Investigating the impact of climate change on hydro-climatological variability and water resources in the Upper Indus Basin

Nathan Forsythe

A Thesis Submitted for the Degree of

Doctor of Philosophy

Newcastle University

Faculty of Science, Agriculture and Engineering

School of Civil Engineering and Geosciences

January 2013

Abstract

The Indus is crucial for Pakistan; economically and for water and food security. This thesis makes substantial contributions to fundamental understanding of local hydro-climatological processes in the Upper Indus Basin (UIB), essential as changes to water resources potentially affect millions of people.

Drawing on a range of available data sources, complex vertical gradients are identified in several climate variables including cloud cover. The study confirms previously identified seasonally and diurnally asymmetrical temperature trends, which result in year round increasing diurnal temperature range, continue to the recent record, and describes some of the underlying causal mechanisms.

Furthermore, for the first time, a stochastic weather generator is used to provide downscaled time series for 2071-2100 for two contrasting "climate scenarios" for the UIB: (i) using change factors from a Regional Climate Model (RCM) under the SRES A2 emissions scenario, (ii) extrapolating from recent observed climatic trends.

A new semi-distributed basin-scale hydrological model is assembled using existing and adapted model algorithms to simulate cryosphere-hydrology interactions, including snowmelt and basic glacial mechanics. Calibrated catchment models – one glacial (Hunza) and one snowmelt-dominated (Astore) regime – are run to provide probabilistic estimates of potential hydrological changes. The RCM-derived scenario – featuring strong summer warming (> 5°C) – projects large decreases in glacial volumes (>90% and >80% mass loss in Astore and Hunza respectively) and one month earlier peak flows. The historical trends-based scenario – featuring net annual warming (0.7°C) but moderate summer cooling (~1.5°C) – also projects earlier peak flows but stable glacial areas and suppression of summer runoff from energy input constraints on melting.

Acknowledgements

I would like to thank my advisors Hayley Fowler, Chris Kilsby and David Archer for their patience, guidance, clear thinking and encouragement. Additional vital input to this thesis has been provided by Stephen Blenkinsop, Aidan Burton and Greg O'Donnell without whom the present work would have achieved far less.

I am grateful to United States National Science Foundation who awarded me the Graduate Research Fellowship which allowed me to undertake my postgraduate studies. Additional financial support has been provided by the British Council, the Philip Leverhulme Prize, the School of Civil Engineering and Geosciences and Newcastle University.

Further thanks are due to David Archer (again), Prof M. Saeed Shah (formerly of CEWRE, UET-Lahore) and Mr Abdul Majeed (retired Chief Forecaster, PMD) for the help in acquiring additional data to extend the local observational records available to the present work. Thanks are also due to the Global Change Impact Studies Centre for generous access to the output of their PRECIS RCM simulations. Special thanks go out to Tomas Holderness without whose PyRaster toolkit this thesis would have been far less spatial affair. Andrew Hardy also deserves thanks for his work on development of spatial climate data products derived from AVHRR imagery.

Immeasurable thanks are owed to my family, especially my mother Katy, for their support throughout the PhD process. Lastly, a special note of gratitude for Peg who has miraculously been here to help me across the finish line.

Glossary of acronyms and specialist terminology

AET: actual evapotranspiration

albedo: a fractional number (0 to 1) quantifying the amount of solar radiation reflected (not absorbed) by a given surface; may be made specific to a certain wavelength or spectral band, e.g. near infrared albedo as opposed to visible wavelength albedo.

APHRODITE: a gridded dataset of estimated historical precipitation over much of Asia and the Oceania; produced from ground-based observations and geostatistical interpolation techniques

AR4: Fourth Assessment Report by the IPCC

ASTER: Advanced Spaceborne Thermal Emission and Reflection instrument for producing satellite imagery, flown aboard the NASA Terra spacecraft

AVHRR: Advanced Very High Resolution Radiometer, an early multi-spectral satellite imagery instrument flown on successive generations of NOAA satellites since the late 1970s

AWS: automatic weather station

c10: shorthand for the first decile limit (10^{th} percentile) of a statistical distribution

c25: shorthand for the lower quartile limit (25^{th} percentile) of a statistical distribution

c75: shorthand for the upper quartile limit (75^{th} percentile) of a statistical distribution

c90: shorthand for the last decile limit (90^{th} percentile) of a statistical distribution

CCF: cloud cover fraction, the percentage of a given unit surface area covered by cloud

CER: cloud effective radius, an estimate of the mean or effective radius of the water droplets or ice crystals composing the cloud

cloud macrophysical properties: large-scale properties of cloud cover, including areal extent, thickness/height and mean/representative altitudes of cloud top and cloud base.

cloud microphysical properties: "structural" properties at the "unit volume" or near molecular level including the amount of water in a unit area, the "effective radius" of droplets (liquid water) or crystals (ice particles) as well as the relative "opacity" (cloud optical thickness).

CMA: continuous melt area, fraction of unit area or a geographic unit (e.g. catchment) where Tmin remains above freezing, i.e. Tmin > 0°C

COT: cloud optical thickness, a measure of the cloud's opacity to visible spectrum light

CRE: cloud radiative effect, the net effect – through reflective and/or insulative properties – of clouds on the radiative energy balance either for the (ground) surface or the atmospheric column.

CRU: Climate Research Unit of the University of East Anglia

CRU-WG: Weather Generator software package by CRU (often used in conjunction with RainSim) for generation of coherent synthetic (stochastic) time-series of key climate variables

CTP: cloud top pressure, the estimated atmospheric pressure of the representative/mean cloud top height in a give target area

CV: coefficient of variation, statistical ratio of the standard deviation divided by the mean

CWP: cloud water path, is a measure (in mass per unit area) of the amount of water contained in the cloud within the (surface area of) the target pixel

ddf: "degree-day factor", an empirical coefficient, with units depth of melt per (positive) temperature increment and time-step (i.e. mm * °C-1 * day-1), relating the available energy to drive melt processes to near-surface air temperature

DEM: digital elevation model

DTR: diurnal temperature range (Tmax minus Tmin)

ECMWF: European Centre for Medium-Range Weather Forecasting

ELA: equilibrium line altitude, the elevation on a given glacier at which ablation is balanced by accumulation (through direct precipitation); i.e. where spot mass balance is neutral (zero)

ENSO: El Niño Southern Oscillation, the primary mode of climatic variability in the Tropical Pacific, usually quantified via differentials in sea surface temperatures (SSTs) between the western and eastern tropical Pacific Ocean

EOS: Earth Observation System, the NASA initiative under which the Terra and Aqua spacecraft (carrying instruments including MODIS and ASTER) were launched

ERA-40: meteorological reanalysis project by ECMWF covering Sep. 1957 to Aug. 2002.

ERA-Interim: meteorological reanalysis project by ECMWF covering Jan. 1979 to present day.

ETM: Enhanced Thematic Mapper, a specific instrument flown on some Landsat spacecraft

GCM: general circulation model, also referred to as global climate model

GDEM: a global coverage high-resolution digital elevation model (DEM) produced from stereo pair imagery captured by the ASTER instrumental

GHG: green-house gas, an umbrella term for gases which contribute to radiative forcing (green-house effect) of the Earth's atmosphere

GPCP: GlobalPrecipitation Climatology Project

GRACE: Gravity Recovery and Climate Experiment, a pair of satellites capable of measuring minute fluctuations in the Earth's gravity field, allowing measurement of large scale (km^3) fluctuations in regional water (groundwater, surface water, or glacial ice)

HadAM3P: a (non-coupled0 GCM by MetOffice Hadley Centre with only an atmospheric component, sea surface temperatures (SSTs) supplied as boundary conditions

HKH: Hindu Kush – Karakoram – Western Himalaya mountain region

HMA: high mountain Asia

hypsometry: the distribution of surface area with respect to elevation

ICIMOD: International Centre for Integrated Mountain Development

insolation: the amount of incoming solar radiation

IOD: Indian Ocean Dipole, a teleconnection index quantifying atmospheric circulation conditions over the Indian Ocean

IPCC: Intergovernmental Panel on Climate Change

IRBM: integrated river basin management

IWE: ice water equivalent, the equivalent mean depth measured in liquid water of ice mass covering a unit area or geographic unit (e.g catchment)

IWRM: integrated water resources management

Landsat: a series of satellites carrying remote sensing instruments for production of multi-spectral satellite imagery; operational since the 1970s

lapse rate: the rate at which temperature decreases with increasing elevation or altitude

LST: land surface temperature

LWin: cumulatively daily incoming long-wave radiation

MEI: Multivariate ENSO Index, a teleconnection index synthesising several individual metrics, one of a number of indices quantifying ENSO conditions

MODIS: Moderate Resolution Imaging Spectrometer, an instrument producing multi-spectral imagery flown aboard the NASA Terra and Aqua spacecraft

MOIG: Mediterranean Oscillation Israel to Gibraltar, a teleconnection index quantifying atmospheric circulation conditions over the Mediterranean Sea

MRI: Mountain Research Initiative

NAO: North Atlantic Oscillation, an index quantifying the atmospheric circulation conditions in the North Atlantic, defined as the difference in sea level atmospheric pressure between the Azores and Iceland

NASA: U.S. National Air and Space Administration, a primary supplier of remotely sensed (satellite imagery-derived) spatial data products for climatological applications

NOAA: U.S. National Oceanic and Atmospheric Administration

NWP: numerical weather prediction

NW UIB: a geographic unit comprising the tributary catchments of Gilgit, Hunza, Shigar, Astore as well as the Indus main channel from the gauging station at Besham Qila downstream to the upstream stations at Yogo (on the Shyok) and Kharmong (on the Indus); this area supplies the bulk of runoff in the UIB

orographic gradient: vertical profile describing local influence of topography on precipitation

PET: potential evapotranspiration

PMD: Pakistan Meteorological Department

PRECIS: ("Providing Regional Climates for Impacts Studies"), a Regional Climate Model (RCM) from the UK MetOffice Hadley Centre

PyRaster: a software package, written in the Python programming language, facilitating translation of climatological data and the results of hydrological simulations to raster format for display in geographic information systems

RainSim: a software package for generating synthetic (stochastic) time-series of precipitation data

RCM: regional climate model

RH: relative humidity

RMSE: root mean squared error, a metric for the average difference between two data series, often where one series represents observations and the other series simulated or predicted values

RS-EO: remote sensing for earth observation

SCA: snow covered area, expressed as a fraction or percentage of a unit area or geographic unit (e.g. catchment)

SOI: Southern Oscillation Index, a teleconnection index based on difference in atmospheric pressure between Darwin (Australia) and Tahiti, one of a number of indices quantifying ENSO conditions

SPOT: « Système Pour l'Observation de la Terre » (in english: "System for Earth Observation") a high resolution satellite imagery instrument operating at visible wavelengths

SRES: Special Report on Emissions Scenarios, a document by the IPCC establishing a set of reference scenarios (e.g. A1B, A2, B1) for projected greenhouse gas emissions in the 21st century

SRM: Snowmelt Runoff Model, a hydrological model incorporating meltwater generation based on predefined (usually observed) time-series of SCA

SRTM: Shuttle Radar Topography Mission, a data source developed by NASA to generate digital elevation models (DEMs)

SST: sea surface temperature

sublimation: transformation of solid water (snow or ice) into water vapour

SVP: saturation vapour pressure, partial pressure at which air becomes saturated (RH=100%); SVP is a function of atmospheric pressure and temperature

SWE: snow water equivalent, the equivalent mean depth measured in liquid water of snowpack covering a unit area or geographic unit (e.g catchment)

SWin: cumulatively daily incoming shortwave radiation

Tavg: Daily mean near-surface air temperature, usually calculated as the mean of Tmin and Tmax.

Tday: day-time LST (from local solar noon satellite overpass) analogous to Tmax

Tmax: daily maximum near-surface air temperature

Tmin: daily minimum near-surface air temperature

Tn: alternate shorthand for Tmin

Tnight: night-time LST (from local solar midnight satellite overpass) analogous to Tmin

Tx: alternate shorthand for Tmax

TRMM: Tropical Rainfall Monitoring Mission

UIB: the Upper Indus Basin, catchment area upstream of Tarbela reservoir on the Indus main channel

vpd: vapour pressure deficit the expression, in units of (partial) atmospheric pressure, of the "shortfall" between the amount of moisture (water vapour) the atmosphere is capable of holding (for a given temperature and absolute pressure) and the water vapour present at that instant.

VIC: Variable Infiltration Capacity hydrological model (developed and maintained by the University of Washington [USA])

VICwCDiP: adapted model, "Variable Infiltration Capacity with Cryosphere Dynamics in Python", i.e. the version of the VIC model adapted/developed for the present study;

VSO: UK Volunteer Service Organisation, a non-governmental organisation providing technical support in developing countries and emerging nations

WAPDA: Pakistan Water and Power Development Authority, government agency responsible for monitoring of river discharge

WG1: Working Group One, the committee within the IPCC tasked with study of physical (scientific) study of the present climate and potential climate change

WH: Western Himalaya region

Table of Contents

Abstract ii
Acknowledgements iii
Glossary iv
Table of Contents ix
List of Figures xvii
List of Tables xxxviii

Chapter One Introduction 1
1.1 Background to the project 1
1.1.1 Socio-economic importance of UIB water resources and hydrological knowledge 1
1.1.2 Research gaps in present understanding of UIB hydro-climatology for current and future conditions 3
1.2 Principal research aims 4
1.3 Structure of thesis 6

Chapter Two Literature Review 7
2.1 Introduction 7
2.2 Priority themes for investigation 7
2.2.1 Key elements for climate change studies supporting natural resources management in a development context 8
2.2.2 Mountain specific issues for hydroclimate and water resources research 9
2.2.3 Contrast and comparison in evolving water resources management challenges in a different developing mountainous context 11
2.3 Previous studies of the hydro-climatology of the Upper Indus 12
2.3.1 Foundational research by Archer and Fowler 12
2.3.2 Understanding the hydro-climatology of the UIB and potential teleconnections 17
2.3.3 Analysis of recent climate trends and potential causal mechanisms in the UIB and other mountain regions 19
2.3.4 Projections of future climate change in IPCC AR4 23
2.4 Glaciology of the Upper Indus 26
2.4.1 Landmark glaciological studies by K. Hewitt 26
2.4.2 Glaciological studies of the Upper Indus Basin by other authors 29

2.4.3 Regional glacial mass balance assessments for the UIB and larger Himalayan region 32
2.5 Modelling of water resources in the UIB 36
2.5.1 General guidelines for hydrological modelling of mountainous catchments 36
2.5.2 Hydrological modelling techniques applied to the specific simulation challenges of the UIB 38
2.5.3 Melt-runoff modelling by snow cover as a proxy for mass balance 40
2.5.4 Surface energy balance and glacial mass balance modelling 43
2.5.5 Context of previous studies of potential climate change impacts on UIB hydrology 46
2.6 Summary 47

Chapter Three Present Hydro-climatology of the Upper Indus Basin 48
3.1 Abstract 48
3.2 Introduction 49
3.3 Relevant data sources for characterisation of UIB hydro-climatology 53
3.3.1 River discharge gauging by WAPDA 54
3.3.2 PMD long-record meteorological observing stations 57
3.3.3 AWS stations operated by WAPDA 58
3.3.4 Numerical meteorological simulation generalities 60
3.3.5 ERA-40 Meteorological Reanalysis Data 61
3.3.6 ERA-Interim Meteorological Reanalysis Data 62
3.3.7 PRECIS RCM 64
3.3.8 Remote sensing earth observation (RS-EO) from satellite imagery generalities 66
3.3.9 RS-EO from the Tropical Rainfall Monitoring Mission (TRMM) 67
3.3.10 RS-EO from Moderate Resolution Imaging Spectrometer (MODIS) data products generalities 68
3.3.11 MODIS spatial data proxies for meltwater-generation inputs 69
3.3.12 Cloud properties by MODIS atmospheric data products 70
3.3.13 MODIS albedo estimates 71
3.4 Locally observed hydrology 71
3.4.1 UIB hydrological regimes 71
3.4.2 Interannual variability in of UIB hydrology 74
3.4.3 Incremental contributions to large-scale UIB discharge 75
3.4.4 Climate drivers of UIB hydrology 77
3.5 Quantitative indices of mass inputs to UIB hydrological system 77

3.5.1 Precipitation generalities 77
3.5.2 Precipitation climatology from PMD and AWS data 78
3.5.3 Estimated precipitation from ECMWF reanalysis data 82
3.5.4 Precipitation estimates from the Tropical Rainfall Monitoring Mission (TRMM) 89
3.5.5 Precipitation estimates from RCM to downscale reanalysis: PRECIS driven by ERA-40 95
3.5.6 Summary discussion of precipitation data sources and issues 99
3.5.7 Snow Covered Area 100
3.6 Quantitative indices of energy inputs to UIB hydrological system 105
3.6.1 Temperature (air and surface) generalities 105
3.6.2 Diurnal extremes of 2m air temperature and LST 106
3.6.3 Diurnal Temperature Range (DTR) 112
3.6.4 Continuous Melt Area 120
3.7 Secondary climate-drivers of UIB hydrology 122
3.7.1 Relative Humidity (RH) 122
3.7.2 Cloud Cover: generalities and local observations 128
3.7.3 Reanalysis estimates of cloud-cover 129
3.7.4 Cloud cover estimates from MODIS (mod06L2) 136
3.7.5 Albedo 144
3.8 (Reanalysis) estimates of surface energy balance in the UIB 146
3.8.1 ERA-40 estimated UIB surface energy balance 146
3.8.2 ERA-Interim estimated UIB surface energy balance 149
3.9 A Vertical hydro-climatology of the UIB 151
3.9.1 Orographic precipitation gradients 151
3.9.2 Vertical snow covered area (SCA) profiles 154
3.9.3 Lapse rates and isotherms for air and surface temperature 156
3.9.4 Profiles of surface-cloud parameter relationships 160
3.9.5 Vertical profiles of ground surface albedo 166
3.10 Hydroclimate relationships in the UIB 167
3.11 Summary & Discussion 176
3.11.1 Summary of key data sources and relevant characteristics 176
3.11.2 Discussion of key topographically-driven climate sensitivities 179
3.11.3 Discussion of critical limitations of present sources of spatial data 180
3.11.4 Concluding remarks 181

Chapter Four Assessment of climate trends and their drivers in the UIB from the available observational record 183
4.1 Introduction 183
4.2 Assessment of trends in local observations and meteorological reanalysis 185
4.2.1 Contextual remarks on trend analysis in the UIB 185
4.2.2 Timeframe (analysis window) sensitivity 185
4.2.3 Examination of evidence for seasonally and diurnally asymmetrical temperature change 189
4.2.4 Assessment of the spatial coherence of estimated trends 194
4.2.5 Statistical significance of spatial trends 200
4.2.6 Summary of trend rate analysis findings 200
4.3 Pre-requisite analyses for investigation of air temperature change causal mechanisms 201
4.3.1 Impetus and conceptual framework for investigation of causal mechanisms 201
4.3.2 Inter-variable correlations in diurnal air temperature components 203
4.3.3 Testing of relationships between air temperature variables from local observations and reanalysis 205
4.4 Assessment of potential causal mechanisms of change 208
4.4.1 Conceptual presentation of potential forcings 208
4.4.2 Coherence of energy balance air-temperature relationships in ERA-Interim 212
4.4.3 Energy balance residual correlations to air temperature 215
4.4.4 Sensible heat flux correlations to energy balance residual and air temperature 218
4.4.5 Detailed point-based (grid cell & station) examination of potential causal mechanisms 223
4.4.6 Initial summary of investigation of causal mechanisms 229
4.5 Inter-variable relationships for precipitation (point-based analysis) 229
4.5.1 Correlations between precipitation variables from gridded numerical data sources and local observations 230
4.5.2 Inter-variable correlations between precipitation and relative humidity 233
4.6 Investigation of relationships between large-scale circulation and UIB climate variability 234
4.6.1 Characterisation of circulation patterns with relationship to the UIB 234
4.6.2 Background of circulation teleconnections and context with regards to the UIB 240

4.6.3 Correlation testing between teleconnections and UIB climate variables 242
4.7 Summary and discussion 246
4.7.1 Summary 246
4.7.2 Discussion 248

Chapter Five Plausible scenarios of future climate in the Upper Indus Basin 250
5.1 Introduction 250
5.2 Presentation and background of available RCM simulation PRECIS forced by HadAM3P 252
5.3 Bias assessment of available RCM outputs for the UIB 254
5.3.1 Methodological approach to RCM bias assessment for the UIB 254
5.3.2 Precipitation climatology comparison between PRECIS_AM3Pcntrl and PRECIS_ERA40 255
5.3.3 Near-surface air temperature climatology comparison between PRECIS_AM3P and PRECIS_ERA40 257
5.3.4 Implications of climatology comparison between PRECIS_AM3Pcntrl and PRECIS_ERA40 for interpretation of climate change projections 262
5.3.5 Bias assessment of PRECIS_ERA40 and PRECIS_AM3Pcntrl versus local observations (PMD) 263
5.4 Calibration and validation of a weather generator approach for observed UIB climate 269
5.4.1 Background on RainSim and the CRU Weather Generator 269
5.4.2 Results for calibration of present climate time-series 271
5.5 Construction of future climate scenarios for the UIB 277
5.5.1 Spatial assessment of change factors from PRECIS_AM3P (2080s vs control) 277
5.5.2 Selected scenarios of plausible future climate conditions for assessment of potential changes to UIB water resource availability 283
5.5.3 Implementation of selected scenarios in synthetic time-series 288
5.6 Discussion and conclusions 298

Chapter Six Construction and validation of a hydrological model adapted for the UIB 301
6.1 Abstract 301
6.2 Introduction 302
6.3 Approach adopted for hydrological modelling including meltwater generation 304

6.4 VIC with Cryosphere Dynamics in Python (VICwCDiP) model capabilities 305
6.5 Meteorological input data (climate forcings) 307
6.6 VICwCDiP model construction and pre-initialisation 310
6.7 Model simulation , generalities and initialisation 315
6.8 Simulation Phase I: Distribution of meteorological inputs 316
6.8.1 Precipitation distribution 316
6.8.2 Temperature distribution 319
6.8.3 Examples of orographic precipitation factors and Tair offsets 319
6.8.4 Extrapolation of additional variables 320
6.9 Simulation Phase II: Land surface processes and crysophere dynamics 320
6.9.1 Calculation of fractional snow covered area (SCA) 320
6.9.2 Approximation of mean surface albedo and net (absorbed) shortwave solar radiation 321
6.9.3 Approximation of surface temperature (Tsurf) 322
6.9.4 Simulation of snowpack density evolution 323
6.9.5 Calculation of meltwater generation 325
6.9.6 Post-melt updating of SCA and remaining land surface processes 329
6.9.7 Glacial vertical mass redistribution and volume and aeral change calculations 329
6.9.8 Aggregation of band specific quantities to grid cell means 332
6.10 Simulation Phase III: Soil moisture accounting module 332
6.11 Model Calibration and validation 333
6.11.1 Assessment of calibration and validation using standard performance metrics 333
6.11.2 Graphical presentation of calibration and validation 336
6.11.3 Assessment of simulated mass fluxes and land surface states 344
6.12 Raster/GIS visualisation of model outputs 349
6.13 Grid-cell level simulation of glacial dynamics 350
6.14 Discussion 358

Chapter Seven Contrasting scenarios of future UIB hydrology 361
7.1 Introduction 361
7.2 Context of previous studies of potential climate change impacts on UIB hydrology 362
7.3 Simulation procedure for synthetic time series 364
7.4 Control climate (1961-1990) 364

7.4.1 Performance of VICwCDiP model 364
7.4.2 Flux trajectories over 300-year control simulations 367
7.5 Future Climate Scenarios 371
7.5.1 RCM-driven Scenario 371
7.5.2 Observation-led scenario 375
7.5.3 Flux trajectories over 300-year simulations of future scenarios 379
7.5.4 Comparison of results from the two scenarios 384
7.6. Uncertainty from model stochastic “natural” variability 390
7.7 Grid cell level consideration of glacial trajectories 396
7.8 Discussion 398

Chapter Eight Conclusions 402
8.1 Summary 403
8.2 Conclusions regarding principal research aims 407
8.2.1 Improving the spatial and temporal characterisation of present hydro-climatology of the UIB 407
8.2.2 Assessing climate trends and their drivers in the UIB from the available observational record 410
8.2.3 Developing plausible scenarios of future climate for the Upper Indus Basin 415
8.2.4 Constructing and validating a hydrological model for the UIB 418
8.2.5 Examining the implications of contrasting future scenarios on UIB hydrology and cryosphere 418
8.3 Key findings 420
8.4 Recommendations for future research 421

Appendix A Supplemental material to Chapter 3 423
A.1 Temperature climatologies from diverse data sources 423
A.2 Sample preliminary period monthly means from AVHRR-derived spatial data products 428

Appendix B Supplemental material to Chapter 4 430
B.1 Time-series of normalised, standardised anomalies of climate observations aggregated for key seasons. 430
B.2 Statistical significance of linear trends in ERA-Interim 450
B.3 Teleconnections 452

Appendix C Supplemental material to Chapter 5 468
C.1 Results of calibration and validation of synthetic time-series for Gilgit and Skardu 468
C.2 Results of perturbation of synthetic time-series for Gilgit and Skardu 473

Appendix D Supplemental material Chapter 6 478
D.1 Glossary 478
D.2 Reasoning for development of VICwCDiP 488
D.3 Additional detail on equations used in VICwCDiP 489
D.3.1 Catchment model construction: Elevation parameters 489
D.3.2 Catchment model construction: soil parameters 492
D.3.3 Extrapolation of additional atmospheric variables 494
D.3.4 Simulation of snowpack density evolution 496
D.3.5 Glacial vertical mass redistribution and volume and areal change calculations 498
D.3.6 Determination of mass fluxes at the soil surface 501
D.3.7 Calculation of soil water storage and gravity drainage between soil layers 505
D.3.8 Calculation of baseflow 506
D.4 Comparison of simulated hydrological results from 5km and 10km versions of Astore and Hunza catchments in VICwCDiP 508
D.5 Comparison of simulated results to MODIS climatologies for secondary calibration variables (SCA, LST) from land surface process approximations 514
D.6 Raster/GIS visualisation of model VICwCDiP outputs for Astore and Hunza 5km calibration runs 518

Appendix E Supplemental material Chapter 7 524
E.1 Projected values for key hydrological fluxes and mean cryosphere states 524
E.2 Grid cell level consideration of glacial trajectories 528

Bibliography 532

List of Figures

Figure 1.1 Map of the core Upper Indus contributing area and key infrastructure.. 1

Figure 2.1 Figure 3 of Archer (2004) showing the estimated annual cycles of freezing isotherms in the UIB. 13

Figure 2.2 Figure 2 of Young & Hewitt (1993) showing the spatial configuration, including vertical profile of a typical Karakoram glacier. 27

Figure 2.3 APHRODITE period mean “pixel station density ratio” from 1961 to 1989. 42

Figure 3.001 Basic conceptualisation of surface energy balance fluxes, simplified from Figure 7 in Kiehl and Trenberth (2007). 49

Figure 3.002 Conceptual illustration of annual cycle of key seasonally-varying vertically-driven atmospheric and land surface processes in the UIB portrayed in terms of vertical profiles along mountain slopes. 51

Figure 3.003 Map of the core Upper Indus contributing area and key infrastructure. 52

Figure 3.004 Hypsometry of the Upper Indus to Besham showing percentage of area in each elevation band (Pct Area) and cumulative percentage (Cumul Pct) below or level with the given elevation. 53

Figure 3.005 Location of primary UIB discharge gauging stations operated by WAPDA shown against a background of surface elevation (m asl) from the NASA SRTM90 DEM. 55

Figure 3.006 Incremental contributing area to primary WAPDA discharge gauges. 56

Figure 3.007 PMD primary long-record meteorological stations located in permanent settlements (towns) in valley bottoms. 58

Figure 3.008 Automatic Weather Stations (AWS) in the UIB operated by WAPDA. Boundaries shown are for primary WAPDA gauged tributaries. 59

Figure 3.009 Composite of three types of local (point) hydroclimate observation locations. 60

Figure 3.010 Position and relative orography of ERA40 reanalysis grid cells used for analysis. 62

Figure 3.011 Position and relative orography of ERA-Interim reanalysis grid cells used for analysis. 63

Figure 3.012 Overlay of locations/spatial domains of hydroclimate data analysed. 64

Figure 3.013 Selected (named) analysed PRECIS grid cells. Grid cells are coloured according to orographic height (m asl). 65

Figure 3.014 Selected analysed PRECIS grid cells with local (point) observation locations. 66
Figure 3.015 Mean annual total precipitation estimates (mm) from TRMM, global coverage (E-W between 50N & 50S)..... 68
Figure 3.016 Discharge in mixed and nival regime tributaries. 73
Figure 3.017 Discharge at glacial regime tributaries. 73
Figure 3.018 Discharge at Indus main channel gauging points. 73
Figure 3.019 Incremental relative contributions to total flow in the Indus at Besham, by month, ... 76
Figure 3.020 Incremental absolute contributions to total flow in the Indus at Besham, by month. 76
Figure 3.021 Historical observations (1961 to 1990) of mean monthly precipitation (pp) at Gilgit (G), Skardu (S) and Astore (A). 80
Figure 3.022 Available (sample) observations of precipitation from AWS in Gilgit & Hunza catchments. 80
Figure 3.023 Available (sample) observations of precipitation from AWS in the Astore catchment..... 81
Figure 3.024 Precipitation records (1979 to 2001) from selected cells in the ERA-40 reanalysis: UIB West (UIBW), UIB Central (UIBC) and UIB East (UIBE)..... 82
Figure 3.025 Precipitation records (1979 to 2001) from selected cells in the ERA-Interim reanalysis: Hunza.Skardu (HnSk), Khunjerab.KunlunShan (KhTs) and Hushe.K2 (HsK2)..... 83
Figure 3.026 Precipitation records (1979 to 2001) from selected cells in the ERA-Interim reanalysis: Gilgit.Chilas (GgCh), Besham.Naran (BeNr) and Vale-of-Srinigar (VaSr)..... 83
Figure 3.027 A comparison for precipitation records from 4 independent data sources..... 85
Figure 3.028 Mean annual total precipitation (mm) from ERA-Interim (1979 to 2007). 86
Figure 3.029 Mean annual total wet days (precipitation > 0.1 mm) from the ERA-Interim reanalysis (1979 to 2007). 87
Figure 3.030 Mean monthly contributions to annual total precipitation from the ERA-Interim reanalysis (1979 to 2007). 88
Figure 3.031 Mean monthly contributions to annual total wet days from the ERA-Interim reanalysis (1979 to 2007). 88
Figure 3.032 Mean annual total precipitation estimates from TRMM (1998 to 2010). 90
Figure 3.033 Mean monthly contributions to annual total precipitation, TRMM spatial aggregates vs point observations, TRMM and PMD records from 1998 to 2010; AWS records (as available) from 1994 to 1998..... 92

Figure 3.034 Seasonal scatter plots of local (PMD) precipitation observations to TRMM estimates for 1998 to 2010 for Astore (top row) and Gilgit (bottom row). 94

Figure 3.035 Mean monthly contributions to annual total precipitation estimates by TRMM (1998 to 2010). 95

Figure 3.036 Mean annual total simulated precipitation from PRECIS downscaling of ERA40 (1961 to 1989) to 50km resolution. 96

Figure 3.037 Mean annual total wet days from PRECIS downscaling of ERA40 (1961 to 1989) to 50km resolution. 96

Figure 3.038 Mean monthly contributions to annual total precipitation from PRECIS downscaling of ERA40 (1961 to 1989) to 50km resolution. 98

Figure 3.039 Mean monthly contributions to annual total wetdays from PRECIS downscaling of ERA40 (1961 to 1989) to 50km resolution. 98

Figure 3.040 Annual cycle of Snow Covered Area (SCA) for the period 2000 to 2010 monthly means and first and last deciles (c10 & c90) from MODIS for primary tributary catchments. 101

Figure 3.041 Boundaries of primary tributary catchments as used in analysis of MODIS data products 101

Figure 3.042 MODIS SCA “surface state” by month for NW UIB. 103

Figure 3.043 Historical observations of 2m mean daily maximum (Tx) and minimum (Tn) air temperature at Gilgit (G), Skardu (S) and Astore (A) from 1961 to 1990. 106

Figure 3.044 Mean daily 2m air temperature from ERA-40 for eight analysed grid cells (1962 to 2001). 107

Figure 3.045 Mean daily 2m air temperature from ERA-Interim (1979 to 2007) for twelve analysed grid cells. 108

Figure 3.046 Monthly means of daily maximum 2m air temperature, 1995 to 1998, from four available data sources: PMD, AWS, ERA-40 and ERA-Interim. 109

Figure 3.047 Monthly means of daily minimum 2m air temperature, 1995 to 1998, from four available data sources: PMD, AWS, ERA-40 and ERA-Interim. 109

Figure 3.048 Comparison of MODIS LST to air temperature at Astore PMD for the MODIS (Terra) observational record, 2000 to 2010. 112

Figure 3.049 Annual cycle of mean diurnal temperature range (DTR) from PMD stations, 1961 to 2001. 113

Figure 3.050 Annual cycle of mean diurnal temperature range (DTR) from AWS stations from 1995 to 1998. 113

Figure 3.051 Annual cycle of mean diurnal temperature range (DTR) from ERA-40 for eight analysed grid cells, 1962 to 2001. 114

Figure 3.052 Annual cycle of mean diurnal temperature range (DTR) from ERA-Interim for eight analysed grid cells, 1979 to 2007. 114

Figure 3.053 Annual cycle of diurnal range in land surface temperature for period (2000 to 2010) monthly means and first and last deciles (c10 & c90) from MODIS for primary tributary catchments. 115

Figure 3.054 Monthly means of daily (diurnal) 2m air temperature range (DTR), 1995 to 1998, from four available data sources: PMD, AWS, ERA-40 and ERA-Interim. 117

Figure 3.055 Mean monthly DTR (°C) from the ERA-Interim reanalysis, 1979 to 2007. 119

Figure 3.056 Mean monthly DTR (°C) from MODIS, 2000 to 2010. 119

Figure 3.057 Mean monthly DTR (°C) from ERA40-driven PRECIS, 1961 to 1989. 120

Figure 3.058 Continuous Melt Area CMA) for period (2000 to 2010) monthly means and first and last deciles (c10 & c90) from MODIS for primary tributary catchments. 121

Figure 3.059 Historical (local) observations of relative humidity at Astore, 1981 to 1999. 123

Figure 3.060 Available (sample) observations of relative humidity from two AWS units, Shandur (3719 m asl) and Khunjerab (4733 m asl), 1994 to 1999. 124

Figure 3.061 Estimate of annual cycle of near surface relative humidity from ERA-40, single grid cell example. 125

Figure 3.062 Estimate of annual cycle of near surface relative humidity from ERA-Interim, single grid cell example. 125

Figure 3.063 Estimate of annual cycle of near-surface morning (00z, 05h local time) relative humidity from ERA-Interim, two sample grid cells, 1979 to 2007. 126

Figure 3.064 Estimate of annual cycle of near surface afternoon (12z, 17h local time) relative humidity from ERA-Interim, two sample grid cells, 1979 to 2007. 127

Figure 3.065 Historical (local) manual observations of low cloud at Astore, 1981 to 1999. 129

Figure 3.066 Mean daily low cloud fraction from ERA-40 for eight analysed grid cells (1962 to 2001). 130

Figure 3.067 Mean daily low cloud cover from ERA-Interim (1979 to 2007) for twelve analysed grid cells. 131

Figure 3.068 Mean day-time low cloud fraction from ERA-40 for two sample grid cells, 1962 to 2001. 131

Figure 3.069 Mean night-time low cloud fraction from ERA-40 for two sample grid cells, 1962 to 2001. 132

Figure 3.070 Estimate of annual cycle of day-time “low cloud” fraction from ERA-Interim, two sample grid cells, 1979 to 2007. 132

Figure 3.071 Estimate of annual cycle of night-time “low cloud” fraction from ERA-Interim, two sample grid cells, 1979 to 2007. 133

Figure 3.072 ERA-Interim gridded estimates of period mean day-time total cloud cover, 1979 to 2007. 134

Figure 3.073 ERA-Interim gridded estimates of period mean night-time total cloud cover, 1979 to 2007. 135

Figure 3.074 ERA-Interim gridded estimates of period mean cloud cover diurnal range (day minus night), 1979 to 2007. 135

Figure 3.075 MODIS spatially aggregated estimates of total cloud cover, day (left) and night (right), in NW UIB. 137

Figure 3.076 MODIS (mod06L2) estimates of period mean day-time total cloud cover, 2000-2009 138

Figure 3.077 MODIS (mod06L2) estimates of period mean night-time total cloud cover, 2000-2009 139

Figure 3.078 MODIS (mod06L2) range (day minus night) mean night-time total cloud cover, 2000-2009 139

Figure 3.079 Detailed composite view of NW UIB period monthly means of cloud cover fraction (CCF) MODIS cloud cover. 140

Figure 3.080 MODIS spatially aggregated estimates of cloud microphysical properties in NW UIB, 2000 to 2004. 143

Figure 3.081 MODIS spatially aggregated estimates of albedo for three UIB tributary catchments -- NW UIB, Hunza, Astore -- from 2001 to 2010. 145

Figure 3.082 Estimate of annual cycle of surface energy balance components from ERA-40, single grid cell example, mean monthly values of daily accumulated energy fluxes (kWh/day), 1962 to 2001 147

Figure 3.083 Estimate of annual cycle of surface energy balance state from ERA-40, eight analysed grid cells), 1962 to 2001. 149

Figure 3.084 Estimate of annual cycle of surface energy balance components from ERA-Interim, single grid cell example, mean monthly values of daily accumulated energy fluxes (kWh/day), 1979 to 2007 150

Figure 3.085 Estimate of annual cycle of surface energy balance state from ERA-Interim, twelve analysed grid cells, 1979 to 2007. 150

Figure 3.086 Indications of UIB orographic precipitation gradient and variability from local observations (PMD, AWS) from 1995 to 1997. 153

Figure 3.087 Assessment of indications of vertical precipitation gradient from TRMM 3b43, annual total period statistics, 2000 to 2010 154

Figure 3.088 Mean monthly vertical profile of MODIS snow covered area (SCA) for the NW UIB ablation season, 2000 to 2010 155

Figure 3.089 Vertical profile of interannual variability in MODIS snow covered area (SCA) for the Gilgit catchment in months of annual maximum (February) and minimum (August) SCA, 2000 to 2010 156

Figure 3.090 Lapse rates derived using local observations from PMD & the AWS network. 157

Figure 3.091 Mean seasonal vertical profile of MODIS day-time land surface temperature (LST) for the NW UIB, 2000 to 2010 158

Figure 3.092 Mean seasonal vertical profile of MODIS night-time land surface temperature (LST) for the NW UIB, 2000 to 2010 158

Figure 3.093 Mean seasonal vertical profile of MODIS LST DTR for the NW UIB, 2000 to 2010. 159

Figure 3.094 Mean monthly estimations for 0°C isotherm elevations from local observations (PMD, AWS) and MODIS LST (2000 to 2010) for the NW UIB for both day-time/maximum and night-time/minimum temperatures. 160

Figure 3.095 Vertical profiles of cloud-cover fraction (CCFday and CCFnight), MODIS, 2000 to 2009. 162

Figure 3.096 Vertical profiles of cloud top pressure (CTPday and CTPnight), MODIS, 2000 to 2009. 165

Figure 3.097 Mean vertical profiles of MODIS albedo for the NW UIB, 2000 to 2010. 167

Figure 3.098 Example regression relationships between climatic indicators (predictors) of hydrological variability and observation variation in runoff. 168

Figure 3.099 Conceptual diagram of vertical profile of snowpack depth (left); SCA versus elevation in seasonal transition from accumulation to ablation (right). 169

Figure 3.100 Vertical patterns of interannual variability in SCA for Astore and Gilgit in peak snow cover months (February, March). 171

Figure 3.101 Example regression relationships between climatic indicators (predictors) of hydrological variability and observation variation in runoff. 173

Figure 3.102 Example regression relationships between climatic indicators (predictors) of hydrological variability and observation variation in runoff. 175

Figure 3.103 hypsometric concentration of catchment area and resultant sensitivity to fluctuations in 0°C isotherms. 180

Figure 4.01 Timeframe (analysis window) sensitivity for trends in mean temperature (Tavg) from multiple data sources – local observations (PMD), ERA-40, ERA-Interim and PRECIS_ERA40. 187

Figure 4.02 Timeframe (analysis window) sensitivity for trends in total precipitation (Precip) from from multiple data sources – local observations (PMD), ERA-40, ERA-Interim and PRECIS_ERA40. 188

Figure 4.03 Monthly linear trends in near-surface air temperature from local observations (PMD) and ERA-Interim for 1979 to 2007 for UIB: A) maximum (Tmax), B) average (Tavg), and C) minimum (Tmin) temperature. 191

Figure 4.04 Further consideration of the diurnal temperature conundrum including discrepancies between data sources. Diurnal components: Tmax in panels A, B, C; Tmin in panels D, E, F. Time periods: 1961 to 1990 in panels A, D; 1962 to 2001 in panels B, E; 1979 to 2007 in C, F. 192

Figure 4.05 Additional diurnal conundrums and discrepancies as shown in temperature trends from local observations (PMD), ERA-40 and PRECIS_ERA40 (P40) for 1961 to 1990 for diurnal phases: A) Tmax, B) Tavg and C) Tmin. 193

Figure 4.06 Pearson's correlation of precipitation with time using ERA-Interim (1979 to 2007). 195
Figure 4.07 Pearson's correlation of precipitation with time using PRECIS_ERA40 (1979 to 2007). 196
Figure 4.08 Pearson's correlation of Tmax with time using ERA-Interim (1979 to 2007). 197
Figure 4.09 Pearson's correlation of Tmax with time using PRECIS_ERA40 (1979 to 2007). 198
Figure 4.10 Pearson's correlation of Tmin with time using ERA-Interim (1979 to 2007). 198
Figure 4.11 Pearson's correlation of Tmin with time using PRECIS_ERA40 (1979 to 2007). 199
Figure 4.12 ERA-Interim, 1979 to 2007, Pearson's correlation between Tmax & DTR for January, Eurasia sub-domain. 205
Figure 4.13 ERA-Interim, 1979 to 2007, Pearson's correlation between Tmin & DTR for January, Eurasia sub-domain. 205
Figure 4.14 Pearson's correlation, 1979 to 2007, between near-surface air temperature diurnal components provided by ERA-Interim and local observations (PMD). 207
Figure 4.15 Pearson's correlation, 1961 to 1989, between near-surface air temperature diurnal components provided by PRECIS_ERA40 and local observations (PMD). 208
Figure 4.16 Surface energy balance (components and time-step residual) example from ERA-Interim for (a) day-time, (b) net daily and (c) night-time diurnal phases. . 210
Figure 4.17 Simple conceptualisation of near-surface air temperature forcings. 211
Figure 4.18 ERA-Interim, 1979 to 2007, Pearson's correlation between daytime total cloud fraction (TCFday) and daytime energy balance residual (EBRday). 213
Figure 4.19 ERA-Interim, 1979 to 2007, Pearson's correlation between night-time total cloud fraction (TCFnight) and night-time energy balance residual (EBRnight). 213
Figure 4.20 Pearson's correlation between mean total cloud fraction (TCFavg) and total daily energy balance residual (EBRtot) for ERA-Interim (1979 to 2007)..... 214
Figure 4.21 Pearson's correlation between total daily energy balance residual (EBRtot) mean daily 2m air temperature (Tavg) for ERA-Interim (1979 to 2007)..... 216
Figure 4.22 Pearson's correlation between day-time energy balance residual (EBRday) and daily 2m maximum air temperature (Tmax) for ERA-Interim (1979 to 2007). 216
Figure 4.23 Pearson's correlation between night-time energy balance residual (EBRnight) and daily 2m minimum air temperature (Tmin) for ERA-Interim (1979 to 2007). 217

Figure 4.24 Pearson's correlation between day-time energy balance residual (EBRday) and daytime sensible heat flux (SHFday) for ERA-Interim (1979 to 2007). 219

Figure 4.25 Pearson's correlation between night-time energy balance residual (EBRnight) and night-time sensible heat flux (SHFnight) for ERA-Interim (1979 to 2007). 219

Figure 4.26 Pearson's correlation between day-time sensible heat flux (SHFday) and Tmax for ERA-Interim (1979 to 2007). 221

Figure 4.27 Pearson's correlation between night-time sensible heat flux (SHFnight) and Tmin for ERA-Interim (1979 to 2007). 221

Figure 4.28 Pearson's correlation between ERA-Interim total cloud fraction (TCFavg) and near-surface air temperature components from local observations (PMD), 1979 to 2007 224

Figure 4.29 Mean annual cycle (1961 to 2001) of diurnal range in near-surface air temperature (DTR) from local observations (PMD). 225

Figure 4.30 Pearson's correlation between PRECIS driven by ERA-40 total cloud fraction (TCFavg) and 2m air temperature (Tair) components from local observations (PMD) for 1961 to 1989. 226

Figure 4.31 Pearson's correlation, between ERA-Interim energy balance components – SWnet and LWnet – and near-surface air temperature components from local observations (PMD), 1979 to 2007. 227

Figure 4.32 Pearson's correlation between ERA-Interim energy balance components – SHFnet and LHFnet – and near-surface air temperature components from local observations (PMD), 1979 to 2007. 228

Figure 4.33 Pearson's correlation, between precipitation variables from ERA-Interim and local observations (PMD), 1979 to 2007 230

Figure 4.34 Pearson's correlation, between precipitation variables from PRECIS_ERA40 and local observations (PMD), 1961 to 1989. 232

Figure 4.35 Pearson's correlation between precipitation variables from local observations (PMD) and relative humidity (relhumid) from ERA-Interim [1979 to 2007] and PRECIS driven by ERA-40 [1961 to 1989]. 233

Figure 4.36 ERA-Interim average mean sea level pressure (MSLP) [millibars] for January, Eurasia sub-domain (1979 to 2007). 235

Figure 4.37 ERA-Interim average mean sea level pressure (MSLP) [millibars] for July, Eurasia sub-domain (1979 to 2007). 235

Figure 4.38 ERA-Interim, period mean 10m wind direction (compass degrees) for January, Eurasia sub-domain, 1979 to 2007. 236

Figure 4.39 ERA-Interim, period mean 10m wind direction (compass degrees) for July, Eurasia sub-domain, 1979 to 2007. 236

Figure 4.40 ERA-Interim period mean 500mb wind direction (compass degrees) for January, Eurasia subdomain, 1979 to 2007 237

Figure 4.41 ERA-Interim period mean 500mb wind direction (compass degrees) for July, Eurasia subdomain, 1979 to 2007. 237

Figure 4.42 ERA-Interim period mean annual cycle for 500mb wind direction (compass degrees), UIB sub-domain, 1979 to 2007. 239

Figure 4.43 ERA-Interim period mean annual cycle for 10m wind direction (compass degrees), UIB sub-domain, 1979 to 2007. 239

Figure 4.44 Invariant orographic height (surface) [m asl] from ERA-Interim. 240

Figure 4.45 Schematic presentation of major candidate teleconnections tested for influence on local climate of the UIB. 241

Figure 4.46 Illustration of “oscillation frequencies” in selected teleconnection indices, 1957 to 2007..... 241

Figure 4.47 ERA-Interim mean 200mb zonal (west to east, westerly positive) wind speed [m/s] for January, Eurasia sub-domain (1979 to 2007). 245

Figure 4.48 ERA-Interim mean 200mb zonal (west to east, westerly positive) wind speed [m/s] for July, Eurasia sub-domain (1979 to 2007). 246

Figure 5.01 Selected analysed PRECIS grid cells with GTOPO30 orography..... 255

Figure 5.02 Ratio of mean monthly precipitation amounts from PRECIS_AM3Pctrl to PRECIS_ERA40. 256

Figure 5.03 Ratio of mean monthly precipitation amounts from PRECIS_AM3Pctrl and PRECIS_ERA40 for twelve selected grid cells. 257

Figure 5.04 Spatial, pixel-wise difference of mean air temperature (Tavg) from the two simulations (PRECIS_AM3Pctrl minus PRECIS_ERA40)..... 258

Figure 5.05 Spatial, pixel-wise difference of diurnal temperature range (DTR) from the two simulations (PRECIS_AM3Pctrl minus PRECIS_ERA40)..... 258

Figure 5.06 Spatial, pixel-wise difference of mean maximum daily air temperature (Tmax) from the two simulations (PRECIS_AM3Pctrl minus PRECIS_ERA40)..... 259

Figure 5.07 Spatial, pixel-wise difference of mean minimum daily air temperature (Tmin) from the two simulations (PRECIS_AM3Pctrl minus PRECIS_ERA40)..... 259

Figure 5.08 Difference (PRECIS_AM3Pctrl minus PRECIS_ERA40) of mean daily maximum air temperature (Tmax) for twelve selected grid cells. 260

Figure 5.09 Difference (PRECIS_AM3Pctrl minus PRECIS_ERA40) of mean daily minimum air temperature (Tmin) for twelve selected grid cells..... 260

Figure 5.10 Difference (PRECIS_AM3Pctrl minus PRECIS_ERA40) of mean diurnal temperature range (DTR) for twelve selected grid cells. 261

Figure 5.11 Ratio of mean monthly contribution to mean annual total precipitation between local observations and PRECIS_ERA40 and PRECIS_AM3Pctrl..... 265

Figure 5.12 Difference in mean monthly DTR between local observations and PRECIS_ERA40 and PRECIS_AM3Pcntrl control (PRECIS minus observations). .. 267

Figure 5.13 Statistics calculated by RainSim for observed, fitted and simulated time-series for rainfall measured at Astore. 272

Figure 5.14 Comparison of statistics between observations (obs) and simulated (RainSim) control-climate time-series for precipitation amounts at Astore. 273

Figure 5.15 Comparison of statistics between observations (obs) and simulated (RainSim) control-climate time-series for “wet day” occurrence at Astore. 275

Figure 5.16 Comparison of statistics between observations (obs) and simulated (WGout) control-climate time-series for near surface air temperature at Astore. 276

Figure 5.17 Spatial, pixel-wise change factors for mean precipitation amounts from PRECIS_AM3P, i.e. ratio of mean monthly precipitation amounts from PRECIS_AM3Pfutr and PRECIS_AM3Pctrl. 279

Figure 5.18 Spatial, pixel-wise change factors for precipitation variance from PRECIS_AM3P, i.e. ratio of monthly precipitation variance from PRECIS_AM3Pfutr and PRECIS_AM3Pctrl. 279

Figure 5.19 Spatial, pixel-wise change factors for wet day occurrence from PRECIS_AM3P, i.e. ratio of monthly wet day occurrence from PRECIS_AM3Pfutr and PRECIS_AM3Pctrl. 280

Figure 5.20 Spatial, pixel-wise change factors for mean daily air temperature (Tavg) from PRECIS_AM3P, i.e. difference in Tavg between PRECIS_AM3Pfutr and PRECIS_AM3Pctrl. 281

Figure 5.21 Spatial, pixel-wise change factors for mean diurnal temperature range (DTR) from PRECIS_AM3P, i.e. difference in DTR between PRECIS_AM3Pfutr and PRECIS_AM3Pctrl. 281

Figure 5.22 Spatial, pixel-wise change factors for variance of daily air temperature (Tavg) from PRECIS_AM3P, i.e. difference in Tavg between PRECIS_AM3Pfutr and PRECIS_AM3Pctrl. 282

Figure 5.23 Spatial, pixel-wise change factors for variance of diurnal temperature range (DTR) from PRECIS_AM3P, i.e. difference in DTR between PRECIS_AM3Pfutr and PRECIS_AM3Pctrl. 282

Figure 5.24 Additional diurnal conundrums and discrepancies as shown in temperature trends from local observations (PMD), ERA-40 and PRECIS_ERA40 (P40) for 1961 to 1990 for diurnal phases: A) Tmax, B) Tavg and C) Tmin. 284

Figure 5.25 Change factors for precipitation descriptor statistics based on scenarios from PRECIS_AM3P and extrapolated from trends in local observations. 286

Figure 5.26 Change factors for air temperature descriptor statistics based on scenarios from PRECIS_AM3P and extrapolated from trends in local observations. 287

Figure 5.27 Comparison of statistics between observations and simulated perturbed-climate time-series from PRECIS_AM3P scenario for precipitation amounts at Astore. 291

Figure 5.28 Comparison of statistics between observations and simulated perturbed-climate time-series from PRECIS_AM3P scenario for near surface air temperature at Astore. 293

Figure 5.29 Comparison of statistics between observations and simulated perturbed-climate time-series from locally-observed trends scenario for precipitation amounts at Astore. 295

Figure 5.30 Comparison of statistics between observations and simulated perturbed-climate time-series from locally-observed trends scenario for near surface air temperature at Astore. 297

Figure 6.01 Overall conceptual schematic of the Variable Infiltration Capacity with Cryosphere Dynamics in Python (VICwCDiP) model developed in this thesis. 303

Figure 6.02 Example of verification of correspondence between observed and modelled input air temperature for the base meteorological station at Astore showing data from 1981 to 1995, daily values re-aggregated to a monthly time-step. 309

Figure 6.03 Spatial discretisation of the Astore (a to c) and Hunza catchments (d to f) for raster degree-day modelling. 311

Figure 6.04 Examples of grid cell internal distribution of area by defined sub-grid elevation bands used in VICwCDiP surface discretisation. 312

Figure 6.05 Conceptual illustration of the relationships in VICwCDiP between glacial driving stress, thickness and bed-slope relationships. 313

Figure 6.06 Conceptual illustration of glacial footprint geometry at the sub-grid level used in VICwCDiP. 315

Figure 6.07 Conceptual illustration of glacial cross section and longitudinal geometry of the glacial mass used in VICwCDiP. 315

Figure 6.08 Calibrated orographic precipitation gradients for Astore and Hunza catchments with comparison to other published studies. 318

Figure 6.09 Derived linear lapse rates for daily mean 2m air temperature (Tavg) used in VICwCDiP as Tair. 319

Figure 6.10 Conceptual illustration of process of snowpack density evolution in VICwCDiP. 323

Figure 6.11 Conceptual schematic of soil moisture accounting module of Variable Infiltration Capacity with Cryosphere Dynamics in Python (VICwCDiP) model. 332

Figure 6.12 Calibration and validation results for the Astore catchment. 337

Figure 6.13 Calibration and validation results for the Hunza catchment. 338

Figure 6.14 Calibration and validation results in reproducing annual hydrological cycle and its variability for the Astore and Hunza catchments. 340

Figure 6.15 Calibration and validation results in glacial mass and areal extent (fraction of catchment) for the Astore and Hunza catchments. 343

Figure 6.16 Calibration and validation results for hydrological mass inputs and outputs for the Astore and Hunza catchments. 346

Figure 6.17 Validation results for simulation of snow covered area (SCA) land surface temperature (LST) for the 10km versions of the Astore and Hunza catchment models. 348

Figure 6.18 Geographic detail for location of example glaciated areas for the Astore catchment. 351

Figure 6.19 Results of simulated glacial mechanics for 10km grid cell 36.15N 74.75E in Hunza. 352

Figure 6.20 Results of simulated glacial mechanics for 5km grid cell 36.125N 74.725E in Hunza. 354

Figure 6.21 Results of simulated glacial mechanics for 5km grid cell 36.175N 74.775E in Hunza. 356

Figure 7.01 Annual cycles of A) hydrological mass input (precipitation) and outputs (evapotranspiration, baseflow and direct overland flow/hortonian runoff), B) total runoff, C) snow covered area (SCA) and D) land surface temperature (LST) for the 3,000 simulated years of control climate. 365

Figure 7.02 As for Figure 7.01 but for the Hunza catchment. 366

Figure 7.03 Trajectory and spread of results hydrological modelling of synthetic control climate for the Astore catchment. 368

Figure 7.04 As for Figure 7.03 but for the Hunza catchment. 369

Figure 7.05 Annual cycles from hydrological modelling of RCM-based (PRECIS_AM3P) climate scenario for the Astore catchment. 373

Figure 7.06 As for Figure 7.05 but for the Hunza catchment. 374

Figure 7.07 Annual cycles from hydrological modelling of climate scenario extrapolated from local trends (PMD) for the Astore catchment. 377

Figure 7.08 As for Figure 7.07 but for the Hunza catchment. 378

Figure 7.09 Trajectory and spread of results hydrological modelling of RCM-based (PRECIS_AM3P) climate scenario for the Astore catchment 380

Figure 7.10 Trajectory and spread of results hydrological modelling of RCM-based (PRECIS_AM3P) climate scenario for the Hunza catchment. 381

Figure 7.11 trajectory and spread of results hydrological modelling of the “observation-led” future climate scenario for the Astore catchment. 382

Figure 7.12 Trajectory and spread of results hydrological modelling of the “observation-led” future climate scenario for the Hunza catchment. 383

Figure 7.13 Relative changes for hydro-climatological variables calculated between the defined future scenarios and the synthetic baseline for the Astore catchment..... 385

Figure 7.14 Relative changes for hydro-climatological variables calculated between the defined future scenarios and the synthetic baseline for the Hunza catchment..... 386

Figure 7.15 Relative changes in annual totals (or means) for hydro-climatological variables calculated between the defined future scenarios and the synthetic baseline for the Astore catchment. 387

Figure 7.16 As for Figure 7.15 but for the Hunza catchment. 388

Figure 7.17 “Box-plot” style presentation of projected annual totals for key hydrological fluxes and mean cryosphere states for the Astore (panels A to C) and Hunza catchments (panels D to F). 392

Figure A.01 Available (sample) observations, 1994 to 1999, of 2m mean daily maximum (Tx) and minimum (Tn) from AWS in Gilgit & Hunza catchments. 423

Figure A.02 Available (sample) observations, 1995 to 1998, of 2m mean daily maximum (Tx) and minimum (Tn) from AWS in the Astore catchment. 424

Figure A.03 Mean daily maximum 2m air temperature from ERA-40 for two sample grid cells, UIB West and UIB East, from 1962 to 2001. 424

Figure A.04 Mean daily minimum 2m air temperature from ERA-40 for two sample grid cells, UIB West and UIB East, from 1962 to 2001. 425

Figure A.05 Mean daily maximum 2m air temperature from ERA-Interim for two sample grid cells, Besham.Naran and Hushe.K2, from 1962 to 2001. 425

Figure A.06 Mean daily minimum 2m air temperature from ERA-Interim for two sample grid cells, Besham.Naran and Hushe.K2, from 1962 to 2001. 426

Figure A.07 Annual cycle of day-time land surface temperature (LST) for period (2000 to 2010) monthly means and first and last deciles (c10 & c90 from MODIS for primary tributary catchments. 426

Figure A.08 Annual cycle of night-time land surface temperature (LST) for period (2000 to 2010) monthly means and first and last deciles (c10 & c90 from MODIS for primary tributary catchments. 427

Figure A.09 example development phase AVHRR-derived spatial data product for SCA. 428

Figure A.10 example development phase AVHRR-derived spatial data product for LSTday. 428

Figure A.11 example development phase AVHRR-derived spatial data product for CCFday. 429

Figure B.01 Time-series of normalised, standardised annual mean Tavg anomalies from local observations (PMD), ERA-40 and PRECIS_ERA40 (P40) for 1961 to 1990..... 430

Figure B.02 Time-series of normalised, standardised annual mean Tavg anomalies from local observations (PMD) and ERA-40 for 1962 to 2001. 430

Figure B.03 Time-series of normalised, standardised annual mean Tavg anomalies from local observations (PMD), ERA-40 and ERA-Interim (ERA-Int) for 1979 to 2001..... 430

Figure B.04 Time-series of normalised, standardised annual mean Tavg anomalies from local observations (PMD) and ERA-Interim (ERA-Int) for 1979 to 2007..... 431

Figure B.05 Time-series of normalised, standardised ONDJFM mean Tavg anomalies from local observations (PMD), ERA-40 and PRECIS_ERA40 (P40) for 1961 to 1990.....431

Figure B.06 Time-series of normalised, standardised ONDJFM mean Tavg anomalies from local observations (PMD) and ERA-40 for 1962 to 2001.....431

Figure B.07 Time-series of normalised, standardised annual mean Tavg anomalies from local observations (PMD), ERA-40 and ERA-Interim (ERA-Int) for 1979 to 2001.....432

Figure B.08 Time-series of normalised, standardised ONDJFM mean Tavg anomalies from local observations (PMD) and ERA-Interim (ERA-Int) for 1979 to 2007.....432

Figure B.09 Time-series of normalised, standardised JJA mean Tavg anomalies from local observations (PMD), ERA-40 and PRECIS_ERA40 (P40) for 1961 to 1990.....432

Figure B.10 Time-series of normalised, standardised JJA mean Tavg anomalies from local observations (PMD) and ERA-40 for 1962 to 2001.....433

Figure B.11 Time-series of normalised, standardised JJA mean Tavg anomalies from local observations (PMD), ERA-40 and ERA-Interim (ERA-Int) for 1979 to 2001.....433

Figure B.12 Time-series of normalised, standardised JJA mean Tavg anomalies from local observations (PMD) and ERA-Interim (ERA-Int) for 1979 to 2007. 433

Figure B.13 Time-series of normalised, standardised annual mean Tmax anomalies from local observations (PMD), ERA-40 and PRECIS_ERA40 (P40) for 1961 to 1990.....434

Figure B.14 Time-series of normalised, standardised annual mean Tmax anomalies from local observations (PMD) and ERA-40 for 1962 to 2001.....434

Figure B.15 Time-series of normalised, standardised annual mean Tmax anomalies from local observations (PMD), ERA-40 and ERA-Interim (ERA-Int) for 1979 to 2001.....434

Figure B.16 Time-series of normalised, standardised annual mean Tmax anomalies from local observations (PMD) and ERA-Interim (ERA-Int) for 1979 to 2007.....435

Figure B.17 Time-series of normalised, standardised ONDJFM mean Tmax anomalies from local observations (PMD), ERA-40 and PRECIS_ERA40 (P40) for 1961 to 1990.....435

Figure B.18 Time-series of normalised, standardised ONDJFM mean Tmax anomalies from local observations (PMD) and ERA-40 for 1962 to 2001.....435

Figure B.19 Time-series of normalised, standardised annual mean Tmax anomalies from local observations (PMD), ERA-40 and ERA-Interim (ERA-Int) for 1979 to 2001.....436

Figure B.20 Time-series of normalised, standardised ONDJFM mean Tmax anomalies from local observations (PMD) and ERA-Interim (ERA-Int) for 1979 to 2007. 436

Figure B.21 Time-series of normalised, standardised JJA mean Tmax anomalies from local observations (PMD), ERA-40 and PRECIS_ERA40 (P40) for 1961 to 1990.....436

Figure B.22 Time-series of normalised, standardised JJA mean Tmax anomalies from local observations (PMD) and ERA-40 for 1962 to 2001..... 437

Figure B.23 Time-series of normalised, standardised JJA mean Tmax anomalies from local observations (PMD), ERA-40 and ERA-Interim (ERA-Int) for 1979 to 2001... 437

Figure B.24 Time-series of normalised, standardised JJA mean Tmax anomalies from local observations (PMD) and ERA-Interim (ERA-Int) for 1979 to 2007. 437

Figure B.25 Time-series of normalised, standardised annual mean Tmin anomalies from local observations (PMD), ERA-40 and PRECIS_ERA40 (P40) for 1961 to 1990..... 438

Figure B.26 Time-series of normalised, standardised annual mean Tmin anomalies from local observations (PMD) and ERA-40 for 1962 to 2001..... 438

Figure B.27 Time-series of normalised, standardised annual mean Tmin anomalies from local observations (PMD), ERA-40 and ERA-Interim (ERA-Int) for 1979 to 2001..... 438

Figure B.28 Time-series of normalised, standardised annual mean Tmin anomalies from local observations (PMD) and ERA-Interim (ERA-Int) for 1979 to 2007..... 439

Figure B.29 Time-series of normalised, standardised ONDJFM mean Tmin anomalies from local observations (PMD), ERA-40 and PRECIS_ERA40 (P40) for 1961 to 1990..... 439

Figure B.30 Time-series of normalised, standardised ONDJFM mean Tmin anomalies from local observations (PMD) and ERA-40 for 1962 to 2001..... 439

Figure B.31 Time-series of normalised, standardised annual mean Tmin anomalies from local observations (PMD), ERA-40 and ERA-Interim (ERA-Int) for 1979 to 2001..... 440

Figure B.32 Time-series of normalised, standardised ONDJFM mean Tmin anomalies from local observations (PMD) and ERA-Interim (ERA-Int) for 1979 to 2007..... 440

Figure B.33 Time-series of normalised, standardised JJA mean Tmin anomalies from local observations (PMD), ERA-40 and PRECIS_ERA40 (P40) for 1961 to 1990.... 440

Figure B.34 Time-series of normalised, standardised JJA mean Tmin anomalies from local observations (PMD) and ERA-40 for 1962 to 2001..... 441

Figure B.35 Time-series of normalised, standardised JJA mean Tmin anomalies from local observations (PMD), ERA-40 and ERA-Interim (ERA-Int) for 1979 to 2001... 441

Figure B.36 Time-series of normalised, standardised JJA mean Tmin anomalies from local observations (PMD) and ERA-Interim (ERA-Int) for 1979 to 2007. 441

Figure B.37 Time-series of normalised, standardised annual mean DTR anomalies from local observations (PMD), ERA-40 and PRECIS_ERA40 (P40) for 1961 to 1990..... 442

Figure B.38 Time-series of normalised, standardised annual mean DTR anomalies from local observations (PMD) and ERA-40 for 1962 to 2001..... 442

Figure B.39 Time-series of normalised, standardised annual mean DTR anomalies from local observations (PMD), ERA-40 and ERA-Interim (ERA-Int) for 1979 to 2001..... 442

Figure B.40 Time-series of normalised, standardised annual mean DTR anomalies from local observations (PMD) and ERA-Interim (ERA-Int) for 1979 to 2007..... 443

Figure B.41 Time-series of normalised, standardised ONDJFM mean DTR anomalies from local observations (PMD), ERA-40 and PRECIS_ERA40 (P40) for 1961 to 1990. 443

Figure B.42 Time-series of normalised, standardised ONDJFM mean DTR anomalies from local observations (PMD) and ERA-40 for 1962 to 2001. 443

Figure B.43 Time-series of normalised, standardised annual mean DTR anomalies from local observations (PMD), ERA-40 and ERA-Interim (ERA-Int) for 1979 to 2001..... 444

Figure B.44 Time-series of normalised, standardised ONDJFM mean DTR anomalies from local observations (PMD) and ERA-Interim (ERA-Int) for 1979 to 2007..... 444

Figure B.45 Time-series of normalised, standardised JJA mean DTR anomalies from local observations (PMD), ERA-40 and PRECIS_ERA40 (P40) for 1961 to 1990. ... 444

Figure B.46 Time-series of normalised, standardised JJA mean DTR anomalies from local observations (PMD) and ERA-40 for 1962 to 2001..... 445

Figure B.47 Time-series of normalised, standardised JJA mean DTR anomalies from local observations (PMD), ERA-40 and ERA-Interim (ERA-Int) for 1979 to 2001... 445

Figure B.48 Time-series of normalised, standardised JJA mean DTR anomalies from local observations (PMD) and ERA-Interim (ERA-Int) for 1979 to 2007. 445

Figure B.49 Time-series of normalised, standardised annual total precipitation anomalies from local observations (PMD), ERA-40 and PRECIS_ERA40 (P40) for 1961 to 1990..... 446

Figure B.50 Time-series of normalised, standardised annual total precipitation anomalies from local observations (PMD) and ERA-40 for 1962 to 2001..... 446

Figure B.51 Time-series of normalised, standardised annual total precipitation anomalies from local observations (PMD), ERA-40 and ERA-Interim (ERA-Int) for 1979 to 2001..... 446

Figure B.52 Time-series of normalised, standardised annual total precipitation anomalies from local observations (PMD) and ERA-Interim (ERA-Int) for 1979 to 2007. 447

Figure B.53 Time-series of normalised, standardised ONDJFM total precipitation anomalies from local observations (PMD), ERA-40 and PRECIS_ERA40 (P40) for 1961 to 1990..... 447

Figure B.54 Time-series of normalised, standardised ONDJFM total precipitation anomalies from local observations (PMD) and ERA-40 for 1962 to 2001..... 447

Figure B.55 Time-series of normalised, standardised ONDJFM total precipitation anomalies from local observations (PMD), ERA-40 and ERA-Interim (ERA-Int) for 1979 to 2001..... 448

Figure B.56 Time-series of normalised, standardised ONDJFM total precipitation anomalies from local observations (PMD) and ERA-Interim (ERA-Int) for 1979 to 2007. 448

Figure B.57 Time-series of normalised, standardised JJA total precipitation anomalies from local observations (PMD), ERA-40 and PRECIS_ERA40 (P40) for 1961 to 1990..... 448

Figure B.58 Time-series of normalised, standardised JJA total precipitation anomalies from local observations (PMD) and ERA-40 for 1962 to 2001..... 449

Figure B.59 Time-series of normalised, standardised JJA total precipitation anomalies from local observations (PMD), ERA-40 and ERA-Interim (ERA-Int) for 1979 to 2001..... 449

Figure B.60 Time-series of normalised, standardised JJA total precipitation anomalies from local observations (PMD) and ERA-Interim (ERA-Int) for 1979 to 2007..... 449

Figure B.61 ERA-Interim, 1979 to 2007, 2-tailed significance of correlation with time (year index), Precipitation..... 450

Figure B.62 ERA-Interim, 1979 to 2007, 2-tailed significance of correlation with time (year index), Tmax..... 450

Figure B.63 ERA-Interim, 1979 to 2007, 2-tailed significance of correlation with time (year index), Tmin..... 451

Figure B.64 Teleconnection testing for relationships between DTR (ERA-Interim, 1979 to 2007) and MEI for concurrent response (L00). 452

Figure B.65 Teleconnection testing for relationships between Tmin (ERA-Interim, 1979 to 2007) and MEI for concurrent response (L00). 452

Figure B.66 Teleconnection testing for relationships between TCFavg (ERA-Interim, 1979 to 2007) and MEI for concurrent response (L00). 453

Figure B.67 Teleconnection testing for relationships between precipitation (ERA-Interim, 1979 to 2007) and MEI for concurrent response (L00)..... 453

Figure B.68 Teleconnection testing for relationships between DTR (PRECIS_ERA40, 1961 to 1989) and MEI for concurrent response (L00). 454

Figure B.69 Teleconnection testing for relationships between Tmin (PRECIS_ERA40, 1961 to 1989) and MEI for concurrent response (L00). 454

Figure B.70 Teleconnection testing for relationships between TCFavg (PRECIS_ERA40, 1961 to 1989) and MEI for concurrent response (L00). 455

Figure B.71 Teleconnection testing for relationships between precipitation (PRECIS_ERA40, 1961 to 1989) and MEI for concurrent response (L00). 455

Figure B.72 Teleconnection testing for relationships between DTR (ERA-Interim, 1979 to 2007) and NAO for concurrent response (L00). 456

Figure B.73 Teleconnection testing for relationships between Tmin (ERA-Interim, 1979 to 2007) and NAO for concurrent response (L00). 456

Figure B.74 Teleconnection testing for relationships between TCFavg (ERA-Interim, 1979 to 2007) and NAO for concurrent response (L00). 457

Figure B.75 Teleconnection testing for relationships between precipitation (ERA-Interim, 1979 to 2007) and NAO for concurrent response (L00). 457

Figure B.76 Teleconnection testing for relationships between DTR (PRECIS_ERA40, 1961 to 1989) and NAO for concurrent response (L00). 458

Figure B.77 Teleconnection testing for relationships between Tmin (PRECIS_ERA40, 1961 to 1989) and NAO for concurrent response (L00). 458

Figure B.78 Teleconnection testing for relationships between TCFavg (PRECIS_ERA40, 1961 to 1989) and NAO for concurrent response (L00). 459

Figure B.79 Teleconnection testing for relationships between precipitation (PRECIS_ERA40, 1961 to 1989) and NAO for concurrent response (L00). 459

Figure B.80 Teleconnection testing for relationships between DTR (ERA-Interim, 1979 to 2007) and MEI for 4-month lag-time (L04)..... 460

Figure B.81 Teleconnection testing for relationships between Tmin (ERA-Interim, 1979 to 2007) and MEI for 4-month lag-time (L04)..... 460

Figure B.82 Teleconnection testing for relationships between TCFavg (ERA-Interim, 1979 to 2007) and MEI for 4-month lag-time (L04)..... 461

Figure B.83 Teleconnection testing for relationships between precipitation (PRECIS_ERA40, 1961 to 1989) and MEI for 4-month lag-time (L04)..... 461

Figure B.84 Teleconnection testing for relationships between DTR (PRECIS_ERA40, 1961 to 1989) and MEI for 4-month lag-time (L04)..... 462

Figure B.85 Teleconnection testing for relationships between Tmin (PRECIS_ERA40, 1961 to 1989) and MEI for 4-month lag-time (L04)..... 462

Figure B.86 Teleconnection testing for relationships between TCFavg (PRECIS_ERA40, 1961 to 1989) and MEI for 4-month lag-time (L04)..... 463

Figure B.87 Teleconnection testing for relationships between precipitation (PRECIS_ERA40, 1961 to 1989) and MEI for 4-month lag-time (L04)..... 463

Figure B.88 Teleconnection testing for relationships between DTR (ERA-Interim, 1979 to 2007) and NAO for 4-month lag-time (L04). 464

Figure B.89 Teleconnection testing for relationships between Tmin (ERA-Interim, 1979 to 2007) and NAO for 4-month lag-time (L04). 464

Figure B.90 Teleconnection testing for relationships between TCFavg (ERA-Interim, 1979 to 2007) and NAO for 4-month lag-time (L04). 465

Figure B.91 Teleconnection testing for relationships between precipitation (ERA-Interim, 1979 to 2007) and NAO for 4-month lag-time (L04). 465

Figure B.92 Teleconnection testing for relationships between DTR (PRECIS_ERA40, 1961 to 1989) and NAO for 4-month lag-time (L04). 466

Figure B.93 Teleconnection testing for relationships between Tmin (PRECIS_ERA40, 1961 to 1989) and NAO for 4-month lag-time (L04). 466

Figure B.94 Teleconnection testing for relationships between TCFavg (PRECIS_ERA40, 1961 to 1989) and NAO for 4-month lag-time (L04). 467

Figure B.95 Teleconnection testing for relationships between precipitation (PRECIS_ERA40, 1961 to 1989) and NAO for 4-month lag-time (L04). 467

Figure C.01 Statistics calculated by RainSim for observed, fitted and simulated time-series for rainfall measured at Gilgit 468

Figure C.02 Comparison of statistics between observations (obs) and simulated (RainSim) control-climate time-series for precipitation amounts at Gilgit 468

Figure C.03 Comparison of statistics between observations (obs) and simulated (RainSim) control-climate time-series for “wet day” occurence at Gilgit 469

Figure C.04 Comparison of statistics between observations (obs) and simulated (RainSim) control-climate time-series for “dry day” occurence at Gilgit 469

Figure C.05 Statistics calculated by RainSim for observed, fitted and simulated time-series for rainfall measured at Skardu 470

Figure C.06 Comparison of statistics between observations (obs) and simulated (RainSim) control-climate time-series for precipitation amounts at Skardu 470

Figure C.07 Comparison of statistics between observations (obs) and simulated (RainSim) control-climate time-series for “wet day” occurrence at Skardu..... 471

Figure C.08 Comparison of statistics between observations (obs) and simulated (RainSim) control-climate time-series for “dry day” occurrence at Skardu 471

Figure C.09 Comparison of statistics between observations (obs) and simulated (WGout) control-climate time-series for near surface air temperature at Gilgit..... 471

Figure C.10 Comparison of statistics between observations (obs) and simulated (WGout) control-climate time-series for near surface air temperature at Skardu 472

Figure C.11 Comparison of statistics between observations and simulated perturbed-climate time-series from PRECIS_AM3P scenario for precipitation amounts at Gilgit 473

Figure C.12 Comparison of statistics between observations and simulated perturbed-climate time-series from PRECIS_AM3P scenario for wetday occurrence at Gilgit .. 473

Figure C.13 Comparison of statistics between observations and simulated perturbed-climate time-series from PRECIS_AM3P scenario for near surface air temperature at Gilgit 473

Figure C.14 Comparison of statistics between observations and simulated perturbed-climate time-series from PRECIS_AM3P scenario for precipitation amounts at Skardu..... 474

Figure C.15 Comparison of statistics between observations and simulated perturbed-climate time-series from PRECIS_AM3P scenario for wetday occurrence at Skardu 474

Figure C.16 Comparison of statistics between observations and simulated perturbed-climate time-series from PRECIS_AM3P scenario for near surface air temperature at Skardu 474

Figure C.17 Comparison of statistics between observations and simulated perturbed-climate time-series from PRECIS_AM3P scenario for precipitation amounts at Astore 475

Figure C.18 Comparison of statistics between observations and simulated perturbed-climate time-series from PRECIS_AM3P scenario for wetday occurrence at Astore. 475

Figure C.19 Comparison of statistics between observations and simulated perturbed-climate time-series from PRECIS_AM3P scenario for near surface air temperature at Astore 475

Figure C.20 Comparison of statistics between observations and simulated perturbed-climate time-series from locally-observed trends scenario for precipitation amounts at Gilgit 476

Figure C.21 Comparison of statistics between observations and simulated perturbed-climate time-series from locally-observed trends scenario for wet day occurrence at Gilgit 476

Figure C.22 Comparison of statistics between observations and simulated perturbed-climate time-series from locally-observed trends scenario for near surface air temperature at Gilgit 476

Figure C.23 Comparison of statistics between observations and simulated perturbed-climate time-series from locally-observed trends scenario for precipitation amounts at Skardu 477

Figure C.24 Comparison of statistics between observations and simulated perturbed-climate time-series from locally-observed trends scenario for wet day occurrence at Skardu 477

Figure C.25 Comparison of statistics between observations and simulated perturbed-climate time-series from locally-observed trends scenario for near surface air temperature at Skardu 477

Figure D.01 Examples of grid cell internal distribution of area by defined sub-grid elevation bands used in VICwCDiP surface discretisation. 490

Figure D.02 Conceptual illustration of the relationships between glacial driving stress, thickness and bed-slope relationships. 491

Figure D.03 Calibrated relationships between lower soil layer depths and mean cell surface elevation as used in the VICwCDiP model. 493

Figure D.04 Conceptual illustration of the soil moisture extraction function as implemented within the VICwCDiP) model. 502

Figure D.05 Conceptual illustration of the relationship between fractional infiltration capacity and fractional saturated area. 504

Figure D.06 Conceptual illustration of the relationship between fractional baseflow and fractional relative soil moisture. 506

Figure D.07 Calibration and validation results in reproducing annual hydrological cycle and its variability for the Astore catchment. 508

Figure D.08 Calibration and validation results in reproducing annual hydrological cycle and its variability for the Hunza catchment. 509

Figure D.09 Calibration and validation results in glacial mass and areal extent (fraction of catchment) for the Astore catchment. 510

Figure D.10 Calibration and validation results in glacial mass and areal extent (fraction of catchment) for the Hunza catchment. 511

Figure D.11 Calibration and validation results in hydrological mass inputs and outputs for the Astore catchment. 512

Figure D.12 Calibration and validation results in hydrological mass inputs and outputs for the Hunza catchment. 513

Figure D.13 Calibration and validation results in simulation of snow covered area (SCA) for the Astore catchment. 514

Figure D.14 Calibration and validation results in simulation of snow covered area (SCA) for the Hunza catchment. 515

Figure D.15 Calibration and validation results in simulation of land surface temperature (LST) for the Astore catchment 516

Figure D.16 Calibration and validation results in simulation of land surface temperature (LST) for the Hunza catchment. 517

Figure D.17 Period mean raster output calibration results of hydrological mass input and output components for the Astore and Hunza catchments. 518

Figure D.18 Period mean raster output calibration results of land surface temperature (LST) for the Astore and Hunza catchments 519

Figure D.19 Period mean raster output calibration results of snow covered area (SCA) for the Astore and Hunza catchments. 520

Figure D.20 Raster output calibration results of glaciated area (fraction) for the Astore and Hunza catchments. 521

Figure D.21 Spatial patterns of period mean annual totals of glacial mass balance components for the calibration simulations in both the Astore and Hunza catchments. 522

Figure D.22 Period mean raster output calibration results of relative contributions of snow and ice to combined meltwater generation for the Astore and Hunza catchments. 523

Figure E.1 example grid cell glacial variable trajectories from synthetic baseline climate for the Hunza catchment 529

Figure E.2 example grid cell glacial variable trajectories from RCM-driven future climate scenario (PRECIS_AM3P A2 2080s) for the Hunza catchment. 530

Figure E.3 example grid cell glacial variable trajectories from “observation-led” future climate scenario (extrapolated from local trends [PMD]) for the Hunza catchment. 531

List of Tables

Table 2.1 Table 4 of Archer and Fowler (2004) showing the calculated relative precipitation trends from 1961 to 1999 for available UIB meteorological stations..... 14

Table 2.2 Table 3 of Fowler and Archer (2006) showing the calculated relative temperature trends from 1961 to 1999 for available UIB meteorological stations..... 16

Table 2.3 Summary of climate drivers, causal mechanisms and temperature responses in mountainous regions, adapted (synopsized) from Rangwala and Miller (2012). 22

Table 3.01 Description of key seasonally-varying vertically-driven atmospheric and surface process characteristics. 52

Table 3.02 Primary discharge gauge record length and range (historical period). Catchment areas are based on Archer (2003). 56

Table 3.03 Primary Pakistan Meteorological Department (PMD) long-record stations in the UIB..... 58

Table 3.04 AWS stations in the UIB operated by WAPDA used in this study with variables analysed. 59

Table 3.05 Position and modelled orography (m asl) of ERA40 reanalysis grid cells used for analysis. 62

Table 3.06 Position and modelled orography (m asl) of ERA-Interim reanalysis grid cells used for analysis..... 64

Table 3.07 Spatial and temporal resolution of MODIS SCA and LST products used in this thesis. 70

Table 3.08 Mean observed runoff by month (mm) for UIB river discharge gauging stations. 74

Table 3.09 Interannual variability in UIB runoff as measured by the coefficient of variation (CV). 75

Table 3.10 Contingency table describing colour-coding in Figure 3.042. 103

Table 3.11 Summary table showing archetypal seasonal “surface state” conditions associated with each hydrological regime type. 105

Table 3.12 Correlations of March Snow Covered Area vs Cumulative Winter (Oct-Mar) Precipitation. 170

Table 3.13 Correlations of Land Surface Temperature (LST) vs 2-m air temperature (point observations)..... 172

Table 3.14 Correlation between spatial variables within individual sub-catchments. 172

Table 4.1 Values of Pearson's correlation coefficient corresponding to specific statistical significance levels as a function of the record lengths for the data sets analysed. 200

Table 5.1 RMSE for monthly fractional contribution to annual total precipitation for PRECIS_ERA40 and PRECIS_AM3Pcntrl as compared to monthly relative distribution of annual total precipitation from local observations (PMD). 266

Table 5.2 RMSE for monthly DTR (°C) for PRECIS_ERA40 and PRECIS_AM3P as compared to monthly relative DTR from local observations (PMD). 268

Table 6.1 Summary of required meteorological input data for simulation by VICwCDiP. 309

Table 6.2 Calibrated orographic gradient function parameters for the Astore and Hunza catchments. 317

Table 6.3 Examples of orographic precipitation factors and air temperature offsets for individual sub-grid elevation bands and cell spatial mean from two example grid cells, one each from Astore and Hunza catchments. 320

Table 6.4 Calibrated values for components of degree-day melt factors for snow and ice as determined for Astore and Hunza catchments. 329

Table 6.5 Hydrological model performance metrics (quantitative relationships between simulated and observed runoff). 334

Table 6.6 Annual total mass fluxes for key hydrological inputs and model outputs for the VICwCDiP model calibration and validation runs. 344

Table 7.1 Summary of previous published studies of hydrological impacts of climate change on the UIB. 362

Table 7.2 Summary of seasonally aggregated change factors for two key variables in the selected future climate scenarios. 371

Table D.1 Soil parameters applied uniformly to all grid cells throughout the VICwCDiP models of the Astore and Hunza catchments. 492

Table E.1 Probabilistic estimates of 30-year statistics for Astore annual total hydrological fluxes. 524

Table E.2 Probablilistic estimates of 30-year statistics for Hunza annual total hydrological fluxes. 524

Table E.3 Probabilistic estimates of 30-year statistics for Astore annual cryosphere states & fluxes. 525

Table E.4 Probabilistic estimates of 30-year statistics for Hunza annual cryosphere states & fluxes. 525

Table E.5 Probabilistic estimates of relative changes to 30-year statistics for Astore annual total hydrological fluxes. 526
Table E.6 Probablilistic estimates of relative changes to 30-year statistics for Hunza annual total hydrological fluxes. 526
Table E.7 Probabilistic estimates of relative changes to 30-year statistics for Astore annual cryosphere states & fluxes. 527
Table E.8 Probabilistic estimates of relative changes to 30-year statistics for Hunza annual cryosphere states & fluxes. 527

Chapter 1: Introduction

1.1 Background to the project

1.1.1 Socio-economic importance of UIB water resources and hydrological knowledge

The Upper Indus Basin (UIB) covers a vast expanse of high-mountain Asia (Figure 1.1). Its water resources are of the utmost importance to the wellbeing of Pakistan. Water from the Indus and its tributaries is the dominant supply source for Pakistan's irrigation, domestic consumption and hydropower demands (Archer *et al.* 2010).

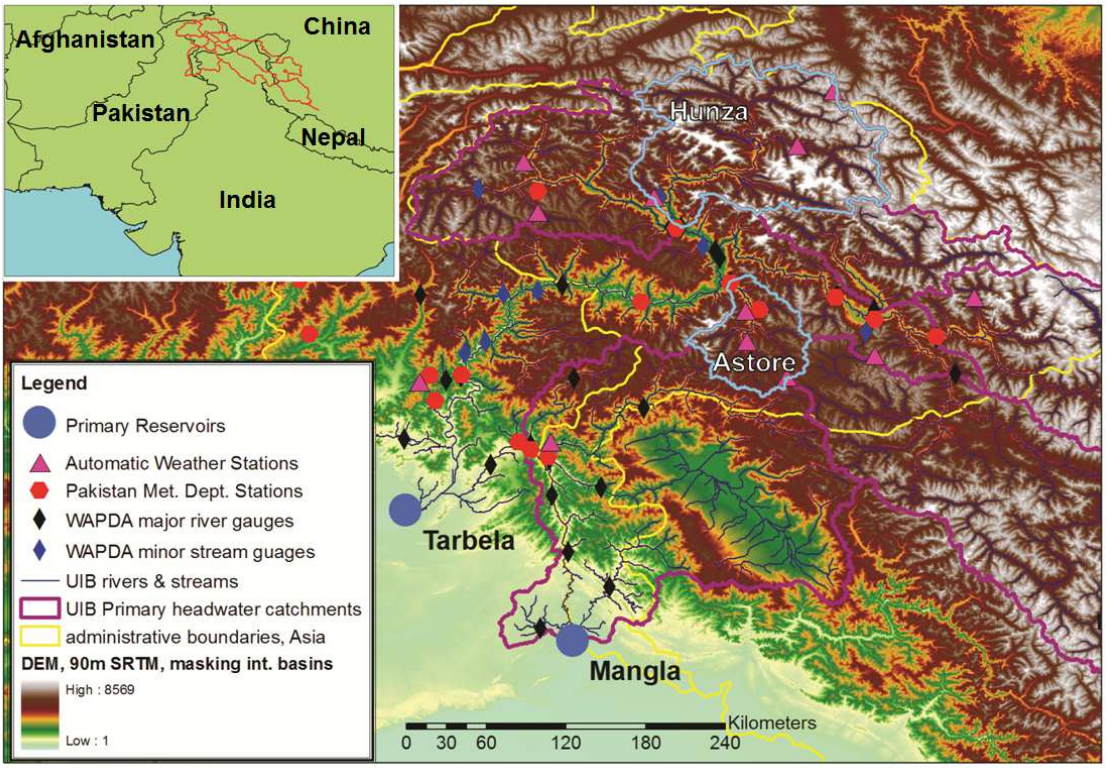

Figure 1.1 Map of the core Upper Indus contributing area and key infrastructure.

Flow from the Indus underpins local incomes and nutrition through irrigated agriculture and electricity supplies through hydropower. To partially summarise the comprehensive overview of water resources management issues in the Indus Basin by Archer *et al*. (2010):

- Agricultural output from irrigated land provides 85% of cereal grain (wheat, rice) harvests as well as all sugar production.
- The agricultural sector accounts for 45% of the total labour force in Pakistan, and exports are dominated by goods derived from agricultural production – textiles (67%) and food items (11%).

- The hydropower generation of the Tarbela dam alone supplies nearly 20% of national electricity demand.

Thus the Indus River is the lifeblood of Pakistan, and without its contribution, Pakistan's existing problems of food security and electrical load-shedding would be much greater. Present water resources management challenges in the UIB are primarily due to the considerable interannual variability in flows and in the timing of the rising limb of the meltwater-driven hydrograph. In the future this variability will continue to complicate resource management, but water stresses in Pakistan will above all be driven by high demographic growth (Archer *et al*., 2010). In downstream areas – i.e. below Tarbela reservoir – absolute per capita water scarcity will be the primary challenge in the future and the resulting difficulties in meeting food security needs is likely to become the driving concern.

Pakistan's further socio-economic development thus depends largely on optimisation of its precious water resources. The two principal potential applications of hydrological insight into the UIB for support of development initiatives are: i) improvement of present operational water resources management (water allocation in irrigation) via skilled seasonal forecasts; and ii) improved infrastructure design and long term planning via confident characterisation of future water availability, including its variability. In addressing the need for improved knowledge management to support enhanced water productivity, Karki *et al*. (2011) note, "*Disruption in the hydrological regime can have serious impacts on people's lives in the basin* ..." Thus, as Karki *et al*. (2011) point out, key priorities are: i) improved understanding of present hydro-climatic variability and potential future changes, and ii) expanded use of available remote sensing data sets.

The core understanding of the hydrological behaviour of sub-catchments of the UIB needed to enable skilled forecasting is also crucial to providing insight into likely water availability in the next few decades. Further prerequisites for this output are the assessment of the plausibility of available climate projections for the region and then the translation of these projections into likely changes in the mean values and interannual variability of regional hydrological cycles. Relationships identified between the meteorological point observations of temperature and precipitation – two parameters which are the primary indicators of mass and energy inputs into the meltwater hydrological system – and available gridded data products capturing spatial and temporal variability at scales ranging village/valley sub-catchments to tributary basins

will guide assessment of the implications of future climate projections on water availability within and downstream of the UIB.

1.1.2 Research gaps in present understanding of UIB hydro-climatology for current and future conditions

Despite substantial exploratory work – by the advisors of this thesis – in quantifying the relationships between observed local climatic conditions and gauged runoff, there remain many significant research gaps regarding UIB hydro-climatology. These gaps have not been wholly filled by the work of independent research groups who previously focused on the use of gridded data sets and future climate projections to drive hydrological models.

Areas yet to be clarified include:

- the spatial means and vertical gradients of key climate variables which provide additional information – beyond that provided by point observations of precipitation and near-surface air temperature – regarding mass and energy inputs to the UIB meltwater hydrological system;
- the direction and magnitude of rates of change in precipitation and near-surface air temperature, including detail of seasonal (monthly) and diurnal asymmetry, within the observed record up through the past decade;
- the proximal causal mechanisms driving observed variability and change, including the existence of specific local climate sensitivities and potential feedbacks;
- the role and degree of influence of teleconnections – indices of large-scale atmospheric circulation – on local UIB climate;
- the degree of coherence (agreement) between available future projections of UIB climate – from global and regional climate models – and the trajectory suggested by extrapolation of trends in the observed record;
- the sensitivity of the hydrological system to the vertical gradients in precipitation (mass input) and temperature (energy input);
- the present state of – and probable implications of projected climate scenarios for – the mass balance of glaciers in the major UIB tributary basins;

The research gaps listed above are identified and framed in this thesis through the imperative to characterise and quantify the net implications of these hydro-climatological issues for future water resource availability.

1.2 Principal research aims

In light of the enumerated research gaps, the aims and objectives of the present project have been formulated as follows:

1. Improving the spatial and temporal characterisation of present hydro-climatology of the UIB

- To explore the available multi-decadal records from local observations of river discharge, precipitation and air temperature in order to quantify annual cycles and interannual variability.
- To analyse the available global meteorological reanalyses and remote sensing spatial climate data products which provide complementary indicators of the mass and energy inputs to the UIB hydrological system.
- To develop a detailed climatology for the UIB of secondary meteorological variables, i.e. beyond precipitation and temperature, which may be expected to either act as proximal causal mechanisms in local climate variability or influence net runoff through modulation of meltwater generation or evaporative processes (or both).
- To assess the estimates of surface energy balance fluxes in the UIB from available global meteorological reanalyses both to provide a benchmark reference for later melt process simulation as part of the hydrological modelling and to provide the foundation for identification of causal mechanisms in air temperature variability in the UIB.
- To perform a detailed characterisation of the vertical gradients -- with respect to underlying surface elevation -- in key climate variables either through use of observations from multiple ground-based stations or through use of available remote sensing spatial climate data products.

2. Assessing climate trends and their drivers in the UIB from the available observational record

- To verify previous findings regarding seasonally and diurnally asymmetrical temperature change.
- To assess the coherence of estimated trends. This will include examination of the spatial coherence of trends found in meteorological reanalyses as well as the testing of relationships (correlations) between air temperature variables from local observations and reanalyses.

- To assess potential causal mechanisms of asymmetrical temperature change via testing of correlations between air temperature variables from gauges and reanalyses and cloud cover and energy balance components within the ERA-Interim reanalysis..
- To examine relationships (correlations) between locally-observed precipitation and precipitation estimates from gridded data sources (ERA-Interim and ERA-40 downscaled by PRECIS RCM) and additional potential links between large-scale circulation characteristics and local mass input to the hydrological system.
- To investigate the influence of large-scale atmospheric circulation patterns on the UIB as quantified by correlations between teleconnections and local climatic conditions.

3. Developing plausible scenarios of future climate for the Upper Indus Basin

- To assess available RCM outputs (HadAM3P downscaled by PRECIS) for the UIB. Bias will be assessed both between HadAM3P downscaled by PRECIS and local observations as well as between HadAM3P downscaled by PRECIS and ERA-40 downscaled by PRECIS.
- To calibrate and validate a stochastic downscaling model of the present climate to establish the appropriateness and adequacy of the method for the UIB and to provide baseline synthetic time-series for use in time-slice modelling studies of future hydrological conditions.
- To derive change factors -- extracted from available RCM outputs (HadAM3P downscaled by PRECIS) and extrapolated using trends estimated from local observations -- for precipitation and air temperature in order to construct contrasting scenarios of future climate.
- To implement the selected scenarios in synthetic time-series by perturbing the previously calibrated stochastic downscaling model.

4. Constructing and validating a hydrological model for the UIB

- To develop a hydrological model using, wherever possible, proven methodologies to enable the simulation of key land surface processes -- including snowpack transformation to ice through compaction, vertical transfer of glacial ice through basal sliding and evolution of glacial volume (area and thickness) -- in order to accurately reproduce the key aspects of UIB hydrology.

- To calibrate and validate this model for archetypal catchments representing the dominant UIB hydrological regimes, i.e. nival (seasonal snowpack) and glacial, using the available meteorological input data from the observed record.

5. Examining the implications of contrasting future scenarios on UIB hydrology and cryosphere

- To use long synthetic time-series for future climate scenarios to drive the calibrated meltwater runoff models for the two archetypal UIB tributary catchments.
- To further use the output of the scenario-driven simulations to assess projected glacial trajectories in terms of mass and areal extent.

1.3 Structure of thesis

This thesis is divided into eight chapters. Chapter 1 gives an introduction, including the socio-economic context and aims and objectives of the thesis. Chapter 2 provides a synthesis of the relevant existing literature. Chapter 3 draws on a wide range of available data sources to present a comprehensive characterisation of the present hydro-climatology of the UIB. Chapter 4 examines the available historic record for evidence of on-going change and indications of causal mechanisms, both local and global, driving this change. Chapter 5 describes the development of contrasting scenarios of future climate – based on projections from a regional climate model (RCM) and extrapolations of observed trends – using stochastic methods to produce synthetic time series of precipitation and temperature. Chapter 6 describes the adaptation of a hydrological model capable of simulating the key processes of inter-seasonal (and interannual) water storage and runoff generation with sufficient spatial resolution to capture the key factors driving variability in UIB river flows. Chapter 7 then applies the scenarios introduced in Chapter 5 to the hydrological model in Chapter 6. This permits probabilistic assessment of the likely consequences of these scenarios for glacial mass balance trajectories and future hydrological conditions, including both likely mean values and interannual variability. Lastly, Chapter 8 delivers the conclusions of the present project and recommends key priorities for future research.

Chapter 2: Literature Review

2.1 Introduction

Before embarking on a comprehensive exploration of the findings and contributions of the present work, it is essential to provide the context constituted by previous work in the same domain – thematically as well as geographically – and to explore known issues and challenges in studies of this nature. These issues will influence attempts to address the key research questions. It is also worthwhile to review the broader context of climatology and the potential impacts of climate change on water resources across the wider Himalayan mountain arc in particular and more generally in mountainous regions across the globe.

To be clear, the literature reviewed in this chapter will focus on the present "knowledge gap" and potential approaches to filling, rather than on technical issues related to specific datasets or methods. The necessary context and references for the latter will be provided directly in the relevant chapters of this thesis.

2.2 Priority themes for investigation

It would perhaps be best to begin by reviewing the "known unknowns", i.e. the areas identified by previous literature surveys as key issues for investigation in terms of hydroclimatic and water resources research but with an emphasis on mountainous regions. The themes addressed in sections 2.2.1 to 2.2.3 have been identified as crucial for the following reasons:

- Support of natural resources management in development context: While from an academic viewpoint the pursuit of knowledge for its own sake is a worthwhile endeavour, from an engineering perspective the purpose of research is to support, through improved understanding of physical systems, efforts to enhance human welfare. Thus while undertaking fundamental hydro-climatological research it is crucial to keep in mind the imperative of applying knowledge gained to improving infrastructure systems and resource productivity in the geographical region of study.
- Mountain specific issues: The natural physical processes at work in the hydrology of mountainous catchments are quite different from those in river basins of lower elevation or lower topographic relief. It is critical to bear in mind

these specificities when approaching research questions related to mountainous catchments.

- Contrasts with challenges in other regions with similar contexts: It is logical when undertaking a complex and challenging research project to consider how other authors have approached similar problems. Although not a perfect analogue in terms of the climate processes, the tropical Andes do provide a valuable parallel as a region with substantial topographical relief, high population growth in demand areas and relatively sparse ground-based observations.

2.2.1 Key elements for climate change studies supporting natural resources management in a development context

Wilby *et al*. (2009) reviewed downscaling techniques from the perspective of their utility and appropriateness for provision of risk information for climate change adaptation and development planning. Taking this viewpoint, they grouped available techniques based on their resource intensiveness, namely their needs in input information, technical capacity and computing resources. Bearing in mind these demands, they catalogued the advantages and drawbacks of each method.

Wilby *et al*. (2009) stressed that the timescales at which natural resource management and infrastructure planning are conducted, ten to fifty years, are considerably shorter than many future climate projections which tend to focus on climate conditions at the end of the twenty-first century. Over this shorter timescale there is relatively less uncertainty in terms of global mean temperature changes due to the "locked-in" nature of emissions and thermal inertia in the planet's oceans. Furthermore, considerable uncertainty remains over the magnitude and direction of changes in precipitation in both the near and longer term. Climate patterns in the near term are dominated by regional patterns and interannual variability.

Wilby *et al*. (2009) went on to point out how the secondary models for impacts assessment driven by the reviewed downscaling techniques add to the uncertainty involved in characterising future climate related risks for resource management and development planning. Looking forward to how integration of climate science outputs into development planning can be facilitated, they identified three core areas: i) fundamental science; ii) uncertainty; and ii) decision support systems. The former two themes fall within the classical sphere of academic (and institutional) research, and as

such the current challenges and remaining knowledge gaps are relatively well identified. The integration of climate science outputs into decision support systems, however, is a less traditional area of focus. Wilby *et al*. (2009) stress the need to render climate risk information comprehensible to decision makers at a range of geographical levels, from the local to national, in both the public and private sectors. They suggest that potential climate change impacts could be communicated to practitioners in terms relative to their professional experience with present climate variability. Confrontation of these relative indicators with present levels of system resilience and vulnerability could aid in prioritising actions and investments for climate change adaptation. In closing, Wilby *et al*. (2009) propose a twofold approach for climate risk-driven development planning. First, climate scenario-led risk identification can help to identify likely critical impacts of change. Second, analysis of vulnerability of existing infrastructure to observed present variability can identify weaknesses which should be urgently remedied.

Continuing to explore the theme of strategies to support climate change adaptation, Wilby and Desai (2010) proposed a framework for evaluation of adaption measures oriented toward "low regret" interventions. This variant on the work of Heltberg *et al*. (2009), while recognising that all actions have opportunity costs and resource requirements and hence cannot be entirely regret free, endorses the search for measures that yield benefits under all plausible scenarios. Such measures would include both "hard engineering solutions" (physical infrastructure) and "soft solutions" including institutional issues and resource allocation. Efficiency, demand management, supply diversification and capacity building are core tenets of this approach.

In relation to the present study, improved hydrological understanding of the UIB is crucial to understanding variability and probable evolution of water availability as well as potential evapotranspiration. This knowledge is crucial to accurately assessing supply-demand balance.

2.2.2 Mountain specific issues for hydroclimate and water resources research

Under the auspices of the Mountain Research Initiative (MRI), Viviroli *et al*. (2011) compiled a comprehensive review of commonalities between mountain regions across the world in terms of key hydrology research gaps, water resources management challenges and water governance policy needs. They stressed the importance of mountain regions as sources of water supply for adjacent lowland areas. In consultation with regional experts they found that the regions with greatest water stress – measured

by supply shortfalls compared with demand – were often those with the least institutional capacity to adapt to a changing climate. In terms of research gaps they noted the urgency to reduce uncertainty regarding future glacial mass balance and runoff magnitude and variability. They identified the imperative both for greatly increased ground-based observation programmes – with increased access to the data gathered – and for consistent/standardised regional scenarios of future climate. They insisted on the need to extend analysis frameworks beyond natural systems to take into account land-use changes, socio-economic impacts and infrastructure systems, especially engineered storage in the form of large reservoirs. The latter are expected to play an even more crucial role in management of a resource projected to become increasingly variable under global warming.

In light of increasingly daunting challenges for water resources, Viviroli *et al*. (2011) insisted on the need for better linkages – communication and responsiveness – between scientists, resource managers and policy makers. Increased involvement of stakeholders in resource management processes was identified as a potential pathway for reinforcing catchment level policy making. They concluded by asserting that in seeking to guarantee robust applied research there is no substitute for substantial funding of sound science.

Adopting a similar approach to Viviroli *et al*. (2011), Karki *et al*. (2011) focussed their attentions solely on the Indus Basin. Unsurprisingly, they found similar scientific priorities as identified for other river basins: improved spatial characterisation of precipitation, more detailed robust down-scaled climate scenarios, increased up-take of opportunities afforded by remote sensing, improved understanding of glacial mechanics and melt processes, the incorporation of socio-economic issues in resource impact assessments, engagement with stakeholders regarding water governance. They particularly stressed a potential role for integrated water resources management (IWRM) and integrated river basin management (IRBM) in the Indus basin. They noted the urgency of increasing resilience of water resources management structures given the seemingly inescapable increases in water stress Pakistan is facing – even if absolute resource volumes remain stable – due purely to demographic growth. They conclude by advocating enhanced coordination, improved data sharing and development of methodologies explicitly linking upstream, physical science-driven supply characterisation with downstream, socio-economically-driven demand issues.

2.2.3 Contrast and comparison in evolving water resources management challenges in a different developing mountainous context

Approaches used to assess water resources in similar regions, in this case mountainous catchments in developing and data scarce regions, can provide a useful comparison to methods applied in the basin of interest. An evaluation by Buytaert *et al*. (2010) of uncertainties in downscaling climate projections using RCMs and related challenges for water resources assessments under changing climate conditions in the tropical Andes provides an interesting and useful counterpoint to work in the UIB. Analysing projections of temperature and precipitation – both at General Circulation Model (GCM) resolution from the Intergovernmental Panel on Climate Change (IPCC) 4th Assessment Report (AR4) (Christensen *et al*., 2007; IPCC, 2007) multi-model ensemble and from the UK Met Office GCM HadAM3P as dynamically downscaled by the PRECIS (Jones *et al*., 2004) Regional Climate Model (RCM) – Buytaert *et al*. (2010) found that projections of future climate, especially precipitation, were problematic at the scale of RCM resolution (~50km) as well as the GCM scale (>150km). They posited that poor performance for precipitation, as evidence by spatially dependent biases in both GCMs and RCMs, was the inability to accurately simulate climate processes – such as orographic precipitation and local convective rainfall – occurring at spatial scales unresolved by either type of model. Nevertheless they noted that the improved characterisation in RCMs of the atmospheric circulation features which drive precipitation might lead to better simulation results regionally. They noted that there exists both scope to improve GCMs – to reduce the range of multi-model projections – and a need to refine the spatial resolution of RCMs in order to adequately represent key climate processes.

Buytaert *et al*. (2010) concluded that faced in the medium term with "irreducible uncertainties" in projected future climate, it was crucial from a water resources management perspective to develop strategies by which reducing vulnerabilities and enhancing robustness render systems more adaptable. They make specific note of the "no regret" intervention approach expounded by Heltberg *et al*. (2009) which actively seeks to identify actions which provide net benefits under all of the plausible scenarios of future change.

Buytaert and De Bievre (2012) then complemented the assessment of uncertainties in climate change projections for the tropical Andes with an analysis of the implications for water resources of projected climate change coupled to projected

demographic growth. They found that while uncertainties regarding both the magnitude and sign/direction of net climate change impacts on water resources are pervasive, at least the direction, if not the magnitude, of demographic change in the countries and watersheds of the tropical Andes is in little doubt. In their analysis even the slowest rate of population growth resulted in reductions of per capita water availability – with reference to present climate and population conditions – than the lower bound of the interquartile range predicted by climate change (with present population) in a 19 member multi-model GCM ensemble. Additionally for two of four case studies, the reduction in per capita water availability from the "high growth" scenario exceeded the reduction from the range for the multi-model ensemble, i.e. for the most severe GCM projections. Furthermore, their analysis considered only mean climatic conditions and did not explore the effects of changes to interannual variability. Hence, the added stress of demographically-driven demand growth superimposed upon resource fluctuations in drought years under future climate conditions highlights the likelihood of quite drastic transient declines in per capita water availability. These findings mirror analysis by Archer *et al*. (2010) on the likely impact of demographic growth in Pakistan on per capita water availability in the Upper Indus where projected growth is expected to contribute to substantial water stress.

2.3 Previous studies of the hydroclimatology of the Upper Indus

2.3.1 Foundational research by Archer and Fowler

Some of the most important and most widely cited work on the Upper Indus has been carried out by the advisors of the present project. In groundbreaking initial work on the hydrology of the UIB, Archer (2003) defined its archetypal hydrological regimes – glacial, nival (seasonal snowfall) and pluvial (direct rainfall runoff) – in terms of their dominant climatic controls. Archer (2003) found:

- In glacial regimes, thanks to their massive storage of ice, annual runoff is governed (limited) by Summer (June, July, August) energy inputs, most easily quantified by local air temperature observations.
- In nival regimes, most of the annual precipitation falls as snow in cold seasons and at high elevation, while Summer energy inputs are regularly adequate to cause melting of all available snow pack. Hence the controlling element in annual runoff is the accumulated cold season precipitation.

- Because a relatively small fraction of precipitation falls as snow, pluvial regimes simply exhibit the classical rainfall-runoff response to concurrent mass inputs.
- Because both glacial and nival regimes require energy inputs to convert accumulated solid precipitation into runoff, their annual hydrographs are shaped by the fraction of the catchment experiencing melt-conducive conditions. Annual hydrographs in pluvial catchments are simply shaped by precipitation seasonality.

In a mountainous context such as the UIB, the variation of temperature with elevation is a key index controlling hydrological response. Archer (2004) quantified the mean rates of vertical temperature variation on a seasonal basis for average temperatures using available local observations. Archer (2004) found a mean annual lapse rate of 0.70°C $100m^{-1}$ for average daily temperatures. These rates of change are referred to as lapse rates as they are driven by the general adiabatic lapse rate but also influenced by local conditions. Using these local lapse rates, Archer (2004) also extrapolated the monthly mean freezing isotherms – the elevation at which the average temperature equals 0°C – for both daily maximum and minimum temperatures. The annual freezing isotherm elevations found by Archer are shown in Figure 2.1 (his Figure 3).

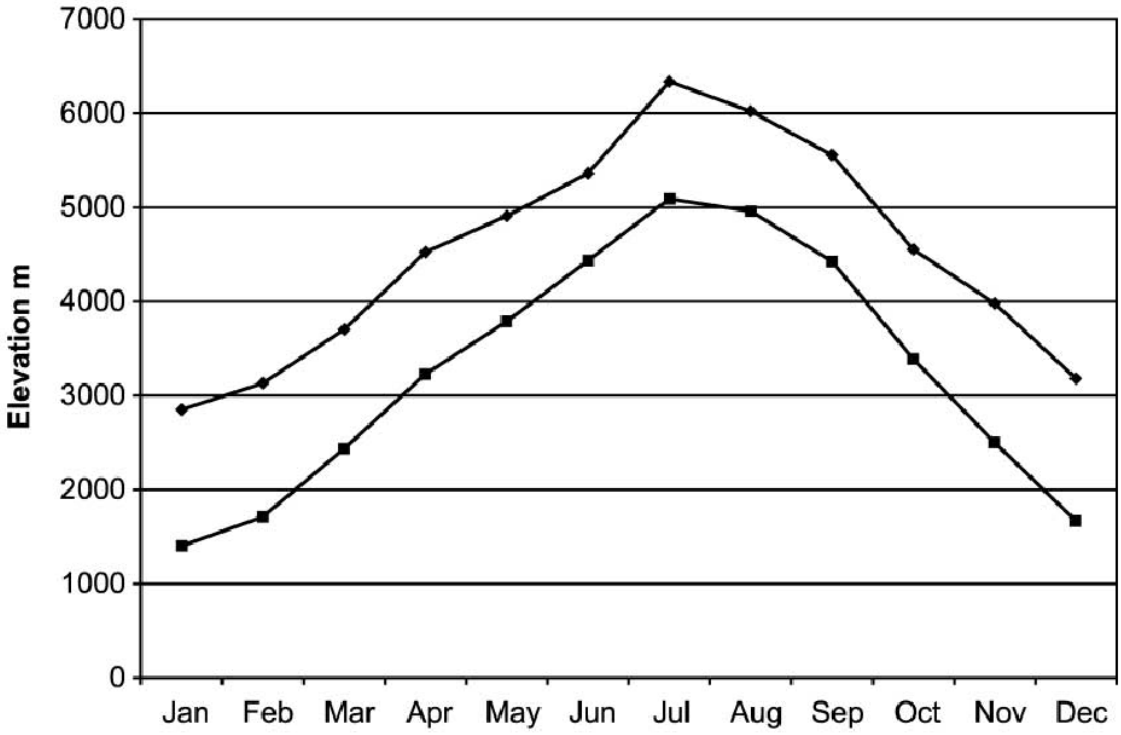

Figure 2.1: Figure 3 of Archer (2004) showing the estimated annual cycles of freezing isotherms in the UIB.

In the hydrological cycle, precipitation is a climate input of paramount importance. Archer and Fowler (2004) investigated the spatial patterns in correlations between precipitation observations at long record meteorological stations throughout the UIB. They found that cold season precipitation is positively correlated throughout the region, but that a sub-regional separation exists for Summer (monsoon) precipitation. One zone exhibits substantial monsoonal precipitation and corresponds to the foothills and front range of the mountains. The second zone, to the north, has very limited Summer precipitation. Correlations between stations from the same zone are positive, but correlations across the division are negative.

Another aspect examined by Archer and Fowler (2004) were recent precipitation trends found in the local observational record. Table 2.1 (their Table 4) below presents a summary of the relative precipitation trends (as a percentage of the period mean) from 1961 to 1999 in the available stations.

Station	*J-D*	*J-M*	*A-J*	*J-S*	*O-D*	*O-M*	*A-S*
Drosh	-1	+3	-8	-7	+6	+4	-8
Gilgit	**+10**	+1	+9	+5	+11	+3	+8
Bunji	***+13***	-7	+10	**+19**	+23	+4	+14
Astore	+5	+3	-3	**+18**	+16	+5	+3
Skardu	**+14**	**+18**	+3	***+17***	+19	**+18**	+8
Srinagar	+1	+3	-6	+7	-8	+1	+2
Dir	**+11**	**+14**	+9	+5	+18	**+16**	***+7***
Shahpur	**+11**	**+17**	+9	+8	+6	**+16**	***+8***
Puran	+1	+7	-2	-1	-2	+4	-1
Shinkiari	+1	**+10**	-4	-1	+3	+7	-2
Bold Italics show stations north of the Himalayan divide. Notes on siginificance of trend: **Bold** = P < 0.05 ***Bold Italic*** = P < 0.01							

Table 2.1: Table 4 of Archer and Fowler (2004) showing the calculated relative precipitation trends from 1961 to 1999 for available UIB meteorological stations. Trends for 3 and 6-month periods show change per decade as a percentage of the period average.

As can be seen in Table 2.1 they found predominantly increasing precipitation especially for the three primary long-record stations: Gilgit, Skardu and Astore.

Archer and Fowler (2004) also investigated links between interannual precipitation variability and indicators of large scale atmospheric circulation known as teleconnections. Specifically they assessed correlations between UIB precipitation and circulation patterns over the northeastern Atlantic, as quantified by the North Atlantic Oscillation (NAO) index. The NAO is defined as the difference in sea level atmospheric pressure (SLP) between Gibraltar and Reykjavik and is well recognised indicator conditions in the North Atlantic, a key feature of global atmospheric circulation (Jones *et al.* 1997, Marshall *et al.* 2001). Archer and Fowler found frequent positive correlations between the NAO and UIB precipitation in cold season months but

negative correlations for Summer months. This suggests that a positive NAO phase is linked to intensified temperate westerly weather systems which provide increased cold season precipitation, but that in Summer months these systems interfere with monsoonal activity with a net result of precipitation decreases.

Fowler and Archer (2005) extended their study of precipitation teleconnections by expanding the atmospheric structures assessed to include circulation over the tropical Pacific in the form of the El Niño Southern Oscillation (ENSO) as quantified by the Multivariate ENSO index (MEI). ENSO is large-scale circulation phenomenon primarily manifested in sea surface temperature (SST) differentials between different areas of the tropical Pacific (Diaz *et al*., 2001). The MEI is a quantitative measure of the ENSO phase and state using a principal components analysis of a combination of SLP and SST measures for the region (Wolter and Timlin, 2011). A strongly positive MEI (El Niño phase) was found to coincide with increased Winter precipitation in the UIB, while a negative MEI (La Niña phase) coincided with decreased autumn (September, October, November) and early winter (December) precipitation. Correlations between the MEI and Summer precipitation were too weak to be considered conclusive, although positive MEI values were correlated to reductions in UIB Summer air temperature, perhaps indicating increased cloud cover (leading to reductions in incoming solar radiation).

As with high latitude zones, mountainous regions are expected to experience greater magnitudes of change than the global mean response to anthropogenic forcing (Beniston *et al*., 1997). It was thus logical that Fowler and Archer (2006) would investigate trends in the historical record of local UIB temperature observations. Unsurprisingly they found a net annual mean temperature increase at the primary long-record stations between 1961 and 1997. In contrast to general expectations of global warming, they found increasing year round diurnal temperature range (DTR). While globally increases in daily minimum temperatures are expected to exceed increases in daily maximum temperatures thus reducing DTR (Easterling, 1997; Jones, 1999), Fowler and Archer (2006) found seasonal asymmetry in temperature trends. For daily maximum temperature they found increases during Autumn and Winter (December, January, February) as well as for the annual aggregate. For daily minimum temperature, however, they found decreases during Summer and Autumn as well as for the annual aggregate. In terms of the net effect of these asymmetrical changes, they found Summer average temperature to be decreasing while Winter and annual aggregate average

temperature were found to increase. The values of trend rates are given in Table 2.2 (their Table 3).

(a)					
Station	Annual	Winter (DJF)	Spring (MAM)	Summer (JJA)	Autumn (SON)
Dir	**-0.26**	-0.03	***-0.41***	**-0.35**	-0.19
Drosh	+0.01	+0.15	+0.02	-0.04	-0.03
Bunji	**-0.52**	+0.07	**-0.32**	**-0.99**	**-0.66**
Gilgit	-0.13	***+0.17***	-0.08	**-0.38**	-0.15
Astore	-0.08	-0.07	-0.06	***-0.30***	+0.01
Skardu	**+0.21**	**+0.38**	***+0.24***	-0.05	**+0.26**
Srinagar	**+0.19**	**+0.51**	+0.07	-0.05	+0.08
(b)					
Station	Annual	Winter (DJF)	Spring (MAM)	Summer (JJA)	Autumn (SON)
Dir	+0.07	**+0.51**	-0.19	-0.06	+0.10
Drosh	+0.05	+0.11	+0.11	+0.03	-0.08
Bunji	**+0.20**	**+0.27**	+0.16	-0.01	**+0.35**
Gilgit	**-0.29**	+0.10	-0.20	-0.86	-0.16
Astore	-0.05	-0.07	-0.18	-0.19	***+0.28***
Skardu	**+0.52**	**+0.55**	**+0.46**	+0.30	**+0.75**
(c)					
Station	Annual	Winter (DJF)	Spring (MAM)	Summer (JJA)	Autumn (SON)
Dir	**-0.58**	**-0.60**	**-0.60**	**-0.62**	**-0.48**
Drosh	-0.05	***+0.22***	-0.06	-0.12	-0.04
Bunji	**-0.45**	+0.02	**-0.32**	**-0.75**	**-0.62**
Gilgit	**-0.67**	+0.06	**-0.47**	**-1.11**	**-1.17**
Astore	-0.13	-0.08	+0.06	**-0.41**	-0.08
Skardu	***-0.17***	+0.23	-0.05	**-0.43**	**-0.34**

Table 2.2: Table 3 of Fowler and Archer (2006) showing the calculated relative temperature trends from 1961 to 1999 for available UIB meteorological stations: (a) mean, (b) mean maximum, and (c) mean minimum showing change in °C decade^{-1}. **Bold p** < 0.05. ***Bold italic p*** < 0.10.

In addition to identifying these surprising asymmetrical patterns, Fowler and Archer (2006) also extrapolated the implications of these temperature trends for glacial regime catchment hydrology. Decreasing summer temperature in fact represents a reduction in the energy inputs needs to drive glacial meltwater generation. They found that a 1°C reduction in summer mean temperature would be expected to result in 16% and 17% reductions in summer runoff respectively for the Hunza and Shyok catchments.

Looking beyond fundamental hydroclimatology to potential applications for improved water resources management, Archer and Fowler (2008) explored the predictability of Summer runoff from nival regimes using locally observed predictors available with sufficient lead times for practical use in water resources management planning. Based on simple linear regression techniques applied to the discharge observations for the Jhelum basin above Mangla reservoir and its tributaries, they found that by using locally observed precipitation and temperature as predictors that skilful

forecasts could be made for Spring runoff (rising limb) as well as the melt season (April to September) totals but that forecasting of the recessing limb of the melt season (July to September) was more difficult. Given Pakistan's dependency on irrigated agriculture for economic activity and food security, forecasting of water availability could play a key role in optimising crop yields and economic returns.

Continuing their focus on the assessment of practical needs and opportunities for improving water resources management in the Indus Basin, Archer *et al*. (2010) produced a holistic assessment of the challenges faced in managing Indus river flows sustainably. They focused particularly on the implications of projected population growth on water availability and withdrawal demands. Pakistan's population is projected to increase by a factor of between 1.5 and 2.5 over the next four decades, hence per capita water availability will be divided by the same factor if the absolute quantity of the resource remains constant. Depending on their sign (direction), changes in Indus runoff could accentuate or mitigate these reductions. It is a primary aim of the present study to assess potential changes to the quantitative resource.

Archer *et al*. (2010) also considered a number of other phenomena with the potential to influence water volumes available for extraction from the Indus. These additional factors included reservoir sedimentation, the need for reserved discharge levels for ecological requirements and potential declines in groundwater levels. Looking beyond the physical resource, the authors also assessed the institutional potential (scientific capacity, water governance systems) to cope with resource management challenges; concluding that, while fragmentation of responsibility and influence of vested interests on decision making hampered productive resource use, increasing local scientific capacity provided hope for future prospects.

2.3.2 Understanding the hydroclimatology of the UIB and potential teleconnections

Of course while the work of Archer and Fowler has been both ground-breaking and comprehensive, other authors have contributed to the detailed hydroclimatological study of the UIB.

Working at field sites in the nival regime Kunhar catchment in the Jhelum basin, de Scally and Gardner (1990) assessed moisture fluxes and melt rates for snowpack in both undisturbed and avalanched conditions. Regarding melt rates, de Scally and Gardner (1990) found both that melt rates in the Western Himalaya, as quantified by degree-day melt factors, exceed those in other mountainous regions around the globe

and that, locally, degree-day factors for avalanched snow (5.6 +/-0.6 mm $°C^{-1}$ day^{-1}) are statistically greater than for undisturbed snowpack (4.3 +/-1.1 mm $°C^{-1}$ day^{-1}). In terms of vapour fluxes, de Scally and Gardner (1990) observed occurrences of condensation as well as expected sublimation. As de Scally and Gardner (1990) point out, condensation is potentially a very important vapour flux because the latent heat released from 1 mm of moisture phase change (vapour to liquid) is sufficient to cause 7.5 mm of melt.

Work by de Scally (1994) on the Jhelum basin set the stage for the seasonal forecasting study by Archer and Fowler (2008) described above. Drawing on a combination of meteorological observations, field measurements of seasonal snowpack and runoff estimates from river stage gauging, de Scally (1994) investigated the relative contributions of snowmelt and Summer (monsoon) precipitation to annual total runoff in Jhelum sub-basins. Noting the "steep vertical and horizontal gradients of snow accumulation", de Scally (1994) concluded that in most years annual total runoff in the Jhelum was dominated by Winter/cold season accumulated snow pack, with relatively limited influence from Summer monsoon rainfall.

Also during his work in the Jhelum, de Scally (1997) investigated air temperature lapse rates using observations made during high elevation field studies over two years – 1986 and 1987 – and found rates of between generally between 0.7 and 0.8 °C per 100 m. These values are close to the 0.7°C found by Archer (2004).

There is considerable scientific uncertainty regarding orographic precipitation gradients in the UIB. One of the most striking statements was made by a pioneering glaciologist (Kick, 1980) regarding vertical precipitation variation in the Nanga Parbat massif. Kick (1980) reported that precipitation was less than 120 mm $year^{-1}$ below 2500m and rose to more than 8000 mm $year^{-1}$ at elevations above 4500m.

Accurate quantification of precipitation inputs is absolutely critical in any hydrological study. Winiger *et al*. (2005) used a range of available data sources including high elevation automatic weather stations (AWS) to assess orographic precipitation gradients and sub-regional rainfall regimes. Using nine years (1991-1999) of AWS precipitation measurements they found the best fit function to describe the relationship between elevation and annual precipitation to be exponential in form. This equation will be presented graphically in Chapter 6 (section 6.8.1).

Fowler and Archer are not the only authors to have studied potential teleconnections of large scale atmospheric circulation to climate variability in the UIB.

Syed *et al*. (2006) investigated the links between UIB winter precipitation and NAO and ENSO indices. Syed *et al*. (2006) found that both a positive NAO phase and a warm ENSO phase were correlated to increased UIB Winter precipitation. In both cases the causal mechanism appeared to be a trough in atmospheric pressure developing over Central Asia, roughly centred to the east of the Caspian Sea. According to Syed *et al*. (2006), the orientation and magnitude of the trough varied depending on whether it was caused by ENSO or the NAO.

Building on his statistical study of observed climate data, Syed *et al*. (2010) was able to reproduce the previously identified links between UIB Winter precipitation and both the NAO and ENSO using an RCM, RegCM3, driven by boundary conditions from the European Centre for Medium-range Weather Forecasting (ECMWF) ERA-40 reanalysis (Uppala *et al*., 2005). The simulations in RegCM3 confirmed the intensification of storm activity from westerly disturbances originating over the Eastern Mediterranean caused by development of a trough in atmospheric pressure centred to the east of the Caspian Sea. Storm intensity was assessed quantitatively as vertically integrated moisture convergence. Analysis of both positive NAO and warm ENSO cases showed enhanced moisture transport from source zones to Northern Pakistan thus indicating a physical mechanism for the causal link identified in the previous study. Interestingly, Syed *et al*. (2010) found that while increased moisture inputs under a positive NAO were drawn from geographically diverse sources including the Mediterranean, Caspian and Arabian Seas as well as the Persian Gulf, additional moisture during warm ENSO conditions were drawn only from the latter two sources.

2.3.3 Analysis of recent climate trends and potential causal mechanisms in the UIB and other mountain regions

Fowler and Archer (2006) were not the first authors to identify diurnal and seasonal asymmetry in near surface air temperature trends in South Asia. Kumar *et al*. (1994) analysed daily minimum and maximum temperatures – deriving daily means and diurnal temperature range (DTR) – for 121 meteorological stations throughout India which he grouped into various sub-regions. Trends were assessed over three time windows: 1901 to 1987, 1901 to 1950 and 1951 to 1987. For his “northwest” region, which included stations from the Greater Himalaya as well as the adjacent Indian Punjab and Rajasthan, Kumar found seasonal asymmetry in that “trends in both the sub-periods are dominated by the monsoon and post-monsoon seasons, and the winter trends

opposing them." He also found signs of diurnal asymmetry, with increasing daily maximum and decreasing minimum temperatures, leading to increasing DTR in the northwest India region, as found also by Fowler and Archer (2006) in the UIB.

A recent paper by Shahid *et al*. (2012) has also found increasing DTR in the monsoon period in Bangladesh, although they found decreasing DTR in winter and pre-monsoon periods. Increasing DTR in pre- and post-monsoon periods, as well as during the monsoon itself, has also been found for some stations in NE India by Jhajharia and Singh (2011).

Bhutiyani *et al*. (2010) investigated trends monthly means of daily mean temperatures, rather than DTR, using available observation records of century or more from northwestern Himalayan stations in India. Using both linear and non-parametric (Mann-Kendall) trend tests, they found widespread increasing temperatures, with the strongest increases in Winter (DJF), in this sub-region adjacent to the UIB. They also investigated variability in precipitation and snowfall. Using power spectrum analyses they identified apparent epochal cycles in precipitation with a periodicity ranging from 30 to 60 years. Bhutiyani *et al*. (2010) also noted decreasing trends in winter snowfall which they attributed to a changing distribution of the fractions of precipitation falling in liquid (rain) and solid (snow) forms. They hypothesised that this shift in phase distribution was due to the Winter warming they had identified in the same study.

With regards to the wider Himalayan mountain arc, a recent review paper by Rangwala and Miller (2012) cites Bhutiyani (2007) and Kothawale (2010) for the Indian Himalaya and Shrestha (1999) for the Nepal Himalaya. These studies concluded that maximum temperatures have been increasing more rapidly than minimum temperatures in the recent historical record. Bhutiyani and Shrestha (1999) suggested that monsoonal circulation was linked to this diurnal asymmetry while Kothawale (2010), like Fowler and Archer (2006) for the UIB, found that warming is occurring fastest in the Winter season. A paper by Khattak *et al*. (2011) also published similar results to Fowler and Archer (2006) for the UIB region. Khattak *et al*. (2011) applied Mann-Kendall non-parametric trend tests to the available local observational record. They also found statistically significant decreasing trends in Summer Tmin (-0.45°C decade^{-1}) and Winter Tmax (+0.45°C decade^{-1}) as well as increasing Summer precipitation (6mm decade^{-1}).

The recent review paper by Rangwala and Miller (2012) on climate change and its elevation dependency in mountain regions provides an understanding of both the

recent improvements and the remaining challenges in mountain climatology. Ambitious and comprehensive in scope, they summarise the sometimes contradictory results of dozens of studies covering mountain ranges on four continents recognising that, fundamentally, mean annual temperature trend rates are inadequate to describe the on-going change in mountainous regions. They suggest that changes in diurnal – daily minimum and maximum – as well as seasonal – Winter, Spring, Summer, Autumn – temperatures must be studied in order to understand the complex processes at work in these regions.

After a wide-ranging geographical review, Rangwala and Miller (2012) then systematically examined elevation-linked causal mechanisms which could explain the differences between regions as well as potential discrepancies between studies within a given region. Table 2.3 (derived from their Table 2) reproduces Rangwala and Miller (2012)'s summary of climate drivers, the physical mechanisms by which they act and their diurnal and seasonal effects. Table 2.3 (Table 2 of Rangwala and Miller, 2012) is reproduced here because it provides an excellent synthesis of potential proximal causal mechanisms which cause temperature trends in mountain regions to deviate from global patterns. Some of these mechanisms are investigated by the present study. The results of this investigation are presented in Chapter 4 of this thesis.

Climate drivers	Physical mechanisms	Seasonal effects	Diurnal response
Changes (reductions) in surface albedo from changes (decreases) in snow and ice extent and or changes in surface properties (dust/debris)	Change (increase) in surface absorption of incoming solar (shortwave) radiation	Focused around freezing level (0°C isotherm), thus at low elevation in Winter, middle elevation in Spring and high elevation in Summer	Increases Tmax, although the effect may be buffered or offset if available soil moisture allows for latent heat release (evapotranspiration)
Changes (increases) in daytime cloud cover	Change (reduction) in incoming solar (shortwave) radiation	Seasonal effects are proportional to absolute incoming shortwave radiation hence vary with annual solar cycle (greatest in Summer)	Suppresses Tmax, effect would be greatest when relative change is largest, i.e. when initial cloud cover is minimal
Changes (increases) in night-time cloud cover	Change (increase) in downward longwave (thermal) radiation	Seasonal effects are proportional to the relative share of longwave radiation in the overall energy balance, hence inversely proportional to annual solar cycle (greatest in Winter)	Increases Tmin
Increases in specific humidity (q)	Change (increase) in downward longwave (thermal) radiation although this effect is highly sensitive to the absolute specific humidity: effects are much greater when q is less than 0.005 kg/kg.	Seasonal effects are proportional to the relative share of longwave radiation in the overall energy balance, hence inversely proportional to annual solar cycle (greatest in Winter) but also inversely proportional to annual humidity cycle (greatest when air initially driest)	Increases Tmin
Changes (increases) in non-absorbing aerosols (e.g. sulphates)	Change (reduction) in incoming solar (shortwave) radiation Increases cloud albedo and cloud "lifetime"	Dependent on seasonal (anthropogenic) emissions	Decreases Tmax Limited increases in Tmin through increased cloud radiative effects Effect is expected to be localised near the emission source
Changes (increases) in absorbing aerosols (e.g. dust, black carbon)	Change (reduction) in incoming solar (shortwave) radiation but increases mid-tropospheric heating Inhibits cloud cover Decreases cloud albedo Decreases albedo of snow cover	Dependent on seasonal (anthropogenic) emissions and proportional to absolute incoming shortwave radiation	Increases Tmin Increases Tmax through reduced cloud radiative effects Effect is expected to be localised near the emission source
Changes (increases) in soil moisture	Change in surface energy balance through increased latent heat fluxes (surface cooling) and decreased sensible heat fluxes (soil to air heating)	Proportional to soilwater influx, may be due to either meltwater infiltration or liquid precipitation (rainfall), hence will follow the seasonality of these two mass inputs to soil-water system	Suppresses DTR; Suppresses Tmax in Summer

Table 2.3: Summary of climate drivers, causal mechanisms and temperature responses in mountainous regions, adapted (synopsized) from Rangwala and Miller (2012).

Rangwala and Miller (2012) conclude by reiterating the spatial complexity of mountain regions and hence the complexity of the patterns of net effects from alternating reinforcing and counteracting sensitivies. They reaffirm the need for increased ground-based observations, greater use of remote sensing technologies and climate modelling at spatial resolutions adequate to capture the complexity of mountain environments.

Amongst the studies cited by Rangwala and Martin (2012), Dai *et al*. (1999) took a global approach in assessing the factors influencing DTR. Drawing on both local observations from a targeted climatological experiment – the First International Satellite Land Surface Field Experiment (FIFE) – as well as a range of global observations, Dai *et al*. (1999) found that cloud cover acts strongly to suppress DTR due its oppositely signed effects on Tmax – which it decreases by reducing incoming solar radiation – and Tmin, which is increased with increased cloud cover by limiting net out-going longwave (thermal radiation). It follows that DTR responds positively to an increasingly energetic climate, i.e. shows positive correlations to incoming shortwave (solar) radiation, latent heat flux and sensible heat flux. Detailed examination of the FIFE results presented by Dai *et al*. (1999) clearly indicates that a more energetic climate would be expected in drier conditions not only due to reduced cloud cover but also in the case of reductions in atmospheric water vapour (specific humidity) and soil moisture. The latter in particular produced statistically significant correlations to sensible heat flux in the FIFE observations.

2.3.4 Projections of future climate change in IPCC AR4

Climate change impact assessments, including studies of likely future hydrological conditions, require projections of probable future climate. One of the most common methods of integrating disparate climate forcing mechanisms, such as those discussed above, is through atmospheric circulation models. Development of these models logically draws comprehensive on climatology.

The Intergovernmental Panel on Climate Change (IPCC) is the forum through which advances in climatology and related fields are periodically compiled and reviewed to assess the present state of knowledge and remaining research gaps in humanity's understanding of the mechanisms and implications of the evolving climate in the "anthropocene" epoch (Zalasiewicz *et al*., 2010). The IPCC is divided into three working groups by area of focus: i) Working Group I, "The physical science basis"; ii) Working Group II, "Impacts, adaptation and vulnerability" and iii) Working Group III,

"Mitigation of Climate Change". The IPCC periodically releases comprehensive "assessment reports". It's most recent, the fourth assessment report (AR4) was released in 2007.

The IPCC (Christensen *et al*., 2007) addressed the issue of regional climate projections in Chapter 11 of the WG1 report of AR4. Section 11.4 specifically dealt with projected climate change for Asia. For the purpose of climate projections, in AR4 WG1 11.4 (Christensen *et al*., 2007) the IPCC subdivided Asia into a number of sub-regions. Two of these, "Central Asia" and "the Tibetan Plateau" overlap the UIB. AR4 11.4 (Christensen *et al*., 2007) explored the projected changes, and the associated uncertainty, for future precipitation and near surface air temperature across Asia via the mechanisms expected to drive these changes.

At the time of the AR4's compilation, scientific consensus pointed toward:

- greater warming than the global mean in both Central Asian and the Tibetan Plateau;
- increased precipitation across much of Asia, including the Tibetan Plateau, during the northern hemisphere ("boreal") winter;
- decreased boreal summer precipitation in Central Asia and simultaneous decreases in "monsoonal flows" and large-scale tropical circulation;

It was recognised however that local changes could exhibit significant departures from regional trends in part because of complex topography as well as the proximal influence of maritime water bodies.

Because Asia in general, including the UIB, covers substantial zones of contact and interaction between westerly and monsoonal weather systems, changes to tropical circulation are expected to have considerable impact on the shape of future regional climate. Modelling studies frequently projected reductions in the tropical atmospheric circulation related to monsoonal activity. An emerging consensus, however, pointed to increased moisture transport overwhelming weakened circulation and yielding net increases in related precipitation. One on-going obstacle to the projection of future Asian climate was continuing uncertainty regarding the role of ENSO in Asian monsoonal processes. (Christensen *et al*., 2007)

In sub-regions, including Central Asia and the Tibetan Plateau, where westerly weather systems were expected to play a dominant role, uncertainty remained as to the probable geographic extent of drying projected for the Eastern Mediterranean and western Asia and hence whether these precipitation changes would manifest as far east

as the UIB (Christensen *et al*., 2007). With regards to temperature, it was expected that considerable roles would be played by the spread of broader arctic warming in Winter, the changes to spatial extent of snow cover in the primary accumulation seasons, Winter and Spring, as well as the sub-regions' severe continentality – i.e. the lack of maritime climate influence.

In terms of evaluating circulation model skill and biases, a general "cold and wet" bias was found across Asia in GCM outputs. For Central Asia and the Tibetan Plateau in particular, the lack of spatially representative observations was a substantial obstacle to judging the accuracy of simulated climatologies. AR4 did recognise that the topographic complexity was a difficult challenge for GCMs and even moderate resolution RCMs to overcome (Christensen *et al*., 2007).

In terms of specific projections from GCM experiments, a multi-model ensemble (MMD-A1B) approach projected nearly 4°C of warming for both Central Asia (3.7°C) and the Tibetan Plateau (3.8°C) by the end of the 21st century. Limited RCM studies of the sub-regions that were available for AR4 suggested elevation dependency – i.e. increasing warmer rates with increasing elevation – and strong potential snow cover-albedo feedback, i.e. increasing shortwave (solar) radiative absorption with decreasing snow cover.

The generation of GCMs available for AR4 showed greater range, or spread, in precipitation projections between different models in an ensemble than between different emissions scenarios simulated by a single model. In other words the choice of GCM(s) played a dominant role in the projected future climate.

With regard to seasonal changes, in Central Asia dry (low precipitation) conditions were projected to become more frequent for Spring, Summer and Autumn, while high precipitation events were projected to become more frequent during Winter.

In WG1 Chapter 11 (Christensen *et al*., 2007), the IPCC also highlighted commonalities and divergences in climate change projections with mountainous regions worldwide. The difficulty for the coarse resolution GCMs, and even moderate resolution RCMs, to accurately simulate physical processes, including accumulation and ablation of seasonal snowpack and glacial ice, driven by the topographical complexity of mountain ranges was logically highlighted. In 2007 there were already limited cases of RCMs being running at extremely high spatial resolutions – 1km to 5km – over limited time periods in order to adequately represent the geographic complexity of mountainous regions (Christensen *et al*., 2007), but the "computational cost" inhibited

their implementation over the simulation lengths normally required for climate modelling. Nothing of this resolution has yet been run over the Himalayan region and the highest resolution runs currently available are 25 to 50 km resolution for this region. Even some the RCM simulations over the Himalaya being performed as part of the CORDEX project (Jacob *et al*., 2012a, Ozturk *et al*., 2012) which will be integrated into the upcoming Fifth Assessment Report (AR5) are being run at 50km resolution.

2.4 Glaciology of the Upper Indus

Glaciology is an important discipline which is integrated into the present work through the need to model glacial behaviour as the interannual storage of precipitation inputs and their release as meltwater runoff.

Mountainous regions are often referred to as the water towers of the world (Viviroli *et al*., 2009). Glaciers fulfil this reservoir function literally, providing long term water storage in solid form. Nevertheless, glacial behaviour is far from static. Glacial dynamics include a constant flux between accumulation and ablation modulated by vertical mass transport. This occurs potentially across kilometres of elevation change by mechanisms including basal sliding and avalanching.

The remote and rugged nature of UIB glaciers – specifically the extreme elevational range, the lack of transportation infrastructure and the distance from large settlements for logistical support – make field investigations almost prohibitively difficult. Thus the number of field studies is more limited than in other regions. This renders the few available ground observations even more valuable.

2.4.1 Landmark glaciological studies by K. Hewitt

Ken Hewitt is another author with an impressive body of work on the Upper Indus, although more focused on glaciology than hydrology. Hewitt's work in the Karakoram and Western Himalaya spans several decades and is considered a definitive reference on the evolution of glaciers in the region.

Young and Hewitt (1993) provided a concise overview of glacial spatial configuration which is, of course, controlled by elevation [Figure 2.2] while detailing their expert view on the imperatives for improved glaciological monitoring. Key distinct zones within a typical Karakoram glacier include debris covered areas often located on glacial tongues near the terminal moraine, additional ablation areas – where meltwater

processes occur when input energy is sufficient – which may be bare ice or crevassed and high altitude accumulation zones. Accumulation zones are separated from the ablation areas by a key feature known as the equilibrium line altitude (ELA). This is the elevation where net annual ablation is balanced by accumulation, yielding a neutral mass balance. Below the ELA the net mass balance is negative in terms of vertical processes – direct precipitation and melting – but mass losses may be balanced by ice transport from above by avalanching and basal sliding. Correspondingly locally positive mass balance conditions above the ELA may be compensated by transfer of ice to lower zones. Thus it is possible for an entire glacier to be effectively in a state of dynamic equilibrium despite steep gradients in precipitation and ablation rates.

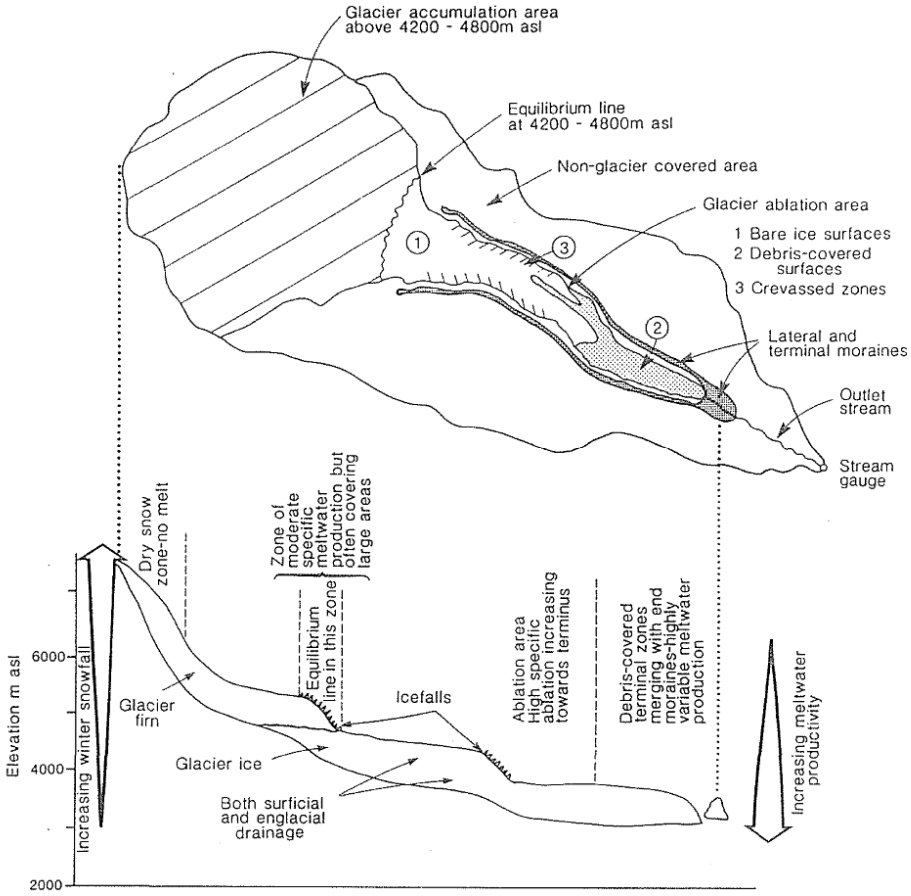

Figure 2.2: Figure 2 of Young & Hewitt (1993) showing the spatial configuration, including vertical profile of a typical Karakoram glacier.

The Biafo glacier is one of the emblematic cryospheric features of the Upper Indus headwaters. Hewitt *et al.* (1989) spent considerable time studying this important glacier. Hewitt *et al.* (1989)'s physical characterisation of the Biafo underlines its immensity. The glacier has a length of 68km and an area of 628km^2. This alone represents 0.09% of the surface area of the full Indus Basin. Hewitt *et al.* (1989) estimated the equilibrium line elevation (ELA) at 4650m. Field investigations using

ground penetrating radar provide an estimated ice thickness of 1400m for the ELA (Hewitt *et al*., 1989). Hewitt *et al*. (1989) estimated the annual mass input at 0.6 km^3 and annual melt at 0.7 km^3. This amount of meltwater alone represents 0.9% of the UIB runoff to the gauging station at Besham. Summer ablation season melt rates were estimated at 50 to 90 mm day^{-1} on clean ice (Hewitt *et al*., 1989). This is the equivalent of 5 to 7 m yr^{-1} at 4000m. Although this may seem substantial, according to Hewitt *et al*. (1989) the value is still inferior to the 9m yr^{-1} estimate reported for the Batura glacier.

In terms of the historical behaviour of the Biafo, records analysed by Hewitt *et al*. (1989) indicate glacial retreat from the early 20th century until 1975, followed by a decade of advance by the glacial tongue. In studying meltwater generation processes on the Biafo, Hewitt *et al*. (1989) found that debris cover suppresses melting, especially below 3600m. According to Hewitt *et al*. (1989) these conditions are widespread throughout the Karakoram and are evidence of glacial "nourishment" by avalanching which entrains debris during vertical movement of snow.

Natural dams leading to glacial outburst floods can present catastrophic if infrequent risks dynamic glacial regime catchments. Hewitt (1982) analysed historical accounts and any available quantitative information from records of outburst flood events. Hewitt (1982) found that, historically, outburst events appeared to group into active/frequent and dormant/quiescent phases. Focussing in detail on probable sediment transport, he also found that a return to a phase of more frequent events, such as observed in the early 20th century, would pose a substantial threat of reducing the operating lifetime of major impounding reservoirs in the Indus basin.

Generally global warming is expected to lead to widespread glacier retreat, and indeed in recent decades glaciers have receded in many regions around the world (Kaser *et al*., 2006). Field investigations in the Karakoram by Hewitt (2005) throughout the 1990s, however, showed evidence of glacial expansion and thickening, albeit primarily restricted to extremely high elevation zones. In his search for causal mechanisms to explain this apparently anomalous behaviour Hewitt (2005) considered a range of potential influences including recent climatic changes influencing mass (precipitation) and energy (temperature) inputs, vertical distribution of precipitation, supraglacial debris and dust, and glacier thermal regimes concluding primarily that the lack of monitoring networks hampers improvements in UIB glaciology.

Hewitt (2005) identified the elevation zone between 4500m and 6000m as the range of net accumulation and net ablation in the zone from 3500m to 4300m, with regional ELAs oscillating near 4500m. He further pointed out that glaciers are complex, sensitive systems and it is not immediately evident whether recent glacier growth is primarily attributable to increases in mass inputs (greater snowfall), decreases in energy inputs (cooling Summer temperatures) or a combination of the two. He concluded that while regional glacial expansion, set against a backdrop of global glacial retreat, might seem reassuring; if enhanced ice storage also indicated reduced runoff from glacial regime catchments, as found by Fowler and Archer (2006), there would be serious negative consequences for downstream population dependent on meltwater for irrigation needs.

Hewitt (2011) has continued to investigate the potential causal mechanisms behind recent glacial growth in the Karakoram. In reviewing the leading candidates for attribution, he also provided a concise summary of the climatic and physiographic characteristics that set the mountainous headwaters of the UIB apart from other glacierised regions of the world:

"In the Karakoram, high mountain processes serve to concentrate climatic conditions for glacierization, notably:

1. Processes that enhance and concentrate snowfall: an orographic condition that generates maximum precipitation in glacier source areas. Inputs of 1000–2000 mm (w.e.) are an order of magnitude greater than at valley weather stations and comparable to ''maritime'' glaciers, despite the extreme continentality. An all-year accumulation regime magnifies the effect.

2. Avalanche concentration: a terrain or ruggedness effect in glacier source areas, of which 60–90% are steep rockwalls. Snowfall, rapidly concentrated down slope, is deposited near or below snowlines, accelerating transformation to glacier ice.

3. Ablation buffering: ice tongues at lower elevations, where temperatures are higher and the ablation season longer, are protected by heavy debris covers.

4. Areas with the greatest ablation losses and water yield: these occur where debris covers are thin or absent but have short ablation seasons and respond sensitively to summer weather. On the one hand, increases in "thin" debris cover here are likely to increase ablation. On the other hand, if ablation seasons get shorter or cloudiness and summer precipitation increase, their impact on ablation will diminish."

2.4.2 Glaciological studies of the Upper Indus Basin by other authors

The Astore catchment in the extreme Western Himalaya is smaller than other Indus tributaries, has a lower fractional glacial cover and its individual glaciers are physically smaller than many found in the Karakoram to the north. Its glaciers thus receive somewhat less attention than others. Nevertheless, Shroder *et al*. (2000)

conducted extensive fieldwork on the Shaigri and Sachen glaciers on the slopes of the Nanga Parbat massif. All three glaciers have extensive debris cover, associated by Shroder *et al*. (2000) with frequent large ice avalanches and rock fall from overlooking slopes. Velocity measurements carried out on the Shaigri glacier, at a middle elevation transect, indicate mean surface velocities of near 12 cm day^{-1} which is equivalent to 43 m $year^{-1}$ of downslope movement.

The Bagrot valley located on the southern slopes of Rakaposhi empties into the Gilgit River between its confluence with the Hunza (upstream) and its junction with the main channel of the Indus. The Bagrot offers a rare level of accessibility relative to other glacierised sections of the UIB. Mayer *et al*. (2010) conducted an extensive field study on the Hinarche glacier, the largest in the Bagrot Valley. The study measured a number of glacier characteristics including debris cover, movement and melt rates. Use of a temporary automatic weather station (AWS) in conjunction with observations from the long-record station at Gilgit allowed calculation of a local air temperature lapse rate, found to be 0.63°C per 100m. Glacial surface velocities were found to vary with elevation, from as low as 14cm day^{-1} (50m $year^{-1}$) to 50cm day^{-1} (190m $year^{-1}$), with an estimated mean velocity of 35cm day^{-1} equivalent to movement of 130m $year^{-1}$. Based on ablation stake measurements and observations by the AWS, a mean degree-day melt factor of 4.08mm $°C^{-1}$ day^{-1} was estimated for the glacial tongue.

Perhaps most interestingly, using remote sensing imagery from the Landsat ETM and ASTER instruments, glacial (areal) extent was found to be unchanged in 2009 compared with 2000 (Mayer *et al*., 2010). This alone does not indicate a neutral mass balance, however, as glacier thinning or thickening could take place even within static boundaries.

Amongst the many debris covered glaciers in the Karakoram, the Baltoro glacier is one of the largest. It begins on the southern slopes of K2 (8611m asl) and neighbouring peaks covering roughly 1500km^2, with a maximum ice-flow length of 62km. Mihalcea *et al*. (2006) analysed observations from a 2004 field campaign, including records from two AWS as well as ablation stakes and data loggers with temperature sensors for measurement of debris thermal properties. The AWS observations indicated an air temperature lapse rate of 0.75°C per 100m.

One of the primary objectives of the study was to investigate the effect of debris cover on ablation rates. The Baltoro observations appear to confirm the assumption that debris cover suppresses ablation: calculated degree-day factors ranged from 7.73 mm

$°C^{-1}$ day^{-1} for 1cm (0.01m) debris thickness to 1.13 mm $°C^{-1}$ day^{-1} for 40cm (0.40m). It must be noted, however, that degree-day factors for bare ice were also highly variable, ranging from 1.3mm $°C^{-1}$ day^{-1} to 5.8mm $°C^{-1}$ day^{-1}. Integrating calculated ablation rates based on degree-day factors estimated for individual elevation bands and extrapolated air temperatures based on the aforementioned lapse rates, Mihalcea *et al*. (2006) estimated a cumulative annual meltwater production volume of $1.3km^3$ from the Baltoro above 3900m asl. Below this elevation, the authors expected ablation to be nearly negligible due to insulation from thick debris cover.

Following on from their field investigations, Mihalcea *et al*. (2008) used imagery from the Advanced Spaceborne Thermal Emission and Reflection Radiometer (ASTER) at 90m horizontal spatial resolution to derive a methodology for the estimation of glacial debris cover thickness from remotely sensed surface temperatures. The method did produce the expected pattern of increasing debris thickness with decreasing elevation, i.e. the thickest debris cover nearest the terminus/snout. The authors noted, however, a number of limitations, including problems with sub-pixel scale heterogeneity from physical features (meltwater ponds, crevasses, etc.) as well as a generalised minor positive bias, i.e. overestimation of debris thickness in absolute terms. Correspondingly, ablation estimates based on derived debris thickness slightly underestimated actual melting rates in pixels with quite thin measured debris cover (less than 3cm).

Remote sensing has multiple potential applications in glaciology. Quincey *et al*. (2009) applied emerging methodologies for "feature-tracking" to spaceborne radar from three generations of satellites to the study of ice flow velocities on the Baltoro Glacier. A sporadic 15-year record – from 1993 to 2008 – of velocity estimates based on remote sensing was compared to limited ground-based – differential global positioning system (DGPS) – observations made during field investigations. Derived spatial patterns of velocity conformed to expectations as minimum velocities were calculated longitudinally at the glacier terminus with increasing movement rates corresponding to increasing elevation below the confluence of major ice streams. Transversally, velocity distribution was found to depend on the selected transect. In some cases minimum velocities were found at the edges of ice extent, while in others the flow was relatively constant across the glacial width.

Temporally, when imagery from Winter was compared to Summer scenes, it was found that velocities were greater in the latter. This tracks with the general

understanding of meltwater enhancement (lubrication) of basal sliding. Calculated velocities were also compared to estimated climate inputs. Precipitation estimates were drawn from both reanalysis (ERA-40) (Uppala *et al*., 2005) and the remote sensing Tropical Rainfall Monitoring Mission (TRMM 3b43v06) data product (Huffman *et al*., 2007). ERA-40 also provided air temperature estimates. The authors found that, in terms of interannual variability, peak velocities appeared to coincide with what were expected to be the largest Winter precipitation accumulations (mass gain) and Summer melt events (meltwater sliding enhancement).

2.4.3 Regional glacial mass balance assessments for the UIB and larger Himalayan region

While the mechanics of processes on individual glaciers must be understood to have an accurate understanding of likely responses to changing climate conditions, water resources assessments tend to focus on larger – catchment and basin – spatial scales. Recently a number of studies have been published examining regional mass balance trends in the Karakoram and wider Himalaya. The findings of these studies appear to lend credence to the earlier findings of Archer and Fowler (2004) and Fowler and Archer (2006) that recent local climate trends show increasing mass (precipitation) inputs and decreasing energy (Summer air temperature) inputs to the UIB glacio-hydrological system.

A quite recent technological development in large (basin) scale water resources assessment is the availability of spaceborne measurements of "gravity anomalies" on the Earth's surface. When large (km^3 scale) volumes of water are displaced by regional changes in groundwater levels or glacial mass balance, the Earth's gravity field changes infinitesimally. These minute changes can be detected by instruments carried aboard satellites launched in the last decade. At present the spatial discrimination (horizontal resolution) of these methods is on the order of hundreds of kilometres, although emerging numerical techniques are helping to refine this. Nevertheless, because the density of water is roughly constant, changes in gravity can be translated into volumetric estimates of continental or basin-scale fluctuations in water storage.

Jacob *et al*. (2012b) used measurements by the Gravity Recovery and Climate Experiment (GRACE) platform to assess global cryospheric – glacier and icecap – contributions to sea level rise over the length of the GRACE observational record. The glaciers of the Himalaya, Karakoram and Hindu Kush (HKH) along with the Pamirs,

Kunlun Shan, Tien Shan, Qilian Shan and Tibetan Plateau, collectively referred to by Jacob *et al*. (2012b) as High Mountain Asia (HMA), showed a limited or mixed mass balance signal. This is in marked comparison to other many global regions where mass losses were clear and unequivocal. Given that their results differed from previous studies (e.g. Matsuo and Heki, 2010), Jacob *et al*. (2012b) explored potential sources of error, such as signal contamination, including groundwater depletion in the irrigated plains adjacent to HMA as well as tectonic processes (crustal uplift), concluding that near neutral mass balance for the available record, with considerable interannual and sub-regional variability, appeared the most probable characterisation of the current HMA cryosphere.

Another recently developed technique operating on a very different spatial scale involves the use of digital elevation models (DEMs) referenced to particular moments in time – effectively three-dimensional snapshots – to determine changes in glacial volume by a processes known as 'surface matching'. Using this method, "stable" features of the images, basically solid rock, are used to correct for distortions and alignment issues. Once the invariant sections of the images have been matched, the variable or dynamic portions of the images, i.e. snow and ice cover, are "differenced" to calculate the changes in elevation on a pixel by pixel basis. These elevation differences are then integrated spatially to calculate volumetric changes over the observed glacial extent. Applying an assumed ice density and the time lag between the images then permits calculation of a rate of mass balance change.

Considering alternate density assumptions of either uniform ice density (900kg m^{-3}) or for differentiated densities for the accumulation (600kg m^{-3}) and ablation (900kg m^{-3}) zones, using imagery from February 2000 (NASA SRTM) and December 2008 (SPOT5), Gardelle *et al*. (2012) found that in the Karakoram regional mass balance was near to zero (the change was less than the uncertainty bounds). This regional apparently stable pattern, however, masked considerable sub-regional heterogeneity. Gardelle *et al*. (2012) noted both thinning (elevation reduction) and thickening (elevation gain) rates of as much as 16m per year, although rapid rates of height change were largely limited to "surge-type" glaciers.

Although the finding of relatively neutral mass balance in the Karakoram does tally with other findings described here (e.g. Hewitt, Jacob *et al*. 2011), the spatial heterogeneity observed using this method, along with the well recognised influence of interannual climate variability and the fact that Gardelle *et al*. (2012) used imagery from

only two dates spanning a period of only 8 years, dampen the significance accorded to these findings. Clearly this is a technique with substantial potential, for example in the calibration and validation of hydrological models, but analysis of imagery spread over a longer time period with more frequent scenes would be required prior to drawing conclusions on longer-term mass balance trends for any region.

Using similar techniques to Gardelle *et al*. (2012), Kääb *et al*. (2012) cast a geographically wider net using satellite laser altimetry from the ICESat platform (for 2003 to 2009) to contrast with the NASA SRTM DEM (for Feb 2000). Kääb *et al*. (2012) then assessed elevation changes for glaciated areas across nearly the entire length of the Himalayan mountain range, from Afghanistan to Bhutan. Seventeen distinct observational "campaigns" (sets of altimetry coverages) were available within the 2003 to 2009 record. These campaigns could effectively be seasonally categorised as Autumn, late Winter/early Spring and early Summer. The Autumn scenes effectively represent annual post-ablation conditions while the Winter scenes potentially show annual maximum accumulation, at least for those sub-regions with substantial precipitation inputs from Winter westerly weather systems. For reasons of excessive variability, Summer scenes were discarded. The remaining Autumn and Winter scenes allowed Kääb *et al*. (2012) to assess the interannual variability and therefore estimate present trends. The resultant findings showed generalised mass loss across the Himalayan mountain arc albeit with substantial sub-regional differences, including a marked difference in the Karakorum which showed near neutral mass balance. Interestingly Kääb *et al*. (2012) found statistically indistinguishable rates of elevation change between "clean ice" and debris covered glacial tongues at equivalent elevations. This finding was mirrored by Gardelle *et al*. (2012). The debris-covered characterisation in the Kääb *et al*. (2012) and Gardelle *et al*. (2012) approaches apparently did not, however, assess debris cover thickness which was shown by Mihalcea *et al*. (2008) to have a substantial impact on the magnitude of the effect debris cover on melt rates, as described in Section 2.4.2.

Scherler *et al*. (2011) also comment on this in their analysis of remotely-sensed frontal changes and surface velocities from glaciers in the greater Himalaya between 2000 and 2008. More than 65% of the monsoon-influenced glaciers were found to be retreating, but heavily debris-covered glaciers, common in the rugged central Himalaya, with stagnant low-gradient terminus regions typically had stable fronts. In contrast, more than 50% of observed glaciers in the westerlies-influenced Karakoram region in the northwestern Himalaya were found to be advancing or stable. Their study showed

that there is no uniform response of Himalayan glaciers to climate change and highlighted the importance of debris cover for understanding glacier retreat, an effect so far neglected in predictions of future water availability.

Focusing on the Karakoram region, but bringing in more data sources than Gardelle *et al*. (2012), Iturrizaga (2011) provided an overview of trends in 20th century and recent glacier fluctuations since the end of the 19th century in the Karakoram Mountains on the basis of field observations carried out in the period of 1992-2006 on 57 glaciers. They used historical documents, such as photographs and travel reports, and air and satellite images. A considerable part of the Karakoram glaciers show signs of glacier retreat, but most of the longer glaciers (> 45 km), such as the Baltoro and Batura glaciers, were rather stationary in the last century. On the whole, the dynamics of the Karakoram glaciers was found to be different from the neighbouring mountain ranges, such as the Himalayas and Tienshan, which are characterized by a dominant glacier retreat.

Another study of glacial volume fluctuations drawing on remote sensing, but only using satellite imagery for glaciated area, was conducted by Bolch *et al*. (2012). They estimated glacial thicknesses based on theoretical relationships between basal driving stress and surface slope. This is a similar approach to that used in the (concurrent) present study (see section 6.6.1) although Bolch *et al*. (2012) used a reference stress (pressure) of 1.5 bar whereas the work described in this thesis assumed a reference stress of 1.0 bar following the value retained by Naz (2011). They also applied an area-volume scaling method to provide alternative estimates to the stress-slope approach. With regards to glacial mass balance trajectories across the Himalayan mountain, the findings of Bolch *et al*. (2012) corroborated the emerging consensus of general mass loss from the Central Himalaya eastward with tentative evidence of fluctuating or positive mass gain in the Karakoram.

Many studies have reported on the region-wide variability in the response of glaciers to global warming, particularly in the Himalayan region. For example, Schmidt and Nusser (2012) report changes in 181 small glaciers in Ladakh, northwest India, between 1969 and 2010, a region between the predominantly receding glaciers of the Central Himalaya and some advancing ice masses of the Karakoram, using a similar approach to Gardelle *et al*. (2012) based on satellite images (Corona, SPOT, Landsat). Glaciated area in this region decreased by about 14% and the average ice front retreat amounts to 125 m from 1969-2010, but with high interannual variability. This suggests

that extrapolation even on a regional scale is problematic and a consideration of differing responses of various glacier types and glacier sizes is of utmost importance, as well as the influence of topography and climate upon glacier response (Scherler *et al*., 2011).

Further widening the geographical focus, Sarikaya *et al*. (2012) used ASTER imagery to assess changes in glacial length are areal extent in the Hindu Kush and a adjacent massifs. This area covers parts of Afghanistan as well as Pakistan. They found contrasting patterns of change within the study area with evidence of retreat in the western and southern Hindu Kush but expansion in the massifs in the Hunza basement.

2.5 Modelling of water resources in the UIB

Hydrological modelling has come to be seen as crucial in water resources assessments both for testing hypotheses regarding system sensitivities and causal linkages as well as for projection of future water availability under various forcing scenarios. Mountainous regions are particularly challenging cases for modelling owing to steep topographic gradients and sparse data availability. Amongst these the UIB is one of the most complex due to its sheer scale and remoteness. Efficiently orienting new modelling work requires a thorough knowledge of achievements and limitations of previous studies.

Additional previous studies on hydrological modelling of projected future UIB climate conditions will be examined separately in detail in Chapter 7, but the salient points are synopsised here in section 2.5.5.

2.5.1 General guidelines for hydrological modelling of mountainous catchments

Burlando *et al*. (2002) in their review paper provided not only a critical survey of existing hydrological modelling methodologies for mountainous catchments but also a roadmap to guide future model development. Focussing on the need to balance physical realism against input data constraints, Burlando *et al*. (2002) enumerated the advantages and drawbacks of conceptual and physically-based approaches to modelling meltwater runoff generation in mountainous catchments. Recognising that hydrological modelling of catchments with extensive cryosphere fraction comprises three phases – snow accumulation and redistribution, ablation and meltwater routing – Burlando *et al*. (2002) stressed the need for “internal validation” of modelled variables beyond runoff

alone. In terms of data limitations at appropriated scales, Burlando *et al*. (2002) suggested that "nested" climate models could potentially provide realistic estimates of topographically forced input variables such as wind speed and direction while remote sensing imagery could provide validation data including snow cover and albedo. Despite acknowledging the utility of spatial data sets from numerical sources, they also stressed the need to carry out as much field-based data collection as possible in order to provide calibration and ground-truthing for the distributed data sources. In terms of long-term sensitivity to climate variable and change, they endorsed mass balance evaluations driven with synthetic time-series of temperature and precipitation from stochastic models.

With regards to future model development, Burlando *et al*. (2002) outlined their vision for an "ideal" model for mountain hydrology, asserting that such a model should be spatially distributed – a priori rasterised – while conceptually-based, albeit structured to represent physical processes via methods appropriate to the available input data. Burlando *et al*. (2002)'s ideal mountain model would also be computationally efficient – i.e. not overly processor intensive – in order to permit "extensive simulations", including large numbers of model runs to test parameter sensitivity and long simulations to probabilistically assess potential outcomes of future climate scenarios. Furthermore, the ideal model should be able to be transferred between catchments with relative ease thanks to parameterisations which can be derived from readily available catchment descriptors (topography, etc). There are, however, contradictory opinions. Kult *et al.* (2012) consider that conceptual models, including those require explicit input of snow cover data such as the Snowmelt Runoff Model (SRM) (Martinec *et al.*, 2007), are more appropriate for the Upper Indus judging that physically-based models are not viable for the UIB due to the lack of a dense network of field observations. On balance the present work considers Burlando *et al*'s (2002) conclusions more rigorous and substantive compared to the relatively simplistic if not facile approach advocated by Kult *et al.* (2012).

In keeping with Burlando *et al*. (2002)'s directive that thorough understanding of physical processes must inform development of ablation/meltwater generation models, of particular relevance is the detailed study by Marks and Dozier (1992) of snow surface energy fluxes at two sites in a test catchment in the Sierra Nevada mountains of California. This site is particularly pertinent to the present work because its latitude, near 36°N, is quite similar to that of the UIB. Collecting observations over a complete accumulation and ablation sequence – from November 1985 to July 1986 –

they individually assessed each component of the energy balance – net solar radiation, net thermal radiation, sensible heat flux, latent heat flux, ground (conductive) heat flux and advection (from rain on snow). They found that outside the ablation season energy exchange at the snow surface was dominated by turbulent energy exchange, i.e. latent heat flux (from sublimation) and sensible heat flux (between the surface and air), but that during peak melting periods net solar radiation was the governing factor. Considering the snow season as a whole, they found that net turbulent heat exchange would be limited because the direction of energy transfer of the two components – away from the ground for latent heat, toward the ground for sensible heat – was opposed due to the 0°C upper threshold of snow surface temperature governing the sign of sensible heat flux. They further found that ground (conductive) heat exchange and advection were negligible in comparison with other fluxes. Both the monthly absolute values and relative contributions of individual energy balance components reported by Marks and Dozier (1992) can provide an element of internal validation, as recommended by Burlando *et al*. (2002), for physically-oriented conceptual models which estimate one or more of the energy balance components. Coarse resolution values of energy components from meteorological reanalysis or regional climate models (RCMs) can provide a third element to this triangle.

2.5.2 Hydrological modelling techniques applied to the specific simulation challenges of the UIB

Two of the key challenges in hydrological modelling studies are: i) the specification of inputs for which there is a high level of uncertainty, chiefly precipitation; and ii) the approach taken to model calibration and validation.

1. Spatial distribution of precipitation in an environment dominated by orographic effects: Accurate representation of the spatial and temporal variability of the mass input (precipitation) to the hydrological system is one of the most challenging yet essential tasks in modelling mountain catchments. Point based observations can provide meaningful quantitative indicators of temporal variability (Archer and Fowler 2008) but do not represent mean catchment conditions in terms of the absolute magnitude as most stations are located at low elevations on valley floors. In other words although, due to elevation differences, the annual precipitation and mean temperature measured by local observations are not of the same magnitude as the values of the catchment spatial

means, the patterns of anomalies – i.e. wet years, dry years, cold years, warm years – do indicate larger-scale conditions in the basin.

In the UIB this is especially true of meteorological stations located in relatively arid valley floors below the slopes where substantial orographically enhanced precipitation occurs. At present there is a lack of detailed physically-based information available in the UIB with which to characterise vertical precipitation gradients and reduce related uncertainty.

Immerzeel *et al*. (2012) took an interesting approach in attempting to derive the orographic precipitation gradient of the Hunza basin. Using a glacial inventory from the International Centre for Integrated Mountain Development (ICIMOD), elevation data from the ASTER Global Digital Elevation Map (GDEM) (Krieger *et al*., 2011) and three years (2001 to 2003) of available high elevation AWS meteorological data, they applied a degree-day method to calculate potential ablation across a range of elevation bands. Then, assuming a neutral glacial mass balance for the simulated period, Immerzeel *et al*. (2012) applied spatial interpolation techniques based on a reference elevation field to determine the precipitation coefficients necessary to provide the require mass input.

The study acknowledged that substantial uncertainty persisted, in large part linked to the choice of degree-day factor values for "clean" and debris-covered ice and hence the magnitude of meltwater generated by energy inputs. Using a degree-day method, energy inputs are indexed by air temperatures which are spatially extrapolated from point observations using lapse rates. In this case Immerzeel *et al*. (2012) selected a lapse rate of 0.68°C per 100m. Nevertheless, the approach is an interesting one, the results of which will be compared to the findings of the present study in Chapter 6. In summary, Immerzeel *et al*. (2012) estimated a mean catchment annual precipitation of 688 mm $year^{-1}$ for the selected period. This represents a coefficient of 2.6 with regards to the mean of the absolute observations by the three AWS used.

2. Choice of method for calibration and validation in catchment with complex land surface processes: The question of what constitutes an optimal approach to hydrological model calibration is contentious regardless of the geographical context. The problems of data scarcity for model construction, model forcing and model evaluation are accentuated in mountainous regions such as the UIB. Pelicciotti *et al*. (2012) undertook a rigorous exploration of potential calibration strategies in the context of data

constraints faced in the UIB. Using a meltwater generation model based on an "enhanced temperature index method" – intended as a compromise between a simple degree-day approach and a fully resolved surface energy balance – Pellicciotti *et al.* (2012) assessed the effects of using both different combinations of validation data – runoff observations only, remotely sensed snow covered area (SCA) data, or both together – as well as a selection of model performance criteria – Nash-Sutcliffe efficiency, logarithmic Nash-Sutcliffe efficiency, volume error, coefficient of determination and snow cover efficiency – on validated model behaviour. They found that the use of multiple validation data sets as well as multiple performance criteria during an automated calibration procedure improved model performance scores for all criteria. Pellicciotti *et al.* (2012) also postulated the applicability to the UIB of results from other mountainous regions which indicated that short record simulation of the full energy balance using locally observed secondary meteorological variables – radiative fluxes, wind speed, humidity – would improve characterisation of catchment melt processes and thus improve calibration of hydrological models based on simpler methods, e.g. simple degree-day, or enhanced temperature index.

Pelicciotti *et al*'s (2012) work, while concurrent with this study, by its advocacy of using non-hydrological variables – e.g. SCA – as additional constraints on model calibration and validation supports the methodology, described in Chapter 6 of this thesis, used here to tune and assess the performance of the VICwCDiP model. In the case of the present study, the decision to use multiple – and relatively independent – variables as performance metrics was motivated by the desire to avoid finding the "right answer for the wrong reasons", i.e. to avoid producing the expected hydrological cycle by systematic misrepresentation of meteorological inputs or land surface processes, especially cryosphere dynamics, or some combination thereof.

2.5.3 Melt-runoff modelling by snow cover as a proxy for mass balance

Pellicciotti *et al.* (2012)'s use of SCA in model validation raises the pertinent subject of the use of remote sensing data products in snowmelt hydrology. Tahir *et al.* (2011a) analysed snow covered area (SCA) data for the Hunza basin from the Moderate Resolution Imaging Spectrometer (MODIS); specifically the MOD10a2 8-day aggregate maximum snow cover extent (Hall *et al.*, 2001). Tahir *et al.* (2011a) assessed the MODIS SCA for short term (decadal) trends as well as correlation to observed river discharge at the catchment outlet (Dainyor Bridge). In terms of annual cycles, Tahir *et*

al. (2011a) found that MODIS SCA in Hunza was inversely proportional to both air temperature and river discharge. In other words, as would be expected, increasing temperature leads to snow cover ablation and increased river flows. As for the detection of trends in the available MODIS record, the intrinsic climatic variability (noise) of the UIB complicates the determination of underlying climate tendencies (signal). Tahir *et al*. (2011a) subdivided the Hunza catchment into three elevation zones and separately assessed SCA for Winter (Nov to Feb) and Summer (June to Sept) finding statistically significant trends – using Mann Kendall's tau – only in high elevation Winter SCA. This may be a result of the trend of increasing Winter precipitation in recent decades as reported by Archer and Fowler (2004).

While Pelliciotti *et al*. (2012)'s suggestion to use SCA for model validation has considerable merit, other approaches are possible. Some snowmelt hydrological models use SCA as input data rather than calculating it as an output. Tahir *et al*. (2011b), building on his analysis of MODIS SCA in the Hunza basin, used one such model, the Snowmelt Runoff Model (SRM) to simulate present and potential future runoff in the catchment. One advantage of the SRM approach is that it effectively renders precipitation observations redundant for meltwater dominated catchments. This is achieved by assigning a calibrated runoff yield for SCA per degree-day. As such, Tahir *et al*. (2011b) did not need to orographically correct either the local point-based precipitation observations or the spatial precipitation estimations from the APHRODITE dataset (Yatagai *et al*., 2009) which uses a purely distance-weighted (not physically-based) interpolation method but draws only on low elevation observations in the UIB [Figure 2.3]. Furthermore, Tahir *et al*. (2011b) did not account for glaciers other than to apply a higher degree-day factor to the elevation band with nearly permanent snow cover.

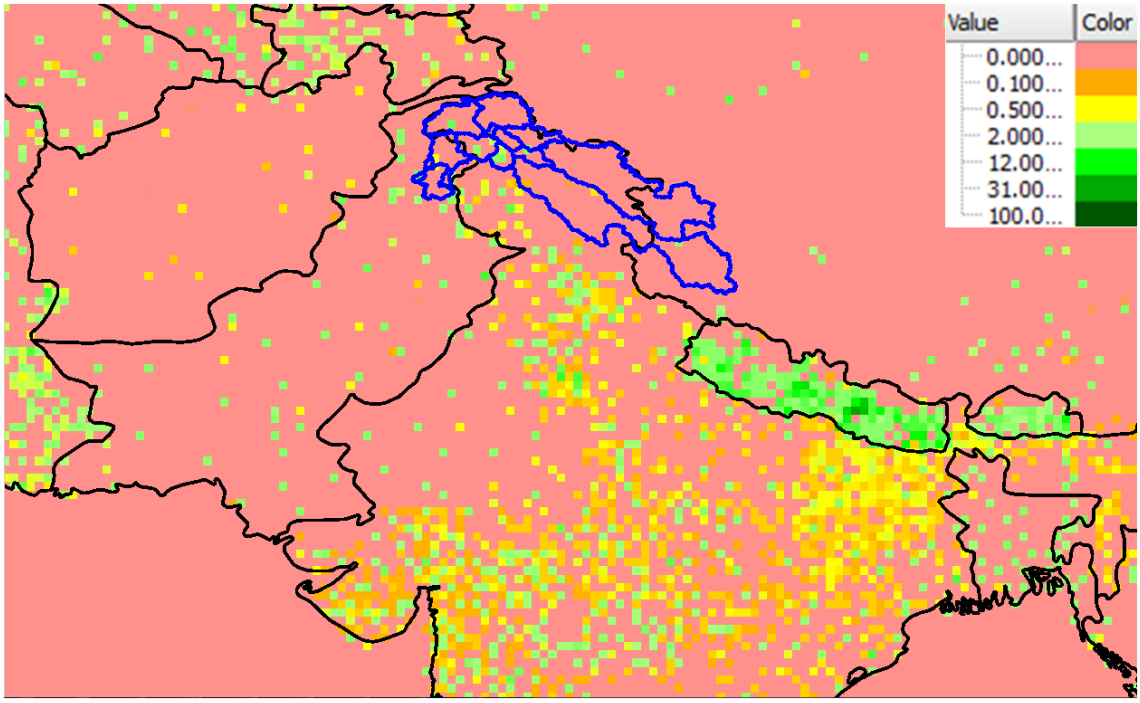

Figure 2.3: APHRODITE period mean "pixel station density ratio" from 1961 to 1989. Colour scale is in the upper right corner. Higher numerical values indicate greater spatial density of observations. National boundaries are black lines. Catchment boundaries of gauged Indus tributaries are blue lines.

The most obvious limitation of SRM is that it requires predefined SCA scenarios to be able to simulate future conditions, rather than calculating snow cover changes based on the interplay of future temperature and precipitation. To his credit, Tahir *et al.* (2011b) recognised this uncertainty in both the sign and magnitude of change in both air temperature and SCA. The choice of combinations of temperature and SCA change are somewhat puzzling however, given the observed relationship found in Tahir *et al.* (2011a), as temperature and SCA increases are paired in some scenarios. Because the calibrated SCA yield is not then revised for the scenario simulations, scenarios with increased temperature and stable or increasing SCA inevitably project increased runoff. Thus, the drawback of SRM is that it does not explicitly require conservation of mass. As a result predicted runoff may not reflect realistic catchment inputs from precipitation.

Another study which used SRM for modelling water resources availability under changed climate conditions, albeit with a grander spatial scale, was carried out by Immerzeel *et al.* (2010) who attempted to assess the implications of climate change on water resources in five major Asian river basins: the Indus, Ganges, Brahmaputra, Yangzte and Yellow rivers. The study was based on satellite-derived precipitation estimates from the TRMM platform, but these were critically not corrected for bias resulting from underestimation of orographically-enhanced precipitation. A further explanation of the potential and limitations of the TRMM dataset will be provided later

in this chapter as well as in Chapter 3. In summary, however, underestimation of orographically-enhanced precipitation in the UIB results in substantial misrepresentation of total catchment accumulation. Thus, unsurprisingly, Immerzeel *et al*. (2010) concluded that, at the present, mass balance in the Indus basin is substantially negative. In terms of future projections, the study utilised future climate projections from a "mini-ensemble" of five global climate models (GCMs) – CCMA-CGCM3, GFDL-CM2, MPIM-ECHAM5, NIES-MIROC3 and UKMO-HadGEM1 – under the SRES A1B emissions scenario to force two separate SRM glacier scenarios, one a "best guess" approximation of likely areal changes and another "worst case" scenario with complete deglacierisation. In general, Immerzeel *et al*. (2010) projected moderate decreases in water availability with reduced meltwater from glaciers which was partly compensated for by increased precipitation inputs. However, the reported results presented only projected period mean conditions and did not explore the effects of interannual variability.

Commendably, Immerzeel *et al*. (2010) addressed the crucial issue of food security by a relating upstream runoff to downstream irrigation demand by a simple method referred to as the "normalised melt index" (NMI). Projected changes in water availability under the future climate scenarios were translated into impacts on crop yields via the NMI. While addressing the issue of potential impacts of climate change on human nutrition is laudable, the neglect of interannual variability, specifically drought years, implies that the projected effects of climate change on continental food security – threatened caloric sufficiency for 4.5% of the study are population – found by this study may, in fact, be seriously underestimated.

2.5.4 Surface energy balance and glacial mass balance modelling

Immerzeel *et al*. (2011) adopted a more sophisticated approach for the (much smaller scale) assessment of potential climate change impacts on the hydrology of the Langtang catchment in Nepal. The approach used to model the Langtang is in many ways quite similar to the independently developed one that will be presented in Chapters 6 and 7 of this thesis. The underlying glacial mechanics are simulated with variations on the equations – relating glacial thickness and assumed bed-slope to basal driving stress and downslope displacement – used in the present work. The extremely high spatial resolution (90m) used to simulate the relatively small (360km^2) Langtang catchment, however, allows for inter-cell ice mass transfers. This degree of spatial detail

is impressive, but may be prohibitive in computing requirements for larger catchments. In further demonstrations of model complexity, Immerzeel *et al*. (2011) also implemented sub-glacial hydrological storage and refined degree-day factors on a grid cell basis to reflect slope aspect using an approach previously applied in the Langtang by Konz *et al*. (2007).

Scenarios of future climate were derived using bias correction – mean and standard deviation – of transient runs of the five GCMs used in the continental scale study (Immerzeel *et al*., 2010). The resultant scenarios show a mean annual warming of 0.06°C $year^{-1}$ and an annual precipitation increase of 1.9 mm $year^{-1}$. The transient GCM outputs allow the model to simulate a relatively gradual rate of deglaciation – rather than a block response to abrupt shifts in temperature which are imposed by the use of time slice climate scenarios – but the projected future glacial extent at the end of the study period (2100) still shows a drastic reduction in the cryosphere: between 60% and 90% reduction in glacial area and 70% to 95% reduction in glacial volume.

Despite the striking projected cryospheric response to climate change, the projected hydrological response, at least in terms of mean flow, is much less alarming. Interestingly, the projected increases in future runoff despite the deglaciation, which is more than compensated for by increased mean precipitation, foreshadow some of the (scenario-dependent) findings of the present work (Chapter 7). In contrast to the tributaries of the Upper Indus and the catchments of the Karakoram and Western Himalaya, however, the precipitation seasonality in the Langtang is concurrent with the hydrological cycle so there is no projected shift in the timing of peak flows.

Of course not all climate change impact assessments simulate physical catchments. Rees and Collins (2006) performed a comparison study to test the differences in the response of two otherwise identical synthetic catchments based on differences in regional climate regimes. They designed their synthetic catchments as a series of nested sub-catchments. The smallest of these contained a 50km^2 glacier, the only perennial ice pack in the pseudo-basin. The climate forcing data, from the Climate Research Unit (CRU) 0.5° gridded data set (New *et al*., 2000), were specified as if the "western" catchment was centred on the location of the Batura glacier in the Hunza basin and the "eastern" catchment was centred on the Laptang glacier in Nepal. The hypsometry of the synthetic catchments was specified as an amalgamation of the real terrain in these two locations. Climate data were adjusted for temperature lapse rates and orographic precipitation based on studies by previous authors including Young and

Hewitt (1993). Input precipitation was assigned as rainfall or snow depending on the time-step air temperature.

The glacial volume was broken into elevation bands, with each filled by a regular prism with a wedge-shaped cross section. Initial thicknesses were assigned as a function of the position along the glacier length, with a maximum at the mid-point and identical minima at the peak and terminus/snout. Ice ablation was only allowed when snowpack in an elevation band was exhausted; this approach will also be used in this thesis. Modelled glacial area was allowed to vary by holding geometric relationship of the cross-section constant.

The model (pseudo)calibration indicated that glacial mass balance was moderately net negative under present climate conditions. Future climate was modelled as a transient trajectory with precipitation held constant but temperature increased at an annual rate of 0.06°C $year^{-1}$. Hence, with constant mass input and increasing energy input, the glacial mass balance could only become increasingly negative with time. This approach resulted in the total deglaciation of the "western" catchment less than 100 years after simulation initialisation while the "eastern" catchment was projected to become ice-free at 120 years after simulation start. River discharge under the future scenario was projected to initially increase as glacial melt rates compensated glacial retreat but eventually a point was reached when glacial area was no longer sufficient and discharge decreased until the catchment became completely ice-free. Thereafter, the only change in discharge came from gradually increasing evapotranspiration due to temperature rises.

This study is noteworthy as it was one of the earliest to explicitly model glacial ice mass and to accommodate variable glaciated area. The choice of climate input data and the manner in which climate data was specified, i.e. lacking in realistic climate variability, limit the realism of the study however. Furthermore, the acceptance of net negative mass balance for the "western" catchment is questionable based on numerous studies (e.g. Gardelle *et al*., 2012, Hewitt, 2005) cited above of "real-world" Karakoram glaciers. Nevertheless, it did set an ambitious benchmark for glacio-hydrological modelling studies. The hydrological modelling – incorporating cryospheric dynamics – described in this thesis (Chapters 6 and 7) aims to further develop modelling of variable glacial volumes as follows:

- by permitting either net positive or negative mass balance by simulation of glacial accumulation, through snowpack density simulation, as well as ablation by degree-day meltwater generation modelling.
- by accounting for climatic variability through the use of synthetic time-series of present (control) climate and projected future climate scenarios generated using stochastic modelling (RainSim and CRU-Weather Generator).

2.5.5 Context of previous studies of potential climate change impacts on UIB hydrology

This thesis is not the first work to explore the potential hydrological implications of climate change for the Upper Indus and its tributary catchments. Three of the most notable publications are Akhtar *et al*. (2008), Immerzeel *et al*. (2008) and Bocchiola *et al*. (2011). The three studies were relatively uniform in their primary conclusions:

- Under scenarios with unchanged glaciated area the three studies found increasing runoff due to increased mass (precipitation) and energy (temperature) inputs increasing rainfall and snowmelt contributions to runoff as well as well as increased glacial melt.
- Under scenarios with moderate deglaciation the reductions in glacial meltwater generation are roughly compensated for by increased rainfall and snowmelt from increased precipitation.
- Under scenarios specifying total glacial loss the increases in rainfall and snowmelt from increased precipitation were not able to offset the reductions in glacial meltwater.

While these studies have the merit of having attempted to address urgent research questions in terms of both their geoscientific and socio-economic importance, they also have substantial methodological limitations. Chief among these shortcomings, in addition to drawing upon only a single scenario of future climate for their simulations, is the reliance by all three studies upon predefined, static conditions of glaciated area. Inextricably linked to this assumption of static glaciated area is effectively infinite (inexhaustible) glacial mass, such that glacial melt is constrained only by available energy inputs which are quantified (indexed) by air temperature using degree-day melt methods. As such, the uncertainty in future glacial mass balance is not fully explored, nor is the realism of the predefined scenario of changes in glacial area assessed.

As described in Chapter 6, the VICwCDiP model developed in this thesis also uses a degree-day index approach for calculating glacial melt, but, in addition to energy constraints, meltwater generation is also limited by explicit accounting of the available glacial mass (volume). While, as discussed in Chapter 6, the VICwCDiP model used in this study itself has notable limitations regarding uncertainties in the calibrated orographic gradients and melt degree-day factors as well as, in its present form, a lack of horizontal spatial variability, it does provide substantial advances on the previous studies cited above.

2.6 Summary

This chapter has provided an overview of key literature related to the research themes addressed in this thesis. Logically hydrological and climatological studies of the geographical area of interest are uppermost in the list of priority literature. The ground-breaking – and much cited – work by advisors of this thesis, Archer and Fowler, provides a foundation for understanding the links between local climate and hydrology. In light of the extensive glacial cover in the UIB, it was also important to survey relevant glaciological literature. This included both research conducted by field measurements as well as studies based on remote sensing data. Given the objectives of this study, it was also imperative to review hydrological modelling studies to date to identify strengths and weaknesses. These would be extremely helpful in guiding development of the VICwCDiP model used in this study.

Chapter 3: Present Hydro-climatology of the Upper Indus Basin

3.1 Abstract

The Upper Indus Basin (UIB) is a highly complex hydro-climatic system. The atmospheric and land surface processes that generate the runoff nourishing the Indus and its tributaries exhibit tremendous temporal and spatial variation. These variations are governed primarily by two factors: i) the annual cycle of incoming solar (shortwave) radiation which in turn drives annual cycles of air and surface temperature; and ii) the cooling of air temperature with increasing elevation (atmospheric lapse rate). Together these two phenomena shape the spatial and temporal distribution of solid precipitation as snow and ice. They also determine the timing of snow cover accumulation and ablation.

Additional factors further complicating hydrological processes in the UIB are the timing, magnitude and distribution of precipitation and atmospheric humidity (as relative humidity & cloud cover). Precipitation is obviously the controlling mass input of the hydrological cycle. However, there is substantial scientific uncertainty regarding the amount of annual precipitation as well as its spatial distribution within the UIB (see Archer and Fowler, 2004, for example). Humidity is also important in determining eventual runoff because it influences the amount of mass input "lost" to evapotranspiration (Thornthwaite, 1948), in warm zones & seasons, and sublimation (Jackson and Prowse, 2009) in cold zones & seasons. In addition, cloud cover modulates runoff generation by forcing the surface energy balance (Chen *et al.,* 2000). Cloud cover can act as both a positive (warming) force by trapping outgoing (thermal or longwave) radiation – primarily at night – as well as, in the daytime, a negative (cooling) force by blocking incoming (shortwave) radiation, most notably in the summer months (Shupe and Intrieri, 2004).

This chapter presents in detail the mean annual cycles and measures of variability in these and other important climatic parameters. Drawing on a wide range of data, these are shown for hydro-climatic variables and processes for point locations, spatial aggregates (catchment means) and as gridded maps. The unprecedented level of detail presented here provides significant improvement upon previously published research – both by adapting previous methodologies (e.g. Archer 2003, Archer 2004, etc.) to assimilate new data sources, and for the first time, by fully taking into account

the vertical dimension including the distribution of area with elevation – in quantifying the underlying processes which drive the UIB hydro-climatology.

3.2 Introduction

In its simplest expression, the terrestrial water cycle consists of water falling as rain then running downhill into a river and ultimately the sea. The added complication in the UIB is that water most often falls as snow, particularly as most precipitation is in winter months, sometimes on glaciers, with melting delayed until summer months, before flowing down through the valleys and onward toward the sea. In other words, an understanding of the local surface energy balance is crucial to characterising the hydrological cycle of the UIB.

The simplest conceptual model of the surface energy balance describes how incoming (shortwave) solar radiation is in part reflected and in part absorbed by the atmosphere and the surface, and then how the portion absorbed is redistributed, as sensible and latent heat fluxes, and re-emitted as outgoing thermal (longwave) radiation. A basic conceptual schematic, simplified from a more complex, quantitative version in Kiehl and Trenberth (1997, their Fig. 7), is provided in Figure 3.001.

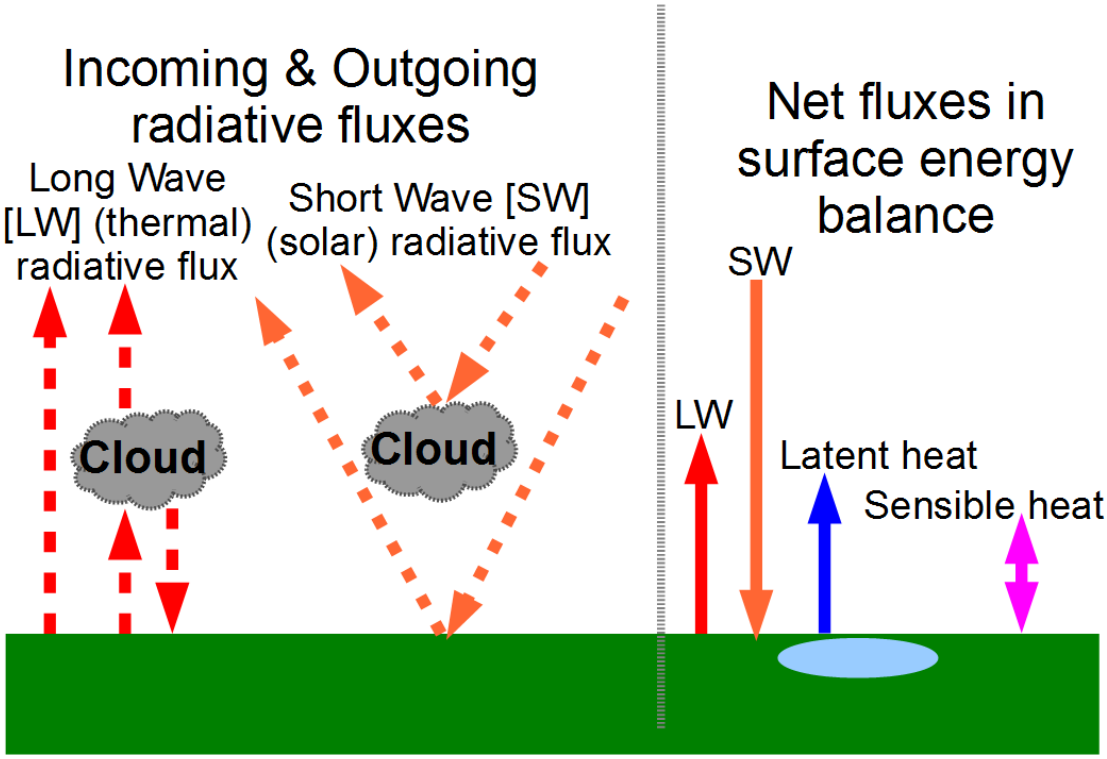

Figure 3.001: Basic conceptualisation of surface energy balance fluxes, simplified from *Figure 7* in Kiehl and Trenberth (2007).

The energy input, incoming solar radiation, is in part reflected by clouds prior to reaching the earth's surface. A very small fraction is also absorbed directly by the atmosphere. The remaining radiative flux is in part absorbed and in part reflected by the surface. The fraction of the incoming energy which is reflected is determined by the properties of the surface and is quantified as a parameter known as "albedo". Values for albedo thus range from 0 to 1 (0% to 100%). Highly reflective surfaces, for example snow, have high albedos. Dark, absorbtive surfaces, such as asphalt or dark rocks, have low albedos. Estimates of surface albedo for the UIB derived from satellite imagery (remote sensing) will be presented later in this chapter.

The amount of incoming solar radiation (at the top of the atmosphere [TOA], independent of cloud reflection) at a given point on the earth's surface is determined by its latitude and the position of the earth in its orbit around the sun Fasullo and Trenberth (2008b). A point located on the equator will have maximum solar radiation (most direct insolation , lowest solar zenith angle) and experience no solar component to its annual cycle, i.e. effectively identical TOA insolation from one day to the next. A point located near to one of the poles will have minimum mean solar radiation (most oblique insolation, highest solar zenith angle) and experience a very pronounced annual cycle with very little TOA insolation in winter and considerably more in summer Fasullo and Trenberth (2008a). The UIB, covering latitudes from roughly 31N latitude to 37N latitude, experiences considerable variation in incoming solar radiation over the course of the annual cycle. This variation drives the annual cycle of the surface energy balance and hence the hydrological cycle.

The energy absorbed by the surface is redistributed in one of three mechanisms. Firstly, depending on the relative temperatures of the surface and the air immediately above (Sade 2011), energy can be redistributed in what is termed the sensible heat flux. This flux can operate in either direction (the surface emitting or absorbing) and in general will follow regular patterns in the diurnal and annual cycles. Secondly, absorbed energy is also re-emitted as (thermal) "blackbody radiation" with rate depending on the surface temperature according to the Stefan-Boltzmann law (Delany and Semmer, 1998).

In hydrological terms, the most important radiative flux is the third type, known as the "latent heat flux". The latent heat flux is the energy that is transferred through a state change in (a mass of) water. In the UIB the latent heat flux includes both energy serving to melt ice and snow (solid to liquid phase change) and that used for

evapotranspiration (liquid to vapour phase change). The latent heat flux is modulated by a variety of factors specific to each phase change. Some of these will be examined in detail later in this chapter.

Further complicating the surface energy balance in the UIB is its immense vertical topographic (elevation) range. This is due to the atmospheric lapse rate which causes air to cool with an increase in elevation (altitude). The air temperature interacts with water in all three of its phase states. With atmospheric water vapour, the lapse rate cooling of air temperature results in greater cloud frequency over higher elevation sections of the catchment. The air temperature further determines whether precipitation will fall as liquid (rain) or solid (snow). Hence rain is rare at high elevations, even in summer, and snow is rare in the lower valleys, even in winter. Once snow begins to accumulate, air temperature strongly influences whether or not it will melt. This shapes the surface albedo because snow is more reflective then the soil and (sparse) vegetation in the UIB. This link between albedo and air temperature becomes a feedback loop in the surface energy balance driving the amount of incoming solar radiation which is absorbed and available for meltwater generation. For these reasons an understanding of the vertical dimension is critical to characterising the hydro-climatology of the UIB. As such, vertical profiles of key parameters will be presented later in this chapter. This distinctive vertical and seasonal variation is presented in Figure 3.002 and Table 3.01.

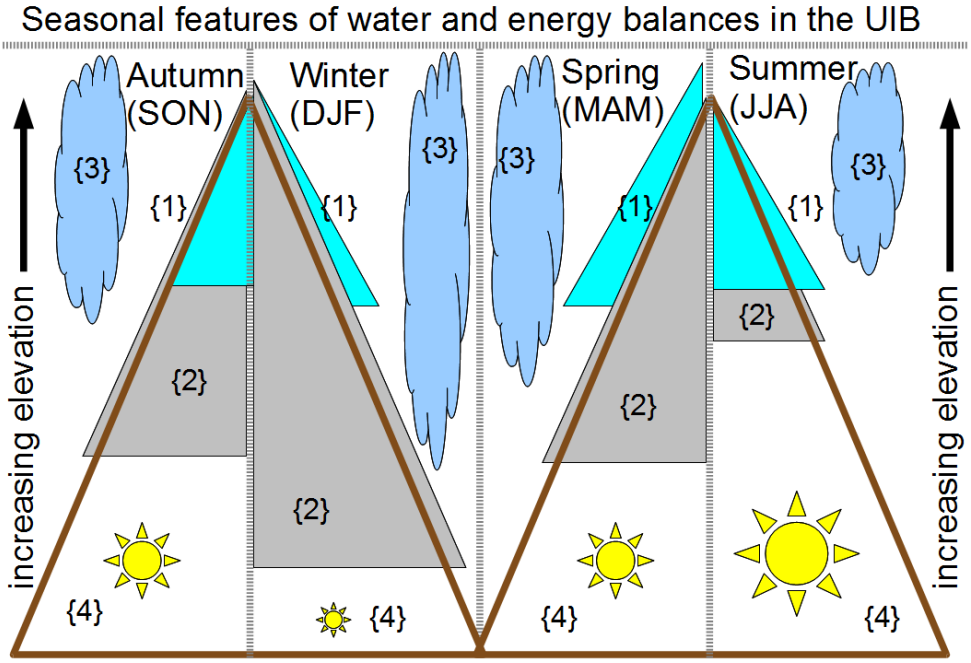

Figure 3.002: Conceptual illustration of annual cycle of key seasonally-varying vertically-driven atmospheric and land surface processes in the UIB portrayed in terms of vertical profiles along mountain slopes. Numbers in { } brackets refer to Table 3.01 for which this figure serves as a visual aid. nb: The offsets between the grey and blue triangles representing cryospheric components and the brown lines representing ground surface conceptually illustrates seasonally varying depth and mass during phases of accumulation and ablation.

Season // Component	Autumn (SON)	Winter (DJF)	Spring (MAM)	Summer (JJA)
{1} Glaciers / perennial icepack	Ablation ceases, annual mass recovery begins on bare ice	Annual mass recovery continues	Annual maximum accumulation; ablation of tongues begins	Strong ablation below Tmin 0C isotherm
{2} Seasonal snowpack	Fresh seasonal snowpack begins to accumulate	Maximum (or near maximum) accumulation	Snowpack ripens and ablation develops	Snowpack ablates completely (in normal years)
{3} Clouds & Humidity	Moderate cloud and humidity	Maximum cloud and humidity	Moderate cloud and humidity	Limited cloud and humidity
{4} Radiation & Albedo	Moderate incoming SW; Significant area of bare earth (lower albedo)	Minimum incoming SW; Surface very reflective = maximum albedo	Moderate incoming SW; limited area of bare earth (high albedo)	Maximum incoming SW; increased latent heat flux; minimum albedo
Hydrological state	Recession of summer melt/flood via baseflow	Maximum water storage; little to no melt, baseflow only	Melt of from low to mid-elevation snowpack	Maximum melt and evaporation; maximum runoff

Table 3.01: Description of key seasonally-varying vertically-driven atmospheric and surface process characteristics. Numbers in { } brackets refer to conceptual illustration provided in Figure 3.002.

Figure 3.003 provides an overview of the core hydrological contributing area of the UIB as well as the location of key infrastructure and hydro-climatological observing stations.

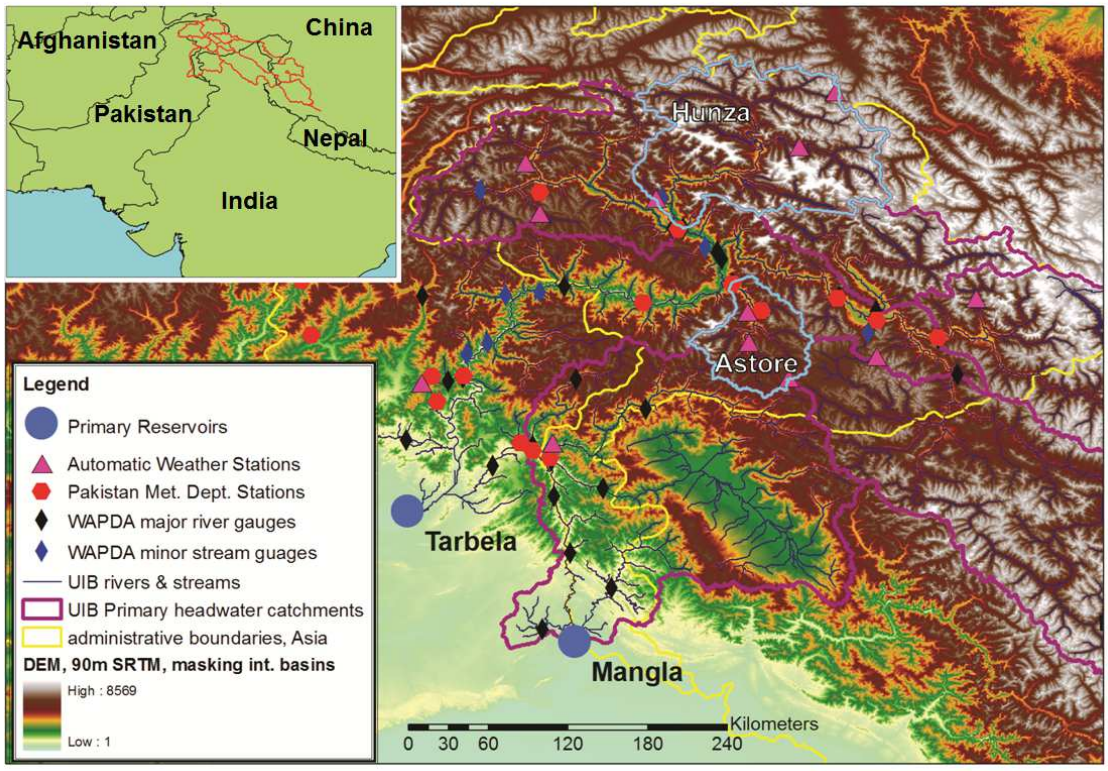

Figure 3.003 Map of the core Upper Indus contributing area and key infrastructure.

The scale of vertical range and variation within the UIB has few analogues elsewhere in the world. Elevation ranges from below 1000 m where the river emerges on the plains at the two major controlling reservoirs of Tarbela and Mangla (Figure

3.003) to several mountain peaks above 8000 m. As shown in Figure 3.004, the mean elevation of the catchment to Besham, the gauging station upstream from the Tarbela Dam, is above 4000 m. This means that the greater part of the catchment surface is thrust up into the middle troposphere (ground level atmospheric pressures from 700 mb to 500 mb). The vertical red lines in Figure 3.004 represent atmospheric pressure levels often used by meteorologists as key heights for summary of circulation and weather processes (e.g. Trenberth 1995). The behaviour of climate variables, such as diurnal variations in specific and relative humidity, wind strength and direction and cloud formation, are significantly different at these pressure levels than near to the ground surface. In the UIB, however, these pressure levels are in fact 'near ground surface level'. Given that the aforementioned parameters play key roles in precipitation processes and diurnal energy balance, an understanding of the impact of the unique range of elevation of the UIB on their variation is essential.

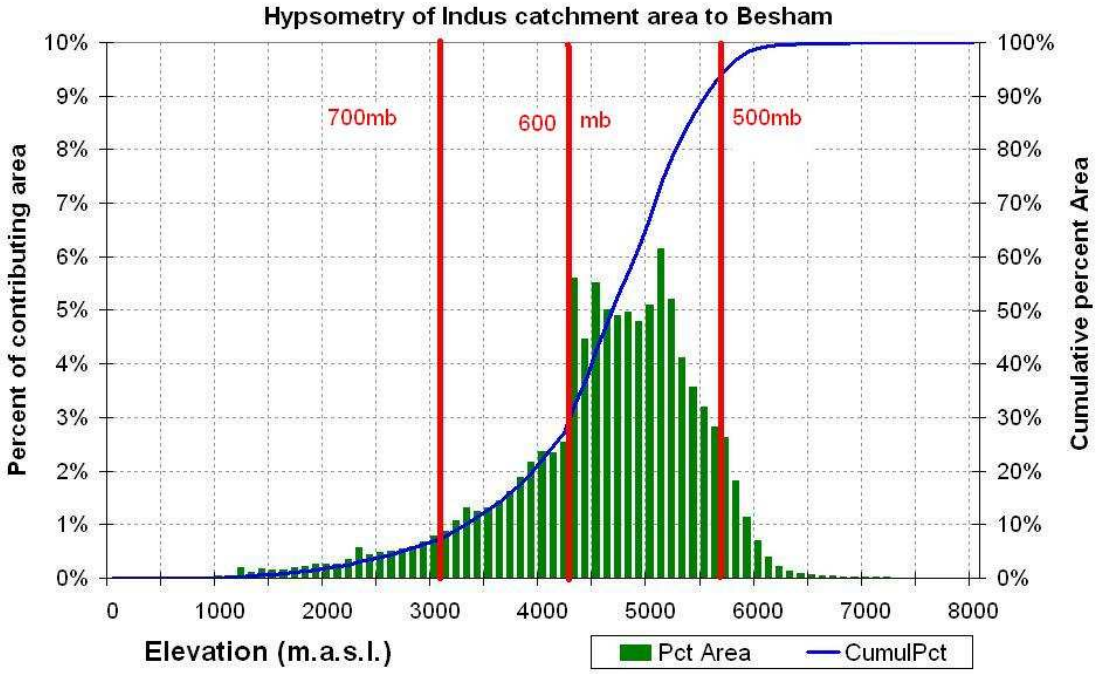

Figure 3.004 Hypsometry of the Upper Indus to Besham showing percentage of area in each elevation band (Pct Area) and cumulative percentage (Cumul Pct) below or level with the given elevation. Also shown are the approximate altitudes of key atmospheric pressure levels hence indicating the fraction of catchment exposed to widely reported wind patterns.

3.3 Relevant data sources for characterisation of UIB hydro-climatology

Given the physiographic and climatological complexity of the region, and above all the potential impacts on human development of hydrological variability, it is important to analyse all reliable, relevant sources of hydro-climatic data in order to characterise these earth systems as comprehensively and coherently as possible. A

substantial challenge at present for local water resources management initiatives in the UIB is the availability of hydro-climatological data at the appropriate scales. This situation is accentuated by the complex geopolitical situation in the region, and especially the tensions and suspicions over finite water resources, as a result of which data providers are hesitant to offer international researchers access to observations, especially of river discharge.

In the interests of clarity, it is worthwhile to affirm the usage of a number of terms in the context of the present work. Unless otherwise noted, in keeping with standard climatological notation, seasons are defined as three-month periods beginning on the first calendar day of the first month and ending on the last calendar day of the third month as follows: i) Winter is from December to February (DJF), ii) Spring is from March to May (MAM); iii) Summer is from June to August (JJA); iv) Autumn is from September to November (SON). For the purposes of UIB hydro-climatology, it is useful to define two additional periods: a) "warm months/season" from April to September (AMJJAS) also known in South Asia as "Kharif"; b) "cold months/season" from October to March (ONDJFM) also known locally as "Rabi".

In the figures presented in the follow sections showing the locations of point based observations, the station markers are overlaid on the elevations provided by a digital elevation model (DEM) derived from the NASA Shuttle Radar Topography Mission 90m horizontal resolution (SRTM90) with post-processing funded the Consultative Group for International Agricultural Research (CGIAR) (Jarvis *et al.* 2008). The post-processing involved void-filling (Reuter *et al.* 2007) and was of sufficient effectiveness to enable the SRTM90 DEM to be used to delineate the catchment boundaries and stream courses of the UIB. The vectorised version of these boundaries and stream links are also overlain on the aforementioned figures.

3.3.1 River discharge gauging by WAPDA

The Pakistan Water and Power Development Authority (WAPDA) operates several river gauging stations in the UIB on the main channel of the Indus and its primary tributaries. Most often these stations consist of a staff (level) gauge from which discharge is extrapolated by means of a rating curve. These gauges are located at sites where current profiling is possible – either beneath bridges or where a small pulley-driven cable basket system has been erected – in order to periodically check and update the rating curve.

Figure 3.005 shows the locations of the primary WAPDA gauge records analysed in this study. The bulk of this data was originally acquired by Archer (2003) while providing expert technical support to WAPDA on behalf of the German aid agency GTZ under the auspices of the UK Volunteer Service Organisation (VSO). Subsequent partial, incremental updates have been acquired informally through personal contacts with Pakistani scientists and academics working both nationally and abroad.

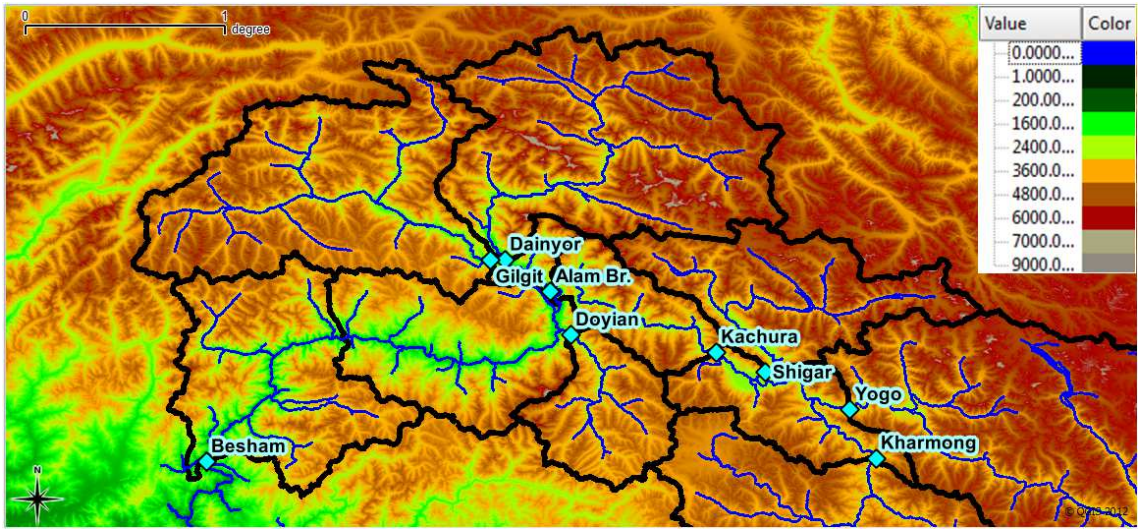

Figure 3.005 Location of primary UIB discharge gauging stations operated by WAPDA shown against a background of surface elevation (m asl) from the NASA SRTM90 DEM.

Logically all of these gauges are located within the administrative jurisdiction of WAPDA (i.e. within Pakistan). Figure 3.006 shows the contributing areas to each of these gauges. Because significant portions of the Upper Indus tributary catchments are the subject of geopolitical disputes, the location of borders on maps of the area can be contentious. From a hydrological standpoint the situation is somewhat simpler. While Pakistan, India and China all claim various portions of the headwater catchments, most of the key contributing areas in terms of runoff generation are presently controlled by Pakistan. Table 3.02 gives the name of the tributary measured by each gauge as well as the length of record available to this project. As alluded to above, river discharge is a highly sensitive issue in regional politics, and gaining access to observations through official channels is extremely difficult. Of particular note, at present, the river gauging data available to this project is only at the spatial scale of tributary river basins and has little temporal overlap with existing validated spatial climate data products derived from remote sensing imagery: Astore river 2000–2008; Gilgit river 2000–2008; Hunza river 2001–2004 , 2008; Indus main channel at Besham Qila 2000–2002.

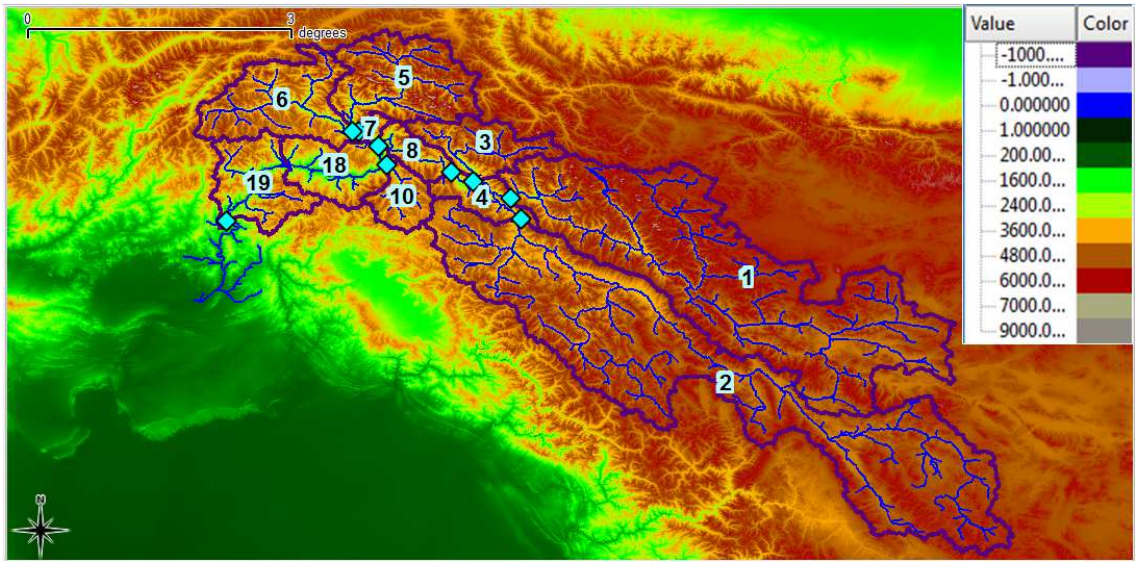

Figure 3.006 Incremental contributing area to primary WAPDA discharge gauges. Label numbers refer to gauging stations listed in Table 3.02. Units on the map refer to topographic surface provide by SRTM90 DEM (m asl).

River	***Gauging Station***	***Label number in Figure 3.006***	***Catchment area (km^2)***	***Record length & range***
Shyok	Yogo	**1**	65,025	35 years; 1973 to 1997, 1999 to 2008
Indus	Kharmong	**2**	72,500	16 years; 1982 to 1997
Shigar	Shigar	**3**	6,650	12 years; 1985 to 1997
Indus	Kachura	**4**	146,100	39 years; 1970 to 2008
Hunza	Dainyor Bridge	**5**	13,925	40 years; 1966 to 2004, 2008
Gilgit	Gilgit Town	**6**	12,800	41 years; 1961 to 1972, 1980 to 2008
Gilgit	Alam Bridge	**7**	27,525	39 years; 1966 to 1967, 1969 to 1998, 2000 to 2001, 2004 to 2008
Indus	Partab Bridge	**8**	176,775	47 years; 1962 to 2008
Astore	Doyian	**10**	3,750	35 years; 1974 to 2008
Indus	Shatial Bridge	**18**	187,275	15 years; 1983 to 1997
Indus	Besham (Qila)	**19**	196,425	32 years; 1969 to 1997, 2000 to 2002

Table 3.02 Primary discharge gauge record length and range (historical period). Catchment areas are based on Archer (2003). nb: There remains some uncertainty regarding the precise contribution area of the large arid upstream subcatchments (Skyok, Indus above Kharmong) due to the presence of closed basins (salt lakes) in this relatively flat subregion. Data frequency prior to 2000 are daily, from 200 onwards are monthly. Periods listed are complete at the relevant timestep.

In terms of data quality, taken at face value one might consider WAPDA river gauging data dubious given the physical conditions – highly irregular and or shifting channel/bed geometry, difficult access for proper velocity profiling and limited metadata, and lack of information regarding updating/maintenance of rating curves – associated with these observations. Even recognising this caveat, however, several of the WAPDA gauging records show both very good internal consistency and coherent response (correlation) to climate drivers as will be demonstrated in this chapter. This

quality was first recognised by Archer (2003), and the present work only serves to reinforce this finding.

3.3.2 PMD long-record meteorological observing stations

Sparse, but spatially representative, point observations of temperature and precipitation are available from long record meteorological stations operated by the Pakistan Meteorological Department (PMD). The relatively low station spatial coverage density, however, leaves doubt as to whether these data adequately represents the heterogeneities which may occur at smaller spatial scales. The primary data available from these stations are daily precipitation and daily minimum and maximum temperature, although some additional climate parameters are monitored as well. Some of these stations have been operating for several decades and provide invaluable insight into the long term climate variability of the region (e.g. Archer and Fowler, 2004; Fowler and Archer, 2006). The locations of the gauges analysed for this work are shown in Figure 3.007. The records were obtained from the work of Archer and Fowler (2004) and Fowler and Archer (2006) and updated to near present-day using online data from the PMD website (for precipitation or extended piecemeal via good-will agreements with scientists and academics of Pakistani origin (for near-surface air temperature). Archer and Fowler validated the initial dataset and checked it for inconsistencies (2004). The same methodology was applied to the updated records.

We therefore have access to temperature observations up to 31 December 2007 and precipitation observations to 31 August 2010 for primary long record stations. Table 3.03 gives the elevation (in meters above sea level) as well as details on the availability (record length, etc.) of key parameters for each station. These stations are located in settlements (towns) in valley bottoms of the UIB tributary catchments. They are thus situated well below the catchment mean elevation. Despite this limitation, they provide a self-consistent record, which, although not measuring the absolute areal mean conditions, still yields a very important representation of interannual variability in climate parameters.

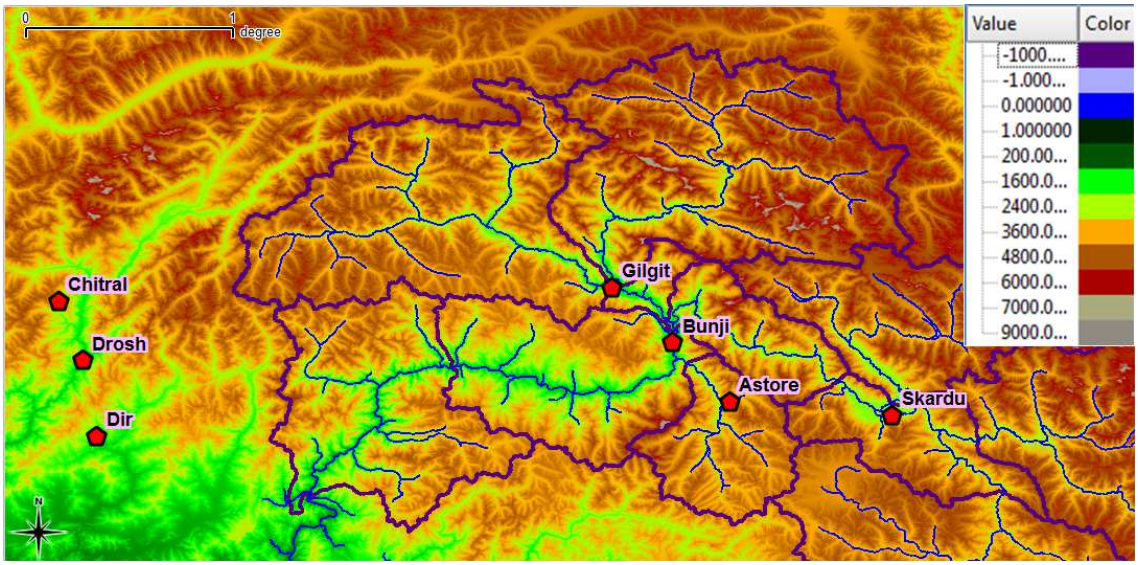

Figure 3.007 PMD primary long-record meteorological stations located in permanent settlements (towns) in valley bottoms. Boundaries shown are for primary WAPDA gauged tributaries. Units on the map refer to topographic surface provide by SRTM90 DEM (m asl).

Station	***Elevation (m asl)***	***Precipitation record***	***Temperature record***	***Additional variables***
Gilgit	1460	Daily, 1958 to 2010	Daily, 1958 to 2007	n/a
Skardu	2210	Daily, 1958 to 2010	Daily, 1958 to 2007	n/a
Astore	2394	Daily, 1953 to 2010,	Daily, 1981 to 1999 Monthly, 1962 to 2007	Daily: cloud (oktas) & relative humidity 1981 to 1999
Bunji	1372	Daily, 1993 to 2007 Monthly, 1952 to 2007	Daily, 1993 to 2007 Monthly, 1961 to 2007	n/a
Chitral	1499	Daily, 1993 to 2007 Monthly, 1965 to 1991, 1993 to 2007	Daily, 1993 to 2007 Monthly, 1965 to 2007	n/a
Drosh	1465	Daily, 1993 to 2007 Monthly, 1950 to 2007	Daily, 1993 to 2007 Monthly, 1961 to 2007	n/a
Dir	1425	Daily, 1993 to 2007 Monthly, 1967 to 2007	Daily, 1993 to 2007 Monthly, 1967 to 2007	n/a

Table 3.03 Primary Pakistan Meteorological Department (PMD) long-record stations in the UIB

3.3.3 AWS stations operated by WAPDA

In the mid-1990s a network of automatic weather stations (AWS) were installed at significant elevations by the "Snow and Ice Hydrology Project" initiative of WAPDA. Since that time the AWS have operated continuously (i.e. to the present day). The AWS were installed at as high an elevation as logistically feasible, although generally still significantly below the catchment mean elevation and certainly below key zones of accumulation and melt both for seasonal snowfall (nival) and perennial ice (glacial) catchment regimes. Even so, the existence of these records potentially provides very useful data for improving the vertical profiling of key parameters (including the

development of realistic lapse rates) and for validating other data sources (e.g. remote sensing from satellite imagery or numerical simulation results from meteorological reanalysis or regional climate models [RCMs]). Unfortunately, only the first few years of such records (1994–1998, which does not overlap with the observational record of recent NASA remote sensing satellite platforms) have been made available for use in this study, so their impact here is limited. Figure 3.008 shows the location of the AWS records analysed in this study. Table 3.04 provides details of the unit elevation, available record length and variables analysed for each AWS.

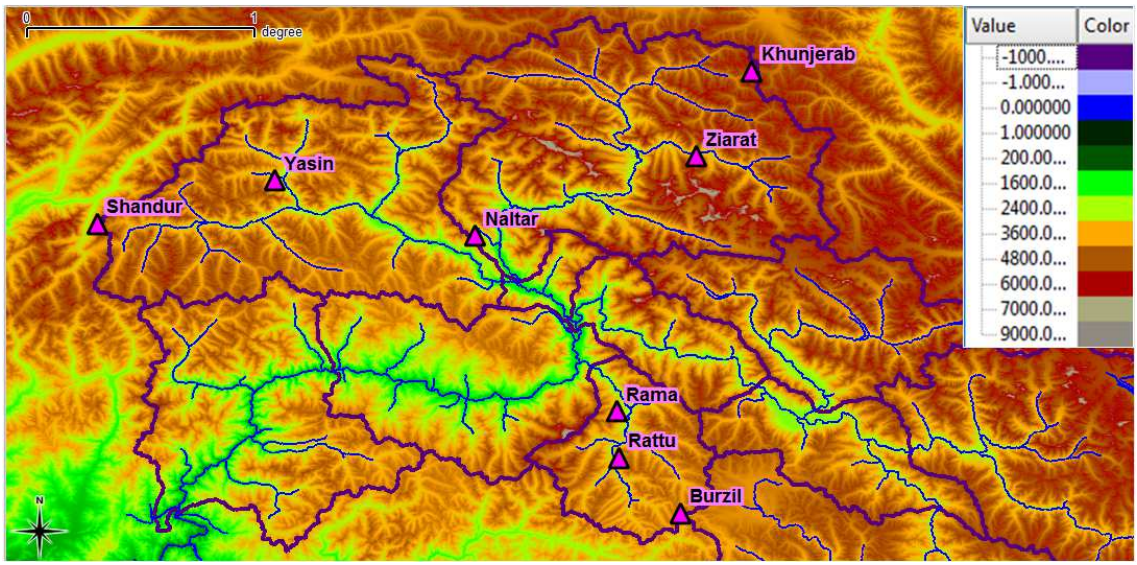

Figure 3.008 Automatic Weather Stations (AWS) in the UIB operated by WAPDA. Boundaries shown are for primary WAPDA gauged tributaries. Units on the map refer to topographic surface provide by SRTM90 DEM (m asl).

Station	***Elevation (m asl)***	***Data availability***	***Variables analysed***
Khunjerab	4733	06/1994 to 11/2000	Relative Humidity (min & max)
Shandur	3719	07/1994 to 11/2000	Relative Humidity (min & max)
Yasin	3353	06/1994 to 03/1999	Precipitation, Temperature
Naltar	2810	06/1994 to 03/1999	Precipitation, Temperature
Ziarat	3688	06/1994 to 03/1999	Precipitation, Temperature
Rama	3140	06/1994 to 08/1998	Precipitation, Temperature
Rattu	2920	06/1994 to 08/1998	Precipitation, Temperature
Burzil	4101	06/1994 to 08/1998	Precipitation, Temperature

Table 3.04 AWS stations in the UIB operated by WAPDA used in this study with variables analysed. All data are at the daily time-step.

Figure 3.009 shows a composite of the three types of available point observations – i) river discharge gauging, ii) long-record meteorological stations, and iii) AWS high-elevation units – in relation to the contributing area within the UIB.

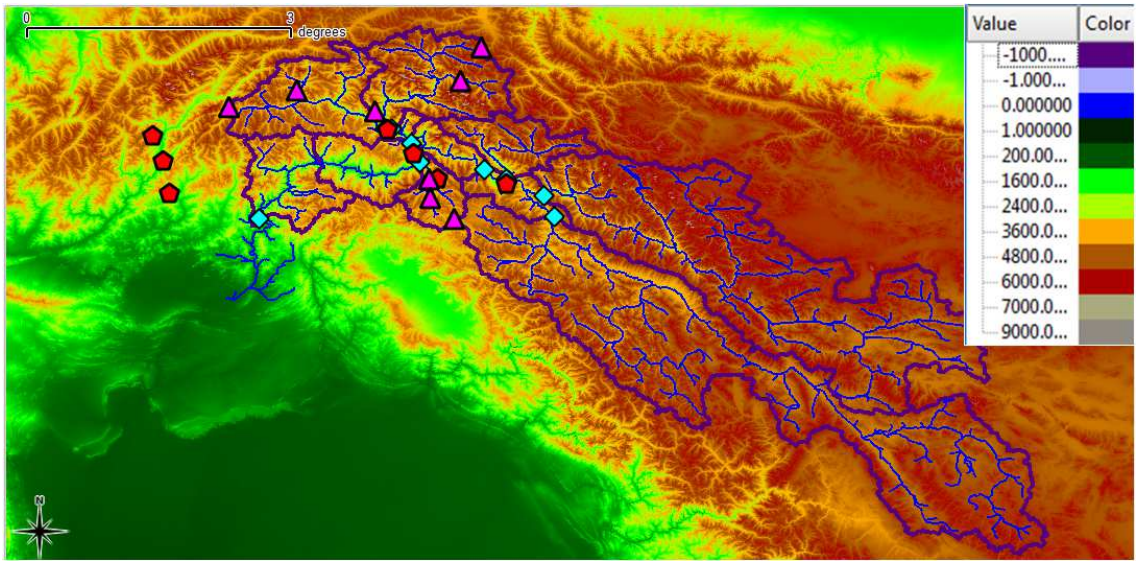

Figure 3.009 Composite of three types of local (point) hydroclimate observation locations.. Boundaries shown are for primary WAPDA gauged tributaries. Units on the map refer to topographic surface provide by SRTM90 DEM (m asl).

3.3.4 Numerical meteorological simulation generalities

To overcome these ground-based data limitations, the adequacy of spatial remotely sensed climate data products to act as analogues for point meteorological observations and the scalability in the climate drivers of hydrological variability between tributary basins and village/valley catchments will be tested. Numerical meteorological simulation is best known from its use in weather forecasting, technically referred to as numerical weather prediction (NWP). Beyond this familiar application, use of gridded data produced by numerical simulation of atmospheric circulation has become widespread in hydro-climate studies both of present conditions and potential future scenarios.

One form of numerical meteorological simulation is a direct outgrowth of the development of models for NWP. In order to initialise forecast models, input values of existing conditions must be provided from a range of data sources. These data sources may include ground-based point observations, climate parameter estimations from satellite imagery (remote sensing), vertical profiles of the atmosphere from radiosondes and of the ocean near-surface from instrumented buoys, as well as observations made by airplanes and ships (Bengtsson and Shukla 1988, Brown 1987). The process of synthesising this data into a coherent, usable format for a given model is known as data assimilation. Over the decades which NWP has been in use a tremendous amount of input data has thus been assimilated.

The data – in spatiotemporal resolution and type of observations – and the models using them to generate forecasts have of course evolved significantly over the

years. Meteorological reanalysis projects have been undertaken to reassess the complete available historical record of assimilated data using the most modern and sophisticated numerical models of atmospheric circulation. The models are run in an "analysis and short-term forecasting" mode to synthesise a coherent representation of the state of the atmosphere and land surface for key climatological parameters (Paolino *et al.* 1995). The completed sequence of outputs from the series of model runs over the timeframe of the reanalysis project forms a continuous time series of estimated (fitted) values globally for the modelled parameters.

3.3.5 ERA-40 Meteorological Reanalysis Data

ERA-40 was a major reanalysis carried out by the European Centre for Medium-Range Weather Forecasting (ECMWF) (Uppala *et al.* 2005). It covers the period from 01/09/1957 to 31/08/2002. Hence, despite its name, ERA-40 provides a continuous 45-year time-series for its modelled variables/parameters. The model was run on a roughly 125km horizontal spacing at a 6-hour time-step. A complete archive of post-processed analysis data are available at a lower spatial resolution (2.5x2.5 decimal degrees) from an ECMWF data server (http://data.ecmwf.int) (Kallberg *et al.*, 2007).

Given the time period covered and the variety of data-sources assimilated, the input data are non-homogeneous. The ERA-40 reanalysis effectively spans three distinct periods of meteorological observation: i) the pre-satellite era of the 1950's and 1960's; ii) the early satellite era in the 1970s to mid-1980s; and, iii) the satellite-intensive era beginning in the late 1980s (Uppala *et al.* 2005). This observational asymmetry ranging from the relatively "data-poor" for early years and "data-rich" period toward the end of the record undoubtedly skews the shape of the resultant time-series because the overall (sum) balance of biases from the individual biases particular to each type observation will change from decade to decade (Sugahara *et al.* 2012).

In addition to the inhomogeneity of the assimilated data, the ERA-40 reanalysis, as with any numerical meteorological simulation, presents biases due to the specific numerical formulations used to represent meteorological processes. These formulations are often referred to as "model physics". One such well-known bias in ERA-40 relates to overestimates of precipitation, especially over tropical regions. Difficulties with the model initialisation, also referred to as model "spin up", results in excess precipitation (Betts *et al.* 2003). Despite this weakness, relative patterns in spatial (wet versus dry areas) variability and seasonal anomalies may be well represented.

Figure 3.010 shows the location of the ERA-40 grid cells analysed in this study and the indicative names applied to them. Table 3.05 also gives the cell centre coordinates in latitude and longitude and the modelled orographic height for each cell.

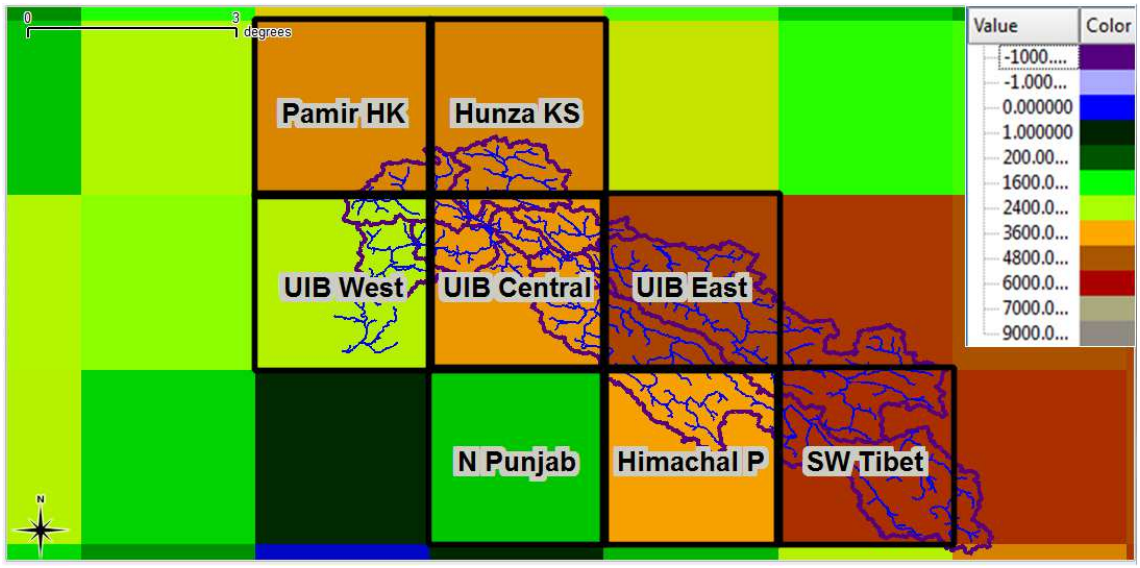

Figure 3.010 Position and relative orography of ERA40 reanalysis grid cells used for analysis. Grid cells are coloured according to orographic height (m asl). Labels correspond to the naming system applied throughout this thesis.

Project grid cell name	Latitude of cell centre (decimal degrees)	Longitude of cell centre (decimal degrees)	Orographic Height assigned by ERA-40 (m)
Pamir HK	37.5	72.5	4102
Hunza KS	37.5	75.0	4157
UIB West	35.0	72.5	2572
UIB Central	35.0	75.0	3855
UIB East	35.0	77.5	5033
N Punjab	32.5	75.0	1131
Himachal P	32.5	77.5	3711
SW Tibet	32.5	80.0	5311

Table 3.05 Position and modelled orography (m asl) of ERA40 reanalysis grid cells used for analysis.

3.3.6 ERA-Interim Meteorological Reanalysis Data

ERA-Interim is a more recent and on-going reanalysis project also by ECMWF (Dee *et al*. 2011). The model is run at an approximately 80km horizontal spatial resolution. Post-processed archived analysis results were initially made available at a grid resolution of 1.5 decimal degrees, but later released at "full resolution" (0.75 decimal degrees). Data is available publicly via the ECMWF data server (see URL address above). Its record covers the period from 01/01/1979 to present (analysed to 31/07/2011). As ERA-Interim covers the "modern satellite" epoch, the assimilated data is substantially less heterogeneous than that used by ERA-40. It was intended to tackle a number of shortcomings in ERA-40 primarily linked to the data assimilation process.

Unsurprisingly, most measures (moisture transport, energy balance) show superior performance by ERA-Interim compared to ERA-40 (Berrisford *et al*. 2011, Betts *et al.* 2009).

Figure 3.011 shows the location of ERA-Interim grid cells analysed in this study and the indicative names applied to them. The selected grid cells were initially chosen prior to the public release by ECMWF of ERA-Interim data at "full resolution" (0.75 decimal degrees). Thus the initial analyses were carried out with coarser (aggregated) outputs (1.50 decimal degrees) and the selected cells at this resolution provided a rough coverage of the core 'runoff generation' areas within the UIB as well as adjacent areas with contrasting (sub-) climates for comparison purposes. When, during the course of the present project, "full resolution" data was made publically available, a decision was taken to retain the grid cells at the cell-centres of the initial selection, thus preserving the desired survey of regional sub-climates. Table 3.06 also gives the cell centre coordinates in latitude and longitude and the modelled orographic height for each cell.

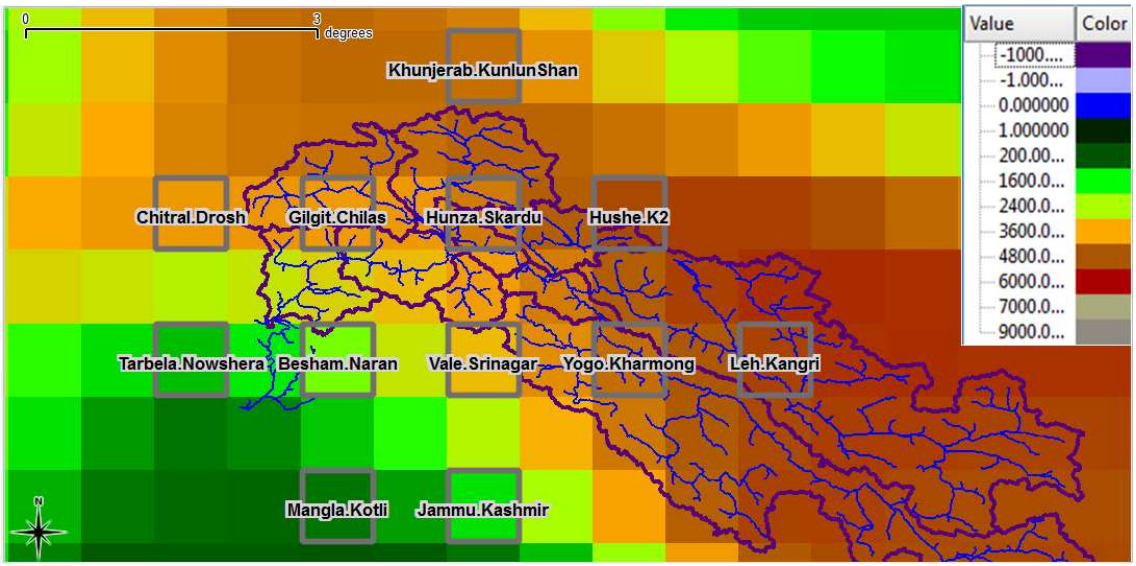

Figure 3.011 Position and relative orography of ERA-Interim reanalysis grid cells used for analysis. Grid cells are coloured according to orographic height (m asl).

Project grid cell designation (name)	Latitude of cell centre (decimal degrees)	Longitude of cell centre (decimal degrees)	(static) Orographic Height ERA-Interim (m)
Chitral.Drosh	36.0	72.0	3832
Tarbela.Nowshera	34.5	72.0	1060
Gilgit.Chilas	36.0	73.5	3809
Besham.Naran	34.5	73.5	2153
Mangla.Kotli	33.0	73.5	480
Khunjerab.KunlunShan	37.5	75.0	4412
Hunza.Skardu	36.0	75.0	4274
Vale.Srinagar	34.5	75.0	3358
Jammu.Kashmir	33.0	75.0	1375
Hushe.K2	36.0	76.5	4953
Yogo.Kharmong	34.5	76.5	4445
Leh.Kangri	34.5	78.0	5061

Table 3.06 Position and modelled orography (m asl) of ERA-Interim grid cells used for analysis.

Figure 3.012 shows the spatial domains of the ERA-40 and ERA-Interim cells combined with the location of the local (point) observations.

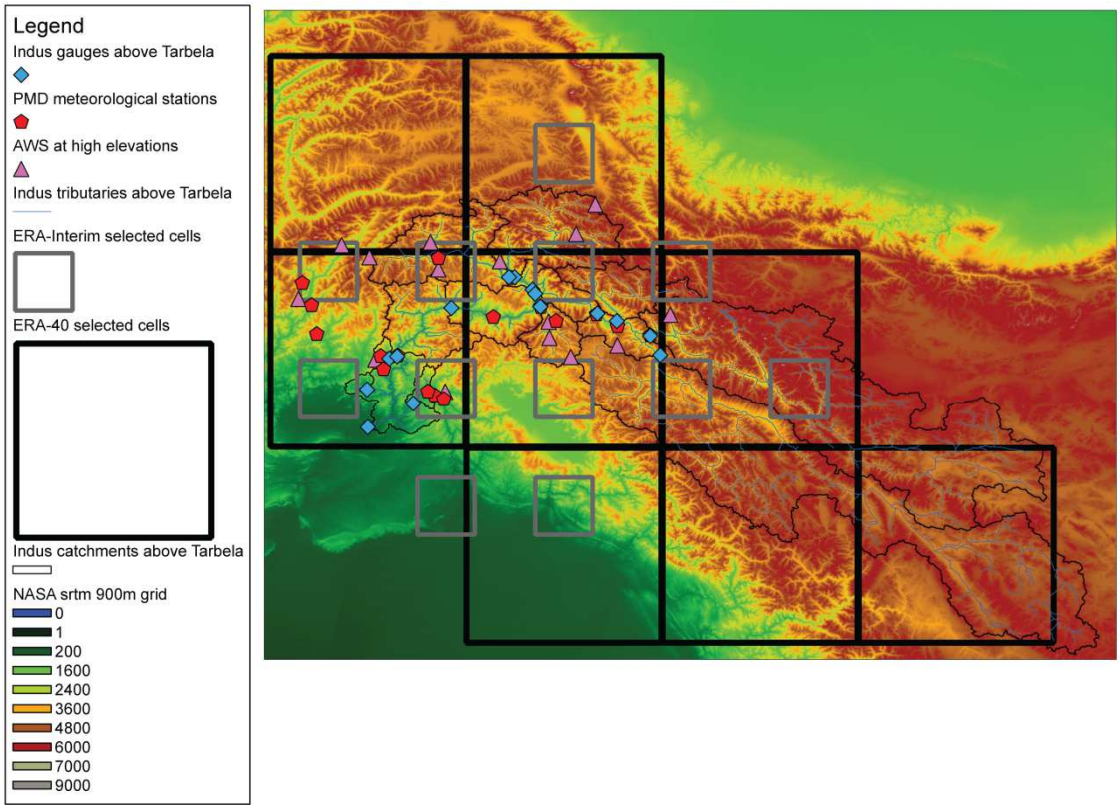

Figure 3.012 Overlay of locations/spatial domains of hydroclimate data analysed.

3.3.7 PRECIS RCM

Regional climate models (RCMs) have primarily been used to dynamically downscale the global projections of future climate from global climate models (GCMs) to specific regions or locations. Because the numerical formulations (model physics)

used in RCMs are similar to those used for reanalysis, they can also be used to downscale the reanalysis results to provide a finer resolution output which better incorporates the regional topography and other local factors.

One popular RCM used primarily to study developing regions is the PRECIS ("Providing Regional Climates for Impacts Studies") model (Jones *et al*. 2004) from the Hadley Centre of the UK Met Office. PRECIS is essentially the HadRM3P RCM (Jones *et al*. 1995) with simplified user controls and pre-packaged boundary (forcing) conditions. PRECIS has been used in the present work for the downscaling of future climate scenarios (see Chapter 5) as well as to examine at a higher-resolution the output from the ERA-40 reanalysis. The PRECIS results here are from simulations at a 0.50 decimal degree resolution. These simulations were carried out by the Global Change Impact Studies Centre (GCISC) in Islamabad, Pakistan (Islam *et al.* 2009).

The 12 grid cells within the UIB domain selected for analysis overlie the meteorological stations as shown in Figures 3.013 and 3.014. Figure 3.013 shows the cell locations with indicative names and relative elevations. Figure 3.014 shows the cell locations with respect to the local (point) observations.

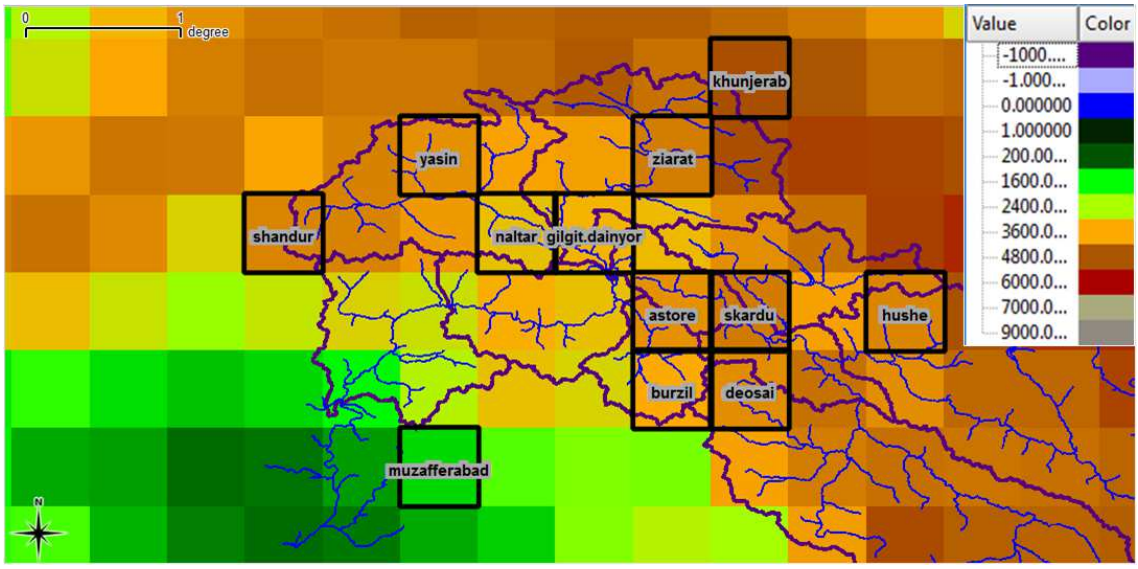

Figure 3.013 Selected (named) analysed PRECIS grid cells. Grid cells are coloured according to orographic height (m asl).

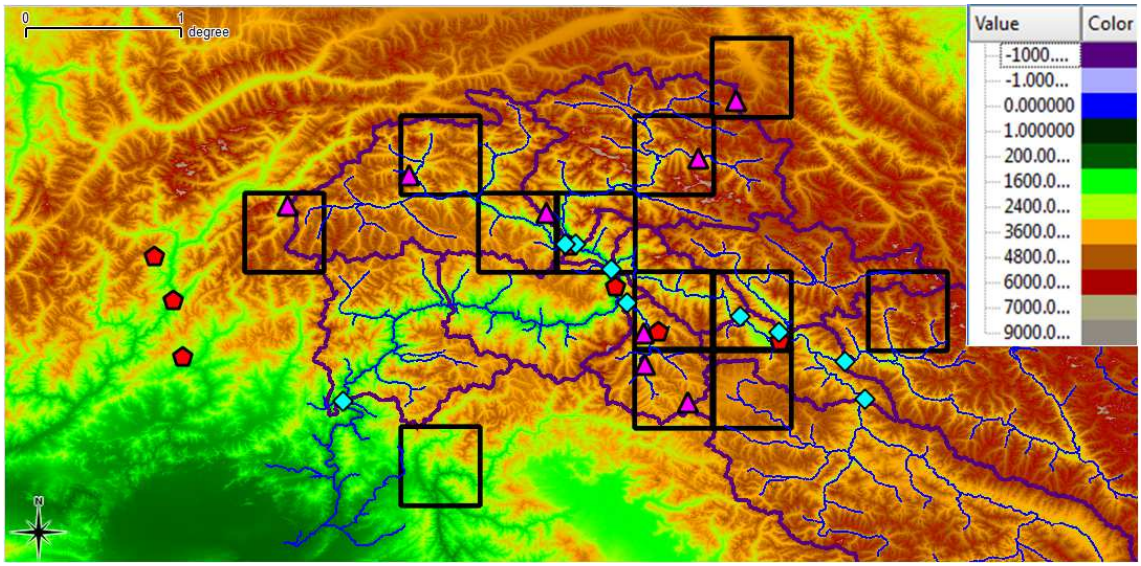

Figure 3.014 Selected analysed PRECIS grid cells with local (point) observation locations.

3.3.8 Remote sensing earth observation (RS-EO) from satellite imagery generalities

An additional valuable, but recent, source of data for hydro-climatological studies are data products derived from satellite imagery, commonly referred to as "remote sensing" data. Satellite imagery-derived remote sensing products use algorithms based on relationships between the radiometric properties (albedo/reflectance, thermal emittance temperatures) and the atmospheric and land surface processes of interest to climatologists and hydrologists to create spatial data products that act as a direct measures or quantitative indicators of these processes (Brutsaert *et al.*, 1988). While providing valuable insights into predominant meteorological conditions over vast often sparsely instrumented areas, these spatial climate data products do have substantial limitations and shortcomings.

The temporal frequency of remote sensing observations is one important shortcoming. At present there is an inverse relationship between frequency and (horizontal) spatial resolution of these products. The popular MODIS data products have a maximum horizontal resolution of 500m to 1km and are derived from twice-daily overpasses of the target area (Justice *et al.*, 2002). This spatial resolution provides adequate detail with which to assess sub-catchment-scale conditions, i.e. on the order or tens to hundreds of square kilometres. However, data products with better horizontal resolution (sub- 100m) are necessary for studying smaller spatial areas, such as individual glaciers, and these often have observational frequencies of only once every two weeks or more (e.g. sixteen days for ASTER and Landsat ETM+ (Liu *et al.*, 2009)). In contrast, the remotely-sensed data products with the best frequency of observation – from geostationary satellites – have historically had coarse spatial resolutions (> 40km),

only detailed enough for continental (or synoptic) scale studies although this has improved in successive technological generation of the instruments (Bikos *et al.*, 2006).

3.3.9 RS-EO from the Tropical Rainfall Monitoring Mission (TRMM)

As will be discussed later in this chapter, precipitation is a notoriously difficult parameter to capture accurately in spatial terms. One hope for improving these observations is remote sensing data products from multi-sensor (and multi-satellite) algorithms. The most prominent of these data products presently available is produced by the Tropical Rainfall Monitoring Mission (TRMM) (Huffman, 2007).

A preliminary assessment was made of the usefulness of TRMM precipitation estimates for the region; a detailed analysis has been published in Forsythe *et al*. (2012) and will be reproduced here. These estimates are derived from a multi-sensor system which assimilates observations from multiple satellites gauge-adjusted with the Global Precipitation Climatology Project (GPCP) dataset (Huffman, 2011). This constellation of data sources includes the TRMM instrument itself which carries both a passive microwave imager and space-borne rainfall radar which provide high resolution assessment of precipitation rates within the satellite's window of view (swath width). These high resolution observations are very limited in observational frequency; with direct repeat observations only approximately twice per month. The TRMM specific observations, however, are merged with additional passive microwave observations from several other satellite-borne instruments (SSM/I, DMSP, AMSR-E, AMSU-B, etc.) as well as the near continuous low resolution infrared and thermal imagery from geostationary weather satellites. This multi-sensor composite can thus provide a balance between good spatial resolution and high frequency observation, although due to the present limited number of passive microwave-equipped satellites there are substantial gaps in the spatio-temporal coverage of the higher resolution data needed to calibrate the lower resolution continuous imagery from the geostationary platforms (Huffman, 2007).

The data used here are from the 3B43v006 data product (Huffman, 2007) which provides a continuous time series of monthly estimated precipitation totals at 0.25 decimal degree horizontal resolution from Jan 1998 to present. Comparisons to available local long-record observations of precipitation and limited river discharge data strongly suggest that the TRMM estimates provide a good quantitative indicator of monthly rainfall mass input rather than a measure of absolute magnitude (shown later in

this chapter). In this they are similar to the local long-record meteorological observations which also do not directly represent catchment wide precipitation but do correlate well as indicators of mass inputs for seasonal snowmelt driven catchments (e.g. Archer, 2003; Archer and Fowler, 2008). Figure 3.015 illustrates the global spatial coverage and spatial variability of TRMM estimates of mean annual total precipitation for 1998 to 2010.

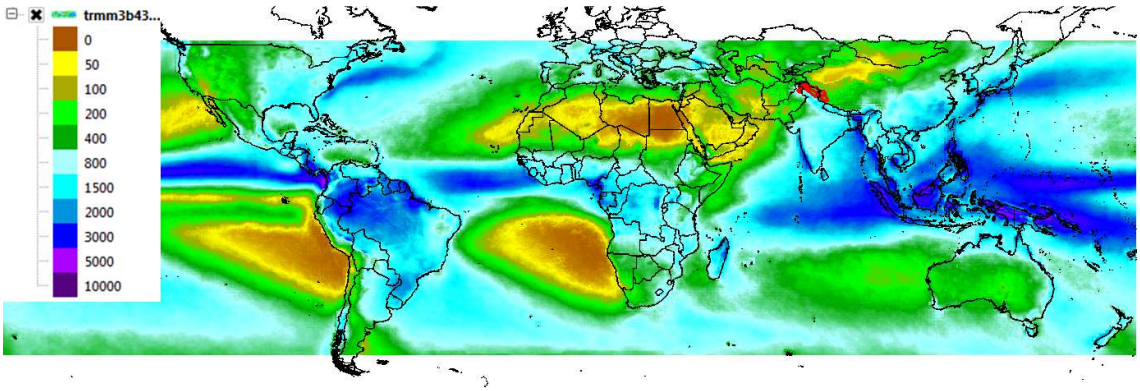

Figure 3.015: Mean annual total precipitation estimates (mm) from TRMM, global coverage (E-W between 50N & 50S). For relative spatial reference the boundary of the UIB is shown in bright red.

3.3.10 RS-EO from Moderate Resolution Imaging Spectrometer (MODIS) data products generalities

Another widely-used family of remote sensing data products are those produced by radiometric observations from the Moderate Resolution Imaging Spectrometer (MODIS) instrument flown on the "Terra" and "Aqua" Earth Observation System (EOS) satellite platforms operated by NASA (Justice *et al.*, 2002). The large number of spectral (radiometric) bands (thirty-six) measured by MODIS enables diverse algorithms to produce a wide range of spatial data products relating to atmospheric and land surface processes. These spatial data products are of especially great value to scientists studying regions where field observations are difficult and sparse. Note however that the data analysed in the present work are almost exclusively from MODIS-Terra.

Radiometrically-derived data products do, however, have important limitations in their capacity to accurately assess parameters of interest to hydro-climatologists. The spatial data products have their theoretical basis in identified relationships between the intensity of emission of electromagnetic radiation at specific wavelengths (spectral bands) and specific surface or atmospheric properties (e.g. Hall *et al.* 2001, Platnick *et al.* 2003). While MODIS data products are quite robust due to the high number of available spectral bands there is still potential for misidentification of radiometrically

similar climate features. This is perhaps best illustrated by the challenge of accurately differentiating snow versus cloud (both are cold and "bright"); crucial as algorithms for determination of snow cover (SCA) and land surface temperature (LST) routinely employ "cloud-masking" approaches.

Even the sophisticated MODIS products are sensitive in this regard to a number of thresholds and viewing conditions (Ackerman, 2008). In other mountainous study areas, the systematic misidentification of snow as cloud in the transition zone between snow-covered and snow-free areas has been found to occur in earlier versions of the MODIS snow algorithm (Klein, 2003). The ground-based data available to this study does not allow assessment of whether such issues have been resolved in the current version of the algorithm; we simply assume that the estimates are as good as they can be. Independent of cloud-masking issues, the topography of the study area for mountainous regions may also affect the accuracy of snow-cover detection. In winter, for example, large shadows resulting from low sun angles can result in under-detection of snow in steep terrain (Sorman, 2007). Given these limitations, it may be prudent to consider spatial data products as quantitative indicators of hydrometeorological conditions rather than as absolute measures of the physical state of the target catchment.

3.3.11 MODIS spatial data proxies for meltwater-generation inputs

The primary MODIS data products for consideration in this study are snow covered area (SCA) and land surface temperature (LST). SCA and LST respectively provide indices of the mass and energy inputs to the hydrological (melt-runoff generation) system. The SCA and LST data products from the Moderate Resolution Imaging Spectrometer (MODIS) instrument aboard the NASA Earth Observation Terra platform presented here were acquired as eight-day temporal aggregates over the period from March 2000 to July 2010. The temporal aggregates cover consecutive Julian days: 01 January to 08 January, 09 January to 16 January, etc. Thus there are forty-six time-steps for each calendar year, with the last aggregate – starting Julian day 361 – overlapping the following year by two or three days. For SCA the eight-day rasters provide 500m horizontal resolution maximum snow cover extent (product MOD10A2) (Hall *et al.,* 2001). For LST the eight-day rasters provide 1km horizontal resolution mean surface temperature for day-time (near local noon) and night-time (near local midnight) overpasses (product MOD11A2) (Wan, 2008). In order to compare the MODIS data to local observations, the eight-day rasters were further aggregated by

calculating pixel by pixel means from groups of four eight-day rasters to provide proxies of calendar month averages. This spatio-temporal aggregation is summarised in Table 3.07.

MODIS parameter	snow covered area (SCA)	land surface temperature (LST)
MODIS dataset designation	MOD10A2	MOD11A2
MODIS source spatial resolution	500m nominal	one kilometre nominal
MODIS source temporal resolution	eight-day maximum	eight-day mean
analogous to local observation parameter	precipitation (cumulative cold season)	two-metre air temperature
further temporal aggregation	means of four eight-day rasters centred on calendar months	means of four eight-day rasters centred on calendar months

Table 3.07 Spatial and temporal resolution of MODIS SCA and LST products used in this thesis.

3.3.12 Cloud properties by MODIS atmospheric data products

As explained in the introduction to this chapter, cloud-cover can also play a key role in modulating the surface energy balance throughout the UIB. This energy balance sensitivity can have important impacts on the timing and magnitude of meltwater runoff-generation and thus river flows. Furthermore, as will be discussed in later chapters, there is evidence that changes in cloud-cover regimes – especially diurnally asymmetric changes in the amount and location of daytime and night-time cloud-cover – could significantly influence future and current local temperature trends. For these reasons, detailed characterisation of the cloud-cover regime within the UIB is of great scientific interest. In this domain spatial data products from MODIS can again be of significant value. In this study, analysis is limited to those parameters directly related to the macrophysical and microphysical cloud properties likely to influence the surface energy balance.

The MODIS cloud data presented here were compiled by pre-processing and aggregating a large number of "swath" images from the available observational record. Swath images are data products from 5 (temporal) minute (300 seconds) snapshots by the MODIS instrument of its field of view. These scenes are not, in their initial format, mapped onto commonly used coordinate systems and thus require considerable pre-processing before analysis can take place.

The cloud macrophysical properties analysed here are "cloud fraction" and "cloud-top (atmospheric) pressure" (Platnick, *et al.* 2003). The former is simply the estimate of the amount of cloud (0 to 100%) in the target pixel. The latter is an estimate of cloud-top height. These relatively simple parameters can provide important

descriptors/indicators of the nature of the clouds present and their likely influence on the local energy balance. This influence is commonly referred to as “cloud forcing” or “cloud radiative effect”.

The cloud microphysical properties analysed here include “cloud optical thickness”, “cloud effective radius” and “cloud water path” (Platnick, *et al.* 2003). Cloud optical thickness is a measure of the cloud’s opacity to visible spectrum light. Cloud effective radius is, as its name would indicate, an estimate of the mean or effective radius of the water droplets or ice crystals composing the cloud. Cloud water path is a measure (in mass per unit area) of the amount of water contained in the cloud within the (surface area of) the target pixel. Each of these parameters is often used in attempts to quantify the cloud radiative effect (for example see Dong *et al.* 2005, Ebell *et al.* 2011, Shupe and Intrieri 2004).

3.3.13 MODIS albedo estimates

An additional relatively simple, yet crucial, parameter than can be assessed spatially by MODIS is albedo. As explained in the chapter introduction, estimates of albedo are essential to developing complete characterisations of the local surface area energy balance, including both its annual cycle and interannual variability. In mountainous regions surface albedo is closely linked with snowcover cycles and snowpack evolution (Sun *et al.,* 1999) and its characterisation is important for accurately modelling meltwater generation. The MODIS data product offers high spatial resolution aggregated at a consistent timestep. Furthermore MODIS albedo data has been shown in validation studies (Jin *et al.,* 2003) to agree well with a range of comparable data sources including imagery from other spaceborne instruments and ground-based observations during field campaigns. This project chose to analyse the MODIS data product designated MCD43a3 (Wang *et al.* 2012) as will be presented later in the chapter.

3.4 Locally observed hydrology

It is difficult to overstate the importance of the runoff from the Upper Indus to livelihoods in the basin. Food and energy security depend respectively on irrigated agriculture and hydropower. Without these contributions Pakistan would face far greater difficulties in cereal grain and electricity production. This economic dependency adds urgency to improving understanding of the hydro-climatology of the UIB.

3.4.1 UIB hydrological regimes

An understanding of the hydro-climatology of the UIB begins with an understanding of the three distinct hydrological regimes found in the UIB (Archer, 2003). The classic pluvial regime characterised by direct rainfall runoff is only found in the UIB in the lower elevation, foothills catchments near to major reservoirs. Pluvial regime catchments in the UIB can be significant in terms of risk of downstream flash flooding, but due to their relatively limited surface area are minimal contributors to basin annual runoff (volumes). For this reason, pluvial regime catchments are not presented in detail in this thesis.

The two dominant hydrological regime types in the UIB are both characterised by the accumulation of solid precipitation during the cold (winter) season and its ablation during the warmer (summer) months. Both regimes have minimal baseflow in the cold season, a rising limb in the late spring and recession in the early autumn. Peak flow occurs in the summer months, modulated by the availability of mass and energy inputs.

These two regimes are differentiated, however, by the dominant control (constraint) on melt season runoff. Melt runoff in nival (seasonal snowfall) regime catchments is governed by available mass input (accumulated snowpack from the preceding winter). Examples of nival regime catchments in the UIB include the Indus above Kharmong, the Astore river (gauged at Doyian) and the Ghizer branch of Gilgit river (gauged at Gilgit Town) (Archer, 2003). Alternatively, melt runoff in glacial (perennial icepack) regime catchments is governed by available melt energy (summer temperature). Examples of glacial regime catchments include the Shyok (gauged at Yogo), the Shigar (gauged at Shigar Town), and the Hunza (gauged at Dainyor Bridge). These cycles are thus driven by the predominant temperature conditions, which can be characterised as the fraction of the catchment where night-time temperatures remain above 0°C. In nival regimes, the accession limb of the melt hydrograph rises quickly in spring with warming temperatures but recedes in mid-summer once the seasonal snowpack is exhausted. In glacial regimes the accession limb of the hydrograph lags rising temperatures marginally, but flows remain high until the catchment begins to cool in late summer.

The annual cycle, along with the range of interannual variability (first [c10] and last [c90] deciles), of discharge for the major gauged tributaries (WAPDA data) are shown in Figures 3.016 to 3.018. While both the shape of the annual cycle and the

relative range of interannual variability is consistent in all of the primary gauged catchments, the absolute river discharge rates (Figures 3.016 to 3.018) and the runoff contributions (Table 3.08) vary considerably.

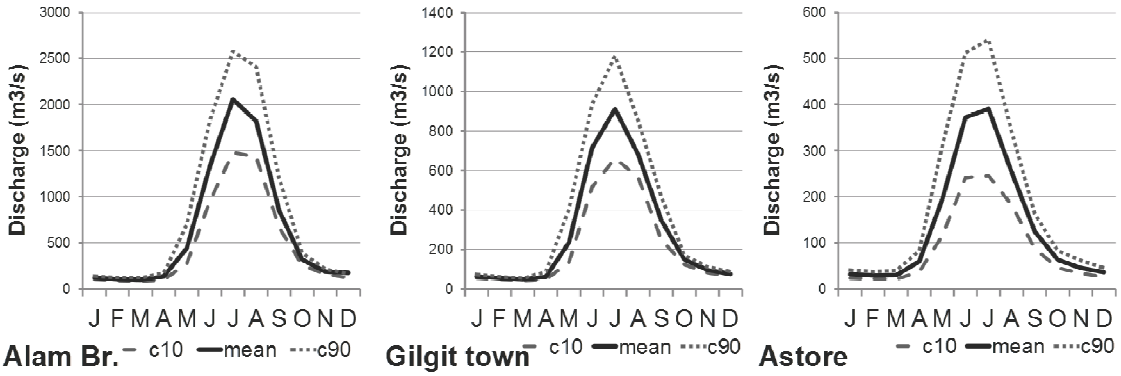

Figure 3.016 Discharge in mixed and nival regime tributaries. Each example stations draws on all of the available gauging record years: Alam Br. (mixed regime) 1966-67, 1969-98, 2000-01, 2004-08; Gilgit town (nival regime) 1961-72, 1980-2008; Astore (nival regime) 1974-2008. Note differences in vertical scale.

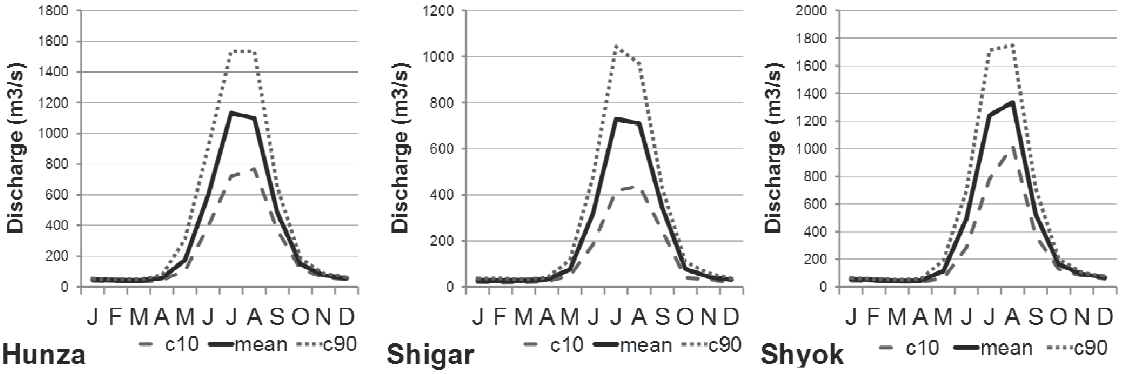

Figure 3.017 Discharge at glacial regime tributaries. Each example stations draws on all of the available gauging record years: Hunza (glacial regime) 1966-2004, 2008; Shigar (glacial regime) 1985-1997; Shyok (glacial regime) 1973-1997, 1999-2008. Note differences in vertical scale.

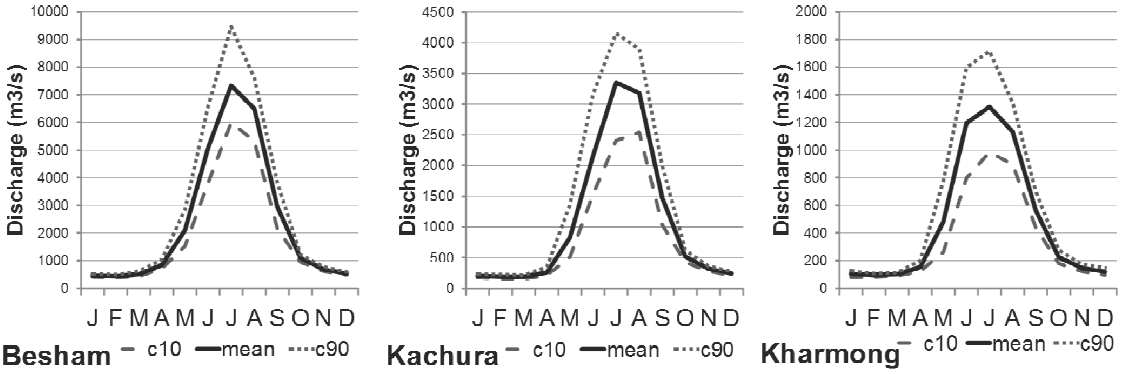

Figure 3.018 Discharge at Indus main channel gauging points. Each example stations draws on all of the available gauging record years: Besham (mixed regime) 1969-97, 2000-02; Kachura (mixed regime) 1970-2008; Kharmong (nival regime) 1983-97. Note differences in vertical scale.

River	Indus	Indus	Indus	Shyok	Shigar	Gilgit	Hunza	Gilgit	Astore
Station	Besham	Kachura	Kharmong	Yogo	Shigar	Alam	Dainyor	Gilgit	Doyian
Jan	6.1	3.7	3.7	2.2	11.3	11.7	9.2	13.1	22.3
Feb	5.3	3.1	3.5	1.8	10.1	9.1	7.6	10.3	18.6
Mar	6.8	3.4	3.7	1.8	11.4	9.4	7.9	10.1	20.9
Apr	11	4.6	5.6	1.8	12.3	12.6	10.7	12.5	41.1
May	28.6	15.1	17.7	4.7	30.8	42.8	33.6	49.1	139.1
Jun	66.9	38.2	44.1	19.6	124.4	125.2	110.8	144.5	257.3
Jul	99.9	61.4	48.4	51.1	293.6	200.1	217.7	190.7	279.2
Aug	88.5	58.3	41.7	55	285.9	177.1	211.4	142.4	180.6
Sep	38.7	26	20.8	20.8	133.9	79.9	89.8	70.3	86.1
Oct	14.9	9.4	8.2	6.7	31.6	30.9	28.7	31.2	44.9
Nov	8.9	5.6	5.3	3.7	17.1	17.5	14.1	19.5	31.3
Dec	7.1	4.4	4.3	2.7	12.6	16.9	10.7	15.7	25.7
Annual Total	**382.7**	**233.2**	**207.0**	**171.9**	**975.0**	**733.2**	**752.2**	**709.4**	**1147.1**

Table 3.08 Mean observed runoff by month (mm) for UIB river discharge gauging stations.

These absolute differences in runoff are determined primarily by the ratio of highly active cryosphere area, with large meltwater yields, to arid high mountain desert and secondarily by governing constraints in climatic inputs – snowpack for nival regimes and summer melting energy in glacial regimes. Thus the largest gauged areas – the Shyok gauged at Yogo and the Indus main channel gauged at Kharmong, Kachura and Besham – have the lowest annual runoff totals, less than 400mm/year, because the areas yielding large runoff volumes are "diluted" by vast largely barren areas, while the smaller gauged tributaries – the Gilgit to Gilgit town and Alam Bridge, the Astore to Doyian, the Hunza to Dainyor Bridge and the Shigar to Shigar town – high high annual runoff totals, greater than 700mm/year, because the nival regimes have deep mean annual snowpack accumulation while the glacial catchments have large percentages of glacial cover which in both cases yield high mean meltwater volumes.

In contrast, the absolute values of discharge are determined by the product of mean runoff depth by catchment. Hence despite having lower unit contributions by surface area, the accumulated river flows are largely a function of total catchment area (provided previously in Table 3.02) as seen in the vertical axes of the graphs in Figures 3.016 to 3.018.

3.4.2 Interannual variability in of UIB hydrology

All regimes demonstrate considerable interannual variability. In most years shortfalls (below mean runoff) in contributions from one regime type (glacial or nival)

are at least partial compensated by surplus (greater than mean) from the other type; Table 3.09 shows the coefficient of variation [CV] – i.e. the standard deviation divided by the mean – values for annual and summer runoff for individual gauged tributaries. Catchments with a single dominant regime type tend to experience larger CVs than those with mixed regimes (e.g. Indus at Besham and Kachura, Gilgit at Alam Bridge). In the headwater reaches the glacial and nival regimes are dominant. In these areas river flows during the melt season, locally referred to as the Kharif—from April to September—dominate annual runoff volumes, with summer (June to August) runoff often accounting for 65 to 75 % of annual totals (Table 3.09). The large range of observed interannual variability—+75 to −45% of period mean for a nival regime, +60% to −40% of period mean for a glacial regime—in summer runoff volumes is striking (Figures 3.016 to 3.018). The CVs for summer runoff (given in Table 3.09) in the primary gauged catchments range from 13 to 26%.

River	Station	Mean annual total runoff (mm)	CV for annual runoff	JJA mean contribution (fraction) of annual runoff	CV for JJA runoff
Indus	Besham	382.7	0.133	0.666	0.154
Indus	Kachura	233.2	0.169	0.676	0.180
Indus	Kharmong	207.0	0.177	0.647	0.206
Shyok	Yogo	171.9	0.200	0.730	0.240
Shigar	Shigar	975.0	0.257	0.721	0.326
Gilgit	Alam Bridge	733.2	0.137	0.683	0.176
Hunza	Dainyor	752.2	0.205	0.717	0.205
Gilgit	Gilgit	709.4	0.139	0.671	0.178
Astore	Doyian	1147.1	0.204	0.624	0.204

Table 3.09 Interannual variability in UIB runoff as measured by the coefficient of variation (CV).

3.4.3 Incremental contributions to large-scale UIB discharge

While runoff as a measure quantifies the hydrological processes on a unit area basis, it does not indicate the absolute quantity of water which will be available for human and ecosystem needs at key points in the channel network. Figures 3.019 and 3.020 show the relative and absolute contributions of the incremental gauged catchment areas to the total flow in the Indus at Besham (Qila). Besham is the last gauging station on the Indus main channel upstream of the large reservoir at Tarbela.

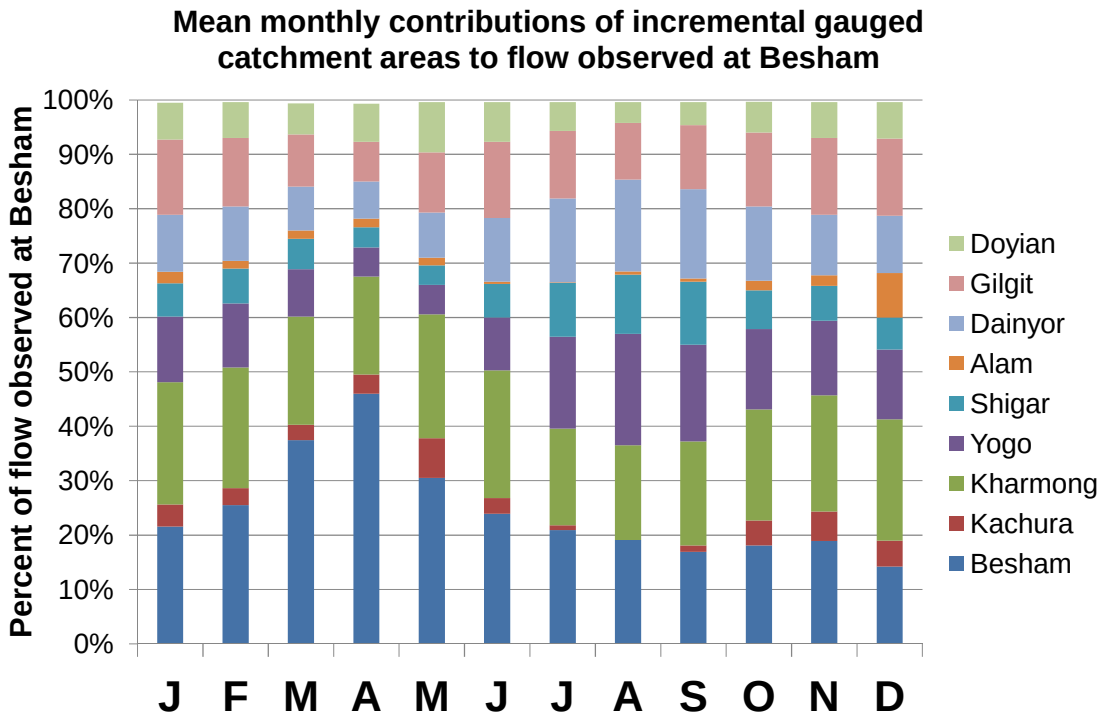

Figure 3.019 Incremental relative contributions to total flow in the Indus at Besham, by month

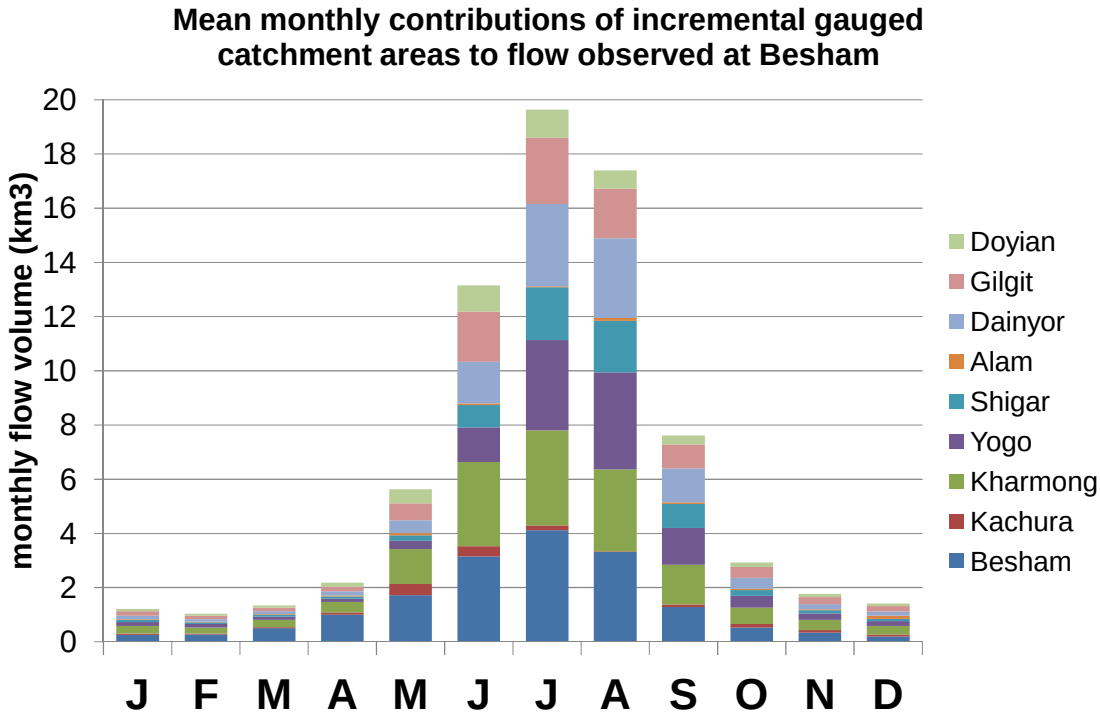

Figure 3.020 Incremental absolute contributions to total flow in the Indus at Besham, by month

As with the absolute discharge at individual tributary gauging stations, the incremental contributions of gauged tributaries – or of the incremental area between consecutive gauging stations along the main channel – to total observed flow at Besham (Figure 3.020) are largely linked to the extent of surface area. As discussed in the

preceding sections, the annual cycle – timing, relative magnitude – of these contributions is largely similar and driven by the annual meltwater cycle.

Detailed study of the relative contributions to monthly totals (Figure 3.019) does yield some further interesting insights. Although the absolute runoff generated by the incremental area immediately above the Besham station does follow a similar annual cycle to the other hydrographs examined here, it provides a substantially higher relative contribution to total flow at Besham in early spring – March and April – than during the remainder of the year. This is most likely due to the fact that this area receives substantial winter snowpack accumulation but is at a marginally lower elevation than other nival regime areas (e.g. Astore, Gigit/Ghizer valley) and hence experiences initial melting some weeks earlier than higher elevation areas to the north. In contrast, the expansive, high elevation and relatively arid glacial tributary Shyok (gauged at Yogo) contributes a minimum fraction of the flow at Besham in March and April, but substantial portions of total flow in July, August and September while glaciers continue to melt after seasonal snowpack has been exhausted in the nival tributaries. To a degree the other gauged incremental surface areas vary between these two poles, with nival regimes providing greater relative contributions in spring and minimally in summer, while glacial regime areas contribute relatively less in spring but substantially greater fractions in late summer.

3.4.4. Climate drivers of UIB hydrology

To this point, while individual tributaries have been identified as either nival or glacial regimes and the characteristics defining regime types have been explained, little quantitative evidence has been presented to demonstrate the differences in catchment responses to various climatic forcings. This evidence will in due course (section 3.10) be presented, but beforehand the climatologies of mass and energy inputs to the UIB hydrological system will be quantitatively characterised.

3.5 Quantitative indices of mass inputs to UIB hydrological system

3.5.1 Precipitation generalities

Precipitation is the mass input to the hydrological cycle but is notoriously difficult to capture accurately in spatial terms. Precipitation is a discrete process in time and space and thus very difficult to interpolate realistically. For this reason alone, it is

vital to draw upon all available, credible sources of data when attempting to characterise this key variable. Furthermore, there is generally a much higher degree of (relative) interannual variability in precipitation time series when compared with other climate variables such as temperature. As such, a substantial record length is often necessary before the "signal" of the annual rainfall cycle can be separated from the "background noise" (intrinsic variability).

Quantifying the annual cycle and interannual variability of precipitation is crucial to understanding the seasonality and interannual variability in catchment hydrological response because in most cases (pluvial and nival regimes) this response is governed by the mass input to the hydrological system. Even in glacial regime catchments quantification of the precipitation input is necessary to evaluate the mass balance state and assess the long term prospects for future runoff.

More particularly with regards to the UIB and its nival catchments, the spatial distribution of precipitation, specifically the distribution of precipitation with respect to elevation, is crucial to understanding the timing of the annual runoff cycle. The interplay of the annual temperature cycle, as the 0°C isotherm – i.e. the elevation at which water freezes – moves upward from late winter to high summer, with the vertical distribution of snowpack will drive the timing of meltwater generation which feeds river flows.

It is relevant at this point to recognise that in a more orthodox and ideal context the historical record coverage of each individual data source would allow for selection of a common reference period for the collective set of observations. This unfortunately is not the case. Given the often minimal overlap between the datasets it is deemed that restricting comparisons to such a limited time window would counter-productively inhibit exploration of the range of interannual variability in the recorded in the data sources with multi-decadal length. The reader is referred again to Tables 3.03 and 3.04 for details on the period covered by local observations.

3.5.2 Precipitation climatology from PMD and AWS data

Precipitation observed by the PMD long-record meteorological stations in the UIB follows a general pattern with a strong mode, i.e. concentration of relatively wet months, in Spring (or late Winter) with normally a lesser contribution from the summer (monsoon) months. The autumn months are usually quite dry although large rain and snowfall events are occasionally recorded (Figure 3.021). As can be seen in the lower

quartile values (c25) for wet days (wd; days with measured precipitation of 0.1mm or more), it is not uncommon for entire months to pass without observed precipitation in the valley floors where the long-record stations are located. Furthermore given the arid yet variable nature, the mean values are strongly influenced by infrequent large magnitude events. Hence, the monthly means sometimes approach or even surpass the upper quartile (c75) values.

Another interesting aspect of the precipitation observations from the long-record stations is that while Archer (2003) and Archer and Fowler (2008) demonstrated that they are valuable quantitative indicators of interannual variations in mass inputs to the hydrological system, they are also clearly not representative absolute measures of catchment spatial mean accumulations. The working hypothesis is that the observations in valley bottoms represent the lower end of a vertical precipitation gradient that increases with elevation, with a maxima likely situated well above 4500 m asl before declining in the rarefied conditions at extreme altitudes (e.g. Hewitt 2011, Winiger *et al.* 2005, Immerzeel *et al.* 2012). Comparison of the absolute accumulations from Gilgit (1465 m asl), Skardu (2210 m asl) and Astore (2394 m asl) as shown in Figure 3.021 does however suggest that there are additional factors at play given that values at Skardu are much closer to Gilgit despite the difference in elevation while Astore is much more humid than Skardu despite the minimal elevation difference (less than 200m vertically). This may well be partially due to sub-regional differences in precipitation regimes. Another potential explanation is that geometric aspects (e.g. orientation aspect, concavity, declivity) of topography surrounding the observation station strongly influences the absolute quantities of precipitation observed. In the absence of much increased spatial coverage of ground-based observation, improved understanding of the causal mechanisms influencing spatial distribution of precipitation in the UIB, or any other region of similar topographically complexity, would likely very require high resolution numerical weather simulation (Rasmussen *et al.*, 2011).

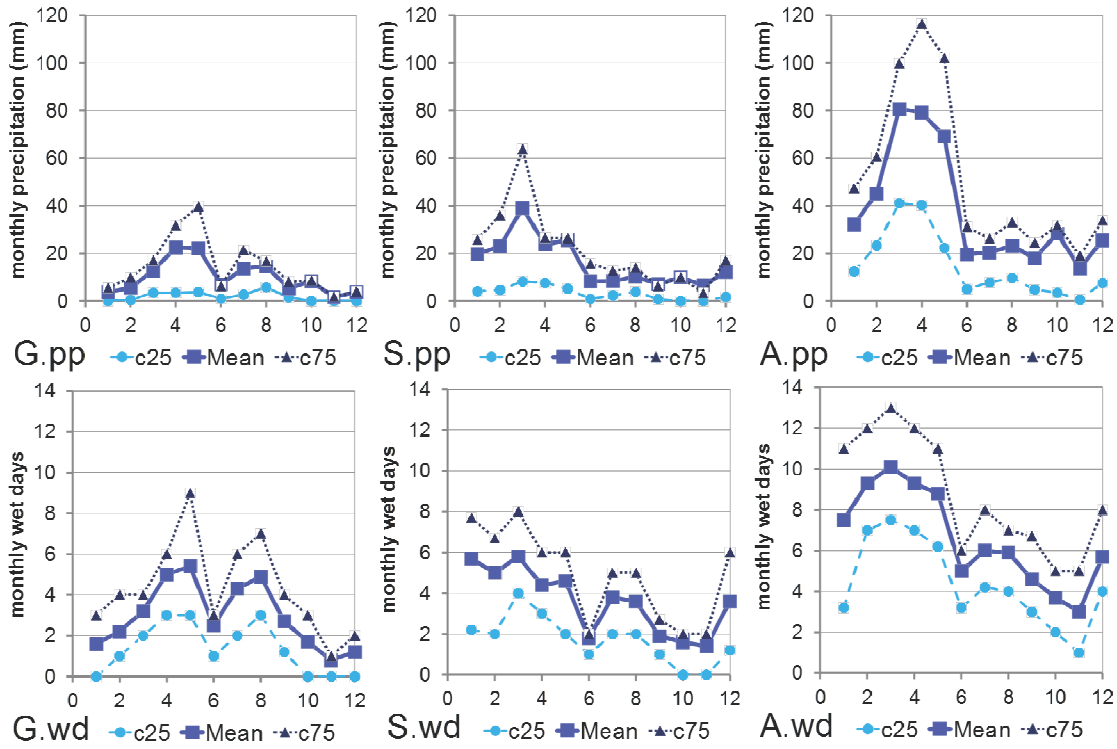

Figure 3.021 Historical observations (1961 to 1990) of mean monthly precipitation (pp) at Gilgit (G), Skardu (S) and Astore (A). Wet days ("wd") are calculated as days with precipitation > 0.1mm. In addition to the means, the lower ("c25") and upper ("c75") quartile boundaries are also given.

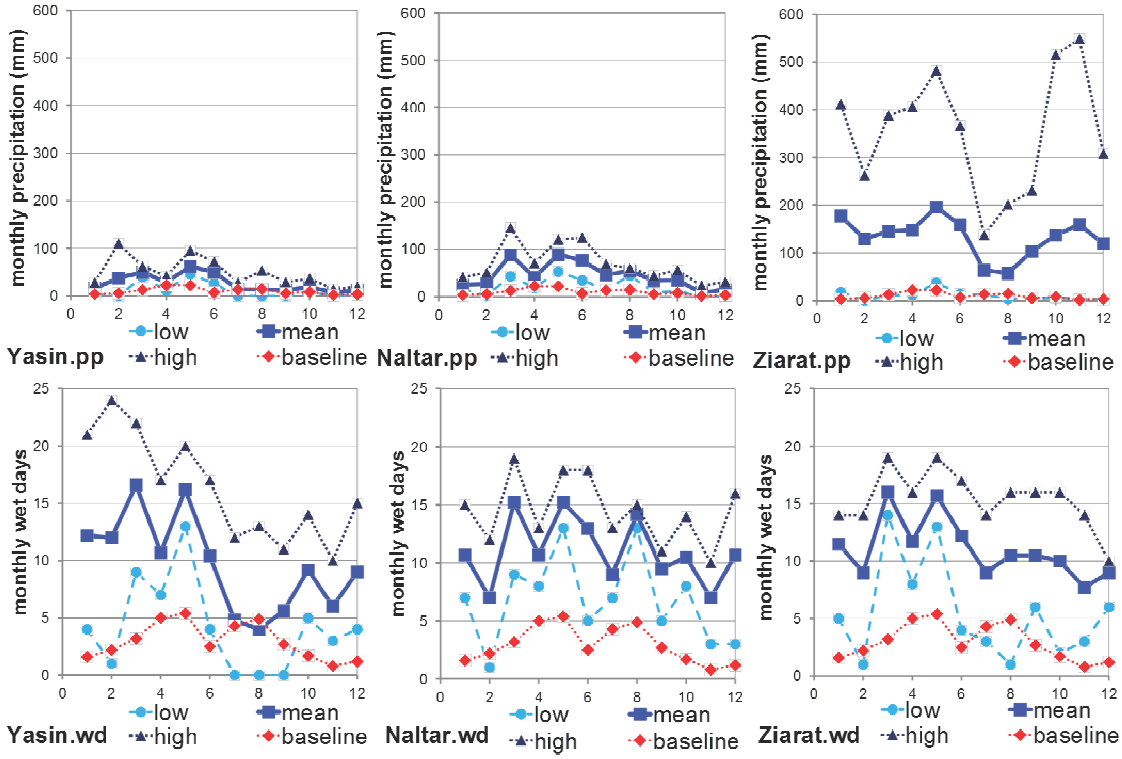

Figure 3.022 Available (sample) observations of precipitation from AWS in Gilgit & Hunza catchments. Precipitation ("pp") is given as cumulative monthly depth (mm). Wet days ("wd") are calculated as days with precipitation > 0.1mm. In addition to the means, the lower ("c25") and upper ("c75") quartile boundaries are also given. Baselines are provided by the 1961 to 1990 period climate normal (means) at Gilgit (PMD).

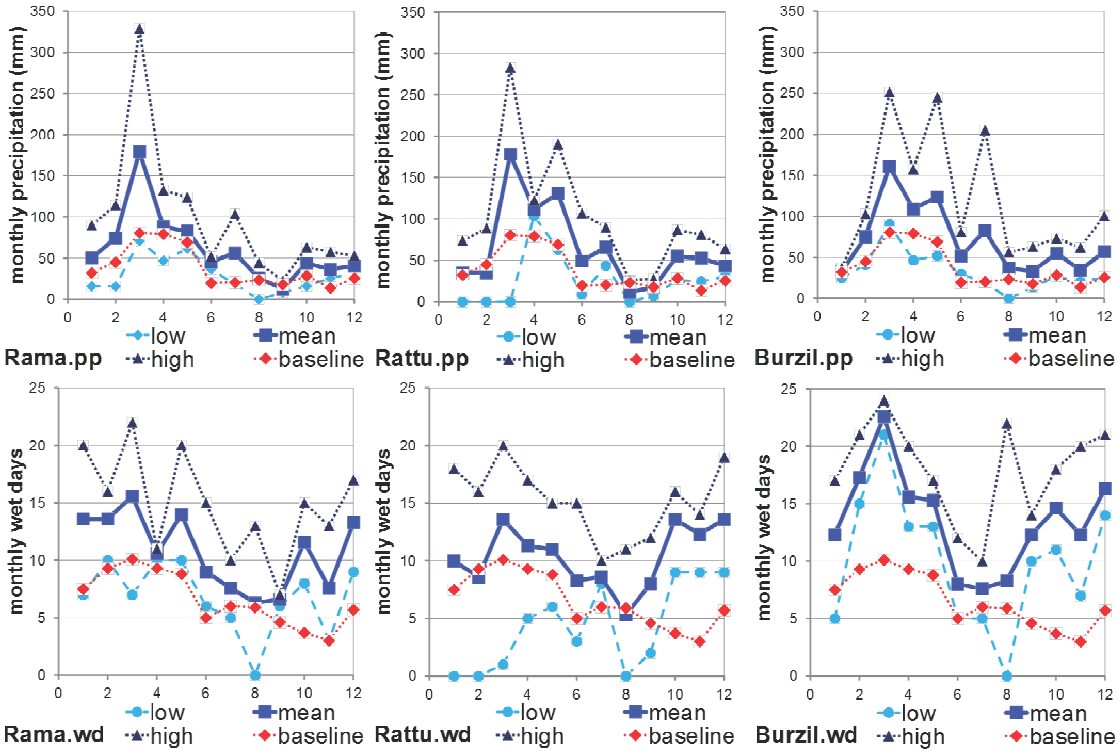

Figure 3.023 Available (sample) observations of precipitation from AWS in the Astore catchment. Precipitation ("pp") is given as cumulative monthly depth (mm). Wet days ("wd") are calculated as days with precipitation > 0.1mm. In addition to the means, the lower ("c25") and upper ("c75") quartile boundaries are also given. Baselines are provided by the 1961 to 1990 period climate normal (means) at Astore (PMD).

Despite the fact that they draw on only a handful of record-years, the precipitation data from selected AWS stations (Figures 3.022 and 3.023) largely corroborate the patterns of seasonality found in the PMD data. These stations experience relatively wet conditions in late winter and early spring with generally drier summers. This mean distribution of precipitation within the annual cycle suggests relatively limited influence of monsoonal weather systems on overall high elevation precipitation in the UIB reaffirming the established pattern from the long-record valley stations.

The AWS stations do, however, experience substantially more wet days in general as well as greater accumulated precipitation as can be seen in comparing the high-elevation observations to the local valley station baseline climate normals (1961 to 1990 monthly means from Gilgit PMD for Figure 3.022 and Astore PMD for Figure 3.023). Although the initial temptation would be to infer meaning regarding the intensity (per day or event) of precipitation as well, in light of the extremely short available record length it would be more prudent to refrain from drawing conclusions until additional data becomes available.

There are also observations by the AWS units of significant precipitation events in late Autumn and early Winter. All of these differences are, preliminarily, attributed to the orographically-enhanced precipitation assumed to occur throughout the UIB in all seasons. Further study of this phenomenon is of course merited, but would necessitate access to additional years of data from the AWS record either for observation-based analysis alone or as validation data for high spatial resolution climate simulations.

3.5.3 Estimated precipitation from ECMWF reanalysis data

The annual distribution of precipitation found for the selected grid cells from the ERA-40 and ERA-Interim reanalysis projects is shown in Figures 3.024 to 3.026. As described in sections 3.3.5 and 3.3.6, the record periods for ERA-40 and ERA-Interim respectively are from September 1957 to August 2002 and from January 1979 to present day. For this reason a common reference period of January 1979 to December 2001 is chosen for presentation here. In each case the simulated (hindcast) precipitation is compared to the reference mean monthly precipitation (1979 to 2001) from the most humid local meteorological station, Astore PMD.

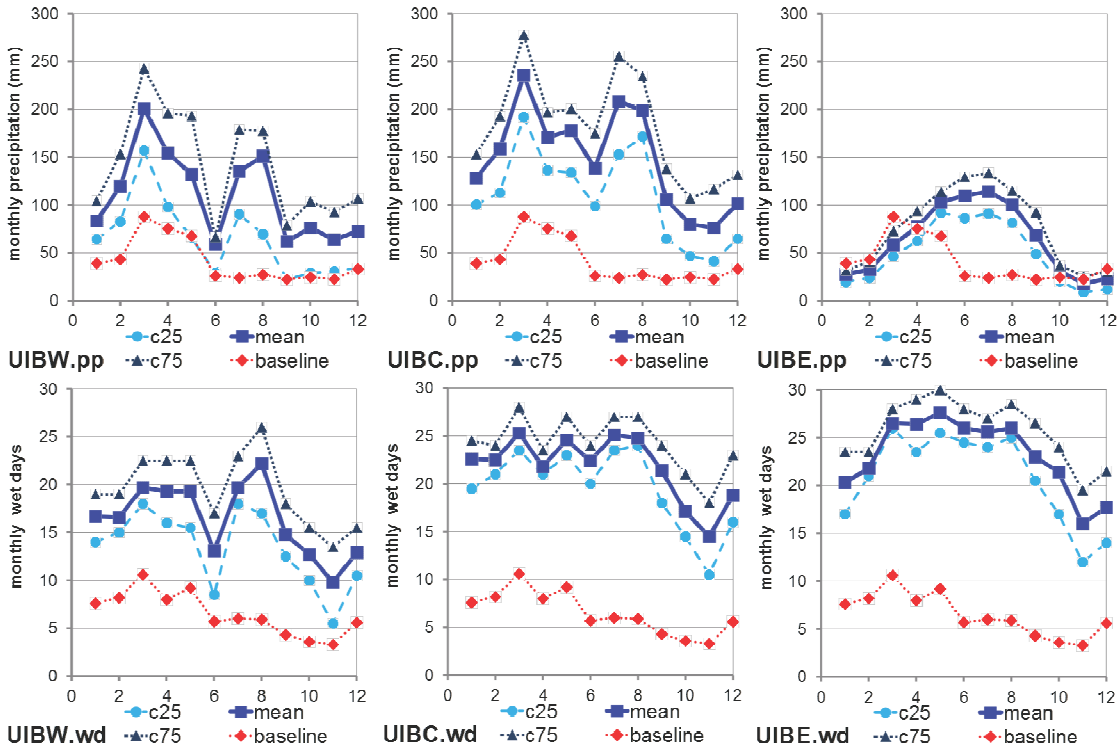

Figure 3.024 Precipitation records (1979 to 2001) from selected cells in the ERA-40 reanalysis: UIB West (UIBW), UIB Central (UIBC) and UIB East (UIBE), with "baseline" from Astore PMD for the same period for comparison.

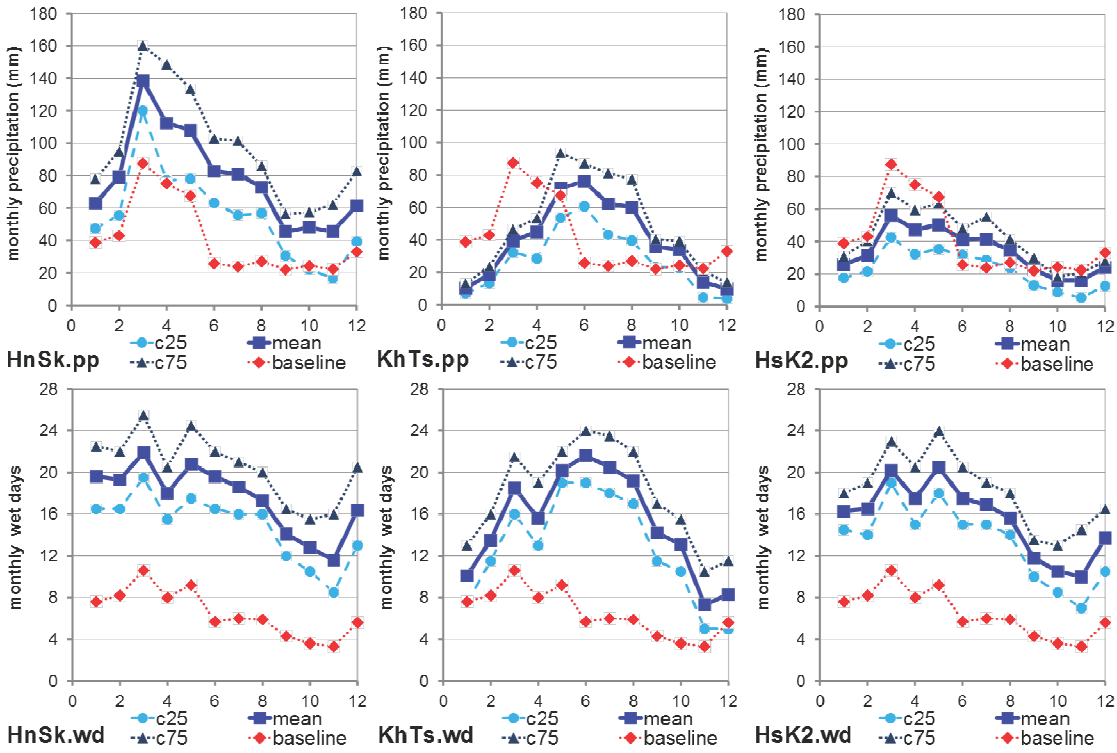

Figure 3.025 Precipitation records (1979 to 2001) from selected cells in the ERA-Interim reanalysis: Hunza.Skardu (HnSk), Khunjerab.KunlunShan (KhTs) and Hushe.K2 (HsK2), with "baseline" from Astore PMD for the same period for comparison.

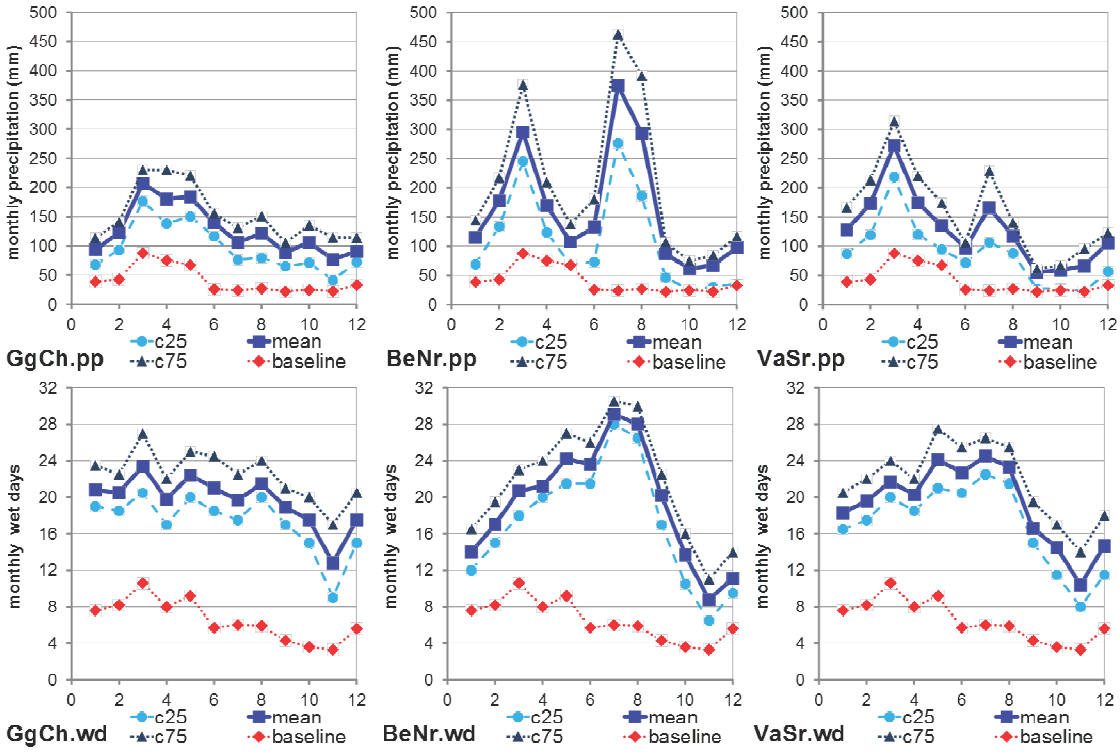

Figure 3.026 Precipitation records (1979 to 2001) from selected cells in the ERA-Interim reanalysis: Gilgit.Chilas (GgCh), Besham.Naran (BeNr) and Vale-of-Srinigar (VaSr), with "baseline" from Astore PMD for the same period for comparison.

When viewing Figures 3.024 to 3.026, one aspect that stands out is relatively limited interannual variability (narrow inter-quartile range) in the precipitation

simulated by reanalyses when compared to the ground-based observations (PMD, AWS). There also, between the two reanalysis data sets, indications of three distinctive patterns of rainfall seasonality which might represent real precipitation regimes within the study area. The first and seemingly dominant pattern mirrors that found for the point observations, i.e. with an annual mode in Spring and a variable/potential secondary/minor Monsoonal mode. Examples of this are UIBW and UIBC from ERA-40 along with HnSk, HsK2, GgCh and VaSr from ERA-Interim. The second pattern observed is nearly pure bi-modal behaviour in the BeNr grid cell from ERA-Interim. Interestingly this grid cell is at the same latitude, and further west, than the VaSr cell yet appears to show substantial greater monsoonal influence, i.e. increase in precipitation amount and frequency in Summer (June to August) linked to weather systems forming the South Asian monsoon. The lower modelled grid cell elevation (see Figure 3.011) might play a role in this difference. Lastly, a distinct seasonal regime appears in the UIBE grid cell from ERA40 with an annual precipitation distribution that appears to have a similar shape to the annual temperature cycle (see section 3.6). Geographically this would be situated over the higher elevation south-eastern Karakoram nearer to the Tibetan plateau. Verification of sub-regional precipitation regimes is another potential application nested, high-resolution numerical weather simulation. As will be seen in section 3.5.5, it is already standard practice to "drive" RCMs with meteorological reanalysis. The logical extension of this, i.e. nesting higher resolution models within RCMs is already being carried out for regions similar to the UIB (e.g. Rasmussen *et al.*, 2011).

As can be more easily seen in Figure 3.027, the accumulated monthly totals in the ECMWF reanalysis data are substantially greater than those measured by the long-record valley (PMD) stations, although the magnitude of observations at the AWS stations is similar in some cases. This could be because the modelled mean elevations of the reanalysis grid cells more closely represent the elevations of the AWS stations – and also the mean catchment elevations – but further study is warranted. Both ERA-40 and ERA-Interim simulate a greater annual total number of wet days than observed by the AWS stations. This may be due to a "drizzle effect" which is seen in many numerical meteorological models which tends to overestimate the frequency of low intensity precipitation events (e.g. Goddard *et al.* 2001). One of the most interesting aspects of Figure 3.027 is the close agreement of reanalysis records with AWS records in some cases (e.g. UIB.C/Va.Sr & Burzil; Kh.Ts & Naltar) at least in seasonality if not always

in magnitude of precipitation accumulation, despite substantial differences in seasonality of precipitation frequency, i.e. wet days.

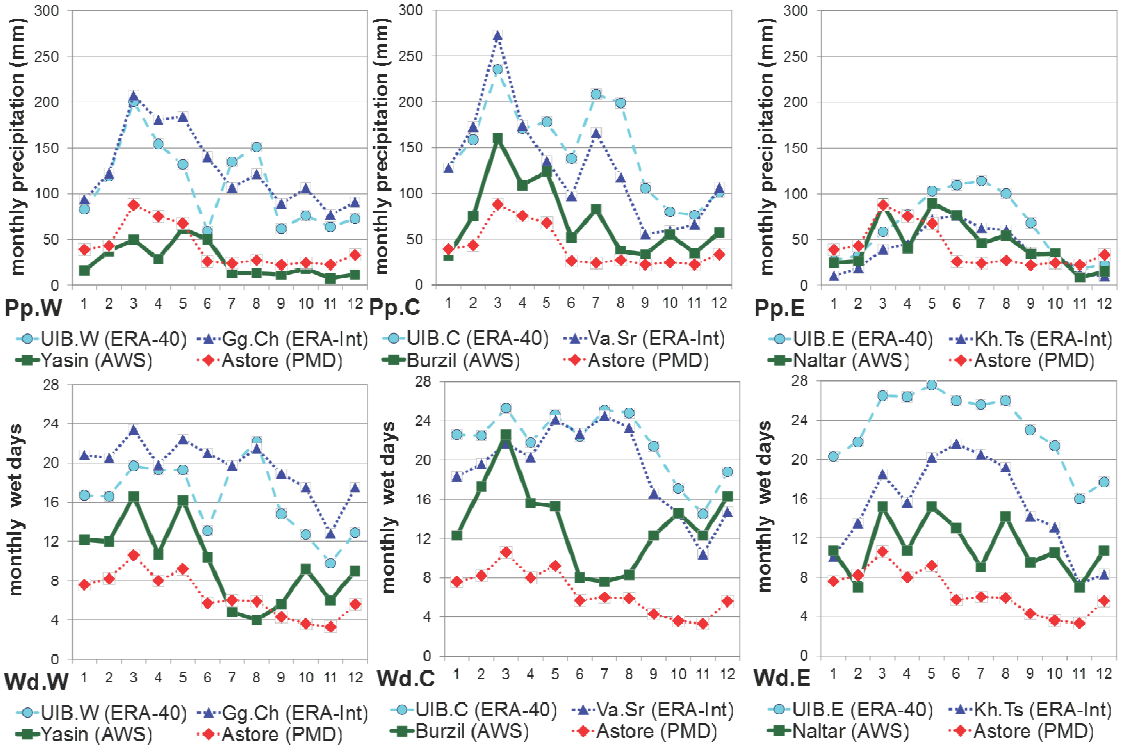

Figure 3.027 A comparison for precipitation records from 4 independent data sources. Time-periods are from1979 to 2001 (ERA-40, ERA-Interim, PMD) except for AWS observations where records are as indicated in Table 3.04.

Clearly, the precipitation regimes seen in the reanalysis precipitation climatologies find echoes in the local observations. The limited spatial extent and distribution (with respect to elevation) of the latter and the spatially aggregating character of the former, however, make some discrepancies between the data sources inevitable. The reanalysis precipitation climatologies are of particular interest because the estimated annual accumulations are similar in magnitude to the annual runoff depths calculated through WAPDA river gauging.

In addition to “synthetic station records” created by extracting time series of individual grid cells, the spatial resolution of the ERA-Interim reanalysis justifies presenting it as large-scale rasters (maps). Figures 3.028 and 3.029 respectively show the annual total precipitation and wet days for an analysis window covering the UIB and contiguous regions. In both figures the orographic controls on precipitation are clear. For wet days, the higher values are roughly uniformly distributed over the mountains and upland plateaus (western Tibet), with lower numbers of wet days in the low-lying areas in the southwest (lower Indus valley) and northwest (Taklimakan Desert). For total annual precipitation, the control of the available moisture sources is clear: the

greatest totals occur along the front range of the Himalayas in areas benefitting from monsoonal rains as well as from winter storms. The “leeward highland regions” (northern Hindu Kush/Karakoram and Tibetan Plateau) have moderate totals. The areas with lowest accumulated precipitation are also those with the fewest wet days.

Previous studies of spatial precipitation have often drawn upon gridded data sets interpolated from point-based station records using purely geometric techniques (e.g. APHRODITE, described by Yatagai *et al.* 2009) which do not take into account physical mechanisms such as orographic enhancement of precipitation. In the opinion of this author such methods may be appropriate where station density itself is great enough to capture the physical processes governing precipitation. In areas such as the UIB, however, where station density is severely limited and station locations are recognised as not representative in absolute terms of catchment spatial mean accumulation amounts, that approach is neither rigorous nor sound. Other studies (e.g. Winiger *et al.* 2005, Immerzeel *et al.* 2012) have used hydrological modelling to “back-calculate” precipitation inputs required to “close the hydrological mass balance” in light of observed runoff or assumed glacial mass balance conditions. Spatial studies based on upon data from TRMM data products will be considered in section 3.5.4. In summary the spatial assessments presented here of direct outputs from meteorological reanalysis as well as RCM simulations driven by reanalysis (section 3.5.5) provide a novel contribution, at least for the study area in question.

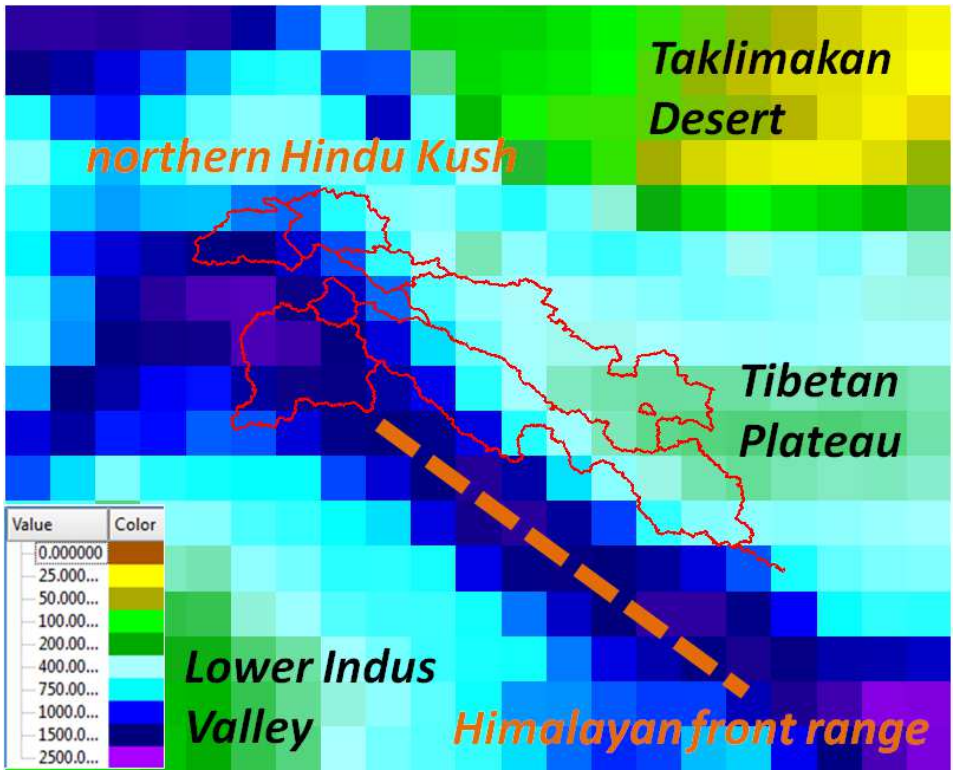

Figure 3.028 Mean annual total precipitation (mm) from ERA-Interim (1979 to 2007).

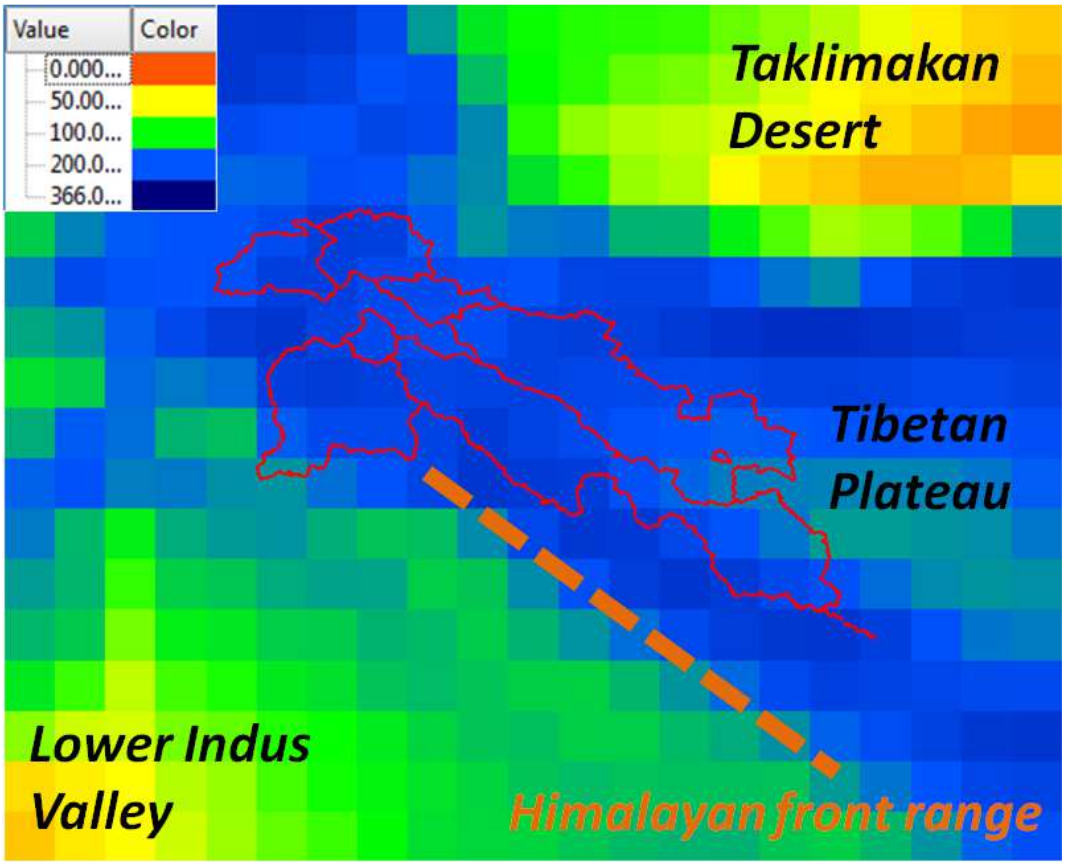

Figure 3.029 Mean annual total wet days (precipitation > 0.1 mm) from the ERA-Interim reanalysis (1979 to 2007).

The annual cycles of precipitation and wet days, expressed as monthly contribution to annual totals, are shown in Figures 3.030 and 3.031. Because the values are computed relative to the annual total the units are dimensionless (0 - 100%). This approach was adopted to normalise, or remove the bias from the information provided by sometimes discordant data sources. In the near total absence of definitive, spatially-representative ground-truthing this seemed a viable approach to allow competing precipitation climatologies to be assessed objectively. Furthermore, given the scientific uncertainty regarding orographic precipitation gradients in the UIB, it is inevitable that for hydrological simulation purposes scaling of observations as precipitation inputs will be performed in order to achieve model calibration and validation. As such the seasonality of precipitation will play an equally important role to its magnitude in achieving project objectives.

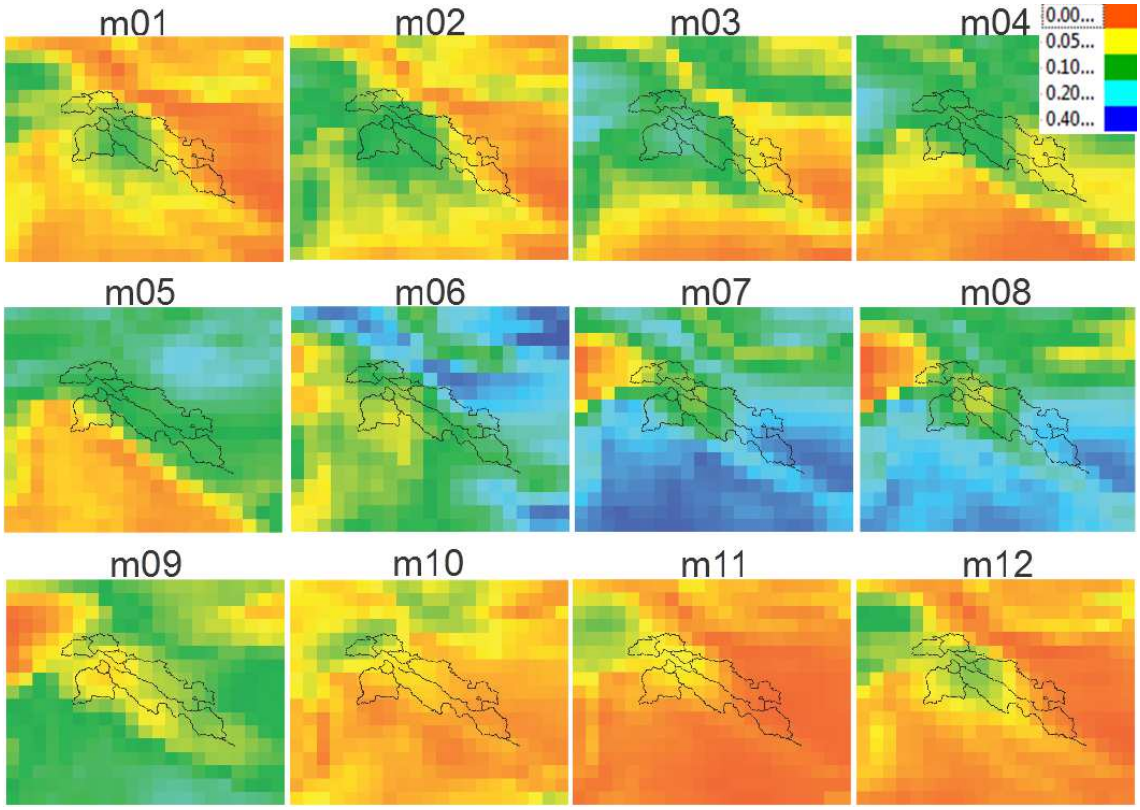

Figure 3.030 Mean monthly contributions to annual total precipitation from the ERA-Interim reanalysis (1979 to 2007).

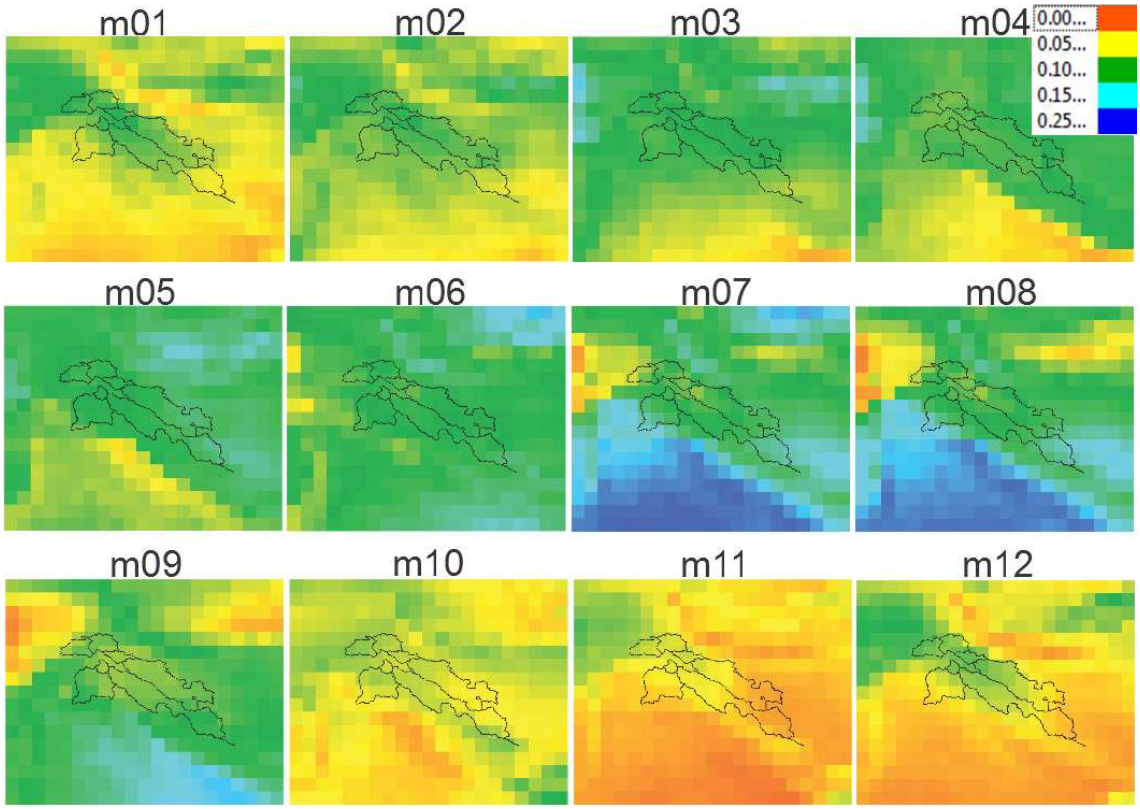

Figure 3.031 Mean monthly contributions to annual total wet days from the ERA-Interim reanalysis (1979 to 2007).

Figures 3.030 and 3.031allow one to begin to visualise sub-regional precipitation regimes. Although there are differences between wet day numbers and accumulated precipitation, the individual monthly contributions indicate which blocks of grid cells behave in a (roughly) coherent manner. Of key interest to the present study is the core area of the NW UIB -- centred on the Gilgit, Hunza, Astore and Shigar tributary catchments – which shows its own pattern of monthly contributions (seasonality). The pattern shown in the Figures (3.025 and 3.026) – where selected grid cells are treated as synthetic gauges – can be seen spatially in Figures 3.030 and 3.031. This can be most easily visualised in the minimal autumn contributions to annual totals of both precipitation and wet days for this area. It can also be recognised in the strong pre-monsoonal (February to June) contributions to annual precipitation (Figure 3.030).

This pattern is climatically distinct from the surrounding sub-regions which could roughly be termed the Hindu Kush/Pamir (northwestern half of the northwestern quadrant), the Indo-Gangetic plain (southern central region tapering east and west), the Taklimakan Destert (northern half of northeast quadrant) and the Tibetan Plateau (southern half of northeast quadrant). These adjacent sub-regions show individual seasonal concentrations of precipitation events – evidenced by maxima in monthly contributions to annual totals – which could be assumed to derive from the specific atmospheric circulation systems which deliver moisture bearing air masses to the region. Hence the Indo-Gangetic plain for example shows maxima of contributions to annual totals from July and August as the precipitation climatology of this sub-region is dominated by (South Asian) monsoonal rainfall concentrated in these months. An objective classification of these preliminarily identified climate regimes was not conducted in the context of the present work, but the data (ERA-Interim) seem favourable and thus this is a likely element of future work.

3.5.4 Precipitation estimates from the Tropical Rainfall Monitoring Mission (TRMM)

While the reanalyses output provides estimates of precipitation based on projected meteorological behaviour, the data from the Tropical Rainfall Monitoring Mission (TRMM) are derived from direct observations of the atmosphere by satellite-borne instruments (Huffman *et al.,* 2007). The specific data product analysed in this study, 3B43 (Huffman *et al.,* 2011), is derived from data another TRMM data product (2B31) which is further “corrected” using observations from a network of ground-based rainfall gauges. Figure 3.032 shows the period mean annual total precipitation estimates

from TRMM for the UIB (for the available time period from 1998-2010) and its contiguous regions.

In general terms the sub-regional distribution of precipitation is similar to that found in ERA-Interim (Figure 3.028). Closer inspection, however, shows that while in TRMM the central axis of maximum precipitation is squarely over the foothills of the Himalaya, in ERA-Interim this axis is positioned slightly behind (to leeward) of the front range. This can be gauged visually in comparing the two figures (3.028 & 3.032) and noting the relative positions of the band of maximum precipitation and the catchment boundary of the Indus above Kharmong (which runs roughly parallel). It could be assumed that this difference is attributable to the difference in time periods: 1998 to 2010 for TRMM, but 1979 to 2007 for ERA-Interim. As will be argued in the remainder of this section, however, a more plausible explanation is that the discrepancy results from differential bias in the TRMM data product with respect to the physical mechanism driving the precipitation event, i.e. TRMM better detects convective precipitation than orographic precipitation. This finding mirrors that by Ward *et al.* (2011) for another mountainous region, the Andes, who also identified differential bias as a function of precipitation mechanism.

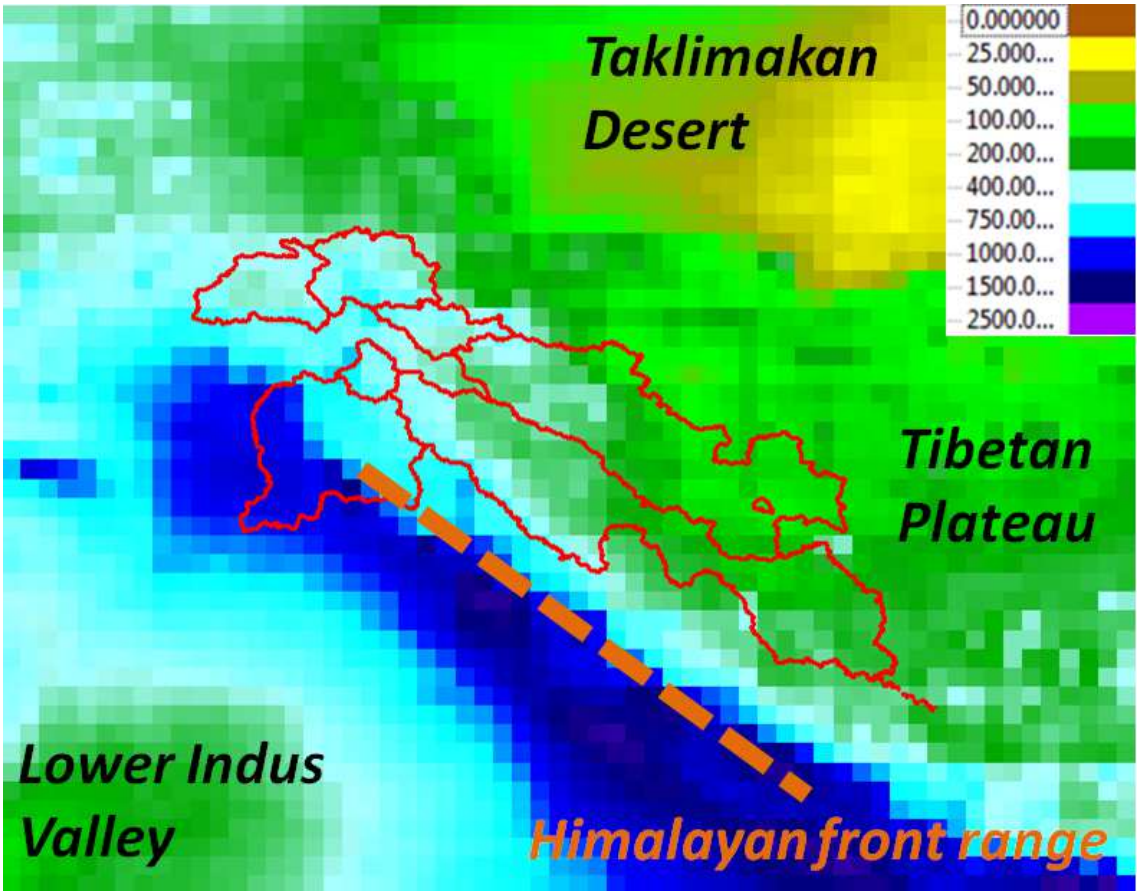

Figure 3.032 Mean annual total precipitation estimates from TRMM (1998 to 2010).

This simple (contrasting) inspection of different data sources clearly demonstrates the need to determine the characteristics and biases of each type of precipitation estimate before it can be used in any modelling study as unverified assumption that any individual data set was accurate in absolute as well as relative terms could introduce additional bias in subsequent analyses, for example understanding precipitation in one season or geographic area and implicitly exaggerating the relative importance of precipitation at another time or location.

As its name suggests, TRMM was primarily destined to provide observed precipitation in the equatorial and tropical regions where precipitation is dominated by intense convective activity. Precipitation in the UIB tends to be dominated by orographically enhanced stratiform precipitation. To assess the impact these differences in rainfall mechanism could engender in terms of measurement bias, spatial aggregates (catchment area means) were compared to point observations from the PMD and AWS stations.

First the seasonality (monthly contributions to annual total) from the TRMM estimates and point observations were compared (Figure 3.033; first panel shows comparison to PMD, second to AWS data). The AWS data clearly demonstrate a spring-time concentration in precipitation, thus corroborating that seen in the PMD long-record stations. This directly contrasts with the TRMM values which show a “dual mode”: a peak in late winter and again during the monsoon months. To be clear the orthodoxy of this comparison is hampered by the fact that the available data records for the AWS stations do not overlap with the operational period of the TRMM satellite. Nevertheless previous analyses with ground-based precipitation observations have demonstrated that while trend detection (see Chapter 4) is highly sensitive to the choice of analysis period, derivation of period means and characterisation of seasonality (mean monthly contributions to mean annual totals) are far less so. This is attested by the contrast between the differences in TRMM versus PMD observation results from identical time periods (1998 to 2010) and the similarities between the PMD observations and AWS measurements despite the use of different time windows (1994 to 1998 for AWS).

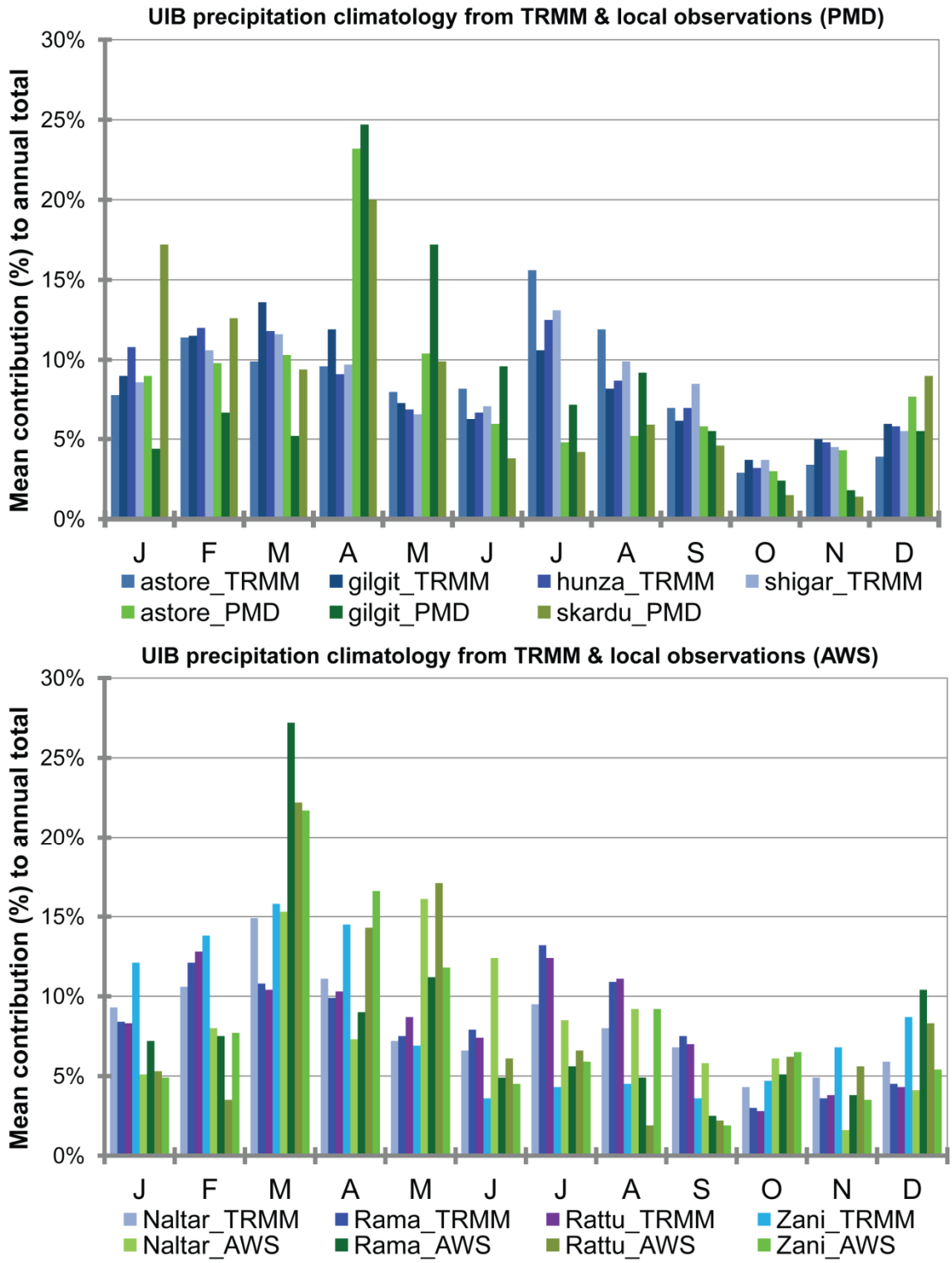

Figure 3.033 Mean monthly contributions to annual total precipitation, TRMM spatial aggregates vs point observations, TRMM and PMD records from 1998 to 2010; AWS records (as available) from 1994 to 1998.

This disagreement between TRMM and local observations is further evidenced when comparing seasonal scatter plots of TRMM estimates versus local observations for Astore and Gilgit (Figure 3.034) using a common observation period from 1998 to 2010. The ratio of TRMM to local observations is clearly greater in Summer (JJA) than in Spring (MAM). This may be due to the underestimation of stratiform precipitation –

enhanced in the UIB by orographic lifting – compared with the convective precipitation that traditionally dominates in the tropics and subtropics where the TRMM initiative is focused. The relative contributions of stratiform and convective precipitation to total accumulation in the UIB will vary from season to season although stratiform would always be expected to remain the dominant mechanism. Thus it is logical that the relationship between TRMM precipitation estimates and local observations (PMD) for Summer (JJA), when the fractional contribution of convective precipitation to total accumulation would be at its annual maximum, would differ from the relationship between the two data sources for Spring (MAM) when convective precipitation would contribute relatively less to total UIB total accumulations. By this reasoning of dominant precipitation mechanism, Autumn (SON) and Winter (DJF) would be expected to resemble the Spring (MAM) rather than Summer (JJA) in the relationships between TRMM precipitation estimates and local observations.

Orographic precipitation poses technical problems for both infrared-derived and passive microwave-based rainfall estimation algorithms (Dinku, 2008). This seasonally varying bias (differing scale factor) complicates the use of TRMM as an indicator for interannual variability of runoff in UIB subcatchments. Even so, as will be shown later in this chapter, TRMM precipitation estimates, separated into Winter (ONDJFM) and Monsoon (JJA) measures, still have potential as (complementary) predictors of melt season runoff.

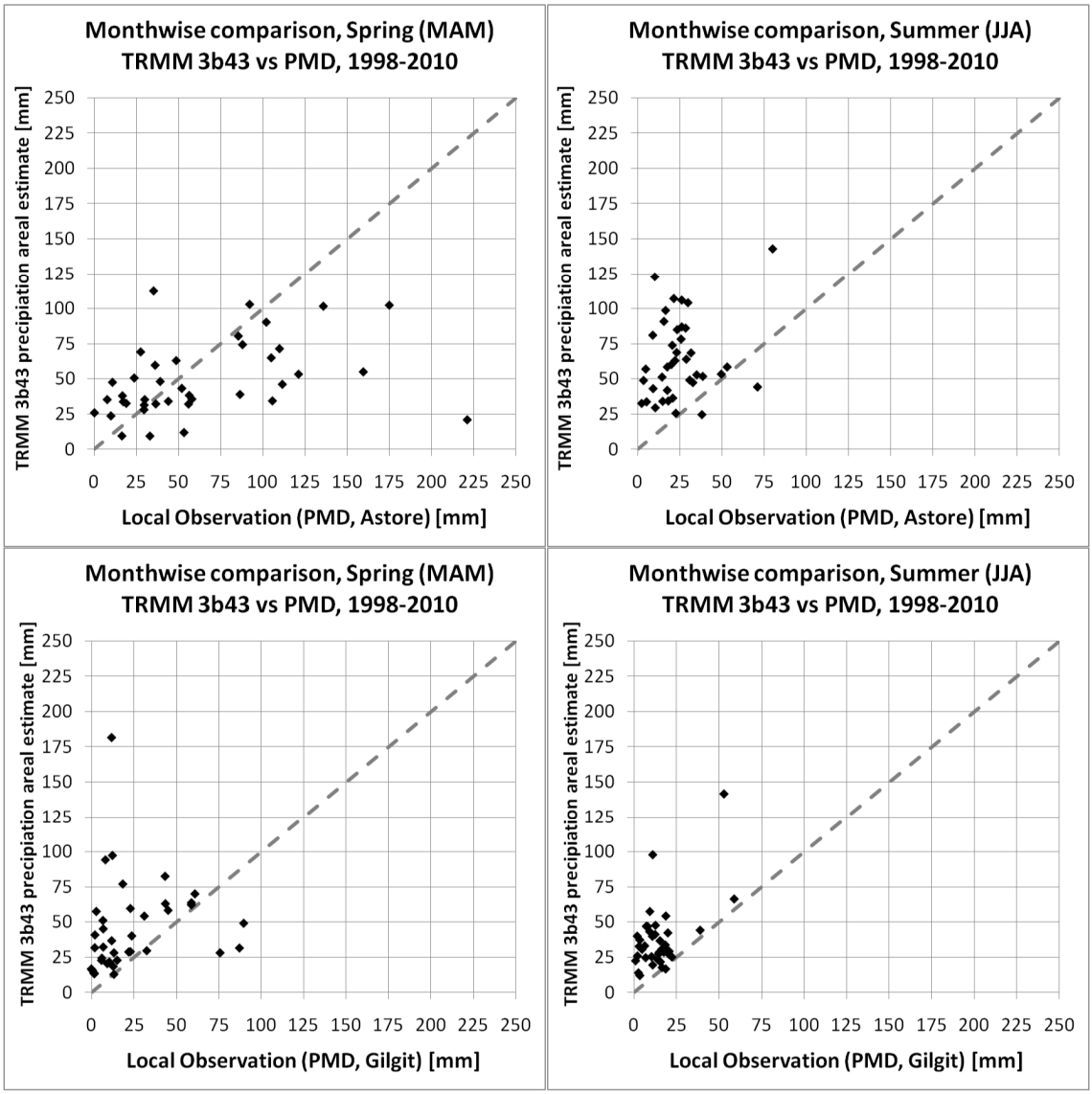

Figure 3.034 Seasonal scatter plots of local (PMD) precipitation observations to TRMM estimates for 1998 to 2010 for Astore (top row) and Gilgit (bottom row).

In a separate consideration, assessment of monthwise and pixelwise distribution of mean contributions to annual precipitation provides a further element for the classification sub-regional scale precipitation regimes. This is shown in Figure 3.035. Although “noisier” (less spatially coherent) than the ERA-Interim estimates, very similar regime-zones emerge from the TRMM data. The core NW UIB zone appears, however, marginally less coherent than in ERA-Interim. This is perhaps due to the mechanisms and biases described above.

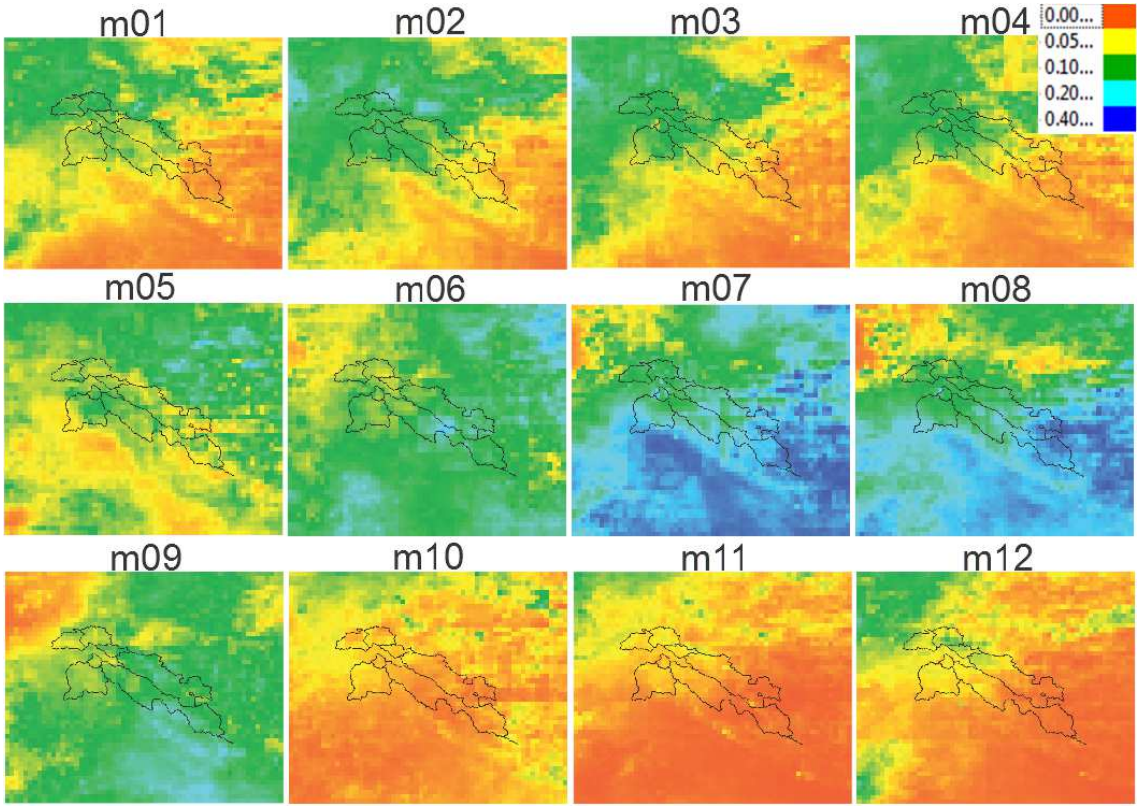

Figure 3.035 Mean monthly contributions to annual total precipitation estimates by TRMM (1998 to 2010).

3.5.5 Precipitation estimates from RCM to downscale reanalysis: PRECIS driven by ERA-40

One significant drawback to the ERA-40 reanalysis data is its coarse spatial resolution (2.5 degrees). Use of ERA-40 as boundary conditions to drive an RCM (PRECIS; HadRM3), however, allows the information from the reanalysis to be downscaled to better reflect sub-regional variations driven by topography (Akhtar *et al.*, 2009). The downscaling performed by the PRECIS simulation output available to this study (Islam *et al.*, 2009) delivers a spatial resolution of roughly 50km (0.5 degrees). The resultant estimates of annual total precipitation and wet days are shown in Figures 3.036 and 3.037.

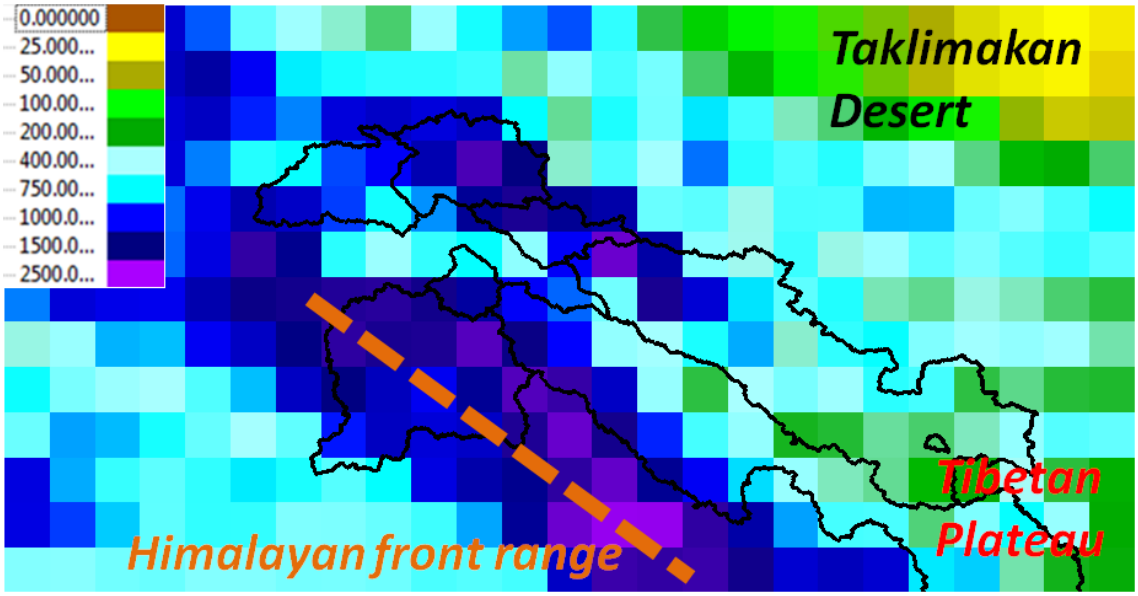

Figure 3.036 Mean annual total simulated precipitation from PRECIS downscaling of ERA40 (1961 to 1989) to 50km resolution.

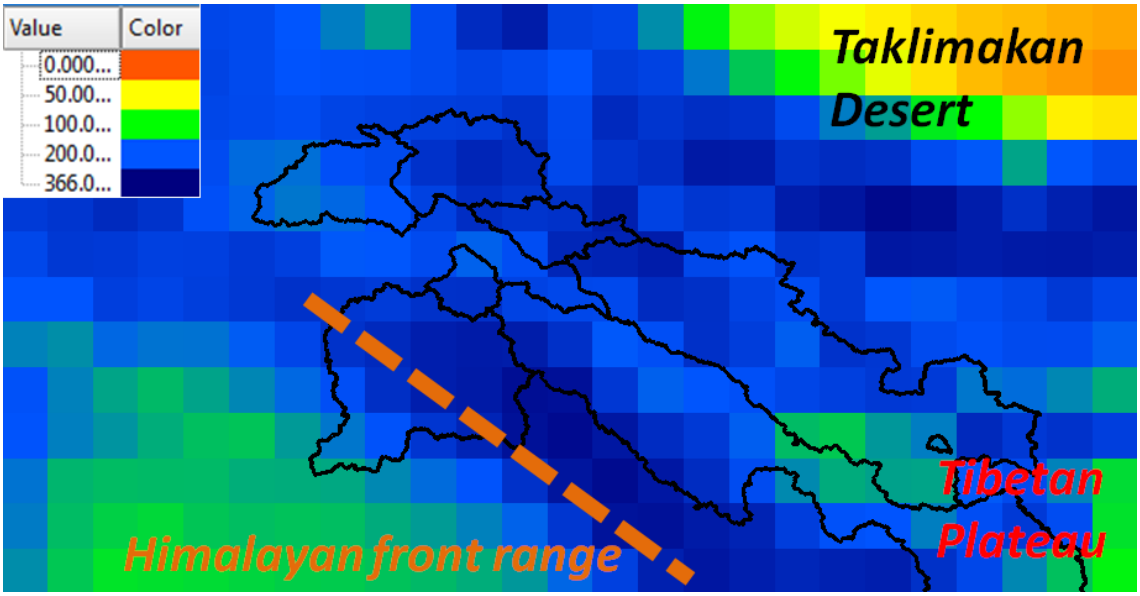

Figure 3.037 Mean annual total wet days from PRECIS downscaling of ERA40 (1961 to 1989) to 50km resolution.

Even for the mean annual total precipitation (Figure 3.036), the similarities and differences between PRECIS downscaling of ERA40 (hereafter designated PRECIS_ERA40) and the other spatial precipitation datasets, ERA-Interim (Figure 3.028) and TRMM (Figure 3.032), are striking. Despite the differences in the assimilation and forecasting model used by the two reanalyses – ECMWF model cycle 23R4 for ERA-40 and model cycle 31R2 for ERA-Interim (Betts *et al.* 2009) – as well as the difference in time period analysed – 1961 to 1989 for PRECIS_ERA40, 1979 to 2007 for ERA-Interim – the band of maximum regional accumulation in both ERA-Interim and PRECIS_ERA40 is centred on and oriented along the front range of the

Western Himalaya (WH). This is in contrast to TRMM which, as stated above, shows the band of maximum regional accumulation oriented parallel to the front range but offset and centred over the foothills and adjacent plains. There are nevertheless differences between PRECIS_ERA40 and ERA-Interim in the spatial patterns of annual accumulations. Most interestingly, while ERA-Interim shows a single coherent band of large annual accumulations over the WH with limited penetration to the Karakoram and Hindu Kush, PRECIS_ERA40 in addition to the primary band over the WH also shows a narrower secondary band over the Greater Karakoram and northeastern Hindu Kush. This secondary band is separated from the primary by an area with lower annual totals.

In general the spatial patterns for the annual wet day totals for PRECIS_ERA40 (Figure 3.037) are quite similar to those from ERA-Interim (Figure 3.029). There are indications that the increased spatial resolution may yield improved resolution of the orographic influences on precipitation frequency (as quantified by annual total wet days). Given the difference in analysed time periods – 1961 to 1989 for PRECIS_ERA40, 1979 to 2007 for ERA-Interim – presented here, more robust conclusions would require comparison of identical temporal subsets, i.e. 1979 to 1989. In light of the relatively minor difference in spatial resolution between the two data sets, further analysis would likely be more justified in the event additional models at yet higher spatial resolutions (e.g. 25km or better) become available.

Thus spatial patterns found in PRECIS_ERA40 precipitation and wet day estimates broadly match those in found in the marginally coarser resolution (80km vs 50km) ERA-Interim reanalysis. The improved representation of orographic (elevation-driven) precipitation effects is not entirely conclusive, but there is some visual indication that the drier microclimate of the Indus main channel valley bottom and the humid accumulation zones of the major Karakoram glaciers (e.g. Biafo, Baltoro, Biafo, Siachen) are captured. There also appear to be differences in how the relative influences/impacts of westerly and monsoonal moisture sources are resolved. Care must be taken, however, when crediting RCMs with accurate representation of processes, such as the monsoonal weather systems, which are driven by convective activity. This is because in present RCMs the simulation of convective processes must be approximated by via parameterisations since the spatial resolution of the models is not adequate to directly model the physical processes involved.

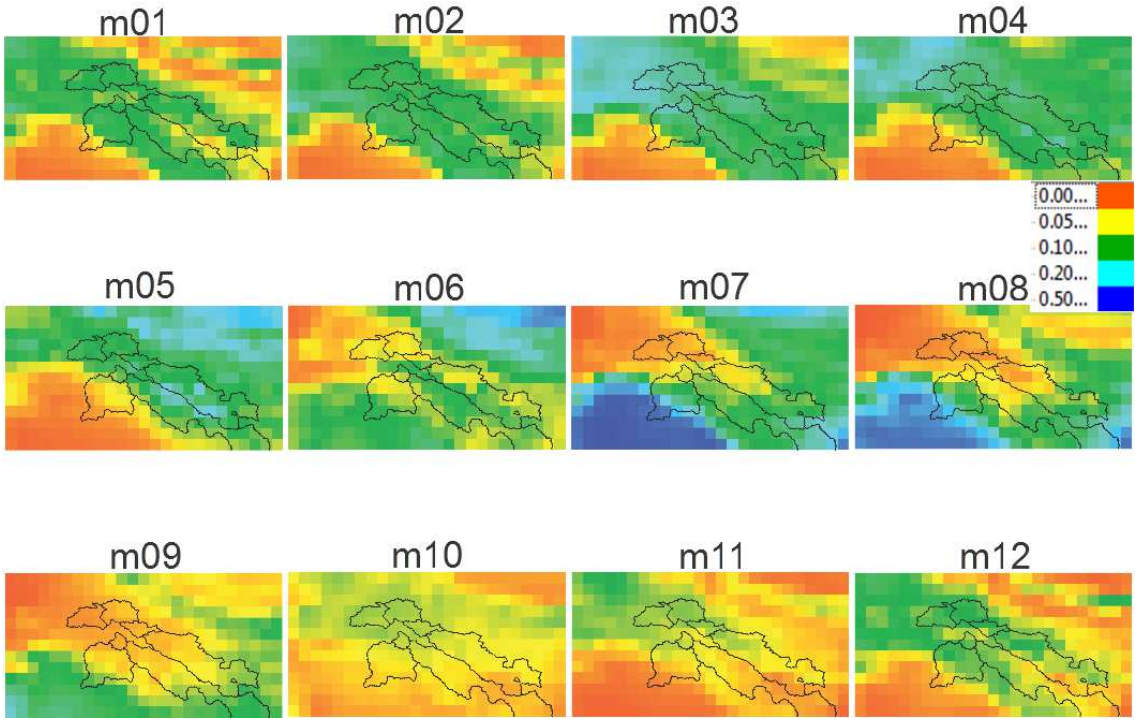

Figure 3.038 Mean monthly contributions to annual total precipitation from PRECIS downscaling of ERA40 (1961 to 1989) to 50km resolution.

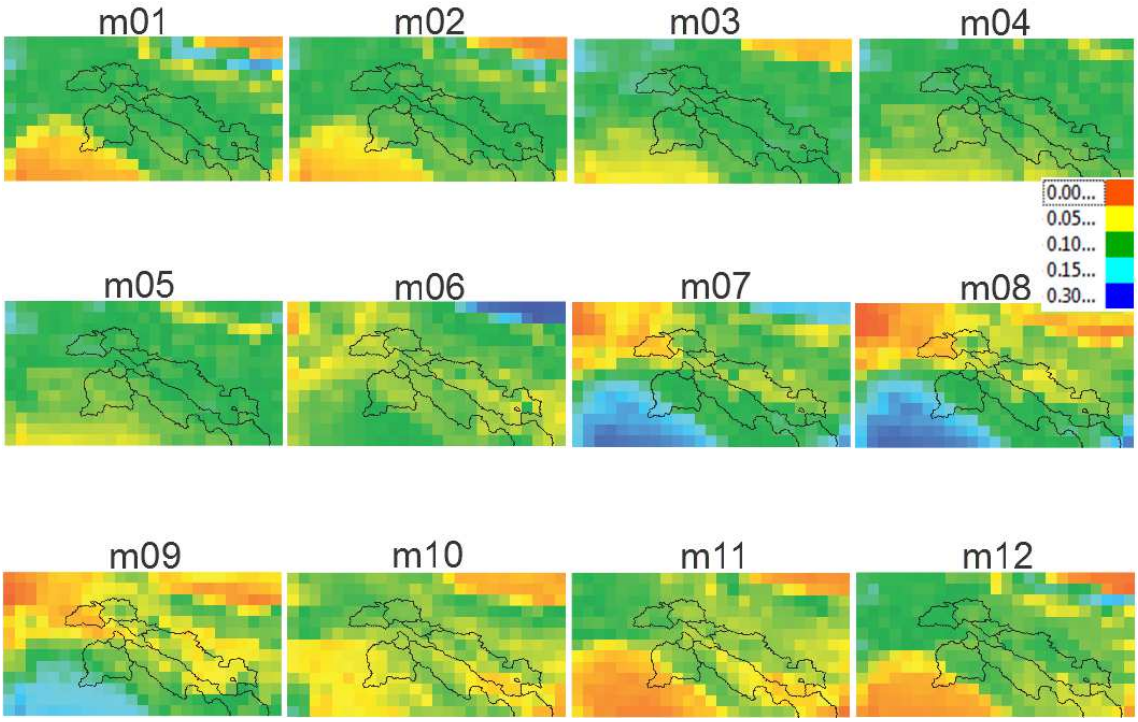

Figure 3.039 Mean monthly contributions to annual total wetdays from PRECIS downscaling of ERA40 (1961 to 1989) to 50km resolution.

While the annual totals of precipitation and wet days give indications of the sub-regional variations in overall mass inputs to the river systems of the sub-continent, the detailed analysis of the mean monthly contributions to annual totals can help to identify the dominant climatic influences by revealing the timing of weather systems which deliver precipitation. Figures 3.038 and 3.039 consequently show the annual cycle for

mean monthly contributions to annual rainfall and total wet days respectively and are apt for direct comparison to the equivalent Figures, 3.030 and 3.031, for ERA-Interim. In general PRECIS_ERA40 and ERA-Interim yield quite similar results, as would be expected based on the close agreement, described above, between the spatial patterns of annual totals.

In the PRECIS outputs there appears to be less monsoonal penetration beyond the foothills/windward front range than in ERA-Interim. With regards to precipitation seasonality in the core NW UIB hydrological contributing area, the PRECIS outputs tend to more strongly emphasize the dominance of the spring-time primary mode and lessen the contribution of the summertime/monsoonal secondary mode.

It would be hoped that increased PRECIS model horizontal resolution in a 25km/0.25decimal-degree simulation would yield further improvements in characterisation of orographic precipitation effects and geographic delimitation of monsoonal versus westerly dominance in precipitation regimes. An ensemble of 25km RCM runs for the South Asian domain by the Hadley Centre of the UK Met. Office has been completed (Bhaskaran, UK Met Office, personal communication, 26 Nov 2012), but not yet available to this study. Given the topographical complexity of the UIB, however, truly satisfactory simulation of the complex local precipitation regimes might require even further increases in spatial resolution (e.g. 5km grid spacing or less).

3.5.6 Summary discussion of precipitation data sources and issues

It is abundantly clear from this section (3.5) that the estimates of annual total precipitation and of its monthly distribution vary greatly depending upon data source. Consequently, it is important to point out that modelling assumptions, and ultimately the conclusions, about the UIB cryosphere – glacial ice and seasonal snowpack – mass balance based on the difference in mass input (precipitation) and mass output (runoff) will depend entirely on the source of the precipitation estimate and how it is interpreted to represent the spatial mean values for the basin. If it is assumed that the values measured in either the PMD long-record (valley) stations or estimated by the TRMM 3B43 data product are accurate as absolutes, and also assuming accuracy in absolute terms of runoff depths calculated from WAPDA river gauging, then the assumption is that mass balance is severely negative, i.e. mass input (precipitation) is greatly exceed by mass output (runoff plus evapotranspiration). The logical extension of this thinking is then that glacially volumes will of necessity be decreasing in order to compensate for

the mass shortfall of inadequate precipitation. If the values from the ECMWF reanalysis projects are assumed to be close to the true spatial averages, however, the assumption that net positive mass balance is probable, i.e. that input from precipitation exceeds output in runoff and evapotranspiration, may be retained.

Reality is likely much more nuanced than either of these two simplistic assumptions. The present work will attempt to provide the maximum possible clarification and constraint on these issues as the currently available data allow.

3.5.7 Snow Covered Area

Snow covered area (SCA) is not a direct metric of accumulated precipitation. Rather it shows the areal extent of solid precipitation (snow and ice), independent of accumulated depth, for a given period of time. Due to the orographic control on precipitation in the UIB, coupled with the approximately linear relationship between temperature and elevation, however, there is a strong link between the degree of snow cover and the accumulated catchment snowpack. Thus SCA can act as an indicator of the preceding season's precipitation. SCA is also important because of its contribution to land surface albedo and thus its influence on the surface energy balance.

For this project, SCA was available as raster imagery produced from radiometric observations by the MODIS instrument. Because of its strong links to catchment hydrology SCA was spatially aggregated (areal mean) to the catchment areas of the primary gauged UIB tributary basins. The annual SCA cycle, along with an estimate of the range of interannual variability (first [c10] and last [c90] deciles), for six spatial units is shown in Figure 3.040. For clarity, the boundaries of these six units are shown in Figure 3.041.

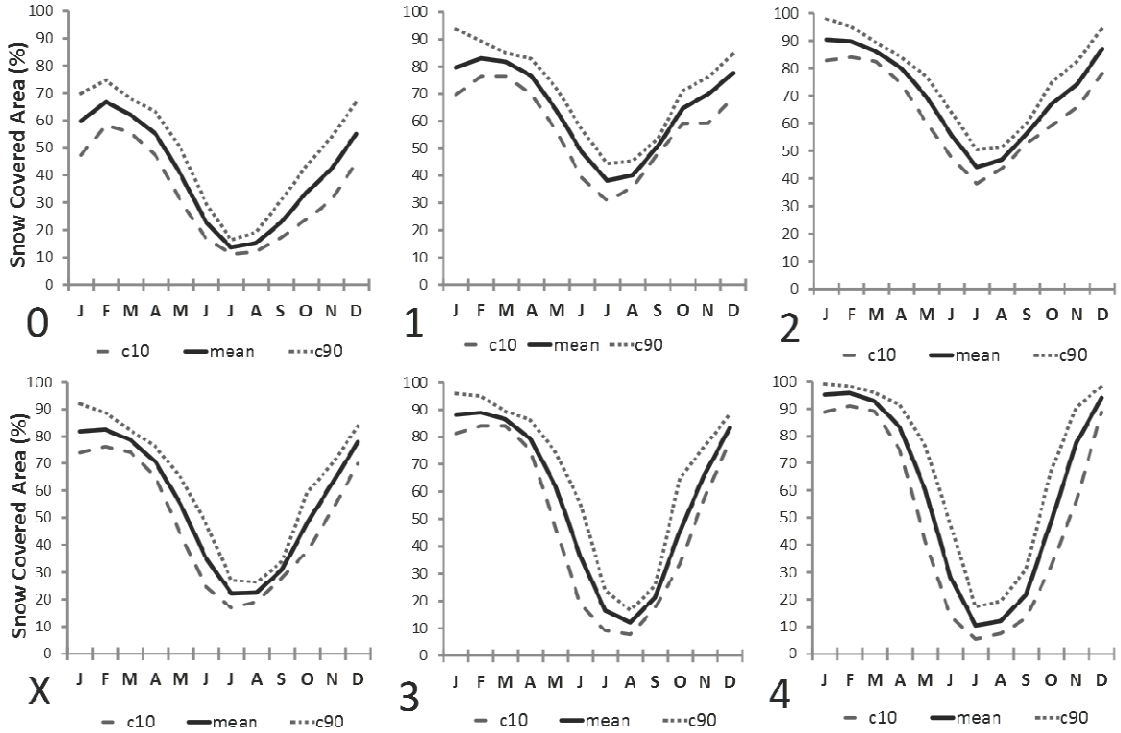

Figure 3.040 Annual cycle of Snow Covered Area (SCA) for the period 2000 to 2010 monthly means and first and last deciles (c10 & c90) from MODIS for primary tributary catchments – [0] the Upper Indus above Besham, [1] the Hunza above Dainyor bridge, [2] the Shigar above Shigar town, [X] the NW UIB sector (1+2+3+4 plus main channel valley between Besham and Yogo/Kharmong), [3] the Gilgit/Ghizer above Gilgit town, and [4] the Astore above Doyian. Boundaries are shown in Figure 3.041.

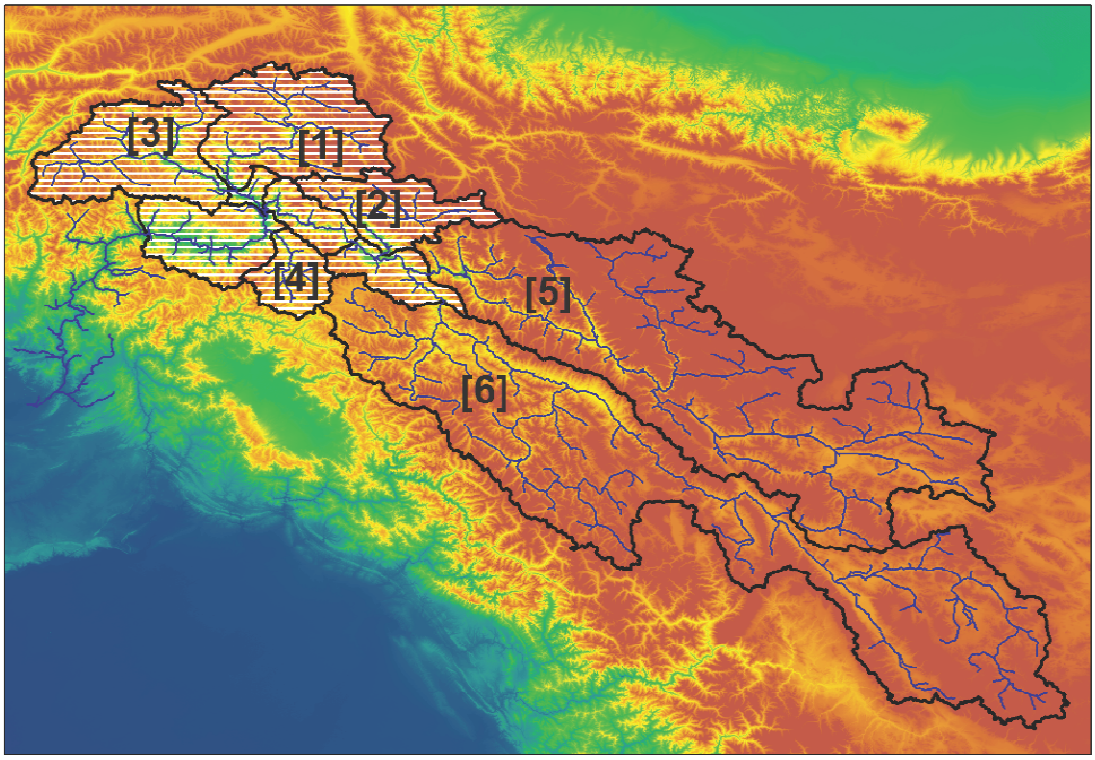

Figure 3.041 Boundaries of primary tributary catchments as used in analysis of MODIS data products – [1] the Hunza above Dainyor bridge, [2] the Shigar above Shigar town, , [3] the Gilgit/Ghizer above Gilgit town, and [4] the Astore above Doyian.

The differences between catchments in the shape of their annual SCA cycles, as shown in Figure 3.040, align with established hydrological regime types. Catchments with high annual SCA minima, Hunza and Shigar, are also those with high glacial melt contributions (glacial regime) and minimal hydrological responsiveness to year to year variation in observed precipitation. Those with low annual SCA minima, Gilgit and Astore, are snowmelt-dominated catchments (nival regime) dependent on annual replenishment of the snowpack from winter precipitation. Nival regime catchments tend to have very little contributing area above 6000 m asl. The relative variability in annual SCA minima (values for c10 compared to c90) is striking, particularly for the nival regime catchments, Astore and Gilgit, where c90 is roughly twice that of c10 for the minimum SCA month. This difference could interpreted as a nuance on the behaviour of nival regime catchments. It is generally assumed for nival regime catchments that available cumulative energy to drive the melt process will nearly always be adequate to completely exhaust the available snowpack. If the the interannual variability indicated by MODIS is representative of real physical variability in minimum annual snowpack extent it would imply that melt energy may in fact as a constraint, albeit secondary, to runoff in UIB nival catchments. On the other hand, given the challenges involved in SCA detection in geographical contexts as complex as the UIB, the apparent variability seen in MODIS may in fact simply be artefacts in the data due to processing algorithm errors.

Figure 3.042 shows, with varying degrees of detail, images of the mean monthly land surface state classified by the snow-presence (from SCA) and surface temperature. The term “land surface state” as employed here refers to the surface condition defined by a combination of parameters of interest from land surface process perspective, and in this case specifically a cryospheric viewpoint: whether or not snow cover is present and whether the surface is above or below the freezing point. Land surface temperature will be presented separately, in detail, later in this chapter, but in these figures the key consideration are whether: night-time LST (Tnight) remains above freezing (Tnight > 0°C) and whether day-time LST (Tday) remains below freezing (Tday < 0°C). Table 3.10 provides a “contingency table” to summarise how colours were assigned in these figures.

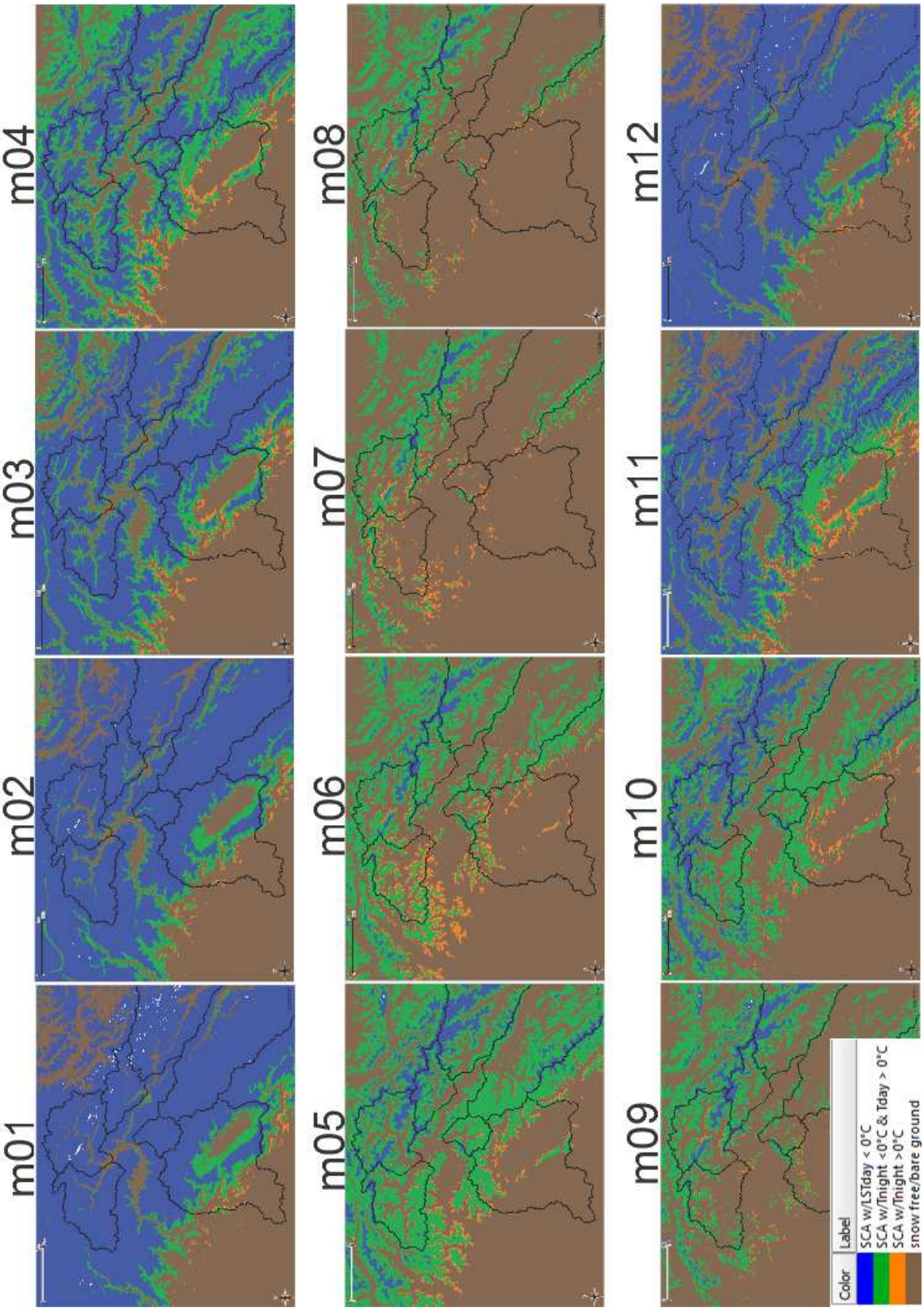

Figure 3.042 MODIS SCA "surface state" by month for NW UIB.

Land Surface Temperature (LST)	Monthly mean SCA	
	SCA < 25%	SCA > 25%
Tnight > 0°C	brown	orange
Tnight < 0°C < Tday		green
Tday < 0°C		blue

Table 3.10 Contingency table describing colour-coding in Figure 3.042.

To clarify, an arbitrary decision was made to represent a pixel (1km horizontal resolution in this case) as snow-free if the period mean SCA was less than 25%. If so, the pixel was assigned the colour brown. If snow was determined to be present (SCA > 25%), the day-time and night-time LST were considered to provide further classification. These locations are expected to function hydrologically as in the classic "direct rainfall-runoff" mode.

It is important to note here that on a long-term mean basis, night-time temperatures are uniformly cooler than day-time temperatures. If night-time LST remains above freezing (Tnight > 0°C), the pixel was assigned the colour orange. These pixels are locations where limited snowpack and glacier "tongues" will be surrounded by bare ground and where melt is expected to be rapid. These conditions are generally spatially quite limited.

If day-time LST does not reach freezing (Tday < 0°C), the pixel was assigned the colour blue. These are areas where input energy is not expected to be adequate to result in the melt of snow or icepack. Thus for the month in question they do not contribute hydrologically (although mass movement to lower/warmer areas by avalanching may occur).

In the remaining case, day-time LST reaches 0°C or greater but night-time LST falls below 0°C thus suggesting a diurnal cycle of melt and refreezing. These pixels were assigned the colour green. Locations in these conditions are expected to contribute most to ablation of the ephemeral (seasonal) snowpack.

This classification of "surface state" thus illustrates the essential spatial articulation between hydrological inputs of mass (SCA) and energy (LST) in the UIB and shows why detailed consideration of temperature is so crucial to study of the basin's hydrology.

In essence the annual "surface state" cycle can provide another method of defining the differences between the pluvial, nival and glacial hydrological regimes in the UIB. This is summarised in Table 3.11.

Season	seasonal "surface state" typology by hydrological regime		
	pluvial regime	nival regime	glacial regime
Winter	limited if any snow cover, most area Tday > 0C	Snow cover nearly total, most area Tnight < 0C	Snow cover nearly total, most area Tnight < 0C
Spring	area nearly snow free, SCA likely to show Tnight > 0C	SCA still extensive, but most area rapidly shows Tday > 0C	SCA still extensive, Tday < 0C still widespread
Summer	area entirely snow free, Tnight > 0C	remaining SCA minimal, Tday > 0C through	substantial remaining SCA, but only highest elevation areas keep Tnight < 0C
Autumn	area nearly snow free, SCA likely to show Tnight > 0C	SCA begins to replenish, transition from Tday >0C at beginning of season to Tday < 0C at end of season	SCA rapidly extends toward annual maximum; most area quickly shows Tday < 0C

Table 3.11 Summary table showing archetypal seasonal "surface state" conditions associated with each hydrological regime type.

As presented in Table 3.11, the annual "surface state" cycle can provide an additional means of identifying catchment hydrological regime type. Areas with only minimal Winter snow cover are likely to experience rapid Spring melt and exhibit dominantly direct rainfall-runoff response characteristic of pluvial regime catchments. Nival regime catchments in contrast will have widespread Winter SCA although the snowpack surface temperature will rise rapidly through Spring and ablation will be nearly complete by early Summer. Finally, glacial regime catchments will have substantial Summer SCA and surface temperatures will remain below freezing except from late spring to early autumn. In conclusion, because it can be easily displayed geographically, "surface state" can be a very effective descriptor for rapidly assessing meltwater-hydrological conditions spatially.

3.6 Quantitative indices of energy inputs to UIB hydrological system

3.6.1 Temperature (air and surface) generalities

Temperature is the simplest available index of energy input to the meltwater-generation runoff process. As such its analysis is the prerequisite to more sophisticated evaluation of the surface energy balance. When considering how to assess cycles and variability in (air and surface) temperature, the issue of visualisation method arises. Local observations are almost always point based (e.g. thermometers) and time-series do illustrate well temporal cycles and variability. The catchment land surface processes, above all meltwater generation, which motivate hydrologists' interest in temperature are spatial integrators. Thus, point observations, while useful in quantifying relative temporal anomalies in catchment energy inputs, will only provide meaningful absolute

measures of catchment conditions if they happen to be sited so as to observe a point where spatial mean occurs (e.g. at the mid-point or median of catchment elevation range). Otherwise, mean spatial conditions must either be extrapolated using topographic relationships (temperature lapse rates) or assessed through spatial data products. In light of these issues, this study will assess both point-based and spatial data sets for air and surface temperature.

3.6.2 Diurnal extremes of 2m air temperature and LST

Evidence (e.g. Forsythe *et al.* 2012b) suggests that in the UIB the extremes of the diurnal temperature cycle play a vital role in modulating hydrological processes. In the UIB, at any given point or elevation, the annual cycle of temperature follows a roughly sinusoidal pattern with an annual maxima centred on July-August and an annual minima centred on January-February. This can be seen from point observations – PMD (1961 to 1990) and AWS (1994 to 1999) – and in analysis of individual grid cells from reanalysis products – ERA-40 (1962 to 2001) and ERA-Interim (1979 to 2007). Figure 3.043 illustrates this with historical observations from the PMD long-record stations. Equivalent figures for the other data sources are found in Appendix A (section A.1).

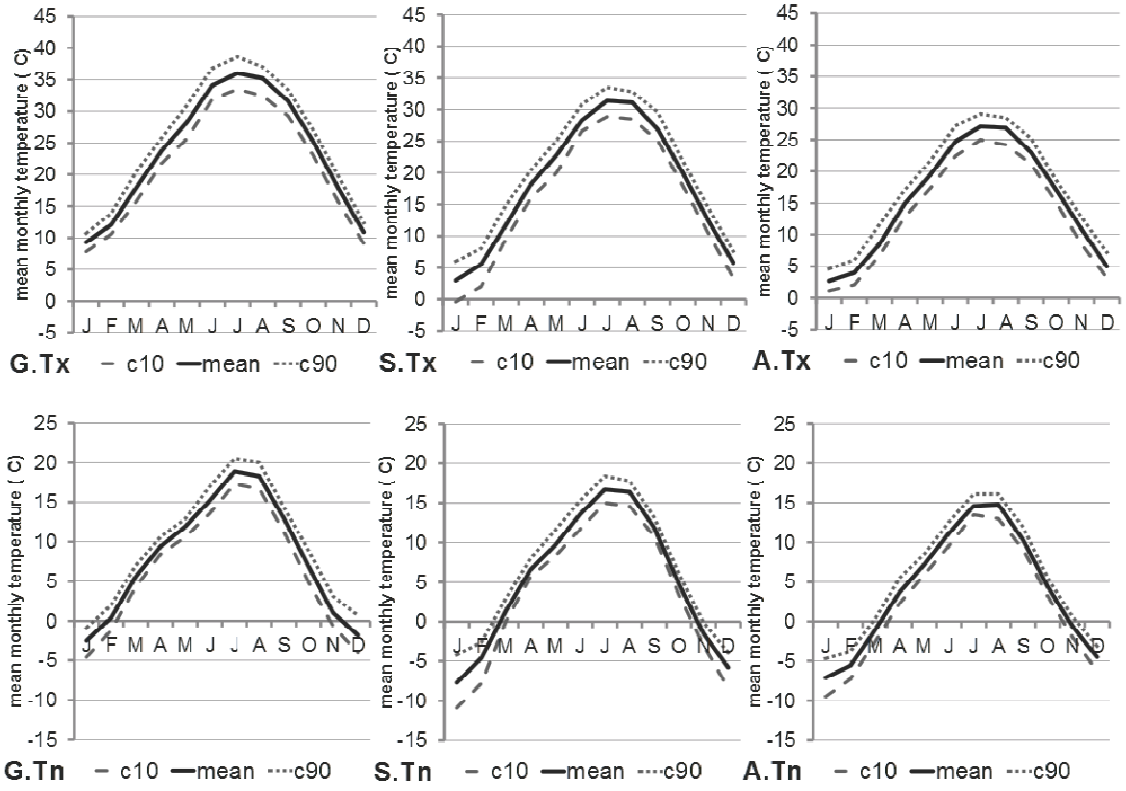

Figure 3.043 Historical observations of 2m mean daily maximum (Tx) and minimum (Tn) air temperature at Gilgit (G), Skardu (S) and Astore (A) from 1961 to 1990. Elevations of the meteorological stations are as follows: i) Gilgit, 1460 m asl; ii) Skardu, 2210 m asl; iii) Astore 2394 m asl.

Key points to retain with regards to the PMD and AWS temperature records:

- There is above all consistency in the shape and timing of annual temperature cycles.
- The differences between station temperature mean values in a given month can be attributed to elevation differences (higher elevations are cooler then lower ones).
- The shape of warm season temperature peaks, centred around Summer, is generally broader for daily maximum temperature (Tx) than for daily minimum temperature (Tn).
- There does appear to be variability between stations in the amplitude of the annual temperature cycle which is not necessarily related to elevation. This might be due either to site-specific issues, or sub-regional climate differences, e.g. Astore PMD and the AWS located in the Astore catchment have a small amplitude annual cycle than stations situated further north.

Individual reanalysis grid cells are modelled as having a uniform elevation. Hence, differences in temperature between adjacent grid cells are (primarily) due to differences in elevation. This is illustrated in Figures 3.044 and 3.045 showing period mean annual cycles of daily mean near-surface air temperature for selected grid cells respectively from ERA-40 and ERA-Interim.

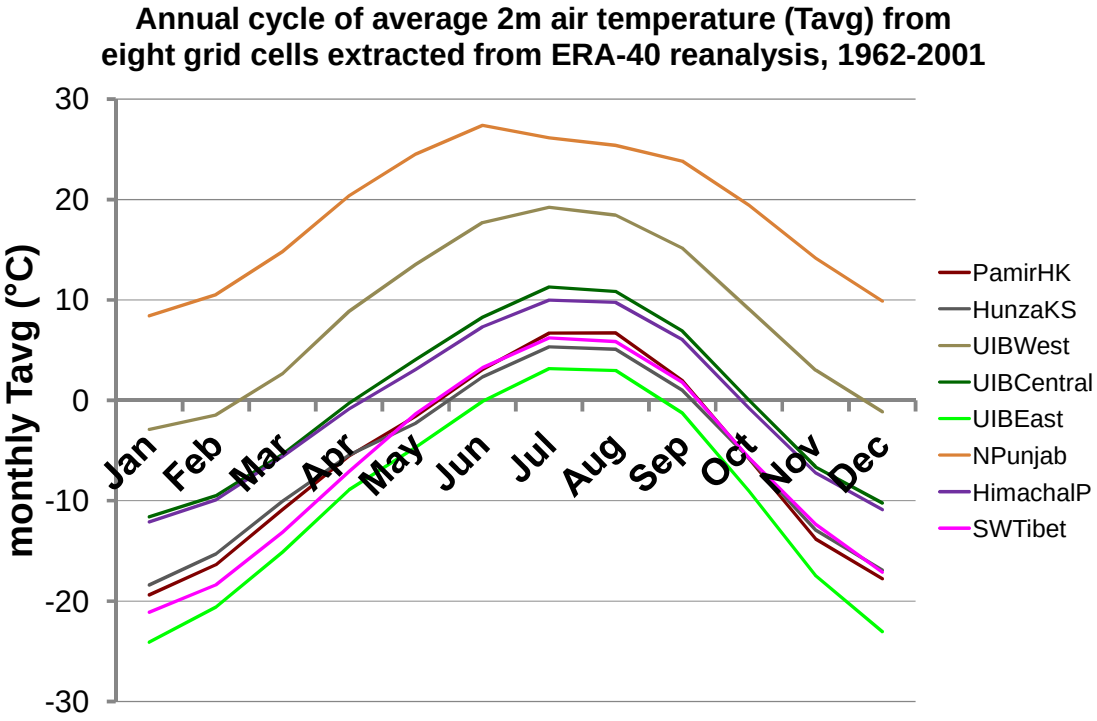

Figure 3.044 Mean daily 2m air temperature from ERA-40 for eight analysed grid cells (1962 to 2001). Grid cell mean elevations are given in Table 3.05.

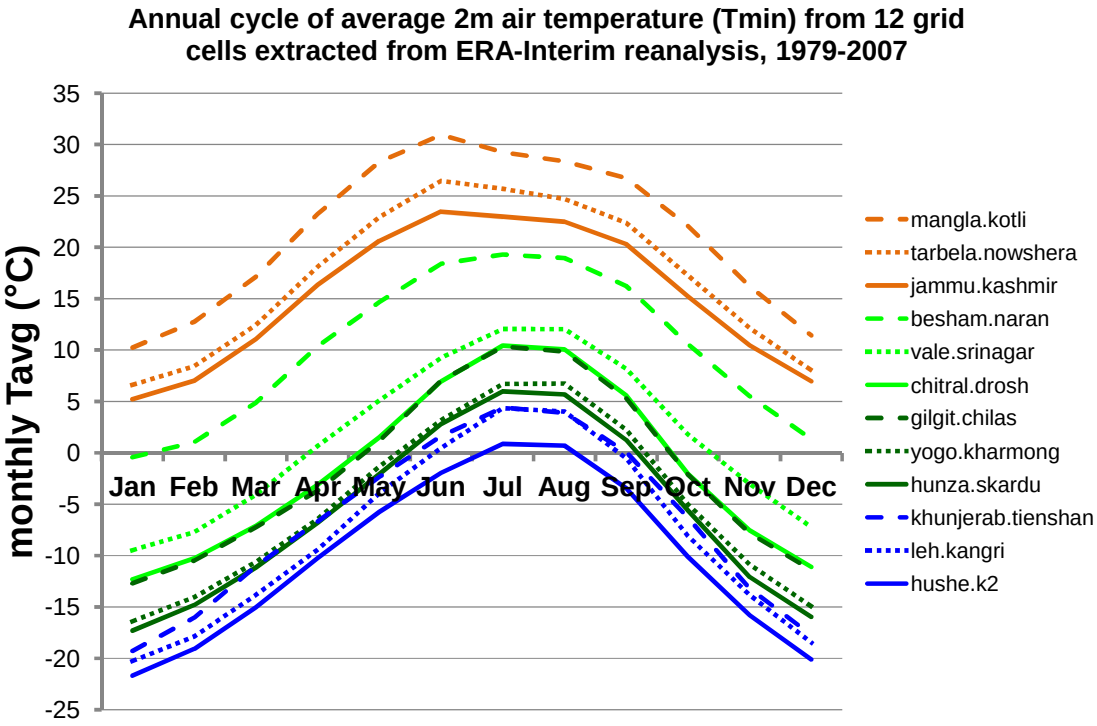

Figure 3.045 Mean daily 2m air temperature from ERA-Interim (1979 to 2007) for twelve analysed grid cells. Grid cell mean elevations are given in Table 3.06.

With regards to the meteorological reanalyses, ERA-40 and ERA-Interim, temperature records, with the exception of relatively low elevation grid cells with substantial monsoon influence – NPunjab in Figure 3.044, Mangla.Kotli, Tarbela.Nowshera and Jammu.Kashmir and Besham.Naran in Figure 3.045– where annual maxima in daily maximum or daily mean temperature may occur in June, the shape and timing of annual temperature cycles are very consistent throughout the sub-region. Absolute differences in temperature between grid cells in any given month can thus be largely attributed to modelled mean grid cell elevation (higher elevation cells are cooler).

As can be seen in the Figure 3.043 (and corroborated by the corresponding figures for other data sources in Appendix 1, section A.1) with measures of interannual variability – c10 & c90 or "low" and "high" – in the transitional seasons (Spring, Autumn) the magnitude of month to month change caused by the annual temperature cycle is likely to predominate over periodic anomalies (interannual variability). Thus the UIB near-surface air temperature climatology follows the expected pattern for regions located outside the tropics.

Example comparisons between air temperature data sources for selected areas can be seen in Figures 3.046 and 3.047, respectively showing monthly means of daily maximum and daily minimum temperatures for the common observational period –

January 1995 to December 1998 – between the four data sources considered in this section: PMD, AWS, ERA-40 and ERA-Interim.

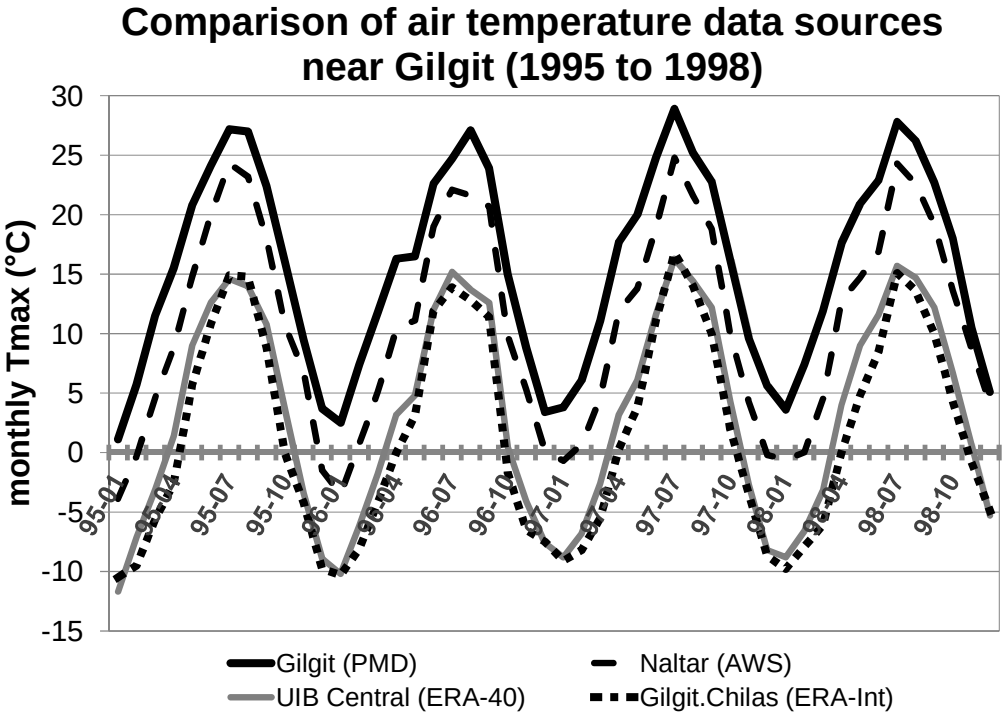

Figure 3.046 Monthly means of daily maximum 2m air temperature, 1995 to 1998, from four available data sources: PMD, AWS, ERA-40 and ERA-Interim. Representative elevations are as follows: i) Gilgit (PMD, 1460 m asl; ii) Naltar (AWS), 2810 m asl; iii) UIB Central (ERA-40) 3855 m asl; iv) Gilgit.Chilas (ERA-Int), 3809 m asl.

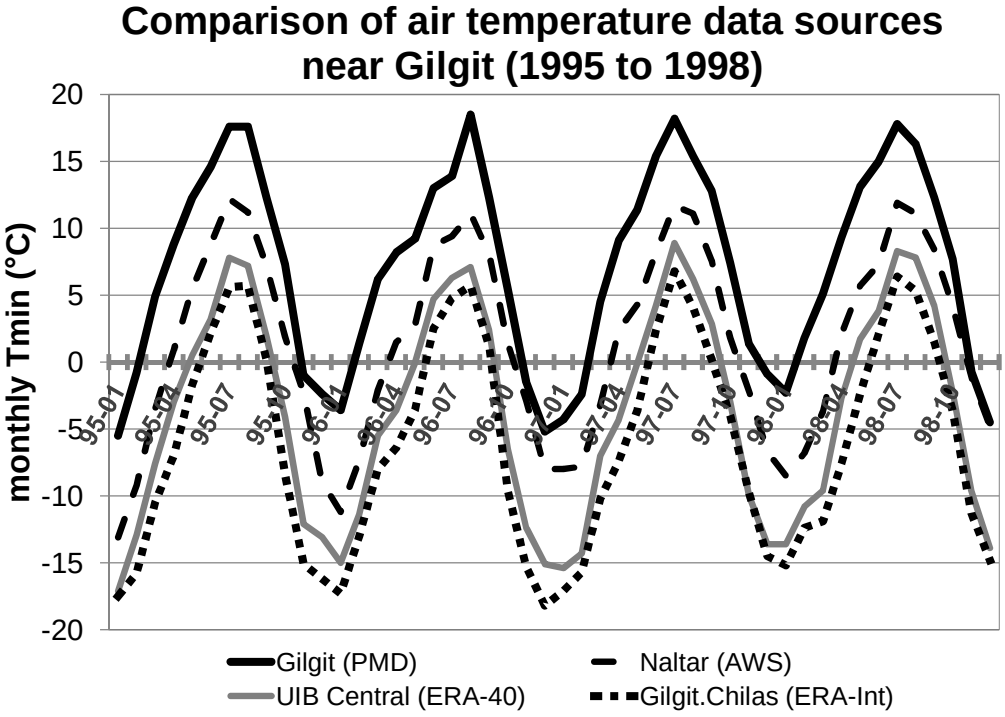

Figure 3.047 Monthly means of daily minimum 2m air temperature, 1995 to 1998, from four available data sources: PMD, AWS, ERA-40 and ERA-Interim. Representative elevations are as follows: i) Gilgit (PMD, 1460 m asl; ii) Naltar (AWS), 2810 m asl; iii) UIB Central (ERA-40) 3855 m asl; iv) Gilgit.Chilas (ERA-Int), 3809 m asl.

The stations (PMD, AWS) and grid cells (ERA-40, ERA-Interim) selected for Figures 3.046 and 3.047 were chosen for their geographical proximity (see Figures 3.007, 3.008, 3.010 and 3.011 for location details) in order to better illustrate the similarities and divergences between the different sources of data. The similarity in elevations between the ERA-40 grid cell (3855 m asl) and ERA-Interim grid cell (3809 m asl) is coincidental given their substantial differences in area and geographical boundaries. Nevertheless this closeness in height helps to illustrate the governing role elevation plays in temperature variability at the sub-regional level. The very close agreement in absolute terms for Tmax (Figure 3.046) between the two reanalysis data sets for the period in question is in clear contrast to the non-negligible differences between them for Tmin (Figure 3.047) over the same period. The offset in Tmin – generally slightly warmer in ERA-40 than ERA-Interim – in this example might either be due to changes in the ECMWF analysis and forecasting model between the two reanalyses, or because the critical factors governing night-time temperatures in both models are more localised than those which drive Tmax.

Looking in detail at the interannual variations for each data source across the short common record, similarities are relativity clear between the PMD and AWS observations, especially for Tmax. Tracking of anomalies between the ground-based observations and reanalysis estimates is less immediately obvious, but does not imply that the latter are unable to reflect local temperature anomalies, i.e. particularly warm or cold years. Strength of relationships between the local observations (PMD) and reanalysis data sources for near-surface air temperature was tested by calculating the Pearson's correlation coefficients between them. Results of this analysis are presented in Chapter 4 (section 4.3.3).

Spatially-aggregated (remotely sensed) land surface day-time and night-time temperature (LST) from MODIS shows a similar sinusoidal pattern to those from point observations and reanalysis grid cells. Figures for the annual cycle of spatial means for primary UIB gauged tributary catchments can be found Appendix 1, section A.1. The spatially aggregated mean night-time LST (Tnight) in particular provides an indicator of catchment hydrological regime. Catchments where the spatial mean T_{night} struggles to exceed 0°C in the summer months are catchments with a glacial melt regime. For these catchments, anomalies in Summer temperature govern interannual variability in runoff. Catchments where T_{night} regularly exceeds freezing in July and August exhibit a nival (seasonal snowfall) regime. In these catchments, melt season runoff variability is governed by accumulated precipitation from the previous Winter and Spring.

In order to provide context on the relationship between air temperature and LST, Figure 3.048 compares average daily air temperature (Tavg) at Astore PMD to the mean of LST_{day} and LST_{night} (LST_{avg}) for the corresponding pixel from the MODIS 5km horizontal resolution LST data product (MOD11C3). As can be seen in Figure 3.048, Astore PMD Tavg and LSTavg for the pixel corresponding to the meteorological station track very closely in warm months (Summer) while in cold months (Winter) LST_{avg} diverges becoming substantially colder than Tavg at the time of annual minimum. This may be due to the fact that LST is calculated only for "clear sky" (i.e. cloud-free) conditions. Similar relationships are found throughout the UIB between point observations and individual MODIS pixels. The Astore (PMD) station was chosen because it is used in the development of future climate scenarios (Chapter 5) and as climate data input for the hydrological model used in this study (Chapter 6).

Normally, i.e. under "all sky" (both cloudy and clear) conditions, given that the land surface is the medium or interface of primary energy exchange between solar radiation and near surface air, both maximum and minimum surface temperature values are expected to be more extreme – warmer highs, colder lows – than the corresponding 2m air temperature at the same location. Because satellite imagery-derived (remotely sensed) LST values are calculated from "clear sky" conditions only, a systematic bias is introduced. Because cloud cover tends to raise minimum temperatures by reducing net outgoing long-wave (thermal) radiation, "clear sky" night-time conditions will appear colder than the broader mean. The magnitude of differences between "all sky" and "clear sky" conditions will vary somewhat from site to site depending on the frequency of cloud cover at the location in question. Spatial patterns of cloud cover as estimated by both reanalysis (ERA-Interim) and remote sensing (MODIS) data sources are examined in sections 3.7.4 and 3.7.5.

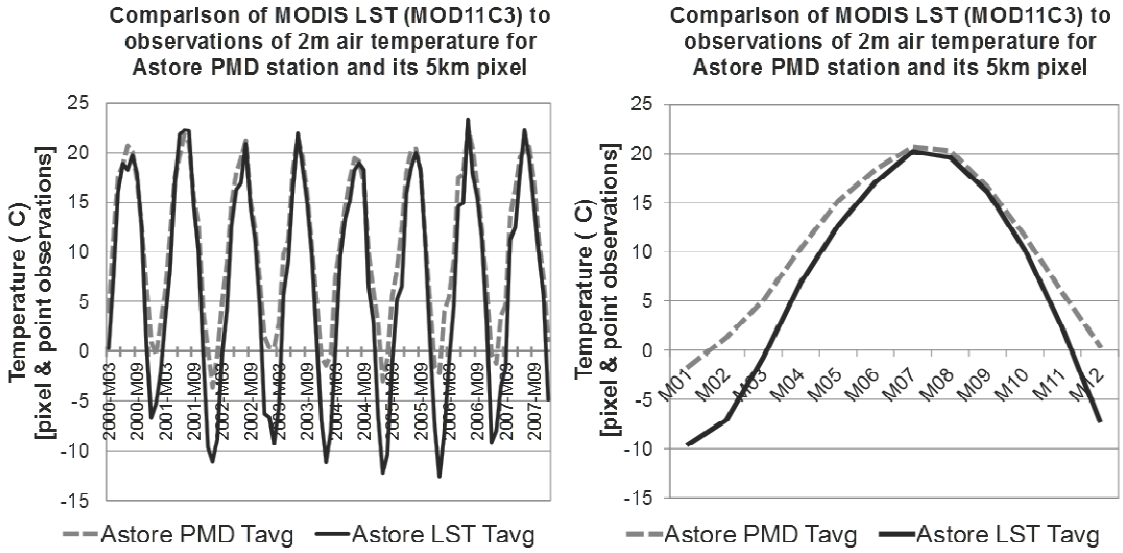

Figure 3.048 Comparison of MODIS LST to air temperature at Astore PMD for the MODIS (Terra) observational record, 2000 to 2010.

3.6.3 Diurnal Temperature Range (DTR)

The continental geographical position of the UIB tends to accentuate the diurnal temperature range (DTR) in the region. DTR is the difference between daily maximum (day-time) and minimum (night-time) temperature. UIB DTR values throughout the year are large compared to those that would be expected in other climate regimes, e.g. maritime, low-land tropical (Geerts 2003, Jackson and Forster 2010).

The relative shape of the annual DTR cycle (discretised as monthly means) can provide insight into land surface processes and dominant weather regimes. Figures 3.049 to 3.052 provide observations and estimates of DTR from point sources (PMD & AWS) and reanalysis projects. Broadly two types of annual patterns are found and, as will be shown later in this section, phases and magnitudes of DTR suppression for both types of cycle generally coincide with periods and intensities of peak cloud cover.

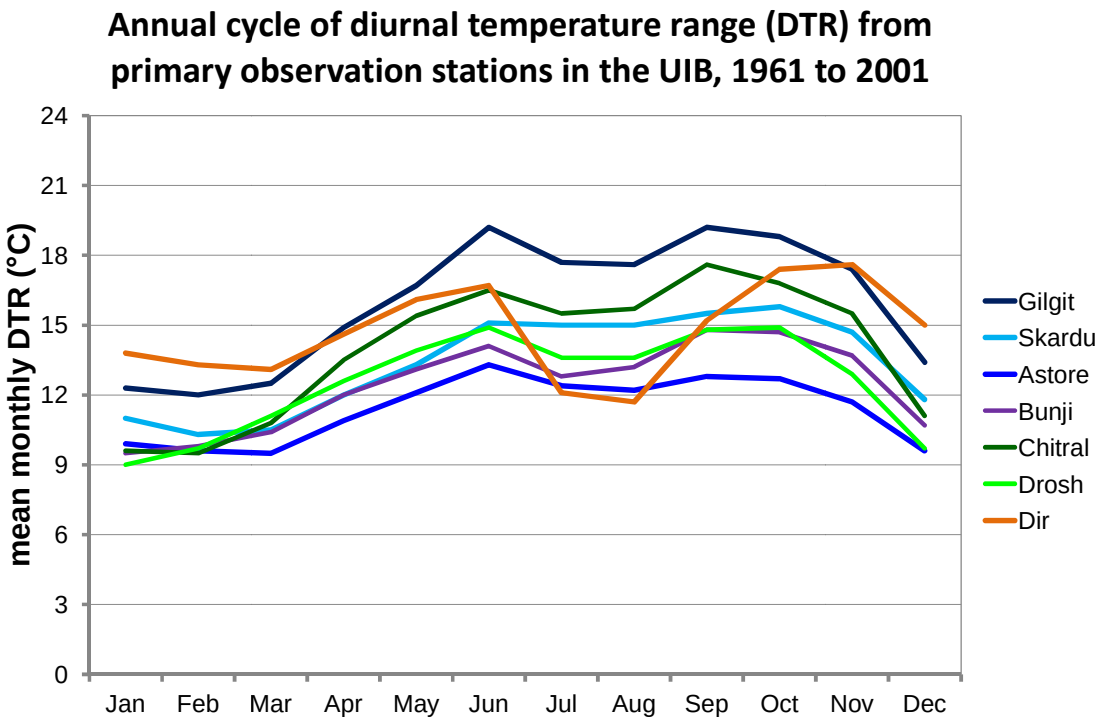

Figure 3.049 Annual cycle of mean diurnal temperature range (DTR) from PMD stations, 1961 to 2001.

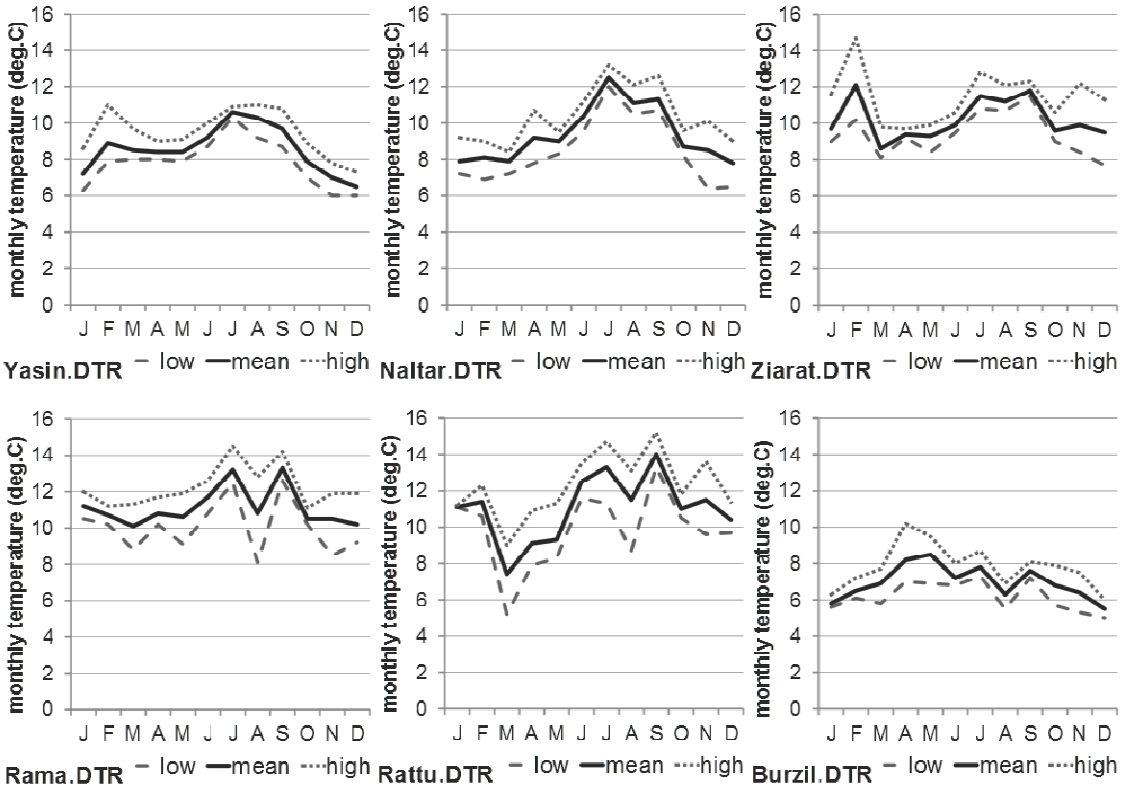

Figure 3.050 Annual cycle of mean diurnal temperature range (DTR) from AWS stations from 1995 to 1998.

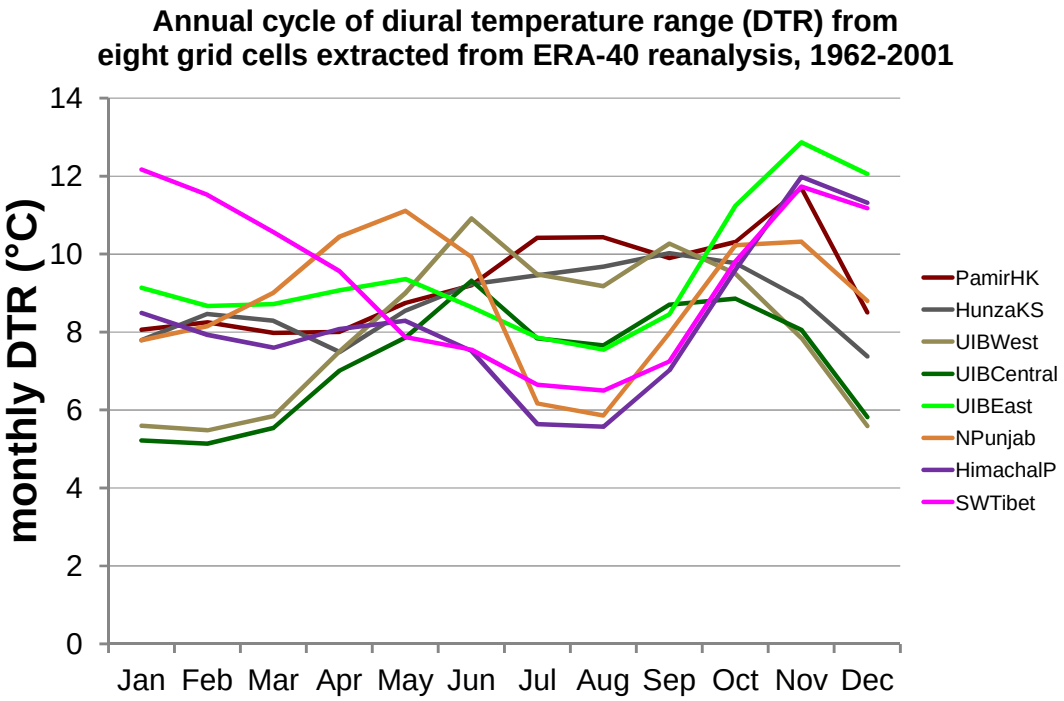

Figure 3.051 Annual cycle of mean diurnal temperature range (DTR) from ERA-40 for eight analysed grid cells, 1962 to 2001.

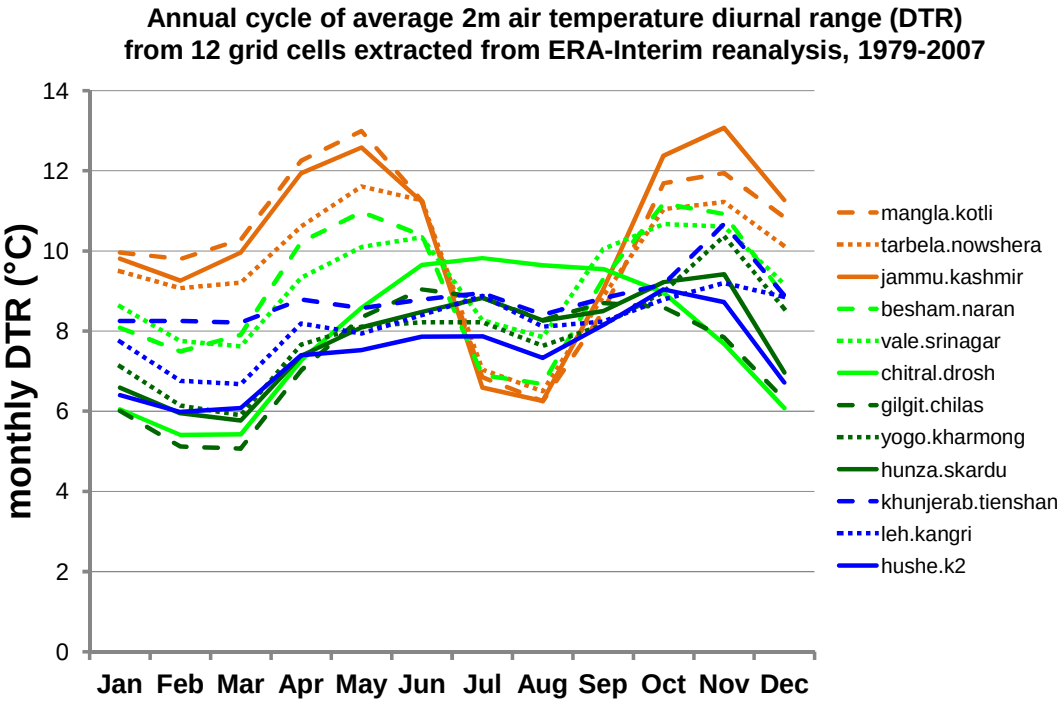

Figure 3.052 Annual cycle of mean diurnal temperature range (DTR) from ERA-Interim for eight analysed grid cells, 1979 to 2007.

As seen in Figures 3.058 to 3.061, the first type of annual DTR cycle is associated with those areas having a humid cold season and an arid summer. In these cases cold-season snowcover reduces winter DTR because its high albedo reduces absorption of incoming solar radiation thus limiting daytime warming of the surface and air immediately above it. DTR here reaches its annual maximum in the summer as

ablation nears completion. This archetype covers the majority of UIB stations (and grid cells) analysed in this study.

The second type of annual DTR cycle is found in areas with both a humid winter and summer but arid transitional seasons. In this case, one annual DTR minimum still occurs in winter, but a secondary minimum also occurs in summer when the presence of monsoonal weather systems (thick cloud, high humidity) reduces daily maximum temperatures (Tmax) to a greater extent than daily minimum temperatures (Tmin). This occurs because day-time cloud cover reduces incoming (shortwave) solar radiation thus lowering Tmax, while night-time cloud cover drives relative increases in Tmin by limiting out-going (long-wave) thermal radiation. To clarify during large monsoonal events both Tmax and Tmin may fall due to the large reduction in total incoming radiative energy, but the fall in Tmax is expected to exceed the fall in Tmin thus reducing DTR as well.

Another potential source of DTR reduction is the transfer of energy via latent heat involved in snow and ice ablation processes during the peak melt season. In this case the bimodal annual DTR maxima occur in late spring and mid-autumn. This pattern is less common, but still found in both long-record meteorological station observations (PMD; Figure 3.049) and reanalysis data (Figures 3.051 and 3.052).

The PMD station which best exemplifies this pattern is Dir, one of the southernmost analysed in this study. There is however perceptible, if limited, DTR reduction in summer in two (Gilgit, Astore) of the three primary long-record stations used throughout this study. The degree of summer DTR buffering in the affected reanalysis grid cells is accentuated, and perhaps exaggerated. The ERA-40 grid cells (Figure 3.051) most clearly affected are those selected for analysis – NPunjab, HimachalP and SWTibet – in the to the south and east of the primary study area, although perceptible buffering also occurs in the three core UIB grid cells (UIBWest, UIBCentral and UIBEast). In ERA-Interim (Figure 3.061) the grid cells most affected are again those on the southern boundary of the study area – Mangla.Kotli, Tarbela.Nowshera and Jammu.Kashmir – but once again grid cells – Besham.Naran and Vale.Srinagar – close to the central UIB area also show noticeable Summer DTR reduction.

Interestingly, the patterns in high-elevation AWS observations (Figure 3.050) and spatially aggregated remote sensing (MODIS LST, Figure 3.053) do not divide into these two categories of Summer annual maxima or Summer reduction. Although some

of the AWS stations do seem to fit the humid winter, arid summer pattern, the curves are not as smooth/regular. This is probably due to the very limited record length – only four complete years of AWS data – available to this project for analysis. One clear example of the liability of attempting to use records of extremely short length is can be seen in that some (Yasin, Ziarat, Rattu) of the AWS stations do show spikes (maxima) in late winter (February). This is suspected to be an artefact (erroneous measurement) in the data because it does not track with patterns that are otherwise coherent across independent data sources and for a range of time periods. Unfortunately the short available AWS record length renders definitive confirmation of this difficult.

The less regular nature of annual DTR cycles is further illustrated by the time series of four separate data sources (PMD, AWS, ERA-40, ERA-Interim) for the available common record period (1995 to 1998) shown in Figure 3.054. The DTR variability in this short window reveals that while the underlying annual cycle is visible, especially for Gilgit (PMD), it is considerably less smooth than the broadly sinusoidal patterns of Tmax and Tmin. In terms of agreement between data sources, the results appear mixed. The four data sources track quite closely at times (e.g. 1996), but there are divergences especially in summer months (e.g. 1995, 1998) and by ERA-40 (grid cell UIB Central).

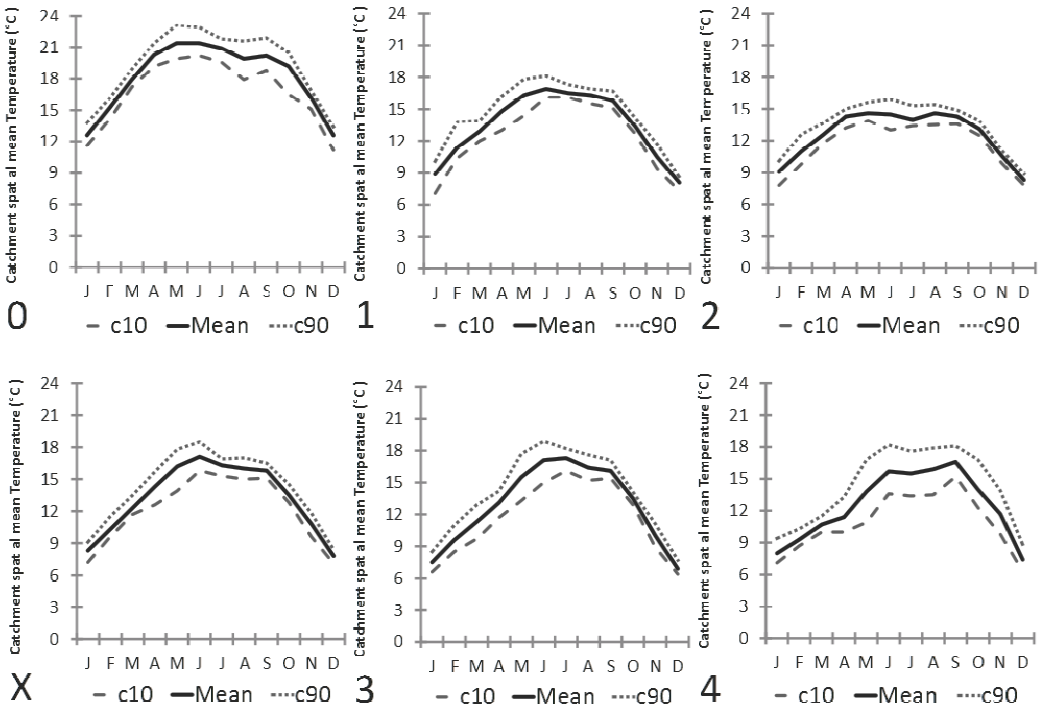

Figure 3.053 Annual cycle of diurnal range in land surface temperature for period (2000 to 2010) monthly means and first and last deciles (c10 & c90) from MODIS for primary tributary catchments – [0] the Upper Indus above Besham, [1] the Hunza, [2] the Shigar, [X] the NW UIB sector (1+2+3+4 plus main channel valley between Besham and Yogo/Kharmong), [3] the Gilgit/Ghizer, and [4] the Astore. Boundaries are shown in Figure 3.041.

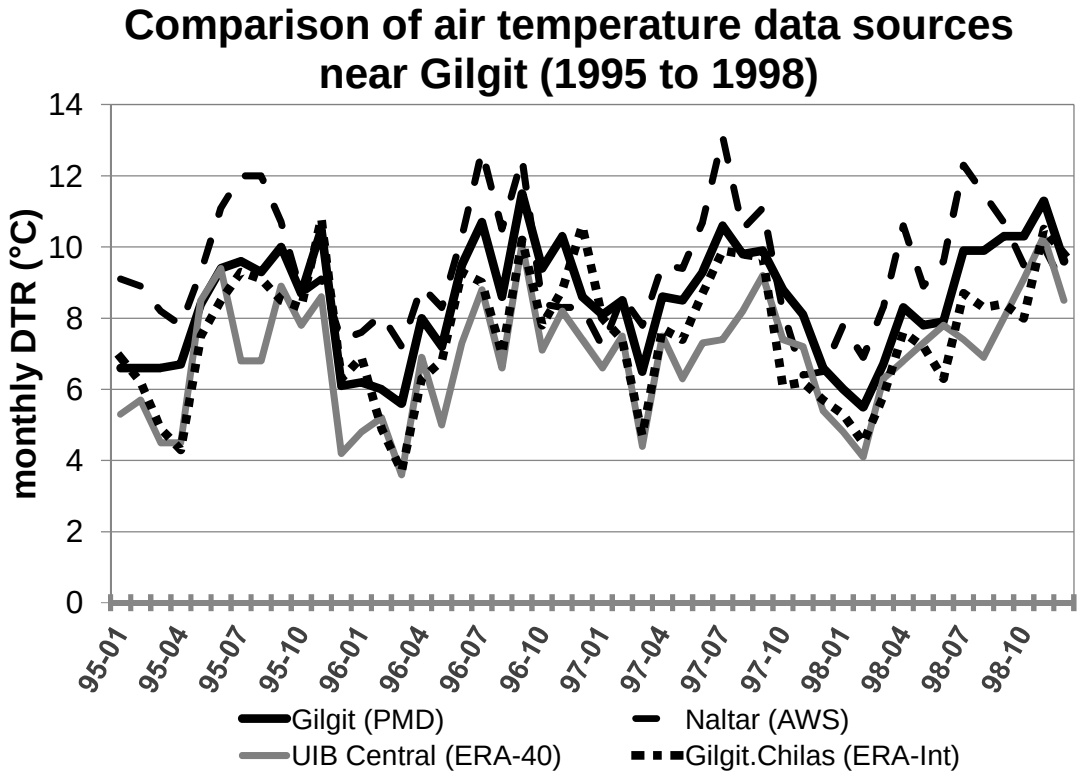

Figure 3.054 monthly means of daily (diurnal) 2m air temperature range (DTR), 1995 to 1998, from four available data sources: PMD, AWS, ERA-40 and ERA-Interim. Representative elevations are as follows: i) Gilgit (PMD, 1460 m asl; ii) Naltar (AWS), 2810 m asl; iii) UIB Central (ERA-40) 3855 m asl; iv) Gilgit.Chilas (ERA-Int), 3809 m asl.

The spatially aggregated MODIS DTR, on the other hand, generally shows a regular, dominant "humid winter, arid summer" pattern for all locations in the UIB. There are two potential explanations for this. First, the algorithm used for MODIS LST depends on "clear sky" i.e. cloud-free conditions. This inherently biases the MODIS LST product against the buffering effects of humid weather and toward anti-cyclonic/high-pressure weather conditions. A second explanation is that the "humid winter, arid summer" best represents the spatial mean conditions in the catchments (rather than the PMD data which tells us primarily about DTR in the valleys).

Detailed examination of the summer months in the spatial aggregates, and in particular the measures of interannual variability, c10 & c90, provides tentative evidence of limited DTR reduction. At a regional scale the apparent absolute reductions in MODIS DTR are small. The amount of interannual variability (c90 minus c10), however, is greater in catchments to the south and east, i.e. Astore and Shigar as well as in the ensemble of the Upper Indus above Besham (hence including the western Tibetan Plateau), than for the areas concentrated in the northwest, i.e. Gilgit, Hunza and larger the NW UIB zone. This difference between groups of catchments suggests a similar sub-regional disctinction in local temperature climatology to that inferred from the local

observations and reanalysis data. The short length (10 years) of the present MODIS record, however, limits the conclusions which may be drawn in this regard.

Looking beyond LST alone, and comparing MODIS DTR to 2m air DTR, both the relatively small summer DTR buffering as well as the absolute range of the annual cycle – with winter DTR near 10°C and summer DTR in the range of 15°C to 20°C – provides a close analogue to the long-record PMD stations (Figure 3.049). In fact it appears superior in this regard to the reanalysis grid cell estimates (Figures 3.051 and 3.052).

Evidence for DTR as an indicator of climate regime can be seen in the available gridded/raster DTR data from ERA-Interim, MODIS and PRECIS driven by ERA-40 (PRECIS_ERA40) (Figures 3.055 to 3.057). These figures show the geographical distribution of the winter and summer phasing of DTR suppression. In the winter through late spring, DTR is lowest over the high mountains, moderate over the foothills and highest in the low elevation areas. From early summer the monsoonal influence suppresses DTR along the Himalayan front range, expanding across the plains as the monsoon intensifies, then diminishing and quickly disappearing in early- to mid-autumn. There are nuances in the estimates of DTR magnitudes and in the precise spatial limits of the zones of westerly and monsoonal influence depending on which of the three data sources – ERA-Interim, MODIS or PRECIS_ERA40 – is consulted, but these discrepancies can largely be explained by the biases and spatial resolution unique to each.

ERA-Interim has a relatively coarse spatial resolution (80km) and as such the variability which might be expected at a point-scale would likely be muted resulting, among other effects, in lower magnitude DTR (ERA-Interim regional DTR maximum = 15°C). MODIS, in contrast, with is small pixel size (1km or 5km) more closely resembles the point scale. MODIS also, as noted above, only observes LST under “clear-sky” conditions, i.e. high incoming solar radiation conditions. Thus MODIS DTR would be expected to have a large magnitude (MODIS regional DTR maximum = 40°C). PRECIS_ERA40 has an intermediate spatial resolution compared to ERA-Interim and MODIS and hence could be expected show an intermediate magnitude DTR. Spatial resolution and whether the data source operates under “all sky” or only “clear sky” (cloud-free) conditions will also shape how the influence of atmospheric circulation, e.g. South Asian monsoon, on DTR is detected by each data source.

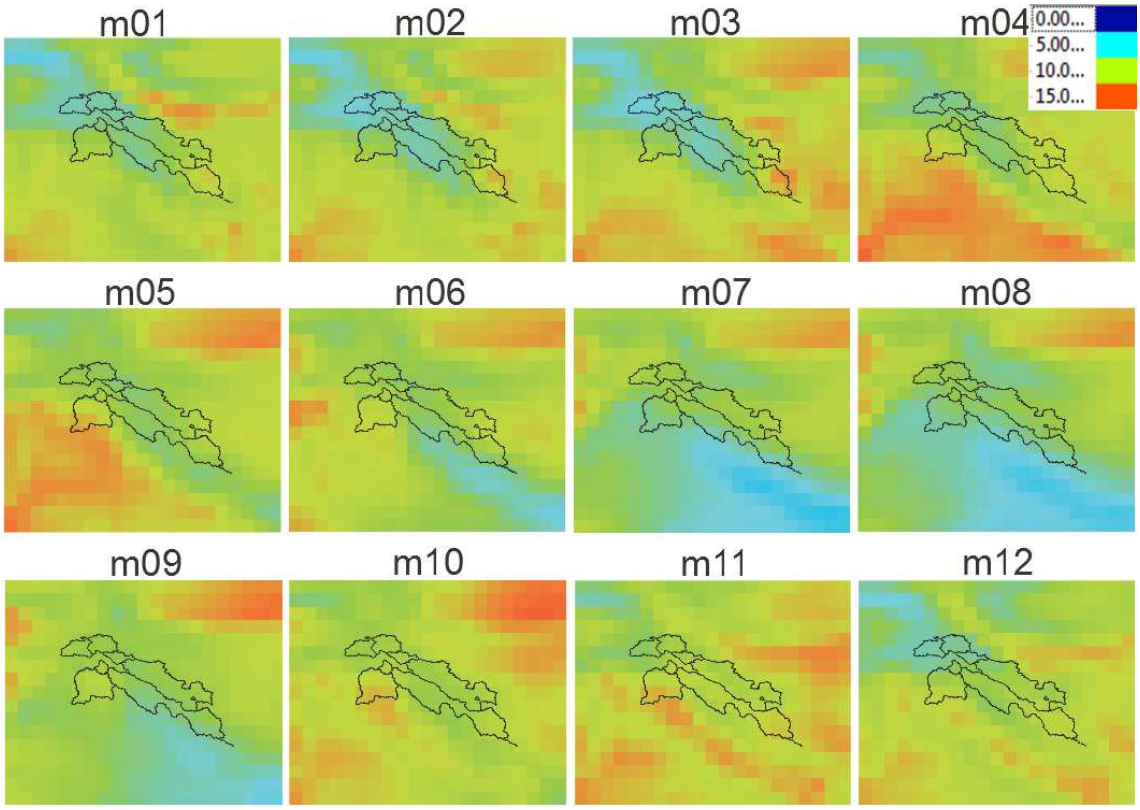

Figure 3.055 Mean monthly DTR (°C) from the ERA-Interim reanalysis, 1979 to 2007.

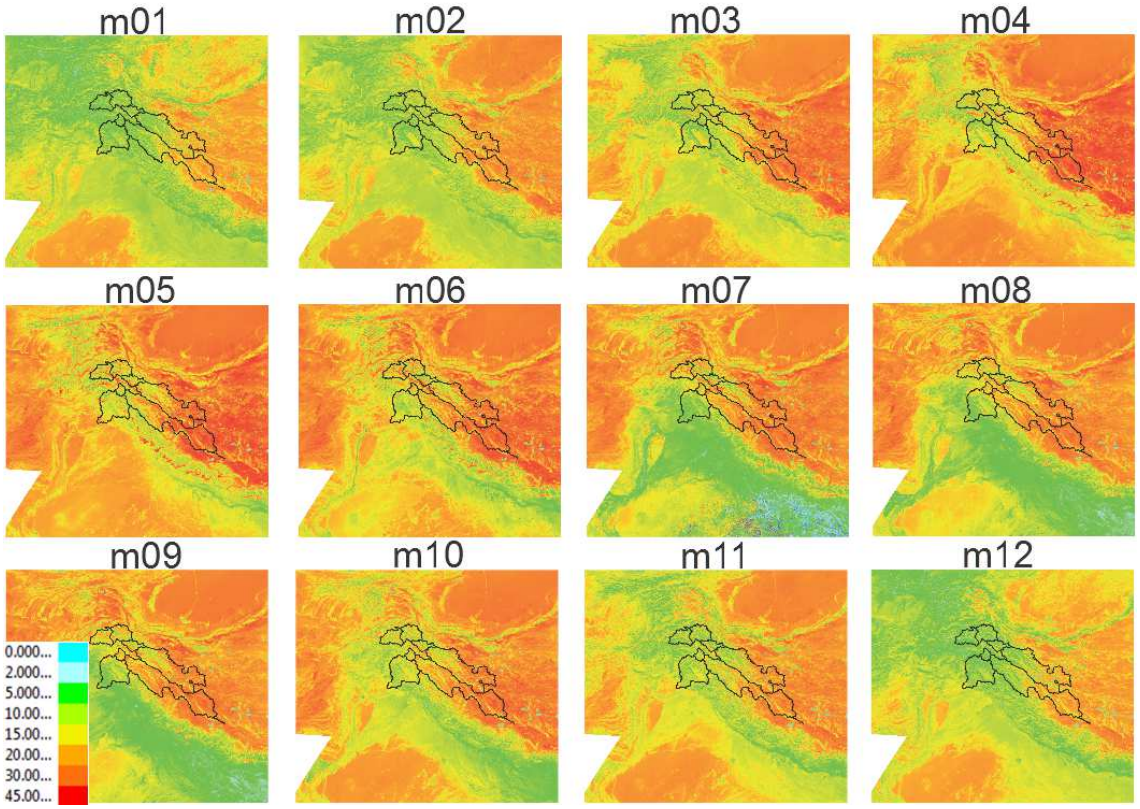

Figure 3.056 Mean monthly DTR (°C) from MODIS, 2000 to 2010.

It should be made clear here that in these spatial representations, MODIS DTR is defined in fact as LST_{day} minus LST_{night}, which on most climatic timescales is equivalent to Tmax minus Tmin given the most frequent daily timing of maximum and

minimum temperature. Ocasionally, however, LSTnight does exceed LSTday. Physically this is likely due to strong influences of convective precipitation activity near the time of LSTday observation, i.e. within roughly 90 minutes of local solar noon, which cools the land surface but clears later allowing sufficient post-observation solar heating that LSTnight exceeds LSTday. As can be seen Figure 3.065 this is a very infrequent occurence both spatially and temporally. In the present study it is observed almost exclusively in the Gangetic plain adjacent to the Central Himalaya during the period of peak monsoonal activity (July).

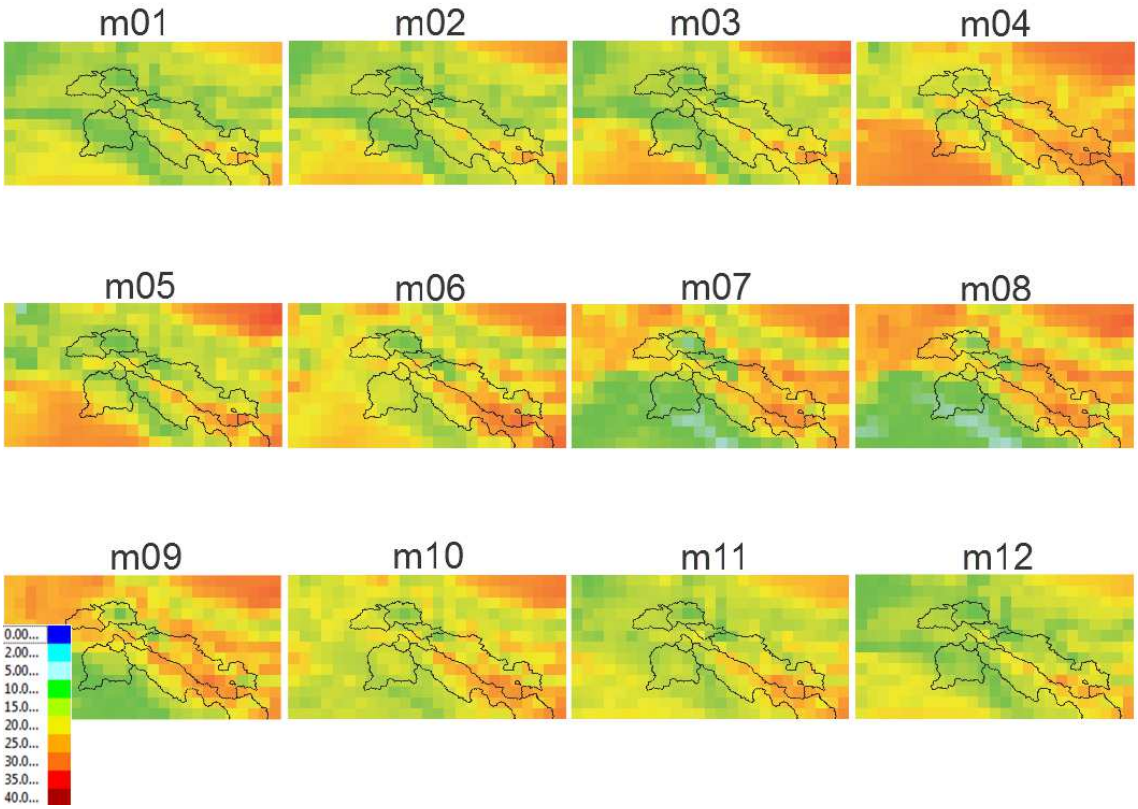

Figure 3.057 Mean monthly DTR (°C) from ERA40-driven PRECIS, 1961 to 1989.

3.6.4 Continuous Melt Area

This section summarises original work undertaken in this PhD but published prior to the completion of this as Forsythe *et al.* (2012a) and Forsythe *et al.* (2012b).

While the contribution of precipitation inputs to snowpack mass balance is immediately obvious, the energy controls on meltwater generation processes are less intuitive. Daily minimum temperatures are a key element, as night-time refreezing disrupts meltwater processes (Bengtsson, 1982). A key metric for assessing thermal constraints to runoff generation is thus the fraction of the catchment where monthly mean night-time temperatures remain above 0°C: referred to here as the "continuous melt area" (CMA) (Forsythe *et al.*, 2012a).

As with SCA, differences in the shape of annual cycles of CMA, as shown in Figure 3.058 for the six primary tributary catchments, are indicative of differing hydrological regime types. While for nival regime catchments (Gilgit [3], Astore [4] in Figure 3.058) annual SCA minima showed the greatest relative variability, for glacial regime catchments (Hunza [1], Shigar [2] in Figure 3.058) the relative variability of annual maximum CMA is the key parameter in interannual climate variability. These glacial regime catchments have a low mean annual CMA maximum but a large relative variability (ratio of c90 to c10). Nival regime catchments, in contrast, regularly attain very high CMA maxima as little of their area remains melt-free during the high summer. Another interesting element from Figure 3.058 is the consistency of the very large ranges in CMA during the early stages of the ablation phase (May and June). This can affect the timing of peak flows for both regime types as well as the availability of meltwater for irrigation during crucial crop growth phases. Some of this variability could be a result of apparent seasonal low elevation night-time LST inversions found when studying the "parent data product" (MOD11A2). At present it is unclear whether this phenomenon is a real climatic feature of the UIB, perhaps linked to local-scale cloud cover variations, or an artefact resulting from a particular element in the MODIS product algorithm.

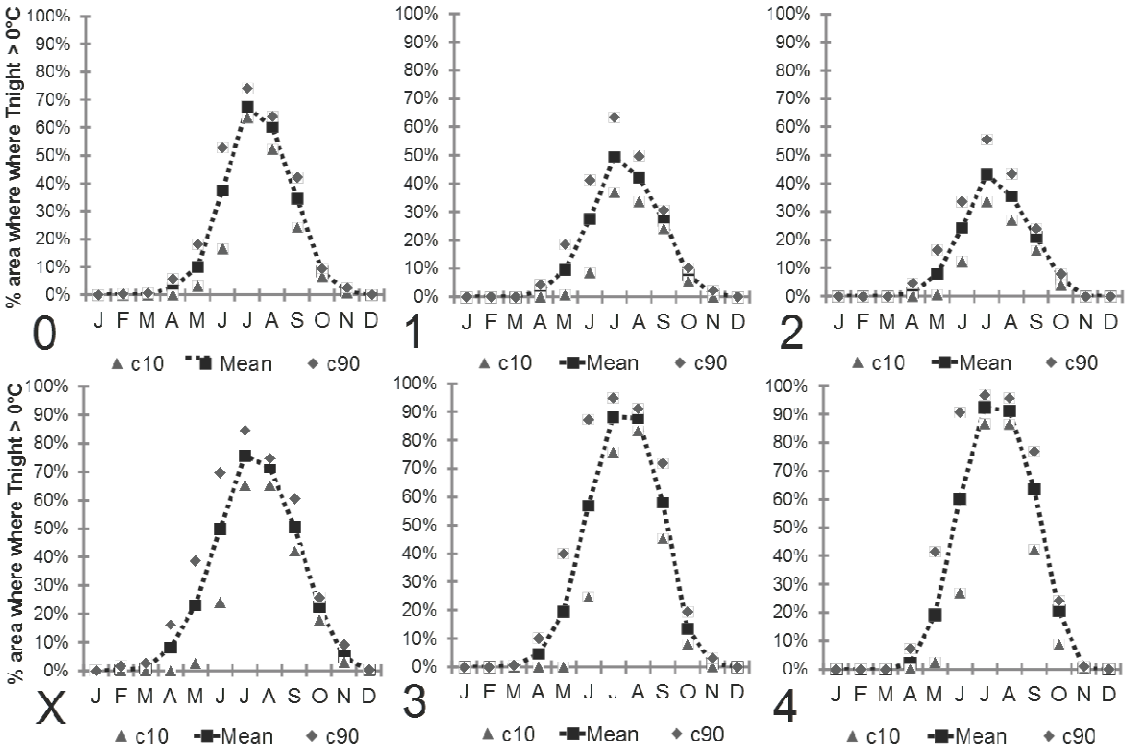

Figure 3.058 Continuous Melt Area (CMA) for period (2000 to 2010) monthly means and first and last deciles (c10 & c90) from MODIS for primary tributary catchments – [0] the Upper Indus above Besham, [1] the Hunza, [2] the Shigar, [X] the NW UIB sector (1+2+3+4 plus main channel valley between Besham and Yogo/Kharmong), [3] the Gilgit/Ghizer, and [4] the Astore. Boundaries are shown in Figure 3.041.

3.7 Secondary climate-drivers of UIB hydrology

Although observations (and estimates) of precipitation and temperature provide key indices respectively of mass and energy inputs to the UIB hydrological system, there are additional climate parameters which substantially influence both the surface energy balance – hence controlling timing of the melt cycle – as well as the water balance – by influencing evaporative losses – and as such merit analysis in a comprehensive study of the hydroclimatology of the UIB.

3.7.1 Relative Humidity (RH)

Relative humidity (RH) – the instantaneous ratio of water vapour pressure to saturation vapour pressure (a function of temperature) – is a key parameter in classical hydrology. It strongly influences the potential evaporative losses of surface water and near-surface soil moisture. It is also indicative of likely cloud cover.

Figures 3.059 to 3.064 show observations (PMD, AWS) and estimates – from ERA-40 and ERA-Interim reanalyses – of the annual cycle of relative humidity in central locations in the UIB. These independent data sources cover a range of overlapping time periods: i) PMD, 1981 to 1999; ii) AWS, 1994 to 1999; iii) ERA-40, 1961 to 1990; iv) ERA-Interim, 1979 to 2007. As with DTR, there are two archetypal patterns in annual humidity cycles. The first, familiar from the high elevation NW UIB, shows an annual RH maximum during the wet winter and a minimum in the dry summer. The second pattern typifies the climate of the monsoonal plains, with low RH values in autumn through spring and a distinct maximum in the summer. Many observing stations and modelled grid cells in the UIB show a mixture or hybrid of these two types of regime.

Focusing first on the ground-based observations, the daily minimum (local afternoon) RH at Astore PMD (2394 m asl) is roughly the same as the daily minimum measured at the AWS stations Shandur (3719 m asl) and Khunjerab (4733 m asl). The daily maximum RH at the AWS stations, however, is substantially higher than the daily maxima (local morning) at Astore throughout the year. This difference has potentially important hydrological implications because the vertical gradient, if any, in day-time relative humidity will, along with temperature and incoming solar radiation, modulate the magnitude of potential evapotranspiration. Detailed investigation of the RH gradient and its causal mechanisms is beyond the present scope of this study.

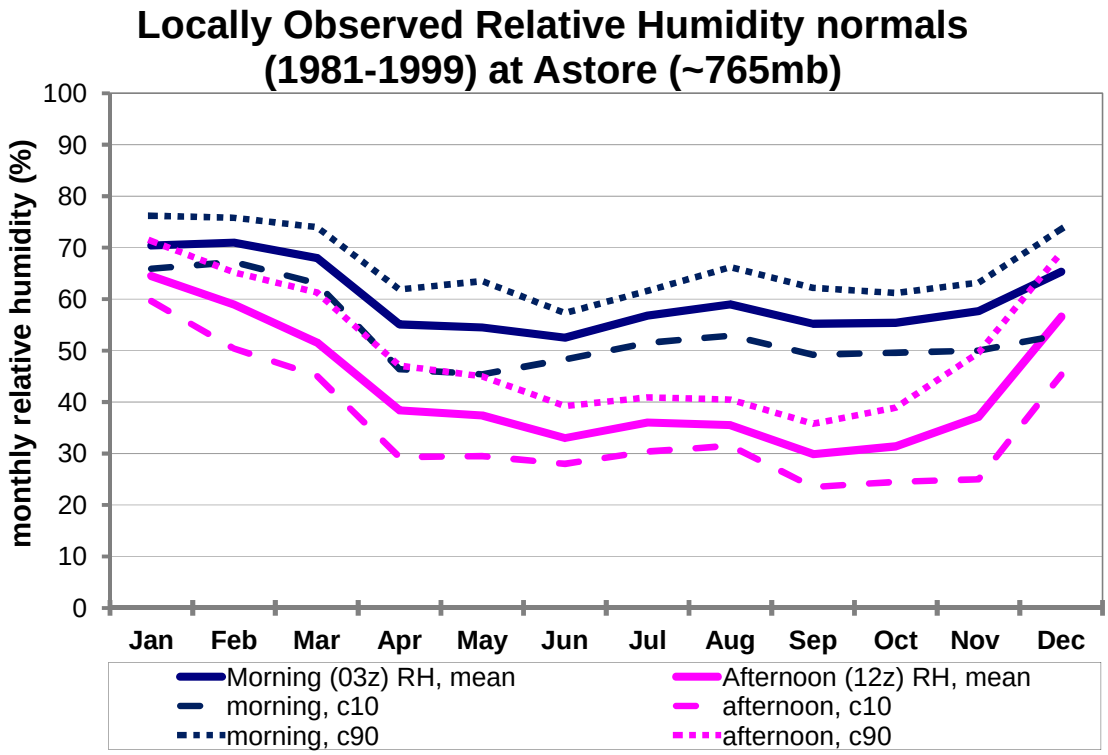

Figure 3.059 Historical (local) observations of relative humidity at Astore, 1981 to 1999.

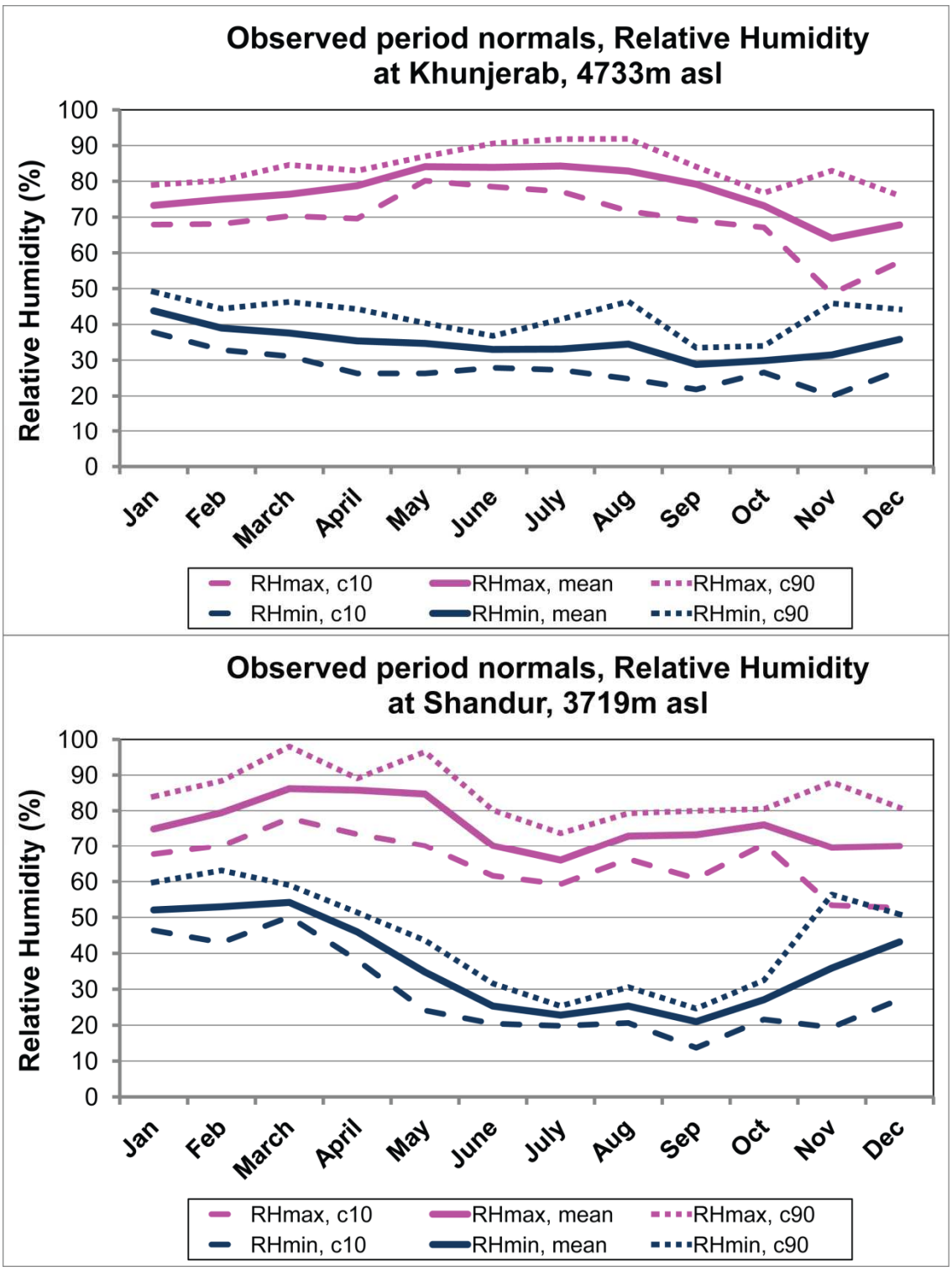

Figure 3.060 Available (sample) observations of relative humidity from two AWS units, Shandur (3719 m asl) and Khunjerab (4733 m asl), 1994 to 1999.

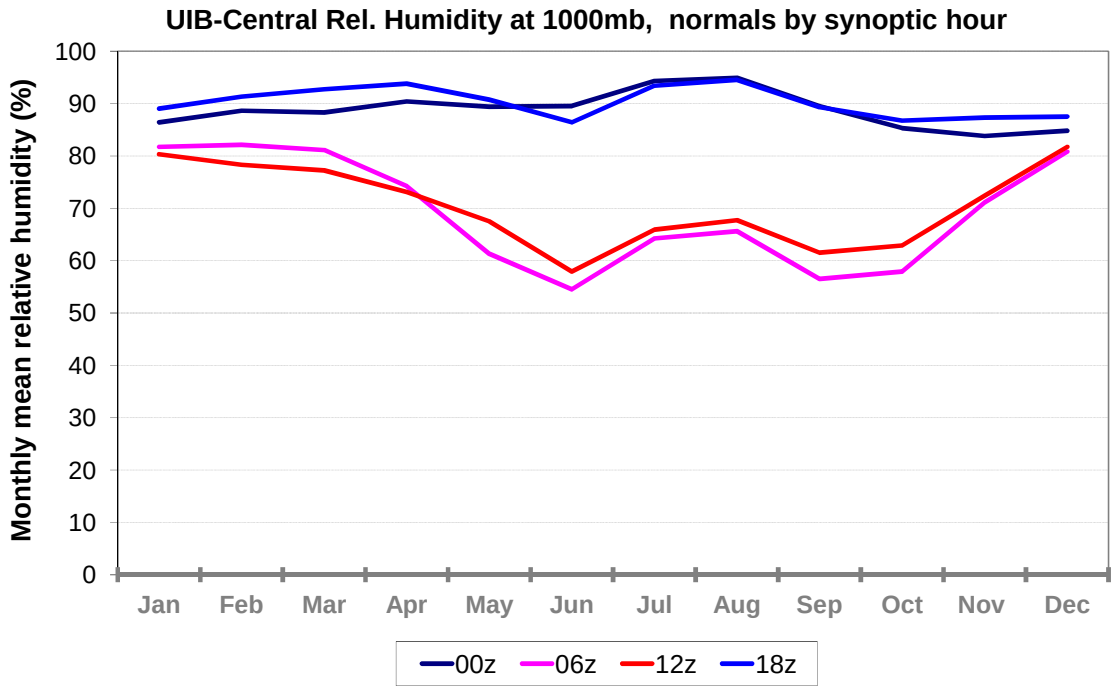

Figure 3.061 Estimate of annual cycle of near surface relative humidity from ERA-40, single grid cell example (UIB Central modelled mean elevation 3855 m asl), values for each "synoptic hour", climatic normals (means 1961 to 1990).

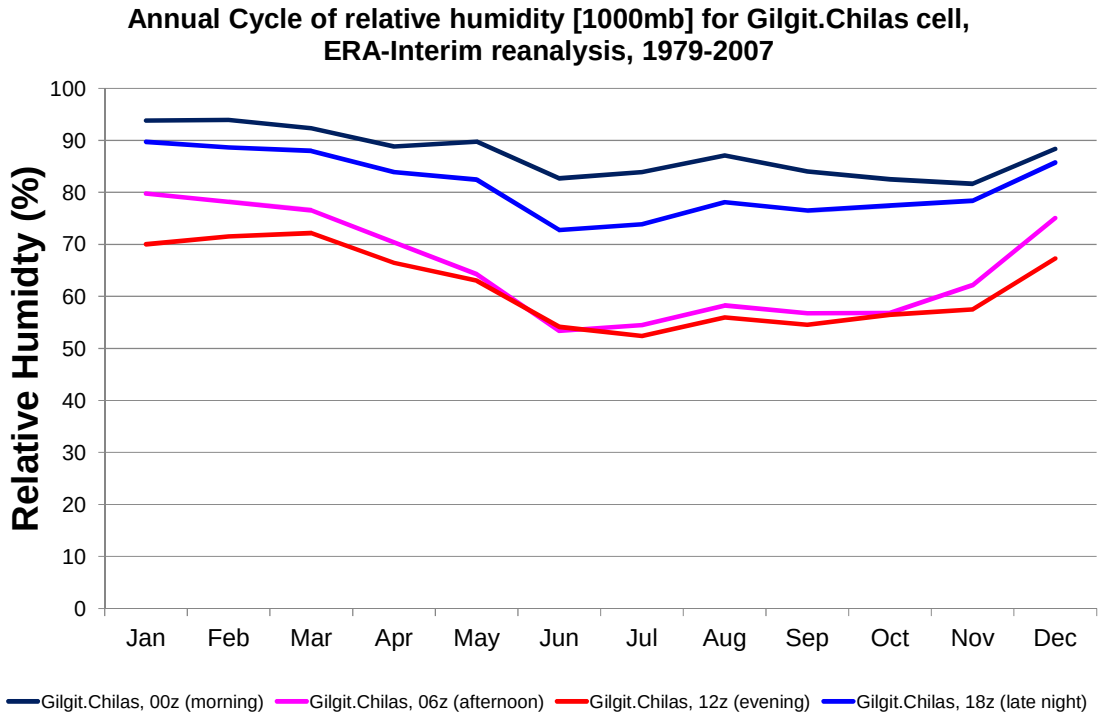

Figure 3.062 Estimate of annual cycle of near surface relative humidity from ERA-Interim, single grid cell example (Gilgit.Chilas modelled mean elevation 3809 m asl), values for each "synoptic hour", 1979 to 2007.

It is interesting to compare RH estimates from the two reanalysis projects, ERA-40 (Figure 3.061) and ERA-Interim (Figure 3.062). As was shown for air temperature, two cells with very similar modelled mean elevations – UIB Central (3855 m asl) and

Gilgit.Chilas (3809 m asl) – are presented here to offer the opportunity to compare outputs without the need make assumptions regarding the altitudinal effects. In general both the diurnal and annual cycles are roughly similar. There is substantially less diurnal range in RH in ERA-40 in winter than estimated by ERA-Interim. ERA-40 also shows a greater incremental increase in RH during the summer months than ERA-Interim, but this may be a realistic reflection of the fact that the larger "footprint" of the UIB Central (ERA-40) cell extends further south and east (see Figure 3.012) than the Gilgit.Chilas cell (ERA-Interim). Conversely, there is greater difference between local night-time (18z) and local morning (00z) RH in ERA-Interim than in ERA-40 where the two synoptic time steps are nearly interchangeable.

Comparing the reanalysis RH estimates to the available local observations, the outputs from ERA-40 and ERA-Interim are much closer to the values observed by the AWS stations (Figure 3.069) for daily maximum RH. This is perhaps due to the modelled grid cell elevations being quite similar to the spot elevation at Shandur as well as being closer to the elevation of Khunjerab than of Astore (Figure 3.068). In contrast the daily minimum RH values for all local observations are substantially lower than those estimated by the reanalysis outputs. It is not clear at this point whether this is due to inadequate diurnal heating in the ECMWF reanalyses, mass balance errors or other causes. In any case, resolution of the discrepancy is beyond the scope of the present study.

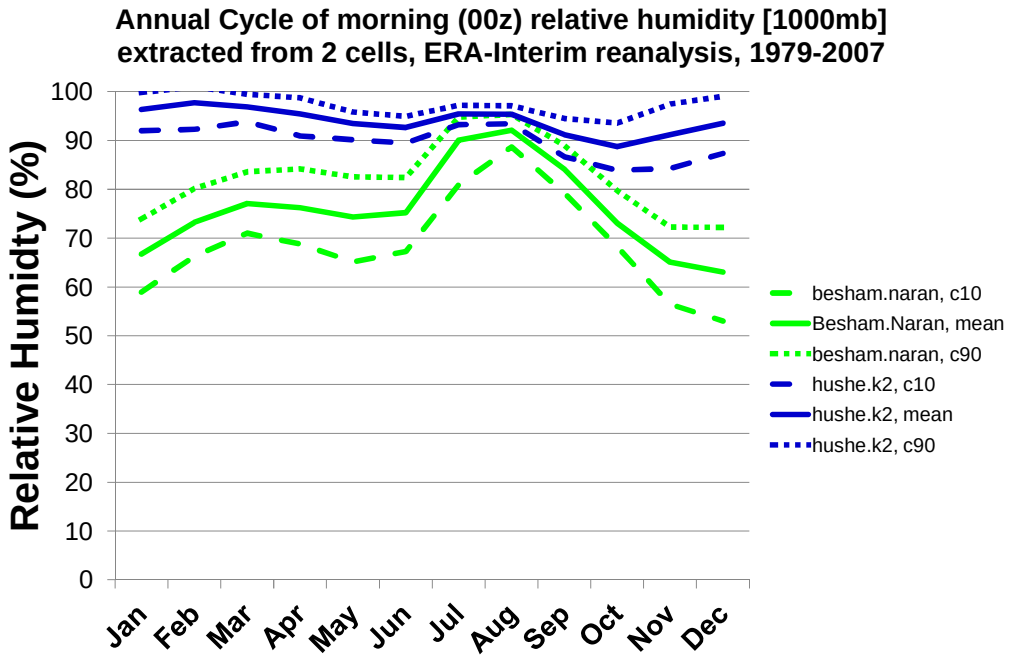

Figure 3.063 Estimate of annual cycle of near surface morning (00z, 05h local time) relative humidity from ERA-Interim, two sample grid cells, Besham.Naran (modelled elevation 2153m asl) and Hushe.K2 (modelled elevation 4953 m asl), mean values and indicators of interannual variability (c10 & c90), 1979 to 2007.

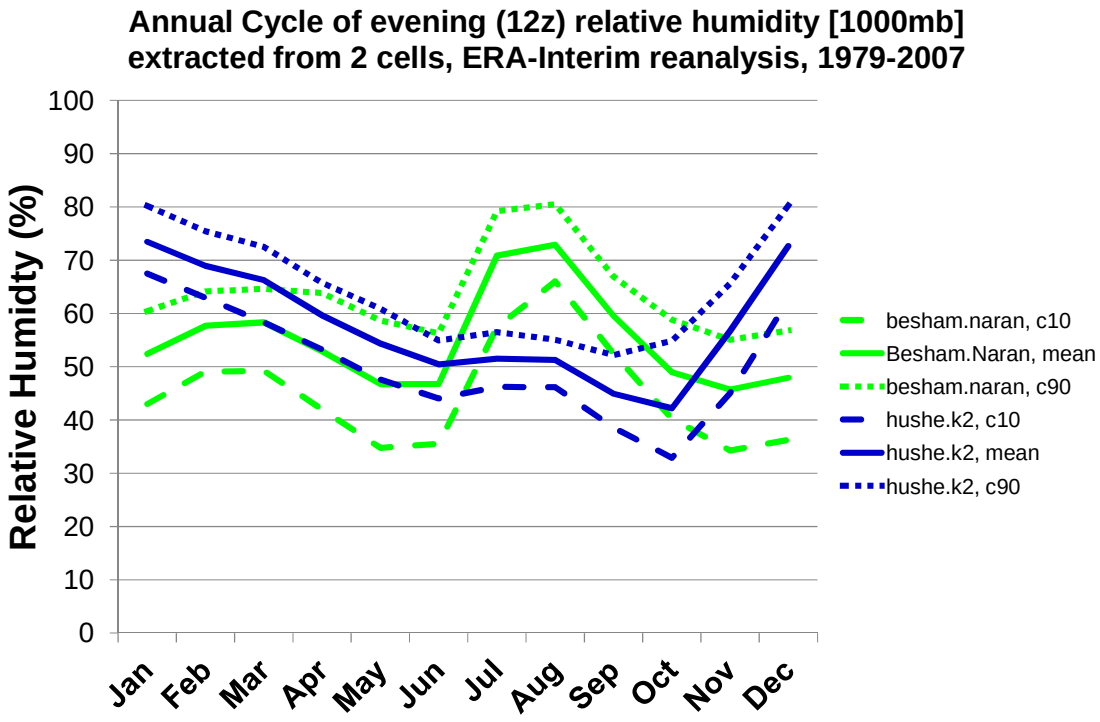

Figure 3.064 Estimate of annual cycle of near surface afternoon (12z, 17h local time) relative humidity from ERA-Interim, two sample grid cells, Besham.Naran (modelled elevation 2153m asl) and Hushe.K2 (modelled elevation 4953 m asl), mean values and indicators of interannual variability (c10 & c90), 1979 to 2007.

Shifting from differences between reanalyses and local observations to sub-regional differences identified within ERA-Interim, Figures 3.063 and 3.064 show respectively annual cycles local morning (daily maximum) and local afternoon (daily minimum) RH for two grid cells. These grid cells were chosen both for their differences in modelled mean elevation – Besham.Naran (2153m asl) and Hushe.K2 (4953 m asl) – but also for the assumed difference in climatic sub-regime implied by their geographical separation: Besham.Naran is centred over outlet of the Indus main channel from the mountains to the plains while Hushe.K2, as its name implies, is centred over some of the highest peaks in the Greater Karakoram. As can be seen in Figure 3.063, daily maximum RH for the Hushe.K2 grid cell is estimated close to saturation (RH > 90%) throughout the year. This might be attributed to its high elevation. In contrast, in the Besham.Naran grid cell daily maximum RH only regularly exceeds 85% in the summer months. This influx of moisture is assumed to correspond to transport by monsoonal weather systems. With regards to daily minimum RH (Figure 3.064), for Besham.Naran the minimum value tracks roughly parallel to the daily maximum throughout the year. For the Hushe.K2 grid cell, however, diurnal range – daily maximum minus daily minimum – in RH exhibits its own annual cycle. In winter the Hushe.K2 RH diurnal range is quite small but grows larger as the year progresses reaching a maximum in late

summer and early autumn. It could be assumed that this annual cycle is driven by diurnal heating following the annual solar (insolation) cycle as well as being moderated my local snow cover and cloud cover.

Returning to a broader view of available RH data sources, in all cases it is expected that the daily maximum will occur during the early morning, with a minimum in the late afternoon. This is assumed to occur because – barring precipitation events – the water vapour present locally will have limited variation, but the saturation vapour pressure, as a function of air temperature, will vary substantially. The strong UIB diurnal temperature cycle is thus a driver and amplifier of the RH diurnal cycle.

3.7.2 Cloud Cover: generalities and local observations

The precise – and differentiated – effects of cloud cover on the diurnal temperature cycle and surface are a key area of uncertainty for both climate scientists and hydrologists. Modelling of cloud formation and dispersal of cloud characteristics is extremely complex and an area in need of on-going refinement. Analysis of all available, credible data sources for cloud characteristics – frequency, macrophysical and microphysical properties – will help to compile a high-resolution cloud climatology for the UIB. This should be useful both in understanding the present cloud radiative effects (CRE) on the local energy balance as well as for evaluation of the realism/coherence of the outputs of various numerical meteorological simulations.

Cloud cover fraction in the UIB is substantial in all seasons as well as dynamic/variable at a range of time-steps (sub-daily to interannual). For readily apparent reasons, cloud is difficult to observe quantitatively with precision at ground-based meteorological stations with only limited automated equipment. Nevertheless, methodologies have been developed for manual cloud-cover observations. This project has access to a limited amount of such observations for a single station (Astore PMD, twice daily observations 1981 to 1999). These observations of low cloud are presented in Figure 3.074. It can be seen that in general the level of low cloud at Astore is low – between 10 and 20% in the morning and this is relatively stable throughout the day in winter months (from Nov to Feb). However, from May to September the amount of low cloud increases during the afternoon, to 20 to 40%. As will be seen in the remainder of this section, these observations do not correspond particularly well with estimates from either reanalysis or remote sensing products.

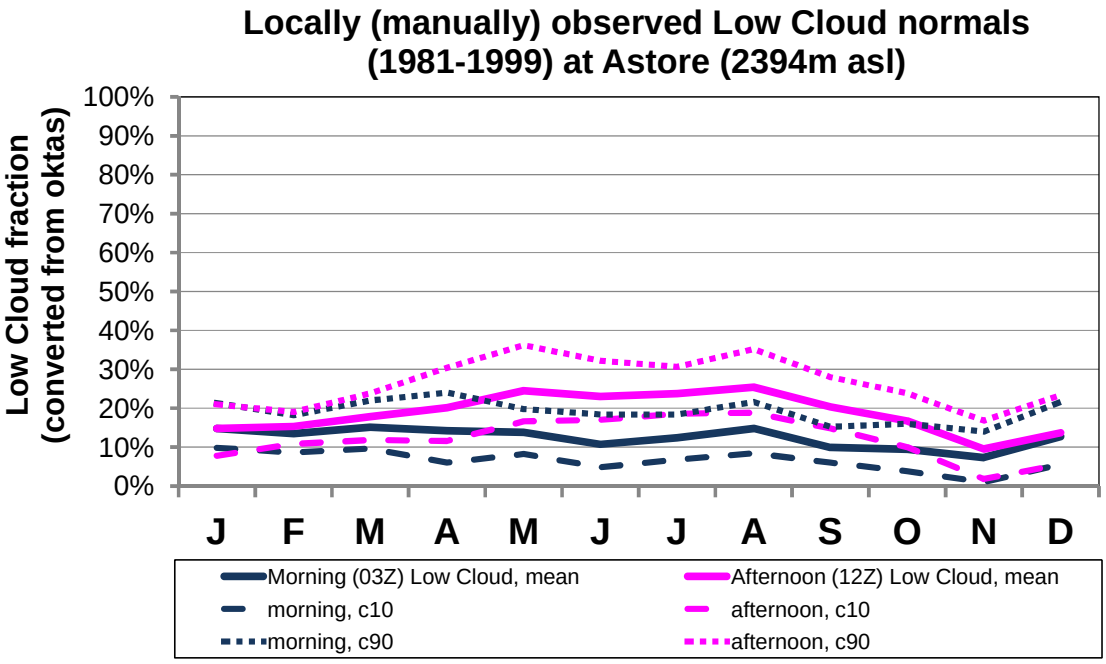

Figure 3.065 Historical (local) manual observations of low cloud at Astore, 1981 to 1999.

3.7.3 Reanalysis estimates of cloud-cover

Reanalysis cloud cover is an "analysis parameter" in both ERA-40 and ERA-Interim. This means that there is a closer relationship between the observations assimilated (for input into the numerical model) and the resultant output than might be expected if it was instead a "forecast" parameter. Roughly speaking, "analysis parameters" in ECMWF reanalyses are variables that describe the physical state of something relatively continuous (e.g. temperature, humidity). "Forecast parameters" are general fluxes of mass or energy which could be termed "accumulating variables" (e.g. precipitation, incoming solar radiation).

Annual cycles and estimates of interannual variability in "low cloud" cover as modelled by ERA-40 (1962 to 2001) and ERA-Interim (1979 to 2007) are shown in Figures 3.066 to 3.071. As was done for previous variables (air temperature, relative humidity) two grid cells are directly compared within each reanalysis to explore potential regional sub-climates created by elevation differences and geographic separation.

Despite the differences in spatial resolution and changes to model physics in treatment of humidity (Betts *et al.* 2009), the two reanalysis projects produce relatively similar types of annual cycle for daily mean cloud cover (Figures 3.066 and 3.067), i.e. a "humid winter, arid summer" type and a "autumn to spring dry season, summer monsoon" type, although the range of cloud cover in summer months is not as large for

ERA-interim and with lower maxima. Diurnal cycles are a different matter however. ERA-40 estimates greater low cloud cover at night in UIB East, while in UIB West the cloud cover is comparable and lower in both day-time and night-time (Figure 3.068 versus Figure 3.069). ERA-Interim, however, estimates greater low-cloud in day-time than at night (Figure 3.070 versus Figure 3.071) in the north-east (Hushe-K2), whereas in the south-west (Besham-Naran) there is little difference between night and day time cloud cover and it is lower than in the north-west apart from during the summer monsoon.

The cloud cover climatologies described by both reanalyses contrast strongly with the observations from Astore (Figure 3.065). The pattern of winter annual maxima and summer annual minima (for limited monsoonal activity) found in the reanalyses contradicts the locally observed winter annual minimum and broadly constant levels from late Spring to early Autumn. It is probable that much of these discrepancies result directly from the assessment methods: i) local observations were made manually and visually interpreted to a standardised scale; ii) reanalysis cloud cover was calculated based on relative humidity thresholds in modelled atmospheric pressure levels, drawing also on assimilated remote sensing data (satellite imagery).

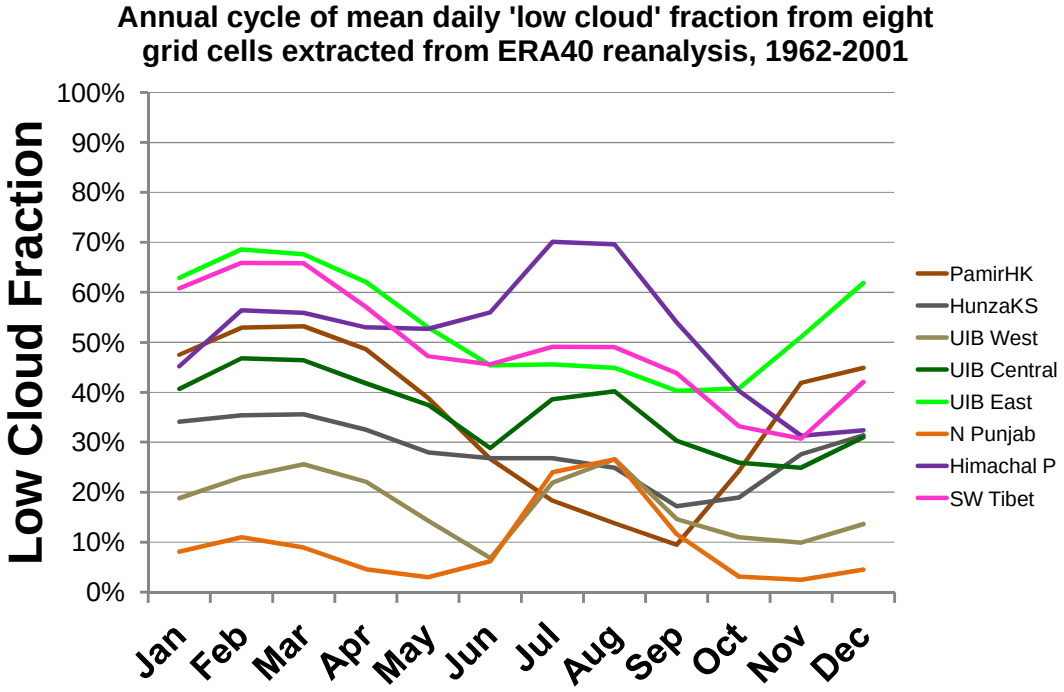

Figure 3.066 Mean daily low cloud fraction from ERA-40 for eight analysed grid cells (1962 to 2001). Grid cell mean elevations are given in Table 3.05.

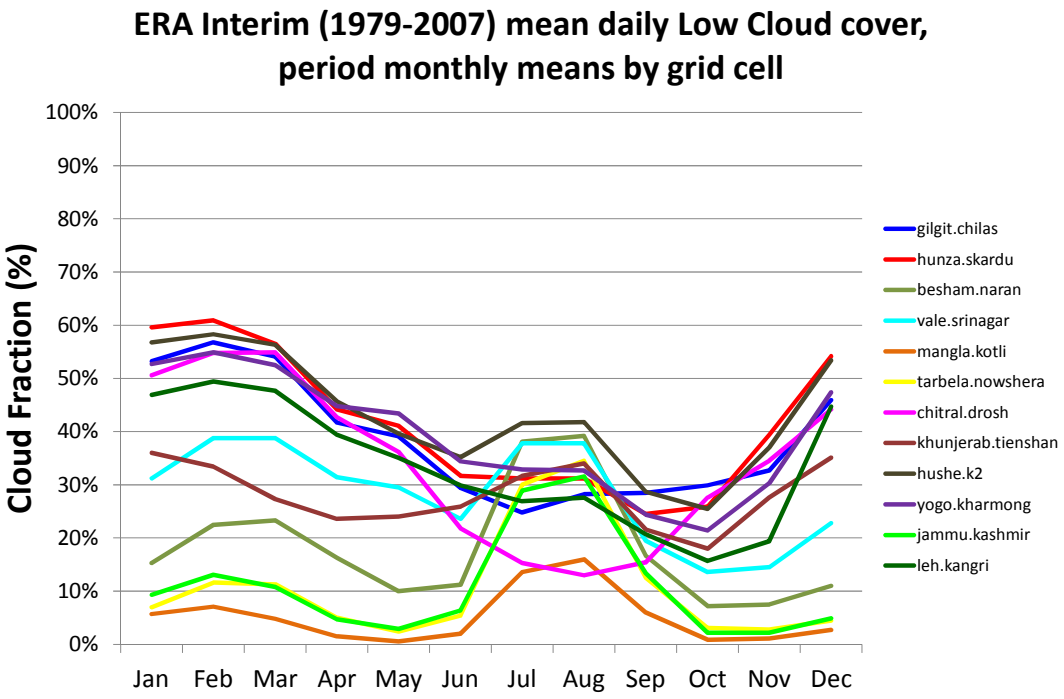

Figure 3.067 Mean daily low cloud cover from ERA-Interim (1979 to 2007) for twelve analysed grid cells. Grid cell mean elevations are given in Table 3.06.

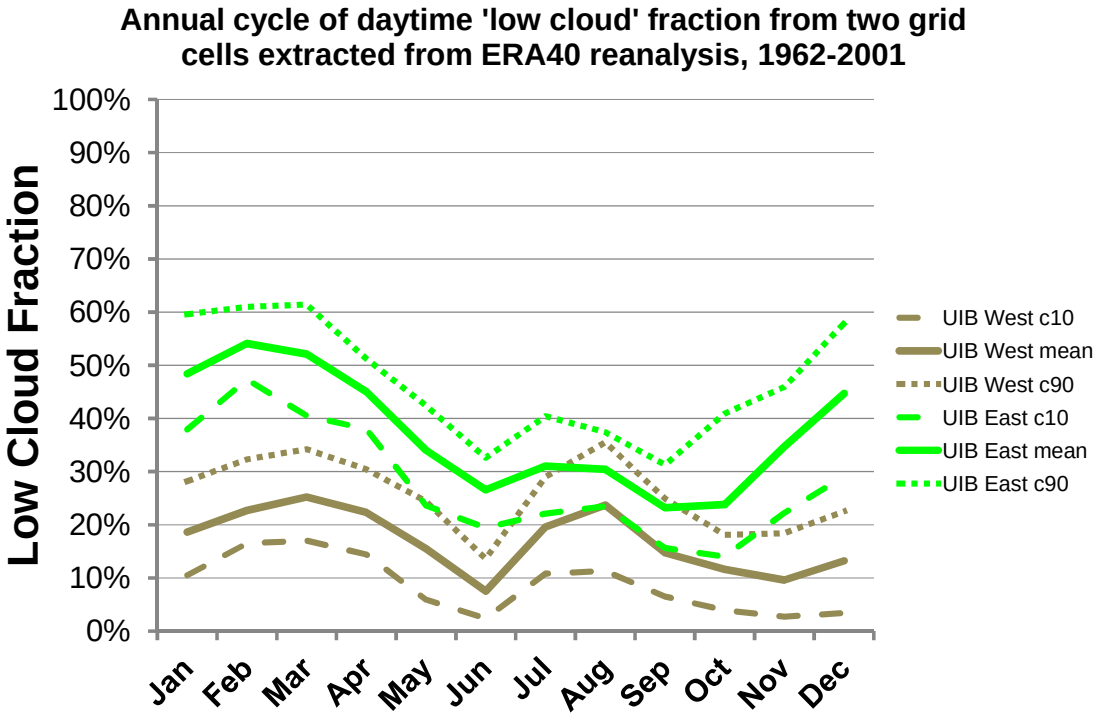

Figure 3.068 Mean day-time low cloud fraction from ERA-40 for two sample grid cells, UIB West (modelled elevation 2572 m asl) and UIB East (modelled elevation 5033 m asl), from 1962 to 2001.

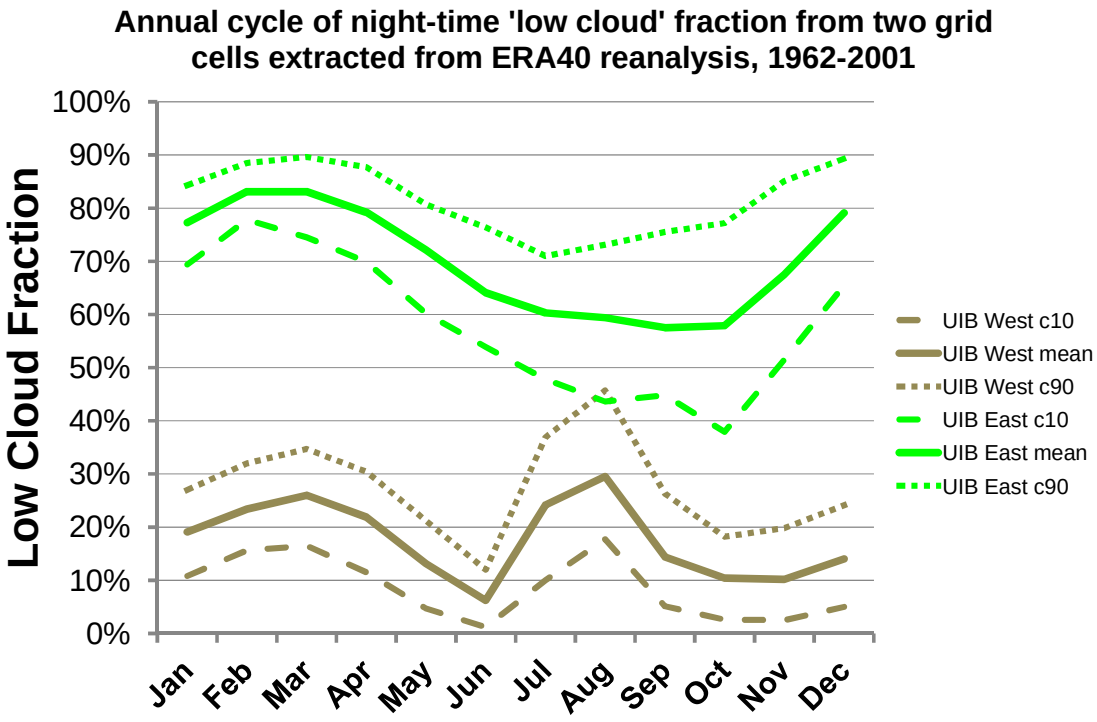

Figure 3.069 Mean night-time low cloud fraction from ERA-40 for two sample grid cells, UIB West (modelled elevation 2572 m asl) and UIB East (modelled elevation 5033 m asl), from 1962 to 2001.

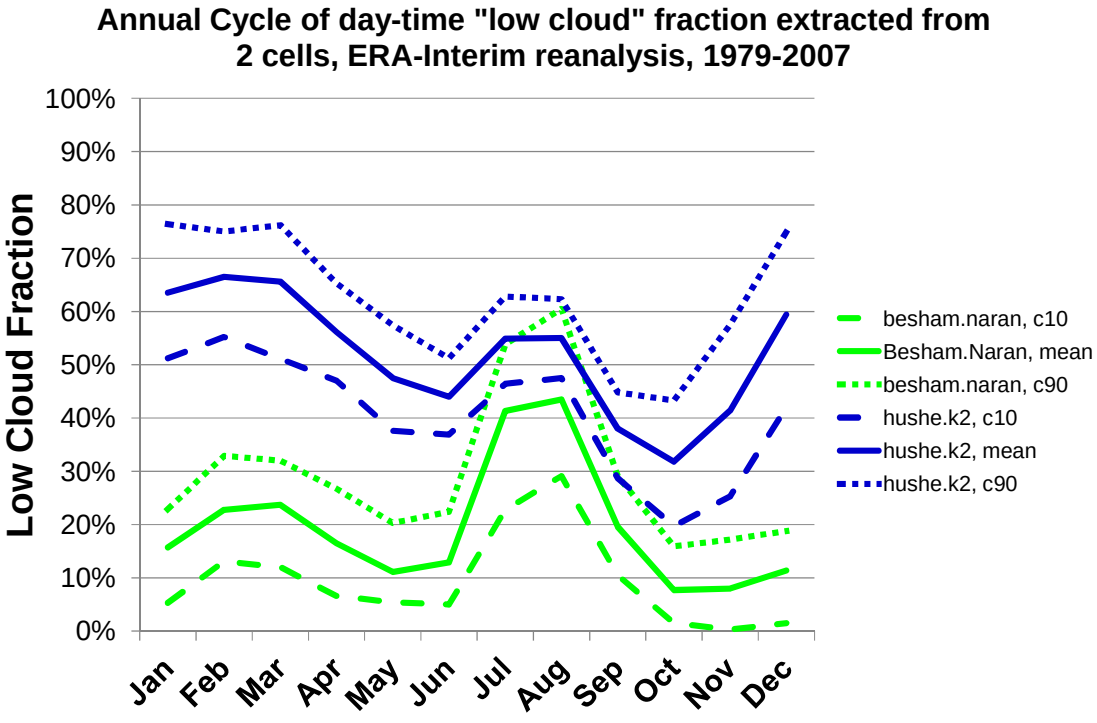

Figure 3.070 Estimate of annual cycle of day-time “low cloud” fraction from ERA-Interim, two sample grid cells, Besham.Naran (modelled elevation 2153m asl) and Hushe.K2 (modelled elevation 4953 m asl), mean values and indicators of interannual variability (c10 & c90), 1979 to 2007.

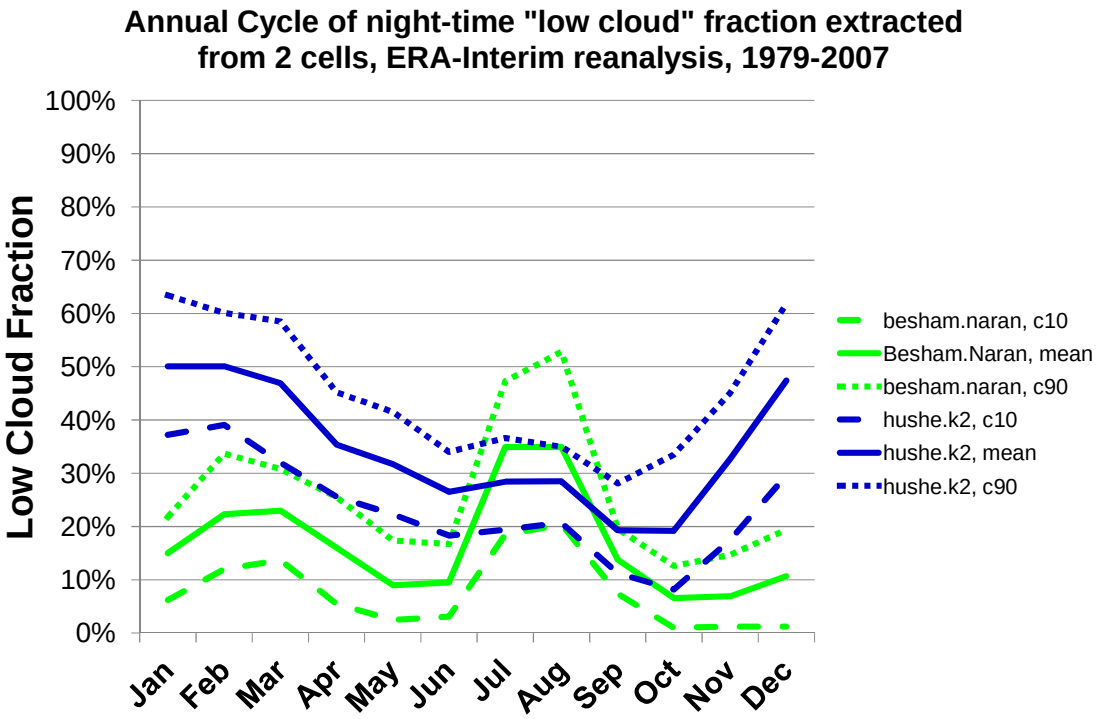

Figure 3.071 Estimate of annual cycle of night-time "low cloud" fraction from ERA-Interim, two sample grid cells, Besham.Naran (modelled elevation 2153m asl) and Hushe.K2 (modelled elevation 4953 m asl), mean values and indicators of interannual variability (c10 & c90), 1979 to 2007.

Using ERA-Interim in gridded/raster form to consider cloud cover patterns across a wider area, cloud appears to be a further element for distinguishing between UIB sub-climates. Figures 3.072 and 3.073 respectively show ERA-Interim estimates for day-time and night-time mean cloud cover over the period from 1979-2007. Topographic influence on cloud cover is evident in every month of the year in both day and night, with the largest values over high elevation terrain. Figure 3.074 shows the diurnal range (day-time minus night-time) in ERA-Interim total cloud estimates. The diurnal range of cloud cover is a variable of interest because complex diurnally asymmetrical patterns of near-surface air temperature variability have been identified in the UIB in recent decades and it is thought that cloud cover plays an important role in shaping this variability. The questions of climatic variability in recent decades in the UIB and its potential drivers is addressed in Chapter 4. It is deemed worthwhile therefore to assess the present mean annual cycles of cloud cover diurnal range as the part of the broader characterisation of UIB cloud climatology.

Over the primary UIB contributing area, total day-time cloud is estimated to exceed night-time cloud throughout the year. For adjacent regions – including the Central Himalaya front-range, the northern Pamir-Kunlun Shan ranges and substantial sections of the Tibetan plateau – however, night-time cloud is estimated to exceed day-

time cloud for much of the year. The low elevation areas – the Indo-Gangetic plain and the Taklimakan desert – appear to follow a similar diurnal cycle to the central UIB with the exception of the incursion of the monsoon in the summer months.

Spatial patterns of statistical significance of the ERA-Interim estimates of cloud cover diurnal range are not addressed directly here, in large part due to the coarse spatial resolution. Some insight on potential seasonal and spatial patterns, however, can be gained by comparing the results of each of the example grid cells between Figures 3.070 and 3.071. In some cases, e.g. hushe.k2 in July or ‘August, the first decile (c10) of the day-time cloud cover will be greater than the last decile (c90) of the night-time cloud cover suggesting a statistically significant diurnal range. In other cases, .e.g. besham.naran more or less year-round, the band of variability between the first and last deciles for day-time and night-time cloud cover will broadly overlap suggesting little statistical significance in the diurnal cloud cover range.

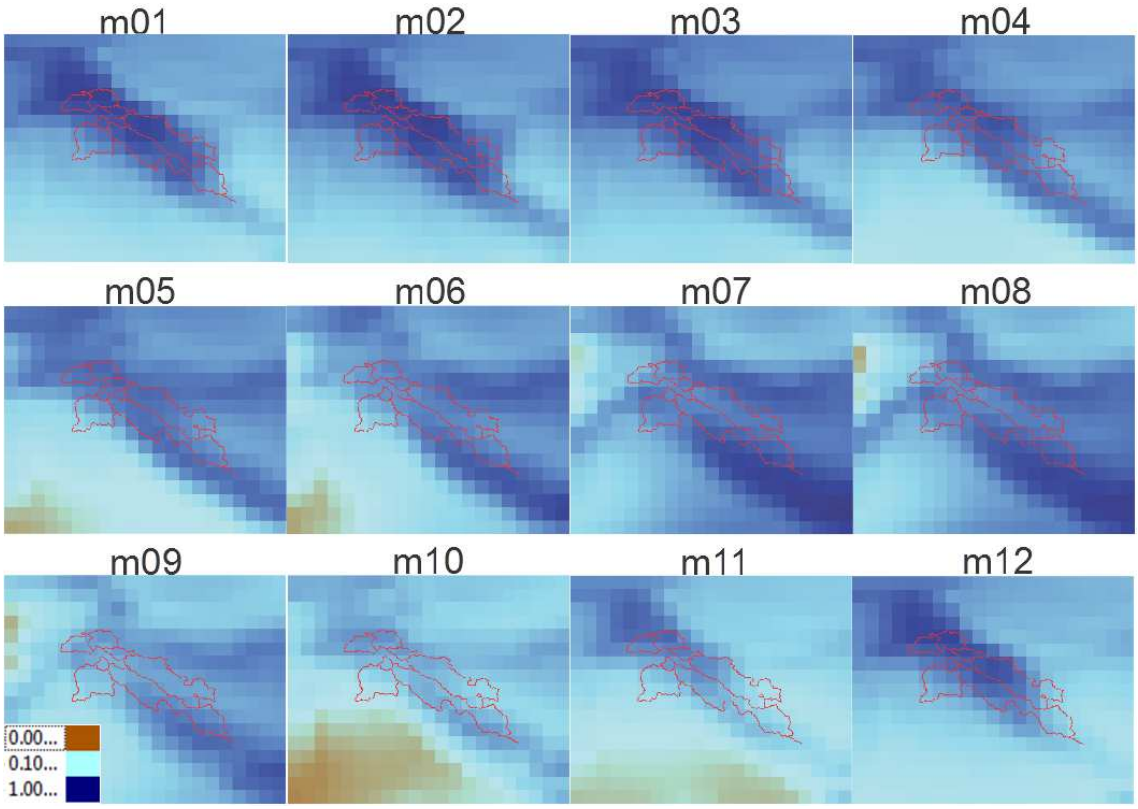

Figure 3.072 ERA-Interim gridded estimates of period mean day-time total cloud cover, 1979 to 2007. For cloud imagery: the colour scale shown indicates reference points between which colour is scaled linearly. Put more simply, a cloud cover frequency of 0.55 is a medium blue, i.e. mid-way between pale blue (0.10) and navy blue (1.00).

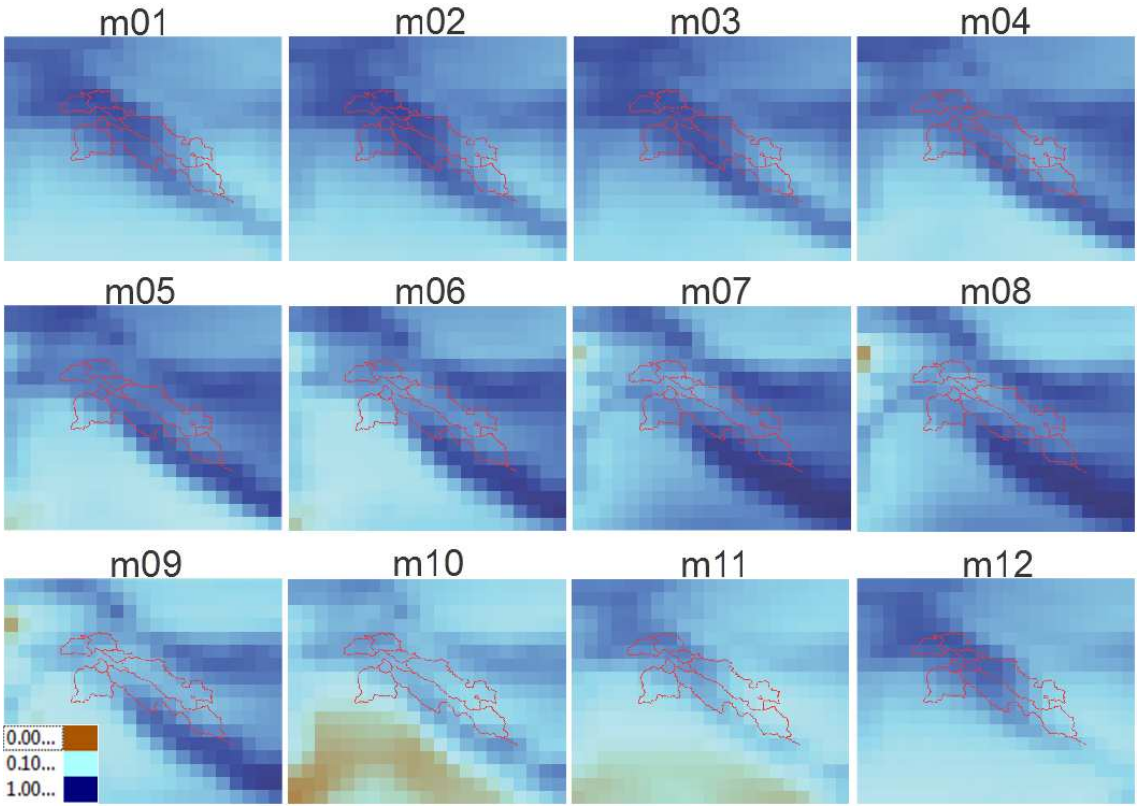

Figure 3.073 ERA-Interim gridded estimates of period mean night-time total cloud cover, 1979 to 2007. For cloud imagery: the colour scale shown indicates reference points between which colour is scaled linearly. Put more simply, a cloud cover frequency of 0.55 is a medium blue, i.e. mid-way between pale blue (0.10) and navy blue (1.00).

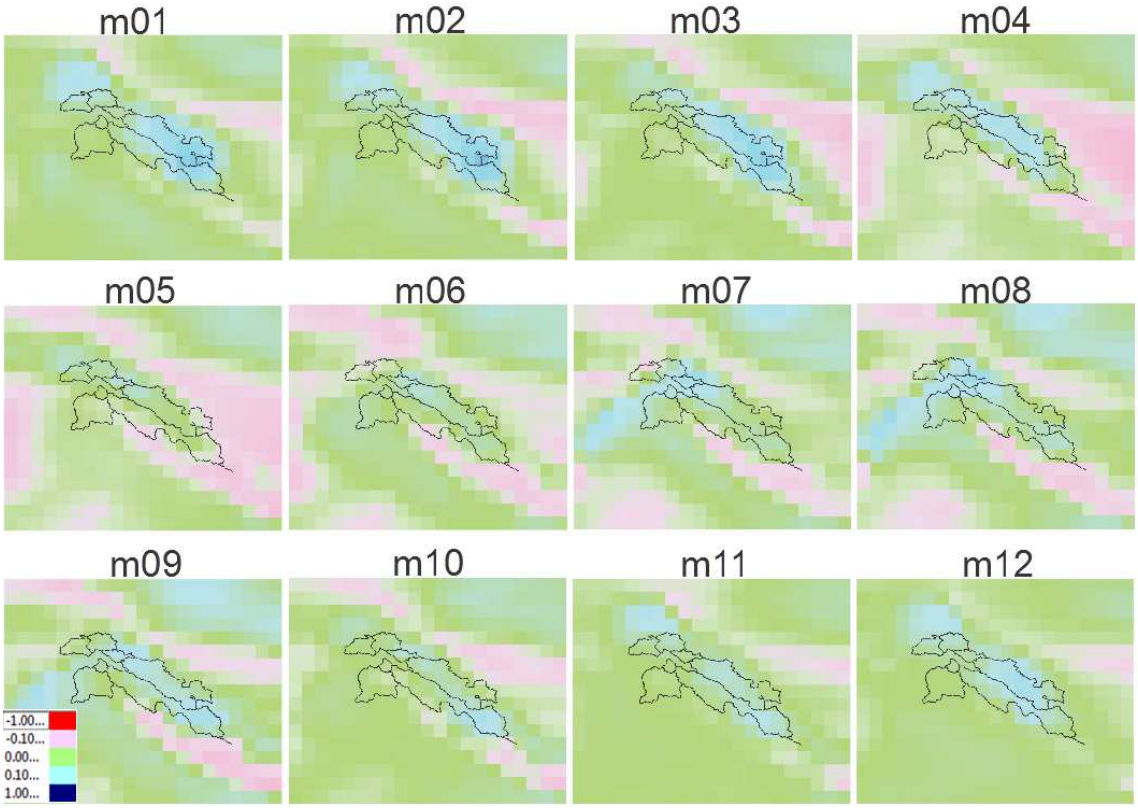

Figure 3.074 ERA-Interim gridded estimates of period mean cloud cover diurnal range (day minus night), 1979 to 2007. For cloud imagery: the colour scale shown indicates reference points between which colour is scaled linearly. Put more simply, a cloud cover frequency of 0.55 is a medium blue, i.e. mid-way between pale blue (0.10) and navy blue (1.00).

3.7.4 Cloud cover estimates from MODIS (mod06L2)

While reanalysis products estimate cloud formation/presence through numerical simulation, including thresholds of relative humidity, data products from remote sensing use algorithms drawing on passive radiometric observations in a range of frequency bands to test for cloud presence. Thus, although the remote sensing algorithms may at times produce false positives or negatives, these data products can be considered as observations. This project has included detailed analysis of a high resolution cloud data product (mod06L2) produced from MODIS imagery (Platnick *et al.* 2003, Li *et al.* 2005, Weisz *et al.* 2007).

The MODIS spatially aggregated annual cycle of total day-time and night-time cloud cover fraction (CCF) for the NW UIB zone – tributary catchments of Shigar, Hunza, Gilgit and Astore plus the main channel from Yogo and Kharmong downstream to Besham – are shown in Figure 3.084. CCF is the fraction (or percent) of a given unit area which is covered by clouds. Even in periods with relatively clear prevailing conditions (first decile/c10), on a mean-monthly catchment-wide basis, the MODIS cloud product (MOD06L2) still indicates substantial CCF (>35%) from both day-time and night-time scenes/overpasses. As seen in Figure 3.075, for much of the year the spatial mean total cloud cover from day-time and night-time scenes are of quite similar magnitudes. This contradicts both the local observations (Astore PMD) as well as the ERA-40 and ERA-Interim reanalyses which indicated substantial (large-scale) diurnal cloud-cycling. The pattern of winter annual maxima and summer annual minima does match the annual cycle found in the reanalysis outputs (ERA-40 and ERA-Interim). This finding, however, contradicts the somewhat questionable manual observations made locally.

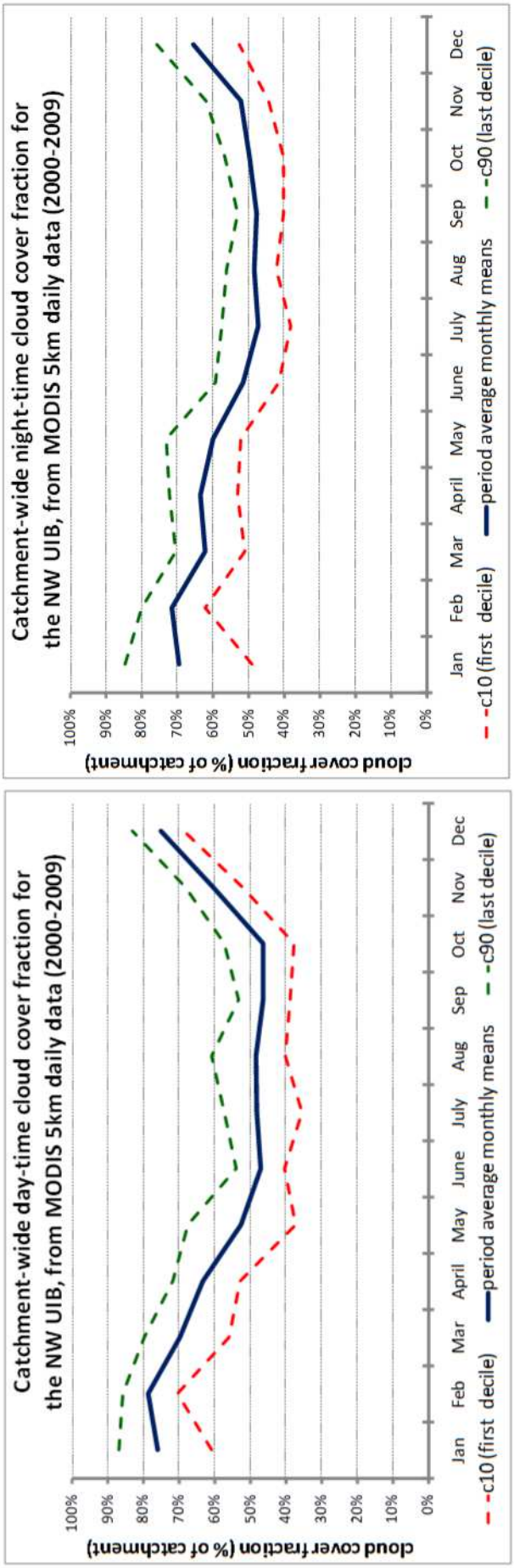

Figure 3.075 MODIS spatially aggregated estimates of total cloud cover, day (left) and night (right), in NW UIB.

As Figures 3.076 to 3.079 show, however, there is considerable spatial variability at the catchment scale. MODIS observations of day-time cloud cover (Figure 3.076), night-time cloud cover (Figure 3.077) and diurnal cloud range (Figure 3.078) largely corroborate the spatial patterns found for these parameters in ERA-Interim, although the absolute values of cloud cover are much higher for MODIS than for the reanalysis products, and the incursion of the monsoon in summer months may be seen more clearly in the MODIS dataset.

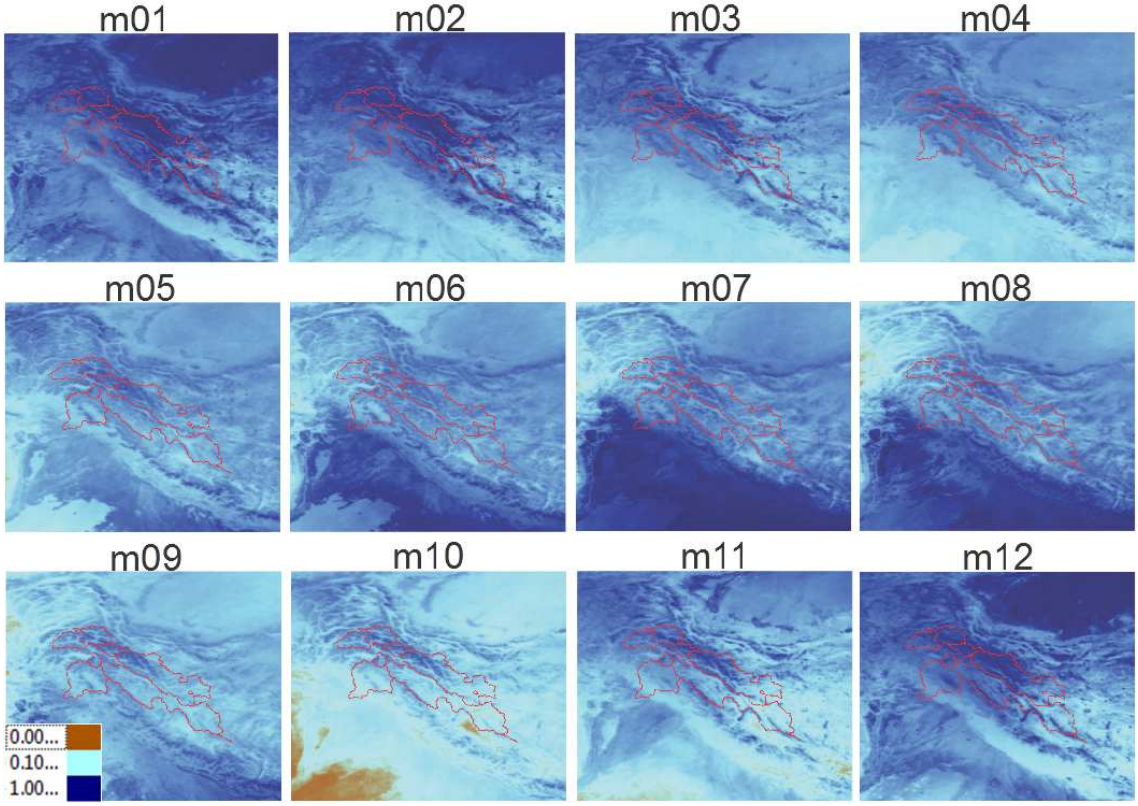

Figure 3.076 MODIS (mod06L2) estimates of period mean day-time total cloud cover, 2000-2009. For cloud imagery: the colour scale shown indicates reference points between which colour is scaled linearly. Put more simply, a cloud cover frequency of 0.55 is a medium blue, i.e. mid-way between pale blue (0.10) and navy blue (1.00).

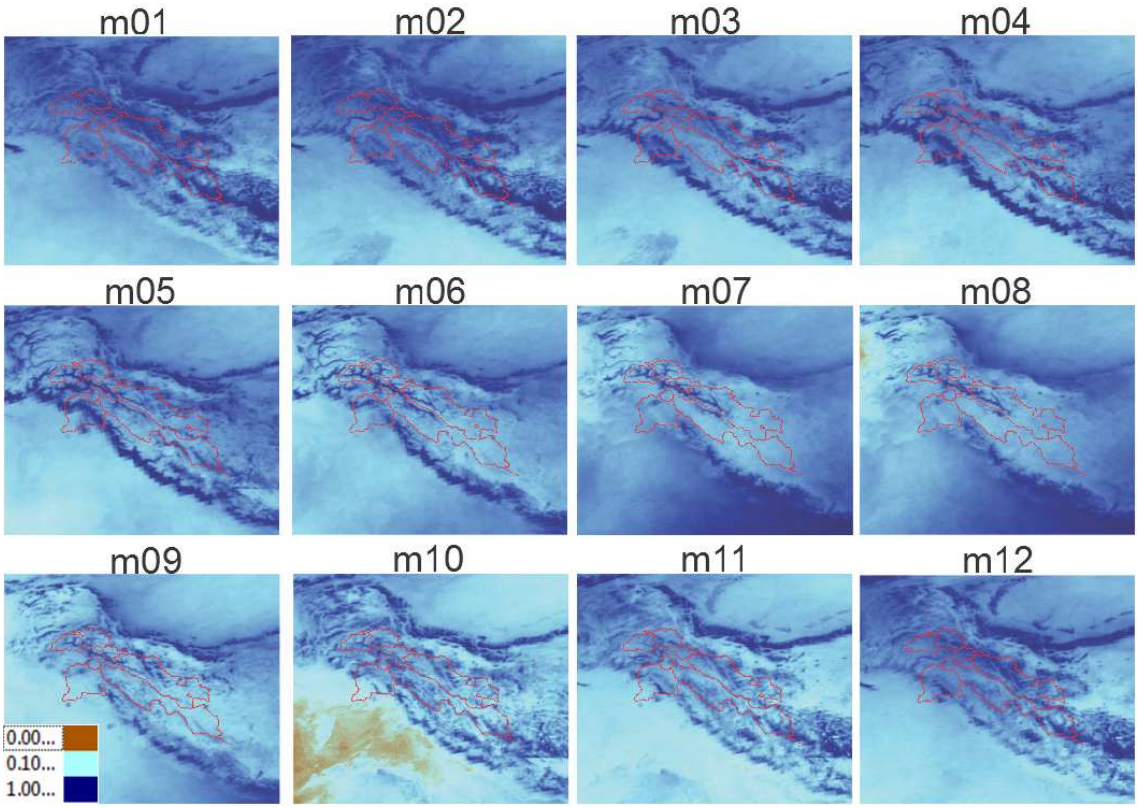

Figure 3.077 MODIS (mod06L2) estimates of period mean night-time total cloud cover, 2000-2009. For cloud imagery: the colour scale shown indicates reference points between which colour is scaled linearly. Put more simply, a cloud cover frequency of 0.55 is a medium blue, i.e. mid-way between pale blue (0.10) and navy blue (1.00).

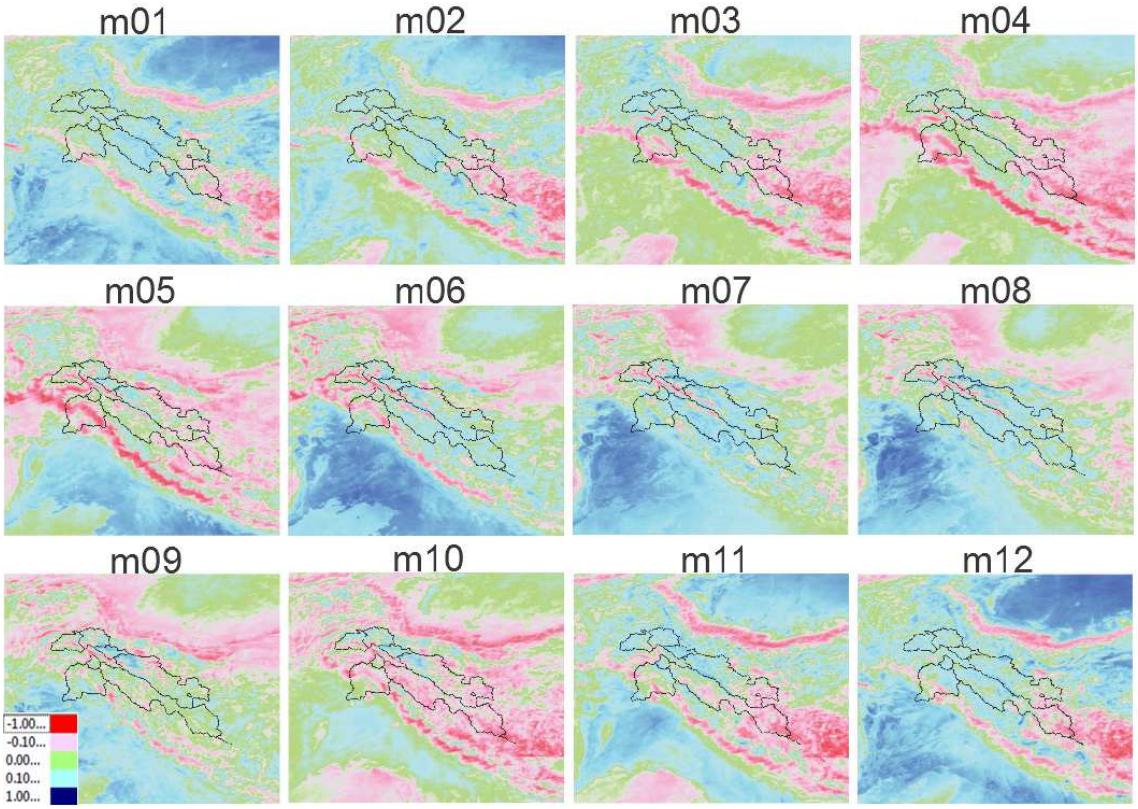

Figure 3.078 MODIS (mod06L2) range (day minus night) mean night-time total cloud cover, 2000-2009. For cloud imagery: the colour scale shown indicates reference points between which colour is scaled linearly. Put more simply, a cloud cover frequency of 0.55 is a medium blue, i.e. mid-way between pale blue (0.10) and navy blue (1.00).

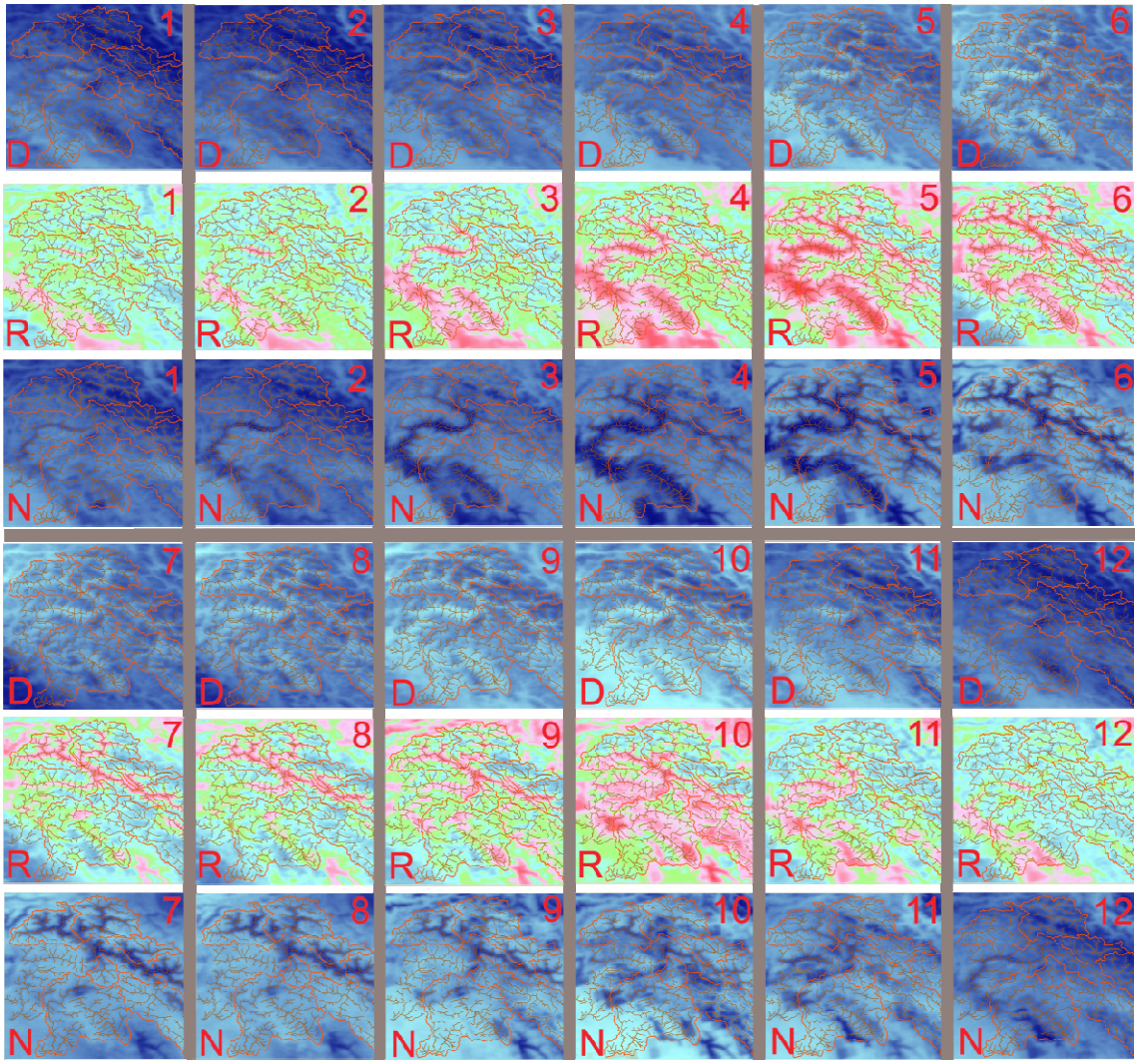

Figure 3.079 Detailed composite view of NW UIB period monthly means of cloud cover fraction (CCF) MODIS cloud cover using Figures 3.85 to 3.87. Component images are coded by diurnal phase with a letter and by calendar month with a number. For diurnal phase: D = CCFday, R = diurnal range {CCFday minus CCFnight}, N = CCFnight. For calendar month, e.g. 1 =January, 12 = December.

Detailed examination of the relative values between the UIB peaks and valley channels – as shown in Figure 3.079 – reveals a well-defined (orographically-driven) sub-regional spatial structure to cloud cover frequency. Furthermore, a phenomenon of particular interest can be seen in Figure 3.079. Comparison of the sequence of month by month images shows a northward & upward migration of night-time cloud (and night vs day excess [{CCFday minus CCFnight} <0]; pink in Figure 3.079) concentrated in the valleys, developing through spring, reaching its highest/northernmost extent in summer and retreating again during autumn. This highly complex spatio-temporal pattern is of interest because it potentially suggests that at least some of the factors influencing local energy balance and hence local temperature variation in the UIB operate at a relatively restricted spatial scale, i.e. far smaller than the gauged tributary catchments. This in turn opens the door to the possibility that trends estimated from long-record meteorological stations located in valley bottoms may be under the influence of physical mechanisms,

i.e. cloud radiative effect, which are not spatially representative of wider catchment conditions.

Looking beyond the simple presence or absence of cloud cover, cloud micro-physical properties – derived for MODIS using algorithms requiring visible wavelengths and thus observed only in daylight – describe the characteristics which differentiate clouds in terms of their potential cloud radiative effect (CRE). Annual cycles for three key parameters –cloud optical thickness, cloud effective radius and cloud water path, as well as the frequency of observation of cloud water path – are shown in Figure 3.080. These parameters are of critical importance because they influence the magnitude of the cloud radiative effect by defining cloud properties beyond just fractional areal cover (see for example Shupe and Intrieri 2004, Dong *et al.* 2005, Ebell *et al.* 2011). Cloud optical thickness (COT) is a measure of the cloud's opacity to visible spectrum light. This influences the amount of incoming shortwave radiation reaching the ground surface beneath the cloud. Cloud effective radius (CER) is an estimate of the mean or effective radius of the water droplets or ice crystals composing the cloud. Cloud water path (CWP) is a measure (in mass per unit area) of the amount of water contained in the cloud within the (surface area of) the target pixel. Both CER and CWP can influence the longwave and shortwave CRE.

The cloud microphysical properties (COT, CER and CWP) show relatively muted annual cycles, with a general tendency toward higher values in colder months (Sept-Jan). Notably, cloud effective radius has an annual minimum during the months of peak monsoon activity (July, August) and cloud optical thickness has an annual minimum during the spring (March to May) which are the months with peak precipitation (originating from westerly weather systems). The precise impact on net radiative effects resulting from variability in cloud microphysical parameters is an issue of continuing uncertainty in climatological circles. In general, increasing values in the microphysical properties here could be expected to increase their contribution to CRE on individual radiative fluxes, but it must be born in mind that CRE on shortwave and longwave radiation act in opposing directions with regards to net surface energy balance. Furthermore, microphysical influence on CRE is expected to be non-linear and some authors (e.g. Ebell *et al.*, 2011) have identified threshold effects which influence which microphysical parameter is dominant for a given set of conditions. Exhaustive investigation of these issues is beyond the scope of the present study and would likely require longer observational records than those presently available in the MODIS data products to robustly sample present climatic variability. Development of a multi-

decadal record of high spatial and temporal resolution cloud microphysics data, for example using the radiometric observations from the AVHRR series of instruments perhaps in conjunction with meteorological reanalysis, could provide an avenue for developing such a record.

The complex diurnal, spatial and seasonal patterns in cloud parameters shown here indicate the challenge posed by the imperative of quantifying the role of cloud in governing temperature variability in the UIB. The detailed characterisation undertaken by this project, however, should provide the first step toward this goal.

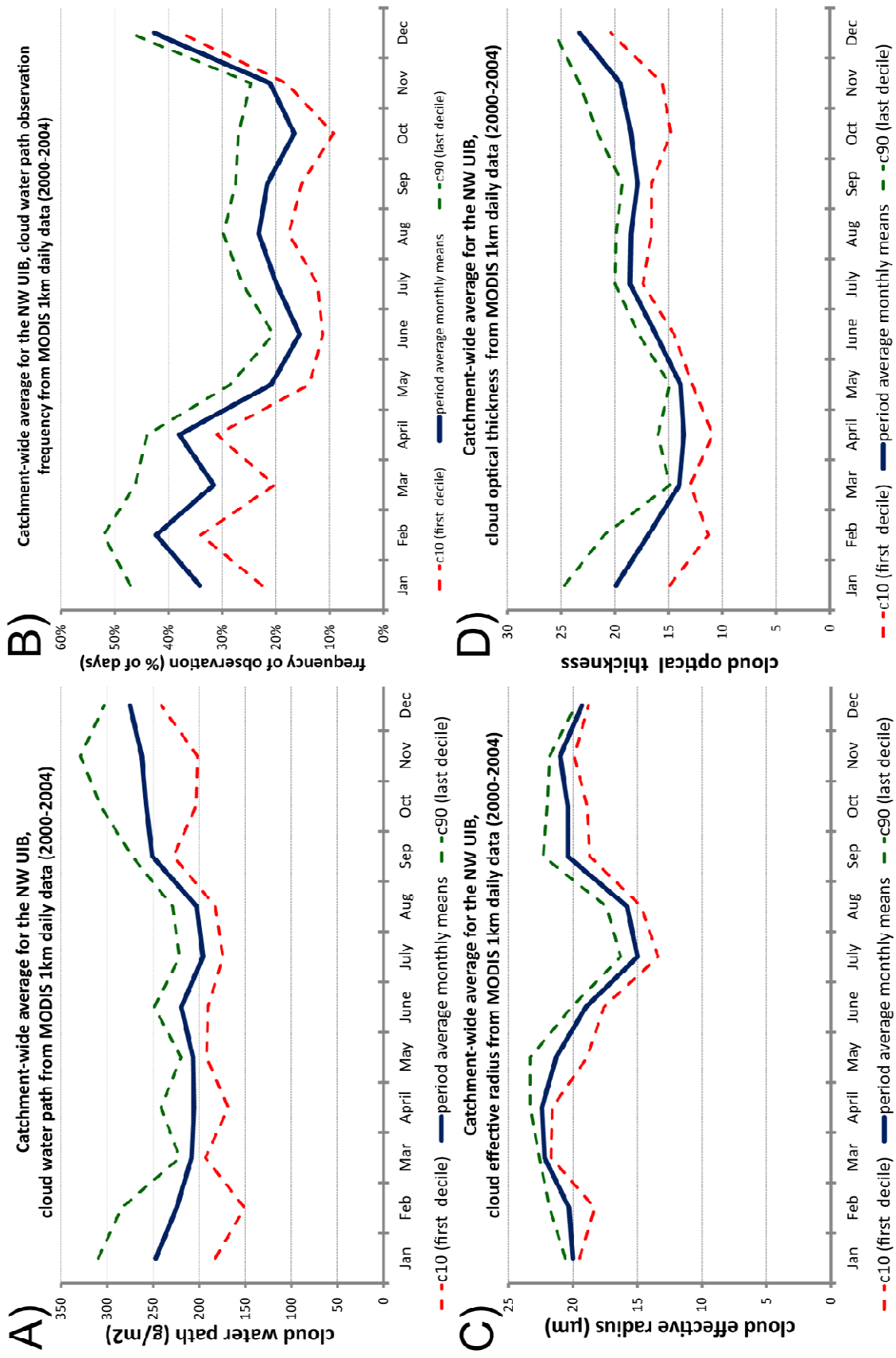

Figure 3.080 MODIS spatially aggregated estimates of cloud microphysical properties in NW UIB, 2000 to 2004. Panels show: A) cloud water path (absolute value); B) cloud water path (frequency of observation); C) cloud effective radius; and D) cloud optical thickness.

3.7.5 Albedo

As described in section 3.3.13, surface albedo is a key parameter in the surface energy balance because it controls the absorption of incoming (shortwave) solar radiation. In the UIB albedo is very strongly linked to snow cover, because snow cover often has an albedo much higher than vegetation or bare ground. Direct estimation (observation) of albedo via remote sensing is possible. This project analysed a MODIS albedo product (mcd43a). The spatially aggregated results – annual cycle and indicators of interannual variability (c10 & c90) – are shown in Figure 3.081. As can been seen in Figure 3.081, in late winter the Astore catchment as a whole reflects approximately 70% (albedo of 0.7) of incoming solar radiation while the Hunza catchment and the wider NW UIB each reflect approximately 50% (albedo of 0.5). Annual albedo minima occur in late summer when snow and ice cover are also at their lowest. In late summer the Astore catchment absorbs roughly 85% of incoming solar radiation (albedo of 0.15), while the Hunza catchment and wider NW UIB each absorb approximately 80% (albedo of 0.2). While these values appear plausible, there is an absence of field observations of albedo in the UIB which would be necessary to provided independent validation of this dataset. Nevertheless, Wang *et al.* (2012) found that the mcd43 data product agreed well with both ground-based measurements and alternative remote sensing estimates from the Landsat platform for a site in Alaska (Barrow) with a prolonged annual cycle of snow cover.

Detailed knowledge of catchment albedo is useful in constraining and/or validating land surface process components in complex hydrological models. This subject will be dealt with in Chapter 6.

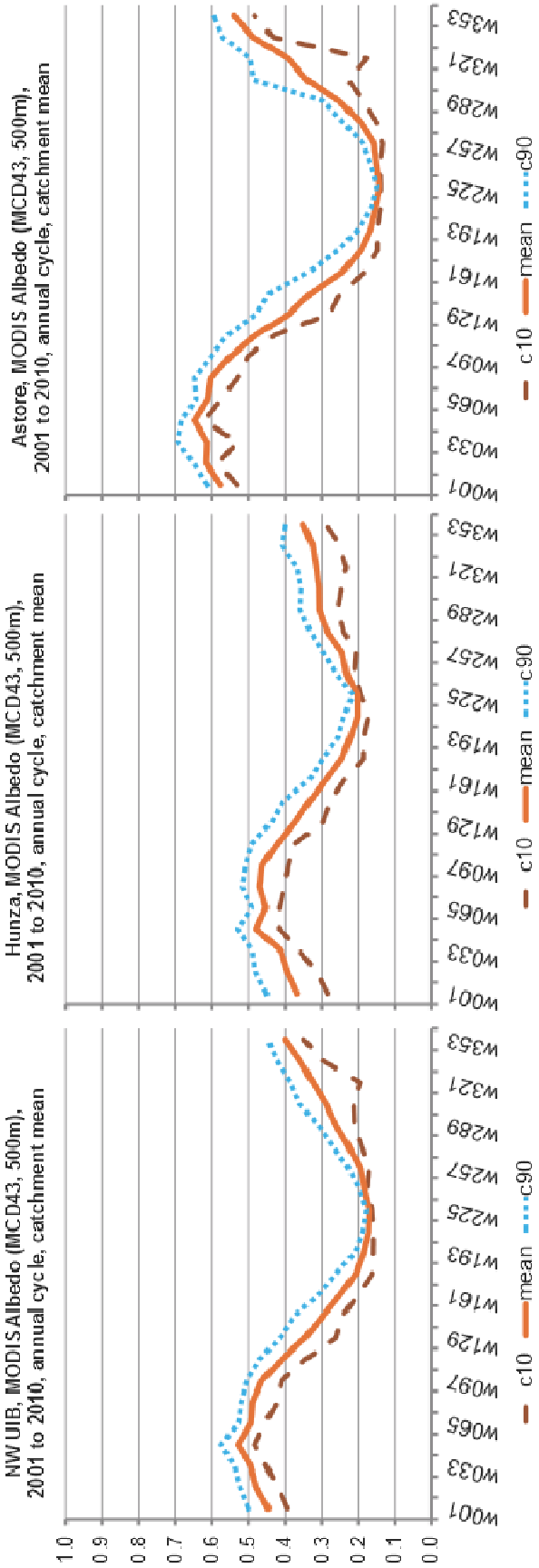

Figure 3.081 MODIS spatially aggregated estimates of albedo for three UIB tributary catchments: NW UIB (left panel), Hunza (middle panel), Astore (right panel) – from 2001 to 2010. Catchment boundaries can be seen in Figure 3.041. The labels on the horizontal axis refer to the first Julian day (1 to 365) of the MODIS 16-day aggregate for which the value is being computed.

3.8 (Reanalysis) estimates of surface energy balance in the UIB

As discussed earlier in this chapter, the surface energy balance controls the timing and, in cases where melt energy is the primary limiting factor (i.e. glacial regime catchments), magnitude of runoff in the UIB. In order to better understand the influence of the surface energy balance on UIB hydrology, this project analysed the surface energy balance components as estimated by the ECMWF reanalysis projects ERA-40 and ERA-Interim.

3.8.1 ERA-40 estimated UIB surface energy balance

Logically the annual surface energy balance cycle in the UIB is dominated by the annual cycle in incoming solar (shortwave) radiation (Figure 3.091). Values for net solar radiation are at annual minimum in the winter when: i) "top of atmosphere" incoming radiation is also at a minimum; ii) substantial cloud cover reduces the amount of solar radiation reaching the surface; and iii) the high surface albedo resulting from widespread, fresh snow cover cause much of the incoming surface radiation to be reflected rather than absorbed (Kiehl and Trenberth 1997, Sade *et al.* 2011). Net solar radiation, in the mountainous NW UIB, reaches an annual maximum in early summer when: i) the "top of atmosphere" incoming radiation is also at a maximum; ii) pre-monsoonal prevailing "mostly clear sky" conditions allow much of the "top of atmosphere" radiation to reach the surface; iii) in terms of surface area, the majority of ephemeral/seasonal snow cover has been ablated.

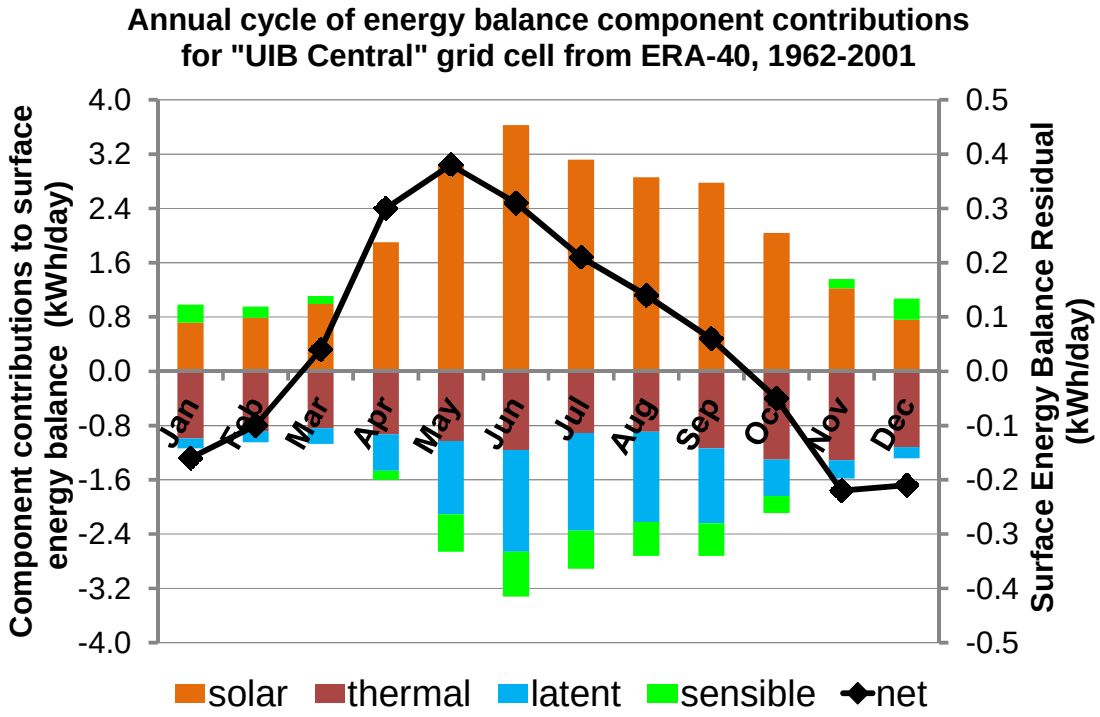

Figure 3.082 Estimate of annual cycle of surface energy balance components from ERA-40, single grid cell example, mean monthly values of daily accumulated energy fluxes (kWh/day), 1962 to 2001.

The sign of net thermal (infrared) radiation is opposite to net solar radiation as it quantifies the release of (infrared wavelength) thermal energy from the surface to the atmosphere. The outgoing thermal flux is dependent upon both surface temperature and overlying cloud and hence has a more complex annual cycle than net solar flux. In terms of magnitude, Figure 3.082 shows that there is a minor maximum in early summer when surface temperatures are high and cloud cover is low to moderate. There is an additional major mode/maximum in autumn when surface temperatures are moderate but relatively clear skies allow more of the emitted radiation to escape into the upper atmosphere (very limited backscatter).

Thoughtful consideration of the influence of snow cover and cloud cover on the two dominant energy balance components – solar (shortwave) and thermal (infrared) – indicate the strong potential for feedback mechanisms in a changing climate. To be explicit, perturbations to incoming moisture regimes from changes to weather system characteristics could substantially alter both cloud formation parameters and snow cover dynamics. This could, in turn, have significant impacts on net available energy which would further perturb the local snow cover and cloud cover cycles. Multi-decadal snow cover data of satisfactory spatial resolution is not currently available, but estimates of cloud cover from reanalysis are spatially and temporally coherent with the reanalysis energy balance estimates. This allows examination of “cloud radiative effects.” Links

between cloud cover, radiation balance components and near-surface air temperature will be explored in Chapte 4 (section 4.4).

Latent heat flux, which quantifies the energy transferred by the state change of water, follows a similar annual cycle to net solar radiation, albeit with an opposite sign (Figure 3.082). In the winter there is minimal available energy to drive snow melt, minimal liquid water available for evaporation and only limited sublimation – direct lost of mass from the snowpack to the atmosphere – hence very little energy is transferred from the surface to the atmosphere as latent heat. In the summer, however, substantial available energy drives considerable snow and ice melt. Liquid water is available on the surface and as moisture in the near-surface soil for evaporation. Thus, latent heat flux is elevated throughout the melt season.

Sensible heat flux, like net thermal flux, quantifies energy exchange between the surface and the overlying air. Sensible heat flux, however, changes in both sign and magnitude over the course of its annual cycle (Figure 3.082). In the winter and early spring, on a mean-basis, near-surface air temperatures exceed surface ("skin") temperature and so there is a modest energy transfer from the overlying air downward. As ablation develops in mid- to late-spring this situation reverses as the surface temperature exceeds the near-surface air temperature on a mean basis. From this point forward in the ablation season, the transfer is from the surface toward the atmosphere although magnitudes remain modest (a fraction of the outgoing thermal flux). The sign changes back again in autumn as ablation ends and substantial snowpack/cover begins to accumulate.

The net result of each of these individual components, in ERA-40, is that the direction of energy transfer is from the surface toward the atmosphere (negative) in the winter, albeit at modest magnitudes (Figure 3.082). In energy balance terms, the potential melt season in the UIB can be equated with the period when the net balance is positive (energy transfer from/through atmosphere to surface). There are, however, sub-regional differences in the timing and magnitude of the net energy balance (residual), as can be seen in Figure 3.083. There appear to be multiple geographic/physiographic dependencies which shape the annual cycle of net surface energy balance residual: elevation, latitude, position with regards to monsoonal versus westerly weather systems. In general, higher (mean) elevation grid cells appear to have amplified residual cycles (higher positive peak, more negative winter phase) compared with lower elevation cells.

Improved spatial resolution could help to separate the competing factors causing the differences found.

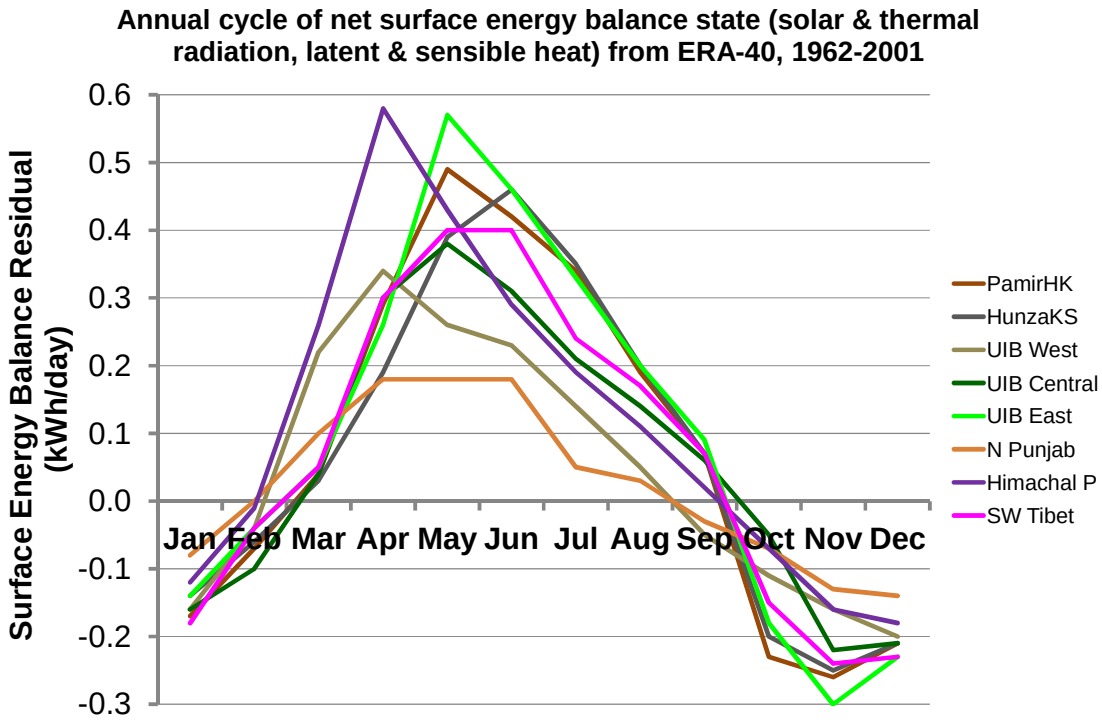

Figure 3.083 Estimate of annual cycle of surface energy balance state from ERA-40, eight analysed grid cells), 1962 to 2001.

3.8.2 ERA-Interim estimated UIB surface energy balance

The "full resolution" ERA-Interim output does present a significant advance over ERA-40 in terms of spatial resolution of available data (0.75 degrees versus 2.5 degrees). Fundamentally, as shown for example in Figure 3.084, the estimated contributions of the individual energy balance components remains similar to that found by ERA-40. The contrasting residual cycles seen when comparing multiple ERA-Interim grid cells do seem to fit general sub-regional patterns (Figure 3.085). The southerly, lower-elevation grid cells covering the foothills show a lower peak annual residual – roughly 0.45 kWh/day – with an annual maximum residual shifted one or two months earlier in the year. As in ERA-40, the high and central mountain grid cells (located behind the "front range") have exacerbated peak annual residual values. In ERA-Interim these values are substantially greater, ranging from 0.8 to 1.0 kWh/day. Elevation appears to play the dual role of both accentuating and delaying the peak residual.

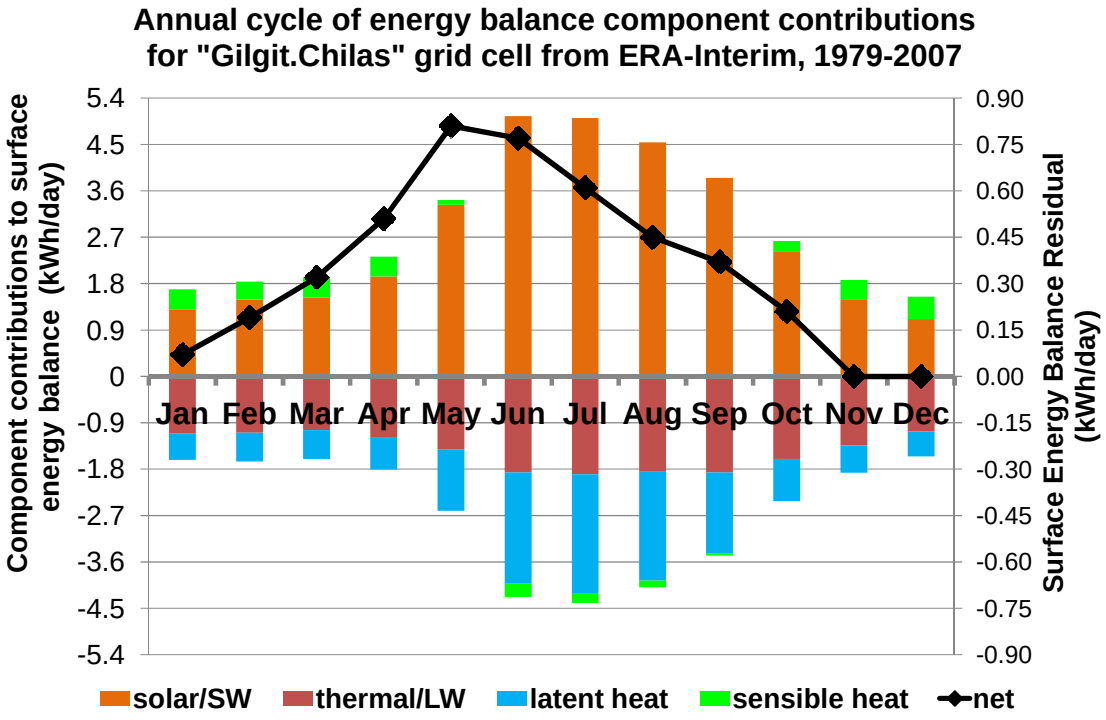

Figure 3.084 Estimate of annual cycle of surface energy balance components from ERA-Interim, single grid cell example, mean monthly values of daily accumulated energy fluxes (kWh/day), 1979 to 2007.

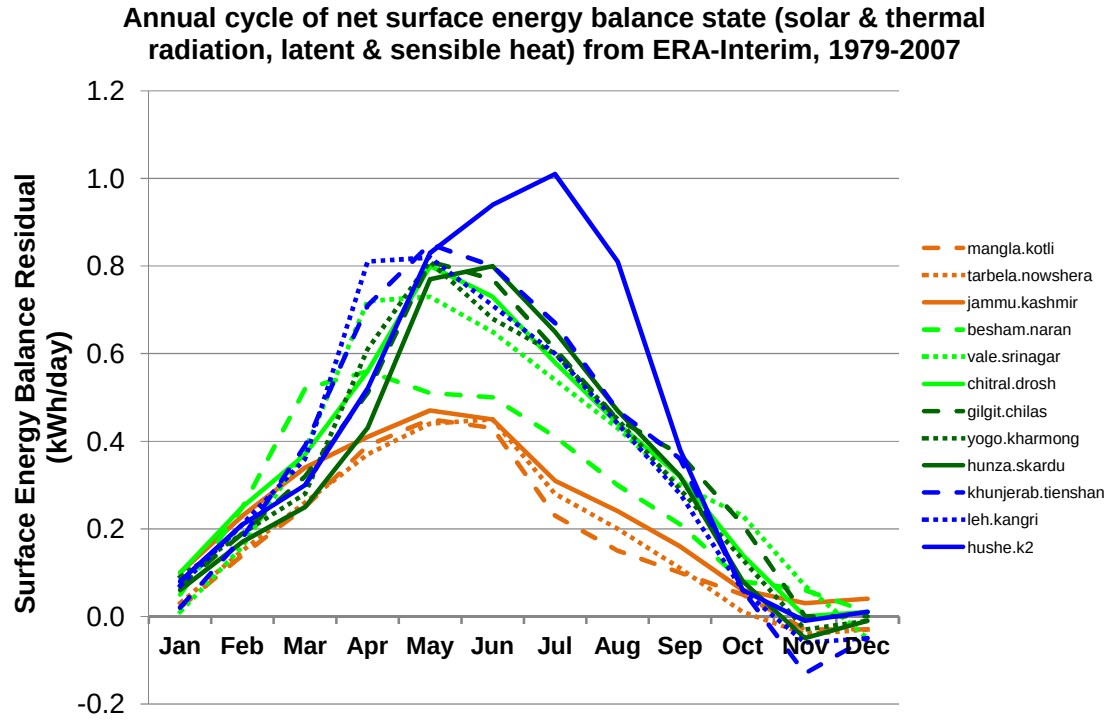

Figure 3.085 Estimate of annual cycle of surface energy balance state from ERA-Interim, twelve analysed grid cells, 1979 to 2007.

Interestingly, in ERA-Interim the net surface energy balance is (roughly) zero in the winter rather than negative as found in ERA-40. There appears to be both a year round positive shift in energy balance residual as well as an accentuation of the magnitude of the annual cycle in ERA-Interim compared to ERA-40. Given that this comparison is of period means and that the periods in question overlap by 22 years

(1979 to 2001) which constitutes more than half of each record, it seems more probable that the differences in energy balance characterisation are due to changes in assimilation and forecasting model formulation.

The surface energy balance component contributions and net residuals shown in this section represent wide spatial averages of the areas covered by the large-scale ERA-40 and ERA-Interim grid cells. Alternatively they can be seen as point simulations for a "synthetic station" having the properties of the grid cell mean. Within individual tributary catchments, or at any other practical water resources management scale, there will of course be tremendous variation. This variation will largely be driven by the vertical gradients in mass as well as energy inputs to the hydroclimate system.

From a hydrological modelling viewpoint, estimates of net shortwave (solar) and net longwave (thermal) radiation are useful in many methods of calculating potential evapotranspiration. Furthermore, if accurate, latent heat flux should reflect, via physical constants, the volume water per unit area experiencing phase changes. These phases would include both melting (solid to liquid) and evaporation (liquid to gas) and thus are particularly relevant for a basin with the diversity of hydrological regimes found in the UIB.

Quantified sensible heat fluxes are primarily of interest when the selected land surface process or hydrological modelling methodology includes full solutions to the surface energy balance. In less sophisticated approaches, the direction of sensible heat flux should reflect the sign of the temperature differential between the land surface and near surface air. The rate of the sensible heat flux might further indicate the magnitude of this temperature differential.

3.9 A Vertical hydro-climatology of the UIB

As explained throughout this Chapter, the consistent gradients of the primary climatic variables in the vertical dimension are one of the key climatic features of this region where the range of elevation change exceeds 7000m.

3.9.1 Orographic precipitation gradients

The orographic precipitation gradient, and its impact on the mass balance of the UIB cryosphere, is perhaps the most critical present area of hydroclimate science uncertainty. This criticality is multi-fold. The orographic precipitation gradient is an

importance source of divergence of expert opinion. The uncertainty associated with this divergence is also of critical importance for water resources management planning because of its dominant role in estimates of current hydrological and cryosphere mass balance in the UIB. This uncertainty stems directly from the paucity of available long-record observations across the range of critical elevations.

To be clear, the local long-record precipitation observations that do exist have been proven to be important indicators of basin-wide mass inputs, but, as is shown elsewhere in this Chapter, they do not provide absolute measurements of catchment averages. This limitation is due to the location of the long-record (PMD) stations in the relatively low elevation arid valley bottoms where the principal towns are situated. Furthermore while the WAPDA-operated AWS network installed in the mid-1990s presents considerable potential for improving observation of the orographic precipitation gradient, measurements remain sparse in the critical zone between 4500 and 5500 m asl which is crucial both because of the large proportion of catchment area within this elevation range and because previous authors (e.g. Winiger *et al.* 2005, Hewitt 2011) have identified it as receiving large amounts of orographically-driven precipitation.

All caveats accepted, the available local observations can be used to provide indications of the orographic gradient and its variability (Figure 3.086). One tentative inference that can be drawn from Figure 3.086 is that the orographic precipitation gradient itself may be a function of the relative amount precipitation, i.e. in wet years the precipitation gradient may increase, while in dry years it may decrease. For the three example years shown in Figure 3.086, the data points suggest that, for the elevation range from 1500m asl to 4500m asl, in a “dry year” the precipitation gradient may be as little 60mm (annual accumulation) per 1000m. In a “wet year”, however, the precipitation gradient could be as high as 500mm (annual accumulation) per 1000m. This order of magnitude difference in potential estimates clearly illustrates the underlying uncertainty.

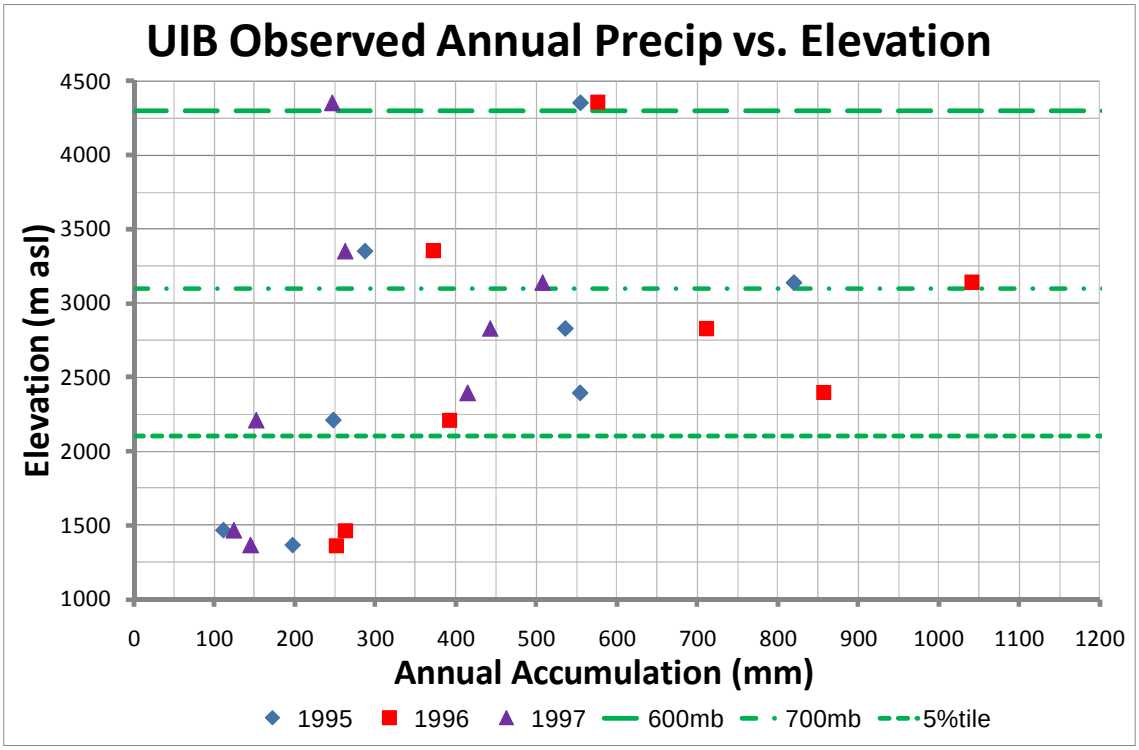

Figure 3.086 Indications of UIB orographic precipitation gradient and variability from local observations (PMD, AWS) from 1995 to 1997. Horizontal lines indicate the elevation of reference atmospheric pressure levels (600mb, 700mb) or UIB hypsometry (5th percentile of UIB surface area with respect to elevation).

The coarse spatial scale (roughly 25km) and technical/method-related biases – discussed earlier in this chapter (section 3.5.4) – inherent in the available remote sensing precipitation estimates from TRMM present even greater obstacles to determining the orographic precipitation gradient in the UIB. For comparison purposes, the derived TRMM relationship between pixel (footprint) mean elevation and mean precipitation – and its variability, c10 & c90 – over its observational record (1998-2010) is presented for annual total precipitation in Figure 3.087. As can be seen in Figure 3.087, TRMM effectively detects no orographic precipitation gradient, rather showing a range of vertical "noise" centred around a uniform mean annual total precipitation of 500mm. Furthermore neither the first (c10) nor last (c90) deciles of annual precipitaton indicate an orographic gradient. TRMM precipitation esimates in individual months, not shown here for brevity, also detects no orographic gradient. This is interpreted as further evidence of TRMM failure to detect orographic enhancement of (stratiform) precipitation in the UIB.

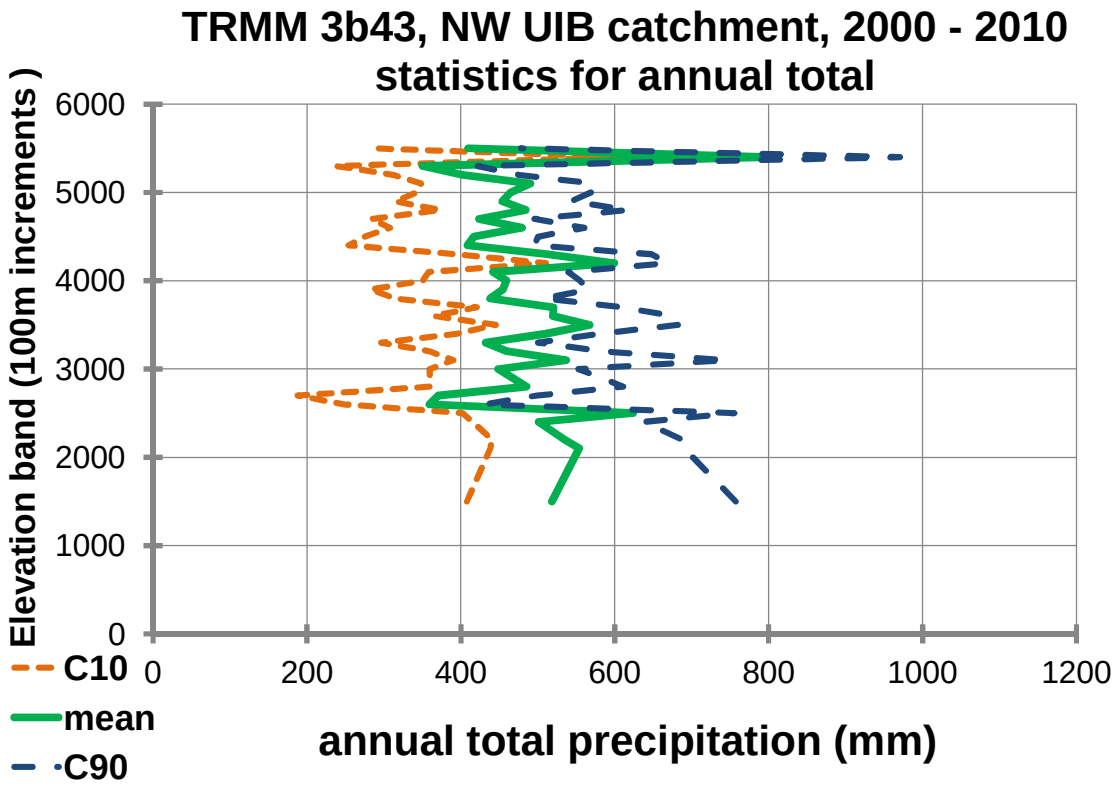

Figure 3.087 Assessment of indications of vertical precipitation gradient from TRMM 3b43, annual total period statistics, 2000 to 2010.

It could be hoped that numerical weather simulation, either meteorological reanalysis or nested RCM downscaling, would provide physically-based means to assess probable orographic precipitation gradient in the absence of access to data from an adequate network of local observations. At present, however, the spatial resolution of the available reanalyses is not refined enough to assess both elevation-driven effects and sub-regional climate regimes. In a multi-resolution nested modelling study of the Colorado Rockies Rasmussen *et al.* (2011) found that validation of modelling outputs using a dense network of ground-based observations, the horizontal resolution necessary for accurate simulation of orographic precipitation was between 18km and 6km. In contrast, the spatial resolution of the ERA-Interim reanalysis is approximately 80km and the PRECIS_ERA40 simulation outputs available to the present study are at 50km resolution. Forthcoming access to 25km resolution PRECIS RCM outputs will likely provide further incremental improvement, but still may not allow a thorough characterisation of the vertical dimension of UIB precipitation climatology.

3.9.2 Vertical snow covered area (SCA) profiles

UIB SCA exhibits a large amount of annual variation over most of the vertical range. Monthly vertical SCA profiles taken from the MODIS Terra product – spatial

means for the NW UIB – are plotted for the ablation season in Figure 3.098. Only above roughly 5000m asl does permanent snowpack (or glacial ice) begin to dominate (i.e. >50% in August). The limited snow cover in the lower portion of the catchment (below 2500m asl), and the higher temperatures there, mean that any available snowpack is quickly melted at the beginning of spring. Above 5500m, summer daily minimum temperature restricts melt by nightly refreezing. Above this elevation, however, accumulated snow is transferred downslope by avalanching and glacial movement (sliding & deformation).

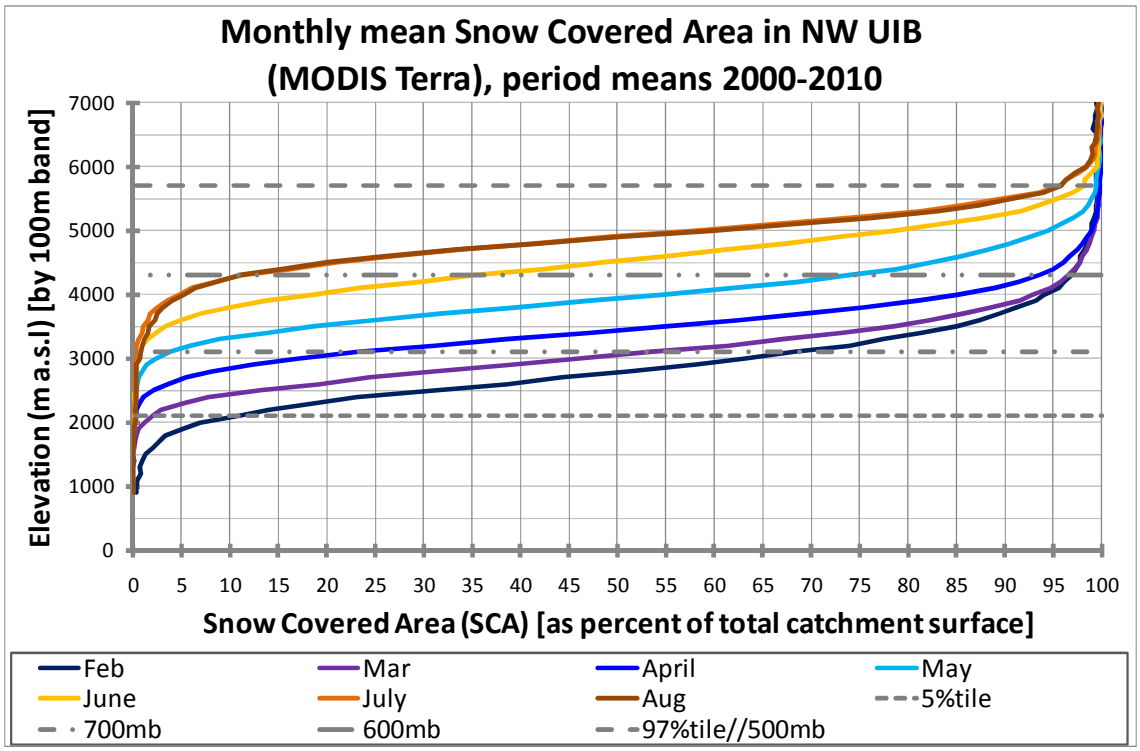

Figure 3.088 Mean monthly vertical profile of MODIS snow covered area (SCA) for the NW UIB ablation season, 2000 to 2010. Horizontal lines indicate the elevation of reference atmospheric pressure levels (500mb, 600mb, 700mb) or UIB hypsometry (5th and 97th percentiles of UIB surface area with respect to elevation).

Interannual hydrological variability in the UIB is primarily driven by the extent and thickness of the available snow pack in the elevation zone between 2500 and 5500m asl – i.e. the mass input – and by how quickly the zero degree isotherm (freezing line) moves upward through the spring and early summer, i.e. the energy input. Figure 3.089 (using the Gilgit catchment as an example of wider UIB patterns) shows the vertical distribution of interannual variability in SCA for February – near annual maximum – and August – near annual minimum, illustrating the vertical concentration of the variability in mass input. The elevation of peak SCA variability in February (late winter) is approximately 2700m asl. At this time, above roughly 3500m winter SCA is reliably complete (>90% in all years observed). Below 2000m, snow is rarely if ever

present. With regards to summer minimum SCA, the elevation of maximum variability is approximately 5000m asl. Above roughly 5500m, even in "high summer", SCA rarely diminishes substantially, and below roughly 4500m ablation is consistently complete (with the exception of glacier tongues).

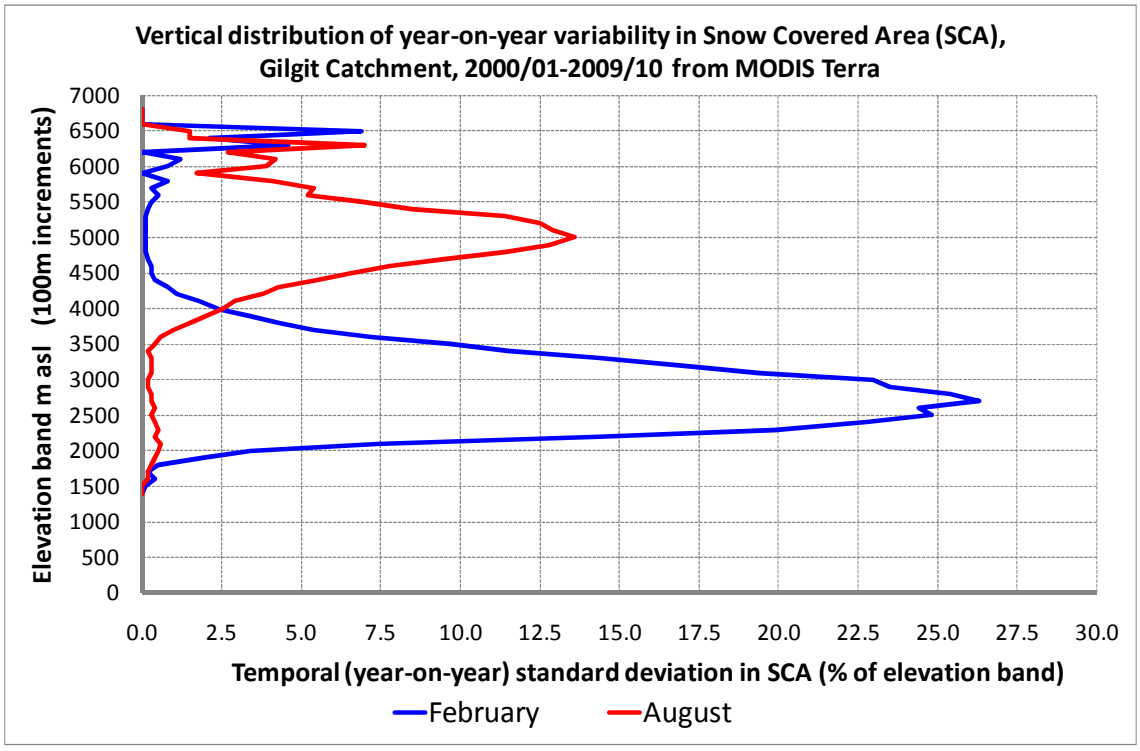

Figure 3.089 Vertical profile of interannual variability in MODIS snow covered area (SCA) for the Gilgit catchment in months of annual maximum (February) and minimum (August) SCA, 2000 to 2010.

The key elevation range for assessment of the available snowpack water equivalent (SWE) for the Gilgit catchment is thus 2000m to 5500m. SCA at the margins of this range for key months – respectively February and August – can provide an indicator of maximum annual SWE accumulation and minimum annual SWE residual. Because the vertical concentrations of interannual variability are regionally driven primarily by the annual temperature cycle and secondarily by precipitation, the results for other UIB tributary catchments are broadly similar to those shown in Figure 3.089.

3.9.3 Lapse rates and isotherms for air and surface temperature

While a tremendous amount of uncertainty surrounds the estimation of the orographic precipitation gradient, establishing the relationship between elevation and near surface air temperature is much simpler (at least for the elevation range with available observations). Figure 3.100 shows the effectively linear decrease in 2m air temperature with elevation shown by local observing stations (PMD and AWS); shown by strong regression relationships. While both minimum temperature (Tmin) and

maximum temperature (Tmax) exhibit effectively linear behaviour with respect to elevation, it should be pointed out that Tmax decreases more quickly than Tmin (~7.5°C per 1000m versus ~6.2°C per 1000m).

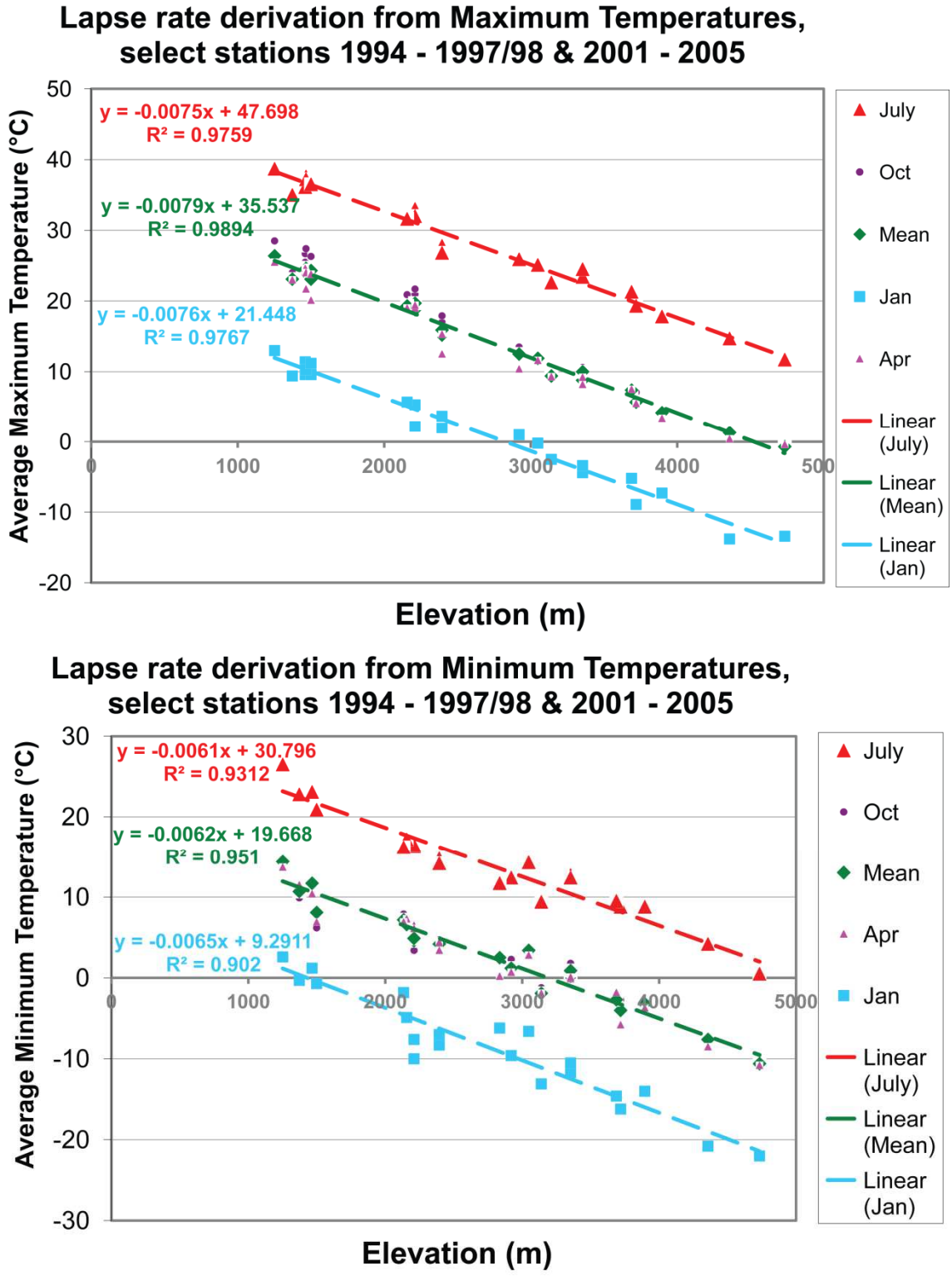

Figure 3.090 Lapse rates derived using local observations from PMD & the AWS network.

Vertical profiles for land surface temperature (LST) from MODIS (mod11a2) are slightly more complex (Figures 3.091 and 3.092), but can still be approximated as

linear, at least within subsections of the vertical range. As such apparent lapse rates for LST_{day} would be ~ 8°C per 1000m and for LST_{night} would be ~ 6.5°C per 1000m.

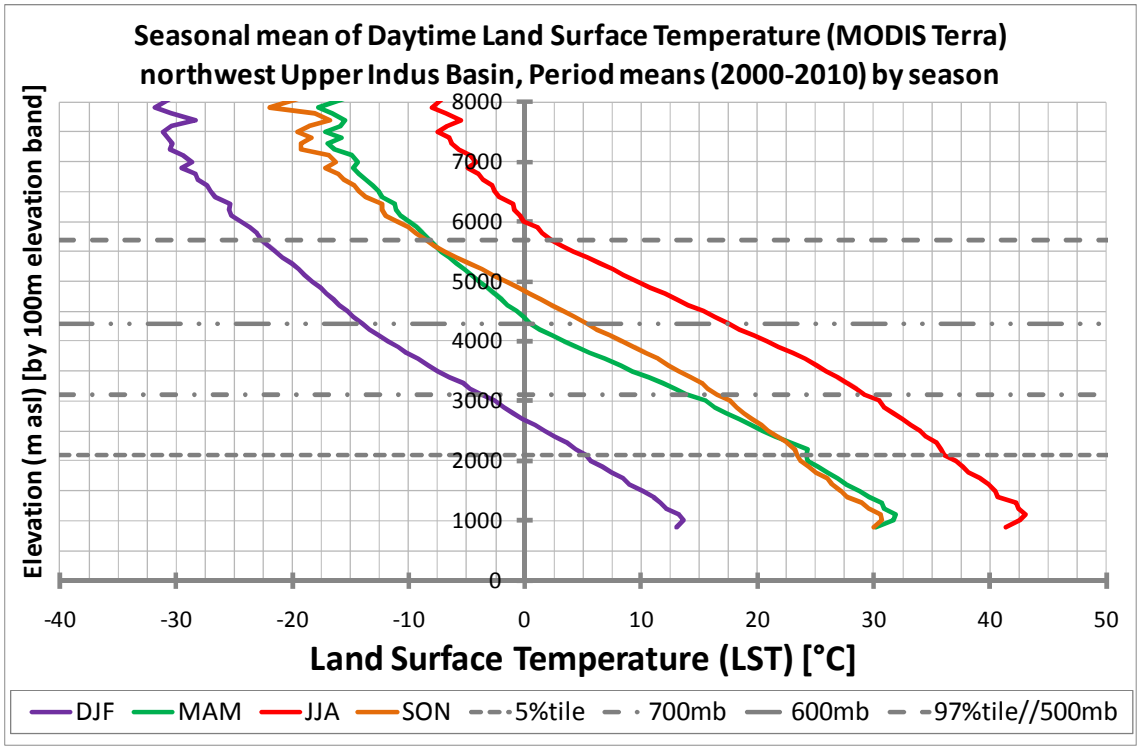

Figure 3.091 Mean seasonal vertical profile of MODIS day-time land surface temperature (LST) for the NW UIB, 2000 to 2010. Horizontal lines indicate the elevation of reference atmospheric pressure levels (500mb, 600mb, 700mb) or UIB hypsometry (5th and 97th percentiles of UIB surface area with respect to elevation).

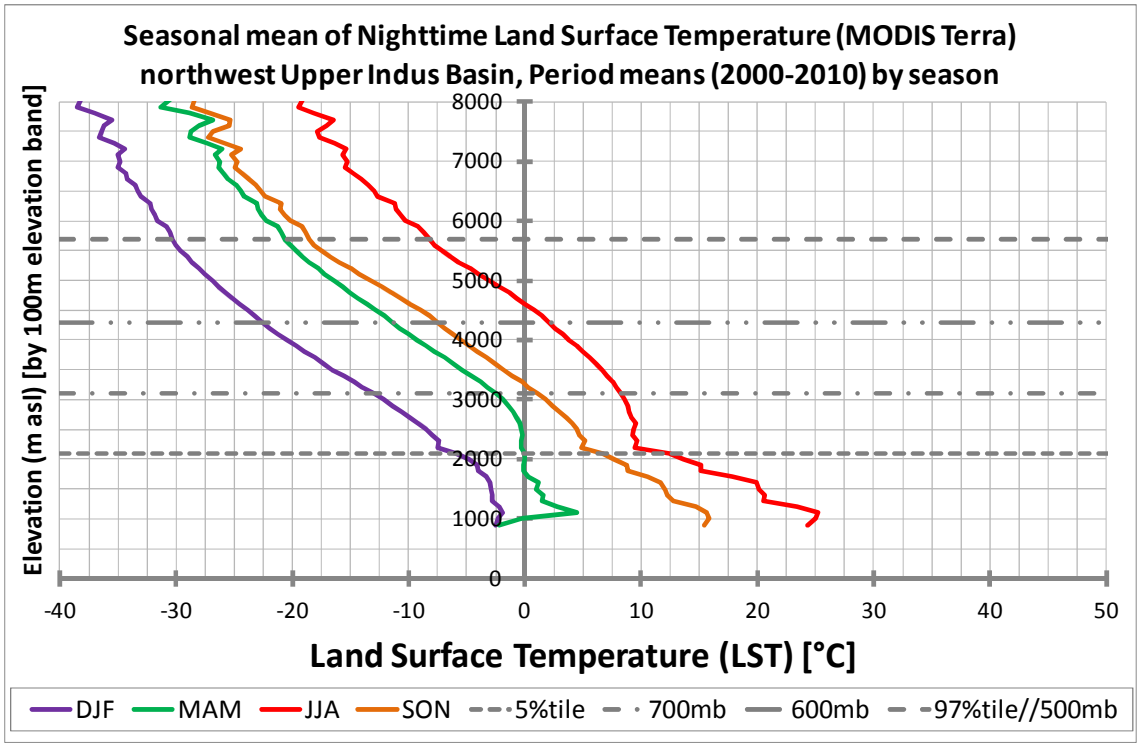

Figure 3.092 Mean seasonal vertical profile of MODIS night-time land surface temperature (LST) for the NW UIB, 2000 to 2010. Horizontal lines indicate the elevation of reference atmospheric pressure levels (500mb, 600mb, 700mb) or UIB hypsometry (5th and 97th percentiles of UIB surface area with respect to elevation).

The most striking feature of the LST vertical profiles are certainly the apparent inversions and discontinuities below 2500m for mean night-time temperatures (Tnight). The effects of the asymmetry between Tnight and Tday in the magnitude of this unexpected behaviour can clearly be seen in the diurnal temperature range (Figure 3.093). In Figure 3.093, autumn and winter land surface DTR profiles appear reasonable, but below 3000m and 4000m respectively spring and summer have strong gradients belying the expectation of a muted DTR lapse rate of ~ 1.5°C per 1000m inferred based on the differential between the broad linear approximations of LSTday (~ 8°C per 1000m) and LSTnight (~ 6.5°C per 1000m) lapse rates.

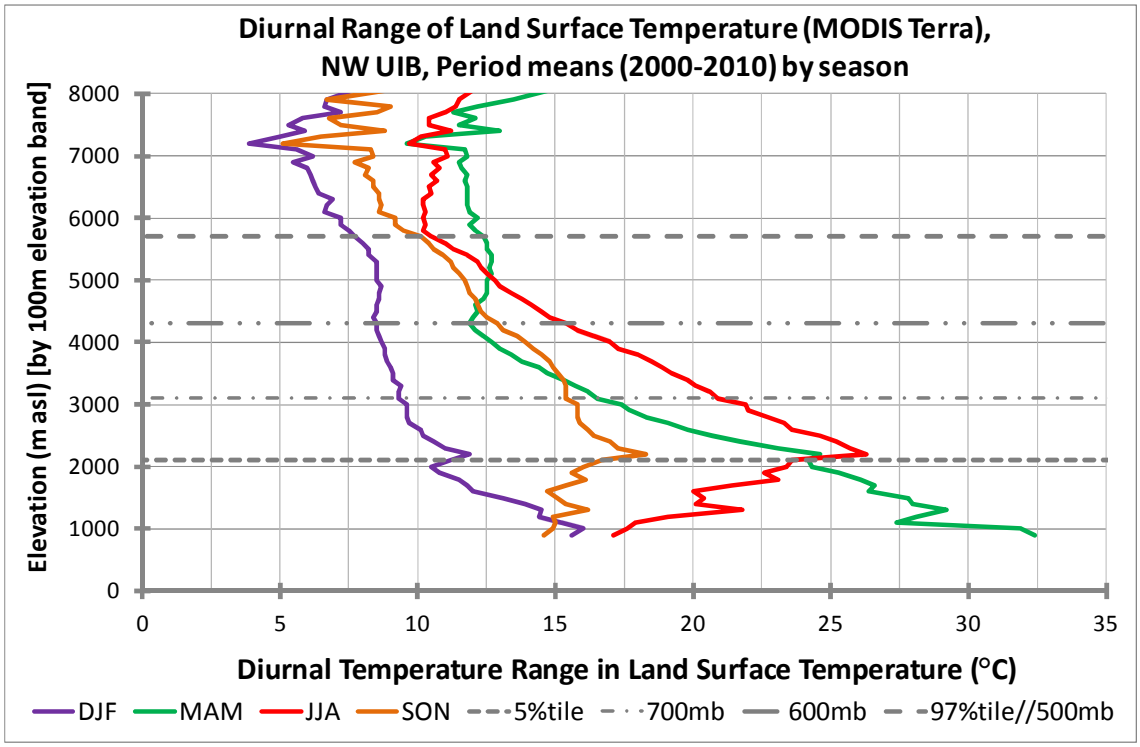

Figure 3.093 Mean seasonal vertical profile of MODIS LST DTR for the NW UIB, 2000 to 2010. Horizontal lines indicate the elevation of reference atmospheric pressure levels (500mb, 600mb, 700mb) or UIB hypsometry (5th and 97th percentiles of UIB surface area with respect to elevation).

Furthermore, the summer and autumn DTR vertical gradients reverse at 2000m asl The causes of this apparent phenomenon are not well understood. One hypothesis is that this is linked to both the dependence of the LST algorithm on "clear sky" conditions (limiting the number/frequency of observations and skewing the results) and on the seasonal behaviour of night-time cloud in the valleys (below 2500m asl).

As can be seen in Figure 3.094, despite the unexpected night-time LST behaviour at lower elevations, there is good correspondence between monthly zero-degree (freezing) isotherms estimated from local observations and MODIS LST. In general the vertical range of greatest interest in any given month will be the zone

between the zero degree isotherms (Tmin/Tnight and Tmax/Tday). This is the zone which is expected to contribute most of the meltwater to catchment runoff. In most months this zone covers a vertical difference of 2000 to 2500m. Potentially of greatest interest are the maximum elevations reached by each isotherm in the summer months. These isotherm values will determine the active range for ablation in the glacierised sections of the catchment.

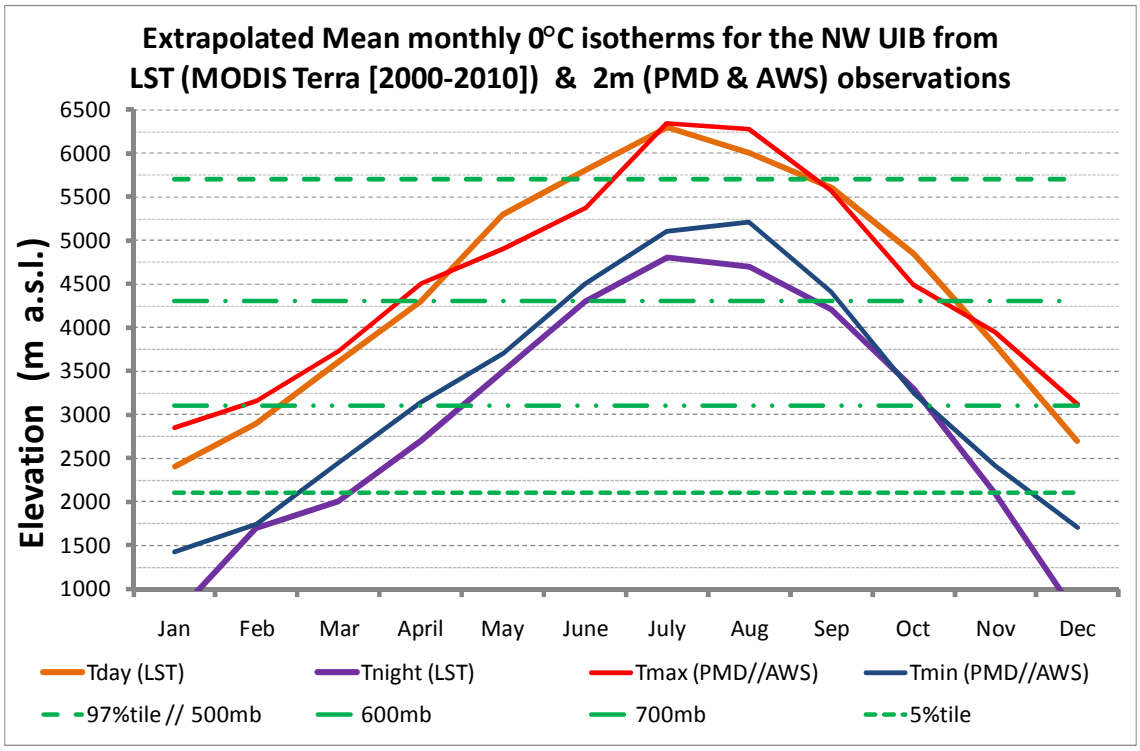

Figure 3.094 Mean monthly estimations for 0°C isotherm elevations from local observations (PMD, AWS) and MODIS LST (2000 to 2010) for the NW UIB for both day-time/maximum and night-time/minimum temperatures. Horizontal lines indicate the elevation of reference atmospheric pressure levels (500mb, 600mb, 700mb) or UIB hypsometry (5th and 97th percentiles of UIB surface area with respect to elevation).

3.9.4 Profiles of surface-cloud parameter relationships

As a reminder, as previously defined in section 3.7.3, CCF is the cloud cover equivalent of snow covered area (SCA), i.e. the fraction (or percent) of a given unit are which is covered by clouds. Although, as shown in Figure 3.075, the spatially aggregated catchment cloud cover fraction (CCF) for both day and night has a moderate range (c10 to c90) of interannual variability, the spatial variability within the catchment even for period means, as shown in Figure 3.079, is considerably greater. As part of the effort to identify the physical mechanisms which drive this spatial variability, the mean CCF for each month of the available MODIS record (2000 to 2010) was analysed as a function of the elevation band of the underlying ground surface as shown Figure 3.105

which presents means for each calendar month and the customary indicators, c10 and c90, or interannual variability.

When examing the results of this analysis, a consistent vertical pattern of CCF distribution as a function of the underlying surface elevation is observed. For CCFday (columns 1 and 3 in Figure 3.095) the vertical pattern nearly monotonically increases with elevation throughout the year, i.e. in every month.

For CCFnight (columns 2 and 4 in Figure 3.095) the vertical patterns are more complex, in every month, with relative maxima at or near the highest and lowest points in the catchment. Which of these relative maxima (valley or summit) is the absolute for a given month is variable. The vertical position of the CCFnight minima is also variable – lower in cold months and moving upward to its highest position in summer.

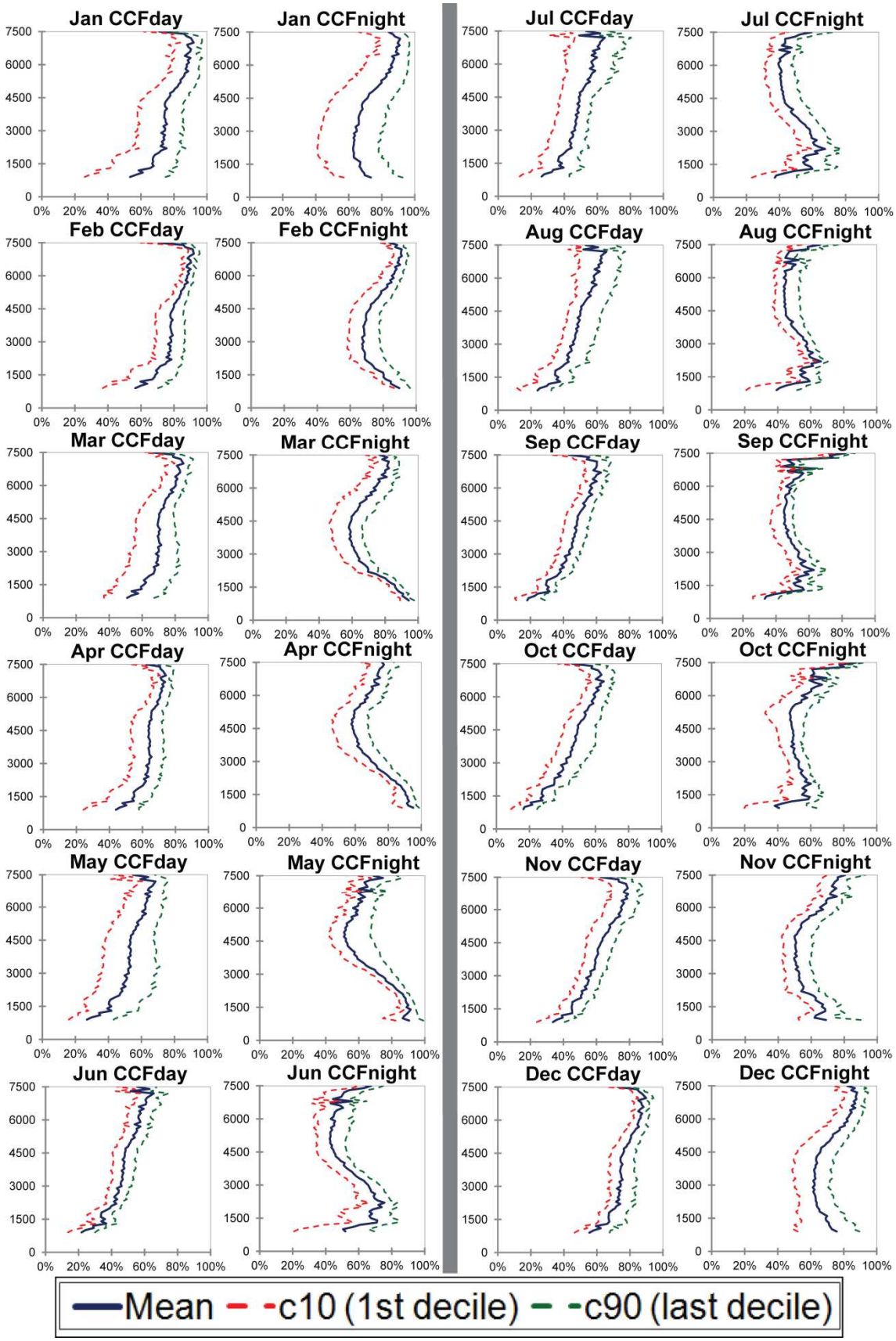

Figure 3.095 Vertical profiles of cloud-cover fraction (CCFday and CCFnight), MODIS, 2000 to 2009. Horizontal axes are as percentage of given elevation band. Vertical axes are (underlying) surface elevation (m asl).

One of the available sub-datasets within the general MODIS cloud data product (MOD06L2) gives an estimate of the atmospheric pressure at the cloud top (upper extremity) of the identified pixels with cloud cover. This variable, derived in part from assumed relationships between thermal detection of cloud top temperature and assumed atmospheric profiles of temperature versus pressure, is referred to as cloud-top pressure (CTP). This is an important parameter because it provides an estimate of one boundary of the vertical cloud structure. In other words, "low clouds" could be differentiated from "high clouds". It does not alone, however, provide an estimate of cloud thickness. Other methods, usually incorporating cloud water path (CWP) and cloud effective radius (CER), can be used in conjunction with CTP to estimate cloud thickness and cloud base altitude/height.

Vertical CTP profiles – converted to atmospheric altitude (m asl) – estimates (versus underlying ground surface) are considerably easier to conceptualise than when expressed in units of pressure (Figure 3.096). As a simplification, CTPday is roughly constant regardless of the elevation of the underlying ground surface while CTPnight tends to roughly parallel the elevation of the underlying ground surface, i.e. increasing as the elevation increases. If cloud cover formation for the UIB is primarily local, rather than arriving externally via synoptic/mesoscale weather systems, it could be expected that the underlying surface would influence cloud processes through diurnal heating and moisture fluxes, e.g. during the day-time rising air warmed by radiative energy exchange with the surface and laden with moisture from evapotranspiration would ascend until relative humidity reached a critical level for cloud formation, then at night these air masses might descend during the nocturnal cooling portion of the diurnal cycle. To be clear, detailed meteorological study of UIB cloud processes is beyond the scope of this thesis.

A more precise description is that the vertical profile of CTPday (as height) is strongly linear in all months with a decrease in gradient/slope from winter to summer. In the warm months, CTPday becomes nearly constant (independent of underlying ground surface). In some months MOD06L2 estimates – after pressure to height conversion – place the cloud below the ground surface at the upper limits of the catchment (above 6000m). This "cloud top below ground" could be due to a mixture of two factors: i) the simplistic method of conversion of pressure to height underestimates the atmospheric pressure at ground level in upper slopes of the catchment; and ii) the 5km pixels for MOD06L2 CTP are highly topographically diverse in the UIB and it may be that in summer day-time fractional cloud cover is concentrated over the lower

sections of each pixel yielding a mean cloud top elevation (where cloud is present) lower than the mean elevation of the underlying ground surface. The former explanation is expected to dominate, but the latter remains plausible as well.

The vertical profile of CTPnight shows a tendency towards non-linearity in the summer months in the lower half of the elevation range, especially above lower elevation ground surface (less than 2000m, e.g. valleys). In these cases there is actually a slight increase in estimated CTPnight (height) over the deepest valleys. At the opposite limit of the elevation range, CTPnight estimates indicate an approximate intersection with the ground surface at the upper boundaries (peaks, ridge lines) of the catchment.

CTP, although not directly linked to cloud radiative effect (CRE), does, by the clear distinction between the forms of the day and night vertical profiles, indicate a potentially fundamental difference in the characteristics/structure of the clouds. These differences may point in turn to substantial differences in CRE between daytime and night-time cloud. The evolution of these cloud structures and the associated CRE could potentially indicate how an imbalance between incoming shortwave (solar) radiation and outgoing long-wave (thermal) radiation might be driving seasonally and diurnally assymetrical patterns of temperature change observed in the UIB over recent decades. This seasonal and diurnal asymmetry of change will be examined in detail in Chapter 4.

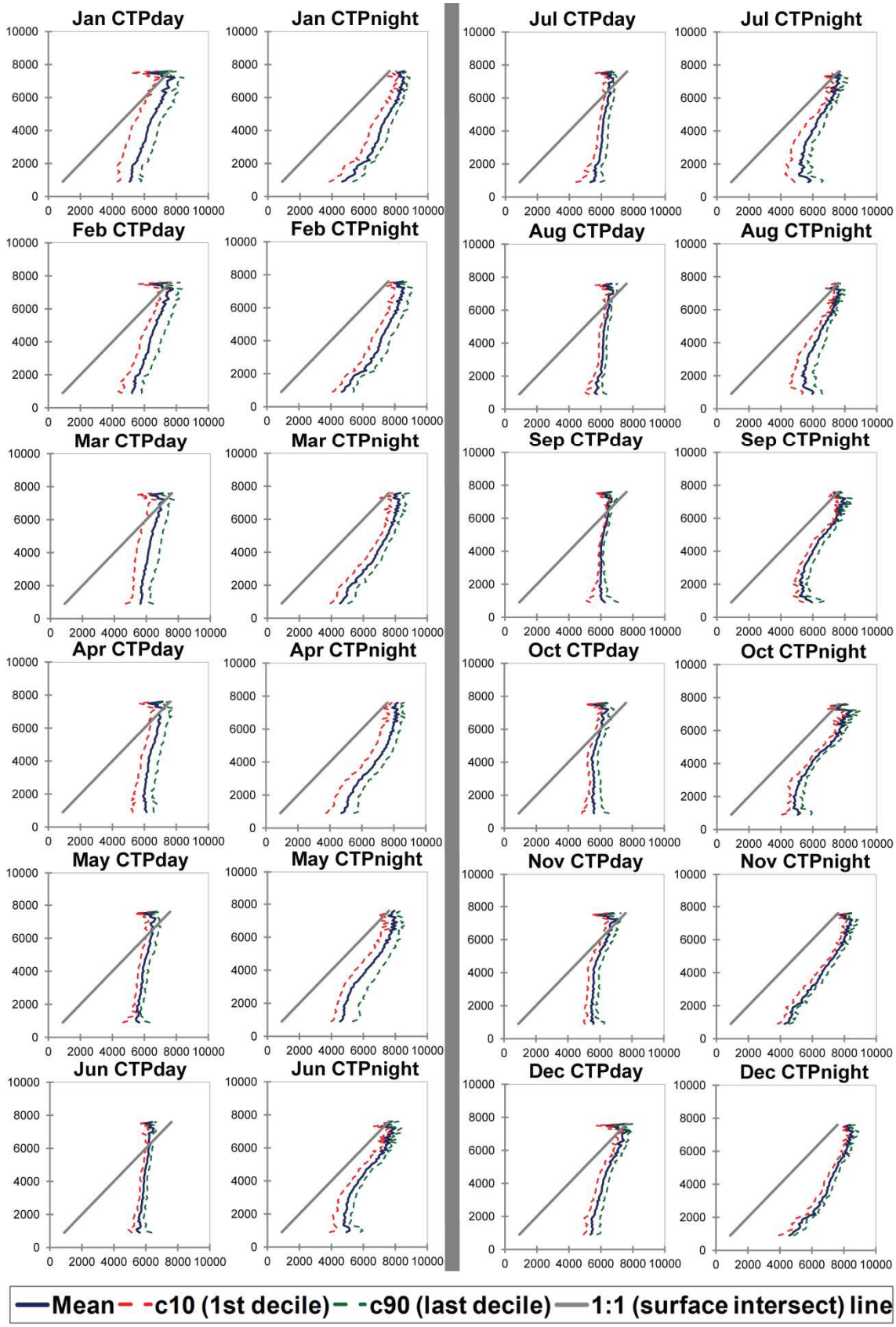

Figure 3.096 Vertical profiles of cloud top pressure (CTPday and CTPnight), MODIS, 2000 to 2009. Horizontal axes estimated cloud top altitude (m asl). Vertical axes are surface elevation (m asl).

Vertical profiles of cloud microphysical parameters (not shown) show minimal influence from elevation. Thus, the cloud properties, where they occur, will generally

reflect a (sub-)regionally standard composition. The exception to this is cloud optical thickness during cold months (Nov to Mar) when there is a positive gradient (increasing opacity) with increasing elevation. Otherwise, the primary mode of variability in cloud parameters remains the change in CCF with underlying surface elevation. Analysis of frequency of quantified observations by MODIS (day-time only due to use of visible wavelength spectral bands) of microphysical parameters corroborates the increasing cloud presence with increasing elevation shown by CCFday, albeit with observation frequency values roughly half of CCFday. In other words, because of the data constraints and quality controls instigated by NASA with regard to cloud microphysical properties, the parameters discussed in section 3.7.5 are only calculated ("observed") for half of the CCF cloud detected pixels, but the analysis of the "observational frequency" of MODIS cloud microphysical properties with respect to underlying surface elevation produces a pattern which matches that found for CCF.

In contrast to CCF, cloud micro-physical properties show much less spatial structure (perhaps linked to less pronounced day-time cloud top pressure variation with elevation), i.e. where present, clouds are relatively homogeneous.

3.9.5 Vertical profiles of ground surface albedo

As explained previously, there is a very strong correspondence between SCA and albedo in the UIB. This is equally true for vertical profiles as for catchment-wide spatial means. Figure 3.097 shows vertical (elevation) profiles of albedo for key weeks (labelled by first julian day) in the ablation season. Although individual pixels appear with albedo values approaching 0.9, in general a spatially averaged albedo of 0.65 is found for elevation bands with complete SCA. Where ablation is complete (0% SCA), albedo values converge at roughly 0.15.

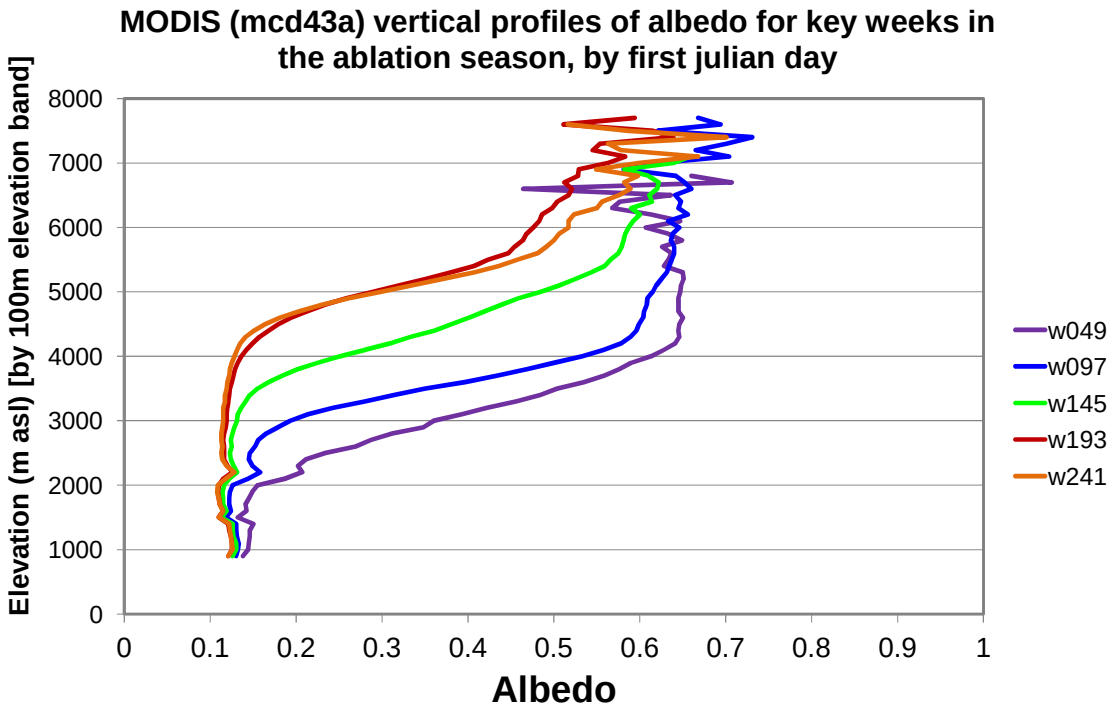

Figure 3.097 Mean vertical profiles of MODIS albedo for the NW UIB, 2000 to 2010. Profiles are shown for key weeks in the ablation season (legend notation: w, first julian day).

Because the vertical distribution of catchment area (hypsometry) of the UIB is far from uniform, a thorough understanding of the vertical profiles of key hydroclimate parameters can help to identify potential sensitivities to present variability and future change. Identifying these sensitivities, so that risks and challenges can be anticipated, is crucial to forward-looking water resources management.

3.10 Hydroclimate relationships in the UIB

A practical reason for study of the UIB's hydroclimatology is to enable improvements in water resources management. While sophisticated techniques exist for hydrological modelling of snow and glacier melt regime catchments, improved hydrological characterisation of the UIB must begin with fundamental conceptual understanding of the relationships between runoff and its key climatological drivers. This section summarises original work undertaken in this PhD but published prior to the completion of this as Forsythe *et al.* (2012a)

Previous studies (Archer, 2003, Archer and Fowler, 2008) have shown significant linear correlations between gauged river flows and observed climate variables, notably concurrent temperature or preceding season precipitation. These relationships differ between the three identified hydrological regimes. Examples of such relationships are shown in Figure 3.098 for the Astore catchment, where runoff is

primarily snow-melt from winter accumulated snowfall, and for the high level Hunza catchment, which is primarily glacier fed. The pool of candidate indicators is limited to climate observations made at local long-record meterological stations. Long (multi-decadal) record length is specified to improve chances of finding statistically significant relationships.

The indicators, as well as summer (June to August) discharge observations, have been transformed to relative anomalies, i.e. the anomaly is calculated by subtracting the record mean from the individual observation then the result is divided by the record mean. For the nival catchment, Astore, the best available locally-observed indicator of catchment output (relative discharge anomaly) is the accumulation season (October to March) precipitation at Astore (PMD station). For the glacial catchment, Hunza, the best indicator is the fraction of the catchment where the minimum night-time temperature is greater than 0°C, as derived from concurrent temperature at Gilgit (PMD), and linear temperature lapse rates based on available regional observations. Such relationships indicate the sensitivity of UIB hydrology to both climate variability and gradually developing trends.

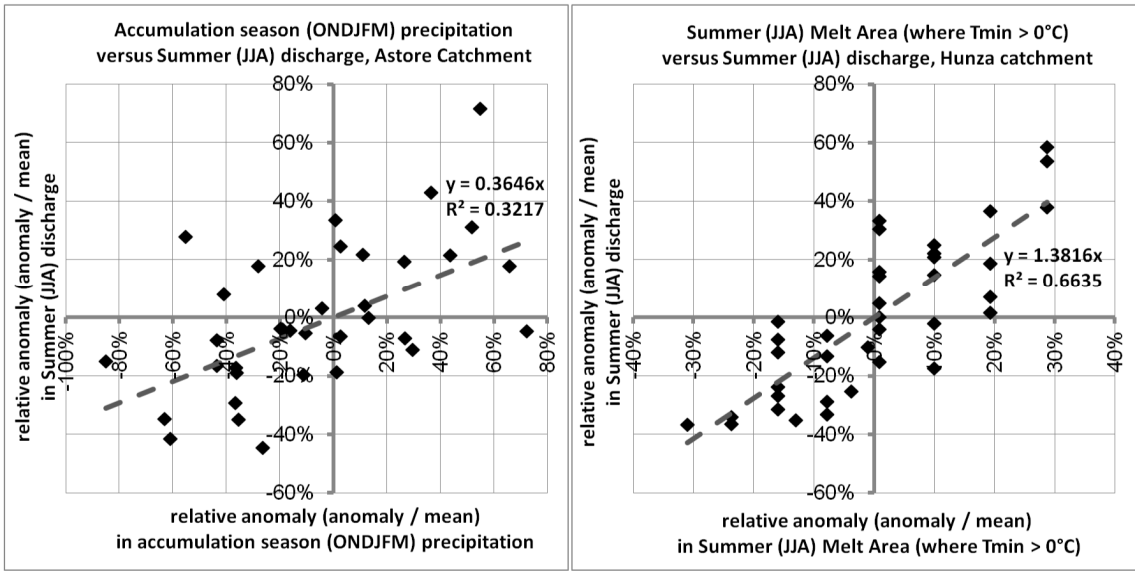

Figure 3.098 Example regression relationships between climatic indicators (predictors) of hydrological variability and observation variation in runoff.

While previously established studies conclusively demonstrate the validity of local (point-based) climate observations for prediction of runoff volumes (e.g. Archer and Fowler, 2008), use of complementary spatial data from remote sensing sources can aid in quantified characterisation of the links between climate inputs – mass and energy – and hydrological outputs (runoff). Thorough examination of the MODIS SCA and LST data products can identify analogues for the ground-based observations used to

characterise the hydrological regimes of the UIB. A spatial analogue for the "point observation & lapse rate"-derived catchment melt area parameter is a case of straight-forward substitution (direct assessment).

Selection of the best analogue for accumulated cold season (October to March) precipitation from the information contained in the SCA data product, however, is more complex. An initial indication is given by the temporal aspect: the need to characterise the state of the catchment at the transition from accumulation to ablation, i.e. in late March or early April. Thus, one option is to select as an indicator the total catchment SCA in March. This is logical in that the SCA will vary relatively consistently as a function of the seasonal snowline (elevation of the transition between snow-covered and snow-free portions of the catchment).

Given the orographically-driven nature of precipitation in mountainous areas, a vertical profile of the accumulated snowpack can be visualised as a wedge beginning at the seasonal snowline and increasing in depth upward toward the elevation of maximum precipitation. This concept is illustrated in Figure 3.099 as is the mean variation of SCA versus elevation by month for the late winter and early spring.

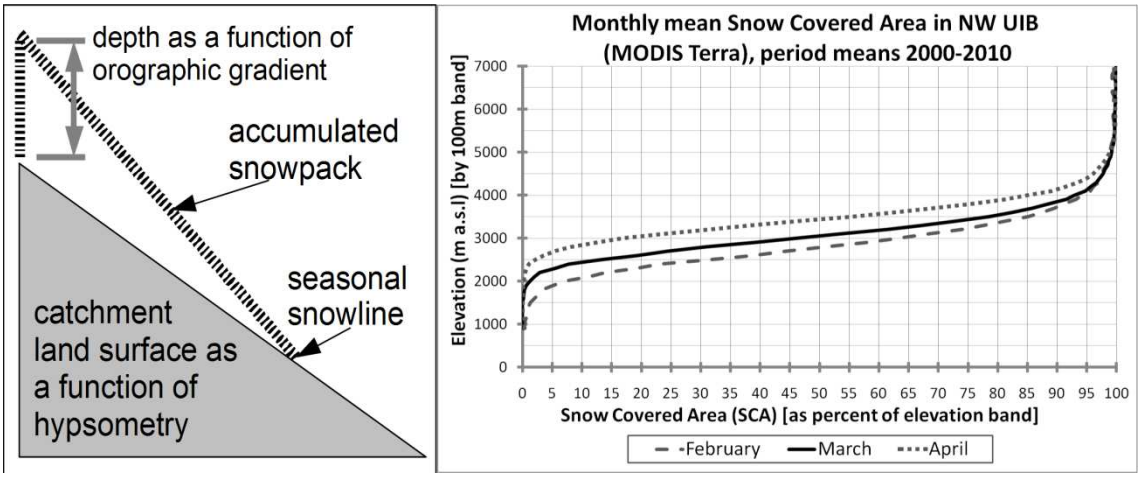

Figure 3.099 Conceptual diagram of vertical profile of snowpack depth (left); SCA versus elevation in seasonal transition from accumulation to ablation (right).

This is of interest because the both the conceptualisation of the seasonal snowpack and the vertical profiles of late winter (February) and early spring (March, April) SCA suggest that the amount of fractional snowcover at or near the seasonal snowline may provide a valuable quantitative indicator of catchment mean or total snowpack. The value of this indicator is that it would provide good "information content", i.e. exhibit substantial (relative) interannual variability. Put another way, an indicator with minimal interannual variability would provide little information on relative conditions of inputs to the hydrological system. The information content of

SCA in relatively low elevation bands can also be seen in Figure 3.089 (vertical profile of interannual variability in MODIS SCA).

Validity of MODIS SCA as a precipitation analogue was tested by assessing the correlation of normalised, standardised anomalies of March SCA to accumulated cold season (October to March) precipitation. March SCA is roughly the annual maxima of SCA in most sub-catchments. The cold season accumulated precipitation forms the available snowpack in the UIB before the melt season flood begins. At present this study has local precipitation observations dating from approximately 1960 to the end of 2007. SCA aggregated—i.e. spatial mean—at a range of spatial scales for the series of eight years from 2000 to 2007 was tested against observed precipitation and number of wet days from each of three long-record meteorological stations. The resulting correlations (Pearson's "r", 2- tailed significance) are given in Table 3.12. Although statistical significance is difficult to achieve due to the short duration of the time series, some of the larger catchments as well as the aggregation of the wetter northwestern sector (i.e., excluding Ladakh & Tibet) of the UIB, do show p-values less than 0.05. At smaller spatial scales, including one case study catchment of 10 km^2, Pearson's "r" values are regularly greater than 0.5 and often 0.6 for one or more of the tested precipitation variables. Based on these results, SCA appears to be a valid spatial analogue, across the range of tested spatial scales, for point observations of precipitation.

Station	Precip. at Gilgit	Precip. at Astore	Precip. at Skardu	Wetdays at Gilgit	Wetdays at Astore	Wetdays at Skardu
Indus to Besham	.358	.590	.086	.466	.455	.307
NW UIB	***.800***	***.760***	**.647**	***.825***	**.678**	***.776***
Hunza to Dainyor	**.683**	***.796***	**.654**	**.710**	**.687**	**.679**
Shigar to Shigar	**.696**	**.732**	**.604**	**.692**	**.686**	***.847***
Gilgit to Gilgit	.587	.452	.496	**.634**	.378	**.666**
Astore to Doyian	**.673**	**.722**	.265	***.816***	**.671**	.535

Table 3.12 (excerpt of Table 3 from Forsythe *et al.* 2012a) Correlations of March Snow Covered Area vs Cumulative Winter (Oct-Mar) Precipitation. Formatting of Table 3.12: values for Pearson's "r" are underline bold italic if the corresponding significance (***p***) is less than ***0.01***, highlighted in simple bold if **p** is than **0.05** and in grey text if p is greater than 0.10.

Another option for indicator selection is to focus on SCA within an elevation band exhibiting the maximum interannual variability for the season of interest. Figure 3.100 shows the interannual variability of SCA versus elevation for two nival regime

catchments, Astore and Gilgit. The zone of greatest variability, where the information potential of the MODIS data product can be maximised, for the end of the accumulation season lies between 2500 and 3000 m asl. For the purposes of illustration, the SCA within the 2700 m asl elevation band has been used here as an analogue for accumulation season (October to March) precipitation.

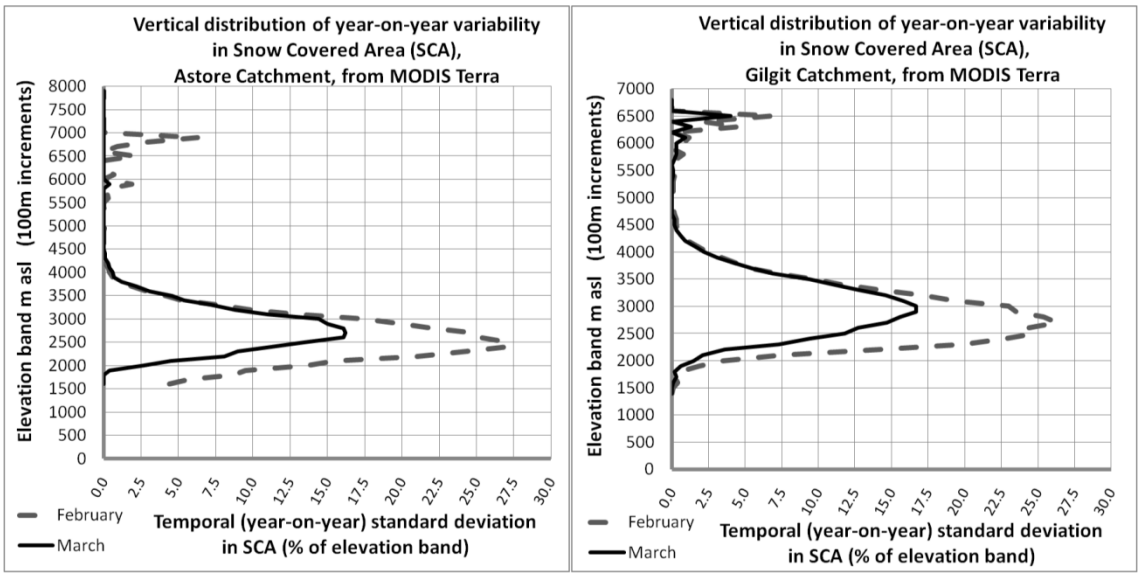

Figure 3.100 Vertical patterns of interannual variability in SCA for Astore and Gilgit in peak snow cover months (February, March).

The validity of MODIS LST as an analogue for 2-m air temperature was tested by aggregating groups of four consecutive 8-day day- and night-time LST measures to create a quasi-monthly time series for the duration of the MODIS instrument record. These monthly time-steps were spatially aggregated using a range of catchment scales. The areally averaged values were then assessed for correlation with the same three long-record meteorological stations which were used to validate the SCA data product (point observations available through December 2007 for minimum and maximum temperature). Both LST and 2-m air temperature values were converted to normalised, standardised anomalies to avoid false correlation strength based solely on the annual temperature cycle. The resulting correlations (Pearson's "r", 2-tailed significance) are given in Table 3.13. Substantial statistical significance ($p<0.01$) is widespread owing to the larger number of time-steps in the record, compared to the precipitation study. Correlations are generally strong for both day-time/Tmax and night-time/Tmin, though somewhat weaker for the latter, across a range of spatial scales, with the exception of the largest aggregations. This widespread correlation strength supports the validity of LST as a spatial analogue for 2-m air temperature.

Station	Astore Tmax vs Tday	Gilgit Tmax vs Tday	Skardu Tmax vs Tday	Astore Tmin vs Tnight	Gilgit Tmin vs Tnight	Skardu Tmin vs Tnight
Indus to Besham	***.457***	***.453***	***.358***	***.283***	.016	.184
NW UIB	***.489***	***.474***	***.309***	***.299***	-.082	**.227**
Hunza to Dainyor	***.725***	***.694***	***.657***	***.660***	***.335***	***.527***
Shigar to Shigar	***.736***	***.655***	***.679***	***.665***	***.310***	***.528***
Gilgit to Gilgit	***.671***	***.709***	***.590***	***.662***	**.219**	***.564***
Astore to Doyian	***.747***	***.710***	***.647***	***.664***	***.339***	***.532***

Table 3.13 (excerpt of Table 4 from Forsythe *et al.* 2012a) Correlations of Land Surface Temperature (LST) vs 2-m air temperature (point observations). Formatting of Table 3.13: values for Pearson's "r" are underline bold italic if the corresponding significance (***p***) is less than ***0.01***, highlighted in simple bold if **p** is than **0.05** and in grey text if p is greater than 0.10.

Of course patterns of anomalies in the two spatial data products – SCA & LST – are not independent, rather they are climatically coupled. To further test the coherence of the spatial data products, correlations of concurrent anomalies between the variables within individual sub-catchments were assessed. This assessment is a substantial simplification of actual system behaviour as it only considers concurrent anomalies and in no way incorporates specific precipitation input or cumulative effects of prolonged/persistent anomalies. Nevertheless, as shown in Table 3.14, the sub-catchments under study can be considered quite responsive systems. Given that large temperature anomalies at the monthly timescale may often be due to dominant synoptic conditions thus persisting across the diurnal cycle, the strong correlation between day and night-time LST is largely to be expected. The results of notable (negative) correlations between SCA and day or night-time LST, however, show that at the monthly time-step most sub-catchments show a concurrent response in snow cover to temperature anomalies. These findings further support the use of the available spatial data products as analogues for the climatic drivers governing runoff generation in the various sub-catchments of the UIB.

Correlation	Indus to Besham	NW UIB	Hunza to Dainyor	Shigar to Shigar	Gilgit to Gilgit	Astore to Doyian
Tday to Tnight	***.779***	***.858***	***.860***	***.856***	***.852***	***.756***
Tday to SCA	***-.443***	***-.414***	***-.561***	***-.552***	***-.603***	***-.648***
Tnight to SCA	***-.339***	***-.286***	***-.477***	***-.473***	***-.496***	***-.560***

Table 3.14 (excerpt of Table 5 from Forsythe *et al.* 2012a) Correlation between spatial variables within individual sub-catchments. Formatting of Table 3.14: values for Pearson's "r" are underline bold italic if the corresponding significance (***p***) is less than ***0.01***, highlighted in simple bold if **p** is than **0.05** and in grey text if p is greater than 0.10.

Figure 3.101 shows available indicators of runoff anomalies from local observations, TRMM and MODIS for the nival regime catchments, Astore and Gilgit. To clarify the limitations of available discharge observations and potential indicators:

- WAPDA discharge data is available (to this study) for Astore from 1974 to 2008.
- WAPDA discharge data is available (to this study) for Gilgit from 1969 to 1998, 2000 to 2001, 2004 to 2008.
- TRMM data is available from January 1998 to present (with approximately 3-month processing lag on latest months).
- MODIS data is available for the instrument on the Terra satellite platform from March 2000 to present (with a variable processing lag depending on the data product, spatial resolutions and temporal aggregation in question).

Hence the common record period for indicators and observations is from mid-2000 to 2008 for Astore, and from 2000 to 2001 and 2004 to 2008 for Gilgit.

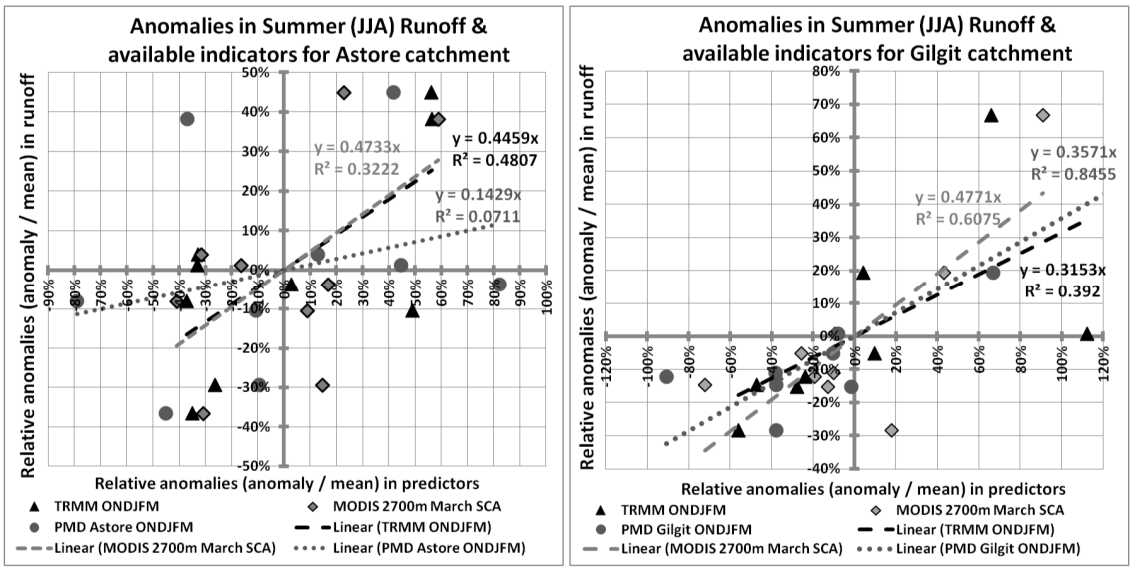

Figure 3.101 Example regression relationships between climatic indicators (predictors) of hydrological variability and observation variation in runoff. Anomalies were calculated as for Figures 3.098.

The same mathematical procedure to calculate relative anomalies used to generate Figure 3.098 was applied in Figure 3.101. While the very limited available observations – nine each for Astore and Gilgit – are inadequate to assess statistical robustness and quantitative uncertainty, the performance of the available indicators is nevertheless encouraging. TRMM performs well for both catchments (R^2 values of 0.48 for Astore and 0.39 for Gilgit as seen in Figure 3.101). TRMM's spatial scale, however, is too coarse to provide the village/valley scale specificity thus precluding its use for community-based management of small scale infrastructure. If available with adequate

lead-time it could be of use for supporting operation of medium-scale infrastructure and resource management planning at the tributary catchment level. The MODIS March SCA in the 2700m elevation band also performs moderately well for both catchments, thus supporting its use as an indicator. The performance of the local (point-based) observations is polarised between the two catchments with R^2 values of 0.07 and 0.84 respectively for Astore and Gilgit. This starkly illustrates the pitfalls of conferring excessive significance to samples based on too few observations. Comparison of the panels for Astore in Figures 3.098 and 3.103 shows how analysing a small number of years, i.e. an inordinately short record-length, for calibration or validation could yield coefficients of variation (R^2) that are substantially higher or lower than would generally be found if a larger sample were selected.

Prediction of runoff in nival regime catchments where concurrent conditions are less important than seasonally accumulated snowpack is less problematic than in glacial catchments where concurrent energy inputs – indexed by temperature – are dominant (Archer and Fowler, 2008). Even so, remote sensing-derived spatial data can contribute to characterisation of the variability and sensitivity of glacial regime catchments. Potential indicators of energy inputs were thus sought both among available local observations of near-surface air temperature as well as in spatial datasets of land surface temperature (LST) derived from satellite imagery (remote sensing).

Figure 3.102 presents potential indicators from local observations and remote sensing for runoff in the Hunza catchment. The selected indicators of energy input are both estimates of continuous melt area (CMA). CMA as derived from MODIS LST was presented in section 3.6.4. It also possible to derive CMA using a time-series of near-surface air temperature from a reference local observing station, e.g. Astore PMD, along with linear lapse rates (see section 3.9.3) and catchment hysometric data, i.e. the cumulative distribution of surface area as a function of elevation.

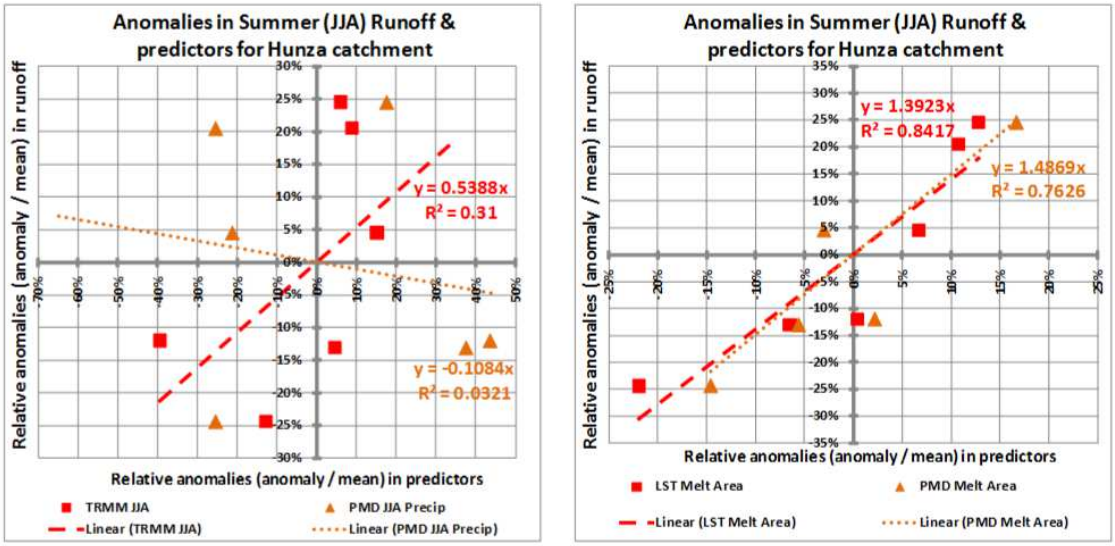

Figure 3.102 Example regression relationships between climatic indicators (predictors) of hydrological variability and observation variation in runoff. Anomalies were calculated as for Figures 3.098 and 3.101.

The CMA estimates from local observations (PMD) and remote sensing (MODIS LST) both agree well with each other and each have good quantitative performance ($R^2 > 0.75$). In contrast, the concurrent mass input indicators from local observations and remotely sensed sources have quite different behaviours. The absence of predictive capacity from local summer (concurrent) precipitation observations is not surprising given the previous work by Archer and Fowler (2008). The apparent predictive potential of the TRMM concurrent precipitation estimates, however, is more surprising. There are two leading hypotheses to explain this. First, the very small number of observations (seasonal averages from six years) does not exclude this result being purely random. Alternatively, if this is veritable predictive potential rather than a data artefact or random result, given TRMM's inherent bias toward convective precipitation, and the relationship between thermal inputs and convective activity, it may be that higher convective precipitation estimates are linked to more intense surface heating which would normally also result in increased glacial melt and runoff. Obviously an increased number of observations (record years) should help to resolve these questions.

Thus for both nival and glacial regime catchments quantitative indicators of climate inputs to the hydrological system from local observations and remote sensing are complementary in characterising runoff response. Improved spatio-temporal characterisation of the hydro-climatology of the UIB will facilitate improved water resources and reduced scientific uncertainty.

3.11 Summary & Discussion

The UIB is a complicated hydro-climate system with complex vertical gradients and spatial variability. Annual cycles and interannual variability add further dimensions to this already challenging scientific subject.

3.11.1 Summary of key data sources and relevant characteristics

Despite its vast, rugged and sparsely instrumented nature, the advent of remote sensing and meteorological reanalysis makes available large amounts of pertinent data for study of the UIB. Each of these data types has its own strengths and limitations, but as a portfolio of available information the complementary elements support the meticulous composition of a complete, coherent description of the UIB hydro-climate system. The key issue for the applicability of any data source to the UIB lies in its spatial representativity and the degree to which it represents an absolute measure of catchment state or simply a quantitative indicator of catchment conditions which must be scaled by coefficient, perhaps as a function of surface elevation. The following list provides a brief summary of the data sources considered in this chapter and their relevant defining characteristics.

1) *Data source (agency and/or observation type)*: **WAPDA river gauging**;

Variables available: Discharge ;

Relevant characteristics (commentary): In practice WAPDA discharge measurements should provide absolute values although stream gauging in a geographical (logistical, hydrological) context such as that of the UIB is highly challenging. Furthermore, if accurate estimates of contributing catchment surface area are available it should be possible to convert the absolute discharge measurements (volume per unit time) to runoff (equivalent depth per unit surface area).

2) *Data source (agency and/or observation type)*: **PMD**;

Variables available: Moderate selection of ground-based weather observations;

Relevant characteristics (commentary): The long-record (multi-decadal) climate stations operated by PMD have been shown both in this thesis and by other authors to meaningfully capture quantitative interannual variability in inputs to the hydrological system, but because these stations are located at relatively low elevations (in permanent settlements in valley floors) far below the spatial mean

surface elevation of the individual tributary catchments the values recorded are representative in absolute terms. For example near-surface air temperature must be projected using lapse rates while for precipitation some estimated or assumed orographic gradient must be applied to extrapolate catchment-wide representative values.

3) *Data source (agency and/or observation type)*: **WAPDA AWS** ;

Variables available: Limited selection of ground-based weather observations;

Relevant characteristics (commentary): In principal the AWS units which have been operating for over 15 years at moderate elevations (close to catchment mean/mode) throughout the (Pakistan controlled) UIB should provide crucial data in their own right as well as the key calibration data to be able to scale PMD low-elevation observations to spatially representive representative values. Unfortunately access to this data is tightly restricted by the operating agency and the present study has had only limitied access to the initial handful of years data (in the mid-1990s).

4) *Data source (agency and/or observation type)*: **ECMWF meteorological reanalysis (ERA-40 and ERA-Interim)**;

Variables available: Complete set of climatological descriptors;

Relevant characteristics (commentary): The estimated values produced by the reanalysis projects from analyses of assimilated data or short-run simulations (hind casts) of key climate variables yields coherent self-consistent global climatologies. Unfortunately for studies focusing on distinct geographic areas the presently available reanalyses were produced and archived on relatively relatively coarse spatial grids (2.5 decimal degrees for ERA-40 and 0.75 decimal degrees for ERA-Interim). As a result the values produced are representative in absolute terms only of the assigned modelled surface elevation in the global reanalysis model and will necessarily lack the influence of small-scale spatial variability. Still the fact that the reanalyses are driven by large scale atmospheric circulation they tend to capture the key aspects of interannual variability. Thus they are similar to the local (PMD) observations in that the they provide valuable information on the timing and amplitude of annual cycles as well as interannual fluctuations, but they may potentially require scaling to be directly applicable to UIB hydro-climatology

5) *Data source (agency and/or observation type)*: **Meteorological reanalysis down-scaled using an RCM (PRECIS_ERA40)**;

Variables available: A limited selection of core climatological descriptors (an exported subset of climatological descriptors from the full down-scaled reanalysis);

Relevant characteristics (commentary): Functionally PRECIS_ERA40 is very similar to the global meteorological reanalyses but offers marginally better spatial resolution.

6) *Data source (agency and/or observation type)*: **Remote sensing from the MODIS instrument**;

Variables available: A substantial range of spatial climate variables (descriptors of land surface or atmospheric states);

Relevant characteristics (commentary): In principle, MODIS should provide estimated absolute values of key land surface and atmospheric state variables. Among the most crucial for the UIB are snow covered area (SCA) and land surface temperature (LST), which as described in section 3.10 can be used to derive indicators of mass and energy inputs to the UIB hydrological system. While these estimates should yield accurate absolute values, the methodologies and underlying radiometric observations are not without biases, thus as with any dataset care must be taken to account for these biases when utilising the data. One bias specific to the metholodology for deriving SCA, LST (and similar ground surface state variables) is that they require “clear sky” conditions for a conclusive determination of the variable value. In other words, if cloud is present in a given pixel, the satellite is unable to make an observation at that point in space and time.

7) *Data source (agency and/or observation type)*: **Remote sensing from the TRMM system**;

Variables available: Estimates of precipitation (and related variables);

Relevant characteristics (commentary): While TRMM is intended to provide absolute areal estimates of precipitation accumulations, it was also designed to function principally in tropical climates where the dominant precipitation mechanism by far is convective rainfall. As discussed at length in sections 3.5.4 and 3.9.1, TRMM is less skilled at detecting stratiform precipitation, especially

orographically-enhanced stratiform precipitation than at detection of convective precipitation. While the ratio of convective to stratiform precipitation in contributions to total accumulation will alway be heavily weighted to the latter, the ratio will vary as a function of the season. In warmer months convection will be become marginally more prevalent even in the mountainous UIB. Thus factors of "virtual undercatch" by TRMM for the UIB will vary from month to month or season to season. Despite these limitations, TRMM has been shown to provide a degree of meaningful quantification of interannual variability of precipitation in the UIB (see section 3.10). The net result of its biases and advantages is that TRMM precipitation data is yet another source of meaningful quantitative information on UIB hydro-climatology which requires scaling to yield physically accurate absolute values.

3.11.2 Discussion of key topographically-driven climate sensitivities

The core NW UIB area distinguishes itself climatically from the contiguous sub-regions through a number of parameters: precipitation seasonality, annual SCA, annual DTR cycle, cloud cover regime, etc. Detailed analysis of the energy balance components and thorough characterisation of vertical gradients in key climate parameters provides the underpinning for understanding key hydro-climate relationships. This in turn paves the way for skilful modelling of present and projected future hydrological conditions.

As can be seen in Figure 3.103, the concentration of UIB surface area in the band between 4000m and 5000m asl corresponds to an elevation where both local observations (PMD and AWS) and remote sensing (MODIS LST) place the Tmin/Tnight zero degree isotherm in the summer months. Interannual seasonal anomalies in temperature can push this isotherm upward or downward. Because of the concentration of catchment area in this zone, these anomalies will in turn have a substantial (disproportionate) effect on the catchment continuous melt area (CMA). As was shown in the section on hydro-climate relationships (section 3.10), CMA is a critical indicator of runoff from glacierised sub-catchments. The ability to skilfully predict summer temperature anomalies is thus a critical objective in supporting water resources management. This sought after forecasting ability would enable anticipation of variations in water availability. Such a capability would be very valuable for infrastructure managers and agricultural planners, allowing optimisation of reservoir

management to support irrigation and hydropower and supporting decisions on the amount surface area to plant as well as crop/seed variety selection.

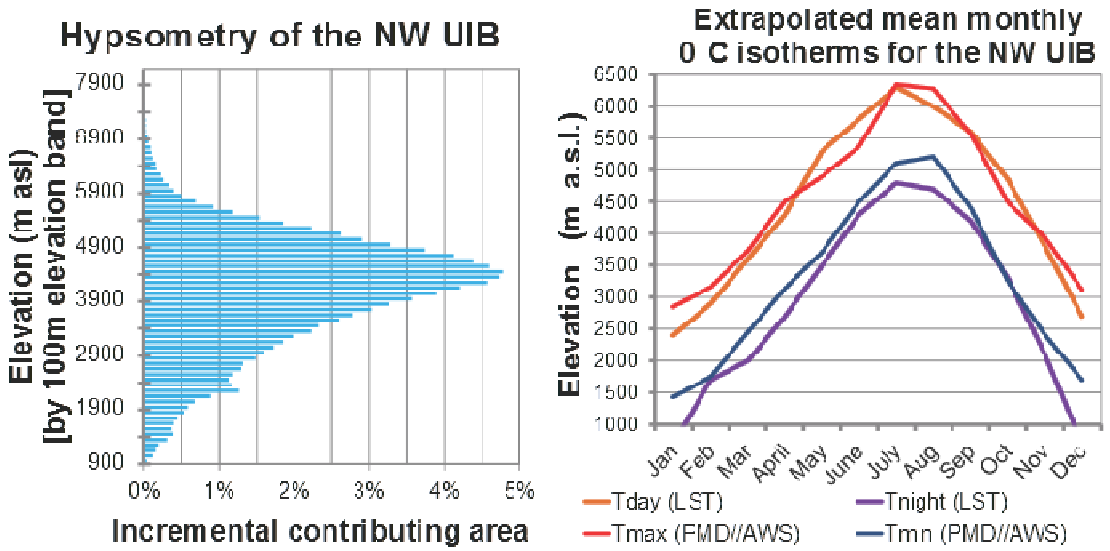

Figure 3.103 hypsometric concentration of catchment area and resultant sensitivity to fluctuations in 0°C isotherms.

3.11.3 Discussion of critical limitations of present sources of spatial data

One difficulty, and thus opportunity for improvement, to the hydro-climate relationship methodology presented in this Chapter is the very limited historical record length of the available remote sensing data products. This short record length is inadequate to fully represent the range of likely hydro-climatological variability. A solution to this problem is the creation of customised spatial data products using existing primary radiometric observations from a succession of satellite-borne instruments originally launched to support weather forecasting. For example, parallel work to that presented here is currently underway on the development of multi-decadal spatial data products – equivalent to MODIS SCA and LST – using imagery from the Advanced Very High Resolution Radiometer (AVHRR) instrument flown on several generations of (US) National Oceanic and Atmospheric Agency (NOAA) satellites (Chokmani *et al.*, 2005, Khlopenkov and Trischenko, 2006, Li and Becker, 1993, Pinheiro *et al.*, 2006). The AVHRR data has similar spatial resolution and observational frequency to the MODIS data products, though with more limited spectral resolution – only five bands – than the more modern instrument. The AVHRR record does, however, extend from 1978 to the present. This long record offers the potential to : i) greatly increase the overlap of the spatial data products with local observations, thus refining quantification of relationships between them; and ii) to extend the range of observations to better capture current spatio-temporal climate variability.

Example figures of preliminary estimates of monthly period means for a sample record period (1998 to 2008) for preliminary AVHRR data products for SCA, LSTday and CCFday are presented in Appendix 1 (section A.2). Visual comparison of these images to their MODIS equivalents suggests a satisfactory level of initial agreement. Rigorous validation is currently underway to assess biases and limitations in this exciting new dataset.

3.11.4 Concluding remarks

Throughout this Chapter a number of potential avenues for future work have been identified. In addition to development of AVHRR-derived spatial data products, some of the most promising and hence urgent include nested numerical weather simulation to better understand the physical precipitation mechanisms shaped by the unique topography of the UIB and the resultant spatial patterns of mass input to the hydrological system.

Above all this Chapter has been intended to serve as the hydro-climatological foundation for sub-sequent chapters by providing the benchmark in terms present-day mean climate and probable bounds (first and last deciles) of interannual variability. This will be crucial for Chapter 4 which examines recent patterns of change in key inputs of mass (precipitation) and energy (near-surface air temperature) to the UIB hydrological system, especially evidence of seasonally and diurnally asymmetrical patterns of change in near-surface air temperature.

The understanding presented in this chapter will also be crucial for work in Chapter 5 which describes development of contrasting plausible future climate scenarios for the UIB. In order to assess projections of future change it is necessary to first assess underlying biases in sources of the projections. Furthermore the methods used in this these for application of climate scenarios is based on stochastic synthetic time-series of control (present) and perturbed (future) climates which require the statistical descriptions of observed climate as core inputs.

The information presented in this chapter is also crucial to construction, calibration and validation of a hydrological model for archetypal UIB tributary catchments (Chapter 6). Hydro-climate data is used both as input to drive the model and as observed standards against which simulated outputs are assessed. Lastly the calibrated hydrological model will be driven by the selected future climate scenarios to

examine potential hydrological impacts of the projected climate change trajectories (Chapter 7).

In conclusion, it is because the material presented in this Chapter provides the foundation for the remainder of this thesis that the subject matter has been dealt with so exhaustively. This thesis is intended to provide a substantial contribution to the hydrological science underpinning water resources management in a region of the world where shortfalls in water availability have immediate and severe consequences for economic well-being and food security.

Chapter 4: Assessment of climate trends and their drivers in the UIB from the available observational record

4.1 Introduction

The Upper Indus Basin is a highly complex hydroclimatic system. Marginal changes in key hydroclimatic variables, principally precipitation and near surface air temperature, both in their means and interannual variability, could have profound implications for water resources management in this region. This sensitivity derives largely from the concentration of large fractions of the total catchment surface area within relatively narrow elevation bands where these variables either fluctuate considerably in magnitude (peak orographic precipitation) or oscillate across key thresholds (freezing, i.e. 0°C, isotherms).

As an integrator of multiple highly variable climate processes, meltwater-generated runoff is itself highly variable. Thus robust assessment of variability and trends in river discharge is highly dependent on access to gauging records of substantial length, preferably with good spatial density. Spatial density in this instance indicates that an individual gauge either receives flow from a limited catchment area, or, if there is an additional gauge upstream, there is only limited incremental area between the gauges. Furthermore, it is preferable that the contributing area, either upstream or incremental, is relatively homogeneous in the characteristics (e.g. land cover, soil characteristics) which influence the hydrological response.

Unfortunately, access to local observation data in contentiously shared trans-boundary basins is highly politicised and hence highly sensitive. Furthermore, in contrast to many climate variables there are effectively no remote sensing analogues to local measurement of river discharge with even moderate spatial resolution and frequency. The presently available gravimetric (mass balance) techniques associated with the NASA Gravity Recovery (GRACE) mission have a minimum time-step of one month and a minimum horizontal discrimination of 400 km (Wahr *et al*., 2004) although developing numerical methods allow the detection of mass change in glacial areas as small as 100km^2 (Jacob *et al*., 2012). Other methods, e.g. river stage altimetry, rely upon either local discharge observations or accurate knowledge of channel geometry to establish a "rating curve" (e.g. Bjerklie *et al*., 2003).

The limited incremental extensions acquired during the present project to the existing hydrological data series for the study area, combined with underlying climatic

variability of the past decade, result in limited additional findings to report regarding hydrological trends beyond the preceding work by Fowler & Archer (2006). An examination of trends in magnitude and time of flows, to which the author of this thesis has contributed, by Sharif *et al.* (in review) found contrasting trends in flow magnitude depending on season and catchment hydrological regime. In terms of magnitude Sharif *et al.* (in review) found indications of increasing flows in moderate elevation (nival regime) catchments but decreasing flows in high elevation (glacial regime) catchments. With regards to timing of flows Sharif *et al.* (in review) found no clear patterns of change in either "spring onset date" (SOT) or "centre of volume" (CoV) dates. These two metrics respectively quantify the timing of melt onset and of the mid-point of annual cumulative discharge.

In light of the limited opportunity to expand upon the work of Fowler and Archer (2006) or Sharif *et al.* (in review) with the presently available data, work presented in this Chapter therefore focuses on assessment of variability and trends in the proximate drivers – i,e. the climate variables most locally, and directly influencing runoff – of hydrological variability (section 4.2). As described in Chapter 3, in the UIB these drivers are mass and energy inputs, as indexed by precipitation and temperature, to the hydrological system.

To better understand the underlying drivers of this variability in system inputs, further analysis is then presented of secondary climate variables – cloud cover, energy balance components, atmospheric water content as represented by relative humidity – in order to identify causal relationships and to provide insight regarding likely trajectories of future change (sections 4.3 to 4.5). The same desire to improve process-based understanding of UIB climatology which prompted the search for local causal mechanisms in UIB climate variability also motivated investigation of links to large-scale atmospheric circulation, particularly investigation of relationships between local climate and large-scale circulation features known as teleconnections (section 4.6). This chapter concludes with reflexions on the implications of the observed patterns of recent change, of identified local causal mechanisms (e.g. relationships between near-surface air temperature and radiative forcings), and of identified large-scale circulation influences on UIB climate (section 4.7).

4.2 Assessment of trends in local observations and meteorological reanalysis

4.2.1 Contextual remarks on trend analysis in the UIB

Chapter 3 of the present work provided a descriptive inventory of the data sources available to this study. This chapter will specifically draw on local meteorological observations (PMD) and outputs from two of the European Centre for Medium-range Weather Forecasting (ECMWF) reanalyses, ERA-40 (Uppala *et al*., 2005) and ERA-Interim (Dee *et al*., 2011). ERA-40 outputs will be analysed both in their "native" coarse spatial resolution (2.5 decimal degrees) and as downscaled using the PRECIS RCM (Jones *et al*., 2004), hereafter referred to as PRECIS_ERA40.

Owing to the inherent variability of the climate system, particularly in the UIB, multi-decadal records are necessary to better understand the nature of that variability and to assess potential, statistically significant trends (Frei and Schar, 2001). Furthermore, owing to this inherent variability, records of moderate length – in the range of 20 to 40 years – are susceptible to the choice of analysis period. In a study of stations in the nearby northwest Himalaya Bhutiyani *et al*. (2010) using power spectrum analysis found underlying periodicities ranging from three to six decades. This suggests that underlying phenomena governing regional precipitation variability are driven by processes or cycles that are multi-decadal in nature. Hence attempts to detect underlying long-term changes, also referred to as "secular change", with records at shorter time-scales than the inherent cyclical variability will be complicated by the need to separate the "natural" or expected fluctuations from those which cause the evolving additional, implicitly anthropogenic, forcing.

4.2.2 Timeframe (analysis window) sensitivity

Four separate time windows were selected – 1961 to 1990, 1962 to 2001, 1979 to 2001, and 1979 to 2007 – these correspond to the common availability of the different data sources presented: i) 1961 to 1990 corresponds to availability of ERA-40 (coarse resolution and PRECIS_ERA40) and local observations; ii) 1962 to 2001 corresponds to availability of ERA-40 (coarse resolution only) and local observations; iii) 1979 to 2001 corresponds to availability of ERA-40 (coarse resolution only), ERA-Interim and local observations; iv) 1979 to 2007 corresponds to availability of ERA-Interim and local observations. It is recognised that the third window, 1979 to 2001, is relatively short (19 years) compared to the widespread three decade standard for climatological studies. Nevertheless it was deemed useful to examine this period

specifically because both ECMWF reanalyses, ERA-40 and ERA-Interim, can be compared to local observations for a common analysis window.

Time-series for these periods have been assessed. The normalised, standardised anomalies – observations with means first subtracted (normalised) then scaled by dividing by standard deviations (standardised) – have been calculated for the representative values (means for temperature, totals for precipitation) of key temporal aggregates – annual, cold season (ONDJFM) and summer monsoonal season (JJA) – for the variables considered in this Chapter. These times-series are shown in Appendix B. These show strong general agreement (in sign if not in magnitude) across data sources for individual anomalies for a given combination of variable, season and year. This agreement is numerically quantified in section 4.3.3 and4.5.1. Additionally, the figures show the observation by the individual data sources of specific seasonal-scale events such as the 2000 to 2003 drought (Archer *et al*., 2010).

For each analysis window, Figures 4.01 and 4.02 illustrate the differences in the sensitivity of linear trend rate estimation between these data sources for near surface (2m) air temperature and precipitation. Trend rates were estimated by simple linear regression from local observations (PMD) and are compared those from to the output of numerical weather analyses – meteorological reanalysis or reanalysis-driven regional climate model simulation. Mann-Kendall was not used to test significance in this case as work published in Forsythe *et al*. (2012b) showed only limited differences in trend sign, correlation magnitude and statistical significance when using linear regression versus Mann-Kendall and Rank-Spearman coefficients.

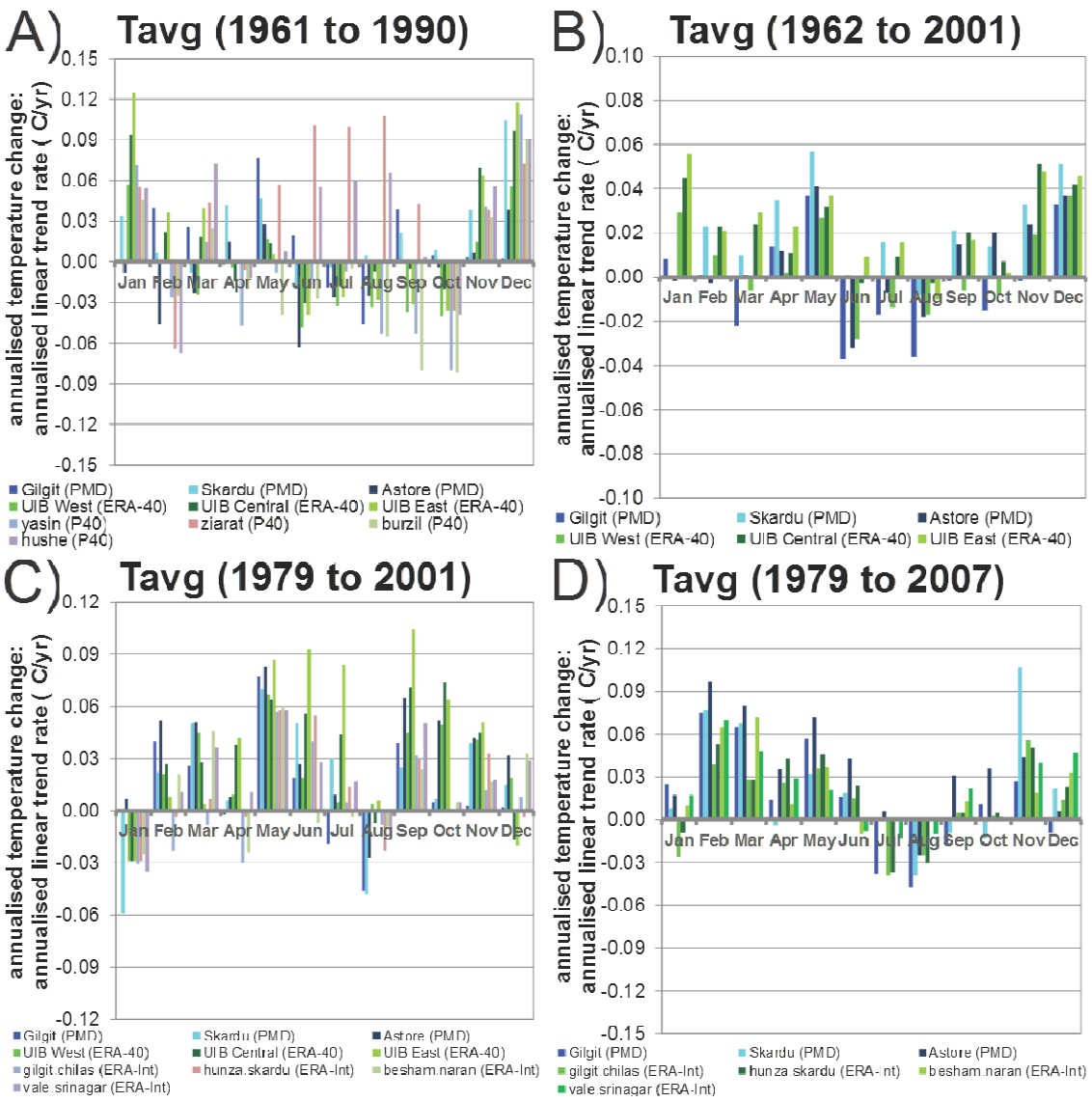

Figure 4.01 Timeframe (analysis window) sensitivity for trends in mean temperature (Tavg) from multiple data sources – local observations (PMD), ERA-40, ERA-Interim (abbreviated ERA-Int) and PRECIS_ERA40 (abbreviated P40) – for the following periods: A) 1961 to 1990; B) 1962 to 2001; C) 1979 to 2001; and D) 1979 to 2007.

For daily mean (Tavg) air temperature (Figure 4.01), the best agreement with local observations is found in ERA-Interim which is the newest and perhaps most sophisticated data source. Agreement between local observations and ERA40 outputs are generally good as well. So too is the agreement with the RCM outputs, PRECIS_ERA40, with the exception of higher elevation grid cells in summer months. Specific examples of these high-elevation grid cells are the "ziarat" and "hushe" cells (locations are shown in Figure 3.013). As can be seen in the upper left panel of Figure 4.01, these grid cells yield oppositely signed trends from the other data sources for June, July and August (1961 to 1990).

For precipitation (Figure 4.02), the level of agreement between trend rates from local observations and numerical analyses is also generally quite good. In this case

though it is ERA-Interim in the summer months for the time window from 1979 to 2007 that diverges from the local observations.

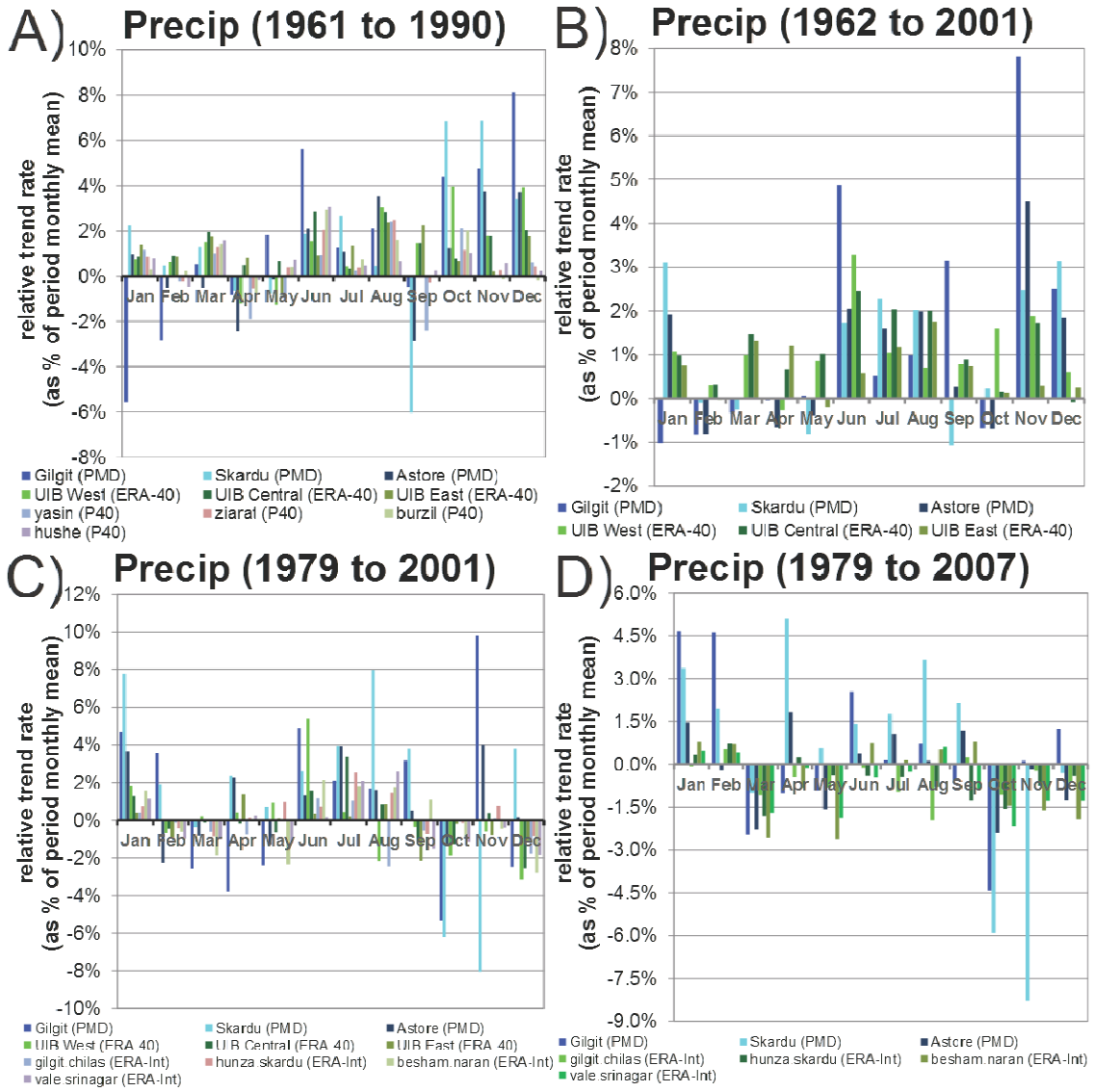

Figure 4.02 Timeframe (analysis window) sensitivity for trends in total precipitation (Precip) from from multiple data sources – local observations (PMD), ERA-40, ERA-Interim (abbreviated ERA-Int) and PRECIS_ERA40 (abbreviated P40) – for the following periods: A) 1961 to 1990; B) 1962 to 2001; C) 1979 to 2001; and D) 1979 to 2007.

Between temperature and precipitation, temperature trends are less sensitive to the choice of time window. In each of the four windows presented a common pattern emerges of warming from autumn through to spring but cooling centred on the hottest months of the year (July, August). There are differences in the magnitude and breadth (number of months) of summer cooling as well as in the magnitude of warming in the other seasons, but the general pattern – of warming in cold months and cooling warm months – remains consistent. This finding confirms and reinforces previous work by Fowler & Archer (2006) who analysed the period from 1961 to 1997. The fact that the pattern remains in the most recent analysis window (1979 to 2007) for both data sources

tested – PMD local observations and ERA-Interim – suggests that whatever processes have been at work continue to act. The fact that the seasonal asymmetry is present in multiple data sources across all four analysis windows strongly indicates that the estimated trends are driven by active physical mechanisms and not simply artefacts misconstrued through random patterns within natural variability.

For precipitation (Figure 4.02) not only the magnitude, but even the sign, of the estimated trend changes between analysis windows. There is some consistency in precipitation increases in the summer months, especially in local observations, but it must be recognised, as was presented in Chapter 3, that the summer months in the UIB are relatively dry compared to the spring. The most important message to glean from this analysis is an appreciation of the endemic temporal variability of precipitation in the UIB and hence the inherent uncertainty regarding likely precipitation in any specific time period – of decadal length or similar – be it for the observed record or projected future. This does not imply shortcomings in any particular data source, but simply underlines the inherently chaotic nature of precipitation magnitude in the UIB.

4.2.3 Examination of evidence for seasonally and diurnally asymmetrical temperature change

The apparent persistence of summer cooling found across the various time windows is not the only noteworthy finding in this analysis. Figure 4.03 shows that recent temperature trends are asymmetrical not only between seasons, but also within the diurnal cycle. Daily maximum air temperatures (Tmax), occurring in the afternoon, have increased in autumn through spring, with effectively negligible change in summer. Daily minimum temperatures, occurring in the pre-dawn hours, show a mixture of trajectories with limited warming or no change from autumn to spring and strong cooling in summer months. Robust agreement is noted on daytime warming and night-time cooling between local observations and ERA-Interim.

Agreement can also be seen, in Figures 4.04 and 4.05, between local observations and ERA40 although it depends on the choice of time window, i.e. good agreement for 1979 to 2001, limited agreement for 1961 to 1990 but poor agreement for 1961 to 2001. This may be due to specific biases introduced by the temporal non-homogeneity of the global observations assimilated by ERA40 over the more than four decades it spans (Uppala *et al.*, 2005). Again the reanalysis-driven RCM outputs (PRECIS forced with ERA40) show moderate agreement with local observations

(Figure 4.05) except for high elevation grid cells in warm months – late spring to early autumn – which show oppositely-signed trends with large magnitudes. This hints at specific sensitivities or feedbacks possibly linked to elevation-dependent parameters such as cloud cover.

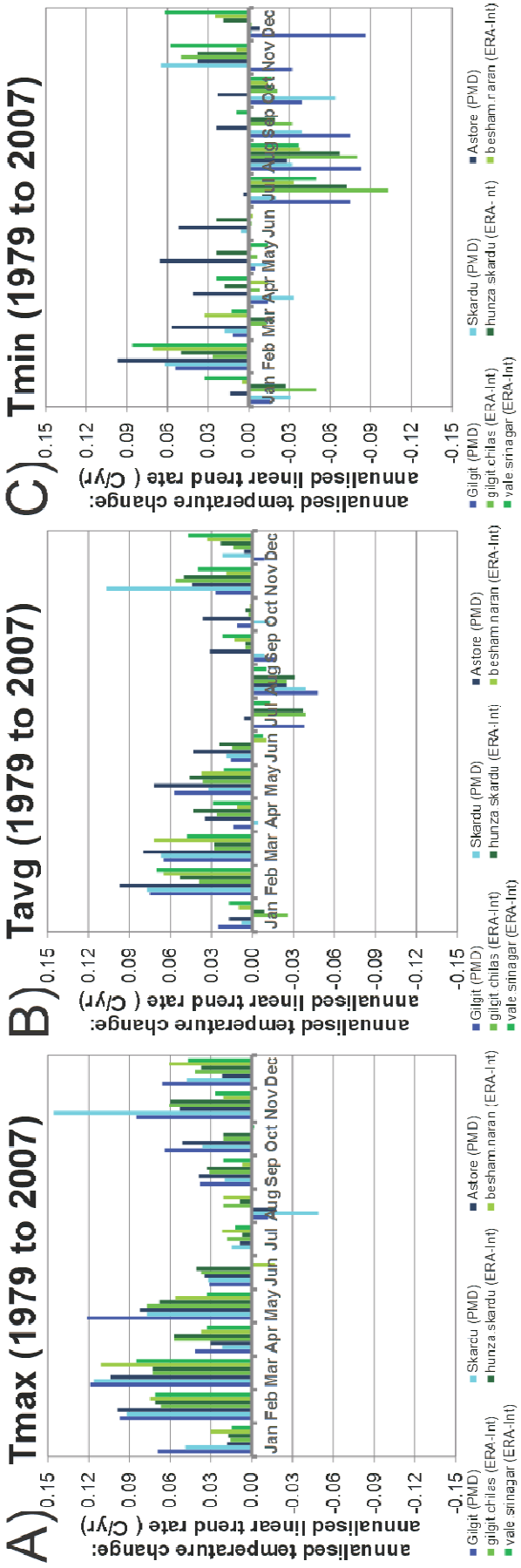

Figure 4.03 Monthly linear trends in near-surface air temperature from local observations (PMD) and ERA-Interim (abbreviated ERA-Int) for 1979 to 2007 for UIB: A) maximum (Tmax), B) average (Tavg), and C) minimum (Tmin) temperature.

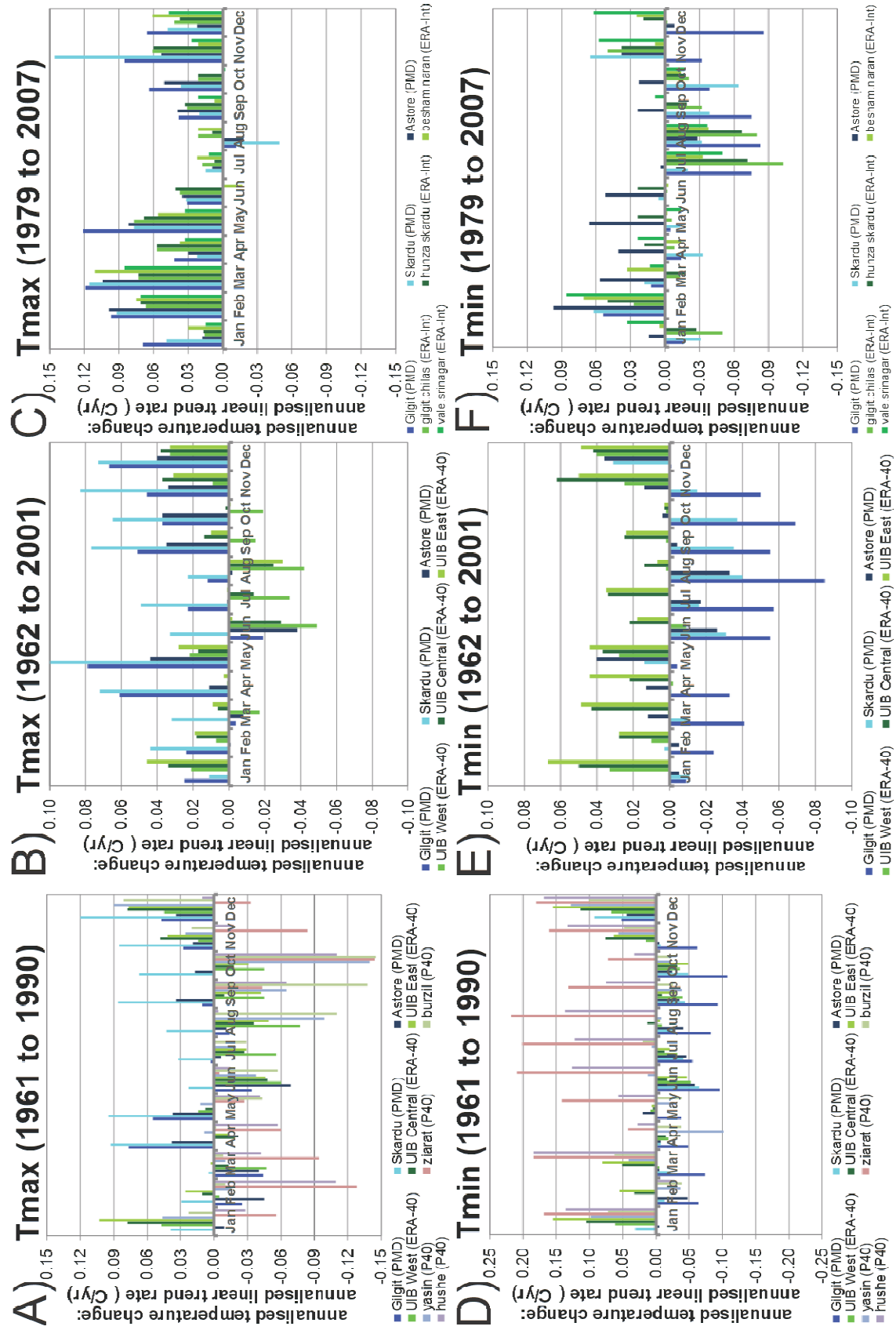

Figure 4.04 Further consideration of the diurnal temperature conundrum including discrepancies between data sources. Diurnal components: Tmax in panels A, B, C; Tmin in panels D, E, F. Time periods: 1961 to 1990 in panels A, D; 1962 to 2001 in panels B, E; 1979 to 2007 in C, F.

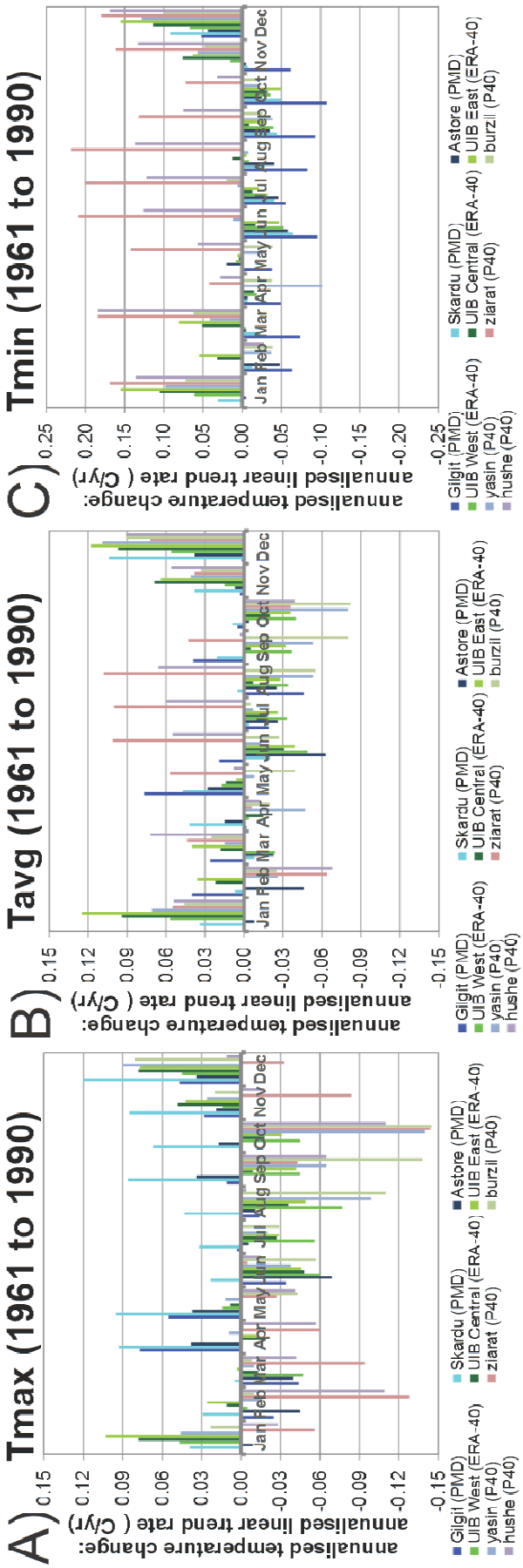

Figure 4.05 Additional diurnal conundrums and discrepancies as shown in temperature trends from local observations (PMD), ERA-40 and PRECIS_ERA40 (P40) for 1961 to 1990 for diurnal phases: A) Tmax, B) Tavg and C) Tmin.

Overall, these findings substantially support and build upon the previous work by Fowler and Archer (2006). Their work provided the initial substantive explanation – decreasing summer melt energy inputs as indexed by near-surface air temperature – of the "Karakoram anomaly" described by Hewitt (2005). The work carried out by the present study and described in this Chapter, however, has added substantially to the present understanding of UIB hydro-climatology by drawing on multiple additional data sources and testing multiple analysis windows where Fowler and Archer (2006) used only a single data source (PMD) primarily limited to a single analysis window (1961 to 1997), although they did test some stations for the late 19th and early 20th century. The use of multiple data sources and testing of multiple analysis windows considerably strengthens the evidence for seasonally and diurnally asymmetrical temperature change in the UIB.

Much of the remainder of this Chapter will be devoted to assessing potential causal mechanisms for these striking patterns of recent change. Identifying these mechanisms is critical to evaluating the plausibility of available scenarios of projected future climate change.

4.2.4 Assessment of the spatial coherence of estimated trends

To further evaluate the applicability of the point-based trend-analysis presented in the preceding section, regional subsets of gridded outputs from ERA-Interim and PRECIS_ERA40 data sources were also tested for linear trends. As for the point-based analysis, trends were assessed by calendar month and each grid cell was analysed as an individual time-series. This was to determine if there are spatially coherent patterns – ideally continuous sub-regions of grid cells with values of similar sign and magnitude – of temporal change for air temperature and precipitation. Optimally these patterns would be clearly attributable to physiographic factors or local climate processes.

To simplify the examination of spatial patterns in temporal trends, the Pearson's correlation coefficient of the selected climate variable with respect to time was used. Pearson's correlation coefficient, whose value ranges from -1 to -1, is often calculated while performing ordinary linear regression and is defined as the covariance between two variables of interest – in this case, the selected climate variable and the time index – divided by the product of the standard deviations of each variable. It is recognised that non-parametric measures of correlation, e.g. Mann-Kendall's tau, are often used for climate data of this type. In the present study, Pearson's correlation was retained for its

simplicity. Work by Forsythe *et al*. (2012b) showed that Mann-Kendall and rank Spearman correlation measures for UIB climate observations were identical in sign and similar in magnitude to the Pearson's correlation coefficient values for the same data series. Further comparisons between the Pearson's correlation values presented here and non-parametric measures can be made by comparing the results in this Chapter to work of Khattak *et al*. (2011).

Figures 4.06 to 4.11 show the spatial patterns in Pearson's correlation coefficient for the selected climate variable with respect to time. Positive correlation values indicate increasing trends. Negative correlation values indicate decreasing trends. In these figures months are labelled alpha-numerically, i.e. 'm01' for January through 'm12' for December. With regards to Figures 4.07, 4.09 and 4.11, the spatial domain for PRECIS_ERA40 provided to the present study was geographically limited hence it is smaller than that of ERA-Interim (Figures 4.06, 4.08 and 4.10), but also omits the extreme southeast corner of the UIB.

Overall, there appears in both ERA-Interim (Figures 4.06, 4.08 and 4.10) and PRECIS_ERA40 (Figures 4.07, 4.09 and 4.11) to be general spatial coherence (contiguous areas similar sign and magnitude) in the results. This implies that patterns of change are being driven by sub-regional responses to large-scale drivers with differences potentially linked to climate regimes as described in Chapter 3.

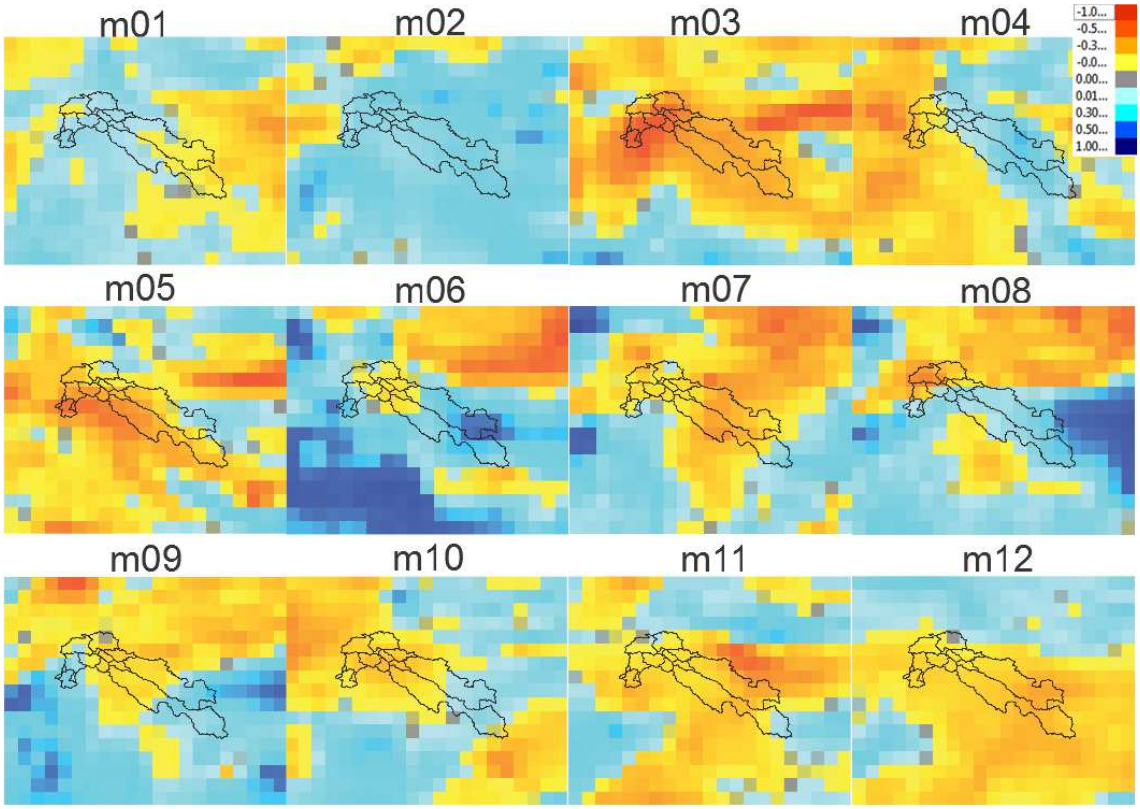

Figure 4.06 Pearson's correlation of precipitation with time using ERA-Interim (1979 to 2007).

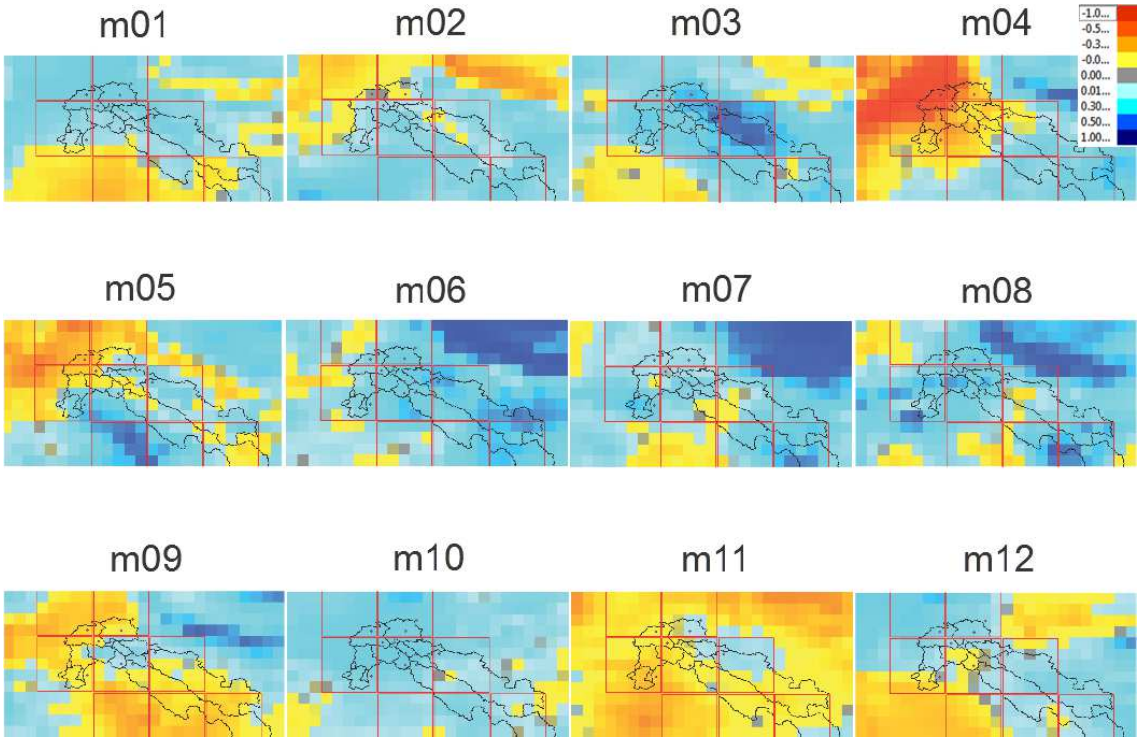

Figure 4.07 Pearson's correlation of precipitation with time using PRECIS_ERA40 (1979 to 2007).

By comparison of Figures 4.06 and 4.07, the spatial assessment confirms the time-window sensitivity of estimation of precipitation trends as the ERA-Interim results bear little resemblance to those from PRECIS_ERA40. Specifically several of the areas of the strongest correlations in each Figure have the opposite signs, e.g. UIB March precipitation decreases from ERA-Interim (Figure 4.06) and decreases from PRECIS_ERA40 (Figure 4.07). This is result primarily provides a spatial confirmation of the timeframe (analysis window) sensitivity of precipitation identified in section 4.2.2 rather than indicating disagreements between the two data sources in terms of precipitation climatology.

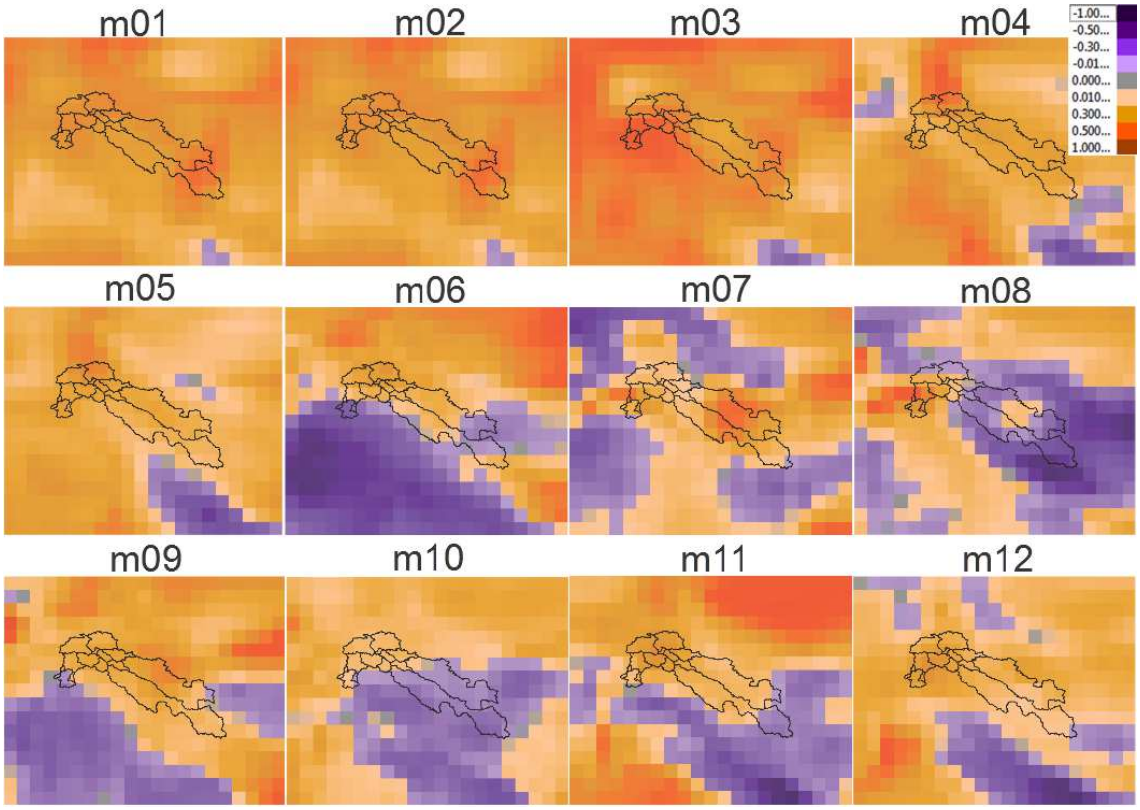

Figure 4.08 Pearson's correlation of Tmax with time using ERA-Interim (1979 to 2007).

Figure 4.08 shows the broad spatial extent of increasing Tmax in the UIB and surrounding sub-regions especially from January (m01) to May (m05). Spatial patterns are more mixed in other months, although correlations remain uniformly positive across the core north-western (NW) UIB – Gilgit/Ghizer, Hunza, Shigar and Astore tributary catchments as well as the Indus main channel from Kharmong and Yogo to Besham – except from June through August when marginal areas show limited negative correlations. This can be related to the point-based assessment shown in Figure 4.03.

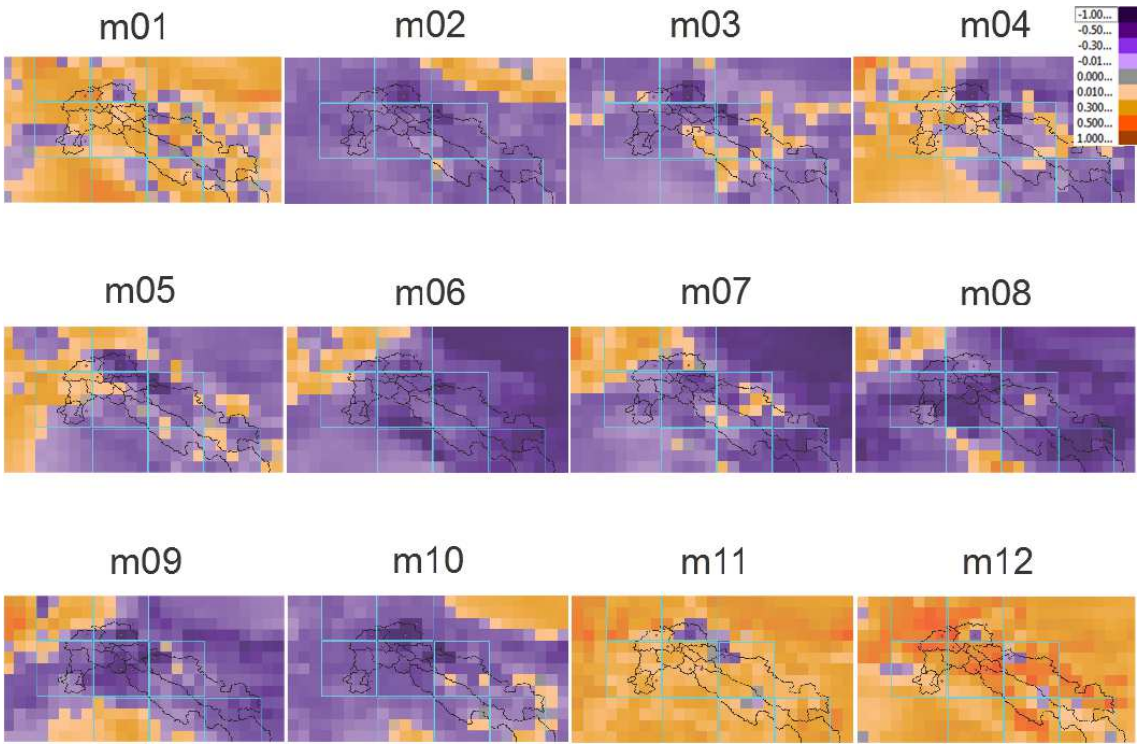

Figure 4.09 Pearson's correlation of Tmax with time using PRECIS_ERA40 (1979 to 2007).

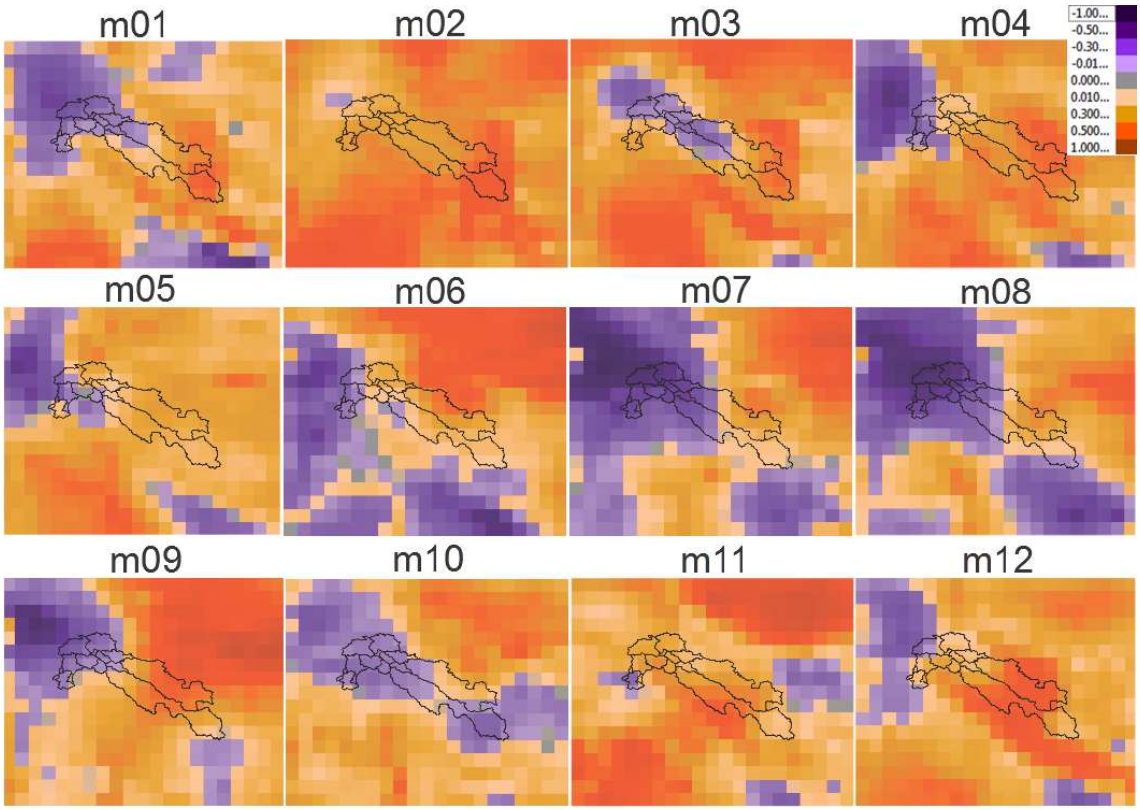

Figure 4.10 Pearson's correlation of Tmin with time using ERA-Interim (1979 to 2007).

Figure 4.10 shows the spatial patterns in temporal trends for Tmin. Of key interest is the geographic extent of decreases in Tmin described in section 4.2.2. The spatial analysis indicates a "super-cell" of decreasing Tmin which, although the radius varies from month to month, is present for much of the year and centred in the northern

Hindu Kush slightly west of the UIB. The spatial examination of Tmin trends (correlation with time) can be related to the point-based assessment shown in Figure 4.03.

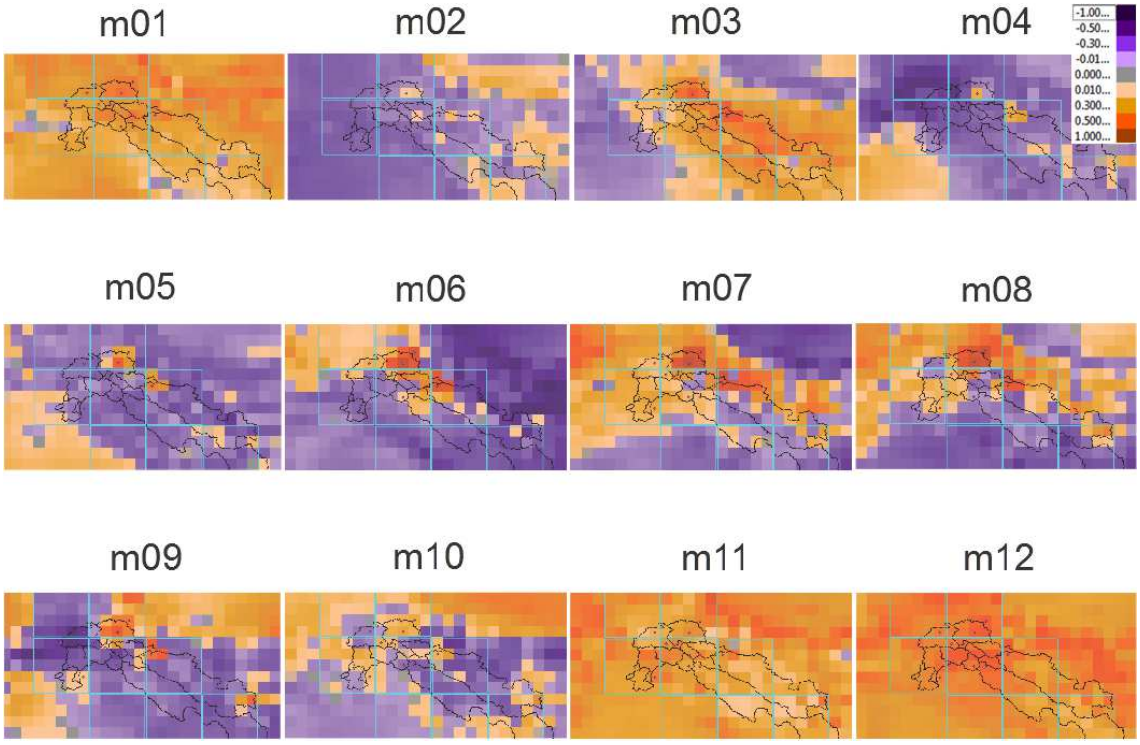

Figure 4.11 Pearson's correlation of Tmin with time using PRECIS_ERA40 (1979 to 2007).

The results from PRECIS_ERA40 (Figures 4.09 and 4.11) for air temperature graphically illustrate the expected condition that RCM outputs will largely be governed by the supplied boundary forcings (either from global meteorological reanalyses or GCMs). In other words, while RCMs can help to improve simulation of scale-dependent processes, i.e. those strongly influenced by local topography (e.g. orographic precipitation), they can only do so within the constraints imposed by the supplied boundary forcings. Thus if the coarse resolution boundary forcing is fundamentally biased in terms of climate responses, downscaling by the RCM is unlikely to resolve the discrepancy. In the case of the spatial data presented here, divergences from local observations in trend sign of diurnal components (Tmax, Tmin) appear across the sub-region. For example, for Tmax, local observations (Figure 4.05) identify strong increases in April (m04) and May (m05) while PRECIS_ERA40 (Figure 4.09) shows strong negative correlations through much of the core NW UIB. Additionally, where local observations (Figure 4.05) indicate strong decreases in summer (June to August) Tmin, PRECIS_ERA40 results show increasing Tmin (Figure 4.11) in the core NW UIB (though there are decreases in many of the adjacent sub-regions). That these results are in conflict with both local observations and results from the more recent ERA-

Interim (Figure 4.10) which underline the importance of using the correct large-scale forcings in addition to adequate spatial resolution in modelling for accurate assessment of climate trends.

4.2.5 Statistical significance of spatial trends

Statistical significance of the Pearson's correlation is calculated using Student's *t*-test. The *t*-statistic in this case is a function of the Pearson's correlation and the sample size, i.e. the record length. The associated statistical significance values for the correlations shown in Figures 4.06 to 4.08 can be found in the corresponding figures in Appendix B (section B1.2). Because of the dependence of the *t*-statistic on record length, the critical thresholds in Pearson's correlation required to attain specific levels of statistical significance are straight-forward to calculate. The two data sources presented here for spatial assessment are respectively 29 years (ERA-Interim) and 30 years (PRECIS_ERA40) in length. The relevant Pearson's correlation thresholds, for a '2-tailed' significance test are shown in Table 4.1.

Record length	90% significant ($p < 0.10$)	95% significant ($p < 0.05$)	99% significant ($p < 0.01$)	99.9% significant ($p < 0.01$)
29 years (ERA-Interim)	0.315	0.365	0.475	0.585
30 years (PRECIS_ERA40)	0.310	0.370	0.465	0.575

Table 4.1 Values of Pearson's correlation coefficient corresponding to specific statistical significance levels as a function of the record lengths for the data sets analysed.

The Pearson's correlation values were tested against the thresholds shown in Table 4.1 as absolute values. Reviewing Figures 4.06 to 4.11, grid cells with positive or negative correlations greater in magnitude than these thresholds are thus statistically significant at the relevant level. Simply put, for the record lengths examined in this analysis, areas with strong positive (or negative) correlations show a meaningful degree of significance. Areas with only weak correlations will not attain these levels.

4.2.6 Summary of trend rate analysis findings

The multiple data sources and analysis windows considered in the preceding sections robustly substantiate on-going seasonally and diurnally asymmetrical temperature trends indicated in the available historical record for the UIB. While increasing temperatures are found in cold seasons (autumn to spring), summer

temperatures have been decreasing in recent decades. The net temperature change (Tavg trend) in each season results from asymmetrical contributions by diurnal phases. From autumn through spring, increasing mean temperatures are mostly driven by increasing (day-time) Tmax, with little substantial change in Tmin. Decreasing summer temperatures, on the other hand, are mostly attributed to decreasing Tmin while Tmax is relatively stable.

While these findings echo both Fowler and Archer (2006) and Khattak *et al*. (2010), the point-based work presented here is supported by a broader range of input data and tested for multiple analysis windows. Furthermore, the spatial assessment, presented in Section 4.2.4, using outputs from meteorological reanalyses – both 'native' resolution and downscaled by an RCM – to examine the coherence of sub-regional patterns of change in the UIB and adjacent areas is an innovation by the present study.

4.3 Pre-requisite analyses for investigation of air temperature change causal mechanisms

4.3.1 Impetus and conceptual framework for investigation of causal mechanisms

If trends in precipitation and temperature in the UIB were relatively monotonic (e.g. uniform warming, uniform drying) and statistically significant across a range of analysis windows for the data sources available for the historical record, then the spatial and temporal patterns highlighted above could be accepted with a degree of confidence and focus could shift to assessment of the likely hydrological impacts and development of potential adaptation measures.

The asymmetrical and inconsistent changes presented in the preceding section, to some extent deviate from what might be expected under the general narrative of a warming world. This does not in any way imply that these findings refute the influence of anthropogenic greenhouse gas emissions on climate change. Notwithstanding the extensive difficulties identified in obtaining reliable assessments of recent climate variability and change in which we may have confidence, the unique physiographic features of the UIB and its location at the intersection of monsoonal and westerly weather regimes also mean that climate change may take a different trajectory here than in other regions. For example, as described in the "Regional Climate Projections" section of the Working Group I contribution to the IPCC 4th Assessment Report (WG1-AR4) (Christensen *et al*. 2007), the Arctic Polar regions are considered very likely to warm faster than the global mean largely due to surface albedo feedbacks from reduced

sea-ice cover. Similarly reported in WG1-AR4 (Christensen *et al.*, 2007), Europe is considered likely to warm more than the global mean with sub-regional changes in precipitation and temperature largely shaped by changes in "storm tracks" of westerly weather systems which are shaped by the North Atlantic Oscillation (NAO).

Thus before the hydrological effects of potential changes in climate inputs – mass (precipitation) and energy (temperature) – can be assessed, it is necessary to evaluate the plausibility of the scenario that projects them. This evaluation requires identification of the physical mechanisms producing the observed (or projected) change and, as far as possible, the dependencies and thresholds of these mechanisms. This evaluation must bear in mind whether the variable under consideration is temporally (and spatially) discrete or continuous. For example, precipitation is a spatially and temporally discrete in its occurrence. Temperature, in contrast, is continuous.

It is precisely the continuous nature of temperature which makes the diurnal asymmetry in trends seen in the UIB so puzzling. While, as will be presented in the following sections, candidate mechanisms which influence air temperature are plentiful, those that could produce the specific pattern of change found in the UIB are not immediately evident. In order for one diurnal component (Tmax or Tmin) to show strong change (warming or cooling) while the other is effectively stationary (no change) one would expect a concurrent compensating causal mechanism to offset the initial forcing. To clarify, Tmax and Tmin are subject to separate concurrent forcings (shortwave [SW] solar radiation, longwave [LW] thermal radiation, sensible heat flux, latent heat flux) with the net influence articulated around mean daily temperature (Tavg).

This could be formulated conceptually as:

$\Delta Tmax = \Delta daytime_forcing + \Delta night_carryover$

$\Delta Tmin = \Delta nighttime_forcing + \Delta day_carryover$

In other words, if the local climate forcing on near-surface air temperature was temporally conserved – i.e. $\Delta daytime_forcing = \Delta day_carryover$, and $\Delta nighttime_forcing = \Delta night_carryover$ – rather than being thermodynamically transferred away either to higher atmospheric levels or to the ground surface, then one would expect the net diurnal forcings to be purely additive. Hence, if the temperature

changes (ΔTmax, ΔTmin) were held in the near-surface air layer, it would for example be expected that day-time SW forcing would directly result in a change in Tmin as well as in Tmax and conversely night-time LW forcing would affect Tmax as well as Tmin. In such a scenario, changes in diurnal components would be identical, i.e. ΔTmax = ΔTmin. Clearly the reality of temperature change in the UIB is more complex than this idealisation.

Thus, to provide a physical explanation for the locally observed asymmetrical temperature trends presented above, mechanisms must be identified which in autumn through spring result in daytime warming (increasing Tmax) while this energy is dissipated (transferred away) during the night such that the trend in Tmin is null. Similarly, mechanism(s) in summer must be identified which cause night-time cooling (decreasing Tmin) but also an adequate day-time energy gain such that the trend in Tmax is null. This search for causal mechanisms is further complicated by the large amplitude of the annual cycle in the UIB of one of the dominant potential forcings, incoming shortwave (solar) radiation [see Chapter 3].

4.3.2 Inter-variable correlations in diurnal air temperature components

Prior to embarking on an exploration of the radiative forcings (surface energy balance) and, in turn, their drivers (principally, cloud and humidity), consideration of the relationships between the individual diurnal air temperature components (Tavg, Tmax, Tmin and DTR) may provide some insight.

Although they may seem self-evident, the following relationships (Pearson's correlation coefficients) are found between air temperature variables observed at individual local meteorological stations, as well as between different stations:

- Tmax is strongly positively correlated to both Tmin and DTR throughout the year. Correlations between these variables at individual stations are generally greater than 0.65. In terms of air temperature variability, this means that when it is warmer (colder) than the mean during the day it tends to be warmer (colder) than the mean at night. Also, when it is warmer (colder) than the mean during the day the DTR tends to be higher (lower). An initial assumption is that increased (decreased) Tmax – i.e. increased (decreased) day-time heating – amplifies (suppresses) the entire diurnal temperature cycle.
- Tmin, however, is strongly negatively correlated with DTR in winter (typical values less than -0.55 at an individual station), but results in other months are

mixed. This is thought to be due to radiative forcing driven by clouds, with night-time positive longwave (thermal) radiative effects raising Tmin with cloud cover but concurrent negative shortwave (solar) effects lowering Tmax with the combined effect of reducing DTR. In warmer months the net positive (warming) effect of reduced daytime cloud cover, i.e. increased absorption of incoming solar radiation, may offset any increased night-time cooling from reduced downward longwave forcing during "clear sky" conditions. These mechanisms will be explored in detail in the following sections.

- Relationships between air temperature variables are quite strongly positively correlated between stations, e.g. Tmin at Gilgit is strongly positively correlated with Tmin at Skardu and Astore. Also, the relationships between variables at a single station hold true to the variables at other stations, e.g. DTR at Astore is negatively correlated to Tmin at Gilgit in the winter months and positively correlated Tmax at Skardu year-round. These relationships appear temporally stable, i.e. independent of time window, having produced highly similar results for the 1961 to 1989 and 1979 to 2007 periods.

Reassuringly, the relationships found between air temperature variables in the local (PMD) observations are mirrored in reanalysis data. Based on analysis of "internal relationships" between variables from ERA-Interim:

- With rare exceptions, Tmax and Tmin are strongly positively correlated, i.e. in months when it's warmer (cooler) than average during the day, it's also warmer (cooler) than average at night.
- With rare exceptions, Tmax and DTR are strongly positively correlated, i.e. in months when it's warmer (cooler) than average during the day, DTR is larger (smaller) than average.
- Over the UIB (mountainous headwaters) itself, Tmin and DTR are strongly negatively correlated, i.e. in months warmer (cooler) than average at night, DTR is smaller (larger) than average. There is, however, a strong spatial exception to this pattern in warm months (Mar to Sep) over the Indo-Gangetic plains adjacent to the UIB where the correlation is moderately to strongly positive

To put these relationships into a larger (sub-global) context, Figures 4.12 and 4.13 respectively show the correlations between Tmax and DTR for January and between Tmin and DTR for July. For Tmax in winter, there is overwhelmingly positive

correlation with some exceptions, notably negative correlation in "high latitude/elevation winter". For Tmin in summer, positive correlations are found under "mild" and/or "moist"/humid conditions, but negative correlations appear under arid condition. Thus Figures 4.12 and 4.13 enable examination of how the relationships between diurnal components of air temperature in the UIB compare both with those in adjacent regions and further afield.

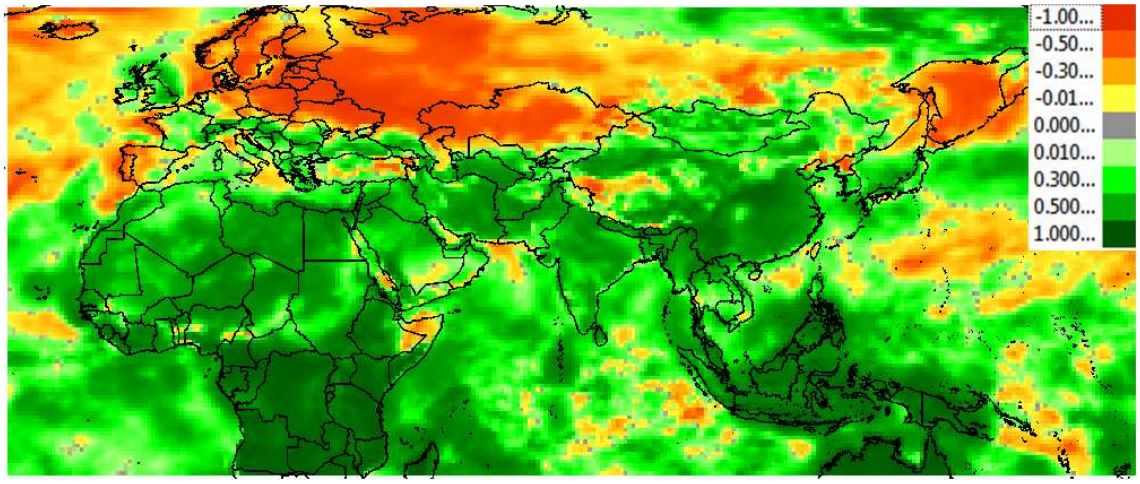

Figure 4.12 ERA-Interim, 1979 to 2007, Pearson's correlation between Tmax & DTR for January, Eurasia sub-domain.

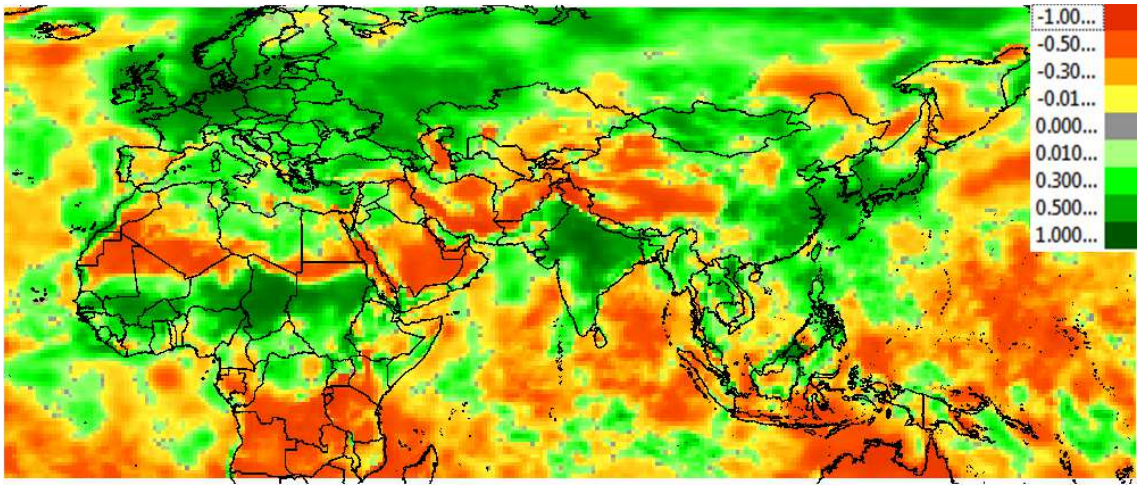

Figure 4.13 ERA-Interim, 1979 to 2007, Pearson's correlation between Tmin & DTR for July, Eurasia sub-domain.

4.3.3 Testing of relationships between air temperature variables from local observations and reanalysis

Before proceeding to a spatial investigation of causal relationships between near-surface air temperate and potential climate drivers, it was deemed useful to provide an additional metric of the validity of the gridded numerical data sources (ERA-Interim and PRECIS_ERA40) in representing the climate of the UIB. To do this, Pearson's

correlation coefficients were calculated between the local (PMD) observations and the air temperature variables from selected grid cells.

Figure 4.14 shows correlations in Tmax and DTR with locally observed air temperature values for three selected grid cells from ERA-Interim. Figure 4.15 provides the same for three selected grid cells from the PRECIS RCM simulation driven by ERA40. In both cases the selected grid cells were chosen to provide a range of climatic sub-regimes in the UIB catchments with the highest runoff contributions. Correlations between Tmax values from the gridded datasets and the range of air temperature variables from local observations are almost uniformly strongly positive. Correlations between gridded DTR and local observations are positive in "warm months" (May to October) for all three cells in PRECIS and the northern two cells in ERA-Interim, with negative correlations with Tmin in colder months. The southern cell (Vale.Srinagar) in ERA-Interim provides a fascinating case for the monsoonal months (June to August). Correlations here to local observations of Tmax and Tmin are negative – with meaningful statistical significance for Tmin – and only weakly positive to locally observed DTR. This will be the cell with the greatest degree of monsoonal weather system influence in its sub-climate. The differences in air temperature response under the contrasting sub-climates will receive further attention later in this Chapter.

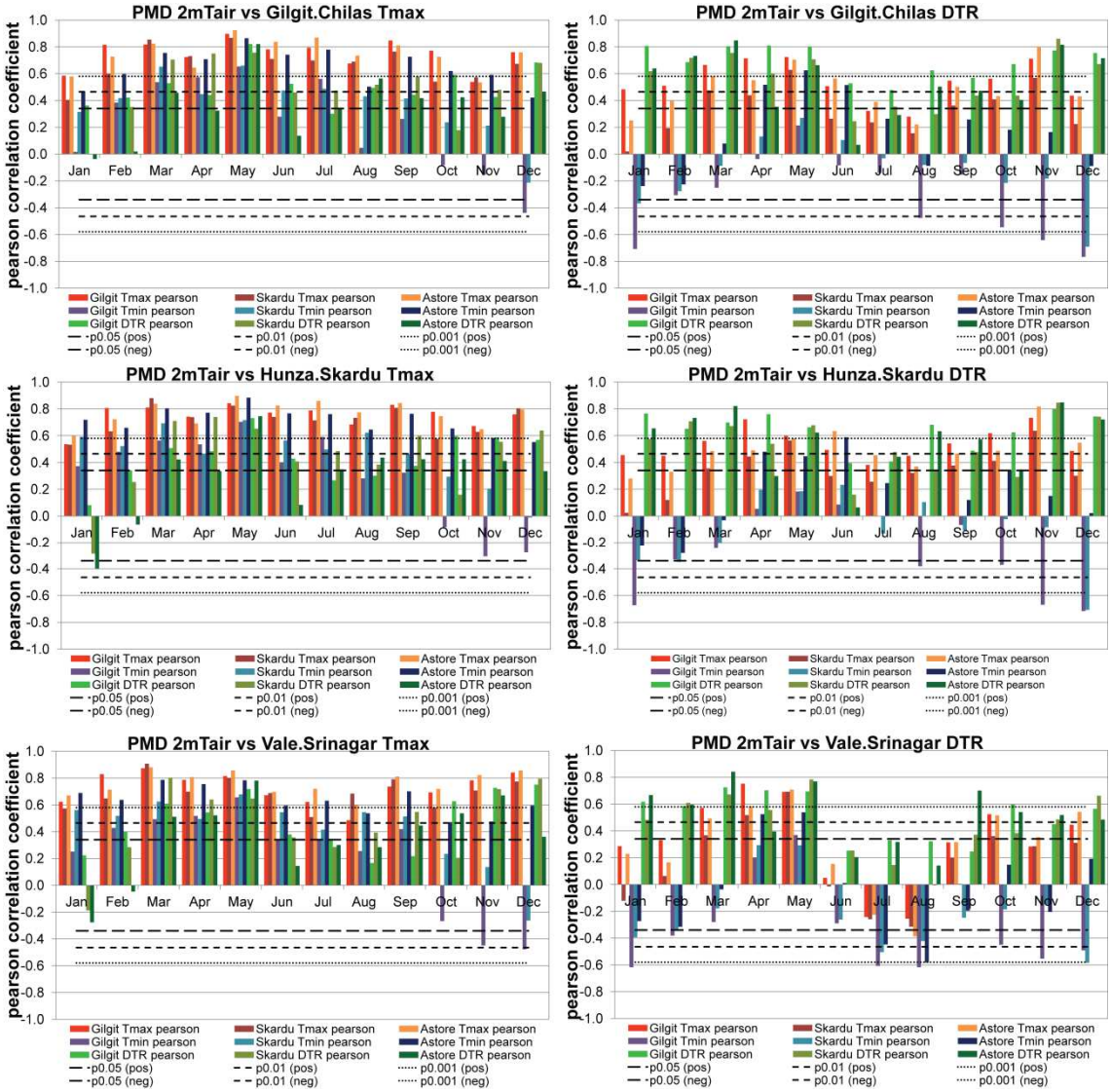

Figure 4.14 Pearson's correlation, 1979 to 2007, between near-surface air temperature diurnal components provided by ERA-Interim and local observations (PMD). The horizontal lines which indicate statistical significance thresholds are annotated by their "p-value" (e.g. "p0.01" for 99% significance). See section 4.2.5 for correspondence between Pearson's correlation coefficient, record length and statistical significance. Locations of the named grid cells and the local observation stations are given in Chapter 3.

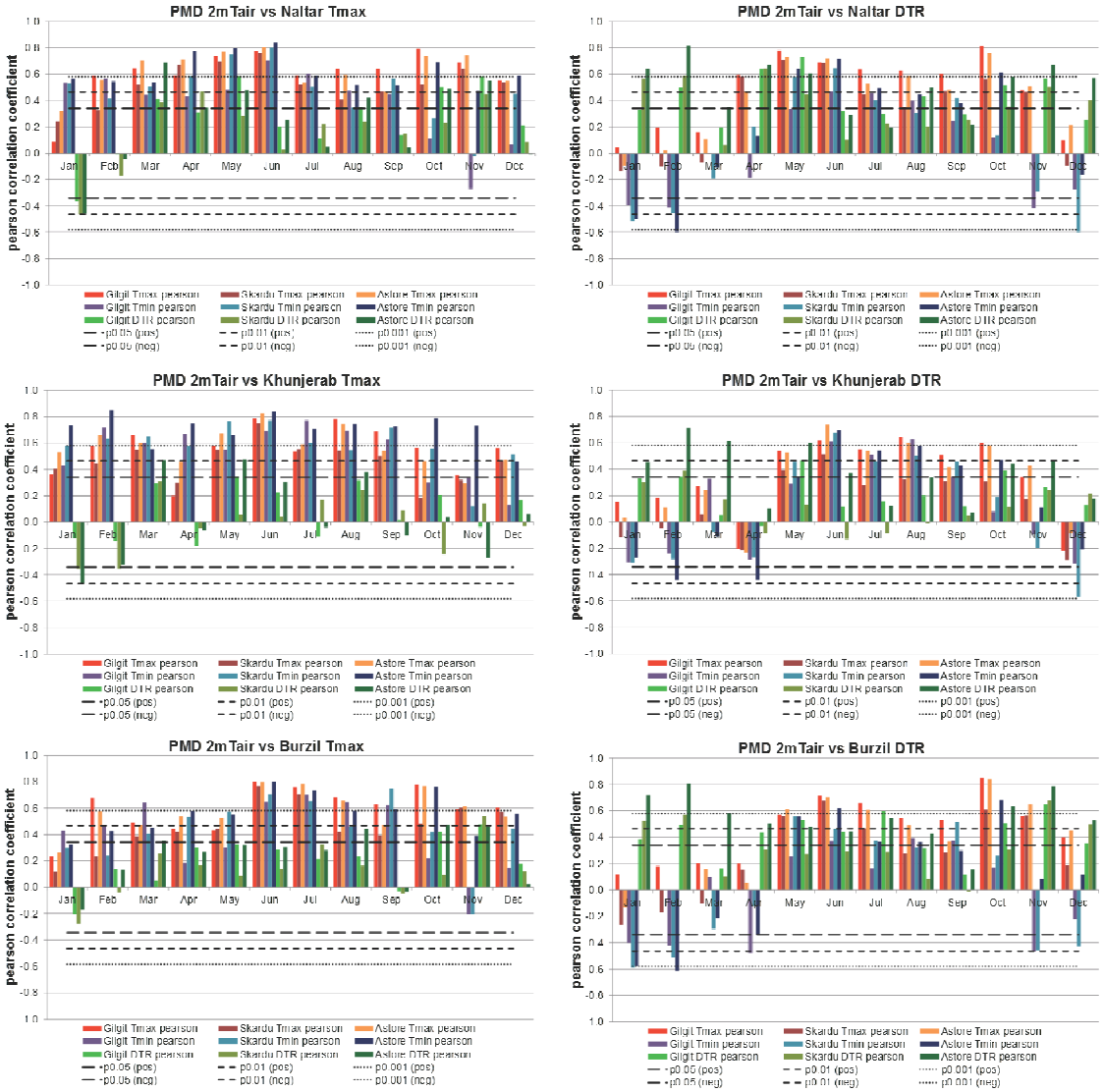

Figure 4.15 Pearson's correlation, 1961 to 1989, between near-surface air temperature diurnal components provided by PRECIS_ERA40 and local observations (PMD). The horizontal lines which indicate statistical significance thresholds are annotated by their "p-value" (e.g. "p0.01" for 99% significance). See section 4.2.5 for correspondence between Pearson's correlation coefficient, record length and statistical significance. Locations of the named grid cells and the local observation stations are given in Chapter 3.

4.4 Assessment of potential causal mechanisms of change

4.4.1 Conceptual presentation of potential forcings

In the search for causal mechanisms driving local trends in near-surface air temperature it is logical to begin by examining the local surface energy balance. In Chapter 3, a simplified conceptualisation of the components of the surface energy balance was presented in section 3.2 (Figure 3.001). Quantified examples of the daytime, night-time and net diurnal contributions of these components – as estimated by ERA-Interim for a sample grid cell – are presented in Figure 4.16. Figure 4.16 shows that, in terms of magnitude (kWh day^{-1} m^{-2}), incoming shortwave (solar) radiation is the

dominant factor in the UIB surface energy balance, but it is counterbalanced by the sum of the other three terms – net longwave (thermal) radiation, sensible heat flux and latent heat flux. At the sub-daily timescale, solar radiation is limited to day-time while thermal radiation is spread across the 24-hours albeit with greater day-time intensity. Although not strictly limited to daylight hours, the magnitudes of sensible and latent heat fluxes are effectively negligible in night-time as these processes are largely driven by incoming solar energy.

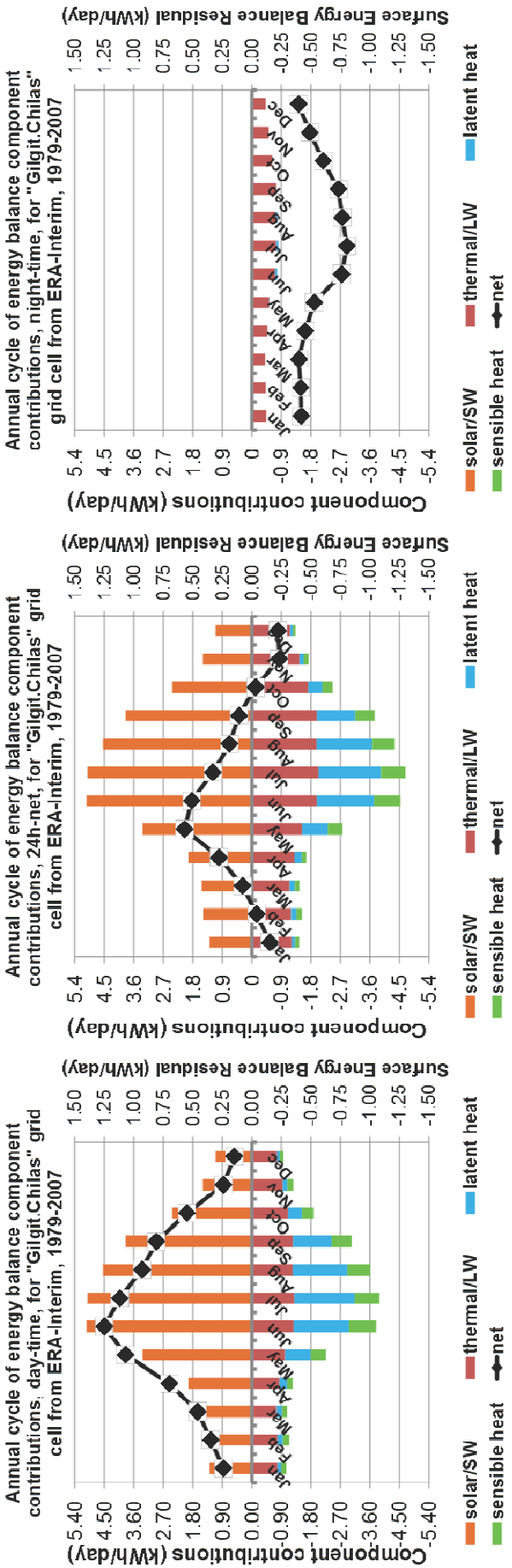

Figure 4.16 Surface energy balance (components and time-step residual) example from ERA-Interim for (a) day-time, (b) net daily and (c) night-time diurnal phases.

Figure 4.17 illustrates a simplified conceptualisation of how these energy balance components provide the proximal mechanisms by which larger-scale elements of atmospheric circulation affect local temperature. The resultant local climate will be shaped by both the characteristics (temperature, humidity) advected by air masses arriving through incoming weather systems as well as variability – and potentially feedbacks – in the local energy balance driven by cloud cover effects and surface processes which are influenced by these characteristics. Because cloud radiative effects (CRE) influence the surface energy balance components of greatest magnitude – i.e. incoming shortwave solar radiation and out-going long-wave thermal radiation – it could be expected that variations in cloud cover will play the dominant role in shaping local air temperature variability. By controlling the net surface energy balance, CRE will shape sensible heat flux. When the net surface energy balance is positive (negative), i.e. net absorption (emission) of energy by the surface, it can also be expected that sensible heat flux will be larger (smaller). The sign and magnitude of sensible heat flux quantifies the direction and amount of energy transfer between the ground surface and the near-surface air mass. The following sections describe work testing the relationships between both the energy balance components on assumed forcing mechanisms and between all of these and diurnal components of near-surface air temperature.

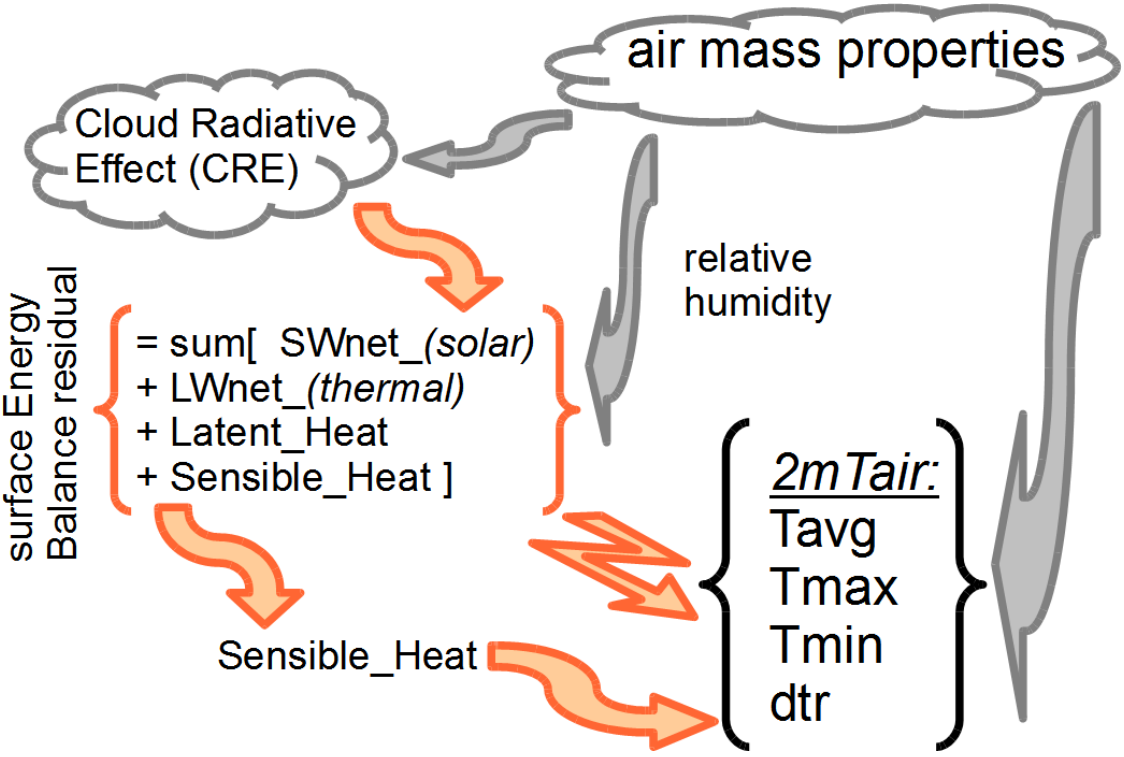

Figure 4.17 Simple conceptualisation of near-surface air temperature forcings.

4.4.2 Coherence of energy balance air-temperature relationships in ERA-Interim

To accurately represent real world physical processes and climatology (as demonstrated by correlations to local observations), one would first expect the ERA-Interim meteorological reanalysis to demonstrate consistent relationships between its own "internal" variables.

Figures 4.18 and 4.19 show respectively the spatial pattern of monthly correlation of daytime total cloud fraction (TCFday) with daytime energy balance residual (EBRday) and of night-time total cloud fraction (TCFnight) with night-time energy balance residual (EBRnight) for a domain containing the UIB and contiguous sub-regions. Figure 4.18 shows almost uniformly strong negative correlations throughout the domain and throughout the year. This is attributed to negative forcing on incoming solar shortwave energy, i.e. clouds reflecting the sun's energy back into space. Figure 4.19 shows almost uniformly positive correlations. This is attributed to positive forcing on outgoing thermal longwave energy, i.e. clouds preventing thermal energy from escaping by reflecting emitted energy back down to the surface.

In terms of statistical significance, as described in section 4.2.5, given the analysed record-length, grid cells with strong correlations exceed thresholds for meaningful significance, e.g. those with absolute correlations >0.365 are significant at 95% ($p = 0.05$) and those with absolute values >0.585 are significant at 99.9% ($p = 0.001$). Thus statistical significance can be visually gauged in Figures 4.18 and 4.19 as well as in subsequent figures in section 4.4 by comparing the relevant correlation threshold, e.g. 0.365 (and -0.365), to the colour scale keys contained within the figures.

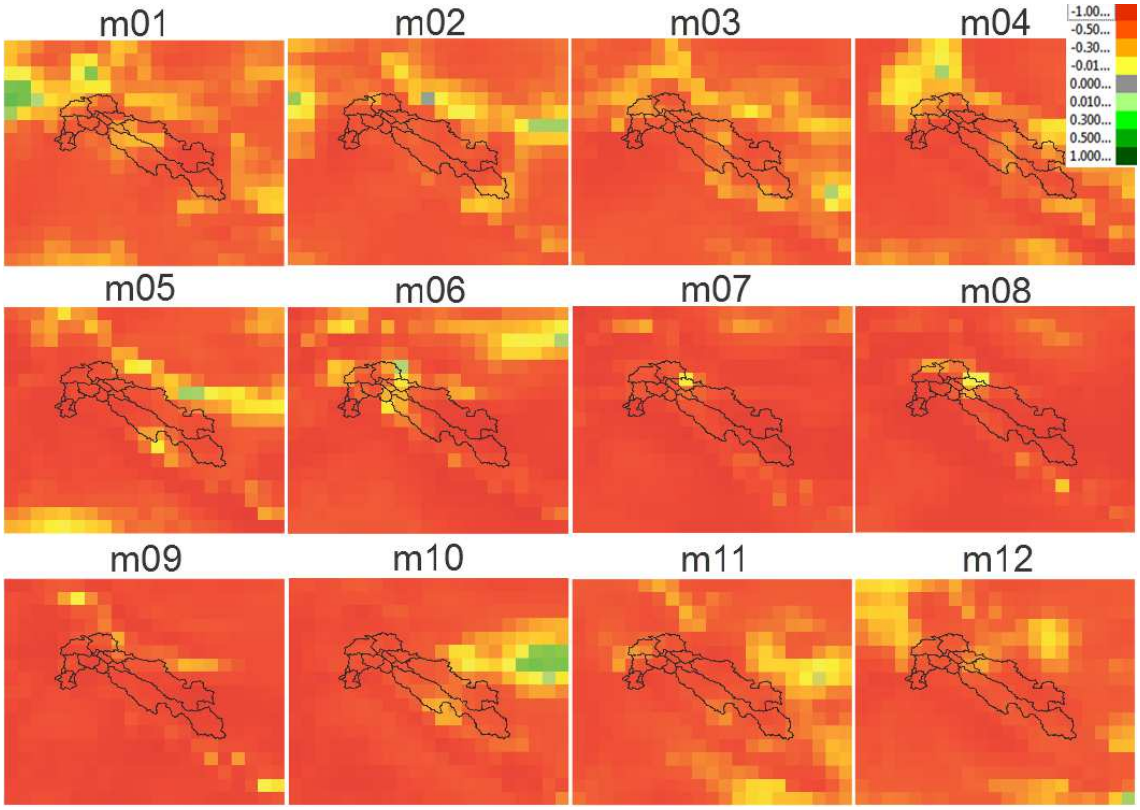

Figure 4.18 ERA-Interim, 1979 to 2007, Pearson's correlation between daytime total cloud fraction (TCFday) and daytime energy balance residual (EBRday).

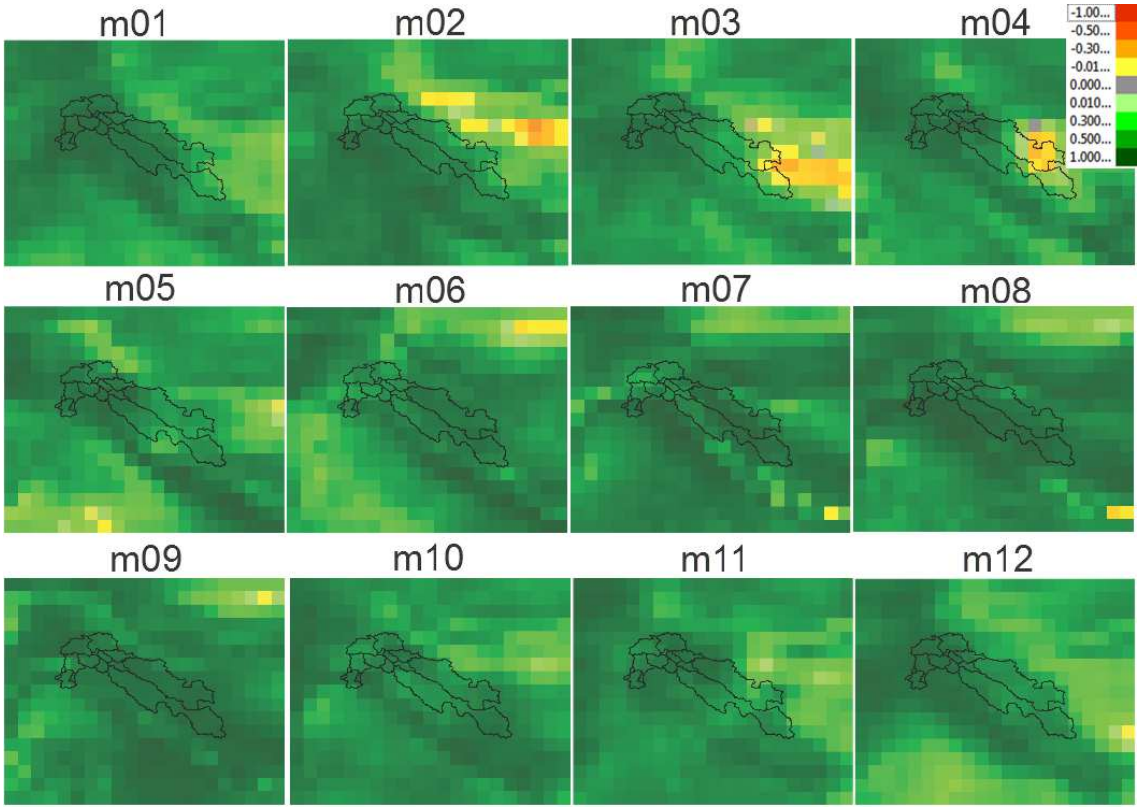

Figure 4.19 ERA-Interim, 1979 to 2007, Pearson's correlation between night-time total cloud fraction (TCFnight) and night-time energy balance residual (EBRnight).

The consistency of these relationships is reassuring, but greater insight can be found by examining the net effect of the individual daytime and night-time forcings, i.e. the correlation of average total cloud fraction (TCFavg) with the total daily energy balance residual (EBRtot) shown in Figure 4.20 where interesting seasonal (temporal) and sub-regional (spatial) patterns emerge. Positive correlations predominate in the cold months and in higher elevations while negative correlations predominate in the summer months and at lower elevations. These generalities, while true, oversimplify patterns which bear further detailed examination. In physical terms, a (net) positive correlation between TCFavg and EBRtot indicates that increasing cloud cover enhances energy absorption, or decreases emission, by the ground surface. Given the clear negative correlations between TCFday and EBRday, which are attributed to decreasing incoming shortwave radiation, it might be assumed that the cases of positive correlation between TCFavg and EBRtot indicate that CRE long-wave forcing is greater in magnitude than CRE shortwave forcing. By similar reasoning, (net) negative correlation between TCFavg and EBRtot thus implies that CRE shortwave forcing is greater in magnitude than CRE long-wave forcing. Negative TCFavg correlations with EBRtot are expected in the summer months when incoming shortwave solar radiation is greatest, whilst negative correlations are logical in the winter months when the ratio of shortwave to longwave radiation is lowest.

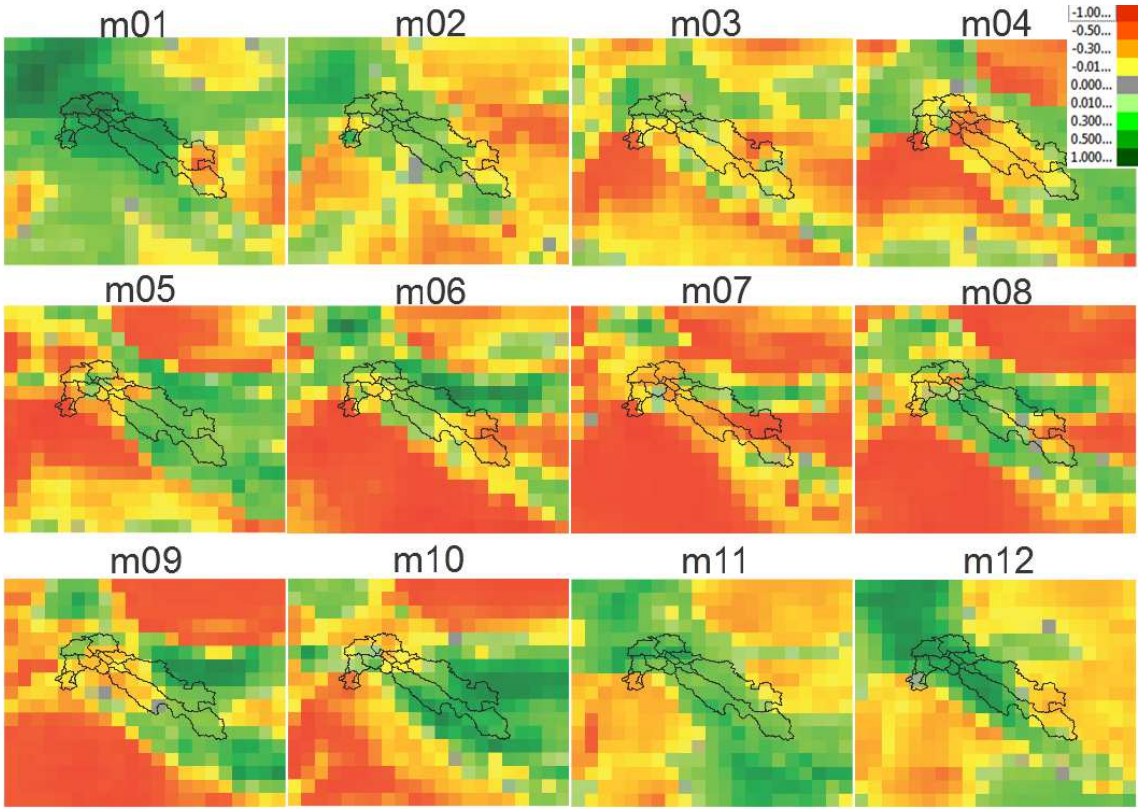

Figure 4.20 Pearson's correlation between mean total cloud fraction (TCFavg) and total daily energy balance residual (EBRtot) for ERA-Interim (1979 to 2007).

The most interesting results are thus cases where sub-regions have positive correlations in summer months or negative correlations in winter months. Examination of Figure 4.20 for such situations reveals that positive correlations can be found in mountainous/high-elevation grid cells in all months, with the lowest and weakest occurrences in July. Negative correlations can also be found in all months, but are most limited in January when they are restricted primarily to the Western Tibetan Plateau. The grid cells covering the core areas of the UIB show a mixture of positive and negative correlations for the months of the melt season (April to September). This may indicate the present delicate balance between the net positive and net negative effects of cloud radiative forcing. This instability (and uncertainty) complicates the evaluation of future climate scenarios because, even if the likely changes in cloud cover (frequency and extent) were accurately projected, the net radiative effect might be misrepresented.

4.4.3 Energy balance residual correlations to air temperature

The surface energy balance is a sophisticated approach to quantifying the energy available for land surface processes such as evaporation or snow and ice melt. Many engineering applications estimate this available energy using index methods based on near-surface air temperature, which is a more easily observed parameter. An example index method relevant to the present thesis is the "degree-day method" for calculation of snowmelt (e.g. Singh *et al*., 2000). In fact, at present there are no local observations of surface energy balance components in the UIB available to the scientific community. There are (as presented in Chapter 3), however, numerous multi-decadal records of daily air temperature variables (Tavg, Tmax, Tmin, DTR). For this reason, any "ground truthing" in terms of quantifying available energy will need to be based on air temperature observations. Therefore, it is important to establish a conceptual bridge between the ERA-Interim reanalysis treatment of the surface energy balance and local observations of air temperature. This bridge is formed by first understanding the internal relationships in ERA-Interim between surface energy balance and air temperature.

Figures 4.21, 4.22 and 4.23 show the correlations respectively of Tavg with EBRtot, Tmax with EBRday, and Tmin with EBRnight. Positive correlations indicate that warmer (cooler) than average temperatures occur when the surface is absorbing more (less) energy than average. Negative correlations indicate that warmer (cooler) than average temperatures occur when the surface is emitting more (less) energy than

average. Once again, statistical significance levels in these Figures can be surmised from the magnitude of the correlation coefficient as described in section 4.2.5.

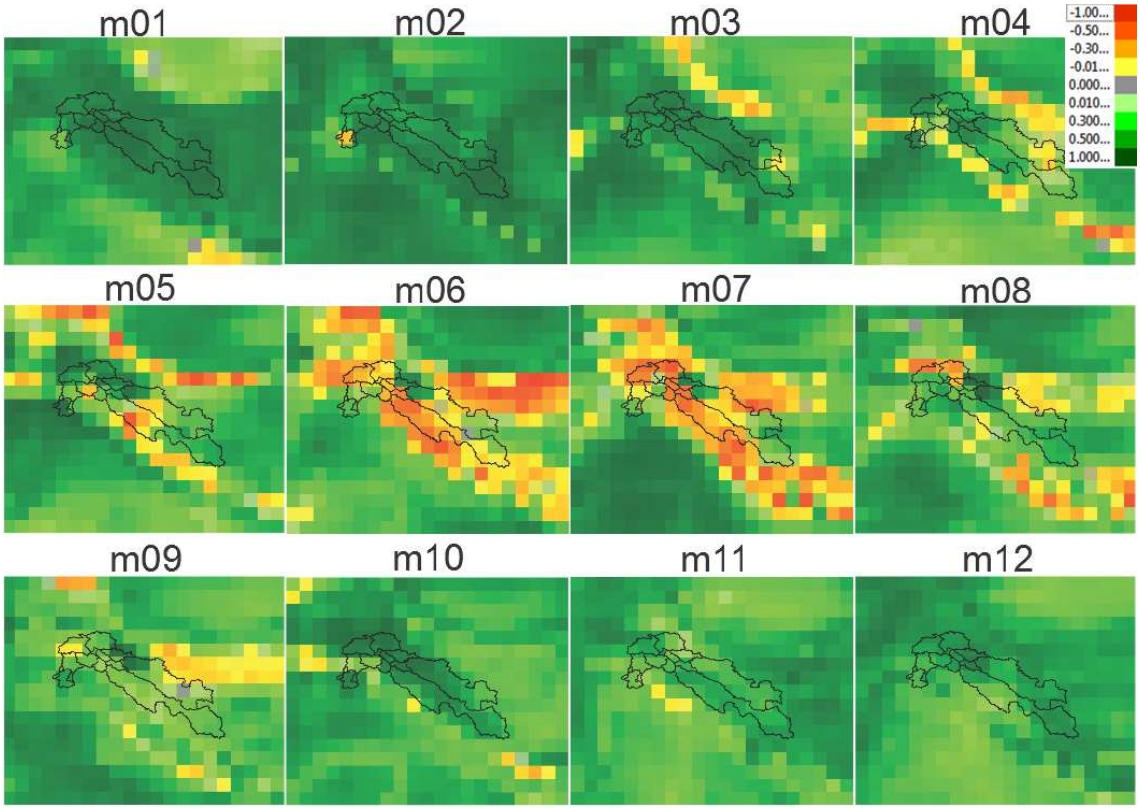

Figure 4.21 Pearson's correlation between total daily energy balance residual (EBRtot) mean daily 2m air temperature (Tavg) for ERA-Interim (1979 to 2007).

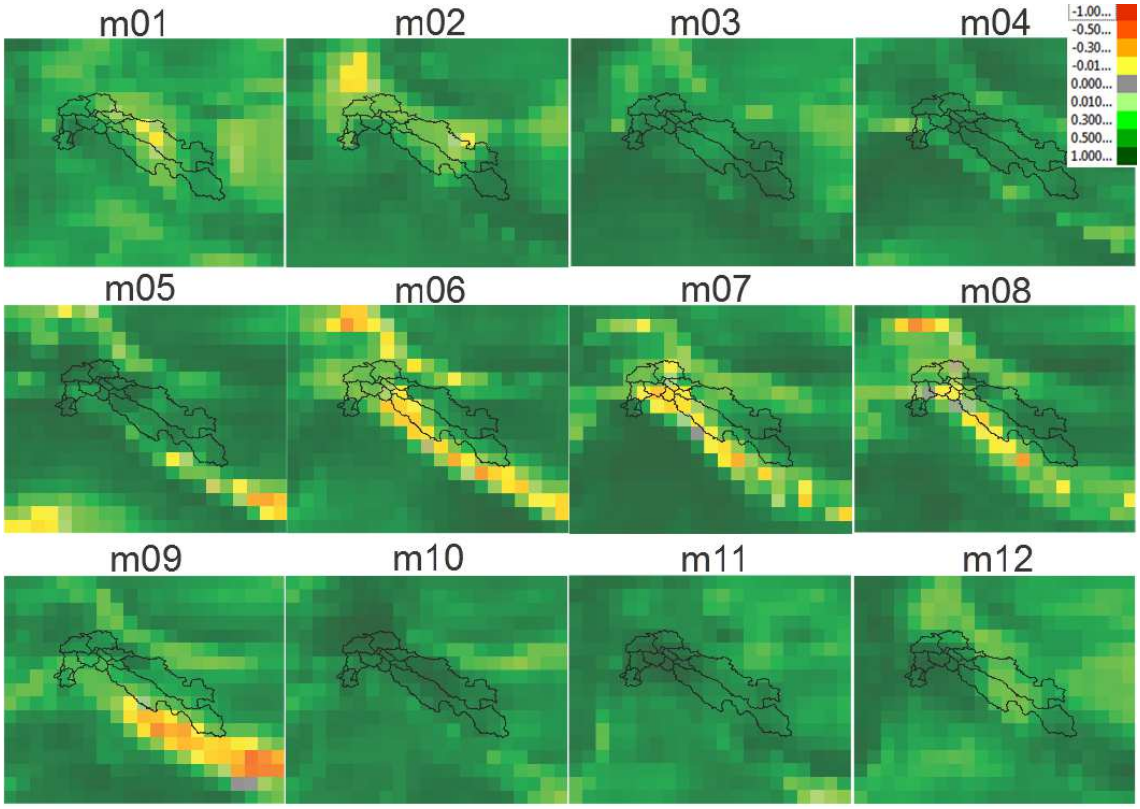

Figure 4.22 Pearson's correlation between day-time energy balance residual (EBRday) and daily 2m maximum air temperature (Tmax) for ERA-Interim (1979 to 2007).

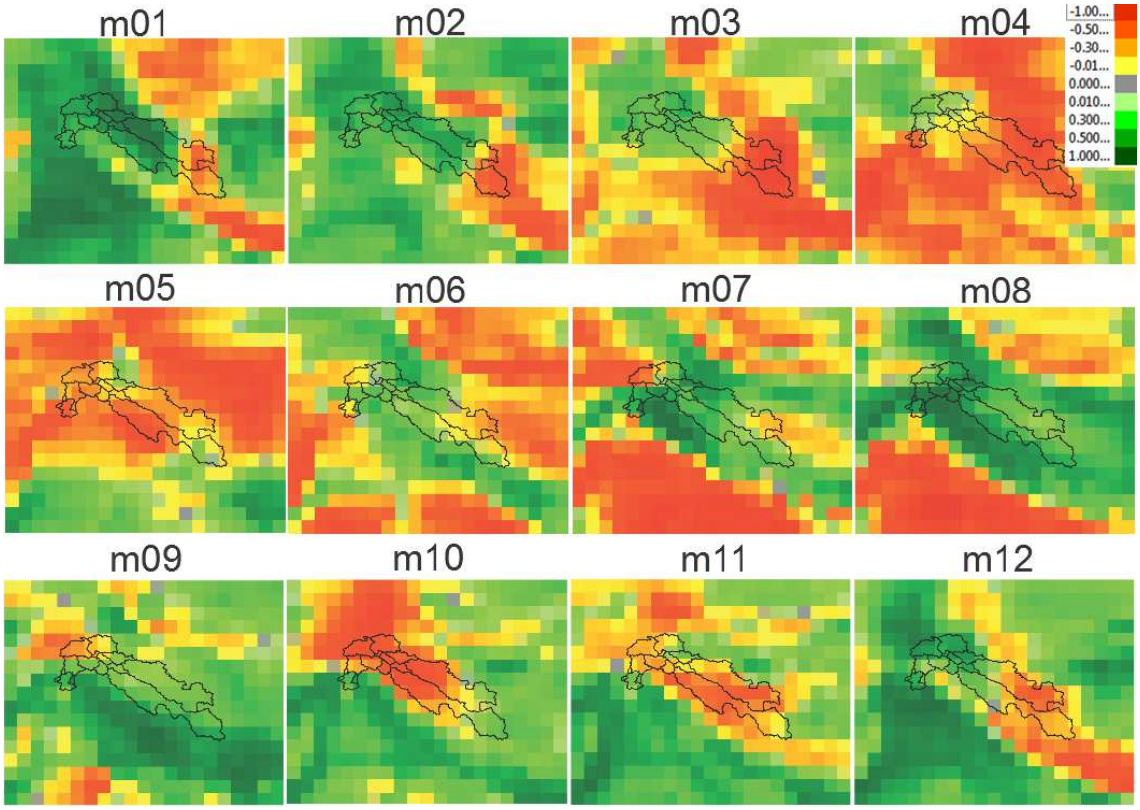

Figure 4.23 Pearson's correlation between night-time energy balance residual (EBRnight) and daily 2m minimum air temperature (Tmin) for ERA-Interim (1979 to 2007).

Tavg correlations to EBRtot (Figure 4.21) are relatively simple. Correlations are positive throughout the selected domain except during the melt season when negative correlations are present in a footprint with a spatial extent that to some degree resembles the area experiencing extensive seasonal snow and glacier melt. Correlations between Tmax and EBRday (Figure 4.22) are similar to those for Tavg but have even stronger positive values and fewer and weaker negatives.

Results of Tmin correlation to EBRnight (Figure 4.23), however, are substantially more complicated. There appear to be coherent sub-regions which, although they expand and contract through seasonal transitions, exhibit uniform annual cycles. The Indo-Gangetic plains adjacent to, and south of, the Himalayan mountain arc behave as a coherent unit throughout the year. In this sub-region during the cold months (September to February), correlations of Tmin with EBRnight are positive, while in warm months (March to August) they are negative. For much of the year the western and eastern sections of Himalayan mountain arc have opposite signs in their correlations of Tmin with EBRnight. The western section corresponds primarily to the northwest UIB (highest runoff area) along with the adjacent Hindu Kush and Pamir ranges, while the eastern section corresponds to the Central Himalaya, although the boundary moves longitudinally with seasonal transitions. From December to April the western section

has positive Tmin to EBRnight correlations while the eastern section shows negative values. In the summer/monsoonal months (June to September), however, the mountain arc appears to behave as a single sub-region. During this period Tmin to EBRnight correlations are positive, albeit of varying strengths, in the sub-region. Physical mechanisms to explain the complexity of the relationship between Tmin and EBRnight have not yet been fully identified, but remain the subject of on-going investigation.

4.4.4 Sensible heat flux correlations to energy balance residual and air temperature

Another mechanism to consider in understanding air temperature forcings is sensible heat flux which should, in theory, be a primary pathway between variability in the surface energy balance and air temperature responses.

Figures 4.24 and 4.25 respectively show correlations of daytime sensible heat flux (SHFday) with daytime energy balance residual (EBRday) and of night-time sensible heat flux (SHFnight) with night-time energy balance residual (EBRnight). It is important to bear in mind the effect of the sign convention on the correlation results. Because energy transfer from the surface to the air (emission) is negatively signed in ERA-Interim while net energy absorption by the surface is positively signed, if greater than mean total energy absorption corresponds to greater (magnitude) than mean sensible heat flux, the correlation value will be negative. If greater than mean total energy absorption corresponds to lesser (magnitude) than mean sensible heat flux, however, the correlation value will be positive.

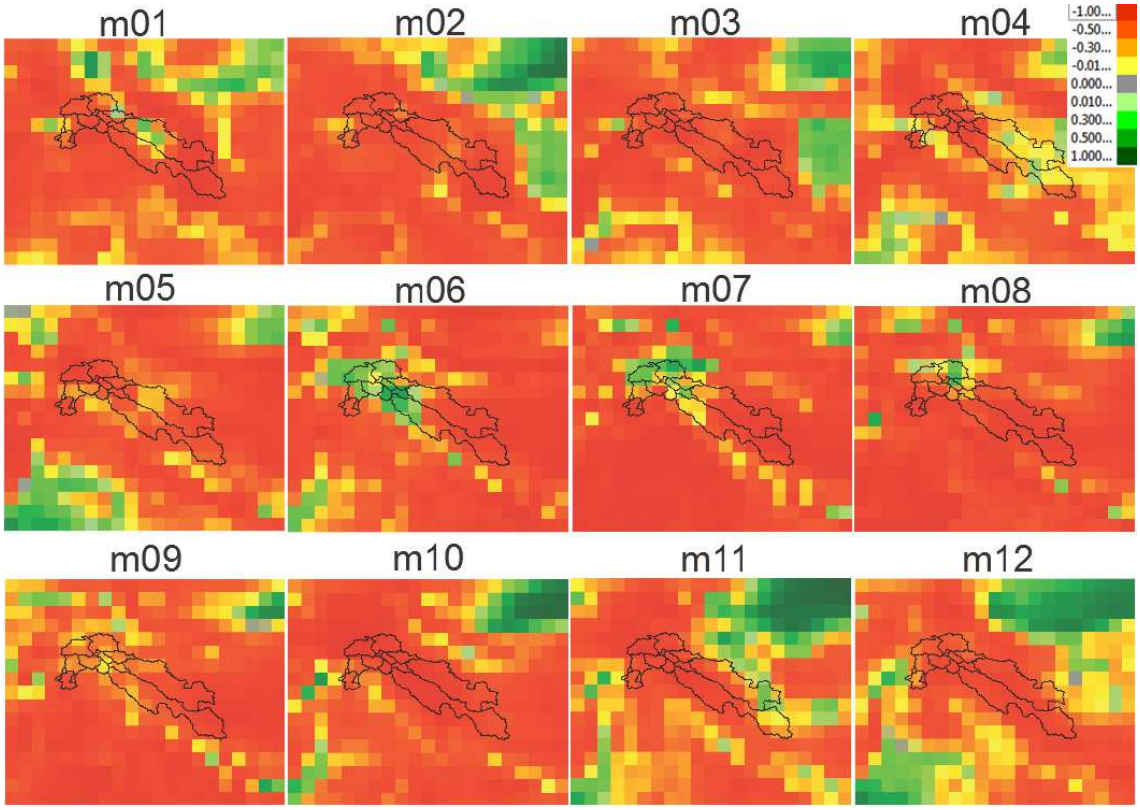

Figure 4.24 Pearson's correlation between day-time energy balance residual (EBRday) and daytime sensible heat flux (SHFday) for ERA-Interim (1979 to 2007).

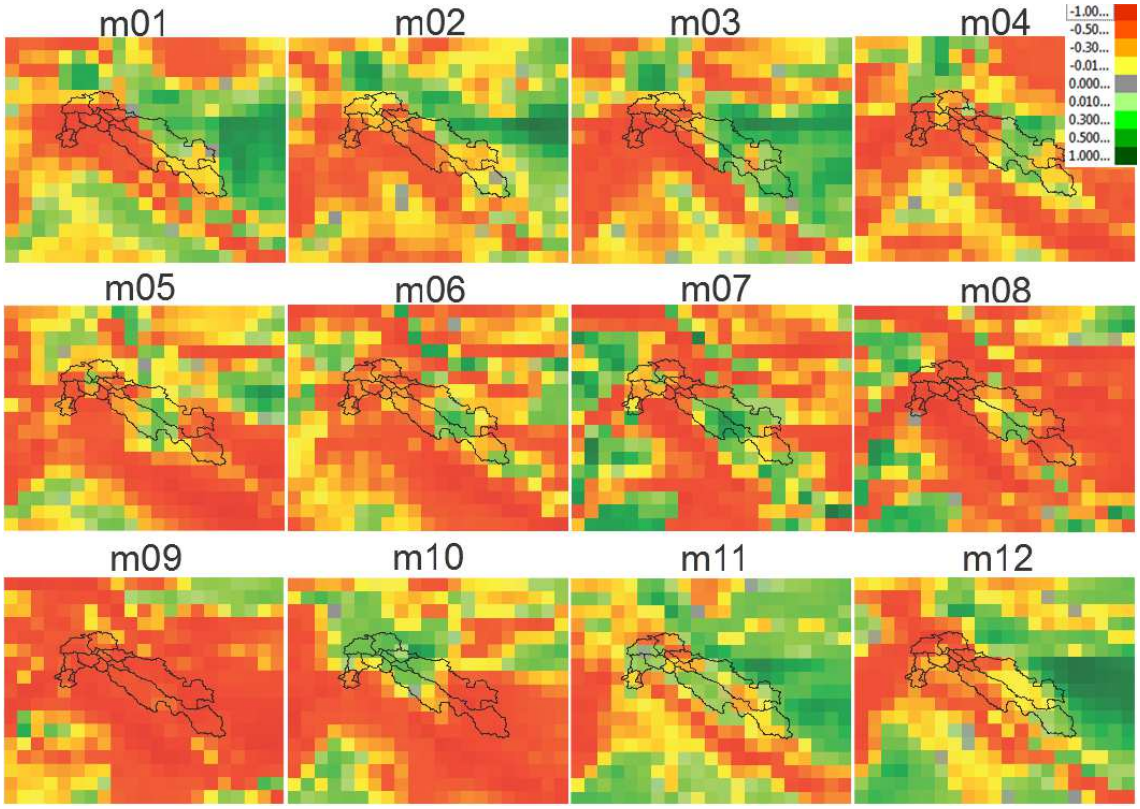

Figure 4.25 Pearson's correlation between night-time energy balance residual (EBRnight) and night-time sensible heat flux (SHFnight) for ERA-Interim (1979 to 2007).

With the exception of the summer/monsoonal months (June to August), correlations of SHFday to EBRday (Figure 4.24) are uniformly negative for the bulk of the domain. In June and July, and to a lesser extent August, there is a small sub-region focused on the north-western UIB where correlations are positive. This indicates that, contrary to the rest of the domain, greater magnitude sensible heat flux occurs in a climate with less total energy exchange. This discrepancy might be due to partitioning of energy in the identified months (June to August) into latent heat flux – resulting from state changes in water (e.g. snowmelt or evapotranspiration) – yielding less energy transfer by sensible heat flux. Nevertheless water state changes have not yet been identified as the physical mechanism responsible for this discrepancy. Identification of the physical mechanism is a key research priority because understanding of the partitioning of the surface energy balance is crucial to understanding future climate and land surfaces responses to radiative forcings associated with climate change.

Figure 4.25 shows that the patterns of correlation between SHFnight and EBRnight are considerably more complex than their day-time counterparts. A positive correlation is found over the western Tibetan Plateau and Kunlun Shan from November through March. Conditions over the Indo-Gangetic plain are mixed. Correlations along the front range of the Himalayan arc, however, are consistently negative.

Despite the uncertainty associated with the consistency of the relationship between sensible heat flux and energy balance residual, the inter-variable relationships within ERA-Interim between sensible heat flux and air temperature could still yield insights into the causal mechanisms shaping air temperature variability and therefore bear examination. Once again because of the sign conventions in ERA-Interim, where warmer temperatures correspond to greater magnitude sensible heat flux, correlation values will be negative.

Figures 4.26 and 4.27 show respectively the correlations of Tmax with SHFday and Tmin with SHFnight. Correlations between Tmax and SHFday (Figure 4.26) are almost interchangeable with those between SHFday and EBRday. In other words, the widespread negative correlations indicate a link between the increased magnitude of sensible heat flux and warmer than average temperatures. This pattern is disrupted in the summer/monsoonal (June to September) months, however, when positive correlations are found centred on the northwest UIB and along the front range of the Central Himalaya.

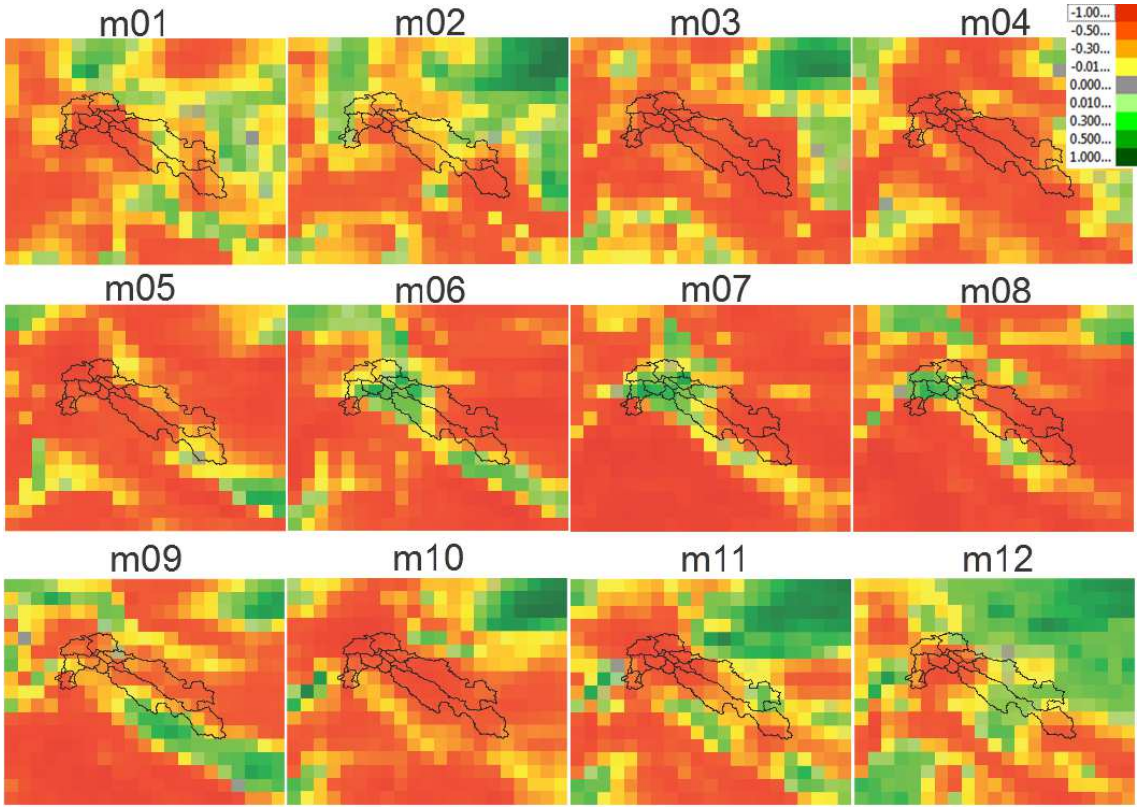

Figure 4.26 Pearson's correlation between day-time sensible heat flux (SHFday) and Tmax for ERA-Interim (1979 to 2007).

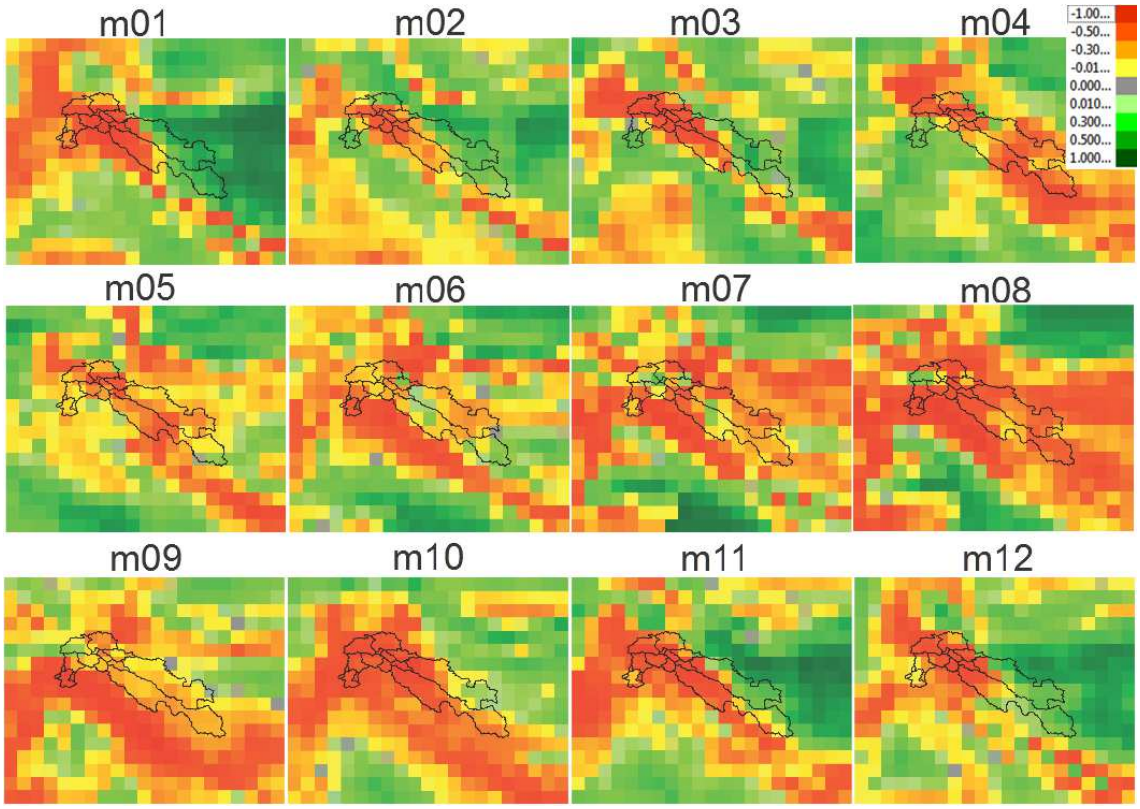

Figure 4.27 Pearson's correlation between night-time sensible heat flux (SHFnight) and Tmin for ERA-Interim (1979 to 2007).

Positive correlations indicate warmer near-surface daily maximum air temperature (Tmax), with smaller transfer of sensible heat from the surface to the air. This could be because land surface temperatures are suppressed by the presence of standing snow and ice cover. In this case seasonal air temperatures rise above freezing, while surface temperature is limited to 0°C until snow and ice cover is fully ablated. If near-surface air temperature is greater than surface temperature, the direction of energy transfer will be away from the air and toward the ground surface. This would account for the positive correlations being largely limited to combinations of grid cells and months where substantial snowmelt is expected. Nevertheless, a broader view of the spatial domain reveals positive correlations in areas unlikely to have snow cover thus additional physical mechanisms may be modulating the relationship between air temperature and sensible heat flux.

Given the relatively small magnitude of SHFnight compared with other energy balance components, the importance of correlations between Tmin and SHFnight should perhaps not be overestimated because it may well not be the dominant factor. Nevertheless the coherence of spatial patterns found in Figure 4.27 is intriguing. As with other inter-variable correlations in night-time parameters, there appear to sub-regions which show coherent behaviour. The core north-western (NW) UIB shows consistent negative values except for during the summer/monsoonal months (June to September) when a handful of grid cells show positive correlations.

Earlier in this section, it was suggested that positive correlation between day-time diurnal components of sensible heat flux and near-surface air temperature may be due to a physical limitation of maximum land surface temperature by the presence of snow or icepack. With regards to night-time relationships between sensible heat flux and near-surface air temperature, however, the broader spatial patterns appear generally opposite to their day-time counterparts. Positive correlations at night are much more widespread and primarily limited to areas with limited topographic relief, especially at lower elevations. Positive correlations within the core NW UIB are extremely limited. While a physical mechanism for the broader positive night-time correlations is not immediately apparent, the opposite sign of day-time and night-time correlations between sensible heat flux and near-surface air temperature in the UIB might be due to the effective absence of night-time latent heat flux. The diurnal cycle of latent heat flux suggests that both snowmelt and evapotranspiration are limited to day-time when incoming solar energy is available to drive these processes. The absence of latent heat flux may result in additional energy partitioning to sensible heat flux during night-time.

4.4.5 Detailed point-based (grid cell & station) examination of potential causal mechanisms

While spatial approaches are useful in understanding the geographic extent of climate processes and phenomena – including trends and inter-variable relationships – it can be difficult to visualise quantitative differences when displayed as colour spectra. Furthermore, "ground truthing" of causal mechanisms requires testing of relationships between indicators of potential forcings and local observations of the key climate variables of interest. Thus it is imperative to examine correlations between results from individual grid cells and local meteorological stations.

Figure 4.28 shows correlations of mean total cloud fraction (TCFavg) and (net) total energy balance residual (EBRtot) with locally observed air temperature variables (PMD) for the three ERA-Interim grid cells already used in this Chapter. The behaviour of the two northern cells, Gilgit.Chilas and Hunza.Skardu, is quite similar and follows expected patterns: correlations of air temperature variables with TCFavg are consistently negative with the exception of Tmin in cold months (October to March) when positive correlations are found. The southern cell, Vale.Srinagar, in contrast, mirrors these patterns except during the summer/monsoon months (June to August) when correlations of TCFavg to air temperature variables are weak or positive except for DTR which remains negative. Notably, these positive correlations for Tmin in July and for Tmax and Tmin in August are statistically significant.

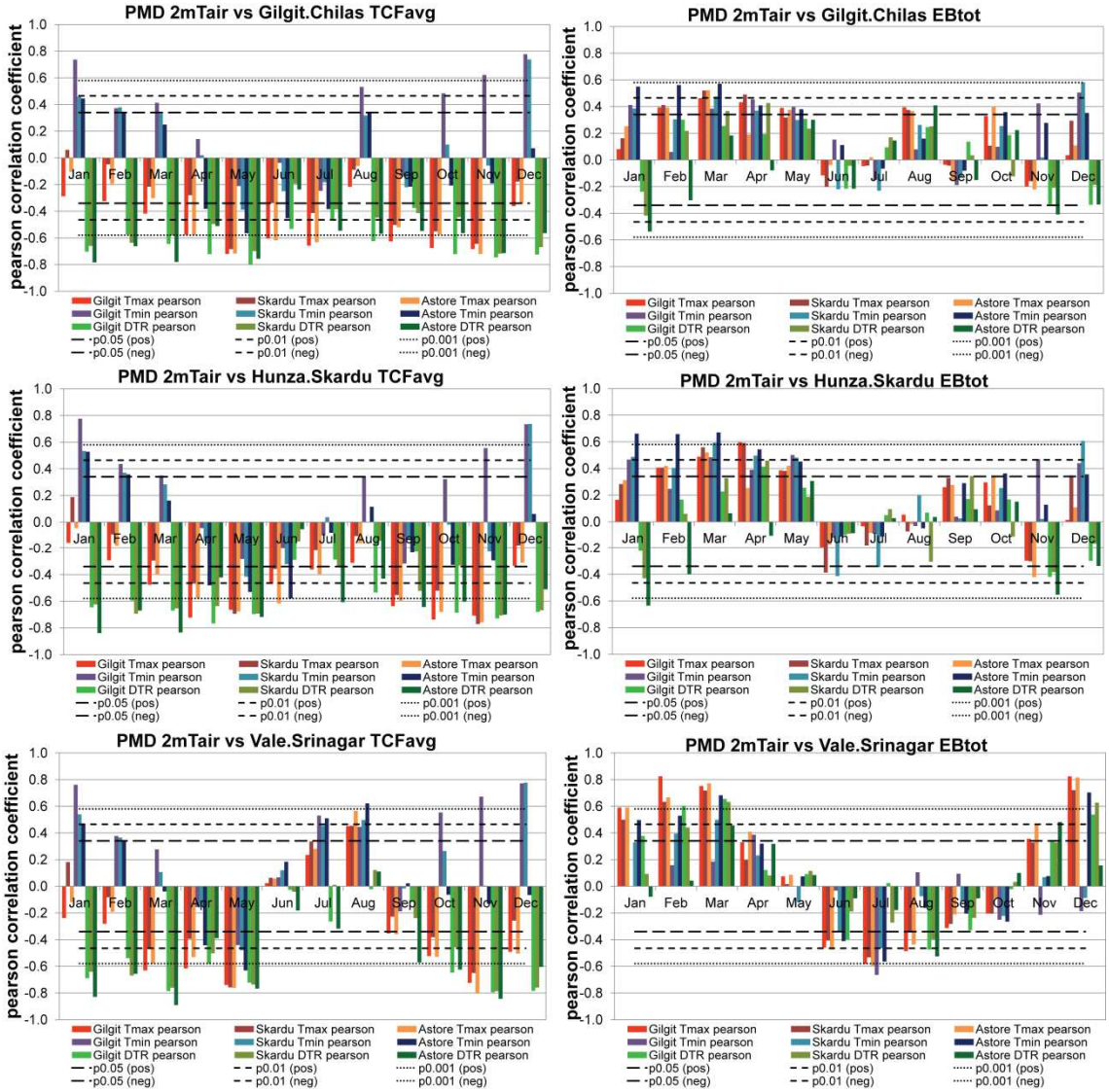

Figure 4.28 Pearson's correlation between ERA-Interim total cloud fraction (TCFavg) and near-surface air temperature components from local observations (PMD), 1979 to 2007.

This does not imply that the conditions modelled in this grid cell are present over and around the UIB observing stations, but that the moderately coarse spatial resolution – 0.75 decimal degrees (~80km) – of the ERA-Interim reanalysis does not allow for simulation of the topographic features and gradients which shape local circulation and surface processes. As can be deduced from the annual cycles of locally observed DTR presented in Chapter 3 (shown here again in Figure 4.29), however, a limited but non-negligible amount of monsoonal influence exists throughout the UIB. Given this and the paradoxical temperature trends presented early in this Chapter, the ERA-Interim cells with both high elevation and substantial monsoonal influence may provide insight into the physical mechanisms responsible for these trends.

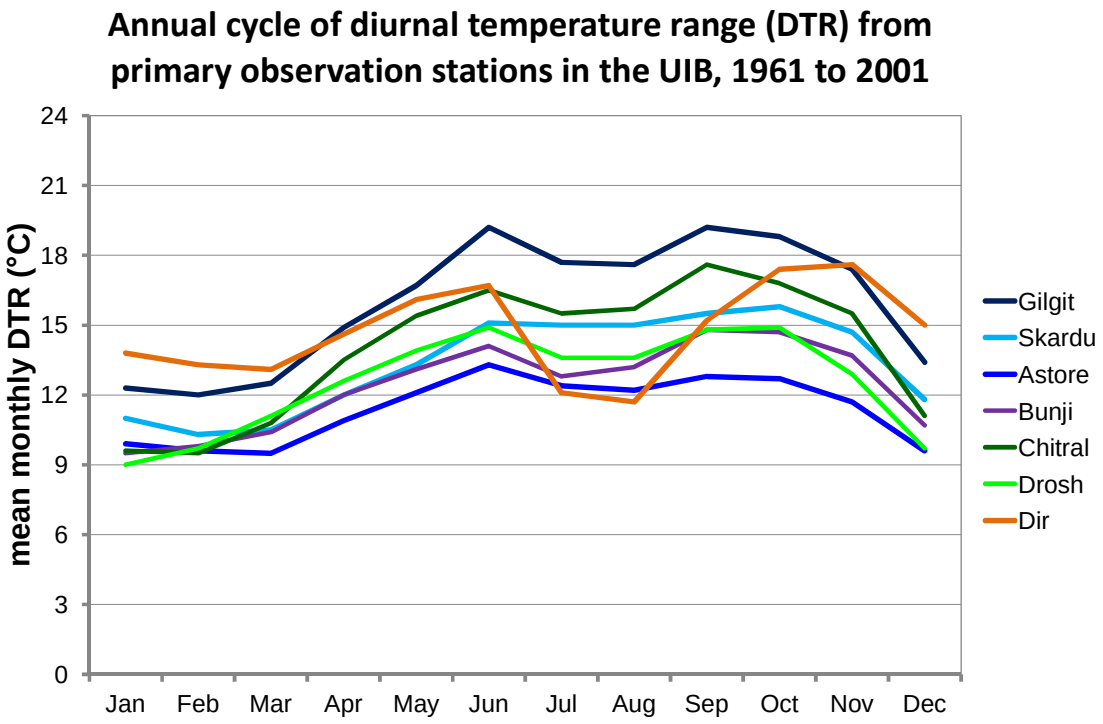

Figure 4.29 Mean annual cycle (1961 to 2001) of diurnal range in near-surface air temperature (DTR) from local observations (PMD). DTR is defined here as Tmax minus Tmin.

It is important to reiterate that values provided by ERA-Interim are not observations. The ECMWF reanalysis assimilates observations to provide a best-fit analysis of initial conditions, for some parameters including air temperature and cloud cover, and then performs simulations to forecast accumulating variables including precipitation and radiative fluxes (Dee *et al.*, 2011). There are thus two levels of uncertainty introduced by the reanalysis process: first during the synthesis and homogenisation of available observations into a coherent set of initial conditions and, second, by the forecasting simulations used to predict the accumulating fields.

Paradoxical relationships between cloud cover and air temperature are not a foregone conclusion in numerical simulation of zones with monsoonal influence, as can be seen in Figure 4.34. This shows correlations between TCFavg from two grid cells of the PRECIS simulation driven by ERA40 and local observations of air temperature. The two grid cells have a latitudinal separation of 2 decimal degrees for their cell centres – roughly 250km north-south distance – and 1.5 decimal degrees for their cell boundaries. The more southerly cell, Burzil, would be expected to experience a substantial degree of monsoonal influence although not a fully monsoonal climate sub-regime in terms of temperature and precipitation seasonality. Both cells, however, have highly similar annual cycles of correlation between cloud cover and local observations of air temperature. This divergence with the results from ERA-Interim may be due to a

difference between the model physics used by PRECIS and that used in the forecast system employed by ERA-Interim. Alternatively, it could be due to differences between the cloud climatologies from ERA40 (use to drive PRECIS) and ERA-Interim.

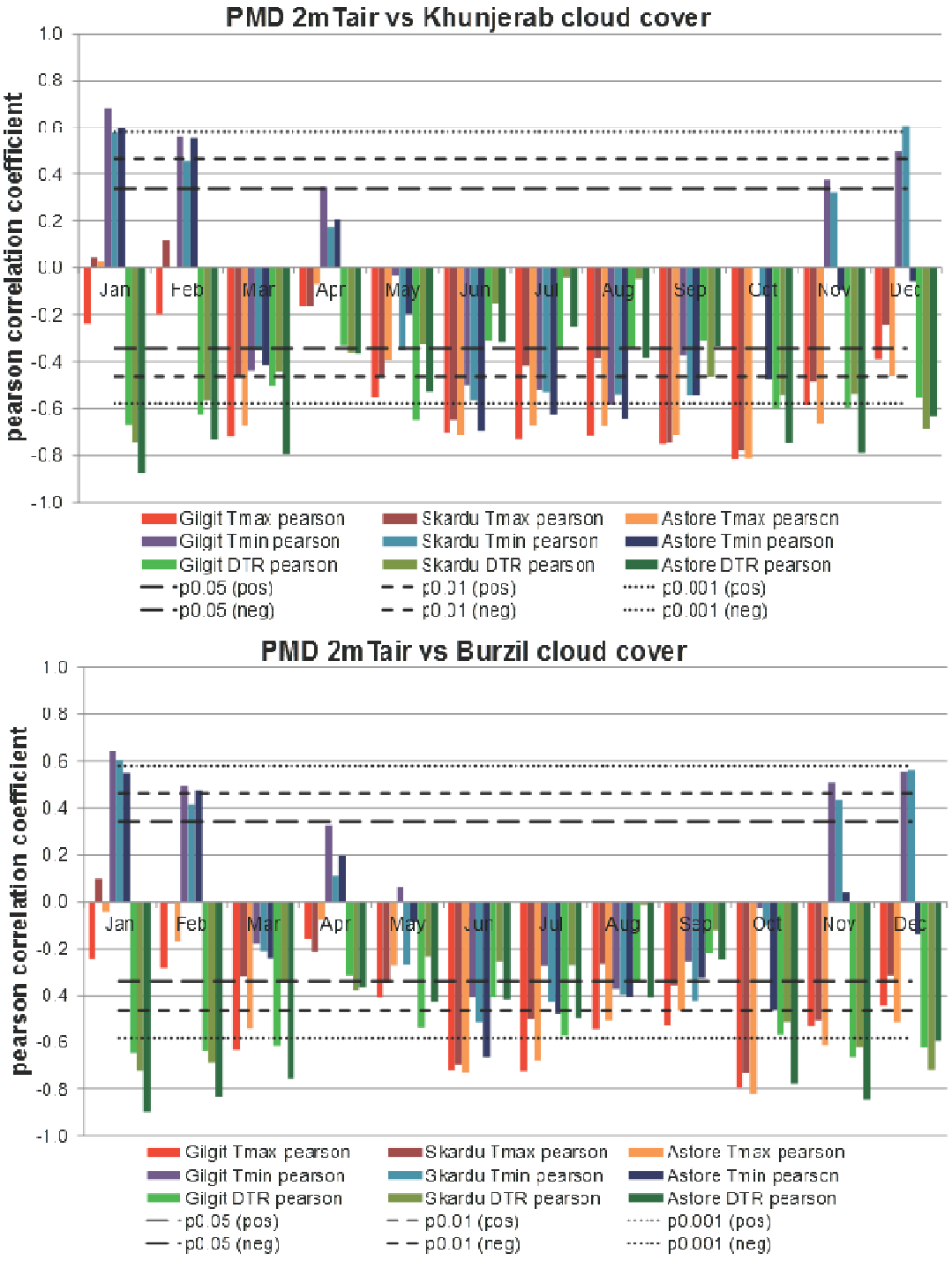

Figure 4.30 Pearson's correlation between PRECIS driven by ERA-40 total cloud fraction (TCFavg) and 2m air temperature (Tair) components from local observations (PMD) for 1961 to 1989.

Returning the focus to the components of the surface energy balance modelled by ERA-Interim, Figure 4.35 shows the correlations of local air temperature observations with net solar shortwave (SWnet) and net thermal longwave (LWnet) radiation, while Figure 4.36 presents the correlations of net sensible heat flux and net

latent heat flux with locally observed air temperature. SWnet correlations for the northern two cells are as would be expected, with positive correlations to Tmax and DTR in all months and Tmin showing negative correlations in winter and positive correlations in warm months. The southern cell, Vale.Srinagar, shows the same patterns except during summer/monsoonal months when correlations are negative with both Tmax and Tmin.

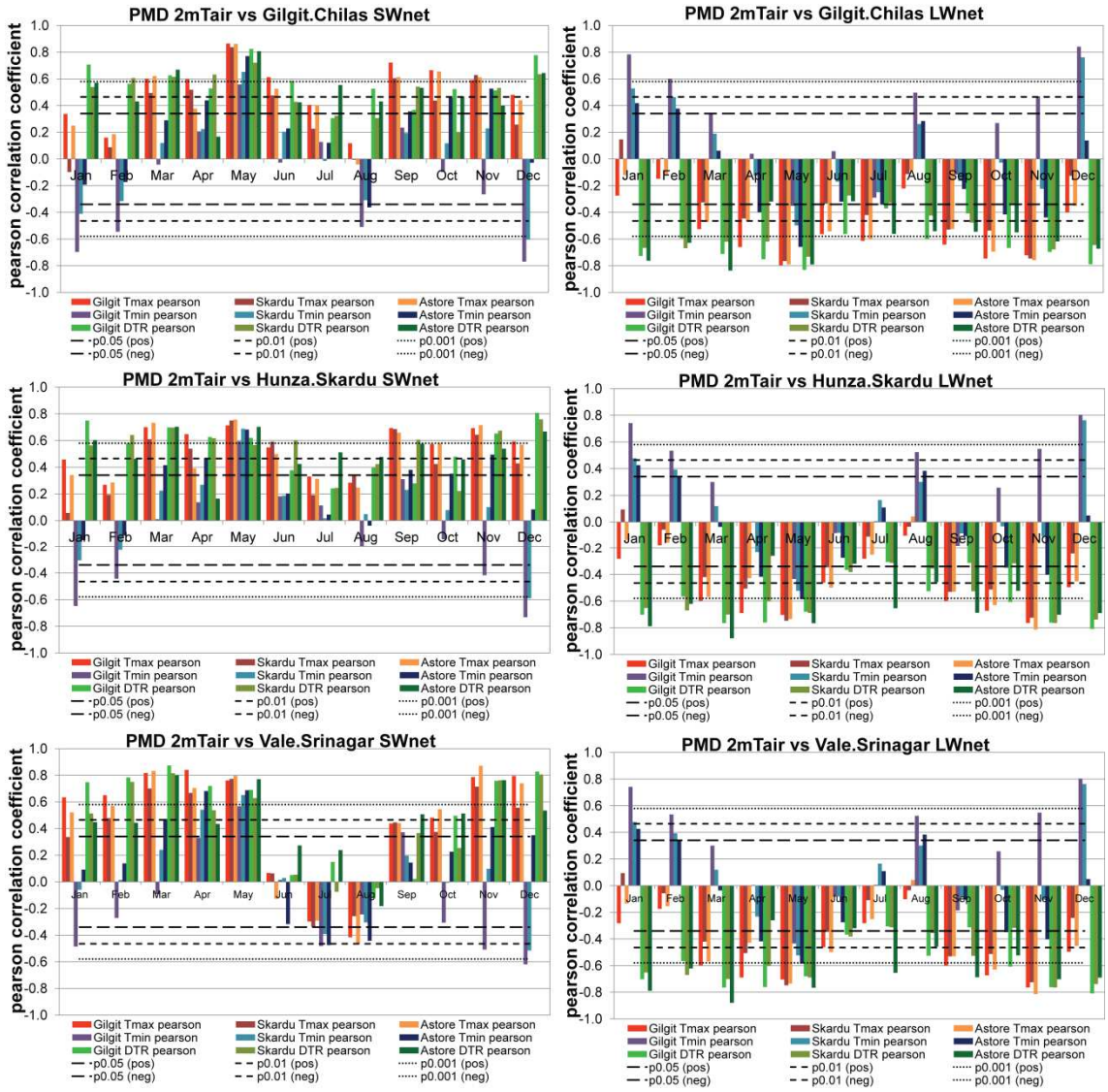

Figure 4.31 Pearson's correlation, between ERA-Interim energy balance components – net shortwave (SWnet) and net long-wave (LWnet) – and near-surface air temperature components from local observations (PMD), 1979 to 2007.

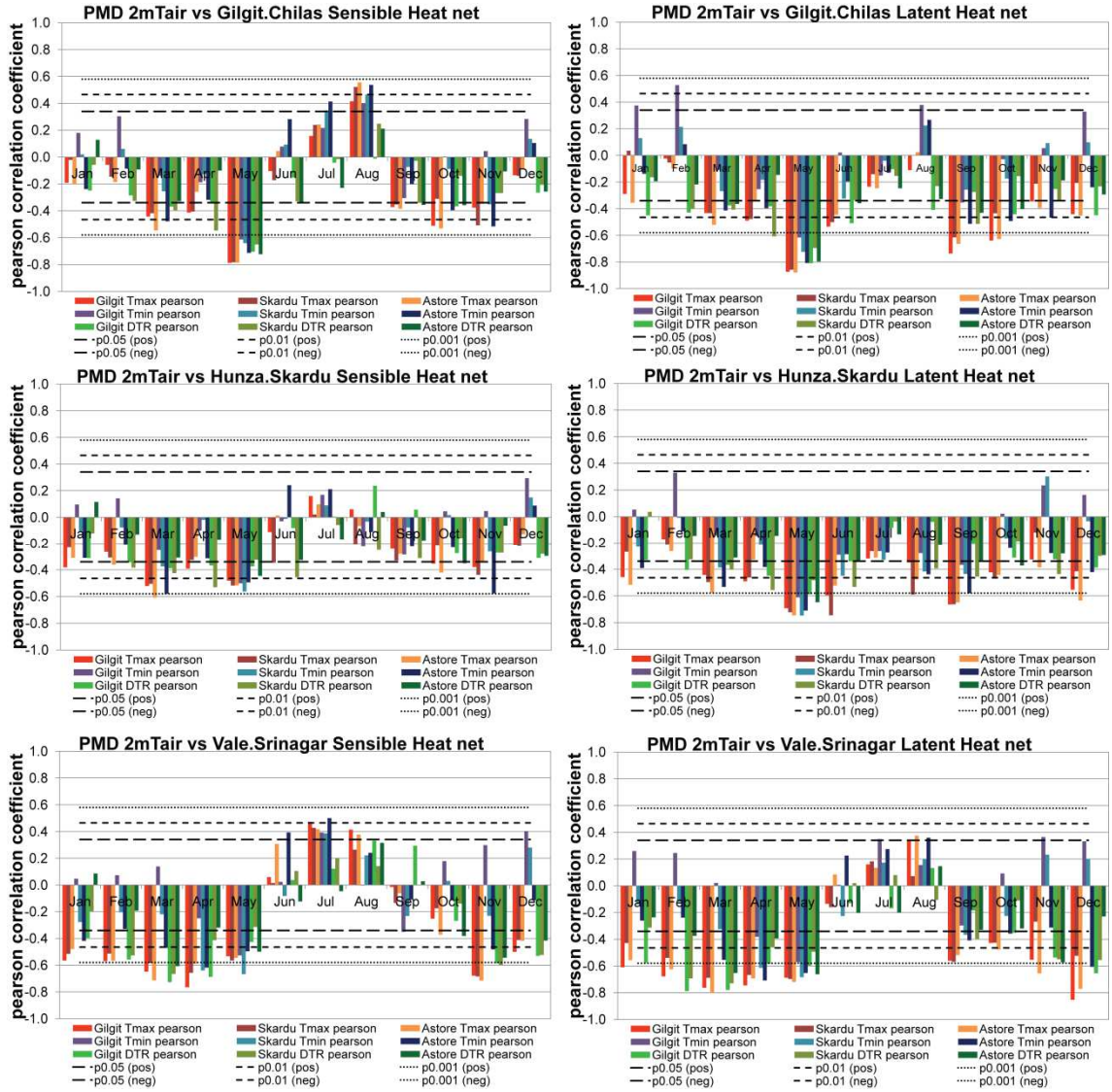

Figure 4.32 Pearson's correlation between ERA-Interim energy balance components – net sensible heat flux (SHFnet) and net latent heat flux (LHFnet) – and near-surface air temperature components from local observations (PMD), 1979 to 2007.

Because of the opposite effect of cloud cover on these two energy balance components, LWnet correlations are expected to show the opposite sign to SWnet which they essentially do for the northern two cells. In this case the southern cell, however, follows the same patterns (signs and magnitudes) in all months as its northern neighbours rather than opposite behaviour during the summer.

Net latent heat flux (LHFnet) is largely driven by incoming solar energy, partitioning some of the energy to enable evaporation and or melting of snow and ice. Owing to the sign conventions in ERA-Interim, latent heat fluxes from evaporation and melt are considered negative, i.e. energy transfers away from the surface. Thus the correlations of LHFnet with locally observed air temperature are expected to follow the same pattern of magnitude but with opposite sign to correlations of SWnet. This is effectively the case for the three selected grid cells.

Net sensible heat flux (SHFnet) is the direct mechanism of exchange between the surface energy balance and near surface air temperature. As such, keeping in mind the ERA-Interim sign conventions, SHFnet correlations with locally observed air temperature would be expected to be uniformly negative. In this case, not only the southern cell, Vale.Srinagar, but also the north-western cell, Gilgit.Chilas, show the opposite behaviour to that expected during the summer/monsoonal months. Furthermore the correlations in the remaining cell are mixed and not statistically significant.

4.4.6 Initial summary of investigation of causal mechanisms

While this detailed consideration of the relationships between air temperature, both locally observed and from numerical gridded analysis, and cloud cover and energy balance components has revealed paradoxical behaviour in the summer/monsoonal months, the identified seasonally and diurnally asymmetrical trends in air temperature have not yet been definitively attributed to plausible physical mechanisms. It is possible that further refinements in the spatial resolution of numerical weather simulation combined with multi-decadal spatial records of land surface temperature (LST), cloud cover and albedo – both "clear sky" and "all atmosphere" – from remote sensing could permit rigorous attribution. These improvements while technically feasible unfortunately fall outside the scope and limitations of the present work.

4.5 Inter-variable relationships for precipitation (point-based analysis)

While the asymmetrical temperature trends are perhaps the most striking present climatological feature of the UIB, further focus on precipitation variability is also required. Confirmation that the numerical, gridded precipitation data sets – e.g. ERA-Interim and PRECIS_ERA40 – show coherent behaviour with regards to local precipitation observations is important for assessment of the plausibility of the overall UIB climatology described by each of these data sources. If the present climate is distorted in the gridded data sources then apparent causal relationships between other climate variables may be erroneous. Furthermore, knowledge of the present relationships between precipitation and humidity in the UIB may help to assess future climate scenarios by comparing projected changes in precipitation to projected changes in humidity.

4.5.1 Correlations between precipitation variables from gridded numerical data sources and local observations

Figures 4.33 and 4.34 show the correlations in locally observed precipitation variables – precipitation amount (PP) and wet days (WD) – with the same variables respectively from the ERA-Interim and PRECIS_ERA40, for three grid cells each as for the air temperature analysis. Given the arid nature of the valley bottoms where the PMD stations are located, wet days (WD) are defined here as the number days in a month with precipitation greater than 0.1mm (i.e. $PP_{day} > 0.1$ mm).

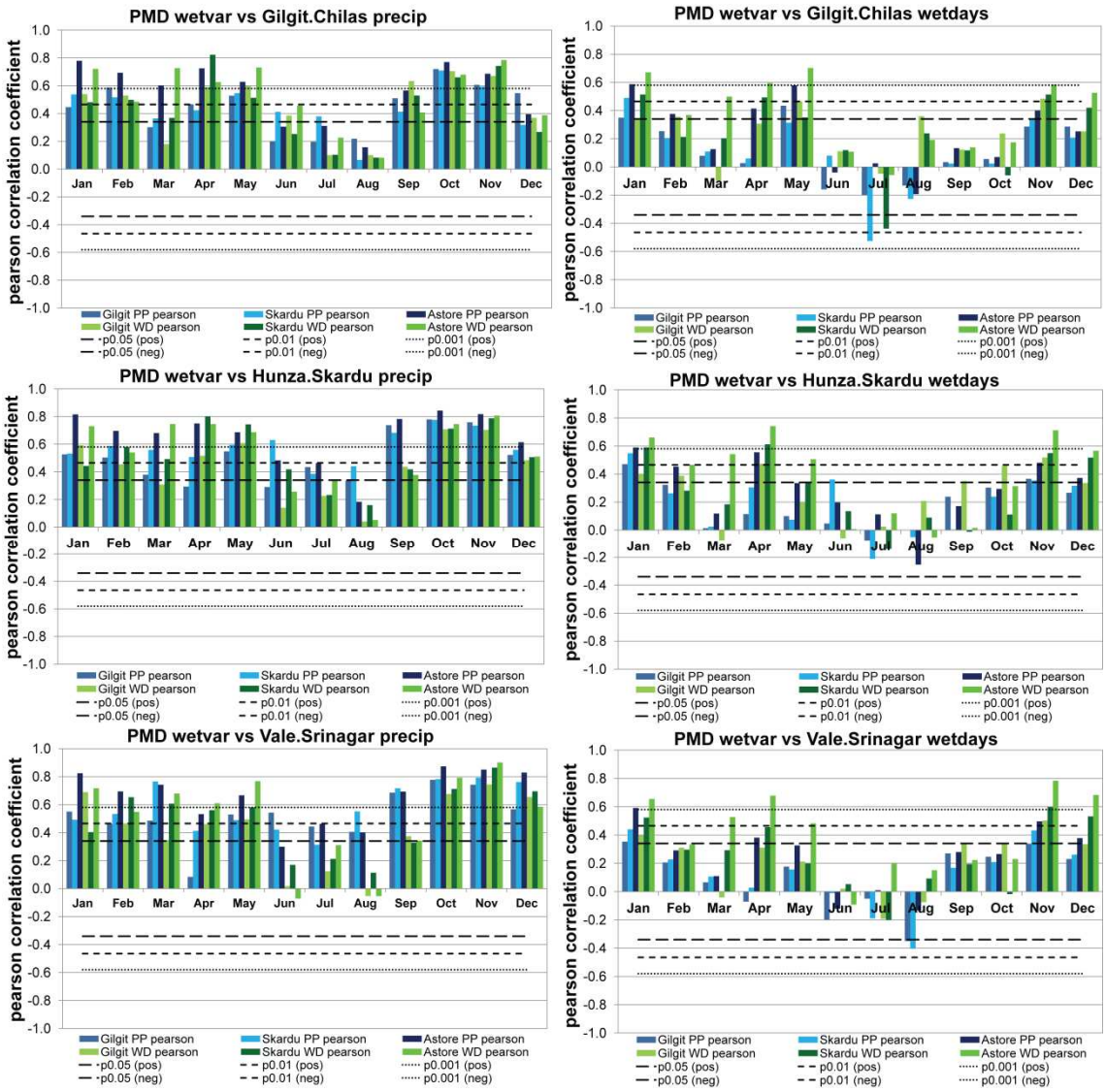

Figure 4.33 Pearson's correlation, between precipitation variables (wetvar = abbreviation of grouping of precipitation-related variables: total precipitation, wetdays occurrence) from ERA-Interim and local observations (PMD), 1979 to 2007, showing 5% (dashed line) and 1% (dotted line) statistical significance levels.

As can be seen in Figure 4.33, correlations of reanalysis PP with local PP and WD are entirely positive with good statistical significance, although relationships in the summer/monsoonal months are relatively weaker. Correlations of reanalysis WD with local PP and WD are still largely positive except in the summer/monsoon period when some (weak) negative correlations are found. These negative correlations may be due to

"drizzle" – i.e. overly frequent, low intensity precipitation – problems in ERA-Interim forecasting modelling if the reanalysis suffers from similar precipitation biases to those seen in GCMs (e.g. Piani *et al.*, 2010). Alternately, the negative correlations may simply be due to differences in the representation of localised convective precipitation when modelled at this spatial scale. Understanding the spatial and temporal distribution of summer rainfall is crucial to UIB hydrology because, as identified by Archer (2004), widespread precipitation events in the UIB during the snow and glacial melt season can actually result in decreasing runoff due to reduction of energy inputs needed to drive melt processes (from cloud cover). Hence it is particularly important to understand discrepancies between local observations and gridded data sources in precipitation variables in this season in order to be aware of potential biases in the over hydro-climatological assessment.

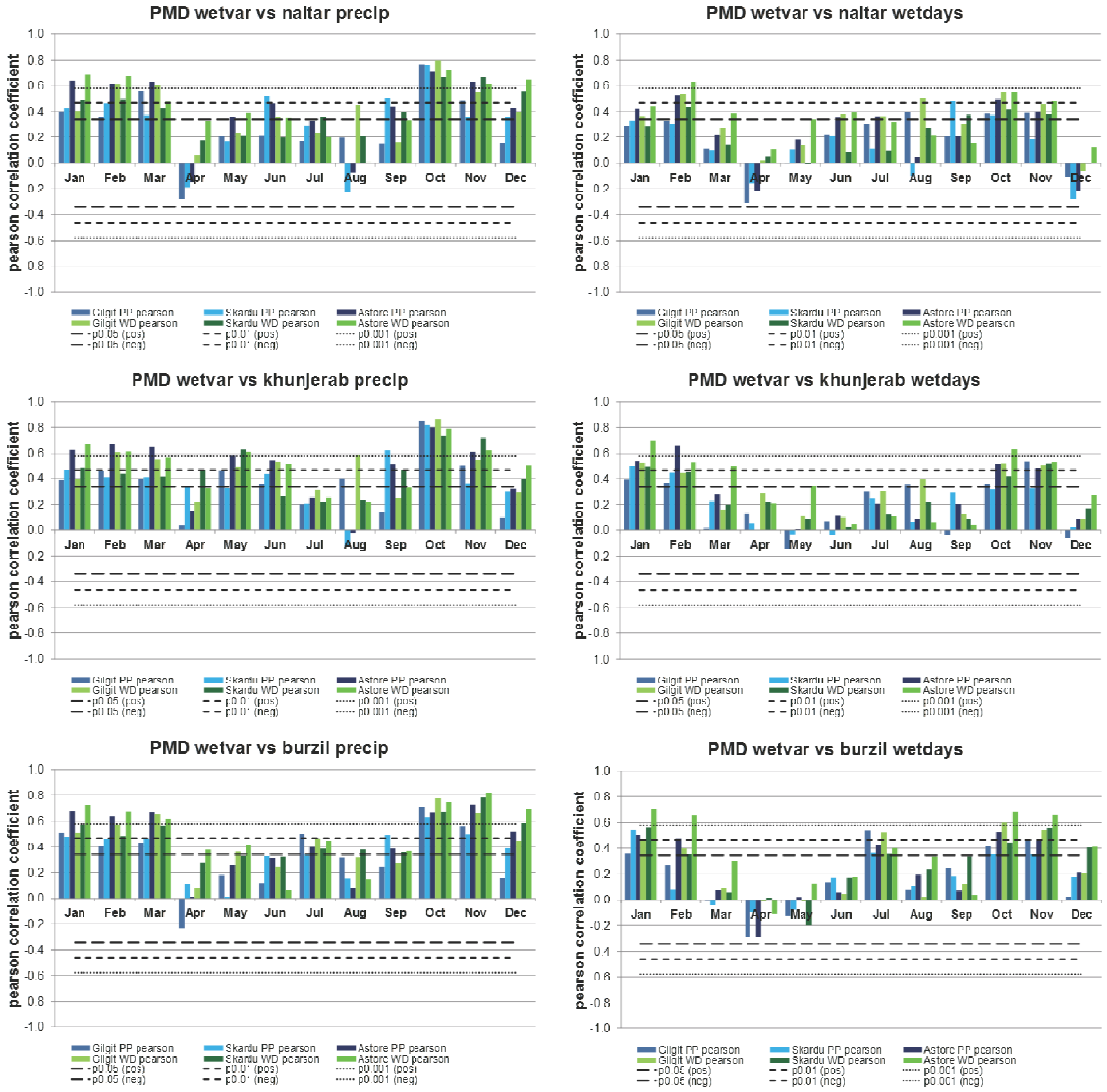

Figure 4.34 Pearson's correlation, between precipitation variables (wetvar = abbreviation of grouping of precipitation-related variables: total precipitation, wetdays occurrence) from PRECIS_ERA40 and local observations (PMD), 1961 to 1989, showing 5% (dashed line) and 1% (dotted line) statistical significance levels.

As Figure 4.34 shows, the relationships between the PRECIS_ERA40 precipitation variables and their locally observed counterparts are quite similar to those between local observations and ERA-Interim, except that PRECIS_ERA40 WD correlations are weakest in Spring rather than Summer. The generally good correspondence between the reanalysis-driven RCM (PRECIS_ERA40) precipitation and local observations is encouraging as an indicator of potential RCM performance over the region. This is a positive sign in terms of the RCM's ability to accurately reproduce not only the range of variability of precipitation but also the patterns – in sign and magnitude – of responses to large-scale forcings.

4.5.2 Inter-variable correlations between precipitation and relative humidity

In an examination of other climatological parameters linked to precipitation, Figure 4.35 shows correlations of relative humidity (RH) from ERA-Interim and PRECIS with locally observed PP and WD. The relationships between gridded RH and local precipitation variables are similar to those for gridded WD. Consideration of the relationship between RH and precipitation variables is pertinent for consideration of future climate scenarios because moisture fluxes are expected to increase in a generally warming climate due to the Clausius-Clapeyron relationship between temperature and saturation vapour pressure, i.e. the moisture carrying capacity of a volume of air (Trenberth *et al*., 2003).

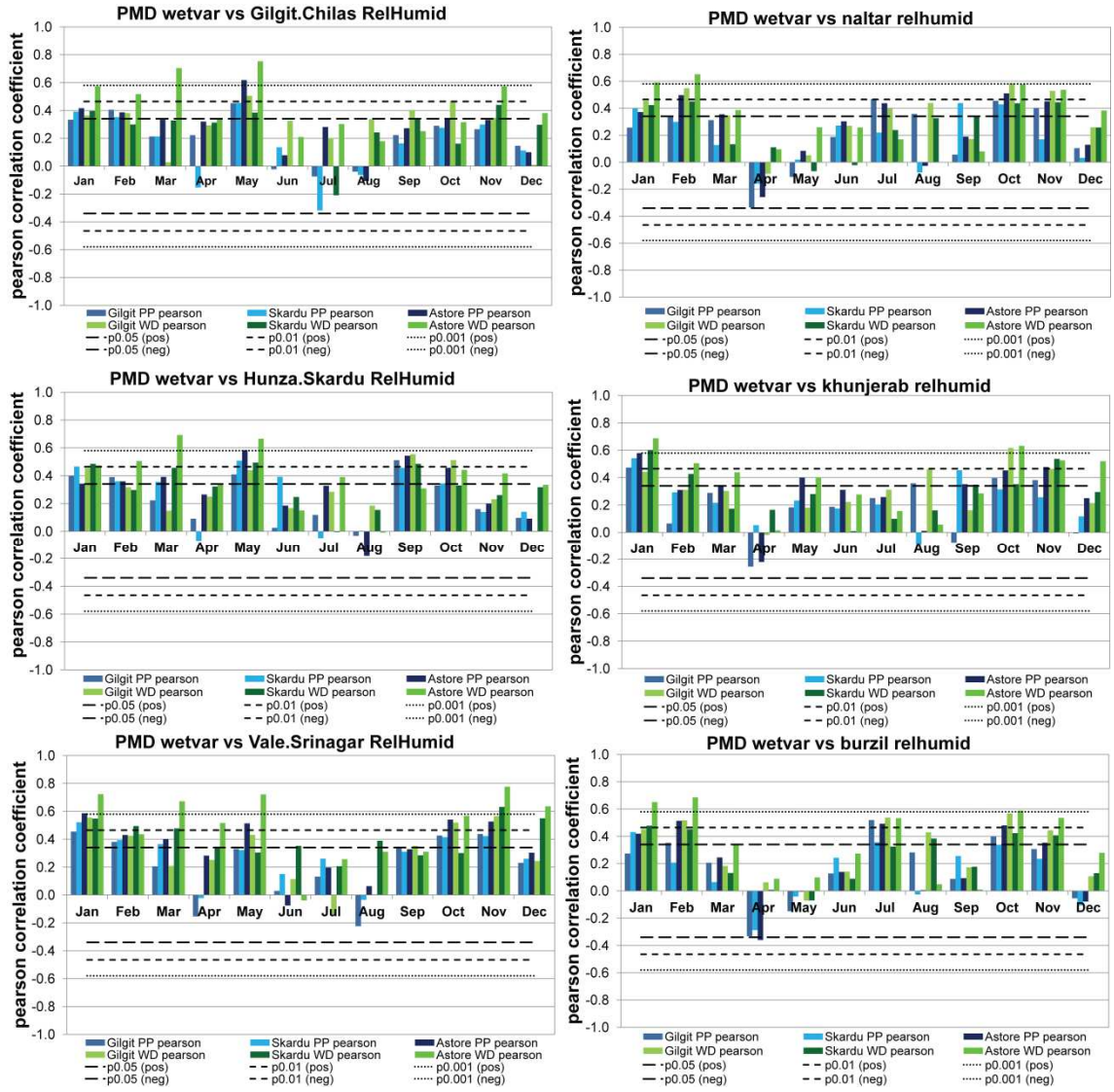

Figure 4.35 Pearson's correlation between precipitation variables (wetvar: total precipitation, wetdays occurrence) from local observations (PMD) and relative humidity (relhumid) from ERA-Interim [1979 to 2007] and PRECIS driven by ERA-40 [1961 to 1989], showing 5% (dashed line) and 1% (dotted line) statistical significance levels.

Clearly, the identified seasonally asymmetrical trends in UIB air temperature, if they persist, could have important implications in this regard. For example, if moisture rich air masses from moisture source regions experiencing strong warming arrive in the UIB where summer cooling is on-going, local RH could be augmented both by an increase in absolute moisture content (specific humidity) and a decrease in the moisture carrying capacity of the air. Alternately if the strong warming in the UIB seen during the present snow accumulation season (October to March) persists, UIB RH might in fact decrease if the moisture carrying capacity of the air increases faster than the increasing influx of absolute moisture content (specific humidity).

4.6 Investigation of relationships between large-scale circulation and UIB climate variability

4.6.1 Characterisation of circulation patterns with relationship to the UIB

To understand the broader patterns of atmospheric circulation and the UIB's place therein, including fluxes from moisture source regions, it is useful to consider the annual cycles of surface pressure and wind speeds at a hemispheric scale. The annual cycles of surface pressure are linked to the annual cycles of absorption of incoming solar shortwave energy by continental landmasses and atmospheric heating from sensible heat flux as a result of this absorption (Trenberth and Solomon, 1994). Wind directions are in turn shaped by pressure gradients.

Figure 4.36 shows the period-mean (1979 to 2007) mean sea level pressure (MSLP) in January for a spatial domain from Iceland in the northwest to Tahiti (i.e. the western tropical Pacific) in the southeast. Figure 4.37 shows period-mean (1979 to 2007) MSLP in July for the same domain. In winter, a substantial area of high pressure forms centred on the severely cold land surface of western Siberia and Mongolia while strong low pressure predominates over the relatively warm sea surface of the mid-to-high latitude oceans. In summer, high-pressure areas dominate over the relatively cool subtropical to mid-latitude oceans while low pressure areas develop over the very hot (> 40°C) land surface in Central and South Asia.

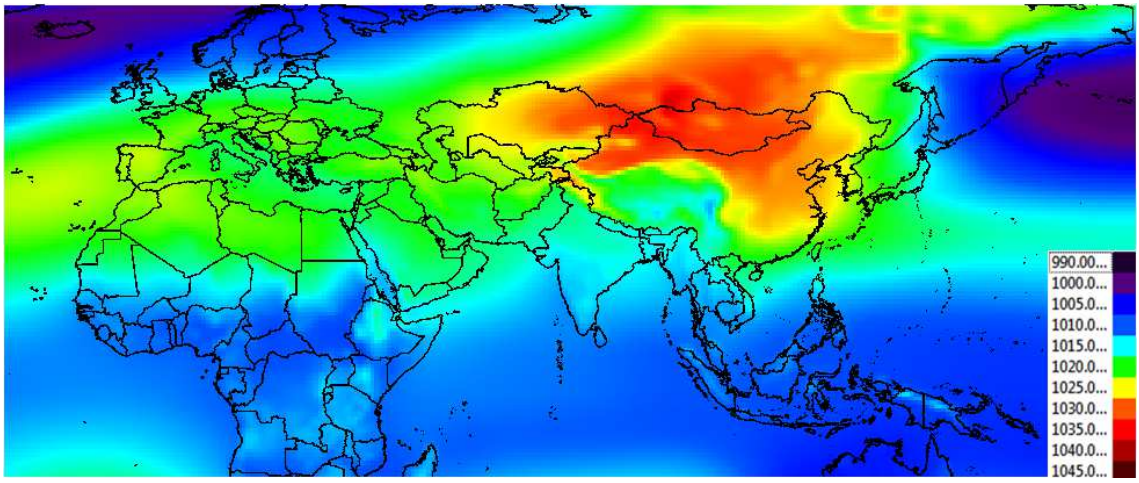

Figure 4.36 ERA-Interim average mean sea level pressure (MSLP) [millibars] for January, Eurasia sub-domain (1979 to 2007).

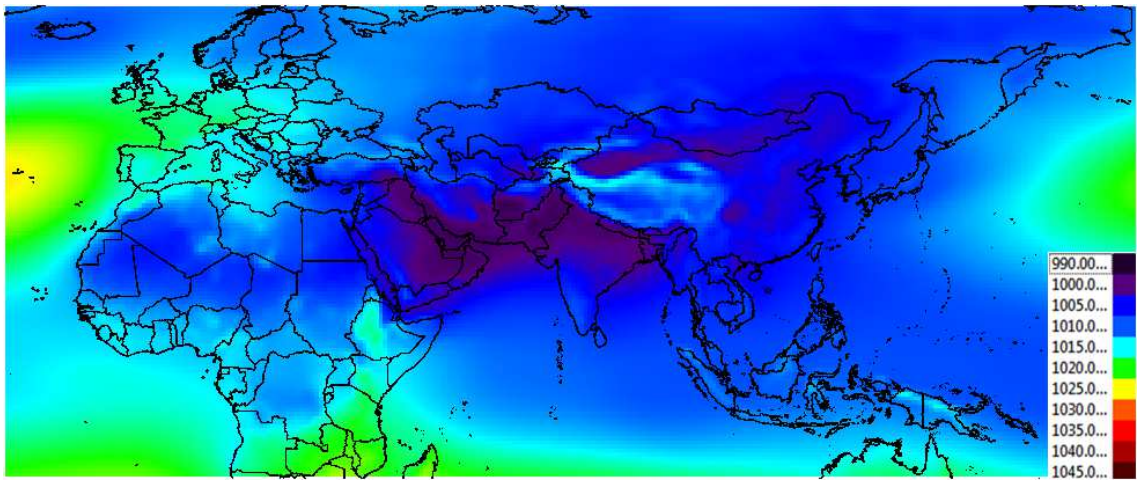

Figure 4.37 ERA-Interim average mean sea level pressure (MSLP) [millibars] for July, Eurasia sub-domain (1979 to 2007).

Figures 4.38 and 4.39 show the near surface (10m) wind directions for January and July respectively for the sub-global eastern hemisphere/Eurasian domain. Wind directions are defined using the meteorological/nautical convention, i.e. a wind blowing directly from south to north would have a direction of 180 degrees and a wind blowing directly from west to east would have a direction of 270 degrees. Wind directions in degrees are secondary values not supplied directly by reanalysis, but rather calculated trigonometrically from the resultant period mean wind components. To clarify, in the ERA-Interim reanalysis directional wind components are supplied separately:

- the “U” or “zonal” component refers to wind velocity along a east-west (longitudinal) axis, with negative values indicating “easterly” wind direction and positive values indicating “westerly wind direction;

- the “V” or “meriodinal” component refers to wind velocity along a north-south (longitudinal) axis, with negative values indicating “northerly” wind direction and positive values indicating “southerly” wind direction.

In order to avoid mathematical discrepancies in attempting to calculate a mean around the 360° to 0° “compass North” discontinuity, the period mean wind direction in degrees for each grid cell was calculated from the period mean “U” and “V” wind components.

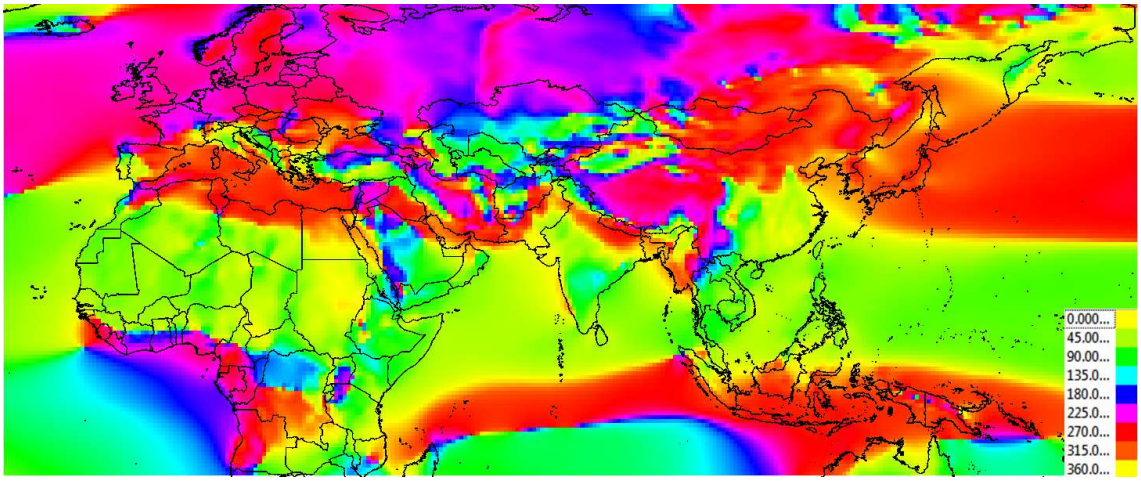

Figure 4.38 ERA-Interim, period mean 10m wind direction (compass degrees) for January, Eurasia sub-domain, 1979 to 2007. To clarify: Yellow => northerly winds (0°); green => easterly winds (90°); blue => southerly winds (180°); red => westerly winds (270°).

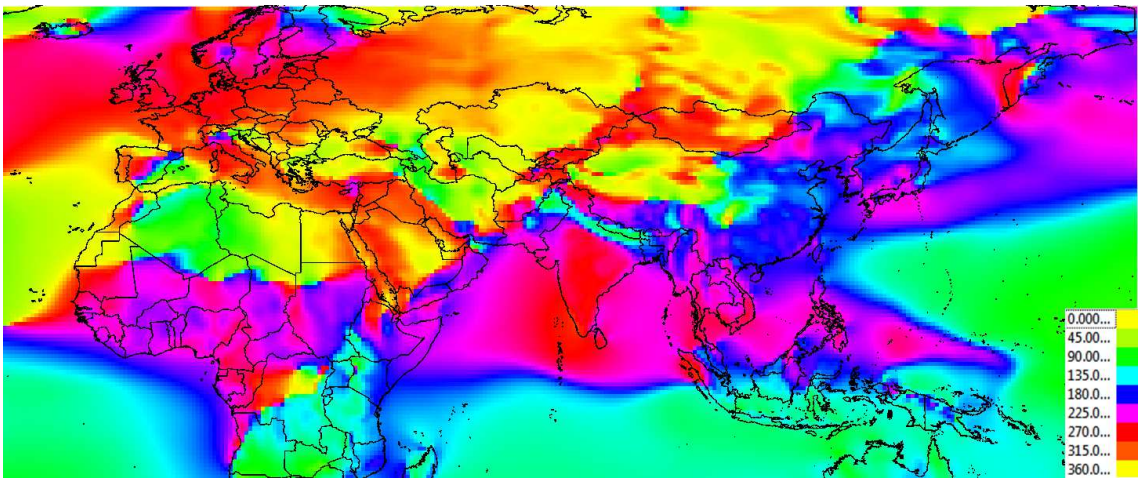

Figure 4.39 ERA-Interim, period mean 10m wind direction (compass degrees) for July, Eurasia sub-domain, 1979 to 2007. To clarify: Yellow => northerly winds (0°); green => easterly winds (90°); blue => southerly winds (180°); red => westerly winds (270°).

The broad patterns of mid-to-high latitude westerly winds and wintertime easterlies in the tropics and subtropics can be clearly seen in Figure 4.38. Figure 4.39 shows the development of the “on-shore” southerly or south-westerly winds in the monsoon season for the tropics and subtropics while westerlies persist in the mid-to-high latitudes. Complicated patterns of wind direction can be seen in both Figures 4.38

and 4.39 in the transition zones between circulation regimes and in regions where topographic features impact upon atmospheric circulation. Although validation studies of ERA-Interim in other regions and climatic contexts (e.g. Szczypta *et al*., 2011) have found strong correlations and limited bias between reanalysis 10m wind velocities and local observations, it is clear that the coarse spatial resolution will inhibit accurate determination of wind speed in areas of high topographic relief where terrain influences near-surface wind speed and direction. It is thus possible that better indications of local atmospheric circulation will be found in wind directions higher in the atmosphere.

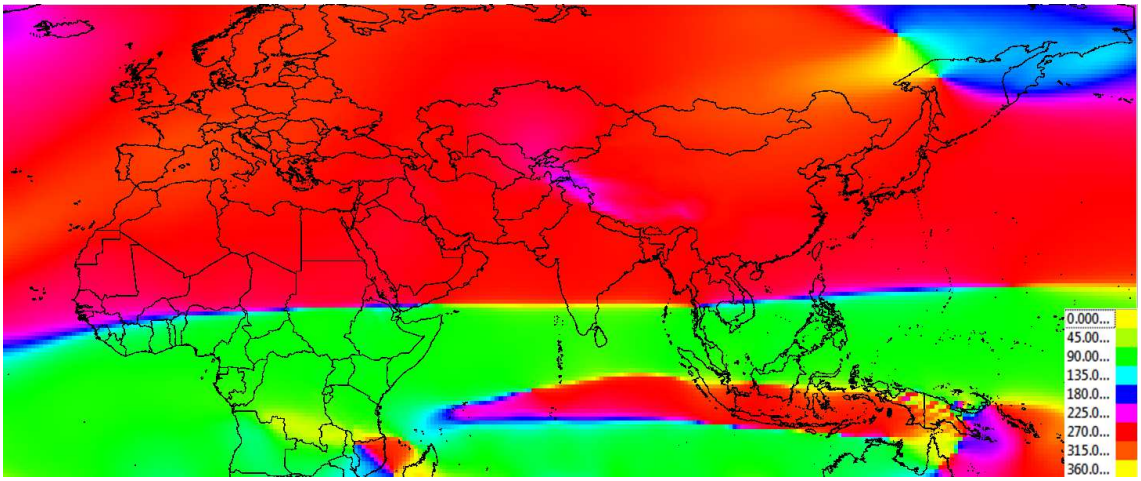

Figure 4.40 ERA-Interim period mean 500mb wind direction (compass degrees) for January, Eurasia subdomain, 1979 to 2007. To clarify: Yellow => northerly winds (0°); green => easterly winds (90°); blue => southerly winds (180°); red => westerly winds (270°).

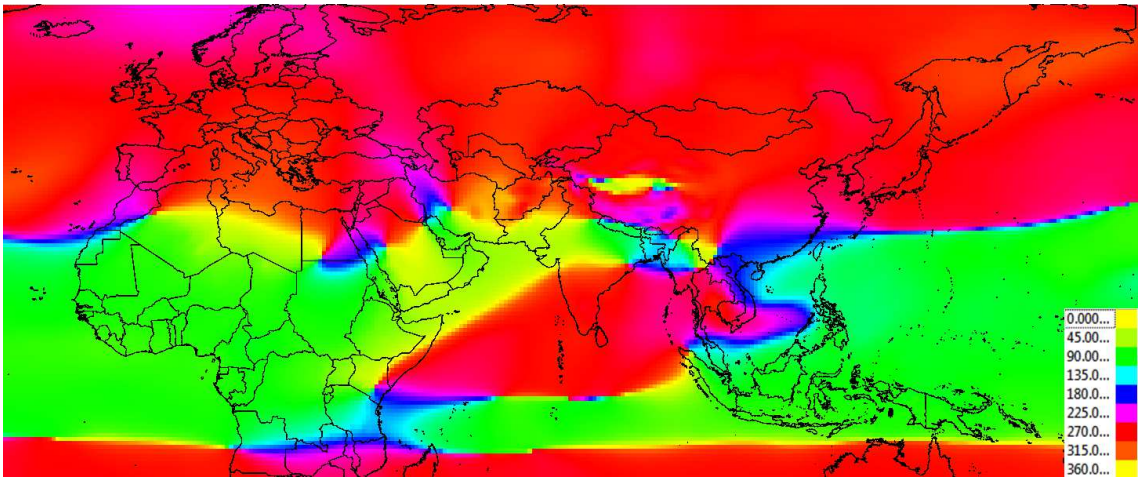

Figure 4.41 ERA-Interim period mean 500mb wind direction (compass degrees) for July, Eurasia subdomain, 1979 to 2007. To clarify: Yellow => northerly winds (0°); green => easterly winds (90°); blue => southerly winds (180°); red => westerly winds (270°).

Patterns of wind direction at the 500mb pressure level, as seen in Figures 4.40 and 4.41 are much more spatially coherent. Comparison of the southern limit of westerly winds in January (Figure 4.40) and July (Figure 4.41) reveals the stark contrast

between atmospheric circulation patterns in the vicinity of the UIB in the cold season versus summer/monsoonal months.

In the January (Figure 4.40) is a vast area of effectively spatially uniform area of westerly winds at the 500mb level over Europe, Asia and even north Africa and the Sahara as far south as 10°N latitude, although the appears to be a moderate (roughly 45 compass degrees) localised anti-clockwise rotation centred over the UIB and likely caused by physical barrier of the Himalayan mountain arc. Southward of 10°N latitude there is a braod band of easterly winds at 500mb albeit with a meridionally (north-south) narrow band of westerlies just south of the equator across nearly the entire width of the Indian Ocean.

In July (Figure 4.41) the northern line of separation between westerlies and easterlies moves northward across the Indian sub-continent moving past 20°N latitude and the southern zone of westerlies expands northward to cover the southern half of the sub-continent. More specifically with respect to the UIB, the adjacent regions remain in a general westerly regime although there is greater spatial variability and a noticeable clockwise (northerly) rotation, although over core areas of the UIB the south-southwesterlies of the cold season persist. Furthermore, “downstream” of the UIB an area of northerlies develops over the central Tibetan Plateau.

The ERA-Interim reanalysis indicates that the 500mb pressure level fluctuates at around 5600 metres above sea-level (m asl). This is above the mean elevation of the UIB but still well below many of the peaks. The detailed focus on the wind directions in the 500mb pressure level given in Figure 4.42 for the UIB sub-domain shows that, even at this high elevation (and coarse spatial resolution), the physical barrier of the Himalayan mountain arc has a substantial impact on wind direction in all months. The progressively increasing disruption (or eddies) caused by this physical barrier as one descends from 500mb (Figure 4.42) to the surface can be seen in Figure 4.43 (10m near surface). In the middle and lower elevations (pressure levels), the Himalayan arc effectively channels and constrains the movement of monsoonal airflow during the summer months. The controlling nature of this barrier can be well understood by considering the relative elevation of the Himalayan mountain arc and adjacent Tibetan plateau with the rest of the hemisphere seen in the invariant surface orographic height [m asl] used in ERA-Interim as shown in Figure 4.44.

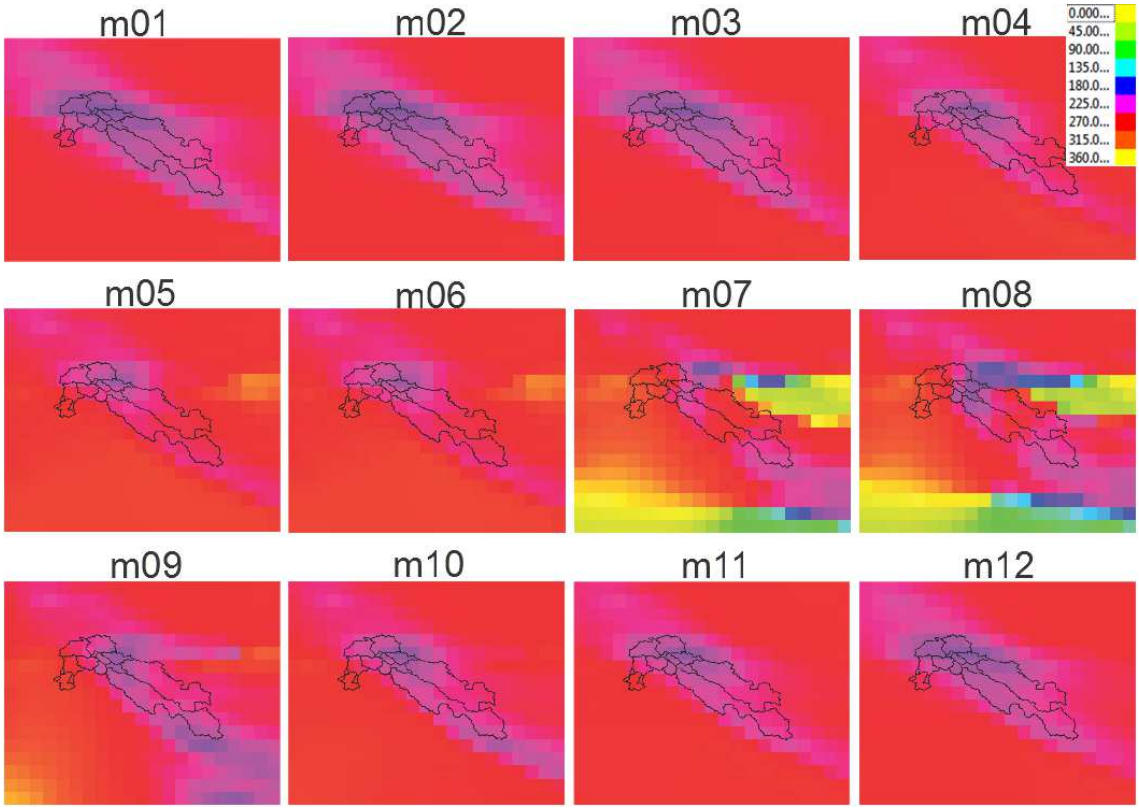

Figure 4.42 ERA-Interim period mean annual cycle for 500mb wind direction (compass degrees), UIB sub-domain, 1979 to 2007. To clarify: Yellow => northerly winds (0°); green => easterly winds (90°); blue => southerly winds (180°); red => westerly winds (270°).

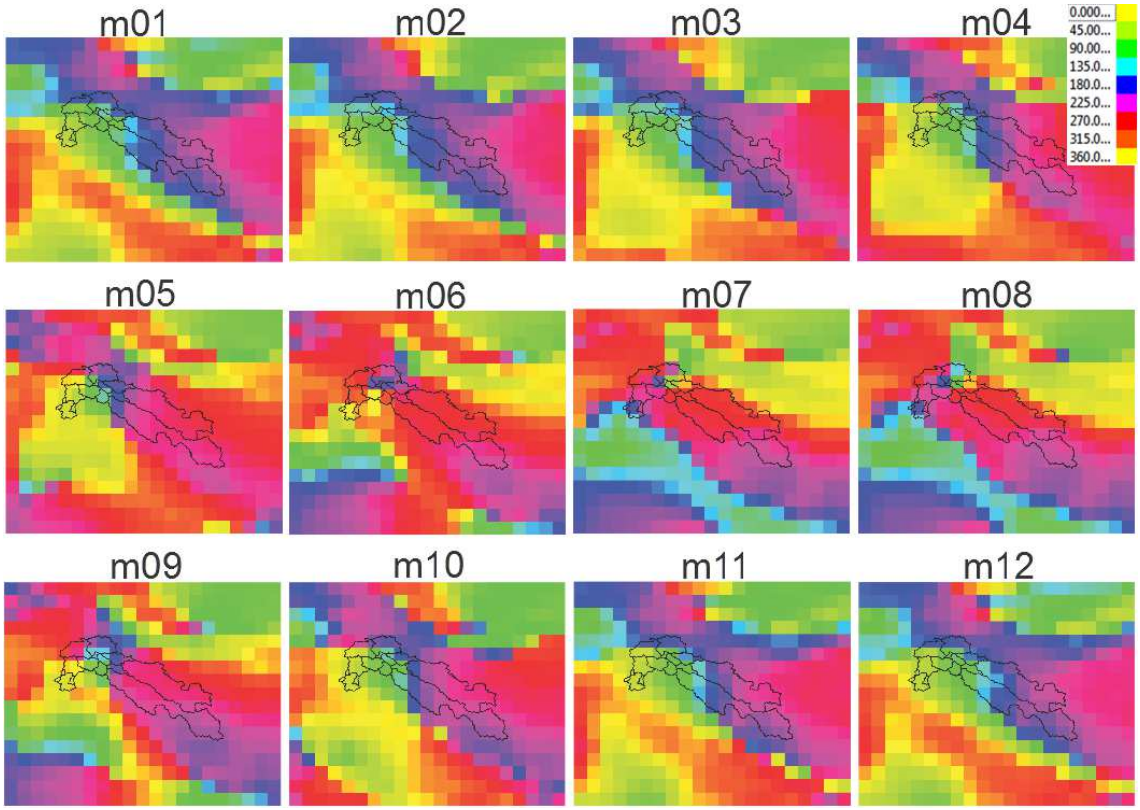

Figure 4.43 ERA-Interim period mean annual cycle for 10m wind direction (compass degrees), UIB sub-domain, 1979 to 2007. To clarify: Yellow => northerly winds (0°); green => easterly winds (90°); blue => southerly winds (180°); red => westerly winds (270°).

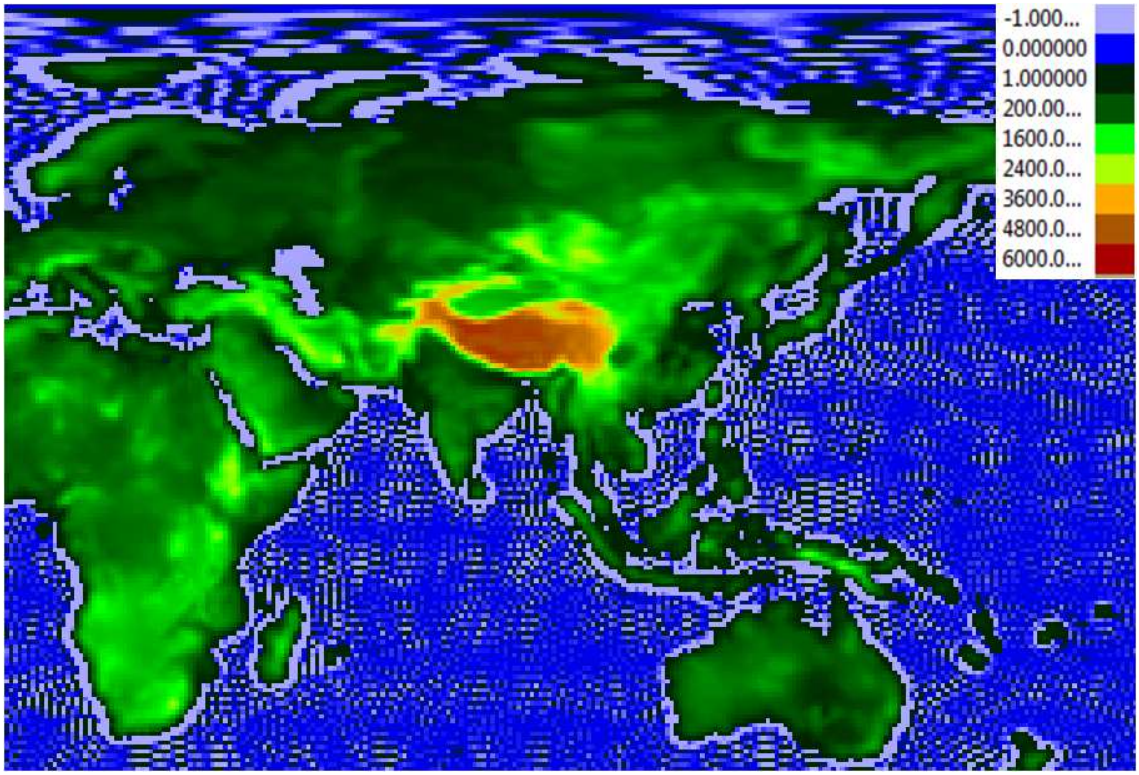

Figure 4.44 Invariant orographic height (surface) [m asl] from ERA-Interim. nb: Artefacts in the oceans are imposed orographical heights deemed necessary in the reanalysis for accurate circulation.

4.6.2 Background of circulation teleconnections and context with regards to the UIB

Understanding the relationships between local atmospheric circulation and larger weather system movement is critical in understanding likely future precipitation and temperature change because, as presented earlier in this chapter, these inputs of mass (precipitation) and energy (air temperature) to the hydrological system will be controlled by the interaction of the characteristics of the incoming air masses with local processes, e.g. surface energy balance. The characteristics of the incoming air masses are shaped in turn by larger-scale features of global atmospheric circulation. These features, often referred to as "teleconnections" for their far reaching influence on sub-regional weather patterns (Angstrom, 1935), are generally quantified as indices of sea surface temperatures or gradients in atmospheric pressure, usually MSLP (e.g. Marshall *et al*., 2001, Diaz *et al*., 2001). Some of these teleconnections can be seen in relation to their influence on the UIB in Figure 4.45.

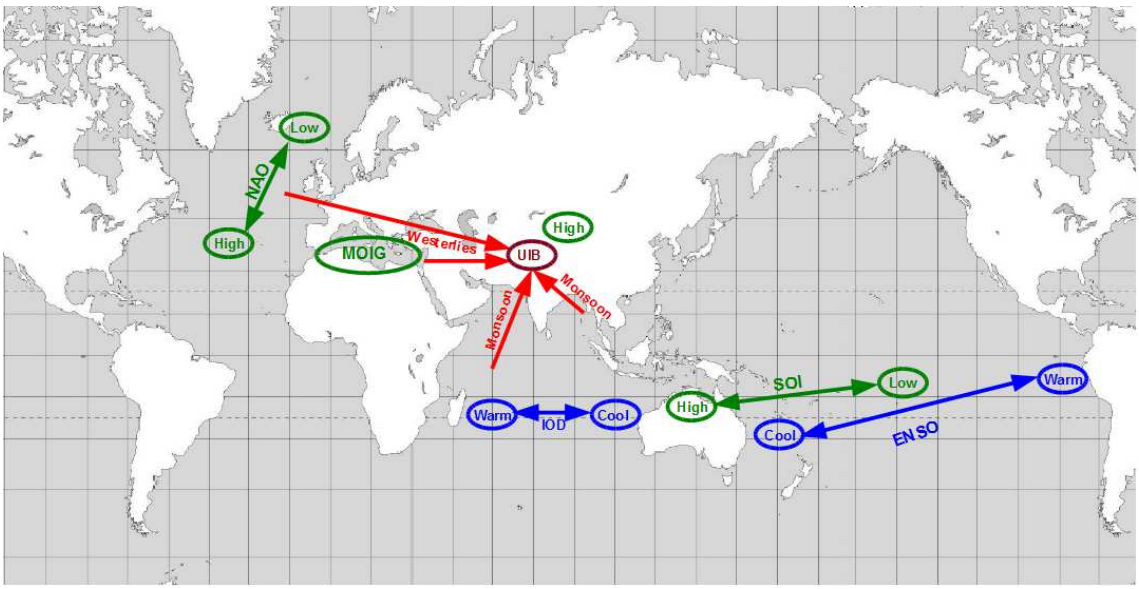

Figure 4.45 Schematic presentation of major candidate teleconnections tested for influence on local climate of the UIB. Pressure-based indices are shown in green while temperature based indices are shown in blue. Simplified weather system tracks are shown in red. Acronyms are as follows: NAO (North Atlantic Oscillation), MOIG (Mediterranean Oscillation Israel-Gibraltar), IOD (Indian Ocean Dipole), SOI (Southern Oscillation Index), ENSO (El Niño Southern Oscillation).

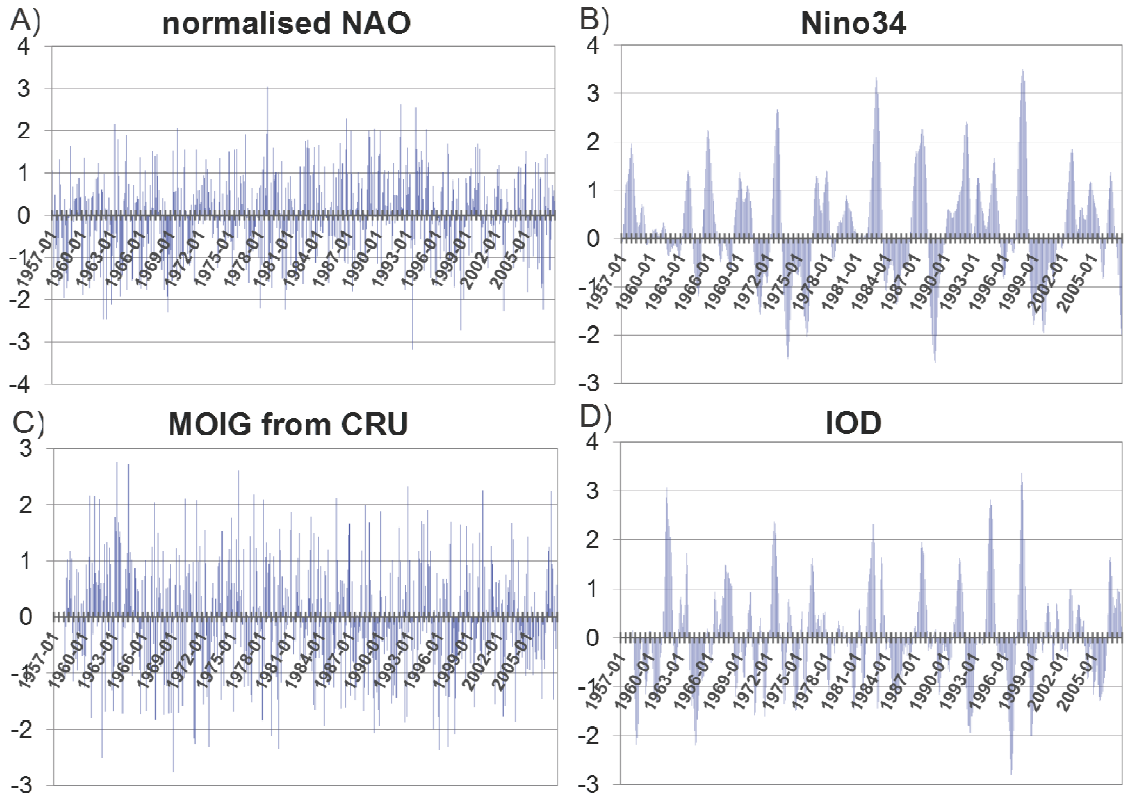

Figure 4.46 Illustration of "oscillation frequencies" in selected teleconnection indices, 1957 to 2007: A) North Atlantic Oscillation (NAO), B) Nino3.4 index of El Nino Southern Oscillation, C) Mediterranean Oscillation index Israel-Gibraltar (MOIG) from Climate Research Unit (CRU), D) Indian Ocean Dipole (IOD).

The behaviour of the indices to some extent depends upon the physical properties of the parameter they quantify. Figure 4.46 shows the behaviour of four indices over a fifty year period. The normalised NAO (North Atlantic Oscillation) and

MOIG (Mediterranean Oscillation Israel-Gibraltar) from CRU are based on atmospheric pressure gradients between two benchmark locations (Jones *et al*., 1997, Palutikof, 2003). Figure 4.46 shows that they frequently – in the space of a few months – oscillate between positive and negative phases. In contrast, the Nino34 (El Niño region 3.4) and IOD (Indian Ocean Dipole) are measures of areally averaged sea surface temperatures (SSTs) in specific regions of the tropical oceans. Therefore, these indices oscillate more slowly, remaining in a single (positive or negative) phase at times for two or three years. This relative stability can be attributed to the inertia or system memory due to relative energy storing nature of the tropical oceans in direct contrast to the relatively transmissive properties of the atmospheric air masses.

4.6.3 Correlation testing between teleconnections and UIB climate variables

This study investigated links between the aforementioned teleconnections and UIB climate as characterised by: i) local observations (PMD, ERA-Interim reanalysis), and ii) PRECIS_ERA40. The relationships were tested by calculating the Pearson's correlation between concatenated time-series of individual calendar months. Relationships were tested for "concurrent" and a range of lagged responses ranging from 1 to 11 months.

Assessment of the relationships at the monthly timescale between selected teleconnection indices and local observations (PMD) of precipitation and air temperature produced results which were weak, inconsistent or contradictory despite the range of "lag-times" considered. Assessment of relationships at the seasonal timescale had previously been carried out by a number of researchers (e.g. Archer and Fowler, 2004; Fowler and Archer, 2005; Syed *et al*., 2006; Yadav *et al*., 2009). These studies primarily focused on the relative effects of conditions in the North Atlantic (NAO) and tropical Pacific (various ENSO indices).

To add a meaningful contribution to this existing work, the present study undertook a spatial assessment, testing the relationships between selected teleconnection indices and the gridded outputs from ERA-Interim and PRECIS_ERA40 for precipitation, cloud cover and air temperature. The motivation for testing the teleconnection relationships to both of these gridded data sources was to test both the temporal stability of the relationships – ERA-Interim was tested for the 1979-2007 period and PRECIS_ ERA40 was tested for 1961-1989 – as well as the agreement in the behaviour of the local parameters from the two gridded sources.

The same range of time lags were tested as for the assessment of relationships to local observations Comparison of the results of relationship strengths for a given index with varying lag times showed the dependence on the rate of variation of the index value itself. For pressure-based indices, the sign of linear correlation could alternate with monthly increments in lead-time, e.g. patterns with 1-month lead-time would be considerably different from 2-months lead-time. In contrast, the correlations of an SST-based index were relatively independent of lead-time because the index would remain in a single phase over the range of lag-times tested, e.g. patterns with 2-months lead-time appeared quite similar to those for 5-months lead-time. As a result, in neither the quickly varying (e.g. NAO, MOIG) nor slowly varying (e.g. MEI, IOD) did key lead-time strengths emerge. For conciseness, the results of only two lead times will be presented here: i) L00 which represents the influence of a teleconnection in the same/concurrent month as the local parameter; and ii) L04 which represents the influence of a teleconnection condition four months prior to the local parameter. These two lead times were selected to contrast the dynamic (fast response) behaviour of the climate system with antecedent conditions which could potentially provide quantitative predictors of future local conditions.

As in the previous seasonal timescale studies, the results presented here will focus on the influence of the NAO and ENSO – as quantified by the Multivariate ENSO Index (MEI) – on conditions in the UIB. As explained in Chapter 2, the MEI is a quantitative measure of the ENSO phase and state using a principal components analysis of a combination of SLP and SST measures for the region (Wolter and Timlin, 2011).

The graphical presentation of the spatial correlations at these two lead times (L00, L04) for the two indices (MEI, NAO) and two gridded data sources (ERA-Interim, PRECIS) for each of four parameters (DTR, Tmin, total cloud fraction, total precipitation) can be found in Appendix B. The salient points can be summarised as follows:

1. With regards to ENSO (MEI), in the spring and late Autumn/early Winter (OND) a positive (negative) phase for the index can be linked to increased (decreased) cloud cover and precipitation broadly across the sub-region/domain. This finding corroborates the earlier work of Fowler and Archer (2005) and Syed *et al.* (2006) who found increasing UIB winter precipitation in El Niño (positive MEI) years. In the winter, when LW cloud forcing can be expected to dominate, this yields increasing (decreasing) Tmin and decreasing (increasing)

DTR. In the late spring however, when SW (incoming solar) cloud forcing dominates, this yields decreasing (increasing) Tmin and increasing (decreasing) DTR.

2. In the summer/monsoonal months (JJAS) there seems to be a sub-regional divide in MEI effects based on sub-climate regimes. During the summer over the high mountains, particularly in the northwest, cloud cover and precipitation increase (decrease) during a positive (negative) ENSO phase, while in the plains these parameters decrease (increase). Again, due to the dominance of SW cloud forcing during these months, the relationships for Tmin and DTR are opposite to those for cloud cover and precipitation. This finding corroborates the earlier work of Fowler and Archer (2005) who found decreasing UIB summer temperatures in El Niño (positive MEI) years.
3. It can be hypothesised that a positive ENSO phase strengthens cyclonic activity ("storminess") from westerly depressions broadly across the region while suppressing monsoonal activity at least over the plains. It is beyond the scope of this project to postulate whether the apparent increase in precipitation over the mountains is due to a displacement of the normal monsoonal rainfall or to increased strength (or further southward movement) of westerly weather systems.
4. NAO correlations show less temporal (commonalities between L00 and L04) or spatial stability (across the domain) in comparison to ENSO. There appears to be better agreement between the gridded data sources at the same lead time (either L00 or L04) than for an individual data source (either ERA-Interim or PRECIS_ERA40) at different lead times. This may suggest that the influence of NAO on UIB climate is consistent across a range of analysis windows – e.g. 1961 to 1989 and 1979 to 2007 – but that the rapidity with which it acts coupled with frequency at which it oscillates may render its use as a predictive indicate difficult at the seasonal timescale – which is of most need for water resources management.
5. At the concurrent timescale (L00), in both the winter and late summer a positive (negative) NAO phase can be linked with increased (decreased) cloud cover, precipitation and night-time temperature (Tmin) as well as decreased (increased) DTR, at least over the NW UIB. This might be attributed to increased cyclonic activity – "stormier" weather – either from strengthened westerly depressions or, in summer, increased monsoonal penetration. As noted above, however, the

spatial coherence of these patterns is relatively limited as are the numerical strength of the correlations.

In an initial assessment it thus appears that both ENSO and NAO can influence the strength of westerly weather systems and monsoonal activity over the UIB and adjacent sub-regions. The present work does not investigate, however, the extent to which these factors interact either synergistically or as opposing forces. Inferences can perhaps be drawn, however, from the distribution of period mean zonal (west to east) wind strengths at the 200mb pressure level from ERA-Interim. This pressure level is in the upper troposphere and often contains the high velocity circulation features known as jet streams (Lu *et al*., 2002). Circulation at this high altitude in turn influences wind speeds, cloud and precipitation.

Figures 4.47 and 4.48 respectively show the January and July period mean zonal wind from ERA-Interim for 1979 to 2007. Figure 4.47 very clearly shows the strong westerly (positive velocity) circulation band centred on approximately 30°N latitude and passing over the UIB. This pattern of westerly flow weakens substantially in summer (Figure 4.48) when the zone of easterly flow expands as monsoonal activity develops. Nevertheless, the band of enhanced westerly flow persists even in July when it moves northward to be centred over roughly 40°N latitude.

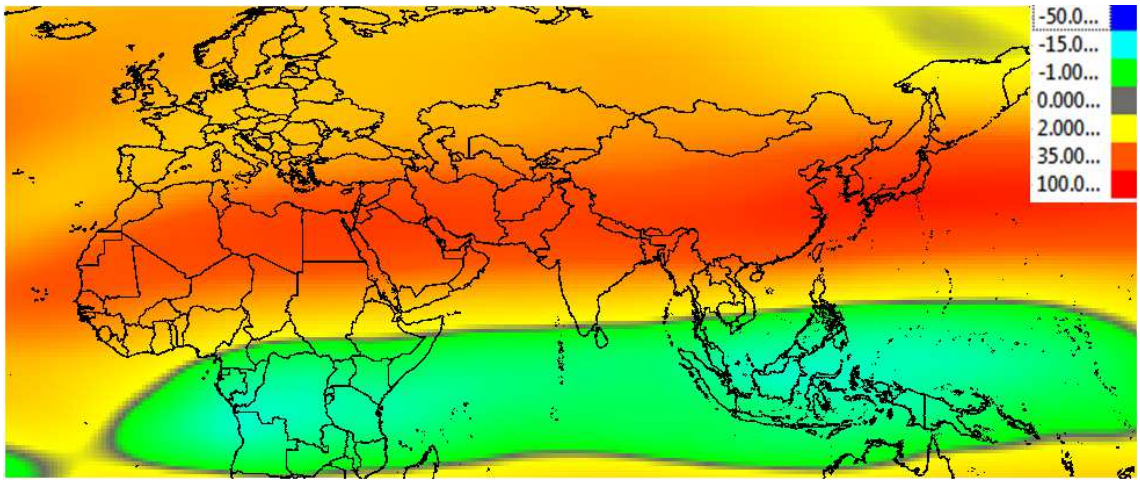

Figure 4.47 ERA-Interim mean 200mb zonal (west to east, westerly positive) wind speed [m/s] for January, Eurasia sub-domain (1979 to 2007).

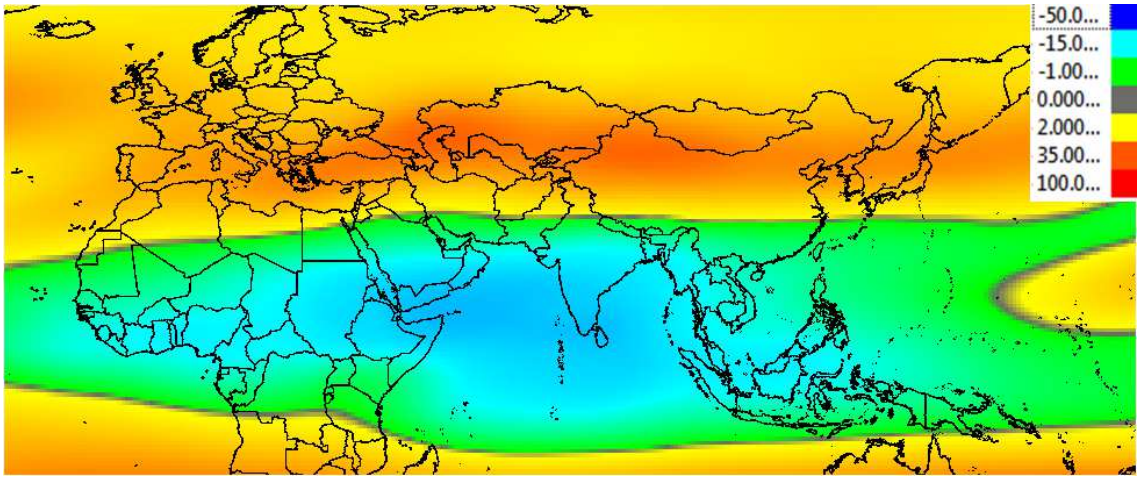

Figure 4.48 ERA-Interim mean 200mb zonal (west to east, westerly positive) wind speed [m/s] for July, Eurasia sub-domain (1979 to 2007).

Drawing on these two figures it is possible to visualise how the NAO and ENSO phenomena may act as levers to influence Eurasian circulation in general, and over the tracking of weather systems over the UIB in particular. In months with westerly dominated weather systems, the NAO is positioned at the "upstream" end, or entrance, of the Eurasian 200mb level circulation jet. In the tropical Pacific, ENSO is positioned at the downstream end, or exit, of the continental section of the 200mb jet. In summer the NAO can influence the trajectory and strength of westerly systems, while ENSO can influence both the northward expansion of the monsoonal systems and the downstream conditions of westerly flow. Ding and Wang (2005) hypothesised along these lines when they described a "circumglobal teleconnection in the Northern Hemisphere summer".

4.7 Summary and discussion

4.7.1 Summary

This study has expanded and improved upon previous assessments of climatic trends in the UIB historical record (Fowler and Archer, 2006; Khattak *et al*., 2010) by drawing on multiple data sources and testing multiple analyses to robustly substantiate on-going seasonally and diurnally asymmetrical temperature trends indicated in the available historical record for the UIB. Furthermore, the spatial assessment, presented in Section 4.2.4, using outputs from meteorological reanalyses – both 'native' resolution and downscaled by an RCM – to examine the coherence of sub-regional patterns of change in the UIB and adjacent areas is an innovation by the present study.

In line with wider global patterns, expected increasing temperatures in cold seasons (autumn to spring) are found for the UIB. Summer temperatures in the study area, however, have been decreasing in recent decades. Examining in detail these seasonally asymmetrical patterns, it is found that the net temperature change (Tavg trend) in each season results from asymmetrical contributions by diurnal phases. From autumn through spring, increasing mean temperatures are mostly driven by increasing (day-time) Tmax, with little substantial change in Tmin during those seasons. Decreasing summer temperatures on the other hand are mostly attributed to decreasing Tmin while Tmax is relatively stable in these months.

Moving beyond simple trend assessment by investigating potential causal mechanisms for the patterns of change observed, the present work has assessed the correlations between the outputs of numerical weather simulations of recent climate (meteorological reanalysis and reanalysis-forced regional climate model simulations). Cloud cover and its effects governing the local energy balance and hence near-surface air temperature are clearly crucial issues. The temperate/mid-latitude surface energy balance response – decreased net shortwave/solar radiation and increased longwave/thermal radiation – to increasing cloud cover appears straightforward. The modelled response to cloud cover variability in the fringes of the monsoonal climate regime/system are more ambiguous.

The present work also investigated potential links between local climate variability and indices of larger-scale atmospheric circulation. The links between these indices and local climate are most often referred to as teleconnections. While previous work has found that modes of variability in both the tropical Pacific/Indian Ocean and North Atlantic/Mediterranean can substantially influence precipitation and temperature in the UIB/Himalaya (Archer and Fowler, 2004; Syed *et al*., 2006; Yadav *et al*., 2009), once again the highly variable nature of the past decade limits the statistical significance of additional findings by this study. Key findings presented in this Chapter include:

- Precipitation in the UIB is highly variable in time as well as space. Assessment of (linear) precipitation trends is highly sensitive to choice of analysis window (starting and ending years).
- Results presented here corroborate and strengthen previous findings (Fowler and Archer, 2006; Khattak *et al.*, 2011) of seasonally and diurnally asymmetrical trends in near surface air temperature.

- Reanalysis estimates of cloud cover correlate strongly with both surface energy balance components and near-surface air temperature. Day-time cloud reduces incoming solar radiation and Tmax. Night-time cloud limits out-going thermal radiation and increases Tmin. Both day-time and night-time cloud reduce DTR.
- Large-scale atmospheric circulation features including both ENSO and NAO have been shown to increase cyclonic activity (storms and precipitation) in the UIB with associated effects for near-surface air temperature. The inherent climatic character of the UIB, however, limits the amount of discernible causal influence (signal) amongst the background variability (noise).

4.7.2 Discussion

As in many regions of the world, the precise regional consequences for the UIB of anthropogenic climate change remain poorly characterised. This lack of clarity stems from the considerable uncertainty regarding both current and future cloud and precipitation climatologies and their effects on local surface energy balance and hydrological processes. In general physical terms, a warming atmosphere will have greater capacity for moisture transport, but the spatial and temporal distribution of these fluxes, including associated evaporation and precipitation, are insufficiently understood at present. This uncertainty is compounded in the UIB by the complexity of local circulation patterns where the climate regimes of westerly and monsoonal weather systems intersect.

Additional complexity stems from the ruggedness of terrain in the UIB which results in steep spatial gradients in orographically-influenced parameters (temperature, cloud cover, precipitation). These are precisely the parameters of greatest interest for understanding the potential impacts of future climate change. This spatial complexity provides a compelling argument in favour of both high resolution meteorological simulation – preferably coupled to a physically-based simulation of land surface and hydrological processes – and the creation of comparable resolution long-record spatial climate data series – e.g. land surface temperature, cloud cover, albedo – from historically available remote sensing records (e.g. AVHRR).

Anecdotal evidence (personal communications with other researchers) at the moment points toward the crucial issue of moisture contributions from the Arabian Sea to local cyclonic activity (either depressions from either westerly waves or tropical origins). The primary coupled oceanic-atmospheric features considered in this study –

i.e. NAO and ENSO – could experience effective state changes in their influence, flipping between interference (analogous to waveform cancelling) and mutual reinforcement (analogous to waveform superposition) regarding local precipitation events and cloud climatologies. The vast uncertainty regarding the thresholds and general controlling parameters/mechanisms of these interactions is a further argument in favour of multi-scale nested climate simulation of the region and development of long-record remote sensing outputs. These analytical tools may hold the key to unravelling the complex local system responses to large scale climate drivers.

Chapter 5: Plausible scenarios of future climate in the Upper Indus Basin

5.1 Introduction

The fate, or trajectory, of water resources in the Upper Indus Basin (UIB) in the coming decades is a matter of great concern. This concern is driven by the importance of this resource for water supply, power generation and above all food security within the catchment as well as in the adjacent irrigated lands which are supplied by abstractions from the river. Thus to assess likely future resource availability, there is a need for plausible scenarios of probable future climate.

Chapters 3 and 4 of this thesis presented the identified links between local climate and UIB hydrology as well as the current understanding of the larger-scale drivers of local UIB climate. This understanding of UIB hydro-climatology provides the foundation for assessing available indications of future climate in order to construct the required scenarios.

The primary sources for such scenarios are projections of future climate produced by global models of atmospheric circulation known as GCMs (general circulation models). At present, due to limitations of hardware capacity confronted with computational requirements, the spatial resolution of GCMs is relatively coarse, often on the order of 200km to 300km, although some higher resolution models operate at 60-100km. Hydrological impact studies, however, are carried out at much finer spatial scales than these.

Furthermore, GCMs are only approximations of the actual climate system as they attempt to model highly complex physical processes with relatively simple numerical formulations (model physics) which are shaped by parameterisations of physical constants. As a result of these simplifications, the model physics and parameterisations inherently introduce biases into the model outputs. Each GCM simulation uses a distinct combination of parameterisations and model physics and hence exhibits a potentially unique pattern of biases where certain parameters will show greater or larger errors in different seasons and in different regions.

Thus in order to be useful in hydrological impact studies, GCM outputs must be downscaled to an adequately fine spatial resolution and corrected for their inherent

biases. A variety of downscaling techniques exist, but these are broadly grouped into two categories.

- i) statistical downscaling which draws upon identified relationships between "predictors" of local climate (predictands) and local climate variables. Amongst the most commonly used of statistical downscaling methods is the "delta change approach" whereby relative changes between 'control' and 'future' GCM runs are applied to time-series of local observations using additive offsets or multiplicative factors known as "change factors";
- ii) dynamical downscaling in which a finer spatial resolution circulation model – referred to as a regional climate model (RCM) – is run over a limited spatial domain using outputs from a GCM as boundary conditions.

Comprehensive reviews of downscaling techniques are available in the literature, notably Fowler et al. (2007).

Even with bias correction – which is based on comparison of historical meteorological observations to GCM "control" simulations of the same time period – a large degree of uncertainty remains over future climate projections. This uncertainty stems from a number of factors including:

- the unknown quantitative trajectory of future anthropogenic greenhouse gas emissions which may not follow the assumed patterns used as GCM inputs.
- Model uncertainties, including resolution, parameterisations, structure, and for RCMs, boundary conditions.
- the predication of stability of model biases, i.e. whether biases between simulated and 'real world' future climate will follow the patterns identified between simulated observed present (control) climate, in a changing climate. This is a specific but noteworthy function of the general model uncertainties.

For these reasons, it is recommended whenever possible to use scenarios from multiple climate model experiments often referred to as 'ensembles'. Unfortunately for this project, only the output from a single RCM – i.e. a pair of simulations, control and future, using one GCM to drive one RCM – was available. For this reason, the results presented in this Chapter are intended to provide a demonstration of methodology rather than an exhaustive exploration of climate projection uncertainty for probable future conditions in the UIB.

5.2 Presentation and background of available RCM simulation PRECIS forced by HadAM3P

One of the most important elements in dynamical downscaling is the choice of GCM which is used to drive the RCM (Jacob et al. 2007; Liang et al., 2008; Pan et al., 2001). In the case of this project, the RCM PRECIS (Jones et al., 2004) – a version of the UK MetOffice Hadley Centre regional model HadRM3 – is driven by the GCM HadAM3P (Pope et al., 2000) also developed by the Hadley Centre. HadAM3P is an atmospheric circulation model only. This means that the mass circulation and energy transfers of the ocean are not directly modelled but rather provided by a set of prescribed (observed) sea surface temperatures (SSTs). This is in contrast to a 'fully-coupled' ocean-atmosphere GCM which simulates both but is much more computationally intensive. As explained above, each GCM brings with it its own set of biases related to model parameterisations and structure. Previous studies have identified the following distinctive elements in HadAM3P results:

- The primary systematic misrepresentations by HadAM3 of global circulation involved excessively high pressures at low latitudes. This bias impacted flow in the Northern Hemisphere (NH) both at the pole and in the 'Icelandic low' (Pope et al., 2000). Pope et al. (2000) also identified seasonal shifts in the timing (earlier onset) and magnitude (greater accumulations) in simulations than in observations of African and Asian tropical rainfall. Furthermore cold biases near the ground surface from the earlier HadAM2b model remained in HadAM3. The largest biases were found in the NH winter (Pope et al., 2000).
- A further circulation bias was identified by Anagnostopolou et al. (2008) who found that the 'Azores High' simulated by HadAM3P was weaker than shown in the National Center for Environmental Prediction (NCEP) reanalysis climatology (Kalnay et al., 1996) and did exhibit the expected geographic expansion over western Europe and the western Mediterranean.
- With regards to modelling of the Pacific Ocean and its influence on global climate, Spencer and Slingo (2003) found that HadAM3 was able to accurately simulate large scale teleconnections by the El Niño Southern Oscillation (ENSO), with modelled climatology in good agreement with observations even though slight errors in tropical climatology can be exacerbated in the tropical influence of ENSO which then propagate into the extra-tropical ENSO response. In contrast to the good ENSO tropical performance, Spencer and Slingo (2003)

also found that simulation of the Northern Pacific and related teleconnections contained inaccuracies, especially in winter.

These elements are important to the UIB because, as presented in Chapter 4, incremental variations in large-scale atmospheric circulation are thought to be critical in influencing local climate variability. This is particularly true of the North Atlantic Oscillation which quantifies the gradient between the Azores High and the Icelandic Low 'upstream' of the UIB in the global Northern Hemisphere mid-latitude westerly circulation pattern. Also of particular importance is the ENSO phenomenon which has been shown to influence both the South Asian monsoon as well as westerly circulation conditions 'downstream' of the UIB.

Excessive precipitation and/or surface temperature biases may also prove problematic for downscaling efforts if they violate the underlying assumption that incremental changes (change factors) between 'control' and 'future' time-slice simulations may be transferred to local conditions. Assumptions could be invalidated if temperature thresholds – i.e. freeze-thaw timing – are incorrectly modelled or if the relationship between circulation regimes and precipitation events are misrepresented (Ehret et al., 2012).

GCMs may be run using a range of forcing scenarios relating to trajectories for global anthropogenic greenhouse gas emissions (GHGs). In this instance, HadAM3P was forced using the 'high-emission' scenario designated 'A2' by the Intergovernmental Panel on Climate Change (IPCC) in their 4th Assessment Report (AR4) (Christensen et al., 2007; IPCC, 2007) for the 2080s time-slice (2071-2100) and a baseline, 1961-1990. The emissions scenarios used in AR4 were set forth in the IPCC "Special Report on Emissions Scenarios (IPCC SRES, 2000). The 'A2' emissions scenario was designed to describe a future with continuous population growth and economically development where globally coordinated efforts to limit emissions growth were muted. It was thus conservative in terms of its optimism regarding climate change mitigation. This conservatism has made it popular in climate modelling simulations as the projected changes are more severe than in scenarios where emissions growth is better constrained. Despite this intended conservatism, latest estimates of emissions growth to date show that emissions growth is in fact in line (i.e within the bounds of historical uncertainty) with the 'A2' scenario (Peters et al., 2013).

5.3 Bias assessment of available RCM outputs for the UIB

5.3.1 Methodological approach to RCM bias assessment for the UIB

Direct comparisons of outputs from RCM simulations to local observations can be problematic in a region as topographically complex as the UIB. Difficulties arise because the current generation of RCMs still operate at a relatively coarse spatial resolution – 0.50 decimal degrees or roughly 50km in the case of the PRECIS outputs – with each grid-cell output representing mean spatial conditions while the available local observations are not spatially representative in absolute terms. This is the case despite local observations providing strong quantitative indicators of interannual variability, as was shown in Chapter 3 of the present work.

Thus the work presented here will focus on methods for quantifying the performance of PRECIS driven by HadAM3P for the study area:

- Spatial comparisons will be made over the relevant sub-domain between outputs from PRECIS driven by HadAM3P for the 'control period' and PRECIS downscaling of ERA-40 for the climate variables influencing UIB hydro-climatology. These comparisons enable examination of the influence of the boundary conditions on the resultant RCM climatology of the UIB.
- For selected parameters where direct, absolute comparison is more applicable, the observations from the primary long-record observing stations will be compared to the values from the overlying PRECIS grid cells.

In principle one would expect the PRECIS driven by boundary conditions from global meteorological reanalysis, in this case ERA40, to provide more realistic simulation of local control-period climate than when PRECIS is driven by a GCM, e.g. HadAM3P for the same time period. The reasoning for this expectation is that ERA-40 boundary conditions are constrained by re-initialisation from data assimilation for each 6-hour time-step of the observed record (Uppala et al., 2005) whereas HadAM3P boundary conditions are free to evolve in the 30-year control simulation (1961-1990) and hence have far greater potential to diverge from observed climate conditions if the GCM formulation contains flawed approximations of key processes or features. The performance of ERA40-driven PRECIS as a description of UIB climatology was presented spatially in Chapter 3 (sections 3.5.5 and 3.6.3) and as correlations of time-series to local observations (PMD) in Chapter 4 (sections 4.3.3 and 4.5.1).

Hence as a spatial analysis PRECIS driven by HadAM3P, hereafter designated PRECIS_AM3P, will be assessed against PRECIS driven by ERA40, hereafter

designated PRECIS_ERA40. To clarify, PRECIS_ERA40 will be compared to the PRECIS_AM3P "control" time-slice simulation of mean "reference climate" (1961 to 1990), hereafter designated PRECIS_AM3P$_{cntrl}$. This differentiates it from the PRECIS_AM3P simulation of projected future climate in the late 21st century (2071 to 2100), hereafter designated PRECIS_AM3P$_{futr}$.

PRECIS_ERA40 and PRECIS_AM3P$_{cntrl}$ will be compared across a common spatial sub-domain of the UIB and its immediate contiguous area. In this inter-comparison of the boundary conditions influence on RCM climatology of the UIB, special focus will be given to twelve selected grid cells spread throughout the primary runoff-contributing areas of the northwest UIB. The location of these cells, also shown in Chapter 3, is given in Figure 5.01.

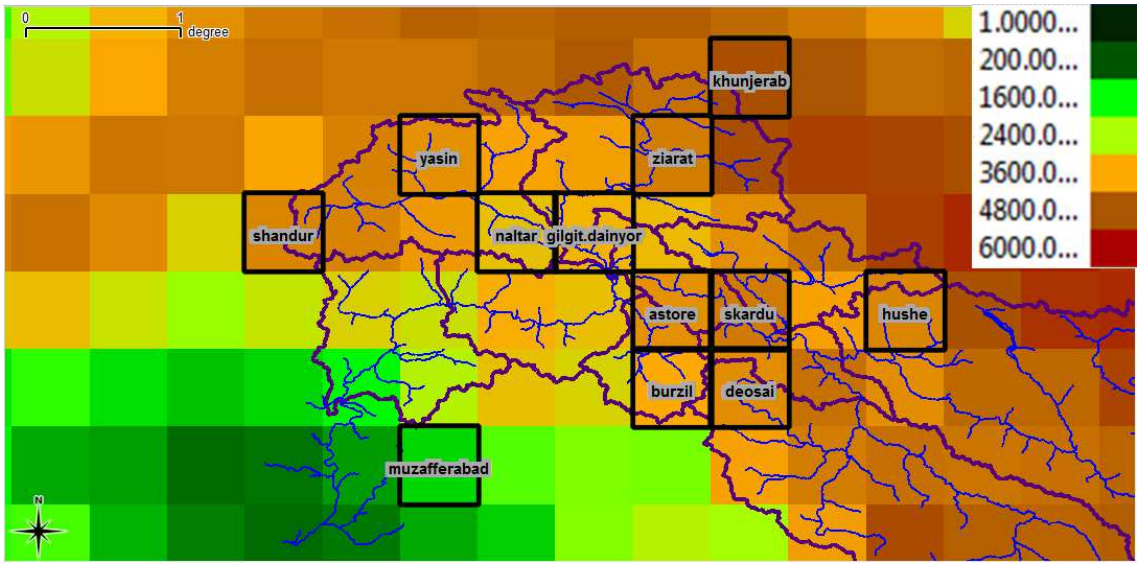

Figure 5.01 Selected analysed PRECIS grid cells with GTOPO30 orography.

5.3.2 Precipitation climatology comparison between PRECIS_AM3P$_{cntrl}$ and PRECIS_ERA40

Figure 5.02 shows the ratio of mean monthly precipitation amounts from PRECIS_AM3P$_{cntrl}$ relative to PRECIS_ERA40. In this, and subsequent figures of gridded spatial data, the calendar months are labelled alphanumerically, e.g. January = "m01", December = "m12". Clear seasonal and geographic patterns are evident. For most of the year PRECIS_AM3P$_{cntrl}$ produces a substantially drier climatology than PRECIS_ERA40 over the mountainous sections of the sub-domain and especially over the northwest UIB. Differences over the core UIB between the two simulations are particularly pronounced in January, June, October and December. In contrast, during the later months of the monsoonal period, i.e. August and September, PRECIS_AM3P$_{cntrl}$ yields a wetter climate than PRECIS40. Also in contrast to the core UIB sub-region, the

lowlands adjacent to the Himalayan arc – the Indo-Gangetic plain – are generally relatively wetter under PRECIS_AM3P$_{cntrl}$ than PRECIS_ERA40 during the warmer months of March through November. These differences may stem from the circulation biases identified by previous studies and summarised in the preceding section.

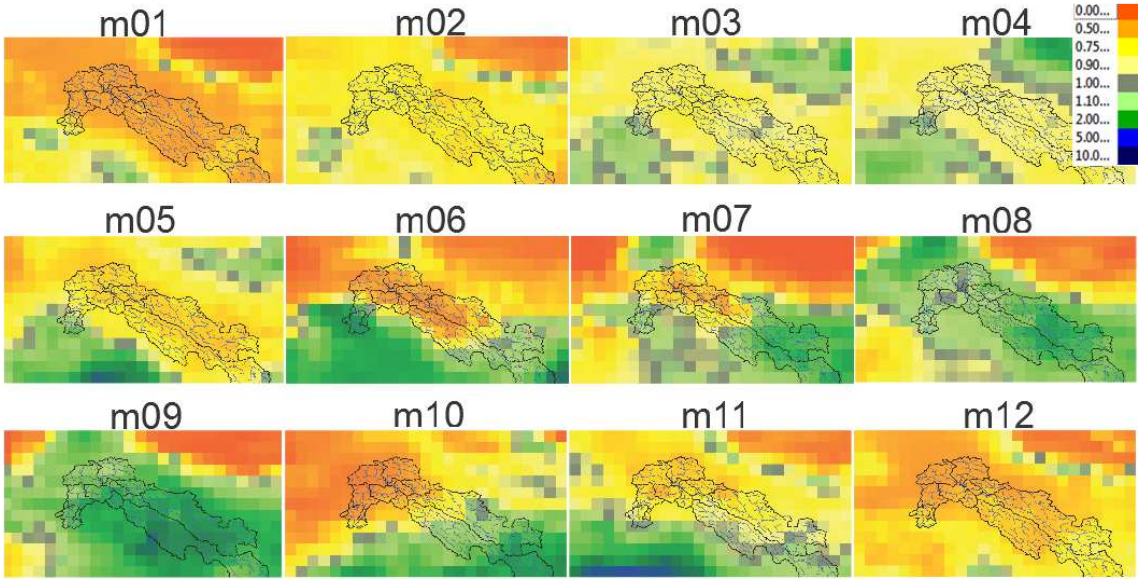

Figure 5.02 Ratio of mean monthly precipitation amounts from PRECIS_AM3Pctrl to PRECIS_ERA40.

Figure 5.03 shows the ratios of mean monthly precipitation amounts for PRECIS_AM3P$_{cntrl}$ and PRECIS_ERA40 for the twelve selected grid cells from the core UIB contributing area. As can be seen, the ratios are relatively spatially homogeneous for much of the year, with sub-regional differences primarily emerging in the monsoonal months. Broadly there is a dry bias in PRECIS_AM3P$_{cntrl}$ with only August and September showing wetter conditions than the reference provided by PRECIS_ERA40. The individual behaviour of the "Muzafferabad" grid cell, the only cell selected from the front-range/foothills sub region, is notable however as it shows wetter tendencies in the pre-monsoon and early monsoon. Also, in September (late monsoon) the grid cells covering the middle mountains (Astore, Burzil, Skardu, Deosai, Hushe) are relatively wet compared to northwestern grid cells (Shandur, Yasin, Naltar, Gilgit.Dainyor, Ziarat, Khunjerab).

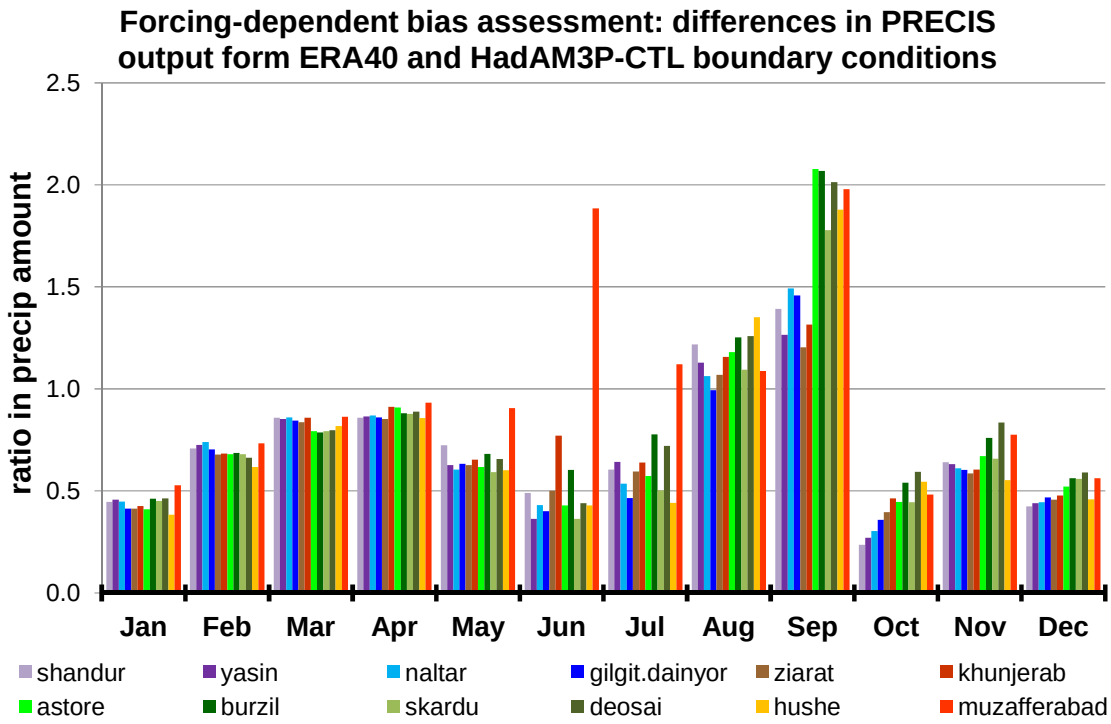

Figure 5.03 Ratio of mean monthly precipitation amounts from PRECIS_AM3Pctrl and PRECIS_ERA40 for twelve selected grid cells.

In Chapter 3 (section 3.5.5) it was shown that there is good general agreement between PRECIS_ERA40 and the moderately coarser resolution ERA-Interim reanalysis. It was noted in section 3.5.5, however, that PRECIS_ERA40 has a stronger spring-time mode for core UIB precipitation than does ERA-Interim. This strong spring-time mode in PRECIS_ERA40 is coherent with the seasonality of precipitation seen in local observations (PMD). Thus, the seasonal pattern of ratios found between PRECIS_ERA40 and PRECIS_AM3P$_{cntrl}$ would appear to suggest a mixed performance by the latter. Whilst underestimation of precipitation in the early Spring (March, April) is marginal, substantial underestimation of precipitation in both mid-Autumn to mid-Winter (October to January) and the late Spring to mid-Summer suggest a potential general dry bias in HadAM3P boundary conditions. Furthermore the excessive precipitation in PRECIS_AM3P$_{cntrl}$ with reference to PRECIS_ERA40 in both August and September suggest problems in both the timing and magnitude of South Asian monsoonal penetration into the UIB by the model.

5.3.3 Near-surface air temperature climatology comparison between PRECIS_AM3P and PRECIS_ERA40

In comparison to PRECIS_ERA40, PRECIS_AM3P$_{cntrl}$ appears to overestimate the magnitudes of both the annual and diurnal temperature cycles through the sub-

domain. This can be seen in Figures 5.04 (Tavg) and 5.05 (DTR) which show the differences – PRECIS_AM3P$_{cntrl}$ minus PRECIS_ERA40 – between the two simulations. The exception to this generalisation appears to be an underestimation of the diurnal temperature range in the plains and adjacent mountainous front-range during the monsoonal months.

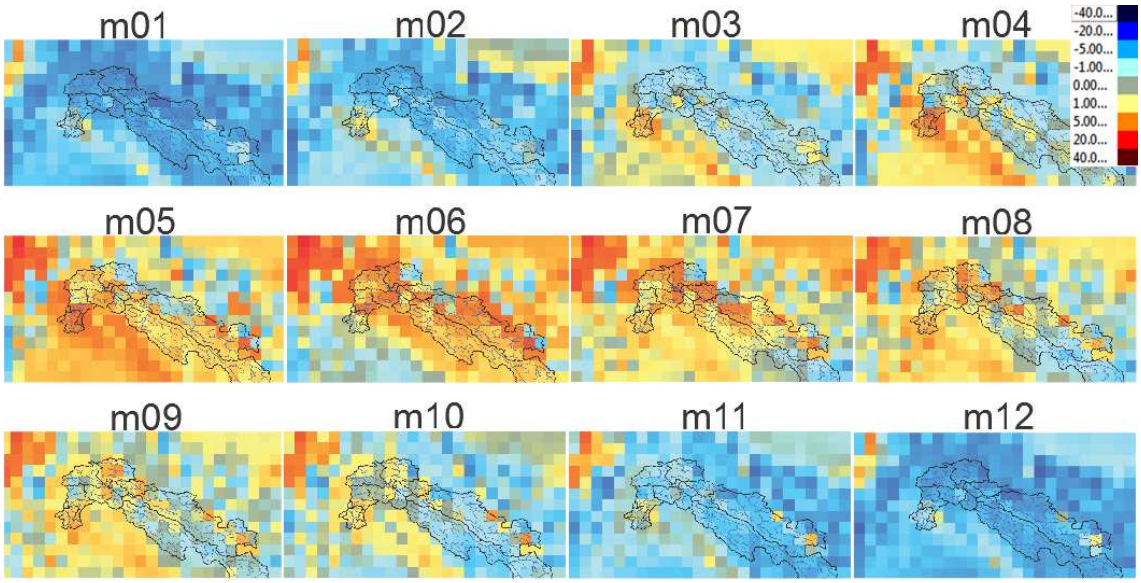

Figure 5.04 Spatial, pixel-wise difference of mean air temperature (Tavg) from the two simulations (PRECIS_AM3P$_{ctrl}$ minus PRECIS_ERA40).

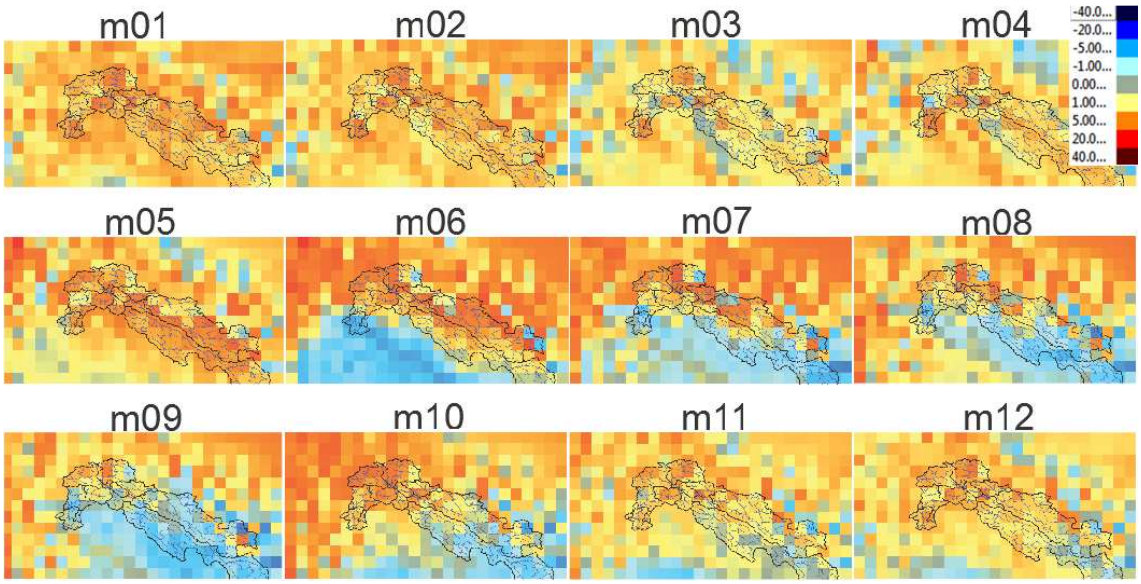

Figure 5.05 Spatial, pixel-wise difference of diurnal temperature range (DTR) from the two simulations (PRECIS_AM3P$_{ctrl}$ minus PRECIS_ERA40).

Confirmation of excessively cold winters and excessively warm winters in PRECIS_AM3P$_{ctrl}$ can be found in Figures 5.06 (Tmax) and 5.07 (Tmin). Generally positive DTR bias confirms greater cold biases in Tmin than Tmax in winter and greater warm biases in Tmax than Tmin in summer. Divergence from this general spatial pattern in the monsoonal season over the plains and adjacent from ranges can be

explained by the weak warm to mild cool biases in Tmax in these sub-regions during the months in question.

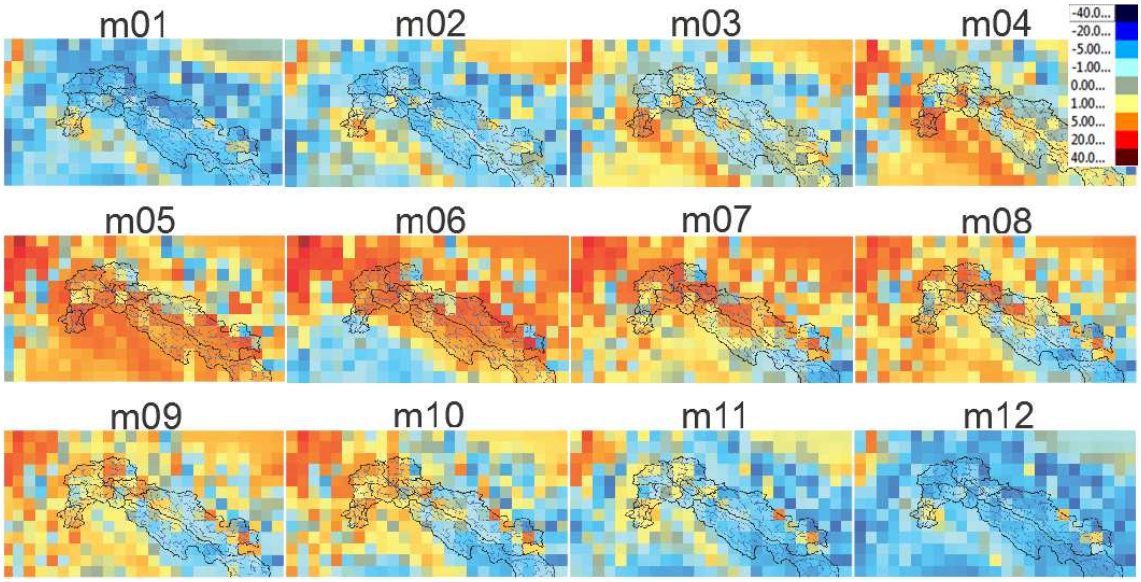

Figure 5.06 Spatial, pixel-wise difference of mean maximum daily air temperature (Tmax) from the two simulations (PRECIS_AM3P$_{ctrl}$ minus PRECIS_ERA40).

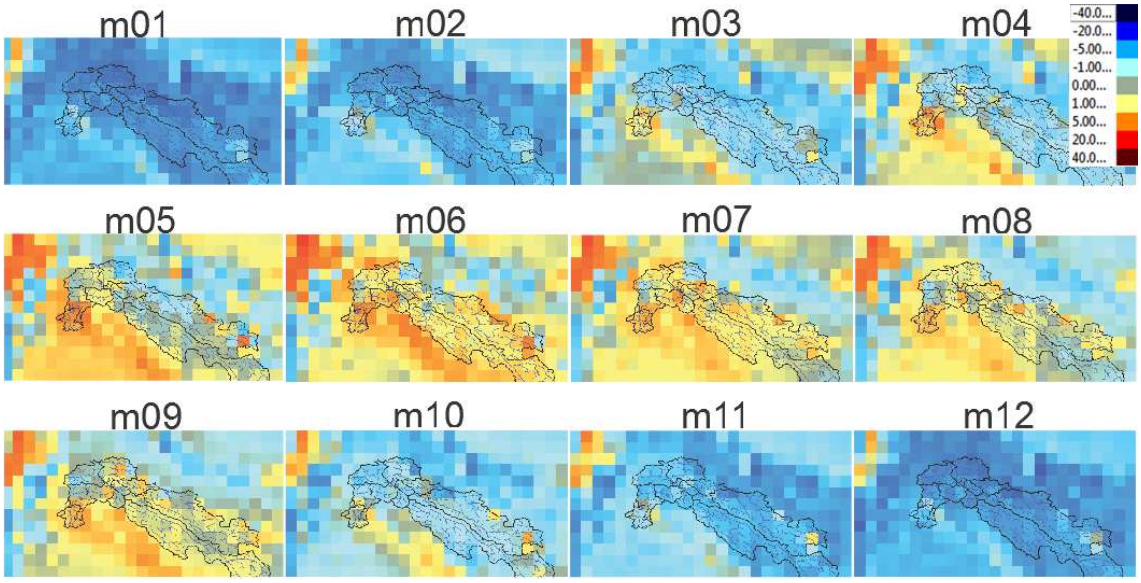

Figure 5.07 Spatial, pixel-wise difference of mean minimum daily air temperature (Tmin) from the two simulations (PRECIS_AM3Pctrl minus PRECIS_ERA40).

Figures 5.08 to 5.10 broadly confirm the excessive annual and diurnal cycles while focusing on the twelve selected core UIB grid cells. Figure 5.08 shows differences in Tmax between PRECIS_AM3P$_{cntrl}$ and PRECIS_ERA40. Figures 5.09 and 5.10 provide the equivalent respectively for Tmin and DTR. At this level of detail, sub-regional differences between different sections of the Himalayan mountain arc begin to manifest themselves.

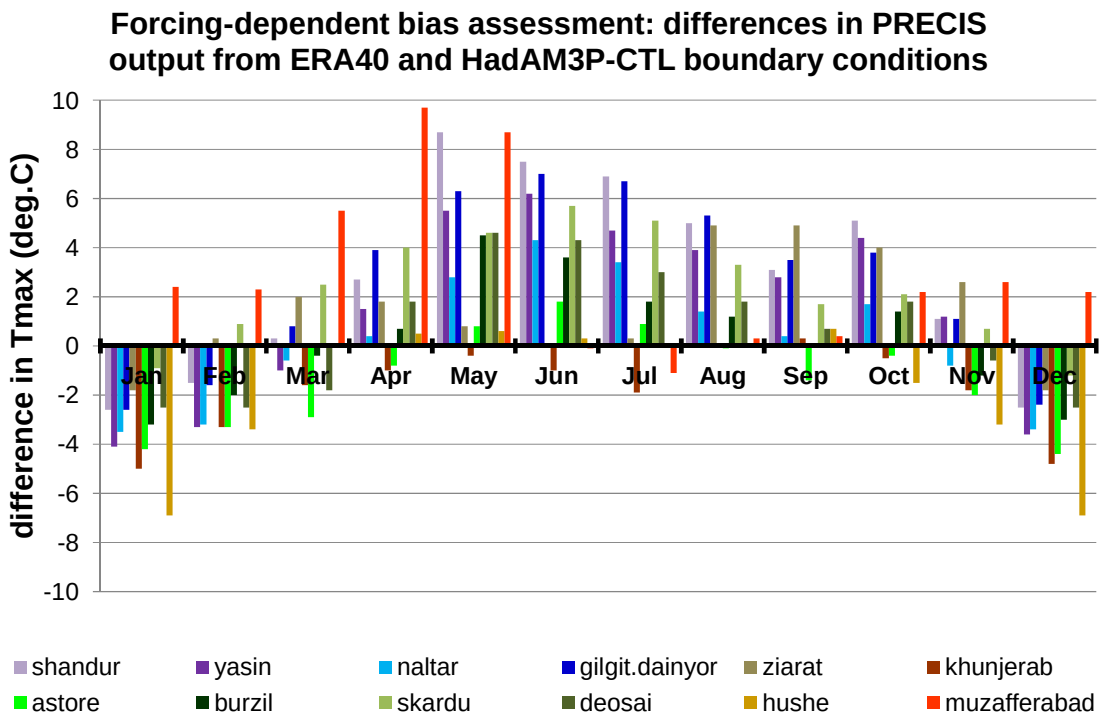

Figure 5.08 Difference (PRECIS_AM3P$_{ctrl}$ minus PRECIS_ERA40) of mean daily maximum air temperature (Tmax) for twelve selected grid cells.

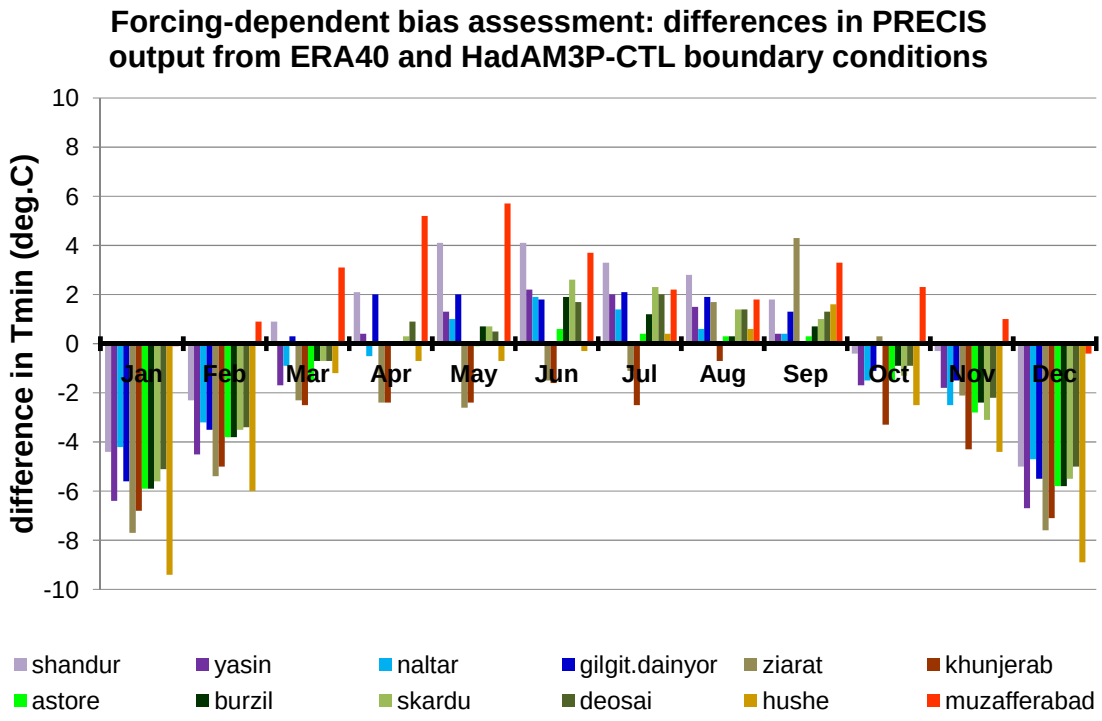

Figure 5.09 Difference (PRECIS_AM3P$_{ctrl}$ minus PRECIS_ERA40) of mean daily minimum air temperature (Tmin) for twelve selected grid cells.

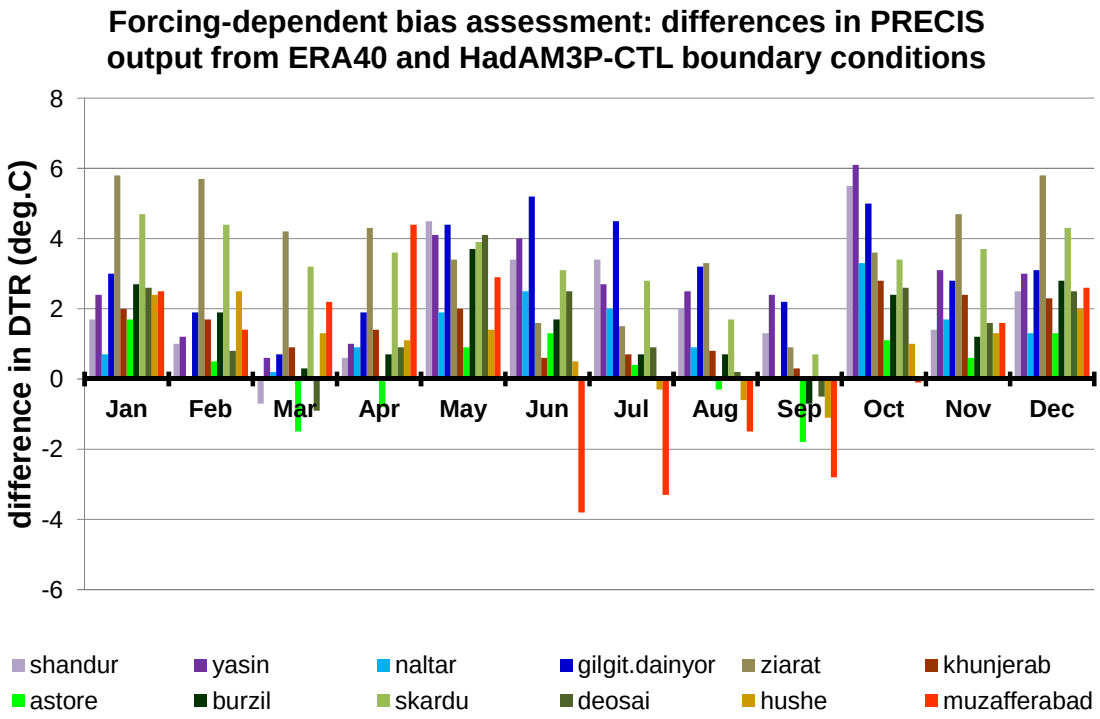

Figure 5.10 Difference (PRECIS_AM3P$_{ctrl}$ minus PRECIS_ERA40) of mean diurnal temperature range (DTR) for twelve selected grid cells.

As with precipitation, the "muzafferabad" grid cell on the front range of the Western Himalaya exhibits distinct behaviour from the other selected grid cells. It might be tempting to consider this a "rogue cell" whose contrasting behaviour is simply an artefact of model instability. In reality, this grid cell was selected as representative of what was expected to be a separate climate sub-regime. Its location on the Himalayan front range, adjacent to the plains and foothills, sets it apart geographically from the other eleven grid cells selected within Hindu Kush, Karakoram and interior Western Himalaya. This area is expected to have greater monsoonal influence due to its southerly location and lower elevation. Detailed study of the behaviour of the "muzzaferabad" grid cell compared the adjacent grid cells by examination of the spatial comparisons (Figures 5.02 and 5.04 to 5.07) and this reveals coherent patterns within the immediate vicinity, hence rebutting the "rogue cell" assumption.

The "muzzaferabad" cell shows a positive bias in Tmax throughout the year except during the monsoonal months (June to September). This is in contrast to the broad regional pattern of negative bias in winter and positive bias from late spring to early autumn. The high mountain grid cells of the western Karakoram – "ziarat", "khunjerab" and "astore" – also deviate from this pattern. They share the regional winter cold bias but in other months show limited or cold bias rather than the generalised warm bias.

The contrasting behaviour of the "muzafferabad" grid cell is also found for Tmin where effectively no bias is found in winter, rather than the very substantial cold bias found in other selected grid cells. The western Karakoram grid cells also again show different behaviour from late spring to early autumn than the cells selected from the adjacent mountainous sub-regions, i.e. the Hindu Kush and Western Himalaya.

Bias in DTR is logically the net (additive) bias from Tmax and Tmin. There is a broad regional net positive bias to DTR, as shown in Figure 5.10, with the exception of the front range "muzafferabad" grid cell which shows negative bias throughout the monsoonal season. There are other minor discrepancies from this overall pattern, but in general cells from a given sub-region, e.g. central Hindu Kush ("shandur" and "yasin"), behave similarly.

5.3.4 Implications of climatology comparison between PRECIS_AM3Pcntrl and PRECIS_ERA40 for interpretation of climate change projections

The comparison of the PRECIS_AM3P$_{cntrl}$ climatology with respect to PRECIS_ERA40 identified an "amplification" of the annual and diurnal temperature cycles as well as the exaggeration of monsoonal influence and apparent underestimation of contributions from westerly weather systems to annual precipitation totals. These apparent biases may indicate sensitivities in PRECIS_AM3P$_{cntrl}$ to changes in specific processes or governing variables responsible for the diurnal and annual cycles in near-surface air temperature as well as the circulation patterns shaping the extent and magnitude of monsoonal activity in the sub-domain and tracking of westerly weather systems. These sensitivities could, in turn, skew even the calculation of relative changes by distorting the simulated responses to absolute climate forcings from projected increases in greenhouse gas concentrations. More positively, the detailed comparison revealed only limited sub-regional discrepancies within core UIB area. The general spatial coherence of grid cells covering the primary NW UIB tributary catchments is encouraging as it indicates that the region may well respond relatively uniformly to changing climate forcings. On the whole, this comparison provides further evidence supporting the use of a weather generator approach for downscaling, i.e. production of synthetic time-series of 'perturbed' local observations, for simulating climate change impacts in the UIB.

5.3.5 Bias assessment of PRECIS_ERA40 and PRECIS_AM3Pcntrl versus local observations (PMD)

It is important to recall and clarify that the term "apparent bias" as used in the preceding section refers to the quantitative differences between what is assumed to be a more realistic simulation of the present climate by PRECIS driven by ERA40 than by the same RCM but driven by the control period outputs from HadAM3P. The reasoning for this presumption of superiority is that the boundary conditions supplied by the reanalysis are constrained multiple times per day over the historical record while those supplied by the GCM are allowed to evolve over the time period of the control simulation, thus allowing any flaws to self-perpetuate and potentially compound.

Ideally, it would be possible to directly assess the performance of each RCM simulation for each climate parameter in each grid cell using independent, spatially representative observations. Unfortunately, the reality of present and historical meteorological observations in the UIB means that long-record climate data series are few in number and sparsely distributed. Furthermore, for the meteorological stations that do exist, owing to the extremely varied mountainous terrain and the lack of confirmation of the modelled surface height; absolute comparison of orographically governed/influenced parameters to their locally observed analogues is not meaningful. Two relative mean comparisons are possible however:

- the mean fractional contribution by month to total annual precipitation;
- the diurnal temperature range (DTR).

1) Locally observed precipitation (PMD) versus PRECIS_AM3P$_{cntrl}$ and PRECIS_ERA40:

The mean monthly fractional contribution to total annual precipitation is an indicator of the accuracy with which the seasonality – which months are relatively wet and dry – of local rainfall patterns is reproduced. The underlying assumption here is that the temporal distribution of precipitation as observed by the local stations is spatially representative even if the absolute amounts are not.

Figure 5.11 shows the mean monthly fractional contribution to total annual precipitation for observations at three stations: Gilgit, Skardu and Astore, in comparison to both PRECIS_ERA40 and PRECIS_AM3P$_{cntrl}$. For two of the stations, Skardu and Astore, RCM performance is relatively consistent and centred around or near unity,

with the exception of the beginning (June) and end (September) of the monsoon season, when respectively PRECIS_ERA40 and PRECIS_AM3P$_{cntrl}$ overestimate the contribution of each month to the annual total precipitation. For the remaining station Gilgit, however, the pattern is substantially different. For Gilgit, the relative importance of late autumn and winter precipitation is substantially overestimated by both PRECIS_ERA40 and PRECIS_AM3P$_{cntrl}$ while the contribution of late spring through early autumn months is underestimated. It is important to point out, however, that despite being located at the outlet of a relatively humid catchment Gilgit is by far the driest station of the three, hence raising doubts about whether scaling between precipitation observed at the meteorological station and the broader spatial average is constant regardless of the month or whether the scaling factor/coefficient may vary seasonally.

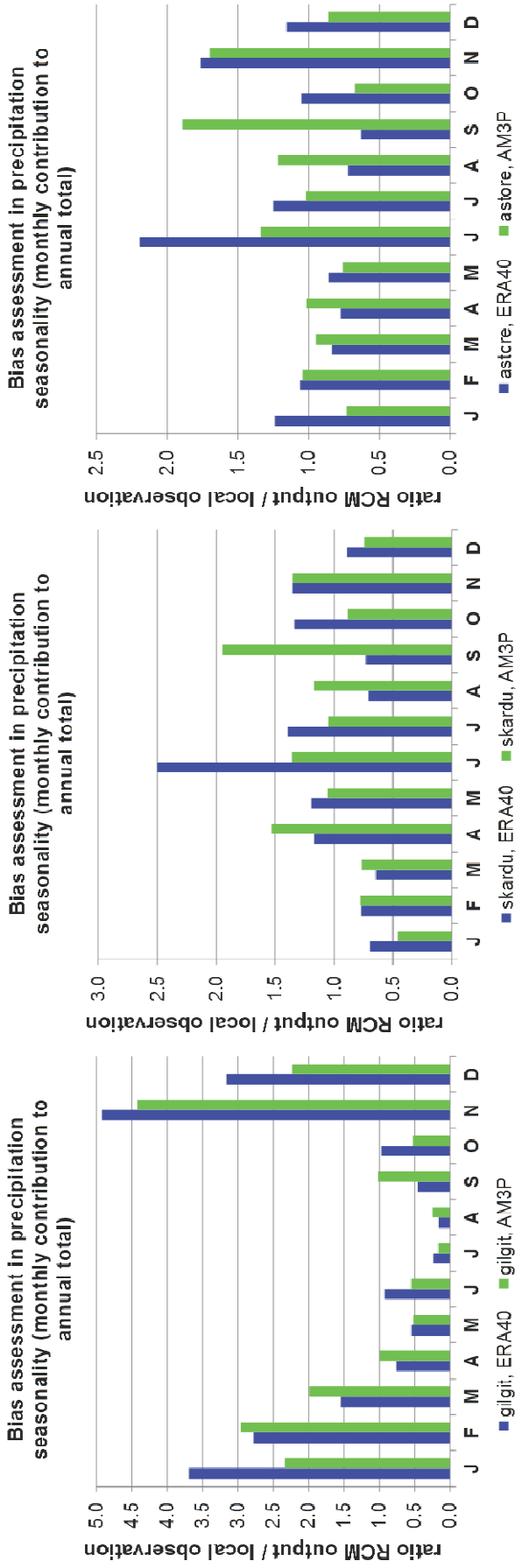

Figure 5.11 Ratio of mean monthly contribution to mean annual total precipitation between local observations and PRECIS_ERA40 and PRECIS_AM3P$_{ctrl}$.

A quantitative performance indicator based on the metric of mean monthly fractional contribution to annual total precipitation, the root mean squared error (RMSE) in terms of fraction of annual total precipitation per month, is shown in Table 5.1.

Simulation	Gilgit PMD	Skardu PMD	Astore PMD
PRECIS_ERA40	0.0648	0.0326	0.0233
PRECIS_AM3P$_{cntrl}$	0.0647	0.0317	0.0185

Table 5.1 RMSE for monthly fractional contribution to annual total precipitation for PRECIS_ERA40 and PRECIS_AM3Pcntrl as compared to monthly relative distribution of annual total precipitation from local observations (PMD).

At face value the RMSE scores in Table 5.1 indicate that performance of the two PRECIS simulations is effectively identical. One explanation for this would be that the difference between the point-based observations and the simulated spatial mean observations dwarfs the differences from the boundary conditions.

2) Locally observed DTR (PMD) versus PRECIS_AM3P$_{cntrl}$ and PRECIS_ERA40:

Diurnal temperature range is expected to have an orographic gradient due to differences between the lapse rates for Tmax and Tmin, but it is substantially less elevation-dependent than either. This aspect makes it the most appropriate near-surface air temperature parameter for evaluation of model performance. Figure 5.12 shows that the three available long-record UIB meteorological stations have starkly contrasting relationships to the RCM outputs from the grid cells overlying them. For Gilgit DTR, bias varies wildly between the two simulations and from month to month, with PRECIS_ERA40 showing little or no bias in April to June as well as October and November. There is a positive bias of 3°C or more in the remaining months, while PRECIS_AM3P$_{cntrl}$ shows a similar annual cycle of bias but with a larger bias of between 1°C and 4°C. In contrast, the DTR bias at Skardu is substantially greater, but relatively constant, with a positive bias of ~9°C by PRECIS_ERA40 and ~12°C by PRECIS_AM3P$_{cntrl}$. Meanwhile, DTR bias for Astore from the two RCM simulations are very similar in each month with an annual minimum of ~5°C and 11°C in September.

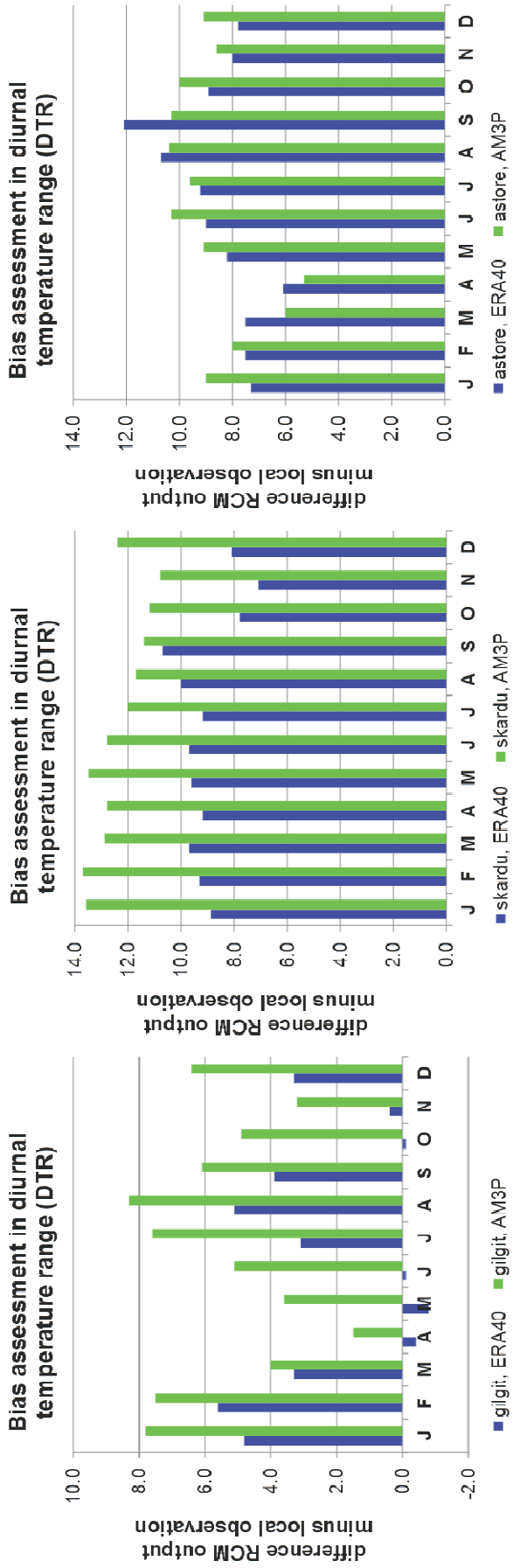

Figure 5.12 Difference in mean monthly DTR between local observations and PRECIS_ERA40 and PRECIS_AM3P$_{cntrl}$ control (PRECIS minus observations).

A quantitative performance indicator based on DTR as metric, the root mean squared error (RMSE) of monthly DTR, is shown in Table 5.2.

Simulation	Gilgit PMD	Skardu PMD	Astore PMD
PRECIS_ERA40	3.26	9.15	8.66
PRECIS_AM3P (control)	5.86	12.43	8.94

Table 5.2 RMSE for monthly DTR (°C) for PRECIS_ERA40 and PRECIS_AM3P as compared to monthly relative DTR from local observations (PMD).

Thus in terms of simulated DTR, for two out of three stations PRECIS_ERA40 is superior (smaller DTR RMSE) to PRECIS_AM3P with the third station showing nearly identical DTR RMSE. The DTR bias assessment also corroborates the characterisation of PRECIS_AM3P as exaggerating the amplitude of the diurnal temperature cycle, with substantial positive bias (overestimation) in every month for all three stations.

In summary, the assumption that PRECIS_ERA40 provides a more accurate representation of UIB climatology to PRECIS_AM3P$_{cntrl}$ is only partially substantiated. While simulation of DTR does appear better in PRECIS_ERA40 (2 out 3 stations), it is difficult to objectively distinguish between PRECIS_ERA40 and PRECIS_AM3P$_{cntrl}$ using selected metrics for the accuracy of precipitation simulation. This could be interpreted as encouraging for the use of PRECIS_AM3P in the projection of future UIB climate conditions. As described in section 4.5.1, strong correlations, with meaningful statistical significance, were found between time-series of precipitation from PRECIS_ERA40 and local observations (PMD) and the present analysis shows PRECIS_AM3P$_{cntrl}$ precipitation simulation to be functionally equivalent to PRECIS_ERA40. In the absence of higher spatial resolution RCM outputs or additional local observations from higher elevation locations, it seems justified that proceeding with PRECIS_AM3P$_{cntrl}$ represents a valid avenue for projection of future climate conditions in the UIB.

5.4 Calibration and validation of a weather generator approach for observed UIB climate

5.4.1 Background on RainSim and the CRU Weather Generator

Given the relatively coarse spatial resolution – 0.5 decimal degrees – of the available RCM simulations as well as the apparent biases identified in the preceding sections, further statistical downscaling is desirable before implementing the projections into hydrological simulations. Previous studies of potential climate change impacts in the Upper Indus (Akhtar et al., 2008; Immerzeel et al., 2009 and Bocchiola et al., 2011) utilised the relatively simple delta change approach, with multiplicative factors for precipitation and additive factors for temperature and no correction of future variance. These studies will be discussed for comparison purposes in Chapter 6. The present study, however, sought to improve upon these existing studies by implementing a more sophisticated technique which is expected to provide better assessment of future changes in climatic variability as well as changes in period means.

Specifically the chosen methodology involves the generation of long "synthetic" weather time-series which allow robust assessment of the statistical distribution of possible future hydrological conditions. The approach used in this study is based around a pair of software tools which together function sequentially as a stochastic weather generator. The first step is the generation of a time-series of "synthetic rainfall" sharing the statistical characteristics of the observed record. This is achieved with the RainSim v3.1.1 software which uses a Neyman-Scott Rectangular Pulses (NSRP) process to model rainfall occurrence (Burton et al., 2008).

The resultant synthetic precipitation time-series is then paired with additional climatic variables (Tmin, Tmax, "sunshine hours", wind speed and vapour pressure) by the Climate Research Unit – Weather Generator (CRU-WG) using regression relationships between rainfall occurrence and these parameters based on transitions between daily rainfall states, e.g. dry-wet, dry-dry, wet-dry (Kilsby et al., 2007). Whilst CRU-WG generates additional variables beyond air temperature these were not deemed useful in the present study (since historical observations were not available with which to calibrate the model). Wind speed and vapour pressure were not used as it was judged infeasible to attempt to accurately model physical mechanisms governing spatial variability of these variables in a region as topographically complex as the UIB.

The "sunshine hours" variable, usually intended for use in calculating potential evapotranspiration (PET), was discarded given its arbitrary and empirical nature. As

will be discussed in Chapter 6, it was instead decided to use the Priestley-Taylor method for calculation of PET. The Priestley-Taylor method requires net shortwave and long-wave radiation at the ground surface. Alternate methods for calculation of these radiation variables were adopted in the absence of their integration by CRU-WG.

The resultant set of self-consistent synthetic weather time-series (in this case for precipitation, Tmin and Tmax) are then validated against the historical record by comparing their statistical descriptors to observations to ensure that the key elements are adequately reproduced. Once the time-series have been validated, typically for the control period of a climate model experiment, a "perturbed" series may be generated using change factors (CF) which quantify changes in descriptive statistics between the reference time period and the future time period of reference. For the variables generated by CRU-WG, these statistics are limited to temperature monthly means and daily variance (Jones et al., 2011) while RainSim allows perturbation of the precipitation time-series by modification of a wider range of statistics including the mean rainfall, variance, proportion of dry days, the skewness of the distribution and the lagged autocorrelation of the time-series (Burton et al., 2008).

Most commonly, these change factors are extracted by comparing results of "time-slice" RCM (or GCM) simulations between future and control runs. The use of change factors to perturb synthetic time-series permits application of scenarios from RCMs (or GCMs) without transferring the inherent biases of these models to new time-series. The crucial caveat here is the assumption that biases are consistent between control and future simulations in a given RCM.

It is worth pointing out that the stochastic approach utilised in RainSim and CRU-WG is truly a state-of-the-art downscaling tool. It has been used to generate the official UK government climate projections (UKCP09, Jones et al., 2009). It has also been used outside the UK for climate change impact assessment assessments on surface water, e.g the Dommel catchment in Belgium and the Netherlands (van Vliet et al., 2012), and groundwater, e.g. the Geer basin in Belgium (Goderniaux et al., 2011). Its present application, in this study, to the UIB is, however, to the author's knowledge the first implementation outside of Europe. It is also consequently the first implementation in a semi-arid climate regime with substantial monsoonal influence. Demonstration of successful validation, as presented in the remaining sections of this Chapter, thus marks an important milestone in the development of this technique and establishment of its

applicability and utility in the broader study of probable future natural resource availability.

5.4.2 Results for calibration of present climate time-series

For the present work synthetic time-series were generated for observed climate conditions for the three primary long-record meteorological stations in the UIB. For brevity only the figures relative to the Astore PMD station, which is used as the "meteorological base station" for the hydrological modelling described in Chapter 6 and 7, will be presented here. Figures for the Gilgit and Skardu stations are presented in Appendix C. The remainder of this section provides graphical illustrations, with commentary, of the validation of the synthetic time-series based upon observed record for these stations.

Figure 5.13 shows the graphical results of the calibration and validation of RainSim for the Astore PMD stations for the observed record (for which daily air temperature is available, i.e. 1981 to 2007). Each key statistic describing the precipitation distribution is considered separately, with comparisons of the "observed", "fitted" and "simulated" values for each calendar month. The "observed" and "simulated" values are calculated using RainSim's analysis mode on the respective observed (input) and simulated (output) time-series. The "fitted" values can be considered the optimised "target" values calculated by RainSim in its "fitting" mode when the parameters required for stochastic simulation are calculated.

Figure 5.13 shows nearly perfect agreement for all statistics in all months. There are, however some minor discrepancies in the "proportion of dry days" (March, April, May) and skewness (June) as numerical techniques used by RainSim are not always able to reconcile all aspects of the defined precipitation distribution. In this case, RainSim adjusts the parameters used to provide the best fit possible according to user-assigned "weights" which prioritise amongst the target statistics. Figure 5.13 shows the preference of the present study, given its general hydro-climatological nature, was the priority matching of the mean and variance. Studies with other objectives might choose different weighting schemes. A study focused on drought might choose to place more emphasis on the "proportion of dry days", perhaps with the addition of "lagged autocorrelation". A study investigation fluvial flooding and hence extreme rainfall, however, might place the greatest weight on skewness followed by variance for example.

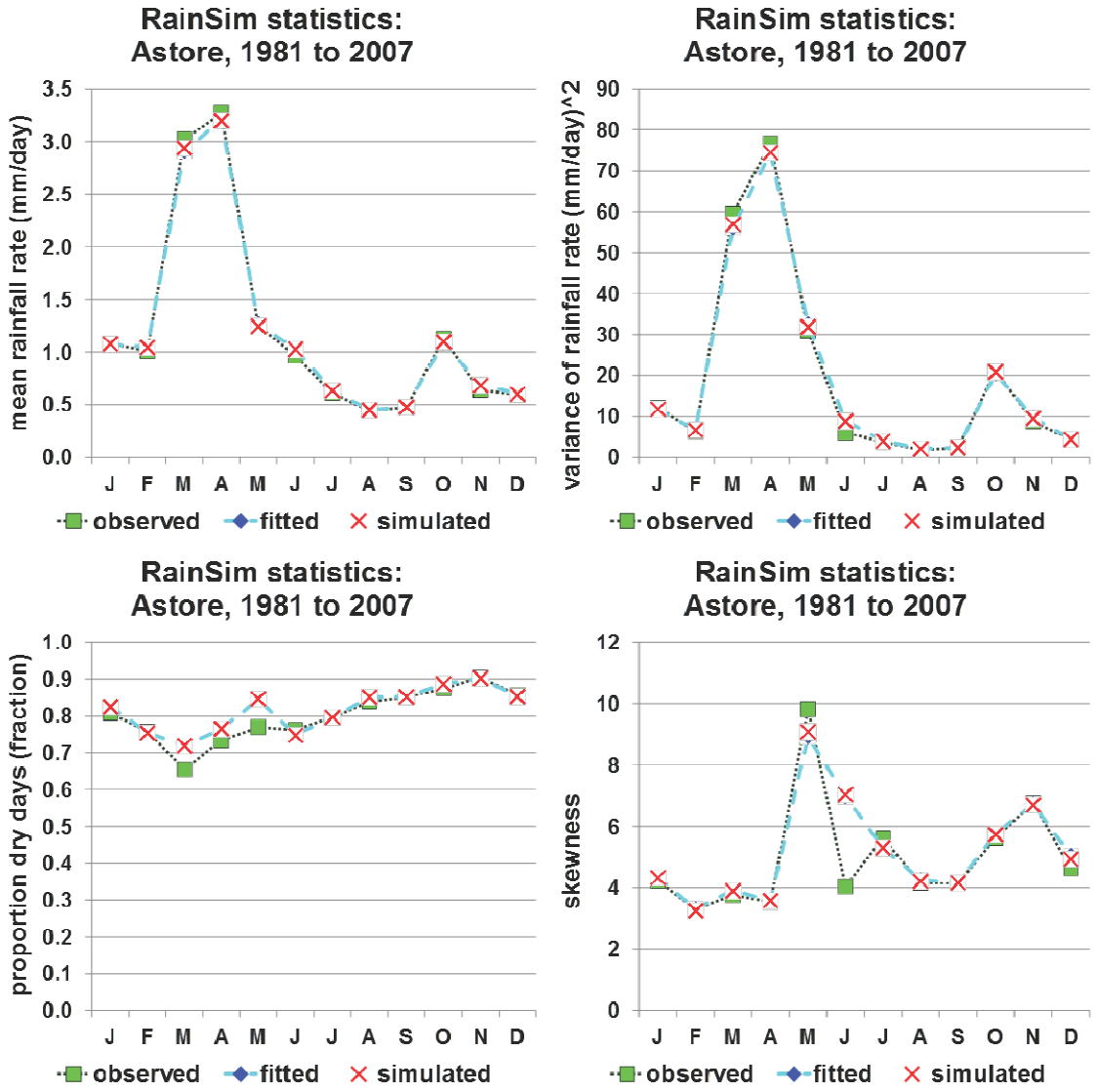

Figure 5.13 Statistics calculated by RainSim for observed, fitted and simulated time-series for rainfall measured at Astore.

While the RainSim statistics shown in Figure 5.13 are useful descriptors in their own right, for hydro-climatological purposes other measures may be more intuitive. The following figures provide alternate descriptors of the precipitation distribution.

Figure 5.14 shows monthly statistics of total precipitation including the mean, median, lower (c25) and upper (c75) quartiles as well as the first (c10) and last (c90) deciles. Finally, Figure 5.14 also shows the "coefficient of variation" (CV), i.e. the ratio of the standard deviation divided by the mean. Agreement is very good for most descriptors in nearly all months. There is some divergence notable in the upper quartile and the last decile (c90) in relatively dry months. This is understandable given that skewness received a relatively light weight during parameter fitting.

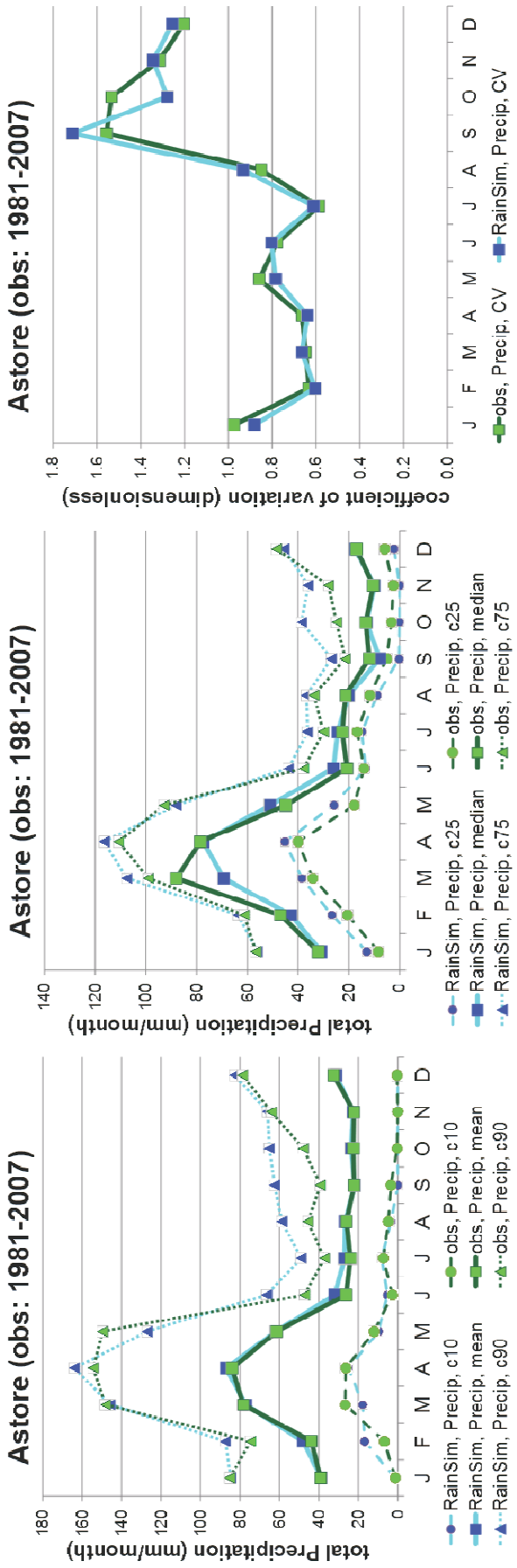

Figure 5.14 Comparison of statistics between observations (obs) and simulated (RainSim) control-climate time-series for precipitation amounts at Astore.

Figure 5.15 shows the monthly statistics of wet days – i.e. the number of days per month with precipitation greater than 0.1mm – including the mean, median, lower (c25) and upper (c75) quartiles as well as the first (c10) and last (c90) deciles. Finally, Figure 5.15 also shows the "coefficient of variation" (CV), i.e. the ratio of the standard deviation divided by the mean. General performance for wet days is much more mixed than for total precipitation. This is understandable since the "proportion of dry days" – which with the proportion of wet days sums to unity (1) – received a lesser weight than the monthly mean (accumulation) and variance of precipitation. Nevertheless, although observed and simulated mean (and median) wet days do not match perfectly, the shape of the annual as well as the general bands of variability, i.e. the quartile bounds and first and last deciles, do show approximate agreement. The agreement on variability measures is further demonstrated by the close match between observed and simulated CV for the first seven months (January to July) of the year. Agreement on CV is moderate for August, September and December, but somewhat disappointing for October and November. The sub-optimal match on October and November CV is, however, perhaps to be expected given that these are the months with the highest absolute CV values both in the observed and simulated wet day statistics.

Figure 5.16 shows the monthly statistics of the diurnal components of near-surface air temperature. The mean as well as the first (c10) and last (c90) deciles are shown for Tmax, Tmin and DTR. Simply put, the agreement between the statistics of the simulated and observed time-series for Tmax and Tmin is excellent not only for the means but also for the first and last deciles. The agreement between simulated and observed statistics for DTR is somewhat less impressive than for Tmax and Tmin, but still quite reasonable.

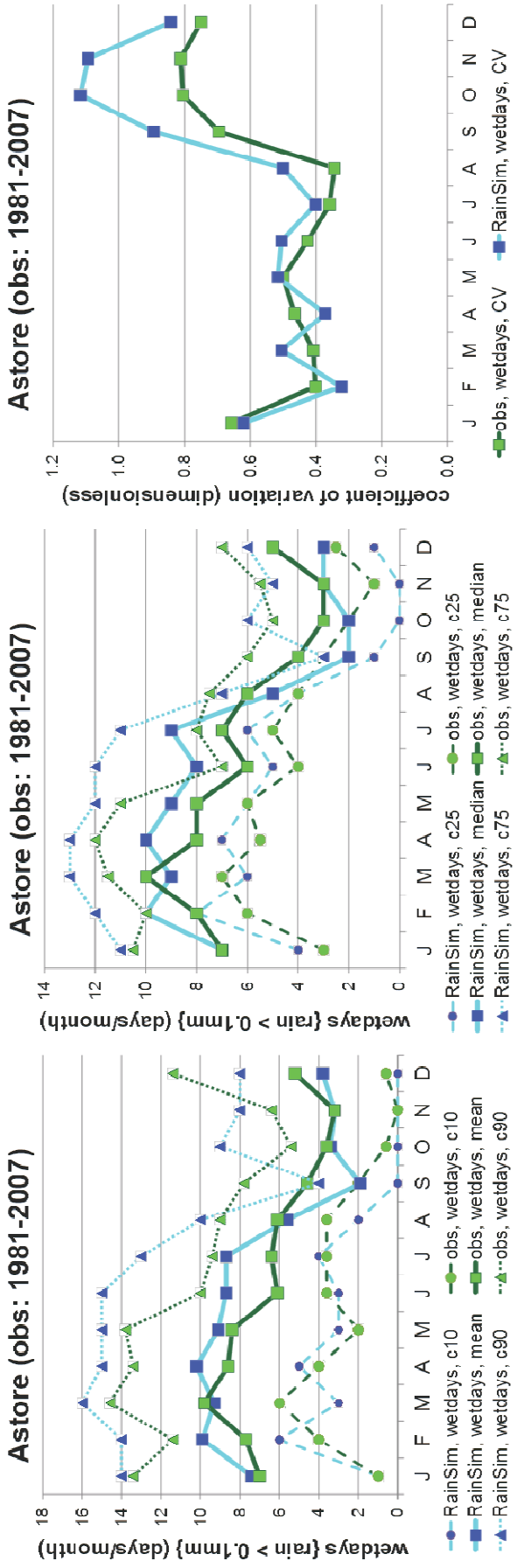

Figure 5.15 Comparison of statistics between observations (obs) and simulated (RainSim) control-climate time-series for "wet day" occurrence at Astore.

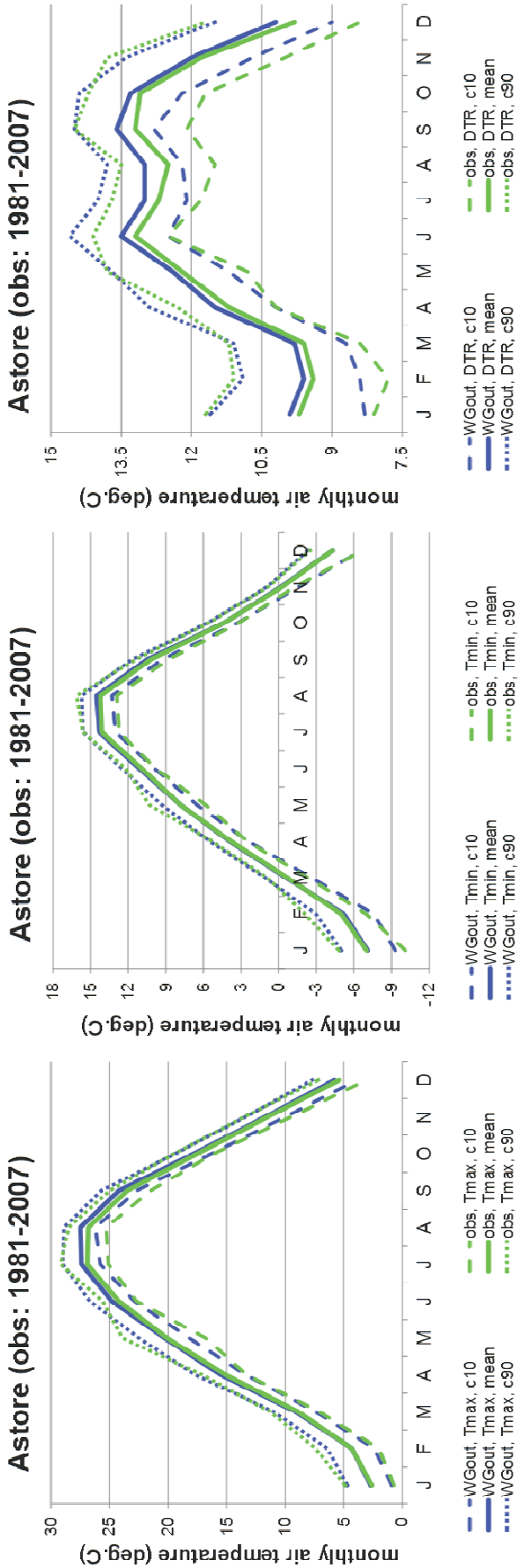

Figure 5.16 Comparison of statistics between observations (obs) and simulated (WGout) control-climate time-series for near surface air temperature at Astore.

In summary, the agreement between observed and simulated statistics for all variables presented here for the Astore (PMD) "control climate" is good. This is satisfying given the large magnitude of annual cycles and considerable interannual variability of local climate in the UIB. The reproduction of the distribution of precipitation amounts is particularly encouraging, although the simulation of precipitation occurrence –"wet days" – is somewhat weaker. Furthermore, although more weight was placed on fitting the "centre" of the distribution – climatological means – rather than accurate simulation of extreme values, there is a good match to the broad range of variability indicated by the first and last deciles (c10 and c90). Similar levels of performance were achieved for Gilgit (PMD) and Skardu (PMD) as can be seen in Appendix C.

5.5 Construction of future climate scenarios for the UIB

5.5.1 Spatial assessment of change factors from PRECIS_AM3P (2080s vs control)

Having validated the ability of the RainSim/Weather Generator pairing to simulate UIB climate parameters satisfactorily, the next step in producing bias-corrected scenarios of future climate requires the extraction of "change factors" by comparing parameter statistics of "future climate" and "control climate" from time-slice RCM simulations. As described previously in this chapter, the available RCM simulations are for a control (1961-1990) and future (2070-2100, SRES A2) time-slice by the Hadley Centre PRECIS model driven by boundary forcings from its HadAM3P GCM ($PRECIS_AM3P_{cntrl}$ $PRECIS_AM3P_{futr}$).

Change factors for climatic means are either multiplicative (coefficients), as in the case of mean precipitation, or additive (constants) as in the case of mean air temperature. Change factors for variance of both precipitation and air temperature are multiplicative. Change factors for precipitation frequency as quantified by "proportion dry days" is slightly more complicated because the resultant descriptor statistic after application of the change factor must respect the absolute physical limit, i.e. it is impossible to have a "proportion dry days" greater than unity (1). In the present study, in cases where substantial drying (reduction of precipitation frequency) was indicated by initially calculated change factors a maximum "proportion of dry days" limit (0.995) was imposed to avoid specifying a null probability of precipitation events. Given that the present study is primarily focused on general climatic means and variability rather than extreme events, change factors were not applied to either skewness or lagged

autocorrelation. Instead, the present observed climatology of these statistics was retained for the future climate scenarios.

Before simply adopting change factors from the individual grid cells overlying the long-record UIB meteorological stations, it is worthwhile to consider the broader sub-regional patterns in change factors provided by the available RCM simulation. Spatial assessment can serve a number of purposes. First, it provides insight into the degree of spatial coherence in patterns of change, hence allowing inferences about the scale and thus the nature of causal mechanisms at work. Secondly, spatial assessment allows verification that the specific grid cells selected for extraction of change factors do not exhibit contrary or "rogue" behaviour to adjacent cells. Alternately spatial means (or other statistics) of multiple grid cells could be used to produce change factors to apply to the point-based (or "single site") generation of stochastic time-series.

Figures 5.17, 5.18 and 5.19 show the monthly change factors respectively for mean precipitation amount, precipitation variance and wet day occurrence. Seasonal and sub-regional patterns are clearly visible. As would be expected there are distinct coherent behaviours for the Indus plains and the Taklimakan desert to the northeast of the Himalayan mountain arc. The mountain arc itself also appears to have sub-regional divisions with separate behaviours. The western end of the arc – i.e. the Hindu Kush, Karakoram and Western Himalaya (HKH) – show winter precipitation increases but decreases in summer/monsoonal rainfall. In contrast the Central Himalaya (eastern limit of the available RCM output subset) shows year-round precipitation increases with the strongest increases in the pre-monsoon to post-monsoon (May to October) period. The sub-regional distinctions are perhaps clearest in Figure 5.18 which shows changes in precipitation variance. Numerical changes in variance track with changes in precipitation amount. Changes in precipitation occurrence (wet day frequency) are relatively limited, suggesting changes primarily in precipitation intensity (of one-day accumulations). There are indications, however, of contrasting changes in wet day frequency within the HKH sub-region during the monsoonal months. The higher elevation, more northerly grid cells show decreasing wet-days from June to September while the relatively lower, southern/foothills grid cells show increasing wet days during these months.

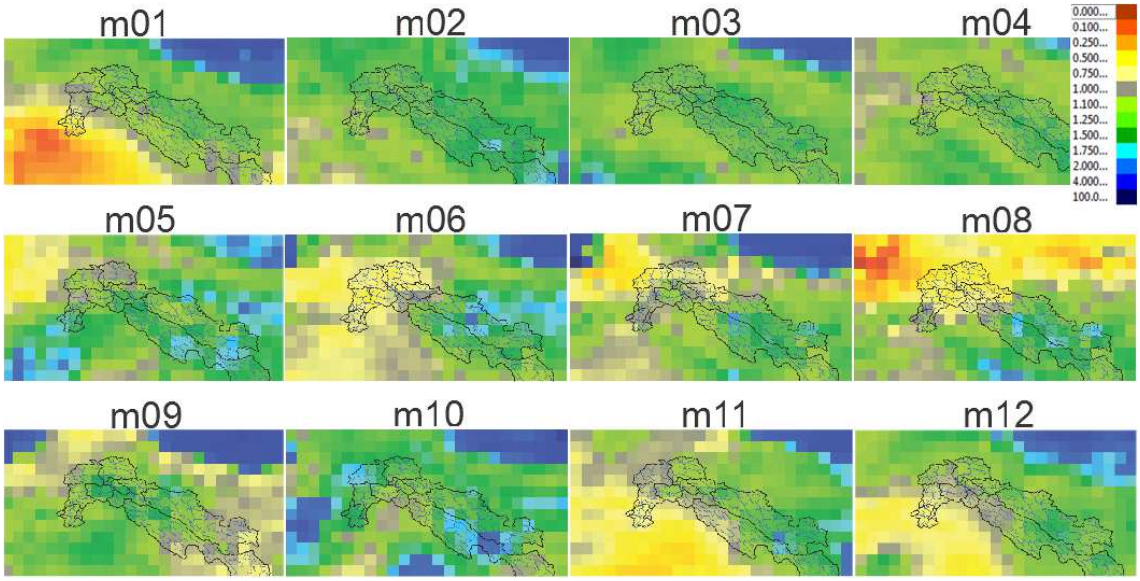

Figure 5.17 Spatial, pixel-wise change factors for mean precipitation amounts from PRECIS_AM3P, i.e. ratio of mean monthly precipitation amounts from PRECIS_AM3P$_{futr}$ and PRECIS_AM3P$_{ctrl}$.

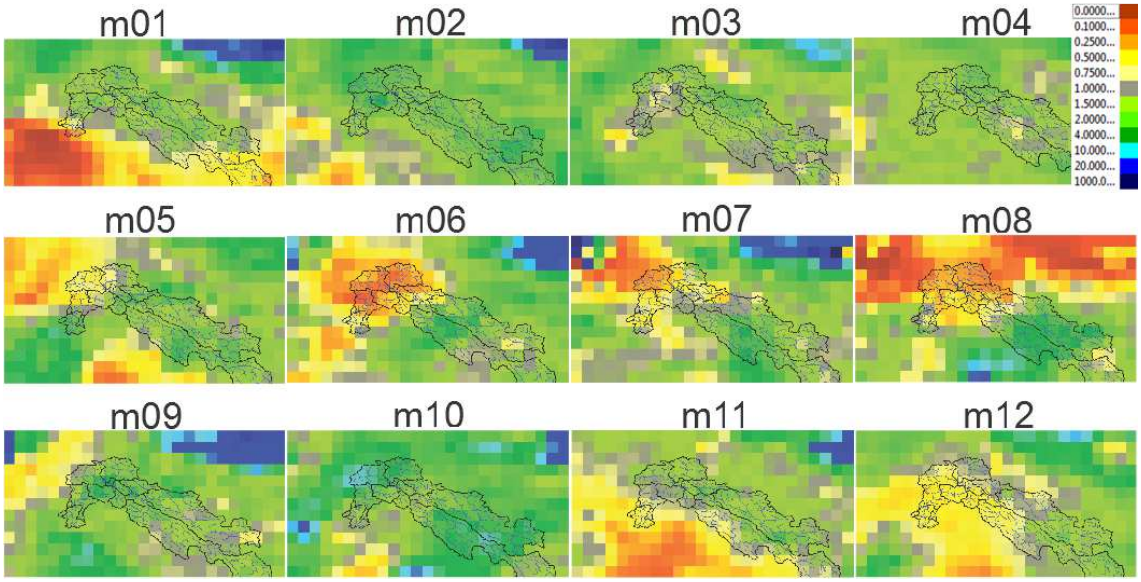

Figure 5.18 Spatial, pixel-wise change factors for precipitation variance from PRECIS_AM3P, i.e. ratio of monthly precipitation variance from PRECIS_AM3P$_{futr}$ and PRECIS_AM3P$_{ctrl}$.

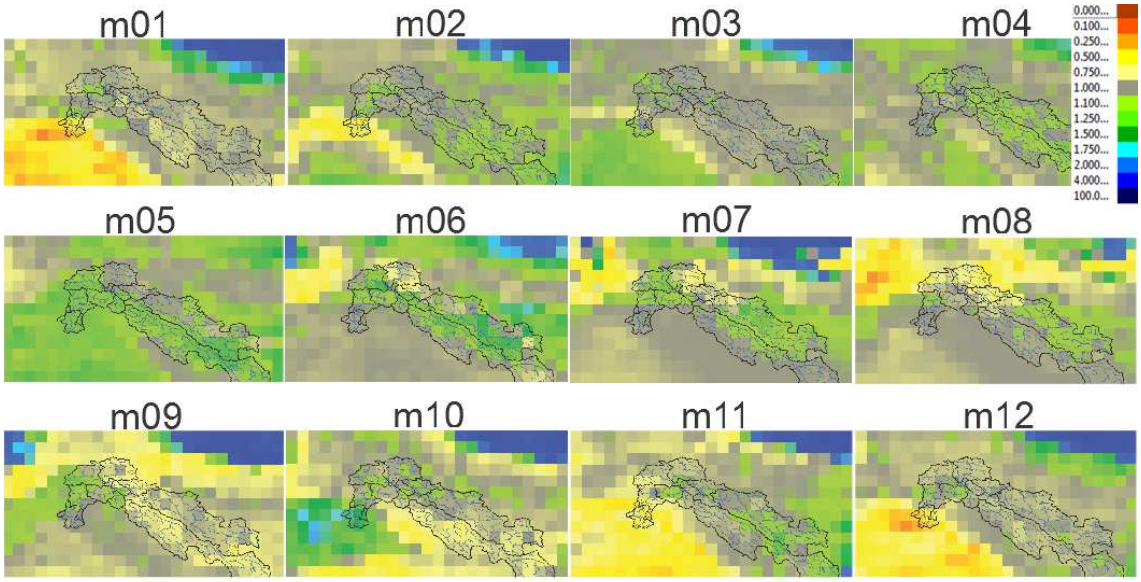

Figure 5.19 Spatial, pixel-wise change factors for wet day occurrence from PRECIS_AM3P, i.e. ratio of monthly wet day occurrence from PRECIS_AM3P$_{futr}$ and PRECIS_AM3P$_{ctrl}$.

In contrast to the fairly distinct sub-regional seasonal patterns of precipitation change, projected changes in mean air temperature are relatively homogeneous across the UIB and contiguous areas. Figures 5.20 and 5.21 show change factors, respectively, for daily mean temperature (Tavg) and diurnal temperature range (DTR). As seen in Figure 5.20, the PRECIS_AM3P time-slice experiment shows year-round temperature increases with only limited variations in the intensity of warming. Figure 5.21 shows broad, albeit mild, regional year-round decreases in DTR. Limited exceptions to this include increasing DTR in several months along a narrow band of cells located at the boundary between the mountains and the plains as well as increasing summer/monsoonal DTR over the Indus plains and the northern HKH. These localised DTR increases appear to be linked to decreases in precipitation, although additional specific analysis has not been performed to verify this.

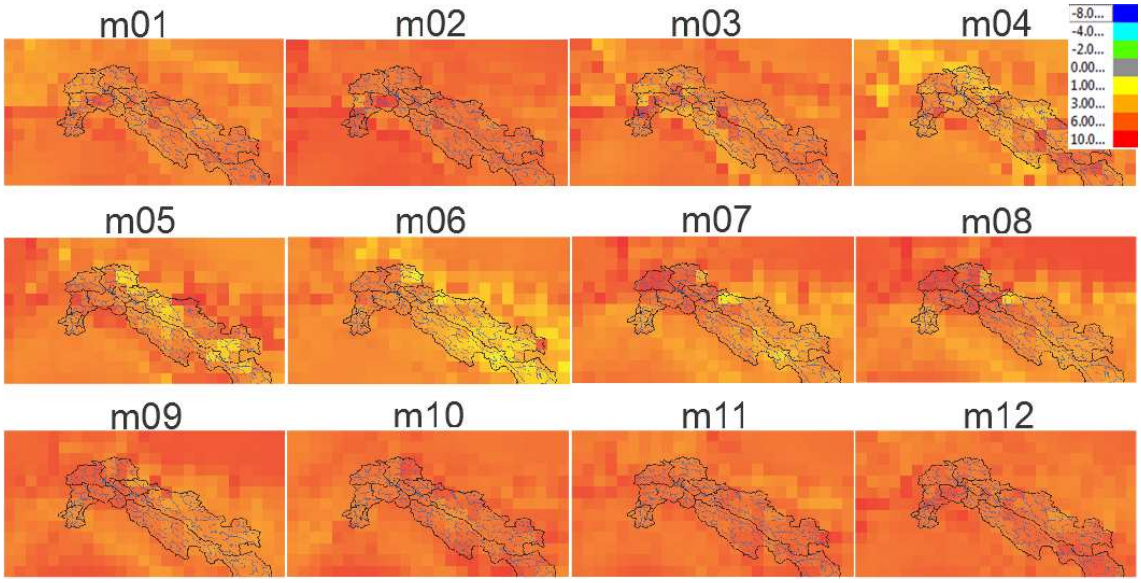

Figure 5.20 Spatial, pixel-wise change factors for mean daily air temperature (Tavg) from PRECIS_AM3P, i.e. difference in Tavg between PRECIS_AM3P$_{futr}$ and PRECIS_AM3P$_{ctrl}$.

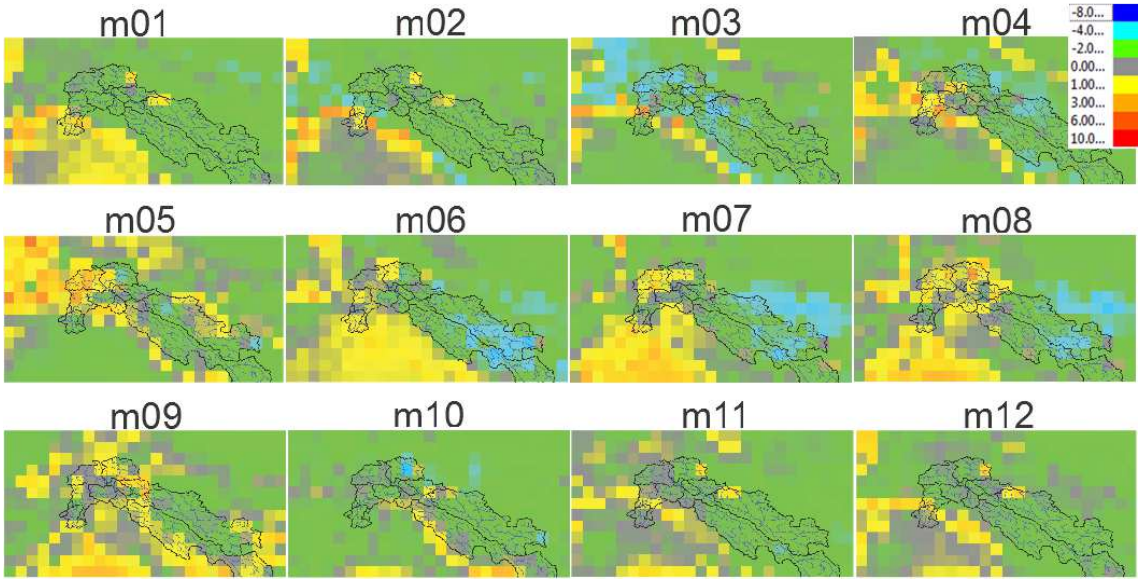

Figure 5.21 Spatial, pixel-wise change factors for mean diurnal temperature range (DTR) from PRECIS_AM3P, i.e. difference in DTR between PRECIS_AM3P$_{futr}$ and PRECIS_AM3P$_{ctrl}$.

Calculated changes in variance of Tavg and DTR are shown respectively in Figures 5.22 and 5.23. Seasonal and sub-regional patterns in changes in temperature variance are less clear (noisier) than for other parameters. For the purposes of the present work these variance changes may be less important than the changes in mean Tavg, although the tentative indications of increasing variance in early spring and early autumn Tavg could indicate increased interannual variability in the timing and duration of the melt season. This question will merit consideration when using synthetic time-series to model potential future hydrological conditions.

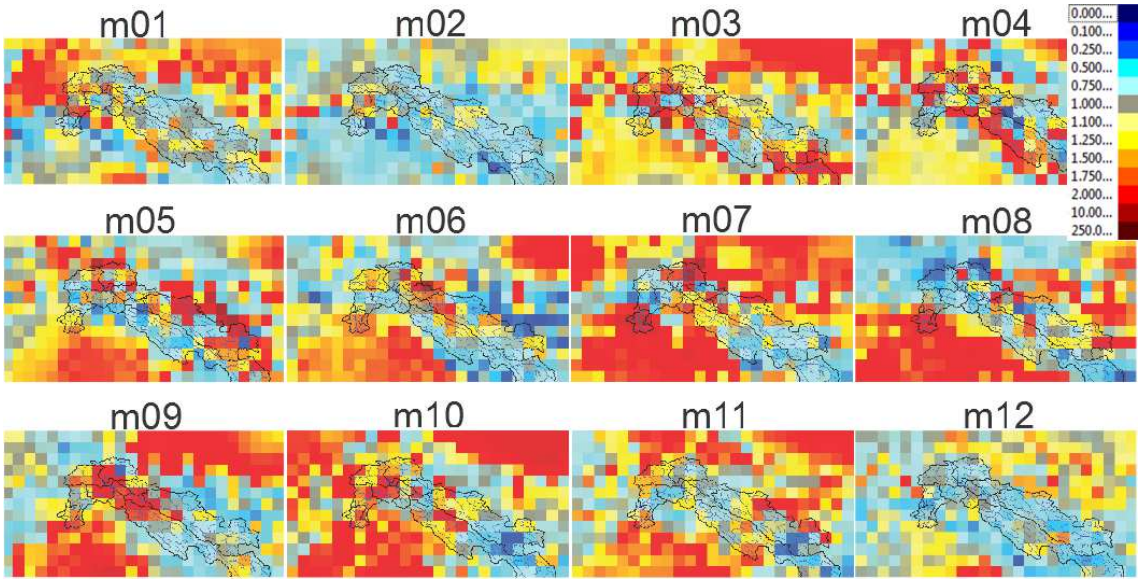

Figure 5.22 Spatial, pixel-wise change factors for variance of daily air temperature (Tavg) from PRECIS_AM3P, i.e. difference in Tavg between PRECIS_AM3P$_{futr}$ and PRECIS_AM3P$_{ctrl}$.

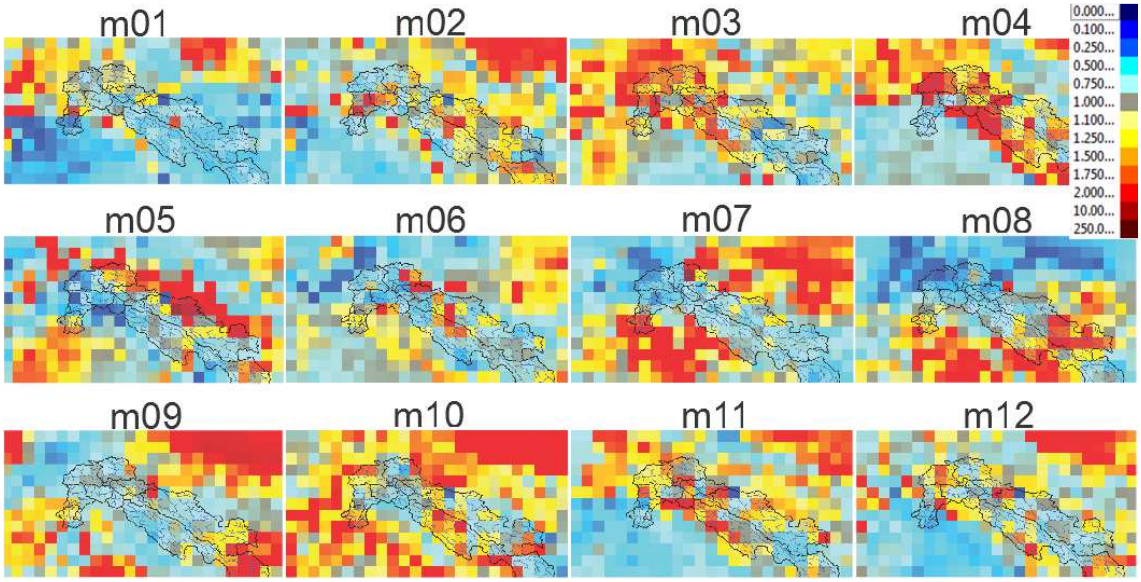

Figure 5.23 Spatial, pixel-wise change factors for variance of diurnal temperature range (DTR) from PRECIS_AM3P, i.e. difference in DTR between PRECIS_AM3P$_{futr}$ and PRECIS_AM3P$_{ctrl}$.

In summary, the spatial assessment of potential change factors from PRECIS_AM3P reveals either largely monotonic region-wide change (Tavg) or relatively coherent spatial patterns (precipitation descriptors, DTR). Thus the PRECIS_AM3P time-slice experiment suggests that the mean temperature response to globally increasing greenhouse gas concentrations will be largely geographically uniform, but that changes to other key climate variables will be modulated by geographical features linked either to surface processes or circulation patterns. The exception to this general spatial coherence is variance of air temperature (Tavg, DTR) which appears more chaotic although there are tentative indications of sub-regional patterns.

The relative importance of changes to temperature variance, however, is limited given the relatively narrow bands of interannual temperature variability compared to the magnitude of its annual cycle. The narrow range of interannual variability in near-surface air temperature for any given month under present UIB climate can be seen in Figure 5.16. The limited temperature range between the first (c10) and last (c90) deciles shows that even with a doubling (change factor ≥ 2.0) of air temperature variance the annual temperature will still over-shadow interannual variability in a given calendar month.

The general spatial coherence of the primary change factors from PRECIS_AM3P encourages their use by suggesting that the simulation is producing consistent responses to physical forcings. The coherence is also reassuring in that the choice of specific cells (within a sub-region) from which to extract change factors appears less critical, i.e. adjacent cells will yield similar if not identical change factors.

5.5.2 Selected scenarios of plausible future climate conditions for assessment of potential changes to UIB water resource availability

The spatially and seasonally homogenous increases in air temperature projected in the change factors extracted from PRECIS_AM3P are in stark contrast to the seasonally and diurnally asymmetrical trends found not only in local observations but also in the PRECIS simulation driven by ERA-40 boundary conditions (PRECIS_ERA40). This was first presented in Chapter 4 (section 4.2.3) of this thesis. As a reminder of specific results presented in Chapter 4, Figure 5.24 shows the estimated air temperature trend rates from local observations (PMD), ERA-40 and selected PRECIS_ERA40 grid cells. As can been seen in Figure 5.24, trend-rates amongst the data sources diverge in all months except for November through January. Discrepancies can be quite large from April through September. This period corresponds to the key snow and glacier melt period when air temperature is an important input of energy to drive melt processes in the UIB hydrological system. The disagreement of PRECIS_ERA40 projections not only with trends from local observations (PMD) but also the coarse resolution reanalysis used as boundary conditions suggests the possibility that there are UIB-specific processes linked to climatic variability which may not be well captured by the PRECIS RCM.

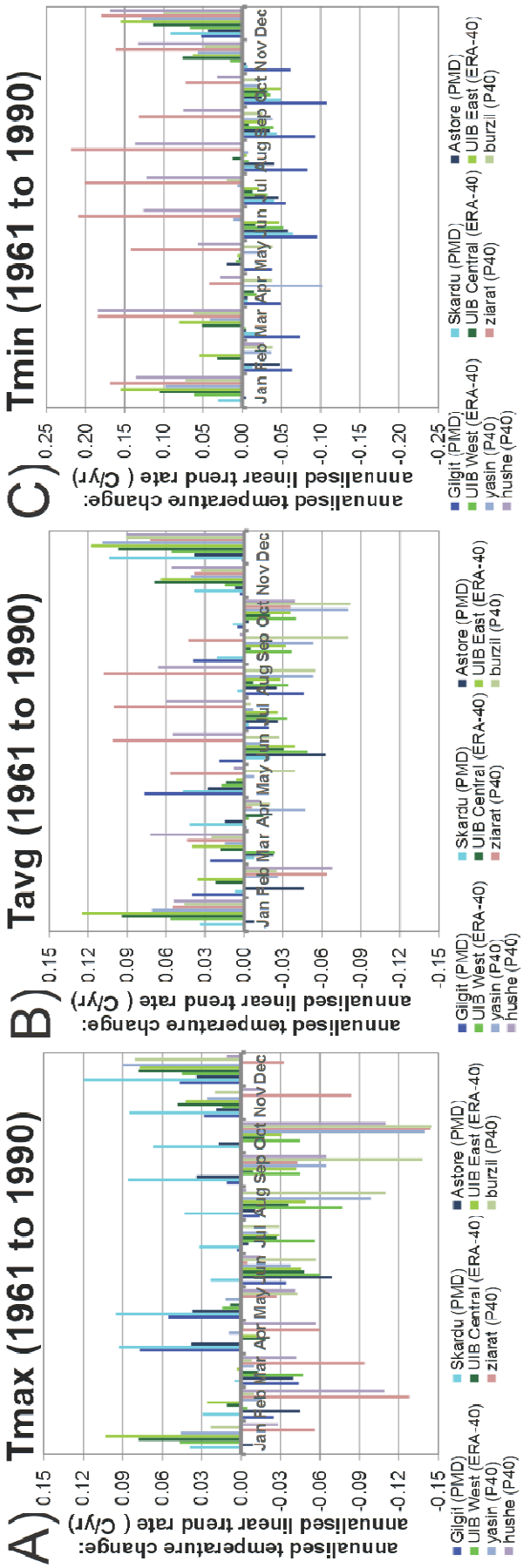

Figure 5.24 (previously Figure 4.05) Additional discrepancies and diurnal asymmetry in temperature trends from local observations (PMD), ERA-40 and PRECIS_ERA40 (P40) for 1961 to 1990 for diurnal phases: A) Tmax, B) Tavg and C) Tmin.

For this reason it is deemed worthwhile to examine the potential divergences in future hydrological conditions which could result depending on whether UIB climate follows the scenario described by downscaled GCM simulation PRECIS_AM3P or the trajectory indicated if recent locally-observed trends persist in the coming decades. It is important to clarify that this comparison of potential climate trajectories is not intended to deliver hydrological projections of equivalent probability, but rather to act as a sensitivity study to highlight the contrasting potential implications for UIB hydrological depending on whether summer cooling (air temperature decreases) or warming (air temperature increases) occur in the coming decades.

In order to provide an envelope (set of rough bounds) illustrating the divergence of potential climate futures resulting from the uncertainty regarding the nature of present, on-going, local climate processes and the ability to model them in future, two scenarios have been retained.

- i) change factors extracted from PRECIS_AM3P. This option represents an orthodox methodological approach as change factors from RCMs are expected to offer potentially greater physical realism, primarily by being constrained by simulated conservation of mass and energy.
- ii) change factors calculated from the mean of locally observed trend rates (from ordinary linear regression) for two time windows: 1961 to 1989 and 1979 to 2007. The mean of the two time windows was taken to limit the influence of any particular events which could distort the trends estimated based on their positioning within the record compared to the selected start and end dates of each analysis window. In effect this is an extremely simple form of temporal smoothing or averaging.

Figures 5.25 and 5.26 show the change factors, respectively for precipitation and air temperature, for these two scenarios for the three long-record UIB meteorological stations. Figure 5.25 shows the hypothesised changes in descriptors of precipitation distribution: precipitation amount, precipitation variance, wet day occurrence and dry day occurrence. The changes in precipitation descriptors extrapolated from locally observed trends are far larger than those projected by PRECIS_AM3P. Of particular interest are large relative increases in Winter (November to February) and Summer (June to August) precipitation amount and frequency (wet days) contrasted by substantial relative decreases in Spring (March, April). In terms of net annual effects, given the dominance of spring-time precipitation in the present climatology, the

increases in other drier months are needed to offset Spring drying. The resultant precipitation climatology yields similar annual total precipitation but with different shifts in seasonal concentrations and frequency of individual events in the different future scenarios.

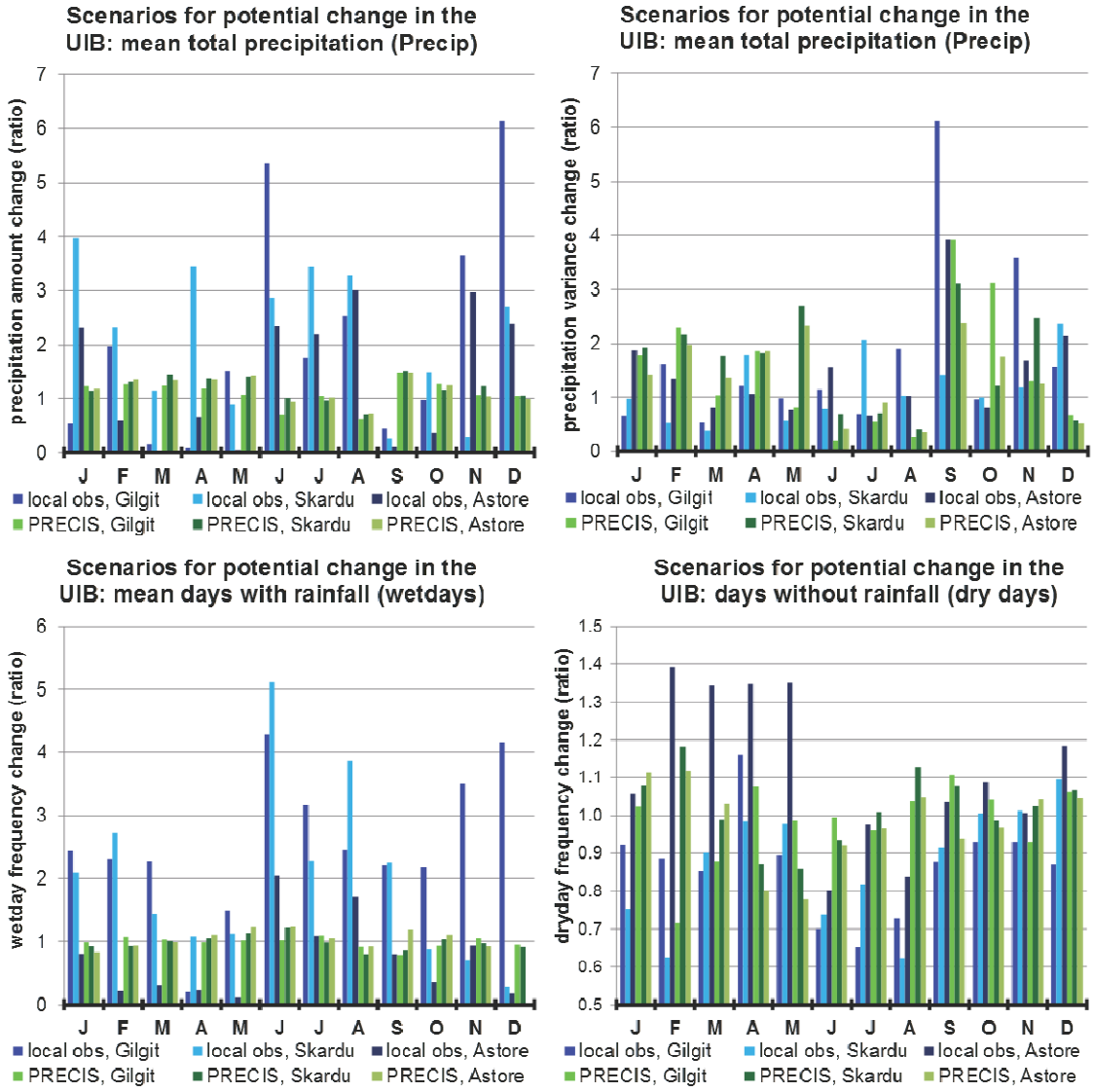

Figure 5.25 Change factors for precipitation descriptor statistics based on scenarios from PRECIS_AM3P and extrapolated from trends in local observations (PMD, abbreviated here as local obs).

In contrast to the trajectory extrapolated from locally observed trends, as seen in Figure 5.25, the changes projected by PRECIS_AM3P are much smaller in magnitude and centred in the opposite seasons. PRECIS_AM3P projects limited relative increases in precipitation amounts – without corresponding changes in frequency – in what are already the wettest months of the year (February to May) thus yielding substantial increases in annual total precipitation. PRECIS_AM3P also projects substantial increases in precipitation variance. The resultant precipitation climatology – increasing accumulation and variability but unchanged frequency – implies a future intensification

of the hydrological cycle with increased mean mass inputs but potentially also a greater range of resource availability between “wet years” and “dry years.”

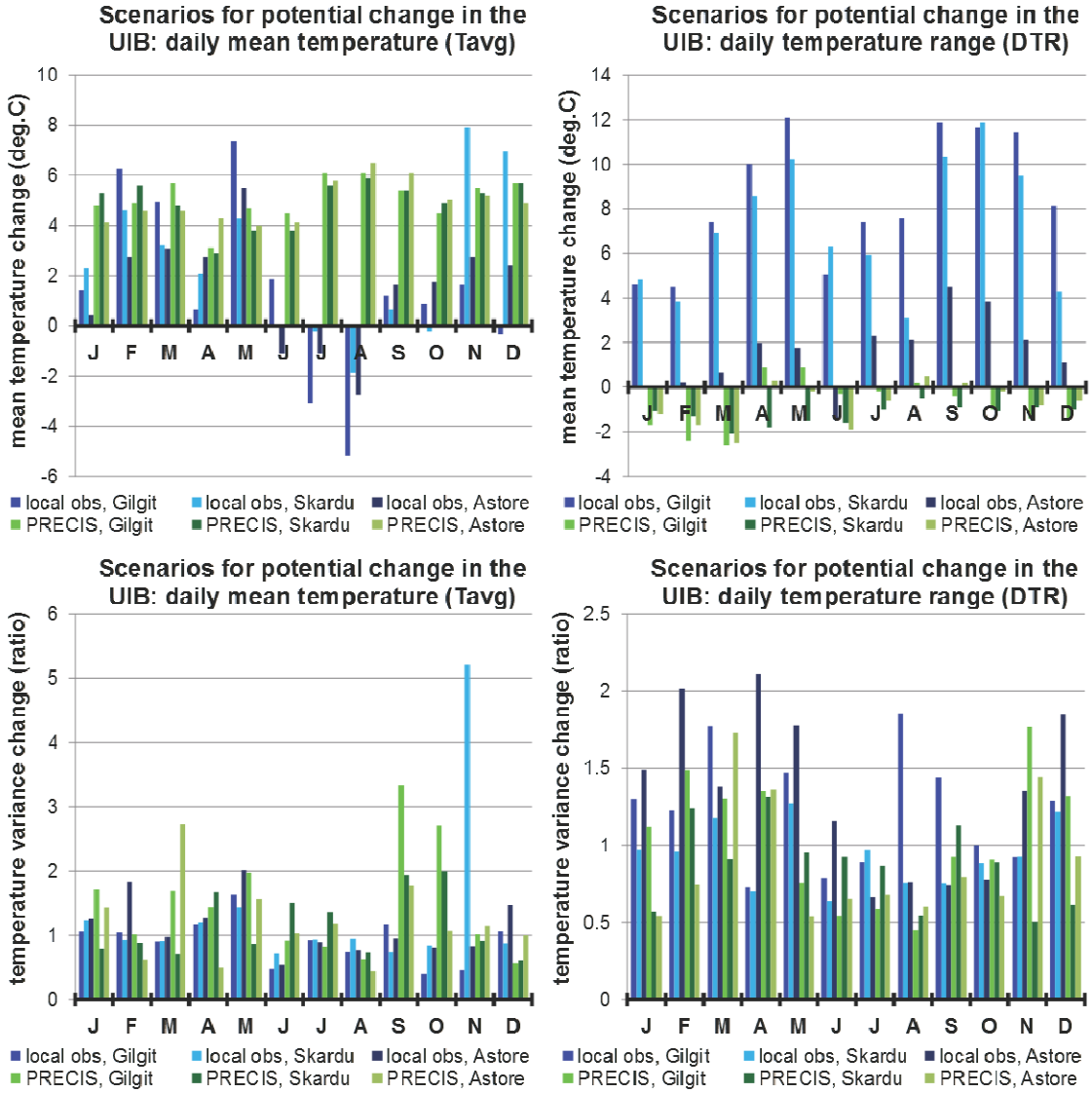

Figure 5.26 Change factors for air temperature descriptor statistics based on scenarios from PRECIS_AM3P and extrapolated from trends in local observations.

As described above, this study chose to use change factors extracted from PRECIS_AM3P in parallel with those derived from extrapolations of locally observed trends in the recent historical record. This decision stems largely the from stark contrast between seasonally and diurnally asymmetrical trends in near-surface air temperature – described in Chapter 4, section 4.2.3 – in the recent record and the monotonic increases air-temperature projected by PRECIS_AM3P presented in section 5.5.1. The divergence between the trajectories suggested by these two sources can be understood by examining Figure 5.26 which presents calculated changes to the mean and variance for both Tavg and DTR. The divergence between the implied future conditions is clear in the changes to the means of both Tavg and DTR. Whilst PRECIS_AM3P projects year-

round increases in Tavg ranging from 4°C to 6°C depending upon the month, the changes to mean Tavg extrapolated from locally observed trends show moderate to strong warming from November to May with substantial cooling in July and August. The divergence between the PRECIS_AM3P projections and extrapolation of local trends is most striking for changes in mean DTR. PRECIS_AM3P projects limited changes – stability to 2°C decreases – without distinction between the seasons. The extrapolation of local trends, however, suggests substantial year-round increases with the greatest increases in spring and autumn. In contrast, while differences in changes to means of Tavg and DTR are striking, changes to the variance of these variables suggested by the two cases are relatively similar.

To be clear, neither change factors from PRECIS_AM3P nor those extrapolated from recent trends are considered robust projections of likely future UIB climate. There are doubts regarding PRECIS_AM3P not only due to the issues evoked in preceding sections of this Chapter, but also because the climatological implications – in terms of circulation patterns and land surface processes – of the extremely rugged terrain and steep topographic gradients in the UIB are unlikely to be well represented by a model spatial resolution of 50km. The extrapolation of locally observed trends on the other hand lacks the constraints provided for an RCM by the conservation of mass and energy fluxes defined by the supplied boundary conditions of the simulation.

Reliable projections would require additional simulation by models both with adequate spatial resolution to capture the climatic effects of severe topographic variability and which had demonstrated a capacity to replicate the response of UIB climate to recent large-scale atmospheric forcing. It is likely that the required spatial resolution would far exceed that of any presently available RCM simulation of the South Asia or Himalayan mountain arc domains. Further details on suggested avenues for additional research will be provided Chapter 8 of this thesis.

In the meantime, the two scenarios presented here outline contrasting pathways for local climate. It is hoped that the degree of contrast between the two is wide enough to capture likely future UIB climate trajectories.

5.5.3 Implementation of selected scenarios in synthetic time-series

After initial attempts to implement the change factors (CFs) presented in Figures 5.25 and 5.26 in RainSim and the CRU-WG, it was decided to retain the initial PRECIS_AM3P CFs but to reduce those extrapolated from local observations trend

rates by 50%, i.e. halving the effective change. This change was made due to the severity of the projected changes in precipitation, especially wet day frequency reductions in presently humid months, and DTR. As will be shown in Chapter 7, even the reduced changes in this scenario still result in substantial differences in projected cryospheric – i.e. ephemeral seasonal snow cover and perennial glacial mass – and hydrological conditions. The retained change factors from locally observed trends still result in substantial changes with respect to present climate conditions, and still provide stark contrast to the PRECIS_AM3P scenario.

Synthetic time-series – 3000 years in total, grouped 100 sets of 30-year sequences – of the perturbed climate conditions for the three primary long-record meteorological stations in the UIB were generated based on the scenarios described in the preceding sections.

In RainSim the time-series is perturbed by substituting the "analysed statistics" of the observed record with the "perturbed statistics" created by multiplying the observed statistics by the change factors (Burton et al., 2008; Kilsby et al., 2007). As described above, the present study chose only to perturb the mean, variance and frequency ("proportion dry days") of precipitation. Skewness and lagged autocorrelation were not modified. Once the "perturbed statistics" have been calculated, the RainSim process of "fitting" parameters and generating ("simulating") time series is performed as for a "control" (observed) precipitation climatology. This perturbed synthetic time-series of precipitation is a primary input for the generation of additional perturbed variables by the CRU-WG.

In addition to the perturbed synthetic time-series of precipitation, the CRU-WG also requires the synthetic time-series of control climate precipitation as well as the air-temperature change factors discussed in preceding sections of this chapter. CRU-WG requires both the control-climate precipitation time-series and the change factors because of its methodology for association of air temperature variability to precipitation occurrence via fitted linear-regression relationships to DTR (Jones et al., 2011). This approach renders it necessary for CRU-WG to separate changes to air-temperature resulting from changes in precipitation occurrence (wet days) from the total projected air temperature change such that distribution of temperature change between "wet days" and "dry days" yields specified net change in climatology. In the present study, near-surface air temperature was perturbed by supplying the CRU-WG with change factors for both mean and variance of DTR as well as Tavg. As discussed in section 5.4.1, the

generation of time-series by the CRU-WG of variables other than air temperature was considered neither pertinent nor appropriate for use in the present study.

Figures 5.27 to 5.30 provide graphical illustrations of the synthetic time-series in comparison to the observed record for Astore (PMD). Equivalent figures for Gilgit (PMD) and Skardu (PMD) are found in Appendix C.

Figure 5.27 shows the projected precipitation climatology of the PRECIS_AM3P scenario. As for the synthetic time-series of control climate precipitation (section 5.4.2), several statistical descriptors – mean, median, lower (c25) and upper (c75) quartiles, the first (c10) and last (c90) deciles as well as the "coefficient of variation" (CV) i.e. the ratio of the standard deviation divided by the mean – are presented here to provide a comprehensive image of the projected distribution of precipitation and wet days. Specifically, with respect to the precipitation climatology projected by PRECIS_AM3P, Figure 5.27 shows that it is relatively close to the observed historical (control) climate with the exception of increases in precipitation amounts during the wettest months of the year (February to May). These increases in precipitation amounts are projected despite relatively unchanged precipitation frequency (wet days), although the projected wet days CV does suggested that the interannual variability of the number of precipitation events per month may increase. The logical interpretation of increasing precipitation amount with unchanged event frequency is a resultant increase in event intensity. Furthermore, with regards to the shape of the distribution of monthly precipitation amounts, the PRECIS_AM3P scenario projects greater relative changes in the higher end of the distribution – i.e. upper quartile (c75) and last decile (c90) – than in the lower end.

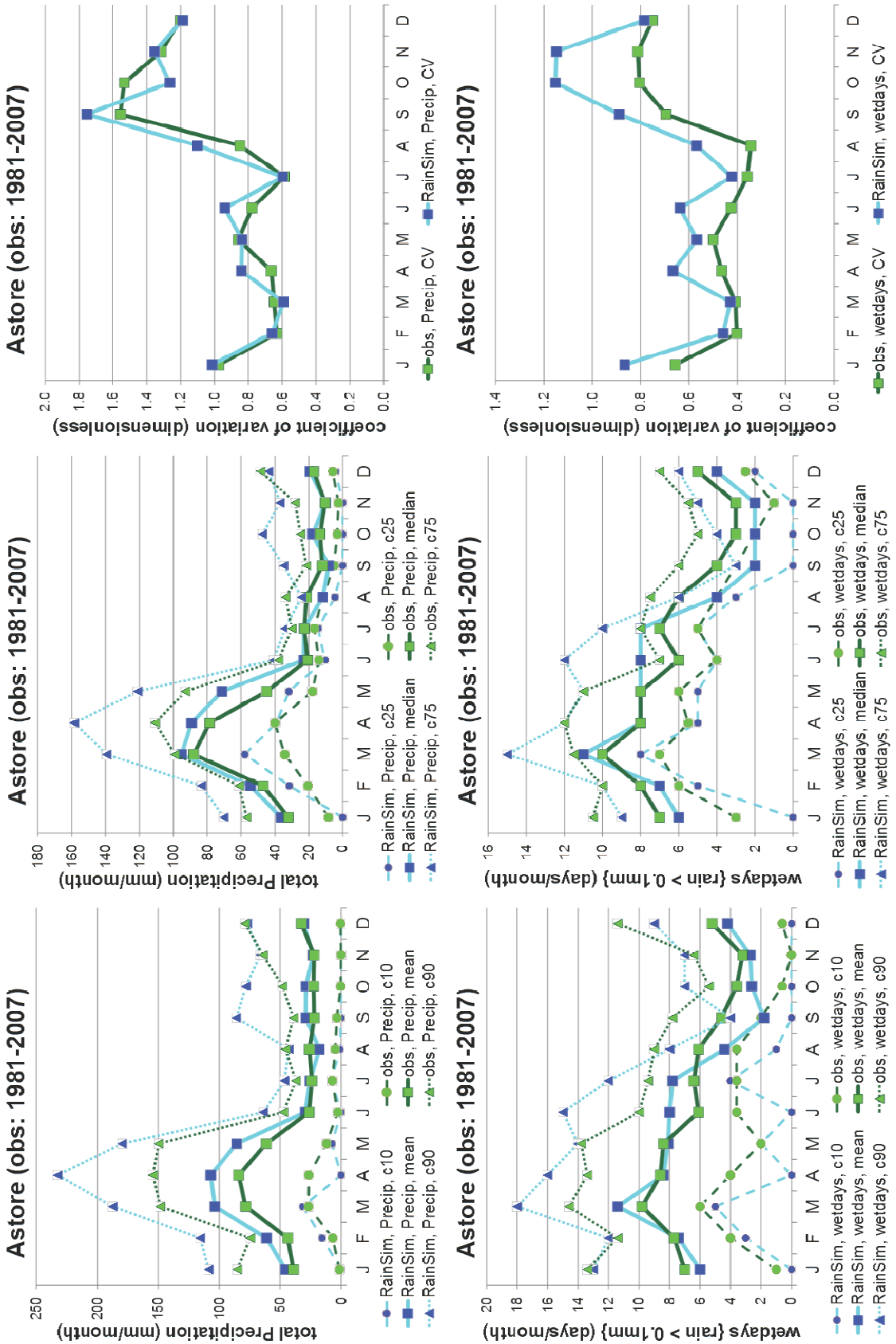

Figure 5.27 Comparison of statistics between observations and simulated perturbed-climate time-series from PRECIS_AM3P scenario for precipitation amounts at Astore.

Figure 5.28 shows the projected near-surface air temperature climatology of the PRECIS_AM3P scenario. As for the synthetic time-series of control climate air

temperature (section 5.4.2), multiple statistical descriptors – mean along with the first (c10) and last (c90) deciles – are presented for Tmax, Tmin and DTR to provide a comprehensive image of the projected distribution of the diurnal components of the near-surface air temperature. As was expected based on the change factors used in the CRU-WG to perturb the control climate time-series, increases in Tmax and Tmin projected by PRECIS_AM3P are relatively uniform throughout the year with marginally greater warming in the Summer months (July, August) which are critical for snow and ice melt processes. The magnitude of the temperature increases are large enough, and the changes in variance limited enough, that the first decile (c10) of the projected climatology is greater than the last decile (c90) of the control climatology for both Tmax and Tmin in months. Changes in DTR, however, are relatively limited with projected decreases in January to March and June and small increases in July and August.

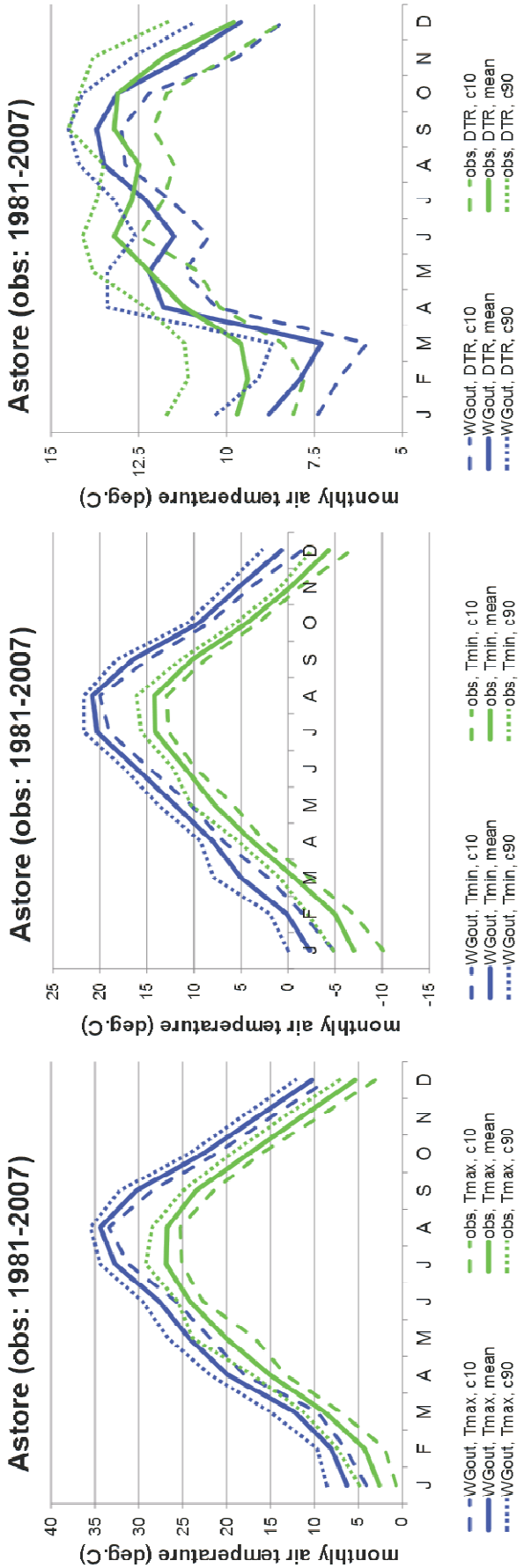

Figure 5.28 Comparison of statistics between observations and simulated perturbed-climate time-series from PRECIS_AM3P scenario for near surface air temperature at Astore.

Figure 5.29 shows the projected precipitation climatology of the scenario extrapolated from locally observed trends in the recent historical record. In contrast to the PRECIS_AM3P scenario, the projected precipitation climatology of the extrapolated trends scenario show a decrease in the wettest spring-time months in both precipitation amounts and wet days. The extrapolated trends scenario also projects increases in both precipitation amounts and wet days for Winter (November to January) as well as Summer (June to August). Thus although April is projected to remain the wettest month, the seasonality of precipitation becomes considerably more complex in this scenario. Furthermore, because the relative decreases in spring-time wet days are greater than the corresponding decreases in precipitation amounts, it can be concluded that the intensity of individual events is projected to increase.

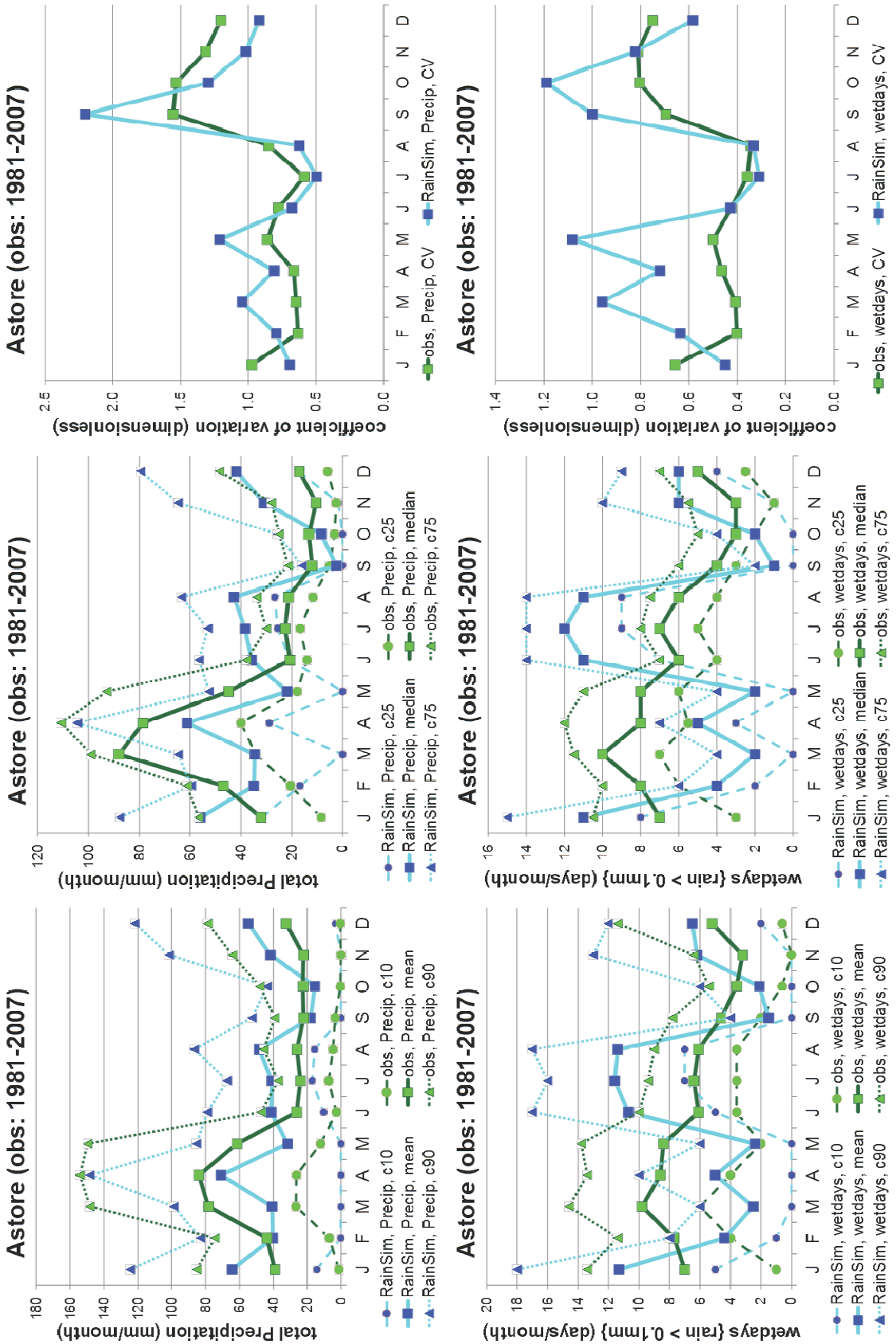

Figure 5.29 Comparison of statistics between observations and simulated perturbed-climate time-series from locally-observed trends scenario for precipitation amounts at Astore.

Figure 5.30 shows the projected near-surface air temperature climatology of the extrapolated trends scenario. As was expected, based on the change factors used in

CRU-WG to perturb the control climate time-series, projected changes to Tmax and Tmin are seasonally asymmetrical. There are moderate year-round increases in Tmax with the exception of the summer (June to August) when Tmax is stable. Tmin, in contrast, is stable year-round with the exception of a moderate warming in May and moderate cooling in July and August. The asymmetrical changes in Tmax and Tmin result in increasing DTR in most months.

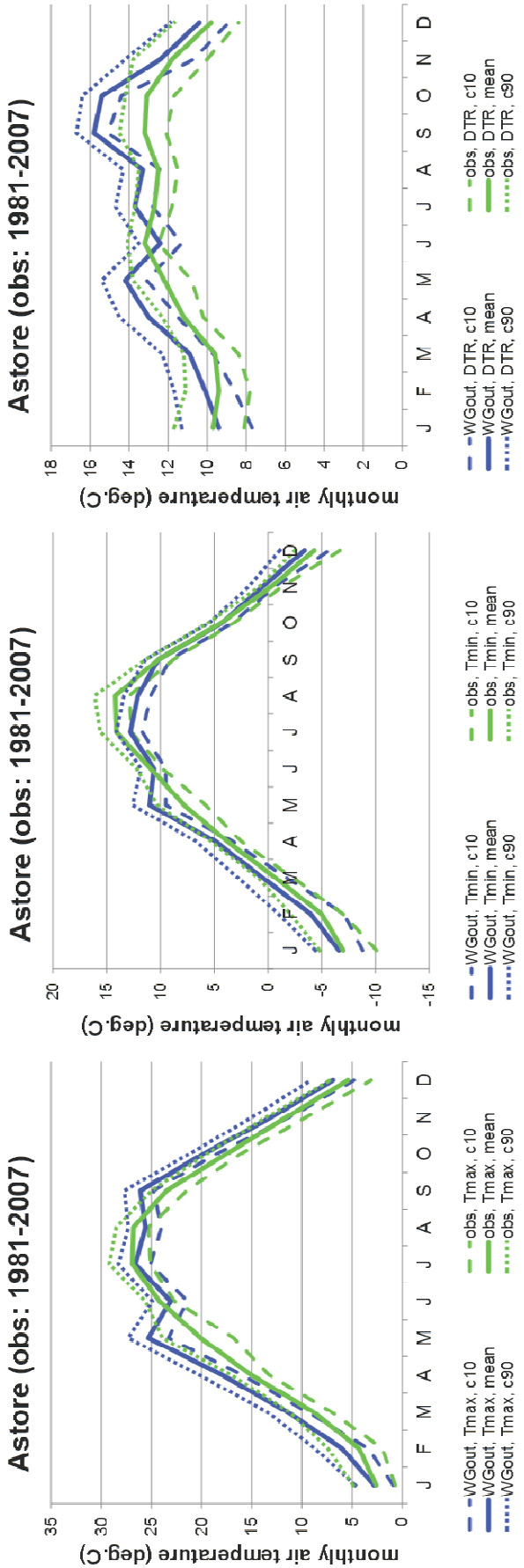

Figure 5.30 Comparison of statistics between observations and simulated perturbed-climate time-series from locally-observed trends scenario for near surface air temperature at Astore.

As can be seen in Figures 5.27 and 5.28, in general the PRECIS_AM3P scenario results in a future climate with moderate precipitation increases concentrated in presently humid months and relatively uniform air temperature increases. As shown in Figures 5.29 and 5.30, the scenario derived from extrapolating trends estimated with local observations results in a future climate that is generally more humid, albeit with substantial shifts in the seasonality of precipitation, i.e. drier springs but more humid winters and summers. In terms of air temperature this scenario carries forward the present trend of year-round increases in DTR. This increase results from asymmetrical changes to Tmax and Tmin.

5.6 Discussion and conclusions

In this chapter, the biases of one RCM, PRECIS, driven by boundary conditions from one GCM, HadAM3P, were assessed both against the same RCM driven by meteorological reanalysis (ERA-40) and against local observations. Although substantial systematic biases were identified in this simulation (PRECIS_AM3P), it may be possible to overcome these limitations to reasonably downscale its projections to individual sites – long-record meteorological stations – using a "weather generator" technique based on perturbing the statistical descriptors of the local observations with change factors extracted from comparison of time-slices – future and "control" – of the RCM/GCM pairing.

Specifically this work used the software packages RainSim (v3.1.1) to generate the synthetic precipitation time-series, present and future, and the Weather Generator from the Climate Research Unit (CRU-WG) to associate air temperature variables to these series. This study is thought to be the first application of the RainSim/CRU-WG coupled tool to a climate domain outside of Europe and is certainly the first application in a semi-arid climate.

After consideration of the divergence of the PRECIS_AM3P projections from the trajectories indicated by trend estimations derived from local observations, it was decided to add a contrasting set of change factors based on extrapolated local trends in order to illustrate the range of potential local climate futures that could occur, resulting from uncertainty regarding the proximate drivers and mechanisms of change (as examined in Chapter 4). As discussed in section 5.5.2, neither scenario source is entirely satisfactory, but in the absence of more reliable projections of future climate, the scenarios developed here will allow at least an effective sensitivity study to examine the

potential hydrological implications of these divergent trajectories for inputs of mass and energy to meltwater runoff generation in the UIB.

The sets of change factors for each scenario were used to generate perturbed climate time-series for the three long-record meteorological stations available to this study. These time-series will be used as inputs for hydrological modelling of glacierised and seasonal snowmelt regime catchments to investigate potential changes in water resource availability in the UIB. The results of this modelling are presented in Chapter 7 of this thesis.

In furthering the present work, it would be advantageous to be able to draw on an "ensemble" of RCM simulations, as is widely adopted now in the assessment of climate change and impacts assessments (e.g. van Vliet et al., 2012), in order to better capture the range of uncertainty identified by available GCM simulations. If possible each RCM/GCM pairing, prior to inclusion in said ensemble, should be tested to assess its capacity to replicate the response of UIB climate to recent large-scale atmospheric forcing. Déqué and Somot (2010) proposed a probabilistic weighting scheme for RCM/GCM pairings based on:

- the relative performance of the RCM to simulate observed climate when driven by reanalysis boundary conditions (e.g. ERA0-40);
- the relative performance of the GCM to reproduce large-scale circulation patterns as measured by regional weather-typing or teleconnection index states.

Ideally these RCM simulations would be at a substantially improved spatial resolution. A recent modelling study for the Colorado Rockies – a region with notable similarities to the UIB – by Rasmussen et al. (2011) showed that a horizontal spatial resolution of better than 18km was necessary to accurately simulate topographic influences on local climate – notably for wind speed and orographically-enhanced precipitation – in rugged mountainous regions. Given that the UIB has a greater elevation range than the Colorado Rockies and potentially steeper topographic gradients, it might be that even higher spatial resolution than that found by Rasmussen et al. (2011) would be necessary to accurately simulation the spatial complexity of UIB climate.

While RCM simulations of the spatial resolution advocated by Rasmussen et al. (2011) are not likely to be available for the UIB in the near future, a perturbed physics ensemble of a single RCM, PRECIS at 25km resolution, driven by 17 separate sets of boundary conditions from HadCM3 simulations – utilising the SRES A2 GHG emissions scenario – will soon be made available to the project team (the author and

advisors) responsible for this thesis. These 17 sets of boundary conditions were created for PRECIS (McSweeney et al., 2012) of HadCM3 simulations as an offshoot of the QUMP project which implemented the methodology advocated by Murphy et al. (2007) for probabilistic projection of future climate change. Thus future work to improve on the contributions in this Chapter by drawing on a more robust set of future projections is already scheduled.

Chapter 6: Construction and validation of a hydrological model adapted for the UIB

6.1 Abstract

This Chapter describes the construction, calibration and validation of a hydrological model adapted to the climatological and land surface process characteristics of the UIB. Rather than attempting to directly implement the model over the entire UIB (upstream of the Tarbela reservoir), it was decided to test the model for two tributary catchments representing the key regional hydrological regimes to establish its performance and suitability prior to embarking on a more ambitious simulation programme.

The choice of methodology for the adapted model was driven both by the objective of improving on previous modelling studies of the UIB and by the constraints of available, reliable meteorological inputs. The improvements sought over previous modelling studies included: i) modelling of snow covered area (SCA) as an output, ii) mass conservative modelling of glacial meltwater; and iii) modelling of glacial catchment fractions variable both in mass (volume) and area. Meteorological inputs act as constraints by the capacity to spatially distribute (scale) them as a function of topography (elevation). At present spatial distribution – through elevation-based scaling – was deemed feasible for precipitation and temperature but not for wind speed or relative humidity.

This chapter describes the methodology adopted to achieve the hydrological modelling objectives in light of the identified constraints. Where the present study has implemented innovative approaches, the original methods are described in detail here. Where existing methods have simply been duplicated, the details of implementation are presented in Appendix D. Following explanation of the methodological innovations contributed by this study, the results of model calibration and validation are presented for the selected catchments. Also described are insights provided into UIB cryospheric processes by the implemented model innovations. The Chapter closes with a discussion of the suitability of the model for use in impact studies, remaining areas for model improvement and identified avenues to achieve these improvements.

For reference, a comprehensive glossary of modelling terminology, particularly symbols and variable names used in the equations in this chapter, is provided in Appendix D.

6.2 Introduction

Simulation of the land-surface processes involved in the hydrological cycle is a favoured method of assessing the probability of hydrologic events which pose physical risks to infrastructure and human systems. This hydrological modelling is used for both determination of present risk levels and assessment of potential impacts of climate change. The formulation of these models ranges from relatively simplistic conceptual/empirical constructs representing system precipitation-runoff responses, to highly complex physically-based representations of land surface processes. Considerable scientific debate remains regarding the optimum balance between physical realism and model performance (Beven, 1989, Beven, 2001, Ewen *et al*., 2006).

Hydrological modelling of mountainous catchments in mid-latitude climates introduces additional elements of complexity. Topographical combined with orographic gradients result in complex spatial patterns for key system inputs. Furthermore, substantial fractions of annual precipitation often fall as snow and are stored on monthly timescales as seasonal snowpack or incorporated into perennial glacial ice, with potentially much longer residence times. Approaches to the modelling of this accumulation and ablation again range from conceptual/empirical methods, such as degree-day models including HBV (Lindstrom *et al*., 1997) and SRM (Schaper *et al*., 1999), to physically-based energy balance formulations, such as that incorporated into recent versions of VIC (Cherkauer *et al*., 2003). Accurate and efficient numerical simulation of these processes is crucial to allow modelling at adequate spatial and temporal resolutions to capture the complexity of catchment behaviour (Burlando *et al*., 2002).

As described in Chapter 3, the Upper Indus Basin (UIB) is overwhelmingly comprised of tributary catchments with dominantly nival (seasonal snow) or glacial hydrological regimes, or mixtures of the two. Hence, the ability to model the snowmelt and mechanistic glacier processes is crucial for the accurate simulation of regional hydrology. This chapter describes the work by the present study to adapt a grid-based hydrological model to the specific constraints and challenges of the UIB and then calibrate and validate that model for two archetypal tributary catchments: the Astore (nival regime) and Hunza (glacial regime). A conceptual diagram of this model is presented in Figure 6.01. This diagram shows the organisation of the adapted model into three “macro-phases”: i) distribution of meteorological input based on vertical gradients or profiles; ii) the simulation of cryosphere dynamics including evolution of snowpack

density, snow and ice melt, and the vertical transfer of glacial mass under gravitational forces; and iii) soil moisture accounting using established methodology.

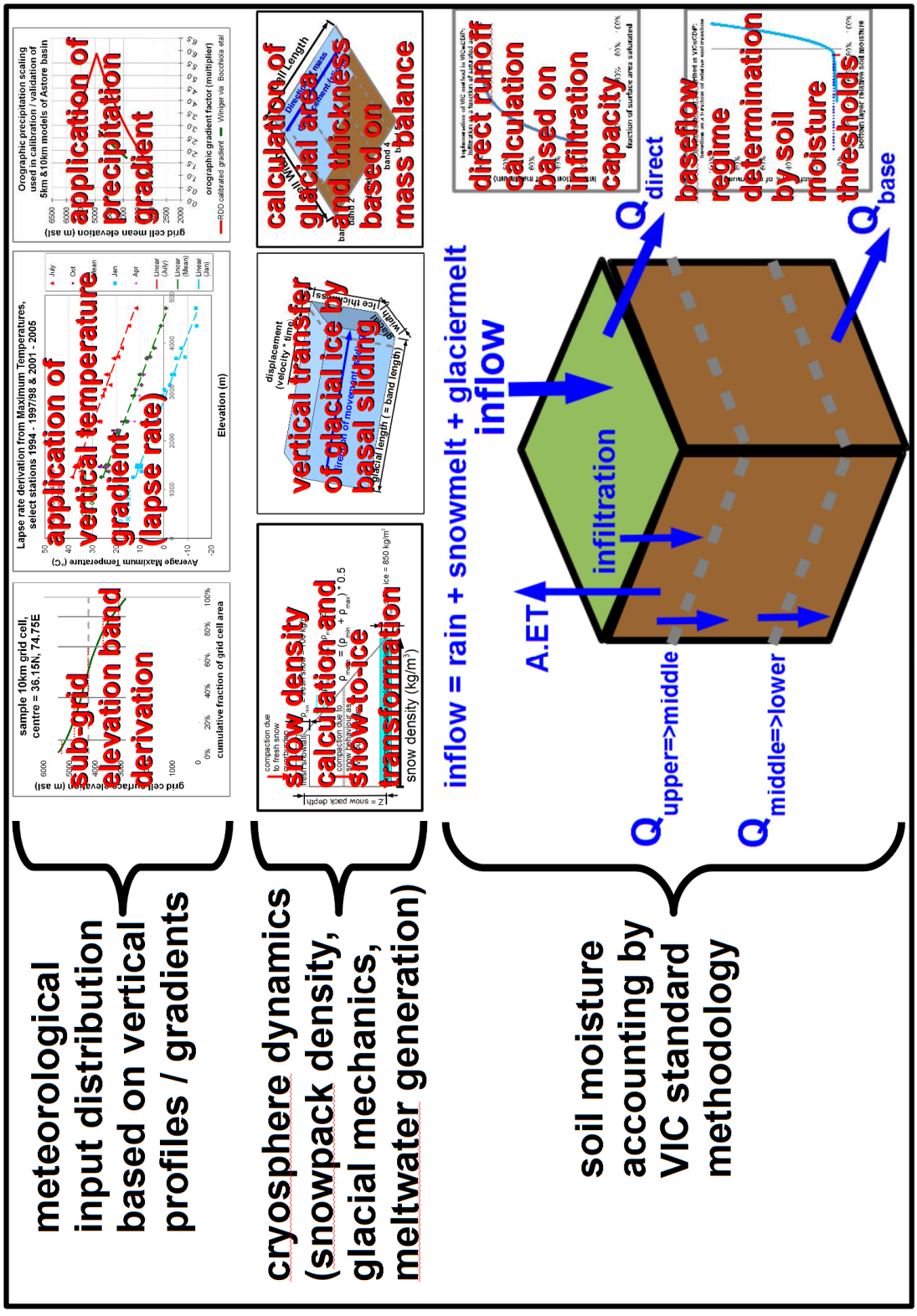

Figure 6.01 Overall conceptual schematic of the Variable Infiltration Capacity with Cryosphere Dynamics in Python (VICwCDiP) model developed in this thesis. nb: Full scale versions of component images are presented (as figures) later in this Chapter or in the associated Appendix (D).

6.3 Approach adopted for hydrological modelling including meltwater generation

This research initially intended to use a pre-existing hydrological model which had been tested for the Upper Indus Basin (UIB). Specifically, it was planned to use a modified version of the Variable Infiltration Capacity (VIC) model which had been adapted to include simplistic glacier mechanics (Naz, 2011). The hydrological component of the VIC model was developed from an approach pioneered in the ARNO model (Todini, 1996). VIC also includes detailed energy balance calculations and vegetative cover properties at the soil surface, snow surface and vegetative canopy levels to provide detailed assessments of energy and mass balance fluxes (Gao *et al*., 2009). Many capabilities of the VIC model are surplus to the requirements of the present project, but its ability to model partial snow cover (Cherkauer and Lettenmaier, 2003) along with the glacial mechanics added by Naz (2011) made it superior to other available candidate models.

Unfortunately, over the course of several months of extensive calibration testing, it was determined that the meteorological input that the current study intended to use was not adequate to meet VIC data requirements for simulation of the full energy balance. A more complete narrative of the issues encountered can be found in Appendix D. At this point it was decided to develop a new model code – implementing the hydrological, snowpack and glacial mechanics methodologies, using algorithms available in the literature, while substituting a "degree-day" based approach (e.g. Singh, 2000) in lieu of the more sophisticated energy balance approach which had hampered the use of VIC. It was decided to code the adapted model in Python in order eliminate compiler dependency issues and thus enhance the platform independence of the model.

Given the capabilities of the adapted model, coded in the Python programming language, to simulate elementary snowpack and glacial mechanics on top of the standard VIC hydrological method it was decided to call this the "Variable Infiltration Capacity with Cryosphere Dynamics in Python" (VICwCDiP) model. A general conceptual diagram has already been presented in Figure 6.01. This diagram illustrates the three main simulation phases – i) distribution of meteorological inputs; ii) simulation of land surface process and cryosphere dynamics; and iii) hydrological partitioning of water balance for runoff yield calculations – which will be discussed in this Chapter.

The concepts and methodology used in model construction as well as the calibration and validation results for two archetypal catchments – Astore (nival) and

Hunza (glacial) – will be presented in the remainder of this Chapter. The decision to model only two, albeit archetypal, catchments was motivated both by logistical – time and computational resources – constraints as well as by the need to demonstrate the validity of the new VICwCDiP model . Development and testing of the VICwCDiP model on the two catchments should be considered as foundational work prerequisite to modelling of the full UIB above the major impounding reservoir at Besham.

6.4 VIC with Cryosphere Dynamics in Python (VICwCDiP) model capabilities

As noted above the capability to model varying, partially snow covered area (SCA), at the sub-grid level, as a model output was a key element in the choice of modelling package. The treatment of SCA as either a model output or input is a key differentiating element between cryospheric modelling approaches; some models, for example the Snowmelt Runoff Model (SRM) (Martinec *et al*., 2007), use spatial and temporal patterns of SCA to drive them. This approach was rejected for two reasons. First because direct calculation of SCA, based on temperature and precipitation, allows for an additional criterion – the accuracy of magnitude and timing in SCA cycles – for calibration and validation. Secondly, the need for SCA as an input would complicate use of the model for climate change impact assessment studies as it the model would need predefined future SCA scenarios (not readily available from Regional Climate Model outputs). In contrast, the methodology selected in this project allows for the independent assessment of the impacts of identified future climate scenarios on SCA extent and duration.

The VIC model spatially discretises catchments into regularly spaced grid cells which in turn are sub-divided into a number of elevations bands for the purpose of improved cryospheric process simulation. Each grid cell is processed individually (sequentially), effectively as a semi-distributed sub-catchment with sub-grid discretisation provided by elevation bands, to simulate the localised cryosopheric and hydrologic behaviour. The hydrological outputs, baseflow and runoff, from the individual cells are then synthesised at the catchment outlet by an external routing model (Lohmann *et al*., 1998). This spatial approach was retained within VICwCDiP, with the use of 0.05 or 0.10 decimal degree (approximately 5km or 10km) horizontal resolution and five elevation bands at the sub-grid scale. Grid cell output file formatting was designed to be compatible with the Lohmann *et al*. routing model, but the primary methods of catchment-wide assessment used the PyRaster toolkit developed by

Holderness (2011) to assemble the results from individual grid cells over a given time period into georeferenced raster images (GeoTiffs) which can be displayed and analysed by geographic information system (GIS) software.

In the VIC model, individualised meteorological records must be specified for each grid cell. This approach is logical for data-rich regions where accurate gridded data sets are available at adequate spatial resolutions. Given the spatially data-sparse nature of the UIB however, it was necessary to extrapolate the cell by cell meteorological records using temperature lapse rates (see Chapter 3, section 3.9.3) and assumed orographic precipitation gradients (see Chapter 3, section 3.9.1). In VICwCDiP a single meteorological "base file" was created for each catchment simulation and applied to all grid cells on purely an elevational basis. Details on the calculation of elevation band statistics and the specification and application of the orographic gradient will be given in later sections of this Chapter. However, more generally, the elevation-band sub-grid approach allows calculation of the fractions of the precipitation falling in liquid (rain) and solid (snow) form.

Broadly the snowpack and glacial mechanics modelling used in the version of VIC modified by Naz (2011) were also adopted in VICwCDiP. Similarly to VIC, portions of the SNTHRM algorithm (Andreadis *et al*., 2009) were adapted for calculation of snowpack density and the transformation of snow to ice. Additional insights from the adapted model formulations described by Saloranta (2012) were useful in adapting the equations for the VICwCDiP implementation. The general glacial mechanics described by Naz (2011) were reproduced in VICwCDiP with the exception that, in addition to volume variability, glaciated area was also rendered variable. Naz's method for derivation of initial glacial thicknesses was also adopted. Details of the formulations are provided in the following sections. Amongst the positive outcomes of this relatively sophisticated methodology for glacial accumulation, mass transport and ablation are insights into the relative balance between snowmelt and glacial melt on a grid cell and catchment basis as well as glacial mass balance trajectories at different elevations as outputs from the model.

A limitation of the VICwCDiP modelling approach, in common with Naz (2011), remains the inability to transfer glacial mass between grid cells. Thus, counter-intuitively, catchment models constructed at coarser spatial resolutions might be more appropriate for catchments with very large individual glacier systems, as smaller grid cells could result in isolation of ablation zones in glacial tongues from accumulation

zones across cell boundaries (at higher elevations). This will be examined in greater detail in later sections of this Chapter.

In terms of more traditional hydrological model outputs, and in the absence of a full energy balance simulation, potential evapotranspiration (PET) in VICwCDiP was calculated using the simpler Priestley-Taylor version (Maidment, 1992) of the Penman-Monteith equation. This choice enables estimation of PET using only air temperature and (approximated) net shortwave and longwave radiation, thus avoiding the need for humidity and wind speed inputs. This an important advantage because interpolation of these two variables over vast elevation differences and topographically complex surfaces would be highly arbitrary in the absence of high spatial resolution – 5km or less – numerical weather simulation. Given that such simulation outputs are not available at present over the study region, simpler methods are deemed more appropriate. Even so, the assumption of spatially constant radiation fluxes is a debatable simplification given links between radiation and cloud cover and the dependency of cloud cover on elevation identified in previous chapters. Dependency of radiation, in terms of energy inputs for melt processes, on topographic controls (e.g. slope, aspect, "hill shade" is also not implemented in the present version of the model. Questions of model performance limitation related to these issues, however, are addressed later in this Chapter.

With regards to the core hydrological results of baseflow and direct runoff, VICwCDiP implements the VIC/ARNO methodology (Todini, 1996, Lohmann *et al*., 1998). VICwCDiP maintains the use of three individual soil layers (per grid cell) where the top layer controls the partition between direct runoff and infiltration and the bottom layer regulates baseflow to the conceptual channel network, while the middle layer serves as both a conduit between the two and a reservoir for groundwater (accumulated infiltration) fluctuations.

6.5 Meteorological input data (climate forcings)

The availability and limitations of meteorological forcings to drive simulations strongly influenced the choice of modelling methodology.

Implementing physically-based modelling to the extent of fully resolving the surface energy balance requires accurate spatial representation of all variables which strongly influence mass and energy fluxes. These include topographically driven variables (wind) and near surface-atmospheric variables (relative humidity) exhibiting

strong (temperature-driven) vertical gradients. Difficulties with interpolation of limited available data for (calculation of) vapour pressure deficit (vpd) as well as only minimal confidence in the spatial representativeness of available near-surface wind speed, rendered resolution of the full energy balance untenable. Thus methods of moderate complexity, focusing primarily on conservation of mass, were adopted for this work.

The baseline hydroclimatology of the UIB, and in particular the annual cycles and interannual variability indicated by the available local long-record meteorological observation stations, was presented in Chapter 3. These local observations along with the global (gridded) meteorological reanalyses – ERA-40 and ERA-Interim –comprise the most reliable observed climate data available as potential inputs to hydrological models of the UIB and its tributary basins.

As will be explained in the following sections dealing with model approach and conceptual structure, the model input meteorological data, whether observed or synthetic, are precipitation, mean daily air temperature (Tavg) and shortwave (SWin) and longwave (LWin) radiation, all specified for the base meteorological station (Astore PMD) and then extrapolated throughout the catchment by calibrated functions using elevation as the single dependent variable.

Because, for the sake of simplicity, orographic scaling was only applied to precipitation amount, and not frequency, Astore (PMD) was used as the base station for meteorological input for models of both the Astore (nival) and Hunza (glacial) catchments despite the availability of the (much drier) long-record Gilgit station in closer proximity to the Hunza. The Astore record was deemed more appropriate for representing precipitation at hydrologically active higher elevations as it has both greater annual precipitation and greater frequency of wetdays and thus using this station achieves a spatial average precipitation (mass input) coherent with the observed runoff (calculated from gauged river discharge).

Furthermore, since the weather generator developed in Chapter 5 requires consistency in the relationship between precipitation occurrence and temperature variability, temperature inputs need to be from the same station as the precipitation data. Unfortunately, temperature data at the daily time-step was not available for the entire available discharge record for the Astore station. A solution to provide estimates where temperature observations were not available was to use normalised, standardised (subtraction of period mean followed by division by period standard deviation) daily time-step anomalies of 2m air temperature (Tavg) from ECMWF reanalysis data (ERA-

40 or ERA-Interim depending on the time period). These anomalies were converted to estimated absolute temperature at Astore by multiplying by the corresponding monthly standard deviation and adding the mean from the observed monthly historical record. To verify the consistency of these estimates, the estimated values were re-aggregated to a monthly time-step and compared to available observations for Astore. Figure 6.02 shows the time series comparison of the observed monthly mean air temperature for Astore PMD with the monthly means of the daily Tavg inputs generated for use in VICwCDiP. Table 6.1 summarises the meteorological input data required by the VICwCDiP model by source.

Variable name	Description	Data source
precipitation	total precipitation (rainfall plus snowfall)	local observations (PMD)
Tavg	daily average near-surface air temperature	local observations (PMD)
SWin	cumulatively daily incoming shortwave radiation	ERA-Interim reanalysis
LWin	cumulatively daily incoming long-wave radiation	ERA-Interim reanalysis

Table 6.1 Summary of required meteorological input data for simulation by VICwCDiP.

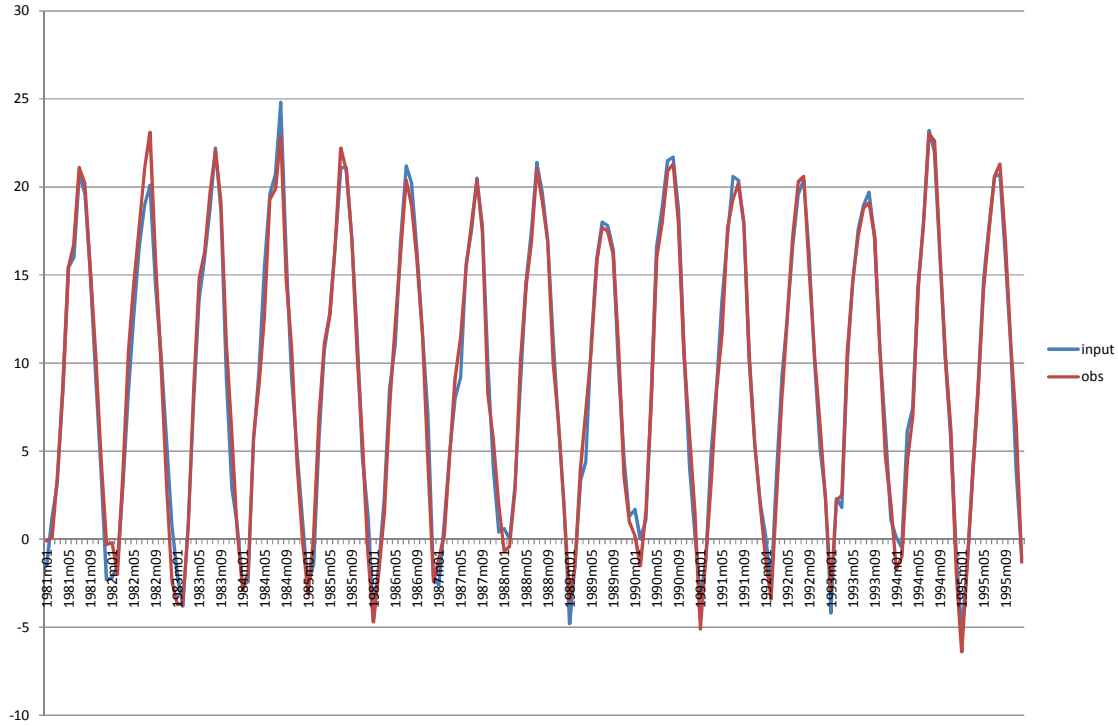

Figure 6.02 Example of verification of correspondence between observed and modelled input air temperature for the base meteorological station at Astore showing data from 1981 to 1995, daily values re-aggregated to a monthly time-step.

Values for shortwave and longwave radiation, which are required for calculation of potential evapotranspiration (PET) using the Priestley-Taylor method, were taken directly from ERA-Interim, if available, or extrapolated from ERA-40 daily normalised,

standardised anomalies and ERA-Interim period statistics if prior to the start of the ERA-Interim (1979/01/01).

6.6 VICwCDiP model construction and pre-initialisation

In the first two phases – i) distribution of meteorological inputs; and ii) simulation of land surface process and crysophere dynamics – of time-step modelling, land surface state values and meteorological inputs are modelled for each grid cell on a elevation band by band basis. In other words each sub-grid elevation band is considered a distinct, homogeneous spatial unit. Once weather-driven land surfaces processes and state values have been computed at the (sub-grid) elevation band level, the values are spatially aggregated to the grid cell level based on the relative areal weighting of each elevation band. This is because soil moisture accounting is performed only at the grid cell (and not elevation band) level. In this Chapter, variables and parameters that are calculated for each specific band are referred to with a general subscript "b(i)." In cases where the previous or subsequent bands in the model chain need to be indicated the subscripts "b(i-1)" or "b(i+1)" are used.

The first step in the construction of a catchment model using VICwCDiP is discretisation of the tributary area into individual grid cells at the selected spatial resolution. Within each grid cell the available topographic data, from a digital elevation model (DEM), is analysed to calculate the characteristics of the individual elevation bands. For the models of the Astore and Hunza – both with versions at 0.05 and 0.10 decimal degrees – catchments were discretised into grid cells using topographic data from the NASA Shuttle Radar Topograpy Mission 90m horizontal resolution (0.000833 decimal degree) DEM (SRTM90) (Jarvis *et al*., 2008). This results in a potential sample of 3600 or 14400 elevation points per modelled grid cell, provided all points within the cell fall within the catchment, i.e. that it is an "interior" rather than "boundary" cell. The process for derivation of elevation band characteristics is described in detail in Appendix D.

As an aside, the difference in hydrological regime between Astore (nival) and Hunza (glacial) is evident in the fraction of glacial coverage in each catchment as shown in Figure 6.03 (i.e. panels a-c vs panels d-f).

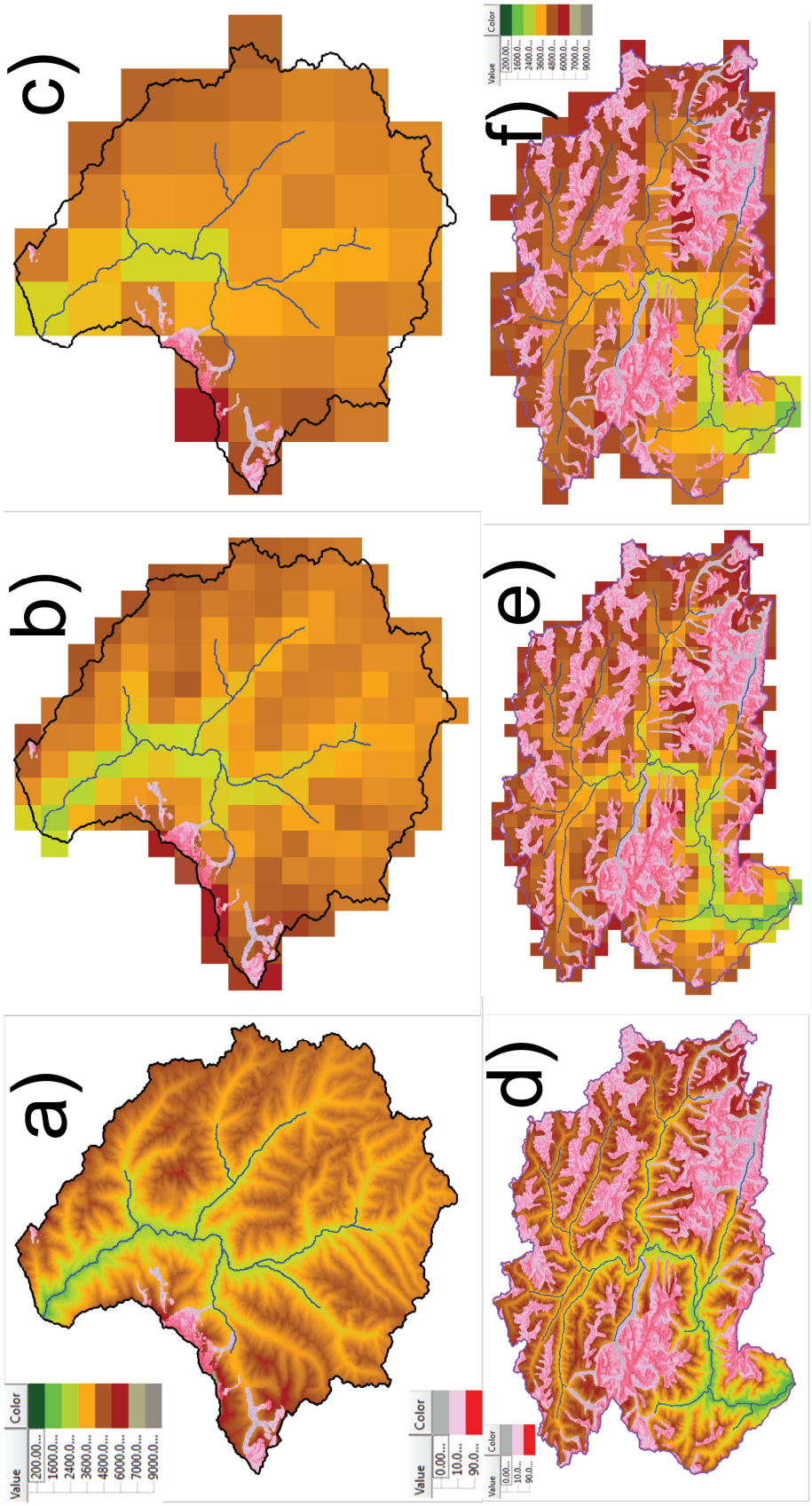

Figure 6.03 Spatial discretisation of the Astore (a to c) and Hunza catchments (d to f) for raster degree-day modelling. Panels a & d: "native" SRTM90 pixel elevations; panels b & e: 5km VICwCDiP model grid cell mean elevations; panels c & f: 10km VICwCDiP model grid cell mean elevations; all panels: glaciated areas are shown as the SRTM90-derived surface slopes. Legends: "earth tones: elevations in m asl. "pink to red" gradations: surface slopes in angular degrees. Overall scales are identical for panels in a give row (i.e a to c and d to f) and can be gauged by the grid cell sizes in the middle panels (b and e, 5km and right panels (c and f, 10km).

Examples of the resultant sub-grid cell discretisation are shown in Figure 6.04. The grid cell shown in the left panel of Figure 6.04, for the Hunza catchment, shows a relatively balanced distribution of area between the five elevation bands. It is typical for the uppermost and lowermost bands to cover a smaller fraction of the cell area than the interior bands and especially the central one. The grid cell shown in the right panel of Figure 6.05, for Astore, provides an example of the situation described above where one or more elevation bands have zero area based on the automated band delineation process. Here specifically the lowest band must be assigned a minimal area in order to allow the model to function. The grid cell internal elevation range in both examples shown is greater than 2000m. This is typical of that found in constructed models of UIB tributary catchments.

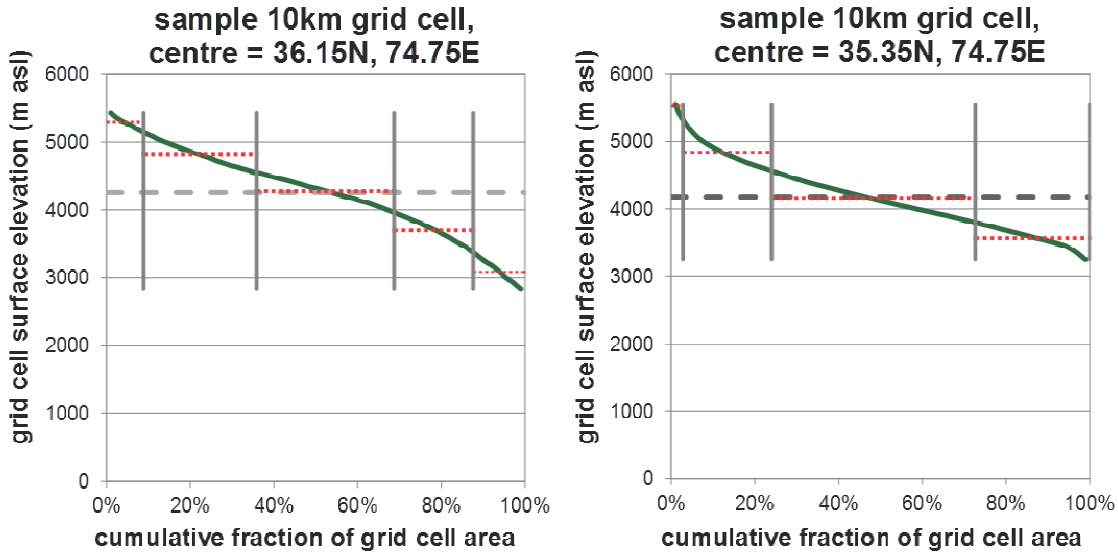

Figure 6.04 Examples of grid cell internal distribution of area by defined sub-grid elevation bands used in VICwCDiP surface discretisation. The cell in the left panel is located in the Hunza catchment. The cell in the right panel is located in the Astore catchment.

To derive the inputs necessary for glacial calculations, available estimates of glacial footprints are used to filter SRTM90 and derive surface slopes. These slope values are processed using the underlying elevation data in an additional iterative loop, with testing against the band limits. The resulting outputs are the fraction of the cell with glacial cover within the elevation band and the mean slope of this glaciated area. The glaciated areas are mapped in Figure 6.03 overlain on the model grid cell elevations respectively for the Astore and Hunza catchments.

For elevation bands containing glaciers, initial glacier thickness is determined using a reformulation of Kessler *et al.*'s (2006) equations of Glenn's flow law as suggested by Naz (2011). This is shown in Equation 6.01:

Equation 6.01:

$$height.ice_{b(i)}\ [m] = \tau_c * (\rho_{ice} * g * sin(\alpha_{b(i)}))^{-1}$$

where: τ_c = 100,000 [Pa] ; ρ_{ice} = 917.0 [kg m^{-3}] ; g = 9.81 [m s^{-2}]; and
$\alpha_{b(i)}$ = mean slope of glacier surface within band [radians]

This derivation relies on the formulation of the gravitational driving stress which is proportional to the ice thickness and inversely proportional to the product of the representative bed (surface) slope with the mean ice density and the acceleration of gravity. The key assumption is provided by Paterson (1994) regarding the near constant/universal representative value of gravitational driving stress – i.e. τ_c = 100 kPa – for temperate mid-latitude glaciers. Figure 6.05 provides a simple conceptualisation of the elements involved. In layman's terms, the theory is that under a state of dynamic equilibrium, glacier thickness will need to be greater (less) at shallower (steeper) slope angles to achieve the driving stress/bed friction conditions widely observed by glaciological field studies.

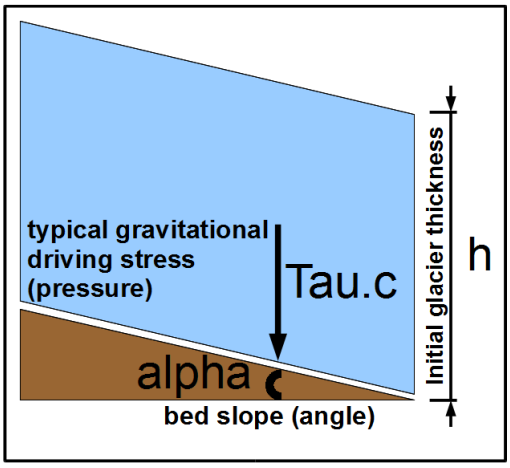

Figure 6.05 Conceptual illustration of the relationships in VICwCDiP between glacial driving stress, thickness and bed-slope relationships, i.e the product of the thickness of the glacier times the vertical component (sine of angular slope) of the bed gradient, the density of ice and the acceleration of gravity are equal to the gravitational driving stress. This derivation is based on the finding by a number of studies globally that due to (the physics of) glacial mechanics the gravitation driving stress tends to converge around a near constant representative value (100kPa).

Given that glaciers are dynamic systems – changing in both lateral extent and volume – this approach is temporally associated with the surface state (glacial thickness) concurrent to the date or period when the DEM was derived and presupposes that the delimitation of glacial footprints match these conditions. The application/adaption here of Paterson's assumptions regarding Glenn's flow law in both the derivation of initial thickness as well as calculation of rates of displacement (basal sliding) is not original but follows the approach adopted by Kessler *et al*. (2006) and Naz (2011).

Once glaciated areas and initial ice thickness have been calculated for each relevant elevation band in each cell, initial ice volume is determined simply by taking the product of the glaciated "footprint" area and the estimated mean thickness. This uniform thickness is clearly an exaggerated simplification but additional idealisations of glaciated geometry were necessary to allow calculation of glacial mass transfer between elevation bands within an individual grid cell.

In the approach used here, glacial ice masses are assumed to advance along a longitudinal axis. At each daily time-step, the distance of glacial advance is calculated in all but the lowest elevation band which is considered blocked, i.e. mass can only be transferred into the lowest band, there is no extracellular ice transport. For the other bands the volume of mass transferred from that band to the adjacent lower band is modelled as the product of the displacement time and the cross-section of the idealised glacial face. Thus it is necessary to define an assumed glacial geometry in the absence of highly detailed cell by cell data on glacial geometries (length, width, thickness).

Each elevation band is therefore assumed to occupy a rectilinear strip across the entire width (dimension perpendicular to the direction of glacial displacement) of the grid cell. The nominal length (dimension parallel to the direction of glacial displacement) of the band is equal to the product of the grid cell length and the elevation band fraction. For bands with glacial cover, the glacial mass is considered to occupy the entire length of the band, i.e. its fraction of the overall cell. This assumption is logically necessary for the intermediate elevation bands to allow continuity of mass transfer since they both receive mass inputs from the adjacent higher band and export mass to the adjacent lower band. For simplicity, the length assumption is extended to the highest and lowest bands. Once the length assumption has been made, it follows logically that the glaciated width is the fraction of the grid cell (and elevation band) equal to the glaciated fraction of the grid cell within the band. It further follows that glacial cross-section is the product of the glaciated width and ice height. These glacial geometry principles are illustrated conceptually in Figures 6.06 and 6.07.

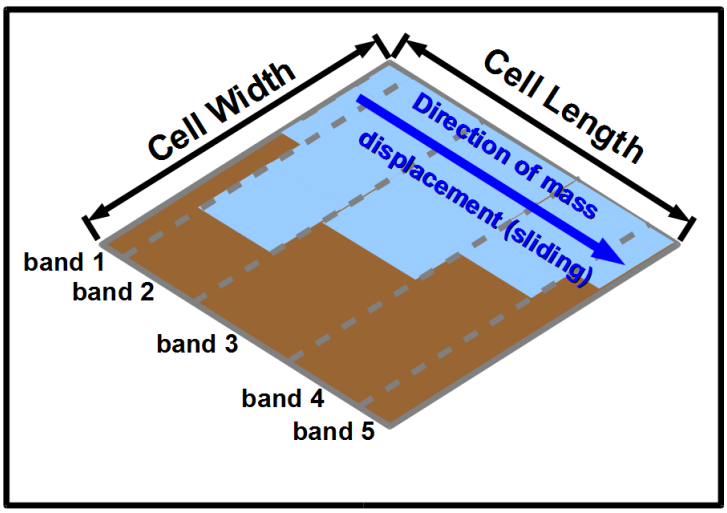

Figure 6.06 Conceptual illustration of glacial footprint geometry at the sub-grid level used in VICwCDiP.

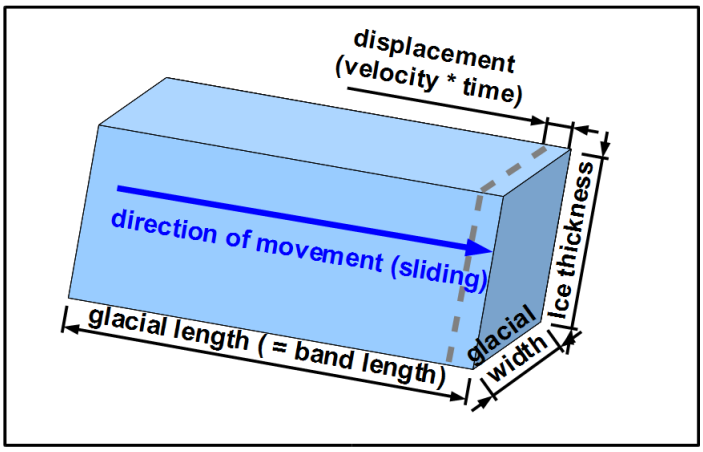

Figure 6.07 Conceptual illustration of glacial cross section and longitudinal geometry of the glacial mass used in VICwCDiP.

Details regarding the selection of parameters for the soil moisture accounting component of the VICwCDiP model, following standard hydrological modelling approaches, are provided in Appendix D.

6.7 Model simulation, generalities and initialisation

Figure 6.01, presented at the start of this Chapter, shows how execution of VICwCDiP for an individual grid cell and time-step can be considered as three distinct phases: i) distribution of meteorological inputs; ii) simulation of land surface process and cryosphere dynamics; and iii) hydrological partitioning of water balance for runoff yield calculations.

At the catchment level VICwCDiP is run by sequentially simulating the hydrological – as well as land surface and cryospheric – responses for each cell in the catchment model for a time-series of available meteorological inputs. This sequential

execution in VICwCDiP is a direct functional implementation of the way in which VIC (Gao *et al*., 2009) operates.

Prior to starting the simulation for a given cell, a variety of location-specific parameters are initialised. In addition to the soil layer descriptive quantities described in Appendix D, the area, elevation and glacial cover characteristics of the five elevation bands composing the grid cell are also imported.

The model is run at a daily (24 hour) time-step. At the beginning of each time-step the snow cover and glacial state quantities are updated either from the initial conditions (first time-step only) or from the results of the preceding time-step.

The following glacier specific quantities are calculated by the model:

Equation 6.02:

$$glacial.ratio_{b(i)}\ [fraction] = glacial.fraction_{b(i)} * (cell.fraction_{b(i)})^{-1}$$

Equation 6.03:

$$IWE.initial_{b(i)}\ [mm] = height.ice_{b(i)} * \rho_{ice} * glacial.ratio_{b(i)}$$

where: $\rho_{ice} = 917.0$ [kg m^{-3}]

The equations above are used to normalise the simulated glacial mass in the cell to an "ice water equivalent" (IWE) as this is necessary for the land-surface process calculations. In the course of model development it was deemed more effective for some processes to use IWE to represent glacial mass and in others to use nominal absolute dimensions, i.e. either area fraction or metres thickness. Considerations included the calculations to be performed, the conceptual coherence of the approach and, above all, the imperative to verify conservation of mass within the model.

6.8 Simulation Phase I: Distribution of meteorological inputs

6.8.1 Precipitation distribution

Once the initial glacial state variables are defined, mathematical equations – as functions of elevation – are used to describe the complex vertical profiles of precipitation amounts in the modelled catchments. Climate inputs are calculated for a band for the given time-step based on the meteorological record and orographic precipitation and air temperature lapse rate equations. While the air temperature behaviour is modelled as a purely linear relationship with elevation (see Chapter 3, section 3.9.3), the formulas defining vertical precipitation gradients are purely empirical and were derived during model calibration to deliver a spatial distribution of catchment mass inputs such that simulated runoff seasonality matched available observations.

The derived formulas are defined using the parameters listed in Table 6.2. The values of each of these parameters are ultimately calibrated, although initial values for $Z_{max.isohyetal}$ were drawn from the literature (Hewitt, 2011). $Z_{max.isohyetal}$ is the critical parameter defining the orographic profiles described here and is defined as the elevation where peak orographically enhanced precipitation is assumed to occur, detailed in Equations 6.04 and 6.05:

Calibration parameters defining the orographic precipitation gradient function	Astore (nival catchment)	Hunza (glacial catchment)
	5km (0.05dd) & 10km (0.10dd)	5km (0.05dd) & 10km (0.10dd)
$Z_{max.isohyetal}$	5000.0	5000.0
β_{submax} (gradient)	0.35	0.35
k.submax (exponent)	3.0	2.75
$\beta_{supermax}$ (gradient)	3.0	2.65
k.supermax (exponent)	5.0	3.0
rain.factor	1.90	1.35

Table 6.2 Calibrated orographic gradient function parameters for the Astore and Hunza catchments.

Equation 6.04

$$orographic.factor_{b(i)} \begin{cases} \text{where } Z_{b(i)} < Z_{max.isohyetal} \\ = \beta_{submax} * [\ Z_{b(i)} * (Z_{metbase})^{-1}\ ]^{k.submax} \\ \text{where } Z_{b(i)} > Z_{max.isohyetal} \\ = \beta_{supermax} * [\ Z_{max.isohyetal} * (Z_{b(i)})^{-1}\ ]^{k.supermax} \end{cases}$$

Equation 6.05:

$$precip_{b(i)} = precip_{metbase} * orographic.factor_{b(i)} * rain.factor$$

In equations 6.04 and 6.05, $Z_{b(i)}$ is mean elevation[m asl] of band "b(i)"; Other parameters, defined in Table 6.2, included exponents (k.submax, k.supermax) and coefficients (β_{submax}, $\beta_{supermax}$ and *rain.factor*).

For both the Astore and Hunza catchment models the meteorological record used was the PMD station at Astore. Hence, the elevation of the meteorological base station $Z_{metbase}$ is equal to 2394m asl.

The resulting orographic precipitation gradient, by which observed rainfall at Astore PMD is multiplied over the elevation range, is shown in Figure 6.10 where it is compared to functions – normalised by Astore annual precipitation – developed by independent studies by Immerzeel *et al*. (2012) and Bocchiola *et al*. (2011). The Immerzeel *et al*. (2012) function was derived from a glacial modelling study in the Hunza catchment which assumed a net neutral mass balance for the years 2001 to 2003 whereas Bocchiola *et al*. (2011) implements findings by Winiger *et al*. (2005) as inputs

to a snow and glacier modelling exercise for the Shigar catchment. To clarify, the values shown for the Immerzeel *et al*. function are crudely approximated from their "Figure 5" because direct calculation would have required access to additional information/data regarding their method for calculation of "reference elevation" in addition to their "optimised precipitation lapse rate" of 0.21%/m. The values for the Bocchiola *et al*. (Winiger *et al*.) function, however, are directly calculated from their "Equation 1" as published in Bocchiola *et al*. (2011).

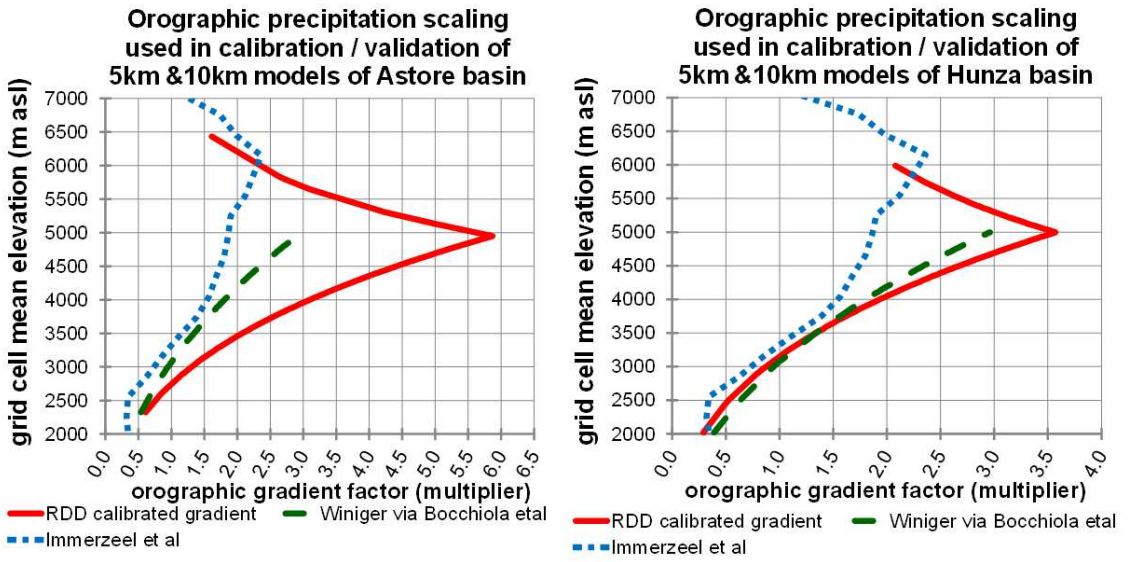

Figure 6.08 Calibrated orographic precipitation gradients for Astore and Hunza catchments with comparison to other published studies by Immerzeel *et al*. (2012) and Bocchiola *et al*. (2011). "RDD calibrated gradient" refers to the "raster degree-day" approach implemented in VICwCDiP.

The approach used in this work admittedly greatly simplifies the complexity of spatio-temporal variability in UIB precipitation patterns:

- The scaling is constant in time, and uniform throughout the catchment, with regards to the reference meteorological base stations. In reality it is understood that the effective orographic precipitation gradient would vary substantially in time and space. This simplification was deemed necessary both due to the absence of information on causal mechanisms of variability in the vertical precipitation gradient and due to the short record length of the high-elevation local (AWS) observations which guided derivation of the orographic precipitation gradient.
- Precipitation gradients are modelled purely as a function of elevation without regard to prevailing wind direction (potential leeward rain shadows) or localised topographic forms, e.g. slope or concavity. Although further model developments might be able to increase the degree of sophistication and thus

physical realism, such work is beyond the constraints and scope of the present project.

6.8.2 Temperature distribution

Mean daily (2m) air temperature (Tair) is determined using a simple linear lapse rate and the base meteorological input record from Astore, as shown in Equation 6.06. The value used here corresponds to the local lapse rate for daily mean temperature, Tavg, as presented in Chapter 3, section 3.9.3. Figure 6.11 provides a visual reminder of the derivation of the linear lapse rate.

Equation 6.06:

$Tair_{b(i)}\ [°C] = Tair_{metbase} - (lapse.rate_{Tair} * (Z_{b(i)} - Z_{metbase}))$

where: $lapse.rate_{Tair} = 0.007$ [°C m^{-1}] i.e. 7°C/1000m

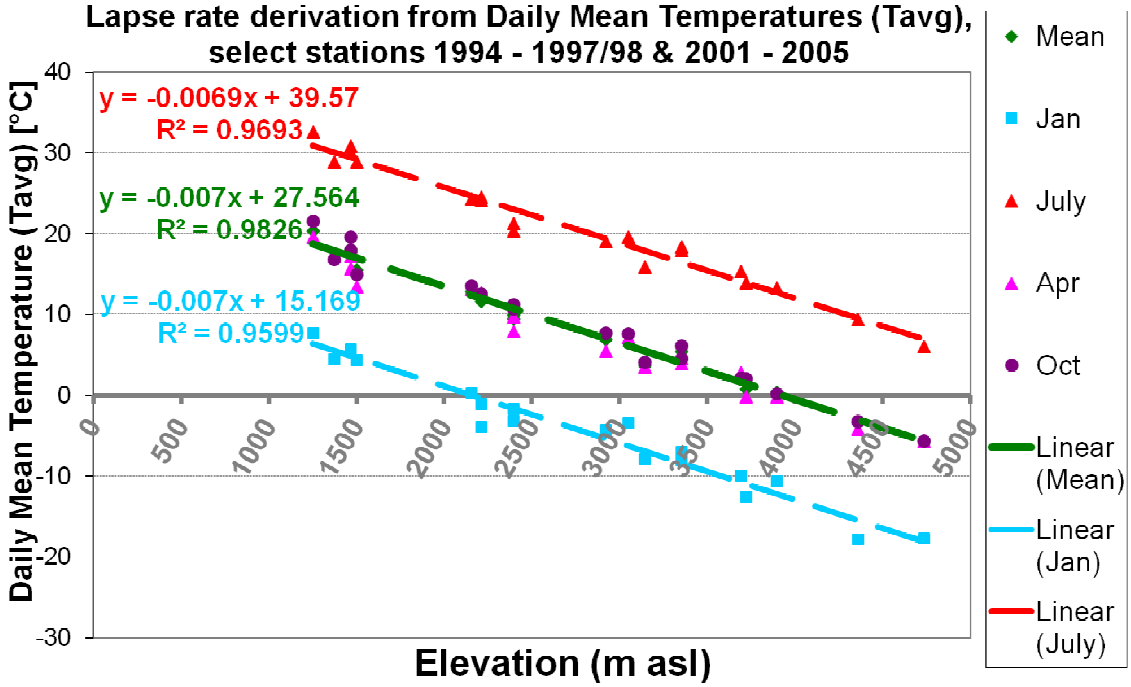

Figure 6.09 Derived linear lapse rates for daily mean 2m air temperature (Tavg) used in VICwCDiP as Tair.

6.8.3 Examples of orographic precipitation factors and Tair offsets

To provide a specific example of how precipitation and air temperature vary within grid cells according to the derived orographic profile and air temperature lapse rates, orographic scaling factors and air temperature offsets were calculated for individual sub-grid elevation bands and for spatial mean grid cell values for each of the two example grid cells previously shown in Figure 6.05. The values are given Table 6.3.

Catchment and grid cell or Station	band.-number$_{b(i)}$	$Z_{b(i)}$ [m asl]	orographic.factor$_{b(i)}$ [dimensionless]	Tair offset$_{b(i)}$ [°C]
Astore PMD	n/a	2394	1.0	0.0
Astore (nival regime) 35.35N, 74.75E	1	5530.3	3.443	-21.9
	2	4842.5	5.503	-17.1
	3	4160.1	3.489	-12.3
	4	3568.8	2.203	-8.2
	5	3567.8	2.201	-8.2
	mean	4181.8	3.564	-12.3
Hunza (glacial regime) 36.15N, 74.75E	1	5296.3	4.236	-20.3
	2	4820.0	3.237	-16.9
	3	4276.5	2.329	-13.1
	4	3699.2	1.563	-9.1
	5	3086.6	0.95	-4.8
	mean	4256.7	2.425	-12.7

Table 6.3 Examples of orographic precipitation factors and air temperature offsets for individual sub-grid elevation bands and cell spatial mean from two example grid cells, one each from Astore and Hunza catchments.

6.8.4 Extrapolation of additional variables

Once Tair has been calculated for the elevation band, the state is determined – solid (snow) or liquid (rain) – of any precipitation occurring during the time-step using a simple 0°C threshold (e.g. Auer, 1974), although this threshold could become a calibrated parameter in future versions of the model.

To enable the calculation of potential evapotranspiration (PET) using the Priestley-Taylor method, we also need to approximate local (near surface atmospheric pressure), saturation vapour pressure (SVP), its gradient (rate of change) and the psychrometric constant (γ) for each elevation band.

Calculation of band Tair permits an approximation of local (near surface) atmospheric pressure. This approximation was drawn directly from the equations used in VIC (Gao *et al*., 2009). These equations are provided in detail in Appendix D.

6.9 Simulation Phase II: Land surface processes and crysophere dynamics

6.9.1 Calculation of fractional snow covered area (SCA)

Next in the modelling sequence, the state of fractional snow covered area (SCA) is determined using an approach similar to VIC. This approach calculates a linearly varying SCA fraction if snow depth is less than a selected critical value which depends upon whether there is fresh snowfall or simply existing standing snowpack (Cherkauer and Lettenmaier, 2003).

These critical snow depths are, strictly speaking, calibration parameters but, in all UIB simulations to date, critical depths of "fresh snow" – i.e. new precipitation in the current time-step ($freshsnow_{b(i)}$) – and "standing snow" – i.e. precipitation occurring prior to the current time-step – for complete snow cover have been defined respectively as 25.0 mm and 100.0 mm as measured in snow water equivalent (SWE).

Thus determination of SCA is a two step procedure. First, if there has been fresh snowfall, i.e. solid precipitation occurring in the time-step in question, an SCA of 1.0 is assigned if the new snow depth (in mm SWE) exceeds the defined threshold (25.0mm). If there has been no new snowfall – or if new snowfall is less than the threshold accumulation – but there is existing snowpack from the previous time-step, then the "standing snow" criterion is evaluated. In this case if the standing snowpack at the start of the time-step ($SWE.initial_{b(i)}$) is greater than the "standing snow" threshold (100.0mm) then SCA is considered complete, i.e. equal to 1.0.

If neither the "fresh snow" nor "standing snow" criteria are satisfied then the fractional SCA is calculated based on Equation 6.07.

Equation 6.07:

$$SCA.initial_{b(i)} = \frac{SWE.initial_{b(i)}}{SWE_{fullSCA}}$$

where $SWE_{fullSCA}$ = 100.0 [mm]

6.9.2 Approximation of mean surface albedo and net (absorbed) shortwave solar radiation

Very sophisticated methods have been developed to estimate the evolution of snow albedo over time, including the method of Sun (1999), available as an option in VIC, which uses physically-based equations considering cloud cover and insolation conditions to estimate the rate of albedo decay. For VICwCDiP a simpler approach was adopted which mirrors that for calculating SCA. If new snowfall is greater than the fresh snow critical depth, the albedo is assigned as the typical fresh snow value. If no snow is present, the albedo is assigned as the "bare ground" representative value. If some standing snow is present then the albedo is calculated by linear scaling with fraction of SCA between the bare ground and "old snow" albedo values as shown in Equation 6.08.

Equation 6.08a:

$$albedo_{currentSCA}\ [fraction] = \begin{cases} \{\ where\ freshsnow_{b(i)} > 25.0 \\ = 0.85 \\ \{\ where\ freshsnow_{b(i)} < 25.0 \\ = 0.65 \end{cases}$$

Equation 6.08b:

$$albedo_{b(i)} = (albedo_{bare} * (\ 1.0 - SCA.initial_{b(i)})\ ) + (albedo_{currentSCA} * SCA.initial_{b(i)}\ )$$

The representative values for bare ground albedo, standing snow albedo and fresh snow albedo could be treated as calibration parameters. However, here the values were derived from analysis of spatial data products for albedo from the MODIS Terra instrument (see Chapter 3, section 3.7.6 and 3.9.5).

Once albedo has been approximated for the elevation band, it is possible to calculate net (absorbed) shortwave radiation, as shown in Equation 6.09.

Equation 6.09:

$$SWnet_{b(i)}\ [W\ m^{-2}] = SWin * (1.0 - albedo_{b(i)}\ )$$

6.9.3 Approximation of surface temperature (Tsurf)

Physically accurate calculation of surface temperature, $Tsurf_{b(i)}$, would require resolution of the full surface energy balance. Given the problems encountered when attempting to use VIC with a full solution of the energy balance, however, a deliberate decision was made to avoid attempting this. As such, a relatively simple method for approximating $Tsurf_{b(i)}$ using $Tair_{b(i)}$ was sought. After considering possible options, it was decided to calculate a correction factor to relate $Tsurf_{b(i)}$ to $Tair_{b(i)}$ using net (absorbed) shortwave radiation. A linear equation for the correction factor was empirically derived using large scale ERA-40 and ERA-Interim reanalysis data for net shortwave radiation and MODIS land surface temperature (LST) data. The resulting formula is presented here as Equation 6.10.

Equation 6.10:

$$Tsurf.correction\ [°C] = (SWnet_{b(i)} * 0.059) - 6.5$$

In cases where $Tair_{b(i)}$ was above freezing (> 0°C) but standing snow was present ($SWE_{b(i)}$ > 0 mm), $Tsurf_{b(i)}$ was assigned as at the freezing point, i.e. 0°C. Otherwise, $Tsurf_{b(i)}$ was calculated as shown in Equation 6.11.

Equation 6.11:

$$Tsurf_{b(i)}\ [°C] = Tair_{b(i)} + Tsurf.correction$$

6.9.4 Simulation of snowpack density evolution

One of the key elements for inclusion in a model to simulate glacial mass trajectories is the replenishment of glacial mass through transformation of accumulated snow into ice by densification. Thus VICwCDiP must incorporate a methodology for calculation of snowpack density as a function of age, temperature and depth/overburden. A simple conceptual illustration of the process is provided in Figure 6.12. As explained in the opening sections of this Chapter, snow density calculations in VICwCDiP use the SNTHRM algorithm (Andreadis *et al.*, 2009). Nuances in the equation formulations detailed by Saloranta (2012) were helpful in arriving at a stable algorithm in the VICwCDiP code. The details of the equations used in the snowpack depth and density calculations are provided in Appendix D, but the conceptual procedure is described in the following paragraphs and shown graphically in Figure 6.10.

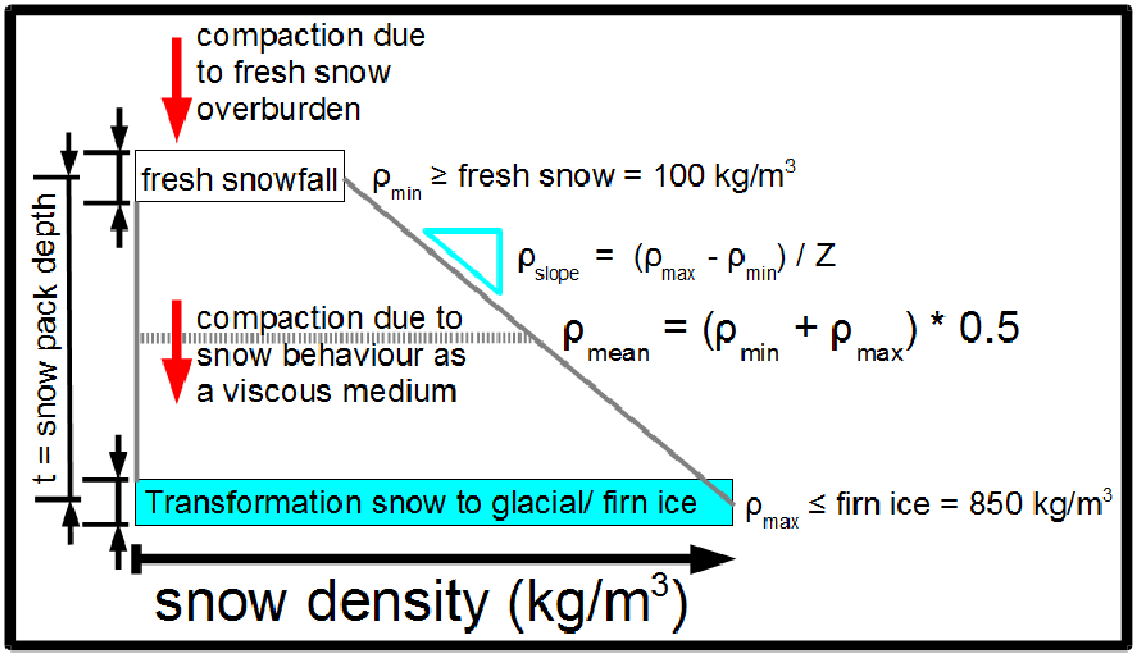

Figure 6.10 Conceptual illustration of process of snowpack density evolution in VICwCDiP.

A number of constant value parameters were necessary to define the snow density algorithm. For simplicity a constant uniform fresh snow density ($\rho_{freshsnow}$) of 100.0 [kg m^{-3}] is adopted. Density is assumed to vary linearly through the pack with the minimum possible density equal to that for fresh snow, and the maximum possible density at the transformation threshold to perennial ice pack. This density, referred to as $\rho_{threshold}$, was assigned the value of 850.0 [kg m^{-3}] and is taken from Singh and Singh (2001). The actual maximum density of snowpack may not reach the upper bound of this threshold value if the prerequisite conditions (pack depth, etc.) do not occur. It is

important to note that this value is different to the assumed mean density of glacial ice at 917.0 [kg m^{-3}] (Singh and Singh, 2001).

The first step in the snow density procedure is to update the pack depth from the value stored at the previous time-step. The previous snow pack water equivalent, SWE.initial, divided by the previous depth value then yields the initial mean pack density. The next step in the density procedure is to calculate the amount of compaction (reduction of pack depth) due to the weight of fresh snow. The amount of allowable compaction is bounded at 10% of the previous snow pack depth. This 'safeguard' limits the amount of compaction occurring during time-steps with very large precipitation amounts which were calculated from the base meteorological record by orographic scaling. This 'safeguard' was implemented because the initial results of process testing in VICwCDiP showed very rapid – on the order of a few days or weeks – transformations of snowpack to glacial ice.

There are a number of potential explanations for this. One is that the numerical simplification of a differential equation (rate of depth change per unit time) to an equation simply yielding compact amount (depth) over the time-step (daily in the present version of VICwCDiP) results in unrealistic results. Another explanation that is judged highly probable is linked to the orographic gradient not in terms of the magnitude of the precipitation – which is viewed with relative confidence – but due to the present inability to implement an orographic gradient with regards to precipitation frequency. As described above, the present method delivers reasonable vertical patterns of accumulation purely by scaling daily precipitation totals. This means however that when it is dry at the base station, it is also considered to be dry across the whole of the elevation range. This is a considerable oversimplification, but at present there is insufficient data on the vertical patterns in precipitation event frequency to implement a more sophisticated method.

The reason that this model shortcoming may affect the simulation of snowpack density is that the intensity of individual precipitation events is likely exaggerated and thus in turn so is the compaction effects of these events on the standing snowpack. Alternative explanations include that the empirical nature of the method limits its applicability to the conditions for which it was developed, i.e. European or North American alpine environments.

The next step in the density procedure is to calculate compaction due to "aging" of the existing snowpack. This requires calculation of characteristic values for snowpack "overburden" and viscosity.

Once again the amount of allowable compaction in this step was bounded to 10% of the updated snowpack depth. Similar limits are used in VIC (Gao *et al*., 2009). Snow depth is thus updated a second time. The limit applied here was implemented so that the timescale for snow to ice transformation would remain physically realistic. The resultant VICwCDiP model behaviour is that snow to ice transformation follows a rough annual cycle roughly proportional to the standing snowpack, i.e. there is little or no transformation from autumn through late winter, until early to mid-spring when, prior to the summer melt season, standing snowpack depth is at its greatest. Transformation then effectively ceases during the summer as the pack overburden is ablated, until the annual cycle begins again with the next accumulation season the following autumn and winter.

As stated at the beginning of this section (6.9.4), the equations used for snowpack depth and density calculations were taken from the VIC source code (Gao *et al*., 2009) which references Andreadis *et al*. (2009). These equations were checked against those of Saloranta (2012).

As stated above, the snow density is considered to vary linearly with the depth of snowpack. This is illustrated conceptually in Figure 6.10. The maximum density within the snowpack, ρ_{max}, can be calculated using simple geometry. The snow to ice transformation procedure enumerated here was implemented based on concepts described by Naz (2011). If the maximum snowpack density is greater than the snow-to-ice transformation threshold density an additional subroutine is activated to calculate the amount of mass transformed and to update the remaining snowpack depth and density.

6.9.5 Calculation of meltwater generation

Now that values for both current SWE and IWE have been updated to account for snow to ice transformation through densification, meltwater generation calculations can be performed using the degree day method (e.g. Singh *et al*., 2000). The degree-day method is an alternative approach to use of the full energy balance to calculate meltwater generation. Under the full energy balance, heat energy exchange at the air-surface interface is resolved to determine the partitioning of energy to melt processes, i.e. latent heat flux of solid to liquid water transformation (Andreadis *et al*., 2009).

Resolution of the full energy balance, however, is demanding both in computational intensity and data requirements. The degree-day method offers a simpler, if empirical approach, by indexing the available energy to drive melt processes to the ambient near-surface air temperature. This index is quantified by means of a calibrated coefficient, referred to as the "degree-day factor", with units depth of melt per (positive) temperature increment and time-step (i.e. mm * °C^{-1} * day^{-1}).

The conceptual approach adopted here for the relationship between snow melt and glacier melt was that they should occur sequentially, i.e. the seasonal snowpack should have been modelled as completely melted prior to the start of glacial melt. This sequential approach follows the approach of Naz (2011) and earlier by Rees and Collins (2005). On the one hand this oversimplifies physical reality by not allowing for spatial variability of snow and ice distribution within the sub-grid (elevation band) domain. On the other hand, at climatic (multi-decadal or longer) timescales, it could be reasonably assumed that glacial ice will be concentrated precisely where seasonal snowpack tends to persist the longest. A further potential change to model formulation could allow ice melt to when SCA falls below a given threshold (e.g. 0.15 or 15%). This threshold would then become a calibration parameter. Testing of the efficacy – i.e. improvement in model performance metrics – of such an increase in complexity is yet another potential task for future VICwCDiP development work.

While seasonal snowpack is present in the model, i.e. $SWE.updated_{b(i)} > 0$, Equations 6.12 and 6.13 are used to describe snow meltwater generation (e.g. following Singh *et al*., 2000).

Equation 6.12:

$$SWE.melt_{b(i)}\ [mm] \begin{cases} \{ \text{where } (SWE.updated_{b(i)} * Tair_{b(i)}) > 0.0 \ ) \\ = min(SWE.updated_{b(i)}, [\ Tair_{b(i)} * ddf_{snow}\ ]) \\ \{ \text{where } (SWE.updated_{b(i)} * Tair_{b(i)}) \leq 0.0 \ ) \\ = 0.0 \end{cases}$$

Equation 6.13:

$$SWE.final_{b(i)}\ [mm] = SWE.updated_{b(i)} - SWE.melt_{b(i)}$$

The snowmelt degree-day factor – designated ddf_{snow} in Equation 6.20 – is a principal calibration parameter in the model described here. The factor has units of millimetres per degree Celsius per day [mm °C^{-1} day^{-1}].

In grid cell elevation bands with glacial ice, i.e. $IWE.updated_{b(i)} > 0$, once the seasonal snowpack has been exhausted simulated glacial melt can proceed and is calculated as in Equations 6.14 to 6.16. This approach is unique to the present work, and an attempt to implement a flexible solution to the complexities introduced by glacial debris cover.

Equation 6.14:

$$ddf_{ice}\ [mm\ °C^{-1}\ day^{-1}] = ddf_{ice.intercept} + (Z_{b(i)} * ddf_{ice.slope})$$

Equation 6.15:

$$IWE.melt_{b(i)}\ [mm] \begin{cases} \{ where\ (IWE.updated_{b(i)} * Tair_{b(i)}) > 0.0 \} \\ = min(IWE.updated_{b(i)}, [\ Tair_{b(i)} * ddf_{ice}\ ]) \\ \{ where\ (IWE.updated_{b(i)} * Tair_{b(i)}) \leq 0.0 \} \\ = 0.0 \end{cases}$$

Equation 6.16:

$$IWE.postmelt_{b(i)}\ [mm] = IWE.updated_{b(i)} - IWE.melt_{b(i)}$$

As can be seen in Equations 6.14 and 6.15 above, a marginally more sophisticated approach was taken to the degree-day melt calculations for ice than for snow. To our knowledge this innovation represents an original contribution by the thesis. For simulations with a strong glacial component, it became clear during model calibration that unless a method of differentiation between melt from glacial tongues/snouts and melt from primary ice fields was implemented then many, if not most, glaciers would experience simulated rapid retreat in the model. The necessity of this added element of sophistication is further corroborated by the finding that debris cover has been shown to suppress melting, especially at low elevations (e.g. Hewitt, 1989).

The reasoning behind the use of an elevation-dependent degree-day factor in part derived from the fact that debris transport to cover glaciated surfaces is largely a gravitationally driven process. As such, it is logical that debris cover is likely to be thicker at lower elevations. Furthermore the finding by Mihalcea *et al*. (2006) that melt suppression by debris cover (above a minimum depth) appears proportional debris depth, can be restated as: 'cleaner' ice will melt more readily in the present of equal amounts of available energy.

This has been quantified in the short record (2001 to 2003) study by Immerzeel *et al*. (2012) on glaciers in the Hunza catchment which used very different ice degree-day melt factors for debris covered (3.0 mm $°C^{-1}$ day^{-1}) and clean-ice glaciers (6.0 mm

$°C^{-1}$ day^{-1}). These findings by previous studies suggested a potential way forward. Although the present work preferred to avoid constraining the model in terms of glacial location or characteristics – in order to allow for "spontaneous" glacier emergence and disappearance when using multi-century synthetic climate forcings – it was hypothesised that, while debris cover over glaciated surfaces would be spatially heterogeneous and governed by a range of factors, at the tributary basin scale debris-cover would correlate negatively with elevation. In other words, glaciated surfaces at lower elevations would be more likely to have thicker debris cover while glaciated surfaces at higher elevations would be more likely to have minimal or no debris cover. Put more simply: 'cleaner' ice would be more prevalent at higher elevations.

This hypothesis provided a rationale for an ice degree-day melt factor that varied with elevation. Specifically, because the debris cover was expected to act as a net insulator (melt inhibitor), the justification existed for an ice degree-day melt factor that increased with elevation. For the time being the simplest linear characterisation was chosen as can be seen in Equation 6.14. In fact, although the capacity to specify an intercept for the linear equation of degree-day was included, for the simulations to date this value has been left at zero.

To be clear this project has no specific data in hand regarding the relationship between debris cover and elevation in the UIB catchments modelled to date. The reasoning above simply appeared coherent in terms of general principles and was convenient in that its implementation appeared to render more coherent and credible simulated patterns of glacial mass and extent variation during calibration runs.

There are a number of reasons that this logic has not been extended to the snow degree-day melt factor – the short 'lifespan' of seasonal snow renders substantial debris accumulation less likely, the net effects of thin debris cover, i.e. albedo-enhanced melting versus insulation-inhibited melting, are not clear – but the primary reason for not implementing a similar linear approach was to preserve simplicity – constant value across the elevation range – given that calibration results did not appear to require added complexity to yield adequate results. The calibrated values of degree-day melt factor components are given in Table 6.4.

Melt calibration parameter	Astore (nival catchment)	Hunza (glacial catchment)
	5km (0.05dd) & 10km (0.10dd)	5km (0.05dd) & 10km (0.10dd)
Snowmelt degree-day factor [mm °C^{-1} day^{-1}]	5.6	6.4
Ice melt degree day intercept $ddf_{ice.intercept}$ [mm °C^{-1} day^{-1}]	0.0	0.0
Ice melt degree day slope [mm °C^{-1} day^{-1} (m asl)$^{-1}$]	0.00220	0.00095

Table 6.4 Calibrated values for components of degree-day melt factors for snow and ice as determined for Astore and Hunza catchments.

6.9.6 Post-melt updating of SCA and remaining land surface processes

With the meltwater components, i.e. SWE.melt and IWE.melt, of soil surface inputs to hydrological processes determined, the model proceeds to update the SCA state and calculate the remaining land surface process descriptors. The SCA update calculations use the same threshold value for standing snowpack, but test the snowpack against the final (post-melt) SWE measure.

Prior to proceeding to the soil moisture accounting module, it is necessary to calculate the potential evaporation (PET) loss from inflow to the soil surface. As explained in section 6.4, the Priestley-Taylor method (Stewart and Rouse, 1976) is used. The equations are detailed in Appendix D.

6.9.7 Glacial vertical mass redistribution and volume and areal change calculations

Another key element needed in a model for simulation of glacial mass trajectories is the gravity-driven redistribution of glacial mass from high-elevation accumulation zones to lower ablation zones. As described in the opening sections of this Chapter, the equations used to calculate glacial movement in VICwCDiP are derived from applications of Glenn's Flow law. These applications were developed by Naz (2011) and Kessler *et al*. (2005) based on earlier fundamental work by Paterson (1994). Using the methodology developed by these studies, two separate, additive components of glacial displacement – deformation and basal sliding – are calculated individually, but both formulated in terms of gravitational driving stress, designated "τ". Equation 6.17 gives the formulation employed in within VICwCDiP to calculate τ.

Equation 6.17:

$\tau\ [Pa] = \rho_{ice} * g * height.ice_{b(i)} * sin(\alpha_{b(i)})$

where: g = 9.81 [m s^{-2}]; ρ_{ice} = 917.0 [kg m^{-3}]

Once the gravitational driving stress has been calculated, the deformation (U_d) and basal sliding (U_s) components of glacial motion can be calculated. The formulations used are shown in Equations 6.18 and 6.19.

Equation 6.18:

$U_d\ [m\ day^{-1}] = 0.4 * A_{Glenn} * height.ice_{b(i)} * (\tau^{3.0})$

where: A_{Glenn} (Glenn's flow law coefficient) = 5.875e-19 [day^{-1} Pa^{-3}]

Equation 6.19:

$$U_s\ [m\ day^{-1}] = typical.slide * e^{[1-\left(\frac{100000.0}{\tau}\right)]}$$

The typical sliding velocity (typical.slide) used in Equation 6.19 could be treated as a calibration parameter in order to tune the vertical redistribution of glacial mass. Here, however, the reference values for each of the two modelled catchments – 0.117 [m day^{-1}] or 42.7 [m $year^{-1}$] (from Shroder *et al.*, 2000) for Astore and 0.230 [m day^{-1}] or 84.0 [m $year^{-1}$] (from Mayer *et al.*, 2010) for Hunza–have been maintained.

As explained by Kessler *et al.* (2006), the total modelled displacement along the axis of glacial travel is the sum of the two displacement components as shown in Equation 6.20

Equation 6.20:

$U_{total}\ [m\ day^{-1}] = U_d + U_s$

In terms of VIC specific implementations, Naz (2011) clarified that the volume of ice transferred from one band to the next lower band is the product of the total displacement times at the glacial face (cross-section). The glacial face is the product of the glacial thickness and the glacial width. The present work contributes incrementally to the definition of the modelled glacial geometry by considering the glacial width as the product of the grid cell width and the ratio of the glaciated fraction within the band to the total cell fraction of the band. These spatial relationships are illustrated conceptually in Figures 6.06 and 6.07 (section 6.6.1). Equations showing the detailed calculation method for mass redistribution are shown in Appendix D.

Once the absolute (modelled) potential volume of ice to be transferred has been calculated, this volume can be confirmed in terms of the fraction of total ice in the band being transferred and the equivalent IWE depth to be removed. This value in IWE depth is then converted into the equivalent IWE depth to be added to the adjacent (downslope) elevation band by multiplying the upslope removed IWE by the ratio of the upslope band cell fraction by the downslope band cell fraction. The equations, which represent

an original interpretation and refinement of the method developed by Naz (2011), used in this procedure are also given in Appendix D. Once the amount of ice being transferred into and out of each band are calculated, it is possible to determine the net IWE change due to ice movement. Given that glacial melt has previously been subtracted from the IWE stock, it is also possible at this point to calculate the final IWE value for the band during the time-step.

Variability of glaciated area was one of a limited number of methodological options where a different approach from the VIC glacier module developed by Naz (2011) was adopted. The decision to render glaciated area variable in the raster degree day model was motivated both by the drive to integrate the capabilities available in few (if any) comparable models and by the potential advantages in terms of assessing catchment-scale glacial mass balance trajectories. By enabling both areal reduction and expansion of glaciated surfaces within VICwCDiP, the potential divergences in contrasting future climate scenarios can be more fully explored. This is critical given the potentially conflicting signs and magnitudes of change between future scenarios as presented in Chapter 5.

The method adopted here to enable areal change in glaciated area was constrained by the constraint of constant glacier length within elevation bands imposed by the conceptual model approach to mass transfer between elevation bands. This limitation requires that any areal change be in terms of lateral expansion or contraction. The amount of lateral change is quantified by use of a consistent cross-section aspect ratio in terms of vertical and lateral change. The calculated volume change is initially distributed between vertical and lateral change by assigning relative change in width as the cube root of the relative change volume and relative change in height as the square of the relative change in width. Hence the product of relative change in width and relative change in height is equal to the relative change in volume as shown in Appendix D.

The potential dimensional changes, however, can only be validated if there is adequate space within the elevation band for any calculated increase in width (area). If the calculated lateral expansion would result in a glacier fraction larger than the cell fraction available in the elevation band, then the updated glacier fraction is set at equal to the band fraction – and glacier width at equal to the cell width – while the remaining relative volumetric change is redistributed as an increase in glacier height. If, however, the potential glaciated area for the band at the end of the time-step is less than the

available band cell fraction, then the equations to update the glacial dimensions are simply validations of the initially calculated potential changes.

This concludes the description of the new "cryosphere dynamics" module of the VICwCDiP model which was developed to enable improved physically-oriented hydrological modelling of nival and glacial hydrological regime catchments.

6.9.8 Aggregation of band specific quantities to grid cell means

The changes in glacial mass and volume are the final element in the elevation band-specific calculations. The atmospheric, land surface and cryosphere quantities calculated in the preceding subroutines are next averaged across the cell according to the areal weights of the individual elevation bands. Once the average cell values have been calculated for each cell, the model enters the hydrological partitioning routines. This is the component of the model that directly reproduces the VIC methodology, specifically its runoff generation module, but recoded in Python.

6.10 Simulation Phase III: Soil moisture accounting module

The hydrological module in VICwCDiP is intended to be a direct implementation of the standard VIC model (Lohmann *et al.*, 1998, Gao *et al.*, 2009). The conceptual operation of hydrological partitioning for an individual grid cell is shown in Figure 6.11 which is adapted from "Figure 1" of Cherkauer *et al.* (2003).

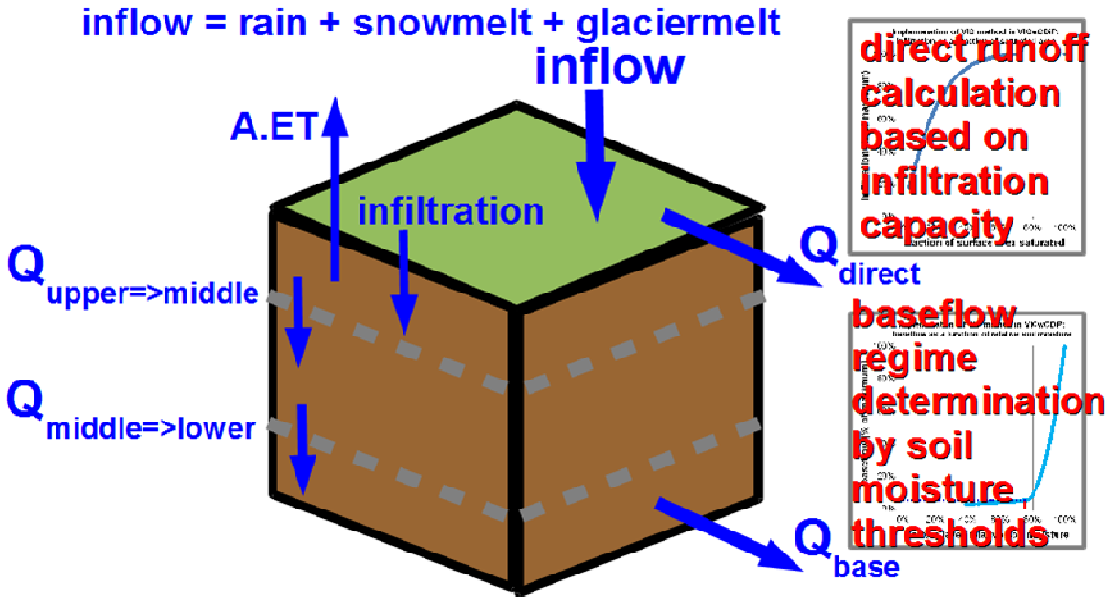

Figure 6.11 Conceptual schematic of soil moisture accounting module of Variable Infiltration Capacity with Cryosphere Dynamics in Python (VICwCDiP) model. This figure based on Figure 1 of Cherkauer *et al.* (2003). nb: Full-size versions of the figures for the infiltration capacity and baseflow curves can be found respectively in Figures D.05 and D.06 (Appendix D).

As can be surmised from Figure 6.11, the soil moisture accounting procedure using standard VIC methodology can be sub-divided into a number of steps:

1) Determination of potential mass fluxes at the surface: this includes an "upward" flux in the form of actual evapotranspiration (AET), a downward flux in the form of infiltration from the surface into the soil system and a lateral flux in the form of direct runoff (Q_{direct}).

2) Calculation of gravity drainage and water storage between discretised modelled soil layers.

3) Calculation of lateral flux in the form of baseflow (Qbase) from the lowest layer of the soil system out to the (theoretical) channel network.

Details on the implementation (formulation) of this VIC methodology in VICwCDiP can be found in Appendix D.

6.11 Model Calibration and validation

6.11.1 Assessment of calibration and validation using standard performance metrics

The model described in this Chapter is clearly ambitious in the range and complexity of physical processes – cryosphere, land surface and hydrological – which it attempts to simulate. This ambition is particularly striking given the scarcity of data available to characterise the sub-catchment scale spatial heterogeneity. Obviously considerable time and computational resources could be devoted to testing parameter sensitivities and increasing the complexity of multiple model subcomponents.

To assess the model performance in simulation of physical processes a split-sample calibration and validation approach was adopted using all of the available flow data for the Astore and Hunza catchments respectively. For Astore, 1974-1995 was used for calibration and 1995-2008 for validation; for Hunza, 1966-1991 was used for calibration and 1991-2004 for validation. At the present iteration of development the model was calibrated manually, with incremental adjustments to key parameters made using the engineering judgement of the the author. The model skill was assessed with a number of traditional metrics such as the monthly Nash-Sutcliffe coefficient, the relative error in annual volumes (the mass balance error), the Root Mean Squared Error (RMSE) in annual volumes and annual coefficient of variation (CV) of annual volumes, and also the Pearson's correlation at the monthly and annual levels. These results are detailed in Table 6.5.

Model and spatial resolution		Simulation type	**Monthly variant of Nash-Sutcliffe R^2**	Relative error in annual volumes	RMSE annual volumes (absolute)	CV (RMSE) annual volumes	Pearson's correlation, monthly, normalised & standardised
Astore	5 km	calibration	**0.801**	0.118	168.8mm	0.149	0.512***
		validation	**0.672**	0.213	276.6mm	0.242	0.268***
	10 km	calibration	**0.775**	0.126	182.9mm	0.162	0.472***
		validation	**0.632**	0.233	297.5mm	0.260	0.252***
Hunza	5 km	calibration	**0.862**	0.169	186.8mm	0.235	0.274***
		validation	**0.648**	0.333	254.2mm	0.382	0.133
	10 km	calibration	**0.864**	0.171	186.4mm	0.234	0.273***
		validation	**0.606**	0.347	269.7mm	0.405	0.152

** => significant at 95.0% (p < 0.05) under 2-tailed T-test.*

*** => significant at 99.0% (p < 0.01) under 2-tailed T-test.*

**** => significant at 99.9% (p < 0.001) under 2-tailed T-test.*

Table 6.5 Hydrological model performance metrics (quantitative relationships between simulated and observed runoff). "Relative error in annual volumes" is the mean absolute annual error normalised by the period mean annual total volume. "CV (RMSE)" is the RMSE of annual volumes normalised by the period mean annual total volume.

Table 6.5 gives a range of metrics of model performance from which a number of general patterns emerge.

- For the grid spacings tested, 5km versus 10km, model spatial resolution has relatively little influence on model skill. This is demonstrated in quantitative terms by the scores for the variety of metrics tested here which differ between resolutions by only a few percent of relative performance.
- With the exception of the Nash-Sutcliffe scores and (absolute) RMSE, a synthesis of the collection of metrics evaluated ("Relative annual error", CV(RMSE) and Pearson's monthly correlation) suggests model performance is better for the nival regime catchment (Astore) than for the glacial regime catchment (Hunza). This may be due to relative model accuracy in simulating snowmelt compared with glacial mass balance (accumulation and ablation) accuracy. Limited performance in simulation of glacial processes could be due to a number of factors, including challenges in fully and accurately simulating the vertical transfer of snow and ice mass within glacial tributary areas and/or the need to provide greater sophistication in techniques for spatially assessing available melt energy (e.g. incorporation of aspect/hillshade or persistent cloud cover).
- Values for the Nash-Sutcliffe efficiency (R^2) calculated on a monthly time-step for the calibration runs are reasonable though not exceptional compared to those

expected generally for rainfall-runoff hydrological model calibration and validation. Given the challenges involved in simulating the complex processes (snowpack transformation to glacial firn, vertical transport of ice between elevation bands by basal sliding) the level of performance attained is considered acceptable for the "proof of concept" level initiative this work represents. This methodology was also used by previously published studies (e.g. Akhtar *et al*., 2008, Tahir *et al*., 2011) whose N.S. R^2 scores are comparable to those shown in Table 6.5.

- For the validation period the relative error in annual runoff volumes is moderate for the snowmelt catchment but poor for the glacial catchment. The same is true for RMSE and CV(RMSE). Pearson's linear correlation between normalised, standardised anomalies at the monthly time-step is somewhat better.
- Scores for all metrics tested here are substantially poorer for validation runs than for calibration runs, especially for the glacial Hunza catchment. Some fluctuation in performance metrics between calibration and validation runs is inevitable. Decreases in model skill scores might even be considered likely in simulations requiring tuning ("over calibration") for a substantial set of model parameters. The glacial dynamics components of VICwCDiP certainly fit this profile of a complex, highly tuned model. Even so the decreases in all metrics, bear further consideration.

A common thread that emerges from the points above is related to the performance of VICwCDiP in short-term simulations, especially requiring detailed modelling of glacial conditions. This is thought to be caused by two separate aspects of the VICwCDiP modelling approach as implemented in this study.

The first element involves the simulated vertical gradients in glacial ice melt and replenishment through mass transport. In the present VICwCDiP configuration, the rate of ablation in lower elevation glacial tongues far exceeds the combined replenishment through local accumulation and vertical transport from higher elevation bands. As a result, over even a brief simulation of a decade or more, glacial tongues are simulated to retreat to the point of disappearance leaving only high-elevation ice fields as active glaciated areas. This is linked to the energy assessment issue noted in the performance assessment summary above. For this reason it was decided to implement a "model spin-up" period of a decade by duplicating the initial decade of meteorological inputs prior to extracting the model outputs for calibration and validation. This "spin-up" period allows the model to reach general dynamic mass balance equilibrium (as opposed to a transient

condition dictated by initial conditions). The issue of vertical gradients in glacial mass balance will be considered in greater detail in section 6.13.

The second potential cause of the poorer performance in validation than calibration runs is the choice of validation time period as well as the selected method for meteorological input. As described in section 6.3, the present method for meteorological inputs uses a master record from a "base station" from which values for climate inputs are assigned to each elevation band in individual grids cell purely as a function of elevation. The ability of individual meteorological stations to act as representative quantitative indicators of broader catchment conditions in the UIB for historical records from the last for decades of the 20th century has been demonstrated by Archer (2003) and Archer and Fowler (2008). More recent work by Forsythe *et al*. (2012) confirmed these findings by extending the work of Archer and Fowler (2008) into the mid-2000s and comparing the indicator performance of local observing stations to spatial indices from remote sensing data products.

Despite this, the poor performance of the validation runs, specifically discrepancies in the final years simulated (late 1990s, early 2000s), might be in part due to a weakening in the stability of the relationship between temperature inputs and runoff in recent years. The deterioration of model performance with progression through the modelled period despite unchanged methodology could support a hypothesis that the (point-based) air temperature measurements made in valley meteorological stations are becoming less spatially representative of catchment scale conditions. An alternative hypothesis, focusing on local hydrological rather than meteorological observations, is that the error structure within the river gauging data may have begun to change (perhaps due to a lack of velocity profiling necessary for updating/maintenance of stage-discharge curves/formulas).

6.11.2 Graphical presentation of calibration and validation metrics

Figures 6.12 and 6.13 (respectively for the Astore & Hunza catchments) show the observed flows from WAPDA against the VICwCDiP simulated flows for the calibration and validation periods for the two different model resolutions, using 5km and 10km grid cells. These figures provide visual confirmation that for a given catchment the model performance was similar at 5 and 10 km resolutions, as indicated by the calibration and validation metric scores reported in Table 6.5. Given this close resemblance, for the remainder of the Chapter only results from the 10km versions of

the catchment models will be shown. Results of the 5km models in comparison to the 10km models are provided in Appendix D.

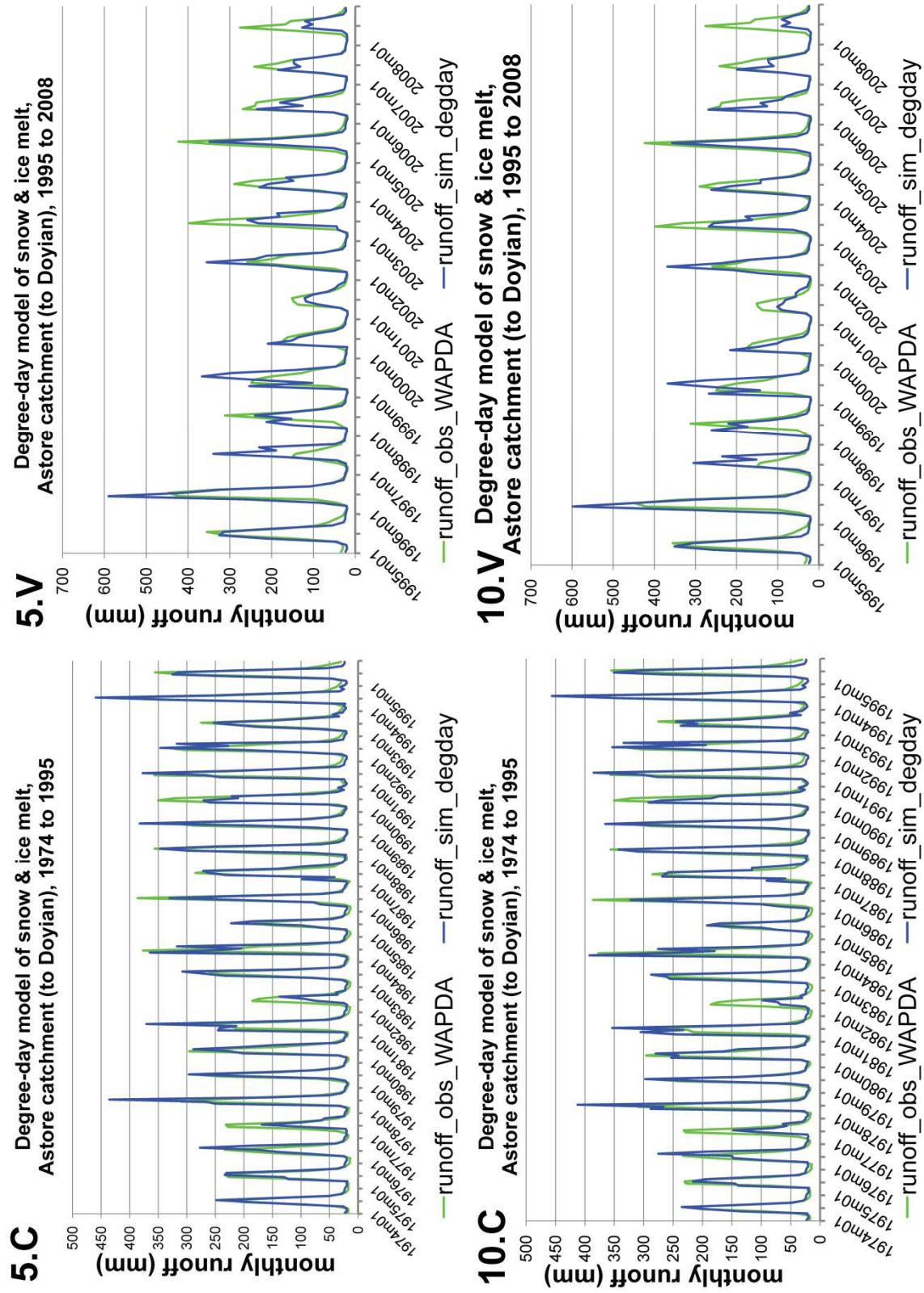

Figure 6.12 Calibration and validation results for the Astore catchment. In this figure observations are labelled "runoff_obs_WAPDA", while simulation results from VICwCDiP are labelled as "runoff_sim_degday". The panels are labelled with reference to model resolution and simulation type as follows: 5.C = 5km calibration; 5.V = 5km validation; 10.C = 10km calibration; and 10.V = 10km validation.

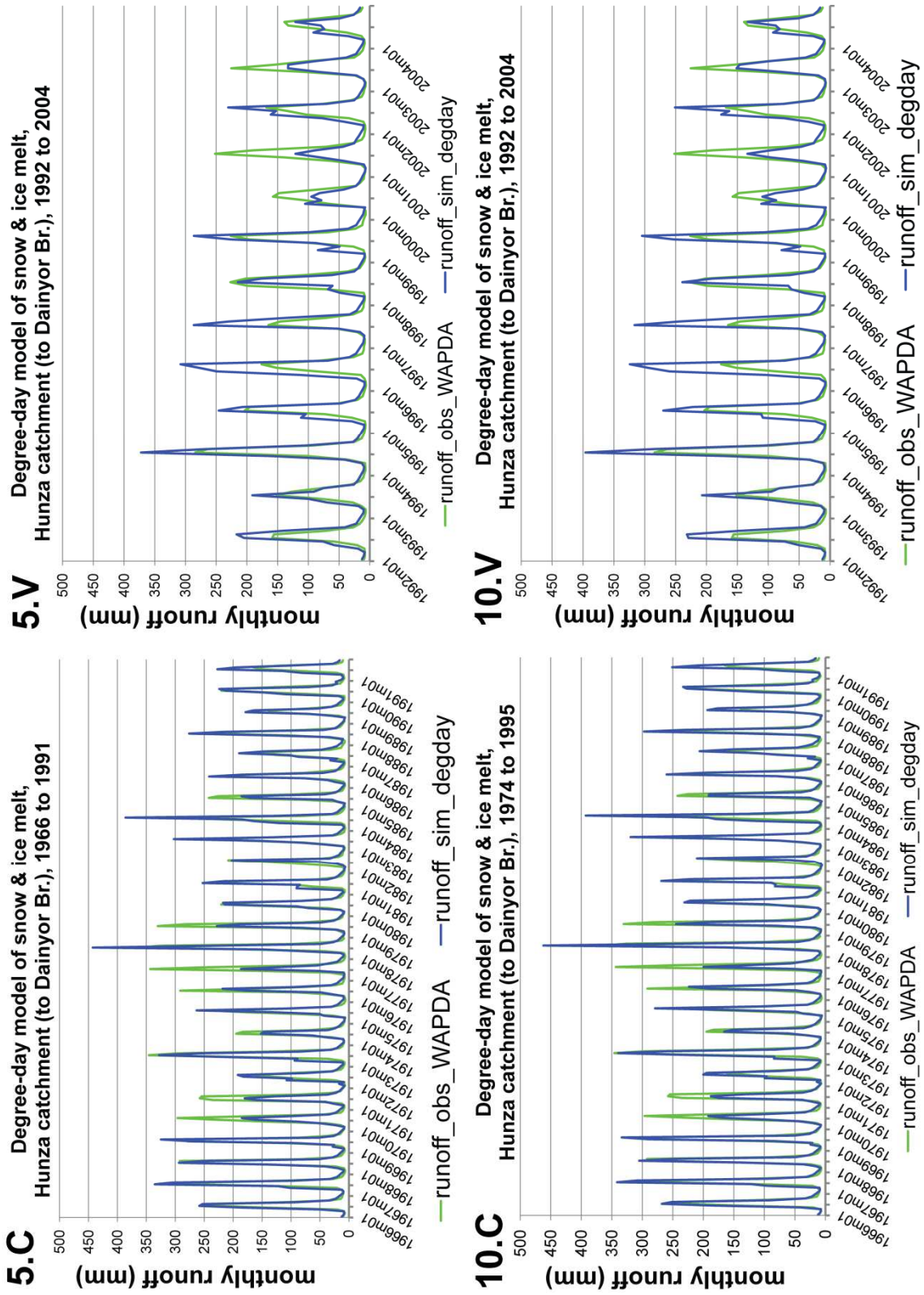

Figure 6.13 Calibration and validation results for the Hunza catchment. Same notation as Figure 6.12.

Figures 6.12 and 6.13 illustrate the consistent performance of the VICwCDiP model in matching the annual hydrological cycles for both catchments as well as the reasonable skill in simulating observed patterns of interannual variability. Further enhancements to VICwCDiP, however, are desirable to improve model skill in

matching specific interannual variations in flow volumes. The scope for improvements in this domain can particularly be seen in the panels for validation period (5.V and 10.V) of Figures 6.12 and 6.13. This performance shortfall was quantified in Table 6.5. Enhancements which could help to remedy these shortcomings could include either refining model inputs or improving process realism.

Figure 6.14 presents the annual hydrological cycle as a measure of the range of interannual variability for each respective time period. The model is clearly capable of replicating the annual cycles of runoff as well as the range of interannual variability – quantified by 10th (c10) and 90th (c90) percentiles – for both the nival (Astore) and glacial (Hunza) test catchments, although the mean model response produces a slight lag at the start of the melt season (rise of runoff) in spring for both catchments and a slight delay at the end of the melt season (fall of runoff) in comparison to observations. Figure 6.14 also shows that the validation for the both catchments is relatively poor – with Astore showing a moderate “dry bias” during the peak summer months and Hunza showing substantial “wet bias” throughout the melt runoff season – in comparison to the results for the model calibration period.

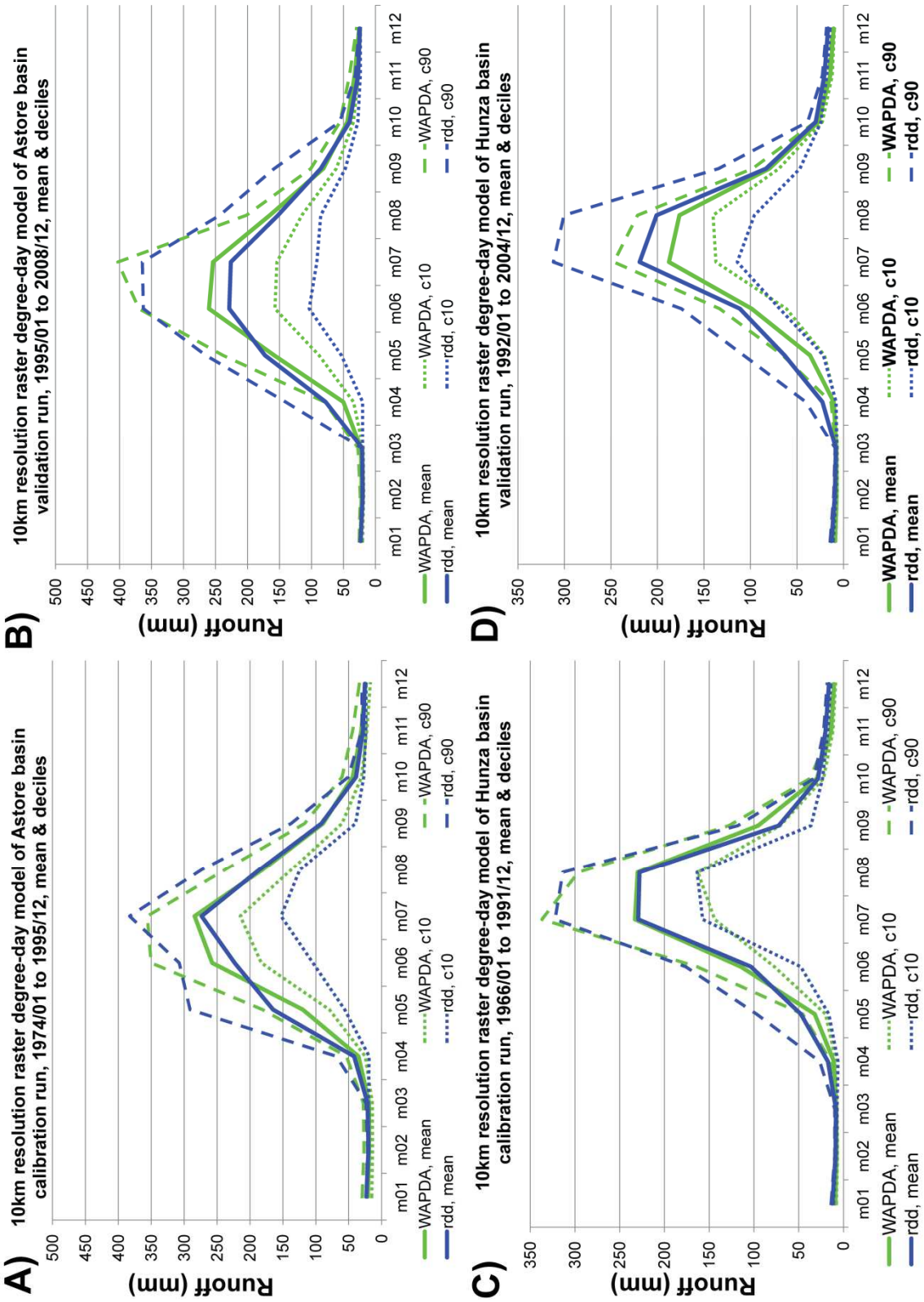

Figure 6.14 Calibration and validation results in reproducing annual hydrological cycle and its variability for the Astore and Hunza catchments. Observations are labelled "WAPDA", while simulation results from VICwCDiP are labelled as "rdd". Months are labelled "m01" (January) to "m12" (December). The panels show as follows: A) Astore calibration; B) Astore validation; C) Hunza calibration; and D) Hunza validation. The panels show mean runoff and 10th and 90th percentiles for monthly flows over the calibration or validation periods respectively.

Figure 6.15 shows the evolution of spatially aggregated glacial mass, as IWE, and areal extent, as a fraction of the catchment area, for the Astore (panels a & b) and

Hunza (panels c & d) catchments during the calibration (panels a & c) and validation periods (panels b & d). Figure 6.15 illustrates the capability of VICwCDiP to simulate variable glacial area as well as mass.

It is important to remember in comparing the panels within Figure 6.15 that the calibration and validation periods used for the Astore and Hunza catchments are different. These differences were driven by the respective availabilities of WAPDA discharge data against which to compare simulated runoff. In effect, the mass balance trajectories are quite similar between the two catchments when common periods are compared. In both catchments simulation results indicate that the 1970s were a period of stable catchment glacial mass. Simulated mass increases were small to negligible in the early 1980s but then accelerated from roughly 1988 and continued until 2000. Simulated mass balance in both catchments is then nearly neutral for the initial years of this century (2001 to 2004). These simulated increasing glacial mass trajectories are coherent with findings reported from both field-based studies (Hewitt, 2005; Hewitt 2011) and remote sensing-driven analyses (e.g. Gardelle *et al.*, 2012; Jacob *et al.*, 2012b).

The simulation of variable glacial extent was one of the more "experimental" model features implemented within VICwCDiP. Given the objective of implementing "conservation of mass" in modelling of glacial meltwater contribution to runoff in UIB catchments, including vertical mass redistribution via basal sliding, it was deemed logical to simulate potential changes in glacial area as well as volume (mass) rather than the latter alone. Details of the formulation of coupled variability in mass and area are presented in Appendix D. In summary, however, it was decided to use a simple geometric relationship to relate areal changes to volumetric changes: changes in glacial area are considered to be the square root of changes in the thickness. Thus the total volumetric change is the product of the area change multiplied by the change in thickness. Constraints are of course imposed to respect the limitations of absolute elevation band surface area.

The results seen in Figure 6.15 of simulated fluctuations in glacial extent appear to indicate much greater relative variability in Astore than Hunza. Caution is prudent, however, with regards to this tentative result. It is expected that the apparent variability in Astore glacial extent is linked to its much smaller overall glaciated area and the greater relative contribution of each glaciated fraction of individual elevation bands in individual grid cells. Another factor in the apparent variability in Astore glacial extent is

likely the relatively lower centroid, in terms of elevation, of overall glacial extent. As explained previously with regards to the imposed model “spin-up” period, in the present version of VICwCDiP simulated glacial tongues at lower elevations melt extremely rapidly indicating a model bias the vertical gradient of melt energy versus mass replenishment. As a result glacial fractions at lower elevations in the calibration and validation simulations may show exaggerated sensitivity to climate variability (meteorological forcing). This current model characteristic also means that apparent stability (near stationarity) in the (spatially aggregated) catchment mean values may mask may mask vertical redistribution of simulated glacial mass and area within the modelled catchments. This issue will be addressed further in section 6.13.

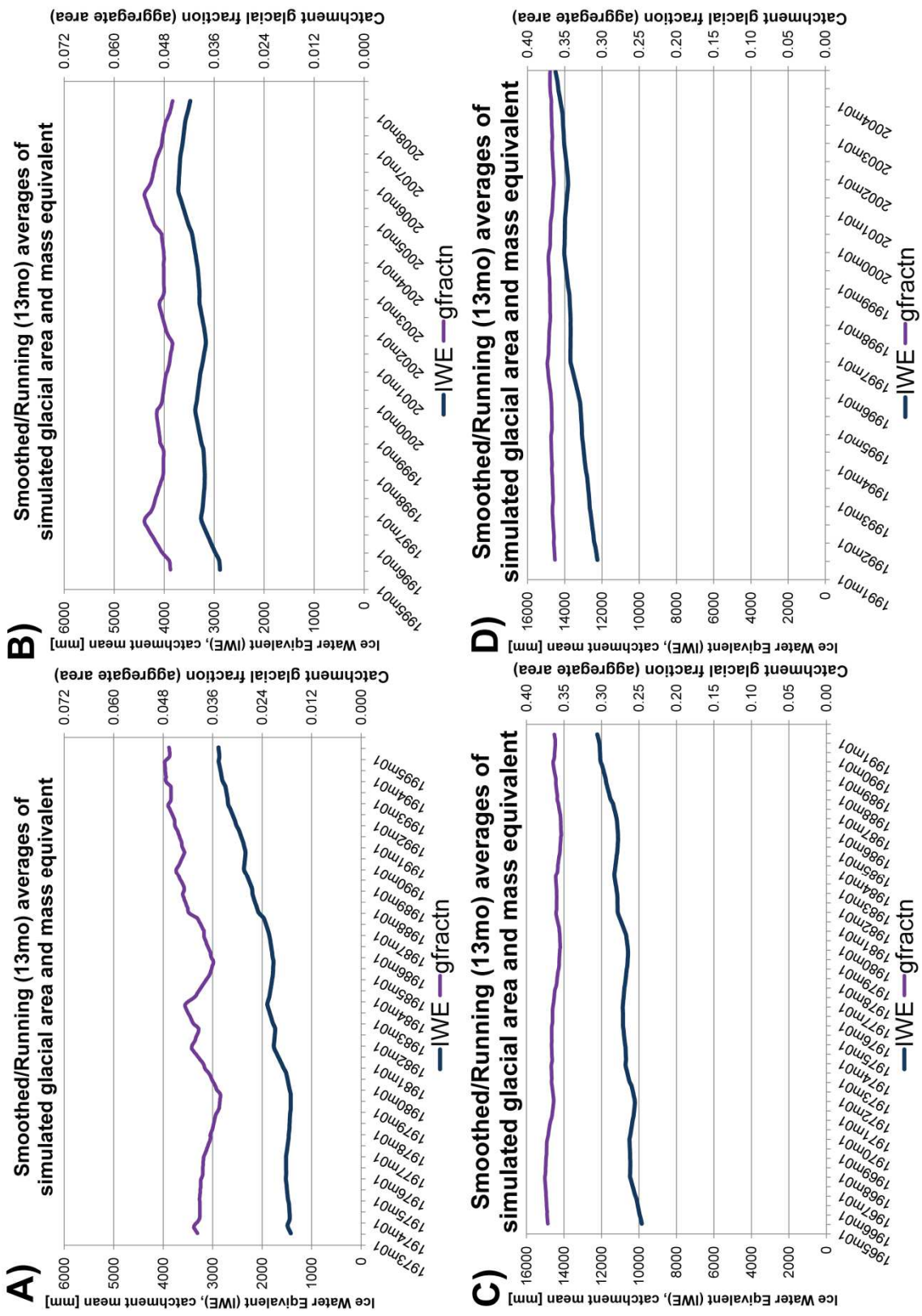

Figure 6.15 Calibration and validation results in glacial mass and areal extent (fraction of catchment) for the Astore and Hunza catchments. In the graphs in this figure, glacial mass is shown as "ice water equivalent" (IWE) and glacial areal extent is labelled "gfractn.". The panels show as follows:A) Astore calibration; B) Astore validation; C) Hunza calibration; and D) Hunza validation.

6.11.3 Assessment of simulated mass fluxes and land surface states

Further confirmation of the limited differences between the results from VICwCDiP at differing spatial resolutions for a given catchment can be found in the mean annual totals of mass fluxes for the calibration and validation runs as shown in Table 6.6. It is important to note that models at different resolutions were manually calibrated using identical values for key calibration parameters including (as presented previously) orographic gradients and melt degree day factors for snow and ice. Furthermore, because meteorological inputs were extrapolated solely on an elevation basis (no horizontal heterogeneity), differences in the model are expected to result only from small differences in spatial aggregation of surface areas at the sub-grid level as well as from the grouping of multiple small glaciers into single grid cells (10km resolution) or the isolation/dissection of physically continuous ices masses between adjacent grid cells (5km resolution). Minor discrepancies between the spatial resolutions for a given catchment and time period might be due to artefacts in the model construction process depending on how well the mean band elevations at the sub-grid level represent conditions on their glaciated fractions. This would be expected to be more likely with relatively coarse grid spacing where larger elevation bands containing small glacial fractions might apply slightly skewed temperature and or precipitation since these are distributed as a function of elevation (of each band as a whole rather than its glaciated fraction alone) in the present VICwCDiP methodology.

Model and spatial resolution		Simulation type	Simulated runoff (baseflow + direct) (mm)	Simulated evaporation (mm)	Snow melt (mm)	Ice melt (mm)	Glacial ice accumulation (mm)	Net glacial mass balance (not localised) (mm)
Astore	5 km	calibration	1177.7	244.3	904.3	134.9	241.1	+106.2
		validation	1118.6	246.1	845.1	136.4	199.3	+62.9
	10 km	calibration	1171.2	282.5	915.2	105.9	179.2	+73.3
		validation	1100.6	285.9	854.2	108.8	147.1	+38.3
Hunza	5 km	calibration	773.0	212.7	650.8	155.9	279.9	+124.0
		validation	768.3	214.9	665.4	109.7	338.2	+228.5
	10 km	calibration	782.0	233.8	665.8	180.5	278.7	+98.2
		validation	802.2	238.8	680.3	161.1	336.4	+175.3

Table 6.6 Annual total mass fluxes for key hydrological inputs and model outputs for the VICwCDiP model calibration and validation runs.

Figure 6.16 shows the annual cycles which sum to the mean annual total mass fluxes presented in Table 6.6. These figures clearly indicate the contrasting seasonalities between precipitation and hydrology (baseflow, direct runoff), with most total runoff occurring during the summer months and most precipitation occurring in winter and

spring months. The timing of the total runoff, like evapotranspiration, is conditioned by the annual cycle of available melt energy – indexed in the present model by air temperature, but in reality also dependent on radiative fluxes. Nival catchments, such as Astore, are differentiated from glacial catchments, such as Hunza where melt magnitude is constrained primarily by energy inputs, as they are governed by mass inputs, i.e. annual precipitation. Given the greater relative variability in precipitation than air temperature, the difference in hydrological regime helps to explain why there are greater differences between the calibration and validation results in terms of magnitude and timing of baseflow and direct runoff in the Astore catchment (Figure 6.16, panels a & b) than the Hunza catchment (Figure 6.16, panels c & d).

In contrast, and as is expected in a glacial regime catchment, the Hunza catchment exhibits less change in direct runoff seasonality between the two simulated time periods (calibration and validation). This is because large influxes to the soil surface in UIB catchments will be dominated by meltwater from snow and ice, and thus for the marginally higher elevation Hunza these events will tend to be concentrated in the peak summer months, whereas the Astore catchment can occasionally experience large spring melt events. The fidelity of the VICwCDiP model in reproducing these expected hydrological regime behaviours is a further encouraging sign of its current performance.

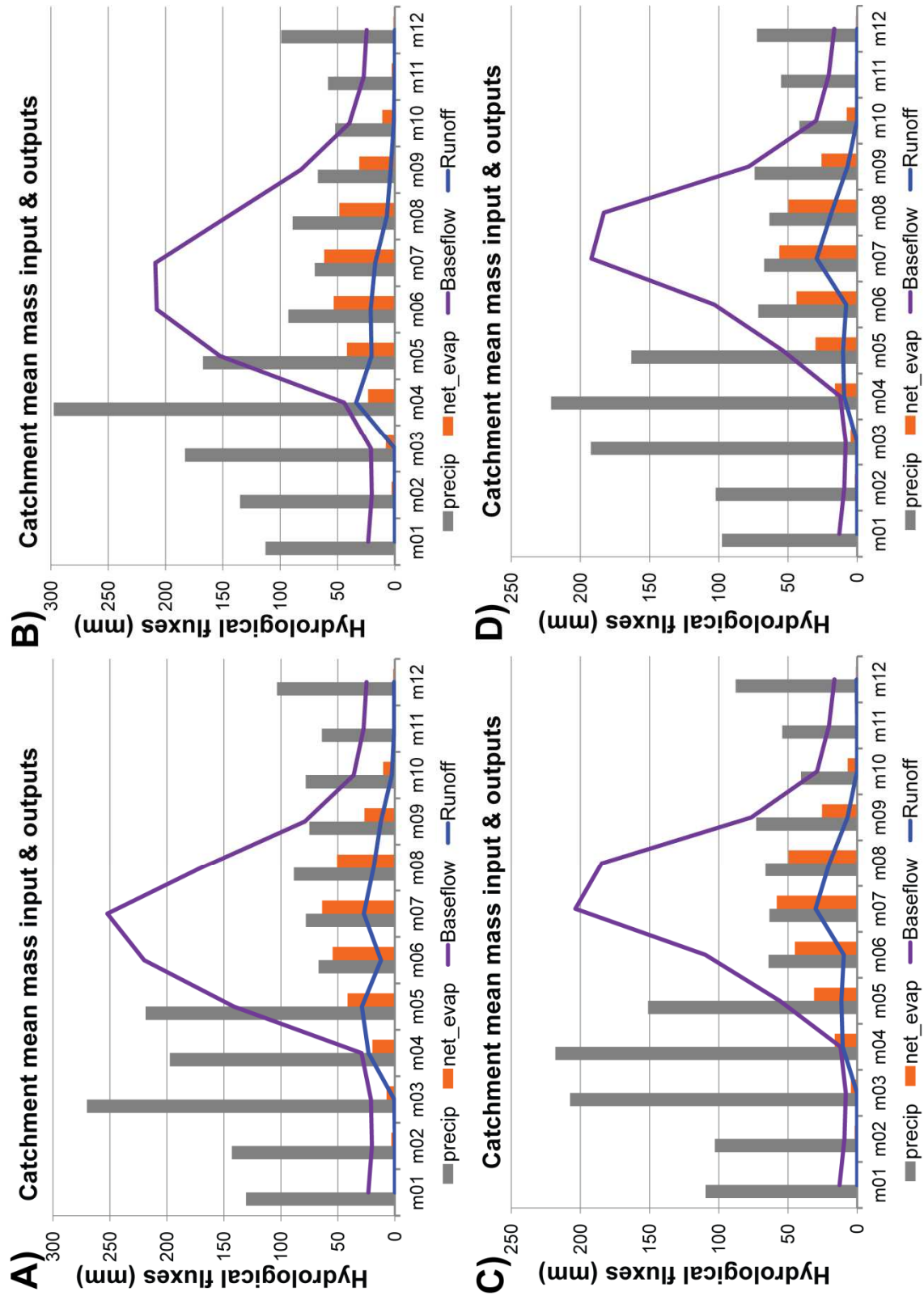

Figure 6.16 Calibration and validation results for hydrological mass inputs and outputs for the Astore and Hunza catchments. In the legends precipitation is abbreviated as "precip." AET is referred to as "net_evap." Baseflow refers to Qbase (base streamflow), and Runoff refers to Qdirect (overland runoff). Months are labelled "m01" (January) to "m12" (December). The panels show as follows: A) Astore calibration; B) Astore validation; C) Hunza calibration; and D) Hunza validation.

Another interesting element that can be seen in Figure 6.16 is that on a period mean basis for both Astore and Hunza (Summer) melt season precipitation inputs are

only equal to or slightly larger than simulated net (actual) evapotranspiration (AET). Thus UIB summer rainfall is only sufficient to compensate for AET rather than contribute substantially to concurrent total runoff (baseflow and direct runoff). This dependence of both the nival and glacial regime catchments on the annual temperature cycle to drive melting of accumulated solid precipitation, be it seasonal snowpack or glacial ice, is further evidence of the coherence and realism of the model formulation.

As described in the preceding sections, in addition to the core hydrological outputs, the VICwCDiP model also calculates the grid cell land surface states of SCA and LST at the sub-grid (elevation band) level. While these calculations are required as intermediate steps in estimating both net shortwave and longwave radiative fluxes, values required for the Priestley-Taylor method, SCA and LST are value outputs in their own right. This value is due to their utility as additional means by which to calibrate and validate hydrological models, such as VICwCDiP, which simulate land surface processes (Pelicciotti *et al*., 2012). In particular, the timing and magnitude of the annual SCA cycle were key elements in tuning both the orographic precipitation gradients and "degree-day melt factors" in model calibration. The results of simulated (catchment spatial average) period means for SCA and LST for the 10km model are compared to the MODIS relevant climatologies in Figure 6.17. While the timeframes for the available MODIS record do not correspond entirely to the historical time periods simulated, they overlap the validation period (Figure 6.17). The full results for the combination of spatial resolutions and time periods for both the Astore and Hunza catchments can be found in Appendix D.

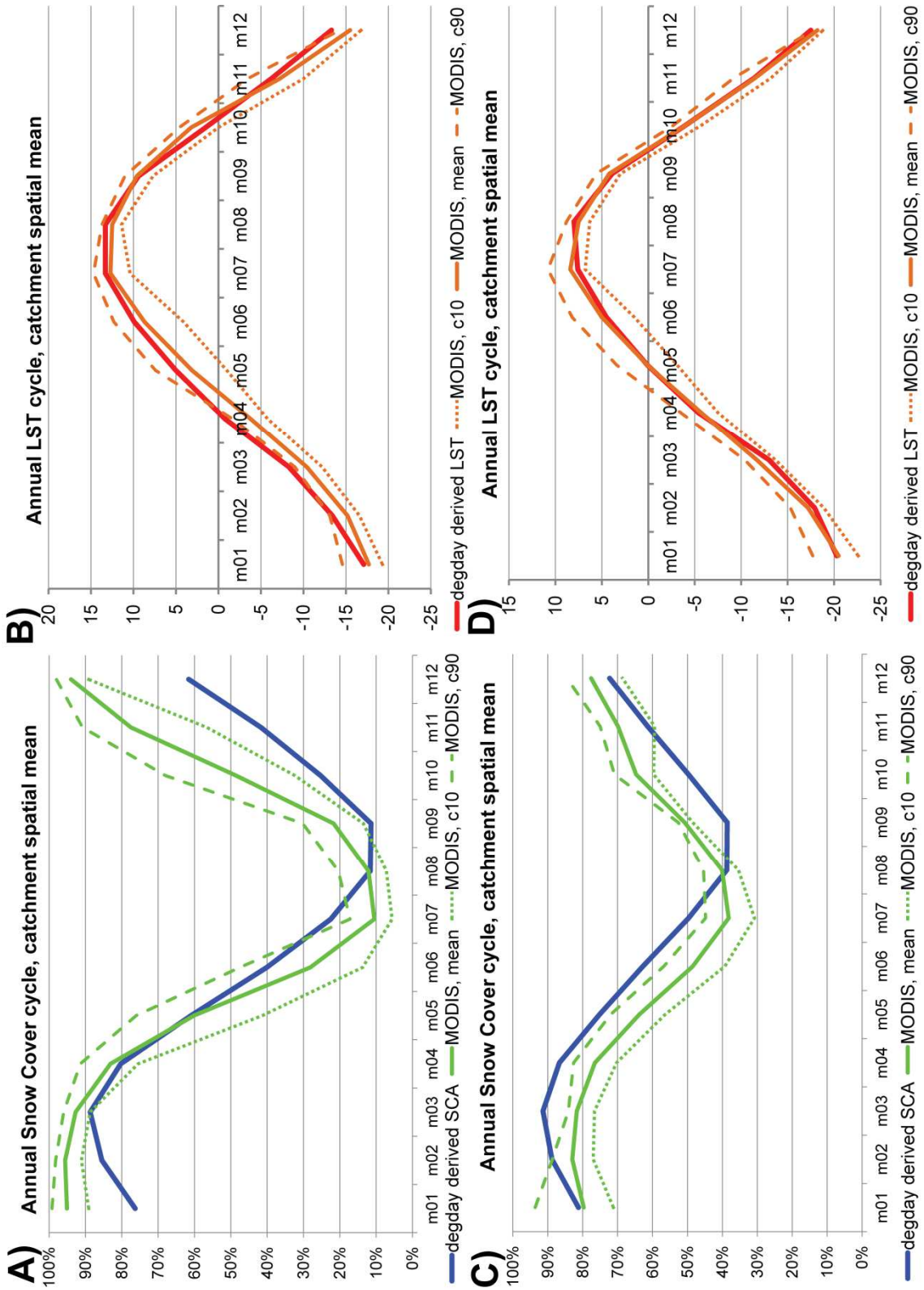

Figure 6.17 Validation results for simulation of snow covered area (SCA) land surface temperature (LST) for the 10km versions of the Astore and Hunza catchment models. Simulated results are prefixed "degday derived". The panels show as follows: A) Astore SCA; B) Astore LST; C) Hunza SCA; and D) Hunza LST.

As can be seen in Figure 6.17, the agreement between simulated and remotely sensed LST is very close.. However, LST was calculated using a simple correction of near-surface air temperature based on an empirical (linear regression) relationship

between net shortwave radiation and the differential between near-surface air temperature and LST.

Achieving agreement between simulated and satellite-derived SCA was considerably more challenging as SCA is dependent upon both the accumulation of mass (solid precipitation) and its removal by energy inputs (temperature). The present version of VICwCDiP does not attempt to simulate the considerable spatial variability of precipitation inputs except in their vertical dimension (via the orographic precipitation gradient). Figure 6.17 shows that despite extensive (manual) calibration work it was not possible to eliminate a degree of systematic bias in the simulated SCA cycles of both the Astore or Hunza catchments. These inherent biases will be taken into account in the "climate change impact assessment" phase of this thesis presented in Chapter 7. This will be accomplished by simulating a "synthetic control climate" time-series of identical length to the time-series to those used in the future climate scenarios (see Chapter 5) to project future hydrological conditions. Thus the projected changes in SCA, as well as in hydrological variables, will be calculated relative to the simulated control climateand its biases, as is standard in climate change impact assessments..

6.12 Raster/GIS visualisation of model outputs

One useful innovation of the VICwCDiP modelling approach adopted in this thesis is the implementation of rasterisation of the model outputs for compatibility with geographic information systems (GIS) via a post-processing step using the RasterIO package for Python developed by Holderness (2011). In future work, this capacity will facilitate the implementation, calibration and validation of horizontal (non-elevation driven) spatial heterogeneity by direct comparison of model land surface state outputs (SCA, LST, albedo) with remote sensing data products based on radiometric observations. Whereas spatially distributed approximations of physical state variables (SCA, LST, albedo) for which remote sensing data products exist can be used in model calibration and validation, spatially distributed estimates of hydrological fluxes and cryosphere state variables can facilitate diagnostics regarding the modelling of related processes.

A "gallery" of raster imagery showing the modelled spatial distribution of key hydro-climate variables/outputs has been assembled using the 5km resolution models of the Astore and Hunza catchments (outputs are very similar for the 10 km model but

using the 5 km model allows for better visualisation). The full gallery is included in Appendix D.

6.13 Grid-cell level simulation of glacial dynamics

As explained in the preceding sections of this Chapter, the VICwCDiP model presented here delivers substantial advances in methodology and the capability to simulate accumulation, vertical transfer and ablation of glacial ice. To accomplish this it is necessary to accurately model vertical gradients in mass fluxes – both precipitation and melt processes – and the mechanics of glacial displacement, be it through basal sliding or avalanching. These are complex physical processes, the simulation of which requires striking a balance between physical realism and the limitations of the available input data and computational resources. Hence, accurate determination of glacial mass balance remains a work in progress.

One of the key aspects of glacial simulation using this methodology is the amalgamation or dissection of the conceptual representations of physically distinct glaciers amongst regularly spaced grid cells. This spatial discretisation determines connectivity in terms of the (downward, gravity-driven) vertical transfer of glacial mass. To illustrate the role that this discretisation issue plays in model performance, examples were chosen from both the Astore and Hunza catchments. It is also hoped that these examples will help to communicate the capabilities and limitations of the VICwCDiP model in its present state.

The example chosen from the Hunza catchment, Figure 6.18, shows how individual glaciers may be dissected. In this example, even at the 10km resolution the example glacier is spread across multiple grid cells, although a single grid cell, which will be considered in detail in the following paragraphs, does cover large areas of both the glacial basin and tongue. At the 5km resolution, however, the broad glacial basin is spread over large sections of four grid cells and the glacial tongue winds through three additional cells. Nevertheless, two individual grid cells can be selected to represent the basin and tongue areas respectively. These two cells will also be considered in detail to examine how the VICwCDiP glacial dynamics modelling performs at the sub-grid scale.

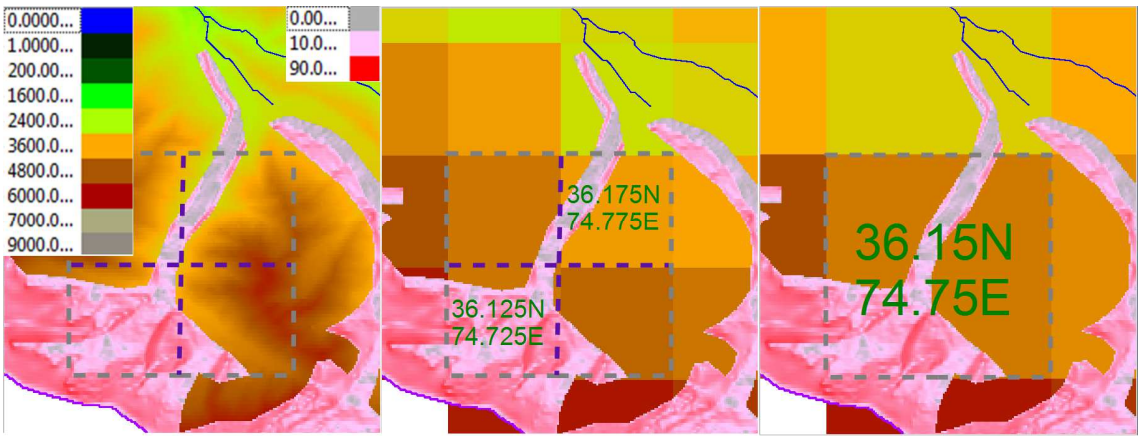

Figure 6.18 Geographic detail for location of example glaciated areas for the Astore catchment. Left panel: "native" SRTM90 pixel elevations; central panel: 5km VICwCDiP model grid cell mean elevations; right panel: 10km VICwCDiP model grid cell mean elevations; all panels: glaciated areas are shown as the SRTM90-derived surface slopes. Legends: "earth tones: elevations in m asl. "pink to red" gradations: surface slopes in angular degrees.

Figures 6.19 to 6.21 provide, for the single 10km grid cell and two 5km grid cells, sub-grid detail on: a) glacial area (as a fraction of each elevation band); b) glacial mass formulated as ice water equivalent (IWE); c) glacial horizontal displacement ("creep"); and d) net inter-band mass transfer (as IWE).

Figure 6.19 shows the 10km grid cell 36.15N 74.75E (designated by its geographic centre). As can be seen in Figure 6.18, this grid cell includes both glacial basin and glacial tongue areas. Figure 6.19 shows that – over the course of the imposed model "spin-up" prior to the beginning of the calibration period – the grid cell has achieved an effective dynamic equilibrium. The results are not ideal as all glacial mass and volume have been lost from the lower two elevation bands (the tongue area). Furthermore, the middle elevation band (b3) only serves as the ablation zone for the glacial mass delivered from the second highest band (b2). Basal sliding (Figure 6.19c) takes place only in the upper two bands (b1 and b2) because in the other bands the ice thickness, which produces the perquisite gravitational driving stress for vertical mass transfer (Figure 6.19d) to occur, has been lost. The values of net mass transfer between bands (Figure 6.19d) are required to sum to zero at each time-step to respect "conservation of mass." Values for the uppermost band (b1) can only be negative (or null) as mass moves out of this band to the adjacent lower band. Similarly mass transfer for the lowest band (b5) can only be positive or null as there is no outlet (other than ablation) for this band. Figure 6.19d shows that the second highest band (b2) both receives mass from b1, because the net transfer rate is positive, and delivers mass to b3 because net transfer for b3 is also positive. Figure 6.19 shows that b3, however, only receives mass because net mass transfer to b4 (panel d) is null and because the glacial

creep (displacement) by basal slide of b3 is null. While the results in Figure 6.19 are not as physically realistic as would be hoped, they are at least coherent and stable, albeit dynamically so, under the fluctuating mass and energy constraints imposed by the meteorological inputs.

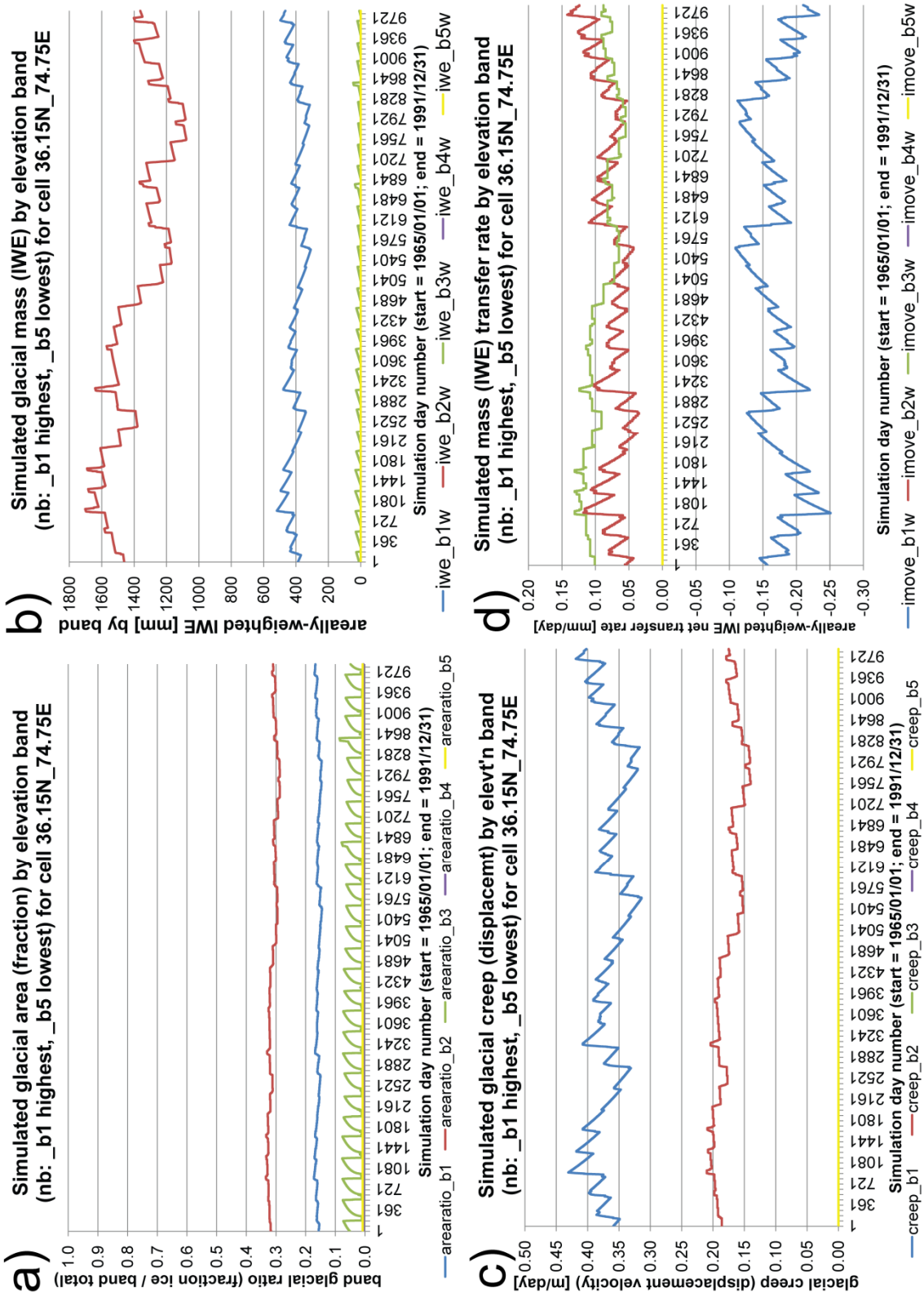

Figure 6.19 Results of simulated glacial mechanics for 10km grid cell 36.15N 74.75E in Hunza. Components include: A) area, B) mass (IWE), C) displacement (creep) and D) mass transfer.

In the 5km model of the Hunza catchment the glacial basin and glacial tongue area of the example glacier are effectively split between multiple grid cells. Figure 6.20 shows the higher elevation 5km grid cell, 36.125N 74.725E (designated by its geographic centre). As can be seen in Figure 6.18, this grid cell covers a substantial portion of the glacial basin for the example glacier. This is the most complicated of the three example grid cells presented here. Panels a and b of Figure 6.20 show that at the beginning of the calibration period (end of imposed model "spin-up") there is still a measurable amount of glaciated area and mass in all five elevation bands. Mass balance in the lower four elevation bands (b2 to b5) is clearly transient at this point in the simulation with the distribution of band behaviours aligning with that seen for the example 10km grid cell by roughly the three-quarter mark of the calibration time period. As such at the end of the calibration period only the upper two bands (b1 and b2) have stable glaciated area and mass with the middle band (b3) serving purely as an ephemeral ablation zone (panels a and b) for annual mass transfers from b2 (panel d).

This example effectively demonstrates that glacial response times simulated by VICwCDiP are variable (10 year "spin-up" period plus the response durations shown in Figure 6.20) as a function of the initial glacial mass (IWE) and the energy inputs (which will largely be governed by the modelled band elevation via the air temperature lapse rate).

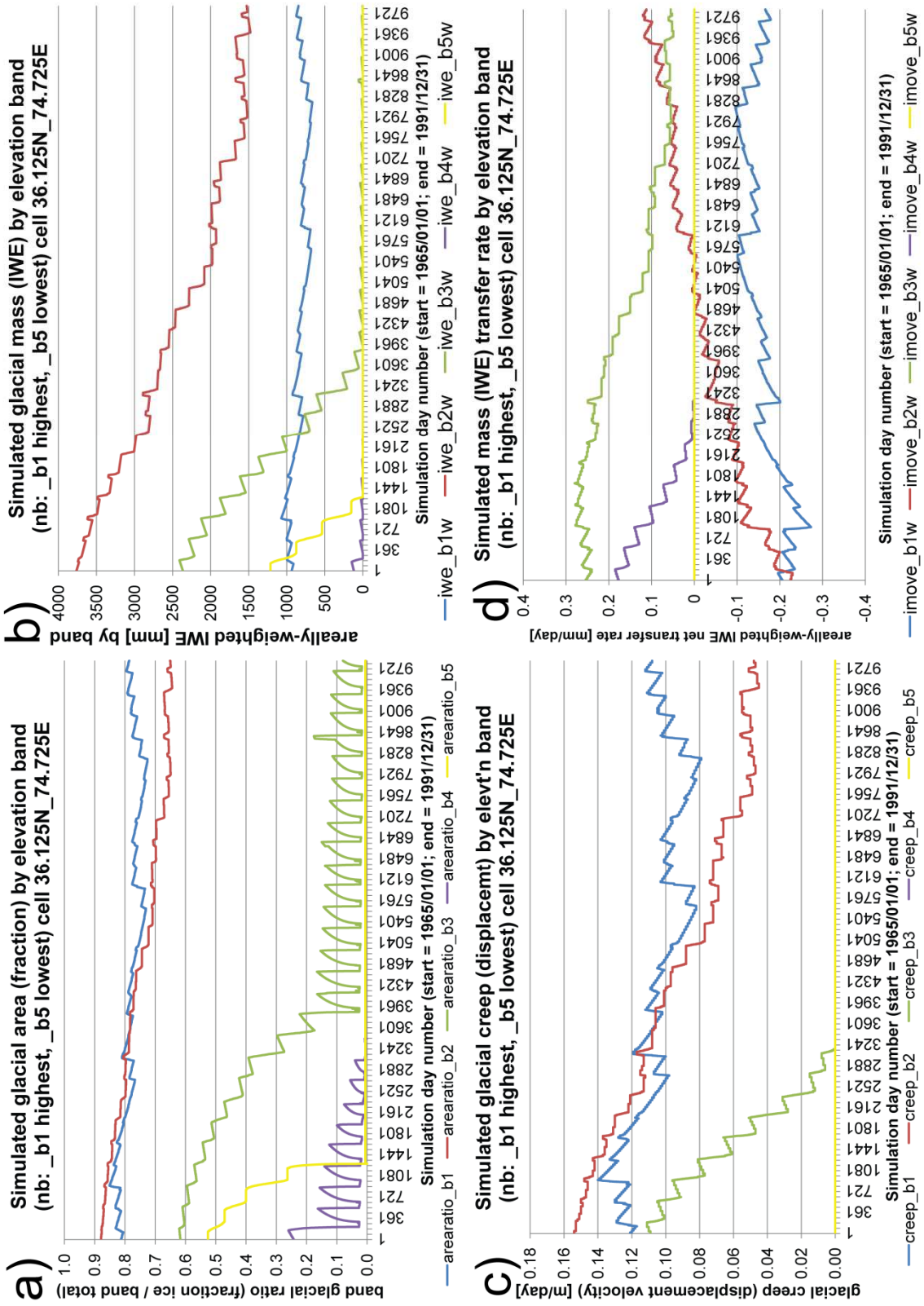

Figure 6.20 Results of simulated glacial mechanics for 5km grid cell 36.125N 74.725E in Hunza. Components include: A) area, B) mass (IWE), C) displacement (creep) and D) mass transfer.

Results are much simpler in the lower elevation 5km grid cell, 36.175N 74.775E (designated by its geographic centre) shown in Figure 6.21. As can be seen in Figure 6.18, this grid cell covers an isolated portion of the glacial tongue for the example glacier. Loss of area (Figure 6.21b) and mass (Figure 6.21b) in the middle three

elevation bands (b2 to b4) are complete prior to the beginning of the calibration period (end of model “spin-up”). A very thick glacial tongue in the lowest elevation band (b5), however, persists until more than mid-way through the calibration period. Thus in this case the model “spin-up” period appears to have been inadequate. Only the highest elevation band (b1) maintains substantial glacial mass throughout the simulation, although the assigned “bed-slope” (derived from surface characteristics calculated from the SRTM90 DEM, see section 6.6) is evidently quite shallow as measurable basal sliding is not projected to develop. As a result of the lack of physical mass outflow (vertical transfer by basal sliding), and what can be inferred as a lack of available energy (air temperature above freezing) to drive melt processes, net mass balance is always positive in b1 and precipitation inputs to this zone are effectively modelled as being sequestered from the catchment hydrological system.

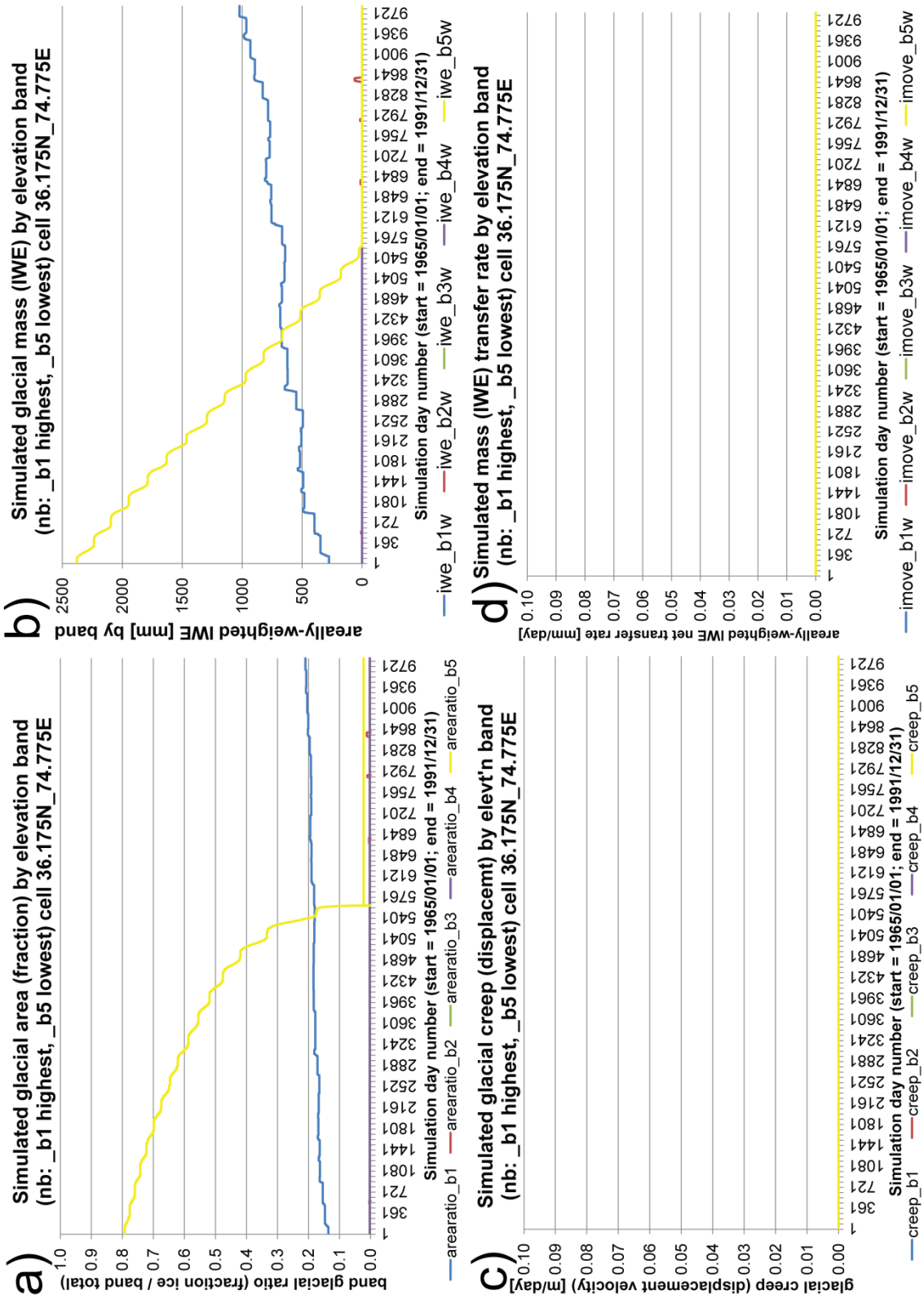

Figure 6.21 Results of simulated glacial mechanics for 5km grid cell 36.175N 74.775E in Hunza. Components include: A) area, B) mass (IWE), C) displacement (creep) and D) mass transfer.

The contrasts of dynamically stable behaviour in the 10km example grid cell with initially transient behaviour in the example 5km cells illustrate two key challenging, if not problematic, aspects of the present VICwCDiP model. Firstly, connectivity of glacial mass transfer is a problematic issue. At present the 10km

resolution offers a clear advantage in allowing better mass transfer from higher to lower elevations across larger distances. As can be seen in Figure 6.18 (and also in Figure 6.03) this is clearly a feature of the "real world" vast glacial systems in large sections of the UIB. This preference for coarser model resolution may seem counter-intuitive as the default assumption in terms of modelling is often that high spatial resolution will yield better accuracy and realism. For this to hold true in the case of simulating UIB glacial systems the modelling methodology would need to be adapted to allow inter-cell mass transfers. This would necessitate a greatly increased spatial resolution such that sub-grid (elevation band) discretisation would no longer be necessary. Such an approach is conceivable and has been implemented by Immerzeel *et al*. (2011) for example for a much smaller glaciated catchment in the Nepal Himalaya. Incorporation of this methodology within (or as a substitute to) VICwCDiP at the scale of UIB tributary catchments (e.g. Astore, Hunza) would primarily depend on the availability of computing resources (processing capacity, disk storage), but is certainly a possible avenue for future model development.

The second issue, highlighted by comparison of the glacial mechanics results from the two spatial resolutions, is the issue of accuracy in the vertical mass balance gradient. While the results from the 10km grid cell model (Figure 6.19) reassuringly indicate that the VICwCDiP will produce a dynamic equilibrium of glacial mass and volume in response to meteorological inputs, the model does not at present reproduce the observed pattern of glaciated area with respect to elevation (glacial hypsometry). Rather the present version of the model appears to simulate equilibrium line altitude (ELA), i.e. the elevation of neutral mass balance, at a substantially higher elevation than those observed in field studies. More worrying the gradient of mass balance (articulated about the ELA) appears too severe. In other words, net ablation is too rapid below the ELA, and net accumulation is too rapid above it. This exaggeration of the mass balance gradient may indicate shortcomings in the present version of the model in the simulation of both energy inputs and vertical mass transfer. Energy inputs at lower elevations may be insufficiently attenuated by inadequate incorporation of dominant debris cover effects over glacial tongues or due to the failure to modulate energy inputs as a function of terrain features (e.g. aspect, hillshade, etc.). Methodology adopted by Konz *et al*. (2007) could serve as a guide specifically for incorporating topographic effects into the degree-day type meltwater simulation approach used in VICwCDiP. Furthermore, the present degree-day method, based upon a daily time-step and thus mean daily temperature, may not adequately account for the implications of the severe diurnal

temperature cycle, with potential refreezing of meltwater, known to predominate in the UIB.

The mass balance gradient articulated about the ELA may also be exaggerated by inadequate vertical mass transfer. Whilst the approach to simulation of basal sliding within the glacial volume is considered to be conceptually robust and well supported by the literature, the model does not simulate mass replenishment of glaciated surfaces by avalanching of seasonal snow from steep surrounding slopes. Avalanche nourishment has been identified by Hewitt (2011) as a key mechanism of mass accumulation for many glaciers in the Karakoram. Thus it may imperative to incorporate at least a simplified model of this process (assumed to occur on an annual or seasonal time-scale) in order to achieve the intended level of accuracy in simulation of UIB cryosphere dynamics.

Despite the identified shortcomings in the the cryosphere components of the present version of VICwCDiP, it is considered that the model, particularly at the 10km spatial resolution, has been established as an adequate platform, upon which further improvement can be made, for accurate simulation of hydrological responses by critical UIB tributary catchments to observed or projected climate forcings.

6.14 Discussion

This Chapter has described an ambitious effort to implement a spatially distributed (rasterised) hydrological model – the VICwCDiP model – incorporating simulation of snowpack and glacial mechanics. This work is based primarily on the existing VIC model while substituting a “degree-day” based approach at a daily time-step for resolution of the full energy balance at a sub-daily time-step. The decision to adopt the simpler “degree-day” method was motivated by complications encountered with sensitivities to sublimation when attempting to calibrate catchment models using the existing VIC code. While sublimation is recognised to play an important role in high elevation cryosphere dynamics, modelling it accurately would require physically realistic (absolute) values for surface wind and humidity at the desired grid cell spatial resolution. This input data is not available at present.

The input data used by the VICwCDiP model is based on the extrapolation of values from a base station record on a purely elevation-driven basis. A simple linear lapse rate is used for daily mean air temperature, while vertical variations in precipitation are extrapolated using more complex functions which are manually fitted

during the calibration process. In the course of future model development this approach could be made more sophisticated either by incorporating additional physiographic/terrain-based elements – such as surface aspect, concavity and hillshade – or by implementing a gridded approach drawing on spatial climatologies derived from remote sensing data products. With regards to the radiation data used to calculate potential evapotranspiration (PET), large-scale values from meteorological reanalysis (ERA-40, ERA-Interim) are applied directly despite previously identified links to cloud cover (see Chapter 4) which itself displays a strong elevation dependency in the UIB (see Chapter 3).

Despite the simplicity of the approach used for meteorological inputs, the model has objectively demonstrated, through the results of calibration and validation runs, the ability to reproduce the annual melt-runoff cycle and range of interannual variability. Furthermore the model has shown at least moderate skill, as evidenced by a range of metrics, to simulate hydrological response to specific interannual variations in mass (precipitation) and energy (temperature) inputs. In addition to traditional hydrological outputs (evapotranspiration, runoff), the model also approximates the surface variables of snow covered area (SCA) and land surface temperature (LST). These surface variables are interesting in their own right, but in hydrological terms their estimation is required for intermediate steps in the calculation of PET. Catchment means for these simulated surface variables match well with climatologies based on remote sensing data products from the MODIS instrument. Considering the present level of model development, the output variables generated by VICwCDiP which could be viewed with the most confidence when simulating projected future climate conditions (as described Chapter 7) are primarily net hydrological fluxes (total runoff, actual evapotranspiration), although the estimation of SCA also appears to be relatively robust. Any calculated future changes, however, would need to be considered as the ratios (or differences) between the simulated results for a given climate scenario with results from a “synthetic control climate” simulation of identical length in order to isolate climate-driven changes from biases which have not yet been eliminated in the present version of VICwCDiP.

Despite these accomplishments in the development of the VICwCDiP model described in this Chapter, it is recognised that there remains considerable potential and impetus to improve the model especially with regard to glacial mechanics. As described in section 6.13, the current model exaggerates the vertical mass balance gradient articulated about the ELA. This shortcoming is manifested as excessive net ablation (mass loss) in shallow (low slope) low elevation glacial tongues and high rates of mass

gain at high elevations. This is thought to result from a combination of over-estimation of energy inputs for ice melt at lower elevations and under-estimation of vertical mass transfer of seasonal snowpack to adjacent glacial ice by (presently not simulated) avalanching.

In future work a number of auxiliary data sources could be drawn upon to reduce uncertainty regarding trajectories of glacial area, volume and (large scale) mass. These include:

- multi-decadal optical imagery and combinations of optical/thermal imagery which could used to delineate glaciated areal extents (e.g. Bolch *et al*., 2008).
- pairs of date-stamped digital elevation models (derived from a range of data sources) which via surface matching techniques could be used to estimate volume changes (e.g. Gardelle *et al*., 2012, Kunz *et al*., 2012);
- large-scale basin wide estimates of mass storage changes using gravimetric techniques and data from the GRACE or similar missions.

Beyond these specific sources of information for tuning simulated glacial mass-balance trajectories during calibration and validation runs, additional staff resources for model development would allow additional simulations to extensively test the model sensitivity to a range of plausible values for each of the primary calibration parameters. This additional testing need not be limited to study areas (catchments) within the UIB. Testing of the VICwCDiP model for catchments in other mountainous geographic regions with better data availability, e.g. the Alps or Andes, could yield further insights to model strengths and limitations.

Nevertheless, it is felt that the work presented in this Chapter demonstrates that the current VICwCDiP model has reached an adequate level of skill not only to act as the foundation for further development but also to be used for preliminary assessment of potential climate change impacts using the synthetic time series described in Chapter 5. The results of these simulations will be presented in Chapter 7.

Chapter 7: Contrasting scenarios of future UIB hydrology

7.1 Introduction

This Chapter integrates the aspects presented in the preceding chapters to present the modelling results of how the hydrology of the UIB may change under contrasting future scenarios. The preceding chapters have described in detail the present hydro-climatology of the UIB (Chapter 3), examined potential causal mechanisms driving recent local climate variability (Chapter 4), assessed contrasting plausible scenarios for future regional climate conditions (Chapter 5) and documented the construction and validation of a hydrological and cryospheric process model developed to deal with the unique challenges posed by the hydrological regimes of the UIB (Chapter 6). This Chapter therefore presents the results of that hydrological model when driven by those future climate scenarios.

7.2 Context of previous studies of potential climate change impacts on UIB hydrology

This thesis is not the first work to explore the potential hydrological implications of climate change for the Upper Indus and its tributary catchments. Three of the most notable publications (Akhtar *et al*., 2008; Immerzeel *et al*., 2009 and Bocchiola *et al*., 2011) are summarised in Table 7.1.

Previous study	Akhtar *et al.* (2008)	Immerzeel *et al*. (2009)	Bocchiola *et al*. (2011)
Catchment(s)	Astore, Gilgit, Hunza	entire Upper Indus above Besham	Shigar
Climate Models and Emissions Scenarios	PRECIS_HadAM3P (RCM), SRES A2	PRECIS, SRES A2	CCSM3 (GCM), SRES A2
Future time slice	2071 - 2100	2071 – 2100	2050 - 2059
Future Climate Conditions (generalised): Change in Summer Air Temperature; Change in Annual Precipitation	Tair : +4.2 to +4.8°C Precip: x1.13 to x1.21	Tair : +4.8°C Precip: x1.19	Tair : +1.9°C Precip: x1.20
Hydrological Model	HBV	SRM	DHM
Orographic Gradient Applied	No.	not explicit (TRMM) Vertical gradients (or rather lack thereof) in TRMM precipitation estimates for the UIB were discussed in section 3.9.1.	Yes: $P_y = (9 * 10^{-6}) * z^{2.22}$ where: "P_y" is annual precipitation [mm] and "z" is surface elevation [m asl] (see Chapter 6 for graphical presentation)
Glaciated Area Change Scenarios Tested	0%, -50%, -100%	0%, -50%, -100%	0%, -10%, -25%, -50%
Future Hydrological Conditions (generalised) as a function of specified relative change from present to future glacial cover [% area reduction]	[0%]: increased flows due to increased mass & energy inputs [-50%]: little annual change but "dampened" annual cycle, increased precipitation roughly compensating decreased glacial melt [-100%]: substantial flow reductions as reduced glacial melt outweighs precipitation increases	[0%]: increased flows due to increased mass & energy inputs [-50%]: little annual change but "dampened" annual cycle, increased precipitation roughly compensating decreased glacial melt [-100%]: substantial flow reductions as reduced glacial melt outweighs precipitation increases	[0% to -25% (inclusive)]: increased flows due to increased mass & energy inputs which offset minor reductions in glacial area [-50%] moderate reduction in flows due to reduced glacial melt

Table 7.1 Summary of previous published studies of hydrological impacts of climate change on the UIB.

As explained in Chapter 2 (section 2.5.5), these three studies were relatively consistent in their primary conclusions:

- Under scenarios with unchanged glaciated area the three studies found increasing runoff due to increased mass (precipitation) and energy (temperature) inputs increasing rainfall and snowmelt contributions to runoff as well as well as increased glacial melt.

- Under scenarios with moderate deglaciation the reductions in glacial meltwater generation are roughly compensated for by increased rainfall and snowmelt from increased precipitation.
- Under scenarios specifying total glacial loss the increases in rainfall and snowmelt from increased precipitation were not able to offset the reductions in glacial meltwater.

While the studies summarised in Table 7.1 attempted to address urgent research questions of both geoscientific and socio-economic importance, they had substantial methodological limitations in common. Chief among these shortcomings, in addition to drawing upon only a single scenario of future climate for their simulations, is their reliance upon predefined, static conditions of glaciated area. Inextricably linked to this assumption of static glaciated area is effectively infinite (inexhaustible) glacial mass, such that glacial melt is constrained only by available energy inputs which are quantified (indexed) by air temperature using degree-day melt methods. As such, the issues of variability and uncertainty in glacial mass balance under future scenarios are not fully explored, nor is the plausibility of the predefined scenario of changes in glacial area assessed.

As described in Chapter 6, the VICwCDiP model developed in this thesis also uses a degree-day index approach for calculating glacial melt but, in addition to energy constraints, meltwater generation is also limited by explicit accounting of the available glacial mass (volume). While, as discussed in Chapter 6, the VICwCDiP model has notable limitations it does provide substantial advances on the previous studies cited above, not only through its incorporation of "conservation of mass" in snowpack and glacial ice modelling, but also through its degree of spatial discretisation – rasterised catchment representation with sub-grid variability in elevation bands – as well as by incorporation of the influence of fractional snow cover – through albedo and surface temperature effects on net radiative fluxes – on potential evapotranspiration (PET). Furthermore, the probabilistic approach to modelling of alternate scenarios using stochastically generated time-series (see Chapter 5) is both more sophisticated and robust than the downscaling approaches used by the studies summarised in Table 7.1.

7.3 Simulation procedure for synthetic time series

As described in Chapter 5, in addition to the two future "perturbed climate" scenarios a synthetic time series for the reference control climate, i.e. representing present conditions (1961-1990), was produced using the RainSim and CRU Weather Generator software packages. In order to provide adequate timeframes over which to assess the projected impacts and to provide multiple simulations of the same set of conditions to provide probabilistic scenarios, 3,000 years of daily synthetic data was generated for each of these three sets of conditions (baseline and two future "perturbed climate" scenarios). Because the "response times to reach dynamic equilibrium" of the glaciological components of the UIB hydrological systems were of interest, each 3,000-year time series was then sub-divided into ten individual 300-year time series and used as input to the VICwCDiP hydrological model described in Chapter 6. As RainSim and the CRU Weather Generator are stochastic models, the appearance of any trends within the 300-year synthetic time-series is purely random and not the result of any simulated physical process – each 300-year time series represents a stationary climate process.

7.4 Control climate (1961-1990)

7.4.1 Performance of VICwCDiP model

The first step in assessing potential hydrological climate change impacts of the selected scenarios is to force the models of each catchment with the synthetic time series of the baseline or control climate simulation (1961-1990). This establishes a baseline of the model performance against which changes can be quantified. This step also provides an additional measure of model validation by testing whether the model reproduces, consistently over a long time period, the current observed land surface processes and hydrology when driven by a stationary climate simulation mirroring present conditions.

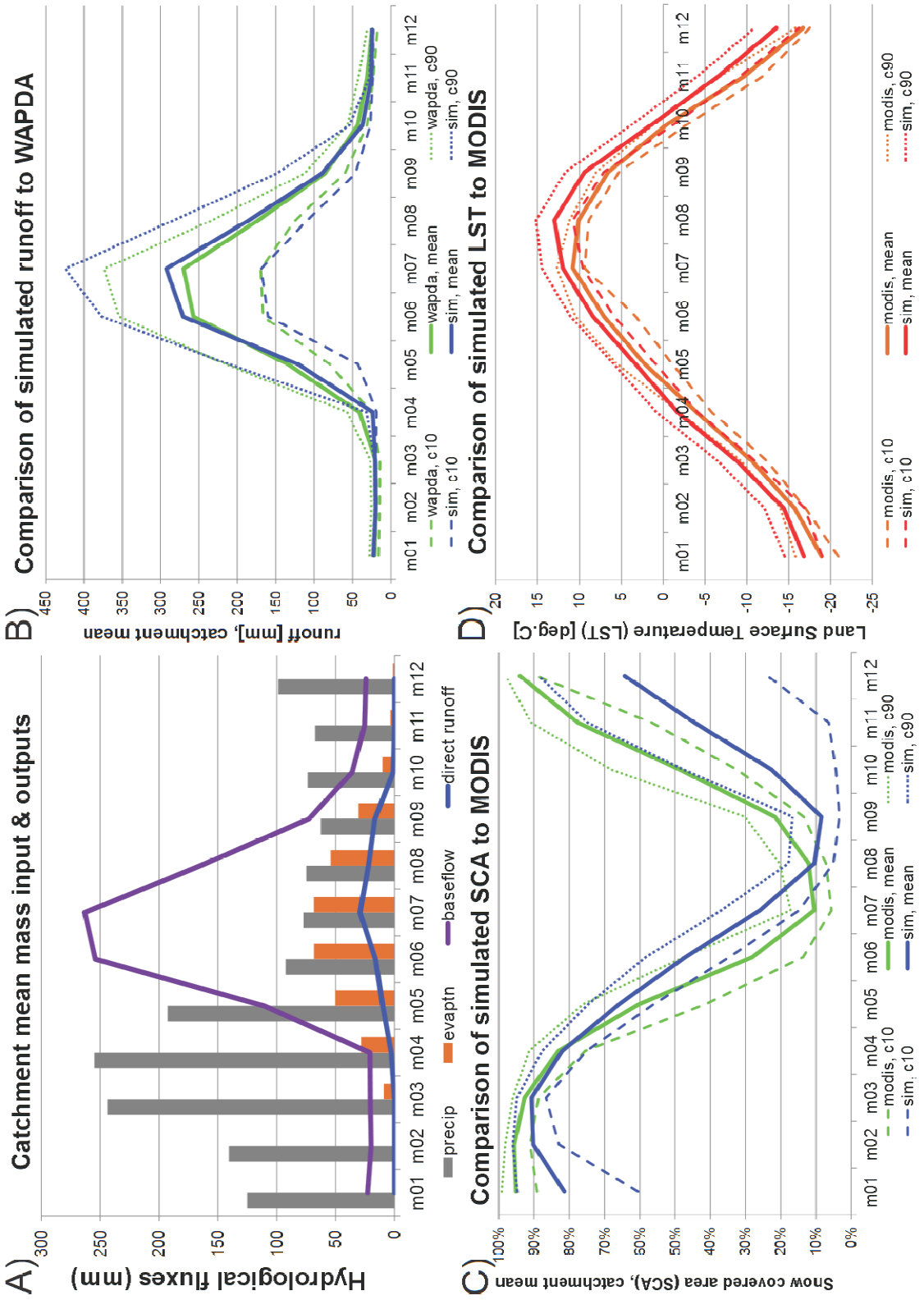

Figure 7.01 Annual cycles of A) hydrological mass input (precipitation) and outputs (evapotranspiration, baseflow and direct overland flow/hortonian runoff), B) total runoff, C) snow covered area (SCA) and D) land surface temperature (LST) for the 3,000 simulated years of control climate. Results are shown from hydrological modelling of the synthetic control climate for the Astore catchment. Panels C & D compare simulated estimates for land surface states (SCA, LST) to the available MODIS climatology (2000-2010). "c10" and "c90" respectively refer to the first and last deciles of the available record for the given variable and data source.

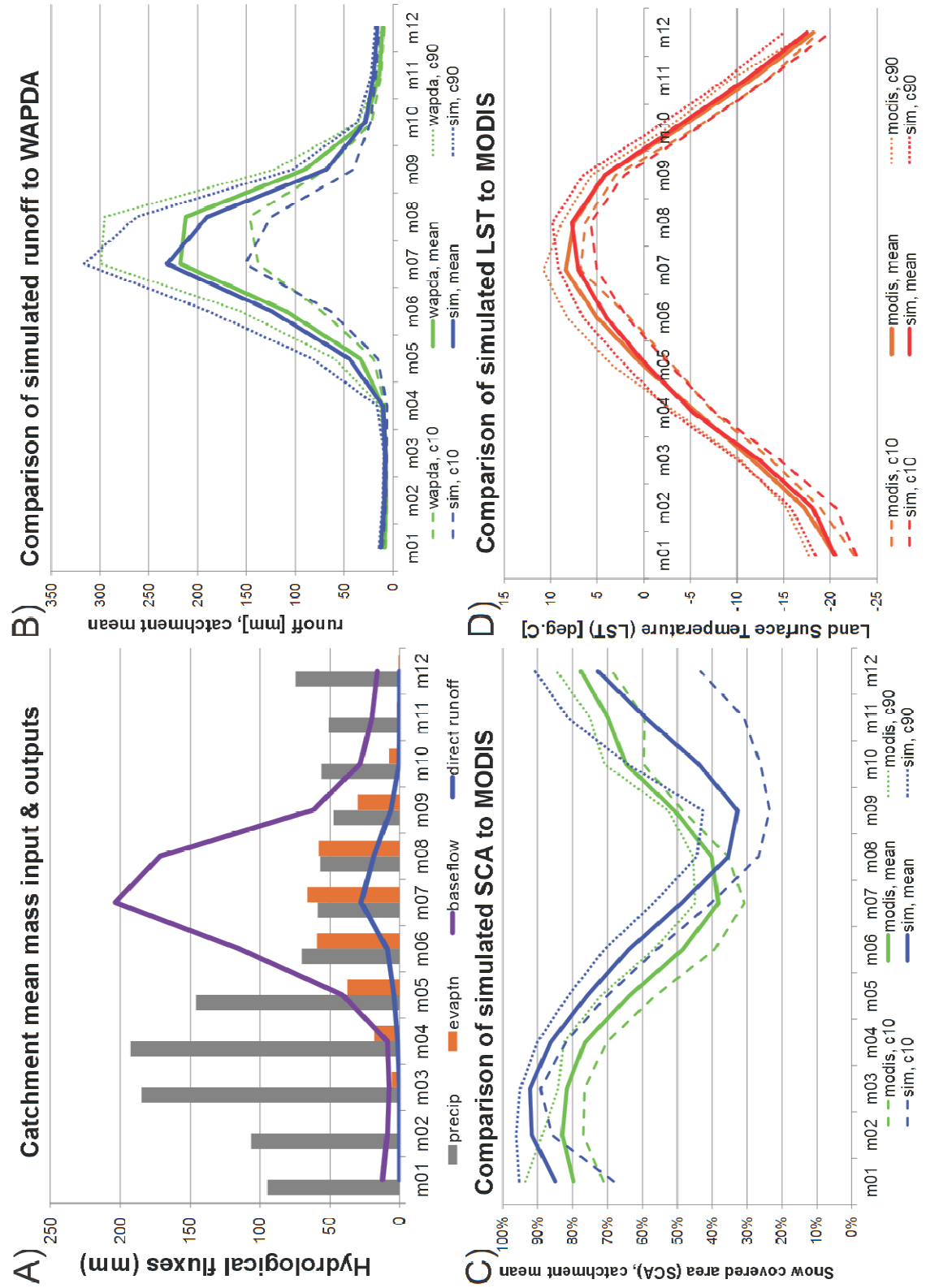

Figure 7.02 As for Figure 7.01 but for the Hunza catchment.

Figures 7.01 and 7.02 show, respectively for the Astore and Hunza catchments, key modelled hydrological and land surface variables. As was the case for the model calibration and validation (Chapter 6), it was not possible to entirely eliminate mean bias from the VICwCDiP model. Nevertheless the biases shown by the control climate

synthetic time-series simulations are similar to those found in the calibration and validation runs described in Chapter 6. This is particularly true for the model output of SCA which, for both Astore (Figure 7.01c) and Hunza (Figure 7.02c), consistently lags the available MODIS climatology during both the mid-to-late ablation and early accumulation seasons, although synchronisation occurs during late accumulation and early ablation phases. In Hunza there is also a slight exaggeration (higher annual maximum, lower annual minimum) to the annual SCA cycle (Figure 7.02c).

With regards to LST, for Astore there is a moderate, uniform warm bias in comparison to air temperature observations (Figure 7.01d). The reason for this discrepancy is not understood at present as this bias is absent from the calibration and validation runs for Astore (see Chapter 6). An albedo feedback via net shortwave radiation seems unlikely given the similarity between synthetic control SCA and calibration SCA. In the absence of an explanation the bias will be taken into account when considering projected LST in the simulations driven by future climate scenarios.

For Hunza, however, simulated LST tracks quite closely with the MODIS climatology except in July when there is a slight cool bias (Figure 7.02D). Focussing on simulated runoff, which is the variable of primary interest in this study, the magnitudes of cool season (annual minima) baseflows as well as the timing of annual melt cycles are very well reproduced (Figure 7.01 and 7.02, panels A and B). However, there are biases in runoff magnitudes for individual months during the melt season, consistent with the VICwCDiP model calibration and validation from Chapter 6. For Astore, the initiation of the melt season in April is underestimated and peak runoff in July and August is slightly overestimated (Figure 7.01b). For Hunza, there is a slight overestimation of runoff during the rising limb of the annual hydrograph and a moderate underestimation during the recession limb (Figure 7.02b).

7.4.2 Flux trajectories over 300-year control simulations

For the baseline simulations, consideration of the spread – variability of the ten 300-year simulations – and trajectories – whether a variable exhibits random variability or a consistent tendency over the course of the model run – is useful both to confirm that the input climate forcing is stationary as well as to aid in visualising the simulated interannual variability and relative magnitudes of different mass fluxes.

Figures 7.03 and 7.04 show, respectively for the Astore and Hunza catchments, the trajectories and spread, as shown by the upper and lower quartile boundaries, for key

hydrological and cryosphere fluxes as well as the areal and mass indicators of catchment glacial volumes over the 300-year simulations.

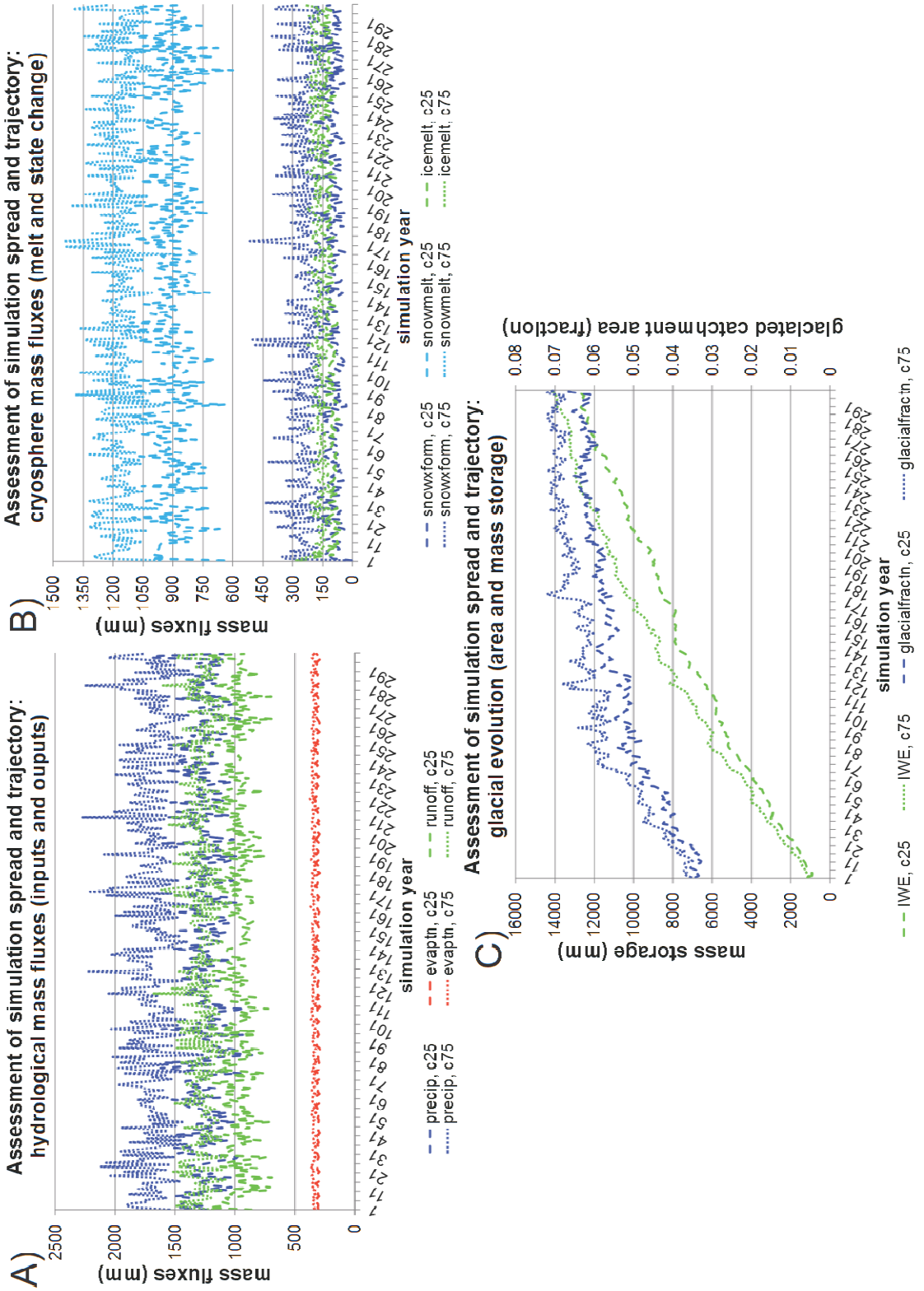

Figure 7.03 Trajectory and spread of results hydrological modelling of synthetic control climate for the Astore catchment. Fluxes are given as annual totals and glacial area and mass are given as annual means. In the figures c25 and c75 respectively refer to the lower and upper quartiles of values at each annual timestep from amongst the ten 300-year long simulations.

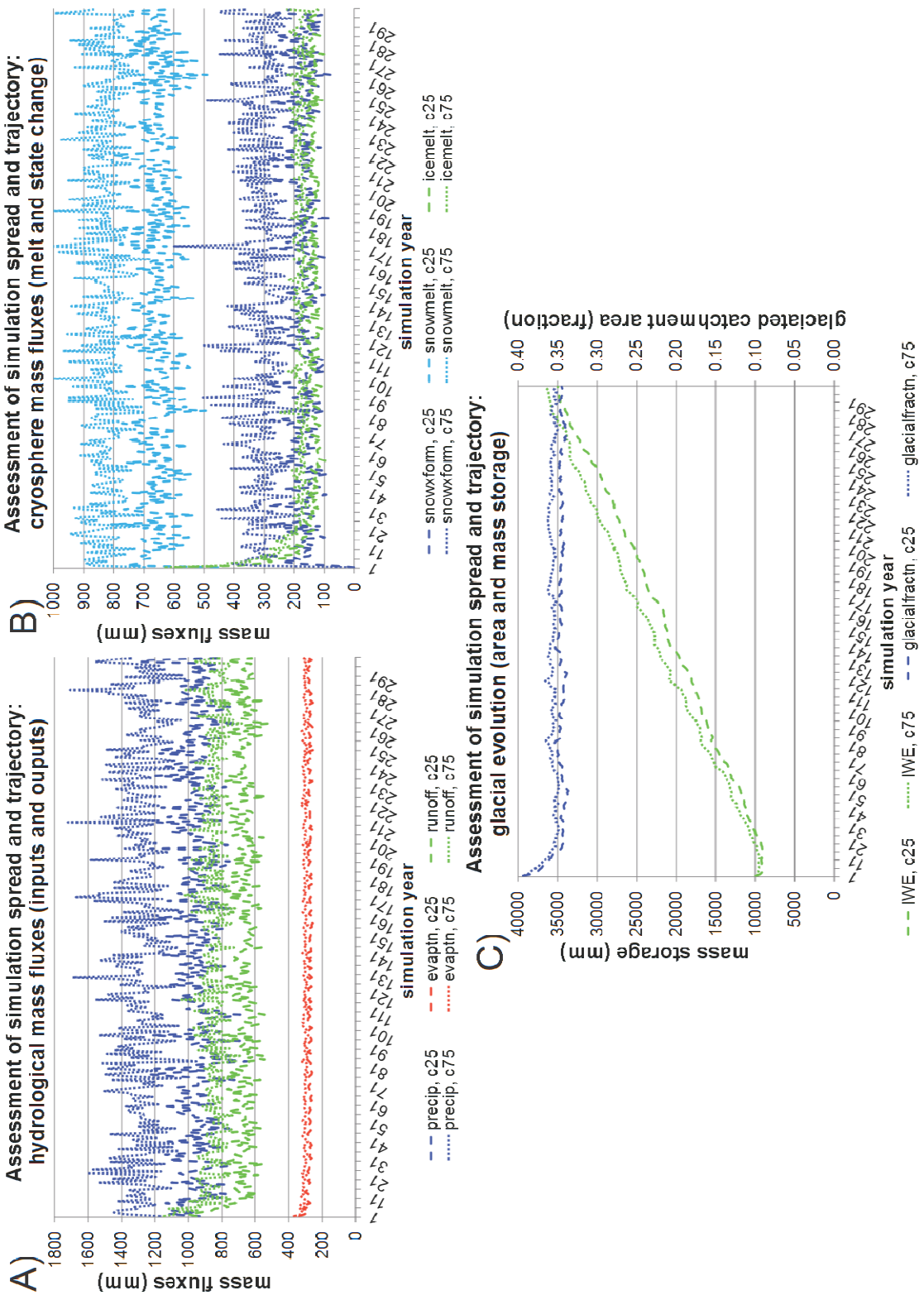

Figure 7.04 As for Figure 7.03 but for the Hunza catchment.

With the exception of glacial area – as a fraction of the catchment surface – the results from Astore and Hunza are very similar in form, if not in magnitude. In the hierarchy of hydrological fluxes, simulated evapotranspiration is very stable, while precipitation is highly variable. Annual runoff also exhibits substantial variability

although less so than input precipitation. Similar patterns emerge for the cryosphere fluxes. With the exception of the first few years of each simulation when the initially specified glacial tongues melt rapidly before being exhausted, glacial ice melt volumes are relatively stable. In future model development work, efforts will be made to improve the accuracy of the vertical distribution of ice melt so that the simulated glacial tongue exhibit similar stability to their real-world counterparts. In the present version of the model, however, it is necessary to neglect the initial decades – a minimum of 20 years although as much 6 decades could be discarded in a more conservative approach – of a multi-century simulation such that the initial low elevation ephemeral glacial tongues have fully ablated.

In both catchments, based on the calibration parameters, snow melt is of considerably larger magnitude than ice melt, after initial glacial tongue retreat. Driven by the intrinsic variability of precipitation inputs, both snow melt and the replenishment of glacial ice pack by transformation of snow into firn are highly variable.

Regardless of its variability, annual glacial ice accumulation regularly exceeds ice melt for both catchments, thus both show effectively monotonically positive glacial mass balances and increasing catchment glacial mass (IWE) under simulated current conditions (1961-1990). The primary difference demonstrated by the two catchments is hence in the trajectory of glacial area. This difference results from the terrain-dependent manner in which glacial mechanics are simulated. For the Hunza catchment, after an initial stabilisation – roughly two decades into the three century simulation – the glaciated area remains roughly constant over time with very little spread between the simulations. For the Astore catchment, however, glacial area tends to increase for most of the model run; roughly doubling over the course of the simulation with substantial spread shown between the ten simulations – a tentative conclusion from this might be that in middle-elevation catchments, ice mass variation is more sensitive to current climatic variability than in high-elevation catchments such as Hunza. Areal increases tend to slow down towards the end of the simulation however; thus it is also possible that the resultant glaciated fraction represents a dynamic equilibrium of replenishment of ablation zones by simulated vertical mass transfer at the sub-grid (elevation band) level.

Despite these tendencies toward increasing glacial mass in both catchments and increasing glacial fraction in the Astore catchment, ice melt remains stable (after the initial period) throughout the simulations. Thus it must be concluded that in the model

simulations glacial volume growth is vertically concentrated above the elevation range where there is adequate available energy for full ablation of annual precipitation mass inputs. This could either indicate that the control climate inherently results in a positive regional net glacial mass balance or that further model improvements are necessary to fully capture the key glacial processes. In all probability, both cases may be true.

7.5 Future Climate Scenarios

As described in Chapter 5, the present study decided to contrast an available RCM-driven scenario (PRECIS_AM3P) with an "observation-led" scenario derived by extrapolating trends identified in the local observational record (PMD). The RCM-driven scenario was derived using a time-slice experiment to calculate change factors between projected UIB climate for the late 21st century (2071 to 2100, hereafter referred to as the 2080s) and the control climate period (1961 to 1990). It was deemed necessary to supplement and contrast this RCM-driven scenario with the "observation-led" scenario because its relatively uniform projections of future temperature change starkly contradict the seasonally and diurnally asymmetrical trends identified in the recent historical data from both local observations and meteorological reanalysis. This asymmetry was examined in Chapter 4.

The two selected future climate scenarios, including their defining change factors and resultant statistical descriptors, are presented in detail in section 5.5. A general grasp, however, of the contrasts between the two scenarios can gained by comparing the seasonal aggregates of change factors for precipitation amount and mean near-surface air temperature (Tavg) shown in Table 7.2.

Future scenario	Precipitation change (factor)				Tavg incremental change (°C)			
	DJF	MAM	JJA	SON	DJF	MAM	JJA	SON
RCM-driven (PRECIS_AM3P 2080s)	*1.176*	*1.374*	*0.896*	*1.256*	*4.5*	*4.3*	*5.4*	*5.4*
Observation-led (extrapolated trends)	*1.383*	*0.623*	*1.757*	*1.073*	*0.9*	*1.8*	*-0.8*	*1.0*

Table 7.2 Summary of seasonally aggregated change factors for two key variables in the selected future climate scenarios.

7.5.1 RCM-driven Scenario

Figures 7.05 and 7.06 show the annual cycles simulated respectively for the Regional Climate Model (RCM)-driven scenario for the Astore and Hunza catchments. For both the Astore and Hunza catchments the overall net hydrological response is an increase in annual total runoff – i.e. baseflow plus direct runoff – with a shift earlier in

the year. Reductions are seen (Figures 7.05b and 7.06b) in mid-to-late summer runoff due to earlier depletion of seasonal snowpack and reduced glacial cover. These reductions are more than offset by large increases (Figures 7.05b and 7.06b) in spring (March, April, May) total runoff in Astore and in mid-Spring to mid-Summer (April to July) total runoff in Hunza.

In terms of SCA, the annual cycle in Astore (Figures 7.05c) follows the same pattern as in the control climate but with a year-round offset (reduction) of 10% of the catchment area. The Hunza catchment (Figures 7.06c) also shows a reduction of 5% to 10% for much of the year except for mid-Summer to mid-Autumn (July to October) when the months on either side of the annual minima have far less SCA than under the control climate. This is due to widespread deglaciation in Hunza under this scenario as substantial sections of the catchment that previously had snow and ice cover year round experience complete ablation every summer as a result of the projected temperature increases.

Under the RCM-driven scenario, quite severe increases in LST (Figures 7.05d and 7.06d) are projected for both the Astore and Hunza catchments. These increases are largely driven by the air temperature increases specified under this scenario. There are, however, relevant elements of the projected LST change linked to the specific methodologies employed in generation of the synthetic time-series and in calculation (approximation) of LST by VICwCDiP. In particular, it is worthwhile to clarify that implications of apparently severe changes in LST should be understood in light of the manner in which they were calculated. As described in Chapter 6, a simple method of calculating LST based on ambient air temperature, snow cover state and a net shortwave radiation correction was implemented in the VICwCDiP model in lieu of a full solution of the surface energy balance equations.

Furthermore, in the calibration and validation phase, incoming shortwave radiation was taken from the ECMWF ERA-Interim meteorological reanalysis. For the synthetic time series, however, because the presently available version of the CRU Weather Generator (Kilsby et al., 2007) that has been adapted to function for the UIB climate does not directly handle radiation variables – instead producing an estimate of the empirical observational variable “sunshine hours” – it was decided to use a simple two-step air temperature index substitution method to provide these secondary variables. The first step consisted of calculating the normalised, standardised anomaly of mean daily air temperature relative to the observational record. This anomaly was

then transformed into an equivalent absolute value for each of the radiation variables by multiplying by the corresponding standard deviation and adding the corresponding mean from the reanalysis reference period.

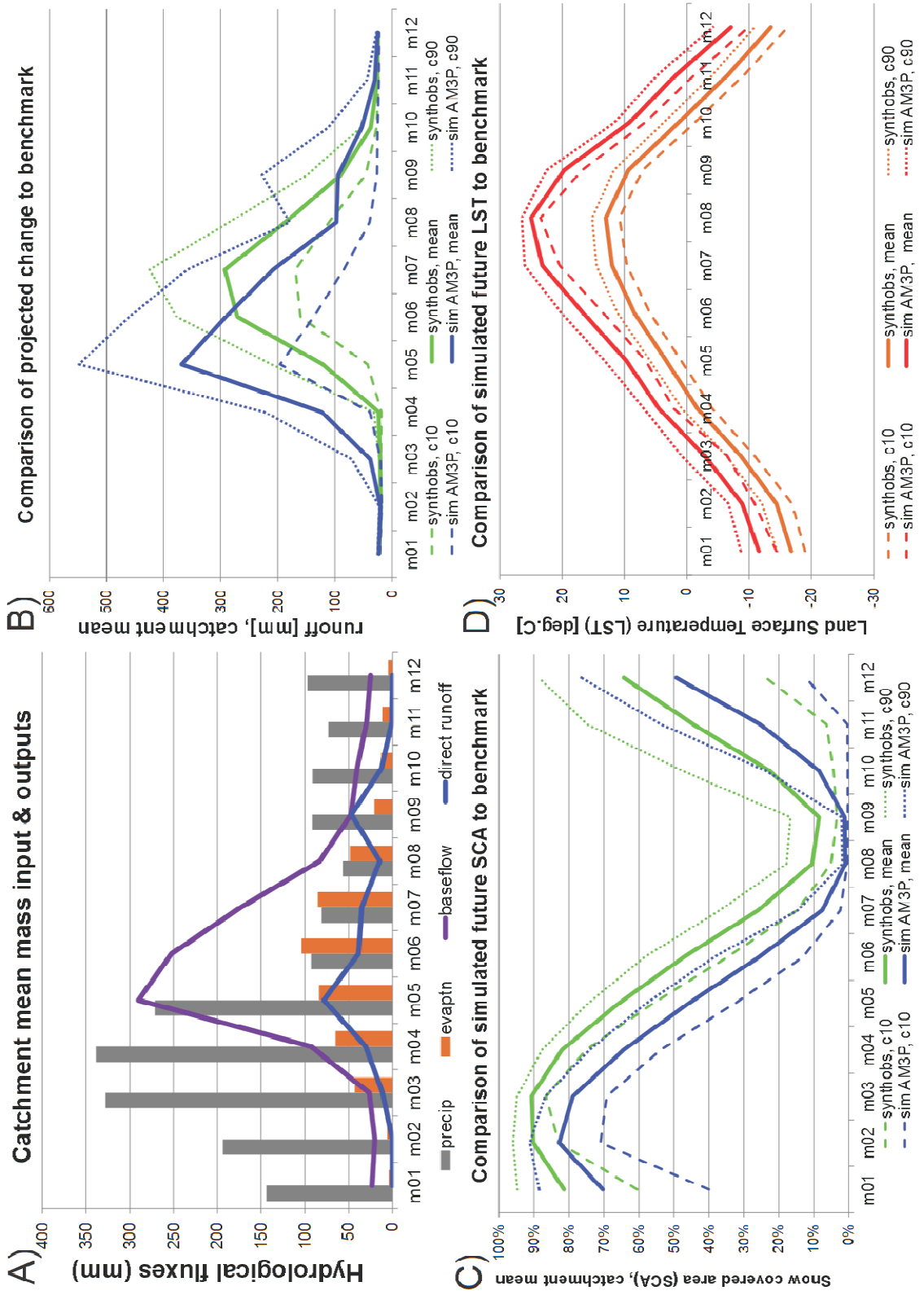

Figure 7.05 Annual cycles from hydrological modelling of RCM-based (PRECIS_AM3P) climate scenario for the Astore catchment. “c10” and “c90” respectively refer to the first and last deciles of the available record for the given variable and data source.

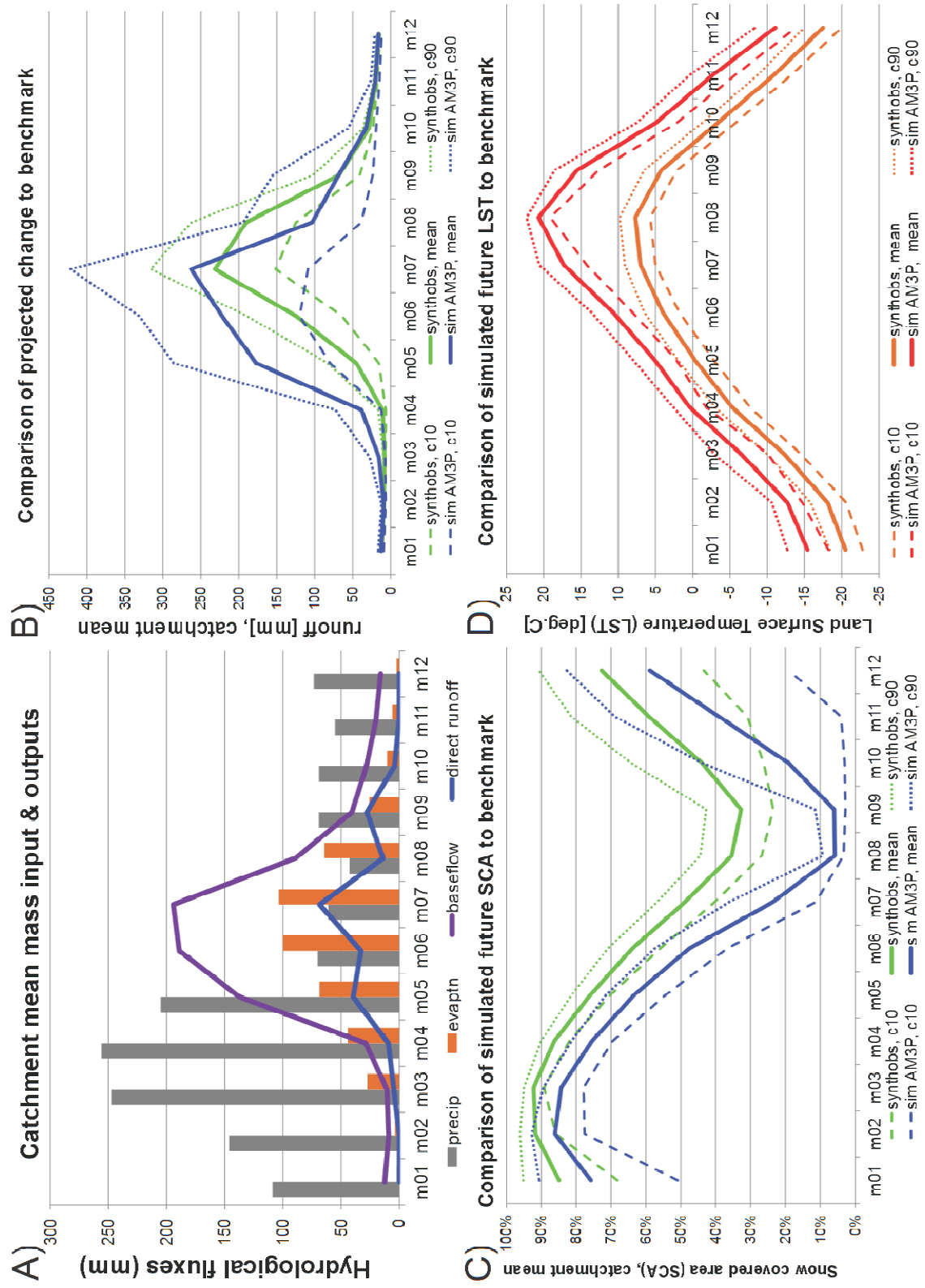

Figure 7.06 As for Figure 7.05 but for the Hunza catchment.

This highly simplified approach is a recognised shortcoming in the current work. Given the previously described correlations of radiation variables to cloud cover (see Chapter 4) it is expected that the Weather Generator approach (Kilsby et al., 2007) –

based on Markov transition states defined by precipitation occurrence – would be well adapted to produce these variables. As problems had been encountered with the specification of secondary variables (beyond air temperature) in the updated Weather Generator (see Chapter 5), it was decided to proceed as described above rather than embarking upon additional testing of synthetic time series. Thus the approach used here was deemed an adequate solution when faced with the time constraints of this thesis but is an opportunity for future development.

A further reason that this approach was considered sufficient was that LST is not used directly in hydrological components of VICwCDiP. Furthermore radiation variables are only used in the model hydrologically for calculation of potential evapotranspiration (see Chapter 6). The combination of the air temperature index method for estimating radiation compounded with the shortwave correction method for LST does, however, effectively square the input air temperature change factor in generating the estimated LST output. Thus, given the uncertainties involved in the mass input (orographic precipitation gradient) and melt energy parameters (degree day factors), the radiation component issue – which is perceptible through the large projected increases in LST – acting via PET is expected to have only limited impact on the overall water balance.

7.5.2 Observation-led scenario

Figures 7.07 and 7.08 show the simulated annual cycles for the Astore and Hunza catchments respectively for the local trend-extrapolated scenarios. The hydrological impact of this reduction in energy inputs can be seen in Figures 7.07b and 7.08b in the suppressed runoff in Summer months (June, July and August). To some extent the reduced Summer runoff in these simulations is compensated for by increased late Spring (May) runoff.

Under the observation-led scenario, the annual SCA cycle shows little change in its amplitude – annual maximum and minimum extent – for either the Astore catchment (Figure 7.07c). The Hunza catchment shows marginal reduction in the amplitude of its SCA cycle (Figure 7.08c) as its annual maximum shows a slight reduction and its annual minimum a slight increase. These limited changes are due to the relatively muted magnitudes of winter warming and summer cooling specified under the observation-led scenario for the Astore (PMD) station used to drive the VICwCDiP model for these catchments (see Chapter 6).

Projected changes to LST similarly muted for both catchments (Figures 7.07d and 7.08d). Again, this is linked to the calculation method described in section 7.5.1 and the limited magnitude of air temperature change in the scenario. Nevertheless incremental changes are discernible with gradual warming from late Winter (February) through mid-Spring (April) culminating in large and significant – projected first decile (c10) exceeding historical last decile (d90) – warming in May. In June and July, however, projected LST returns to historical levels, while August shows substantial cooling. Projected LST in other months under the observation-led scenario is indiscernible from the present (MODIS) climatology. It should again be pointed out that this scenario may underestimate likely changes in LST as the methodology used does not incorporate radiative effects linked to changes in cloud cover (which could be partially inferred from projected changes in precipitation frequency). Hydrologically speaking it is the changes to the radiation variables which are important as they supply energy for evapotranspiration and meltwater generation – while LST for the purposes of the present study is largely symptomatic rather than causal.

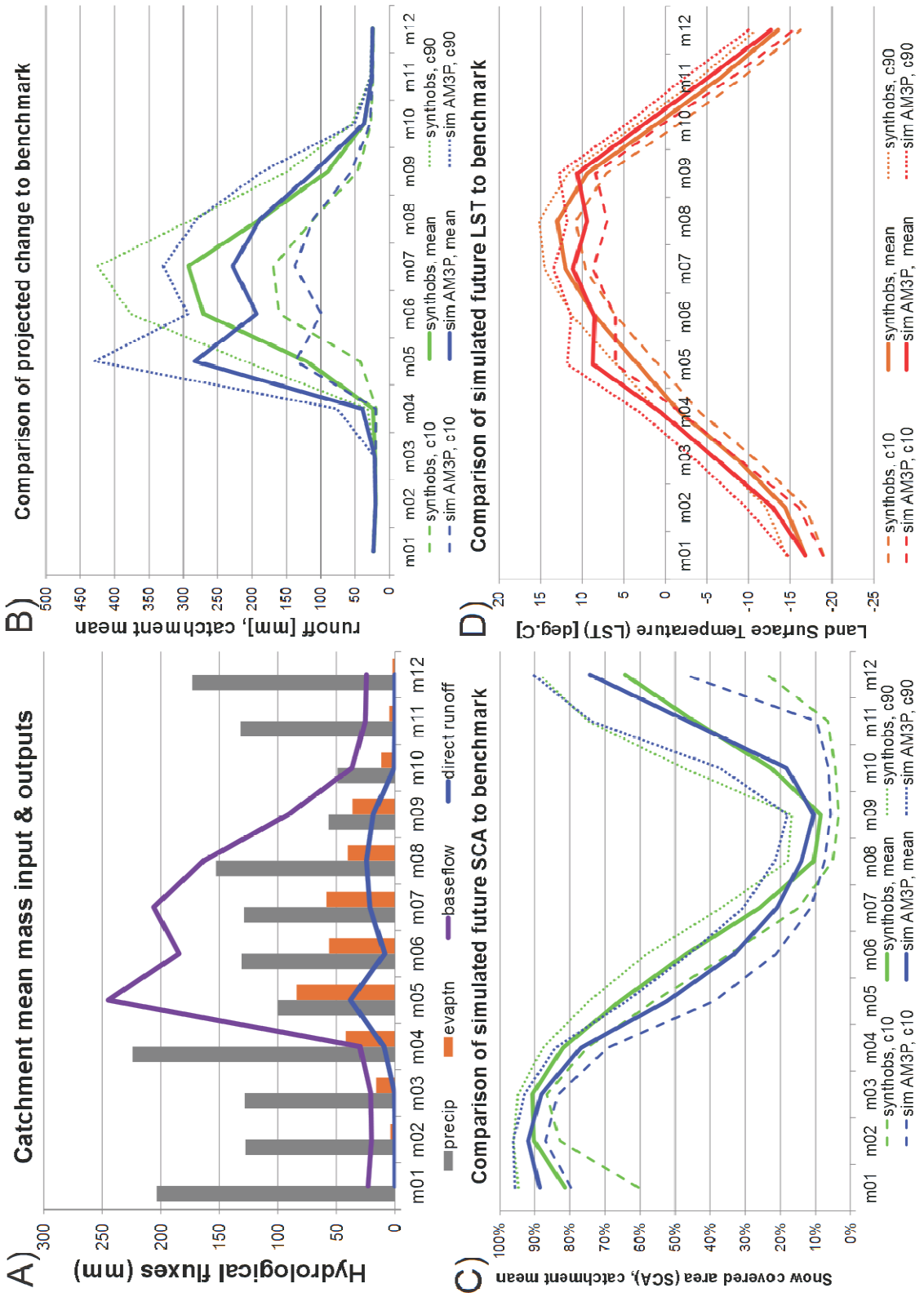

Figure 7.07 Annual cycles from hydrological modelling of climate scenario extrapolated from local trends (PMD) for the Astore catchment. “c10” and “c90” respectively refer to the first and last deciles of the available record for the given variable and data source.

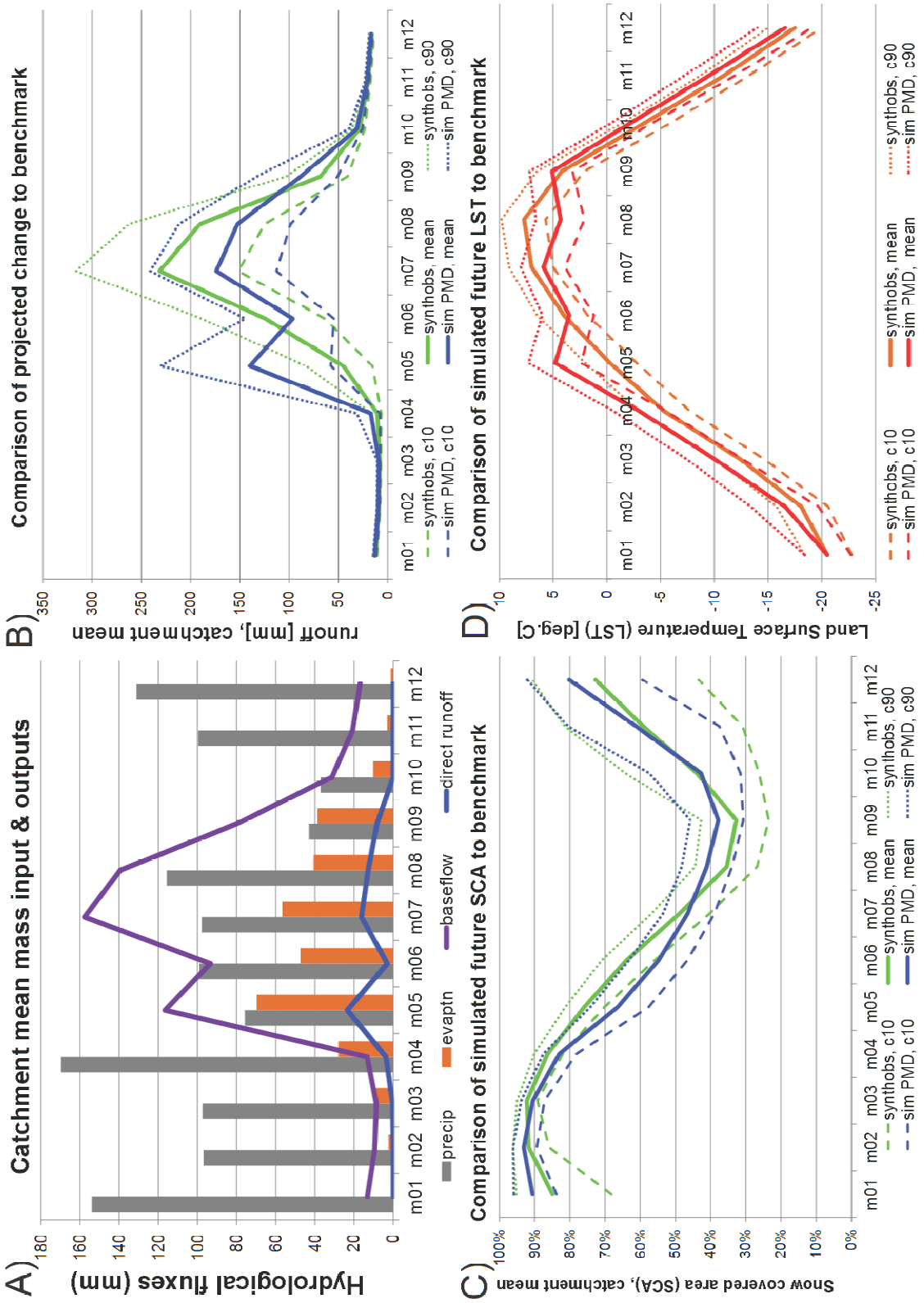

Figure 7.08 As for Figure 7.07 but for the Hunza catchment.

7.5.3 Flux trajectories over 300-year simulations of future scenarios

The divergent projections for Summer energy inputs – as indexed by near-surface air temperature – have profound implications for glacial mass balance in both catchments. These impacts can be seen in trajectories of glacial mass and glacial area (catchment fraction) shown in Figures 7.09 to 7.12. It is difficult to envision more striking differences in glacial mass balance fate than those seen when comparing the glacial volume trajectories projected by the contrasting scenarios. The RCM-driven scenario results in near total deglaciation of the nival regime in the Astore catchment and in the transformation of the glacial regime Hunza catchment into a nival regime catchment with only a small fraction of its present glacial cover. For the scenario extrapolated from observed trends, the glacial volume trajectories are visually quite similar to those found in the baseline control climate simulations, albeit with accelerated rates of mass gain, i.e. millimetres increase per year of IWE.

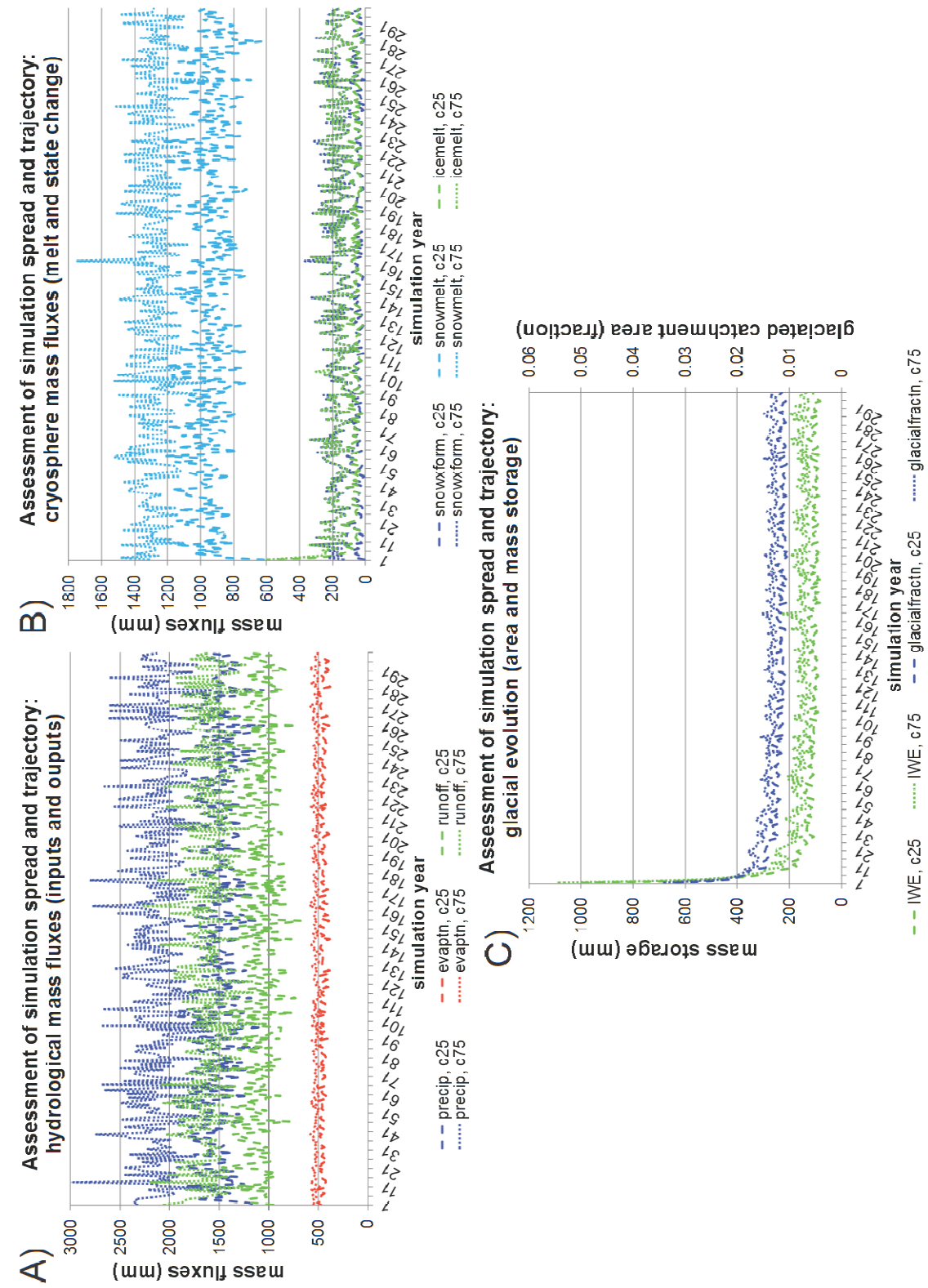

Figure 7.09 Trajectory and spread of results hydrological modelling of RCM-based (PRECIS_AM3P) climate scenario for the Astore catchment

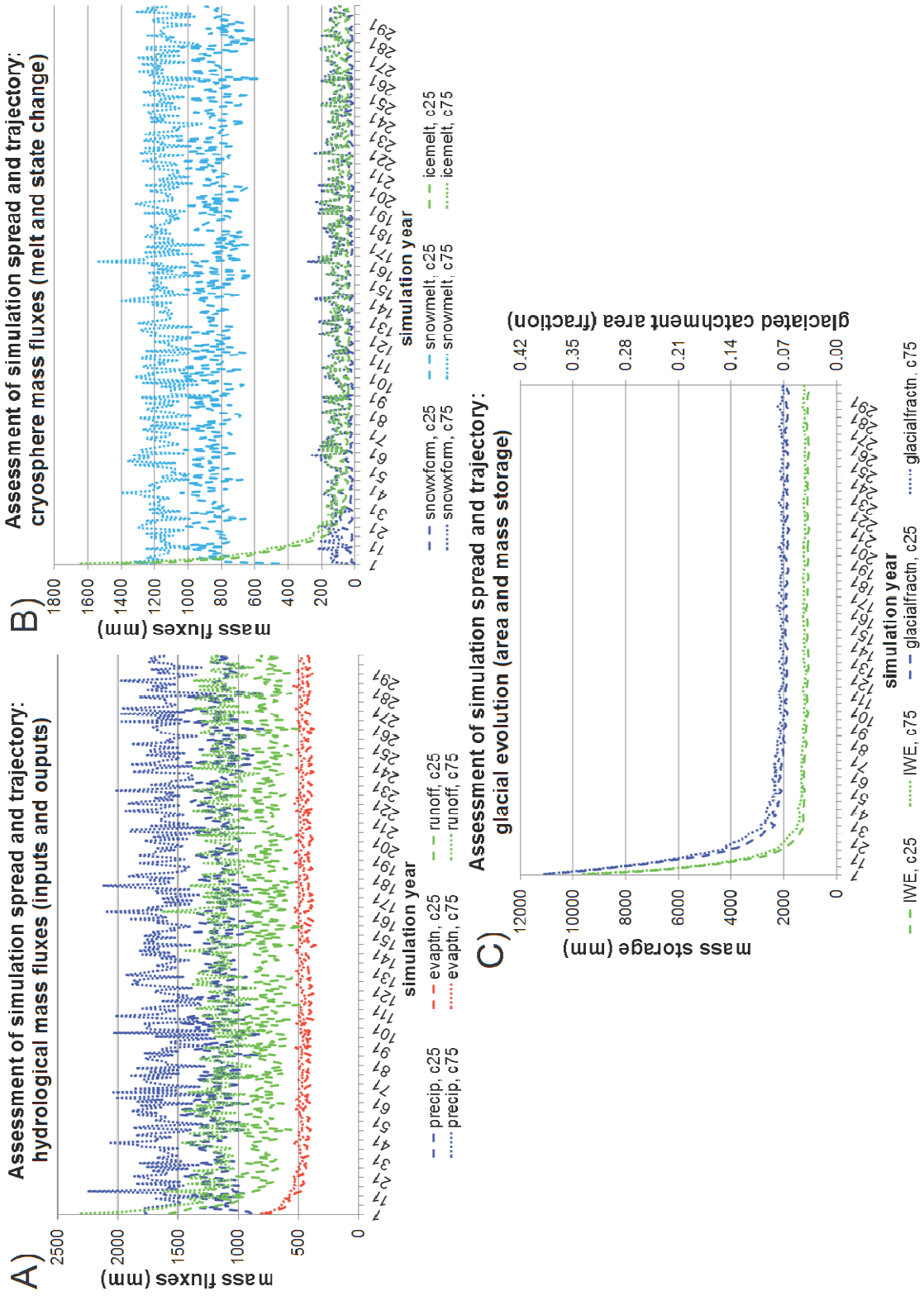

Figure 7.10 Trajectory and spread of results hydrological modelling of RCM-based (PRECIS_AM3P) climate scenario for the Hunza catchment.

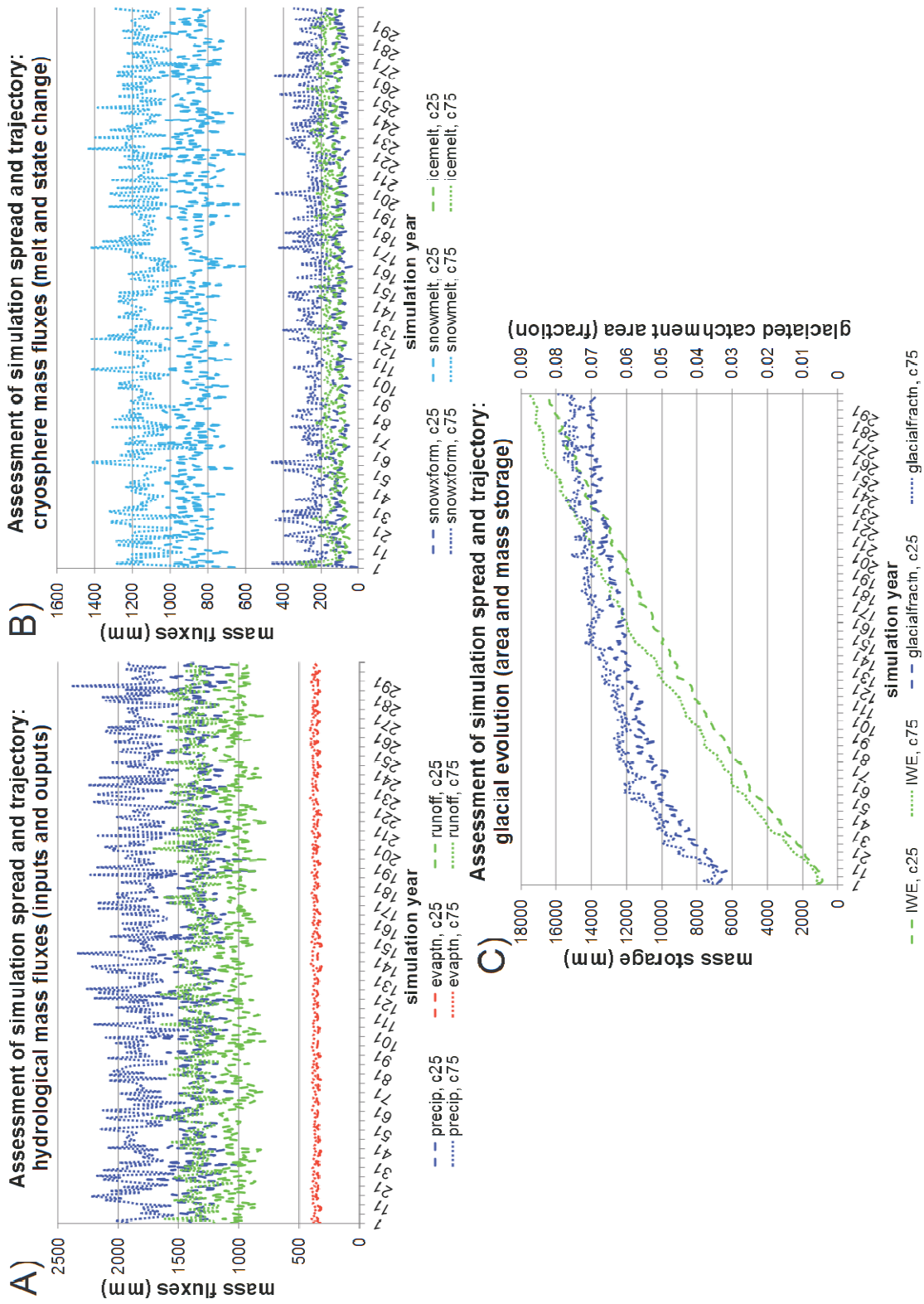

Figure 7.11 trajectory and spread of results hydrological modelling of the “observation-led” future climate scenario (extrapolated from local trends [PMD]) for the Astore catchment.

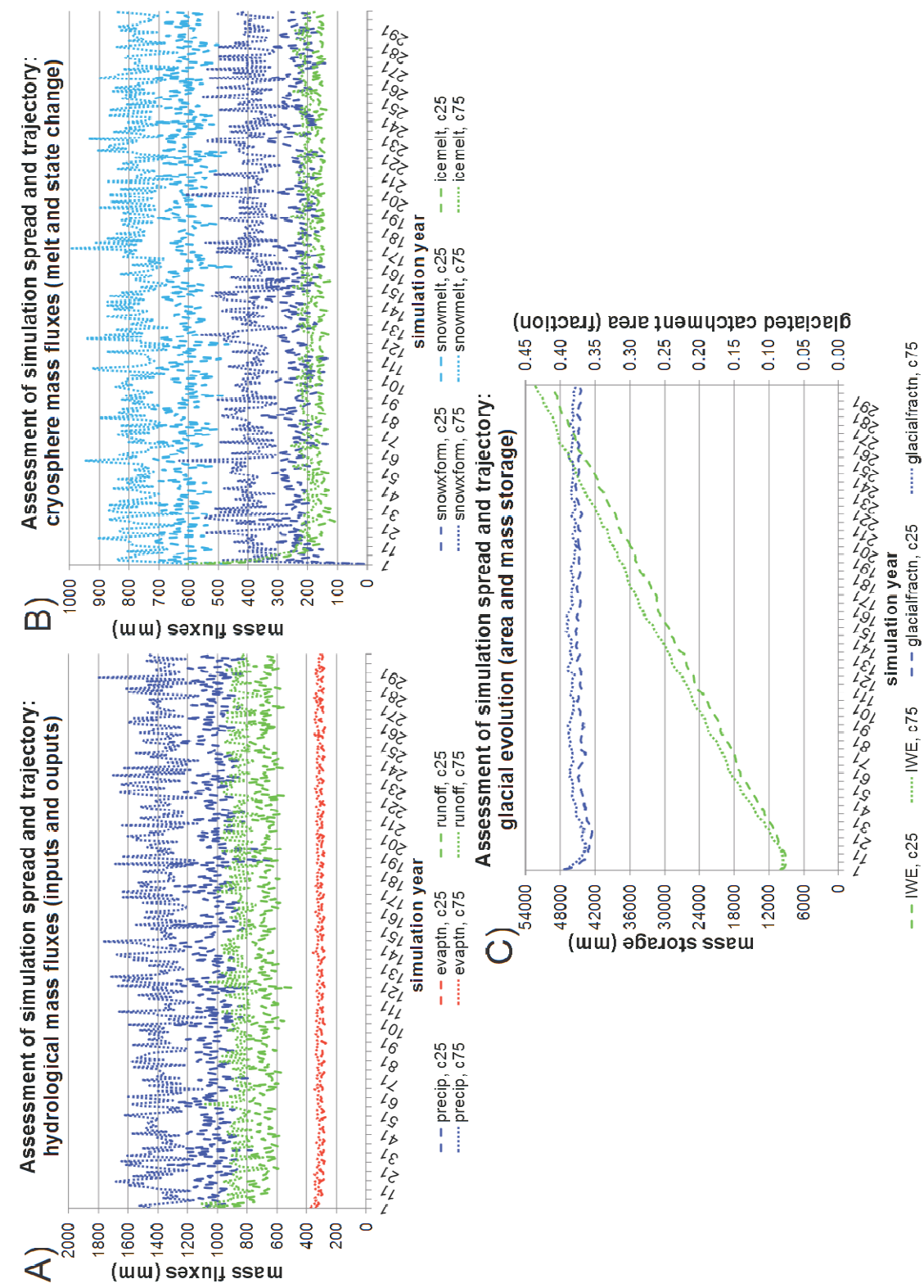

Figure 7.12 Trajectory and spread of results hydrological modelling of the “observation-led” future climate scenario (extrapolated from local trends [PMD]) for the Hunza catchment.

7.5.4 Comparison of results from the two scenarios

In order to provide scale independent metrics of projected hydrological state relative to the present conditions, as well as to separate any underlying bias in the hydrological model from the simulated future conditions, the projected relative changes (the difference between the control and future simulations for the VICwCDiP model) were calculated. These are, as is common practice, presented as ratios for hydrological variables and differences for temperature. The projected changes from the simulation results for the Astore and Hunza catchments can be seen respectively in Figures 7.13 and 7.14.

As explained in Chapter 6, due to the utility of the Astore PMD precipitation record, both catchments were simulated using time-series based on that location as a base station, albeit with individual calibrated orographic precipitation gradients. For that reason the projected changes for input precipitation and air temperature are identical for the two catchments (Figures 7.13 and 7.14, panels A and D). Seasonal aggregates of the monthly change factors were presented above in Table 7.2 (section 7.5).

It is for the same reason that the change factors, shown in Figures 7.13 and 7.14, for the output variables – actual evapotranspiration (AET) [panel B], land surface temperature (LST) [panel E], SCA [panel F] and total runoff [panel C] – also appear relatively similar between the two catchments. This is despite the present difference in hydrological regime of the two catchments: Astore is a nival catchment while Hunza is currently a glacial catchment.

The contrast between the scenarios in projected changes to Summer temperature drives strikingly different catchment responses in terms of the annual snow cover cycle. The Summer air temperature warming of roughly 6°C in the RCM-driven scenario leads to projected substantial reductions (50% or more) in the annual SCA minima of both catchments. This results in the near total ablation of the snowpack in Astore and Hunza, except at the highest elevations. In the local trend-extrapolated scenario, however, the limited Summer cooling results in minor increases in annual SCA minima.

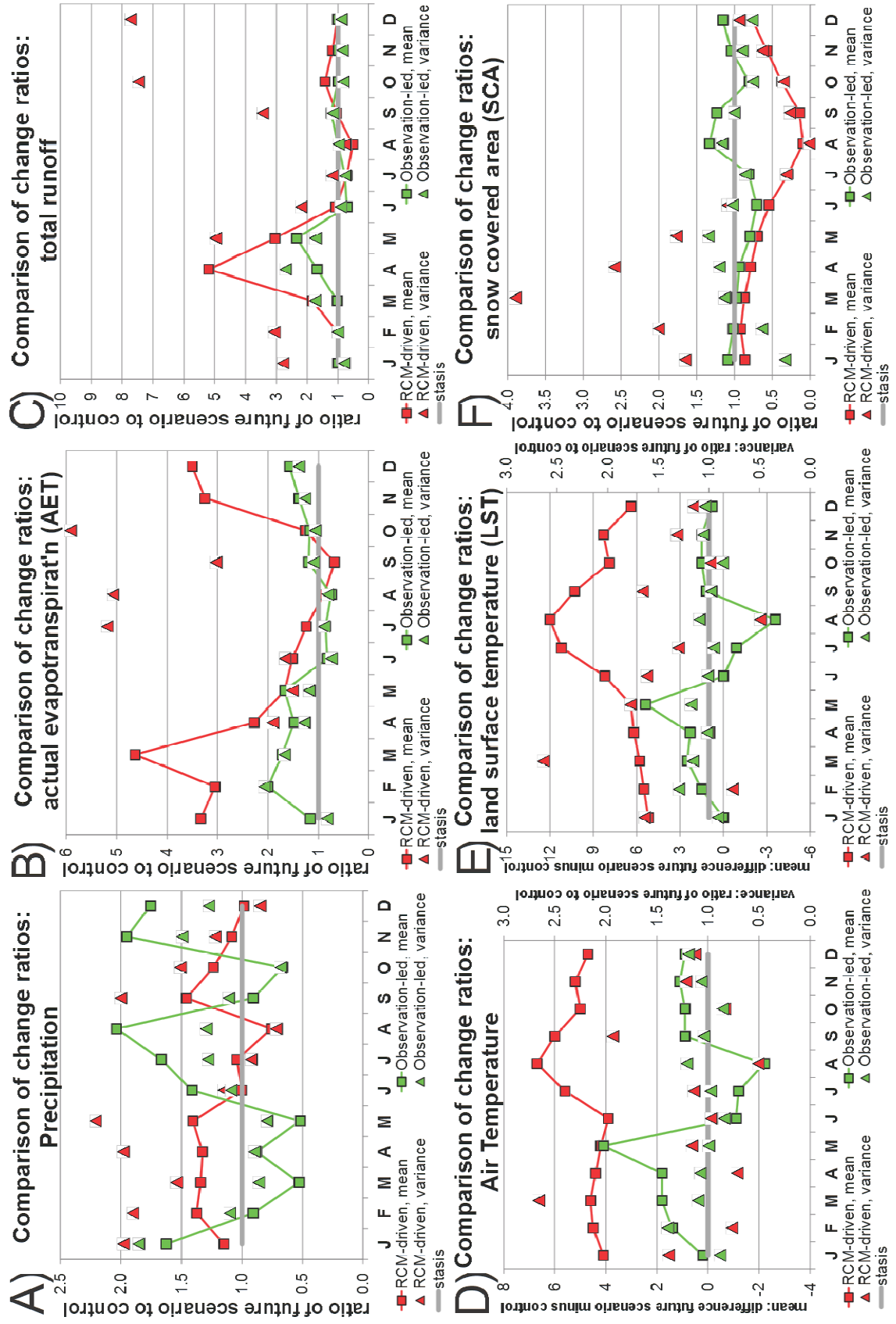

Figure 7.13 Relative changes for hydro-climatological variables calculated between the defined future scenarios and the synthetic baseline for the Astore catchment

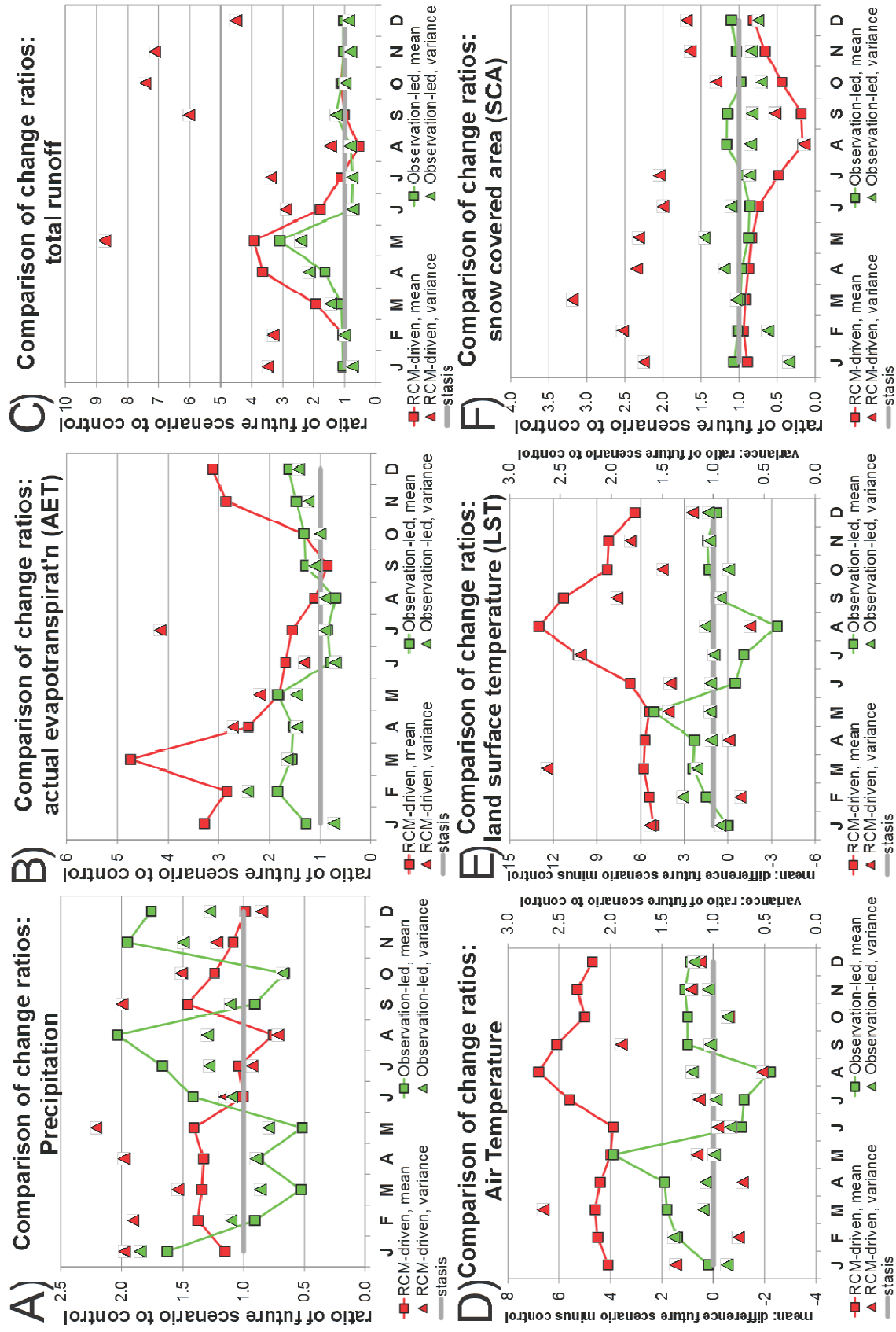

Figure 7.14 Relative changes for hydro-climatological variables calculated between the defined future scenarios and the synthetic baseline for the Hunza catchment

While the patterns of monthly changes shown in Figures 7.13 and 7.14 show complex, asymmetrical patterns of change, the changes in annual totals of key hydrological fluxes and in mean annual values provide more easily understood summaries of net hydrological impacts of the modelled scenarios. These relative changes are shown for Astore and Hunza catchments in Figures 7.15 and 7.16 respectively.

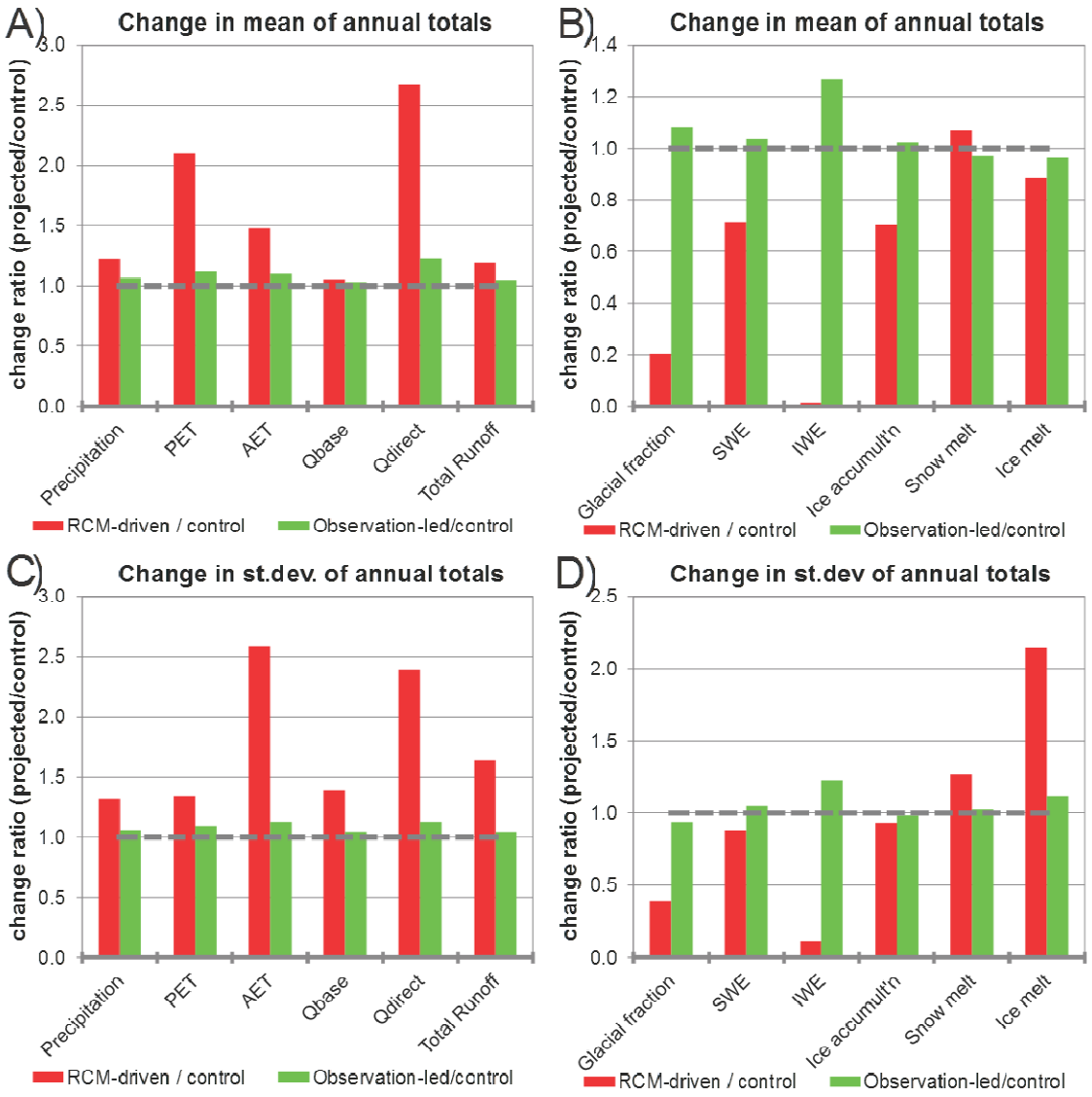

Figure 7.15 Relative changes in annual totals (or means) for hydro-climatological variables calculated between the defined future scenarios and the synthetic baseline for the Astore catchment. Qbase refers to runoff as stream baseflow while Qdirect refers to direct (Hortonian overland) runoff.

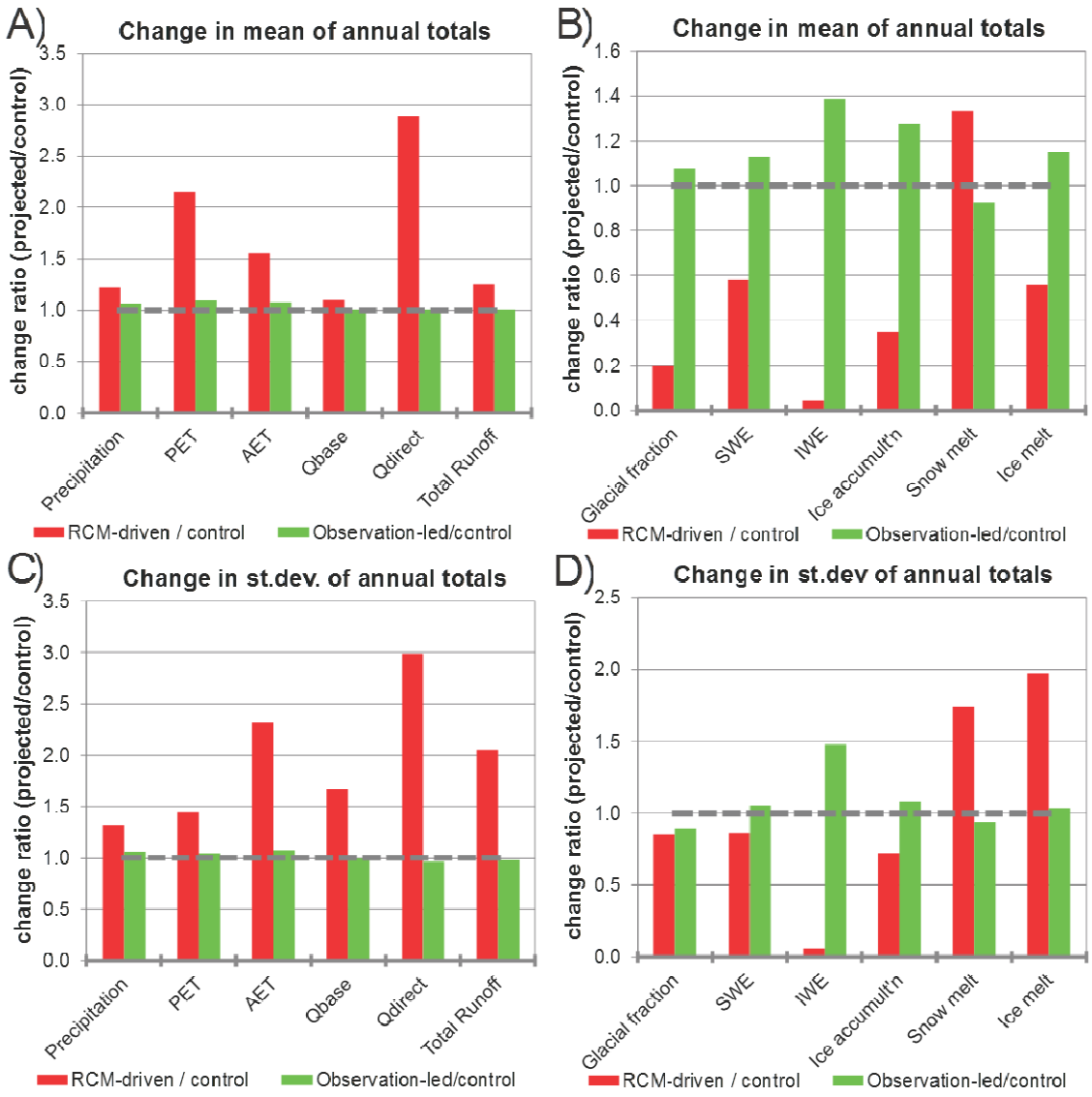

Figure 7.16 As for Figure 7.15 but for the Hunza catchment.

The overall pattern that emerges for changes in the means and standard deviations of annual totals for key hydrological fluxes is one of contrast between the conditions projected by the two modelled future climate scenarios. The RCM-driven scenario – derived from PRECIS_AM3P 2080s – projects sharp increases in fluxes related to energy or intensity of hydrological processes including both PET and AET as well as direct (Hortonian overland) runoff (Qdirect). The increases in PET and AET clearly linked to the projected increases in air temperature which serve to define the RCM-driven scenario. The increase in direct runoff would result from greater influx of moisture at the soil surface, particularly when the upper soil layer is already near saturation. This influx could result either from intense liquid precipitation – if air temperatures are warm enough for precipitation to occur as rain rather than snow – or rapid melting of seasonal snowpack or glacial ice due to large energy inputs. Thus the simulated results of the RCM-driven scenarios for both the Astore and Hunza

catchments track with the general global expectation of intensification of the hydrological cycle (e.g. Frei et al. 1997, Ziegler et al. 2002, Alessandri et al. 2012). In contrast, the observation-led scenario – derived from extrapolated trends – projects relative overall stability (limited change) in total hydrological fluxes despite the substantial changes in seasonality of melt process and runoff described in the preceding paragraphs and sections.

Similarly, the observation-led scenario also projects relative stability in key cryospheric state variables (annual averages) and fluxes (annual totals), while the RCM-driven scenario yields radical changes in these variables. Most strikingly, the RCM-driven scenario projects the essentially complete deglaciation of the Astore catchment and massive deglaciation in the Hunza catchment as can be seen in change ratios for ice water equivalent (IWE). The latter is effectively transformed from a glacial regime catchment to a nival regime catchment (see Chapter 3, section 3.4.1). For both catchments this deglaciation is accompanied by substantial reductions of seasonal snowpack as measured in snow water equivalent (SWE).

While not all of the projected changes appear alarming at first glance, especially in terms of projected future mean annual runoff, caution is to be urged against optimistic interpretation of these results. In the case of the observation-led scenario, the methodology used here is not sophisticated enough to assess the risks potentially associated with rapid high elevation mass accumulation. Such risks might include increased avalanche activity or debris flows triggered by occasional intensity melt events. Either of these phenomena could, in turn, lead to temporary damming – by ice or rubble – of tributary reaches and subsequent potentially devastating outburst floods.

Furthermore the method of extrapolation of trends to construct the observation-led scenario is excessively simplistic. Once again, this scenario was developed due to the contradiction between the nearly uniform changes in near-surface air temperature projected in the RCM-driven scenario with the seasonally and diurnally asymmetrical trends found in the available records of both local observations as well as meteorological reanalyses (ERA-40 and ERA-Interim). Conceptually it would seem likely that the local patterns of change, principally cooling of summer night-time temperatures (Tmin) would eventually be overwhelmed by the “global climate signal” of widespread warming due to increasing atmospheric concentrations of greenhouse gases. This expectation carries the caveat that the temperature trends in recent decades have been dominated by local mechanisms independent of, rather than driven by,

broader patterns of global change. If this is indeed the case, then it would seem likely that probable future UIB climate conditions will lie somewhere between the bounds suggested by the two scenarios presented here. Section 5.6 presented further discussion on potential methodologies for development of additional (intermediate) future climate scenarios for the UIB. Given the prevailing scientific uncertainty decision makers responsible for water resources planning and infrastructure operations would do well to indentify capital investment opportunities and resource management systems which perform well under the range of potential hydrological conditions bounded by scenarios presented in this Chapter. This type of strategy is coherent with the "low regret" approach advocated by Heltberg et al. (2009) and Wilby and Desai (2010).

7.6. Uncertainty from model stochastic "natural" variability

As has been described previously, long (3000-year) daily synthetic time-series were generated and broken up into 300-year segments to simulate potential glacial volume trajectories. Whilst the reasoning for performing 300-year simulations was to investigate for long-term patterns in glacial response to climate forcings, the methods used to derive the future climate scenarios here do not provide "transient evolution" of climate conditions, but rather stochastic descriptions of changed yet stationary climate conditions. Furthermore, the fundamental purpose of the long synthetic time series is not to simulate consecutive centuries of climate, but rather to more fully explore the range of variability in potential climate conditions and in so doing quantify the related hydrological outcomes which could occur over a shorter time period or "climatic normal" (usually 30 years) more appropriate to infrastructure planning.

To this end, each of the ten 300-year simulations for each modelled climate scenario were split into 30-year blocks. The first two 30-year blocks from each 300-year simulation were excluded to remove residual effects of the specified glacial initial conditions (model spin-up or time taken for glacier component of the model to equilibrate). The remaining eighty (8 x 10) 30-year blocks were then analysed to determine summary statistics – mean and standard deviation – of annual characteristic values (totals or averages as appropriate to each variable) for the 30-year period in question. In other words, each scenario yielded eighty potential values for each statistic (30-year mean and 30-year standard deviation) of annual hydrological fluxes and state variables. The distribution of this sample of eighty values for each statistic was then analysed to produce the results presented in this section.

The results of this procedure are given in the “box plot”-style graphs in Figure 7.17 for key hydrological fluxes as well as cryosphere state and flux variables.. Absolute values were examined to enable comparison not only within the distribution for an individual variable, e.g. 5^{th} percentile of precipitation versus 95^{th} percentile of precipitation, but also between variables, e.g. precipitation versus total runoff. For reference the values used to compose Figure 7.17 are given in tables in Appendix E. Interestingly the relative changes in the various descriptors – median, 5^{th} and 95^{th} percentiles – of the statistical distribution of the fluxes are for the most part nearly indistinguishable from the relative changes in the mean values which were shown in Figures 7.15 and 7.16. The details of the relative changes to these descriptors are provided in tables in Appendix E.

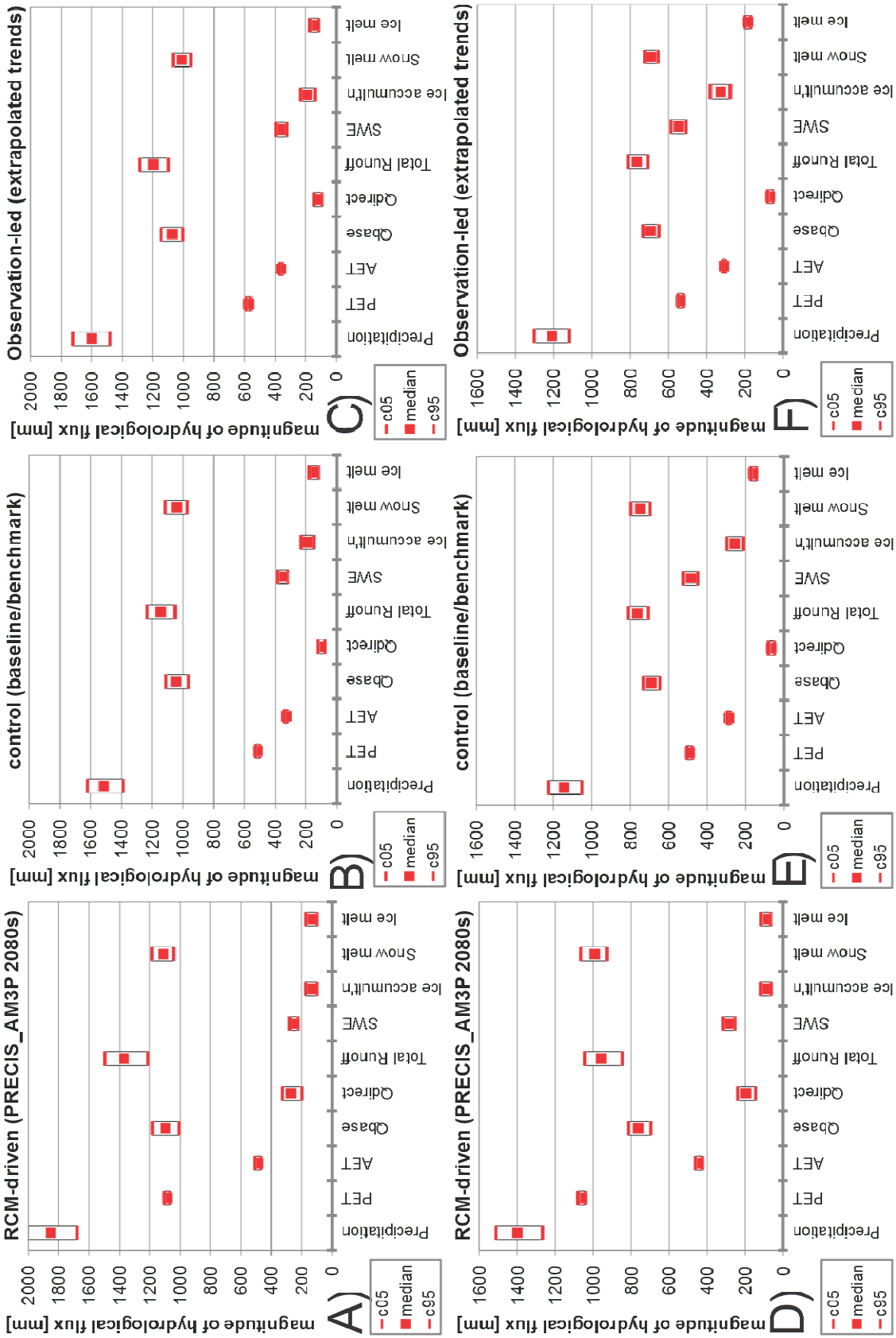

Figure 7.17 “Box-plot” style presentation of projected annual totals for key hydrological fluxes and mean cryosphere states for the Astore (panels A to C) and Hunza catchments (panels D to F). Panels A & D show results for the “RCM-driven” scenario, and panels C & F show results for the “observation-led” scenario. Panels B & E show the control (baseline) results for comparison. Qbase refers to runoff as stream baseflow while Qdirect refers to direct (Hortonian overland) runoff. Values are all expressed in millimetres.

Figure 7.17 show some key points with regard to future hydrological fluxes:

- Mean annual total runoff from the RCM-driven scenario (PRECIS_AM3P 2080s) is projected to be substantially greater than in the control simulations for both Astore and Hunza, albeit with some overlap between the 95th percentile for the baseline and the 5th percentile for the RCM scenario. For Astore the absolute median increase is 226mm (~+20%) whilst for Hunza the increase is 194mm (~+25%).
- Interannual variability in annual total runoff, as quantified by the standard deviation of annual values within a 30-year block, is substantially greater in the RCM scenario than in the control simulations for both Astore and Hunza. For Astore the absolute median increase in the standard deviation is 161mm (~+70%) whilst for Hunza the increase in the standard deviation is 157mm (~+100%).
- For both Astore and Hunza, mean annual total runoff values projected from the observation-led scenario and the control simulation are almost statistically indistinguishable (median projected changes of less than 5%). The same is true of standard deviation of annual total runoff which both for both catchments is also projected to be within 5% of the control simulation.
- Although mean annual total runoff in the RCM scenario is projected to increase compared to the control simulation, actual evapotranspiration (AET) is also projected to increase. In this scenario the ratio of future AET to control AET – 1.47 for Astore, 1.55 for Hunza – is substantially greater than the ratio of future annual total runoff to its control value (1.19 for Astore, 1.25 for Hunza). This is a potential concern considering that runoff from the Upper Indus is impounded at Tarbela reservoir and then used to water the vast irrigated plains in the lower Indus. If AET in the irrigation command areas increases in line with that projected for the UIB, even increased runoff may be inadequate to compensate for the shortfall. Detailed analysis of this issue is, however, beyond the (geographical) scope of the present study.
- Further, although under the RCM-driven scenario, the ratio of future AET to control AET is only about 1.5, future potential evapotranspiration (PET) is projected to more than double: the ratio of future PET to control PET is 2.10 for Astore and 2.15 Hunza. This indicates that soil moisture is a dominant constraint in the relatively humid UIB under projected future conditions (as AET is less than PET). This simple but striking comparison adds urgency to the need to

accurately assess future irrigation demand in the areas served by the Indus Basin Irrigation System.

- While some compensation of increased AET could be hoped for from increased mean (local) precipitation, given that any changes in precipitation amount are expected to be accompanied by even greater changes in interannual precipitation variability this element of the evolving water balance seems likely to further exacerbate supply-demand imbalances rather than to ease them.

Figure 7.17 also shows some key points with regard to the projections of cryosphere variables:

- The trajectories of glaciated area (catchment fraction) and glacial mass have already been commented on earlier in this Chapter, but the numerical values of mean glaciated fraction clearly show the similarities in the results of the observation-led scenario and the control simulations as well as their contrast to the deglaciation projected under the RCM-based scenario.
- With regards to glacial mass balance conditions, for the control simulations as well as for the scenario extrapolated from observed trends, the net mass balance is largely positive for the both Astore and Hunza catchments. For Astore the median estimates of net mass balance yield increases of 39mm per year (190mm accumulation minus 151mm melt) and 48mm (193mm accumulation minus 145mm melt) respectively for the control simulation and observation-led scenario. For Hunza the median estimates of net mass balance yield increases of mm per year (256mm accumulation minus 161mm melt) and 141mm (326mm accumulation minus 185mm melt) respectively for the control simulation and observation-led scenario.
- In contrast, the glacial mass balance in the RCM-based scenario is very nearly zero for both the Astore and Hunza catchments with differences of less than 2mm for both catchments between median estimates of ice accumulation and ice melt. This is because over the long simulations, following the initial rapid deglaciation the catchments reach an effectively steady-state where any annual accumulation of firn ice – through densification of the snowpack in late winter – is ablated the following summer.
- Thus the divergence in projected mass balance between the two scenarios reveals the present scientific uncertainty regarding the fate of UIB glaciers. As

the RCM-driven scenario shows unequivocally, if projected intense summer warming occurs massive reductions in glacial mass and extent will result. If, however, the cooling of summer air temperatures in the UIB (described in Chapter 4) is in fact an unexpected consequence of feedbacks driven by larger-scale global climate change, and as such likely to continue over the next few decades, then UIB glacial volumes appear likely to remain stable or increase. In the event of severe summer cooling runoff from UIB tributaries could be substantially decreased in the absence of adequate energy to drive meltwater generation processes.

- Another element of interest with respect to the RCM-driven scenario is that, as expected rising temperatures year-round, total snowmelt is projected to increase substantially. This is not only due to the projected increase in temperature but also because, as shown in Figures 7.13 and 7.14, precipitation is projected to increase substantially under this scenario in late Winter (February) through Spring (May). Even with the strong warming specified in this scenario, air temperature conditions in large portions of the modelled catchments will remain cold enough that the bulk of this additional precipitation will fall as snow rather than rain. Subsequent melting of this increased snowpack is projected to be rapid due to the increased energy input (indexed by air temperature).
- The difference between the two catchments in the relative magnitude of this increase under the RCM-driven scenario is intriguing. While a projected annual precipitation increase of 22% was applied to both catchments, for Astore the increase in future snowmelt is only 7% while for Hunza snowmelt increases 32%. This difference may be because the transfer of baseline ice accumulation to future snowmelt is less in the Astore catchment than in Hunza. Alternately it could be that a greater fraction of the precipitation increase in Astore is falling as rain than in the Hunza.
- In contrast to the increasing snowmelt projected by the RCM-based scenario, the observation-led scenario projects a slight reduction in snowmelt despite a limited increase in annual precipitation. This reduction – of roughly 3% for Astore and 8% for Hunza relative to the control scenario – is attributed to the reduction in available summer inputs of melt energy. The difference in relative reductions may be explained by lower mean elevation of Astore catchment where increases in May air temperature under the observation-led scenario may better offset the summer cooling. In contrast much of the Hunza catchment

surface will still be experience below-freezing conditions in May and thus marginal warming in that month will yield more limited increases in snowmelt.

- A further noteworthy item in terms of cryospheric variables is the contrast in the ratio of ice melt to snow melt seen both in the different scenarios and in the two catchments. For the Astore catchment, the differences in the ratio of ice melt to snowmelt between the scenarios are relatively muted. The (median projections of) ice melt to snow melt ratios for the three simulations were 0.145, 0.118 and 0.143 respectively for the control, RCM-driven and observation-led scenarios. This limited range is perhaps because Astore is already a nival regime catchment with only limited ice melt but substantial snow melt. For the Hunza catchment the drastic reduction in the ratio of ice melt to snowmelt under the RCM-based scenario – 0.089 projected ratio compared to 0.215 in the control simulation – is in stark contrast to the moderate increase in the ratio (0.266) under the observation-led scenario. The reduction under the RCM-based scenario is understandable given that the catchment is projected to change from a glacial to nival regime under the future climate. The increase in the ratio under the extrapolated trends scenario is, however, thought to occur due more to the larger relative reduction in annual snowmelt caused by input energy constraints (Summer cooling) than to the moderate projected increase in ice melt driven by a strong increase in annual ice accumulation.

In summary the simulation of contrasting scenarios of future climate using the detailed assessment of cryospheric processes as well as hydrological fluxes enabled by the VICwCDiP model clearly illustrate the present uncertainty for both hydrological and glacial conditions depending the specific trajectory of future local climate change in the UIB. These simulations have particularly illustrated the delicately balanced interplay between mass (precipitation) and energy (temperature) inputs to the UIB hydrological system.

7.7 Grid cell level consideration of glacial trajectories

The use of long synthetic time-series for hydrological modelling and cryosphere simulation provide an opportunity to study not only catchment average-scale responses but also glacial behaviour at the grid cell level. Individual grid cells have different sub-grid distributions of elevation and slope, but for the grid cells examined in detail for in each of the three scenarios the cryosphere variables quickly tend toward roughly, if

dynamic, equilibrium states. As at the catchment level, for both the Astore and Hunza grid cells the RCM-driven scenario is confirmed as resulting in eventual deglaciation. In contrast the control time series and the scenario extrapolated from local trends show similar patterns, with nuances in magnitude, of relatively stable glacial volume and movement in the higher elevation bands although melt-out is still rapid and complete in the lower bands.

These results are shown in detail in Appendix E where figures show the results of the first 300-year subset of each of the three synthetic time series for the example grid cells used in Chapter 6. Each figure shows annual means of the glacial mass and the ratio of glacial cover in each elevation band as well as annual totals for glacial displacement (by sliding) and net mass transfer (inward/receiving from above = positive, outward/discharge to below = negative).

To summarise briefly, however, the calibrations of the VICwCDiP model for the Astore and Hunza tributary basins presented in Chapter 6 characterised both catchments – in terms of "degree-day factors" for calculation of snow and ice melt – as highly responsive to changes in mass (precipitation) and energy (temperature) inputs. Thus, modelled glacial volumes in individual grid cells expanded or receded rapidly depending the mass balance state determined by the simulated conditions.

As such the present study strongly indicates the urgency of improving characterisation of spatial gradients and variability in mass (orographic precipitation) and energy (temperature lapse rates). Without accurate quantification of these inputs to the hydrological system, both for historically observed climate and projected future conditions, realistic simulation of likely glacial mass trajectories is infeasible. If the uncertainty regarding the spatial and temporal variability in these inputs can be reduced, then additional spatially detailed information regarding present glacial volume and topography of UIB glaciers would become relevant in efforts to forecast short and medium-term glacial responses to climate variability as well as associated impacts for UIB hydrology. Such information would most probably be provided by a combination of ground investigations and remote sensing imagery.

7.8 Discussion

This chapter has focused on the implications for hydrology and the cryosphere for two starkly contrasting scenarios (presented Chapter 5) of plausible future UIB climate. These implications were calculated using the hydrological model described in Chapter 6. The divergent futures for hydrological and cryosphere variables depicted by the results of the two scenarios are of considerable interest as has been presented in this chapter. The most striking differences between the results of the two scenarios are:

- The massive and rapid deglaciation of both the Astore and Hunza catchments projected under the RCM-driven scenario in contrast to the increasing glacial mass projected under the observation-led scenario.
- The substantial increases in the magnitude of all hydrological fluxes not only in terms of mean values but also especially in terms of interannual variability projected by the RCM-driven scenario in contrast to relative stability in annual total fluxes projected under the observation-led scenario.
- Both scenarios do, however, coincide regarding substantial shifts in the seasonality of meltwater-driven hydrology with accelerated melting in April and May and decreased runoff in the summer season. While the cause of enhanced spring-time melt is strongly warming near-surface air temperatures in April and May under both scenarios, the causes of summer melt reductions are conflicting. Under the RCM-driven scenario decreases in snow and ice melt are due both to early ablation of snowpack (and deglaciation) as well as increased fractions of precipitation falling as rain, even at high elevations, due to severe summer warming. Under the observation-led scenario in contrast, the reduction in summer melt is caused by energy input constraints -- indexed by near-surface air temperature – which result in the aforementioned positive glacial mass balance. Thus while the simulated impacts on the UIB cryosphere under the two scenarios are diametrically opposed, both sets of model results are in fact internally consistent in their hydrological response to starkly contrasting climate forcings.

Although at first glance the hydrological results of the RCM-driven scenario are reassuring, from a perspective of absolute water availability, in terms of projected increases in mean annual runoff, the potential implications of increased evapotranspiration in the irrigation demand areas supplied by the Indus serve to alter the

context in which increased runoff is understood. Far from suggesting increased net water availability, under a scenario projecting substantial warming in irrigation service areas, increased runoff will be desperately needed simply to offset increased crop water demand and maintain crop yields.

Potentially equally confusing, but less worrying, the rapidity of deglaciation simulated under the RCM-driven scenario may be exaggerated. In each of the ten 300-year simulations performed for both the Astore and Hunza catchments reductions of glacial area (-80%) and mass (-90%) were modelled to take place in a matter of decades, i.e. between 20 and 60 years, following the abrupt changes imposed by the model in the simulation driven by the time-series of future climate. The sudden changes in air temperature and precipitation imposed on simulated "present day" glacial volume and extents is analogous to a hypothetical geophysical event resulting in a "step change" in prevailing conditions. There are two primary reasons why the severe and rapid simulated deglaciation may be exaggerated:

1. If the currently selected values of initial glacial volumes substantially underestimate physical reality, greater mass would be available as a buffer or reservoir during the onset of higher temperatures.
2. The temperature changes projected by a time slice RCM simulation will not occur as a step change as applied to the catchment models in the present study, but will rather follow a trajectory dictated by anthropogenic forcings coupled with climatic feedbacks (e.g. methane releases or cloud radiative forcings changing through evolving cloud climatologies). Thus real changes are expected to occur more gradually than those calculated in the initial stages of the synthetic time series simulations.

Additional elements might also bias the model to either overestimate or underestimate ice melt and glacial mass balance:

- A substantial level of statistical uncertainty is expected in the calibrated values of melt parameters (energy input modulation) and orographic gradient (mass input). The constraints of the present project did not permit a rigorous exploration of this uncertainty.
- In the simplistic approach applied in the present study, while climatic means and variability were perturbed to create the synthetic time series used to drive the model, the spatial distribution was left unchanged. It is physically reasonable, however, to expect that causal mechanisms which drive changes in

precipitation and air temperature would also modify temperature lapse rates and the shape of orographic precipitation gradients. Unfortunately, the data sources used to define the future scenarios did not provide the level of spatial information necessary to assess the necessity or form of any elevation-driven or other catchment-scale changes to the spatial distribution of climate variables.

Despite these limitations, the results presented here are considered to provide a substantial contribution to understanding of potential glacial mass trajectories in the UIB in the coming decades. This study represents a substantial improvement in the sophistication and realism in the simulation of large-scale UIB hydrology with regards to previous studies (e.g. Akhtar *et al*., 2008; Immerzeel *et al*., 2009 and Bocchiola *et al*., 2011) where changes in glacial mass and volume were deterministically specified rather than being evaluated for plausibility in terms of mass balance. These previous studies also did not constrain the contributions of glaciated areas in terms of "conservation of mass". Instead the melt-calculation methodologies employed by the three studies cited here allowed glaciated areas to effectively act as "infinite sources" constrained only by available energy (indexed by air temperature).

The work presented in this chapter represents original and meaningful additions to the understanding of potential impacts of climate change on UIB hydrology not only in terms of the sophistication and realism of the methodologies used for simulation of cryospheric processes, but also by its consideration of contrasting future climate scenarios. Whilst the previously cited studies (Akhtar *et al*., 2008; Immerzeel *et al*., 2009 and Bocchiola *et al*., 2011) each considered a single scenario with relatively uniform increases in precipitation and air temperature, the work described in this thesis recognised the differences between projections of future climate by available RCM simulations (e.g. PRECIS_AM3P 2080s presented in Chapter 5 of this thesis) and the trajectories suggested by assessment of recent trends in both local observations and meteorological reanalysis (see Chapter 4 of this thesis).

Whilst the contrasting future climate scenarios – used here to drive the VICwCDiP model for the Astore and Hunza catchments – do not represent ideal projections they do serve together to define potential bounds for future UIB climate and test the sensitivity of the modelled catchments to these contrasting conditions. As such, the RCM-driven scenario shows the likely eventual outcome of strong, sustained regional warming. The observation-led scenario meanwhile helps to understand the

potential implications for UIB hydrology of the perpetuation of the mass-balance dynamics thought to have been occurring in recent decades.

Whilst the present study is squarely oriented toward classical hydrology and water management, there are important water-related impacts of climate change beyond those directly linked to runoff, snow cover and glacial volumes. Food security is likely to be one of the most disrupted elements of human welfare in a warming world as crops are sensitive to available soil moisture as well to energy inputs which can be quantified in a similar “degree-day” approach to that used in the present work. Understanding how projected future climate will affect crop water requirements and productivity/yields is crucial to assessing the socio-economic implications of variable water availability. Future work is envisaged to directly assess these pressing research themes.

Chapter 8: Conclusions

Over the course of this project a number of Indus hydrology-related stories have made headlines in Pakistan and beyond. The most widely reported was clearly the 2010 flooding which affected huge swathes of the country from late July into autumn of that year, inundating vast areas in the irrigated plains along the lower Indus and causing substantial infrastructure damage in the UIB from landslides and debris flows. The flooding and landslides resulted from repeated spatially extensive high intensity precipitation events which, cumulatively, far exceeded mean seasonal totals (Webster et al., 2011). Hong et al. (2011) showed that the magnitude of the precipitation events could be linked to interaction (coupling) between tropical (monsoonal) and extratropical (westerly) circulation. Bhaskaran (UK Met Office, personal communication, 26 Nov 2012) indicated that the monsoonal circulation patterns seen during summer 2011 bear a considerable resemblance to projected future monsoonal circulation regimes seen in outputs from "perturbed physics" ensemble RCM experiments by the UK Met. Office.

Less widely reported internationally, but more frequently occurring in recent years, have been domestic political disputes between Pakistan's provinces over water sharing within the Indus Basin Irrigation System (IBIS). Separately, there are regularly recurring international diplomatic clashes between Pakistan and India regarding the potential impacts of existing and proposed infrastructure on the transboundary Indus and its tributaries in the context of the Indus Waters Treaty of 1960. Thus both domestic and international current political conflicts highlight the already heightened tensions over potential water scarcity in the area served by runoff from the UIB. This is prior to expected decreases in per capita water availability due to demographic growth (Archer et al., 2010).

While the present study was initiated prior to these specific events, the potential risks and challenges from interannual variability in water resources availability, both in scarcity (drought) and abundance (flooding), have been clear for some time and strongly shaped the project's course and structure. It was recognised in the early stages of study that the fundamental characterisation of UIB hydro-climatology required improvement in both temporal and spatial resolution as well as in the range of variables considered. Thus Chapter 3 of this thesis presents a comprehensive – multi-variable and multi-dimensional – portrait of present UIB hydro-climate. It was also clear from the project outset that the patterns of change in precipitation and near-surface air temperature

previously identified in the available historical record of local observations indicated complex processes at work. Chapter 4 documents work to verify and corroborate those initial findings and to investigate potential causal mechanisms. While the available historical record of local observations for both river discharge and meteorological variables anchors understanding of present UIB hydroclimatology, it was recognised that probable future hydrological conditions – driven by local manifestation of global climate change – for the UIB are unlikely to be well represented in this record. Thus Chapter 5 presents the construction of contrasting, plausible scenarios of future climate for the key meteorological variables – precipitation and near-surface air temperature – demonstrated to govern UIB hydroclimatology. In order to translate these future climate scenarios into probable hydrological conditions, it was necessary to identify a hydrological model with adequate land surface, and specifically cryospheric, process representation to accurately simulate the mechanisms of meltwater runoff generation which dominate in the UIB. After months of testing existing software tools, it became clear that the most viable method would be to adapt and program a code implementing diverse approaches into a single model. Chapter 6 describes the construction of the resultant model (VICwCDiP) and the subsequent calibration and validation for two archetypal UIB tributary catchments. Chapter 7 then presents of the results of the VICwCDiP model for the two selected catchments when driven by contrasting future climate scenarios.

8.1 Summary

This study has investigated the hydro-climatological variability of the Upper Indus Basin and the potential implications of climate change for its water resources. The available records of river discharge are limited in both historical length and spatial density. Nevertheless they clearly indicate a complex hydrological system with substantial variability, even under present climate, and unmistakeable sensitivity to variations in both mass (precipitation) and energy (temperature) inputs.

With regards to precipitation, this study considered a wide range of data sources. Large discrepancies between these sources were seen in both monthly and annual (absolute) total accumulations. Some of these differences could be traced to the methodology used for observation or estimation by each data source. Other differences are attributable to the assumed orographic precipitation gradient. Independent of absolute accumulations, the seasonality – i.e. the monthly fractional contribution to

annual totals – indicated three sub-regional precipitation regimes defined by concentrations of peak precipitation in either spring, summer or both. Gridded spatial data sources further supported the existence of multiple sub-regional regimes although the present horizontal resolution is likely inadequate to capture the full complexity of regional patterns.

With regards to temperature, again this study drew upon multiple data sources. In contrast to precipitation, however, there were far fewer discrepancies between these independent measurements and estimates. For the most part, these could be explained by differences in the representative (physical or modelled) elevation associated with the data point. Careful examination of the annual cycles in diurnal temperature range (DTR), however, did reveal a spectrum of temperature response to monsoonal activity concentrated in the months of July and August. At the polar ends of this spectrum – i.e. intense monsoonal activity or complete absence of monsoonal penetration – these could be termed distinct sub-regimes.

In order to support investigations into causal mechanisms driving climate responses in precipitation and temperature, climatologies – mean annual cycles and measures of interannual variability – were developed for relative humidity, cloud descriptive parameters (cloud cover and cloud microphysical properties) and albedo. For similar reasons, global meteorological reanalysis – ERA-40 and ERA-Interim – estimates of regional surface energy balance component fluxes and net residuals were also analysed.

Wherever feasible, vertical gradients were quantified for the climate variables considered and, wherever appropriate, relationships between available indicators of mass or energy inputs to the hydrological system and resultant catchment response were assessed.

In light of the previously identified complexity of trends in the available local historical observational record, evidence of on-going patterns of change and indications of the responsible causal mechanisms at play were of key interest to this study. Results presented here corroborate and strengthen the previously identified patterns of seasonal and diurnal asymmetry of near-surface air temperature change. However, while the sign and magnitude of estimated temperature trends showed only limited sensitivity to the selected analysis window, i.e. choice of start and end years, estimated precipitation trends were greatly influenced by the analysis window. This dramatically illustrates the underlying interannual variability of UIB precipitation and underlines the difficulty in

detecting, much less attributing, changes in precipitation regime in such a climatically variable region.

Returning to the apparently less chaotic, yet nevertheless complex, issue of causal mechanisms for observed near-surface air temperature variability and change, correlations were tested between air temperature datasets and reanalysis estimates of radiative fluxes as well as cloud cover which was expected to play a key role in modulating the surface energy balance. The results of correlation testing revealed inter-variable relationships which were generally coherent with expected responses, notably:

- day-time cloud reducing incoming solar radiation hence reducing net energy balance residuals and daily maximum temperature (Tmax) as well as DTR;
- night-time cloud reducing out-going thermal radiation (though not enough to compensate net energy balance residuals for decreased incoming radiation) and increasing daily minimum temperature (Tmin) and decreasing DTR.

Extremely strong positive correlation between day-time and night-time cloud cover in the reanalysis cloud estimates, however, limited the ability to verify that diurnal differences in cloud radiative effects were responsible for the identified diurnal asymmetry in estimated temperature trends in the available record for the UIB. Furthermore, discrepancies in the spatial patterns of inter-variable correlation raised additional issues which appeared potentially linked to the aforementioned differences in summer DTR response to monsoonal activity.

Looking beyond proximal causal mechanisms of temperature variability, this study also investigated potential large-scale circulation influences on UIB climate via atmospheric teleconnections, e.g. the North Atlantic Oscillation (NAO), the El Niño Southern Oscillation (ENSO). Unfortunately the underlying variability in both local UIB climate observations and the indices of the large-scale atmospheric structures make it difficult to separate the degree of influence (signal) of the latter on the former from the background variability (noise). A spatial (pixel-wise) application of the correlation testing methodology (used for point-based observations) to the gridded data from ERA-interim and the PRECIS-downscaled ERA-40, however, did indicate some tentative insights:

- ENSO (MEI), in the Spring (MAM) and late Autumn/early Winter (OND) can be linked to responses in cloud cover and precipitation broadly across the sub-region/domain. As a result of the relative importance of the incoming solar and out-going thermal components of the surface energy balance, in colder months

increased cloud yields increased Tmin and decreased DTR through “insulation” effects, but from the late Spring increasing cloud actually results in decreasing Tmin and increasing DTR due to decreases in net energy input.

- In the Summer/monsoonal months (JJAS) there seems to be a sub-regional divide in ENSO effects based on sub-climate regimes. For this period, cloud cover and precipitation over the high mountains, particularly in the northwest, respond in opposite directions compared with the adjacent Indo-Gangetic Plains.
- At the concurrent timescale in both the Winter and late Summer, the NAO can be linked with responses in cloud cover, precipitation and night-time temperature (Tmin) as well as DTR, at least over the NW UIB. This might be attributed to increased cyclonic activity – “stormier” weather – either from strengthened westerly depressions from a positive NAO or, in Summer, increased monsoonal penetration.

As stated above, while the analysis of observations from the available historical record anchors current understanding of UIB hydro-climatology, this record is unlikely to contain a substantial sampling of conditions representative of probable local future climate in the face global climatic change. Thus additional methods are required to apply this understanding to produce plausible projections of future UIB climate with which to assess potential hydrological impacts of changes in the mass and energy inputs governing catchment response. In the course of adapting existing methodologies to the cryospheric process simulation and hydrological climate change impact assessment to the challenges and constraints of the UIB, the present study found the following:

- Methodologies established for downscaling of synthetic time-series of climate variables (Burton et al., 2008, Kilsby et al., 2007) used previously primarily in European contexts can be reasonably applied to the climate of the UIB.
- A hydrological model (VICwCDiP) incorporating simplified simulation of cryospheric processes – including snow-density evolution, vertical glacial mass transfer (basal sliding) and variability in glacial extent and thickness – and using temperature-index methods for meltwater generation calculations can achieve adequate representation of catchment response, for both nival and glacial regimes, to local climate forcings as measured by widely used metrics of calibration and validation.
- When driven by contrasting scenarios of future climate, the VICwCDiP model does produce coherent responses both in terms of hydrological outputs (runoff,

evapotranspiration) and cryosphere dynamics (glacial extent and thickness). Where the scenarios agree, e.g. strong air temperature warming in late spring, the response is similar: increased runoff and snowpack ablation in those months. Where the scenarios diverge, however, e.g. summer warming versus summer cooling, the changes in both hydrological and cryospheric response are logically opposed.

Further details on the results of the work with synthetic time-series and hydrological modelling will be given in sections 8.2.3 to 8.2.5.

8.2 Conclusions regarding principal research aims

8.2.1 Improving the spatial and temporal characterisation of present hydro-climatology of the UIB

This project sought to explore the available multi-decadal records from local observations in order to quantify annual cycles and interannual variability. With regard to river discharge, in confirmation of previous research, substantial interannual variability was found. Furthermore, annual cycles of nival and glacial regime catchments were found to be quite similar in terms of timing – i.e. mean contribution of monthly values to annual totals – and in terms of relative variability – i.e. ratio of monthly standard deviation divided by monthly mean – despite melt season and annual variability in runoff totals being controlled by different constraints, respectively mass (precipitation) and energy (temperature), for the two regimes. To be clear, Archer (2003) showed that throughout the UIB annual hydrological cycles are defined by alternating phases of solid precipitation accumulation (winter) and ablation (summer). Low flows, i.e. baseflows, in the winter months are typically of an order of magnitude smaller than peak summer flows and are substantially less variable even in relative terms. Annual variability is thus concentrated in the summer melt season when governing constraints, whether in mass or energy inputs, are materialised.

With regards to precipitation and temperature, the primary contribution of the present study, beyond reaffirming the findings of previously published work (primarily Archer and Fowler, 2004 and Fowler and Archer, 2006) has been their use as a baseline for comparison to other data sources, especially gridded datasets from global meteorological reanalyses and remote sensing spatial climate data products. Detailed examination of these data sources supported the long-standing assumption that while local observations made at meteorological stations in permanent settlements (towns) in

valley bottoms often experience similar relative annual cycles and levels of interannual variability, in terms of absolute values they must be related to wider spatial averages by scaling factors. The gridded data sources also provided evidence of sub-regional climate regimes, especially for precipitation, that would be difficult to identify through the sparse spatial coverage of the long-record local observing stations alone. Further study, preferably drawing on data sources with even higher spatial resolution, would be needed to provide more definitive findings regarding potential sub-regional climate regimes however.

To enable investigation of proximal causal mechanisms in local climate variability, this study sought to develop a detailed climatology for the UIB of secondary meteorological variables, including relative humidity, cloud descriptive parameters and (ground) surface albedo. Analysis of humidity and cloud cover data from ERA-40 and ERA-Interim reanalyses revealed substantial diurnal and annual cycles for both variables. Spatial analysis of cloud parameters from ERA-Interim and, especially, MODIS, further revealed complex sub-regional patterns in cloud climatology. These climatologies may eventually provide the foundation for identifying the causal mechanisms driving identified patterns of asymmetrical temperature change in the observational record.

Also for the purposes of enabling investigation of proximal causal mechanisms in local climate variability, this study sought to assess the surface energy balance fluxes in the UIB by drawing estimates from the meteorological reanalyses from ERA-40 and ERA-Interim. While there were differences in the energy balance estimates from the two reanalyses in terms of magnitude of the fluxes as well as an apparent positive shift in the energy balance residual in ERA-Interim compared to ERA-40, there was substantial agreement. This can be best seen in the shapes of the annual cycles as well as the overall dominant role of incoming solar radiation. Further agreement can be seen in seasonal variations of relative importance of the emissive energy fluxes, thermal long-wave (LW) radiation and latent heat flux (LHF). LW exceeds LHF in the winter (cold) season, but the situation is reversed during the summer season when energy is removed from the ground surface to drive both evaporation and melting of seasonal snowpack and glacial ice. Lastly, there is also moderate agreement between ERA-40 and ERA-Interim on the seasonal cycle of direction (sign) of sensible heat flux (SHF). In cold months positive SHF indicates warming of the surface by energy transfer from the air, while in the summer negative SHF values indicate warming of the near-surface air by energy transfer from the surface.

This project sought to build upon previous research and improve the hydro-climatological understanding of the UIB by a detailed characterisation of the vertical gradients in key climate variables. This was primarily undertaken using remotely sensed spatial data products from the Moderate Resolution Imaging Spectrometer (MODIS) instrument. The following are key findings regarding vertical gradients in MODIS spatial climate data products analysed by this study:

- Vertical variations in snow covered area (SCA) in the UIB are primarily driven by the annual cycle of freezing isotherm elevation which is at its lowest in winter and highest in summer. Thus there are vertical concentrations in interannual variability in SCA clustered around this elevation. For example, in the Gilgit catchment peak interannual variability is near 2700m asl in February but near 5000m asl in August.
- Vertical profiles of land surface temperature (LST) show somewhat more complex vertical patterns than that assumed for near surface air temperature – and supported by linear regression of available ground-based observations. Nevertheless linear approximations of the rate of vertical change in LST are not unreasonable proxies for air temperature change, especially for day-time LST over the range of elevations corresponding to the ground-based observation network. Linearised vertical gradients would be roughly 8°C per 1000m for LST_{day} and 6.5°C per 1000m for LST_{night} while in comparison air temperature lapse rates have been found to be 7.5°C per 1000m for Tmax and 6.2°C per 1000m for Tmin. Freezing (0°C) isotherms also match well for LST_{day} versus Tmax and LST_{night} versus Tmin.
- Vertical patterns, with respect to the underlying ground surface, of cloud cover fraction (CCF) have been assessed and found to contrast markedly between day-time (local noon) and night-time (local midnight) satellite overpasses. Day-time CCF appears monotonic (although not necessarily linear) with a positive CCF-elevation gradient. Night-time CCF, however, appears far more complex with a generally bi-modal vertical pattern showing local maxima – at seasonally varying elevations – in the lower and upper thirds of the elevation range. These complex vertical patterns and diurnal asymmetry are intriguing in the context of identified asymmetrical temperature trends (see section 8.2.2), but the short record length of the MODIS instrument limits use of the cloud cover data product for investigation of causal mechanisms in climate variability. Thus,

development of a comparable spatial data product with substantially longer record length would be of considerable interest and potential advantage.

- Vertical patterns of ground surface albedo demonstrate the dependence of this variable on SCA in the UIB.

This study did not limit itself to MODIS spatial climate data products when drawing on available relevant remote sensing data sources. Monthly precipitation estimates from the Tropical Precipitation Measurement Mission (TRMM) were also assessed as a potential indicator of mass input for catchment scale hydrology. As a remote sensing (satellite imagery) data product, TRMM might be expected to be able to spatially integrate precipitation detected throughout a catchment. Its design, as the name implies, is focused on measurement of convective precipitation which dominates in tropical and sub-tropical latitudes. Precipitation in the mountainous UIB, however, is generated predominantly from orographically-enhanced stratiform processes which are far more difficult for TRMM to detect. Nevertheless there seems to be a degree of uniformity in the "virtual undercatch" by TRMM; over the limited available record it appeared to perform similarly to ground-based observing stations as an effective quantitative, though not absolute, indicator of mass input to the hydrological system. The difficulties for TRMM to provide absolute precipitation estimates extend to the vertical dimension. As shown in section 3.9.1, TRMM was unable to detect an orographic precipitation gradient similar to that found by ground-based observations.

8.2.2 Assessing climate trends and their drivers in the UIB from the available observational record

This study endeavoured to verify previous findings regarding seasonally and diurnally asymmetrical temperature change. This objective was achieved comprehensively as both:

- Analysis of multiple time windows within the local observational record, including extension of analysis into the past decade, showed that the noted patterns (Fowler and Archer, 2006) of strongly increasing Tmax in Autumn, Winter and Spring and with neutral or variable Tmin trends in these seasons contrasted by decreasing Tmin and neutral Tmax in summer are shown to be consistently present over the past four to five decades.
- UIB temperature trends found in the ERA-Interim reanalysis corroborate both the seasonally and diurnally asymmetrical patterns of change seen in local

observations. ERA-40, in contrast. corroborates the seasonal asymmetry in daily mean temperature (Tavg), but subject to the analysis window attributes sub-diurnal contributions – i.e. individual changes in Tmin and Tmax – in contradiction of the local observations.

The distinctive, and perhaps unexpected, character of seasonally and diurnally asymmetrical temperature change found in the available record for the UIB compels further efforts to corroborate it. This study sought to assess the coherence of estimated trends both by verifying the correlation between time-series from local observations with gridded data sources – ERA-Interim and PRECIS-downscaled ERA-40 – and by assessing the coherence of spatial patterns of estimated trend rates within the gridded data sources, finding that:

- The correlations between local observations and corresponding pixels from gridded data sources largely follow expected patterns. Correlations between Tmax values from the gridded datasets and the range of air temperature variables from local observations are almost uniformly strongly positive. Correlations between gridded DTR and local observations are positive in "warm months" (May to October) in most cases with negative correlations to locally-observed Tmin in colder months. Exceptionally an ERA-Interim grid cell with considerable monsoonal activity (June to August) provides a contrasting example. Correlations there to local observations of Tmax and Tmin are negative – with good statistical significance for Tmin – and only weakly positive to locally observed DTR.
- Examination of the geographical patterns within the individual gridded data sources reveals that in general there appears, in both ERA-Interim and PRECIS-downscaled ERA-40, to be general spatial coherence (contiguous areas of similar sign and magnitude), implying that patterns of change are being driven by regionally coherent local processes or relatively uniform response to large-scale or regional forcings rather than isolated, heterogeneous responses limited to the immediate vicinity of the ground-based observations.

This study endeavoured to assess potential causal mechanisms of asymmetrical temperature change via testing of correlations between air temperature variables and cloud cover and energy balance components within the ERA-Interim reanalysis as well as between locally-observed air temperature variables and cloud cover and energy balance components from ERA-Interim and between locally-observed air temperature

variables and ERA-40 reanalysis cloud cover estimates downscaled by an RCM (PRECIS). Key findings in this regard have already been summarised in section 8.1. Further noteworthy results include:

- Interesting seasonal (temporal) and sub-regional (spatial) patterns emerge in the correlation between average total cloud fraction (TCFavg) and total daily energy balance residual (EBRtot). In physical terms, a (net) positive correlation between TCFavg and EBRtot can be assumed to indicate that long-wave forcing is greater in magnitude than shortwave forcing, while a (net) negative correlation implies that shortwave forcing dominates. Positive correlations predominate in cold months and in higher elevations while negative correlations predominate in summer months and at lower elevations. Positive correlations can be found in mountainous/high-elevation grid cells in all months with the lowest and weakest occurrence in July. Negative correlations can also be found in all months, but are most limited in January. The grid cells covering the core areas of the UIB in terms of hydrological contributions (runoff) show a mixture of positive and negative correlations for the months of the melt season (April to September). This may illustrate the present delicate balance between net positive and net negative effects of cloud radiative forcing. This instability (and uncertainty) complicates the evaluation of future climate scenarios because even if the likely changes in cloud cover (frequency and extent) were accurately projected, the net radiative effect might be misrepresented.
- In terms of correlations between gridded near-surface air temperature and energy balance components, Tavg correlations to EBRtot are relatively simple. Correlations are positive throughout the selected domain except during the melt season when negative correlations are present in a footprint with a spatial extent that to some degree resembles the area experiencing extensive seasonal snow and glacier melt. Results of Tmin correlation to EBRnight, however, are substantially more complicated. There appear to be sub-regions – contiguous blocks of grid cells – which, although they expand and contract through seasonal transitions, exhibit uniform annual cycles. The (Indo-Gangetic) plains adjacent to (and south of) the Himalayan mountain arc behave as a coherent unit throughout the year. In this sub-region during the cold months (Sept to Feb) correlations of Tmin with EBRnight are positive, while in warm months (March to August) they are negative.

- Another mechanism to consider in understanding air temperature forcings is sensible heat flux (SHF) which should be, in theory, a primary pathway between variability in the surface energy balance and air temperature responses. With the exception of the summer/monsoonal months (June to August), correlations of SHFday to EBRday are uniformly negative for the bulk of the domain. In June and July, and to a lesser extent August, there is a small sub-region focused on the northwestern UIB where correlations are positive. This indicates that, contrary to the rest of the domain, greater magnitude sensible heat flux occurs in a climate with less total energy exchange. Correlations between Tmax and SHFday indicate a widespread link between increased magnitude of sensible heat flux and warmer than average temperatures. This pattern is disrupted in the summer/monsoonal (June to September) months, however, when occurrences of the opposite relationship are found centred on the northwest UIB and along the front range of the Central Himalaya, yielding a sub-regional and seasonal contradiction with the prevailing linkage.
- While strong correlations have been shown between gridded and locally observed air temperature values, it remains worthwhile to examine correlations between radiative forcing variables from individual (numerical data source) grid cells and air temperature observations at local meteorological stations. For "non-monsoonal" grid cells, correlations of air temperature variables with TCFavg are consistently negative with the exception of Tmin in cold months (October to March) when negative correlations are found. The monsoonal grid cell, in contrast, follows these patterns except during the summer/monsoon months (June to August) when correlations of TCFavg to air temperature variables are weak or positive except for DTR which remains negative.
- In terms of gridded energy flux to local air temperature correlations, the relationships for the net incoming shortwave radiation (SWnet) in "non-monsoonal" grid cells follow expected patterns with positive correlations to Tmax and DTR in all months and Tmin showing negative correlations in winter and positive correlations in warm months. The monsoonal grid cell shows the same SWnet patterns except during the summer/monsoonal months when correlations both with Tmax and Tmin are negative. Sensible heat flux (SHFnet) correlations with locally observed air temperature would be expected to show warming air temperatures with increasing energy emission from the ground surface. In this case, not only the monsoonal cell, but also the northwestern

"non-monsoonal" cell show the opposite behaviour to that expected during the summer/monsoonal months. Furthermore the correlations in the remaining cell are mixed and not statistically significant.

This study aimed to examine relationships (correlations) between locally-observed precipitation and estimates of precipitation and relative humidity from gridded data sources (ERA-Interim and ERA-40 downscaled by PRECIS RCM). Key results of these analyses include:

- Correlations of reanalysis precipitation (PP) with local PP and wet days (WD) is entirely positive with good statistical significance although relationships in the summer/monsoonal months are relatively weaker. Correlations of reanalysis WD with local PP and WD are still largely positive except in the summer/monsoon period when some (weak) negative correlations are found. This may be due to "drizzle" – i.e. overly frequent, low intensity precipitation – problems in ERA-Interim forecasting modelling, or due to simple differences in the representation of localised convective precipitation when modelled at this spatial scale. The relationships between the PRECIS-downscaled ERA-40 simulation precipitation variables and their locally observed counterparts are quite similar to those between local observations and ERA-Interim, except that PRECIS WD correlations are weakest in Spring rather than Summer.
- Correlations of relative humidity (RH) from ERA-Interim and PRECIS with locally observed PP and WD are similar to those for gridded WD. Consideration of the relationship between RH and precipitation variables is pertinent for consideration of future climate scenarios because moisture fluxes are expected to increase in a generally warming climate.

This study sought to investigate the influence of large-scale atmospheric circulation patterns on the UIB as quantified by correlations between teleconnections and local climatic conditions. Further context to this investigation will be provided by the development of a spatial climatology of large-scale atmospheric pressure and regional wind direction using the ERA-Interim reanalysis. The key findings regarding this theme have already been summarised in section 8.1.

8.2.3 Developing plausible scenarios of future climate for the Upper Indus Basin

This study sought to perform an assessment of available RCM outputs (HadAM3P downscaled by PRECIS) for the UIB. This was achieved by quantitative comparisons both between the control run of HadAM3P downscaled by PRECIS (PRECIS_AM3P) and local observations as well as between the control run of HadAM3P downscaled by PRECIS and ERA-40 downscaled by PRECIS (PRECIS_ERA40). Key findings in this respect are as follows:

- With regards to precipitation comparisons between the two PRECIS simulations, for most of the year PRECIS_AM3P produces a substantially drier climatology than PRECIS_ERA40 over the mountainous sections of the subdomain and especially over the northwest UIB. Differences over the core UIB between the two simulations are particularly pronounced in January, June, October and December. In contrast during the later months of the monsoonal period, i.e. August and September, PRECIS_AMP3P yields a wetter climate than PRECIS40.
- With regards to air temperature comparisons between the two PRECIS simulations, if considering PRECIS_ERA40 as the baseline, PRECIS_AM3P appears to overestimate the magnitudes of both the annual and diurnal temperature cycles throughout the sub-region; specifically this is manifested in excessively cold winters and excessively warm winters. Generally positive DTR bias is confirmed with greater cold biases in Tmin than Tmax in Winter and greater warm biases in Tmax than Tmin in Summer.

In terms of comparisons between PRECIS simulations and local observations, absolute comparison of orographically governed/influenced parameters to their locally observed analogues is not strictly meaningful. Two relative mean comparisons, however, are possible: i) mean fractional contribution by month to total annual precipitation; and ii) diurnal temperature range (DTR). The results of this assessment were as follows:

- The mean monthly fractional contribution to total annual precipitation is an indicator of the accuracy with which the seasonality – which months are relatively wet and dry – of local rainfall patterns is reproduced by the RCM control scenario. The underlying assumption here is that the temporal distribution of precipitation as observed by the local stations is spatially representative even if the absolute amounts measured are not. The performance of the two RCM simulations is quite similar for most months. For two of the

three local long-record stations, Skardu and Astore, performance is relatively consistent and centred around or near unity with the exception of the beginning (June) and end (September) of the monsoon season, when respectively PRECIS_ERA40 and PRECIS_AM3P overestimate the contribution of each month to the annual total precipitation. For the remaining station Gilgit, however, the relative importance of late Autumn and Winter precipitation is substantially overestimated while the contribution of late Spring through early Autumn months is underestimated.

- Diurnal temperature range is expected to have an orographic gradient due to differences between the lapse rates for Tmax and Tmin, but it is substantially less elevation-dependent than either. This aspect makes it the most appropriate near surface air temperature parameter for evaluation of model performance. The three available long-record UIB meteorological stations show starkly contrasting relationships to the RCM outputs from the grid cells overlying them. In synopsis, PRECIS_ERA40 does appear superior to PRECIS_AM3P for two out of three stations with the third station effectively showing a tie. The DTR bias assessment also corroborates the characterisation of PRECIS_AM3P as "overly energetic" with substantial positive bias (overestimation) in every month for all three stations.

This project aimed to calibrate and validate a stochastic downscaling model of present climate to establish the appropriateness and adequacy of the method for the UIB. Synthetic time-series were generated using the RainSim and CRU Weather Generator (CRU-WG) software packages. The general fit – i.e. agreement between observed and simulated statistics – for all climate variables is very reasonable. This is quite satisfying given the large magnitude of annual cycles and considerable interannual variability of the local climate in the UIB. Distribution of precipitation amounts is particularly encouraging, although the simulation of precipitation occurrence – the distribution "dry days" versus "wet days" – is somewhat weaker.

This study undertook derivation of change factors – (i) extracted from available RCM outputs (HadAM3P for the 2080s under the SRES A2 scenario downscaled by PRECIS) and (ii) extrapolated using trends estimated from local observations -- for precipitation and air temperature in order to construct contrasting scenarios of future climate. Producing bias-corrected scenarios of future climate from an RCM requires the extraction of "change factors" by comparing climate variable statistics of "future

climate" and "control climate" from time-slice RCM simulations. The key results for precipitation and air temperature are as follows:

- For the western end of the Himalayan arc – i.e. the Hindu Kush, Karakoram and Western Himalaya (HKH) – the PRECIS_AM3P time-slice experiment shows Winter precipitation increases but decreases in Summer/monsoonal rainfall. Numerical changes in variance track with changes in precipitation amounts. There are indications, however, of contrasting changes in wet day frequency within the HKH sub-region during the monsoonal months. The higher elevation, more northerly, grid cells show decreasing wet days from June to September while the relatively lower, southern/foothills grid cells show increasing wet days during these months.
- Changes in mean air temperature are relatively homogeneous across the UIB and contiguous areas. The PRECIS_AM3P time-slice experiment shows year-round temperature increases with only limited variations in the intensity of warming with broad, albeit mild, regional year-round decreases in DTR. Limited exceptions to this include increasing DTR in several months along a narrow band of cells located at the boundary between the mountains and the plains as well as increasing Summer/monsoonal DTR over the Indus plains and the northern HKH. These localised DTR increases appear tentatively linked to decreases in precipitation. Seasonal and sub-regional patterns in changes in temperature variance are less clear (noisier) than for other variables, although the tentative indications of increasing variance in early Spring and early Autumn Tavg could indicate increased interannual variability in the timing and duration of melt season.

This study then intended to implement the selected scenarios in synthetic time-series by perturbing the previously calibrated stochastic model. After initial attempts to implement the change factors (CFs) within RainSim and CRU-WG, it was decided to retain the PRECIS_AM3P CFs but to reduce those extrapolated from local observations trend rates by 50%, i.e. halving the effective change. This change was made due to the severity of the projected changes in precipitation, especially wet day frequency reductions in presently humid months, and DTR. The retained change factors from locally observed trends still result in substantial changes with respect to present climate conditions, and still provide stark contrast to the PRECIS_AM3P scenario.

In general the PRECIS_AM3P scenario results in a future climate with moderate precipitation increases concentrated in presently humid months and relatively uniform air temperature increases. In constrast, the scenario derived from extrapolating trends estimated with local observations results in a future climate that is generally more humid, albeit with substantial shifts in the seasonality of precipitation, i.e. drier Springs but more humid Winters and Summers. In terms of air temperature, this scenario carries forward the present trend of year-round increases in DTR. This increase results from asymmetrical changes to Tmax which increases from Autumn through Winter to Spring but is stable/stationary in Summer and from Tmin which decreases in Summer but is stable/stationary in other months.

8.2.4 Constructing and validating a hydrological model for the UIB

This study developed a hydrological model (VICwCDiP) using, wherever possible, proven methodologies to enable simulation of key land surface processes in order to accurately reproduce the key aspects of UIB hydrology. This was based primarily on a variant of the existing VIC model while substituting a "degree-day" based approach for resolution of the full energy balance. The input data used by the VICwCDiP model is based on the extrapolation of values from a base station record on a purely elevation-driven basis.

This study then calibrated and validated this model for archetypal catchments representing the dominant UIB hydrological regimes. In addition to traditional hydrological outputs (evapotranspiration, runoff), the model, via the intermediate steps required to calculate PET, also simulates the surface variables of snow covered area (SCA) and land surface temperature (LST). Catchment means for these simulated surface variables match well with climatologies based on remote sensing data products from the MODIS instrument.

8.2.5 Examining the implications of contrasting future scenarios on UIB hydrology and cryosphere

This study used long synthetic time-series for future climate scenarios to drive the calibrated meltwater runoff models for the two archetypal UIB tributary catchments in order to probabilistically assess potential hydrological consequences of contrasting future climate scenarios for the 2080s under the SRES A2 emissions scenario. The key findings are as follows:

- Mean annual total runoff from the RCM scenario (SRES A2 for the 2080s)is projected to be substantially greater in the 2080s than in the control simulations for both Astore and Hunza, albeit with some overlap between the 95th percentile for the control and the 5th percentile for the RCM scenario.
- For both Astore and Hunza, mean annual total runoff values projected from the extrapolated trends scenario and the control simulation for the 2080s are almost statistically indistinguishable.
- Interannual variability in annual total runoff, as quantified by the standard deviation of annual values within a 30-year block, is substantially greater in the RCM scenario than in the control simulations for both Astore and Hunza.

This study further used the output of the scenario-driven simulations to assess projected glacial trajectories resulting from the future climate scenarios. The key findings are as follows:

- The trajectories of glaciated area (catchment fraction) and glacial mass show the similarities in the results of the extrapolated trends scenario and the control simulations as well as their contrast to the deglaciation projected under the RCM-based scenario (SRES A2, 2080s). For the control simulations as well as for the scenario extrapolated from observed trends, the net mass balance is largely positive for both the Astore and Hunza catchments. In contrast, after the initial rapid deglaciation the glacial mass balance in for the RCM-based scenario (SRES A2, 2080s) is very nearly zero for both the Astore and Hunza catchments.
- There is substantial contrast in the ratios of ice melt to snow melt seen when comparing the scenarios for the two catchments. For the Astore catchment, the differences between the scenarios in the ratio of ice melt to snowmelt are relatively muted, perhaps because Astore is already a nival regime catchment. For the Hunza catchment, the drastic reduction in the ratio of ice melt to snowmelt under the SRES A2 2080s RCM-based scenario contrasts with to the moderate increase in the ratio under the extrapolated trends scenario. The reduction under the RCM-based scenario is attributed to the projected change from a glacial to nival regime under the future climate. The increase in the ice to snow ratio under the extrapolated trends scenario is however likely due to the notable reduction in annual snowmelt caused by input energy constraints (Summer cooling) rather than to the moderate projected increase in ice melt.

8.3 Key findings

Amongst the wide-ranging results presented in this thesis, the following can be pointed out as key findings:

- The utility of MODIS data products as complementary indicators (to those provided by local precipitation and temperature observations) of mass and energy inputs to the UIB hydrological system has been established by the present study and has been published as Forsythe et al. (2012a) and Forsythe et al. (2012b) and are presented in section 3.10 of this thesis. Vertical aspects are critical in this application as the remotely-sensed indicator of mass input was identified by consideration of the vertical concentration in interannual SCA variability, while the indicator of energy input, dubbed the "continuous melt area" (CMA), was effectively determined by the LST_{night} freezing (0°C) isotherm as CMA is the fraction of the catchment area where LST_{night} remains above freezing.
- UIB temperature trends found in the ERA-Interim reanalysis corroborate both the seasonally and diurnally asymmetrical patterns of change seen in local observations. ERA-40, in contrast. corroborates the seasonal asymmetry in daily mean temperature (Tavg), but subject to the analysis window attributes sub-diurnal contributions – i.e. individual changes in Tmin and Tmax – in contradiction of the local observations.
- The spatially and seasonally homogenous increases in air temperature found in the change factors extracted from PRECIS_AM3P are in stark contrast to the seasonally and diurnally asymmetrical trends found not only in local observations but also in the PRECIS simulation driven by ERA-40 boundary conditions (PRECIS_ERA40). For this reason it is deemed worthwhile to examine the potential divergences in future hydrological conditions which could result depending on whether UIB climate follows the trajectory indicated if recent trends persist in the coming decades rather than the scenario described by the RCM simulation PRECIS_AM3P.
- The VICwCDiP model has objectively demonstrated, through the results of calibration and validation runs for the Astore (nival) and Hunza (glacial) catchments, the ability to reproduce the annual melt-runoff cycle and range of interannual variability in both of the dominant hydrological regimes of the UIB. Furthermore the model has shown at least moderate skill, as evidenced by a

range of metrics, to simulate hydrological response to specific interannual variations in mass (precipitation) and energy (temperature) inputs.

- Although mean annual total runoff in the RCM scenario is projected to increase compared to the control simulation, actual evapotranspiration (AET) is also projected to increase. This is a potential concern considering that runoff from the Upper Indus is impounded at the Tarbela reservoir and then used to water the vast irrigated plains in the lower Indus. If AET in the irrigation command areas increases in line with that projected for the UIB, even increased runoff may be inadequate to compensate for the shortfall. This adds urgency to the need to accurately assess future irrigation demands in the areas served by the Indus Basin Irrigation System.

8.4 Recommendations for future research

While substantial advances have been made in many of themes covered by this thesis, the present study has also served to identify potential further opportunities to improve hydro-climatological understanding of the UIB. Some of the most promising and compelling are as follows:

- Development of multi-decadal equivalents based on the observations by the AVHRR instruments – flown on NOAA satellites since the late 1970s – of the MODIS spatial data products for SCA, LST, CCF and ground surface albedo would facilitate statistically meaningful assessment of recent trends – and their spatial coherence – in these variables. Such multi-decadal records would also facilitate improved simulation of spatial variability in land surface processes by hydrological models such as VICwCDiP. Algorithms for this have been developed and a paper is in revision.
- Extension of the investigation of relationships between local air temperature observations and radiative forcing-related reanalysis variables to include correlations with high-resolution remote sensing of cloud parameters would help to improve understanding of the elevation dependency and catchment-scale spatial coherence of these processes.
- Nested (multi-spatial resolution) downscaling for the UIB of the most recent global meteorological reanalyses – e.g. ERA-Interim – would aid in understanding the physical constraints on orographic precipitation gradients as well as the physical linkages in cloud, water vapour and surface albedo driven

feedback to radiative forcings of regional near-surface air temperature. Outputs from such downscaling simulations could be used as input for UIB-adapted hydrological models such as VICwCDiP to further test skill in reproducing recent hydrological and cryospheric variability in the observed record.

- Assessment of the results of a higher-resolution (25km) 17-member perturbed physics ensemble of RCM simulations for the UIB and adjacent sub-regions, including use of derived change factors in the RainSim and CRU-WG software packages, would enhance characterisation of the range and statistical distribution of plausible UIB future climate scenarios. The resultant synthetic time-series of future scenarios could be used as input for UIB-adapted hydrological models such as VICwCDiP to improve assessment of the range and statistical distribution of future hydrological conditions and regional glacial mass balance trajectory.
- Further development of the VICwCDiP model, or incorporation of its key innovations into other model packages, to better capture key aspects of meltwater generation processes would add greater credibility to projections of future hydrological conditions in nival and glacial regime catchments. Potential avenues include: i) increased sophistication of melt energy modulation – by incorporation of additional topographical (e.g. aspect, hill-shade) or climatic and land surface process (e.g. cloud cover, surface albedo) driven parameters; or ii) incorporation of a complete surface energy balance if credible and sufficiently fine spatial resolution estimates of near surface humidity and wind speed become available.
- Application of the contributions described in this thesis to practical water resources management, especially at the local (village/valley) scale, including for emergency planning and small-scale infrastructure resilience assessment would lend relevance to the work to date and help to justify and guide future research.

Substantial portions of the work packages recommended above have already been initiated including data acquisition for sources produced by external organisations and algorithm validation for bespoke data products. Many of the themes above will be addressed by the author in the context of a research associate appointment funded by a Philip Leverhulme Prize awarded to the lead advisor of this thesis.

Appendix A: Supplemental material to Chapter 3

A.1 Temperature climatologies from diverse data sources

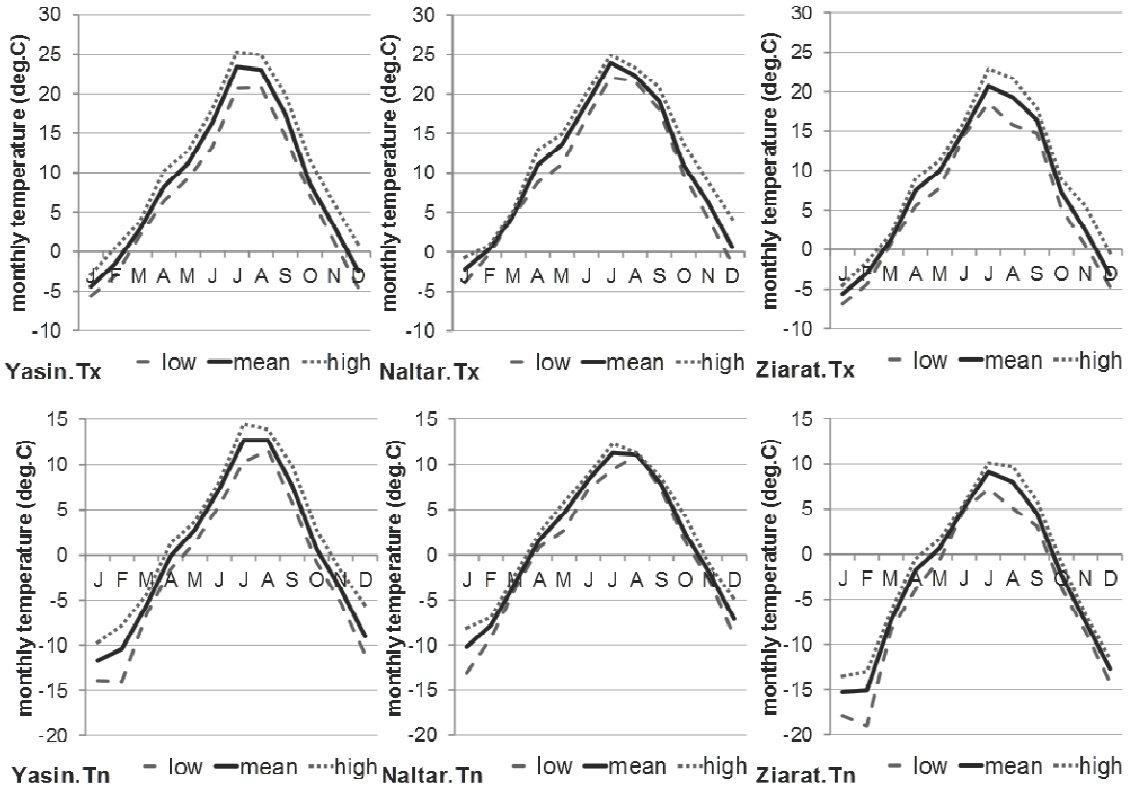

Figure A.01 Available (sample) observations, 1994 to 1999, of 2m mean daily maximum (Tx) and minimum (Tn) from AWS in Gilgit & Hunza catchments. Elevations of the AWS units are as follows: i) Yasin 3353 m asl; ii) Naltar, 2810 m asl; iii) Ziarat, 3688m asl.

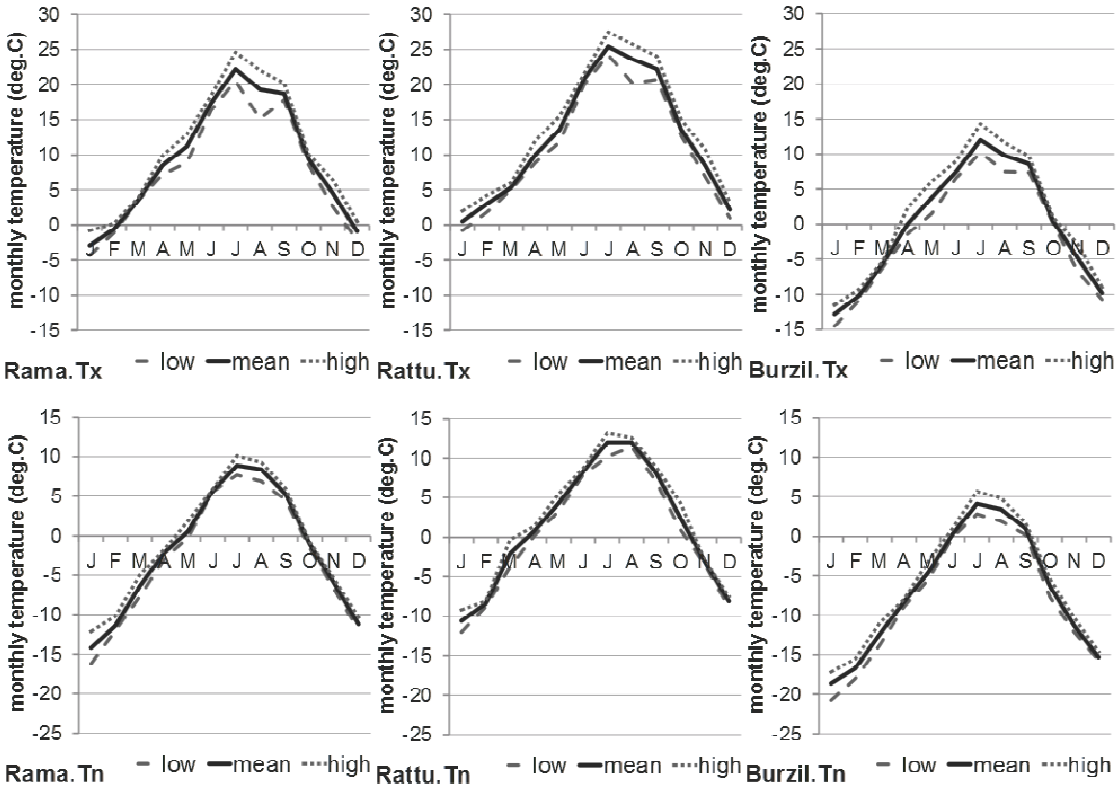

Figure A.02 Available (sample) observations, 1995 to 1998, of 2m mean daily maximum (Tx) and minimum (Tn) from AWS in the Astore catchment. Elevations of the AWS units are as follows: i) Rama, 3140 m asl; ii) Rattu, 2920 m asl; iii) Burzil, 4101 m asl.

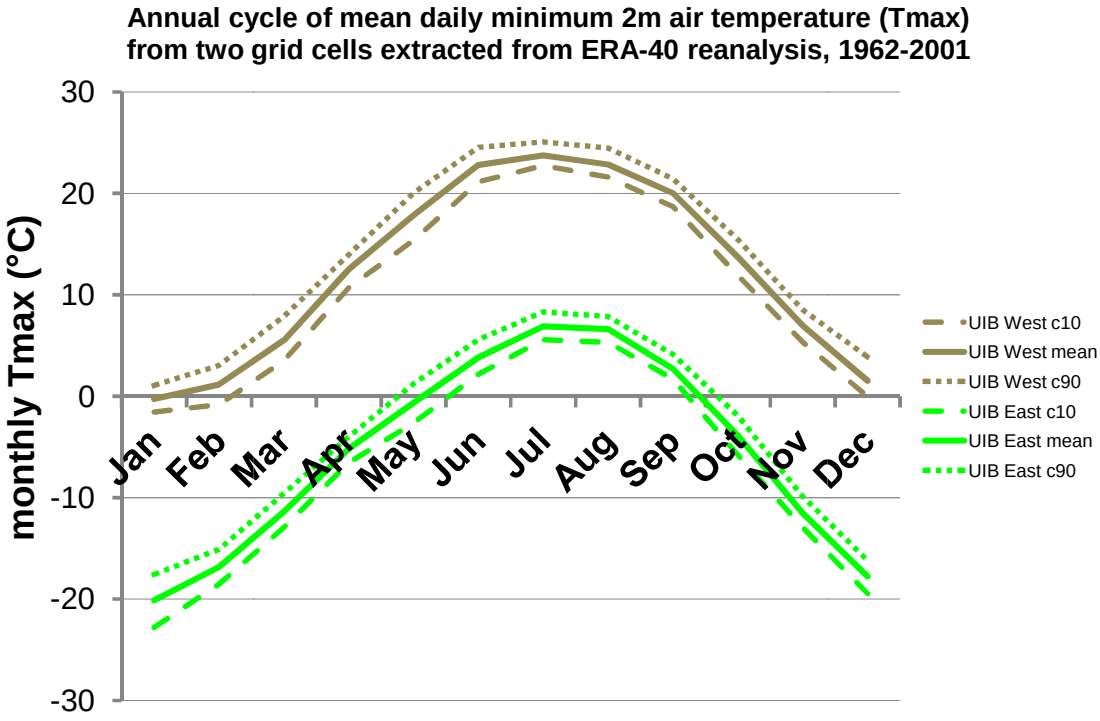

Figure A.03 Mean daily maximum 2m air temperature from ERA-40 for two sample grid cells, UIB West (modelled elevation 2572 m asl) and UIB East (modelled elevation 5033 m asl), from 1962 to 2001.

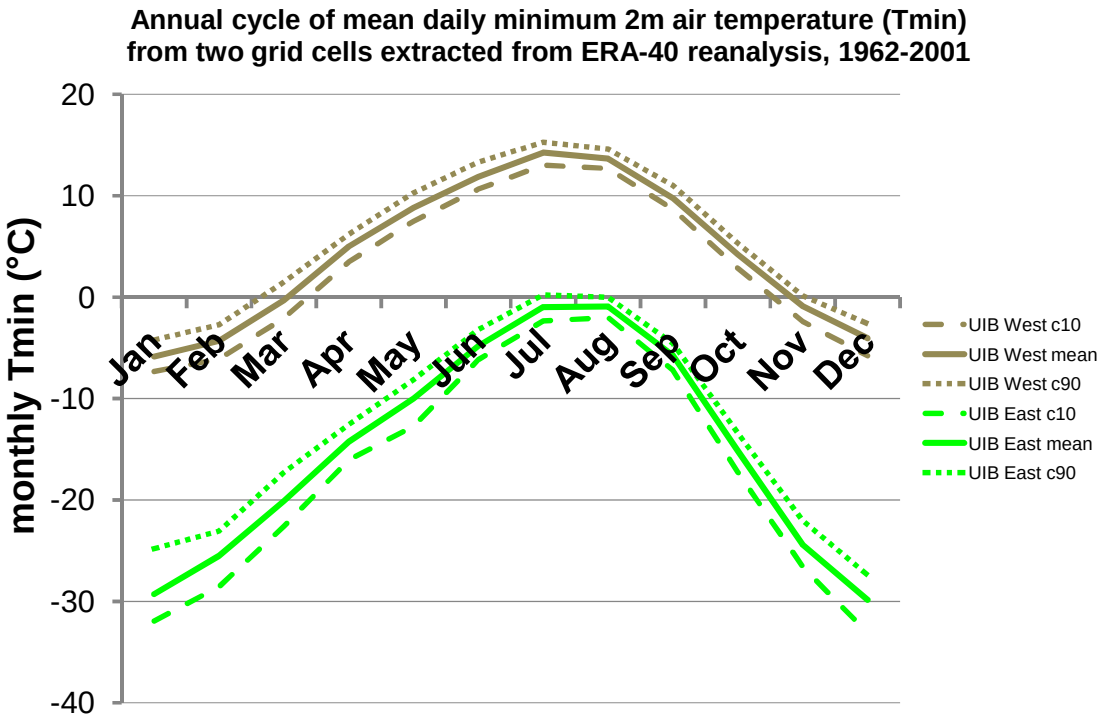

Figure A.04 Mean daily minimum 2m air temperature from ERA-40 for two sample grid cells, UIB West (modelled elevation 2572 m asl) and UIB East (modelled elevation 5033 m asl), from 1962 to 2001.

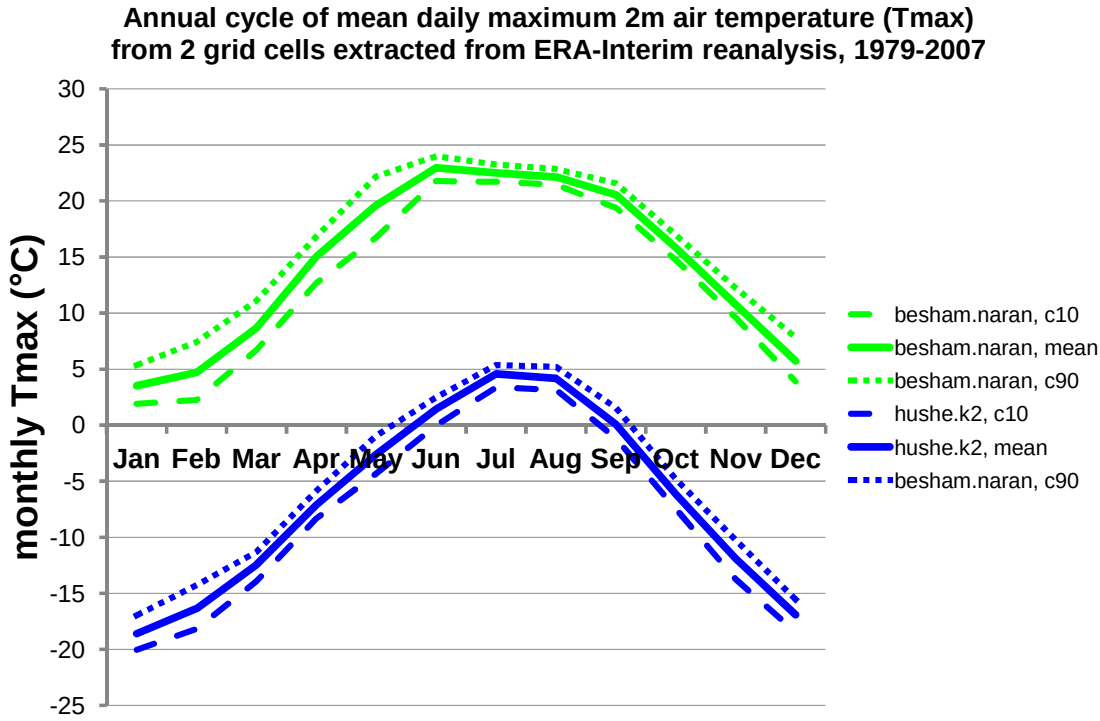

Figure A.05 Mean daily maximum 2m air temperature from ERA-Interim for two sample grid cells, Besham.Naran (modelled elevation 2153m asl) and Hushe.K2 (modelled elevation 4953 m asl), from 1962 to 2001.

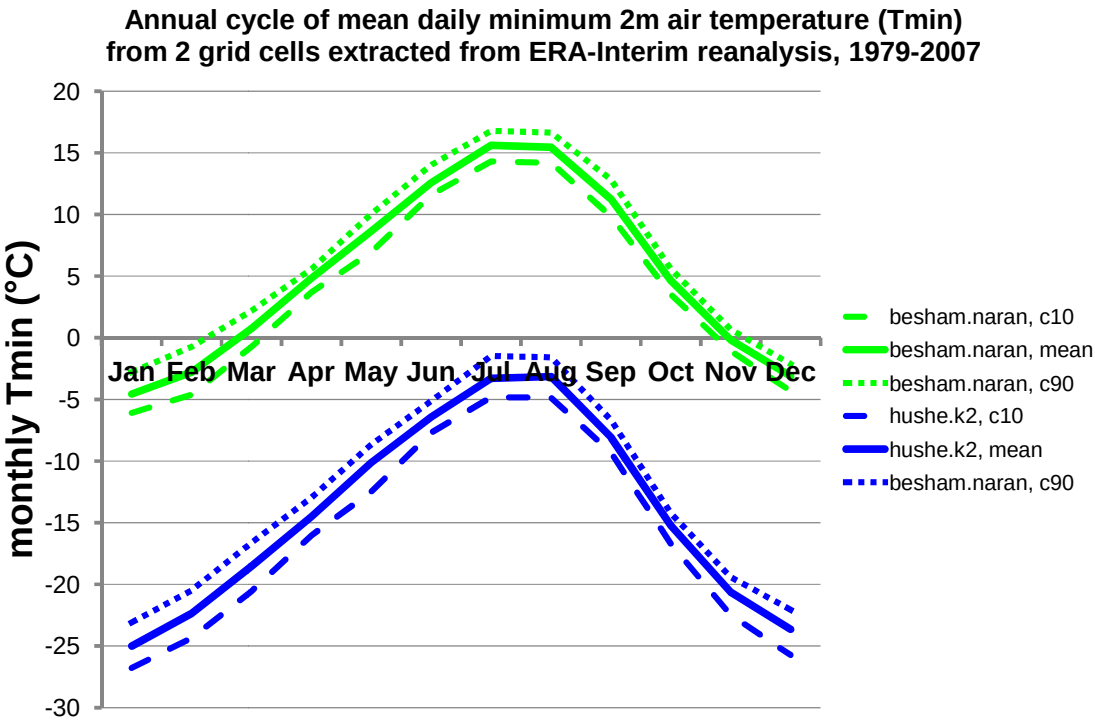

Figure A.06 Mean daily minimum 2m air temperature from ERA-Interim for two sample grid cells, Besham.Naran (modelled elevation 2153m asl) and Hushe.K2 (modelled elevation 4953 m asl), from 1962 to 2001.

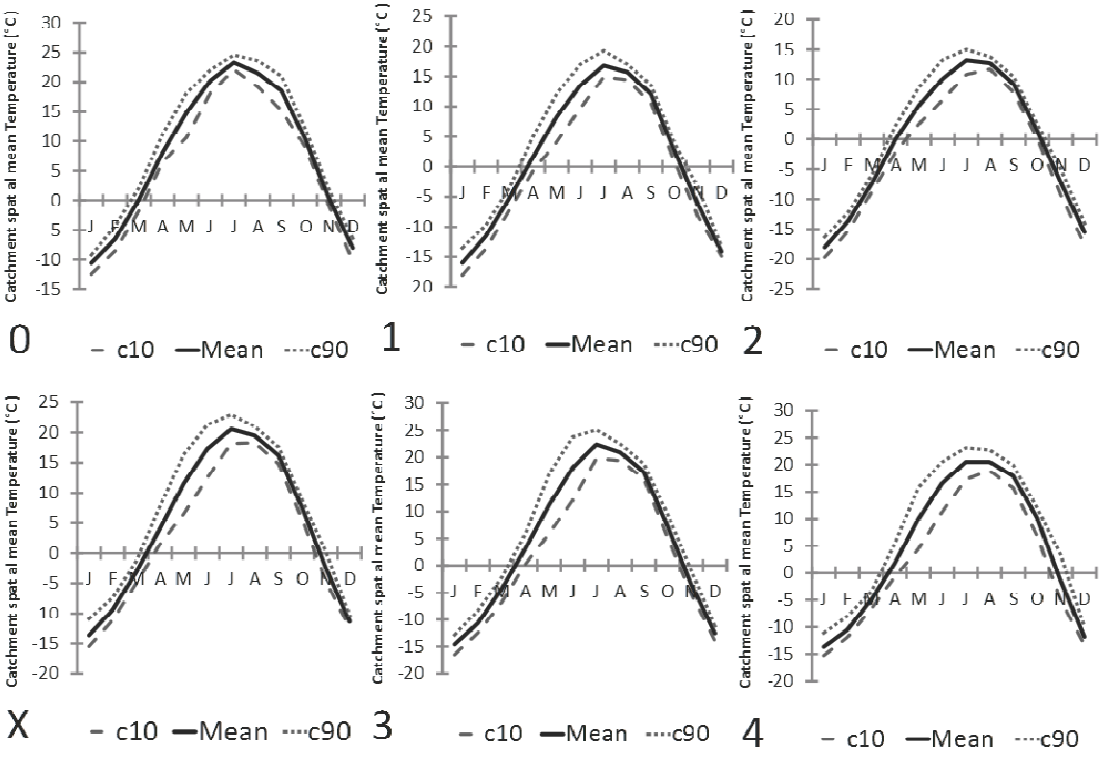

Figure A.07 Annual cycle of day-time land surface temperature (LST) for period (2000 to 2010) monthly means and first and last deciles (c10 & c90 from MODIS for primary tributary catchments – [0] the Upper Indus above Besham, [1] the Hunza, [2] the Shigar, [X] the NW UIB sector (1+2+3+4 plus main channel valley between Besham and Yogo/Kharmong), [3] the Gilgit/Ghizer, and [4] the Astore. Boundaries are shown in Figure 3.041.

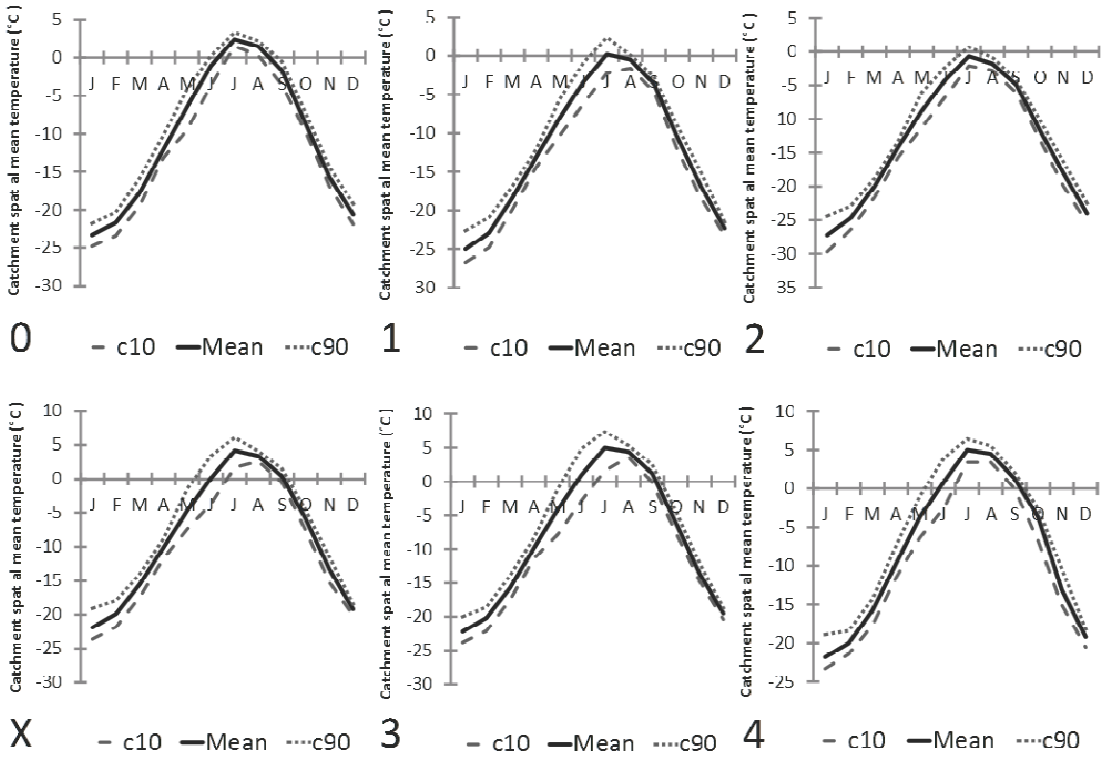

Figure A.08 Annual cycle of night-time land surface temperature (LST) for period (2000 to 2010) monthly means and first and last deciles (c10 & c90 from MODIS for primary tributary catchments – [0] the Upper Indus above Besham, [1] the Hunza, [2] the Shigar, [X] the NW UIB sector (1+2+3+4 plus main channel valley between Besham and Yogo/Kharmong), [3] the Gilgit/Ghizer, and [4] the Astore. Boundaries are shown in Figure 3.041.

A.2 Sample preliminary period monthly means from AVHRR-derived spatial data products

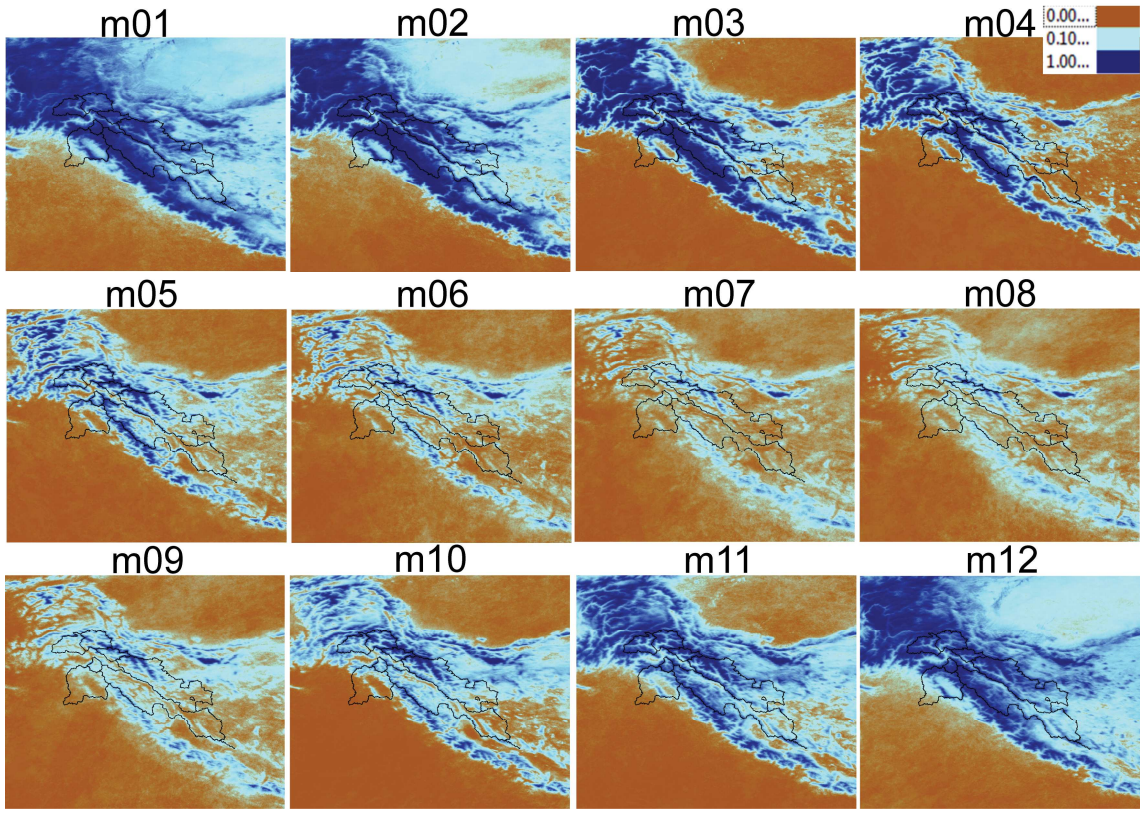

Figure A.09 example development phase AVHRR-derived spatial data product for SCA. Values, in units of fractional cover per pixel, are linearly-interpolated on the provided colour scale (upper right corner).

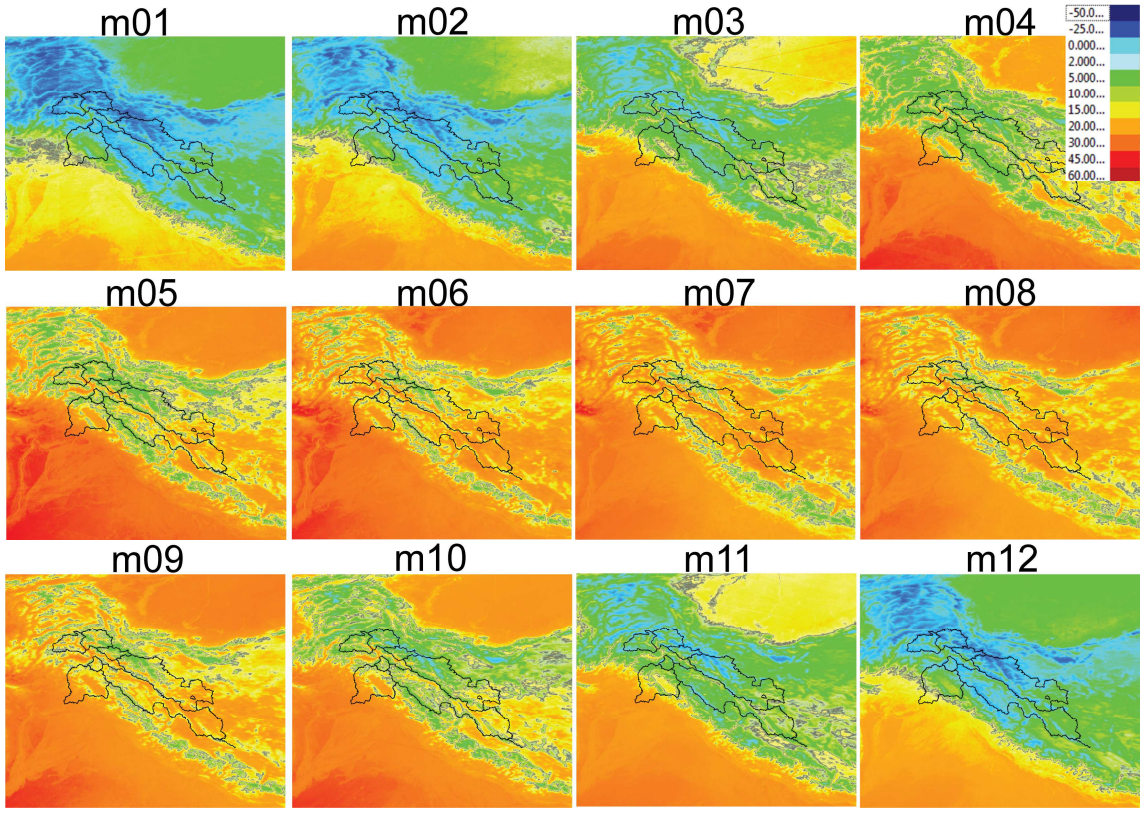

Figure A.10 example development phase AVHRR-derived spatial data product for LST_{day}. Values [°C] are linearly-interpolated on the provided colour scale (upper right corner).

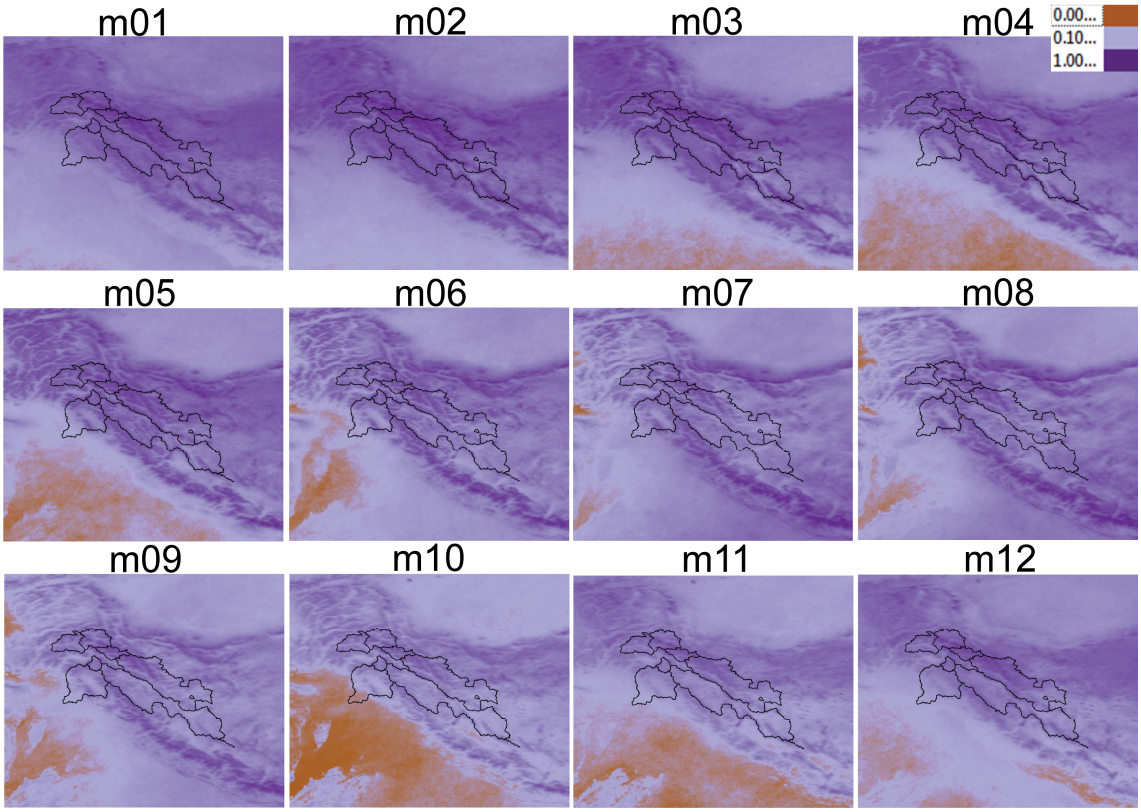

Figure A.11 example development phase AVHRR-derived spatial data product for CCF_{day}. Values, in units of fractional cover per pixel, are linearly-interpolated on the provided colour scale (upper right corner).

Appendix B: Supplemental material to Chapter 4

B.1 Time-series of normalised, standardised anomalies of climate observations aggregated for key seasons.

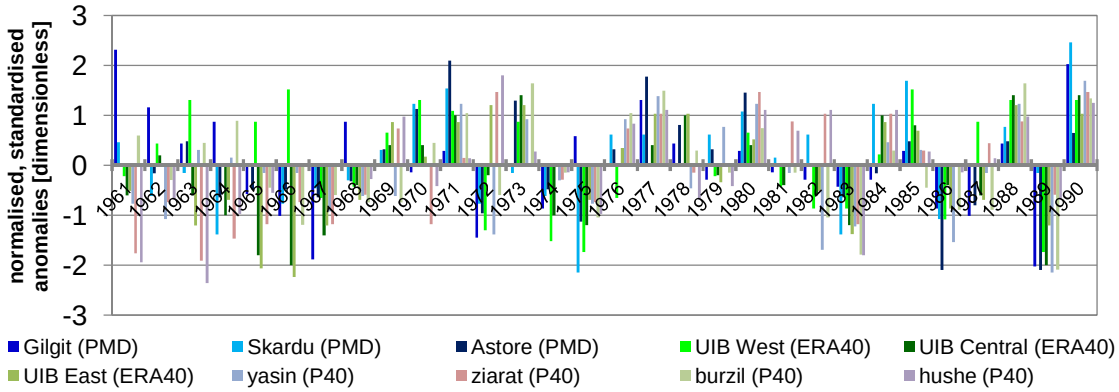

Figure B.01 Time-series of normalised, standardised annual mean Tavg anomalies from local observations (PMD), ERA-40 and PRECIS_ERA40 (P40) for 1961 to 1990.

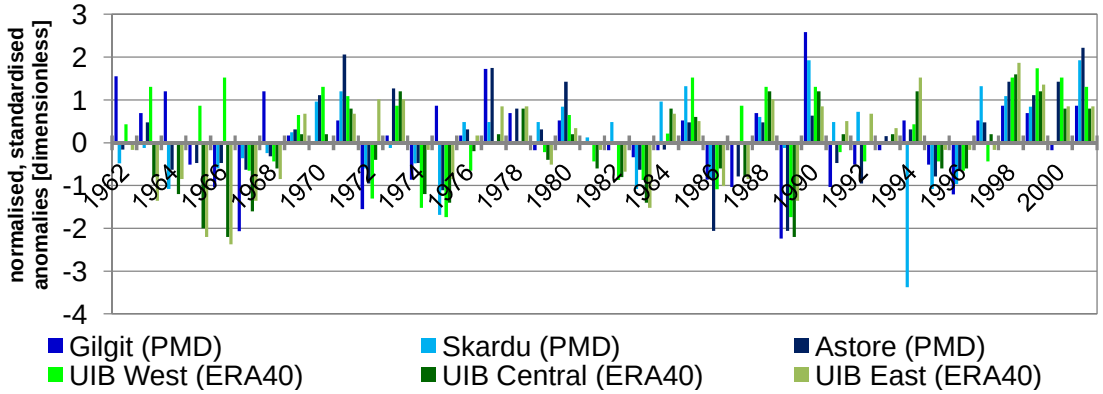

Figure B.02 Time-series of normalised, standardised annual mean Tavg anomalies from local observations (PMD) and ERA-40 for 1962 to 2001.

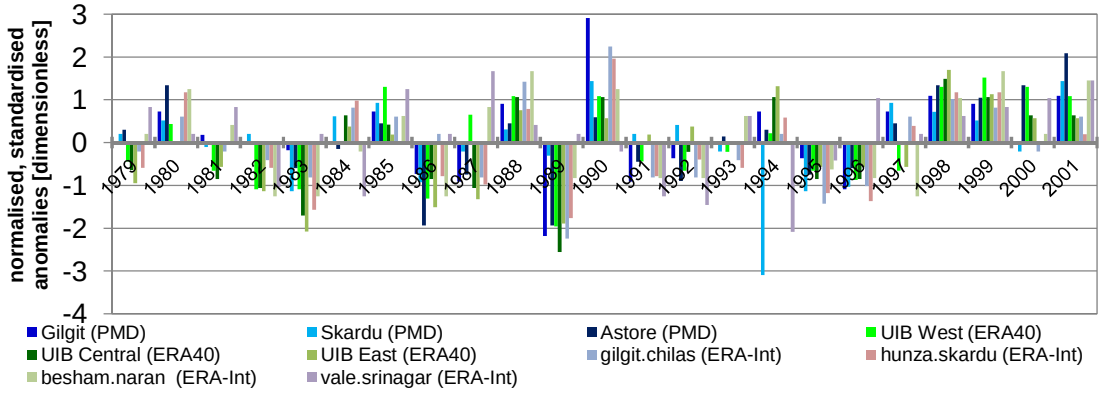

Figure B.03 Time-series of normalised, standardised annual mean Tavg anomalies from local observations (PMD), ERA-40 and ERA-Interim (ERA-Int) for 1979 to 2001.

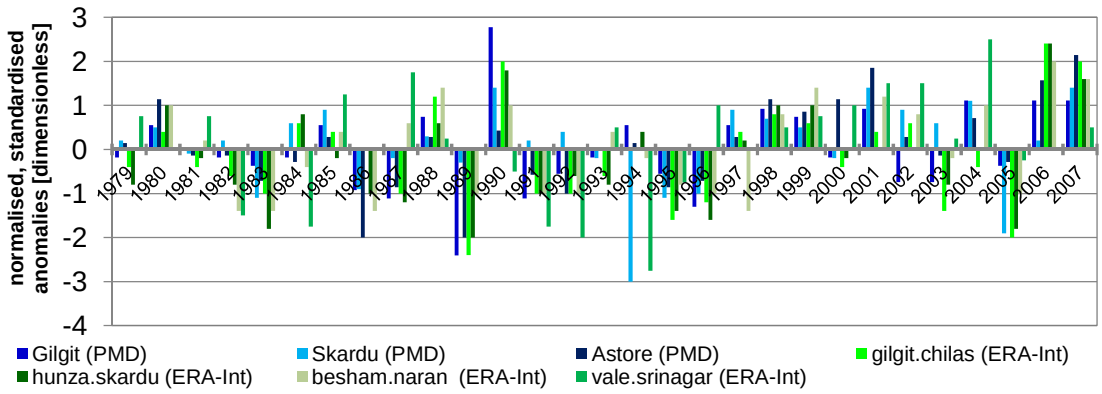

Figure B.04 Time-series of normalised, standardised annual mean Tavg anomalies from local observations (PMD) and ERA-Interim (ERA-Int) for 1979 to 2007.

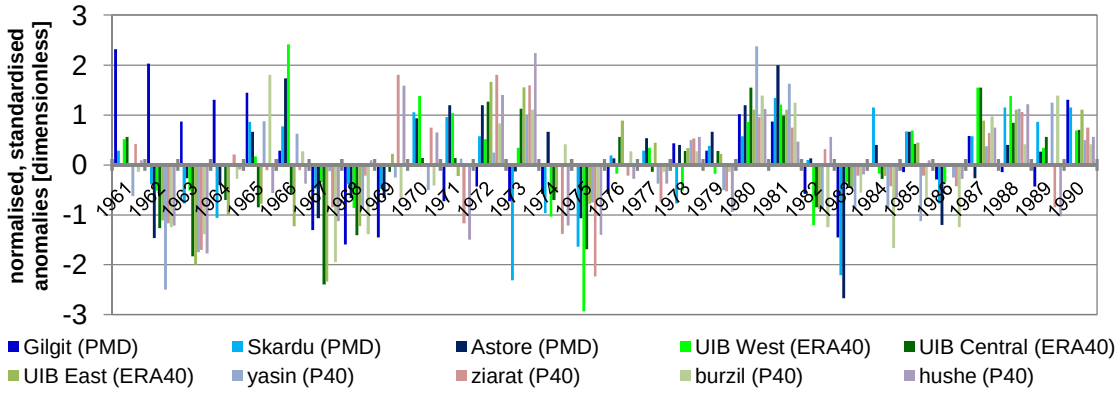

Figure B.05 Time-series of normalised, standardised ONDJFM mean Tavg anomalies from local observations (PMD), ERA-40 and PRECIS_ERA40 (P40) for 1961 to 1990.

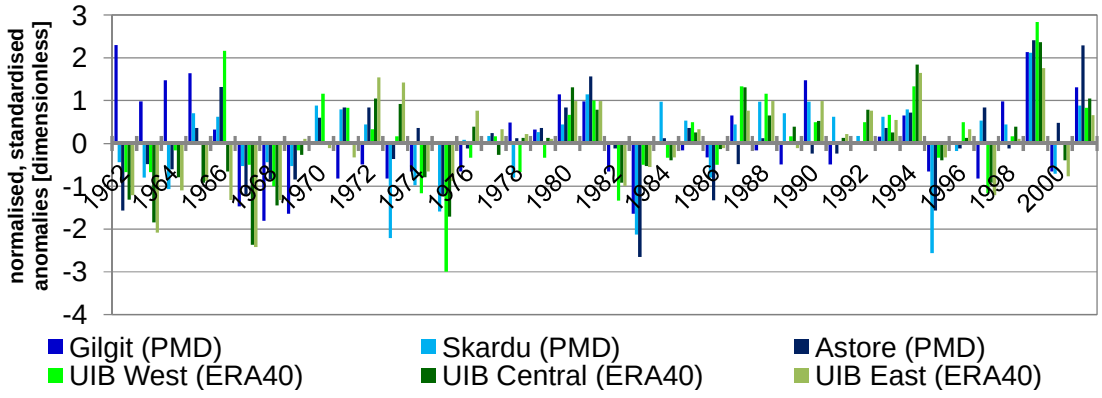

Figure B.06 Time-series of normalised, standardised ONDJFM mean Tavg anomalies from local observations (PMD) and ERA-40 for 1962 to 2001.

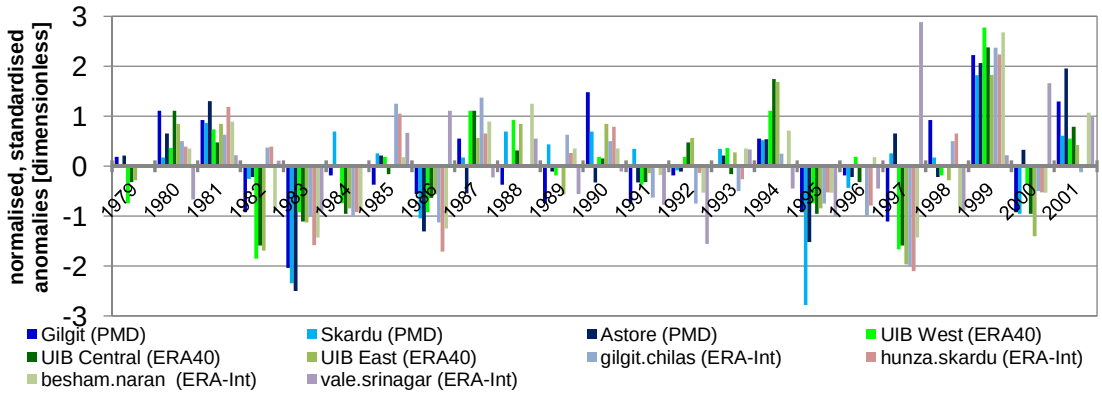

Figure B.07 Time-series of normalised, standardised annual mean Tavg anomalies from local observations (PMD), ERA-40 and ERA-Interim (ERA-Int) for 1979 to 2001.

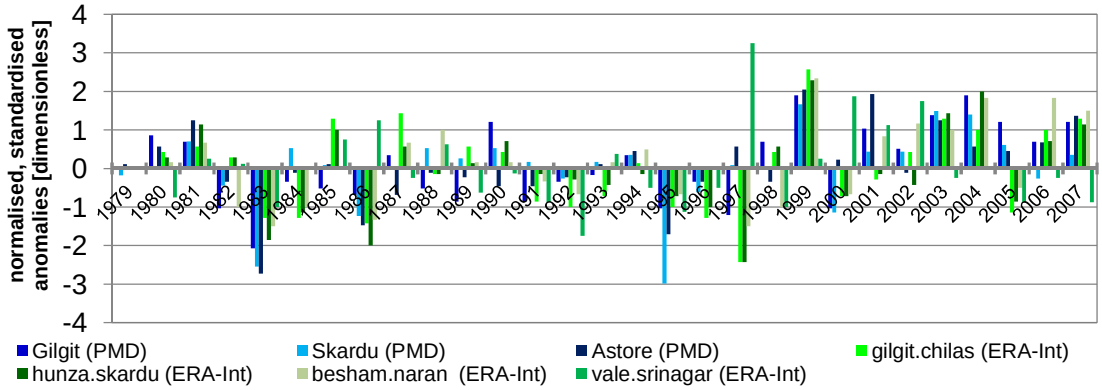

Figure B.08 Time-series of normalised, standardised ONDJFM mean Tavg anomalies from local observations (PMD) and ERA-Interim (ERA-Int) for 1979 to 2007.

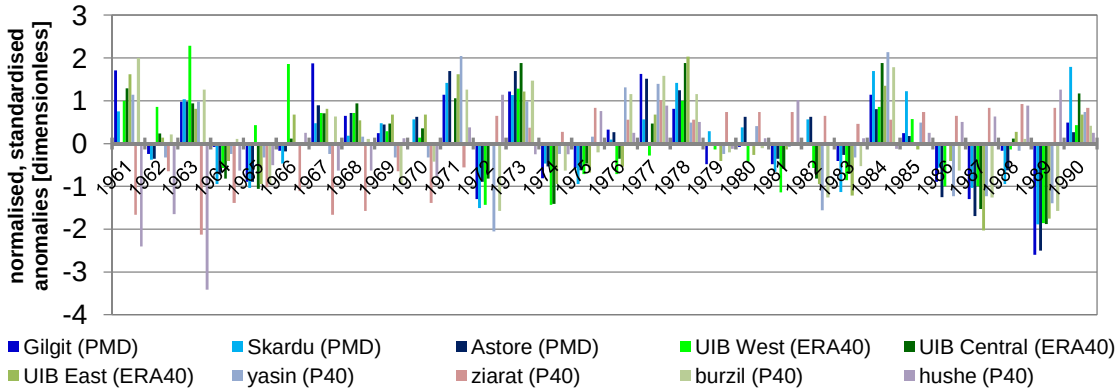

Figure B.09 Time-series of normalised, standardised JJA mean Tavg anomalies from local observations (PMD), ERA-40 and PRECIS_ERA40 (P40) for 1961 to 1990.

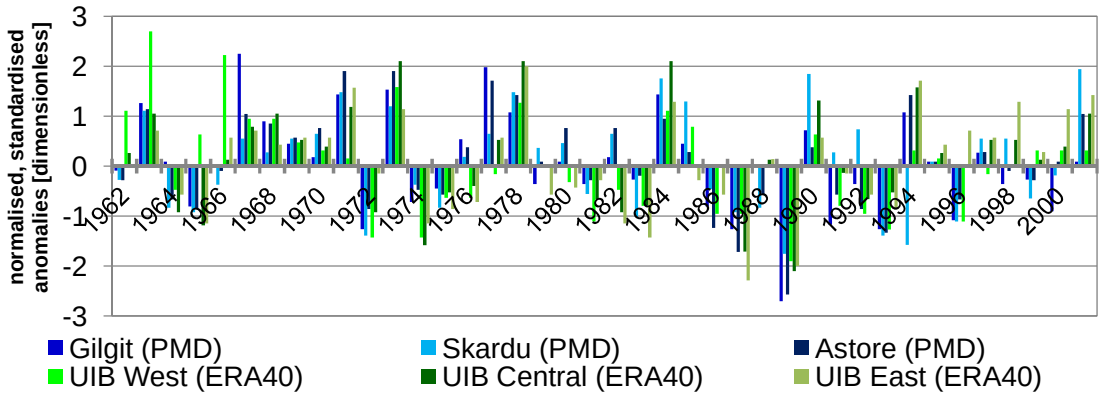

Figure B.10 Time-series of normalised, standardised JJA mean Tavg anomalies from local observations (PMD) and ERA-40 for 1962 to 2001.

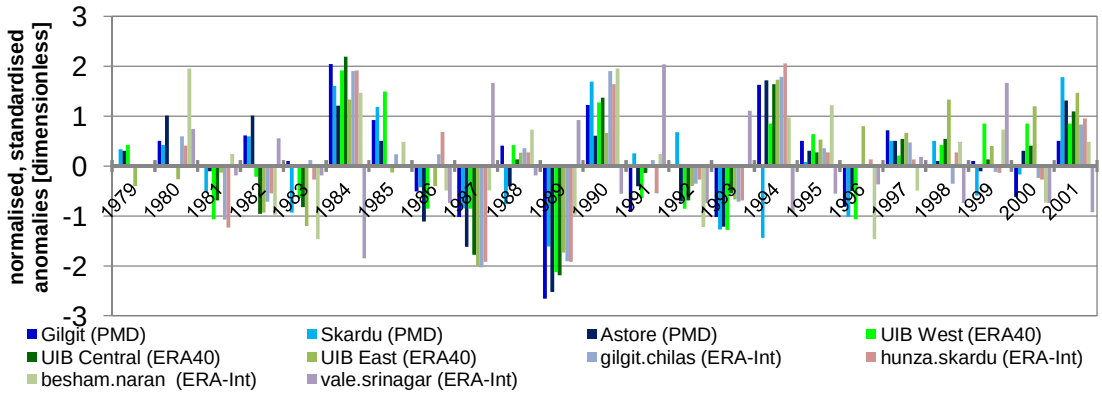

Figure B.11 Time-series of normalised, standardised JJA mean Tavg anomalies from local observations (PMD), ERA-40 and ERA-Interim (ERA-Int) for 1979 to 2001.

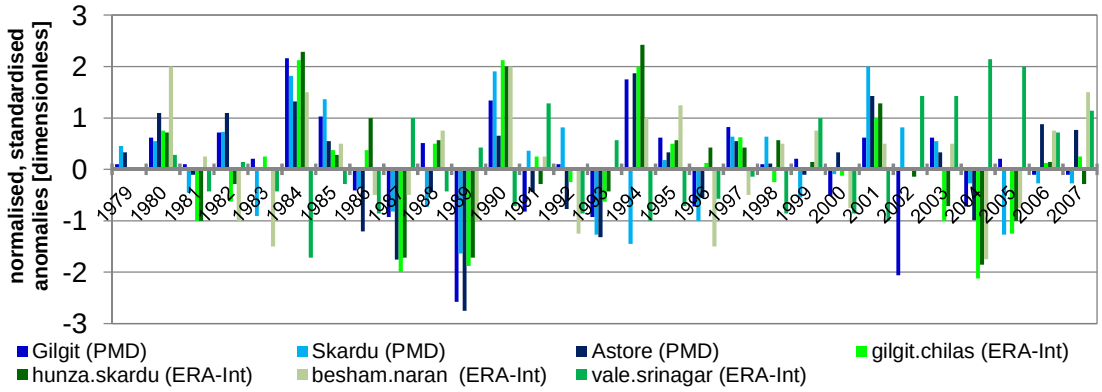

Figure B.12 Time-series of normalised, standardised JJA mean Tavg anomalies from local observations (PMD) and ERA-Interim (ERA-Int) for 1979 to 2007.

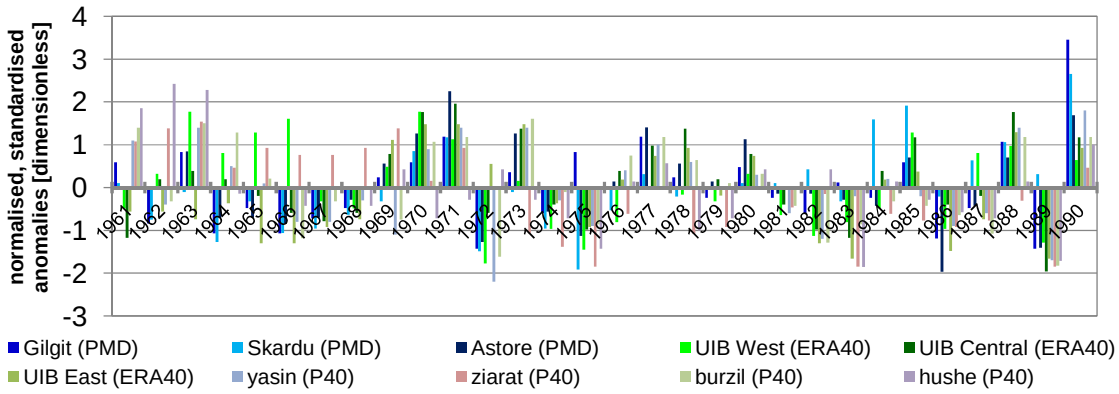

Figure B.13 Time-series of normalised, standardised annual mean Tmax anomalies from local observations (PMD), ERA-40 and PRECIS_ERA40 (P40) for 1961 to 1990.

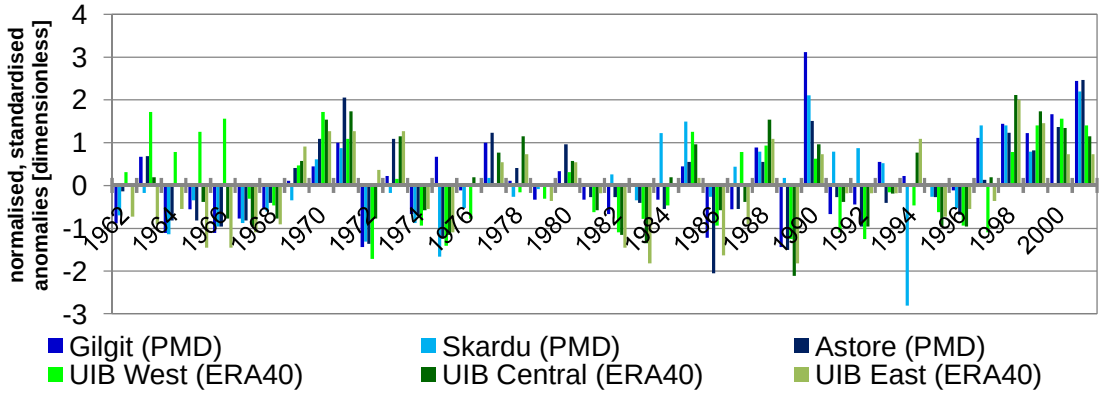

Figure B.14 Time-series of normalised, standardised annual mean Tmax anomalies from local observations (PMD) and ERA-40 for 1962 to 2001.

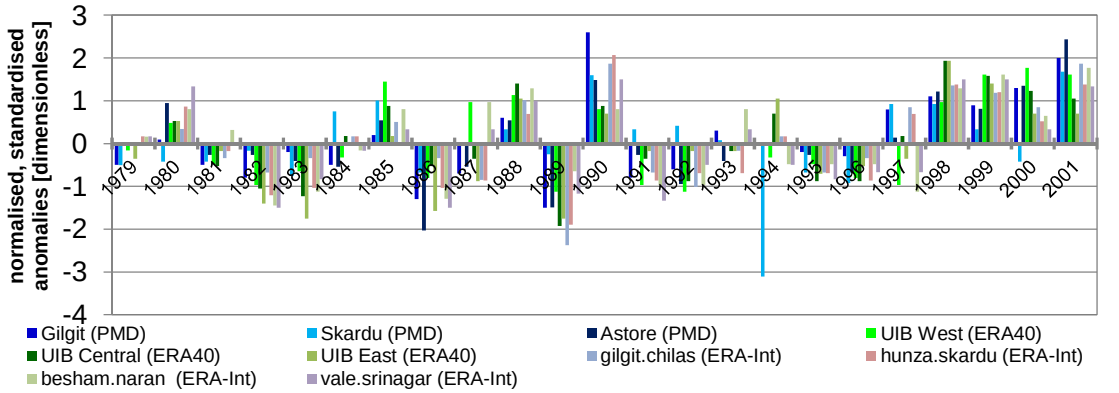

Figure B.15 Time-series of normalised, standardised annual mean Tmax anomalies from local observations (PMD), ERA-40 and ERA-Interim (ERA-Int) for 1979 to 2001.

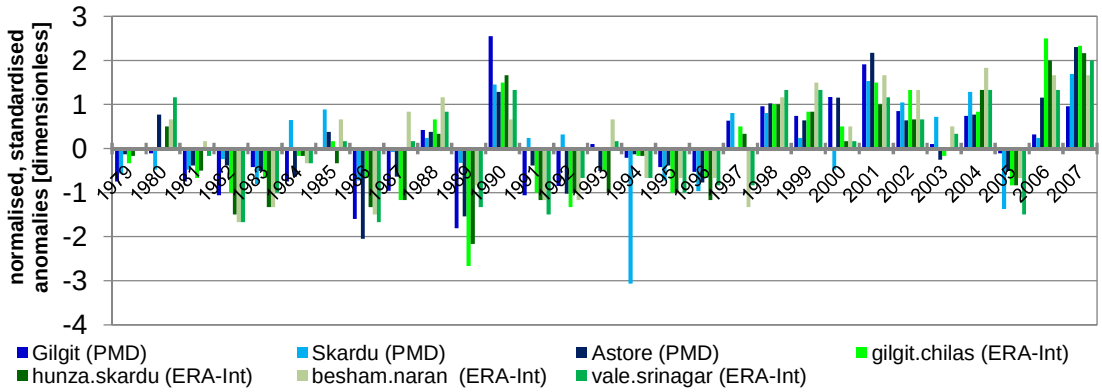

Figure B.16 Time-series of normalised, standardised annual mean Tmax anomalies from local observations (PMD) and ERA-Interim (ERA-Int) for 1979 to 2007.

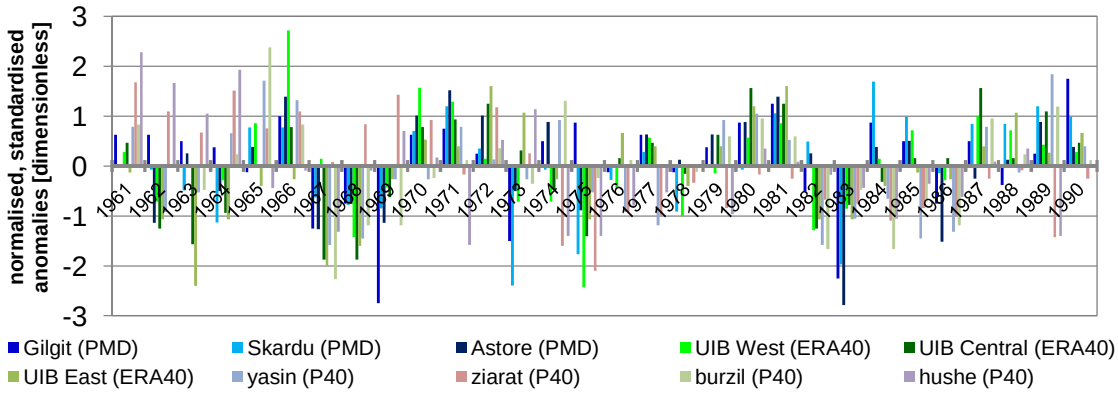

Figure B.17 Time-series of normalised, standardised ONDJFM mean Tmax anomalies from local observations (PMD), ERA-40 and PRECIS_ERA40 (P40) for 1961 to 1990.

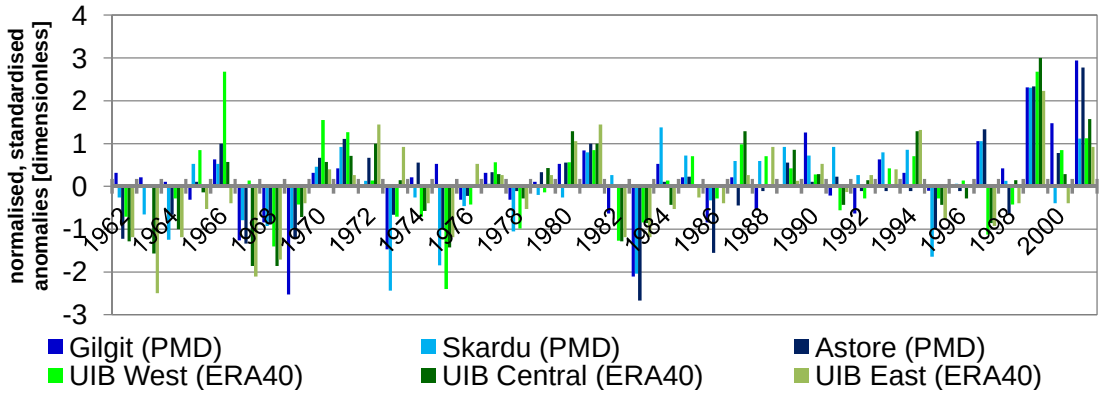

Figure B.18 Time-series of normalised, standardised ONDJFM mean Tmax anomalies from local observations (PMD) and ERA-40 for 1962 to 2001.

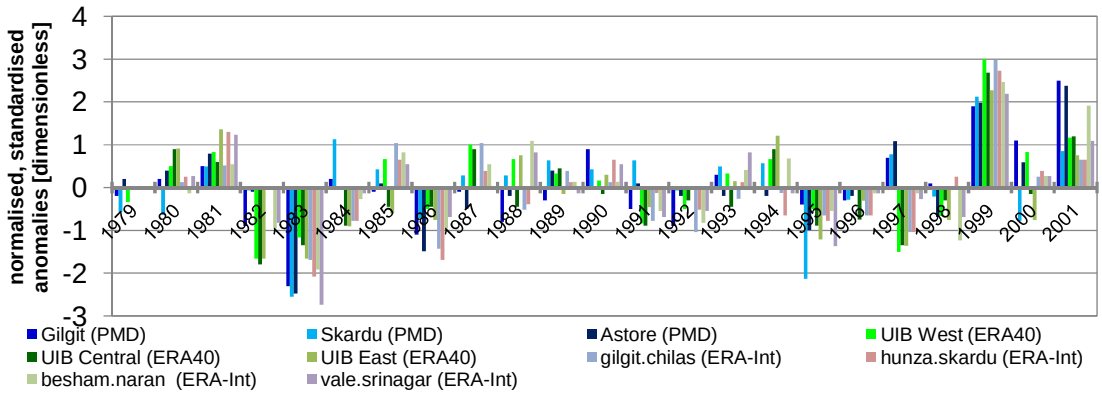

Figure B.19 Time-series of normalised, standardised annual mean Tmax anomalies from local observations (PMD), ERA-40 and ERA-Interim (ERA-Int) for 1979 to 2001.

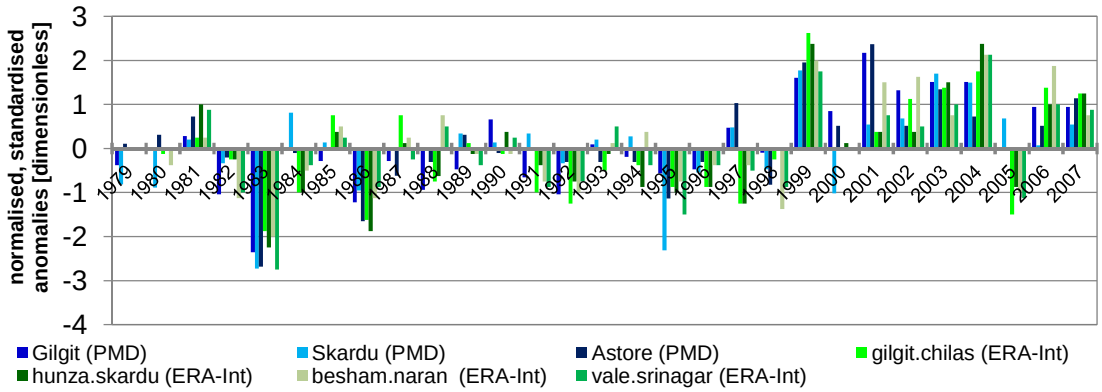

Figure B.20 Time-series of normalised, standardised ONDJFM mean Tmax anomalies from local observations (PMD) and ERA-Interim (ERA-Int) for 1979 to 2007.

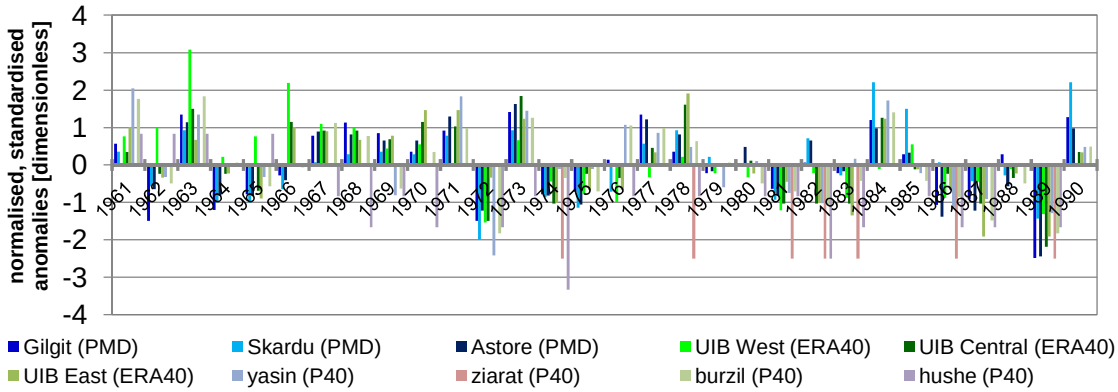

Figure B.21 Time-series of normalised, standardised JJA mean Tmax anomalies from local observations (PMD), ERA-40 and PRECIS_ERA40 (P40) for 1961 to 1990.

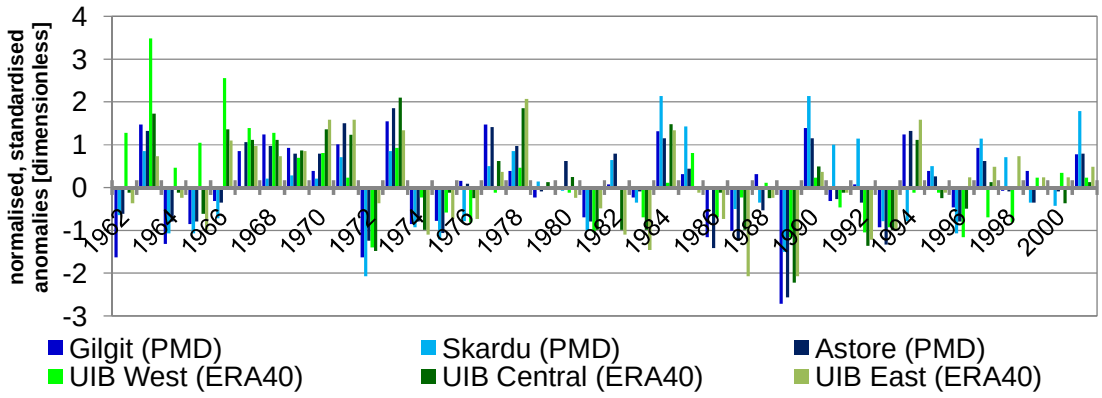

Figure B.22 Time-series of normalised, standardised JJA mean Tmax anomalies from local observations (PMD) and ERA-40 for 1962 to 2001.

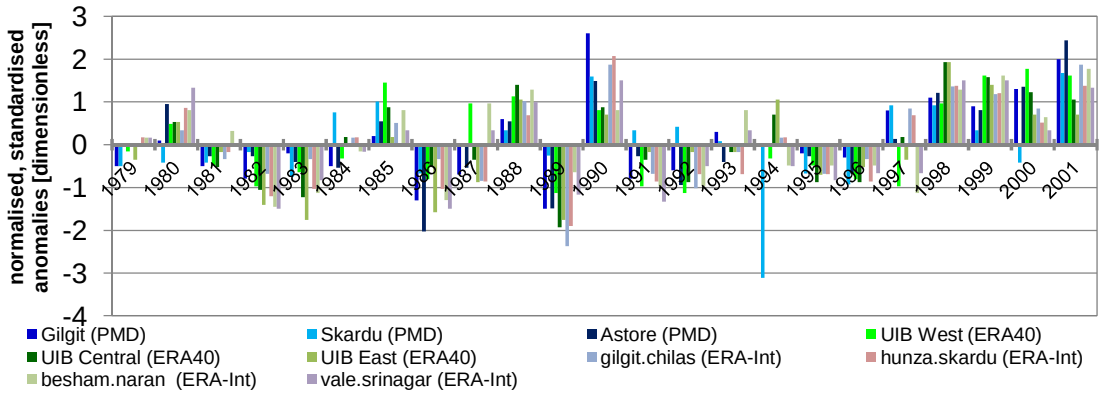

Figure B.23 Time-series of normalised, standardised JJA mean Tmax anomalies from local observations (PMD), ERA-40 and ERA-Interim (ERA-Int) for 1979 to 2001.

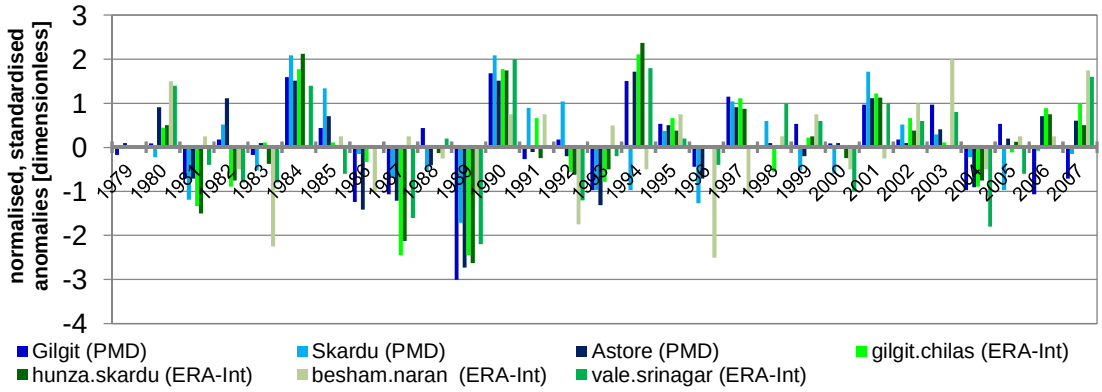

Figure B.24 Time-series of normalised, standardised JJA mean Tmax anomalies from local observations (PMD) and ERA-Interim (ERA-Int) for 1979 to 2007.

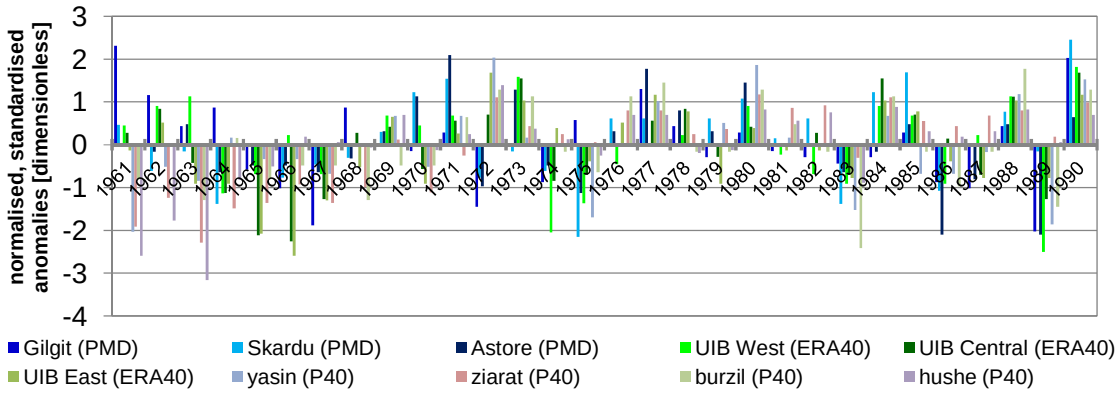

Figure B.25 Time-series of normalised, standardised annual mean Tmin anomalies from local observations (PMD), ERA-40 and PRECIS_ERA40 (P40) for 1961 to 1990.

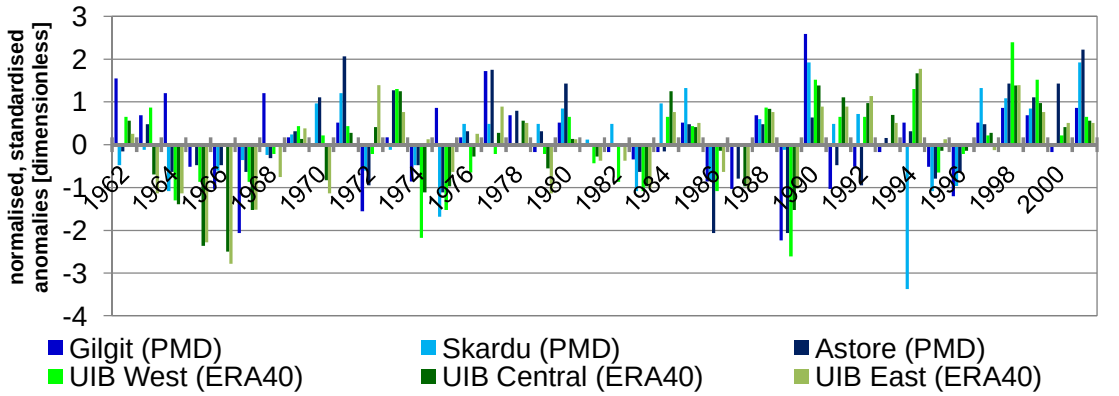

Figure B.26 Time-series of normalised, standardised annual mean Tmin anomalies from local observations (PMD) and ERA-40 for 1962 to 2001.

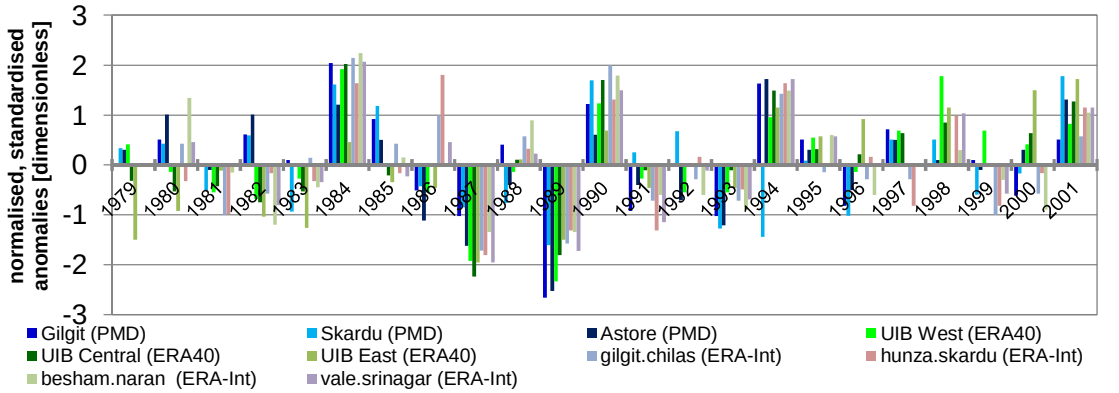

Figure B.27 Time-series of normalised, standardised annual mean Tmin anomalies from local observations (PMD), ERA-40 and ERA-Interim (ERA-Int) for 1979 to 2001.

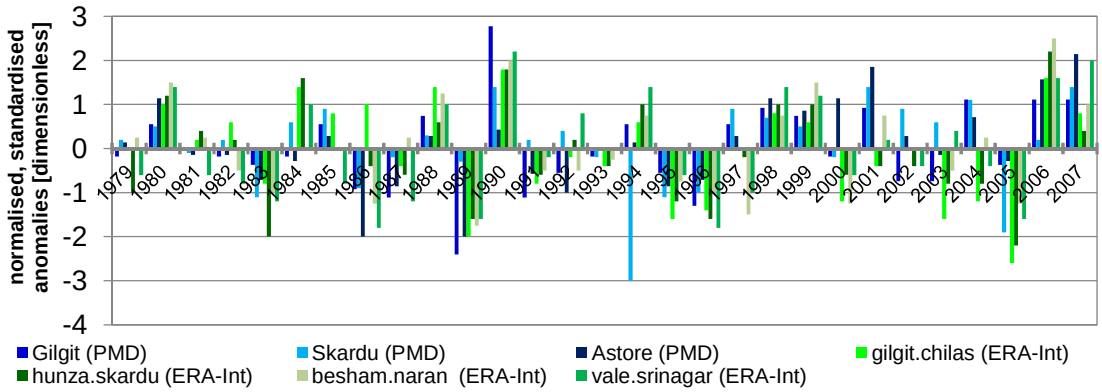

Figure B.28 Time-series of normalised, standardised annual mean Tmin anomalies from local observations (PMD) and ERA-Interim (ERA-Int) for 1979 to 2007.

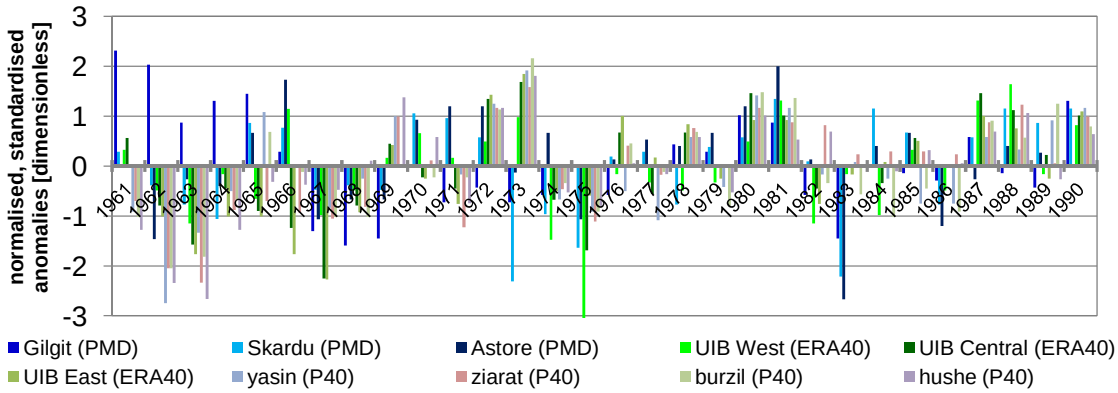

Figure B.29 Time-series of normalised, standardised ONDJFM mean Tmin anomalies from local observations (PMD), ERA-40 and PRECIS_ERA40 (P40) for 1961 to 1990.

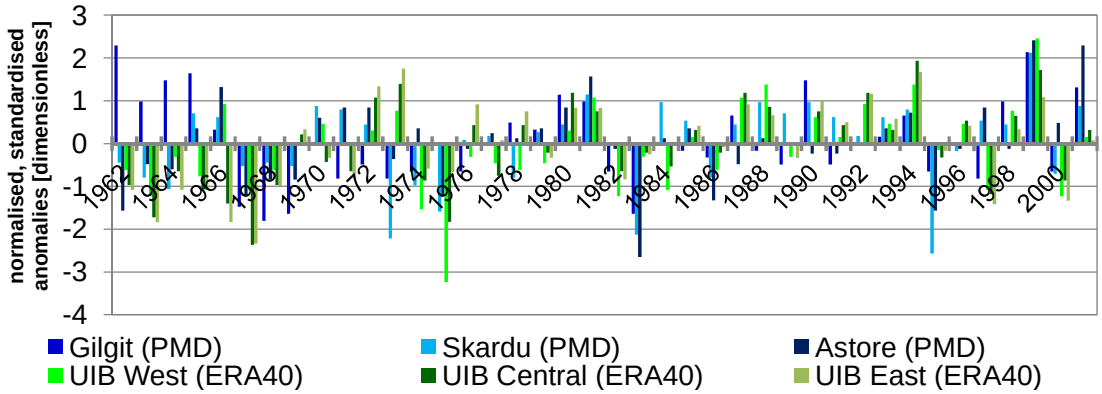

Figure B.30 Time-series of normalised, standardised ONDJFM mean Tmin anomalies from local observations (PMD) and ERA-40 for 1962 to 2001.

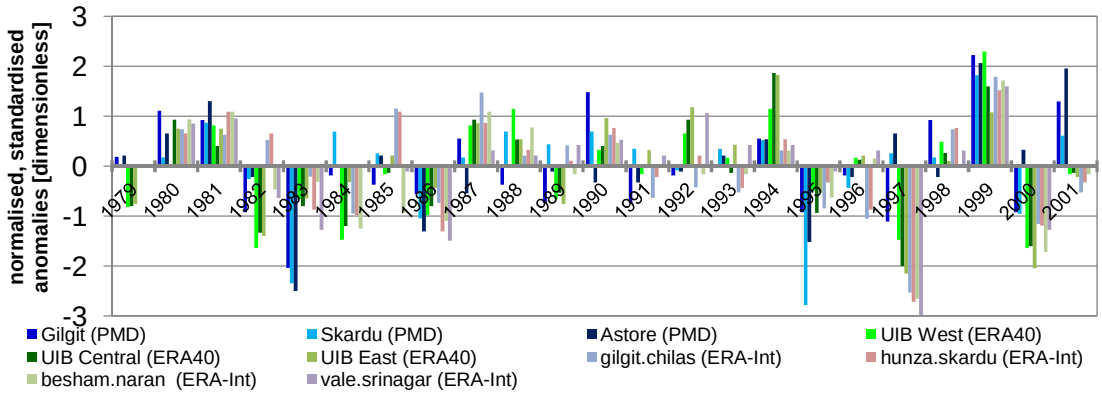

Figure B.31 Time-series of normalised, standardised annual mean Tmin anomalies from local observations (PMD), ERA-40 and ERA-Interim (ERA-Int) for 1979 to 2001.

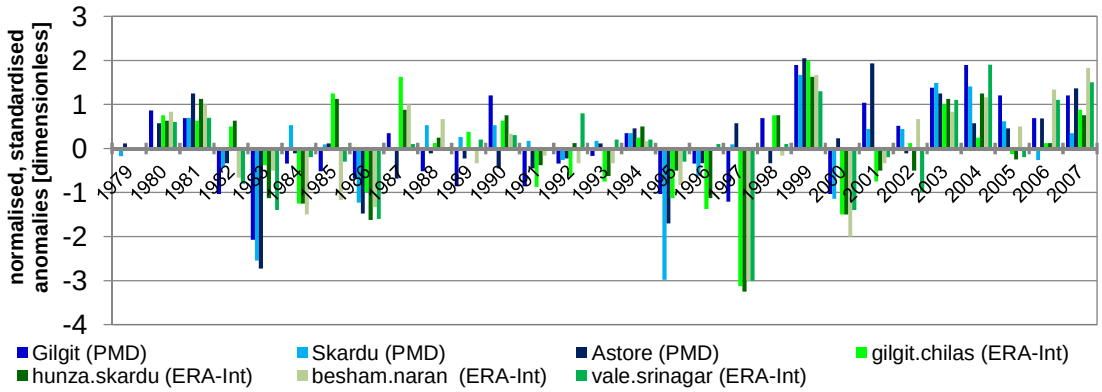

Figure B.32 Time-series of normalised, standardised ONDJFM mean Tmin anomalies from local observations (PMD) and ERA-Interim (ERA-Int) for 1979 to 2007.

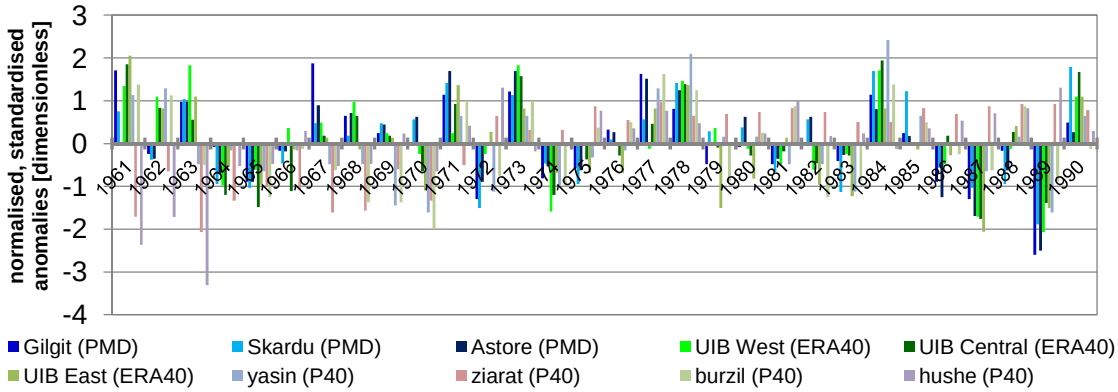

Figure B.33 Time-series of normalised, standardised JJA mean Tmin anomalies from local observations (PMD), ERA-40 and PRECIS_ERA40 (P40) for 1961 to 1990.

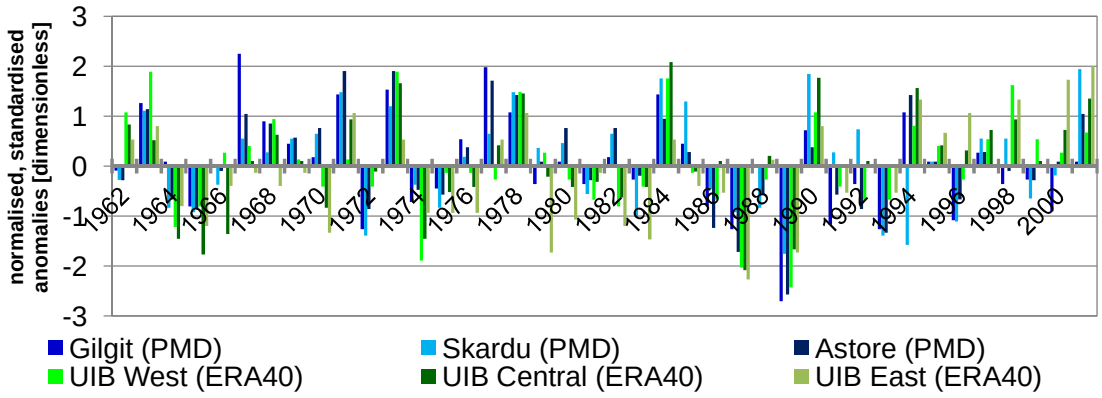

Figure B.34 Time-series of normalised, standardised JJA mean Tmin anomalies from local observations (PMD) and ERA-40 for 1962 to 2001.

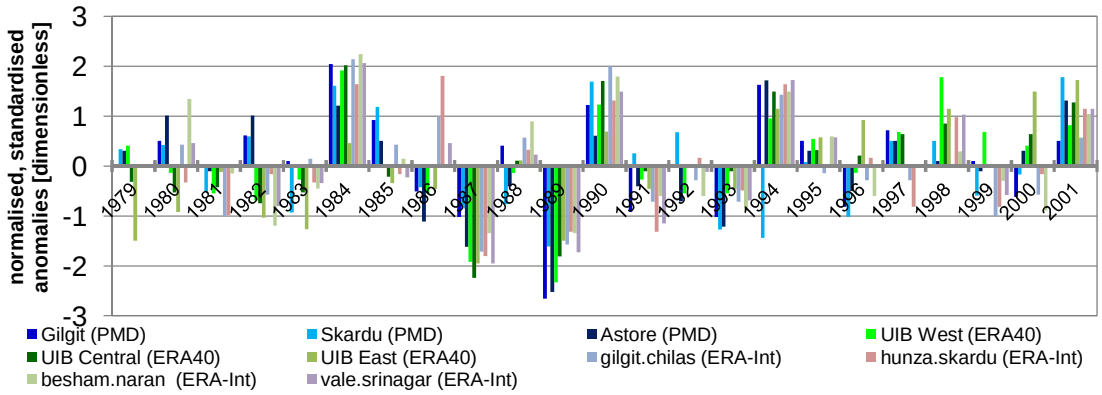

Figure B.35 Time-series of normalised, standardised JJA mean Tmin anomalies from local observations (PMD), ERA-40 and ERA-Interim (ERA-Int) for 1979 to 2001.

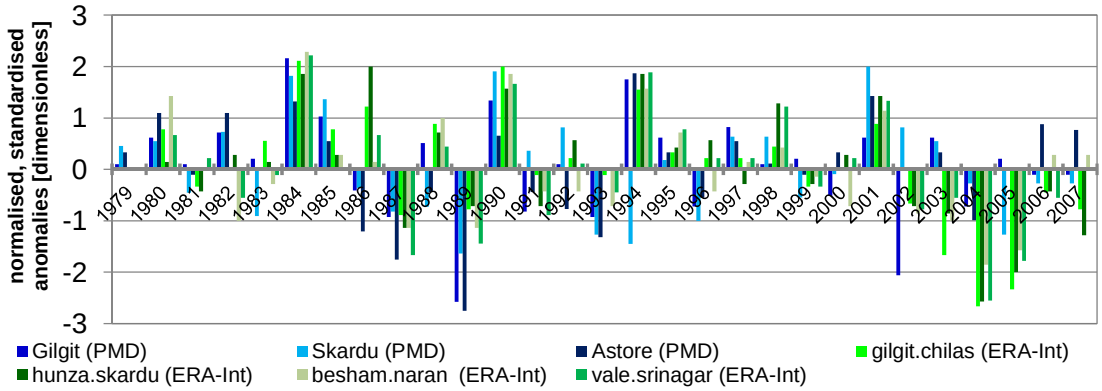

Figure B.36 Time-series of normalised, standardised JJA mean Tmin anomalies from local observations (PMD) and ERA-Interim (ERA-Int) for 1979 to 2007.

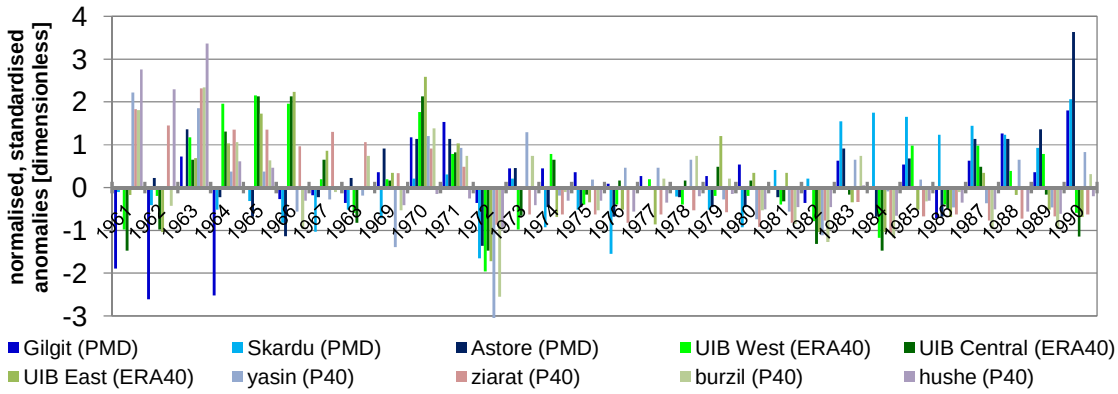

Figure B.37 Time-series of normalised, standardised annual mean DTR anomalies from local observations (PMD), ERA-40 and PRECIS_ERA40 (P40) for 1961 to 1990.

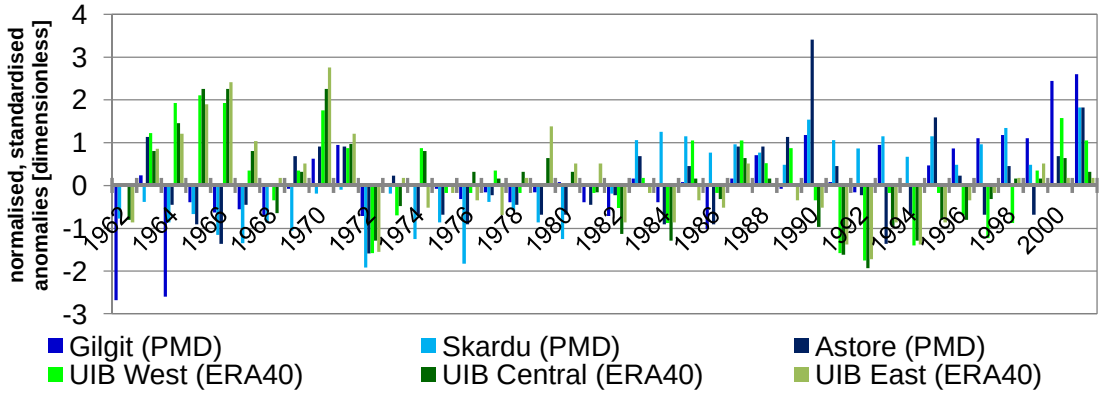

Figure B.38 Time-series of normalised, standardised annual mean DTR anomalies from local observations (PMD) and ERA-40 for 1962 to 2001.

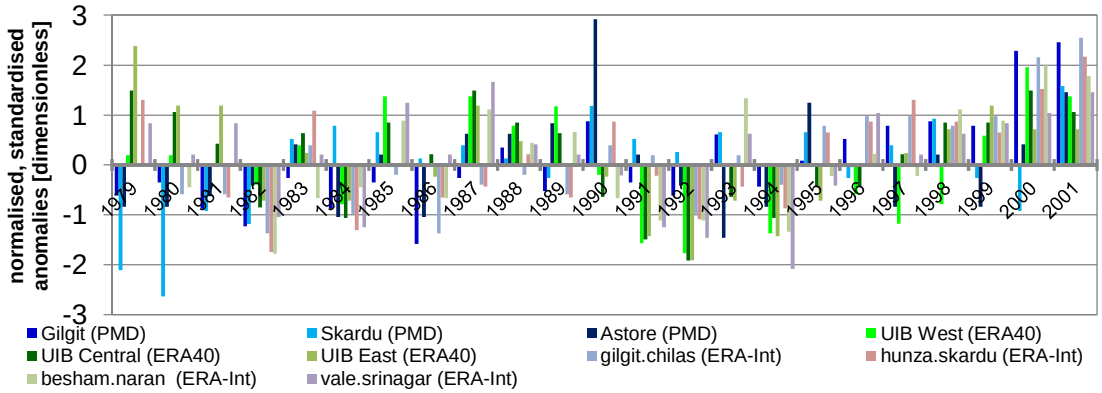

Figure B.39 Time-series of normalised, standardised annual mean DTR anomalies from local observations (PMD), ERA-40 and ERA-Interim (ERA-Int) for 1979 to 2001.

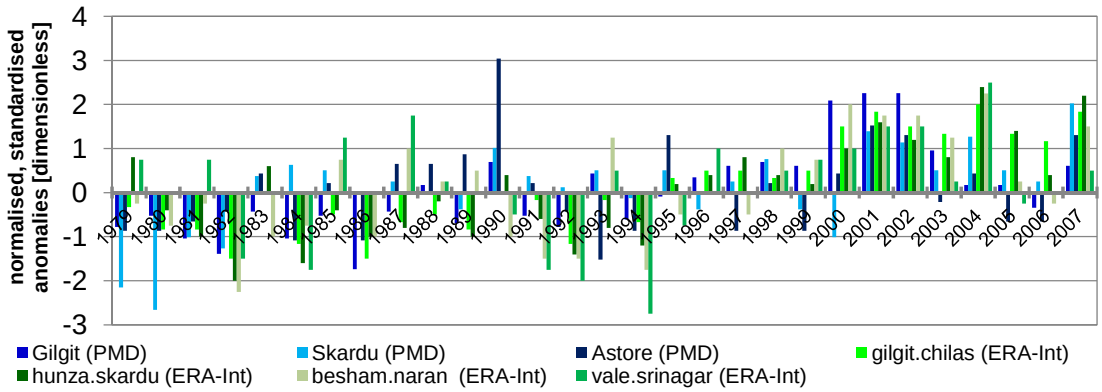

Figure B.40 Time-series of normalised, standardised annual mean DTR anomalies from local observations (PMD) and ERA-Interim (ERA-Int) for 1979 to 2007.

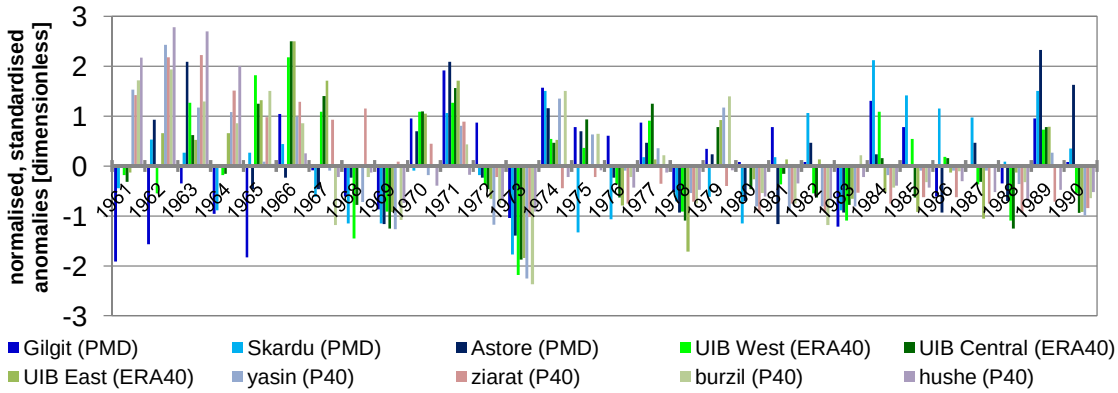

Figure B.41 Time-series of normalised, standardised ONDJFM mean DTR anomalies from local observations (PMD), ERA-40 and PRECIS_ERA40 (P40) for 1961 to 1990.

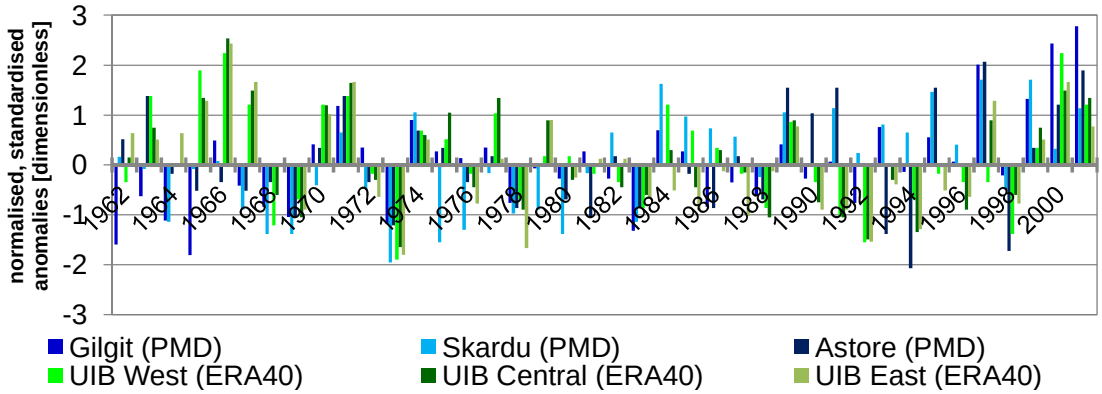

Figure B.42 Time-series of normalised, standardised ONDJFM mean DTR anomalies from local observations (PMD) and ERA-40 for 1962 to 2001.

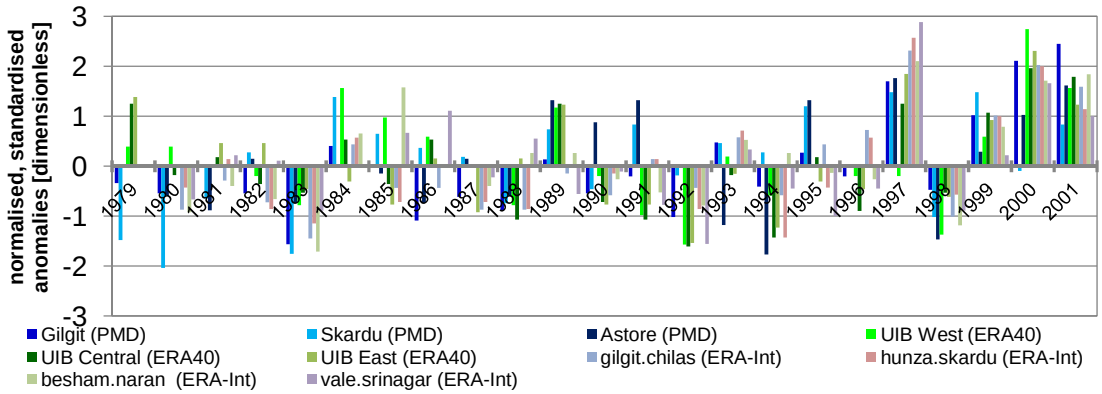

Figure B.43 Time-series of normalised, standardised annual mean DTR anomalies from local observations (PMD), ERA-40 and ERA-Interim (ERA-Int) for 1979 to 2001.

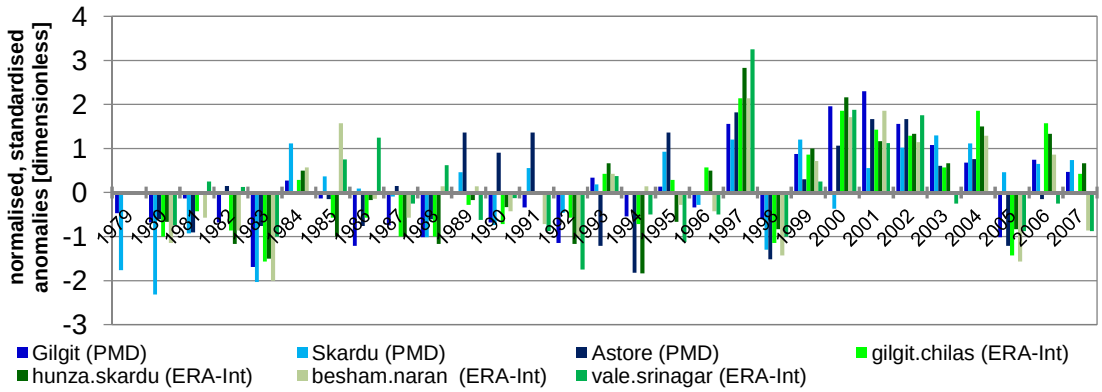

Figure B.44 Time-series of normalised, standardised ONDJFM mean DTR anomalies from local observations (PMD) and ERA-Interim (ERA-Int) for 1979 to 2007.

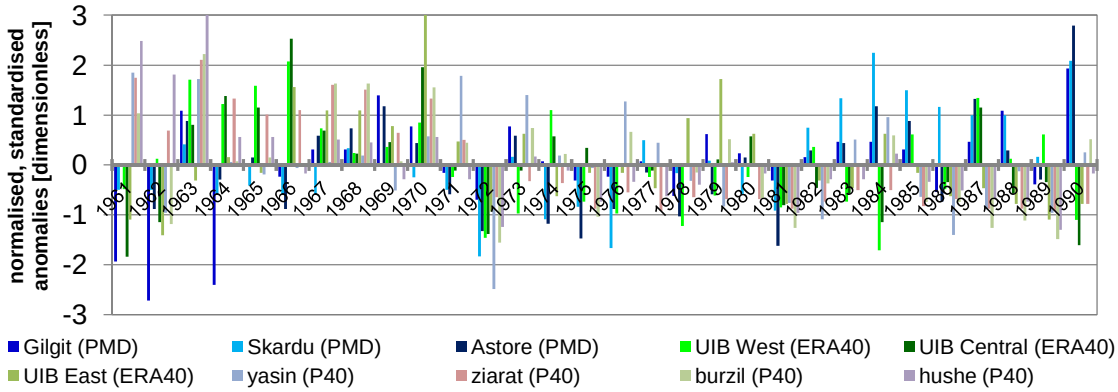

Figure B.45 Time-series of normalised, standardised JJA mean DTR anomalies from local observations (PMD), ERA-40 and PRECIS_ERA40 (P40) for 1961 to 1990.

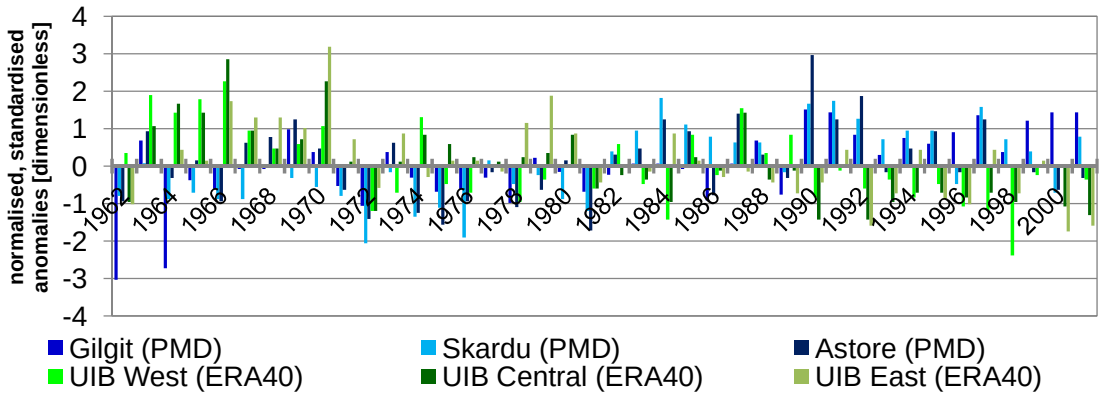

Figure B.46 Time-series of normalised, standardised JJA mean DTR anomalies from local observations (PMD) and ERA-40 for 1962 to 2001.

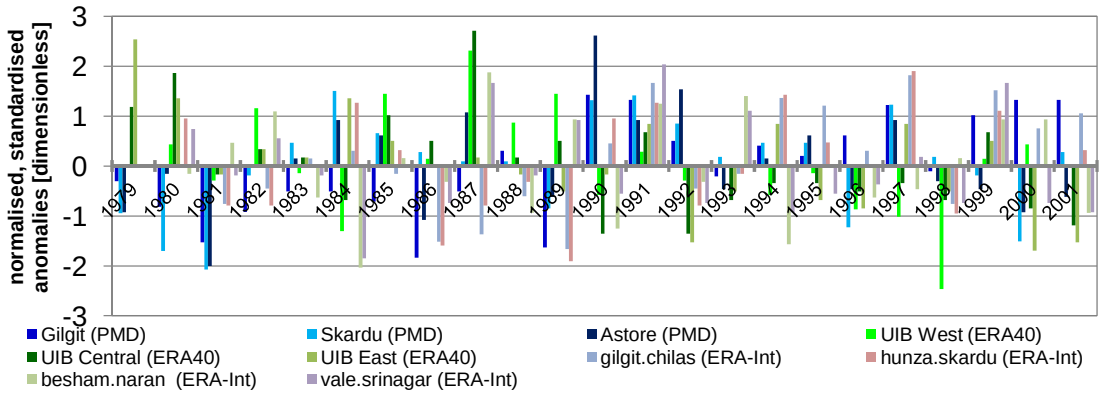

Figure B.47 Time-series of normalised, standardised JJA mean DTR anomalies from local observations (PMD), ERA-40 and ERA-Interim (ERA-Int) for 1979 to 2001.

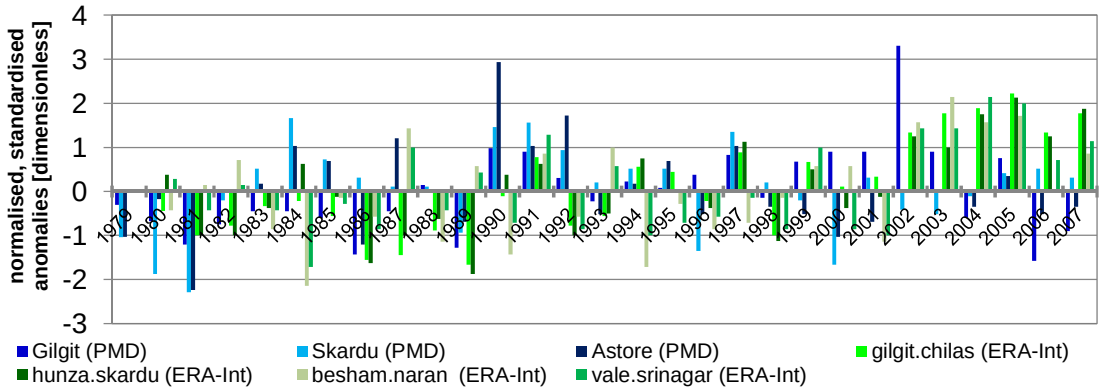

Figure B.48 Time-series of normalised, standardised JJA mean DTR anomalies from local observations (PMD) and ERA-Interim (ERA-Int) for 1979 to 2007.

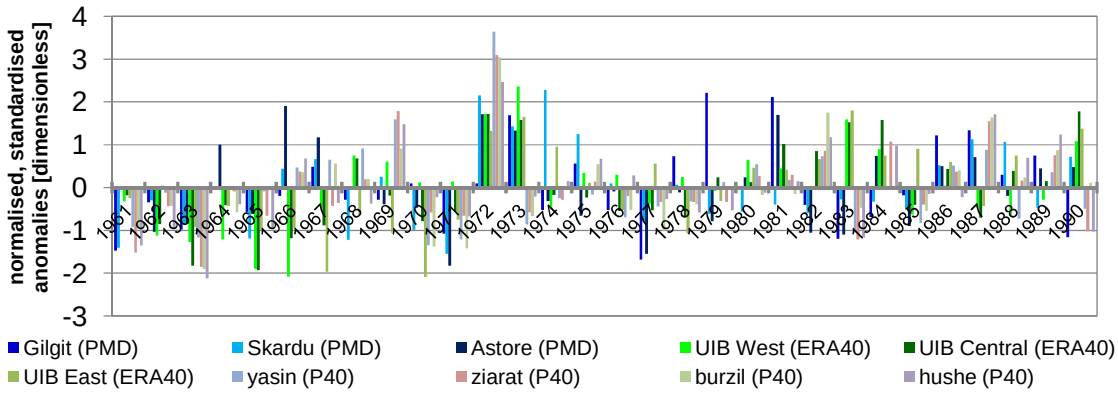

Figure B.49 Time-series of normalised, standardised annual total precipitation anomalies from local observations (PMD), ERA-40 and PRECIS_ERA40 (P40) for 1961 to 1990.

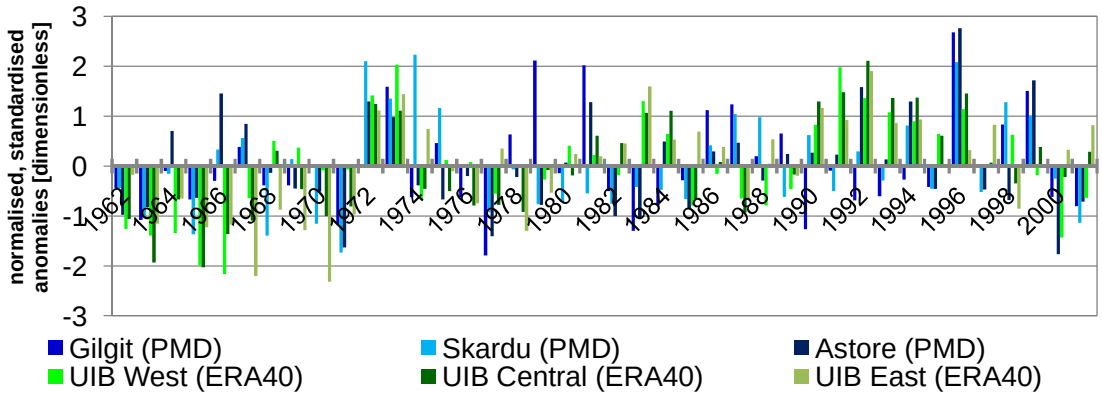

Figure B.50 Time-series of normalised, standardised annual total precipitation anomalies from local observations (PMD) and ERA-40 for 1962 to 2001.

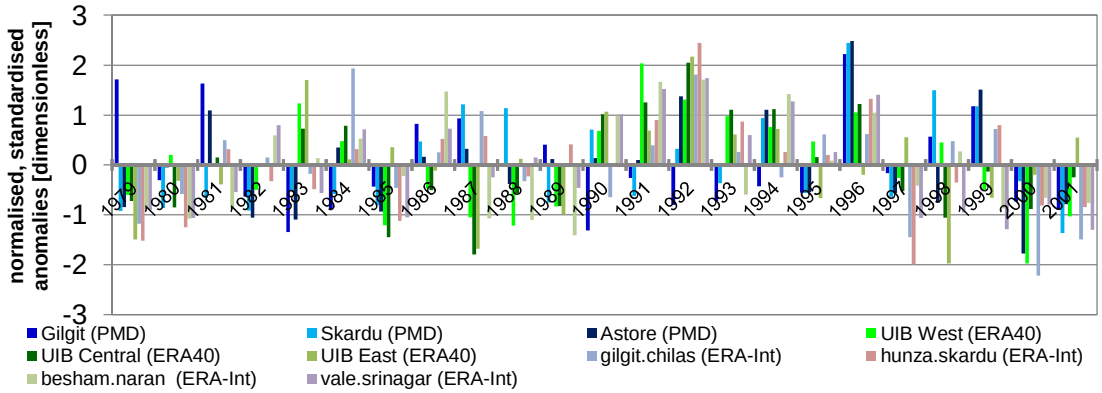

Figure B.51 Time-series of normalised, standardised annual total precipitation anomalies from local observations (PMD), ERA-40 and ERA-Interim (ERA-Int) for 1979 to 2001.

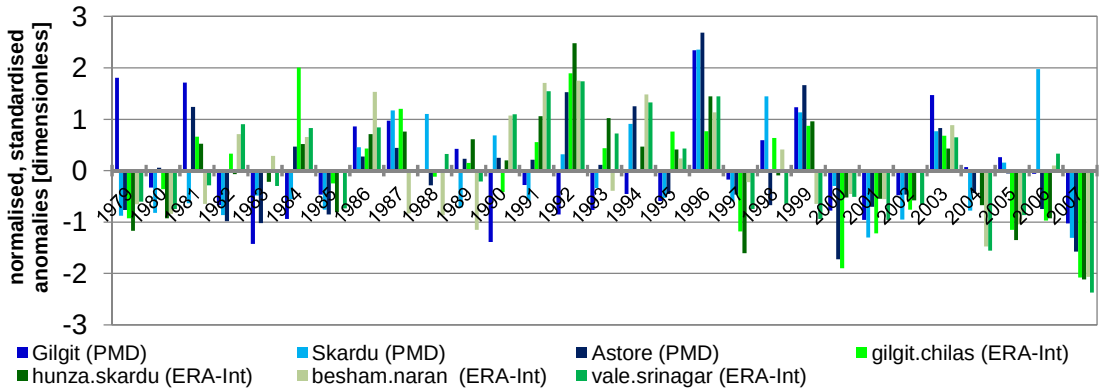

Figure B.52 Time-series of normalised, standardised annual total precipitation anomalies from local observations (PMD) and ERA-Interim (ERA-Int) for 1979 to 2007.

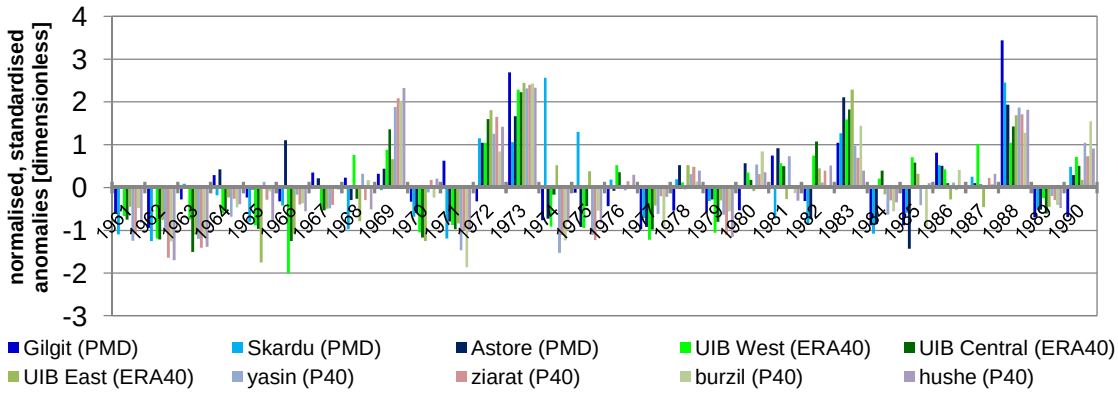

Figure B.53 Time-series of normalised, standardised ONDJFM total precipitation anomalies from local observations (PMD), ERA-40 and PRECIS_ERA40 (P40) for 1961 to 1990.

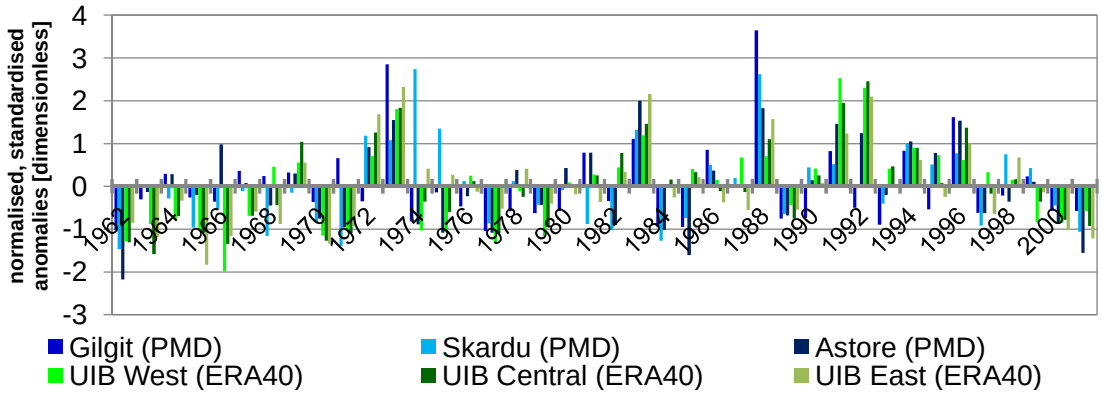

Figure B.54 Time-series of normalised, standardised ONDJFM total precipitation anomalies from local observations (PMD) and ERA-40 for 1962 to 2001.

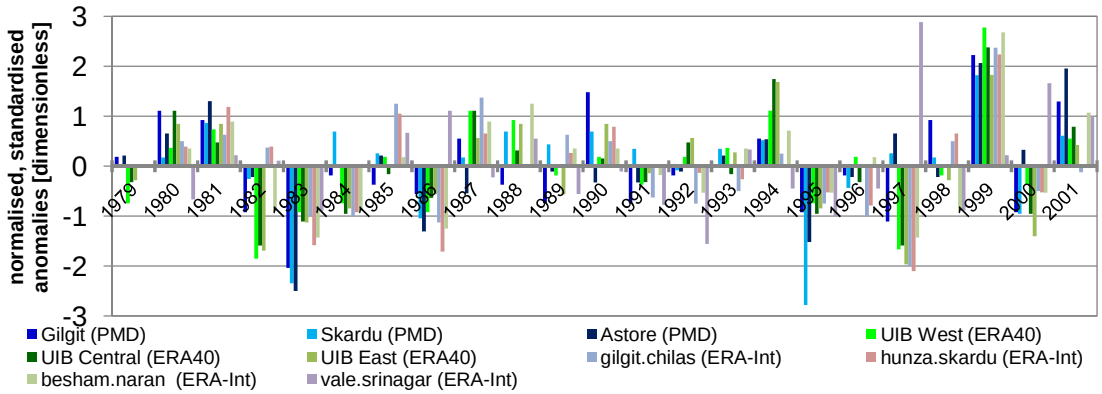

Figure B.55 Time-series of normalised, standardised ONDJFM total precipitation anomalies from local observations (PMD), ERA-40 and ERA-Interim (ERA-Int) for 1979 to 2001.

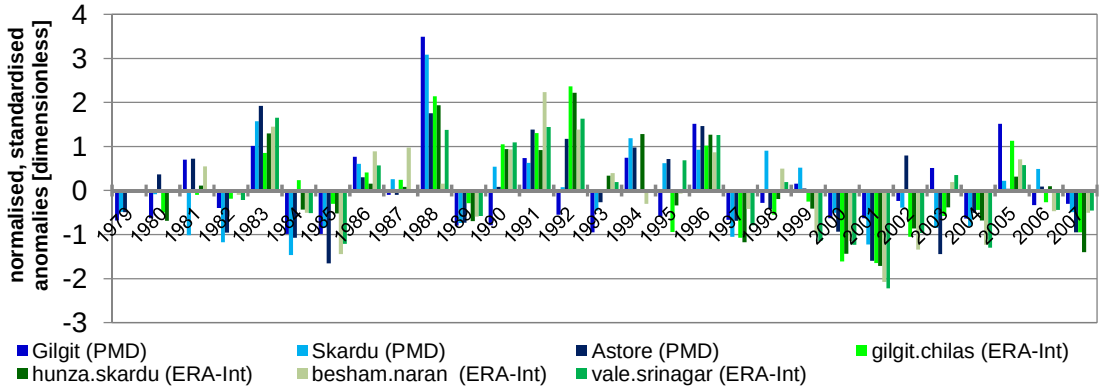

Figure B.56 Time-series of normalised, standardised ONDJFM total precipitation anomalies from local observations (PMD) and ERA-Interim (ERA-Int) for 1979 to 2007.

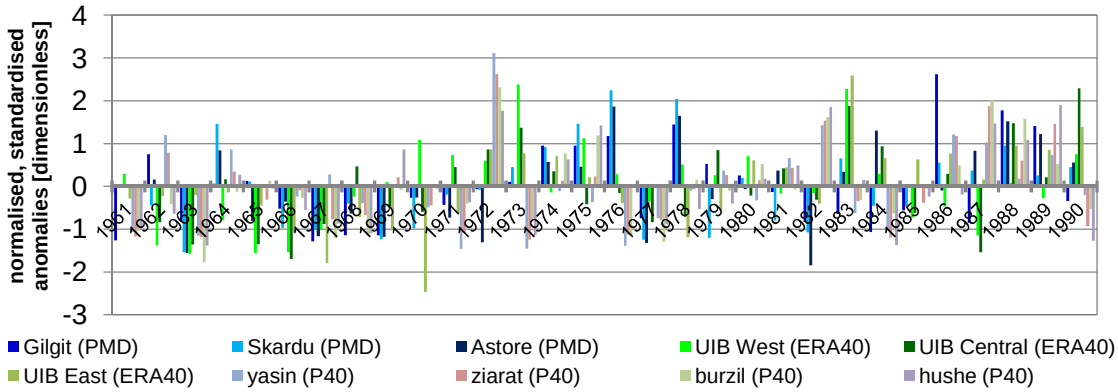

Figure B.57 Time-series of normalised, standardised JJA total precipitation anomalies from local observations (PMD), ERA-40 and PRECIS_ERA40 (P40) for 1961 to 1990.

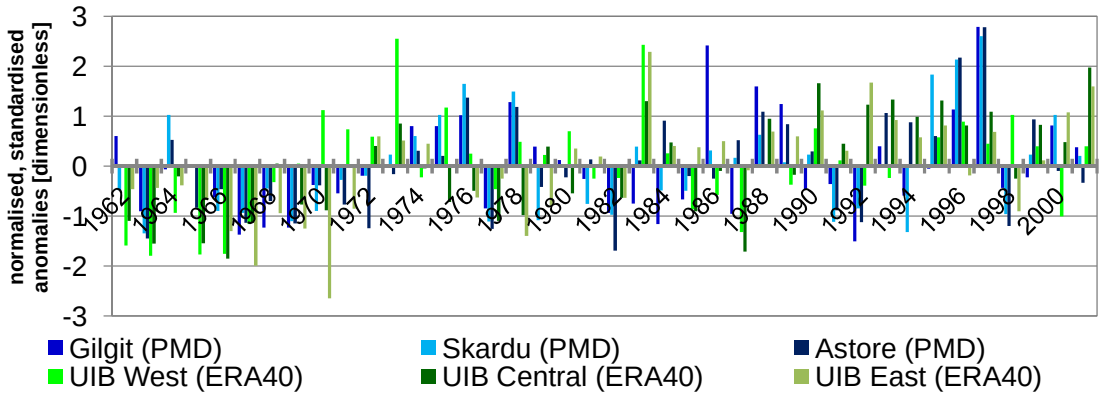

Figure B.58 Time-series of normalised, standardised JJA total precipitation anomalies from local observations (PMD) and ERA-40 for 1962 to 2001.

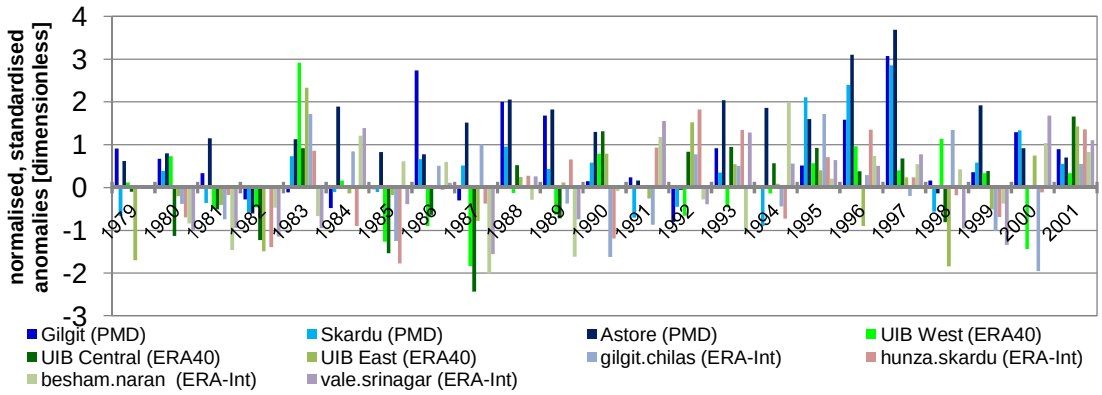

Figure B.59 Time-series of normalised, standardised JJA total precipitation anomalies from local observations (PMD), ERA-40 and ERA-Interim (ERA-Int) for 1979 to 2001.

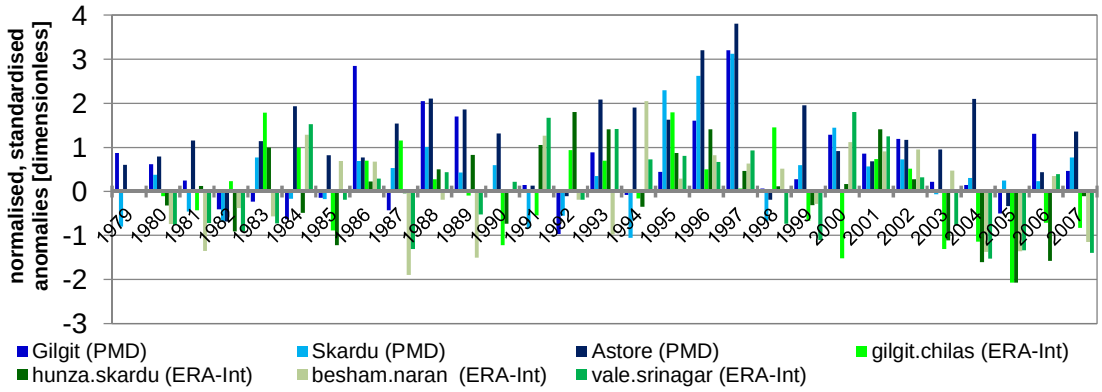

Figure B.60 Time-series of normalised, standardised JJA total precipitation anomalies from local observations (PMD) and ERA-Interim (ERA-Int) for 1979 to 2007.

B.2 Statistical significance of linear trends in ERA-Interim and PRECIS_ERA40.

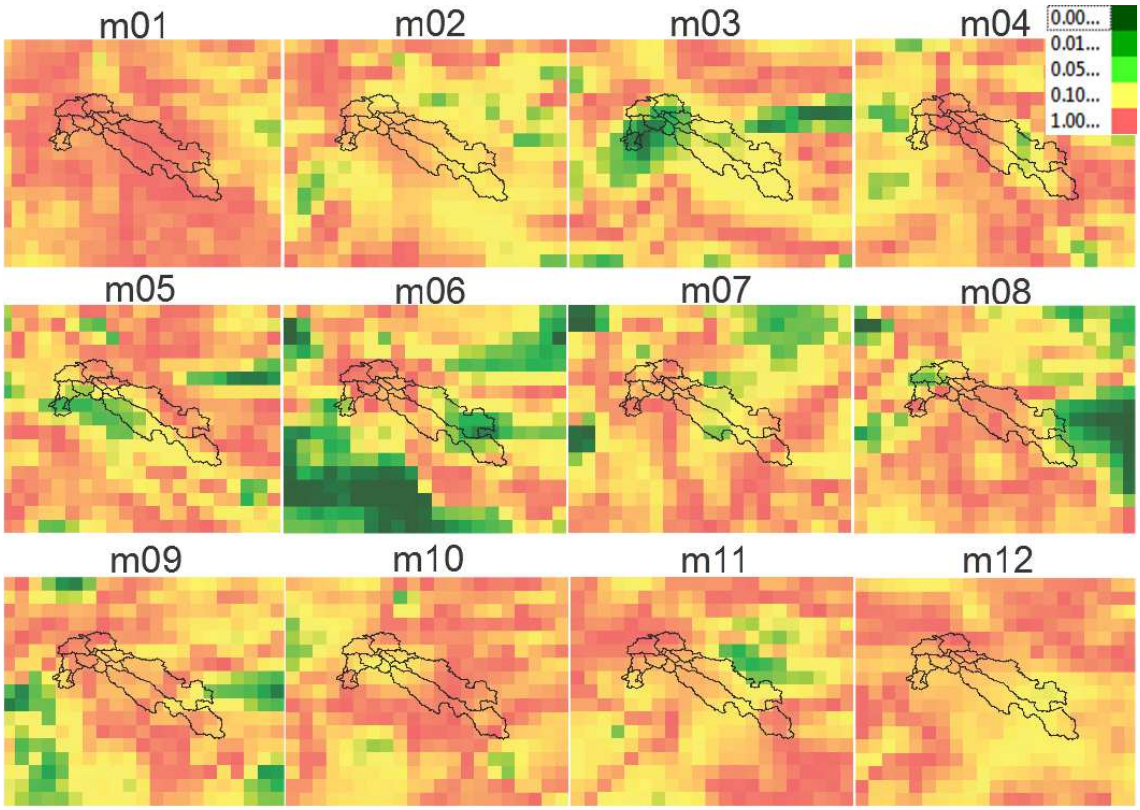

Figure B.61 ERA-Interim, 1979 to 2007, 2-tailed significance of correlation with time (year index), Precipitation.

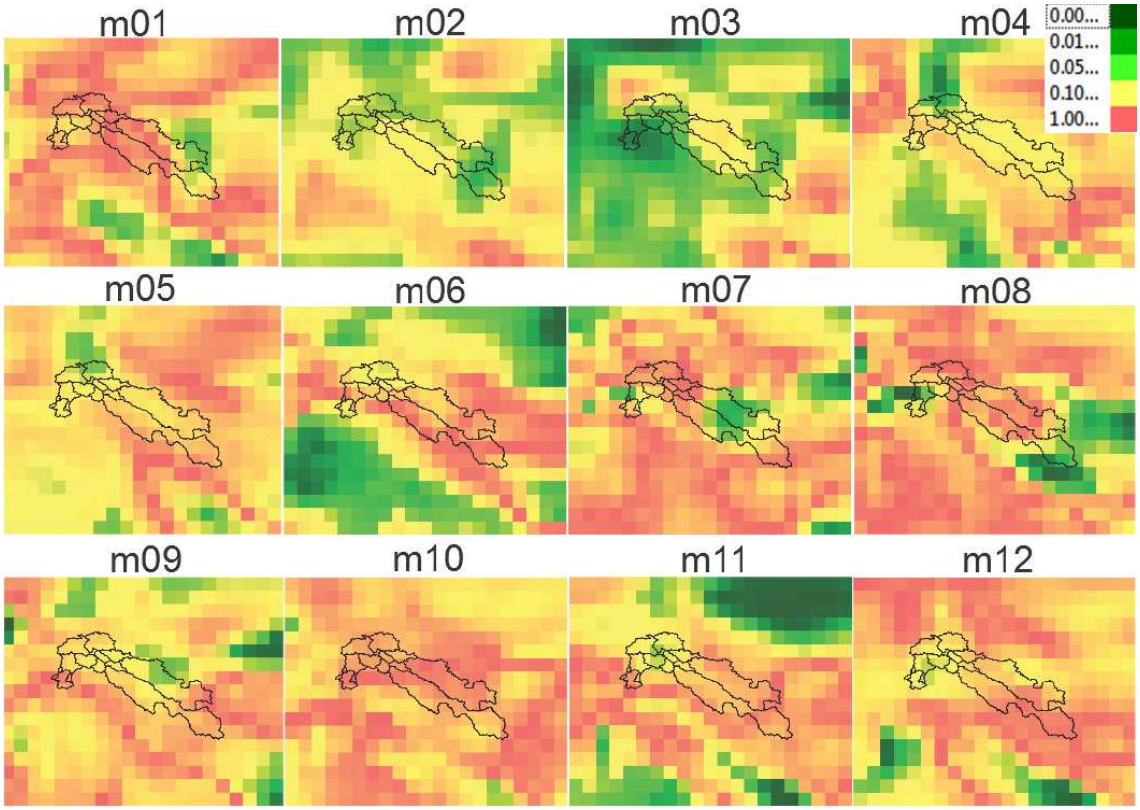

Figure B.62 ERA-Interim, 1979 to 2007, 2-tailed significance of correlation with time (year index), Tmax.

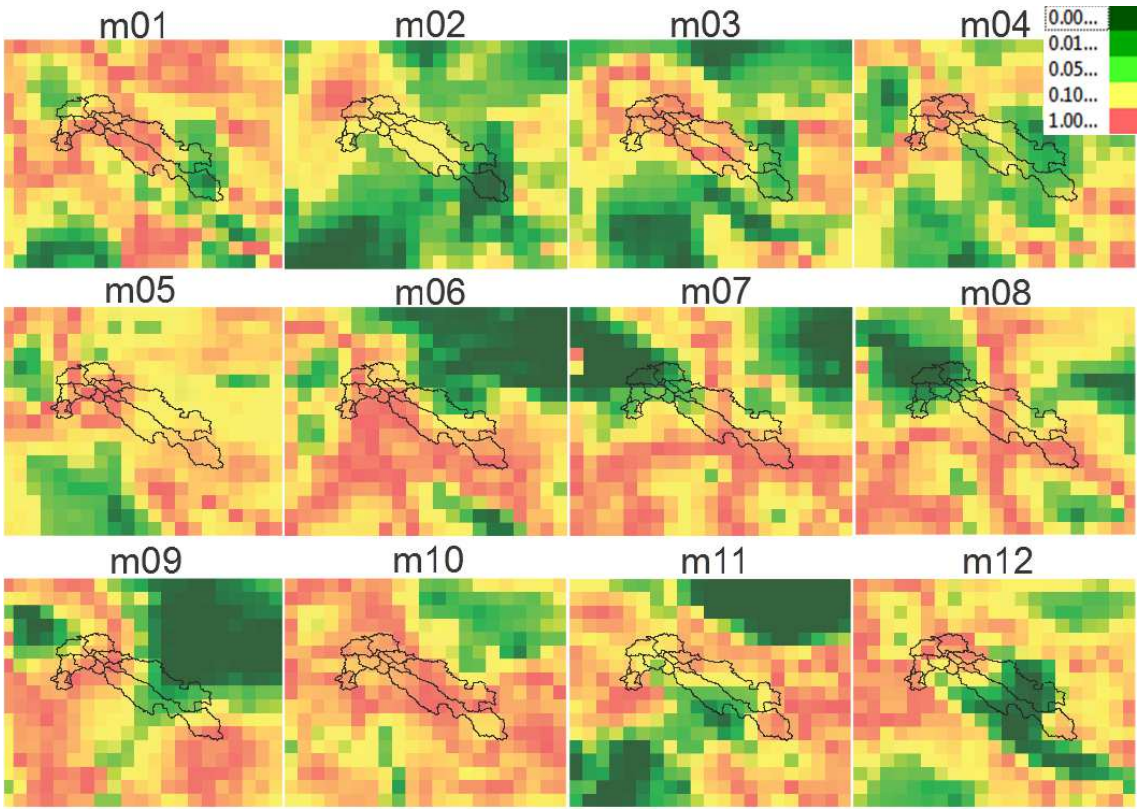

Figure B.63 ERA-Interim, 1979 to 2007, 2-tailed significance of correlation with time (year index), Tmin.

B.3 Teleconnections

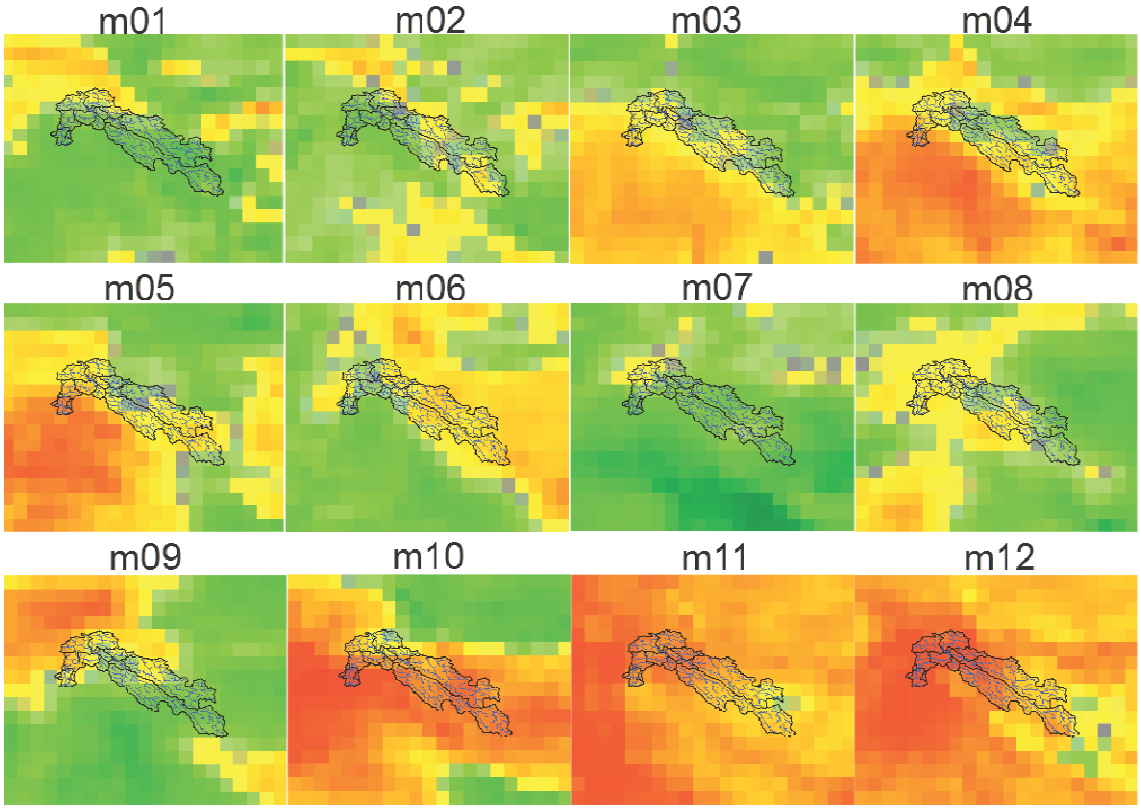

Figure B.64 Teleconnection testing for relationships between DTR (ERA-Interim, 1979 to 2007) and MEI for concurrent response (L00).

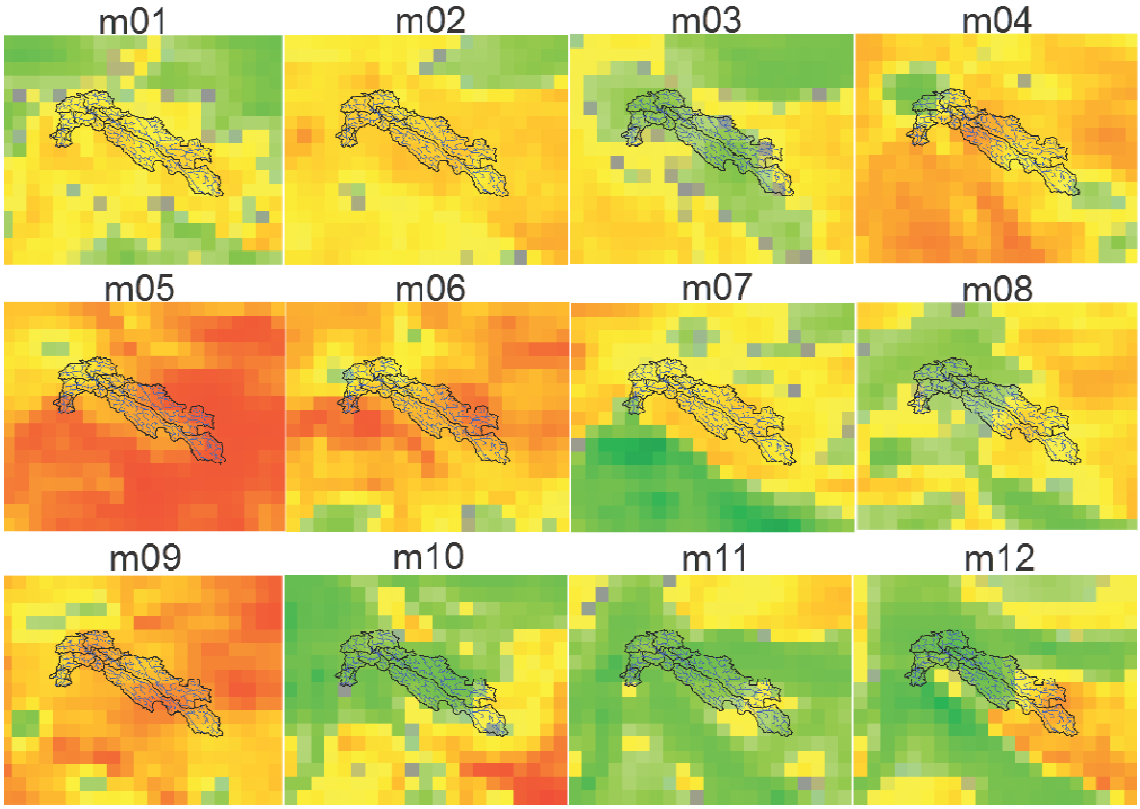

Figure B.65 Teleconnection testing for relationships between Tmin (ERA-Interim, 1979 to 2007) and MEI for concurrent response (L00).

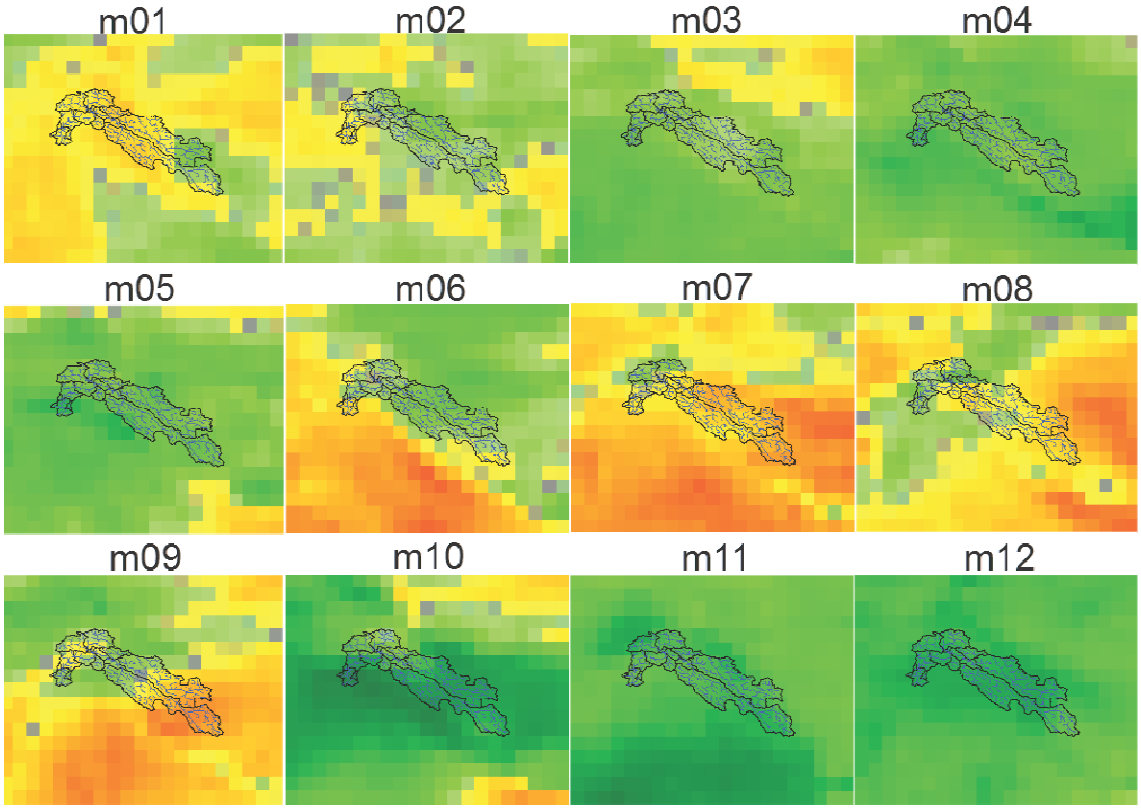

Figure B.66 Teleconnection testing for relationships between TCFavg (ERA-Interim, 1979 to 2007) and MEI for concurrent response (L00).

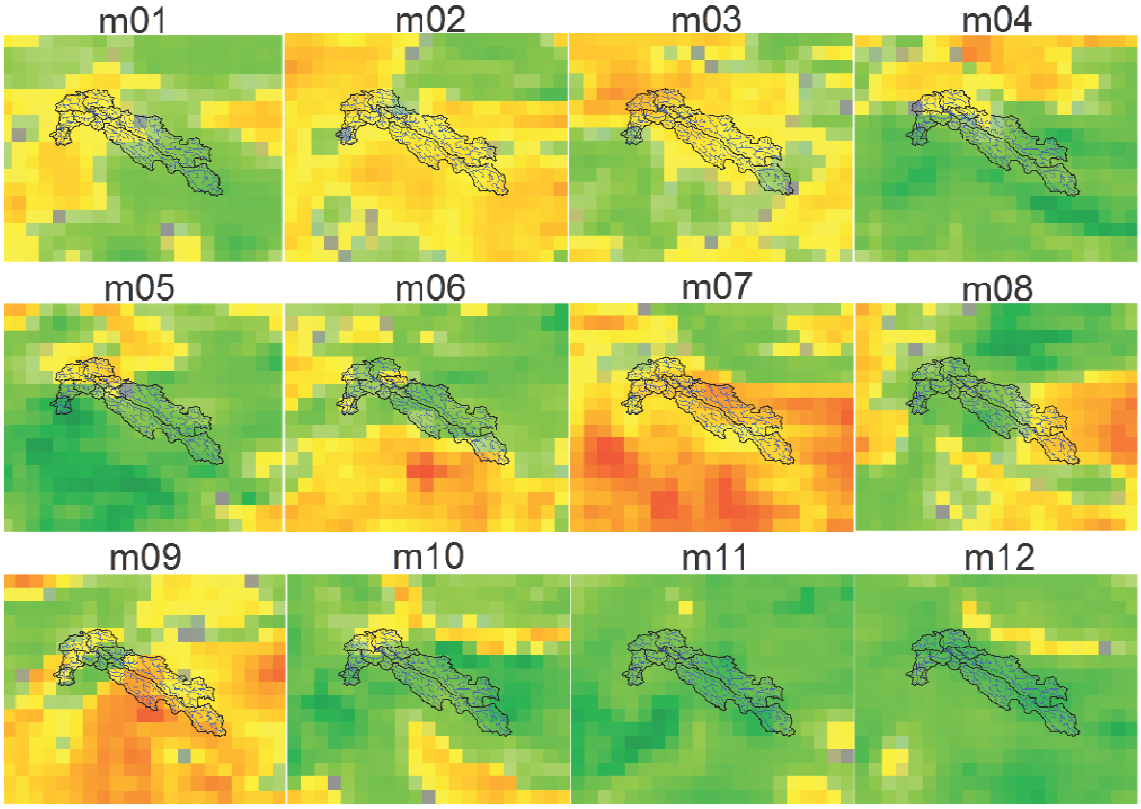

Figure B.67 Teleconnection testing for relationships between precipitation (ERA-Interim, 1979 to 2007) and MEI for concurrent response (L00).

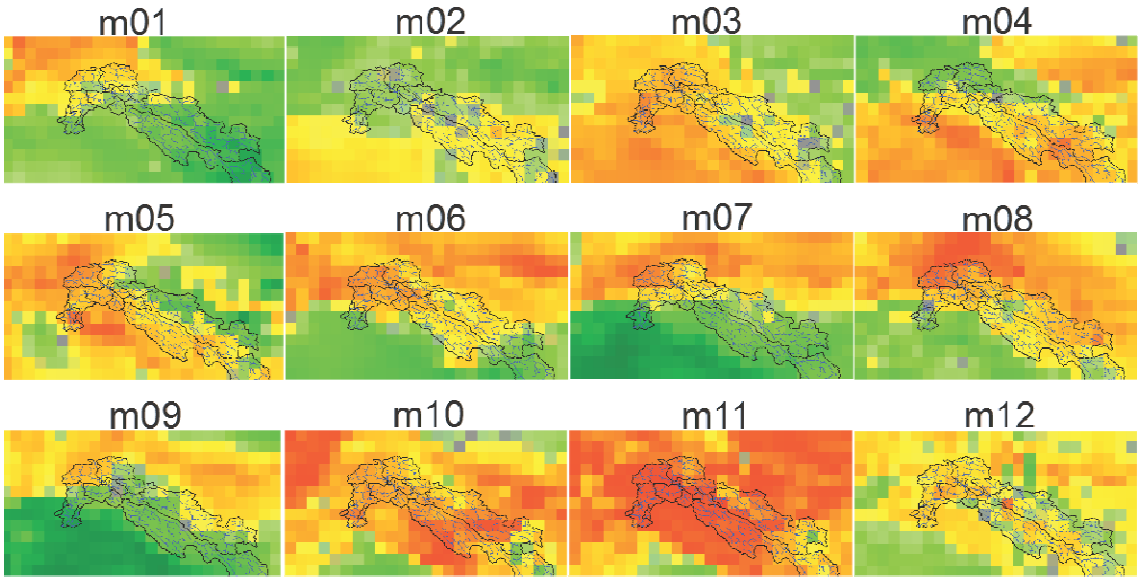

Figure B.68 Teleconnection testing for relationships between DTR (PRECIS_ERA40, 1961 to 1989) and MEI for concurrent response (L00).

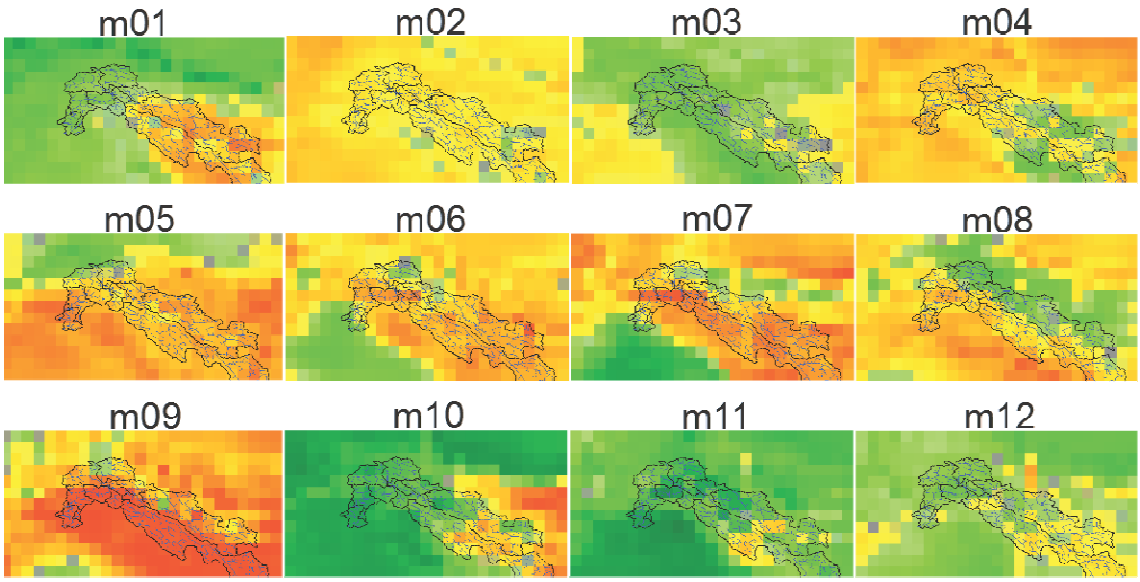

Figure B.69 Teleconnection testing for relationships between Tmin (PRECIS_ERA40, 1961 to 1989) and MEI for concurrent response (L00).

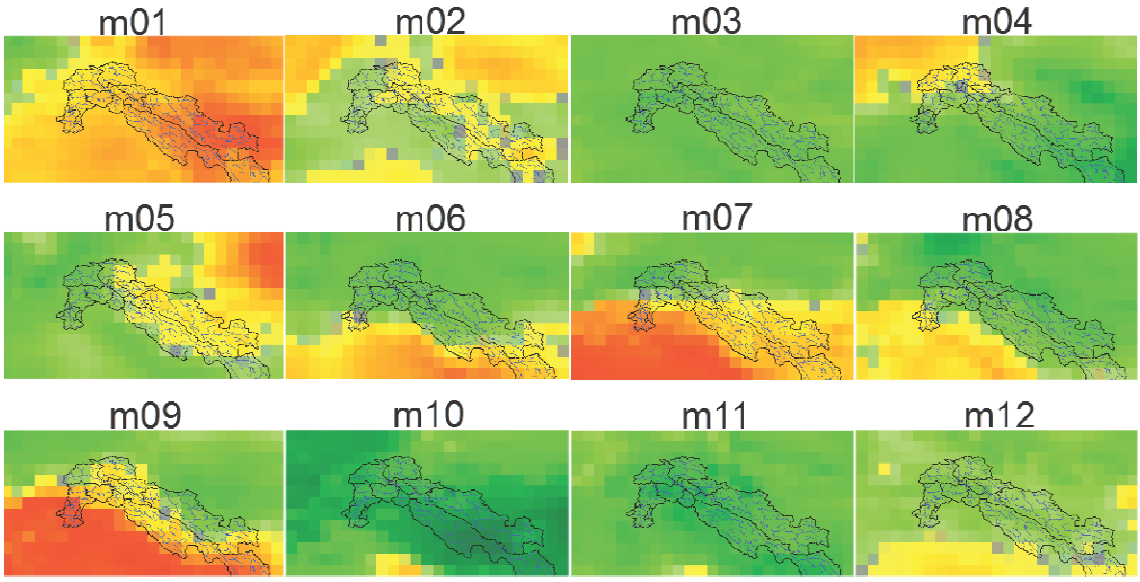

Figure B.70 Teleconnection testing for relationships between TCFavg (PRECIS_ERA40, 1961 to 1989) and MEI for concurrent response (L00).

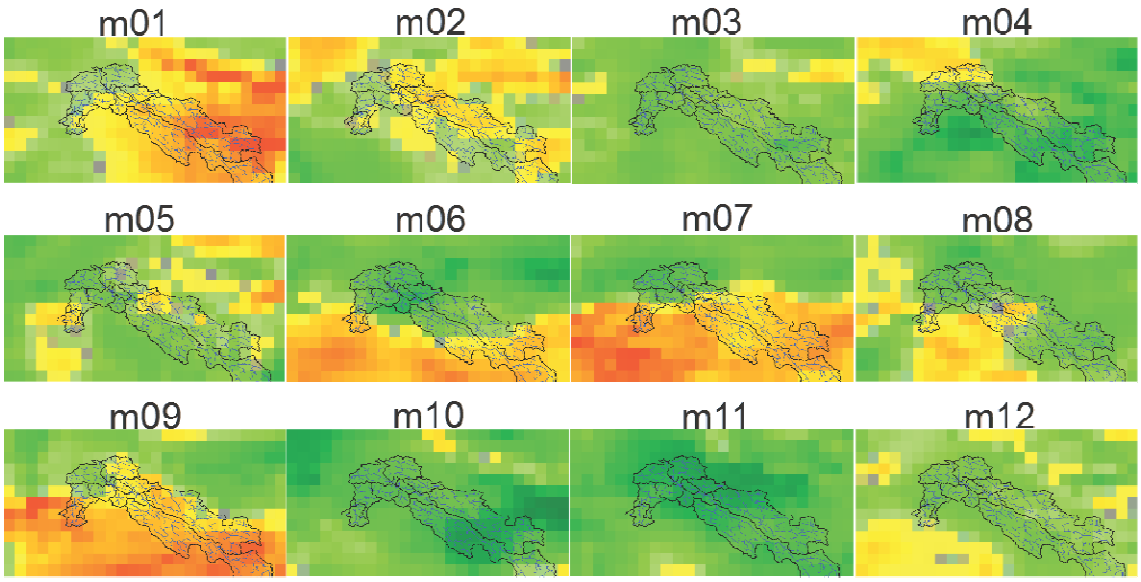

Figure B.71 Teleconnection testing for relationships between precipitation (PRECIS_ERA40, 1961 to 1989) and MEI for concurrent response (L00).

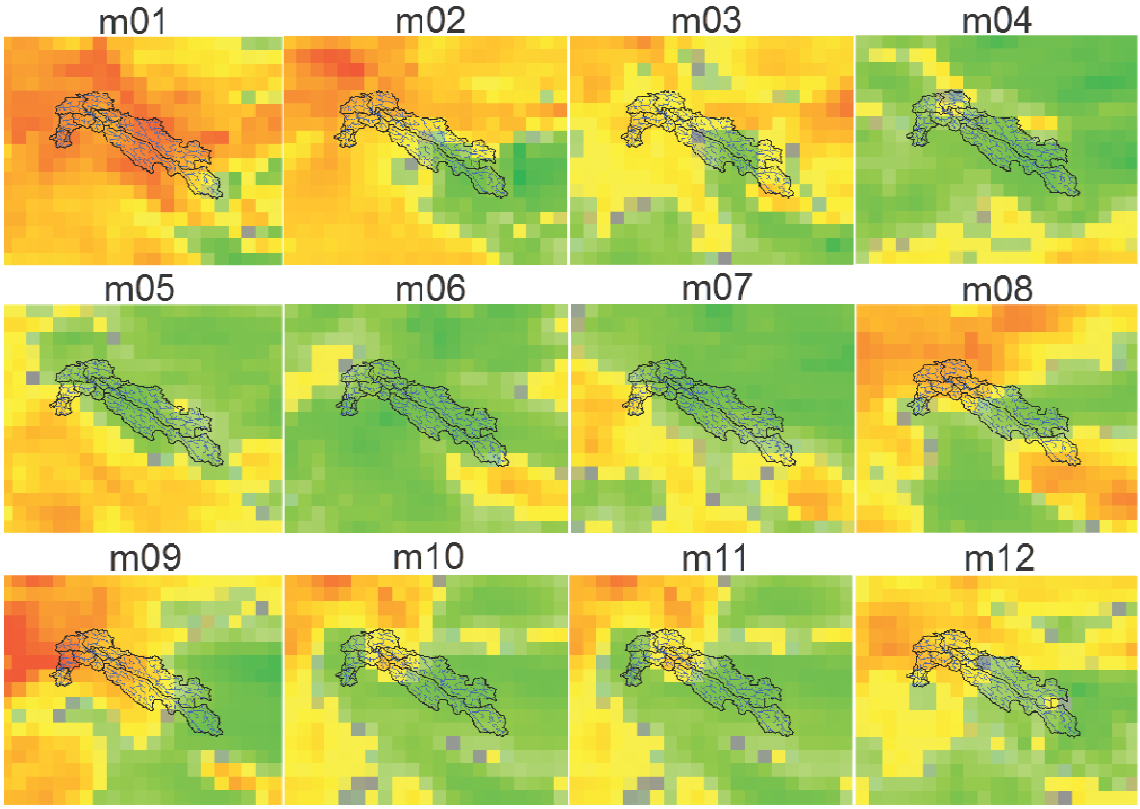

Figure B.72 Teleconnection testing for relationships between DTR (ERA-Interim, 1979 to 2007) and NAO for concurrent response (L00).

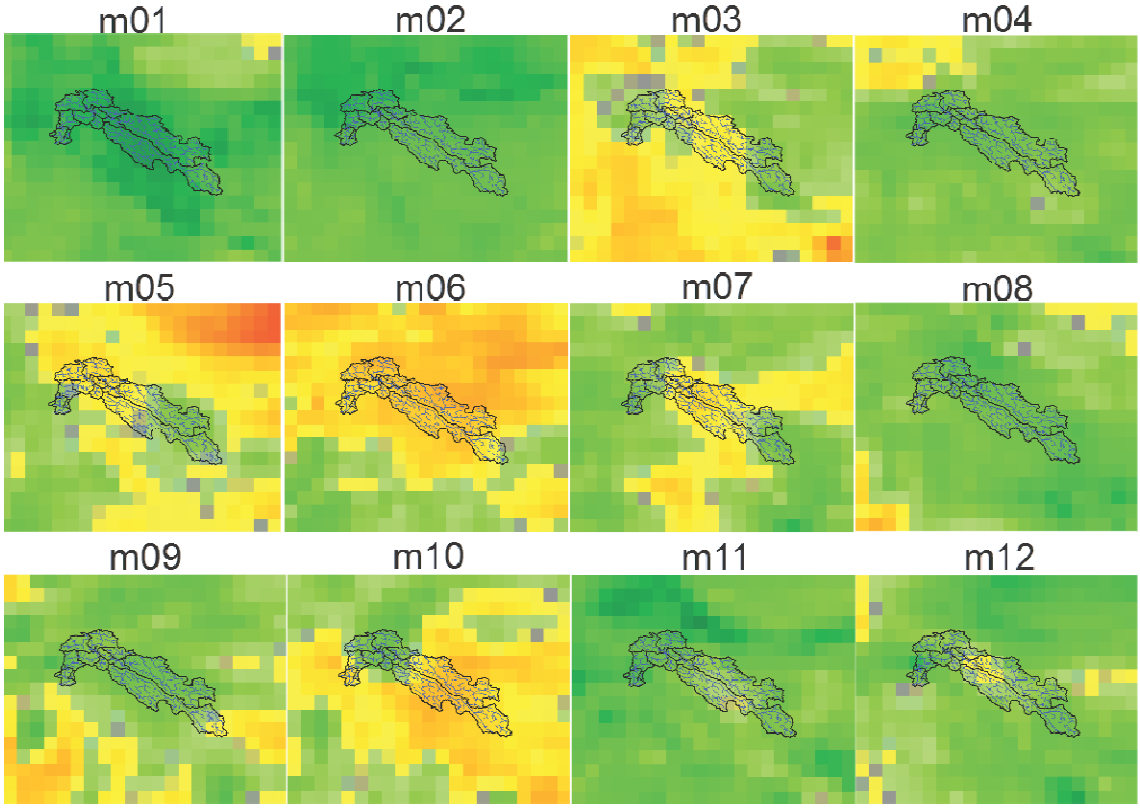

Figure B.73 Teleconnection testing for relationships between Tmin (ERA-Interim, 1979 to 2007) and NAO for concurrent response (L00).

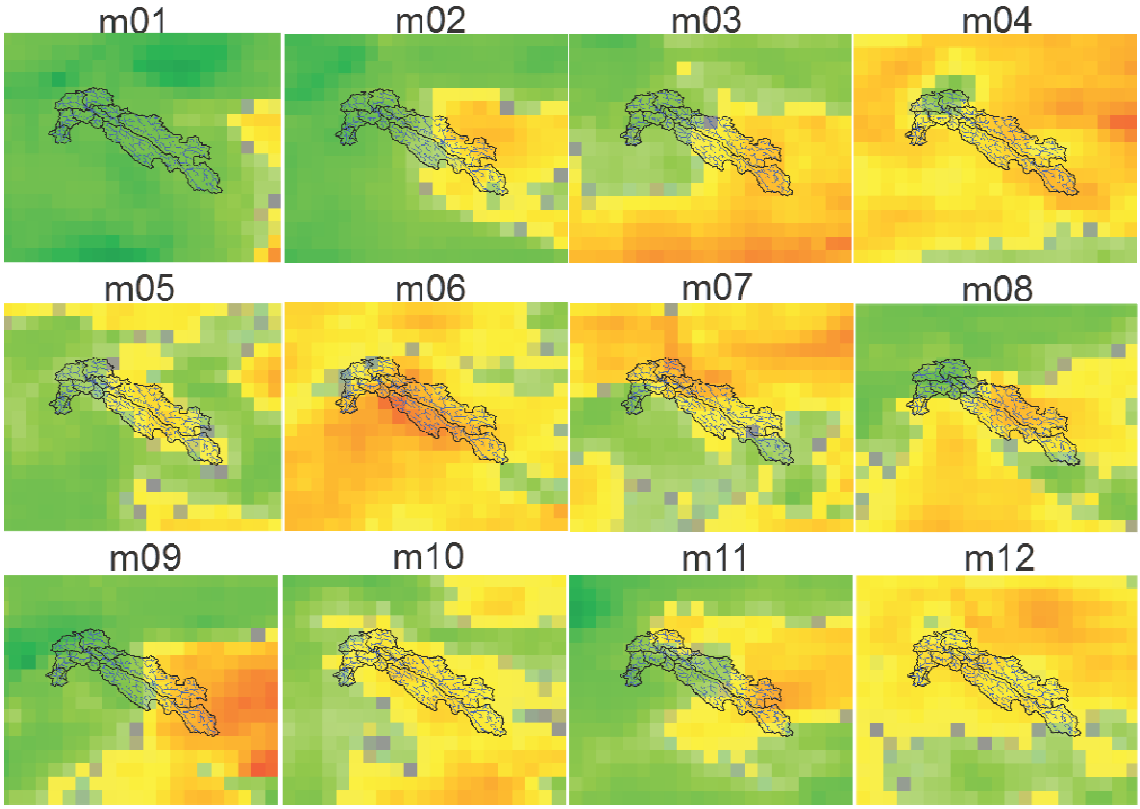

Figure B.74 Teleconnection testing for relationships between TCFavg (ERA-Interim, 1979 to 2007) and NAO for concurrent response (L00).

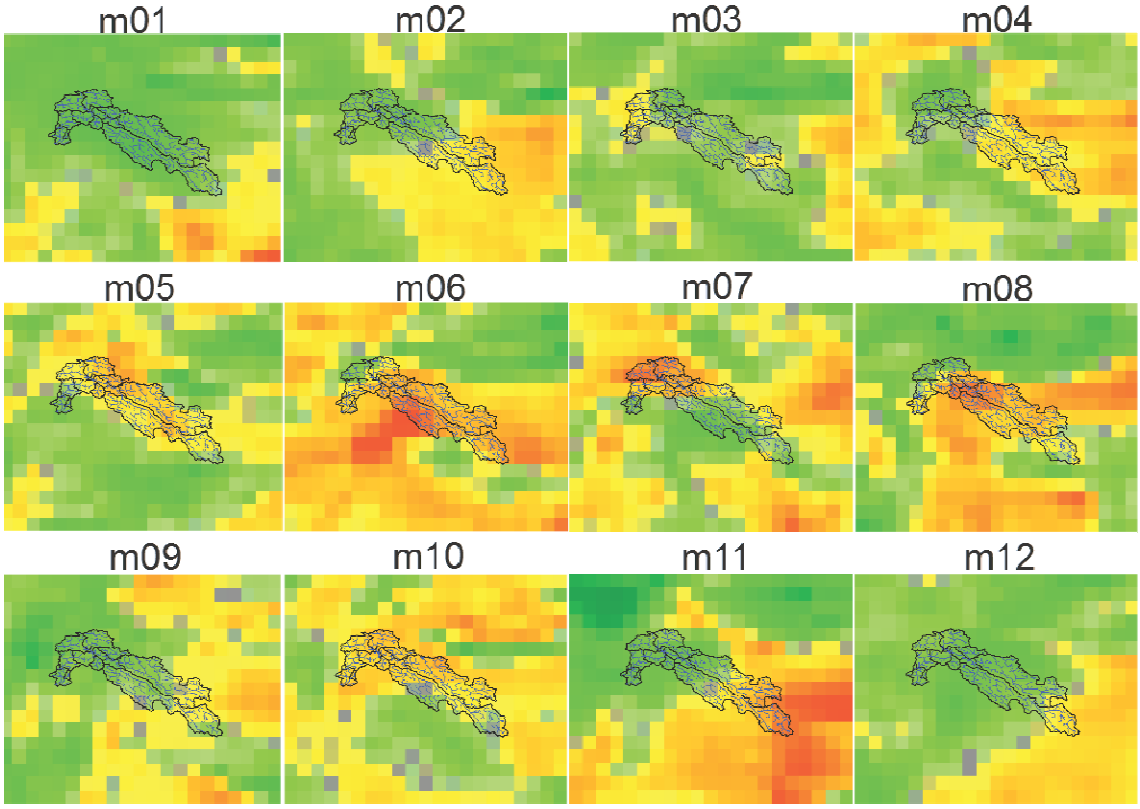

Figure B.75 Teleconnection testing for relationships between precipitation (ERA-Interim, 1979 to 2007) and NAO for concurrent response (L00).

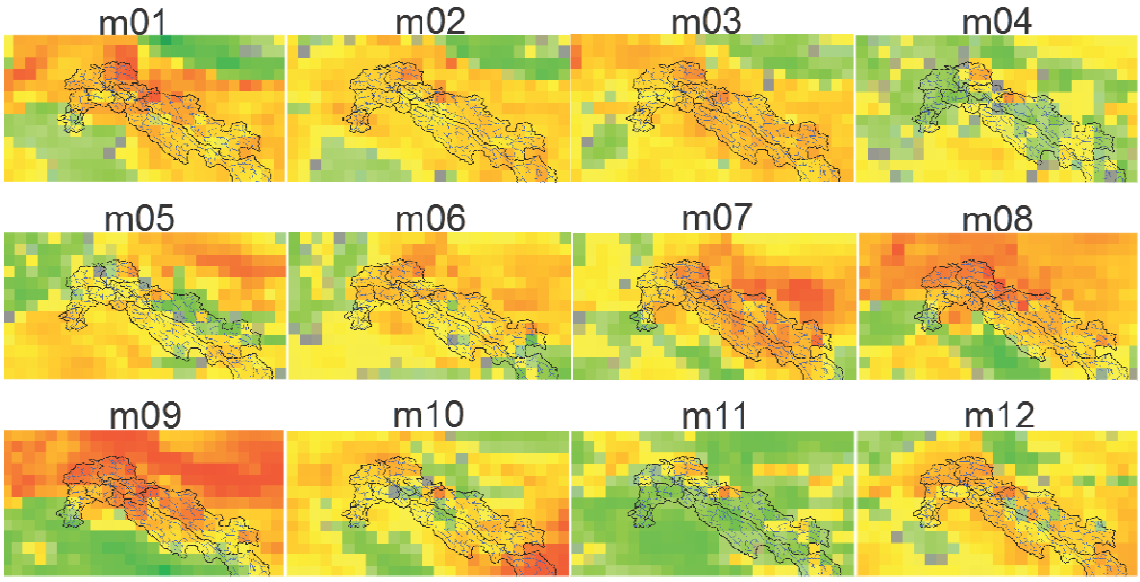

Figure B.76 Teleconnection testing for relationships between DTR (PRECIS_ERA40, 1961 to 1989) and NAO for concurrent response (L00).

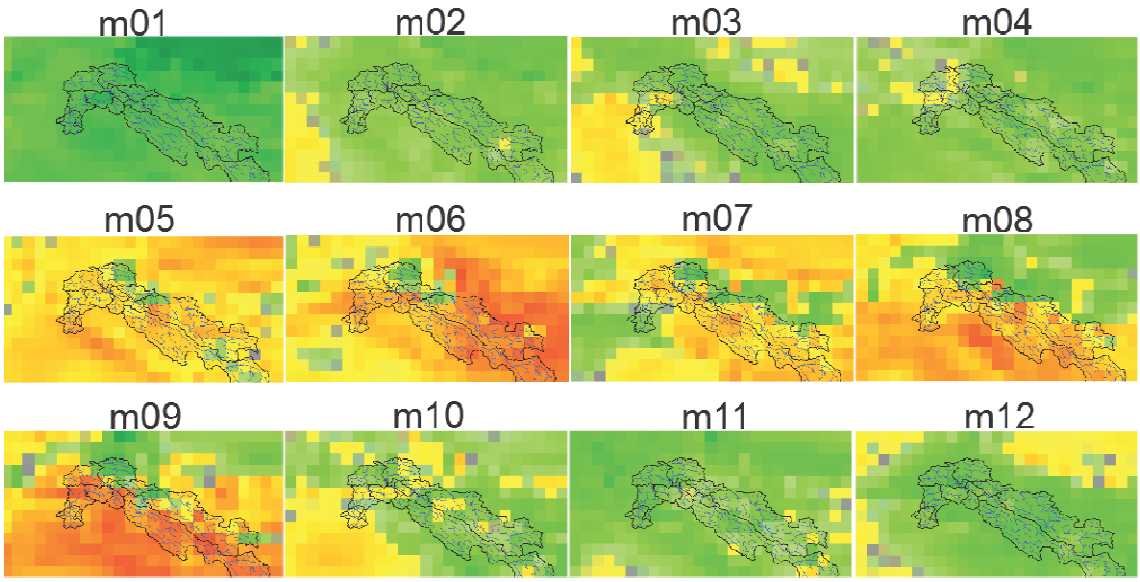

Figure B.77 Teleconnection testing for relationships between Tmin (PRECIS_ERA40, 1961 to 1989) and NAO for concurrent response (L00).

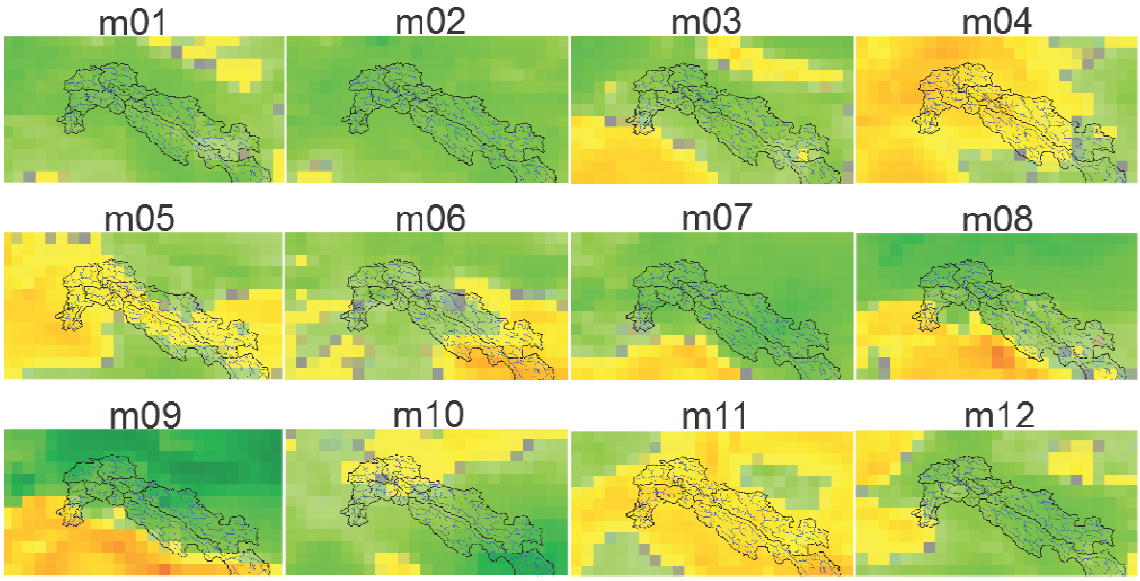

Figure B.78 Teleconnection testing for relationships between TCFavg (PRECIS_ERA40, 1961 to 1989) and NAO for concurrent response (L00).

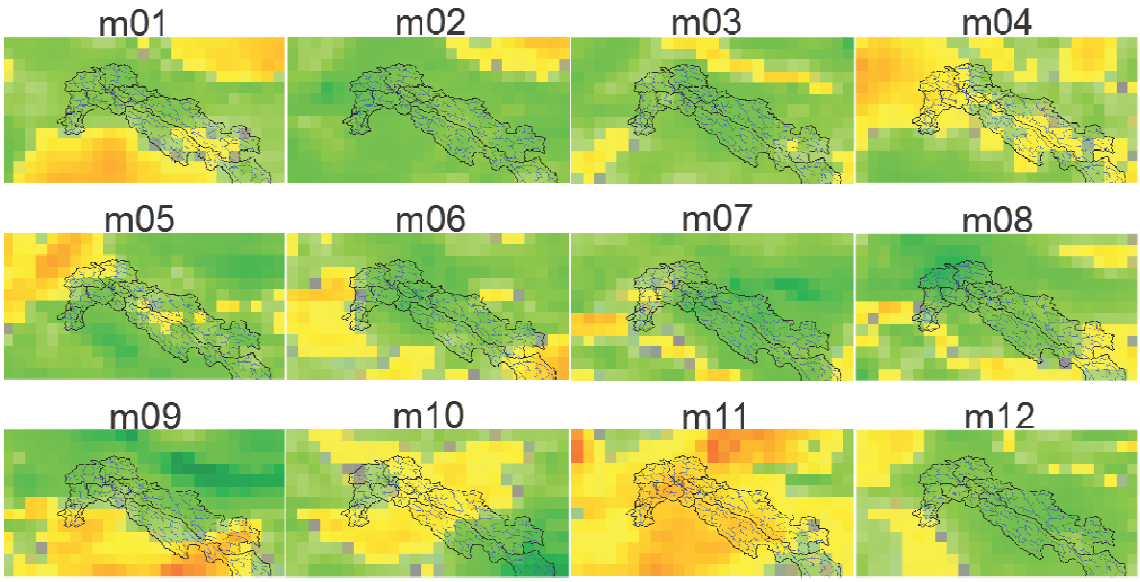

Figure B.79 Teleconnection testing for relationships between precipitation (PRECIS_ERA40, 1961 to 1989) and NAO for concurrent response (L00).

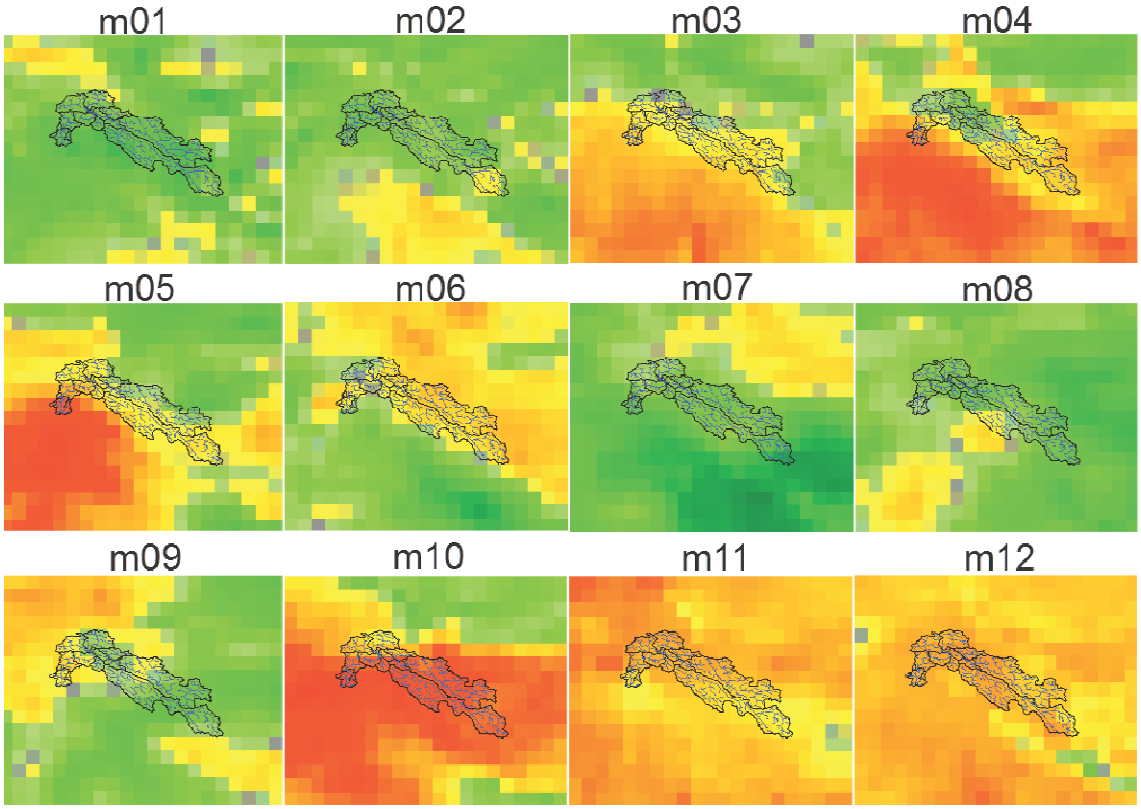

Figure B.80 Teleconnection testing for relationships between DTR (ERA-Interim, 1979 to 2007) and MEI for 4-month lag-time (L04).

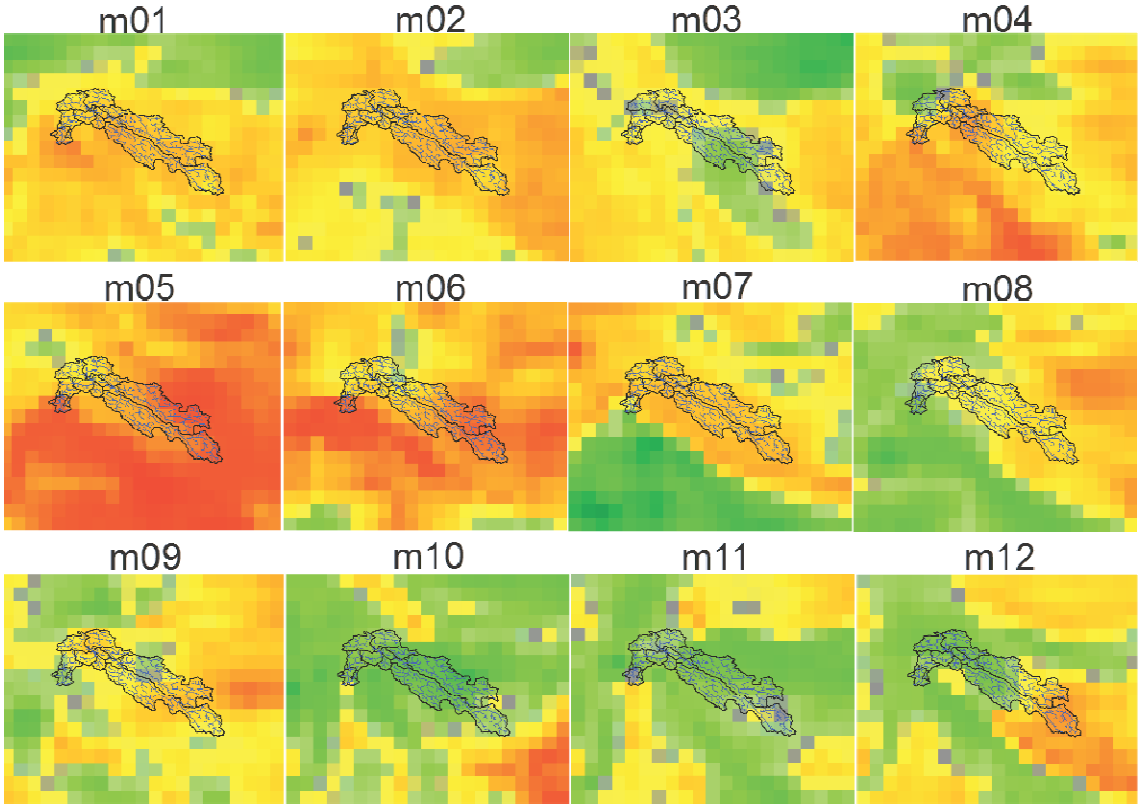

Figure B.81 Teleconnection testing for relationships between Tmin (ERA-Interim, 1979 to 2007) and MEI for 4-month lag-time (L04).

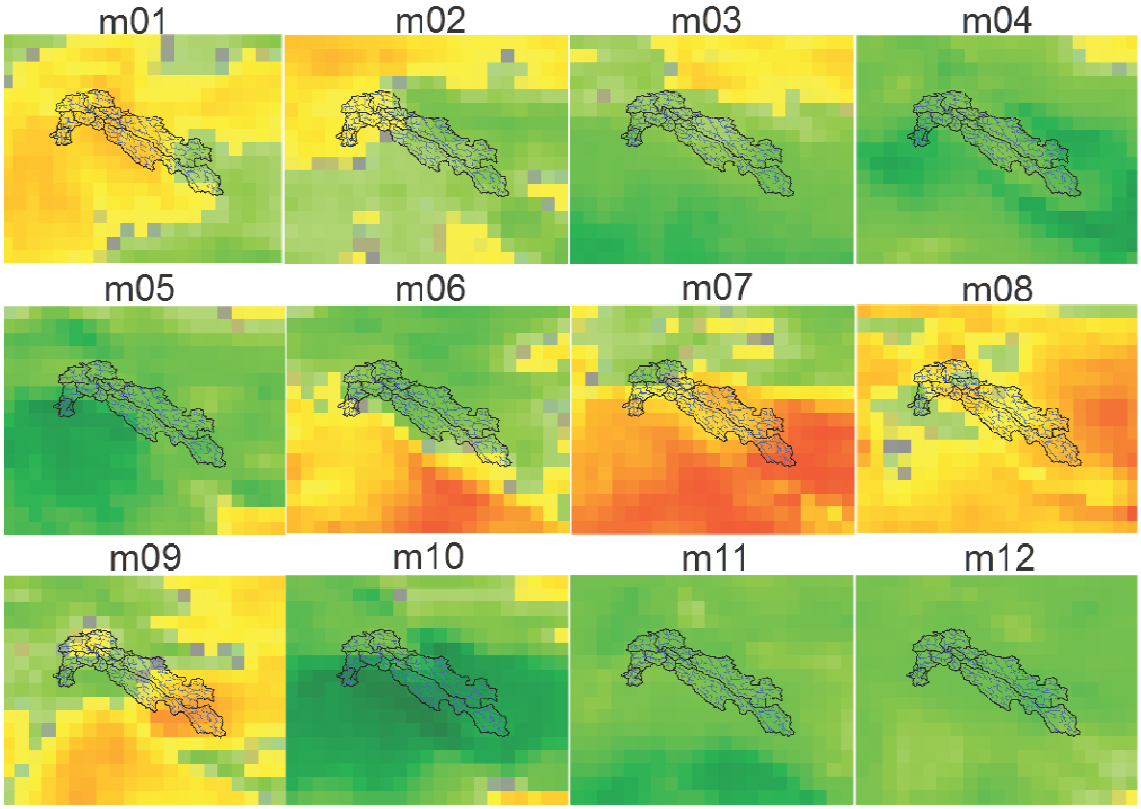

Figure B.82 Teleconnection testing for relationships between TCFavg (ERA-Interim, 1979 to 2007) and MEI for 4-month lag-time (L04).

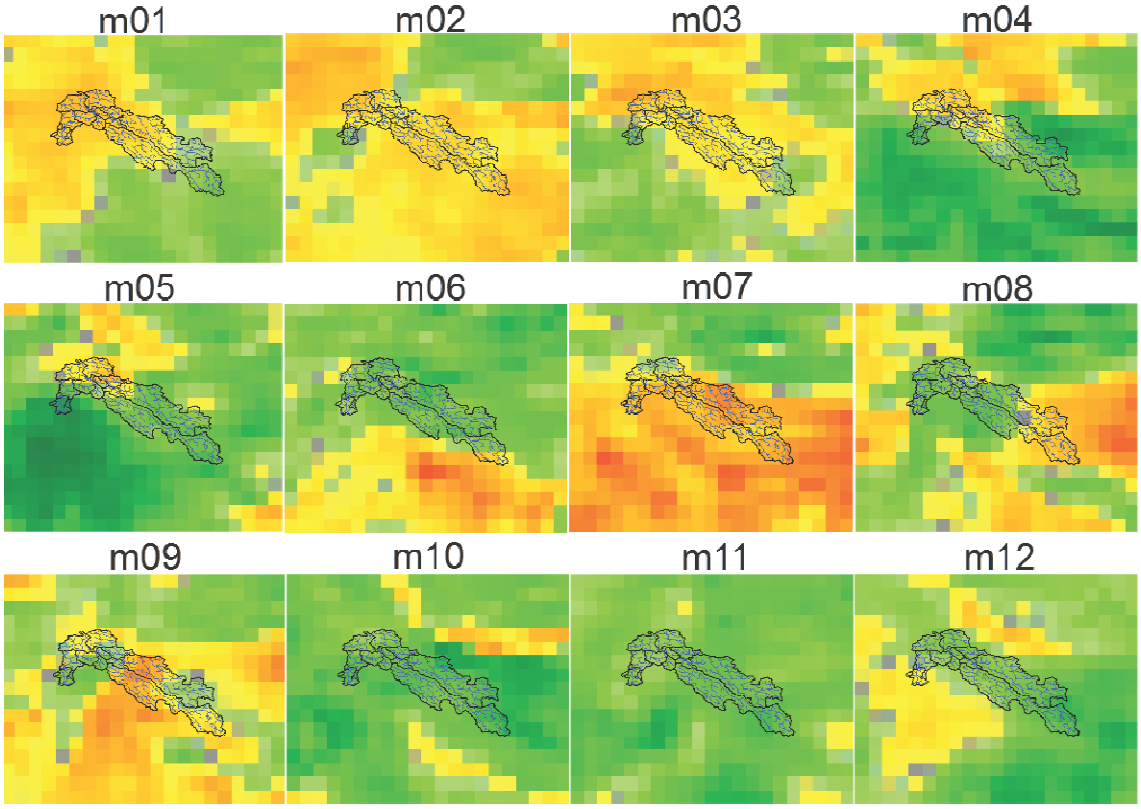

Figure B.83 Teleconnection testing for relationships between precipitation (PRECIS_ERA40, 1961 to 1989) and MEI for 4-month lag-time (L04).

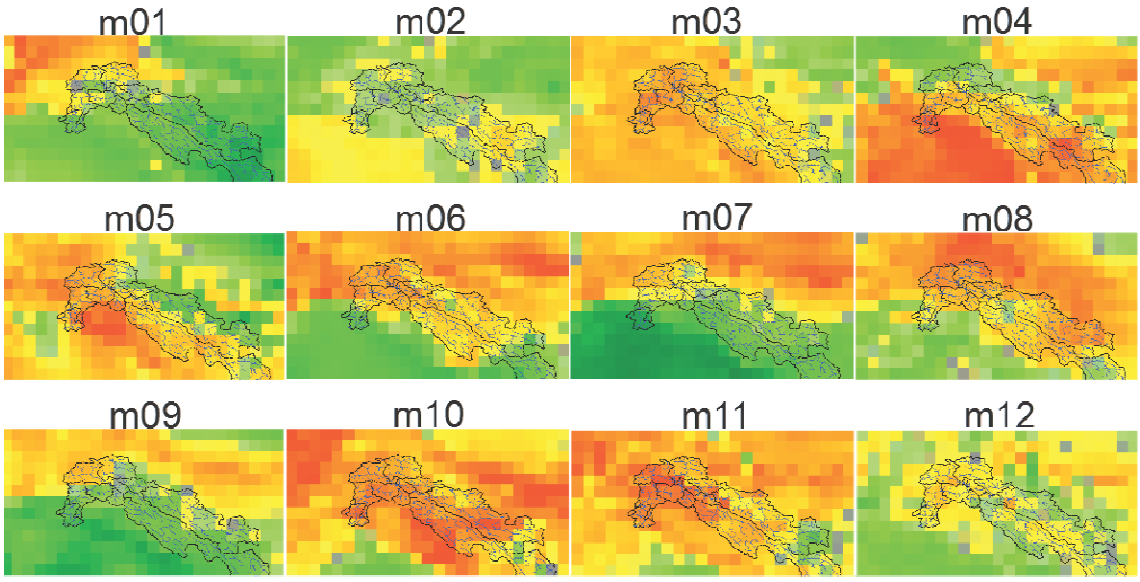

Figure B.84 Teleconnection testing for relationships between DTR (PRECIS_ERA40, 1961 to 1989) and MEI for 4-month lag-time (L04).

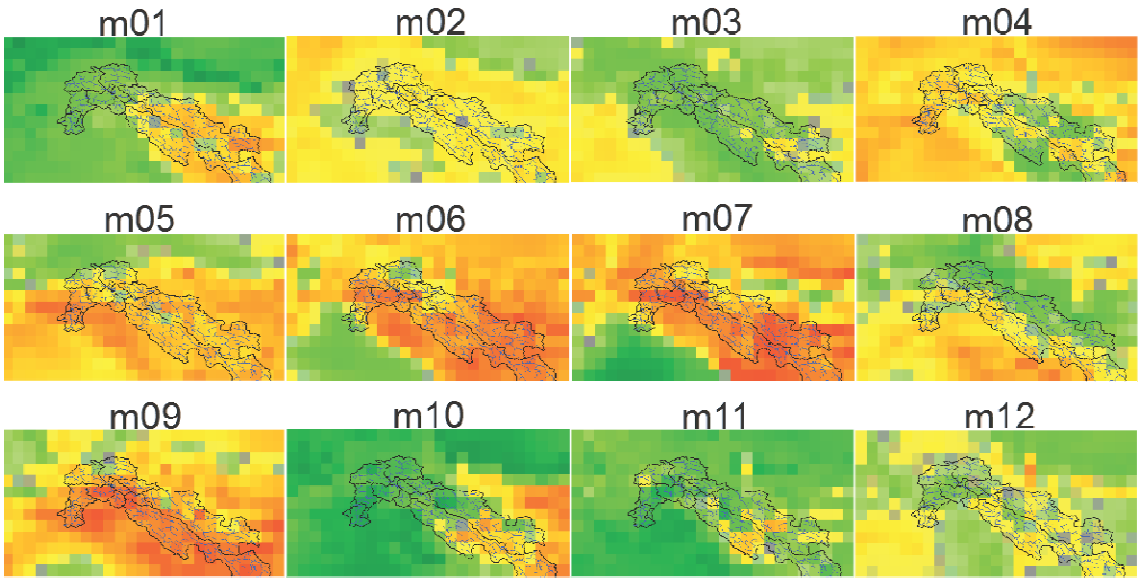

Figure B.85 Teleconnection testing for relationships between Tmin (PRECIS_ERA40, 1961 to 1989) and MEI for 4-month lag-time (L04).

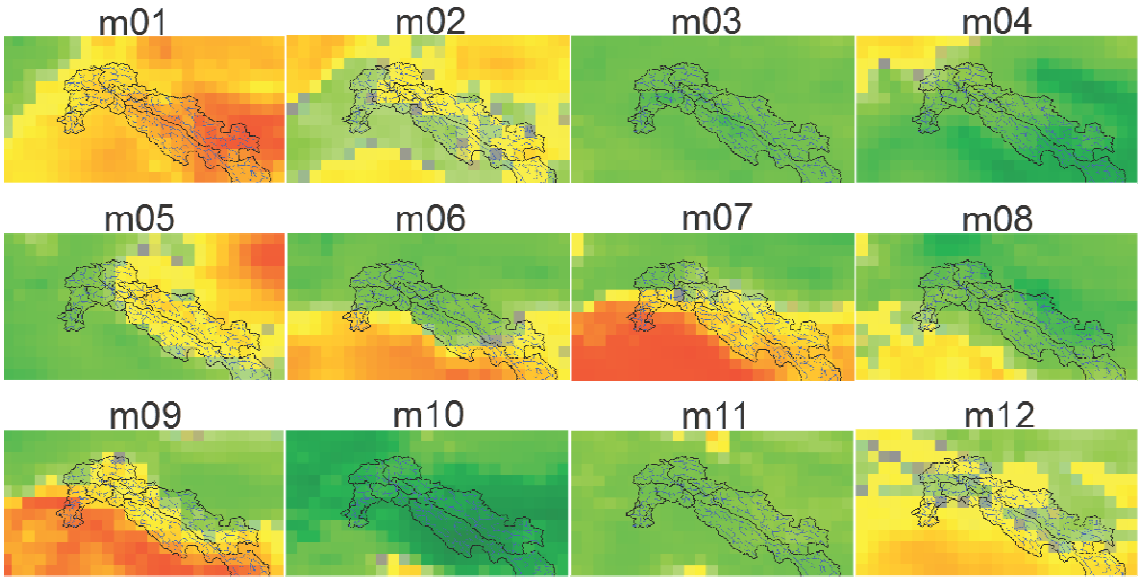

Figure B.86 Teleconnection testing for relationships between TCFavg (PRECIS_ERA40, 1961 to 1989) and MEI for 4-month lag-time (L04).

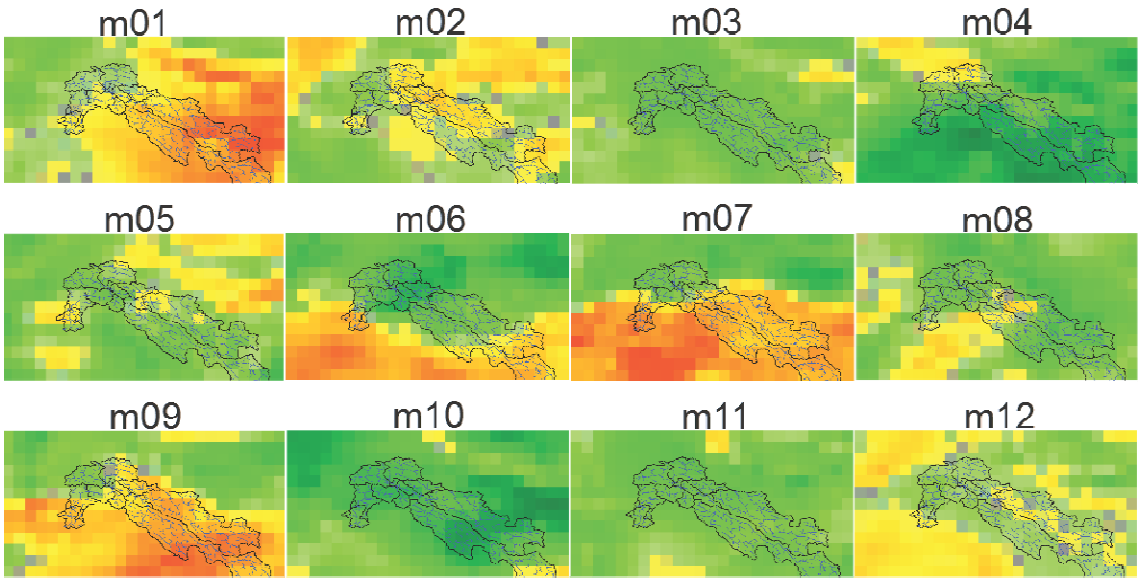

Figure B.87 Teleconnection testing for relationships between precipitation (PRECIS_ERA40, 1961 to 1989) and MEI for 4-month lag-time (L04).

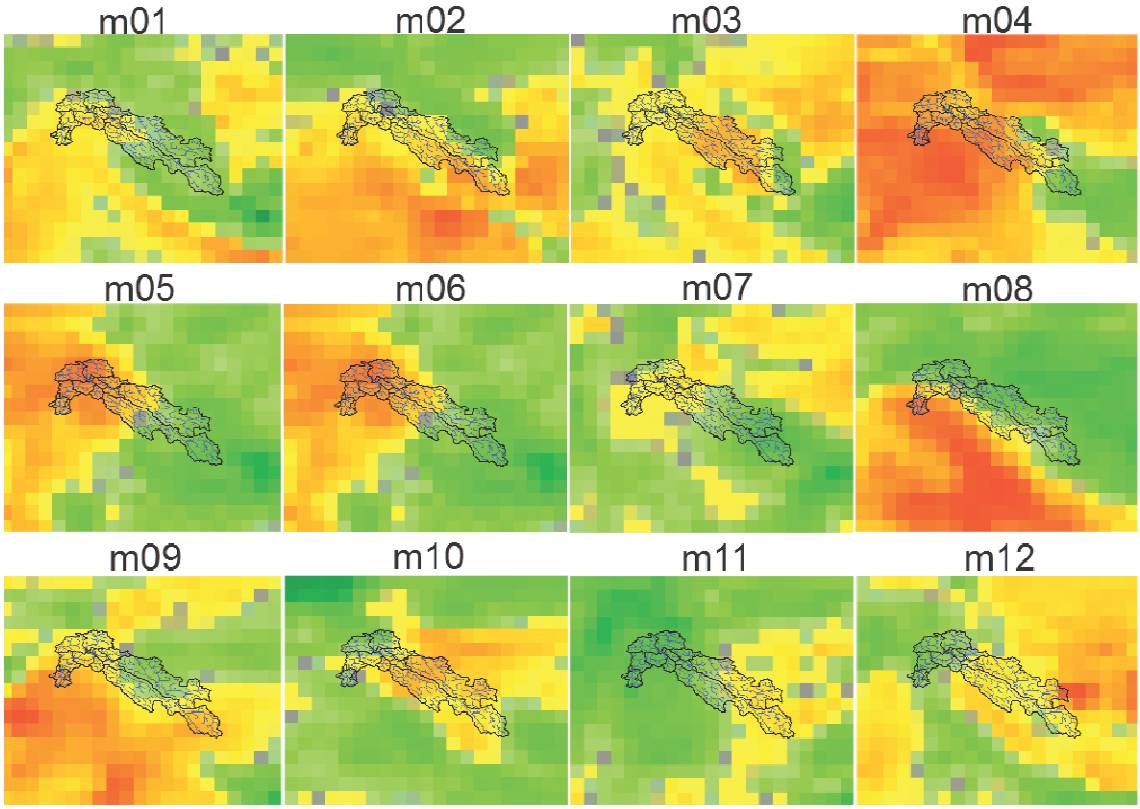

Figure B.88 Teleconnection testing for relationships between DTR (ERA-Interim, 1979 to 2007) and NAO for 4-month lag-time (L04).

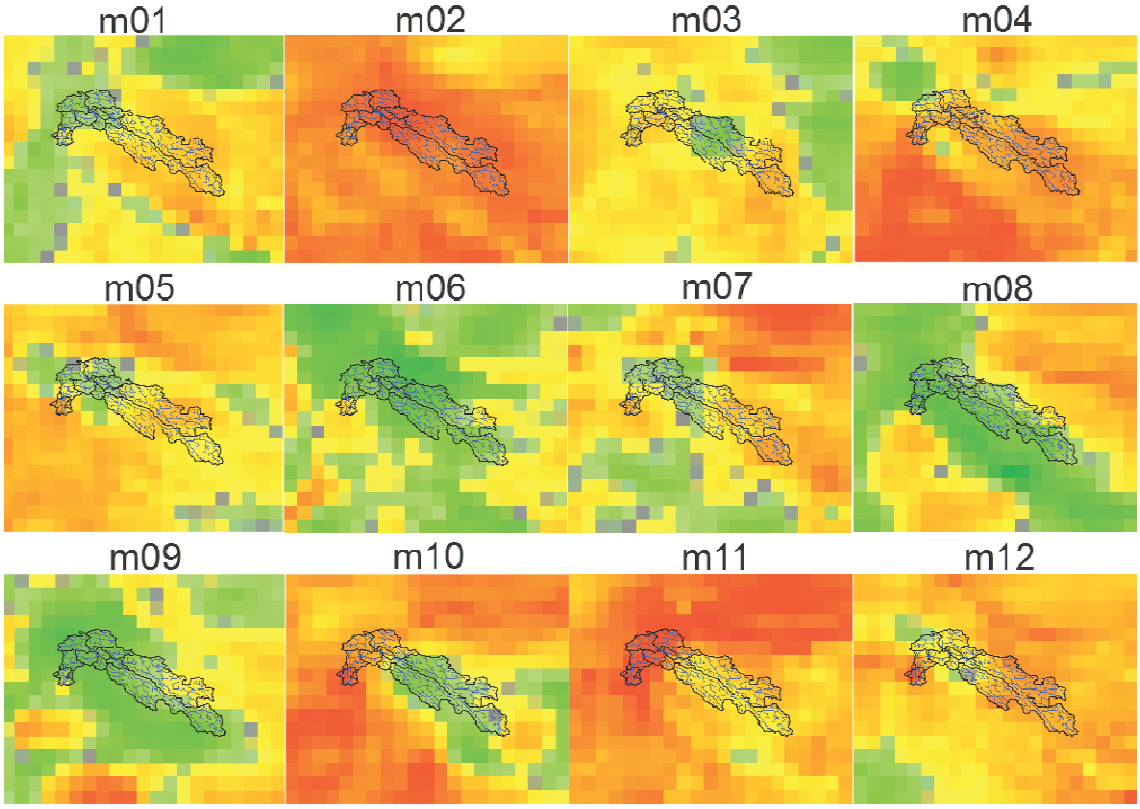

Figure B.89 Teleconnection testing for relationships between Tmin (ERA-Interim, 1979 to 2007) and NAO for 4-month lag-time (L04).

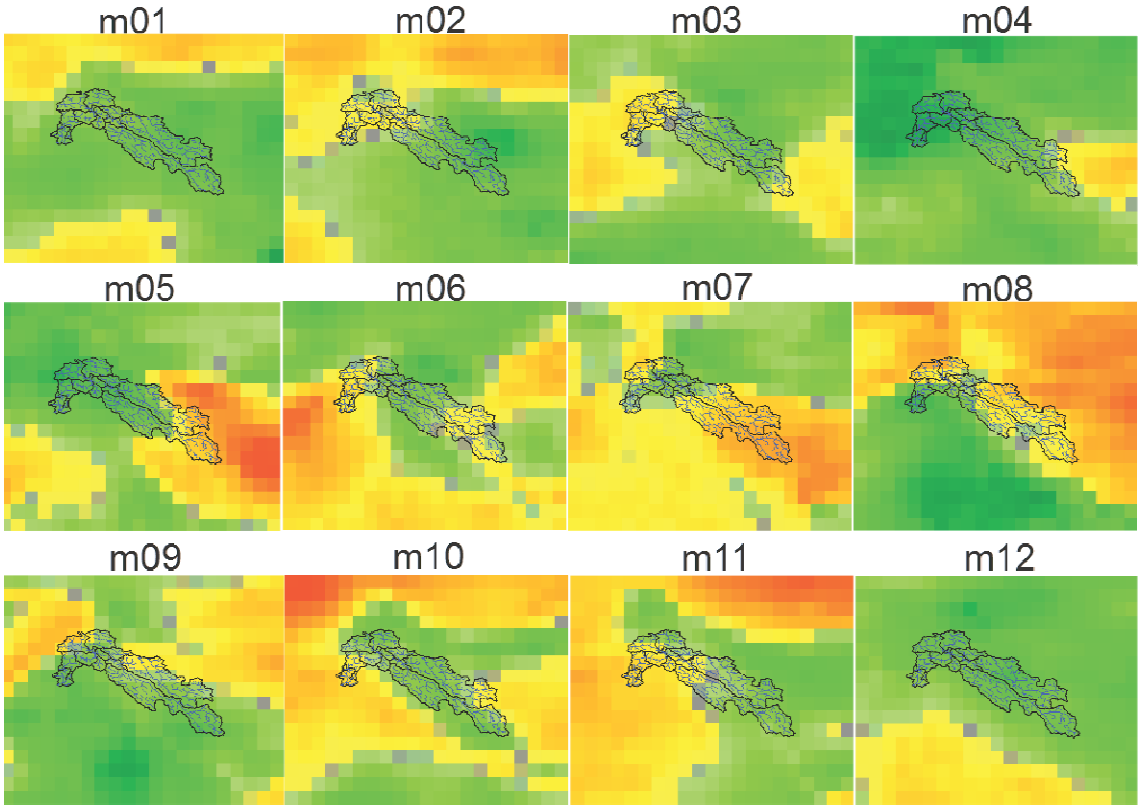

Figure B.90 Teleconnection testing for relationships between TCFavg (ERA-Interim, 1979 to 2007) and NAO for 4-month lag-time (L04).

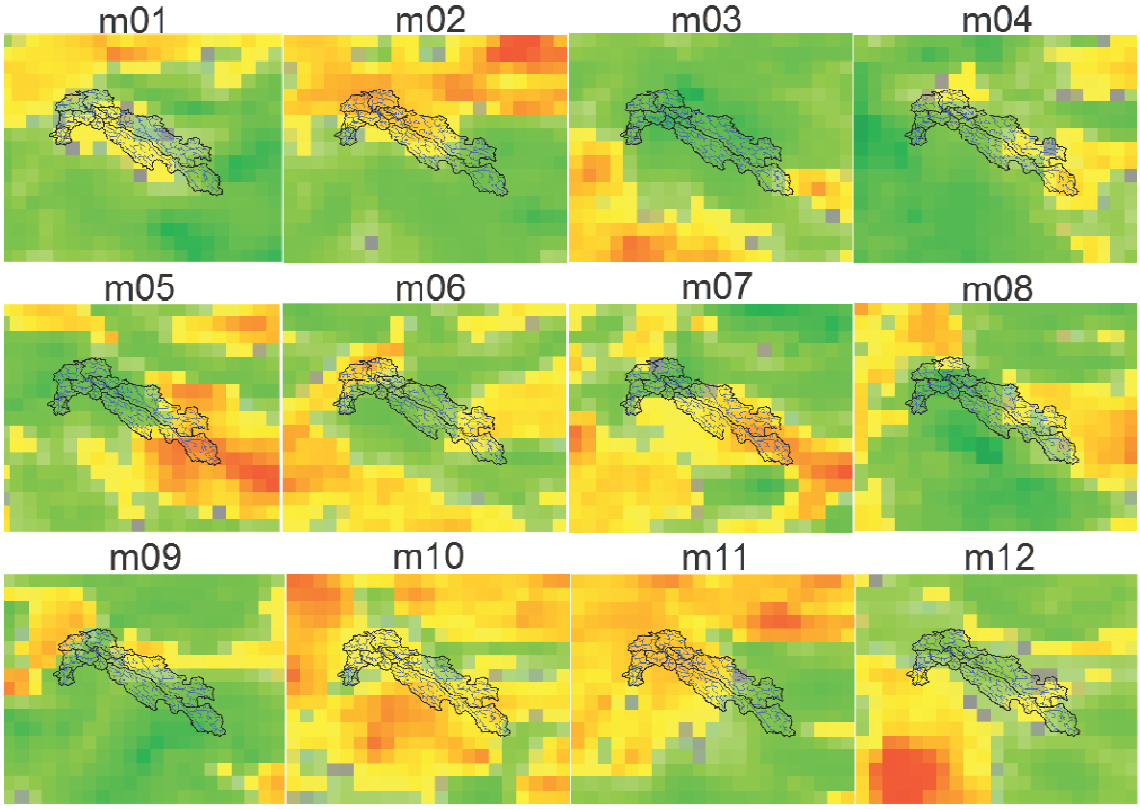

Figure B.91 Teleconnection testing for relationships between precipitation (ERA-Interim, 1979 to 2007) and NAO for 4-month lag-time (L04).

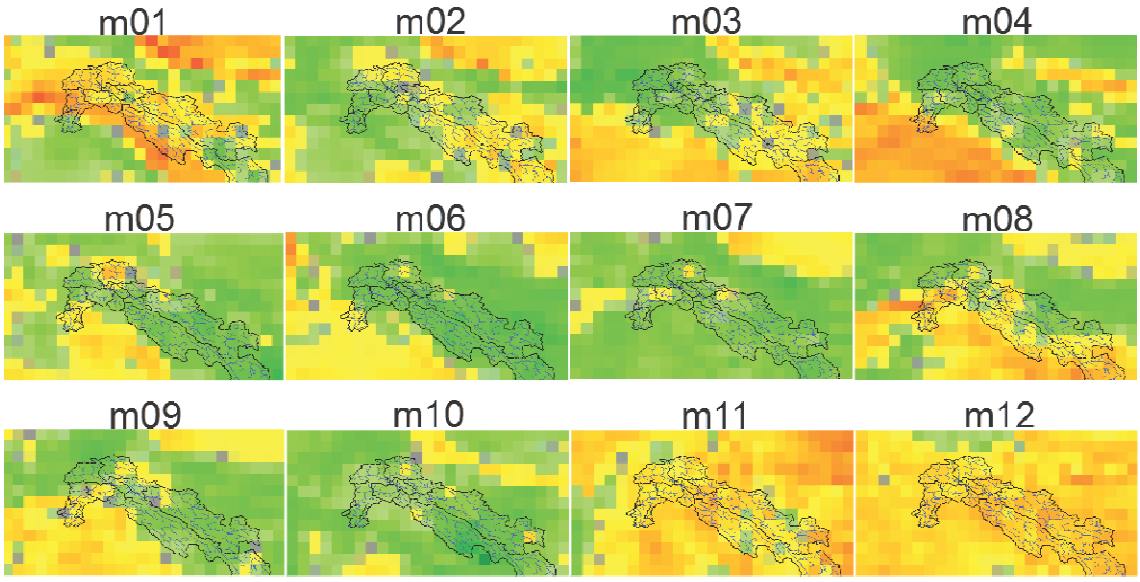

Figure B.92 Teleconnection testing for relationships between DTR (PRECIS_ERA40, 1961 to 1989) and NAO for 4-month lag-time (L04).

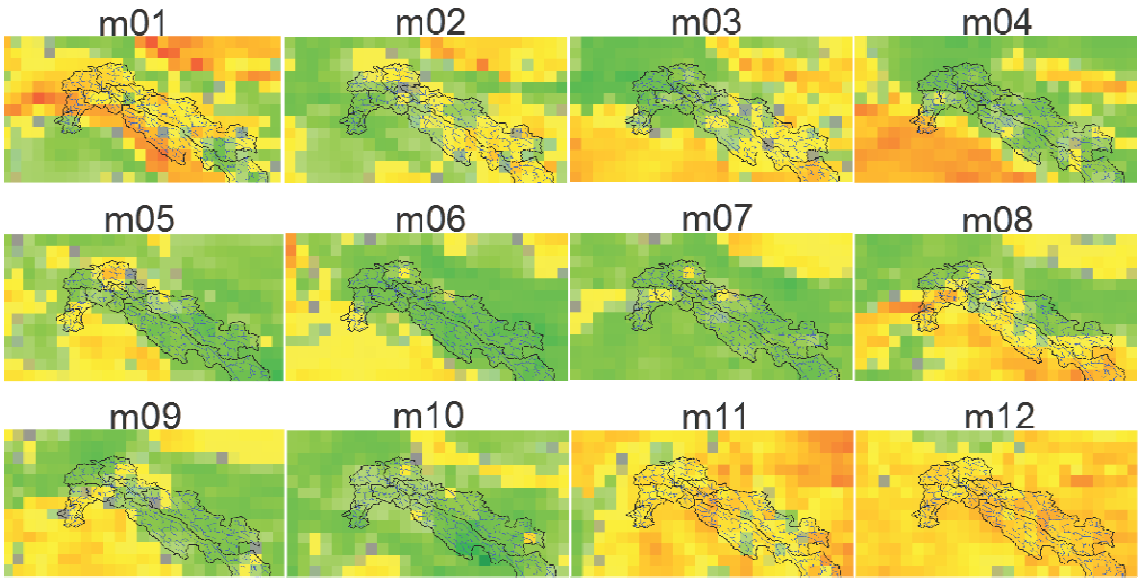

Figure B.93 Teleconnection testing for relationships between Tmin (PRECIS_ERA40, 1961 to 1989) and NAO for 4-month lag-time (L04).

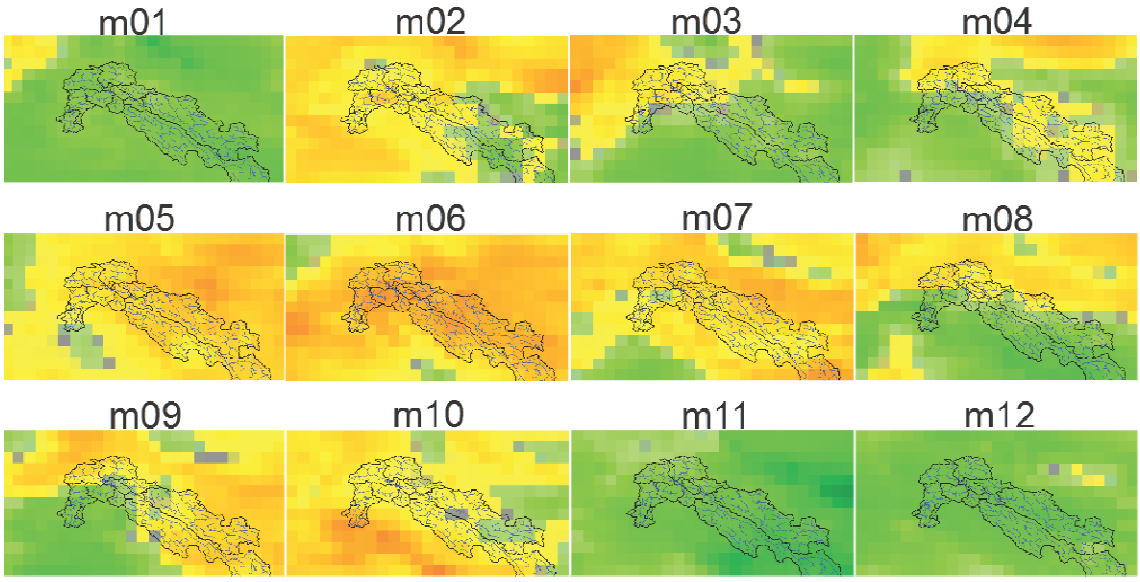

Figure B.94 Teleconnection testing for relationships between TCFavg (PRECIS_ERA40, 1961 to 1989) and NAO for 4-month lag-time (L04).

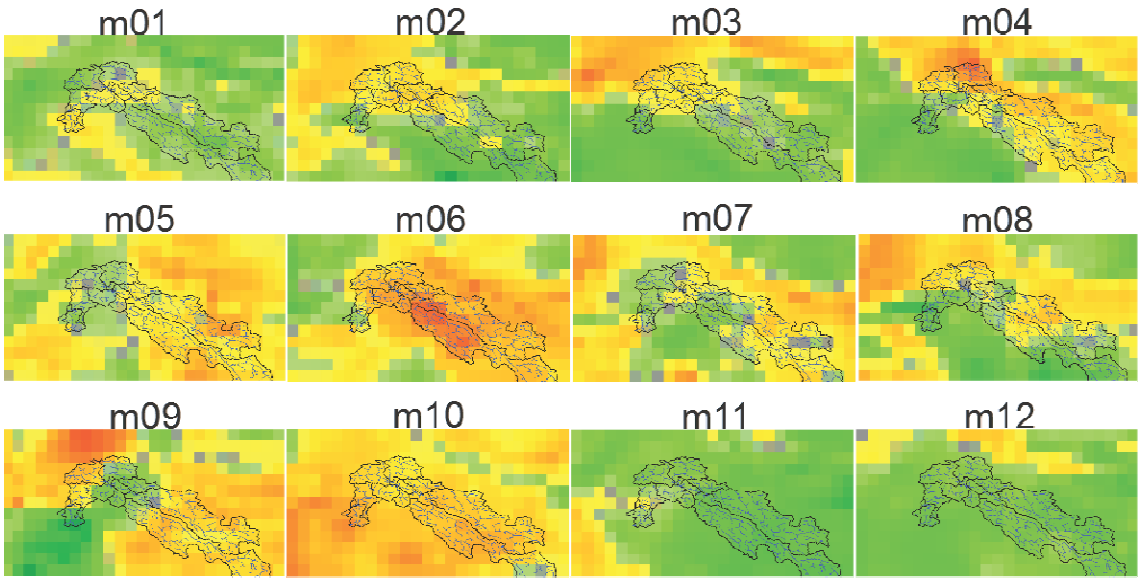

Figure B.95 Teleconnection testing for relationships between precipitation (PRECIS_ERA40, 1961 to 1989) and NAO for 4-month lag-time (L04).

Appendix C: Supplemental material to Chapter 5

C.1 Results of calibration and validation of synthetic time-series for Gilgit and Skardu

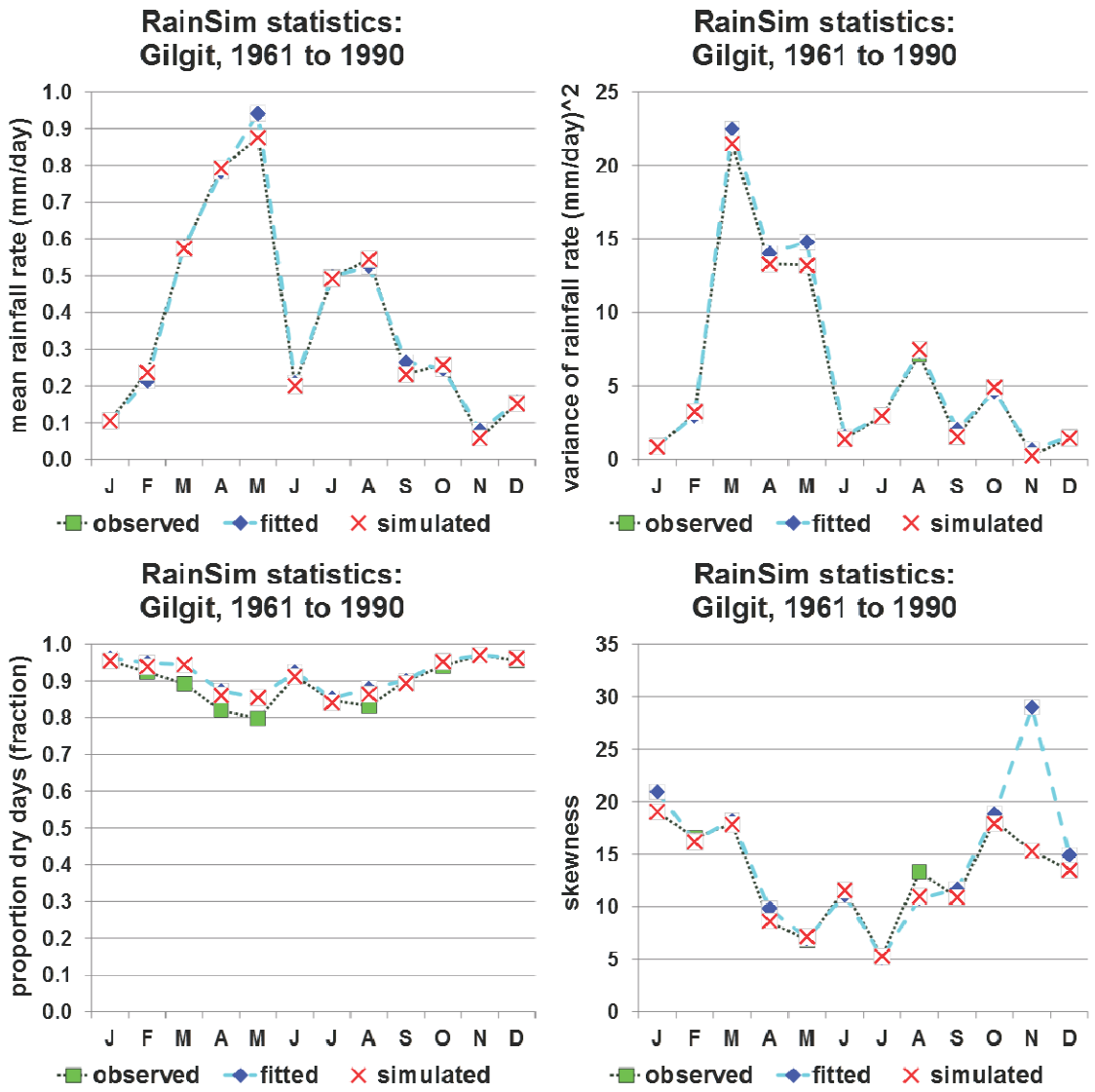

Figure C.01 Statistics calculated by RainSim for observed, fitted and simulated time-series for rainfall measured at Gilgit

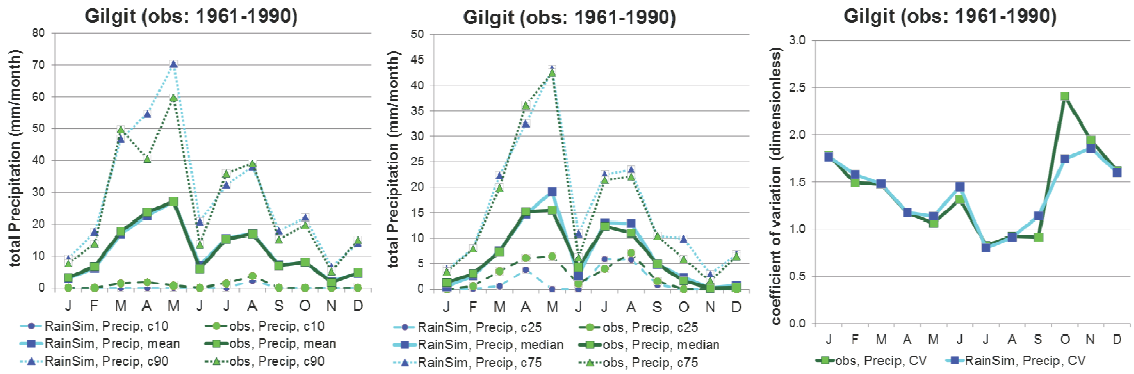

Figure C.02 Comparison of statistics between observations (obs) and simulated (RainSim) control-climate time-series for precipitation amounts at Gilgit

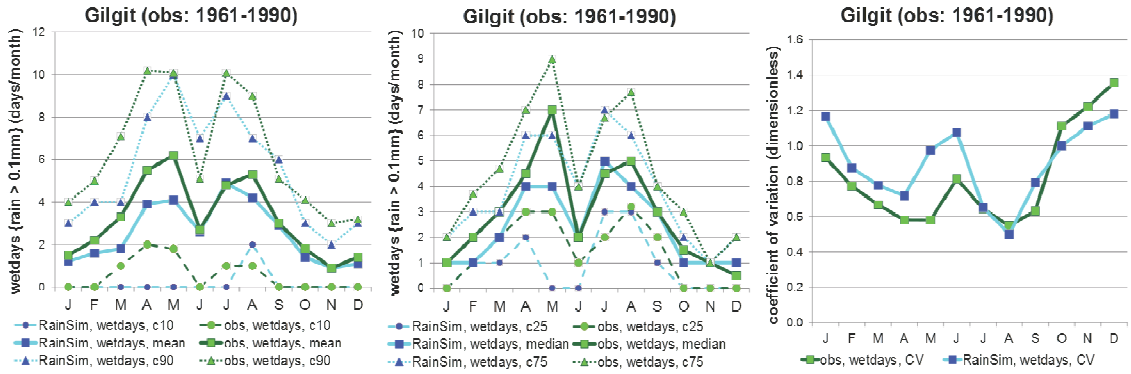

Figure C.03 Comparison of statistics between observations (obs) and simulated (RainSim) control-climate time-series for “wet day” occurence at Gilgit

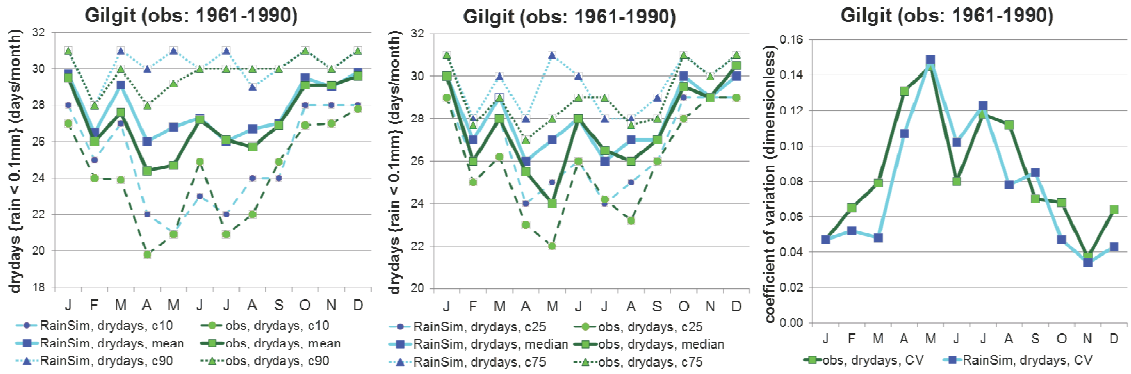

Figure C.04 Comparison of statistics between observations (obs) and simulated (RainSim) control-climate time-series for “dry day” occurence at Gilgit

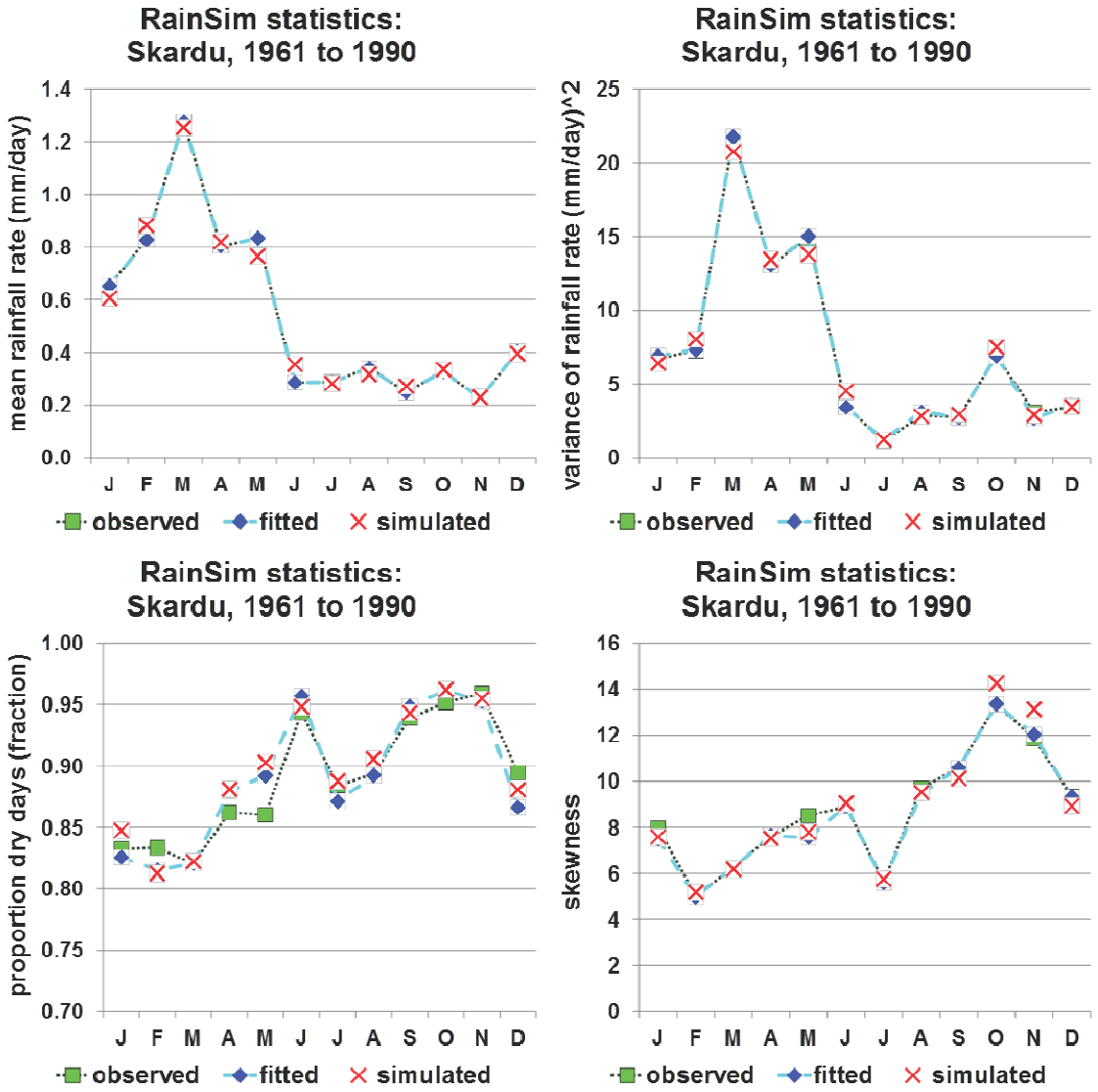

Figure C.05 Statistics calculated by RainSim for observed, fitted and simulated time-series for rainfall measured at Skardu

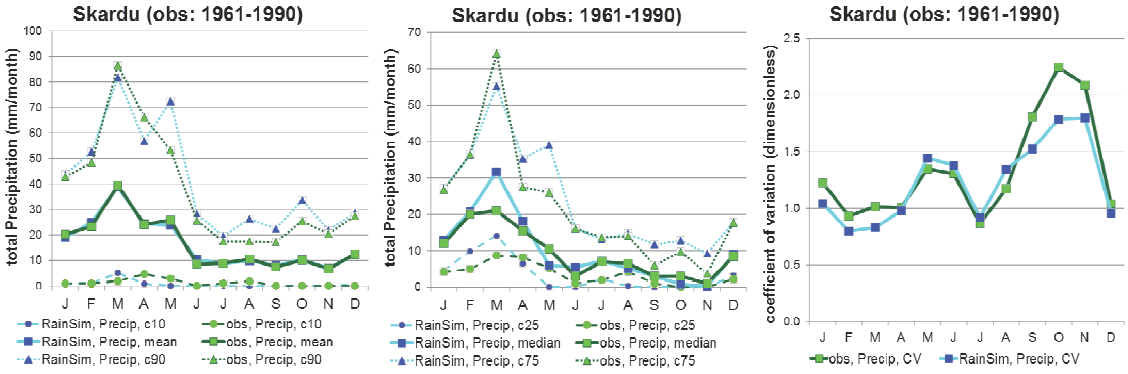

Figure C.06 Comparison of statistics between observations (obs) and simulated (RainSim) control-climate time-series for precipitation amounts at Skardu

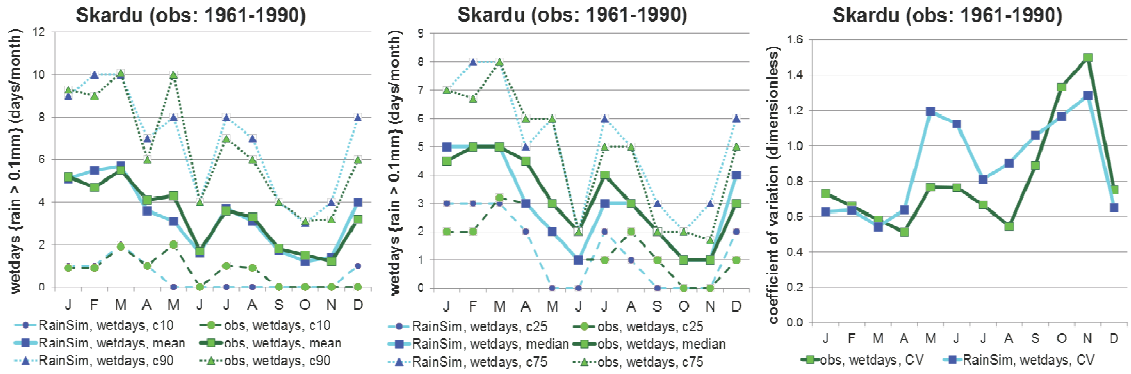

Figure C.07 Comparison of statistics between observations (obs) and simulated (RainSim) control-climate time-series for “wet day” occurrence at Skardu

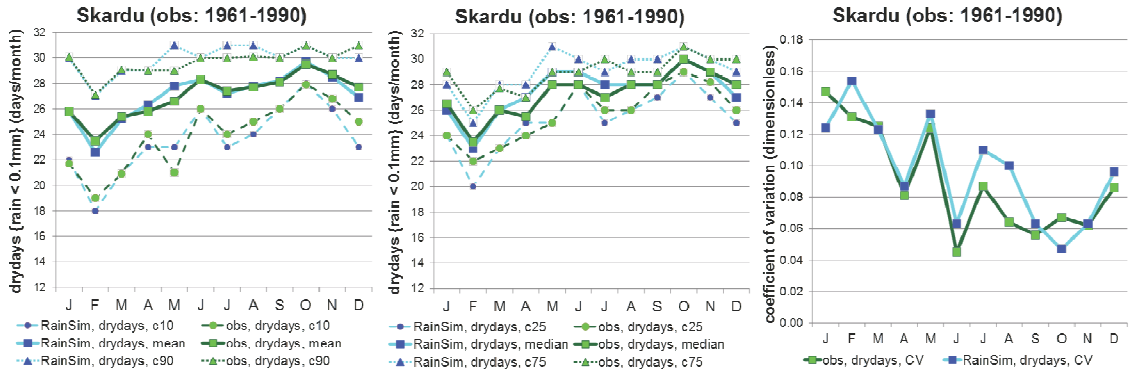

Figure C.08 Comparison of statistics between observations (obs) and simulated (RainSim) control-climate time-series for “dry day” occurrence at Skardu

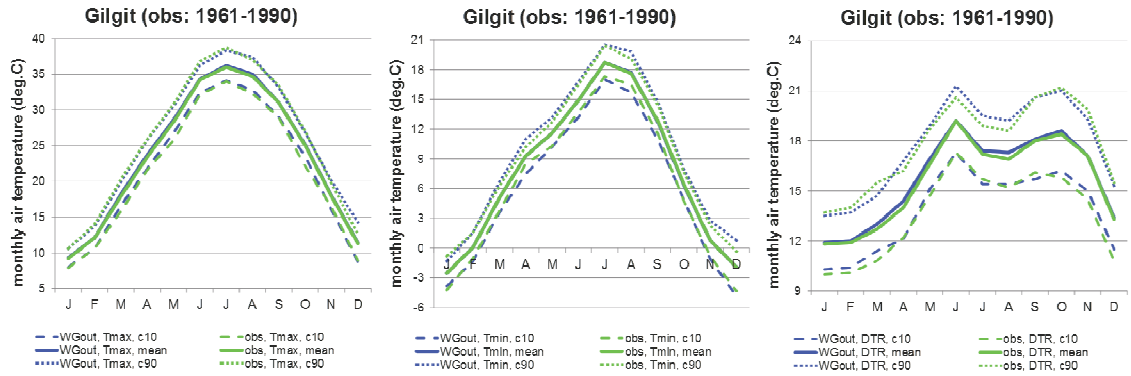

Figure C.09 Comparison of statistics between observations (obs) and simulated (WGout) control-climate time-series for near surface air temperature at Gilgit.

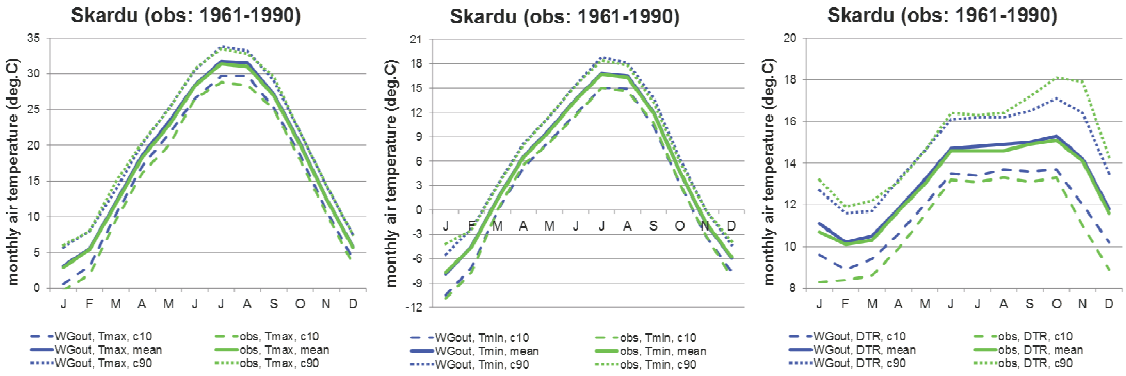

Figure C.10 Comparison of statistics between observations (obs) and simulated (WGout) control-climate time-series for near surface air temperature at Skardu

C.2 Results of perturbation of synthetic time-series for Gilgit and Skardu

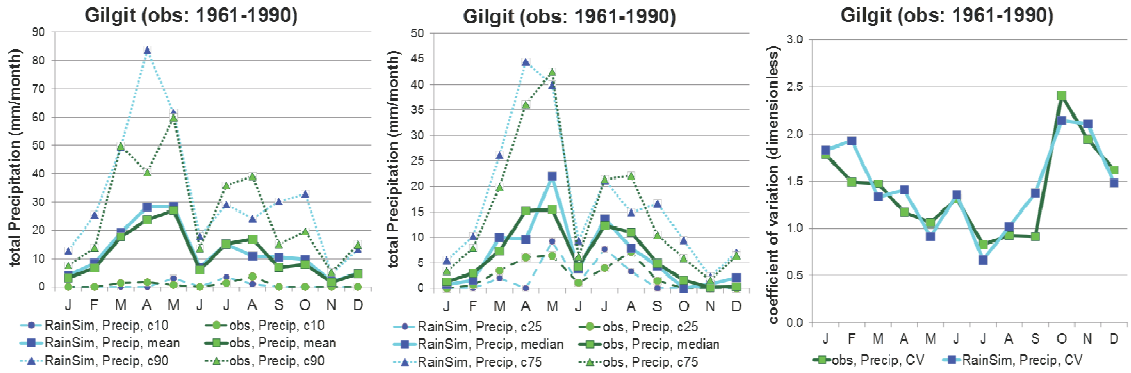

Figure C.11 Comparison of statistics between observations and simulated perturbed-climate time-series from PRECIS_AM3P scenario for precipitation amounts at Gilgit

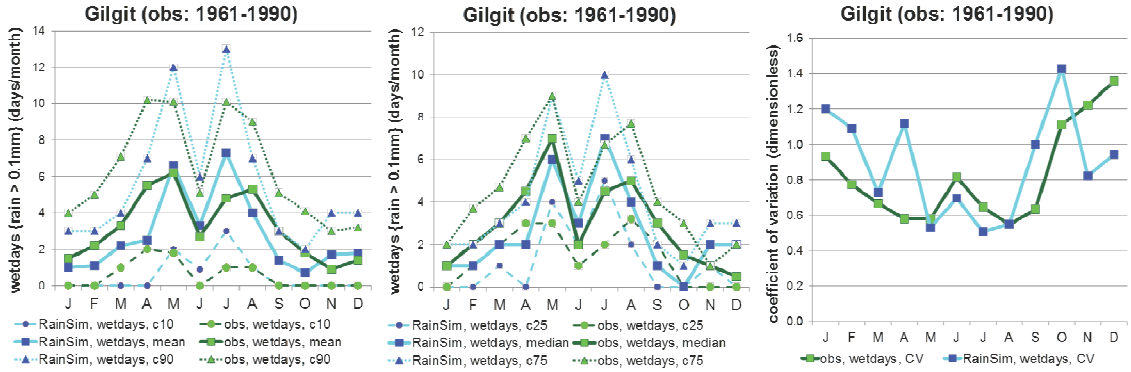

Figure C.12 Comparison of statistics between observations and simulated perturbed-climate time-series from PRECIS_AM3P scenario for wetday occurrence at Gilgit

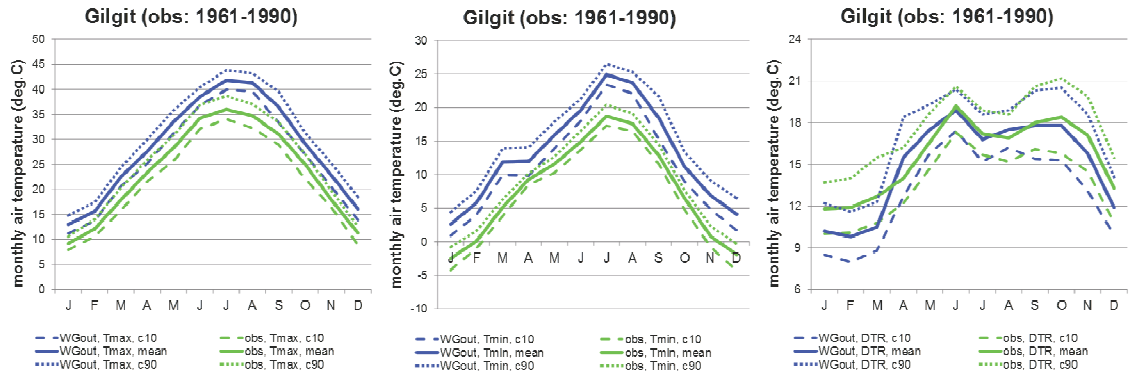

Figure C.13 Comparison of statistics between observations and simulated perturbed-climate time-series from PRECIS_AM3P scenario for near surface air temperature at Gilgit

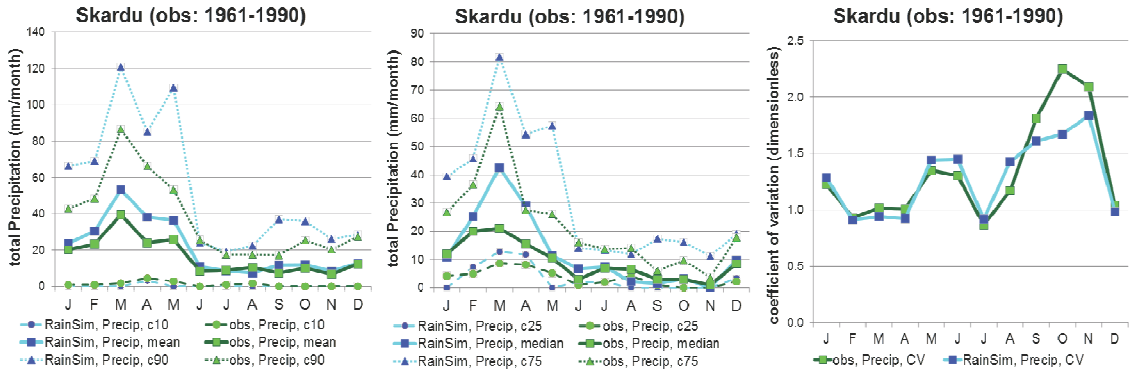

Figure C.14 Comparison of statistics between observations and simulated perturbed-climate time-series from PRECIS_AM3P scenario for precipitation amounts at Skardu

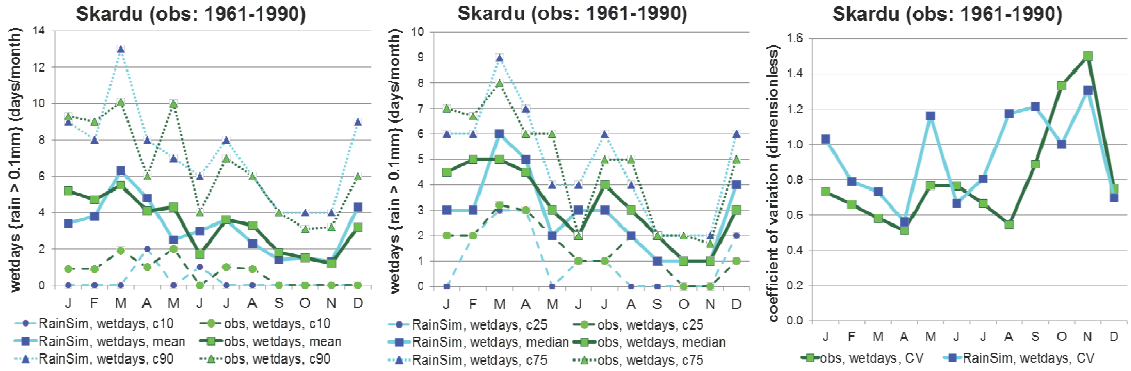

Figure C.15 Comparison of statistics between observations and simulated perturbed-climate time-series from PRECIS_AM3P scenario for wetday occurrence at Skardu

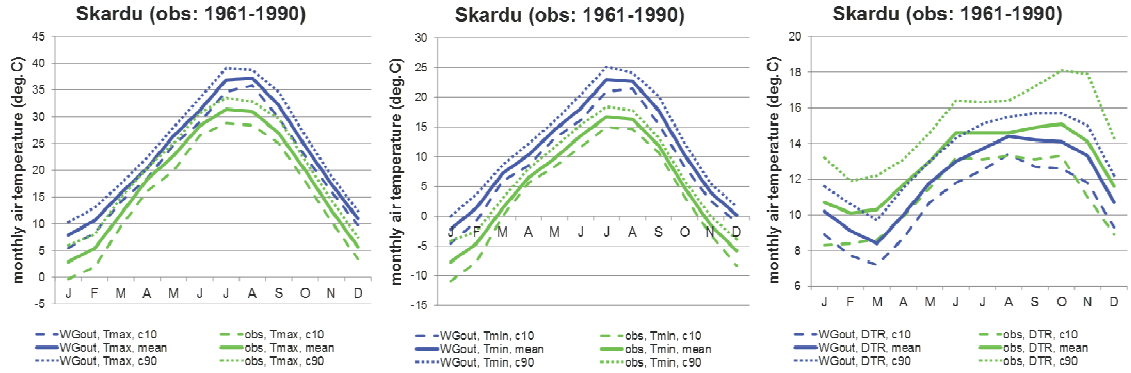

Figure C.16 Comparison of statistics between observations and simulated perturbed-climate time-series from PRECIS_AM3P scenario for near surface air temperature at Skardu

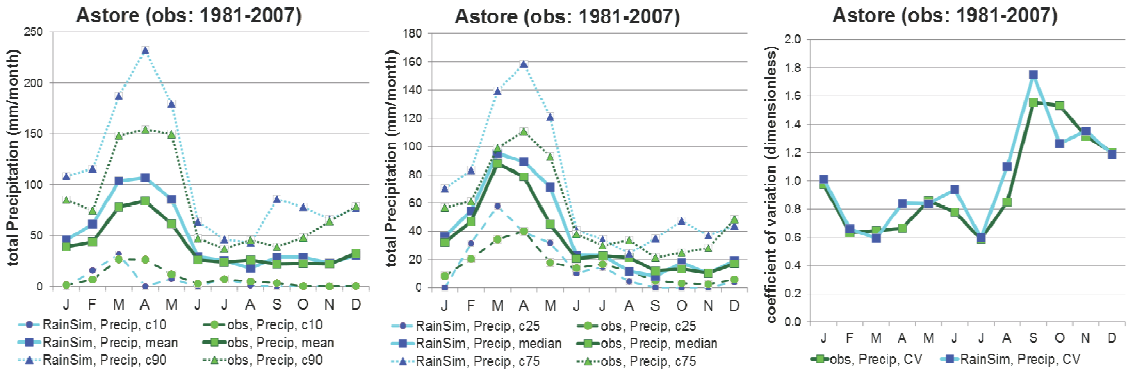

Figure C.17 Comparison of statistics between observations and simulated perturbed-climate time-series from PRECIS_AM3P scenario for precipitation amounts at Astore

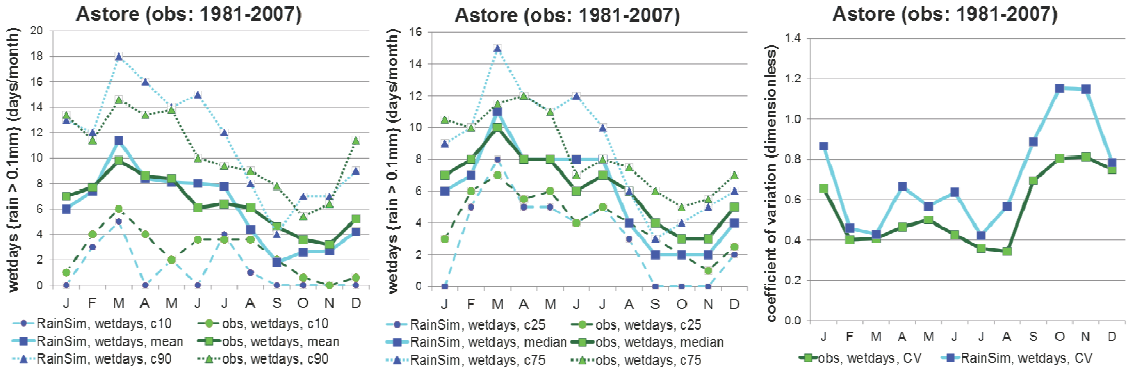

Figure C.18 Comparison of statistics between observations and simulated perturbed-climate time-series from PRECIS_AM3P scenario for wetday occurrence at Astore

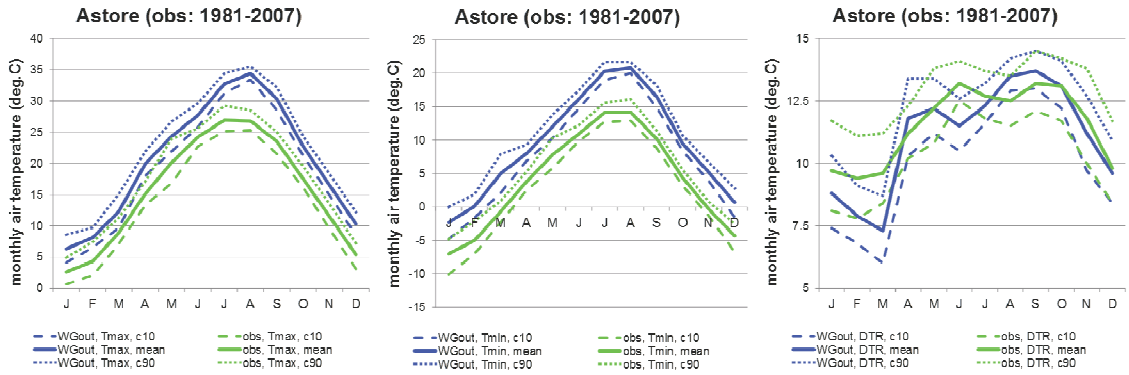

Figure C.19 Comparison of statistics between observations and simulated perturbed-climate time-series from PRECIS_AM3P scenario for near surface air temperature at Astore

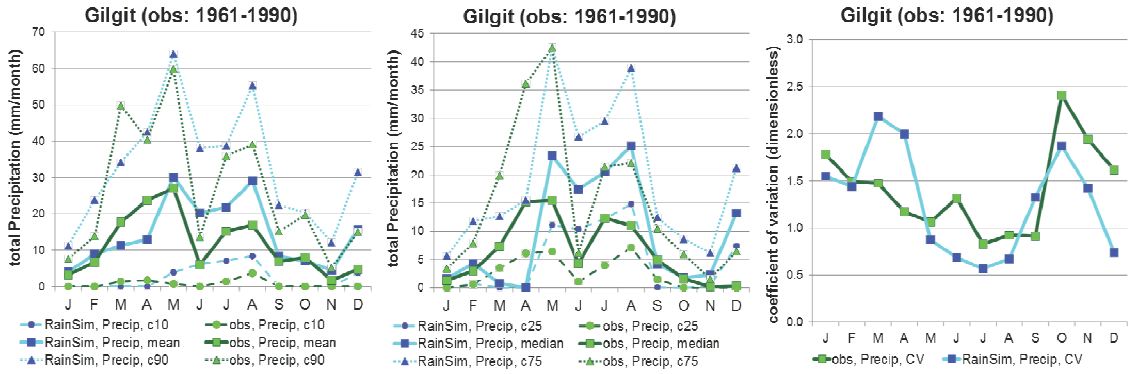

Figure C.20 Comparison of statistics between observations and simulated perturbed-climate time-series from locally-observed trends scenario for precipitation amounts at Gilgit

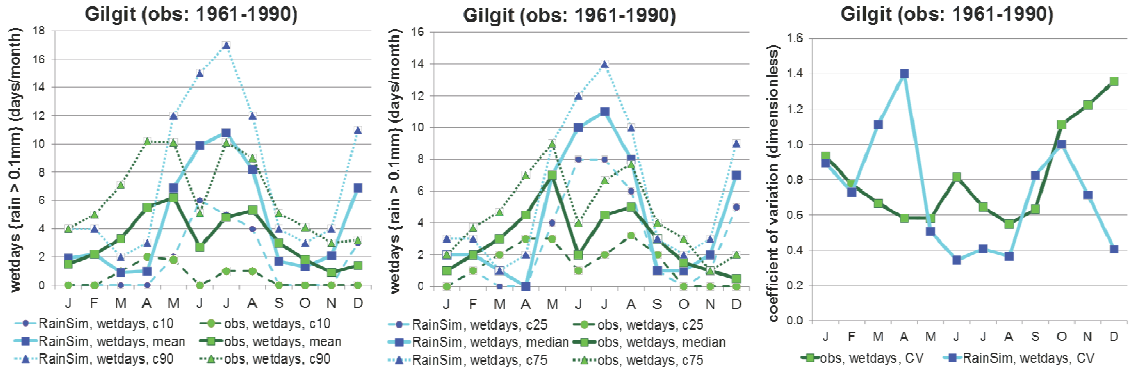

Figure C.21 Comparison of statistics between observations and simulated perturbed-climate time-series from locally-observed trends scenario for wet day occurrence at Gilgit

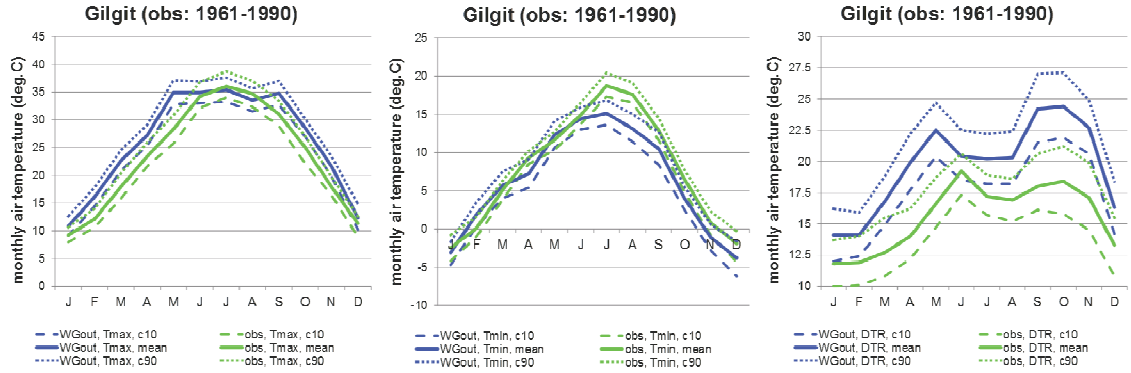

Figure C.22 Comparison of statistics between observations and simulated perturbed-climate time-series from locally-observed trends scenario for near surface air temperature at Gilgit

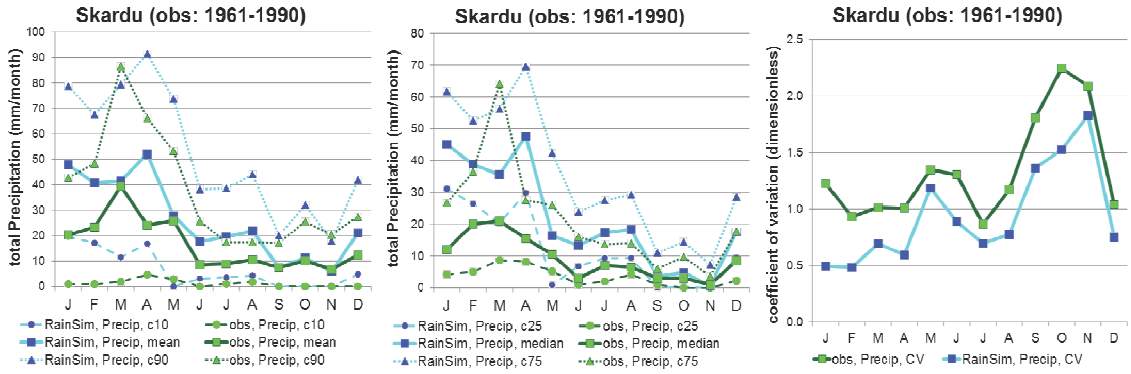

Figure C.23 Comparison of statistics between observations and simulated perturbed-climate time-series from locally-observed trends scenario for precipitation amounts at Skardu

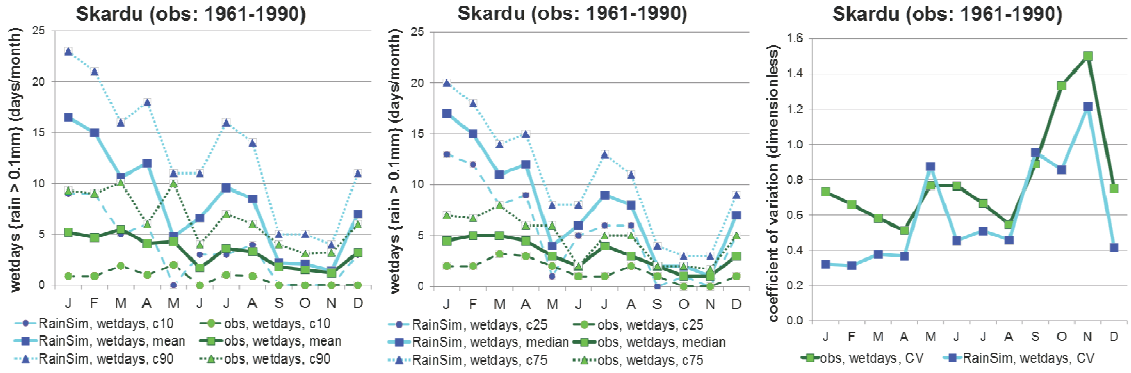

Figure C.24 Comparison of statistics between observations and simulated perturbed-climate time-series from locally-observed trends scenario for wet day occurrence at Skardu

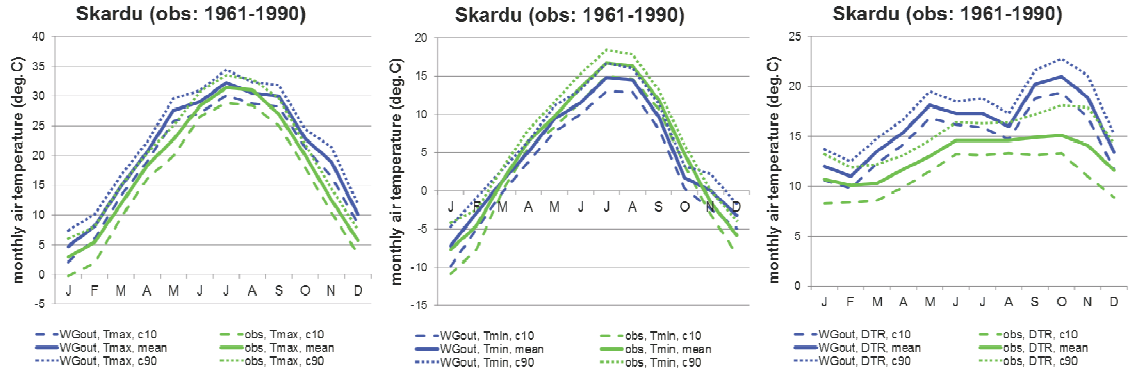

Figure C.25 Comparison of statistics between observations and simulated perturbed-climate time-series from locally-observed trends scenario for near surface air temperature at Skardu

Appendix D: Supplemental material Chapter 6

Additional material for "algorithm theoretical basis document" (ATBD) for VIC with Cryosphere Dynamics in Python (VICwCDiP)

D.1 Glossary

$A_{exponent}$: an intermediate quantity used by VICwCDiP to calculate the fraction of cell surface area which is saturated [dimensionless]

A_{frac}: an intermediate quantity, representing the portion of the grid cell surface assumed to be saturated, used by VICwCDiP to [fraction]

A_{Glenn}: Glenn's flow law coefficient used in calculation of "deformation velocity" (U_d) in simulation of glacial dynamics within VICwCDiP [5.875e-19 day^{-1} Pa^{-3}]

AET: actual evapotranspiration [mm]

$\alpha_{b(i)}$: mean slope of glacier surface within band [radians]

albedo: a fractional number (0 to 1) quantifying the amount of solar radiation reflected (not absorbed) by a given surface; may be made specific to a certain wavelength or spectral band, e.g. near infrared albedo as opposed to visible wavelength albedo.

$albedo_{b(i)}$: the variable name for (broad spectrum) albedo for a given elevation band within a VICwCDiP grid cell, calculated based on the fraction contributions of bare ground and SCA as well as the state of the snowpack (i.e. "fresh" or "standing" snow). [fraction]

$albedo_{bare}$: constant value for bare (i.e. snow-free) ground in VICwCDiP, For the simulations described in this chapter = 0.15. [fraction]

$albedo_{currentSCA}$: albedo of the present state of snow in a given cell/elevation band in VICwCDiP. For the simulations described in this chapter, if fresh snow = 0.85; if standing snow = 0.65. [fraction]

b_1: constant parameter value, = 0.254, used by VICwCDiP in calculation of compaction leading to density changes in standing snowpack

b.exp: constant parameter value, = 0.35, used by VICwCDiP in calculation of compaction leading to density changes in standing snowpack

$band.number_{b(i)}$: the numerical value corresponding to the band order for sub-grid discretisation in a VICwCDiP

basis: intermediate quantity used by VICwCDiP in calculation of direct runoff amounts [dimensionless]

basis.exponent: intermediate quantity used by VICwCDiP in calculation of direct runoff amounts [dimensionless]

basis.product: intermediate quantity used by VICwCDiP in calculation of direct runoff amounts [mm]

β_{submax} : linear gradient (slope) used in calculation of orographic scaling factor when $Z_{b(i)}$ is less than $Z_{max.isohyetal}$ [dimensionless]

$\beta_{supermax}$: linear gradient (slope) used in calculation of orographic scaling factor when $Z_{b(i)}$ is greater than $Z_{max.isohyetal}$ [dimensionless]

"**C**": baseflow exponent in VIC hydrological formulation [dimensionless]

cell.fraction$_{b(i)}$: the fraction of total cell area contained in a given band within a VICwCDiP grid cell [fraction]

cell.length: nominal grid cell lateral width in VICwCDiP which will depend on model spatial resolution, e.g. 0.05 decimal degree (dd) {5km} model will have a cell.width of 5000m and 0.10 dd {10km} model will have a cell.width of 10000m; will be equal to cell.width [m]

cell.width: nominal grid cell lateral width in VICwCDiP which will depend on model spatial resolution, e.g. 0.05 decimal degree (dd) {5km} model will have a cell.width of 5000m and 0.10 dd {10km} model will have a cell.width of 10000m; will be equal to cell.length [m]

change.area$_{b(i)}$: intermediate quantity used by VICwCDiP in calculation of changes in glacier volume as a result of simulated changes in glacial mass (expressed as IWE) [ratio]

change. height$_{b(i)}$: intermediate quantity used by VICwCDiP in calculation of changes in glacier volume as a result of simulated changes in glacial mass (expressed as IWE) [ratio]

change.height2$_{b(i)}$: intermediate quantity used by VICwCDiP in calculation of changes in glacier volume as a result of simulated changes in glacial mass (expressed as IWE) [ratio]

change.volume$_{b(i)}$: intermediate quantity used by VICwCDiP in calculation of changes in glacier volume as a result of simulated changes in glacial mass (expressed as IWE) [ratio]

change.width$_{b(i)}$: intermediate quantity used by VICwCDiP in calculation of changes in glacier volume as a result of simulated changes in glacial mass (expressed as IWE) [ratio]

compaction.exponent1$_{b(i)}$: an intermediate quantity used by VICwCDiP in calculation of compaction leading to density changes in standing snowpack [dimensionless]

compaction.exponent2$_{b(i)}$: an intermediate quantity used by VICwCDiP in calculation of compaction leading to density changes in standing snowpack [dimensionless]

count$_{bands}$: number of elevation bands used for sub-grid discretisation in a given VICwCDiP model [dimensionless]

$\Delta_{snowdepth1.b(i)}$: an intermediate quantity used by VICwCDiP in calculation of compaction leading to density changes in standing snowpack [m]

$\Delta_{snowdepth2.b(i)}$: an intermediate quantity used by VICwCDiP in calculation of compaction leading to density changes in standing snowpack [m]

Δvolume$_{b(i)}$: an intermediate quantity used by VICwCDiP, quantifying relative magnitude of potential downslope ice transfer as a fraction of available glacial volume [ratio]

ddf$_{ice}$: glacial ice melt degree-day factor, a principal calibration parameter in VICwCDiP [mm °C^{-1} day^{-1}]

ddf$_{snow}$: snowmelt degree-day factor, a principal calibration parameter in VICwCDiP [mm °C^{-1} day^{-1}]

depth$_{soil.upper}$: depth of upper soil layer in a given VICwCDiP grid cell [m]

diff$_{max}$: the greater of differences between Z_{max} minus Z_{mean} and Z_{mean} minus Z_{min} [m]

Ds$_{min}$: a secondary calibration parameter, defined as the product of Ds_{max} multiplied by Ds_{crit} [mm]

Ds$_{max}$: a calibration parameter controlling maximum allowable baseflow from a grid cell during a given time-step [mm]

Ds$_{crit}$: a calibration parameter defining the transition from linear to power law baseflow regime as a fraction of Ds_{max} [fraction]

Ds$_{power}$: an intermediate quantity used by VICwCDiP in the calculation of baseflow [dimensionless]

η_0 = constant parameter value, = 3600000.0, related to viscosity of snow used by VICwCDiP in calculation of compaction leading to density changes in standing snowpack [N s m^{-2}]

"e": the 'natural number' from mathematics, approximated as ~2.718281828, used in equations involving 'exponential functions' [dimensionless]

excess.inflow: an intermediate quantity, representing surplus mass input to the soil surface, used in determining direct runoff [mm]

expt {parameter}: a sub-surface/soil property defined as a function of soil pore size distribution parameter, from Campbell's equation for hydraulic conductivity [dimensionless]

FC: (soil water) "field capacity", defined as SMC_{max} minus SMC_{resid} [mm]

freshsnow$_{b(i)}$: the variable name in VICwCDiP for the amount of precipitation in a given time-step falling as snow for a given elevation band within a VICwCDiP grid cell [mm]

γ: psychrometric constant relates the partial pressure of water vapour in the air [kPa °C^{-1}]

g = acceleration of gravity [9.81 m s^{-2}]

glacier.face$_{b(i)}$: the nominal cross-sectional surface, perpendicular to the direction of glacial displacement, used by VICwCDiP to calculate the volume of ice transfer to the adjacent (downslope) elevation band [m^2]

glacier.footprint$_{b(i)}$: the nominal surface area, perpendicular to the direction of glacial displacement, used by VICwCDiP to calculate the volume of ice transfer to the adjacent (downslope) elevation band [m^2] [m^2]

glacial.fraction$_{b(i)}$: the fraction of total cell area which is glaciated contained in a given band within a VICwCDiP grid cell [fraction]

glacial.fraction.final$_{b(i)}$: the fraction of total cell area which is glaciated contained in a given band at the end of a model timestep – i.e. after accumulation from snowpack transformation, ablation/melt, and transport under gravitation stress – within a VICwCDiP grid cell [fraction]

glacial.fraction.update$_{b(i)}$: an intermediate quantity for the fraction of total cell area which is glaciated contained in a given band within a VICwCDiP grid cell, dynamic as a function of the glacial mass balance [fraction]

glacier.length$_{b(i)}$: nominal/virtual length of glaciated portion of an elevation band in VICwCDiP, in order to preserve continuity of ice transfer throughout the grid cells, glacier.length$_{b(i)}$ will be equal to the product of cell.length times cell.fraction$_{b(i)}$ [m]

glacial.ratio$_{b(i)}$: the ratio of glacial.fraction$_{b(i)}$ divided by cell.fraction$_{b(i)}$ for a given elevation band within a VICwCDiP grid cell [dimensionless ratio]

glacier.width$_{b(i)}$: nominal/virtual width of glaciated portion of an elevation band in VICwCDiP, will be less than or equal to the cell.width [m]

glacier.width.final$_{b(i)}$: nominal/virtual width of glaciated portion of an elevation band at the end of a model timestep – i.e. after accumulation from snowpack transformation, ablation/melt, and transport under gravitation stress – in VICwCDiP, will be less than or equal to the cell.width, dynamic as a function of the glacial mass balance [m]

glacier.width.update$_{b(i)}$: an intermediate quantity for nominal/virtual width of glaciated portion of an elevation band in VICwCDiP, will be less than or equal to the cell.width, dynamic as a function of the glacial mass balance [m]

height.ice$_{b(i)}$: initial modelled glacier thickness for a given elevation band within a VICwCDiP grid cell [m]

height.ice.final$_{b(i)}$: modelled glacier thickness for a given elevation band – i.e. after accumulation from snowpack transformation, ablation/melt, and transport under gravitation stress – within a VICwCDiP grid cell [m]

height.ice.update$_{b(i)}$: an intermediate quantity for modelled glacier thickness for a given elevation band within a VICwCDiP grid cell, dynamic as a function of the glacial mass balance [m]

i_0: instantaneous infiltration capacity, used by VIC in calculation of partitioning between direct runoff and infiltration [mm]

infiltration.exponent: an intermediate quantity, which is the inverse of shape$_{base}$, used by VIC in calculation of partitioning between direct runoff and infiltration [dimensionless]

infiltration$_{max}$: maximum daily infiltration depth calculated as a function of and its porosity, used by VIC in calculation of partitioning between direct runoff and infiltration [mm]

inflow: the total sum of mass inputs to the soil surface comprising rainfall, snowmelt and glacier melt [mm]

IWE: ice water equivalent, i.e. the equivalent depth of liquid water over a unit area represented by hypothetical volume of ice [mm]

IWE.final$_{b(i)}$: IWE at the end of a model timestep – i.e. after accumulation from snowpack transformation, ablation/melt, and transport under gravitation stress – in a given elevation band within a VICwCDiP grid cell [mm]

IWE.initial$_{b(i)}$: IWE at the start of a model timestep in a given elevation band within a VICwCDiP grid cell [mm]

IWE.melt$_{b(i)}$: the variable name for amount of IWE reduction through meltwater generation within a timestep for a given elevation band within a VICwCDiP grid cell [mm]

IWE.melt$_{cell}$: as per IWE.melt$_{b(i)}$ but averaged across a VICwCDiP grid cell [mm]

IWE.move.in$_{b(i)}$: an intermediate quantity representing potential IWE transfer into the given elevation band from the adjacent (upslope) band; calculated as part of simulation of glacial dynamics within VICwCDiP [mm]

IWE.move.net$_{b(i)}$: the next transfer – sum of IWE.movein$_{b(i)}$ and IWE.moveout$_{b(i)}$ – of IWE for a given elevation band; calculated as part of simulation of glacial dynamics within VICwCDiP [mm]

IWE.move.out$_{b(i)}$: an intermediate quantity representing potential IWE transfer out the given elevation band to the adjacent (downslope) band; calculated as part of simulation of glacial dynamics within VICwCDiP [mm]

IWE.out.potential$_{b(i)}$: ? [mm]

IWE.postmelt$_{b(i)}$: the variable name for IWE in timestep after reduction by meltwater generation for a given elevation band within a VICwCDiP grid cell [mm]

IWE.previous$_{b(i)}$: IWE at the end of the preceding model timestep in a given elevation band within a VICwCDiP grid cell [mm]

IWE.updated$_{b(i)}$: the variable name for IWE after any transformation of snow to glacial firn ice for a given elevation band within a VICwCDiP grid cell [mm] [mm]

k_c = constant parameter value, = 0.5, used by VICwCDiP in calculation of compaction leading to density changes in standing snowpack [dimensionless]

ksat {parameter}: expression of saturated hydraulic conductivity [mm day^{-1}]

k.submax: exponent used in calculation of orographic scaling factor when $Z_{b(i)}$ is less than $Z_{max.isohyetal}$ [dimensionless]

k.supermax: exponent used in calculation of orographic scaling factor when $Z_{b(i)}$ is greater than $Z_{max.isohyetal}$ [dimensionless]

λ_v = latent heat of vapourisation [2450000.0 J kg^{-1}]

lapse.rate$_{Tair}$: (UIB local) air temperature lapse rate [0.007 °C m^{-1}] i.e. 7°C/1000m

limit.lower$_{.b(i)}$: minimum SRT90 pixel elevation defining the lower limit of a sub-grid elevation band for a given VICwCDiP grid cell

limit.upper$_{.b(i)}$: maximum SRT90 pixel elevation defining the upper limit of a sub-grid elevation band for a given VICwCDiP grid cell

LWin: incoming longwave (thermal) radiation, measured a positive toward the (ground) surface [W m^{-2}]

LWnet$_{b(i)}$: the variable name for net (emitted) longwave (thermal) radiation for a given elevation band within a VICwCDiP grid cell [W m^{-2}]

orographic.factor$_{b(i)}$:orographic scaling factor used to calculate precipitation for a given elevation band within a VICwCDiP grid cell based elevation as reference master/base observation station, e.g. for the Astore and Hunza catchment models, Astore PMD (2394m asl) is used. [dimensionless]

overburden.new$_{b(i)}$: an intermediate quantity used by VICwCDiP in calculation of compaction leading to density changes in standing snowpack [fraction]

overburden.prev$_{b(i)}$: an intermediate quantity used by VICwCDiP in calculation of compaction leading to density changes in standing snowpack [fraction]

PET: potential evapotranspiration [mm]

PET$_{b(i)}$: = the variable name for PET for a given elevation band within a VICwCDiP grid cell [mm]

PET$_{cell}$: = as per $PET_{b(i)}$ but averaged across a VICwCDiP grid cell [mm]

PET.part1: an intermediate quantity used by VICwCDiP in calculation of PET

PET.part2: an intermediate quantity used by VICwCDiP in calculation of PET

ϕ: porosity, i.e. fraction of voids in a unit volume of soil [fraction]

precip$_{b(i)}$: orographically-scaled precipitation calculated for a given elevation band within a VICwCDiP grid cell [mm]

precip$_{metbase}$: precipitation observed (or simulated) at the master/base observation station, e.g. for the Astore and Hunza catchment models, Astore PMD (2394m asl) is used

pressure$_{b(i)}$: the variable name for atmospheric pressure for a given elevation band within a VICwCDiP grid cell, time-varying [Pa]

pressure.exponent: an intermediate quantity used by VICwCDiP in approximation of atmospheric pressure for a given surface elevation.

Q_{base}: baseflow, lateral subsurface mass flux to theoretical drainage network,one of the primary output quantities calculated by VIC [mm]

Q_{direct}: direct runoff, lateral surface mass flux to theoretical drainage network, one of the primary output quantities calculated by VIC [mm]

$Q_{upper=>middle}$: drainage from upper to middle soil layer, subsurface vertical mass flux between soil layers, essential to calculating soil moisture quantities [mm]

$Q_{middle=>lower}$: drainage from middle to lower soil layer, subsurface vertical mass flux between soil layers, essential to calculating soil moisture quantities [mm]

$\rho_{freshsnow}$: the assumed density of freshly fallen snow in VICwCDiP, at present assumed to be a constant density. [100.0 kg m^{-3}]

ρ_{h2o} = the density of liquid water [1000.0 kg m^{-3}]

ρ_{ice} = density of glacial ice [917.0 kg m^{-3}]

ρ_{max}: an intermediate quantity, representing maximum density at the base of the snowpack, used by VICwCDiP in calculation of compaction leading to transformation of snowpack to glacial firn ice [kg m^{-3}]

$\rho_{slope.b(i)}$: an intermediate quantity, representing rate of change of density as function of depth within the snowpack, used by VICwCDiP in calculation of compaction leading to transformation of snowpack to glacial firn ice [kg m^{-4}]

$\rho_{snowpack2.b(i)}$: an intermediate quantity used by VICwCDiP in calculation of compaction leading to density changes in standing snowpack [kg m^{-3}]

$\rho_{snowpack.final.b(i)}$: variable name for the final (post-compaction) for a given elevation band within a VICwCDiP grid cell [kg m^{-3}]

$\rho_{threshold}$ = density at which compacted snow is considered to transform into glacial ice [850.0 kg m^{-3}]

$rainfall_{cell}$: mean liquid rainfall in a given time-step across a grid cell in VICwCDiP [mm]

σ: Stefan Boltzmann constant from thermodynamics [0.000000056696 W m^{-2} K^{-4}]

SCA: snow covered area, a fractional quantity (0 to 1) characterising the amount snow cover within a given unit area.

$SCA.initial_{b(i)}$: the variable name for SCA at the start of a timestep for a given elevation band within a VICwCDiP grid cell [fraction]

$shape_{base}$: a constant parameter, = 0.2, used in intermediate calculations when determining partitioning of inflow between direct runoff and infiltration [dimensionless]

sliding.exponent: an intermediate quantity coefficient used in calculation of "sliding velocity" (U_s) in simulation of glacial dynamics within VICwCDiP. [dimensionless]

soilextraction.coeff: an intermediate quantity used by VICwCDiP during calculation of A.ET [fraction]

$SMC_{layer.initial}$: the model-initialised value of the equivalent depth of water stored in the lower soil layer of a given VICwCDiP grid cell at the start of a simulation time-step [mm]

$SMC_{layer.max}$: the maximum equivalent depth of water which can be stored in the lower soil layer of a given VICwCDiP grid cell [mm]

$SMC_{layer.resid}$: the minimum equivalent depth of water which will be stored in the lower soil layer of a given VICwCDiP grid cell [mm]

SMD: soil moisture deficit, relative representation of amount of volume available to filled by water, mathematically = 1.0 - Θ [fraction]

SMD_{crit}: the critical SMD threshold below A.ET becomes a fraction of, rather than equal to, PET [fraction]

svp: saturation vapour pressure, i.e. the maximum partial pressure of water vapour that the atmosphere can hold under given conditions, i.e total pressure and temperature.

$SVP_{b(i)}$: : the variable name for saturation vapour pressure for a given elevation band within a VICwCDiP grid cell, time-varying [Pa]

svp.coefficient: an intermediate quantity used by VICwCDiP in approximating saturation vapour pressure.

svp.exponent: an intermediate quantity used by VICwCDiP in approximating saturation vapour pressure. [dimensionless]

$SVP.slope_{b(i)}$: the variable name for the rate of change in saturation vapour pressure with respect to temperature pressure for a given elevation band within a VICwCDiP grid cell, time-varying [Pa $°C^{-1}$]

svpslope.coefficient: an intermediate quantity used by VICwCDiP in approximating saturation vapour pressure slope [$°C^{-1}$]

SWE: snow water equivalent, i.e. the equivalent depth of liquid water contained in the snowpack at a particular time and location. [mm]

$SWE_{fullSCA}$: a threshold parameter within VICwCDiP above which SCA is expected to complete or full, i.e SCA = 1.0. In the present study a value of 100.0mm was used for $SWE_{fullSCA}$, i.e. for snowpacks with less than 100.0mm SCA becomes fractional (< 1.0). [mm]

$SWE.final_{b(i)}$: the variable name for SWE in timestep after reduction by meltwater generation for a given elevation band within a VICwCDiP grid cell [mm]

$SWE.initial_{b(i)}$: the variable name for SWE at the start of a timestep for a given elevation band within a VICwCDiP grid cell [mm]

$SWE.melt_{b(i)}$: the variable name for amount of SWE reduction through meltwater generation within a timestep for a given elevation band within a VICwCDiP grid cell [mm]

$SWE.melt_{cell}$: as per $SWE.melt_{b(i)}$ but averaged across a VICwCDiP grid cell [mm]

$SWE.updated_{b(i)}$: the variable name for SWE after any transformation of snow to glacial firn ice for a given elevation band within a VICwCDiP grid cell [mm] [mm]

$SWE.transform_{b(i)}$: the variable name for amount of SWE conversion as a result of any transformation of snow to glacial firn ice for a given elevation band within a VICwCDiP grid cell

SWin: incoming shortwave (solar) radiation, measured a positive toward the (ground) surface [W m^{-2}]

$SWnet_{b(i)}$: the variable name for net (absorbed) shortwave solar radiation for a given elevation band within a VICwCDiP grid cell [W m^{-2}]

τ: the dynamic gravitational driving stress at the base of a modelled glaciated section timestep for a given elevation band within a VICwCDiP grid cell [Pa]

$\boldsymbol{\tau_c}$: near constant/universal representative value of glacial gravitational driving stress [100,000 Pa]

$\boldsymbol{\theta_r}$: residual soil moisture which cannot be gravitationally drained [volumetric fraction]

Θ : normalised water content, alternately relative soil moisture, the ratio of available soil water (SMC_{actual} minus SMC_{resid}) divided by FC [fraction]

$\Theta_{lower.crit}$: a calibration parameter defining the transition from linear to power law baseflow regime in terms of normalise water content (Θ) in the lower soil layer [fraction]

$\boldsymbol{t_{final.b(i)}}$: variable name for final (pre-melt) snowpack depth for a given elevation band within a VICwCDiP grid cell [m]

$\boldsymbol{t_{intial.b(i)}}$: variable name for initial snowpack depth in a given timestep for a given elevation band within a VICwCDiP grid cell [m]

$\boldsymbol{t_{1.b(i)}}$: variable name for an intermediate-stage snowpack depth used by VICwCDiP in calculation of compaction leading to density changes in standing snowpack [m]

$\boldsymbol{t_{2.b(i)}}$: variable name for an intermediate-stage snowpack depth used by VICwCDiP in calculation of compaction leading to density changes in standing snowpack [m]

$\boldsymbol{t_{transform.b(i)}}$: variable name for the reduction in snowpack depth due to transformation of snowpack to glacial firm ice [m]

$\boldsymbol{Tair_{b(i)}}$: Tavg calculated for a given elevation band within a VICwCDiP grid cell [°C]

$\boldsymbol{Tair_{metbase}}$: Tavg observed (or simulated) at the master/base observation station, e.g. for the Astore and Hunza catchment models, Astore PMD (2394m asl) is used

Tavg: Daily mean 2m air temperature, usually calculate as the mean of Tmin and Tmax [°C].

Tmax: daily maximum 2m air temperature [°C].

Tmin: daily minimum 2m air temperature [°C].

$\boldsymbol{Tsurf_{b(i)}}$: (skin) surface temperature calculated for a given elevation band within a VICwCDiP grid cell [°C]

Tsurf.correction: correction factor used to adjust $Tair_{b(i)}$ to approximate $Tsurf_{b(i)}$ [°C]

typical.slide: parameter {optionally calibrated} used in simulation of glacial dynamics within VICwCDiP, observed values, translated from glacial field studies, for the UIB range from 20 to 200 m/year which is equivalent to 0.05 to 0.5 [m day^{-1}]

$\boldsymbol{U_d}$: "deformation velocity" in simulation of glacial dynamics within VICwCDiP [m day^{-1}]

$\boldsymbol{U_s}$: "sliding velocity" in simulation of glacial dynamics within VICwCDiP [m day^{-1}]

$\boldsymbol{U_{total}}$: "total displacement" in simulation of glacial dynamics within VICwCDiP [m day^{-1}]

$Vmove.potential_{b(i)}$: an intermediate quantity representing potential (absolute) ice volume transfer from a higher to adjacent lower elevation band as used in simulation of glacial dynamics within VICwCDiP. [m^3 day^{-1}]

vapour pressure deficit (vpd): the expression, in units of (partial) atmospheric pressure, of the "shortfall" between the amount of moisture (water vapour) the atmosphere is capable of holding (for a given temperature and absolute pressure) and the water vapour present at that instant.

VIC: Variable Infiltration Capacity hydrological model (developed and maintained by the University of Washington [USA])

VICwCDiP model: Variable Infiltration Capacity with Cryosphere Dynamics in Python", i.e. the version of the VIC model adapted/developed for the present study;

$viscosity_{snow.b(i)}$: intermedia quantity used by VICwCDiP in calculation of compaction leading to density changes in standing snowpack

$Z_{b(i)}$: mean elevation of a given elevation band within a VICwCDiP grid cell [m asl]

Z_{max}: maximum SRTM90 pixel elevation within a VICwCDiP grid cell [m asl]

$Z_{max.isohyetal}$: the calibrated elevation of peak orographically enhanced precipitation [m asl]

Z_{mean}: mean of the SRTM90 pixel elevations within a VICwCDiP grid cell [m asl]

$Z_{metbase}$: elevation of the master/base observation station, e.g. for the Astore and Hunza catchment models, Astore PMD (2394m asl) is used

Z_{min}: minimum SRTM90 pixel elevation within a VICwCDiP grid cell [m asl]

$Z_{reference}$: reference height used approximation of atmospheric pressure at ground surface in high elevation environments

D.2 Reasoning for development of VICwCDiP

Unfortunately, over the course of several months of extensive calibration testing, a hypersensitivity to input humidity (specifically when formulated as vapour pressure deficit) was identified in the energy balance module of the VIC model when simulating the hydro-climatic conditions typical of the UIB. This hypersensitivity rendered accurate modelling of UIB tributary catchment hydrology impossible without "over-tuning" the model using physically unrealistic values for model parameters (constants) or bias adjustments to input climatology. The hypersensitivity manifested as large amounts of sublimation in cold months over the modelled snowpack. This, in turn, resulted in the transfer of energy from the snow surface to the atmosphere in the form of accumulated "cold content", i.e. snowpack thermal inertia (Singh, 2001). The "cold content" of the snowpack must be overcome through pack warming or "ripening" during the early spring before melt can begin. Hence, without compensating model tuning, snowmelt simulated in VIC was both delayed and reduced in magnitude in each melt season. VIC incorporates the MTCLIM algorithm (Thornton, 1999) which extrapolates the additional required meteorological parameters for energy balance resolution from maximum and minimum daily temperature, precipitation and windspeed. Use of this module resulted either in similar model results to manually-specified inputs or in MTCLIM specifying a constantly nearly saturated atmosphere with relative humidity between 98 and 99.5%. In this case the model yielded realistic output in terms of snowmelt timing and magnitude but logically also resulted in unrealistically low – i.e. near zero – values of evaporation.

After spending considerable time attempting to unravel the source of these issues, given the total length of code in the overall VIC modelling package and the complexity of linkages between the numerous sub-components (modules), it was decided to develop a new model code – in Python rather than C and Fortran – implementing the intended hydrological, snowpack and glacial mechanics methodologies, using algorithms available in the literature, while substituting a "degree-day" based approach (e.g. Singh, 2000) in lieu of the more sophisticated energy balance approach which had undermined the use of VIC. Given the capability of the adapted model, coded in Python, to simulate elementary snowpack and glacial mechanics on top of the standard VIC hydrological method it was decided to designate this the "Variable Infiltration Capacity with Cryosphere Dynamics in Python" (VICwCDiP) model.

D.3 Additional detail on equations used in VICwCDiP

D.3.1 Catchment model construction: Elevation parameters

The elevation band characteristic derivation process is carried out as follows:

1) Mean elevation for the over grid cell is calculated (for points within the catchment) along with identification of minimum and maximum elevation within the cell. Figure 6.03 shows comparisons for full-resolution elevations provided by SRTM90 with the mean cell elevations at 0.05 and 0.10 degree horizontal resolution respectively of the Astore and Hunza catchments. In all panels of Figure 6.03, areas identified as glaciated are overlain with surface slopes (angular degrees) derived from SRTM90.

2) Width of elevation bands are calculated using Equations 6.001a and 6.001b

Equation D.01a:

$$diff_{max}\ [m] = max((Z_{max} - Z_{mean}), (Z_{mean} - Z_{min}))$$

Equation D.01b:

$$width_{band}\ [m] = (2 * diff_{max}) * (count_{bands})^{-1}$$

3) The upper and lower band limits are next calculated using Equations D.02 and Equation D.03:

Equation D.02:

$$limit.lower_{b(i)}\ [m\ asl] = (Z_{mean} - diff_{max}) + (width_{band} * (band.number_{b(i)} - 1))$$

Equation D.03:

$$limit.upper_{b(i)}\ [m\ asl] = (Z_{mean} - diff_{max}) + (width_{band} * band.number_{b(i)})$$

4) The mean elevation of each elevation band and the fraction of the total cell it covers are calculated using an iterative process which tests the value of each sub-grid elevation point against the band limits derived in Equations 6.02 and 6.03 above. For relatively flat cells, one or more bands – usually the top or bottom band – may have a cell fraction that rounds to zero. In these cases, to avoid numerical discontinuities (dividing by zero) when making glacial volume calculations, a minimum band area and initial glacial footprint – 0.001 of the total cell – are assigned along with a glacial height of zero. This permits numerical stability without violating conservation of mass.

Examples of the resultant sub-grid cell discretisation are shown in Figure D.01. The grid cell shown in the left panel of Figure D.01, in this case located in the Hunza

catchment, shows a relatively balance distribution of area between the five elevation bands. It is typical for the uppermost and lowermost bands to cover a smaller fraction of the cell area than the interior bands and especially the central one. The grid cell shown in the right panel of Figure D.01, in this case located in the Astore catchment, provides an example of the situation described above where one or more elevation bands have zero area based on the automated band delineation process. Here specifically the lowest band must be assigned a minimal area in order to allow the model to function. The grid cell internal elevation range in both examples shown is greater than 2000m. This is typical of that found in the constructed models of UIB tributary catchments.

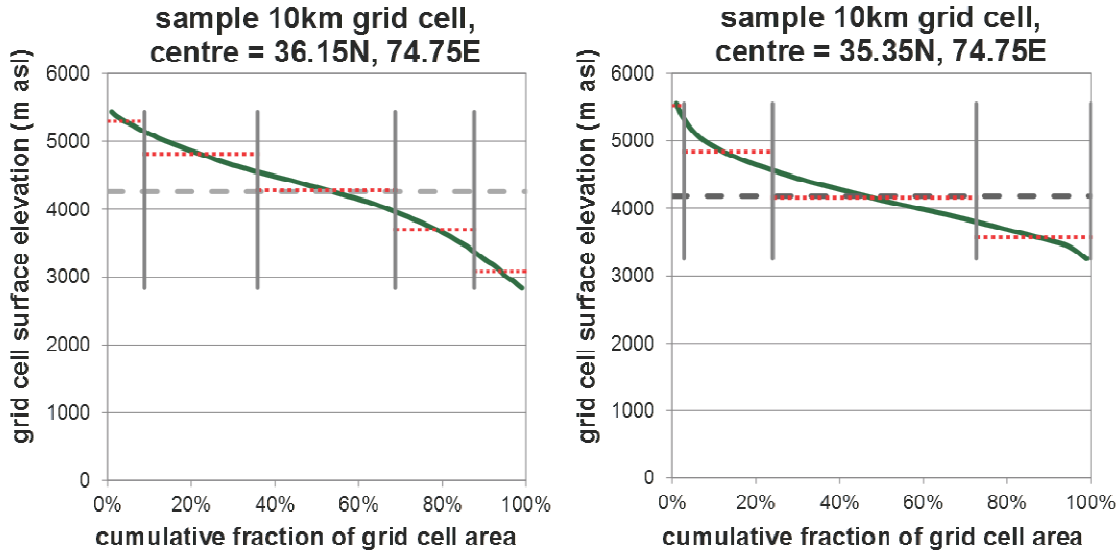

Figure D.01 Examples of grid cell internal distribution of area by defined sub-grid elevation bands used in VICwCDiP surface discretisation.

5) To derive the inputs necessary for glacial calculations, available estimates of glacial footprints are used to filter SRTM90 and derive surface slopes. These slope values are processed using the underlying elevation data in an additional iterative loop, with testing against the band limits. The resulting outputs are the fraction of the cell with glacial cover within the elevation band and the mean slope of this glaciated area. The glaciated areas are mapped in Figure 6.03 and overlain on the model grid cell elevations respectively for the Astore and Hunza catchments.

6) For glaciated bands, initial glacier thickness is determined using a reformulation of Kessler's (2006) equations of Glenn's flow law as suggested by Naz (2011). This is shown in Equation D.04:

Equation D.04:

$$height.ice_{b(i)}\ [m] = \tau_c * (\rho_{ice} * g * sin(\alpha_{b(i)}))^{-1}$$

where: τ_c = 100,000 [Pa] ; ρ_{ice} = 917.0 [kg m^{-3}] ; g = 9.81 [m s^{-2}]; and
$\alpha_{b(i)}$ = mean slope of glacier surface within band [radians]

This derivation relies on the formulation of the gravitational driving stress which is proportional to the ice thickness and inversely proportional to the product of the representative bed (surface) slope with the mean ice density and the acceleration of gravity. The key assumption is provided by Paterson (1994) regarding the near constant/universal representative value of gravitational driving stress – i.e. τ_c = 100 kPa – for temperate mid-latitude glaciers. Figure D.02 provides a simple conceptualisation of the elements involved. In layman's terms, the theory can be stated as that under a state of dynamic equilibrium, glacier thickness will need to be greater (less) at shallower (steeper) slope angles to achieve the driving stress/bed friction conditions widely observed by glaciological field studies.

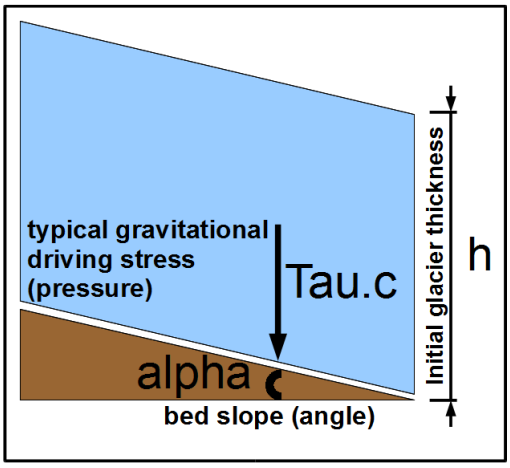

Figure D.02 Conceptual illustration of the relationships between glacial driving stress, thickness and bed-slope relationships, i.e the product of the thickness of the glacier times the vertical component (sine of angular slope) of the bed gradient, the density of ice and the acceleration of gravity are equal to the gravitational driving stress which has in a number of studies to be a near constant.

Given that glaciers are dynamic systems – changing in both lateral extents and volumes – this approach is temporally associated with the surface state (glacial thickness) concurrent to the date or period when the DEM was derived and presupposes that the delimitation of glacial footprints match these conditions. The application/adaption here of Paterson's assumptions regarding Glenn's flow law in both the derivation of initial thickness as well as calculation of rates of displacement (basal sliding) is not original but follows the approach adopted by Kessler et al. (2006) and Naz (2011).

7) Once glaciated areas and initial ice thickness have been calculated for each relevant elevation band in each cell, initial ice volume is determined simply by taking the product of the glaciated "footprint" area and the estimated mean thickness. This uniform thickness is clearly an exaggerated simplification but additional idealisations of glaciated geometry were necessary to allow calculation of glacial mass transfer between elevation bands within an individual grid cell.

D.3.2 Catchment model construction: soil parameters

In addition to elevation band descriptors, it is also necessary to supply values for the sub-surface properties used by the VIC/ARNO to govern the hydrological response. These values must be supplied for each of the three soil layers in each cell. The retained parameters in the specific formulation used in VICwCDiP are the following

a) the 'expt' parameter [dimensionless], itself defined as a function of soil pore size distribution parameter, from Campbell's equation for hydraulic conductivity (Maidment, 1992).
b) the 'ksat' parameter [mm day-1] expression of saturated hydraulic conductivity.
c) the depth [m] of the individual soil layer
d) the residual soil moisture [volumetric fraction] of water which can be gravitationally drained

With the exception of soil depth, which was retained as a calibration parameter, for the Astore and Hunza catchment models, values of these parameters as shown in Table 6.02 were applied uniformly in all cells. The values were determined during the attempted calibration work with the VIC model.

Parameter	Upper soil layer	Middle soil layer	Lower soil layer
drainage exponent	8.454	8.726	8.976
ksat	350	350	350
residual soil moisture (θ_r)	0.087	0.102	0.103

Table D.1 Soil parameters applied uniformly to all grid cells throughout the VICwCDiP models of the Astore and Hunza catchments.

The soil layer depths were retained as a calibration parameter. The upper soil layers were defined with a uniform depth in all cells: a layer depth of 0.15m was eventually adopted for the Astore 5km model and both the 5km and 10km models of Hunza. In the VIC hydrological approach, the upper soil layer effectively governs partitioning between direct runoff (Q_{direct}) and infiltration which eventually leads to

baseflow (Q_{base}). In the catchment models described here a depth of 0.15m yielded appeared a satisfactory balance between direct runoff and infiltration at the monthly timescales of interest to the present work.

The middle and lower soil layers were assigned equal depths as a function of mean cell elevation. The results of the empirical functions used to derive these layer depths are shown in Figure D.03. In addition to the expediency for calibration purposes, there is a logical (geomorphological) justification to decreasing soil depth with elevation. The reasoning is that abrasion from glacial displacement and gravity-driven transport of debris from weathering processes will result increasing sediment deposits in valley bottoms while upper slopes will have relatively thin soil covers over otherwise bare rock.

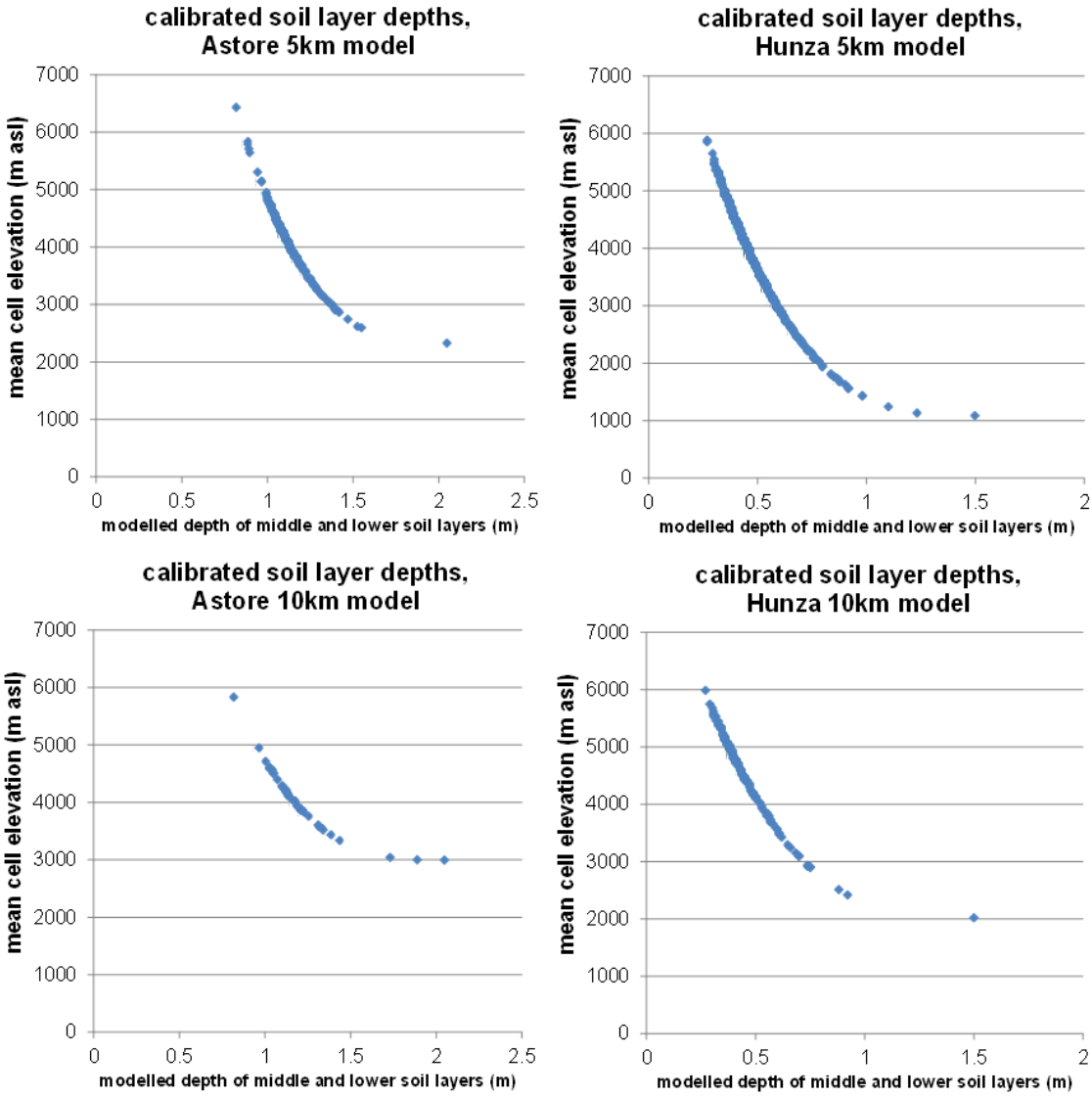

Figure D.03 Calibrated relationships between lower soil layer depths and mean cell surface elevation as used in the VICwCDiP model.

In addition, although all of the soil parameters used in the emulation of the VIC hydrology component (Gao et al., 2009) within the Python-based model could be varied on a grid cell basis, in the absence of detailed information on the spatial variability of soil types within the catchment, it was decided to select catchment-wide values for the following parameters:

- $shape_{base}$: baseflow shape parameter = 0.2; amongst its uses this parameter defines the exponent used in determining the saturated areal fraction as:

Equation D.05:

$$A_{exponent}\ [dimensionless] = (shape_{base} * (1.0 + shape_{base})^{-1})$$

- "C": baseflow exponent = 2.0
- ϕ (porosity, i.e. fraction of voids in a unit volume of soil) = 0.485

These parameter values were selected either as the recommended defaults for VIC or as initial estimates used by Naz (2011). These parameter values are used in combination with individual cell soil layer depths to calculate key soil water capacity quantities as in the hydrological component of the VIC model (Gao et al., 2009):

Equation D.06:

$$infiltration_{max}\ [mm] = (1 + shape_{base}) * \phi * depth_{soil.upper}$$

Equation D.07:

$$SMC_{upper.max}\ [mm] = \phi * depth_{soil.upper} * 1000.0$$

Equation D.08:

$$SMC_{upper.resid}\ [mm] = \theta_r * depth_{soil.upper} * 1000.0$$

Equation D.09:

$$SMC_{upper.initial}\ [mm] = (SMC_{upper.max} + SMC_{upper.resid}) * 0.5$$

The maximum, residual and initial soil moisture equivalents (in mm) are also calculated for the middle and bottom soil layers using the respective layer depths, porosities (ϕ) and residual fractions (θ_r).

D.3.3 Extrapolation of additional atmospheric variables

Estimation of near-surface atmospheric pressure is performed as shown in Equations D.10a and D.10b:

Equation D.10a:

$$Z_{reference}\ [m] = (287 * (g^{-1})) * ((Tairb(i) + 273.15) + 0.5 (lapse.rate_{Tair} * Z_{b(i)})$$

where: g = 9.81 [m s^{-2}]; $lapse.rate_{Tair}$ = 0.007 [°C m^{-1}]

Equation D.10b:

$$pressure.exponent\ [dimensionless] = -1.0 * (Z_{b(i)} * Z_{reference}^{-1})$$

Equation D.10c

$$pressure_{b(i)}\ [Pa] = 101300.0 * e^{pressure.exponent}$$

where: e = ~2.718281828

It is possible to approximate saturation vapour pressure (SVP) and its gradient (rate of change) using only Tair. This is shown in Equations D.11 and D.12:

Equation D.11a

$$svp.coefficient \begin{cases} \{ \text{ where } Tair_{b(i)} > 0 \\ = 1.0 \\ \{ \text{ where } Tair_{b(i)} < 0 \\ = 1.0 + (0.00972 * Tair_{b(i)}) + [0.000042 * (Tair_{b(i)})^{2.0}] \end{cases}$$

Equation D.11b:

$$svp.exponent\ [dimensionless] = (17.269 * Tair_{b(i)}) * (237.3 + Tair_{b(i)})^{-1}$$

Equation D.11c

$$SVP_{b(i)}\ [Pa] = svp.coefficient * 0.61078 * e^{svp.exponent}$$

Equation D.12a:

$$svpslope.coefficient\ [°C^{-1}] = (17.269 * Tair_{b(i)}) * (237.3 + Tair_{b(i)})^{-2.0}$$

Equation D.12b:

$$SVP.slope_{b(i)}\ [Pa\ °C^{-1}] = svpslope.coefficient * SVP_{b(i)}$$

This methodology is also drawn directly from VIC source code and based on Equations 4.2.2 and 4.2.3 from Maidment (1982).

The approximation of surface pressure further allows the estimation of the psychrometric constant (gamma), as shown in Equation D.13.

Equation D.13:

$$\gamma\ [Pa * °C^{-1}] = 1.6286 * (pressure_{b(i)} * (\lambda_v)$$

where λ_v = 2450000.0 [J kg^{-1}]

This is another equation used in VIC and is drawn from Maidment (1982), in this case his equation 4.2.28.

Equations D.14 (e.g. Andreadis et al., 2009) and D.15 (Stewart and Rouse, 1976) show the formulas used to estimate net longwave radiation and PET.

Equation D.14:

$LWnet_{b(i)} = LWin - [\ \sigma * (\ Tsurf_{b(i)} + 273.15\ )^{4.0}\ )\ ]$

where: σ (Stefan Boltzmann constant) = 0.000000056696 [W m^{-2} K^{-4}]

Equation D.15:

$$PET = \frac{1.26 * SVP.slope_{b(i)}}{SVP.slope_{b(i)} + \gamma} * \frac{SWnet_{b(i)} + LWnet_{b(i)}}{1000.0 * \lambda_v} * (1000.0 * 86400.0)$$

where λ_v = 2450000.0 [J kg^{-1}]

D.3.4 Simulation of snowpack density evolution

The first step in the snow density procedure is to update the pack depth from the value stored at the previous time-step. The previous snow pack water equivalent, SWE.initial, divided by the previous depth value then yields the initial mean pack density. The next step in the density procedure is to calculate the amount of compaction (reduction of pack depth) due to the weight of fresh snow. The formulation used is shown in Equation D.16. As stated above, this formulation, including values for key constants, is taken from the VIC source code (Gao et al., 2009) which references Andreadis et al. (2009). These equations were checked against those of Saloranta (2012).

Equation D.16a:

$overburden.new_{b(i)}\ [fraction] = (\ freshsnow_{b(i)} * (SWE.initial_{b(1)} - freshsnow_{b(i)}\ )^{-1}\ )$

Equation D.16b:

$compaction.exponent1_{b(i)} = [(t_{intial.b(i)} * (b_1)^{-1}\ ]^{b.exp}$

where: b_1 = 0.254; b.exp = 0.35 (Saloranta, 2012)

Equation D.16c:

$\Delta_{snowdepth1.b(i)}\ [m] = overburden.new_{b(i)} * compaction.exponent1_{b(i)} * t_{intial.b(i)}$

The amount of allowable compaction is bounded at 10% of the previous snow pack depth. This ‘safeguard’ limits the amount of compaction occurring during time-steps with very large precipitation amounts which were calculated from the base meteorological record by orographic scaling. The over-compaction ‘safeguard’ is implemented as shown in Equation D.17.

Equation D.17:

$$t_{1.b(i)}\ [m] = \begin{cases} \{ \text{where } t_{intial.b(i)} > (\Delta_{snowdepth1.b(i)} * 10.0) \\ = t_{intial.b(i)} - \Delta_{snowdepth1.b(i)} + (freshsnow_{b(i)} * (\rho_{freshsnow})^{-1}) \\ \{ \text{where } t_{intial.b(i)} < (\Delta_{snowdepth1.b(i)} * 10.0) \\ = (t_{intial.b(i)} * 0.9) + (freshsnow_{b(i)} * (\rho_{freshsnow})^{-1}) \end{cases}$$

where $\rho_{freshsnow} = 100.0$ [kg m^{-3}]

The next step in the density procedure is to calculate compaction due to "aging" of the existing snowpack. This requires calculation of characteristic values for snowpack "overburden" and viscosity. Formulas for these quantities and the resultant compaction are shown in Equations D.18 to D.20:

Equation D.18a:

$$overburden.prev_{b(i)} = k_c * g * \rho_{h2o} * (SWE.initial_{b(i)} * 0.001)$$

where: $k_c = 0.5$ [dimensionless]; $g = 9.81$ [m s^{-2}]; ρ_{h2o} =1000.0 [kg m^{-3}]

Equation D.18b:

$$compaction.exponent2_{b(i)} = (C_5 * Tsurf_{b(i)}) + (C_6 * [SWE.initial_{b(i)} * (t_{1.b(i)})^{-1}])$$

where: $C_5 = -0.08$ [°C^{-1}]; $C_6 = 0.021$ [kg m^{-3}]

Equation D.18c:

$$viscosity_{snow.b(i)} = \eta_0 * e^{compaction.exponent2b(i)}$$

where: $\eta_0 = 3600000.0$ [N s m^{-2}] => 3.6 MNs/m^2; e = ~2.718281828

Equation D.18d:

$$\Delta_{snowdepth2.b(i)}\ [m] = overburden.prev_{b(i)} * (viscosity_{snow.b(i)})^{-1} * t_{1.b(i)} * 86400.0$$

Once again the amount of allowable compaction in this step was bounded to 10% of the updated snowpack depth.

Equation D.19:

$$t_{2.b(i)}\ [m] = \begin{cases} \{ \text{where } t_{1.b(i)} > (\Delta_{snowdepth2.b(i)} * 10.0) \\ = t_{1.b(i)} - \Delta_{snowdepth2.b(i)} \\ \{ \text{where } t_{1.b(i)} < (\Delta_{snowdepth2.b(i)} * 10.0) \\ = (t_{1.b(i)} * 0.9) \end{cases}$$

Snow pack depth after compaction is thus known and this combined with current SWE yields the snowpack mean density as shown in Equation D.20.

Equation D.20:

$$\rho_{snowpack2.b(i)}\ [kg\ m^{-3}] = SWE.initial_{b(i)} * (t_{2.b(i)})^{-1}$$

Therefore by geometric derivation the maximum density within the snowpack, ρ_{max}, can be calculated as shown in Equation D.29. The snow to ice transformation

procedure enumerated here was implemented based on concepts described by Naz (2011).

Equation D.21:

$\rho_{max}\ [kg\ m^{-3}] = (\ 2.0 * \rho_{snowpack2.b(i)}\ ) - \rho_{freshsnow}$

where: $\rho_{freshsnow} = 100.0\ [kg\ m^{-3}]$

Using the same geometric reasoning, the density gradient within the snowpack can be calculated using Equation D.22 (Naz, 2011).

Equation D.22:

$\rho_{slope.b(i)}\ [kg\ m^{-4}] = (\rho_{max} - \rho_{freshsnow}) * (\ t_{2.b(i)}\ )^{-1}$

The following Equations D.23 to D.28, which are logically implied by the concepts presented by Naz (2011) and imposed by the core model tenet of 'conservation of mass', outline this procedure.

Equation D.23:

$t_{final.b(i)}\ [m] = (\ \rho_{threshold} - \rho_{freshsnow}\ ) / \rho_{slope.b(i)}$

where: $\rho_{threshold} = 850.0\ [kg * m^{-3}]$; $\rho_{freshsnow} = 100.0\ [kg * m^{-3}]$

Equation D.24:

$t_{transform.b(i)}\ [m] = t_{2.b(i)} - t_{final.b(i)}$

Equation D.25:

$\rho_{snowpack.final.b(i)}\ [kg\ m^{-3}] = (\rho_{threshold} - \rho_{freshsnow}\ ) * 0.50$

where: $\rho_{threshold} = 850.0\ [kg\ m^{-3}]$; $\rho_{freshsnow} = 100.0\ [kg\ m^{-3}]$

Equation D.26:

$SWE.updated_{b(i)}\ [mm] = t_{final.b(i)} * \rho_{snowpack.final.b(i)}$

Equation D.27:

$SWE.transform_{b(i)}\ [mm] = SWE.initial_{b(i)} - SWE.updated_{b(i)}$

Equation D.28:

$IWE.updated_{b(i)}\ [mm] = IWE.initial_{b(i)} + SWE.transform_{b(i)}$

D.3.5 Glacial vertical mass redistribution and volume and areal change calculations

The present work contributes incrementally to the definition of the modelled glacial geometry by considering the glacial width as the product of the grid cell width and the ratio of the glaciated fraction within the band to the total cell fraction of the band. These spatial relationships are illustrated conceptually in Figures 6.06 and 6.07 (section 6.6.1).

Recall Equation 6.02:

$$glacial.ratio_{b(i)}\ [fraction] = glacial.fraction_{b(i)} * (cell.fraction_{b(i)})^{-1}$$

Equation D.29:

$$glacier.width_{b(i)}\ [m] = cell.width * glacial.ratio_{b(i)}$$

Equation D.30:

$$glacier.face_{b(i)}\ [m^2] = glacier.width_{b(i)} * height.ice_{b(i)}$$

Equation D.31:

$$Vmove.potential_{b(i)}\ [m^3\ day^{-1}] = U_{total} * glacier.face_{b(i)}$$

Once the absolute (modelled) potential volume of ice to be transferred has been calculated, this volume can be confirmed in terms of the fraction of total ice in the band being transferred and the equivalent IWE depth to be removed. This value in IWE depth is then converted into the equivalent IWE depth to be added to the adjacent (downslope) elevation band by multiplying the upslope removed IWE by the ratio of the upslope band cell fraction by the downslope band cell fraction.

Equation D.32:

$$glacier.length_{b(i)}\ [m] = cell.fraction_{b(i)} * cell.length$$

Equation D.33:

$$glacier.footprint_{b(i)}\ [m^2] = glacier.width_{b(i)} * glacier.length_{b(i)}$$

Equation D.34:

$$\Delta volume_{b(i)}\ [ratio] = Vmove.potential_{b(i)} * [(glacier.footprint_{b(i)} * height.ice_{b(i)})^{-1}]$$

Equation D.35:

$$IWE.out.potential_{b(i)}\ [mm] = \Delta volume_{b(i)} * IWE.postmelt_{b(i)}$$

Equation D.36:

$$IWE.moveout_{b(i)}\ [mm] = min(IWE.postmelt_{b(i)}, IWE.out.potential_{b(i)})$$

Equation D.37:

$$IWE.move.in_{b(i+1)}\ [mm] = IWE.move.out_{b(i)} * [cell.fraction_{b(i+1)} * (cell.fraction_{b(i)})^{-1}]$$

Equation D.38:

$$IWE.move.net_{b(i)}\ [mm] = IWE.move.in_{b(i)} - IWE.move.out_{b(i)}$$

Once the amount of ice being transferred into and out of each band are calculated, it is possible to determine the net IWE change due to ice movement. Given that glacial melt has previously been subtracted from the IWE stock, it is also possible at this point to calculate the final IWE value for the band during the time-step.

Equation D.39:

$$IWE.final_{b(i)}\ [mm] = IWE.postmelt_{b(i)} + IWE.move.net_{b(i)}$$

Equation D.40:

$$change.volume_{b(i)}\ [ratio] = IWE.final_{b(i)} * (IWE.previous_{b(i)})^{-1}$$

The method adopted here to enable areal change in glaciated area was constrained by the constraint of constant glacier length within elevation bands imposed by the conceptual model approach to mass transfer between elevation bands. This limitation requires that any areal change be in terms of lateral expansion or contraction. The amount of lateral change is quantified by use of a consistent cross-section aspect ratio in terms of vertical and lateral change. The calculated volume change is initially distributed between vertical and lateral change by assigning relative change in width as the cube root of the relative change volume and relative change in height as the square of the relative change in width. Hence the product of relative change in width and relative change in height is equal to the relative change in volume as shown in equations D.41 to D.50 below.

Equation D.41:

$$change.width_{b(i)}\ [ratio] = (change.volume_{b(i)})^{-3.0}$$

Equation D.42:

$$change.height_{b(i)}\ [ratio] = (change.width_{b(i)})^{2.0}$$

Equation D.43:

$$glacier.width.update_{b(i)}\ [m] = glacier.width_{b(i)} * change.width_{b(i)}$$

Equation D.44:

$$height.ice.update_{b(i)}\ [m] = height.ice_{b(i)} * change.height_{b(i)}$$

Equation D.45:

$$glacial.fraction.potential_{b(i)}. = glacial.fraction_{b(i)} * change.width_{b(i)}$$

Equation D.46:

$$glacial.fraction.final_{b(i)}\ [fraction] \begin{cases} \{\ where:\ glacier.width.update_{b(i)} < cell.width\ ) \\ = glacial.fraction.potential_{b(i)} \\ \{\ where\ glacier.width.update_{b(i)} \geq cell.width) \\ = glacial.fraction_{b(i)} \end{cases}$$

Equation D.47:

$$glacial.width.final_{b(i)}\ [m] = \begin{cases} \{\ where:\ glacier.width.update_{b(i)} < cell.width\ ) \\ = glacier.width.update_{b(i)} \\ \{\ where\ glacier.width.update_{b(i)} \geq cell.width\ ) \\ = cell.width \end{cases}$$

Equation D.48:

$$change.area_{b(i)}\ [ratio] = \begin{cases} \{\ where:\ glacier.width.update_{b(i)} < cell.width\ ) \\ = change.height_{b(i)} \\ \{\ where\ glacier.width.update_{b(i)} \geq cell.width\ ) \\ = glacier.width.update_{b(i)} * (glacier.width_{b(i)})^{-1} \end{cases}$$

Equation D.49:

$$change.height.2_{b(i)}\ [ratio] = change.volume_{b(i)} * (change.area_{b(i)})^{-1}$$

Equation D.50:

$$height.ice.final_{b(i)}\ [m] = height.ice_{b(i)} * change.height.2_{b(i)}$$

D.3.6 Determination of mass fluxes at the soil surface

The first step in the soil moisture accounting procedure is to determine the potential mass fluxes at the soil surface. In any given time-step mass influx, i.e. inflow, at the soil surface may be composed of liquid precipitation (rainfall) plus melt from seasonal snowpack and glacial ice, shown in Equation D.50 (Naz, 2011). A first approximation of moisture depth equivalent in the modelled upper soil layer is also made using Equation D.51.

Equation D.50:

$$inflow\ [mm] = rainfall_{cell} + SWE.melt_{cell} + IWE.melt_{cell}$$

Equation D.51:

$$SMC_{upper.1}\ [mm] = SMC_{upper.initial} + inflow - PET_{cell}$$

In keeping with standard hydrological methodology actual evapotranspiration (AET) is determined as a fraction of PET and as a function of soil moisture depletion (SMD). SMD is defined unity (1) minus the normalised water content (Θ) which is itself defined as the ratio available soil moisture (SMC_{actual} minus $SMC_{residual}$) to functional capacity (FWC). The formulations of FWC, Θ and SMD (for the upper soil layer) are shown in Equation D.52.

Equation D.52a:

$FWC_{upper}\ [mm] = SMC_{upper.max} - SMC_{upper.resid}$

Equation D.52b:

$\Theta_{upper.1}\ [fraction] = (SMC_{upper.1} - SMC_{upper.resid}) * (FWC_{upper})^{-1}$

Equation D.52c:

$SMD_{upper.1}\ [fraction] = 1.0 - \Theta_{upper.1}$

Above a critical threshold (SMD_{crit}), AET will be equal to PET. SMD_{crit} is considered to occur at a volumetric water content referred to as the "field capacity" (θ_{fc}) which occurs after normal gravity drainage has taken place following a "wetting event" (e.g. rainfall). Given that SMD_{crit} is often chosen as SMD = 0.5 this indicates that "field capacity" is expected to occur roughly midway between saturation and θ_r. Below the SMD_{crit} threshold AET is calculated as the product of PET multiplied by coefficient which is a function of SMD and SMD_{crit}. The formulation of this method for AET determination is shown in Equations D.53 and D.54 and shown conceptually in Figure D.04.

Equation D.53:

$$soilextraction.coeff\ [fraction] = \begin{cases} \{ \text{where: } SMD_{upper.1} > 0.50 \} \\ = 1.0 - [\ (SMD_{upper.1} - SMD_{crit}) * 2.0\ ] \\ \{ \text{where } SMD_{upper.1} \leq 0.50 \} \\ = 1.0 \end{cases}$$

Equation D.54:

$AET\ [mm] = soilextraction.coeff * PET_{cell}$

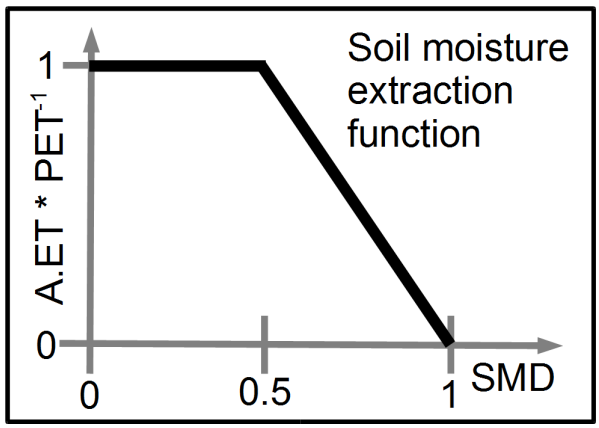

Figure D.04 Conceptual illustration of the soil moisture extraction function as implemented within the VICwCDiP) model.

Following determination of A.ET, the upper layer soil moisture estimate ($SMC_{upper.2}$) is revised as seen in Equation D.55:

Equation D.55:

$$SMC_{upper.2}\ [mm] = SMC_{upper.initial} + inflow - AET$$

The upper level soil moisture estimate is then checked against the layer maximum soil moisture calculated at model initialisation. If the estimated moisture exceeds the layer storage capacity, then the previous estimate is superseded by a value equal to the layer capacity. This verification also indicates whether there is surplus or excess inflow.

Equation D.56:

$$excess.inflow\ [mm] \begin{cases} \{\ where:\ SMD_{upper.2} > SMC_{upper.max} \\ = (inflow - A.ET) - (SMC_{upper.max} - SMC_{upper.initial}\ ) \\ \{\ where\ SMC_{upper.2} \leq SMC_{upper.max} \\ = 0.0 \end{cases}$$

The next step in the hydrological calculation procedure is the calculation of direct runoff using the VIC methodology. Key quantities to calculate include the saturated area fraction (A_{frac}) and instantaneous infiltration capacity (i_0). A_{frac} is a function of the ratio of $SMC_{upper.3}$ divided by $SMC_{upper.max}$ as well as of the areal fraction exponent ($A_{exponent}$) which was calculated at model initialisation (Equation D.05). Instantaneous infiltration capacity (i_0) is a function of maximum infiltration capacity ($infiltration_{max}$) which was calculated at model initialisation (Equation D.06). The formulas for these quantities are shown Equations in D.57 and D.58. The relationship between fractional infiltration rate and fractional surface area is illustrated in Figure D.05.

Equation D.57:

$$Afrac\ [fraction] = 1.0 - [\ 1.0 - (\ SMC_{upper.3} * (SMC_{upper.max})^{-1})\ ]^{A.exponent}$$

Equation D.58:

$$i_0\ [mm] = infiltration_{max} * \left[1.0 - \left(1.0 - A_{frac}\right)^{\frac{1}{shape_{base}}}\right]$$

where: $shape_{base}$ = 0.2 [dimensionless] (see section D.3.2)

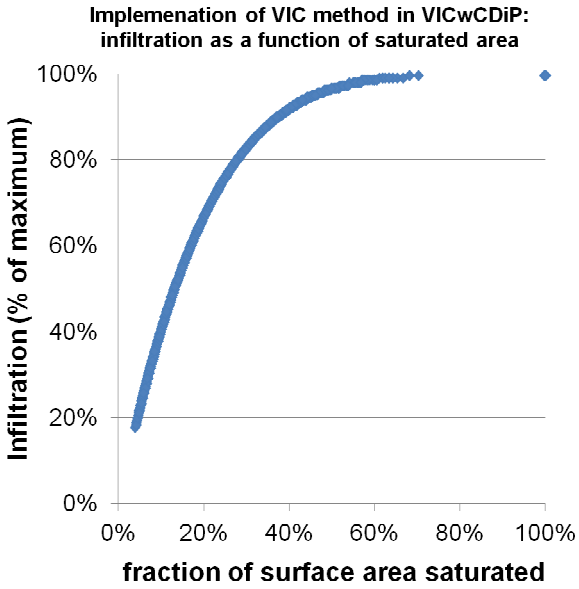

Figure D.05 Conceptual illustration of the relationship between fractional infiltration capacity and fractional saturated area, from VIC standard methodology, implemented within the VICwCDiP) model.

Depending upon the which is larger between maximum infiltration capacity and the sum of instantaneous infiltration capacity plus excess inflow, it may be necessary within the VIC standard methodology (Gao et al. 2009) to use a parameter referred to as "basis". The formulation of basis is given in Equation D.59.

Equation D.59:

$$basis.product\ [mm] = SMC_{upper.max} * \left(1.0 - \left[\frac{i_0 + excess.inflow}{infiltration_{max}}\right]\right)^{(1.0+\ shape_{base})}$$

where: $shape_{base}$ = 0.2 [dimensionless] (see section D.3.2)

The formulation of direct runoff (Q_{direct}) is given in Equation D.60.

Equation D.40:

$$Q_{direct1}\ [mm] \begin{cases} \{\ where:\ (i_0 + \text{excess.inflow}) > infiltration_{max} \\ = max(0,\ (excess.inflow - SMC_{upper.max} + SMC_{upper.3})) \\ \{\ where\ (i_0 + \text{excess.inflow}) \leq infiltration_{max} \\ = max(0,\ (inflow - SMC_{upper.max} + SMC_{upper.3} + basis.product)\ ) \end{cases}$$

The above subroutines complete the preliminary estimation of flux and moisture quantities for the modelled upper soil layer. The next step in the hydrological procedure is to calculate the moisture transfer by gravity driven drainage from the upper to the middle soil layer.

D.3.7 Calculation of soil water storage and gravity drainage between soil layers

If the current estimate of upper layer soil moisture is not greater than the minimum (residual) soil layer moisture, then the soil water is considered trapped by "matric potential" (pore water tension resulting from capillary forces) within the upper soil layer [reference] and drainage to the middle soil layer is considered to be zero. On the other hand, if the estimated upper layer soil moisture is greater than the residual value, gravity drainage is assumed to take place. As shown in Equation D.61, the amount of drainage is then calculated as a function of the upper soil layer saturated hydraulic conductivity, the normalised water content (Θ) (as described in section D.3.6), and the upper soil layer "drainage exponent". In order to respect the primacy of the residual moisture constraint and the gravity-driven drainage approach, the final value for upper to middle soil layer drainage is, as shown in Equation D.62, the minimum of the upper soil layer's "surplus moisture". At this point it is also possible to update the upper layer soil moisture amount post-drainage.

Equation D.61a:

$$\Theta_{upper.3}\ [fraction] = (SMC_{upper.3} - SMC_{upper.resid}) * (SMC_{upper.max} - SMC_{upper.resid})^{-1}$$

Equation D.61b:

$$Q_{upper=>middle.1}\ [mm] = ksat_{upper} * [\Theta_{upper.3}]^{expt.upper}$$

where: $ksat_{upper}$ and expt.upper are invariant model input (see Table 6.02)

Equation D.62:

$$Q_{upper=>middle.final}\ [mm] = min(Q_{upper=>middle.1}, (SMC_{upper.3} - SMC_{upper.resid}))$$

Equation D.63:

$$SMC_{upper.4}\ [mm] = SMC_{upper.3} - Q_{upper=>middle.final}$$

The drainage ($Q_{upper=>middle.final}$) from the upper to middle layer is used to update the soil moisture content of the middle layer. The modelled physical mechanism for drainage from the middle to bottom soil layer uses the identical approach to calculation of drainage from the upper to middle soil layer (SMC_{middle}), i.e. dependent on the internal normalised water content (Θ) of the (middle) layer. Once drainage from the middle to the lower layer ($Q_{upper=>middle.final}$) has been calculated, this in turn is used to update the soil moisture content of the lower layer (SMC_{lower}).

D.3.8 Calculation of baseflow

The updated SMC_{lower} allows calculation of the normalise water content Θ_{lower} is crucial in the VIC standard methodology (Gao et al., 2009) for calculation of baseflow (Q_{base}). This methodology, conceptually illustrated in Figure D.06, considers baseflow to be effectively two-regime process. The initial regime varies linearly as a fraction of maximum baseflow responds to the normalised water content, also referred to as "relative soil moisture". The upper bound of this linear regime is defined by a pair of coordinates along each axis, i.e. a critical fraction of saturation ($\Theta_{lower.crit}$) and a critical fraction of maximum baseflow (Ds_{crit}). Above this threshold, the second "power law" regime pervades.

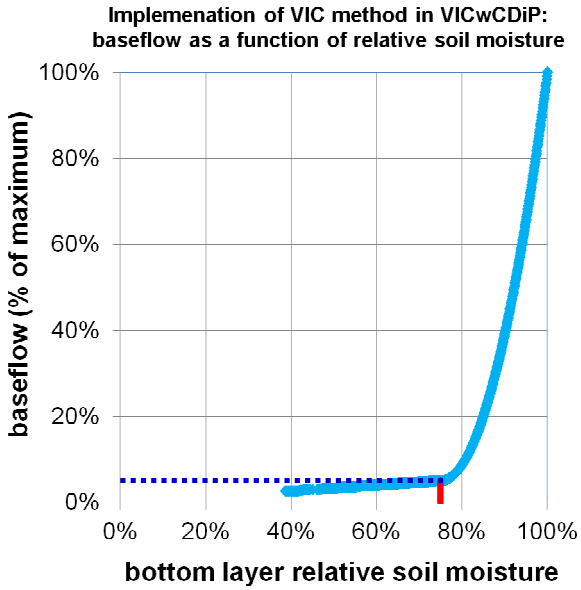

Figure D.06 Conceptual illustration of the relationship between fractional baseflow and fractional relative soil moisture (alternately normalised water content, Θ) from VIC standard methodology, implemented within the VICwCDiP) model.

The relationships described above are illustrated in Figure D.06. The linear regime exists below the critical point which in this example is defined as by the point $\Theta_{lower.crit}$ = 0.75 and = 0.05. Above this point the power law regime dominates. The formulation of Qbase used in VICwCDiP is given in the following equations.

Equation D.64:

$$Ds_{min}\ [mm] = Ds_{max} * Ds_{crit}$$

where: Ds_{max} [mm] and Ds_{crit} [fraction] are calibration parameters

Equation D.65:

$$Q_{base1}\ [mm] \quad \begin{cases} \text{where: } \Theta_{lower.1} < \Theta_{lower.crit} \\ = Ds_{min} * [\Theta_{lower.1} * (\Theta_{lower.crit})^{-1}] \\ \text{where: } \Theta_{lower.1} \geq \Theta_{lower.crit} \\ = Ds_{min} + [Ds_{max} * (1.0 - Ds_{crit}) * \left[\frac{(\Theta_{lower.1} - \Theta_{lower.crit})}{(1.0 - \Theta_{lower.crit})}\right]^{C}] \end{cases}$$

where: C = 2.0 [dimensionless] as described in section 6.6.2, and
where: $\Theta_{lower.crit}$ [fraction] is a calibration parameter

Equation D.66:

$$Q_{base.final}\ [mm] = min(Q_{upper=>middle.1}, (SMC_{upper.3} - SMC_{upper.resid}))$$

Equation D.67:

$$SMC_{lower.2}\ [mm] = SMC_{lower.1} - Q_{base.final}$$

Prior to final verification of the hydrological procedure results, there is a "bottom upwards" check that the estimated soil moisture values do not exceed the capacities of the respective soil layer. If the initial moisture value exceeds the capacity of its soil layer, the moisture is reset to the allowable maximum and the excess is added to the moisture stored in the soil layer above. In the case of the upper soil layer any excess is added to the previously calculated direct runoff. After this verification is performed, time-step hydrological results are saved both for inclusion in model output files as well as to provide initial conditions for the subsequent time-step. One key additional element included in the model output is a "check-sum" which tests the conservation of mass within the hydrological procedure. This "check-sum" considers the following components: inflow, AET, changes in SMC for each of the three soil layers, $Q_{direct.final}$ and $Q_{base.final}$.

D.4 Comparison of simulated hydrological results from 5km and 10km versions of Astore and Hunza catchments in VICwCDiP

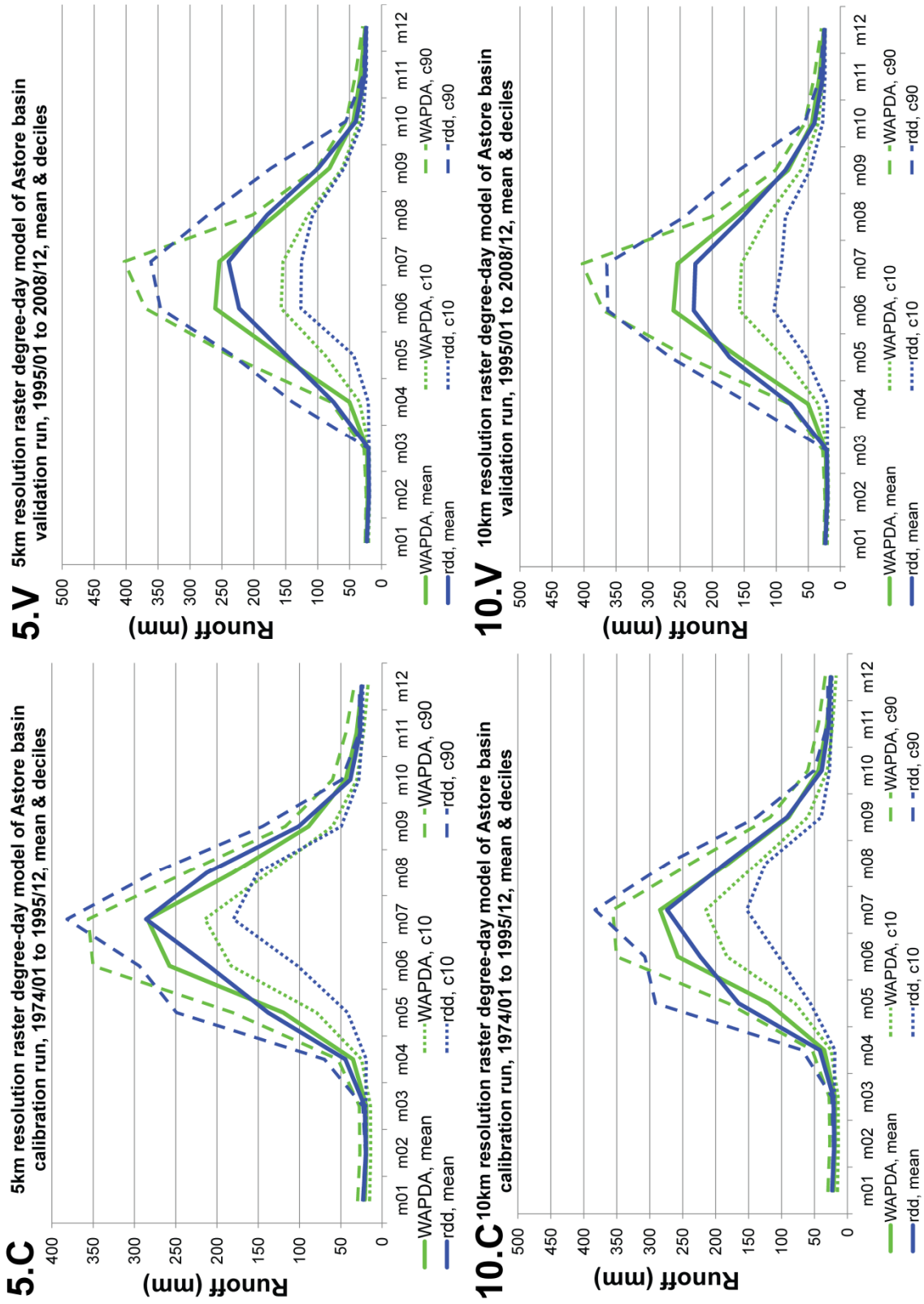

Figure D.07 Calibration and validation results in reproducing annual hydrological cycle and its variability for the Astore catchment. Months are labelled “m01” (January) to “m12” (December). The panels are labelled with reference to model resolution and simulation type as follows: 5.C = 5km calibration; 5.V = 5km validation; 10.C = 10km calibration; and 10.V = 10km validation. WAPDA is the observed runoff and rdd is the raster degree-day model outputs. The panels show mean runoff and 10th and 90th percentiles for monthly flows over the calibration or validation periods respectively.

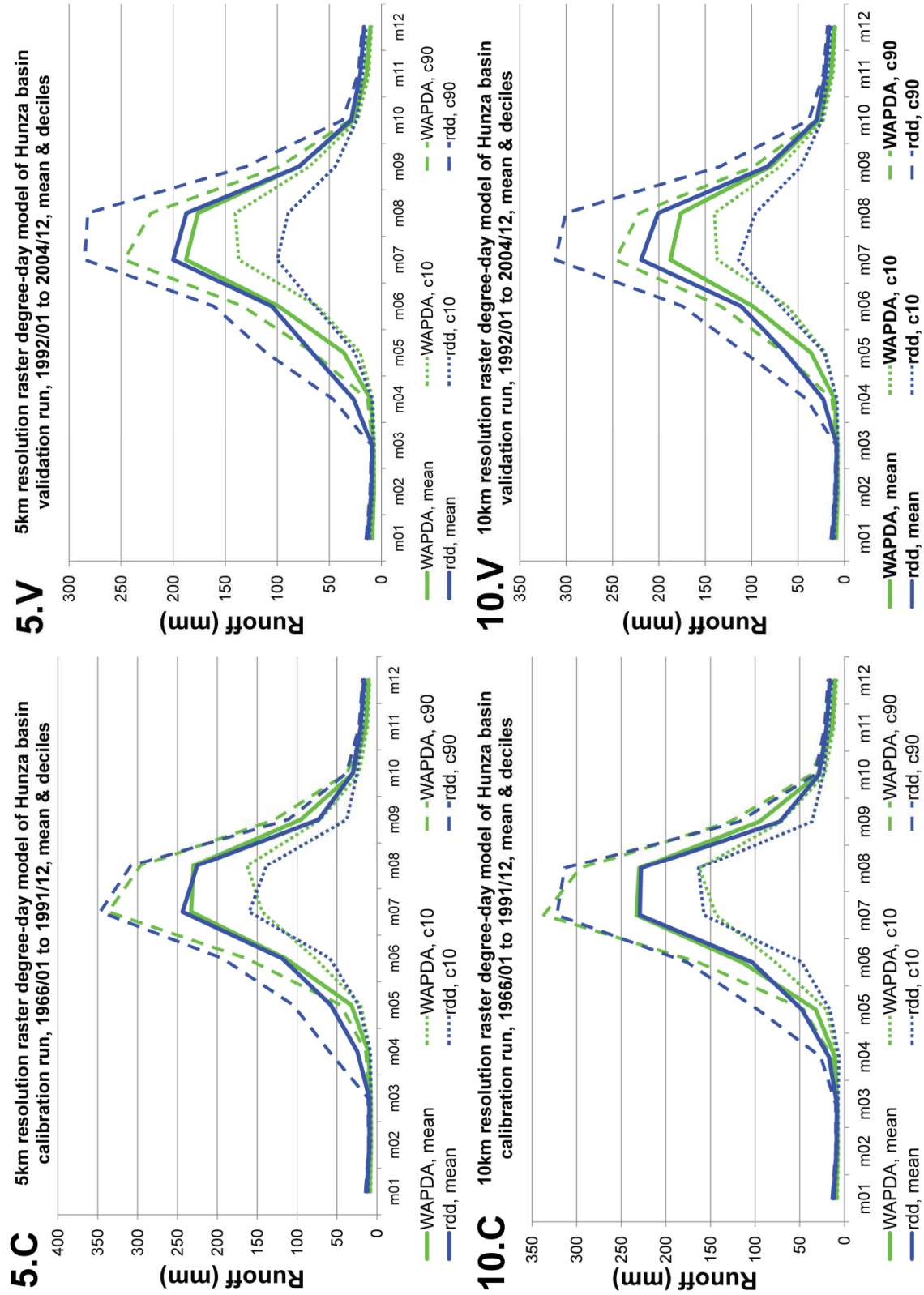

Figure D.08 Calibration and validation results in reproducing annual hydrological cycle and its variability for the Hunza catchment. Months are labelled “m01” (January) to “m12” (December). The panels are labelled with reference to model resolution and simulation type as follows: 5.C = 5km calibration; 5.V = 5km validation; 10.C = 10km calibration; and 10.V = 10km validation. WAPDA is the observed runoff and rdd is the raster degree-day model outputs. The panels show mean runoff and 10th and 90th percentiles for monthly flows over the calibration or validation periods respectively.

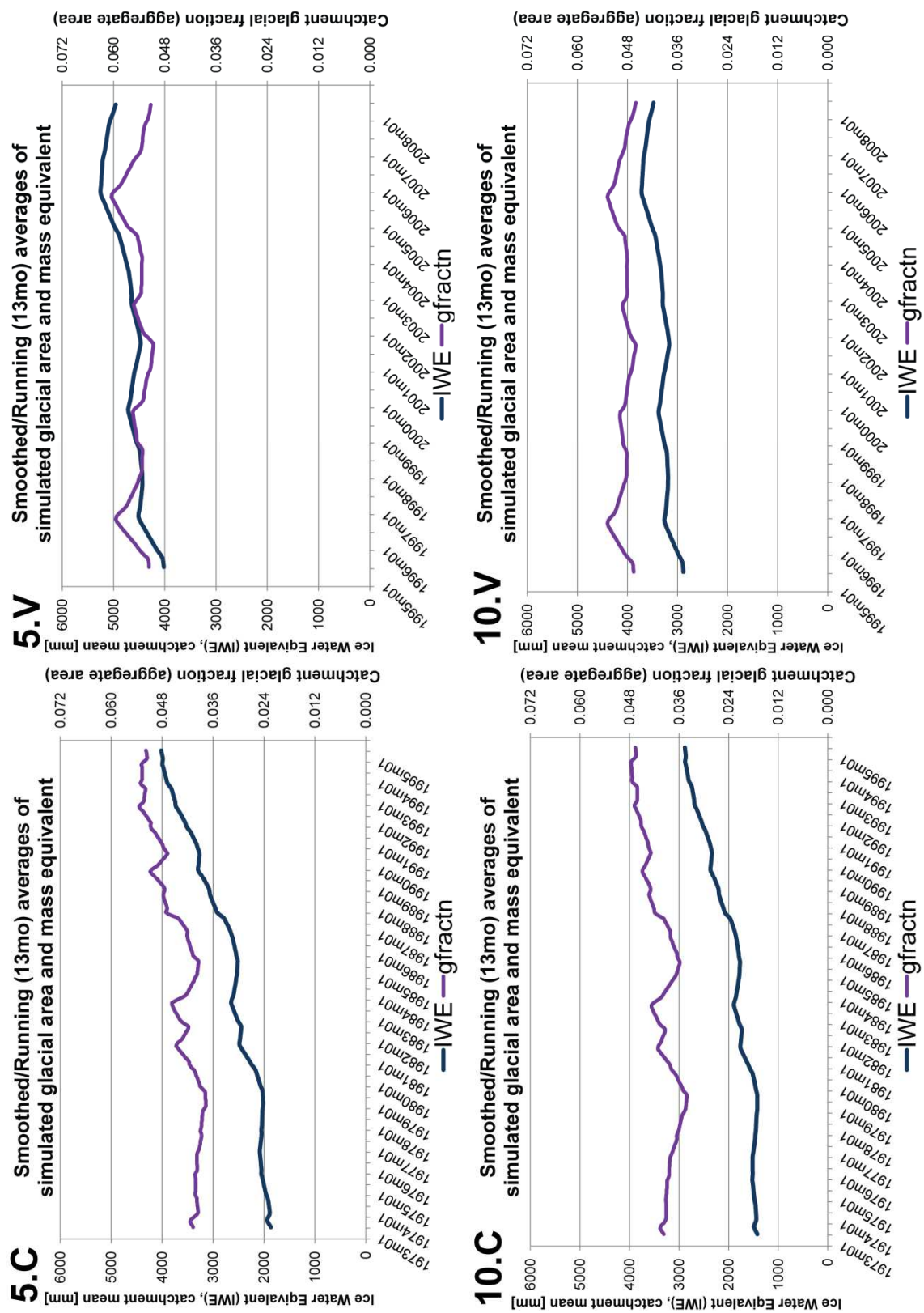

Figure D.09 Calibration and validation results in glacial mass and areal extent (fraction of catchment) for the Astore catchment. In the graphs in this figure, glacial mass is shown as “ice water equivalent” (IWE) and glacial areal extent is labelled “gfractn.” The panels are labelled with reference to model resolution and simulation type as follows: 5.C = 5km calibration; 5.V = 5km validation; 10.C = 10km calibration; and 10.V = 10km validation.

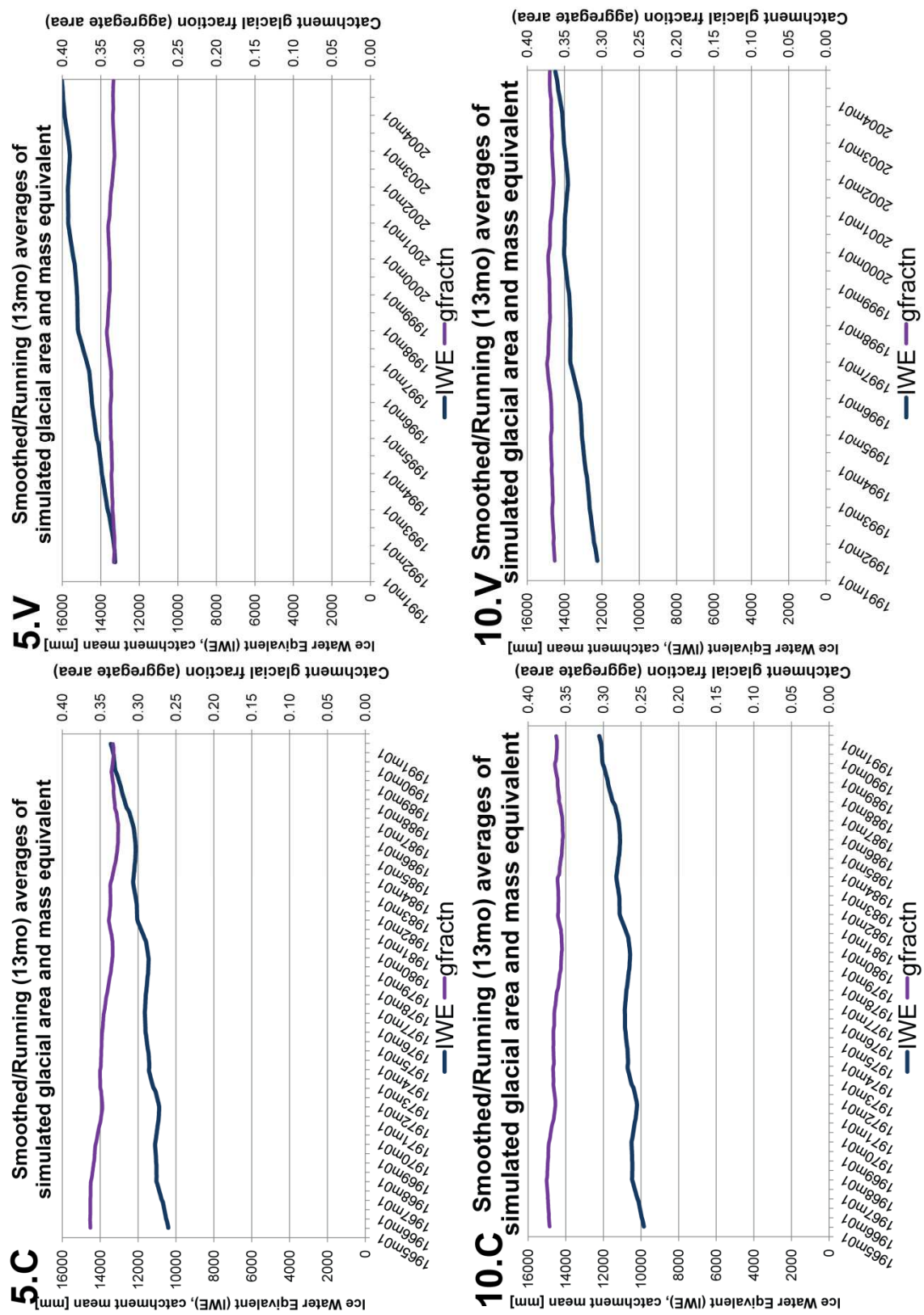

Figure D.10 Calibration and validation results in glacial mass and areal extent (fraction of catchment) for the Hunza catchment. In the graphs in this figure, glacial mass is shown as "ice water equivalent" (IWE) and glacial areal extent is labelled "gfractn." The panels are labelled with reference to model resolution and simulation type as follows: 5.C = 5km calibration; 5.V = 5km validation; 10.C = 10km calibration; and 10.V = 10km validation.

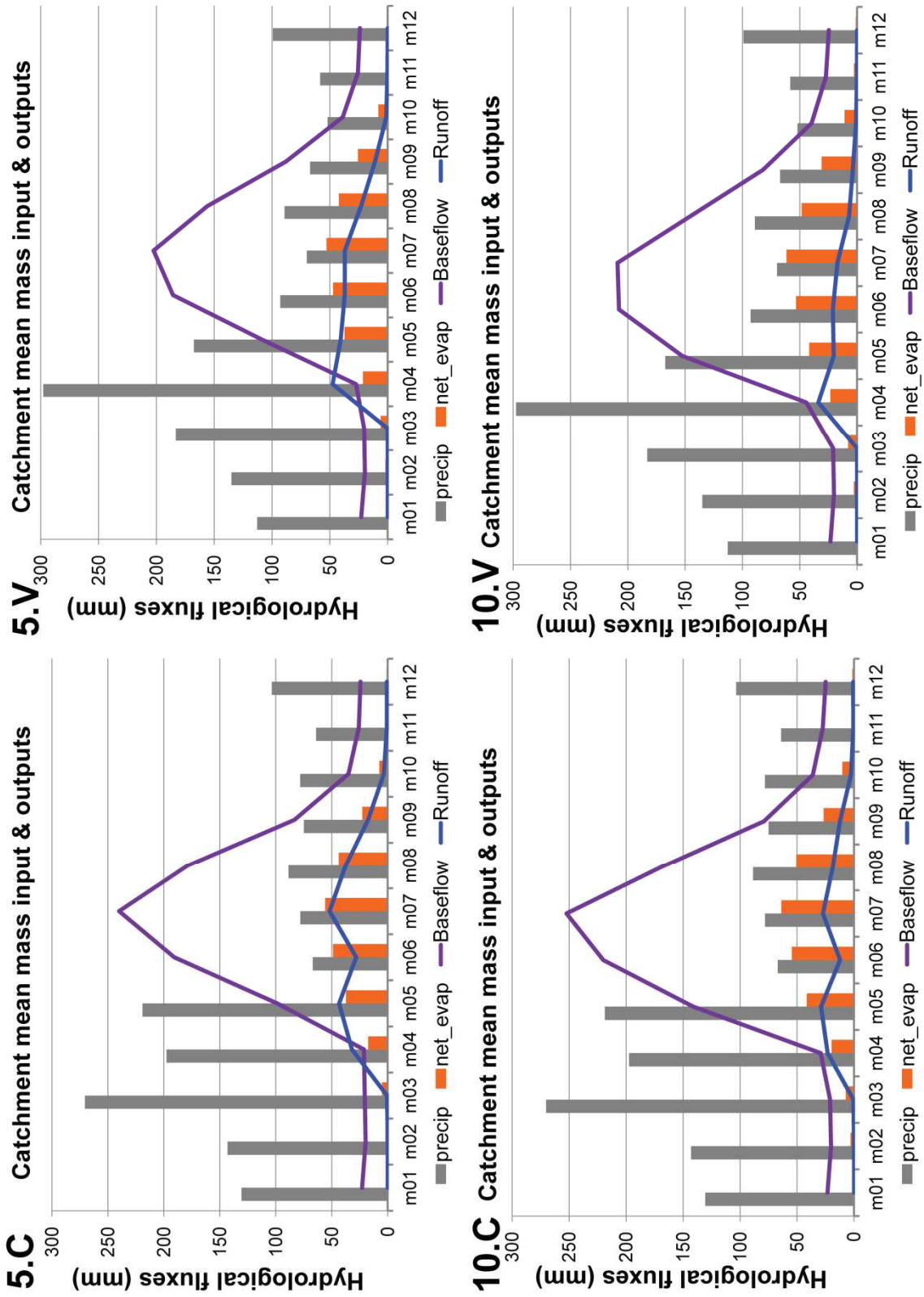

Figure D.11 Calibration and validation results in hydrological mass inputs and outputs for the Astore catchment. In these the legends in these graphs precipitation is abbreviated "precip." AET is referred to as "net_evap." Baseflow refers to Qbase (base streamflow), and Runoff refers Qdirect (overland runoff). Months are labelled "m01" (January) to "m12" (December). The panels are labelled with reference to model resolution and simulation type as follows: 5.C = 5km calibration; 5.V = 5km validation; 10.C = 10km calibration; and 10.V = 10km validation.

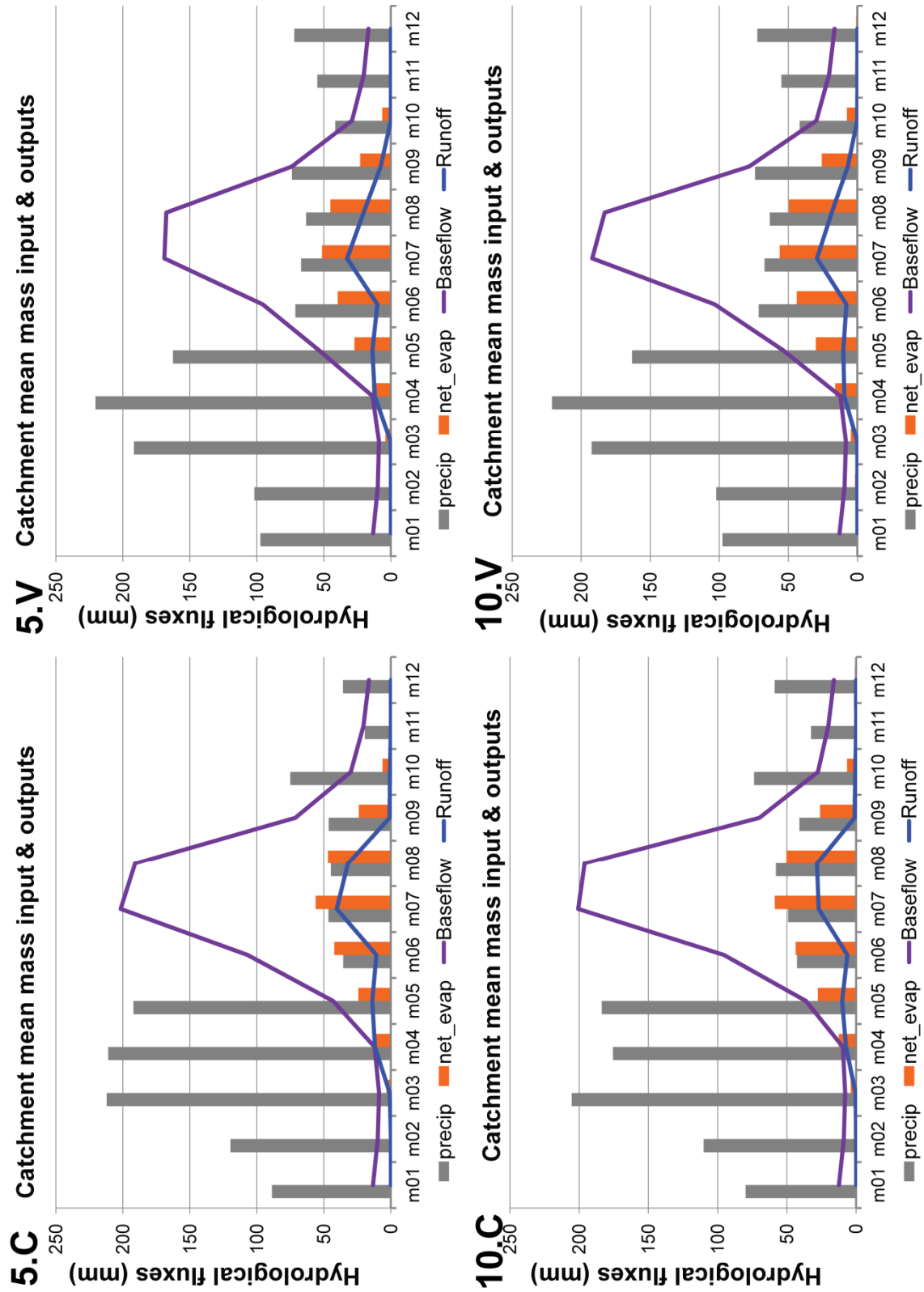

Figure D.12 Calibration and validation results in hydrological mass inputs and outputs for the Hunza catchment. In these the legends in these graphs precipitation is abbreviated “precip.” AET is referred to as “net_evap.” Baseflow refers to Qbase (base streamflow), and Runoff refers Qdirect (overland runoff). Months are labelled “m01” (January) to “m12” (December). The panels are labelled with reference to model resolution and simulation type as follows: 5.C = 5km calibration; 5.V = 5km validation; 10.C = 10km calibration; and 10.V = 10km validation.

D.5 Comparison of simulated results to MODIS climatologies for secondary calibration variables (SCA, LST) from land surface process approximations

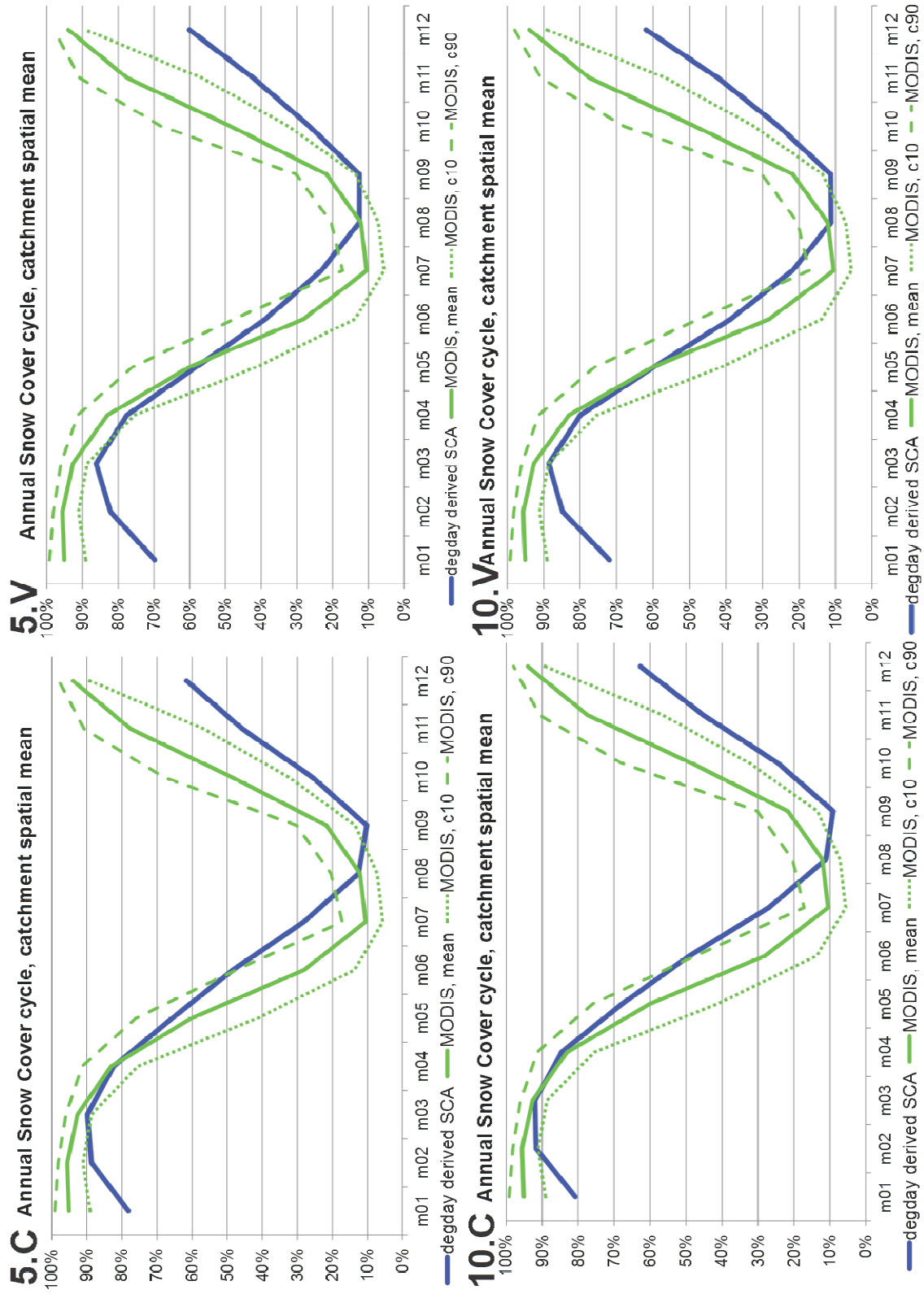

Figure D.13 Calibration and validation results in simulation of snow covered area (SCA) for the Astore catchment. ". The panels are labelled with reference to model resolution and simulation type as follows: 5.C = 5km calibration; 5.V = 5km validation; 10.C = 10km calibration; and 10.V = 10km validation.

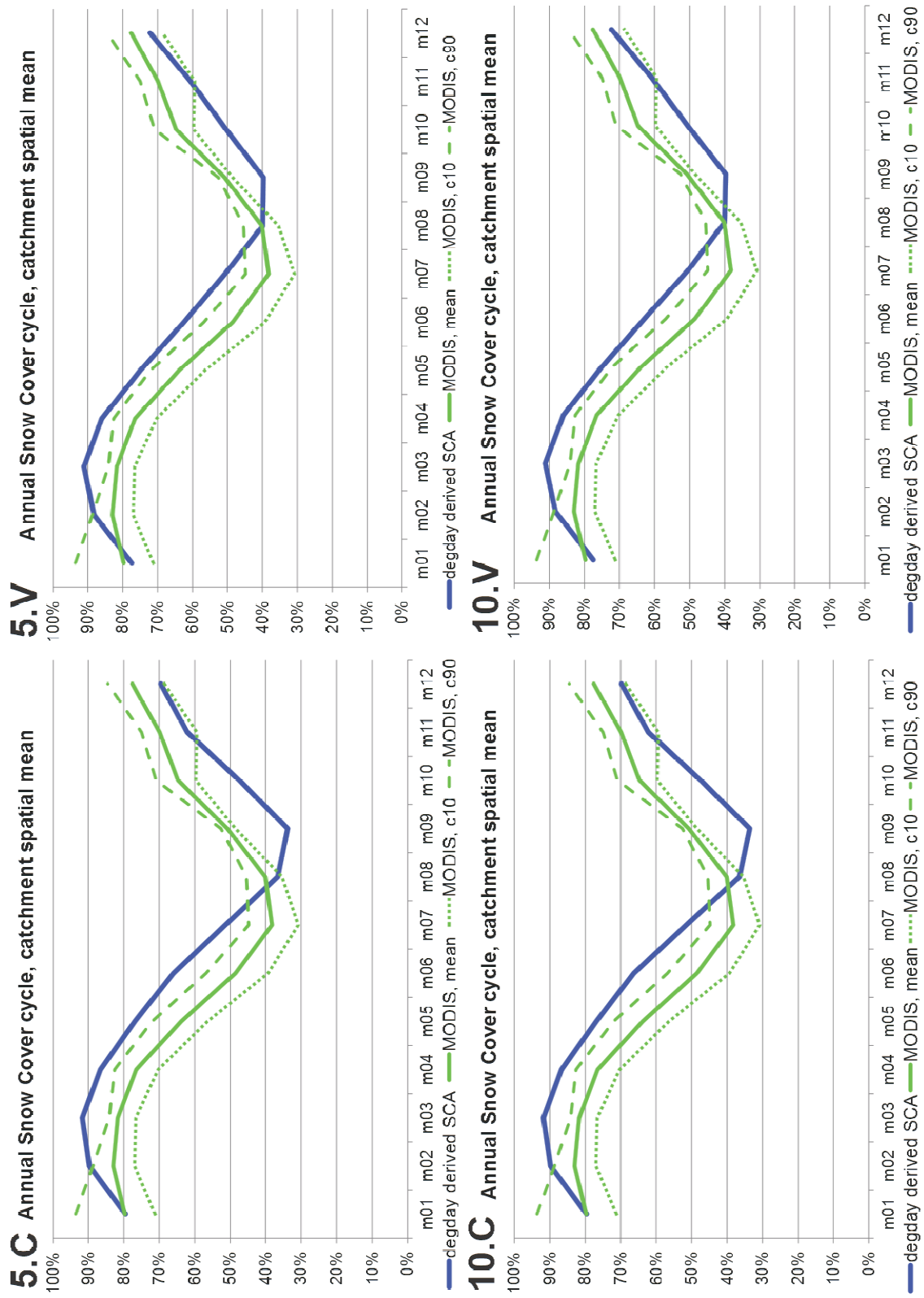

Figure D.14 Calibration and validation results in simulation of snow covered area (SCA) for the Hunza catchment. The panels are labelled with reference to model resolution and simulation type as follows: 5.C = 5km calibration; 5.V = 5km validation; 10.C = 10km calibration; and 10.V = 10km validation.

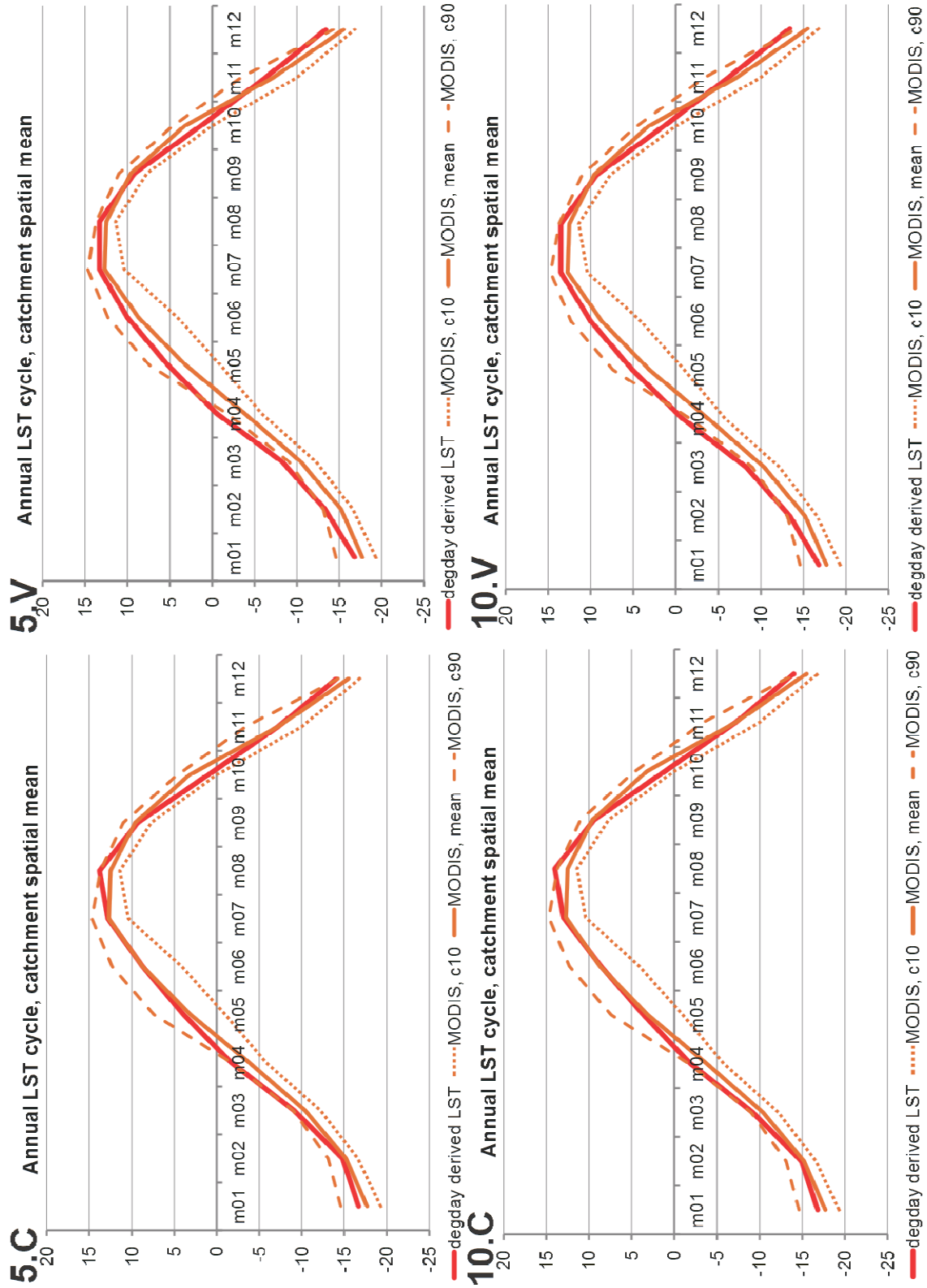

Figure D.15 Calibration and validation results in simulation of land surface temperature (LST) for the Astore catchment. The panels are labelled with reference to model resolution and simulation type as follows: 5.C = 5km calibration; 5.V = 5km validation; 10.C = 10km calibration; and 10.V = 10km validation.

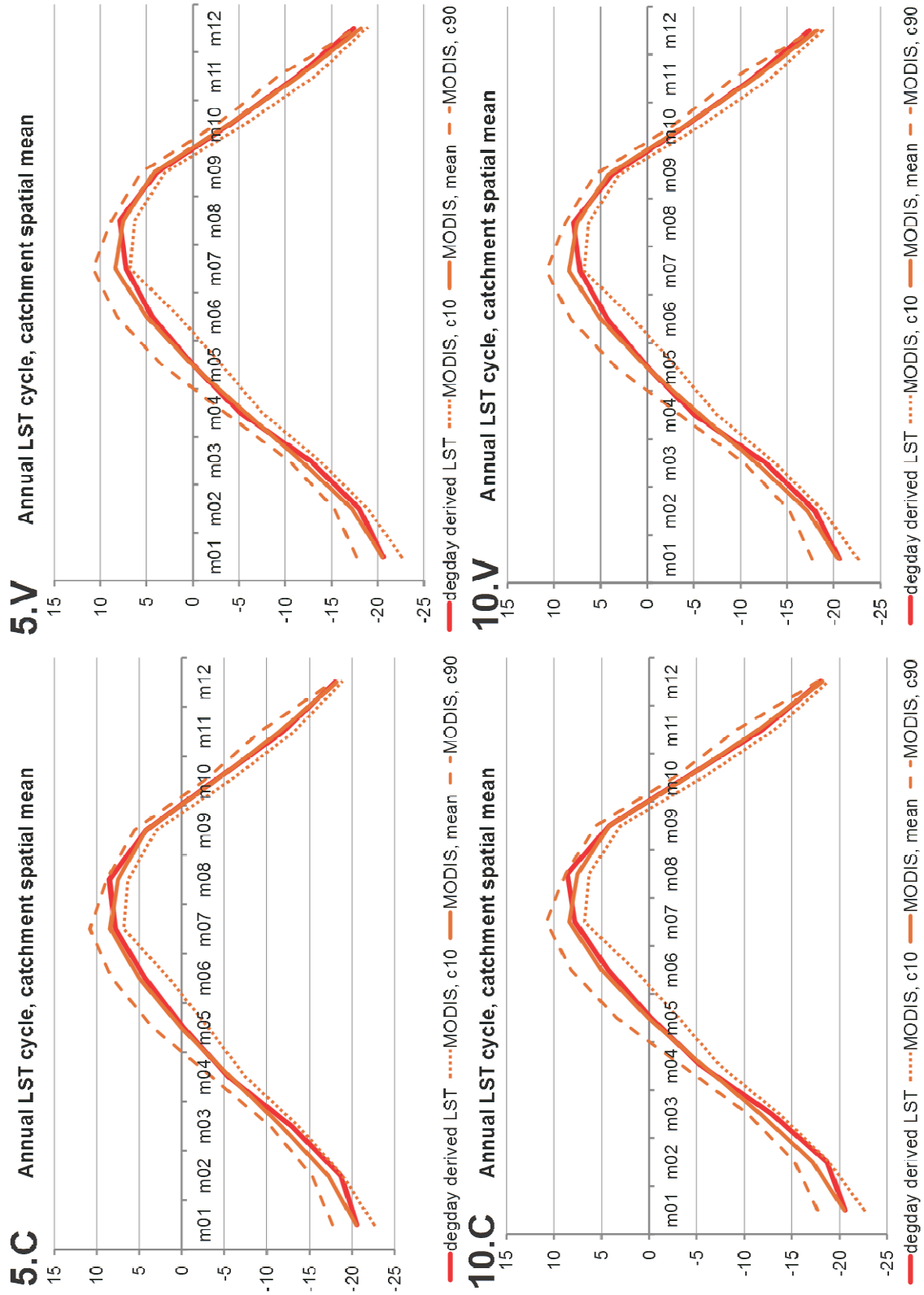

Figure D.16 Calibration and validation results in simulation of land surface temperature (LST) for the Hunza catchment. The panels are labelled with reference to model resolution and simulation type as follows: 5.C = 5km calibration; 5.V = 5km validation; 10.C = 10km calibration; and 10.V = 10km validation.

D.6 Raster/GIS visualisation of model VICwCDiP outputs for Astore and Hunza 5km calibration runs

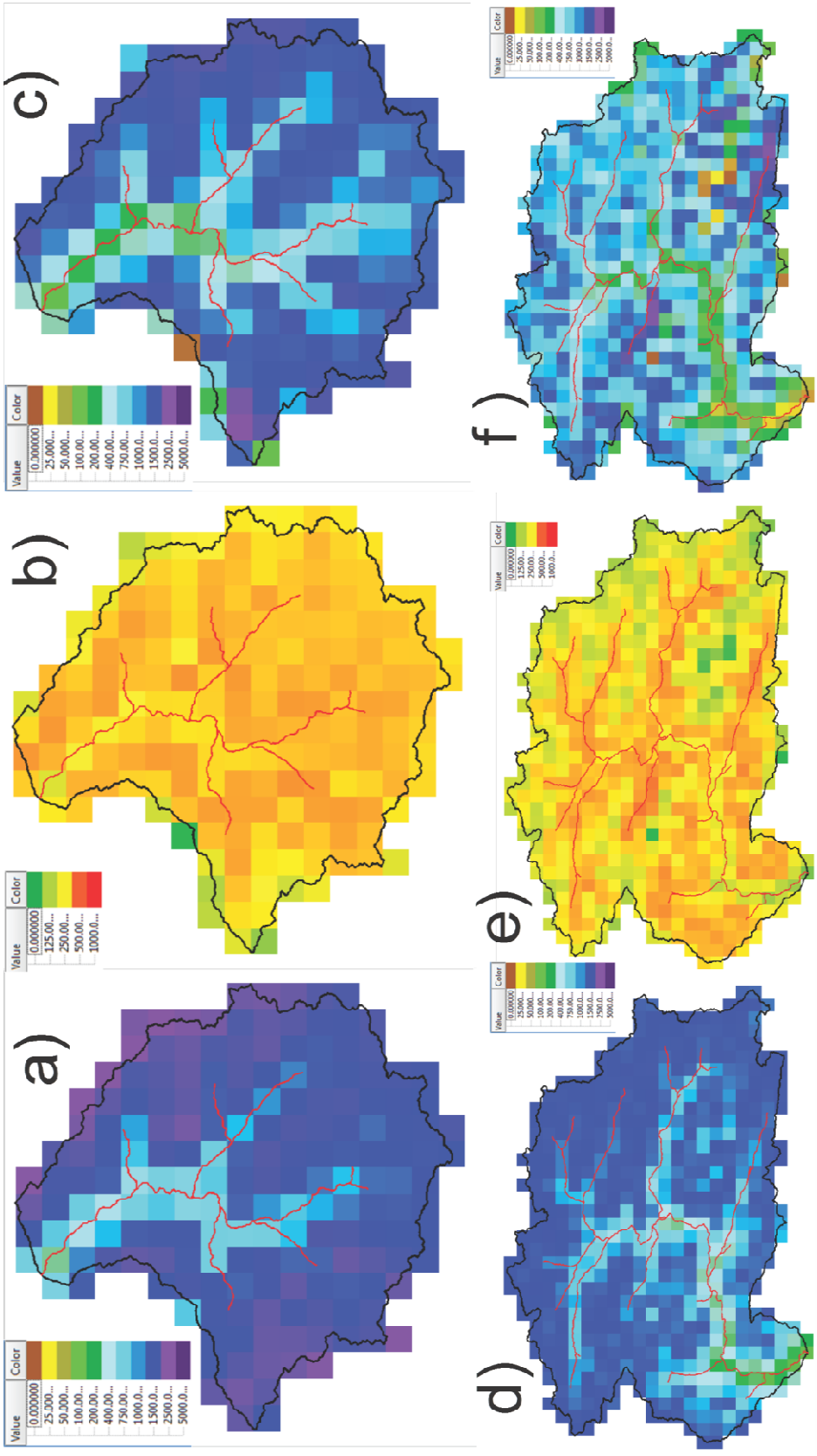

Figure D.17 Period mean raster output calibration results of hydrological mass input and output components for the Astore (panels a to c) and Hunza (panels d to f) catchments, showing precipitation (panels a & d), AET (panels b & e) and total runoff (panels c & f). All values are in millimetres.

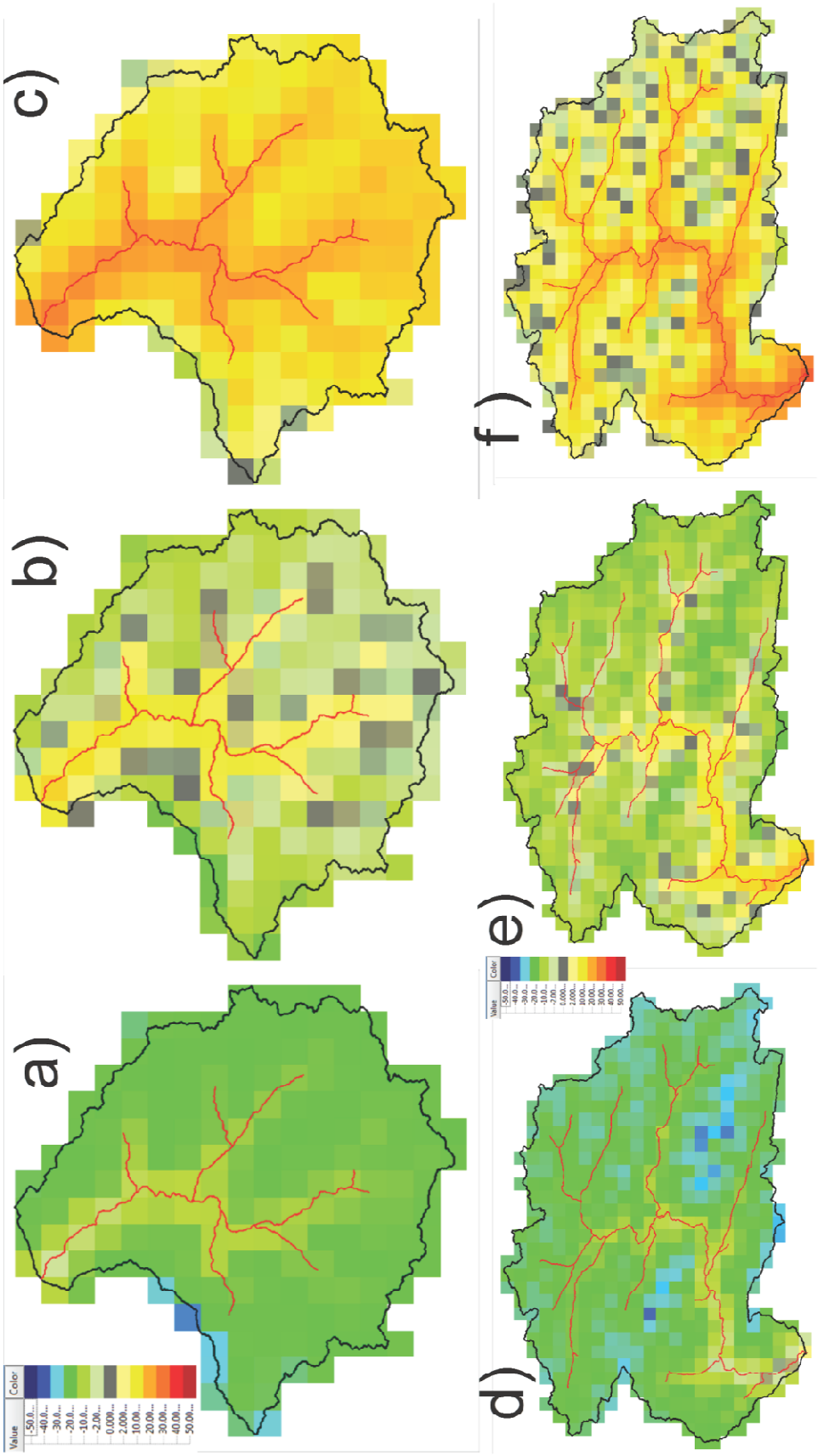

Figure D.18 Period mean raster output calibration results of land surface temperature (LST) for the Astore (panels a to c) and Hunza (panels d to f) catchments, showing January (panels a & d), annual mean (panels b & e) and July (panels c & f). All values are in degrees Celsius.

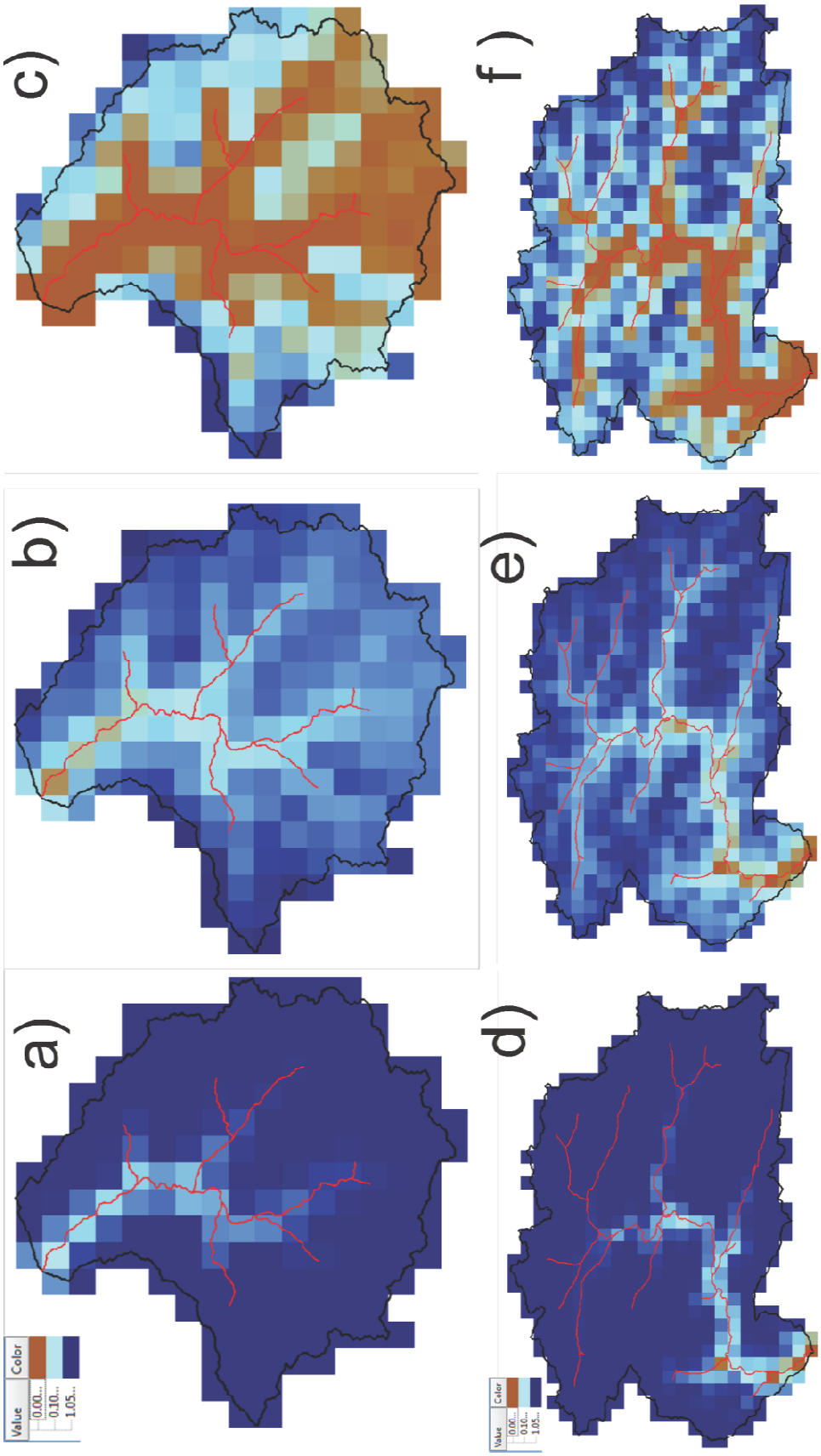

Figure D.19 Period mean raster output calibration results of snow covered area (SCA) for the Astore (panels a to c) and Hunza (panels d to f) catchments, showing February (panels a & d), annual mean (panels b & e) and August (panels c & f). All values are in fractional area (per grid cell).

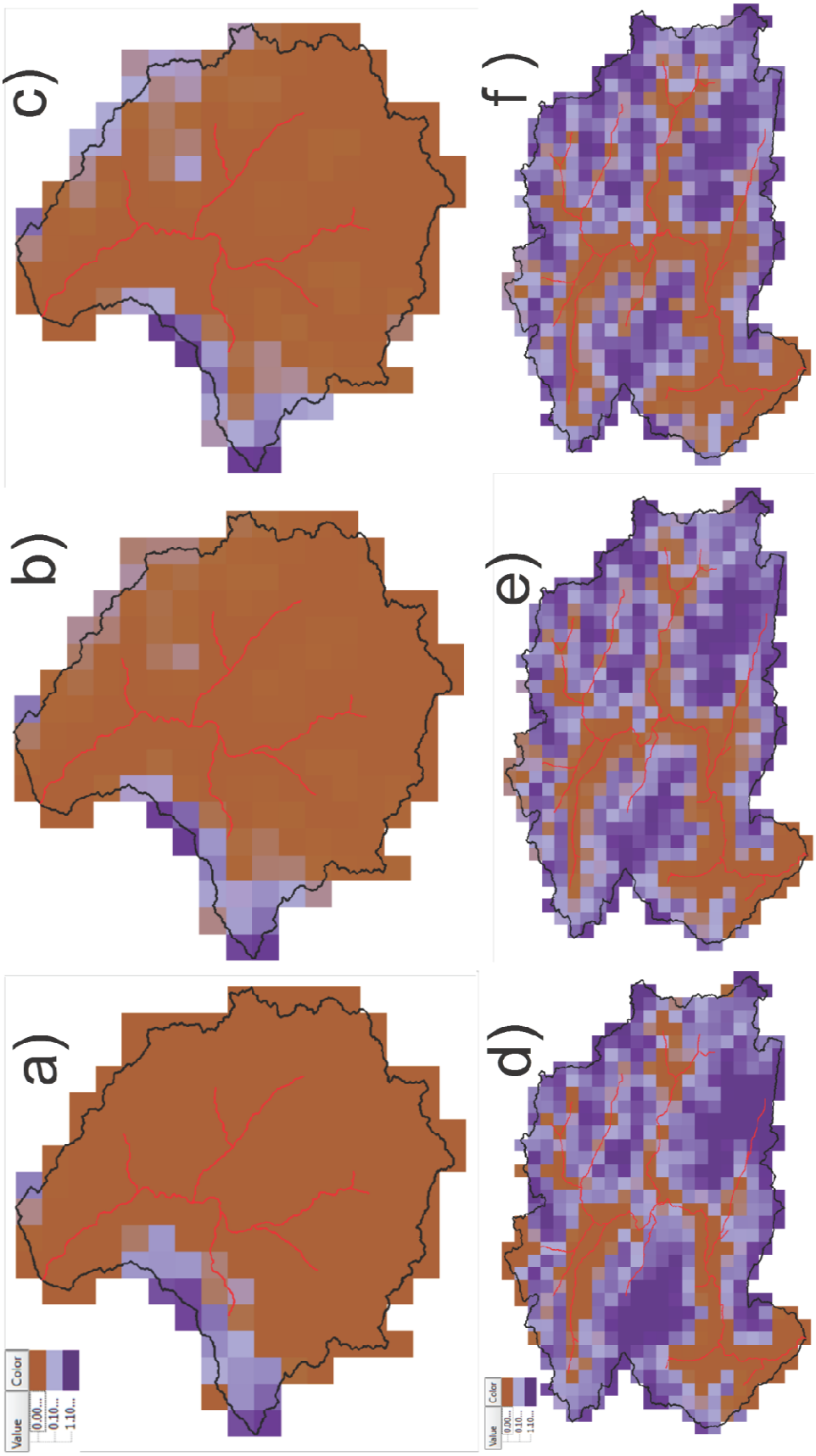

Figure D.20 Raster output calibration results of glaciated area (fraction) for the Astore (panels a to c) and Hunza (panels d to f) catchments, showing simulation initialisation (panels a & d), simulation mean (panels b & e) and simulation end (panels c & f). All values are in fractional area (per grid cell).

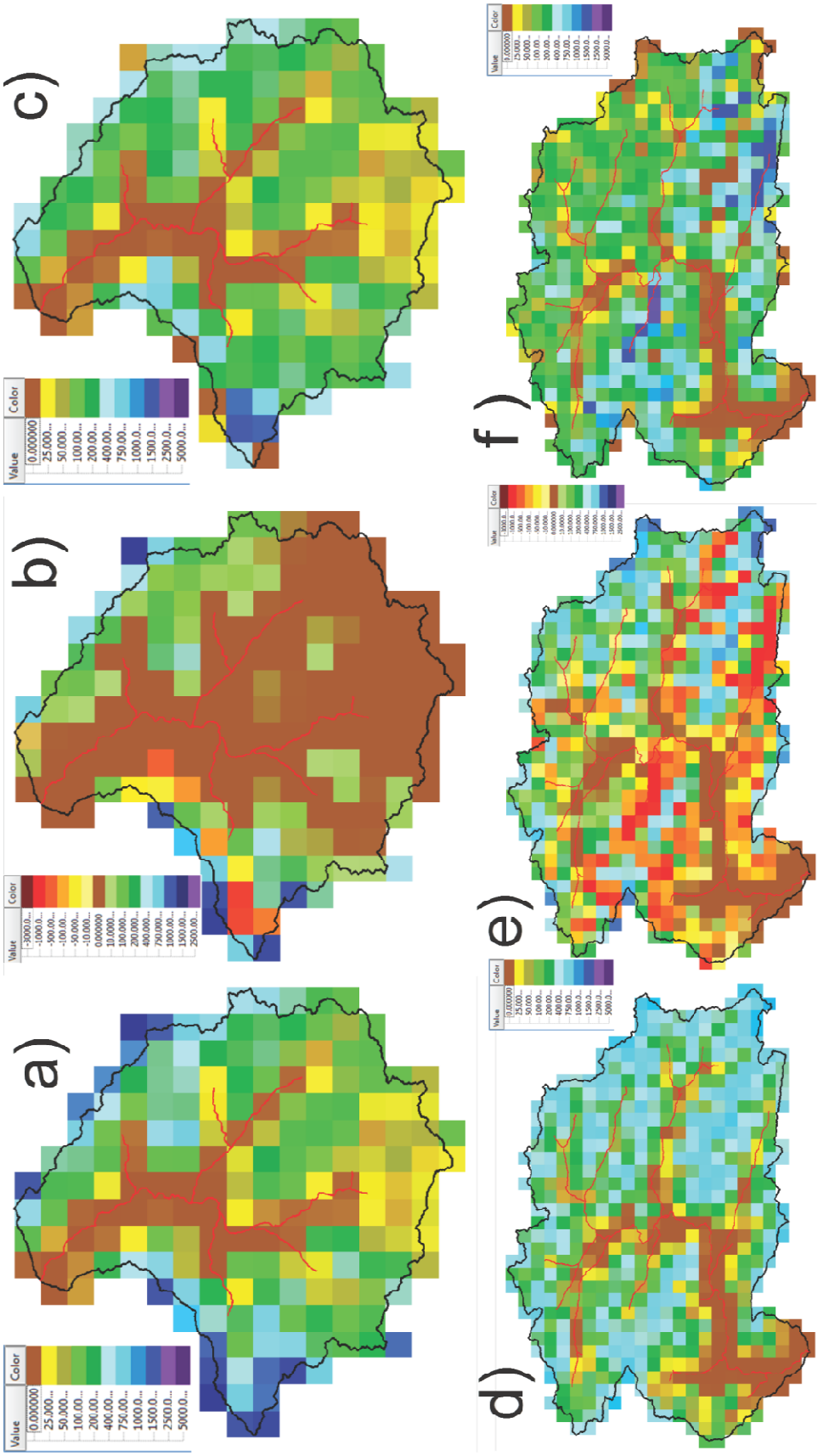

Figure D.21 Spatial patterns of period mean annual totals of glacial mass balance components (accumulation [a, d], ablation [c, f]) and net residual [b, e] for the calibration simulations in both the Astore [a to c] and Hunza [d to f] catchments. All units are in mm.

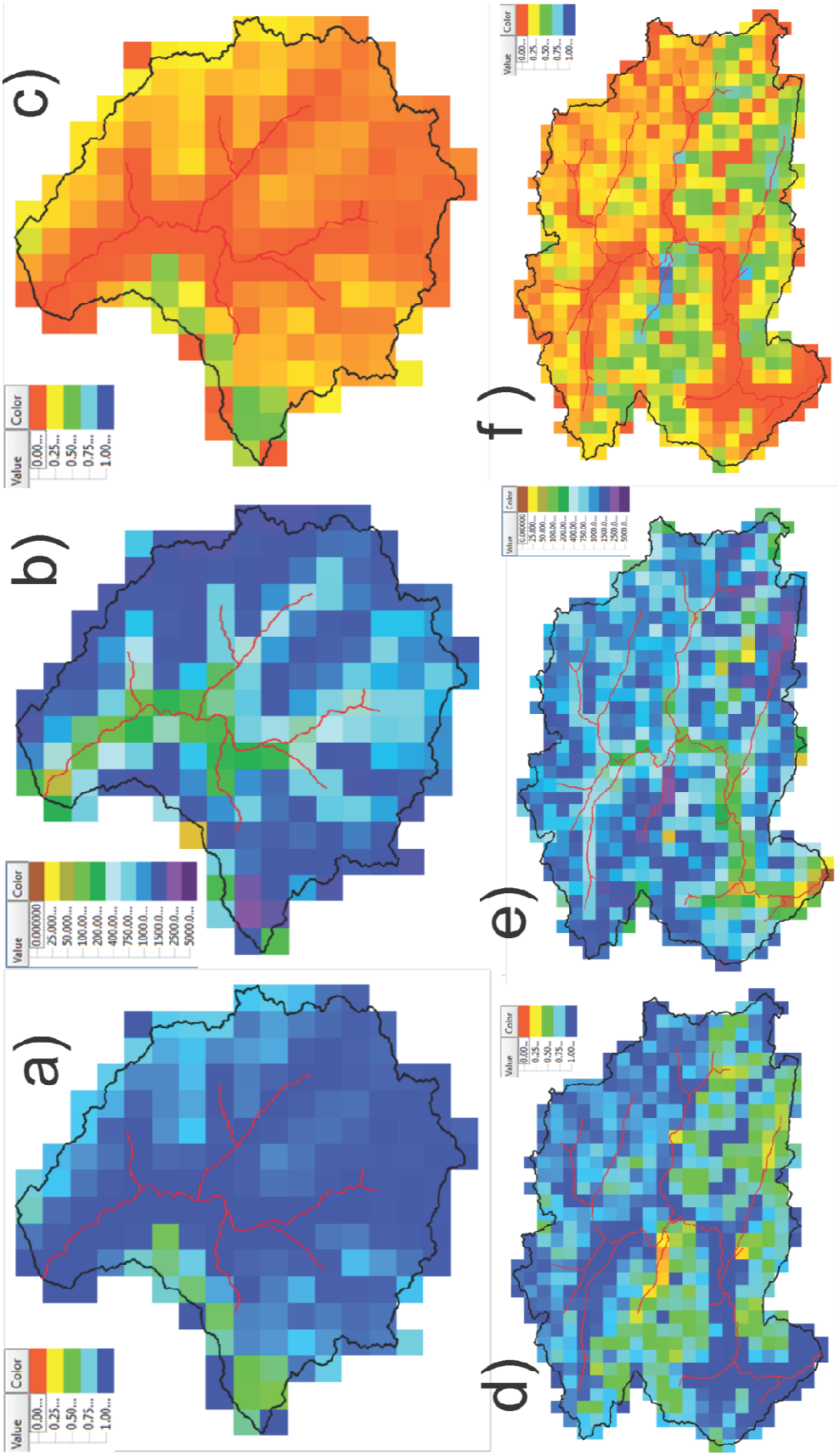

Figure D.22 Period mean raster output calibration results of relative contributions of snow and ice to combined meltwater generation for the Astore (panels a to c) and Hunza (panels d to f) catchments, showing snowmelt fraction of total meltwater (panels a & d), total annual meltwater generation (panels b & e) and glacial of total meltwater (panels c & f). Values in panels a, c, d and f are in fractional volume. Values in panels b and e are in millimetres.

Appendix E: Supplemental material Chapter 7

E.1 Projected values for key hydrological fluxes and mean cryosphere states

Simulation	Statistic	Probability	Precipitation	PET	AET	Total Runoff
Control baseline/-benchmark climate	mean	5th percentile	1390.3	501.0	320.0	1051.8
		Median	1514.7	514.6	329.2	1143.6
		95th percentile	1621.1	529.8	338.7	1232.2
	standard deviation	5th percentile	311.8	35.5	19.0	207.6
		Median	402.5	47.8	25.2	275.2
		95th percentile	534.0	57.5	30.1	334.1
RCM-based scenario (PRECIS-HadAM3P, SRES A2)	mean	5th percentile	1677.2	1067.7	469.5	1211.6
		Median	1852.4	1083.5	486.0	1370.5
		95th percentile	2000.3	1103.8	510.0	1497.0
	standard deviation	5th percentile	425.2	51.6	52.0	353.6
		Median	534.2	63.1	64.1	436.7
		95th percentile	686.2	76.7	79.1	578.8
Scenario extrapolated from locally observed trends	mean	5th percentile	1479.9	560.8	354.2	1097.8
		Median	1598.9	575.1	361.0	1198.1
		95th percentile	1722.7	588.8	371.6	1287.5
	standard deviation	5th percentile	340.7	41.9	22.6	227.9
		Median	435.0	50.3	28.0	282.5
		95th percentile	507.8	63.1	33.7	337.0

Table E.1 Probabilistic estimates of 30-year statistics for Astore annual total hydrological fluxes; all values in mm.

Simulation	Statistic	Probability	Precipitation	PET	AET	Total Runoff
Control baseline/-benchmark climate	mean	5th percentile	1051.4	478.4	280.8	706.2
		Median	1145.5	491.8	287.2	762.8
		95th percentile	1226.0	506.7	295.3	811.0
	standard deviation	5th percentile	235.7	33.5	18.9	116.7
		Median	304.4	44.3	24.3	153.9
		95th percentile	403.8	53.4	28.6	194.3
RCM-based scenario (PRECIS-HadAM3P, SRES A2)	mean	5th percentile	1268.4	1043.1	426.1	847.4
		Median	1400.9	1060.7	446.3	957.6
		95th percentile	1512.8	1080	463.6	1046.1
	standard deviation	5th percentile	321.5	53.6	44.5	256.9
		Median	404.0	64.0	55.8	311.6
		95th percentile	518.9	77.7	67.6	408.4
Scenario extrapolated from locally observed trends	mean	5th percentile	1119.2	523.3	301.9	707.6
		Median	1209.2	538.4	308.6	765.0
		95th percentile	1302.8	550.2	316.0	811.7
	standard deviation	5th percentile	257.6	36.7	20.5	116.3
		Median	328.9	45.5	25.9	149.3
		95th percentile	384.0	57.0	29.7	180.9

Table E.2 Probablilistic estimates of 30-year statistics for Hunza annual total hydrological fluxes; all values in mm.

Simulation	Statistic	Probability	Glacial fraction	IWE [mm]	Ice accum-ulation [mm]	Snow melt [mm]	Ice melt [mm]
Control baseline/-benchmark climate	mean	5th percentile	0.0512	5062.8	150.2	971.8	118.9
		Median	0.0612	9354.0	190.5	1039.1	151.5
		95th percentile	0.0708	13332.1	234.5	1116.1	177.6
	standard deviation	5th percentile	0.0019	148.1	99.2	174.8	37.7
		Median	0.0032	347.3	141.3	230.8	52.9
		95th percentile	0.0061	727.4	190.0	273.2	71.7
RCM-based scenario (PRECIS-HadAM3P, SRES A2)	mean	5th percentile	0.0106	97.2	100.9	1042.5	101.1
		Median	0.0125	129.3	129.8	1111.3	131.3
		95th percentile	0.0139	171.9	173.0	1183.9	171.1
	standard deviation	5th percentile	0.0008	24.6	89.4	235.7	84.1
		Median	0.0013	39.4	123.1	289.7	110.9
		95th percentile	0.0021	75.1	197.7	348.8	171.8
Scenario extrapolated from locally observed trends	mean	5th percentile	0.0542	5959.6	139.5	949.1	115.7
		Median	0.0671	12155.7	193.2	1012.4	144.7
		95th percentile	0.0768	17008.2	233.8	1065.6	172.9
	standard deviation	5th percentile	0.0019	222.6	92.8	192.0	39.7
		Median	0.0029	457.0	136.1	235.3	59.6
		95th percentile	0.0049	806.8	191.3	283.3	82.0

Table E.3 Probabilistic estimates of 30-year statistics for Astore annual cryosphere states & fluxes.

Simulation	Statistic	Probability	Glacial fraction	IWE [mm]	Ice accum-ulation [mm]	Snow melt [mm]	Ice melt [mm]
Control baseline/-benchmark climate	mean	5th percentile	0.3389	15240.5	212.5	696.8	144.2
		Median	0.3506	24728.2	255.9	748.5	161.0
		95th percentile	0.3636	34864.6	298.2	796.8	173.1
	standard deviation	5th percentile	0.0022	472.7	94.6	120.8	28.0
		Median	0.0045	858.4	135.5	149.2	36.3
		95th percentile	0.0076	1304.7	171.9	185.2	46.0
RCM-based scenario (PRECIS-HadAM3P, SRES A2)	mean	5th percentile	0.0634	992.4	63.8	928.1	65.8
		Median	0.0697	1153.4	86.4	993.1	88.8
		95th percentile	0.0763	1295.3	118.9	1067.4	115.9
	standard deviation	5th percentile	0.0022	30.3	60.9	211.2	48.0
		Median	0.0039	48.2	91.8	259.6	70.7
		95th percentile	0.0068	83.9	150.4	321.0	105.4
Scenario extrapolated from locally observed trends	mean	5th percentile	0.3667	19445.6	277.3	654.8	171.8
		Median	0.3772	34728.8	326.3	692.2	184.7
		95th percentile	0.3921	49814.3	381.3	724.7	200.0
	standard deviation	5th percentile	0.0020	805.7	106.0	107.7	30.2
		Median	0.0041	1271.2	145.6	142.2	37.4
		95th percentile	0.0076	1746.8	200.0	166.3	46.6

Table E.4 Probabilistic estimates of 30-year statistics for Hunza annual cryosphere states & fluxes.

Simulation	Statistic	Probability	Precipitation	PET	AET	Total Runoff
RCM-based scenario (PRECIS-HadAM3P, SRES A2)	mean	5th percentile	1.206	2.131	1.467	1.151
		Median	1.222	2.105	1.476	1.198
		95th percentile	1.233	2.083	1.505	1.214
	standard deviation	5th percentile	1.363	1.453	2.736	1.703
		Median	1.327	1.32	2.543	1.586
		95th percentile	1.285	1.333	2.627	1.732
Scenario extrapolated from locally observed trends	mean	5th percentile	1.064	1.119	1.106	1.043
		Median	1.055	1.117	1.096	1.047
		95th percentile	1.062	1.111	1.097	1.044
	standard deviation	5th percentile	1.092	1.180	1.189	1.097
		Median	1.080	1.052	1.111	1.026
		95th percentile	0.950	1.097	1.119	1.008

Table E.5 Probabilistic estimates of relative changes to 30-year statistics for Astore annual total hydrological fluxes; all values dimensionless multipliers.

Simulation	Statistic	Probability	Precipitation	PET	AET	Total Runoff
RCM-based scenario (PRECIS-HadAM3P, SRES A2)	mean	5th percentile	1.206	2.180	1.517	1.199
		Median	1.222	2.156	1.553	1.255
		95th percentile	1.233	2.131	1.569	1.289
	standard deviation	5th percentile	1.364	1.600	2.354	2.201
		Median	1.327	1.444	2.296	2.024
		95th percentile	1.285	1.455	2.363	2.101
Scenario extrapolated from locally observed trends	mean	5th percentile	1.064	1.093	1.075	1.001
		Median	1.055	1.094	1.074	1.002
		95th percentile	1.062	1.085	1.070	1.000
	standard deviation	5th percentile	1.092	1.095	1.084	0.996
		Median	1.080	1.027	1.065	0.970
		95th percentile	0.950	1.067	1.038	0.931

Table E.6 Probablilistic estimates of relative changes to 30-year statistics for Hunza annual total hydrological fluxes; all values dimensionless multipliers.

Simulation	Statistic	Probability	Glacial fraction	IWE	Ice accum-ulation	Snow melt	Ice melt
RCM-based scenario (PRECIS-HadAM3P, SRES A2)	mean	5th percentile	0.207	0.019	0.671	1.072	0.85
		Median	0.204	0.013	0.681	1.069	0.866
		95th percentile	0.196	0.012	0.737	1.06	0.963
	standard deviation	5th percentile	0.421	0.166	0.901	1.348	2.230
		Median	0.406	0.113	0.871	1.255	2.096
		95th percentile	0.344	0.103	1.040	1.276	2.396
Scenario extrapolated from locally observed trends	mean	5th percentile	1.058	1.177	0.928	0.976	0.973
		Median	1.096	1.299	1.014	0.974	0.955
		95th percentile	1.084	1.275	0.997	0.954	0.973
	standard deviation	5th percentile	1.000	1.503	0.935	1.098	1.053
		Median	0.906	1.315	0.963	1.019	1.126
		95th percentile	0.803	1.109	1.006	1.036	1.143

Table E.7 Probabilistic estimates of relative changes to 30-year statistics for Astore annual cryosphere states & fluxes; all values dimensionless multipliers

Simulation	Statistic	Probability	Glacial fraction	IWE	Ice accum-ulation	Snow melt]	Ice melt
RCM-based scenario (PRECIS-HadAM3P, SRES A2)	mean	5th percentile	0.187	0.065	0.300	1.331	0.456
		Median	0.198	0.046	0.337	1.326	0.551
		95th percentile	0.209	0.037	0.398	1.339	0.669
	standard deviation	5th percentile	1.000	0.064	0.643	1.748	1.714
		Median	0.866	0.056	0.677	1.739	1.947
		95th percentile	0.894	0.064	0.874	1.733	2.291
Scenario extrapolated from locally observed trends	mean	5th percentile	1.082	1.275	1.304	0.939	1.191
		Median	1.075	1.404	1.275	0.924	1.147
		95th percentile	1.078	1.428	1.278	0.909	1.155
	standard deviation	5th percentile	0.909	1.704	1.120	0.891	1.078
		Median	0.911	1.480	1.074	0.953	1.030
		95th percentile	1.000	1.338	1.163	0.897	1.013

Table E.8 Probabilistic estimates of relative changes to 30-year statistics for Hunza annual cryosphere states & fluxes; all values dimensionless multipliers.

E.2 Grid cell level consideration of glacial trajectories

Figures show the results of the first 300-year subset of each of the three synthetic time series – control, RCM-derived future and local trends extrapolated future – for the example 10km grid cell used in Chapter 6 from the and Hunza catchment. Each figure shows annual means of the glacial mass (IWE) [panel B] and the ratio of glacial cover to total surface area (fraction) [panel A] in each elevation band as well as annual totals for glacial displacement (by sliding) [panel C] and net mass transfer (inward/receiving from above = positive, outward/discharge to below = negative) [panel D].

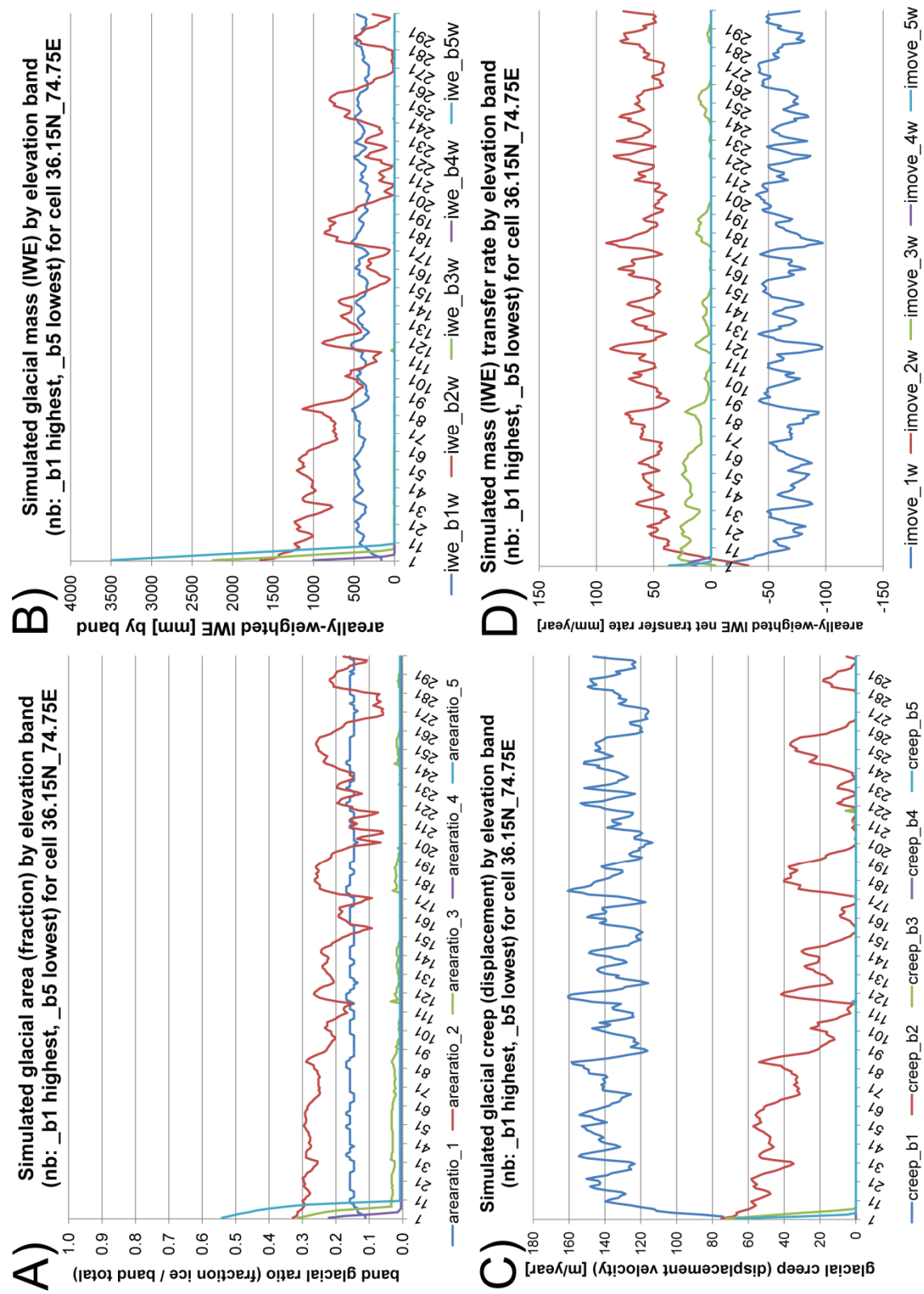

Figure E.1 example grid cell glacial variable trajectories from synthetic baseline climate for the Hunza catchment.

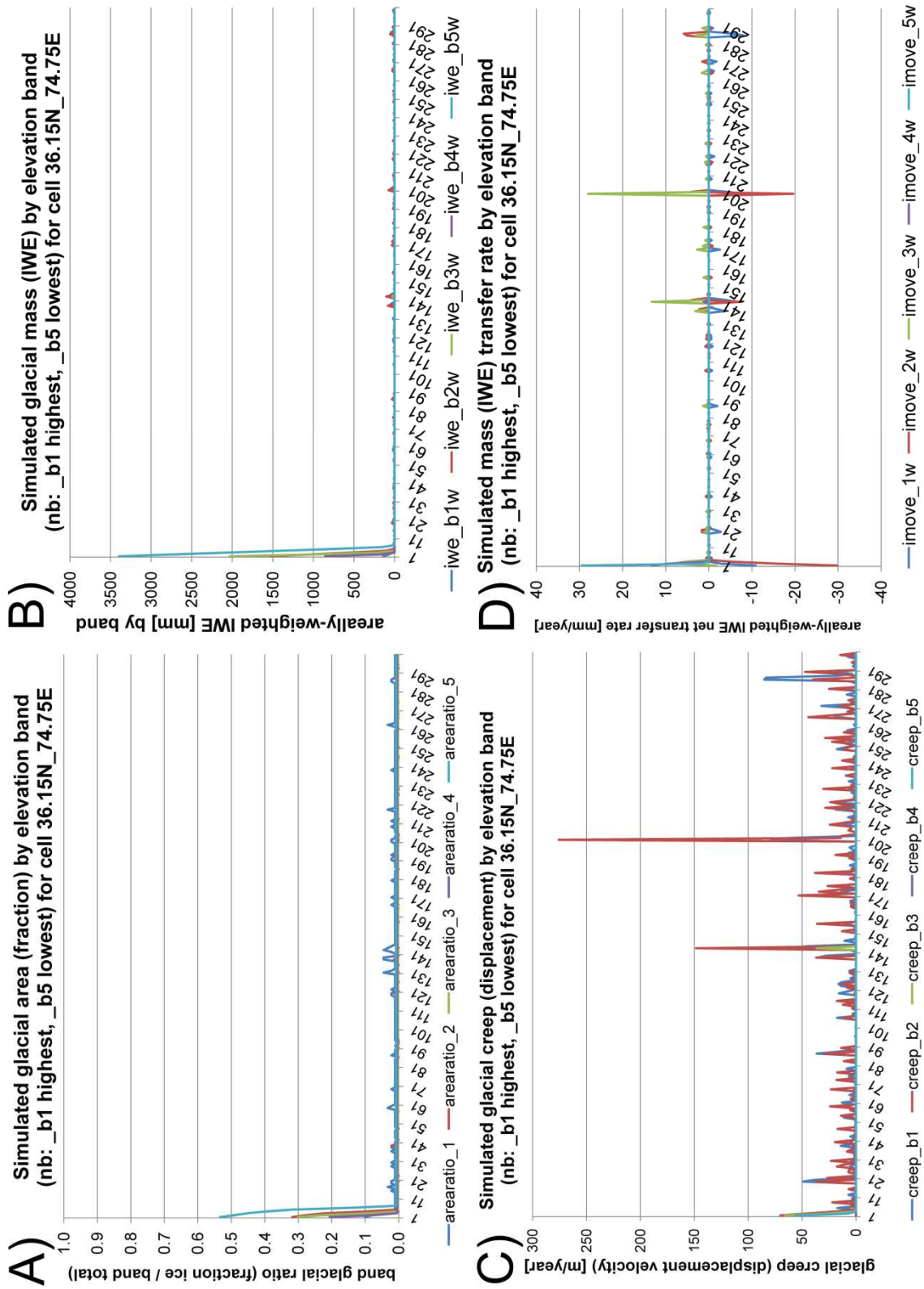

Figure E.2 example grid cell glacial variable trajectories from RCM-driven future climate scenario (PRECIS_AM3P A2 2080s) for the Hunza catchment.

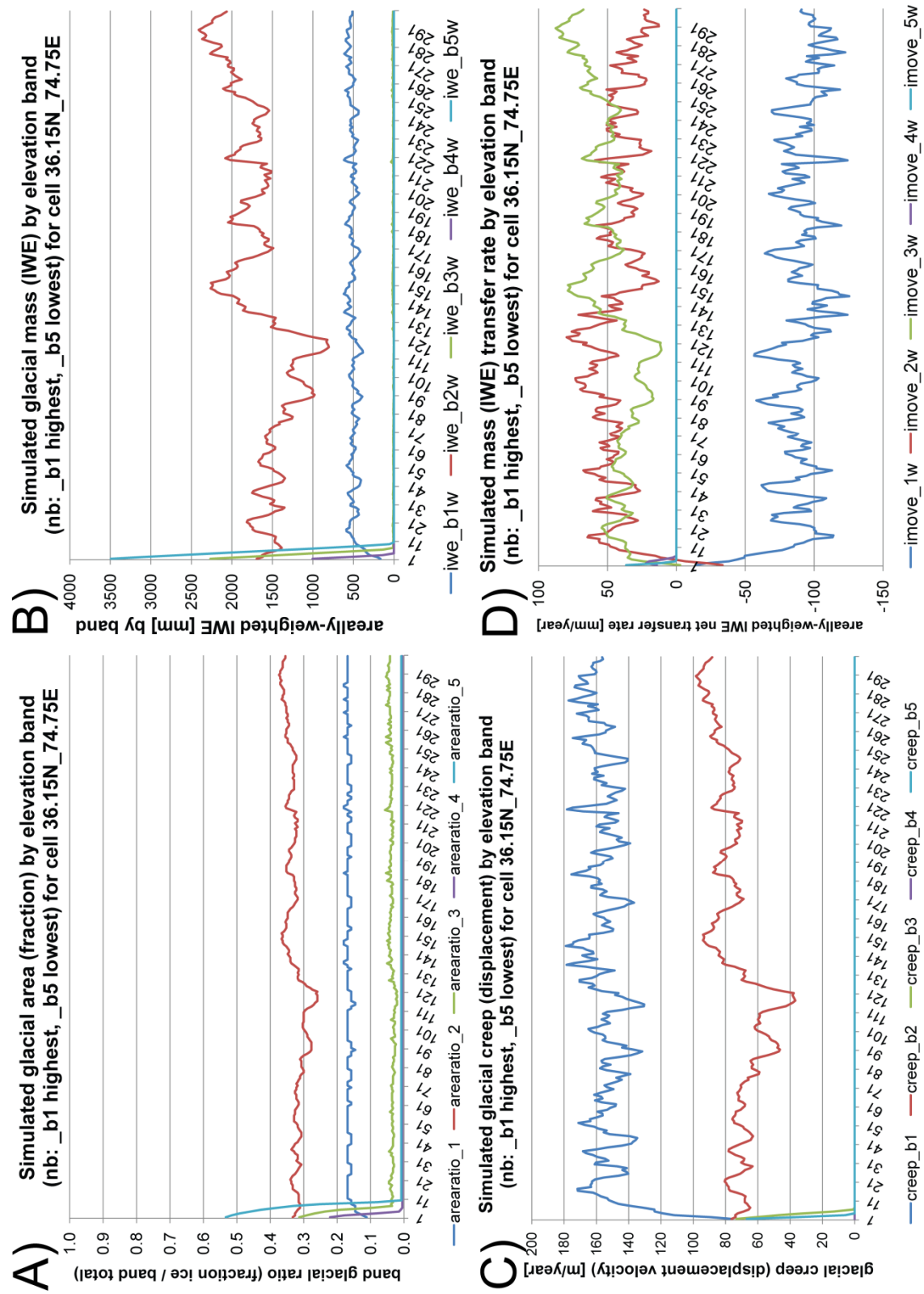

Figure E.3 example grid cell glacial variable trajectories from “observation-led” future climate scenario (extrapolated from local trends [PMD]) for the Hunza catchment.

Bibliography

Ackerman, S.A., Holz, R.E., Frey, R., Eloranta, E.W, Maddux, B.C. and McGill, M., 2008. Cloud Detection with MODIS. Part II: Validation. J. Atmos. Oceanic Technol., 25 (7), 1073–1086. http://dx.doi.org/10.1175/2007JTECHA1053.1

Akhtar, M., Ahmad, N. and Booij, M. J., 2009. Use of regional climate model simulations as input for hydrological models for the Hindukush-Karakorum-Himalaya region. Hydrol. Earth Syst. Sci., 13 (7), 1075-1089. http://dx.doi.org/10.5194/hess-13-1075-2009

Akhtar, M., Ahmad, N., and Booij, M. J., 2008. The impact of climate change on the water resource of Hindukush-Karakorum-Himalaya region under different glacier coverage scenarios, J. Hydrol., 355 (1-4), 148–163. http://dx.doi.org/10.1016/j.jhydrol.2008.03.015

Alessandri, A., Fogli, P. G., Vichi, M. and Zeng, N., 2012. Strengthening of the hydrological cycle in future scenarios: atmospheric energy and water balance perspective, Earth Syst. Dynam., 3 (2), 199-212. http://dx.doi.org/10.5194/esd-3-199-2012

Anagnostopoulou, C., Tolika, K., Maheras, P., Kutiel, H., Flocas, H., 2008. Performance of the General Circulation HadAM3P Model in simulating circulation types over the Mediterranean region. Int J Climatol 28 (2), 185–203. http://dx.doi.org/10.1002/joc.1521

Andreadis, K. M., P. Storck, and D. P. Lettenmaier. 2009. Modeling snow accumulation and ablation processes in forested environments, Water Resour. Res., 45 (5), W05429, http://dx.doi.org/10.1029/2008WR007042

Angstrom, A., 1935. Teleconnections of climate changes in present time. Geography Annals (Geografiska Annaler), 17, 242–258. http://www.jstor.org/stable/519964

Archer, D. R., 2003. Contrasting hydrological regimes in the Indus Basin. J. Hydrol., 274 (1-4), 198–210. http://dx.doi.org/10.1016/S0022-1694(02)00414-6

Archer, D. R., 2004. Hydrological implications of spatial and altitudinal variation in temperature in the Upper Indus Basin. Nord. Hydrol, 35 (3), 209–222.

Archer, D. R. and Fowler, H. J., 2004. Spatial and temporal variations in precipitation in the Upper Indus Basin, global teleconnections and hydrological implications. Hydrol. Earth Syst. Sci., 8 (1), 47–61. http://dx.doi.org/10.5194/hess-8-47-2004

Archer, D. R. and Fowler, H. J., 2008. Using meteorological data to forecast seasonal runoff on the River Jhelum, Pakistan, J. Hydrol., 361 (1-2), 10–23. http://dx.doi.org/10.1016/j.jhydrol.2008.07.017

Archer, D.R, Forsythe, N., Fowler, H.J. and Shah, S.M., 2010. Sustainability of water resources management in the Indus Basin under changing climatic and socio economic conditions. Hydrol Earth Syst Sci 14, 1669–1680. http://dx.doi.org/10.5194/hess-14-1669-2010

Auer, A.H.jr., 1974. The Rain versus Snow Threshold Temperatures. Weatherwise, 27 (2), 67. http://dx.doi.org/10.1080/00431672.1974.9931684

Bengtsson, L., 1982. The Importance of Refreezing on the Diurnal Snowmelt Cycle with Application to a Northern Swedish Catchment. Nordic Hydrology, 13 (1), 1-12.

Bengtsson, L. and Shukla, J., 1988. Integration of Space and In Situ Observations to Study Global Climate Change. Bull. Amer. Meteor. Soc., 69 (10), 1130–1143. http://dx.doi.org/10.1175/1520-0477(1988)069<1130:IOSAIS>2.0.CO;2

Beniston, M., Diaz, H.F. and Bradley, R.S., 1997. Climatic change at high elevation sites: An overview. Climatic Change, 36 (3-4), 233-251. http://dx.doi.org/10.1023/A:1005380714349

Berrisford, P., Kallberg, P., Kobayashi, S., Dee, D., Uppala, S., Simmons, A.J., Poli, P. and Sato, H., 2011. Atmospheric conservation properties in ERA-Interim. Quarterly Journal of the Royal Meteorological Society. 137 (659), 1381-1399. http://dx.doi.org/10.1002/qj.864

Betts, A.K., Ball, J.H., Bosilovich, M., Viterbo, P., Zhang, Y. and Rossow, W. B., 2003. Intercomparison of water and energy budgets for five Mississippi subbasins between ECMWF reanalysis (ERA-40) and NASA Data Assimilation Office fvGCM for 1990–1999, J. Geophys. Res., 108 (D16), 8618, http://dx.doi.org/10.1029/2002JD003127

Betts, A.K., Kohler, M. and Zhang, Y., 2009. Comparison of river basin hydrometeorology in ERA-Interim and ERA-40 reanalyses with observations. J. Geophys. Res., 114 (D2), D02101. http://dx.doi.org/10.1029/2008JD010761

Beven, K., 1989. Changing ideas in hydrology - The case of physically-based models. Journal of Hydrology, 105 (1-2), 157-172. http://dx.doi.org/10.1016/0022-1694(89)90101-7

Beven, K., 2001. How far can we go in distributed hydrological modelling?, Hydrol. Earth Syst. Sci., 5 (1), 1-12. http://dx.doi.org/10.5194/hess-5-1-2001

Bhutiyani, M., Kale, V. and Pawar, N., 2007. Long-term trends in maximum, minimum and mean annual air temperatures across the Northwestern Himalaya during the twentieth century. Clim Chang 85 (1-2), 159–177. http://dx.doi.org/10.1007/s10584-006-9196-1

Bhutiyani, M. R., Kale, V. S. and Pawar, N. J., 2010. Climate change and the precipitation variations in the northwestern Himalaya: 1866–2006. Int. J. Climatol. 30 (4), 535–548. http://dx.doi.org/10.1002/joc.1920

Bikos, D., Weaver, J.F. and Braun, J., 2006. The Role of GOES Satellite Imagery in Tracking Low-Level Moisture. Wea. Forecasting, 21 (2), 232–241. http://dx.doi.org/10.1175/WAF911.1

Bjerklie, D.M., Dingman, S.L., Vorosmarty, C.J., Bolster, C.H. and Congalton, R.G., 2003. Evaluating the potential for measuring river discharge from space. J. Hydrol. 278, 17–38. http://dx.doi.org/10.1016/S0022-1694(03)00129-X

Bocchiola, D., Diolaiuti, G., Soncini, A., Mihalcea, C., D'Agata, C., Mayer, C., Lambrecht, A., Rosso, R., and Smiraglia, C., 2011. Prediction of future hydrological regimes in poorly gauged high altitude basins: the case study of the upper Indus, Pakistan. Hydrol. Earth Syst. Sci., 15 (7), 2059-2075, http://dx.doi.org/10.5194/hess-15-2059-2011

Bolch, T., Buchroithner, M., Pieczonka, T. and Kunert, A., 2008. Planimetric and volumetric glacier changes in the Khumbu Himal, Nepal, since 1962 using Corona, Landsat TM and ASTER data. Journal of Glaciology, 54 (187), 592-600. http://dx.doi.org/10.3189/002214308786570782

Bolch, T., Kulkarni, A., Kääb, A., Huggel, C., Paul, F., Cogley, J. G., Frey, H., Kargel, J. S., Fujita, K., Scheel, M., Bajracharya, S. and Stoffel, M., 2012. The State and Fate of Himalayan Glaciers. Science, 336 (6079), 310-314. http://dx.doi.org/10.1126/science.1215828

Brown, J.A. jr., 1987. Operational numerical weather prediction. Reviews of Geophysics, 25 (3), 312-322. http://dx.doi.org/10.1029/RG025i003p00312

Brutsaert, W., Schmugge, T. J., Sellers, P. J. and Hall, F. G., 1988. Large-scale experimental technology with remote sensing in land surface hydrology and meteorology, Eos Trans. AGU, 69 (18), 561-571. http://dx.doi.org/10.1029/88EO00152

Burlando, P., Pellicciotti, F. and Strasser, U., 2002. Modelling mountainous water system between learning and speculating, looking for challenges. Nordic Hydrology 33 (1), 47–74.

Burton, A., Kilsby, C.G., Fowler, H.J., Cowpertwait, P.S.P. and O'Connell, P.E. 2008. RainSim: A spatial temporal stochastic rainfall modelling system. Environmental Modelling and Software, 23 (12), 1356-1369. http://dx.doi.org/10.1016/j.envsoft.2008.04.003

Buytaert, W. and De Bièvre, B., 2012. Water for cities: The impact of climate change and demographic growth in the tropical Andes. Water Resour. Res., 48 (8), W08503. http://dx.doi.org/10.1029/2011WR011755

Buytaert, W., Vuille, M., Dewulf, A., Urrutia, R., Karmalkar, A. and Célleri, R., 2010. Uncertainties in climate change projections and regional downscaling in the tropical Andes: implications for water resources management. Hydrol. Earth Syst. Sci., 14 (7), 1247-1258. http://dx.doi.org/10.5194/hess-14-1247-2010

Chen, T., Rossow, W.B. and Zhang, Y., 2000. Radiative Effects of Cloud-Type Variations. J. Climate, 13 (1), 264–286. http://dx.doi.org/10.1175/1520-0442(2000)013<0264:REOCTV>2.0.CO;2

Cherkauer, K. A., and D. P. Lettenmaier. 2003. Simulation of spatial variability in snow and frozen soil. J. Geophys. Res., 108 (D22), 8858. http://dx.doi.org/10.1029/2003JD003575

Cherkauer, K. A., Bowling, L. C. and Lettenmaier, D. P., 2003. Variable infiltration capacity cold land process model updates, Global Planet. Change, 38 (1-2), 151–159. http://dx.doi.org/10.1016/S0921-8181(03)00025-0

Chokmani, K., Bernier, M. and Slivitzky, M., 2005. Suivi spatio-temporel du couvert nival du Québec à l'aide des données NOAA-AVHRR. Revue des sciences de l'eau / Journal of Water Science, 19 (3), 163-179. http://id.erudit.org/iderudit/013536ar

Christensen, J.H., B. Hewitson, A. Busuioc, A. Chen, X. Gao, I. Held, R. Jones, R.K. Kolli, W.-T. Kwon, R. Laprise, V. Magaña Rueda, L. Mearns, C.G. Menéndez, J. Räisänen, A. Rinke, A. Sarr and P. Whetton, 2007: Regional Climate Projections. In: Climate Change 2007: The Physical Science Basis. Contribution of Working Group I to the Fourth Assessment Report of the Intergovernmental Panel on Climate Change [Solomon, S., D. Qin, M. Manning, Z. Chen, M. Marquis, K.B. Averyt, M. Tignor and H.L. Miller (eds.)]. Cambridge University Press, Cambridge, United Kingdom and New York, NY, USA.

Dai, A., Trenberth, K.E. and Karl, T.R., 1999. Effects of clouds, soil moisture, precipitation, and water vapor on diurnal temperature range. J Clim 12 (8), 2451–2473. http://dx.doi.org/10.1175/1520-0442(1999)012<2451:EOCSMP>2.0.CO;2

de Scally, F. A. and Gardner, J. S., 1990. Ablation of Avalanched and Undisturbed Snow, Himalaya Mountains, Pakistan, Water Resour. Res., 26 (11), 2757–2767. http://dx.doi.org/10.1029/WR026i011p02757

de Scally, F.A., 1994. Relative importance of snow accumulation and monsoon rainfall data for estimating annual runoff, Jhelum basin, Pakistan. Hydrological Sciences Journal 39 (3), 199–216. http://dx.doi.org/10.1080/02626669409492738

de Scally, F.A, 1997. Deriving Lapse Rates of Slope Air Temperature for Meltwater Runoff Modeling in Subtropical Mountains: An Example from the Punjab Himalaya, Pakistan. Mountain Research and Development, 17 (4), 353-362. http://www.jstor.org/stable/3674024

Dee, D.P., Uppala, S.M., Simmons, A.J., Berrisford, P., Poli, P., Kobayashi, S., Andrae, U., Balmaseda, M.A., Balsamo, G., Bauer, P., Bechtold, P., Beljaars, A.C.M., van de Berg, L., Bidlot, J., Bormann, N., Delsol, C., Dragani, R., Fuentes, M., Geer, A.J., Haimberger, L., Healy, S.B., Hersbach, H., Holm, E.V., Isaksen, L., Kallberg, P., Kohler, M., Matricardi, M., McNally, A.P., Monge-Sanz, B.M., Morcrette, J.-J., Park, B.-K., Peubey, C., de Rosnay, P., Tavolato, C., Thepaut, J.-N. and Vitart, F., 2011. The ERA-Interim reanalysis: configuration and performance of the data assimilation system. Q. J. R. Meteorol. Soc. 137 (656), 553–597. http://dx.doi.org/10.1002/qj.828

Delany, A. C. and Semmer, S. R., 1998. An Integrated Surface Radiation Measurement System. J. Atmos. Oceanic Technol., 15 (1), 46–53. http://dx.doi.org/10.1175/1520-0426(1998)015<0046:AISRMS>2.0.CO;2

Déqué, M. and Somot, S., 2010. Weighted frequency distributions express modelling uncertainties in the ENSEMBLES regional climate experiments. Clim Res, 44 (2-3), 195-209. http://dx.doi.org/10.3354/cr00866

Déqué, M., Somot, S., Sanchez-Gomez, E., Goodess, C.M., Jacob, D., Lenderink, G. and Christensen, O.B., 2012. The spread amongst ENSEMBLES regional scenarios: regional climate models, driving general circulation models and interannual variability. Climate Dynamics, 38 (5-6), 951-964. http://dx.doi.org/10.1007/s00382-011-1053-x

Diaz, H. F., Hoerling, M. P. and Eischeid, J. K., 2001. ENSO variability, teleconnections and climate change. Int. J. Climatol., 21 (15), 1845–1862. (http://dx.doi.org/10.1002/joc.631)

Ding, Q. and Wang, B., 2005. Circumglobal Teleconnection in the Northern Hemisphere Summer. J. Climate, 18 (17), 3483–3505. (http://dx.doi.org/10.1175/JCLI3473.1)

Dinku, T. , Chidzambwa, S. , Ceccato, P. , Connor, S. J. and Ropelewski, C. F., 2008. Validation of highresolution satellite rainfall products over complex terrain. International Journal of Remote Sensing, 29 (14), 4097 - 4110. http://dx.doi.org/10.1080/01431160701772526

Dong, X., Minnis, P. and Xi, B., 2005. A Climatology of Midlatitude Continental Clouds from the ARM SGP Central Facility: Part I: Low-Level Cloud Macrophysical, Microphysical, and Radiative Properties. J. Climate, 18 (9), 1391–1410. http://dx.doi.org/10.1175/JCLI3342.1

Easterling, D.R., Horton, B., Jones, P.D., Peterson, T.C., Karl, T.R., Parker, D.E., Salinger, M.J., Razuvayev, V., Plummer, N., Jamason, P. and Folland, C.K., 1997. Maximum and minimum temperature trends for the globe. Science, 277 (5324), 364–367. (http://dx.doi.org/10.1126/science.277.5324.364)

Ebell K, Crewell, S., Lohnert, U., Turner, D.D., O'Connor, E.J., 2011. Cloud statistics and cloud radiative effect for a low-mountain site. Q. J. R. Meteorol. Soc. 137 (S1), 306–324. (http://dx.doi.org/10.1002/qj.748)

Ehret, U., Zehe, E., Wulfmeyer, V., Warrach-Sagi, K. and Liebert, J., 2012. HESS Opinions: "Should we apply bias correction to global and regional climate model data?". Hydrol. Earth Syst. Sci., 16 (9), 3391-3404. http://dx.doi.org/10.5194/hess-16-3391-2012

Ewen, J., O'Donnell, G., Burton, A. and O'Connell, E., 2006. Errors and uncertainty in physically-based rainfall-runoff modelling of catchment change effects. Journal of Hydrology, 330 (3-4), 641-650. http://dx.doi.org/10.1016/j.jhydrol.2006.04.024

Fasullo, J.T. and Trenberth, K.E., 2008a. The Annual Cycle of the Energy Budget. Part I: Global Mean and Land–Ocean Exchanges. J. Climate, 21 (10), 2297–2312. http://dx.doi.org/10.1175/2007JCLI1935.1

Fasullo, J.T. and Trenberth, K.E., 2008b. The Annual Cycle of the Energy Budget. Part II: Meridional Structures and Poleward Transports. J. Climate, 21 (10), 2313–2325. http://dx.doi.org/10.1175/2007JCLI1936.1

Fowler, H. J. and Archer, D. R., 2005. Hydro-climatological variability in the Upper Indus Basin and implications for water resources. In: T. Wagener et al., Eds., Regional Hydrological Impacts of Climatic Change—Impact Assessment and Decision Making, Proceedings of symposium S6 held during the Seventh IAHS Scientific Assembly at Foz do Iguaçu, Brazil, April 2005).IAHS Publication 295, 131–138.

Fowler, H. J. and Archer, D. R., 2006. Conflicting Signals of Climate Change in the Upper Indus Basin, J. Climate, 19 (17), 4276–4292. http://dx.doi.org/10.1175/JCLI3860.1

Fowler, H.J., Blenkinsop, S. and Tebaldi, C., 2007. Linking climate change modelling to impacts studies: Recent advances in downscaling techniques for hydrological modelling. International Journal of Climatology, 27 (12), 1547-1578. http://dx.doi.org/10.1002/joc.1556

Forsythe, N., Fowler, H.J., Kilsby, C.G. and Archer, D.R., 2012a. Opportunities from remote sensing for supporting water resources management in village/valley scale catchments in the Upper Indus Basin. Water Resources Management, 26 (4), 845–871. http://dx.doi.org/10.1007/s11269-011-9933-8

Forsythe, N., Kilsby, C.G., Fowler, H.J. and Archer, D.R., 2012b. Assessment of Runoff Sensitivity in the Upper Indus Basin to Interannual Climate Variability and Potential Change Using MODIS Satellite Data Products. Mountain Research and Development, 32 (1), 16-29. http://dx.doi.org/10.1659/MRD-JOURNAL-D-11-00027.1

Frei, C., and Schar, C. 2001. Detection Probability of Trends in Rare Events: Theory and Application to Heavy Precipitation in the Alpine Region. Journal of Climate, 14 (8) 1568–1584. http://dx.doi.org/10.1175/1520-0442(2001)014<1568:DPOTIR>2.0.CO;2

Frei, C., Schär, C., Lüthi, D. and Davies, H.C., 1998. Heavy precipitation processes in a warmer climate. Geophysical Research Letters, 25 (9), 1431-1434. http://dx.doi.org/10.1029/98GL51099

Gao, H., Tang, Q., Shi, X., Zhu, C., Bohn, T., Su, F., Sheffield, J., Pan, M., Lettenmaier, D. and E.F. Wood. Water Budget Record from Variable Infiltration Capacity (VIC) Model Algorithm Theoretical Basis Document (Version 1.2). June 19, 2009. http://www.hydro.washington.edu/SurfaceWaterGroup/Publications/Water_Cycle_MEaSUREs_ATBD_VICmodel_submit.doc

Gardelle, J., Berthier, E. and Arnaud, Y., 2012. Contrasting patterns of early twenty-first-century glacier mass change in the Himalayas. Nature Geosci. 5 (5), 322-325. http://dx.doi.org/10.1038/ngeo1450

Geerts, B., 2003: Empirical estimation of the monthly-mean daily temperature range. Theor. Appl. Climatol., 74 (3-4), 145–165. http://dx.doi.org/10.1007/s00704-002-0715-3

Goddard, L., Mason, S.J., Zebiak, S.E., Ropelewski, C.F., Basher, R. and Cane, M.A. 2001. Current approaches to seasonal to interannual climate predictions. Int. J. Climatol., 21 (9), 1111–1152. http://dx.doi.org/10.1002/joc.636

Goderniaux, P., Brouyére, S., Blenkinsop, S., Burton, A., Fowler, H.J., Orban, P. and Dassargues, A., 2011. Modeling climate change impacts on groundwater resources using transient stochastic climatic scenarios. Water Resources Research, 47 (12), art. no. W12516. http://dx.doi.org/10.1029/2010WR010082

Hall, D.K., Riggs, G.A., Salomonson, V.V., Barton, J.S., Casey, K., Chien, J.Y.L., DiGirolamo, N.E., Klein, A.G, Powell, H.W. and Tait, A.B., 2001. Algorithm Theoretical Basis Document (ATBD) for the MODIS Snow and Sea Ice-mapping Algorithms. (http://modis-snow-ice.gsfc.nasa.gov/atbd01.html).

Heltberg, R., Siegel, P. B. and Jorgensen, S. L., 2009. Addressing human vulnerability to climate change: Toward a 'no-regrets' approach. Global Environ.l Chang., 19 (1), 89–99. (http://dx.doi.org/10.1016/j.gloenvcha.2008.11.003)

Hewitt, K., 1982. Natural dams and outburst floods of the Karakoram Himalaya. In: Glen, J. Ed., Hydrological Aspects of Alpine and High Mountain Areas. IAHS-AISH Publication No. 138, pp. 259–269.

Hewitt, K., 2005. The Karakoram Anomaly? Glacier Expansion and the 'Elevation Effect,' Karakoram Himalaya. Mountain Research and Development, 25 (4), 332-340. http://dx.doi.org/10.1659/0276-4741(2005)025[0332:TKAGEA]2.0.CO;2

Hewitt, K., 2011. Glacier change, concentration, and elevation effects in the Karakoram Himalaya, Upper Indus Basin. Mountain Research and Development 31(3),188–200. http://dx.doi.org/10.1659/MRD-JOURNAL-D-11-00020.1

Hewitt, K., Wake, C.P., Young, G.J., David, C., 1989. Hydrological investigations at Biafo Glacier, Karakoram Himalaya: an important source of water for the Indus River. Annals of Glaciology 13, 103–108.

Holderness, T. 2011. Python Spatial Image Processing (PyRaster). https://github.com/talltom/PyRaster

Hong, C.C., Hsu, H.H., Lin, N.H. and Chiu, H., 2011. Roles of European blocking and tropical-extratropical interaction in the 2010 Pakistan flooding. Geophys. Res. Lett., 38 (13), L13806. http://dx.doi.org/10.1029/2011GL047583

Huffman, G.J. and Bolvin, D.T., 2011. TRMM and Other Data Precipitation Data Set Documentation. Laboratory for Atmospheres, NASA Goddard Space Flight Center and Science Systems and Applications, Inc. ftp://precip.gsfc.nasa.gov/pub/trmmdocs/3B42_3B43_doc.pdf

Huffman, G.J., Adler, R.F., Bolvin, D.T., Gu, G., Nelkin, E.J., Bowman, K.P., Hong, Y., Stocker, E.F. and Wolff, D.B., 2007. The TRMM Multisatellite Precipitation Analysis (TMPA): Quasi-Global, Multiyear, Combined-Sensor Precipitation Estimates at Fine Scales. Journal of Hydrometeorology 8 (1), 38 - 55. http://dx.doi.org/10.1175/JHM560.1

Immerzeel, W.W., Droogers, P., de Jong, S. M., and Bierkens, M. F. P., 2008. Large-scale monitoring of snow cover and runoff simulation in Himalayan river basins using remote sensing, Remote Sens. Environ., 113 (1), 40-49. http://dx.doi.org/10.1016/j.rse.2008.08.010

Immerzeel, W.W., Pelicciotti, F., and Shrestha, A. B. 2012. Glaciers as a Proxy to Quantify the Spatial Distribution of Precipitation in the Hunza Basin. Mountain Research and Development, 32 (1), 30-38. http://dx.doi.org/10.1659/MRD-JOURNAL-D-11-00097.1

Immerzeel, W.W., Van Beek, L.P.H. and Bierkens, M.F.P., 2010. Climate change will affect the Asian water towers. Science, 328 (5984), 1382–1385. http://dx.doi.org/10.1126/science.1183188

Immerzeel, W.W., Van Beek, L.P.H., Konz, M., Shrestha, A.B. and Bierkens, M.F.P., 2011. Hydrological response to climate change in a glacierized catchment in the Himalayas. Climatic Change 110 (3-4), 721-736. http://dx.doi.org/10.1007/s10584-011-0143-4

IPCC, 2007. Climate Change 2007: Impacts, Adaptation and Vulnerability. Contribution of Working Group II to the Fourth Assessment Report of the Intergovernmental Panel on Climate Change, M.L. Parry, O.F. Canziani, J.P. Palutikof, P.J. van der Linden and C.E. Hanson, Eds., Cambridge University Press, Cambridge, UK, 976pp.

IPCC SRES (2000), Nakicenovic, N., and Swart, R., ed. (book), Special Report on Emissions Scenarios: A special report of Working Group III of the Intergovernmental Panel on Climate Change, Cambridge University Press, ISBN 0-521-80081-1, 978-052180081-5.

Islam, S.U., Rehman, N. and Sheikh M.M., 2009. Future change in the frequency of warm and cold spells over Pakistan simulated by the PRECIS regional climate model. Climatic Change, 94 (1-2), 35-45. http://dx.doi.org/10.1007/s10584-009-9557-7

Iturrizaga, L., 2011. Trends in 20th century and recent glacier fluctuations in the Karakoram Mountains. Zeitschrift für Geomorphologie, Supplementary Issues, 55 (3), 205-231. http://dx.doi.org/10.1127/0372-8854/2011/0055S3-0059

Jackson, L.S. and Forster, P.M., 2010. An Empirical Study of Geographic and Seasonal Variations in Diurnal Temperature Range. J. Climate, 23 (12), 3205–3221. http://dx.doi.org/10.1175/2010JCLI3215.1

Jackson, S.I. and Prowse, T.D., 2009. Spatial variation of snowmelt and sublimation in a high-elevation semi-desert basin of western Canada. Hydrol. Process. 23 (18), 2611–2627. http://dx.doi.org/10.1002/hyp.7320

Jacob, D., Bärring, L., Christensen, O.B., Christensen, J.H., De Castro, M., Déqué, M., Giorgi, F., Hagemann, S., Hirschi, M., Jones, R., Kjellström, E., Lenderink, G., Rockel, B., Sánchez, E., Schär, C., Seneviratne, S.I., Somot, S., Van Ulden, A., Van Den Hurk, B., 2007. An inter-comparison of regional climate models for Europe: Model performance in present-day climate. Climatic Change, 81 (1, SUPPL. 1), 31-52. http://dx.doi.org/10.1007/s10584-006-9213-4

Jacob, D., Elizalde, A., Haensler, A., Hagemann, S., Kumar, P., Podzun, R., Rechid, D., Remedio, A.R., Saeed, F., Sieck, K., Teichmann, C., and Wilhelm, C., 2012a. Assessing the Transferability of the Regional Climate Model REMO to Different COordinated Regional Climate Downscaling EXperiment (CORDEX) Regions. Atmosphere, 3 (1), 181-199. (http://dx.doi.org/10.3390/atmos3010181)

Jacob, T., Wahr, J., Pfeffer, T. W. and Swenson, S., 2012b. Recent contributions of glaciers and ice caps to sea level rise. Nature 482, 514–518. (http://dx.doi.org/10.1038/nature10847).

Jarvis A., Reuter, H.I., Nelson, A. and Guevara, E., 2008. Hole-filled seamless SRTM data V4, International Centre for Tropical Agriculture (CIAT), available from http://srtm.csi.cgiar.org.

Jhajharia, D. and Singh, V. P., 2011. Trends in temperature, diurnal temperature range and sunshine duration in Northeast India. Int. J. Climatol., 31 (9), 1353–1367. (http://dx.doi.org/10.1002/joc.2164)

Jin, Y., Schaaf, C. B., Woodcock, C. E., Gao, F., Li, X., Strahler, A. H., Lucht, W. and Liang, S., 2003. Consistency of MODIS surface BRDF/Albedo retrievals: 2. Validation. Journal of Geophysical Research, 108 (D5), 4159. http://dx.doi.org/10.1029/2002JD002804

Jones, P. D., Harpham, C., Goodess, C. M. and Kilsby, C. G., 2011. Perturbing a Weather Generator using change factors derived from Regional Climate Model simulations, Nonlin. Processes Geophys., 18, 503-511. http://dx.doi.org/10.5194/npg-18-503-2011

Jones, P. D., Jonsson, T. and Wheeler, D., 1997. Extension to North Atlantic Oscillation using early instrumental pressure observations from Gibraltar and South-West Iceland. Int. J. Climatol., 17 (13), 1433-1450. http://dx.doi.org/10.1002/(SICI)1097-0088(19971115)17:13<1433::AID-JOC203>3.0.CO;2-Phttp://dx.doi.org/10.1002/(SICI)1097-0088(19971115)17:13<1433::AID-JOC203>3.0.CO;2-P

Jones, P. D., Kilsby, C. G., Harpham, C., Glenis, V. and Burton, A., 2009. UK Climate Projections science report: Projections of future daily climate for the UK from the Weather Generator. University of Newcastle, UK.

Jones, R.G., Murphy, J.M. and Noguer, M., 1995. Simulation of climate change over Europe using a nested regional-climate model. I: Assessment of control climate, including sensitivity to location of lateral boundaries. Quarterly Journal of the Royal Meteorological Society, 121 (526 B), 1413-1449. http://dx.doi.org/10.1002/qj.49712152610

Jones, P. D., New, M., Parker, D. E., Martin, S. and Rigor, I. G., 1999. Surface air temperature and its changes over the past 150 years. Rev. Geophys., 37 (2), 173–199. http://dx.doi.org/10.1029/1999RG900002

Jones, R.G., Noguer, M., Hassell, D.C., Hudson, D., Wilson, S.S., Jenkins, G.J. and Mitchell, J.F.B., 2004. Generating high resolution climate change scenarios using PRECIS, Met Office Hadley Centre,Exeter, UK, 40pp. http://www.metoffice.gov.uk/media/pdf/6/5/PRECIS_Handbook.pdf

Justice, C.O., Townshend, J.R.G., Vermote, E.F., Masuoka, E., Wolfe, R.E, Saleous, N., Roy, D.P. and Morisette, J.T., 2002. An overview of MODIS Land data processing and product status. Remote Sensing of Environment, 83 (1-2), 3-15. http://dx.doi.org/10.1016/S0034-4257(02)00084-6

Kääb, A., Berthier, E., Nuth, C., Gardelle, J. and Arnaud, Y., 2012. Contrasting patterns of early twenty-first-century glacier mass change in the Himalayas. Nature 488 (7412), 495-498. http://dx.doi.org/10.1038/nature11324

Kållberg, P., Adrian Simmons, Sakari Uppala, Manuel Fuentes. 2007. "ERA-40 Project Report Series No. 17: The ERA-40 Archive." European Centre for Medium Range Weather Forecasts. Reading, England. (available at http://www.ecmwf.int/publications/library/ecpublications/_pdf/era/era40/ERA40_PRS17_rev1.pdf).

Kalnay, E., Kanamitsu, M., Kistler, R., Collins, W., Deaven, D., Gandin, L., Iredell, M., Saha, S., White, G., Woollen, J., Zhu, Y., Chelliah, M., Ebisuzaki, W., Higgins, W., Janowiak, J., Mo, K.C., Ropelewski, C., Wang, J., Leetmaa, A., Reynolds, R., Jenne, R. and Joseph, D., 1996. The NCEP/NCAR 40-Year Reanalysis Project. Bull. Amer. Meteor. Soc., 77 (3), 437–471. http://dx.doi.org/10.1175/1520-0477(1996)077<0437:TNYRP>2.0.CO;2

Karki, M.B., Shrestha, A.B. and Winiger, M., 2011. Enhancing knowledge management and adaptation capacity for integrated management of water resources in the Indus River Basin. Mountain Research and Development 31 (3), 242–251. http://dx.doi.org/10.1659/MRD-JOURNAL-D-11-00017.1

Kaser, G., Cogley, J.G., Dyurgerov, M.B., Meier, M.F., Ohmura, A., 2006. Mass balance of glaciers and ice caps: consensus estimates for 1961–1994. Geophys. Res. Lett. 33 (19), L19501. http://dx.doi.org/10.1029/2006GL027511

Kessler, M. A., R. S. Anderson, and G. M. Stock. 2006. Modeling topographic and climatic control of east-west asymmetry in Sierra Nevada glacier length during the Last Glacial Maximum, J. Geophys. Res., 111, F02002. http://dx.doi.org/10.1029/2005JF000365

Khattak, M.S., Babel, M.S. and Sharif, M., 2011. Hydro-meteorological trends in the upper Indus River basin in Pakistan. Clim Res 46 (2), 103-119. http://dx.doi.org/10.3354/cr00957

Khlopenkov, K.V. and Trishchenko, A.P., 2006. SPARC: New cloud, snow, and cloud shadow detection scheme for historical 1-km AVHHR data over Canada. Journal of Atmospheric and Oceanic Technology 24 (3), 322-343. (http://dx.doi.org/10.1175/jtech1987.1

Kick, W., 1980. Material for a glacier inventory of the Indus drainage basin–the Nanga Parbat massif. World Glacier Inventory. Proceedings of the Reideralp Workshop, 1978. IAHS-AISH Publication 126. 105–109.

Kiehl, J. T. and Trenberth, K.E., 1997. Earth's Annual Global Mean Energy Budget. Bull. Amer. Meteor. Soc., 78 (2), 197–208. http://dx.doi.org/10.1175/1520-0477(1997)078<0197:EAGMEB>2.0.CO;2

Kilsby, C.G., Jones, P.D., Burton, A., Ford, A.C., Fowler, H.J., Harpham, C., James, P., Smith, A. and Wilby, R.L., 2007. A daily weather generator for use in climate change studies. Environmental Modelling and Software, 22 (12), 1705-1719. http://dx.doi.org/10.1016/j.envsoft.2007.02.005

Klein, A.G. and Barnet, A.C., 2003. Validation of daily MODIS snow cover maps of the Upper Rio Grande River Basin for the 2000–2001 snow year. Remote Sensing of Environment 86 (2), 162–176. http://dx.doi.org/10.1016/S0034-4257(03)00097-X

Konz, M., Uhlenbrook, S., Braun, L., Shrestha, A. and Demuth, S., 2007. Implementation of a process-based catchment model in a poorly gauged, highly glacierized Himalayan headwater. Hydrol Earth Syst Sci 11 (1993), 1323–1339. http://dx.doi.org/10.5194/hess-11-1323-2007

Kothawale, D., Munot, A. and Kumar, K.K., 2010. Surface air temperature variability over India during 1901–2007, and its association with ENSO. Clim Res 42 (2), 89–104. http://dx.doi.org/10.3354/cr00857

Krieger, T., Curtis, W. and Haase, J., 2011. Global Validation of the ASTER Global Digital Elevation Model (GDEM) Version 2. Report to the ASTER GDEM Version 2 Validation Team.

Kult, J., Choi, W. and Keuser, A., 2012. Snowmelt runoff modeling: Limitations and potential for mitigating water disputes. Journal of Hydrology, 430-431, 179-181. http://dx.doi.org/10.1016/j.jhydrol.2012.01.043

Kumar, K.R., Kumar, K.K. and Pant, G.B., 1994. Diurnal asymmetry of surface temperature trends over India. Geophysical Research Letters 21 (8), 677–680. http://dx.doi.org/10.1029/94GL00007

Kunz, M., King, M.A., Mills, J.P., Miller, P.E., Fox, A.J., Vaughan, D.G. and Marsh, S.H., 2012. Multi-decadal glacier surface lowering in the Antarctic Peninsula, Geophys. Res. Lett., 39 (19), L19502. http://dx.doi.org/10.1029/2012GL052823

Li, J., Huang, H.-L., Liu, C.-Y., Yang, P., Schmit, T. J., Wei, H. and Weisz, E., 2005. Retrieval of Cloud Microphysical Properties from MODIS and AIRS. J. Appl. Meteor., 44 (10), 1526–1543. http://dx.doi.org/10.1175/JAM2281.1

Li, Z.L. and Becker, F., 1993. Feasibility of Land Surface Temperature and Emissivity Determination from AVHRR Data. Remote Sens. Environ. 43 (1), 67-85. http://dx.doi.org/10.1016/0034-4257(93)90065-6

Liang, X.-Z., Kunkel, K.E., Meehl, G.A., Jones, R.G. and Wang, J.X.L., 2008. Regional climate models downscaling analysis of general circulation models present climate biases propagation into future change projections. Geophysical Research Letters, 35 (8), L08709. http://dx.doi.org/10.1029/2007GL032849

Lindstrom, G., Johansson, B., Persson, M., Gardelin, M. and Bergstrom, S., 1997. Development and test of the distributed HBV-96 model, J. Hydrol., 201, 272–288. http://dx.doi.org/10.1016/S0022-1694(97)00041-3

Lohmann, D., Raschke, E., Nijssen, B., and Lettenmaier, D. P., 1998. Regional scale hydrology; I, formulation of the VIC-2L model coupled to a routing model, Hydrol. Sci. J., 43 (1), 131– 141. http://dx.doi.org/10.1080/02626669809492107

Liu, Y., Xin, X. and Liu, Q., 2009. Modis and Landsat ETM+ scaling study on the daily evapotranspiration over heterogeneous landscapes. Geoscience and Remote Sensing Symposium 12-17 July 2009, IEEE International IGARSS 2009, 3, 662-665. http://dx.doi.org/10.1109/IGARSS.2009.5417847

Lu, R.-Y., Oh, J.-H. and Kim, B.-J., 2002. A teleconnection pattern in upper-level meridional wind over the North African and Eurasian continent in summer. Tellus, Series A: Dynamic Meteorology and Oceanography, 54 (1), 44-55. http://dx.doi.org/10.1034/j.1600-0870.2002.00248.x

Maidment, D.R. 1992. Handbook of hydrology. McGraw-Hill. New York (USA).

Marks, D. and Dozier, J., 1992. Climate and energy exchange at the snow surface in the alpine region of the Sierra Nevada, 2, Snow cover energy balance. Water Resour. Res. 28 (11), 3043-3054. http://dx.doi.org/10.1029/92WR01483

Marshall, J., Kushnir, Y., Battisti, D., Chang, P., Czaja, A., Dickson, R., Hurrell, J., McCartney, M., Saravanan, R. and Visbeck, M., 2001. North Atlantic climate variability: phenomena, impacts and mechanisms. Int. J. Climatol., 21 (15), 1863–1898. http://dx.doi.org/10.1002/joc.693

Martinec, J., Rango, A., & Roberts, R. (2007). Snowmelt runoff model: User manual. Las Cruces: New Mexico State University.

Matsuo, K. and Heki, K., 2010. Time-variable ice loss in Asian high mountains from satellite gravimetry. Earth Planet. Sci. Lett. 290 (1-2), 30–36. http://dx.doi.org/10.1016/j.epsl.2009.11.053

Mayer, C., Lambrecht, A., Mihalcea, C., Belò, M., Diolaiuti, G., Smiraglia, C. and Bashir, F., 2010. Analysis of glacial meltwater in Bagrot Valley, Karakoram: Based on short-term ablation and debris cover observations on Hinarche Glacier. Mountain Research and Development 30 (2), 169–177. http://dx.doi.org/10.1659/MRD-JOURNAL-D-09-00043.1

McSweeney, Carol F., Jones, R.G. and Booth, B.B.B., 2012. Selecting Ensemble Members to Provide Regional Climate Change Information. J. Climate, 25 (20), 7100–7121. http://dx.doi.org/10.1175/JCLI-D-11-00526.1

Mihalcea, C., Mayer, C., Diolaiuti, G., Lambrecht, A., Smiraglia, C. and Tartari, G., 2006. Ice ablation and meteorological conditions on the debris-covered area of Baltoro glacier, Karakoram, Pakistan. Ann. Glaciol., 43 (1), 292–300. http://dx.doi.org/10.3189/172756406781812104

Mihalcea, C., Mayer, C., G. Diolaiuti, D'Agata, C., Smiraglia, C., Lambrecht, A., Vuillermoz, E., and Tartari, G., 2008. Spatial distribution of debris thickness and melting from remote-sensing and meteorological data, at debris-covered Baltoro Glacier, Karakoram, Pakistan, Ann. Glaciol., 48 (1), 49–57. http://dx.doi.org/10.3189/172756408784700680

Murphy, J.M., Booth, B.B.B., Collins, M., Harris, G.R., Sexton, D.M.H. and Webb, M.J., 2007. A methodology for probabilistic predictions of regional climate change from perturbed physics ensembles. Philosophical Transactions of the Royal Society A: Mathematical, Physical and Engineering Sciences, 365 (1857), 1993-2028. http://dx.doi.org/10.1098/rsta.2007.2077

Naz, B. S., 2011. The Hydrologic Sensitivity of the Upper Indus River to Glacier Changes in the Karakoram Himalayas, PhD Dissertation, Purdue University, West Lafayette, IN.

New, M., Hulme, M. and Jones, P., 2000. Representing twentieth-century space-time climate variability. Part II: Development of 1901-96 monthly grids of terrestrial surface climate. Journal of Climate, 13 (13), 2217-2238. http://dx.doi.org/10.1175/1520-0442(2000)013<2217:RTCSTC>2.0.CO;2

Ozturk, T., Altinsoy, H.A., Türke, M. and Kurnaz, M.L., 2012. Simulation of temperature and precipitation climatology for the Central Asia CORDEX domain using RegCM 4.0. Clim Res 52, 63-76. http://dx.doi.org/10.3354/cr01082

Palutikof, J.P., 2003: Analysis of Mediterranean climate data: measured and modelled. In: Bolle, H.J. (ed): Mediterranean climate: Variability and trends. Springer-Verlag, Berlin

Pan, Z., Christensen, J.H., Arritt, R.W., Gutowski Jr., W.J., Takle, E.S., Otieno, F., 2001. Evaluation of uncertainties in regional climate change simulations. Journal of Geophysical Research D: Atmospheres, 106 (D16), 17735-17751. http://dx.doi.org/10.1029/2001JD900193

Paolino, D. A., Yang, Q., Doty, B., Kinter, J. L., Shukla, J. and Straus, D. M., 1995. A Pilot Reanalysis Project at COLA. Bull. Amer. Meteor. Soc., 76 (5), 697–710. http://dx.doi.org/10.1175/1520-0477(1995)076<0697:APRPAC>2.0.CO;2

Paterson, W. S. B. (1994), The Physics of Glaciers, 3rd ed., 481 pp., Elsevier, New York.

Pellicciotti, F., Buergi, C., Immerzeel, W.W., Konz, M., Shrestha, A.B., 2012. Challenges and uncertainties in hydrological modeling of remote Hindu Kush-Karokoram-Himalayan (HKH) basins: Suggestions for calibration strategies. Mountain Research and Development 32(1):39–50. (http://dx.doi.org/10.1659/MRD-JOURNAL-D-11-00092.1)

Peters, G.P., Andrew, R.M., Boden, T., Canadell, J.G., Ciais, P., Le Quéré, C., Marland, G., Raupach, M.R., Wilson, C., 2013. The challenge to keep global warming below 2C. Nature Climate Change, 3 (1), 4-6. http://dx.doi.org/10.1038/nclimate1783

Piani, C., Haerter, J.O. and Coppola, E., 2010. Statistical bias correction for daily precipitation in regional climate models over Europe. Theoretical and Applied Climatology, 99 (1-2), 187-192. http://dx.doi.org/10.1007/s00704-009-0134-9

Pinheiro, A.C.T., Mahoney, R., Privette, J.L. and Tucker, C.J., 2006. Development of a daily long term record of NOAA-14 AVHRR land surface temperature over Africa. Remote Sensing of Environment 103 (2), 153–164. http://dx.doi.org/10.1016/j.rse.2006.03.009

Platnick, S., King, M.D., Ackerman, S.A., Menzel, W.P., Baum, B.A., Riedi, J.C. and Frey, R.A., 2003. The MODIS cloud products: algorithms and examples from Terra. IEEE Transactions on Geoscience and Remote Sensing, 41 (2), 459-473. http://dx.doi.org/10.1109/TGRS.2002.808301

Pope, V.D., Gallani, M.L., Rowntree, P.R. and Stratton, R.A., 2000. The impact of new physical parameterizations in the Hadley Centre climate model: HadAM3. Clim Dyn 16(2–3), 123–146. http://dx.doi.org/10.1007/s003820050009

Quincey, D. J., Copland, L., Mayer, C., Bishop, M., Luckman, A., and Beló, M., 2009. Ice velocity and climate variations for Baltoro Glacier, Pakistan, J. Glaciol., 55(194), 1061–1071. (http://dx.doi.org/10.3189/002214309790794913)

Rangwala, I. and Miller, J.R., 2012. Climate change in mountains: a review of elevation-dependent warming and its possible causes. Climatic Change 114 (3-4), 527-547. (http://dx.doi.org/10.1007/s10584-012-0419-3)

Rasmussen, R., Liu, C., Ikeda, K., Gochis, D., Yates, D., Chen, F., Tewari, M., Barlage, M., Dudhia, J., Yu, W. and Miller, K., 2011. High-Resolution Coupled Climate Runoff Simulations of Seasonal Snowfall over Colorado: A Process Study of Current and Warmer Climate. J. Climate, 24 (12), 3015–3048. http://dx.doi.org/10.1175/2010JCLI3985.1

Rees, H.G., and Collins, D.N., 2005. Regional differences in response of flow in glacierfed Himalayan rivers to climatic warming. Hydrological Processes 20 (10), 2157–2169. http://dx.doi.org/10.1002/hyp.6209

Reuter, H.I, Nelson, A. and Jarvis, A., 2007. An evaluation of void filling interpolation methods for SRTM data. International Journal of Geographic Information Science, 21 (9), 983-1008. http://dx.doi.org/10.1080/13658810601169899

Sade, R., Rimmer, A., Iggy Litaor, M., Shamir, E. and Furman, A., 2011. The sensitivity of snow-surface temperature equation to sloped terrain. Journal of Hydrology, 408 (3-4), 308-313. http://dx.doi.org/10.1016/j.jhydrol.2011.08.001

Saloranta, T. M., 2012. Simulating snow maps for Norway: description and statistical evaluation of the seNorge snow model, The Cryosphere, 6 (6), 1337-1366. http://dx.doi.org/10.5194/tc-6-1323-2012

Sarikaya, M.A., Bishop, M.P., Shroder, J.F. and Olsenholler, J.A., 2012. Space-based observations of Eastern Hindu Kush glaciers between 1976 and 2007, Afghanistan and Pakistan. Remote Sensing Letters, 3 (1), 77-84. http://dx.doi.org/10.1080/01431161.2010.536181

Schaper, J., Martinec, J. and Seidel, K., 1999. Distributed mapping of snow and glaciers for improved runoff modelling. Hydrological Processes, 13 (12-13), 2023-2031. (http://dx.doi.org/10.1002/(SICI)1099-1085(199909)13:12/13<2023::AID-HYP877>3.0.CO;2-A)

Scherler, D., Bookhagen, B. and Strecker, M.R., 2011. Spatially variable response of Himalayan glaciers to climate change affected by debris cover. Nature Geoscience, 4 (3), 156-159. http://dx.doi.org/10.1038/NGEO1068

Schmidt, S., Nüsser, M., 2012. Changes of high altitude glaciers from 1969 to 2010 in the Trans-Himalayan Kang Yatze Massif, Ladakh, Northwest India. Arctic, Antarctic, and Alpine Research, 44 (1), 107-121. http://dx.doi.org/10.1657/1938-4246-44.1.107

Shahid, S., Harun, S.B. and Katimon, A., 2012. Changes in diurnal temperature range in Bangladesh during the time period 1961-2008. Atmospheric Research, 118, 260-270. http://dx.doi.org/10.1016/j.atmosres.2012.07.008

Sharif, M., Archer, D. R., Fowler, H. J. and Forsythe, N., 2012 (in review for HESS). Trends in timing and magnitude of flow in the Upper Indus Basin. Hydrol. Earth Syst. Sci. Discuss., 9, 9931-9966. http://dx.doi.org/10.5194/hessd-9-9931-2012

Shroder, J.F., Bishop, M.P., Copland, L. and Sloan, V.F., 2000. Debris covered glaciers and rock glaciers in the Nanga Parbat Himalaya, Pakistan. Geogr. Ann., 82A(1), 17–31. http://dx.doi.org/10.1111/j.0435-3676.2000.00108.x

Shrestha, A.B., Wake, C.P, Mayewski, P.A. and Dibb, J.E., 1999. Maximum temperature trends in the Himalaya and its vicinity: an analysis based on temperature records from Nepal for the period 1971–94. J Clim, 12 (9), 2775–2786. http://dx.doi.org/10.1175/1520-0442(1999)012<2775:MTTITH>2.0.CO;2

Shupe, M.D. and Intrieri, J.M., 2004. Cloud radiative forcing of the Arctic surface: The influence of cloud properties, surface albedo, and solar zenith angle. Journal of Climate, 17 (3), 616-628. http://dx.doi.org/10.1175/1520-0442(2004)017<0616:CRFOTA>2.0.CO;2

Singh, P., Kumar, N. and Arora, M., 2000. Degree-day factors for snow and ice for Dokriani Glacier, Garhwal Himalayas. Journal of Hydrology, 235 (1-2), 1–11. http://dx.doi.org/10.1016/S0022-1694(00)00249-3

Singh, P. and V.P. Singh. 2001. Snow and Glacier Hydrology. 742pp. Kluwer Academic Publishers. Dordrecht (Netherlands).

Sorman, A. U., Akyurek, Z., Sensoy, A., Sorman, A. A., and Tekeli, A. E., 2007. Commentary on comparison of MODIS snow cover and albedo products with ground observations over the mountainous terrain of Turkey. Hydrol. Earth Syst. Sci., 11, 1353–1360. http://dx.doi.org/10.5194/hess-11-1353-2007

Spencer, H. and Slingo, J.M., 2003. The simulation of peak and delayed ENSO teleconnections. Journal of Climate, 16 (11), 1757–1774. http://dx.doi.org/10.1175/1520-0442(2003)016<1757:TSOPAD>2.0.CO;2

Stewart, R. B. and Rouse, W. R.,1976. A simple method for determining the evaporation from shallow lakes and ponds. Water Resour. Res., 12 (4), 623–628, (http://dx.doi.org/10.1029/WR012i004p00623)

Sugahara, S., Porfirio da Rocha, R., Yuri Ynoue, R. and Bomfim da Silveira, R., 2013. Spurious shifts in the pattern of diurnal variation of sea level pressure of reanalysis datasets. Clim Dyn, 40 (1-2), 175-186. http://dx.doi.org/10.1007/s00382-012-1338-8

Sun, S., Jin, J. and Xue, Y., 1999. A simple snow-atmosphere-soil transfer model. Journal of Geophysical Research, 104 (D16), 19587 - 19597. http://dx.doi.org/10.1029/1999JD900305

Syed, F.S., Giorgi, F., Pal, J.S. and King, M.P., 2006. Effect of remote forcings on the winter precipitation of central southwest Asia part 1: observations, Theor. Applied Climatology 86: 147–160. http://dx.doi.org/10.1007/s00704-005-0217-1

Syed, F.S., Giorgi, F., Pal, J.S. and Keay, K., 2010. Regional climate model simulation of winter climate over Central-Southwest Asia, with emphasis on NAO and ENSO effects. Int J Climatol, 30 (2), 220-235. http://dx.doi.org/10.1002/joc.1887

Szczypta, C., Calvet, J.-C., Albergel, C., Balsamo, G., Boussetta, S., Carrer, D., Lafont, S. and Meurey, C., 2011. Verification of the new ECMWF ERA-Interim reanalysis over France. Hydrology and Earth System Sciences, 15 (2), 647-666. http://dx.doi.org/10.5194/hess-15-647-2011

Tahir, A. A., Chevallier, P., Arnaud, Y. and Ahmad, B., 2011a. Snow cover dynamics and hydrological regime of the Hunza River Basin, Karakoram Range, Nothern Pakistan. Hydrol. Earth Syst. Sci. 15 (7), 2275-2290. http://dx.doi.org/10.5194/hess-15-2275-2011

Tahir, A.A., Chevallier, P., Arnaud, Y., Neppel, L. and Ahmad, B., 2011b. Modeling snowmelt-runoff under climate scenarios in the Hunza River basin, Karakoram Range, Northern Pakistan. Journal of Hydrology, 409 (1-2), pp. 104-117. http://dx.doi.org/10.1016/j.jhydrol.2011.08.035

Thornton, P. E. and Running, 1999. An improved algorithm for estimating incident daily solar radiation from measurements of temperature, humidity, and precipitation, Agric. For. Meteorol., 93 (4), 211 –228. http://dx.doi.org/10.1016/S0168-1923(98)00126-9

Thornthwaite, C.W., 1948. An Approach toward a Rational Classification of Climate. Geographical Review, 38 (1), 55-94. http://www.jstor.org/stable/210739

Todini, E. 1996. The ARNO rainfall-runoff model. Journal of Hydrology 175 (1-4) 339-382. http://dx.doi.org/10.1016/S0022-1694(96)80016-3

Trenberth, K.E., 1995. Atmospheric circulation climate changes. Climatic Change, 31 (2-4), 427-453. http://dx.doi.org/10.1007/BF01095156

Trenberth, K.E., and Solomon, A. 1994. The global heat balance:Heat transports in the atmosphere and ocean. Clim. Dyn. 10: 107–134. http://dx.doi.org/10.1007/BF00210625

Trenberth, K.E., Dai, A., Rasmussen, R.M, and Parsons, D.B. 2003. The Changing Character of Precipitation. Bull. Amer. Meteor. Soc., 84, 1205–1217. http://dx.doi.org/10.1175/BAMS-84-9-1205

Uppala, S.M., Kallberg, P.W., Simmons, A.J., Andrae, U., Da Costa Bechtold, V., Fiorino, M., Gibson, J.K., Haseler, J., Hernandez, A., Kelly, G. A., Li, X., Onogi, K., Saarinen, S., Sokka, N., Allan, R.P., Andersson, E., Arpe, K., Balmaseda, M.A., Beljaars, A.C.M., Vande Berg, L., Bidlot, J., Bormann, N., Caires, S., Chevallier, F., Dethof, A., Dragosavac, M., Fisher, M., Fuentes, M., Hagemann, S., Holm, E., Hoskins, B.J., Isaksen, L., Janssen, P.A.E.M., Jenne, R., McNally, A.P., Mahfouf, J.-F., Morcrette, J.-J., Rayner, N.A., Saunders, R.W., Simon, P., Sterl, A.. Trenberth, K.E., Untch, A., Vasiljevic, D., Viterbo P. and Woollen, J., 2005. The ERA-40 re-analysis. Quarterly Journal of the Royal Meteorological Society 131 (612) 2961-3012. http://dx.doi.org/10.1256/qj.04.176

van Vliet, M.T.H., Blenkinsop, S., Burton, A., Harpham, C., Broers, H.P. and Fowler, H.J., 2012. A multi-model ensemble of downscaled spatial climate change scenarios for the Dommel catchment, Western Europe. Climatic Change, 111 (2), 249-277. http://dx.doi.org/10.1007/s10584-011-0131-8

Viviroli, D., Archer, D. R., Buytaert, W., Fowler, H. J., Greenwood, G. B., Hamlet, A. F., Huang, Y., Koboltschnig, G., Litaor, M. I., López-Moreno, J. I., Lorentz, S., Schädler, B., Schreier, H., Schwaiger, K., Vuille, M. and Woods, R., 2011. Climate change and mountain water resources: Overview and recommendations for research, management and policy. Hydrol. Earth Syst. Sci., 15 (2), 471–504. http://dx.doi.org/10.5194/hess-15-471-2011

Viviroli D, Messerli B, Schädler B, Weingartner R, 2009. Water towers in a changing world. Mountain waters, a key resource for development. Kohler T, Maselli D, eds. Mountains and Climate Change – From Understanding to Action. Contribution to the 15th World Climate Conference in Copenhagen, DK (COP15). Swiss Agency for Development and Cooperation (SDC), Bern, CH, ISBN 978-3-905835-16-8, p. 12–16.

Wahr, J., S. Swenson, V. Zlotnicki, and I. Velicogna (2004), Timevariable gravity from GRACE: First results, Geophys. Res. Lett., 31 (11), L11501. http://dx.doi.org/10.1029/2004GL019779

Wan, Z., 2008. New refinements and validation of the MODIS Land-Surface Temperature/Emissivity products. Remote Sensing of Environment 112 (1), 59–74. http://dx.doi.org/10.1016/j.rse.2006.06.026

Wang, Z., Schaaf, C.B., Chopping, M.J., Strahler, A.H., Wang, J., Román, M.O., Rocha, A.V., Woodcock, C.E. and Shuai, Y. 2012. Evaluation of Moderate-resolution Imaging Spectroradiometer (MODIS) snow albedo product (MCD43A) over tundra. Remote Sensing of Environment, 117 (15), 264-280. http://dx.doi.org/10.1016/j.rse.2011.10.002

Ward, E., Buytaert, W., Peaver, L. and Wheater, H., 2011. Evaluation of precipitation products over complex mountainous terrain: A water resources perspective. Advances in Water Resources, 34 (10), 1222-1231. http://dx.doi.org/10.1016/j.advwatres.2011.05.007

Webster, P.J., Toma, V.E. and Kim, H.M., 2011. Were the 2010 Pakistan floods predictable?. Geophys. Res. Lett., 38 (4), L04806. http://dx.doi.org/10.1029/2010GL046346

Weisz, E., Li, J., Menzel, W. P., Heidinger, A. K., Kahn, B. H. and Liu, C.-Y., 2007. Comparison of AIRS, MODIS, CloudSat and CALIPSO cloud top height retrievals, Geophys. Res. Lett., 34 (17), L17811, http://dx.doi.org/10.1029/2007GL030676

Wilby, R.L. and Dessai, S., 2010. Robust adaptation to climate change. Weather 65 (7), 180–185. http://dx.doi.org/10.1002/wea.543

Wilby, R.L., Troni, J., Biot, Y., Tedd, L., Hewitson, B.C., Smith, D.G. and Sutton, R.T., 2009. A review of climate risk information for adaptation and development planning. Int. J. Climatol. 29 (9), 1193–1215. http://dx.doi.org/10.1002/joc.1839

Winiger, M., Gumpert, M., and Yamout, H., 2005. Karakoram–Hindu Kush–western Himalaya: Assessing high-altitude water resources. Hydrol. Processes, 19 (12), 2329–2338. http://dx.doi.org/10.1002/hyp.5887

Wolter, K. and Timlin, M. S,. 2011. El Niño/Southern Oscillation behaviour since 1871 as diagnosed in an extended multivariate ENSO index (MEI.ext). Int. J. Climatol., 31 (7), 1074–1087. http://dx.doi.org/10.1002/joc.2336

Yadav, R. K., Rupa Kumar, K. and Rajeevan, M., 2009. Increasing influence of ENSO and decreasing influence of AO/NAO in the recent decades over northwest India winter precipitation, J. Geophys. Res., 114 (D12), D12112, http://dx.doi.org/10.1029/2008JD011318

Yatagai, A., Arakawa, O, Kamiguchi, K., Kawamoto, H., Nodzu, M.I. and Hamada, A., 2009. A 44-year daily gridded precipitation dataset for Asia based on a dense network of rain gauges. SOLA 5, 137–140. http://dx.doi.org/10.2151/sola.2009-035

Young, G.J., and Hewitt, K., 1993. Glaciohydrological features of the KarakoramHimalaya: Measurement possibilities and constraints. In: Young GJ, editor. Snow and Glacier Hydrology. International Symposium, Kathmandu, Nepal, 16–21 November 1992. Proceedings. IAHS Publication 218. Geneva, Switzerland: IAHS [International Association of Scientific Hydrology], pp 273–283.

Zalasiewicz, J., Williams, M., Steffen, W. and Crutzen, P., 2010. The New World of the Anthropocene. Environmental Science & Technology, 44 (7), 2228-2231. http://dx.doi.org/10.1021/es903118j

Ziegler, A.D., Sheffield, J., Wood, E.F., Nijssen, B., Maurer, E.P. and Lettenmaier, D.P., 2002. Detection of intensification of the global water cycle: The potential role of FRIEND. IAHS-AISH Publication, (274), pp. 51-60. http://iahs.info/redbooks/a274/iahs_274_051.pdf